Numéro d'ordre : 2002-13

ANNÉE 2002

THÈSE

présentée devant
le POLITECNICO DI TORINO et l'ÉCOLE CENTRALE DE LYON
pour obtenir le double titre *Italo-Français* et le titre *Européen* de
DOCTEUR
spécialité MÉCANIQUE DES FLUIDES et ACOUSTIQUE

par

Damiano CASALINO

ANALYTICAL AND NUMERICAL METHODS IN VORTEX-BODY AEROACOUSTICS

Soutenue le 8 avril 2002 devant la Commission d'Examen

JURY

Président :	Prof.	A. COGHE
Examinateurs :	Prof.	M. ROGER
	Dr.	M. JACOB
	Prof.	G. P. ROMANO
	Prof.	E. CARRERA
Rapporteurs :	Prof.	M. HIRSCHBERG
	Prof.	W. SCHRÖDER

Dipartimento di Ingegneria Aeronautica e Spaziale
Politecnico di Torino

et

Laboratoire de Mécanique des Fluides et d'Acoustique, UMR CNRS 5509
École Centrale de Lyon

Numéro d'ordre : 2002-13 ANNÉE 2002

THÈSE

présentée devant
le POLITECNICO DI TORINO et l'ÉCOLE CENTRALE DE LYON
pour obtenir le double titre *Italo-Français* et le titre *Européen* de
DOCTEUR
spécialité MÉCANIQUE DES FLUIDES et ACOUSTIQUE

par

Damiano CASALINO

ANALYTICAL AND NUMERICAL METHODS IN VORTEX-BODY AEROACOUSTICS

Soutenue le 8 april 2002 devant la Commission d'Examen

JURY

Président :	Prof.	A. COGHE
Examinateurs :	Prof.	M. ROGER
	Dr.	M. JACOB
	Prof.	G. P. ROMANO
	Prof.	E. CARRERA
Rapporteurs :	Prof.	M. HIRSCHBERG
	Prof.	W. SCHRÖDER

Dipartimento di Ingegneria Aeronautica e Spaziale
Politecnico di Torino

et

Laboratoire de Mécanique des Fluides et d'Acoustique, UMR CNRS 5509
École Centrale de Lyon

Preface

This work deals with that branch of Aeroacoustics concerning the noise generated by the interaction between vortical flows and rigid surfaces. It is the outcome of a PhD research shared among the *Dipartimento di Ingegneria Aeronautica e Spaziale* at Politecnico di Torino and the *Laboratoire de Mécanique des Fluides et d'Acoustique* at Ecole Centrale de Lyon.

Results concerning a nominal two-dimensional flow, the rod-airfoil configuration, are brought together with a description of the noise generation mechanisms in fluid-body interactions.

The rod-airfoil configuration is the object of part I, where I summarized my analytical contributions to the vortex-airfoil interaction problem and to the development of numerical methodologies of aeroacoustic prediction.

The description of the sound generation mechanisms in fluid-body interactions is the object of part II. This constitutes the theoretical basis on which I founded my PhD education.

Therefore, part I constitutes my PhD Thesis and part II should be assumed as formally separated by part I. However, because of the great engagement required by writing part II, my opinion and feeling are to include it in the present work and to consider part I and part II as substantially joined. Of course, part I is in its definitive form, because it represents the outcome of a time constrained research. On the contrary, thanks to its formal autonomy, part II will be reviewed in the next future.

Damiano Casalino

Contents

I

Interaction Noise from an Airfoil in the Wake of a Cylinder

Preface to part I

The first part of the present work is concerned with the aeroacoustic characterization of a low Mach number rod-airfoil configuration, in which vortices shed from the rod are intercepted by the airfoil, generating aerodynamic sound. Such a configuration was conceived at the Laboratoire de Mécanique des Fluides et d'Acoustique (LMFA) of the Ecole Centrale de Lyon (ECL) as an effective benchmark for both analytical and numerical predictions of the aerodynamic noise from lifting surfaces in vortical flows.

A preliminary analytical study of the aerodynamic and acoustic field in a rod-airfoil configuration founds the basis for successive experimental and numerical investigations. Furthermore, two chapters can be inserted in the larger context of the numerical methodologies of aeroacoustic prediction. These are chapter 6 and chapter 7, the former dealing with a new interpretation of the acoustic analogy approach, the latter concerning with the aeroacoustic treatment of a *nominal* two-dimensional flow.

Acknowledgments must be made to Prof. Michel Roger of ECL for the fatherhood of the rod-airfoil experiment, and to Prof. Gianfranco Chiocchia of PT for having inspired to the author the analytical approach for the vortex-airfoil interaction aerodynamics. The author is particularly indebted to Prof. Chiocchia for his useful teachings in the field of unsteady aerodynamics.

1

Introduction

The interaction between an unsteady flow and a solid structure immersed in the flow generates aerodynamic sound, even when the structure is sufficiently rigid to not vibrate under the action of the fluid.

A flow perturbed by vortical disturbances is a particular case of unsteady flow. The vortical disturbances can be produced by fluid motion relative to solid boundaries or by the instability of a free shear-layer separated from a steady surface.

Velocity fluctuations in proximity of a solid boundary induce hydrodynamic pressure fluctuations. This coupling mechanism between vortical and pressure fluctuations is commonly referred to as *surface blockage effect*. The pressure field in the vicinity of the body feeds a far acoustic field. Thus, aerodynamic sound is generated as a by-product of the surface blockage effect. If the characteristic size of the body is not far higher than the acoustic wavelength, then the surface blockage effect provides a sound generation mechanism of *dipole* type.

A portion of the kinetic energy of a vortical flow can be directly converted into acoustic energy. This sound generation mechanism is of *quadrupole* type and is related to the unsteady Reynolds stresses in a turbulent flow. At low Mach numbers, the blockage effect provides a more effective conversion mechanism of vortical kinetic energy into acoustic energy. Therefore, the dipole radiation dominates on the quadrupole one.

In several engineering configurations devices are arranged so that downstream bodies are embedded in the wakes from upstream bodies. Typical examples are those of a bank of heat exchanger tubes in which vortices from upstream cylinders impinge on downstream cylinders, a turbomachinery stage where the wakes from inlet vanes are chopped by the rotor blades, and a helicopter rotor whose blades can interact with the tip-vortices shed from the preceeding blades. In the present study vortices are shed from a rod and are convected towards a downstream airfoil. Both the rod and the airfoil generate aerodynamic sound. However, the more effective aeroacoustic sources are located near the airfoil leading edge where the vortical flow induces pressure fluctuations of higher amplitude.

A vortex-airfoil interaction is predominantly affected by three factors: the distance of the oncoming vortex, the size of the vortex core and the orientation of the vorticity field with respect to the airfoil leading edge.

When a vortex impinges directly onto an airfoil leading edge it is distorted and split, provided that the leading edge is sufficiently sharp with respect to the vortex viscous core. When the vortex size is quite smaller than the curvature radius of the leading edge, the interaction dynamics is strongly affected by the geometrical configuration (airfoil angle of attack, offset between the vortex core and the leading edge, etc.). Both the distortion of the vorticity field and the sensitivity of the vortex trajectory are due to the nonlinear character of the flow.

In the present work we investigate the influence of the vortex distortion and the vortex trajectory on the vortex-airfoil interaction noise. Experimental measurements of wall pressure correlations are performed on the airfoil surface in order to detect the influence of the airfoil angle of attack on the trajectory of the incident vortices. Analytical models of the vortex-airfoil interaction problem are developed which allow to relate the acoustic radiation to the vortex kinematic in proximity of the airfoil. Numerical solutions of the Navier-Stokes equations are performed in order to describe quantitatively the vortical flow in the wake of the rod and past the airfoil.

The orientation of the incident vorticity with respect to the airfoil leading edge has a deep influence on the physics of the vortex-airfoil interaction process. In terms of unsteady loading and sound generation, the most severe conditions occur when the airfoil leading edge is parallel to the vorticity vector. Based on this assumption, a two-dimensional analysis is hereafter performed.

The flow past a circular rod remains two-dimensional up to Reynolds numbers of about 180. At higher values, three-dimensional fluctuations are superimposed on the dominant vortex shedding. Consequently, the pressure on the rod surface and the velocity in the near wake exhibit a random amplitude modulation. Furthermore, due to the rapid distortion of the vorticity field near the airfoil leading edge, a strong vortex-airfoil interaction is an intimately three-dimensional phenomenon.

Because of the intrinsic three-dimensional character of both the vortex dynamics in the wake of a rod and a direct vortex-airfoil interaction, the flow in the rod-airfoil configuration is two-dimensional only *nominally*. A spanwise statistical model is thus proposed as an alternative to a three-dimensional aerodynamic computation. The model allows to perform aeroacoustic predictions on the base of a two-dimensional aerodynamic field, but accounting for the three-dimensional character of the flow.

Aeroacoustic predictions of external flows are usually based on the *acoustic analogy* by Lighthill [1]. In the present work we use the Ffowcs Williams & Hawkings' [2] acoustic analogy formulation which extends Lighthill's model to flows confined by surfaces in arbitrary motion. The traditional approach based on a *retarded time* integral formulation is re-interpreted as an *advanced time* approach. This new numerical methodology allows to perform an aeroacoustic prediction parallelly to an aerodynamic simulation. Moreover, it does not require the iterative solution of a retarded time equation.

1.1 A Brief Description of the Vortex Dynamics in a Rod-Airfoil Configuration

The main terminology used throughout part I is herein presented with reference to the rod-airfoil configuration sketched in Fig.1.1, and to the following qualitative description of the vortex dynamics in the rod-airfoil configuration.

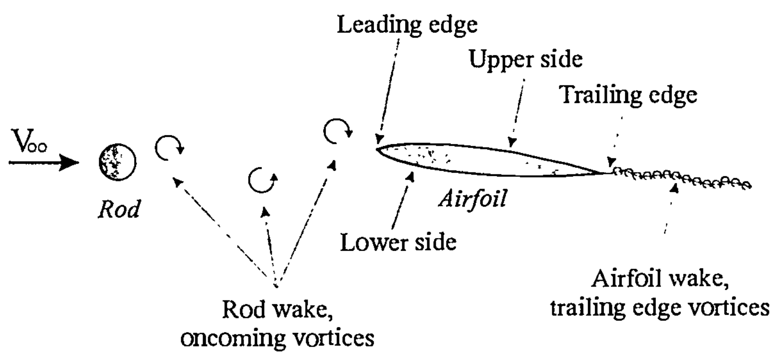

FIGURE 1.1: Rod-airfoil configuration.

The wake behind a rod is unstable at values of the Reynolds number higher than about 49. This instability is responsible for an *alternate* and *periodic* formation of counter-rotating vortices: clockwise and counterclockwise vortices shed from the upper and lower side of the cylinder, respectively. Thus, a double row of staggered vortices is convected in the wake of the cylinder. This flow configuration was analytically described by von Kármán in 1912 and is thus referred to as *Kármán vortex street.*

In 1878 Strouhal [3] had already observed that a rod of diameter d, moving at a velocity U, generates sound of frequency $f_0 = \mathrm{St}\, U/d$, where St is a constant. Later on, Rayleigh [4] related this tonal sound emission to the periodic vortex shedding from the rod. As confirmed by innumerable experiments, the Strouhal number St is equal to 0.19-0.20 in a wide range of Reynolds numbers.

In a rod-airfoil configuration the vortex street intercepts the airfoil. The resulting interaction generates aerodynamic forces on the airfoil and aerodynamic noise in the far field. This interaction can be accompanied by a variety of mechanisms: vortex distortion near the airfoil leading edge, vortex splitting in two fragments convected along the two airfoil sides, boundary-layer separation and consequent formation of secondary vortices at the leading edge, spanwise velocity fluctuations, etc. At the airfoil trailing edge, the fluid viscosity is responsible for a vortex shedding process: a vortical wake is shed by the trailing edge and is convected downstream of the airfoil. The intensity of the wake depends on the instantaneous conditions of the flow past the airfoil. Therefore, the trailing edge vortex shedding is an unsteady process. In the present work this is modeled as a continuous vortex-sheet as well as a sequence of discrete vortices.

The pressure fluctuations induced by the oncoming vortical disturbances on the airfoil surface act as acoustic sources. Clearly, the frequency of the radiated noise depends on the frequency of the aerodynamic process. If the airfoil chord is much smaller than the acoustic wavelength, the far pressure field is not affected by the way the sources are distributed upon the airfoil surface. In this case the airfoil is *acoustically compact* and the acoustic field depends only on the total aerodynamic force exerted on the airfoil. As a result, the directivity of the acoustic intensity is essentially that of a dipole with a radiation axis normal to the free-stream direction. On the contrary, if the airfoil is not acoustically compact, the directivity of the far pressure field depends on the source distribution upon the airfoil surface. In this case, noise is mainly generated in proximity of the airfoil leading edge and is diffracted by the remaining part of the airfoil.

1.2 Theoretical and Practical Relevance of the Rod-Airfoil Configuration

Due to its physical completeness, the rod-airfoil configuration allows a basic investigation of different sound generation mechanisms covering several aspects of practical interest. Therefore, the rod-airfoil configuration is herein considered as an academic benchmark for numerical methods of aeroacoustic prediction.

The rod-airfoil configuration combines true broad band noise with a narrow band noise generation. The latter is due to the airfoil interaction with the *Kármán vortex street.* Since this flow configuration is only partially coherent in time and in the spanwise direction, the radiated sound is not purely tonal. The true broad band part of the acoustic spectrum is generated by the airfoil interaction with small scale turbulent structures. These are convected in the wake of the rod as well as generated by the impact of large scale vortices onto the airfoil leading edge. Therefore, the rod-airfoil acoustic spectrum is characterized by:

- a prominent peak corresponding to the Strouhal frequency;
- a slight broadening about the Strouhal frequency, which is due to:
  a) three-dimensional vortex dynamics in the wake of the rod and near the airfoil leading edge;
  b) nonlinear effects during the impingement of large scale vortices onto the airfoil leading edge;
- A true broad band behaviour due to the airfoil interaction with small scale turbulent structures.

Many analytical formulations in linear aerodynamics describe the airfoil response to a turbulent oncoming flow as a superposition of effects, each related to a sinusoidal velocity perturbation which is referred to as a *gust*. In a similar way, many aeroacoustic models describe the acoustic spectrum radiated by an airfoil in a turbulent stream as resulting from the superposition of effects, each related to one spectral component of the incoming vortical flow. In a rod-airfoil configuration the vortex street in the wake of the rod acts as a periodic upwash gust convected past the airfoil. Therefore, placing a rod ahead of an airfoil is an effective way to investigate the airfoil response to a gust of wavenumber depending on the rod diameter, and to explore the limits of validity of some analytical models of aeroacoustic prediction.

From a numerical point of view, the rod-airfoil configuration is a good benchmark for a Computational Fluid Dynamics (CFD) code. For the sake of a rod-airfoil aeroacoustic prediction, a CFD code is required to simulate both the large scale coherent structures, which exhibit a quasi-periodic behaviour, and the small scale turbulent structures, which exhibit a random behaviour. In the present study two-dimensional unsteady Reynolds Averaged Navier-Stokes (RANS) computations are performed. These are expected to reproduce:

- the large scale coherent structures in the wake behind the rod;
- nonlinear effects during a direct vortex-airfoil interaction, although constrained in a two-dimensional domain.

The large scale vortices generate the radiation peaks at the Strouhal frequency and higher harmonics. The nonlinear effects may be *partially* responsible for the acoustic spectral broadening about the Strouhal peak.

1.3 Part I Overview

Part I is concerned with a low Mach number rod-airfoil configuration. The following subjects are treated:

1. an analytical description of the unsteady aerodynamic field of a Kármán vortex street convected past a Kármán-Trefftz airfoil;
2. an analytical description of the acoustic field generated by a vortex-airfoil interaction;
3. a parametric study of the vortex-airfoil interaction problem by using the approaches in items 1 and 2;
4. an experimental study of the rod-airfoil configuration;
5. the development of numerical methodologies and computational libraries[1] for aeroacoustic predictions based on the Ffowcs Williams & Hawkings' acoustic analogy formulation (FW-H);
6. an analytical modeling of the spanwise statistical behaviour of a nominal two-dimensional flow;
7. a RANS prediction[2] of the unsteady flow in the rod-airfoil configuration for two airfoil angles of attack, and an acoustic prediction based on the computed aerodynamic field.

[1] A rotor noise prediction code has been developed by the author in the present context. This is referred to as *Advantia* throughout this work.

[2] The author's direct contribution to the RANS simulation is restricted to the mesh generation, to the computation management and to the post-processing of the presented results. The existing CFD code *Proust* is used, which has been developed in a turbomachinery context at LMFA.

The above seven items are the object of the next seven chapters. An overview of part I is reported below.

In chapter 2 an analytical model of the aerodynamic vortex-airfoil interaction problem is presented. The *circulation theory* is employed in order to describe, by means of a conformal mapping technique, the kinematics of a given distribution of line-vortices convected past a thick cambered airfoil. A Kutta condition is imposed at the airfoil trailing edge and results in a continuous vortex shedding in the airfoil wake. In a first approach, the wake is described as a vortex-sheet convected along a rectilinear path at the free-stream velocity. In a second approach, the wake is described as a distribution of line-vortices freely convected at the local flow velocity.

In chapter 3 a characterization of the aeroacoustic source distribution on the airfoil surface is performed by splitting the time derivative of the pressure field in four bilateral contributions. These account for the oncoming vortex contribution, the airfoil wake contribution, the vortex-airfoil interaction contribution and the wake self-interaction contribution. Furthermore, a matched asymptotic expansion of the hydrodynamic pressure field past the airfoil and the far acoustic field is performed in order to describe how the vortex kinematics past the airfoil affects the acoustic far field.

In chapter 4 the aerodynamic formulation developed in chapter 2 is exploited in order to predict the unsteady aerodynamic field of a given distribution of line-vortices convected past an airfoil. The pressure field on the airfoil surface is then used to calculate the radiated acoustic field by means of a FW-H acoustic analogy formulation, as described in chapter 3.

In chapter 5 the rod-airfoil experiment is presented and the experimental results are discussed. Emphasis is given to the effects of the airfoil angle of attack on both the acoustic far field and the wall pressure field. The former is measured at about one acoustic wavelength from the airfoil mid-point and exhibits the spectral behaviour described in section 1.2. The latter is described by means of two-point statistical measurements on both the rod and the airfoil surface. The rod results provide a description of the spanwise statistical behaviour of the vortex shedding process and give evidence of a three-dimensional vortex dynamics in the wake of the rod. The airfoil results shed light on some effects of the airfoil angle of attack on the trajectories of the oncoming vortices.

In chapter 6 results concerning the numerical validation of the rotor noise code *Advantia* are presented. *Advantia* was developed in the present context in order to perform aeroacoustic predictions on the base of a FW-H acoustic analogy formulation. Several test cases are discussed, which show the applicability of *Advantia* to:

- arbitrarily moving surfaces;

- penetrable integration surfaces;

- a listener moving at a constant velocity along an arbitrary path.

The classical *retarded time* formulation is herein re-interpreted as an *advanced time* formulation. This offers the advantage of an acoustic prediction parallel to an aerodynamic prediction. Thus, the concept of a post-process acoustic prediction is partially surpassed. Moreover, since the advanced time is an algebraic function of the emission time, the advanced time approach does not require the iterative solution of a retarded time equation.

In chapter 7 a description of the three-dimensional vortex dynamics in the wake of a rod provides the conceptual basis for the development of a new aeroacoustic methodology for nominal two-dimensional flows. The method is based on a spanwise statistical model that allows to perform aeroacoustic predictions by using a two-dimensional flow, but accounting, to some extent, for the three-dimensional character of the real flow. The statistical approach is used to predict the noise generated by a circular cylinder flow.

In chapter 8 results are presented of a numerical aeroacoustic characterization of the rod-airfoil configuration. An unsteady RANS aerodynamic computation and a FW-H acoustic prediction are performed for two airfoil angles of attack. Both aerodynamic and acoustic results are checked against experimental data.

2

Vortex-Airfoil Interaction: Aerodynamic Modeling

As discussed in section 1.1, an airfoil embedded in the oscillating wake of a cylinder is a source of quasi-tonal noise. The acoustic radiation is maximum at the Strouhal frequency, being generated by the interaction between the airfoil and the large scale vortices shed from the rod.

In the present chapter a semi-analytical model is developed for the vortex-airfoil interaction problem. The flow is assumed to be two-dimensional, ideal, incompressible and irrotational. Therefore, the *circulation theory* [5] and the conformal mapping technique are employed in order to determine the unsteady pressure field induced by a line-vortex on the surface of a Kármán-Trefftz airfoil. A zero velocity Kutta condition is imposed at the airfoil trailing edge. As a consequence, a vortical wake is shed from the trailing edge into the field. Two approaches are used to describe the airfoil wake:

1. a *fixed-wake* model,

2. a *free-wake* model.

In the first approach, the airfoil wake is described as a vortex-sheet convected along a constant rectilinear path at the free-stream velocity. The wake intensity γ is thus determined by solving at each time-step an integral equation for γ, with the right-hand side depending on the instantaneous positions of the oncoming vortex. The kernel of the integral equation is a function of the geometrical parameters of the airfoil.

In the second approach, the airfoil wake is described as a distribution of discrete vortices convected at the local flow velocity. At each time-step a *wake vortex* is shed from the trailing edge and its circulation is such that it cancels the velocity induced at the trailing edge by the other vortices in the field.

The Kutta condition is a way to model the behaviour of a real viscous flow past a sharp trailing edge. Thus, it is not a physical condition. As a consequence, spurious forces and spurious acoustic sources may be generated at the trailing edge if the Kutta condition is not properly stated. In the present chapter emphasis is given to the vortex shedding process concerning the generation of spurious forces and spurious acoustic sources at the airfoil trailing edge.

The analytical model first developed for an isolated vortex convected past a Kármán-Trefftz airfoil is then applied to a given distribution of line-vortices. Two distributions are considered:

1. a double row of counter-rotating vortices,

2. a circular cloud of equal vortices.

The former distribution is used to model a Kármán vortex street. The latter is used to describe a vortex of finite size which can undergo a distortion in proximity of the airfoil leading edge. Furthermore, as shown in chapter 4, a Kármán vortex street can be also described as a double row of counter-rotating clouds of line-vortices.

2.1 Introduction

A vortical flow on the surface of a body is a common source of unsteady loading, sound and vibrations.

In several engineering configurations devices are arranged so that downstream bodies are embedded in the wakes from upstream bodies. Typical examples are those of a bank of heat exchanger tubes in which vortices from upstream cylinders impinge on downstream cylinders, a turbomachinery stage where the wakes from inlet vanes are chopped by the rotor blades, and a helicopter rotor whose blades may interact with the tip-vortices shed from the preceeding blades.

A vortex-airfoil interaction is predominantly affected by four factors:

- the orientation of the oncoming vortex with respect to the airfoil leading edge,
- the distance of the oncoming vortex,
- the characteristic wavelength of the vorticity field,
- the mean flow incidence.

The orientation of the oncoming vorticity vector with respect to the airfoil leading edge depends on the value of two angles. The first is that formed by the vorticity vector and its projection onto the airfoil plane. The second angle is that formed by the projection of the vorticity vector onto the airfoil plane and the airfoil leading edge. The latter angle is usually referred to as *skew* angle. Both the unsteady pressure field on the airfoil surface and the vortex dynamics past the airfoil depend on these two angles.

The effects of the vorticity orientation on the pressure field can be examined by considering a vortical disturbance with spatial periodicity, frozenly convected past a thin airfoil. Such a flow configuration is usually referred to as a *gust*. As shown by Graham [6] (see section 10.3.2 of part II), the space of solutions of a gust-airfoil interaction problem can be divided into two sub-spaces, depending on the value of a gust parameter. This parameter is related to the free-stream Mach number and to the skew angle. In terms of unsteady loading and sound generation, the most severe conditions occur when the airfoil leading edge is parallel to the vorticity vector. Therefore, two-dimensional analyses are commonly performed, although a strong vortex-airfoil interaction is an intimately three-dimensional phenomenon.

The effect of the vorticity orientation on the vortex dynamics is mainly related to the distortion of the vorticity field. This process takes different forms depending essentially on the orientation of the vorticity vector and the thickness of the airfoil. A normal vortex-airfoil interaction, for example, involves both a vortex bending and a vortex chopping. In the case of a thin airfoil, the vortex is chopped but not significantly bended. The vortex chopping is accompanied by a *compression* of the vortex core on one side of the airfoil and an *expansion* on the opposite side. Both the compressed and the expanded portions of the vortex propagate away from the surface as the vortex moves along the airfoil. The terms compression and expansion do not denote phenomena related to the compressibility of the fluid but to the strength of the vorticity field. A review of this interaction mechanism is given by Marshall & Grant [7].

A parallel vortex-airfoil interaction is accompanied by a deformation of the vorticity field in the plane normal to the airfoil span. The smaller is the distance between the oncoming vortex and the airfoil, the stronger is the vortex distortion. Hence, we will refer to as *direct interaction* a parallel interaction with the vortex impinging directly onto the airfoil leading edge[1]. Accordingly, a *nearly*

[1] A direct interaction is commonly referred to in literature as *head-on* interaction.

direct interaction occurs when the deviation of the vortex trajectory from the airfoil plane is a small fraction of the airfoil thickness.

The vorticity field is strongly distorted during a direct or nearly direct interaction. Furthermore, the pressure field induced on the airfoil surface depends on the vorticity distribution especially when the vortex is at a small distance from the airfoil. As a result, the vortex distortion must be taken into account when a prediction is made of the unsteady loading and noise generated by a vortex-leading edge interaction.

The characteristic wavelength of the vorticity field is the *size* of an isolated vortex, as well as the wavelength of a gust. In the case of a Kármán vortex street from an upstream rod, for example, the wavelength of the vorticity field is the distance between two vortices on the same row. The influence of the gust wavelength on the unsteady flow past an airfoil is combined with the influence of the skew angle. In fact, as shown by Graham [6], the gust parameter affecting the interaction dynamics depends on both the skew angle and the gust wavelength. The influence of the size of an isolated vortex can be related to the distortion of the vorticity field. The vortex distortion, in fact, is a nonlinear rearrangement mechanism occurring when the curvature radius of the leading edge and the impinging vortex have a comparable scale. On the contrary, when the vortex is of small size compared to the curvature radius of the leading edge, say *compact*, the flow nonlinearity is responsible for a strong dependence of both the vortex trajectory and the induced pressure field on the upstream position of the vortex. In these terms the size of an oncoming vortex affects the dynamics of a vortex-airfoil interaction. Moreover, as observed by Kaykayoglu & Rockwell [8], when a compact vortex moves along the airfoil surface, it induces a wavelike pressure disturbance. The amplitude and the wavelength of this convected disturbance affect both the resulting unsteady loading and interaction noise.

The mean flow incidence has a strong influence on a vortex-airfoil interaction. Effects related to the flow acceleration past the leading edge (suction, boundary layer separation, etc..) are exalted by the presence of an impinging vortical disturbance, with consequences on both the unsteady loading and the sound generation. As shown by Goldstein *et al.* [9], the quadrupole noise from a loaded airfoil is proportional to the mean flow circulation. At high airfoil angle of attacks, the quadrupole contribution tends to become comparable to the dipole one. This is a consequence of the distortion of the impinging vortical disturbances induced by the mean flow gradients in proximity of the airfoil leading edge.

Gursul & Rockwell [10] investigated the interaction between a vortex street and an elliptical airfoil. Experiments were carried out in a water channel. The vortex streets impinging onto the elliptical airfoil were generated by using upstream plates of different thickness. The Reynolds number based on the plate thickness was in the range 309 – 619. The free-stream velocity was $U_\infty = 9.65 \times 10^{-2}$ s and kept constant in the experiments. Gursul & Rockwell showed that such interaction process is strongly affected by two factors:

- the wavelength of the oncoming vorticity field, that is the distance between two next vortices on the same row,

- the offset distance between the axis of the vortex street and the streamwise axis of the elliptical airfoil.

Two vortex streets of different wavelength were considered: a large scale vortex street, and a small scale vortex street. Thus, three flow configurations were observed:

a) both the small scale and the large scale vortex streets, at small values of the offset distance, are split into two separate rows which embrace the airfoil.

b) Both the small scale and large scale vortex streets, at large values of the offset distance, are convected along one side of the airfoil and preserve their structure.

c) When one row impinges directly on the airfoil leading edge, only the large scale vortices are split into less coherent structures. Moreover, these vortices are stretched in the cross-stream direction, but no boundary-layer separation occurs. The small scale vortex street, on the contrary, behaves as described in a) or in b).

Horner *et al.* [11] investigated the interaction between a vortex and a rotating blade. The blade had an NACA-0015 symmetric section of chord 0.149 m. The wind tunnel speed was 47 m/s, whereas the rotor tip velocity was 59.25 m/s. Different blade-vortex intersection configurations were investigated by means of Particle Image Velocimetry (PIV). During a direct blade-vortex interaction, the PIV data showed some basic mechanisms. In proximity of the leading edge the vortex is first deformed and then split into two fragments which are convected along the two airfoil sides. Because of the opposite induction effect of the image vortex system, the convection velocity is different along the two airfoil sides. The slower fragment spreads across the surface, whereas the faster one undergoes a slight distortion. As the vortex fragments approach the trailing edge, secondary vortices are shed into the airfoil wake. Finally, a further interaction occurs in the airfoil wake between the main vortex fragments and the secondary vortices.

Lee & Bershader [12] investigated a direct blade-vortex interaction by means of holographic interferograms. The blade section was an NACA-0012 of 0.05 m chord and the span extended by 0.05 m. The chord based free-stream Reynolds number was in the range $0.9 \times 10^6 - 1.3 \times 10^6$. The free-stream Mach number was in the range $0.5 - 0.7$. Lee & Bershader observed that the impinging vortex induces two opposite pressure peaks near the leading edge. These peaks collapse as the vortex passes above the leading edge. As a consequence, a pressure wave is radiated from the airfoil into the field. Moreover, a boundary-layer separation on the lower side of the leading edge was observed. This implies that the effects related to the viscosity of the fluid play an important role in a strong blade-vortex interaction.

Boundary-layer separation and trailing edge vortex shedding are effects related to the viscosity of the fluid. The latter have stimulated an exciting debate in the past on whether the presence of a vortex-sheet behind an airfoil leads to a reduction of the noise radiation or not. Howe [13] considered a turbulent eddy frozenly convected by a low subsonic flow along an acoustically compact airfoil. He concluded that the imposition of a Kutta condition cancels the trailing edge diffraction contribution and leads to a reduction of the airfoil interaction noise.

A review of the vortex-airfoil interaction problem can be found in chapter 10 of part II where emphasis is given to the interaction noise generation. The problem of the trailing edge noise is reviewed in chapters 8 and 9 of part II.

In the present chapter a semi-analytical model for the vortex-airfoil interaction problem is developed on the base of the circulation theory [5]. The model is applied to describe the interaction between a Kármán-Trefftz airfoil and a given distribution of line-vortices. The effects of the vortex distortion are accounted for by describing the oncoming vortex as a cloud of line-vortices. The effects of the fluid viscosity are modeled by employing a trailing edge Kutta condition.

2.2 The Aerodynamic Problem

In this section a discrete-vortex formulation of the aerodynamic problem is presented.

An ideal, incompressible, irrotational flow around a Kármán-Trefftz airfoil is herein described by exploiting the circulation theory [5]. A conformal mapping technique is used to impose the boundary condition on the airfoil surface. Additionally to a steady Kutta condition, a zero velocity unsteady Kutta condition is imposed at the airfoil trailing edge. As a result, a vortical wake is shed into the field and adds to the preexisting vortices convected past the airfoil.

In a first step, a free-wake formulation is developed by modeling the airfoil wake as a vortex-sheet convected downstream at the free-stream velocity. As a result, an integral equation for the wake intensity is obtained. In a second step, a free-wake formulation is developed by modeling the wake as a distribution of discrete vortices. Emphasis is given to the unsteady Kutta condition and to the existence of spurious acoustic sources at the trailing edge.

The model of an oncoming double row of counter-rotating vortices is presented, and its interaction with the airfoil is discussed. Furthermore, a circular cloud of vortices is proposed as a way to describe an oncoming vortex of finite size.

Some analytical results concerning the vortex-airfoil interaction problem are summarized in appendix 2 A. Some numerical aspects of the discrete-vortex method are discussed in appendixes 2 B, 2 C and 2 D.

2.2.1 Flow Model

In this subsection the theoretical background of the vortex method is briefly recalled in the light of the present study.

An unsteady flow can be assumed to be incompressible if the following two conditions are satisfied

$$M \ll 1 \tag{2.1}$$

$$\frac{LM}{c_0 T} \ll 1 \tag{2.2}$$

where M, L and T are the Mach number, the length scale and the time scale of the flow, respectively. The former is the steady-state condition of incompressibility, whereas the latter condition requires that the time for an acoustic perturbation to cover the distance L is not greater than the time scale T of the flow unsteadiness.

In the present study, a double row of counter rotating vortices is shed from a rod and is convected past an airfoil of chord $c = 0.1$m. Although the origin of the double row is not directly taken into account in the analytical model, the resulting length and time scales govern the modeling choices. In the experiments and simulations described in chapters 5 and 8, respectively, the double row of vortices is shed from a $d = 0.016$m rod at the reduced frequency $\mathrm{St} = f_0\, d/V_\infty \simeq 0.2$. Thus, the vortex shedding period is

$$T_{\mathrm{St}} = \frac{d}{\mathrm{St} V_\infty} \simeq \frac{5d}{c}\frac{c}{V_\infty} \tag{2.3}$$

On the other hand, the time required by an oncoming vortex to cross the airfoil is

$$T_c \simeq \frac{c}{V_\infty} \tag{2.4}$$

Hence, the length scale L of the unsteady flow past the airfoil is c, whereas the time scale is

$$T = \min\left(T_{\mathrm{St}}, T_c\right) \simeq \frac{c}{V_\infty} \tag{2.5}$$

As a result, the condition (2.2) provides $M^2 \ll 1$. Since a free-stream Mach number $M_\infty \simeq 0.06$ is hereafter considered ($V_\infty = 20\,\mathrm{m/s}$), both the conditions (2.1) and (2.2) are satisfied and the flow can be supposed to be incompressible.

The dynamics of the vorticity field $\omega = \nabla \times \mathrm{v}$ in an incompressible flow is governed by the equation

$$\frac{\mathrm{D}\omega}{\mathrm{D}t} = (\omega \cdot \nabla)\,\mathrm{v} + \nu \nabla^2 \omega \tag{2.6}$$

where $\mathrm{D}/\mathrm{D}t$ denotes the Lagrangian derivative. Equation (2.6) shows that the vorticity is a material property of the fluid particles, convected at the local fluid velocity with some deformation and viscous diffusion. Taking the integral of equation (2.6) on a material surface which is enclosed by a contour C

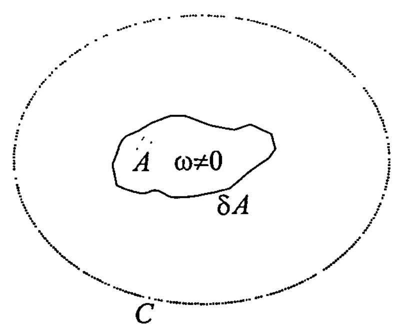

FIGURE 2.1: Contour integration around a non-vanishing vorticity region.

shows that the circulation Γ about C can only change by diffusion of vorticity through the contour (see Fig.2.1), namely

$$\frac{D\Gamma}{Dt} = -\nu \oint_C (\nabla \times \boldsymbol{\omega}) \cdot d\mathbf{l} \tag{2.7}$$

where

$$\Gamma = \iint_A \boldsymbol{\omega} \cdot \mathbf{n}\, dS = \oint_{\delta A} \mathbf{v} \cdot d\mathbf{l} \tag{2.8}$$

and use of the Stokes' theorem has been made. The restriction of this result to ideal fluids was first derived by Lord Kelvin and states that, for negligible viscosity, the circulation is conserved.

Given an arbitrary differentiable velocity field, there exists a scalar function ϕ, called the scalar potential, and a vector function $\mathbf{A}$, called the vector potential, which are such that

$$\mathbf{v} = \nabla\phi + \nabla \times \mathbf{A} \tag{2.9}$$

and satisfy the relationships

$$\nabla^2\phi = \nabla \cdot \mathbf{v} \tag{2.10}$$

and

$$\nabla^2\mathbf{A} = -\nabla \times \mathbf{v} \equiv -\boldsymbol{\omega} \tag{2.11}$$

provided that $\mathbf{A}$ satisfies the condition

$$\nabla \cdot \mathbf{A} = 0 \tag{2.12}$$

According to Lamb [14], this result must be attributed to Helmholtz and is usually referred to as the Helmholtz decomposition theorem. It can be noticed that equation (2.12) can be always satisfied by adding to $\mathbf{A}$ an inconsequential irrotational vector field $\nabla\eta$, namely

$$\mathbf{A}' = \mathbf{A} + \nabla\eta \tag{2.13}$$

such that $\nabla^2\eta = -\nabla \cdot \mathbf{A}$ and $\mathbf{A}'$ satisfies equation (2.12).

The Helmholtz decomposition states that a vector velocity field can be decomposed into an irrotational part $\mathbf{v}_{irr}$ and a solenoidal part $\mathbf{v}_{Sol}$, such that

$$\mathbf{v}_{Sol} = \nabla \times \mathbf{A} \quad \text{and} \tag{2.14}$$

$$\mathbf{v}_{irr} = \nabla\phi \tag{2.15}$$

From equations (2.14) and (2.11) it follows that

$$\nabla^2\mathbf{v}_{Sol} = -\nabla \times \boldsymbol{\omega} \tag{2.16}$$

whereas, from equations (2.10) and from the continuity equation

$$\frac{\partial \rho}{\partial t} + \nabla \cdot (\rho \mathbf{v}) = 0 \tag{2.17}$$

it follows that

$$\nabla^2 \phi = -\frac{1}{\rho}\frac{\mathrm{D}\rho}{\mathrm{D}t} \tag{2.18}$$

Hence, the dynamics of the vorticity field is described by the solenoidal part of the velocity field, whereas the acoustic aspects of the flow are related to the irrotational part of the velocity field.

The present study deals with a two-dimensional flow. In a two-dimensional flow, the term $(\boldsymbol{\omega} \cdot \nabla)\,\mathbf{v}$ which describes the rate of deformation of vortex lines, also called *vortex stretching*, vanishes and the vorticity has only one component ω in the direction normal to the flow plane. Thus, the vorticity transport equation (2.6), neglecting viscosity, becomes

$$\frac{\mathrm{D}\omega}{\mathrm{D}t} = 0 \tag{2.19}$$

Moreover, a Lagrange stream function $\psi(x, y, t)$ can be introduced, such that

$$u_{Sol} = \Psi_y, \qquad v_{Sol} = -\Psi_x \tag{2.20}$$

the existence of ψ being guaranteed by the solenoid nature of $\mathbf{v}_{Sol}$. Evaluating $\nabla \times \mathbf{v}_{Sol}$ yields

$$\nabla^2 \psi\, \hat{k} = -\omega\, \hat{k} \tag{2.21}$$

where $\hat{k}$ denotes the unit vector normal to plane of the flow. This Poisson equation for the stream function ψ is equivalent to that for the solenoidal velocity (2.16), as can be verified by evaluating the curl of equation (2.21). A solution of the Poisson equation (2.21) is

$$\psi(x, y, t) = -\frac{1}{2\pi} \iint\limits_{\mathcal{A}} \omega(x', y', t) \ln |\mathbf{r} - \mathbf{r}'|\, \mathrm{d}x'\, \mathrm{d}y' \tag{2.22}$$

where $\mathcal{A}$ denotes a fluid portion of non-vanishing vorticity and $|\mathbf{r} - \mathbf{r}'| = \sqrt{(x - x')^2 + (y - y')^2}$. Thus, differentiating under the integral sign provides

$$\begin{aligned} u_{Sol} &= -\frac{1}{2\pi} \iint\limits_{\mathcal{A}} \frac{\omega(x', y', t)\ (y - y')}{|\mathbf{r} - \mathbf{r}'|^2}\, \mathrm{d}x'\, \mathrm{d}y' \\ v_{Sol} &= \frac{1}{2\pi} \iint\limits_{\mathcal{A}} \frac{\omega(x', y', t)\ (x - x')}{|\mathbf{r} - \mathbf{r}'|^2}\, \mathrm{d}x'\, \mathrm{d}y' \end{aligned} \tag{2.23}$$

For a two-dimensional fluid motion a notation in complex variables is convenient and will be used throughout the present chapter. Thus, introducing the complex velocity $V_{Sol} = u_{Sol} + \mathrm{i}\, v_{Sol}$, equations (2.23) can be written as

$$V^*_{Sol}(z, t) = \frac{1}{2\pi \mathrm{i}} \iint\limits_{A} \frac{\omega(z', t)}{z - z'}\, \mathrm{d}z' \tag{2.24}$$

where $z = x + \mathrm{i}\, y$ is the complex co-ordinate and $\mathrm{d}z' = \mathrm{d}x'\, \mathrm{d}y'$. The superscript $*$ denotes the complex conjugate. The equivalence between the expressions (2.23) and (2.24) is guaranteed by the identity

$$\frac{1}{z - z'} = \frac{(x - x') - \mathrm{i}\,(y - y')}{|z - z'|^2} \tag{2.25}$$

If the vorticity is supposed to be confined to a number of points z_j, the vorticity distribution is given by

$$\omega(z) = \sum_j \Gamma_j \, \delta(z - z_j) \tag{2.26}$$

where Γ_j is the circulation of each line-vortex in the field. In this case the solenoidal velocity obtained from equation (2.24) takes the form

$$V^*_{Sol}(z) = \sum_j \frac{1}{2\pi \mathrm{i}} \frac{\Gamma_j}{z - z_j} \tag{2.27}$$

Solution methods based on this kind of vorticity distribution are called *discrete-vortex methods.* Many reviews of vortex methods for two-dimensional flows are available. The reader should refer to the works of Clements & Maull [15], Saffman & Baker [16], Leonard [17], Aref [18] and Sarpkaya [19]. Furthermore, some discrete-vortex methods applied to the vortex-airfoil interaction problem are described in section 10.4.1.1 of part II.

In the following subsections, an application of a vortex method to the vortex-airfoil interaction problem will be discussed and attention will be drawn to the trailing edge problem.

2.2.2 The Kutta Condition and the Physical Role of Vortex Shedding

In actual flows, due to the action of viscous forces, vorticity is generated at solid boundaries. In a high-Reynolds-number flow, the region with rotational flow is in general limited to a thin region near the boundary. However, at sharp corners or on a strongly curved part of the boundary, the boundary layer can separate, forming a free shear layer.

An inviscid flow model is devoid of the physical mechanism of the boundary layer separation which must be forced by imposing a Kutta condition. At a sharp edge, in an unsteady potential flow, the Kutta condition results in a generation of a thin vortical layer, which removes the singular behaviour of the flow at the edge. As a result, the velocity remains finite at the separation point.

Different methods to impose the Kutta condition are quoted in literature. Depending on the way in which the boundary conditions are satisfied, either by using a conformal mapping or by using a boundary element method, the implementation of the Kutta condition takes different forms. Since the Kutta condition is not a physical condition but only a model of the flow behaviour near a trailing edge, spurious effects can be generated by this model. Typically, spurious forces and spurious acoustic sources may be produced. In the present chapter we show that a discrete-vortex model of the airfoil wake, in which a vortex is shed at each time-step from the airfoil trailing edge and is convected at the local flow velocity, does not introduce significant spurious forces and spurious acoustic sources.

The *physical* effects of the vortex shedding from a trailing edge on the vortex-airfoil interaction noise are discussed in chapters 8 and 9 of part II. In a quite simplified picture of the flow, we see that the vortex shedding has a smoothing effect on the flow behaviour at the trailing edge. In other words, the boundary layer separation from a sharp edge reduces the suction forces due to the acceleration of the flow past the edge. This smoothing effect ultimately results in a reduction of both the aerodynamic forces and the acoustic sources[2] in proximity of the trailing edge.

A simple model problem solved by Howe [20] and described in section 6.5 of part II illustrates the role of the vortex shedding on the interaction noise. Consider a line-vortex in proximity of the edge of a semi-infinite rigid plate ($x < 0, y = 0$). By assuming, for simplicity, that the shed vorticity rolls up into a concentrated vortex, the total radiated sound at $\mathbf{r} = r(\cos\theta, \sin\theta)$, as $r \to \infty$, is given by

$$p(\mathbf{r}, t) \simeq \frac{\rho \sin(\theta/2)}{\pi\sqrt{r}} \left\{ \Gamma \left[\frac{\mathrm{D}\psi}{\mathrm{D}t}\right]_{\Gamma} + \Gamma_{sh} \left[\frac{\mathrm{D}\psi}{\mathrm{D}t}\right]_{\Gamma_{sh}} \right\} \tag{2.28}$$

[2]Physical forces and acoustic sources, indeed.

where Γ and Γ_{sh} are the circulation of the oncoming and shed vortex, respectively. The function ψ is the imaginary part of the complex potential $W = \phi^* + \mathrm{i}\psi = -\mathrm{i}\sqrt{x + \mathrm{i}y}$ of an ideal flow past the edge. The terms $[\mathrm{D}\psi/\mathrm{D}t]$ denote the rate at which the vortex path crosses the streamlines of the ideal flow past the semi-infinite plate, evaluated at the retarded position of the vortex. Hence, because Γ and Γ_{sh} have opposite signs and the oncoming and shed vortices cross the streamlines $\psi = \text{const}$ in the same direction, the sound generated by the shed vortex tends to cancel the sound generated by the oncoming vortex. As a general result, the vortex shedding process reduces the trailing edge contribution to the interaction noise.

2.2.3 A Fixed-Wake Formulation of the Vortex-Airfoil Interaction Problem

In this subsection an analytical model of the vortex-airfoil interaction problem is presented. Use of the conformal mapping technique is made in order to describe the unsteady flow past a Kármán-Trefftz airfoil. The vorticity shed from the airfoil trailing edge is supposed to be convected at the free-stream velocity along a constant rectilinear path.

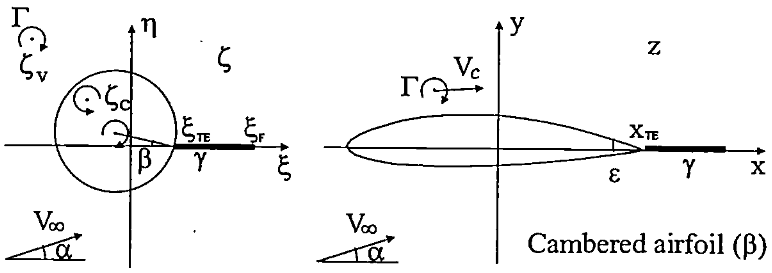

FIGURE 2.2: Kármán-Trefftz conformal mapping.

Consider a Kármán-Trefftz conformal transformation which maps the outer region of a circle in the complex ζ-plane into the outer region of an airfoil in the complex z-plane, namely

$$z = (\theta/4)\,\frac{(\zeta+1/4)^\theta + (\zeta-1/4)^\theta}{(\zeta+1/4)^\theta - (\zeta-1/4)^\theta} \tag{2.29}$$

where $\theta = 2 - \epsilon/\pi$, with ϵ denoting the value of the trailing edge angle. The circle has its center at $\zeta_c = \xi_c + \mathrm{i}\eta_c$. It intersects the real axis at $\xi_{TE} = 1/4$ and has radius $R_c = \sqrt{(\xi_{TE} - \xi_c)^2 + \eta_c^2}$. The point ξ_{TE} maps into the airfoil trailing edge $x_{TE} = \theta/4$, as sketched on Fig.2.2.

Performing the change of variable $\zeta' = \zeta - \zeta_c$ and letting a line-vortex of circulation Γ occupy the position ζ_v, the complex potential field can be written as

$$W(\zeta') = W_s + W_v + W_w \tag{2.30}$$

where W_s denotes the steady potential of a Kármán-Trefftz airfoil in the otherwise uniform flow, W_v is the contribution of the oncoming vortex, and W_w is the potential of the wake shed from the airfoil trailing edge, as required by an unsteady Kutta condition. In the present study the Kutta condition is imposed by requiring that the flow velocity is finite at the trailing edge.

Quantities in the following expressions are all made dimensionless by the free-stream velocity V_∞ and by the airfoil chord.

The steady contribution is given by

$$W_s(\zeta') = \mathrm{e}^{-\mathrm{i}\alpha}\zeta' + \frac{R_c^2}{\zeta'}\,\mathrm{e}^{\mathrm{i}\alpha} + \mathrm{i}\frac{\Gamma_s}{2\pi}\ln\zeta' \tag{2.31}$$

where α is the airfoil angle of attack and $\Gamma_s = 4\pi R_c \sin(\alpha+\beta)$ is the airfoil steady circulation which depends on the airfoil camber $\beta = \tan^{-1}[\eta_c/(\xi_{TE}-\xi_c)]$ and the airfoil angle of attack α. The steady circulation Γ_s is chosen such that a steady Kutta condition is satisfied at the trailing edge.

The vortex contribution has the following expression

$$W_v(\zeta') = -\mathrm{i}\frac{\Gamma}{2\pi}\left\{\ln\left(\zeta'-\zeta_v'\right) - \ln\left(\zeta' - \frac{R_c^2}{\zeta_v'^*}\right) + \ln\zeta'\right\} \tag{2.32}$$

where the first and the second term describe the potential fields of a vortex at ζ_v' and its image within the circle, respectively. The third term denotes the potential of a vortex which has been placed at the center of the circle in order to cancel the effect of the image vortex when the oncoming one is infinitely far from the airfoil (see Fig.2.3). Clearly, when more than one oncoming vortex is present in the field, formulae accounting for the vortex induction must be extended by summation.

Finally, by describing the airfoil wake as a vortex-sheet on the real axis ξ, extending from ξ_{TE} to ξ_F, the wake contribution takes the form

$$W_w(\zeta') = -\frac{\mathrm{i}}{2\pi}\int_{\xi_{TE}}^{\xi_F}\left\{\ln\left(\zeta'-\zeta_w'\right) - \ln\left(\zeta' - \frac{R_c^2}{\zeta_w'^*}\right)\right\}\gamma(\xi_w)\,\mathrm{d}\xi_w \tag{2.33}$$

where $\gamma(\xi_w)$ is the specific circulation of the shed vorticity and ξ_F is the downstream end of the wake (see Fig.2.2).

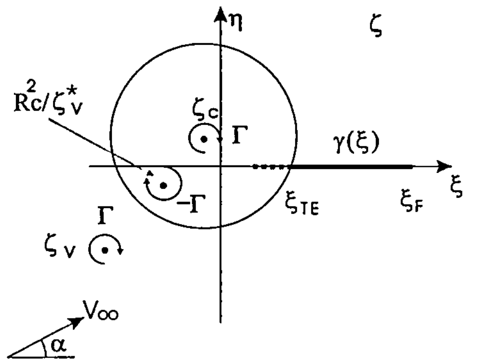

FIGURE 2.3: Aerodynamic configuration in the ζ-plane.

Now, in order to account for the flow unsteadiness, the motion of the oncoming vortex must be taken into account in the complex formulation. Therefore, the following history is assumed to describe the vortex-airfoil interaction process.

a) A vortex of given intensity is located at an arbitrary upstream position, sufficiently far from the airfoil. As a result, a vanishing velocity is induced at the trailing edge and the vortex-sheet has a vanishing circulation γ. The circulation around the airfoil is thus initially due to the only steady-state contribution Γ_s.

b) As the vortex moves towards the airfoil, a wake is progressively shed from the trailing edge, allowing the Kutta condition to be instantaneously fulfilled. The instantaneous reaction of the flow around the airfoil is a consequence of both the incompressible and inviscid character of the flow: the flow perturbations induced by the oncoming vortex propagate at an infinite velocity, no relaxation effects occur at the trailing edge.

c) The trajectory of the oncoming vortex is instantaneously perturbed from the steady-state streamlines by the induction of the whole vorticity field, namely, the image vortex, the wake already shed into the field and the image system of the wake.

The circulation of the wake progressively shed from the trailing edge depends on the instantaneous perturbation induced by all the preexisting vortical disturbances (the oncoming vortex, the wake already shed and the respective images) at the trailing edge. A physically consistent condition requires that the velocity induced at the trailing edge is finite. This condition is equivalent to a zero velocity condition applied onto ξ_{TE} in the circle plane. Hence, the circulation of the vortex-sheet can be determined by requiring that it induces a velocity at ξ_{TE} which exactly cancels the velocity induced by the preexisting vortical disturbances. This is the form of the unsteady Kutta condition adopted in the present fixed-wake approach.

Since the steady potential satisfies the Kutta condition at the trailing edge by definition, the zero velocity Kutta condition in the circle-plane takes the form

$$(V^*)_{\xi_{TE}} = \left(\frac{\mathrm{d}W_v}{\mathrm{d}\zeta}\right)_{\xi_{TE}} + \left(\frac{\mathrm{d}W_w}{\mathrm{d}\zeta}\right)_{\xi_{TE}} = 0 \tag{2.34}$$

Introducing equations (2.32) and (2.33) into equation (2.34), setting $\zeta'_{TE} = R_c\,\mathrm{e}^{-\mathrm{i}\beta}$ and rearranging, we obtain

$$\int_{\xi_{TE}}^{\xi_F} \frac{2R_c\cos\beta + \xi - \xi_{TE}}{R_c\,\mathrm{e}^{-\mathrm{i}\beta}\,(\xi - \xi_{TE})}\,\gamma(\xi)\,\mathrm{d}\xi = \Gamma\,\phi(\zeta_v) \tag{2.35}$$

where

$$\phi(\zeta_v) = \frac{1}{R_c\,\mathrm{e}^{-\mathrm{i}\beta} - \zeta'_v} + \frac{1}{R_c\,\mathrm{e}^{-\mathrm{i}\beta}} - \frac{\zeta'^*_v}{\zeta'^*_v R_c\,\mathrm{e}^{-\mathrm{i}\beta} - R_c^2} \tag{2.36}$$

Clearly, when more than one oncoming vortex are present in the field, the expression of ϕ must be extended by summation.

Then, changing to the airfoil-plane and using the identity $\gamma(x)\,\mathrm{d}x = \gamma(\xi)\,\mathrm{d}\xi$ lead to the integral equation

$$\int_{x_{TE}}^{x_{TE}+V_\infty t} \left\{1 - 4\,R_c\cos\beta\left[1 - \left(\frac{x+\theta/4}{x-\theta/4}\right)^{\frac{1}{\theta}}\right]\right\}\gamma(x)\,\mathrm{d}x = \Gamma\phi(\zeta_v) \tag{2.37}$$

The upper limit of integration results from having supposed that the wake is convected at the free-

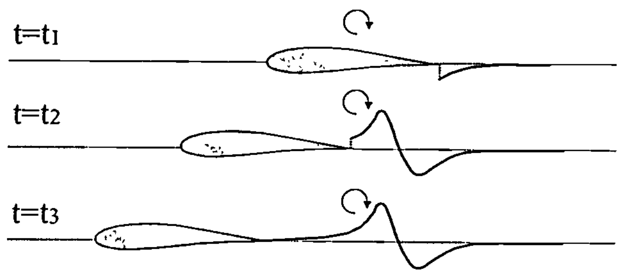

FIGURE 2.4: Vortex shedding from the trailing edge as the airfoil moves towards an upstream vortex.

stream velocity V_∞ along the real axis x.

As the vortex approaches the airfoil, new vorticity is generated and convected downstream. Equivalently, as the airfoil moves towards the vortex (see Fig.2.4) it leaves back a wake at rest[3]. Therefore, space and time are in the present analysis two explicit forms of a same convective variable $(x - V_\infty t)$. It is thus expedient to express the wake in a body reference frame by means of the Galilean transformation $\sigma = -x + x_{TE} + \tau$, with $\tau = V_\infty t$. As a result, equation (2.37) takes the form

$$\int_0^\tau \left\{1 - 4R_c\cos\beta\left[1 - \left(\frac{\tau-\sigma+\theta/2}{\tau-\sigma}\right)^{\frac{1}{\theta}}\right]\right\}\gamma(\sigma)\,\mathrm{d}\sigma = \Gamma\phi(\zeta_v) \tag{2.38}$$

[3]A wake at a rest herein denotes a non convected wake.

with the initial condition $\gamma(0) = 0$. This condition is consistent with the assumption of zero initial velocity at the trailing edge.

Interestingly, for $\zeta_c = 0$ and $\theta = 2$, which correspond to a flat-plate, the kernel in equation (2.38) reduces to

$$\sqrt{\frac{\tau + 1 - \sigma}{\tau - \sigma}} \tag{2.39}$$

which is the same of the integral equation obtained by Wagner [21] for an impulsive start of a flat-plate at a small incidence.

2.2.4 The Oncoming Vortex Trajectory

The known term ϕ, as stated in equation (2.36), is a function of the vortex position ζ_v at the current time τ. The related position in the z-plane is given by

$$z_v(\tau) = z_v^o + \int_0^\tau V_c(z_v)\,\mathrm{d}\tau' \tag{2.40}$$

where z_v^o is the initial position of the vortex. Making use of the Routh's theorem, the convection velocity V_c takes the form

$$V_c^\star(z_v) = \left(\frac{\mathrm{d}\tilde{W}}{\mathrm{d}\zeta}\right)_{\zeta_v}\left(\frac{\mathrm{d}\zeta}{\mathrm{d}z}\right)_{\zeta_v} - \mathrm{i}\frac{\Gamma}{4\pi}\left(\frac{\mathrm{d}^2\zeta/\mathrm{d}z^2}{\mathrm{d}\zeta/\mathrm{d}z}\right)_{\zeta_v} \tag{2.41}$$

where $\tilde{W} = W + \mathrm{i}\,(\Gamma/2\pi)\ln\left(\zeta' - \zeta_v'\right)$ is the overall complex potential deprived of the vortex self-contribution. A vortex, in fact, cannot induce on itself.

Since the vortex velocity V_c is an implicit function of time, equation (2.38) must be solved by successive updates of the vortex position. Moreover, in order to account for the wake contribution, an integral extending from 0 to τ must be calculated at each time-step. The numerical aspects related to the time integration are described in appendix 2 B.

The numerical simulation is started by locating the vortex at a distance from the airfoil such that the velocity $V_{\xi_{TE}}$ induced at the trailing edge is a fraction ε of the free-stream velocity V_∞. Therefore, as ε goes to zero, $|z_v^o|$ goes to infinity and ε behaves like a cut-off parameter for the Kutta condition. The (dimensionless) velocity induced by the oncoming vortex at ξ_{TE} has modulus

$$V_{TE} = \frac{2\Gamma}{\pi}|\phi(\xi_v^o, \eta_v^o)| \tag{2.42}$$

where (ξ_v^o, η_v^o) are the initial co-ordinates of the vortex and the function ϕ is defined in equation (2.36). Hence, setting $V_{TE} = \varepsilon$ yields

$$|\phi(\xi_v^o, \eta_v^o)| = \frac{\pi\,\varepsilon}{2\Gamma} \tag{2.43}$$

If the value of y_v^o is prescribed, equation (2.43) provides two values of x_v^o: the upstream one gives the initial position of the vortex, whereas the downstream one can be used as a stop flag for the numerical simulation.

2.2.5 A Free-Wake Formulation of the Vortex-Airfoil Interaction Problem

The integral equation (2.38) provides the circulation of a vortex-sheet convected at the free-stream velocity along the real axis and satisfying the zero-velocity Kutta condition at the airfoil trailing edge.

The airfoil wake can be also described as a distribution of discrete vortices convected at the local flow velocity. This free-wake model permits to investigate the effects related to a fixed wake approximation which is very frequently made in analytical aeroacoustics.

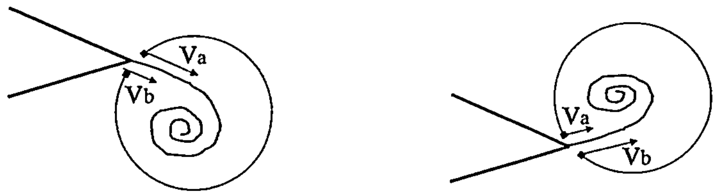

a) $\frac{d\Gamma_w}{dt} > 0$. b) $\frac{d\Gamma_w}{dt} < 0$.

FIGURE 2.5: Vortex roll-up at a sharp trailing edge.

In order to impose a physically consistent Kutta condition we can form the following qualitative picture of the unsteady flow in proximity of the trailing edge. We suppose that the shed vorticity rolls up into a spiral vortex-sheet of overall circulation $\Gamma_w(t)$, as sketched in Fig.2.5. Since the pressure is continuous across the vortex-sheet, applying the unsteady Bernoulli equation along a circle enclosing the rolled-up vortex-sheet yields

$$\frac{1}{2}\left(v_a^2 - v_b^2\right) \equiv v_{sheet}\left(v_a - v_b\right) = -\frac{\mathrm{d}\Gamma_w}{\mathrm{d}t} \tag{2.44}$$

where, as shown in Fig.2.5, v_a and v_b denote the velocities tangential to the sheet, and $v_{sheet} = (v_a + v_b)/2$ is the local convection velocity of the vortex-sheet.

If the vortex-sheet is supposed to be concentrated in a line-vortex of circulation $\Gamma(t)$, as shown in Fig.2.6(a), then the existence of a feeding-sheet must be idealized, which connects the line-vortex to the trailing edge. The feeding-sheet allows the vorticity shed from the trailing edge to be *injected* into the wake vortex. In this case, since the velocity is continuous across the feeding-sheet, applying the

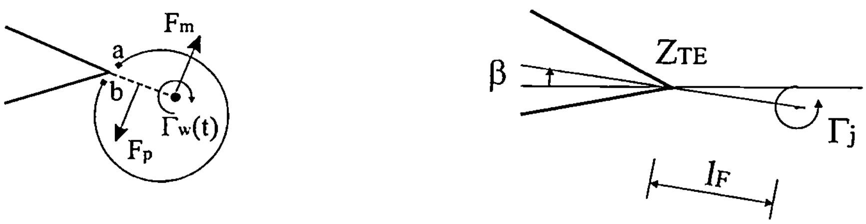

a) Discrete-vortex/feeding-sheet system.

b) Nascent vortex at a trailing edge.

FIGURE 2.6: Unsteady Kutta condition.

unsteady Bernoulli equation along a circle around the line-vortex provides a time-dependent pressure jump across the feeding-sheet, namely

$$\Delta p_{ab} = -\rho\frac{\mathrm{d}\Gamma_w}{\mathrm{d}t} \tag{2.45}$$

As a result, a pressure force acts on the feeding-sheet which is given by

$$F_p = -\mathrm{i}\,\rho\frac{\mathrm{d}\Gamma_w}{\mathrm{d}t}\left(z_w - z_{\mathrm{TE}}\right) \tag{2.46}$$

As argued by Brown & Michael [22], the pressure force on the feeding-sheet must be balanced by a Magnus force generated by assuming that the wake vortex is convected at a velocity which is different from the local flow velocity, namely

$$F_m = -\mathrm{i}\,\rho\Gamma_w(t)\left\{\frac{\mathrm{d}z_w}{\mathrm{d}t} - \frac{\mathrm{d}}{\mathrm{d}z}\tilde{W}^*(z_w)\right\} \tag{2.47}$$

where $\tilde{W}^*$ is the complex conjugate of the local velocity potential deprived of the wake vortex self-contribution. Therefore, balancing the pressure and the magnus force yields

$$V_c'(z_w) = \frac{\mathrm{d}}{\mathrm{d}z}\tilde{W}^*(z_w) - \frac{z_w - z_{\mathrm{TE}}}{\Gamma_w}\frac{\mathrm{d}\Gamma_w}{\mathrm{d}t} \tag{2.48}$$

This differential equation provides a *force-free* correction of the *free vortex* convection velocity $V_c = \mathrm{d}\tilde{W}^*/\mathrm{d}z$ calculated by means of equation (2.41). It can be observed that the correcting term vanishes if the strength of the vortex is constant in time.

The distributed system of forces F_p and F_m involves an unbalanced torque which generates a spurious reaction force on the edge surface. Peters & Hirschberg [23] argued that this unbalanced torque generates a spurious quadrupole edge noise contribution.

An emendation of Brown & Michael [22] equation was proposed by Howe [24] in order to cancel the spurious quadrupole acoustic sources. The vortex convection velocity satisfies the differential equations

$$\begin{aligned}
\frac{\mathrm{d}\mathbf{x}_w}{\mathrm{d}t}\cdot\nabla\Psi_1 + \frac{\Psi_1}{\Gamma_w}\frac{\mathrm{d}\Gamma_w}{\mathrm{d}t} - \mathbf{v}_0\cdot\nabla\Psi_1 = 0 \\
\frac{\mathrm{d}\mathbf{x}_w}{\mathrm{d}t}\cdot\nabla\Psi_2 + \frac{\Psi_2}{\Gamma_w}\frac{\mathrm{d}\Gamma_w}{\mathrm{d}t} - \mathbf{v}_0\cdot\nabla\Psi_2 = 0
\end{aligned} \tag{2.49}$$

where $\mathbf{x}_w = (x_{w_1}, x_{w_2})$ is the instantaneous position of the vortex, $\mathbf{v}_0 = (v_{0_1}, v_{0_2})$ is the free vortex velocity and $\Psi_i(\mathbf{x})$ is the stream function conjugate to $\Phi_i(\mathbf{x})$, $\Phi_i(\mathbf{x})$ denoting the velocity potential of an incompressible flow past the surface of the airfoil that has unit speed in the i-direction at large distance from the airfoil. The stream function $\Psi_i(\mathbf{x})$ satisfies the Cauchy-Riemann relations

$$\begin{aligned}
\frac{\partial\Psi_i}{\partial x_1} = -\frac{\partial\Phi_i}{\partial x_2} \\
\frac{\partial\Psi_i}{\partial x_2} = \frac{\partial\Phi_i}{\partial x_1}
\end{aligned} \tag{2.50}$$

and can be assumed to vanish on the surface of the body.

In the present study the wake is modeled as a distribution of discrete-vortices whose circulation is hold constant in time. Therefore, in principle, a spurious pressure force may act only on the feeding-sheet connecting the trailing edge to a nascent vortex. The circulation of a nascent vortex, in fact, increases, in a time-step, from zero to the value required by the Kutta condition. A force-free shedding model should require an iterative solution of equation (2.49) in the time interval (τ^{j-1}, τ^j), convecting a progressively fed vortex from the trailing edge up to a formation location at which both the Kutta condition and equation (2.49) are satisfied. However, the fictitious pressure force vanishes when the length of the feeding-sheet tends to zero. A simplified treatment is thus proposed by adding, at each time-step, a vortex at a small distance l_F downstream of the trailing edge (see Fig.2.6(b)). The formation length l_F is a parameter of the numerical simulation. The circulation of the nascent vortex is thus determined by applying the Kutta condition onto the trailing edge. More precisely, at each time step τ^j a wake vortex is added at the formation position. Its circulation Γ_w^j is chosen such that the velocity induced at the trailing edge cancels the velocity $V_{\xi_{\mathrm{TE}}}^j$ generated by all the other vortices in the field, i.e.

$$\Gamma_w^j = -\frac{V_{\xi_{\mathrm{TE}}}^j}{V_1} \tag{2.51}$$

where V_1 is the velocity induced at the trailing edge by a unit circulation vortex located at the formation position.

The numerical scheme used to convect each wake vortex is described in appendix 2 B. Furthermore, since a distribution of line-vortices at a small distance from each other is numerically unstable, a blob-vortex method is employed in order to prevent the vortex trajectories to undergo a chaotic behavior. This methodology is described in appendix 2 C and consists in replacing the singular kernel of a line-vortex by an artificial viscous core. Finally, as discussed in appendix 2 D, a vortex amalgamation procedure can be used in order to improve the computational performances of the discrete-vortex method, without affecting the accuracy of the numerical prediction.

2.2.6 The Cloud of Oncoming Vortices

In order to investigate the effect of the vortex distortion during a direct vortex-airfoil interaction, the oncoming vortex can be modeled as multiple, discrete-vortex elements clustered in a circular cloud.

The numerical diffusion of a cloud can be reduced by using a high-order time integration scheme to convect each vortex, and by assuming vortex elements of equal area. In the present work, a four-step Runge-Kutta time integration algorithm is used to convect a single oncoming vortex, as well as each vortex in a cloud (see appendix 2 B). Furthermore, vortices of equal circulation are disposed on circles of different radius with uniform angular spacing. Hence, a condition of constant area elements is ensured by the radial spacing law

$$r_0 = 0 \quad \text{(first vortex in the center of the cloud)} \tag{2.52}$$

$$r_1 = r_{\text{cloud}} \quad (r_{\text{cloud}} \text{ is a parameter of the problem)} \tag{2.53}$$

$$r_k = \sqrt{2r_{k-1}^2 - r_{k-2}^2} \quad \text{for} \quad k \geq 2 \tag{2.54}$$

As a result, the size of the cloud is an implicit function of the parameter r_{cloud}.

The aspect ratio of each vortex element is a strong function of the radial distance. Nevertheless, the vortex trajectories seem to have a quite regular behaviour. Fig.2.7 shows the evolution of a cloud of 101 vortices. The value of the dimensionless inner size is $r_{\text{cloud}} = 0.01$. Interestingly, the initial outer radial compression allows a convergence towards a state of dynamical equilibrium in which an external shell of high vorticity encloses a core of nearly uniform vorticity distribution. Furthermore, as shown in Fig.2.7, secondary structures appear in the external shell.

It is interesting to compare the evolutions of the two clouds of equal size plotted on Fig.2.8. The first on Fig.2.8(a) is a non uniform radial distribution of vortices with inner size $r_{\text{cloud}} = 0.001$. The second on Fig.2.8(b) is a uniform radial distribution of vortices. As shown in Fig.2.9, the non uniform radial distribution preserves the size of the cloud. Conversely, the cloud with a uniform radial distribution undergoes a strong diffusion. After 100 time-steps these two clouds appear as plotted on Fig.2.10. A non uniform radial vortex distribution clearly results in a less chaotic evolution of the cloud.

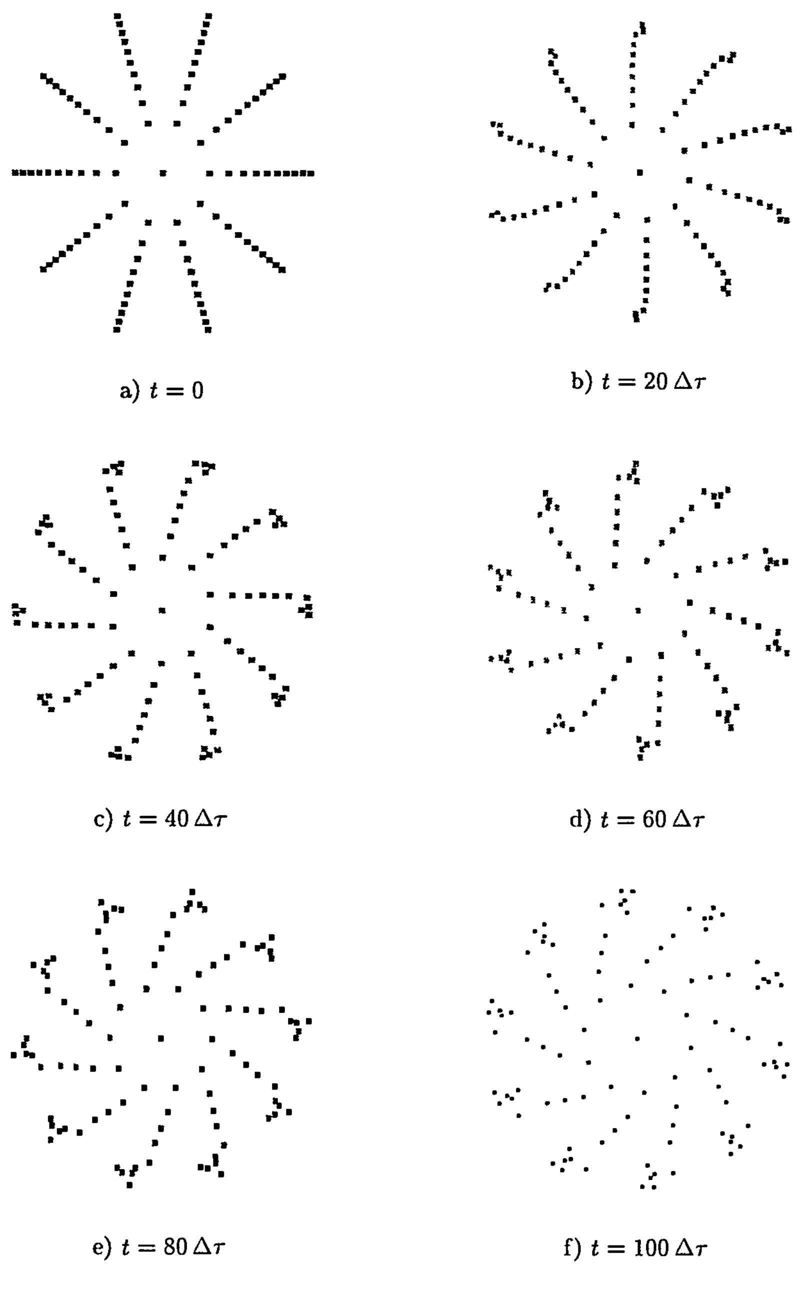

FIGURE 2.7: Evolution of a of cloud of vortices of dimensionless circulation $\Gamma = 1.5 \times 10^{-4}$, starting from a non uniform radially distribution. The dimensionless time-step is $\Delta\tau = 6 \times 10^{-3}$.

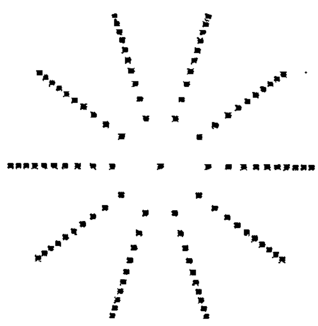

a) Non uniform radial distribution.

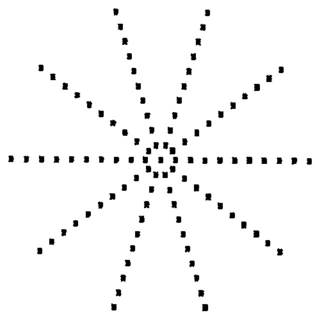

b) Uniform radial distribution.

FIGURE 2.8: Starting distribution of vortices in a cloud ($t = 0$).

a)

b)

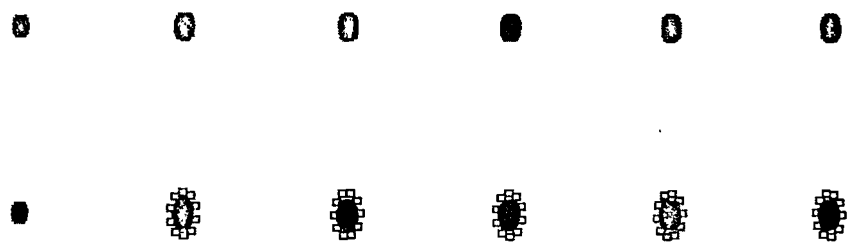

FIGURE 2.9: Cloud evolution (frame rate: $20\Delta\tau$). a): Non uniform radial distribution; b) uniform radial distribution.

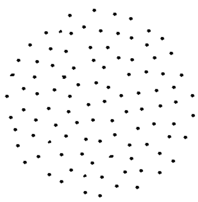

a) The starting cloud is that of Fig.2.8(a).

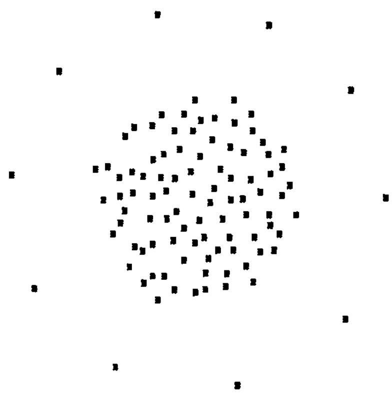

b) The starting cloud is that of Fig.2.8(b).

FIGURE 2.10: Clouds at $t = 100\Delta\tau$.

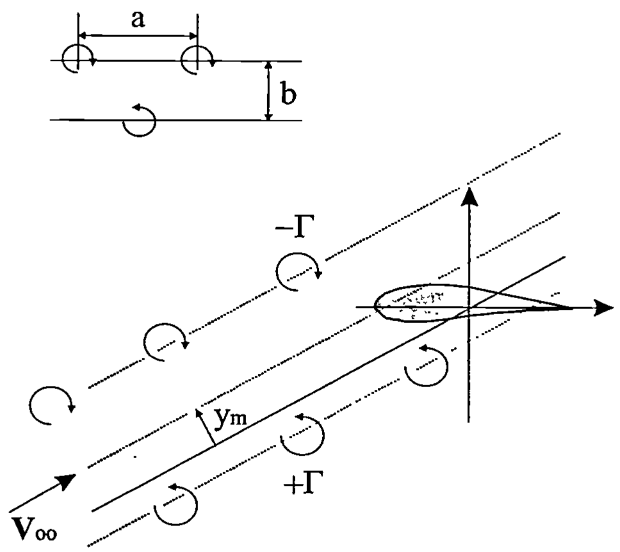

FIGURE 2.11: Interaction between a Kármán vortex street and an airfoil.

2.2.7 The Double Row of Counter-Rotating Vortices

In order to evaluate the acoustic radiation from an airfoil embedded in the wake of a rod, we use the Kármán model of a double row of counter-rotating vortices.

As sketched in Fig.2.11, the distance between the rows is b and the distance between two next vortices on the same row is a. Upper and lower vortices are uniformly staggered so that each vortex on the upper row is above the mid-point of two vortices on the lower row.

A Kármán vortex street is an infinite double row of uniformly spaced counter-rotating vortices. The complex velocity potential of this flow configuration is [25]

$$W(z) = \mathrm{i}\,\frac{\Gamma}{2\pi}\ln\Big(\sin\Big[\frac{\pi}{a}\,(z - \mathrm{i}\,b/2)\Big]\Big) - \mathrm{i}\,\frac{\Gamma}{2\pi}\ln\Big(\sin\Big[\frac{\pi}{a}\,(z - a/2 + \mathrm{i}\,b/2)\Big]\Big) \tag{2.55}$$

where $z = x + \mathrm{i}\,y$ and Γ has the sign of the upper vortices. Since an infinite row does not induces any velocity on itself, the upper row advances with a velocity induced by the lower row and *vice versa.* It should be found by differentiating equation (2.55) that the convection velocity of a Kármán vortex street in a uniform flow is

$$v_c = V_\infty + v_i \tag{2.56}$$

where v_i accounts for the mutual induction effect. It is given by

$$v_i = \frac{\Gamma}{2\,a}\tanh\left(\frac{\pi b}{a}\right) \tag{2.57}$$

and is negative if the upper vortices rotate clockwise. As a result, a Kármán vortex street translates slower than the free-stream.

The model of a Kármán vortex street also provides the following stability condition

$$\cosh\left(\frac{\pi b}{a}\right) = \sqrt{2} \tag{2.58}$$

which yields the equilibrium aspect ratio

$$\frac{b}{a} \simeq 0.281 \tag{2.59}$$

The distance a depends on the diameter d of the cylinder. If f_0 denotes the vortex shedding frequency from the originating rod, it results that

$$f_0 \equiv \mathrm{St}\frac{V_\infty}{d} = \frac{v_c}{a} \tag{2.60}$$

which yields $a \simeq 5\,d$ for a Strouhal number of 0.2.

The circulation Γ of the vortices can be evaluated by using the expression proposed by Sallet [26] for the lift coefficient induced by a Kármán vortex street on a cylinder, namely

$$C_{l_{\max}} = \frac{\Gamma}{2V_\infty d}\left(1 - \frac{3\,|v_i|}{V_\infty}\right) \tag{2.61}$$

which can be solved in Γ with a value of $C_{l_{\max}} \lesssim 0.8$.

The complex potential (2.55) can be differentiated with respect to z in order to determine the velocity field. It is interesting to determine the *upwash*[4] velocity v along the axis of the vortex street ($y = 0$ in (2.55)). Following Ref. [25], the upwash velocity is given by

$$v(t) = \frac{2\pi}{a}\Gamma\cosh\left(\pi\frac{b}{a}\right)\frac{\sin(2\pi f_0\,t)}{\cos^2(2\pi f_0\,t) - \cosh^2(\pi\frac{b}{a})} \tag{2.62}$$

where the dominant frequency f_0 is defined in (2.60). A Fourier decomposition of the upwash velocity (2.62) permits to describe a Kármán vortex street as a superposition of harmonic upwash gusts. Thus, setting

$$v(t) = \sum_{n=-\infty}^{n=\infty} v_n\,\mathrm{e}^{-\mathrm{i}\,n2\pi f_0\,t} \tag{2.63}$$

with

$$v_n = f_0\int_{-\frac{1}{2f_0}}^{\frac{1}{2f_0}} v(t)\,\mathrm{e}^{\mathrm{i}\,n2\pi f_0\,t}\,\mathrm{d}t \tag{2.64}$$

and using the known integral

$$\int_0^\pi \frac{\sin x\sin(nx)}{1 - 2\alpha\cos x + \alpha^2}\,\mathrm{d}x = \begin{cases} \frac{\pi}{2}\alpha^{n-1} & \text{for} \quad \alpha^2 < 1 \\ \frac{\pi}{2}\alpha^{-(n+1)} & \text{for} \quad \alpha^2 > 1 \end{cases} \tag{2.65}$$

yields the harmonic gust components [27]

$$v_n = \frac{-\mathrm{i}\,2\pi\Gamma}{a\left\{\cosh(\pi\frac{b}{a})\left[1 + \tanh(\pi\frac{b}{a})\right]\right\}^n} \quad \text{with } n \text{ odd} \tag{2.66}$$

Interestingly, the upwash velocity induced by the Kármán vortex street along its axis exhibits only odd harmonics.

When more than one oncoming vortex are present in the field, formulae accounting for the vortex induction must be extended by summation. For example, if N_v denotes the number of vortices in a double-row, the right-hand side of the integral equation (2.38) takes the form

$$\phi = 2R_c\sum_{n=1}^{N_v} S_n\frac{(\xi_{TE} - \xi_{v_n})\cos\beta + \eta_{v_n}\sin\beta}{(\xi_{TE} - \xi_{v_n})^2 + \eta_{v_n}^2} \tag{2.67}$$

where $S_n = (-1)^n$.

[4] The velocity normal to the axis of the vortex street constitutes an upwash velocity for an airfoil embedded at zero angle of attack in the vortex street (see Fig.2.11).

2.2.8 The Aerodynamic Force on the Airfoil

The oncoming vortex and the airfoil wake induce an unsteady pressure field on the airfoil surface. As a consequence, an unsteady aerodynamic force **F** and an unsteady aerodynamic moment **M** are exerted on the airfoil.

A way to predict **F** and **M** consists in integrating the unsteady pressure field upon the airfoil surface. By supposing that the fluid is ideal, the density is constant and that the fluid motion is irrotational, the pressure field p is related to the velocity field $\mathbf{v}$ via the generalized Bernoulli equation

$$\frac{\partial \phi}{\partial t} + p + \frac{1}{2} v^2 = \mathcal{F}(t) \tag{2.68}$$

where ϕ denotes the velocity potential and $\mathcal{F}(t)$ is an arbitrary function of time, usually specified by the boundary conditions. A dimensionless complex form of equation (2.68) is given by

$$C_p(z,\tau) = 1 - V(z,\tau)\, V^*(z,\tau) - 2\,\Re\left(\frac{\partial}{\partial \tau} W(\zeta,\tau)\right)_{\zeta(z)} \tag{2.69}$$

where

$$C_p = \frac{p - p_\infty}{\frac{1}{2}\rho v_\infty^2} \tag{2.70}$$

is the pressure coefficient and V is the complex velocity in the airfoil-plane z. The analytical expressions of the complex potential and velocity field can be found in appendix 2 A.

A more effective way to predict the unsteady aerodynamic forces exerted by a perfect, incompressible, irrotational two-dimensional flow on a body is offered by the circulation theory of Kármán & Burgers [5].

The equation of motion for an ideal and incompressible fluid can be written as

$$\frac{\partial \mathbf{u}}{\partial t} = -\nabla\left(p + \frac{u^2}{2}\right) + \mathbf{u} \times \boldsymbol{\omega} + \mathbf{f} \tag{2.71}$$

where $\mathbf{f}$ denotes an external force per unit mass. Equation (2.71) shows that the term $\mathbf{u} \times \boldsymbol{\omega}$ acts as an equivalent body force called the *vortex force*.

Integrating equation (2.71) upon a fixed volume V yields

$$\frac{\partial}{\partial t} \iiint \mathbf{u}\, \mathrm{d}V = -\iint \left(p + \frac{u^2}{2}\right) \mathrm{d}S + \iiint \mathbf{u} \times \boldsymbol{\omega}\, \mathrm{d}V + \iiint \mathbf{f}\, \mathrm{d}V \tag{2.72}$$

In this equation the left-hand side is the rate of change of momentum of the fluid inside V.

A body moving relatively to a fluid can be replaced kinematically by a distribution of image vorticity. This concept, together with balance considerations made on equation (2.72), leads to a relationship between the aerodynamic force exerted on the body and the rate of change of the hydrodynamic impulse. More precisely, in a two-dimensional flow the following quantities can be defined:

- hydrodynamic impulse

$$\mathbf{I} = \iint \omega\, \mathbf{r} \times \hat{k}\, \mathrm{d}A \tag{2.73}$$

- hydrodynamic angular impulse

$$\mathbf{A} = -\hat{k}\, \frac{1}{2} \iint \omega\, r^2\, \mathrm{d}A \tag{2.74}$$

Hence, the total impulse and angular impulse of a given distribution of line-vortices in the presence of a body are given by

$$\mathbf{I} = \sum_i \Gamma_i \mathbf{r}_i \quad \text{and} \quad \mathbf{A} = -\hat{k}\frac{1}{2}\sum_i \Gamma_i r_i^2 \tag{2.75}$$

where a summation over all the vortex pairs (oncoming and image vortices) constituting the flow system has been performed. Finally, the force and the moment exerted by the fluid on the body are given by

$$\mathbf{F} = -\frac{\mathrm{d}\mathbf{I}}{\mathrm{d}t} \quad \text{and} \quad \mathbf{M} = \frac{\mathrm{d}\mathbf{A}}{\mathrm{d}t} \tag{2.76}$$

which shows that the aerodynamic force exerted on the body only depends on the kinematics of the vortex pair system.

2.3 Conclusions

In this chapter we described an analytical model for the vortex-airfoil interaction problem. The formulation was based on the circulation theory and on a Kármán-Trefftz conformal mapping.

The unsteady, incompressible flow of a given distribution of line-vortices past a thick and cambered airfoil was described by using image vortices inside the airfoil. Furthermore, an unsteady Kutta condition was applied by requiring the velocity to be finite at the airfoil trailing edge. As a result, a vortical wake was shed into the field.

Two models of the airfoil wake were described: a fixed-wake model and a free-wake model. The former consists in a vortex-sheet convected at a constant velocity along a rectilinear path, whereas the latter consists in a distribution of discrete-vortices shed from the trailing edge and convected at the local flow velocity. In a fixed-wake model the Kutta condition leads to an integral equation for the wake circulation. The kernel of this equation depends on the geometrical parameter of the airfoil (thickness, camber and trailing edge angle), and the right-hand side depends on the position and circulation of the oncoming vortex. In a free-wake formulation an algebraic equation is solved at each time-step in order to determine the circulation of a nascent vortex that satisfies a zero velocity Kutta condition at the trailing edge.

In chapter 4 results obtained by means of the fixed-wake model will be compared to results obtained by means of the free-wake model. Therefore, the main interest in a fixed-wake formulation lies on the possibility of investigating the physical consistency of an approximation which is commonly made in both unsteady aerodynamics and aeroacoustics.

The main results of the present chapter are essentially two:

- the analytical description of the aerodynamic force exerted on the airfoil as a function of the vortex pair kinematics;

- the analytical description of the potential and velocity field past the airfoil.

In chapter 3 the aerodynamic force and moment exerted on the body will be interpreted as sources of aerodynamic noise. Furthermore, the potential and velocity field will be used to characterize the aeroacoustic source distribution on the airfoil surface.

Appendix 2 A

Analytical Results

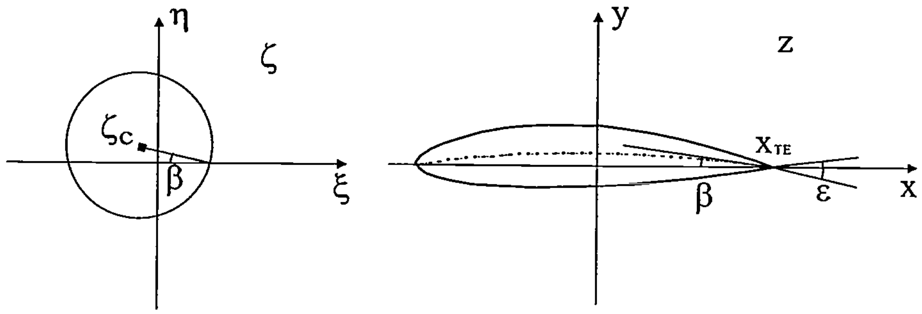

FIGURE 2.12: Kármán-Trefftz conformal mapping.

In this appendix the analytical results of a vortex-airfoil interaction problem are presented. The airfoil is obtained by transforming a circle in the ζ-plane into a Kármán-Trefftz airfoil in the $z-$plane via the conformal mapping transformation

$$z = (\theta/4)\,\frac{(\zeta + 1/4)^{\theta} + (\zeta - 1/4)^{\theta}}{(\zeta + 1/4)^{\theta} - (\zeta - 1/4)^{\theta}} \tag{2.77}$$

where

$$\theta = 2 - \frac{\epsilon}{\pi} \tag{2.78}$$

with ϵ denoting the value of the trailing edge angle (see Fig.2.12). The circle is defined as

$$\zeta = \zeta_c + R_c \mathrm{e}^{\mathrm{i}\,\theta} \qquad -\beta \leq \theta < 2\pi - \beta \tag{2.79}$$

where

$$\zeta_c = \xi_c + \mathrm{i}\eta_c \tag{2.80}$$

is the center of the circle,

$$R_c = \sqrt{(\xi_{TE} - \xi_c)^2 + \eta_c^2} \tag{2.81}$$

is the radius of the circle and

$$\beta = \tan^{-1}\left(\frac{\eta_c}{\xi_{TE} - \xi_c}\right) \tag{2.82}$$

is the airfoil camber. The circle point corresponding to $\theta = -\beta$ maps into the airfoil trailing edge x_{TE}.

In the following paragraphs, the expressions of the complex potential field, velocity field and acceleration field of an isolated vortex convected past a Kármán-Trefftz airfoil are reported. Subscripts s, v and w denote steady, vortex and wake contributions, respectively. If more than one oncoming vortex is present in the field, formulae accounting for the vortex contribution must be extended by summation.

In the expressions below, the wake contribution is supposed to be generated by a fixed vortex-sheet lying on the real axis x. In the case of a free-wake model, the integral over the wake must be replaced by a summation over the wake vortices.

Potential field

$$
\begin{aligned}
W_s(\zeta') &= \mathrm{e}^{-\mathrm{i}\alpha}\zeta' + \frac{R_c^2}{\zeta'}\mathrm{e}^{\mathrm{i}\,\alpha} + \mathrm{i}\frac{\Gamma_s}{2\pi}\ln\zeta' && (2.83)\\
W_v(\zeta') &= -\mathrm{i}\frac{\Gamma}{2\pi}\left\{\ln\Big(\zeta'-\zeta_v'\Big) - \ln\Big(\zeta' - \frac{R_c^2}{\zeta_v'^*}\Big) + \ln\zeta'\right\} && (2.84)\\
W_w(\zeta') &= -\frac{\mathrm{i}}{2\pi}\int_0^\tau \ln\left(\frac{\zeta'-\zeta_w'}{\zeta'-R_c^2/\zeta_w'^*}\right)\gamma(\sigma)\,\mathrm{d}\sigma && (2.85)
\end{aligned}
$$

Velocity and acceleration field

$$
\begin{aligned}
V_s^*(z) &= \frac{\partial\zeta}{\partial z}\left(\mathrm{e}^{-\mathrm{i}\,\alpha} - \frac{R_c^2}{\zeta'^2}\mathrm{e}^{\mathrm{i}\,\alpha} + \mathrm{i}\,\frac{\Gamma_s}{2\pi\,\zeta'}\right) && (2.86)\\
V_v^*(z,\tau) &= -\mathrm{i}\,k\,\frac{\partial\zeta}{\partial z}\left(\frac{1}{\zeta'-\zeta_v'} - \frac{1}{\zeta'-R_c^2/\zeta_v'^*} + \frac{1}{\zeta'}\right) && (2.87)\\
V_w^*(z,\tau) &= -\frac{\mathrm{i}}{2\,\pi}\frac{\partial\zeta}{\partial z}\int_0^\tau\left[\frac{1}{\zeta'-\zeta_w'} - \frac{1}{\zeta'-R_c^2/\zeta_w'^*}\right]\gamma(\sigma)\,\mathrm{d}\sigma && (2.88)\\
\frac{\partial V_v^*}{\partial\tau}(z,\tau) &= -\mathrm{i}\,k\,\frac{\partial\zeta}{\partial z}\,\frac{1}{(\zeta'-\zeta_v')^2}\left(\frac{\partial\zeta}{\partial z}\right)_{\zeta_v'} V_c - \mathrm{i}\,k\,\frac{\partial\zeta}{\partial z}\,\frac{R_c^2/\zeta_v'^{*2}}{(\zeta'-R_c^2/\zeta_v'^*)^2}\left(\frac{\partial\zeta}{\partial z}\right)^*_{\zeta_v'} V_c^* && (2.89)\\
\frac{\partial V_w^*}{\partial\tau}(z,\tau) &= -\frac{\mathrm{i}}{2\,\pi}\frac{\partial\zeta}{\partial z}\int_0^\tau\left\{\frac{1}{(\zeta'-\zeta_w')^2} + \frac{R_c^2/\zeta_w'^{*2}}{(\zeta'-R_c^2/\zeta_w'^*)^2}\right\}\frac{\partial\zeta_w'}{\partial\tau}\gamma(\sigma)\,\mathrm{d}\sigma && (2.90)
\end{aligned}
$$

where V_c denotes the vortex convection velocity in the z-plane.

First order time derivatives of the potential field

$$
\begin{aligned}
\frac{\partial W_v}{\partial\tau}(z,\tau) &= \mathrm{i}\,k\,\frac{1}{\zeta'-\zeta_v'}\left(\frac{\partial\zeta}{\partial z}\right)_{\zeta_v'} V_c + \mathrm{i}\,k\,\frac{R_c^2/\zeta_v'^{*2}}{\zeta'-R_c^2/\zeta_v'^*}\left(\frac{\partial\zeta}{\partial z}\right)^*_{\zeta_v'} V_c^* && (2.91)\\
\frac{\partial W_w}{\partial\tau}(z,\tau) &= \frac{\mathrm{i}}{2\,\pi}\int_0^\tau\frac{1}{\zeta'-\zeta_w'}\,\frac{\partial\zeta_w'}{\partial\tau}\gamma(\sigma)\,\mathrm{d}\sigma + \frac{\mathrm{i}}{2\,\pi}\int_0^\tau\frac{R_c^2/\zeta_w'^{*2}}{\zeta'-R_c^2/\zeta_w'^*}\,\frac{\partial\zeta_w'}{\partial\tau}\gamma(\sigma)\,\mathrm{d}\sigma && (2.92)
\end{aligned}
$$

Second order time derivatives of the potential field

$$
\begin{aligned}
\frac{\partial^2 W_v}{\partial\tau^2}(z,\tau) &= \mathrm{i}\,k\,\frac{1}{(\zeta'-\zeta_v')^2}\left[\left(\frac{\partial\zeta}{\partial z}\right)_{\zeta_v'} V_c\right]^2 + \mathrm{i}\,k\,\frac{1}{\zeta'-\zeta_v'}\,\frac{\partial^2\zeta_v'}{\partial\tau^2}\\
&- \mathrm{i}\,k\,\frac{R_c^2\left(2\zeta'\zeta_v'^* - R_c^2\right)}{\zeta_v'^{*2}\,(\zeta'\zeta_v'^* - R_c^2)^2}\left[\left(\frac{\partial\zeta}{\partial z}\right)^*_{\zeta_v'} V_c^*\right]^2 + \mathrm{i}\,k\,\frac{R_c^2/\zeta_v'^{*2}}{\zeta'-R_c^2/\zeta_v'^*}\,\frac{\partial^2\zeta_v'^*}{\partial\tau^2} && (2.93)\\
\frac{\partial^2 W_w}{\partial\tau^2}(z,\tau) &= \frac{\mathrm{i}}{2\,\pi}\int_0^\tau\frac{1}{(\zeta'-\zeta_w')^2}\left(\frac{\partial\zeta_w'}{\partial\tau}\right)^2\gamma(\sigma)\,\mathrm{d}\sigma\\
&+ \frac{\mathrm{i}}{2\,\pi}\int_0^\tau\frac{1}{\zeta'-\zeta_w'}\left(\frac{\partial^2\zeta_w'}{\partial\tau^2}\right)\gamma(\sigma)\,\mathrm{d}\sigma
\end{aligned}
$$

$$
\begin{aligned}
&- \frac{\mathrm{i}}{2\pi}\int_0^\tau \frac{R_c^2\left(2\zeta'\zeta_w'^* - R_c^2\right)}{\zeta_w'^{*2}\,(\zeta'\zeta_w'^* - R_c^2)^2}\left(\frac{\partial\zeta_w'}{\partial\tau}\right)^2 \gamma(\sigma)\;\mathrm{d}\sigma \\
&+ \frac{\mathrm{i}}{2\pi}\int_0^\tau \frac{R_c^2/\zeta_w'^{*2}}{\zeta' - R_c^2/\zeta_w'^*}\left(\frac{\partial^2\zeta_w'}{\partial\tau^2}\right)\gamma(\sigma)\;\mathrm{d}\sigma
\end{aligned} \tag{2.94}
$$

where

$$
\frac{\partial^2\zeta_v'}{\partial\tau^2} = \left(\frac{\partial^2\zeta}{\partial z^2}\right)_{\zeta_v'} V_c^2 + \left(\frac{\partial\zeta}{\partial z}\right)_{\zeta_v'} A_c \tag{2.95}
$$

with A_c denoting the vortex acceleration in the z-plane.

Mapping rules

$$
\frac{\partial\zeta}{\partial z} = \frac{2}{\theta}\frac{(a_1 - a_2)^2}{a_1 b_2 - a_2 b_1} \tag{2.96}
$$

$$
\frac{\partial^2\zeta}{\partial z^2} = \left(\frac{\partial\zeta}{\partial z}\right)^2 \left[2\frac{b_1 - b_2}{a_1 - a_2} - \frac{a_1 c_2 - a_2 c_1}{a_1 b_2 - a_2 b_1}\right] \tag{2.97}
$$

$$
\zeta_w'(\sigma,\tau) = R_c\,\mathrm{e}^{-\mathrm{i}\,\beta} + \frac{1}{2}\frac{f_1}{f_2 - f_1} \tag{2.98}
$$

$$
\frac{\partial\zeta_w'}{\partial\tau}(\sigma,\tau) = -\frac{1}{2}\frac{f_1 g_2 - f_2 g_1}{(f_2 - f_1)^2} \tag{2.99}
$$

$$
\frac{\partial^2\zeta_w'}{\partial\tau^2}(\sigma,\tau) = -\frac{f_1 h_2 - f_2 h_1}{2\,(f_2 - f_1)^2} + \frac{(f_1 g_2 - f_2 g_1)\,(g_2 - g_1)}{(f_2 - f_1)^3} \tag{2.100}
$$

where

$$
\begin{aligned}
a_{\frac{1}{2}} &= (\zeta \pm 1/4)^\theta \\
b_{\frac{1}{2}} &= \theta\,(\zeta \pm 1/4)^{\theta-1} \\
c_{\frac{1}{2}} &= \theta\,(\theta - 1)\,(\zeta \pm 1/4)^{\theta-2} \\
f_1 &= (\tau - \sigma)^{\frac{1}{\theta}} \\
g_1 &= \frac{1}{\theta}\,(\tau - \sigma)^{\frac{1}{\theta}-1} \\
h_1 &= \frac{1}{\theta}\left(\frac{1}{\theta} - 1\right)(\tau - \sigma)^{\frac{1}{\theta}-2} \\
f_2 &= \left(\tau - \sigma + \frac{\theta}{2}\right)^{\frac{1}{\theta}} \\
g_2 &= \frac{1}{\theta}\left(\tau - \sigma + \frac{\theta}{2}\right)^{\frac{1}{\theta}-1} \\
h_2 &= \frac{1}{\theta}\left(\frac{1}{\theta} - 1\right)\left(\tau - \sigma + \frac{\theta}{2}\right)^{\frac{1}{\theta}-2}
\end{aligned} \tag{2.101}
$$

Appendix 2 B

Time Integration Schemes

In this appendix the time integration schemes used in the numerical solution of the vortex-airfoil interaction problem are described. These are concerned with: i) the trajectory of an oncoming vortex, ii) the integral equation in a fixed-wake formulation, iii) the trajectory of a wake vortex in a free-wake formulation.

The trajectory of an oncoming vortex is calculated by numerical integration of equation (2.40) by means of a four-step Runge-Kutta time integration scheme. The velocity of the vortex is computed at regular time intervals by means of equation (2.41) and the position is updated according to the four-step scheme

$$\begin{aligned} z_v^1 &= z_v^{j-1} + \frac{\Delta\tau}{2} V_c\left(z_v^{j-1}\right) \\ z_v^2 &= z_v^{j-1} + \frac{\Delta\tau}{2} V_c\left(z_v^1\right) \\ z_v^3 &= z_v^{j-1} + \Delta\tau V_c\left(z_v^2\right) \\ z_v^j &= z_v^{j-1} + \frac{\Delta\tau}{6}\left(V_c\left(z_v^{j-1}\right) + 2V_c\left(z_v^1\right) + 2V_c\left(z_v^2\right) + V_c\left(z_v^3\right)\right) \end{aligned} \tag{2.102}$$

where $\Delta\tau$ denotes the time integration step.

The integral equation (2.38) is solved by a second-order collocation scheme where the singularity at $\sigma = \tau$ is numerically integrated. At the time-step τ^j, equation (2.38) can be written as

$$\int_{\tau^{j-1}}^{\tau^j} \left\{1 - 4R_c\cos\beta\left[1 - \left(\frac{\tau-\sigma+\theta/2}{\tau-\sigma}\right)^{\frac{1}{\theta}}\right]\right\}\gamma(\sigma)\,\mathrm{d}\sigma = f\left(\tau^{j-1}\right) \tag{2.103}$$

where the known term is given by

$$f\left(\tau^{j-1}\right) = \Gamma\phi\left(\zeta_v\left(\tau^{j-1}\right)\right) - \int_0^{\tau^{j-1}} \left\{1 - 4R_c\cos\beta\left[1 - \left(\frac{\tau-\sigma+\theta/2}{\tau-\sigma}\right)^{\frac{1}{\theta}}\right]\right\}\gamma(\sigma)\,\mathrm{d}\sigma \tag{2.104}$$

By setting $\tau - \sigma = \Delta\tau\,(1-x)$, equation (2.103) takes the form

$$\int_0^1 K(x)\,\gamma(x)\;\mathrm{d}x = f\left(\tau^{j-1}\right) \tag{2.105}$$

whose kernel is given by

$$K(x) = \Delta t\left\{1 - 4R_c\cos\beta\left[1 - \left(1 + \frac{\theta/2}{\Delta t\,(1-x)}\right)^{\frac{1}{\theta}}\right]\right\} \tag{2.106}$$

Assuming a parabolic behaviour of $\gamma(x)$ in the interval $(-1,1)$ provides

$$\gamma(x) = \gamma_{j-2}\left(\frac{x^2}{2}-\frac{x}{2}\right) + \gamma_{j-1}\left(-x^2+1\right) + \gamma_j\left(\frac{x^2}{2}+\frac{x}{2}\right) \tag{2.107}$$

which can be substituted into equation (2.105) yielding

$$\begin{aligned}&\gamma_j \int_0^1 K(x)\left(\frac{x^2}{2}+\frac{x}{2}\right)\,\mathrm{d}x \\ &= -\gamma_{j-2}\int_0^1 K(x)\left(\frac{x^2}{2}-\frac{x}{2}\right)\,\mathrm{d}x - \gamma_{j-1}\int_0^1 K(x)\left(-x^2+1\right)\,\mathrm{d}x + f\left(\tau^{j-1}\right)\end{aligned} \tag{2.108}$$

These integrals can be evaluated numerically taking their limit values for $x \to 1$. Thus, setting

$$\mathcal{I}_0 = \lim_{x\to 1}\int_0^1 K(x)\left(\frac{x^2}{2}+\frac{x}{2}\right)\,\mathrm{d}x \tag{2.109}$$

$$\mathcal{I}_1 = \lim_{x\to 1}\int_0^1 K(x)\left(-x^2+1\right)\,\mathrm{d}x \tag{2.110}$$

$$\mathcal{I}_2 = \lim_{x\to 1}\int_0^1 K(x)\left(\frac{x^2}{2}-\frac{x}{2}\right)\,\mathrm{d}x \tag{2.111}$$

leads to

$$\gamma_j = \frac{f\left(\tau^{j-1}\right) - \mathcal{I}_1\Gamma_{\gamma-1} - \mathcal{I}_2\Gamma_{\gamma-2}}{\mathcal{I}_0} \tag{2.112}$$

In a free-wake formulation, the trajectory of each wake vortex is computed by the Adams-Bashfort second order scheme, i.e.

$$z_w^j = z_w^{j-1} + \Delta t\left(\frac{3}{2}V_c^{j-1} - \frac{1}{2}V_c^{j-2}\right) \tag{2.113}$$

which is stable when applied to a nonlinear equation. The convection velocity $V_c = V_c(z_w)$ is calculated by means of equation (2.41).

Appendix 2 C

Blob-Vortex Method

In this appendix we describe the method used to desingularize the kernel of a line-vortex.

The velocity induced by a line-vortex at its own location is singular. As a consequence, a line-vortex method is numerically unstable and the trajectories of the vortices have a chaotic behaviour as their number increases or the time-step decreases. Aref [18] demonstrated that a system of line-vortices in free space, moving under their mutual induction effect, is chaotic if the number of vortices is equal to or larger than 4. Instabilities may be damped by smoothing the velocity in a small region, called core, around the center of the vortex. Methods based on a desingularised vortex core are called *blob-vortex methods.*

A line-vortex located in z_j induces the following velocity

$$v^*(z) = \Gamma K_{BS}(z - z_j) \tag{2.114}$$

where $K_{BS}(z) = -\mathrm{i}/2\pi z$ is the Biot-Savart kernel. A simple desingularisation method is based on a viscous core upon which the vorticity ω is uniformly distributed, say Rankine vortex core. If the core is supposed to be a circle of radius δ, the Stokes theorem yields

$$\int_0^\delta \omega\, 2\pi\, r\, \mathrm{d}r = \Gamma \tag{2.115}$$

Thus, since ω is constant within the vortex core, it results that

$$\omega = \frac{\Gamma}{\pi\delta^2} \tag{2.116}$$

The velocity induced in the field for $|z| > \delta$ is equal to the velocity induced by a line-vortex, whereas in the core region $|z| < \delta$ the Stokes theorem yields

$$V(r)\, 2\pi r = \int_{A(r)} \omega \mathrm{d}A \tag{2.117}$$

and, by substituting (2.116)

$$V(r) = \frac{\Gamma}{2\pi\delta^2}\, r \tag{2.118}$$

Concluding, by assuming a Rankine vortex core, the desingularised kernel takes the form

$$K(z) = K_{BS}(z)\, \mathcal{D}\left(|z|\right) \tag{2.119}$$

where

$$\mathcal{D}\left(|z|\right) = \min\left[1, \frac{|z|^2}{\delta^2}\right] \tag{2.120}$$

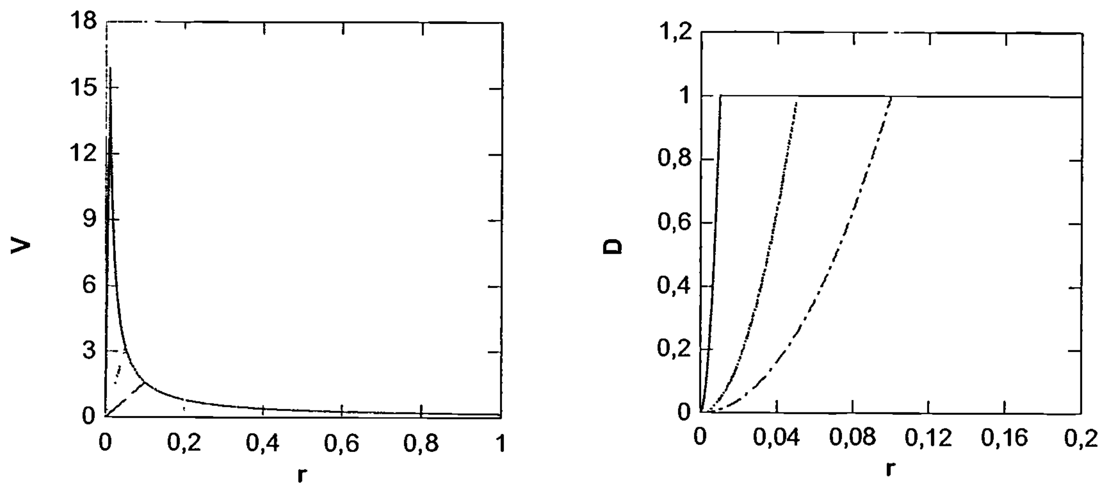

a) Desingularised induced velocity.

b) Desingularised viscous kernel.

FIGURE 2.13: Effect of the cut-off distance δ on the Rankine blob-vortex model (2.120). —— $\delta = 0.01$; - - - - $\delta = 0.05$; - - - $\delta = 0.1$.

The core parameter δ plays the role of an artificial viscosity. It allows the vorticity to have a finite value and to occupy a small but finite region rather than being zero everywhere except at the vortex location where it is infinite. The diffusion of the vorticity within the core is artificial. The cut-off distance δ is indeed a parameter of the computation method and is not cumulative in time.

The induced velocity $v^*(z) = \Gamma K(z - z_j)$ reaches its maximum at a distance δ from the center. It thus results that

$$\delta = \frac{2\pi}{V_{max}} \tag{2.121}$$

As shown in Fig.2.13(a) the radial derivative of the tangential velocity $v^*(z)$ is discontinuous at the cut-off distance δ. Therefore, a different desingularised kernel may be proposed in order to smooth the induced velocity around the maximum value. The desingularised kernel (2.120) can be approximated by the Gaussian kernel

$$\mathcal{D}'\left(|z|\right) = 1 - e^{-\frac{|z|^2}{\beta^2}} \tag{2.122}$$

where the new core parameter β replaces the cut-off distance δ. The induced velocity takes the form

$$V(r) = \frac{\Gamma}{2\pi r}(1 - e^{-\frac{r^2}{\beta^2}}) \tag{2.123}$$

The tangential velocity reaches its maximum value at a distance $r \simeq 1.1208\ \beta$ from the center of the vortex. It thus results that

$$V_{max} \simeq 0.1016\ \frac{\Gamma}{\beta} \tag{2.124}$$

The parameter β may be chosen in order to ensure the same value of V_{max} or the same maximum velocity radius of the desingularised kernel (2.119). In the first case $\beta_1 \simeq 0.8922\ \delta$, while in the second case $\beta_2 \simeq 0.6382\ \delta$. In Fig.2.14 the velocity resulting from the desingularised kernels (2.120) and (2.122) are compared, the latter for the core parameters β_1 and β_2.

The core kernel (2.122) has a physical relevance. By supposing that the vorticity field ω depends only on the radial distance r, equation (2.6) takes the form

$$\frac{\partial \omega}{\partial t} - \nu \left(\frac{\partial^2 \omega}{\partial r^2} - \frac{1}{r}\frac{\partial \omega}{\partial r} \right) = 0 \tag{2.125}$$

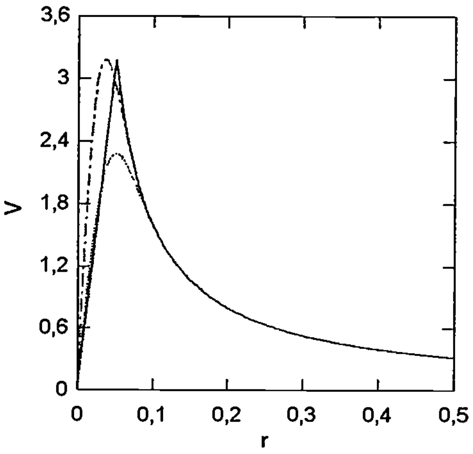

a) Desingularised induced velocity.

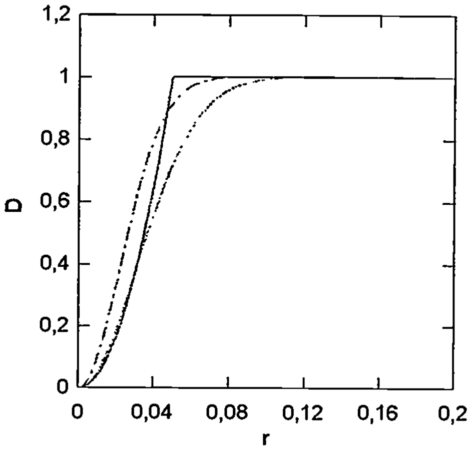

b) Desingularised viscous kernel.

FIGURE 2.14: Comparison between the Rankine blob-vortex model (2.120) and the Gaussian blob-vortex model (2.122). —— $\delta = 0.05$; - - - - $\beta = 0.0446$; – – – $\beta = 0.0319$.

where ν is the laminar viscosity of the flow. If ω is supposed to be initially zero everywhere except for $r = 0$, equation (2.125) has the analytical solution

$$\omega(r,t) = \frac{\Gamma}{\pi 4\nu t} e^{-\frac{r^2}{4\nu t}} \tag{2.126}$$

The related velocity distribution is

$$V(r,t) = \frac{\Gamma}{2\pi r}\left(1 - e^{-\frac{r^2}{4\nu t}}\right) \tag{2.127}$$

A comparison between equations (2.123) and (2.127) shows that the parameter β has an artificial viscous nature, although its effect is not cumulative in time. Thus, a desingularised kernel based on equation (2.122) is well consistent with the viscous diffusion occurring in a vortex core. Finally, it should be observed that

$$\int_0^\infty \omega\,(r)\, 2\pi r \,\mathrm{d}r = \Gamma \tag{2.128}$$

for each value assumed by the variable $4\nu t$. Thus, the Gaussian blob-vortex model (2.122) is integrally equivalent both to a line-vortex, namely $\omega(z) = \Gamma\,\delta(z - z_j)$, and to a Rankine blob-vortex model (2.119).

Different blob-vortex models have been proposed in the past. The most commonly used desingularised kernels are those proposed by Sculley [28], i.e.

$$K(z) = K_{BS}(z)\,\frac{|z|^2}{\delta^2 + |z|^2} \tag{2.129}$$

and by Beale & Majda [29], i.e.

$$K(z) = K_{BS}(z)\left\{1 - \sum_{k=1}^{k_{\max}} a_k \exp\left(-b_k \frac{|z|^2}{\delta^2}\right)\right\} \tag{2.130}$$

In the present work the Gaussian desingularised kernel (2.122) is used, which corresponds to the first term of Beale & Majda's model (2.130). The core parameter β is related to a fixed maximum value of the induced velocity, i.e.

$$\beta = 0.1016\frac{\Gamma}{V_{\mathsf{max}}} \tag{2.131}$$

Appendix 2 D

Amalgamation

In this appendix we describe a technique which permits to improve the computational performances of a free-wake discrete vortex method.

When a free-wake model is used, the number of shed vortices increases progressively as the computation goes on. Thus, in order to contain the computational time, the maximum number of vortices instantaneously present in the field can be fixed to an arbitrary value N_w. At the $(N_w + 1)th$ time-step the first vortex is amalgamated with the second one and takes index 2. Then the nascent vortex takes index 1. At the next time-step the second and the third vortex are amalgamated while the $(N_w + 2)th$ nascent vortex takes index 2. Analogously for successive time-steps.

As shown by Lamb [14], a convected system of line-vortices in free space is characterized by some invariants. An amalgamation process involves only three quantities, namely the circulation of the vortices and their co-ordinates. Consequently, only the total circulation and the position of the center of vorticity can be conserved during an amalgamation process. Hence, the circulation and the position of the resulting vortex are

$$\Gamma_{\text{new}} = \Gamma_1 + \Gamma_2 \tag{2.132}$$

and

$$z_{\text{new}} = \frac{\Gamma_1 \, z_1 + \Gamma_2 \, z_2}{\Gamma_{\text{new}}} \tag{2.133}$$

In the presence of a physical surface, the velocity induced by the amalgamated vortex can differ considerably from the velocity induced by the separated vortices. However, if a sufficiently large number N_w of coexisting vortices is assumed, the distance between the airfoil and the downstream end of the wake where amalgamation occurs is such that the amalgamation process affects the flow past the airfoil only negligibly.

3

Vortex-Airfoil Interaction: Acoustic Modeling

In this chapter we are concerned with an analytical description of the vortex-airfoil interaction noise. The aerodynamic formulation developed in chapter 2 provides a conceptual basis for an aeroacoustic characterization of the vortex-airfoil interaction problem.

In the first section, an acoustic analogy approach based on the Ffowcs Williams & Hawkings [2] formulation is described. It shows that the main sound generation mechanism is related to the time derivative of the pressure field on the airfoil surface. Therefore, an analytical decomposition of the wall pressure field is proposed as a way to investigate the aeroacoustic source distribution on the airfoil surface. The same approach is employed to investigate the effects of the Kutta condition on the sound generation.

In the second section, a linear aeroacoustic model proposed by Howe [30] is used to describe the noise generated by a double row of counter-rotating vortices convected past a flat-plate.

In the final section, a low Mach number model is proposed for the vortex-airfoil interaction noise. It is based on a matched asymptotic expansion of the hydrodynamic pressure field near the airfoil and the acoustic far field. This approach allows to relate the multipole structure of the far pressure field to the aerodynamic force and moment exerted on the airfoil.

3.1 Acoustic Analogy Approach

The Ffowcs Williams & Hawkings [2] (FEW-H) acoustic analogy approach, in the form described in chapter 6, can be used to predict the aerodynamic noise generated by vortical disturbances convected past a Kármán-Trefftz airfoil.

The unsteady aerodynamic field necessary for the acoustic analogy prediction is supplied by the semi-analytical methodology developed in chapter 2.

The FW-H analogy is applied by integrating the aerodynamic field upon the physical surface of the airfoil. In addition, the observer and the airfoil are supposed to translate at the same velocity $-V_\infty(\cos\alpha, \sin\alpha)$.

At low free-stream Mach numbers the aerodynamic noise from a fluctuating flow field in proximity of a rigid surface is essentially due to the pressure fluctuations induced on the surface. Thus, the noise contribution generated *directly* by the velocity fluctuations can be neglected. Accordingly, in the present study, the quadrupole-noise contribution (6.43) is neglected and no volume integrations are performed. Furthermore, the unsteady contribution of the thickness-noise (6.41) vanishes identically because the airfoil has a constant forward velocity and the observer is fixed in a reference frame moving with the airfoil. Therefore, only the loading-noise contribution (6.42) is taken into account. This requires the pressure field and its time derivative to be defined on the airfoil surface. The loading-noise contribution

(6.42) tailored to the present case reduces to

$$\begin{aligned} p'(\mathrm{x},t) &= \frac{p_d}{2\pi} M_\infty \int_0^{L/2} \mathrm{d}Z \int_{\mathcal{L}} \left[\dot{C}_p\right] \frac{\hat{n}_i \hat{r}_i}{R\,(1-M_r)^2} \mathrm{d}\mathcal{L} \\ &+ \frac{p_d}{2\pi} \int_0^{L/2} \mathrm{d}Z \int_{\mathcal{L}} [C_p] \left\{ \frac{\hat{n}_i\,(\hat{r}_i - M_i)}{R^2\,(1-M_r)^2} + \frac{\hat{n}_i \hat{r}_i\,(M_r - M^2)}{R^2\,(1-M_r)^3} \right\} \mathrm{d}\mathcal{L} \end{aligned} \tag{3.1}$$

where $p_d = \rho_0 V_\infty^2/2$ denotes the free-stream dynamic pressure, C_p is the wall pressure coefficient, $\mathcal{L}$ and $L = l/c$ are the dimensionless contour and span of the airfoil, respectively, R is the dimensionless distance between the listener and a point source on the airfoil surface, $\hat{\mathbf{n}}$ is the unit outward normal vector to $\mathcal{L}$ and $\hat{\mathbf{r}}$ is the unit vector in the radiation direction. The square brackets [...] enclose quantities evaluated at the dimensionless retarded time

$$\tau_{\mathrm{ret}} = \tau - R\,M_\infty \frac{-M_r + \sqrt{M_r^2 + 1 - M_\infty^2}}{1 - M_\infty^2} \tag{3.2}$$

where M_r is the surface Mach number in the radiation direction. Equation (3.1) assumes that the three-dimensional flow necessary for the acoustic prediction is obtained through a spanwise repetition of a two-dimensional flow.

Interestingly, equation (3.1) shows that the *far field* depends on the time derivative of the wall pressure coefficient, whereas the *near field* depends on the pressure coefficient. Furthermore, the constants behind the far field and the near field integrals are proportional to M_∞^3 and M_∞^2, respectively.

3.2 Aeroacoustic Sources

The loading-noise contribution (3.1) depends on the wall pressure coefficient and its time derivative. Therefore, the pressure coefficient must be determined in order to perform an aeroacoustic prediction. In chapter 2 we proposed a semi-analytical methodology to describe the incompressible, potential field past a Kármán-Trefftz airfoil. Hence, the Bernoulli equation can be used to determine the unsteady pressure field, i.e.

$$C_p(z,\tau) = 1 - V(z,\tau)\,V^*(z,\tau) - 2\,\Re\left(\frac{\partial}{\partial \tau} W(\zeta,\tau)\right)_{\zeta(z)} \tag{3.3}$$

where C_p is the pressure coefficient and V is the complex velocity in the complex airfoil-plane z.

In order to scrutinize the noise generation mechanisms during a vortex-airfoil interaction, the time derivative of C_p has been analytically obtained, that is

$$\dot{C}_p(z,\tau) = -\frac{\partial V}{\partial \tau} V^* - \frac{\partial V^*}{\partial \tau} V - 2\,\Re\left(\frac{\partial^2 W}{\partial \tau^2}\right)_{\zeta(z)} \tag{3.4}$$

This expression can be split into four contributions, according to the interaction mechanism by which such contributions are originated, i.e.

a) vortex contribution:

$$\dot{C}_{p_v} = -2\,\Re\left(V_s^* \frac{\partial V_v}{\partial \tau} + \frac{\partial^2 W_v}{\partial \tau^2}\right) \tag{3.5}$$

b) wake contribution:

$$\dot{C}_{p_w} = -2\,\Re\left(V_s^* \frac{\partial V_w}{\partial \tau} + \frac{\partial^2 W_w}{\partial \tau^2}\right) \tag{3.6}$$

c) vortex-wake interaction contribution:

$$\dot{C}_{p_{vw}} = -2\,\Re\left(V_v^* \frac{\partial V_w}{\partial \tau}\right) \tag{3.7}$$

d) wake self-interaction contribution:

$$\dot{C}_{p_{ww}} = -2\,\Re\left(V_w^* \frac{\partial V_w}{\partial \tau}\right) \tag{3.8}$$

where subscripts v and w denote the oncoming vortex and wake contributions, respectively. This analytical decomposition is used in chapter 4 to investigate the reciprocal influence of the nonlinear interaction mechanisms on the airfoil unsteady loading and sound generation. The analytical expressions of the various terms involved in the time derivative of the pressure coefficient are listed in appendix 2 A[1].

A final remark concerns the presence of fictitious sources at the trailing edge. As discussed in chapter 2, the Kutta condition is applied in the circle plane by requiring that the velocity in the point ξ_{TE} is zero. Numerically this results in a vanishing but non zero velocity at the airfoil trailing edge x_{TE}. As a consequence, because of the singular behaviour of $\mathrm{d}\zeta/\mathrm{d}z$ as $\zeta \to \xi_{TE}$, aeroacoustic source terms involving $V_v^* + V_w^*$ do not vanish identically and fictitious sources can be generated in proximity of the trailing edge. Thus, exactly at the trailing edge, a zero velocity condition will be explicitly imposed. As a result, the source term at the trailing edge has the form

$$\dot{C}_p = -2\,\Re\left(\frac{\partial^2 W_v}{\partial \tau^2}\right) - 2\,\Re\left(\frac{\partial^2 W_w}{\partial \tau^2}\right) \tag{3.9}$$

Conversely, terms evaluated at a small distance from the trailing edge will be assumed as representative of the flow behaviour in the neighborhood of the trailing edge.

3.3 A Linear Model for the Vortex-Airfoil Interaction Noise

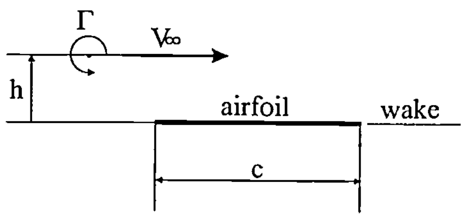

FIGURE 3.1: Interaction between a thin airfoil and a line-vortex.

Consider a flat-plate of chord c ($-c/2 \leq x_1 \leq c/2$, $x_2 = 0$) in a low Mach number stream, such that $M_\infty \ll 1$. Suppose that a vortex of circulation Γ is convected at the free-stream velocity V_∞ along the path $x_2 = h$, parallel to the airfoil chord (see Fig.3.1).

In the low Mach number limit the airfoil is acoustically compact ($c \ll \lambda$, λ denoting the acoustic wavelength). Thus, following Howe [30] (pp. 186-191), the two-dimensional vortex-airfoil interaction generates the far pressure field

$$p(r,\theta,\omega) \simeq \frac{\sin\theta}{2}\sqrt{\frac{\omega}{2\pi\mathrm{i}\, r c_0}}\, F_2(\omega)\, e^{\mathrm{i}\frac{\omega}{c_0} r} \quad \text{for} \quad \frac{r}{\lambda} \to \infty \tag{3.10}$$

[1] The wake contributions in appendix 2 A are defined for a fixed-wake model. Therefore, if a free-wake model is used the integral over the wake must be replaced by a summation over the wake vortices.

where θ is the angle to the mean flow and F_2 is the force exerted on the fluid in the normal direction to the flat-plate. Transforming back to the time domain yields[2]

$$p(r,\theta,t) \simeq \frac{\sin\theta}{2\sqrt{2\pi \mathrm{i}}\; c_0\, r} \int_{-\infty}^{\infty} \sqrt{\omega}\, F_2(\omega)\, \mathrm{e}^{-\mathrm{i}\omega(t-r/c_0)}\, \mathrm{d}\omega \tag{3.11}$$

In a linear aerodynamic context, the force exerted on the fluid by a thin airfoil embedded in a frozenly convected harmonic gust has been obtained by Sears (see section 4.3 of part II) in the form

$$F_2(\omega) = -\pi\, c\, \rho_0\, u_2(\omega)\; V_\infty\, S\!\left(\frac{\omega\, c}{2\, V_\infty}\right) \tag{3.12}$$

where u_2 is the upwash velocity induced by the gust and S is the Sears' function (4.47). The vortex convected along the constant path $x_2 = h$ is described by the vorticity field

$$\Omega(x_1, x_2, t) = \Gamma\delta(x_1 - V_\infty t)\,\delta(x_2 - h) \tag{3.13}$$

The corresponding vorticity wave in the Fourier space is

$$\Omega(x_1, x_2, \omega) = \frac{\Gamma}{2\pi V_\infty}\delta(x_2 - h)\; \mathrm{e}^{\mathrm{i}\frac{\omega x_1}{V_\infty}} \tag{3.14}$$

As shown in section 10.3.1 of part II, a vorticity wave generates an upwash velocity

$$u_2(\omega) = \frac{-\mathrm{i}\,\Gamma}{4\pi^2\, V_\infty}\, \mathrm{e}^{-\left|\frac{\omega h}{V_\infty}\right|}\, \mathrm{e}^{\mathrm{i}\,\frac{\omega x_1}{V_\infty}} \tag{3.15}$$

Thus, substituting into equation (3.12) and integrating equation (3.11) in the limit $h \ll c$ yield

$$p(r,\theta,t) \simeq \frac{\rho_0 \Gamma\, V_\infty\, \sin\theta}{4\,\pi} \sqrt{\frac{M_\infty}{r\, c/2}} \left[\frac{(V_\infty\, t + c/2)\; c/h^2}{1 + (V_\infty\, t + c/2)^2\, /h^2}\right]_{t-r/c_0} \quad \text{for} \quad r \to \infty \tag{3.16}$$

A peak of radiation occurs when the vortex passes by the airfoil leading edge ($t = -c/2\, V_\infty$). Conversely, the acoustic pressure has a regular behaviour as the vortex passes by the trailing edge. This behaviour is a consequence of the aerodynamic transfer function used in equation (3.11). As shown in section 4.3 of part II, the Sears' solution is obtained for a flat-plate with a vortex-sheet behind the trailing edge. The vortex-sheet smoothes the singular behaviour of the flow at the trailing edge. On the contrary, a singular behaviour persists at the leading edge.

The linear model described in this section can be applied to describe the interaction between a Kármán vortex street (see Fig.2.11) and a thin airfoil of chord c at zero angle of attack. In this case the acoustic pressure in the far field takes the form

$$p(r,\theta,t) = \frac{-\rho_0\, \Gamma\, V_\infty\, \sin\theta}{4\,\pi} \sqrt{\frac{M_\infty}{r\, c/2}} \left[\sum_{n=-\infty}^{\infty} \frac{(-1)^n\, (V_\infty\, t + c/2 - n\, a/2)\, (c/2)/(b/2)^2}{1 + (V_\infty\, t + c/2 - n\, a/2)^2\, /(b/2)^2}\right]_{t-r/c_0} \tag{3.17}$$

Then, substituting $\Gamma \simeq C_{l_{\max}} 2\, V_\infty\, d$, as from equation (2.61), and assuming an airfoil span l yield

$$p(r,\theta,t) = \frac{-V_\infty^2 \sqrt{M_\infty}\, \sin\theta}{\sqrt{r}} \frac{\rho_0\, C_{l_{\max}}\, l\, d}{\pi\sqrt{2c}} \left[\sum_{n=-\infty}^{\infty} \frac{(-1)^n\, (V_\infty\, t + c/2 - n\, a/2)\, c/(b/2)^2}{1 + (V_\infty\, t + c/2 - n\, a/2)^2\, /(b/2)^2}\right]_{t-r/c_0} \tag{3.18}$$

Interestingly, this model provides a fifth-power scaling law for the acoustic intensity, i.e.

$$I \propto M_\infty^5 \tag{3.19}$$

[2]The Fourier transform pair herein used is $\hat{f}(\omega) = (2\pi)^{-1} \int f(t)\, \mathrm{e}^{\mathrm{i}\,\omega\, t}\, dt$ and $f(t) = \int \hat{f}(\omega)\, \mathrm{e}^{-\mathrm{i}\,\omega\, t}\, d\omega$.

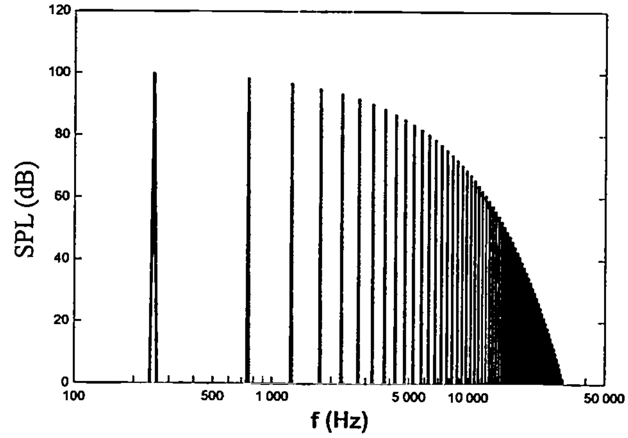

FIGURE 3.2: Spectrum of the acoustic pressure obtained from equation (3.18) with 100 counter-rotating vortices. The following values have been used: $d = 0.016\,\mathrm{m}$, $V_\infty = 20\,\mathrm{m/s}$, $a = 5d$, $b = 0.03\,a$, $C_{l_{\max}} = 0.7$, $c = 0.1\,\mathrm{m}$, $l = 0.2\,\mathrm{m}$, $r = 10\,\mathrm{m}$.

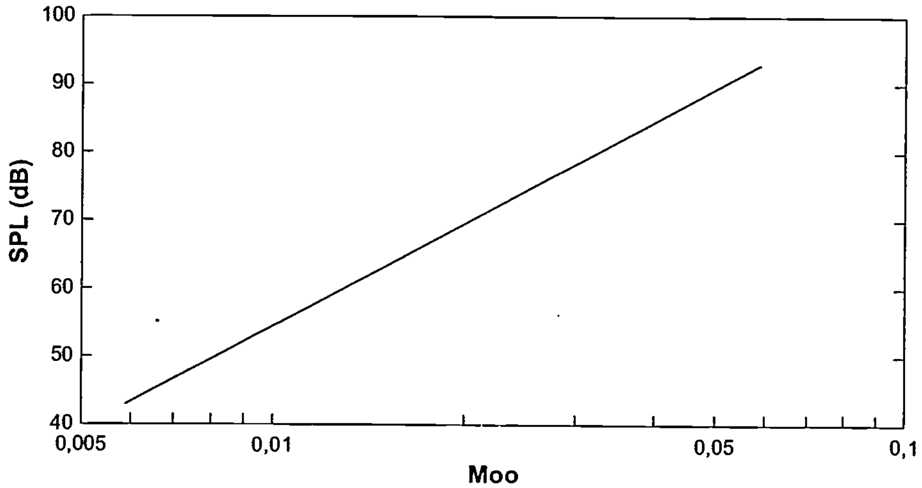

FIGURE 3.3: Maximum peak value of the acoustic radiation obtained from equation (3.18). The same parameters as in Fig.3.2 have been assumed. The free-stream velocity is increased up to the value $V_\infty = 20\,\mathrm{m/s}$.

The acoustic analogy formulation (3.1) shows that, at the leading order in the far field, the acoustic intensity from a compact airfoil scales as M_∞^6. The discrepancy between these results is due to the fact that the model described in this section is based on a *true* two-dimensional field. On the contrary, equation (3.1) is obtained for a two-dimensional flow past a finite span airfoil. This configuration corresponds to a three-dimensional acoustic field. Another interesting result is the $r^{-1/2}$ dependence of the far pressure field on the observer distance.

In Fig.3.2 the spectrum of the acoustic pressure obtained from equation (3.18) is plotted. A Kármán vortex street of 100 vortices convected at a velocity $V_\infty = 20\,\mathrm{m/s}$ has been considered. The radiation peak has a value of 99.5 dB. It is interesting to observe that only odd harmonic peaks arises $(f_0, 3f_0, \ldots)$. This is a clear consequence of the fact that, as shown in subsection 2.2.7, the upwash velocity induced by a Kármán vortex street along its axis exhibits only odd harmonics.

In Fig.3.3 the acoustic intensity against the free-stream velocity is plotted. The results show the fifth-power radiation law.

It is interesting to compare the two-dimensional linear model (3.18) of the noise radiated by a flat-plate embedded at zero incidence in a Kármán vortex street with a three-dimensional linear model.

The acoustic far field of a stationary airfoil in a low Mach number turbulent stream can be evaluated by means of the formula

$$p(r,\theta,t) = -\frac{\sin\theta}{4\pi c_0 r}\left[\frac{\partial F}{\partial \tau}\right]_{\tau=t-r/c_0} \tag{3.20}$$

where F denotes the fluctuating lift induced on the airfoil. Thus setting

$$F(t) = \sum_{n=-\infty}^{n=\infty} F_n\, \mathrm{e}^{-\mathrm{i}\, n 2\pi f_0\, t} \tag{3.21}$$

with

$$F_n = f_0 \int_{-\frac{1}{2f_0}}^{\frac{1}{2f_0}} F(t)\, \mathrm{e}^{\mathrm{i}\, n2\pi f_0\, t}\, \mathrm{d}t \tag{3.22}$$

provides the acoustic spectral components

$$|p_n(r,\theta)| = n\,\frac{\sin\theta}{2c_0 r}\, f_0\, |F_n| \tag{3.23}$$

The lift spectral components F_n can be evaluated by means of Sears' analysis described in subsection 4.3 of part II. It follows that

$$F_n = l\,\pi \rho_0 c V_\infty S_n\, |v_n| \tag{3.24}$$

where S_n denotes the modulus of the complex Sears' function (4.47) evaluated at the nth discrete frequency

$$n\,\frac{\omega_0^*}{2} = n\,\frac{c\pi\, f_0}{V_\infty} \tag{3.25}$$

and v_n denotes the nth spectral component of an upwash impinging gust. In subsection 2.2.7 we obtained the following expression for the upwash velocity along the axis of a Kármán vortex street

$$v_n = \frac{-\mathrm{i}\, 2\pi\Gamma}{a\left\{\cosh\!\left(\pi\frac{b}{a}\right)\left[1+\tanh\!\left(\pi\frac{b}{a}\right)\right]\right\}^n} \quad \text{with } n \text{ odd} \tag{3.26}$$

Considering the approximated Sears' function expression (4.63) of part II gives

$$S_n = \sqrt{\frac{n\, c\pi\, f_0/V_\infty + 0.1811}{0.1811 + 1.569 n\, c\pi\, f_0/V_\infty + 2\pi\,(n\, c\pi\, f_0/V_\infty)^2}} \tag{3.27}$$

Thus, introducing (3.26) and (3.27) into (3.24) provides the lift spectral components F_n that can be substituted into (3.23) in order to evaluate the acoustic spectral components p_n. It thus results that

$$\begin{aligned} |p_n(r,\theta)| \;&=\; \frac{V_\infty^2 M_\infty \sin\theta}{r}\,\frac{\rho_0 2\pi^2\, C_{l_{\max}} \mathrm{St}\, l\, c}{a}\,\frac{n}{\left\{\cosh\!\left(\pi\frac{b}{a}\right)\left[1+\tanh\!\left(\pi\frac{b}{a}\right)\right]\right\}^n} \\ &\quad \sqrt{\frac{n\, c\pi\, f_0/V_\infty + 0.1811}{0.1811 + 1.569\, n\, c\pi\, f_0/V_\infty + 2\pi\,(n\, c\pi\, f_0/V_\infty)^2}} \end{aligned} \tag{3.28}$$

where use of $\Gamma \simeq C_{l_{\max}} 2\, V_\infty\, d$, as from equation (2.61), has been made.

The far pressure field in (3.28) shows that a three-dimensional model provides a sixth-power scaling law for the acoustic intensity, i.e.

$$I \propto M_\infty^6 \tag{3.29}$$

Furthermore, the far pressure field exhibits a r^{-1} dependence on the observer distance. Comparing these results to those obtained through a two-dimensional model confirms that the $I \propto M_\infty^5$ and the $p \propto r^{-1/2}$ predicted by (3.18) are a consequence of the two-dimensional character of the field.

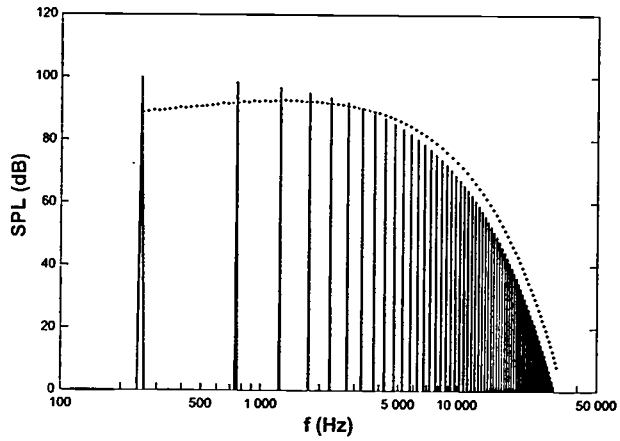

FIGURE 3.4: Spectrum of the acoustic pressure obtained from equation (3.18) with 100 counter-rotating vortices (2D) and from equation (3.28) (3D). The same parameters as in Fig.3.2 have been assumed. —— 2D, - - - - 3D.

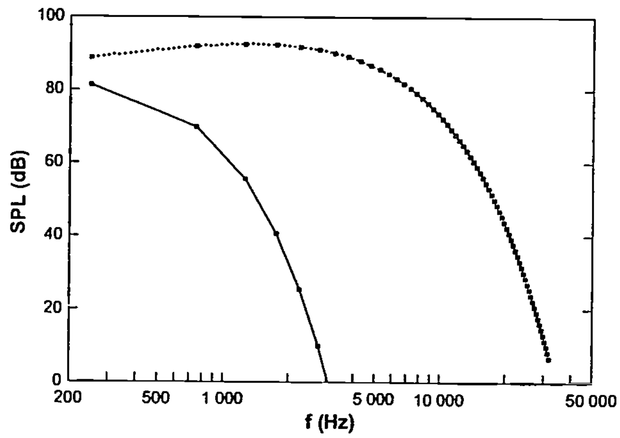

FIGURE 3.5: Spectrum of the acoustic pressure obtained from equation (3.28). The same parameters as in Figs. 3.2 and 3.4 have been assumed. —— $\frac{b}{a} = 0.3$, - - - - $\frac{b}{a} = 0.03$.

In Fig.3.4 a comparison is shown between the two-dimensional result (3.18) and the three-dimensional result (3.28).

Finally, in Fig.3.5 a comparison is shown between the acoustic pressure obtained from equation (3.28) and two values of the aspect ratio b/a of the Kármán vortex street. It is interesting to observe that, at a higher aspect ratio, the harmonic peaks $|p_n|$ exhibit a monotonic decreasing behaviour as n increases.

3.4 A Matched Asymptotic Expansion Model of the Vortex-Airfoil Interaction Noise

Many problems in acoustic have solutions that can be found in the form of a perturbation series

$$p = p_0 + \varepsilon p_1 + \varepsilon^2 p_2 + \dots \tag{3.30}$$

where p is the pressure (or the acoustic velocity potential) and ε is a small dimensionless frequency parameter, say Helmholtz number. When the solution has different expansions in the near and far field, the problem of determining the function p becomes a *singular perturbation problem*. In this

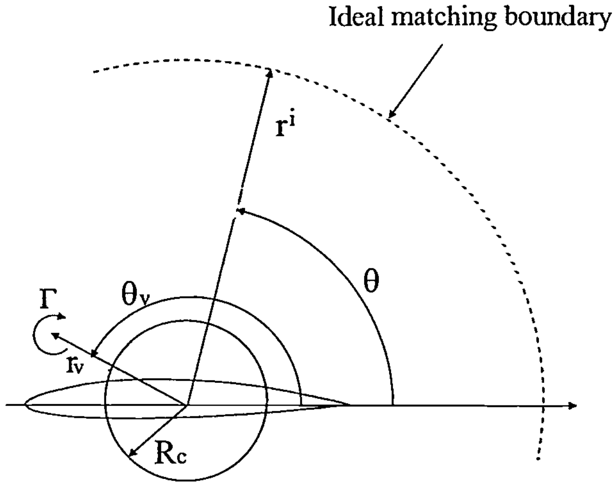

FIGURE 3.6: Matched asymptotic expansion: inner region.

case, separate series must be developed in the near and far field and a method of matched asymptotic expansions must be employed to determine the correct form of each expansion in view of the other, and to determine all the unknown functions and constants appearing in both series by matching the inner and the outer expansions.

By assuming an ideal irrotational flow, the aerodynamic compressible field around the airfoil can be described by the potential equation derived in section 1.4 of part II, with suitable boundary conditions imposed on both the airfoil surface and the wake downstream of the trailing edge. This equation has the form

$$c^2\nabla^2\phi - \frac{\partial^2\phi}{\partial t^2} - \frac{\partial}{\partial t}v^2 - \nabla\phi\cdot\nabla\left(\frac{v^2}{2}\right) = 0 \quad \text{with} \tag{3.31}$$

$$c^2 = c_\infty^2 - (\gamma-1)\,\frac{v^2 - v_\infty^2}{2} - (\gamma-1)\,\frac{\partial\phi}{\partial t} \tag{3.32}$$

where c_∞ is the speed of sound at infinity. Equation (3.31) is uniformly valid, in the near and far field, and can be used to determine an inner and an outer expansion of the potential field.

3.4.1 Inner Problem

The length scale of the inner region is the airfoil chord[3] l. Thus, by supposing that a typical variation of the flow occurs with a circular frequency ω, terms in equation (3.31) stay in the ratio

$$1 : \frac{\omega^2\, l^2}{c_\infty^2} : \frac{\omega\, V_\infty\, l}{c_\infty^2} : M_\infty^2 = 1 : (\omega^* M_\infty)^2 : \omega^* M_\infty^2 : M_\infty^2 = 1 : \varepsilon^2 : \varepsilon M_\infty : M_\infty^2 \tag{3.33}$$

where $\omega^* = \omega\, l/V_\infty$ is the reduced circular frequency and

$$\varepsilon = \omega^* M_\infty \tag{3.34}$$

It follows that, for $\varepsilon \ll 1$ and $M_\infty \ll 1$, equation (3.31) reduces to the Laplace equation

$$\nabla_{x^i}^2\phi = 0 \tag{3.35}$$

where the subscript x^i denotes differentiation with respect to the inner co-ordinates $(x_1^i, x_2^i) = (x_1/l, x_2/l)$.

[3] In this section, c denotes the local speed of sound and l denotes the airfoil chord.

3.4.2 Outer Problem

In the outer region the velocity potential is that of an acoustic disturbance propagating in a moving medium, as described by a linearized form of equation (3.31). Following the analysis of section 1.4 of part II, the linearized potential equation has the form

$$\nabla^2\phi' - \frac{1}{c_\infty^2}\left(\frac{\partial^2\phi'}{\partial t^2} + 2V_\infty\frac{\partial^2\phi'}{\partial x\partial t} + V_\infty^2\frac{\partial^2\phi'}{\partial x^2}\right) = 0 \tag{3.36}$$

where $\phi' = \phi - V_\infty x$ is the potential of the acoustic disturbance. Then, using a Galilean change of variable $x' = x - V_\infty t$, equation (3.36) can be put into the form of the classical acoustic wave equation

$$\nabla'^2\phi' - \frac{1}{c_\infty^2}\frac{\partial^2\phi'}{\partial t^2} = 0 \tag{3.37}$$

Since the acoustic pressure p' is linearly related to the acoustic potential ϕ', the same wave equation is also satisfied by p', namely

$$\nabla'^2 p' - \frac{1}{c_\infty^2}\frac{\partial^2 p'}{\partial t^2} = 0 \tag{3.38}$$

The length scale L of the outer region is the acoustic wavelength λ. For convenience L is set to $\lambda/2\pi$. Furthermore, the acoustic time scale is the same as the aerodynamic one. In other words, a near field perturbation of circular frequency ω generates an acoustic disturbance of the same frequency. As a result, all terms in equation (3.31) have the same order.

Let us introduce the outer co-ordinates $(x_1^o, x_2^o) = (x_1'/L, x_2/L) = (k_0\, x_1', k_0\, x_2)$, where k_0 is the acoustic wavenumber. From the definition (3.34) it follows that

$$\varepsilon = k_0\, l = 2\pi\frac{l}{\lambda} \tag{3.39}$$

Hence, when the Helmholtz parameter ε tends to zero, the inner and the outer length scales become asymptotically disparate.

In cylindrical co-ordinates (r', θ'), with

$$x' = x - V_\infty\, t = r'\cos\theta', \qquad y' \equiv y = r'\sin\theta' \tag{3.40}$$

the wave equation (3.38) becomes

$$\left\{\frac{1}{r'}\frac{\partial}{\partial r'}\left(r'\frac{\partial}{\partial r'}\right) + \frac{1}{r'^2}\frac{\partial^2}{\partial\theta'^2} - \frac{1}{c_\infty^2}\frac{\partial^2}{\partial t^2}\right\}p' = 0 \tag{3.41}$$

which describe the propagation of acoustic disturbances in a convected frame of reference. The general solution of equation (3.41), in the frequency domain, is

$$p'(r', \theta, \omega) = \sum_{n=-\infty}^{n=\infty}\int_{-\infty}^{\infty} a(k)\, Z_{|n|}(\gamma r')\, \mathrm{e}^{\mathrm{i}\, n\theta}\, \mathrm{d}k \tag{3.42}$$

where $k = \omega/c_\infty$ and $\gamma = \mathrm{sgn}(k_0)\sqrt{|k_0^2 - k^2|}$ or $\mathrm{i}\sqrt{|k_0^2 - k^2|}$ according as $|k| \lessgtr |k_0|$, respectively. The function $Z_n(x)$ is any linear combination of Bessel functions (see Ref.[30] (pp. 64-65)). A solution with an outgoing wave behaviour

$$p' \sim (r')^{-1/2}\exp(-\mathrm{i}\, k_0\, r')\, f(\theta) \quad \text{as} \quad r' \to \infty \tag{3.43}$$

is obtained with $Z_n(\gamma r') = H_n^{(2)}(\gamma r')$, where $H_n^{(2)}$ denotes the Hankel function of second kind.

In outer co-ordinates ($r^o = r'/L, \theta'$) the Fourier transform of equation (3.41) has the form

$$\left\{ \frac{1}{r^o} \frac{\partial}{\partial r^o} \left(r^o \frac{\partial}{\partial r^o} \right) + \frac{1}{r^{o2}} \frac{\partial^2}{\partial \theta'^2} + 1 \right\} \hat{p}' = 0 \tag{3.44}$$

Hence, looking for elementary solutions in the form $\hat{p}' = \hat{q}_n \cos(n\theta + \alpha)$, equation (3.44) reduces to an equivalent Bessel equation

$$\left\{ \frac{1}{r^o} \frac{\partial}{\partial r^o} \left(r^o \frac{\partial}{\partial r^o} \right) + \left(-\frac{n^2}{r^{o2}} + 1 \right) \right\} \hat{q}_n = 0 \tag{3.45}$$

For outgoing waves at infinity the solutions are Hankel functions of second kind $H_n^{(2)}(r^o)$.

The Hankel functions $H_n^{(2)}(r^o)$, for small and large values of the argument, have the following asymptotical behaviour [31]

$$\begin{aligned} H_0^{(2)}(x) &\sim \frac{-2\mathrm{i}}{\pi} \ln(x) \quad \text{as} \quad x \to 0 \\ H_n^{(2)}(x) &\sim \frac{\mathrm{i}\ (n-1)!}{\pi} \left(\frac{x}{2}\right)^{-n} \quad \text{as} \quad x \to 0 \end{aligned} \tag{3.46}$$

and

$$H_n^{(2)}(x) \sim \sqrt{\frac{2}{\pi x}} \exp\left\{-\mathrm{i}\left[x - (n/2 + 1/4)\,\pi\right]\right\} \quad \text{as} \quad x \to \infty, \quad \text{with } n \text{ fixed} \tag{3.47}$$

3.4.3 Solution and Matching

Consider now an isolated vortex approaching the airfoil, as sketched in Fig.3.6. The wavelength of the resulting acoustic perturbation is of order

$$\lambda \sim \frac{l}{M_\infty} \tag{3.48}$$

Hence, the outer and the inner co-ordinates are related by

$$r^o = 2\pi\, M_\infty\, r^i \tag{3.49}$$

At a very low Mach number, as relevant to many industrial and marine applications, an incompressible solution is a good approximation of the flow behaviour up to some distance from the airfoil, say $r^i_{\mathrm{M}} = k\, Rc$ ($Rc \simeq 1/4$), where k is some constant. Therefore, the analysis described in section 2.2 can be used to obtain an outer limit of the inner solution to which the outer solution can be matched. The matching boundary is *ideally* fixed at a distance $r^o_{\mathrm{M}} = \pi\, k\, M_\infty/2$. We remark that the matching distance r^o_{M} does not define a real matching boundary. The matching, in fact, is between asymptotic expansions. The necessity of defining an ideal matching distance will be clear later.

Equation (2.69) provides the unsteady pressure field in the incompressible inner region. Therefore it can be used to find an outer expansion of the inner hydrodynamic pressure field.

The vortex contributions (2.32) and (2.87) include a steady term which is related to the presence of a vortex in the center of the circle (ζ-plane). Let then $\tilde{W}_v$ and $\tilde{V}_v$ denote the unsteady part of (2.32) and (2.87), respectively.

Because noise is generated when vortices experience an interaction with the airfoil, it can be assumed that, in the outer limit of the inner region, the velocity induced by the oncoming vortex and by the wake vortices (vortex-sheet in the case of a fixed-wake model) are such that

$$\left|\tilde{V_v}\right| \ll |V_s|\,, \qquad \left|\tilde{V_w}\right| \ll |V_s| \tag{3.50}$$

As a result, the square velocity in equation (2.69) can be approximated as

$$V^2 \simeq |V_s|^2 + 2\Re\left\{V_s\left(\tilde{V}_v^* + V_w^*\right)\right\} \tag{3.51}$$

Hence, the unsteady pressure coefficient takes the form

$$C_p(z,\tau) \simeq -2\Re\left\{V_s\left(\tilde{V}_v^* + V_w^*\right)\right\}h - 2\Re\left(\tilde{W}_v + W_w\right) \tag{3.52}$$

where $h = |\mathrm{d}\zeta/\mathrm{d}z|^2$. It is shown in Fig.3.7 that far enough from the circle center, h tends to the unitary value, uniformly around the airfoil.

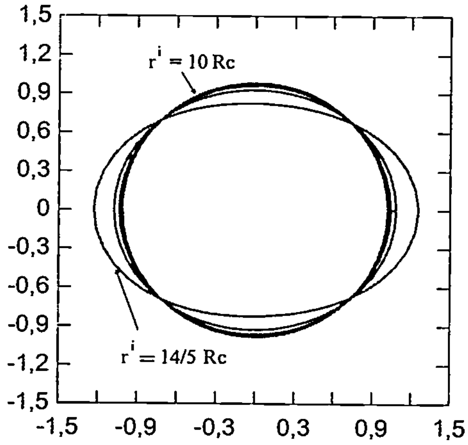

FIGURE 3.7: Polar plot of $h = |\mathrm{d}\zeta/\mathrm{d}z|^2$ for a Kármán-Trefftz conformal mapping of a circle of radius $R_c = 0.25$ into a 12% thickness airfoil of unitary chord. The quasi-elliptical curve is obtained at a distance $r = 14/5R_c$ from the center of the airfoil. The quasi-circular curve is obtained at a distance $r = 10R_c$ from the center of the airfoil.

Furthermore, by assuming that both the oncoming vortex and the wake vortices are at small distance from the airfoil, the expressions (2.33), (2.32), (2.87) and (2.88) can be approximated by introducing the following Taylor series truncated at the second order

$$\begin{aligned}
\ln(\zeta' - \zeta_v') &\simeq \ln\zeta' - \frac{\zeta_v'}{\zeta'} - \frac{1}{2}\frac{\zeta_v'^2}{\zeta'^2} \\
\ln\left(\zeta' - R_c^2/\zeta_v'^*\right) &\simeq \ln\zeta' - \frac{R_c^2}{\zeta'\zeta_v'^*} - \frac{1}{2}\frac{R_c^4}{\zeta'^2\zeta_v'^{*2}} \\
(\zeta' - \zeta_v')^{-1} &\simeq \frac{1}{\zeta'}\left(1 + \frac{\zeta_v'}{\zeta'} + \frac{\zeta_v'^2}{\zeta'^2}\right) \\
\left(\zeta' - R_c^2/\zeta_v'^*\right)^{-1} &\simeq \frac{1}{\zeta'}\left(1 + \frac{R_c^2}{\zeta'\zeta_v'^*} + \frac{R_c^4}{\zeta'^2\zeta_v'^{*2}}\right)
\end{aligned} \tag{3.53}$$

Then, by setting

$$\zeta_v' = r_v e^{\mathrm{i}\,\theta_v} \tag{3.54}$$
$$\zeta_w' = r_w e^{\mathrm{i}\,\theta_w} \tag{3.55}$$

the complex potential and velocity field become

$$\tilde{W}_v(z,\tau) \simeq \frac{\mathrm{i}\Gamma}{2\pi}\left[\frac{r_v^2 - R_c^2}{\zeta'\zeta_v'^*} + \frac{1}{2}\frac{r_v^4 - R_c^4}{\zeta'^2\zeta_v'^{*2}}\right] \tag{3.56}$$

$$W_w(z,\tau) \simeq \frac{\mathrm{i}}{2\pi}\int_0^\tau \left[\frac{r_w^2 - R_c^2}{\zeta'\zeta_w'^*} + \frac{1}{2}\frac{r_w^4 - R_c^4}{\zeta'^2\zeta_w'^{*2}}\right]\gamma(\sigma)\,\mathrm{d}\sigma \tag{3.57}$$

$$\tilde{V^*}_v(z,\tau) \simeq \frac{-\mathrm{i}\,\Gamma}{2\pi\zeta'}\left[\frac{r_v^2 - R_c^2}{\zeta'\zeta_v'^*} + \frac{r_v^4 - R_c^4}{\zeta'^2\zeta_v'^{*2}}\right] \tag{3.58}$$

$$V_w^*(z,\tau) \simeq \frac{-\mathrm{i}}{2\pi\zeta'}\int_0^\tau \left[\frac{r_w^2 - R_c^2}{\zeta'\zeta_w'^*} + \frac{r_w^4 - R_c^4}{\zeta'^2\zeta_w'^{*2}}\right]\gamma(\sigma)\,\mathrm{d}\sigma \tag{3.59}$$

$$\tag{3.60}$$

As a result

$$\tilde{W}_v + W_w = \frac{\mathrm{i}}{2\pi\zeta'}\mathcal{G}(\tau) + \frac{1}{2}\frac{\mathrm{i}}{2\pi\zeta'^2}\mathcal{H}(\tau) \tag{3.61}$$

$$\tilde{V^*}_v + V_w^* = \frac{-\mathrm{i}}{2\pi\zeta'^2}\mathcal{G}(\tau) + \frac{-\mathrm{i}}{2\pi\zeta'^3}\mathcal{H}(\tau) \tag{3.62}$$

where the complex functions $\mathcal{G}$ and $\mathcal{H}$ are defined as

$$\mathcal{G}(\tau) = \mathcal{G}_r + \mathrm{i}\,\mathcal{G}_i = \Gamma\frac{r_v^2 - R_c^2}{r_v}\mathrm{e}^{\mathrm{i}\,\theta_v} + \int_0^\tau \gamma(\sigma)\,\frac{r_w^2 - R_c^2}{r_w}\mathrm{e}^{\mathrm{i}\,\theta_w}\,\mathrm{d}\sigma \tag{3.63}$$

$$\mathcal{H}(\tau) = \mathcal{H}_r + \mathrm{i}\,\mathcal{H}_i = \Gamma\frac{r_v^4 - R_c^4}{r_v^2}\mathrm{e}^{\mathrm{i}\,2\theta_v} + \int_0^\tau \gamma(\sigma)\,\frac{r_w^4 - R_c^4}{r_w^2}\mathrm{e}^{\mathrm{i}\,2\theta_w}\,\mathrm{d}\sigma \tag{3.64}$$

Finally, substituting into equation (3.52) and setting

$$\zeta' = r^i\mathrm{e}^{\mathrm{i}\,\theta} = \frac{r^o}{\varepsilon}\mathrm{e}^{\mathrm{i}\,\theta} \tag{3.65}$$

leads to the following expression for the unsteady pressure coefficient

$$\begin{aligned}
C_p(z,\tau) \simeq & - \frac{\varepsilon}{\pi r^o}\left\{\dot{\mathcal{G}}_r\sin\theta - \dot{\mathcal{G}}_i\cos\theta\right\} \\
& + \frac{h\varepsilon^2}{\pi r^{o2}}\left\{\mathcal{G}_r\sin(2\theta-\alpha) - \mathcal{G}_i\cos(2\theta-\alpha)\right\} - \frac{\varepsilon^2}{2\pi r^{o2}}\left\{\dot{\mathcal{H}}_r\sin(2\theta) - \dot{\mathcal{H}}_i\cos(2\theta)\right\} \\
& + \frac{h\Gamma_s\varepsilon^3}{2\pi^2 r^{o3}}\left\{\mathcal{G}_i\sin\theta + \mathcal{G}_r\cos\theta\right\} + \frac{h\varepsilon^3}{\pi r^{o3}}\left\{\mathcal{H}_r\sin(3\theta-\alpha) - \mathcal{H}_i\cos(3\theta-\alpha)\right\} \\
& - \frac{hR_c^2\varepsilon^4}{\pi r^{o4}}\left\{\mathcal{G}_r\sin\alpha - \mathcal{G}_i\cos\alpha\right\} + \frac{h\Gamma_s\varepsilon^4}{2\pi^2 r^{o4}}\left\{\mathcal{H}_i\sin(2\theta) + \mathcal{H}_r\cos(2\theta)\right\} \\
& - \frac{hR_c^2\varepsilon^5}{\pi r^{o5}}\left\{\mathcal{H}_r\sin\alpha - \mathcal{H}_i\cos\alpha\right\}
\end{aligned} \tag{3.66}$$

This form of the pressure field is assumed as outer limit of the inner behaviour and inner limit of the outer behaviour. It is ideally evaluated at a distance $r^o_{\mathrm{M}} = \pi k M_\infty/2$, with k sufficiently large to ensure a second order inner approximation, but sufficiently small to ensure $r^o_{\mathrm{M}} \ll 1$.

Before matching the outer to the inner solution, the latter should be expressed in a moving frame of reference using the Galilean transformation $x' = x - \tau$ to change (r,θ) into (r',θ'). However, to first-order accuracy, (r,θ) can be replaced by (r',θ') into equation (3.66). This approximation is physically consistent with the fact that noise is mainly generated when the oncoming vortex is in the vicinity of the airfoil, where r and θ are approximately equal to r' and θ'.

In view of the outer limit of the inner solution (3.66), the general outer solution

$$\hat{p'}^o = \sum_n A_n H_n^{(2)}\cos(n\theta + \alpha) \tag{3.67}$$

determined in subsection 3.4.2 can be put into the form

$$
\begin{aligned}
\hat{p'}^{o} &= P^{(1)}H_1^{(2)}(r^o)\sin\theta + Q^{(1)}H_1^{(2)}(r^o)\cos\theta \\
&+ P^{(2)}H_2^{(2)}(r^o)\sin(2\theta) + Q^{(2)}H_2^{(2)}(r^o)\cos(2\theta) \\
&+ P_\alpha^{(2)}H_2^{(2)}(r^o)\sin(2\theta-\alpha) + Q_\alpha^{(2)}H_2^{(2)}(r^o)\cos(2\theta-\alpha) \\
&+ P^{(3)}H_3^{(2)}(r^o)\sin(3\theta) + Q^{(3)}H_3^{(2)}(r^o)\cos(3\theta) \\
&+ P_\alpha^{(3)}H_3^{(2)}(r^o)\sin(3\theta-\alpha) + Q_\alpha^{(3)}H_3^{(2)}(r^o)\cos(3\theta-\alpha)
\end{aligned} \tag{3.68}
$$

Then, taking the limit as $r^o \to 0$, using the asymptotic expressions (3.46) and comparing to (3.66) yield

$$
\begin{aligned}
P^{(1)}K_1 &= -p_d\frac{\varepsilon}{\pi r^o}\hat{\mathcal{G}}_r \\
Q^{(1)}K_1 &= p_d\frac{\varepsilon}{\pi r^o}\hat{\mathcal{G}}_i \\
P^{(2)}K_2 &= -p_d\frac{\varepsilon^2}{2\pi r^{o2}}\hat{\mathcal{H}}_r \\
Q^{(2)}K_2 &= p_d\frac{\varepsilon^2}{2\pi r^{o2}}\hat{\mathcal{H}}_i \\
P_\alpha^{(2)}K_2 &= p_d\frac{h\varepsilon^2}{\pi r^{o2}}\hat{\mathcal{G}}_r \\
Q_\alpha^{(2)}K_2 &= -p_d\frac{h\varepsilon^2}{\pi r^{o2}}\hat{\mathcal{G}}_i \\
P^{(3)}K_3 &= 0 \\
Q^{(3)}K_3 &= 0 \\
P_\alpha^{(3)}K_3 &= p_d\frac{h\varepsilon^3}{\pi r^{o3}}\hat{\mathcal{H}}_r \\
Q_\alpha^{(3)}K_3 &= -p_d\frac{h\varepsilon^3}{\pi r^{o3}}\hat{\mathcal{H}}_i
\end{aligned} \tag{3.69}
$$

where the symbol $\hat{f}$ denotes the Fourier transform of f, $p_d = \frac{1}{2}\rho V_\infty^2$ is the free-stream dynamic pressure and K_1, K_2 and K_3 are the small argument asymptotic limits of the Hankel functions, namely

$$
K_1 = \frac{2\mathrm{i}}{\pi}\frac{1}{r^o}, \quad K_2 = \frac{4\mathrm{i}}{\pi}\frac{1}{r^{o2}}, \quad K_3 = \frac{16\mathrm{i}}{\pi}\frac{1}{r^{o3}} \tag{3.70}
$$

Thus, the coefficients P and Q can be expressed as

$$
\begin{aligned}
P^{(1)} &= -p_d\frac{\varepsilon}{2\mathrm{i}}\hat{\mathcal{G}}_r & Q^{(1)} &= p_d\frac{\varepsilon}{2\mathrm{i}}\hat{\mathcal{G}}_i \\
P^{(2)} &= -p_d\frac{\varepsilon^2}{8\mathrm{i}}\hat{\mathcal{H}}_r & Q^{(2)} &= p_d\frac{\varepsilon^2}{8\mathrm{i}}\hat{\mathcal{H}}_i \\
P_\alpha^{(2)} &= p_d\frac{h\varepsilon^2}{4\mathrm{i}}\hat{\mathcal{G}}_r & Q_\alpha^{(2)} &= -p_d\frac{h\varepsilon^2}{4\mathrm{i}}\hat{\mathcal{G}}_i \\
P^{(3)} &= 0 & Q^{(3)} &= 0 \\
P_\alpha^{(3)} &= p_d\frac{h\varepsilon^3}{16\mathrm{i}}\hat{\mathcal{H}}_r & Q_\alpha^{(3)} &= -p_d\frac{h\varepsilon^3}{16\mathrm{i}}\hat{\mathcal{H}}_i
\end{aligned} \tag{3.71}
$$

Concluding, equation (3.68) with coefficients defined in (3.71), describes a far pressure field which satisfies an outgoing wave behaviour and matches the inner pressure field generated by a low Mach number vortex-airfoil interaction.

3.4.4 Discussion

The complex functions $\mathcal{G}$ and $\mathcal{H}$ have an important physical meaning. As shown in section 2.2.8, a vortex convected past a body induces a force which is proportional to the rate of change of the hydrodynamic impulse of the flow, that is, the hydrodynamic impulse of the pair system constituted by the vortices in the field and their images. The hydrodynamic impulse of a vortex is defined as the product of the circulation and the distance of the vortex from a reference point. Therefore, when a vortex is in proximity of a circle (see Fig.2.3), the lift and drag components of the dimensionless force per unit span are given by

$$C_l = -\frac{\mathrm{d}}{\mathrm{d}\tau}\sum_i \Gamma_i \xi_i' = -\frac{\mathrm{d}}{\mathrm{d}\tau}\left\{\frac{r_v^2 - R_c^2}{r_v}\cos\theta_v\right\}\Gamma \tag{3.72}$$

$$C_d = -\frac{\mathrm{d}}{\mathrm{d}\tau}\sum_i \Gamma_i \eta_i' = -\frac{\mathrm{d}}{\mathrm{d}\tau}\left\{\frac{r_v^2 - R_c^2}{r_v}\sin\theta_v\right\}\Gamma \tag{3.73}$$

Then, using equation (3.63) and considering, for simplicity, only the oncoming vortex contribution, yield

$$C_l + \mathrm{i}\, C_d = -\dot{\mathcal{G}}_v \tag{3.74}$$

Therefore, the rate of change of the real part of $-\mathcal{G}_v$ determines the lift contribution, whereas the rate of change of the imaginary part of $-\mathcal{G}_v$ determines the drag contribution.

In a similar way it can be demonstrated that the rate of change of the function $\mathcal{H}_v$ is related to the aerodynamic moment exerted on the airfoil. Thus, $\mathcal{H}_v$ can be interpreted as a complex form of the hydrodynamic angular impulse of the flow with respect to the origin ζ_c.

The acoustic pressure (3.68) has the form of a multipole expansion where the dipole and quadrupole terms are of the order of ε and ε^2, respectively, as resulting from first- and second-order time derivatives. Therefore, it can be concluded that:

1) the unsteady aerodynamic force exerted on the airfoil generates dipole contributions of first order in ε (terms $P^{(1)}$ and $Q^{(1)}$ containing $\dot{\mathcal{G}}$);

2) the unsteady aerodynamic moment exerted on the airfoil generates quadrupole contributions of second order in ε (terms $P^{(2)}$ and $Q^{(2)}$ containing $\dot{\mathcal{H}}$);

3) the hydrodynamic impulse of the flow generates quadrupole contributions of second order in ε (terms $P_\alpha^{(2)}$ and $Q_\alpha^{(2)}$ containing $\mathcal{G}$).

The far field behaviour can be investigated by using the asymptotical expression (3.47) of the Hankel functions. At the leading order and at an observation angle $\theta = \pi/2$, the acoustic pressure takes the form

$$\hat{p'}^o = \frac{\mathrm{i}\, p_d \sqrt{\varepsilon}}{\sqrt{2\pi\, r^i}}\, \hat{\mathcal{G}}_r\, \mathrm{e}^{-\mathrm{i}\,(\varepsilon r^i - 3\pi/4)} \tag{3.75}$$

Hence, provided that for a vortex-airfoil interaction problem the Helmholtz number is $\varepsilon \simeq 2\pi\, M_\infty$, the vortex-airfoil interaction noise is given by

$$\hat{p'}^o = \frac{\mathrm{i}\, p_d \sqrt{M_\infty}}{\sqrt{r^i}}\, \hat{\mathcal{G}}_r\, \mathrm{e}^{-\mathrm{i}\,(2\pi M_\infty r^i - 3\pi/4)} \tag{3.76}$$

Equation (3.76) exhibits a fifth-power scaling law of the acoustic intensity and a $r^{-1/2}$ dependence of the far pressure field on the observation distance. These results are in agreement with those obtained in section 3.3 by using a two-dimensional linear model (see equation (3.18)).

The analysis developed in this subsection is based on a fixed-wake model, as indicates by the functions $\mathcal{G}(\tau)$ and $\mathcal{H}(\tau)$ in (3.63) and (3.64), respectively. However, the formulation can be straightforwardly extended to a free-wake model by replacing the wake-integrals in the expressions of $\mathcal{G}(\tau)$ and $\mathcal{H}(\tau)$ by summations over wake vortices.

As an interesting result, the functions $\mathcal{G}(\tau)$ and $\mathcal{H}(\tau)$ in (3.63) and (3.64), respectively, show that a wake fixed on the real axis $\eta = 0$ results in unbalanced forces and moments on the airfoil. As a consequence, when a fixed-wake model is employed the dipole and quadrupole acoustic contributions may be overpredicted.

3.5 Conclusions

In this chapter we proposed analytical formulations to describe the acoustic radiation from a vortex-airfoil interaction.

An acoustic analogy formulation was presented, relating the far pressure field to the pressure fluctuations on the airfoil surface. Moreover, an analytical decomposition of the time derivative of the pressure field was proposed as a way to investigate the effects of nonlinear interaction mechanisms on the aerodynamic sound generation.

A two-dimensional linear model proposed by Howe [30] and based on the Sears' gust response function was applied to describe the sound generated by a double row of counter-rotating vortices convected past a flat-plate. It was shown that noise is generated when the vortex passes by the leading edge, and not when it passes by the trailing edge. Furthermore, when a flat-plate is embedded symmetrically in a double row of counter-rotating vortices only odd harmonics acoustic peaks are generated. Finally, consistently with the two-dimensionality of the model, a fifth-power scaling law of the acoustic intensity was obtained ($I \propto M_\infty^5$).

A matched asymptotic expansion model was developed on the base of the analytical results of chapter 2. The model related the multipole structure of the acoustic far field to the aerodynamic force and moment induced by an oncoming vortex and the airfoil wake on the airfoil. More precisely, a force generates a dipole radiation, whereas a moment generates a quadrupole radiation. A fifth-power law of the acoustic intensity was found in agreement with other two-dimensional models. The explicit dependence of the acoustic pressure on the vortex kinematics past the airfoil is an interesting aspect of the proposed model.

4

Vortex-Airfoil Interaction: Results and Discussion

In this chapter we present numerical results concerning with the vortex-airfoil interaction problem. Numerical predictions are made on the base of the aerodynamic and acoustic formulations developed in chapters 2 and 3, respectively.

The aerodynamic problem is solved by means of the discrete-vortex method described in section 2.2. The physical consistency of a fixed-wake approximation is investigated by checking fixed-wake results against free-wake results. In particular, the influence of the wake model on the wall pressure at the airfoil trailing edge is examined.

The acoustic field is predicted by means of the Ffowcs Williams & Hawkings [2] approach described in section 3.1. A parametric study is performed in order to investigate the effects of the free-stream velocity, the vortex distortion and the airfoil geometry.

Finally, numerical predictions of the noise radiated by a Kármán-Trefftz airfoil embedded in a double row of counter-rotating vortices are compared with experimental measurements of the noise generated by an NACA-0012 airfoil in the wake of a cylinder.

Unless otherwise stated, the following geometrical and flow parameters are used in the numerical simulations. The airfoil chord and span are $c = 0.1\,\mathrm{m}$ and $l = 0.3\,\mathrm{m}$, respectively. The acoustic predictions are made at a distance $r = 1.4\,\mathrm{m}$ from the airfoil mid point. Both cambered and symmetrical airfoils are considered. The non zero thickness airfoils have a $\epsilon = 15.5^o$ trailing edge angle, and a 12%percentage thickness. A symmetrical airfoil, obtained with the conformal mapping parameters $\xi_c = -0.01264$ and $\eta_c = 0$, provides a good approximation of an NACA-0012 airfoil. The circulation of the oncoming vortex is obtained through an approximated form of equation (2.61) and results in the dimensionless value $\Gamma = 2C_{l_{\max}} d/c$, where d and $C_{l_{\max}}$ are the diameter and the maximum lift coefficient, respectively, of a hypothetical upstream cylinder from which the oncoming vortex is shed. It is always assumed $d/c = 0.16$. When a double row of vortices is considered, the distance between two next vortices on the same row is $a = 5d$, to which a Strouhal number of 0.2 corresponds. The flow parameters are $V_\infty = 20\,\mathrm{m/s}$, $\rho = 1.225\,\mathrm{kg/m^3}$ and $p_\infty = 101253.6\,\mathrm{Pa}$. The viscous core parameter (see equation 2.131) has a dimensionless value $\beta = 0.01016 M_\infty / M_{\max}$, with $M_{\max} = 0.3$.

When labels are not included in figures these refer to spatial co-ordinates expressed in m. Furthermore, the scales in the y-direction have been frequently shrank in order to enhance the plot resolution.

4.1 Effects of the Vortex Convection Velocity

In this section we investigate some effects related to a vortex *frozen* convection hypothesis. This hypothesis is commonly incorporated by idealized analytical models and consists in supposing that the incident vortex is convected along a rectilinear path at a constant velocity. The frozen convection approximation is herein referred to as *fixed vortex path* approximation. We consider a clockwise line-vortex convected towards a flat-plate at zero angle of attack. This flow configuration is such that a fixed vortex path is physically consistent with a free vortex path, provided that the effect of the vortex self induction near the flat-plate can be neglected. The vortex is initially located at a distance of 0.005 m from the plane of the plate and its circulation is determined by assuming $C_{l_{max}} = 0.1$. Results obtained by considering a fixed vortex path are checked against results obtained by assuming a free vortex path. In the first case a fixed-wake formulation is employed, whereas, in the second case, a free-wake formulation is employed.

4.1.1 Aerodynamic Results

In Fig.4.1(a) the vortex trajectories for the case of a fixed vortex path and that of a free vortex path are plotted. The results show that the leading edge induction effect perturbs the vortex trajectory from a parallel streamline. Furthermore, downstream of the trailing edge, the free-wake formulation provides a slightly diverging vortex path. The wake circulation is plotted in Fig.4.1(b). When a fixed vortex path is assumed, the peak is slightly anticipated because of the greater vortex convection velocity[1].

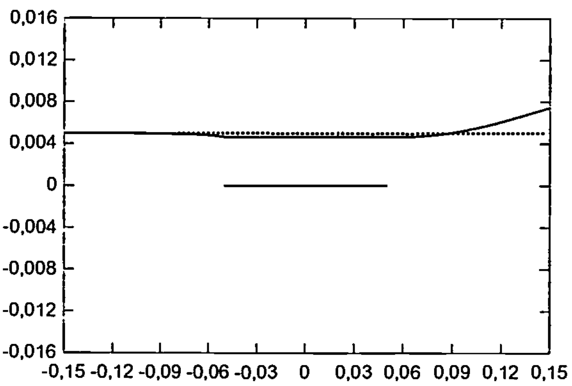

a) Vortex trajectory.

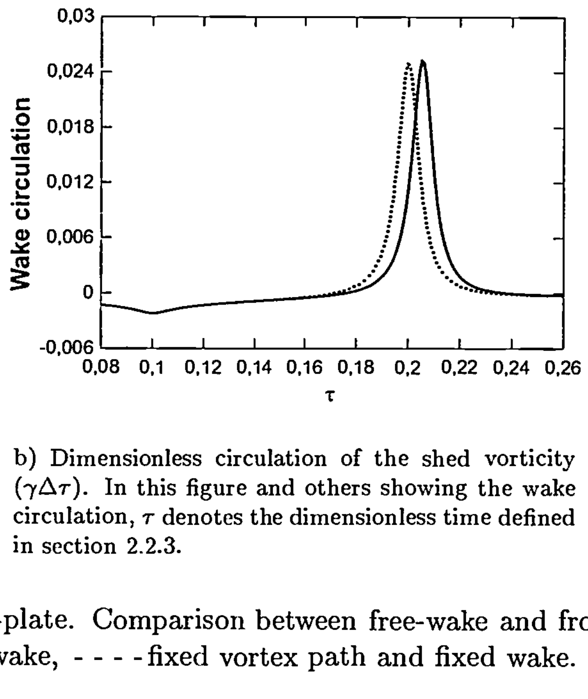

b) Dimensionless circulation of the shed vorticity ($\gamma\Delta\tau$). In this figure and others showing the wake circulation, τ denotes the dimensionless time defined in section 2.2.3.

FIGURE 4.1: Interaction between a vortex and a flat-plate. Comparison between free-wake and frozen convection results : —— free vortex path and free wake, - - - -fixed vortex path and fixed wake.

The flat-plate considered in this section is indeed a Joukowski[2] airfoil of very small thickness ($\sim 5 \times 10^{-6}$), which offers the advantage of a quasi-singular behaviour of the flow at the leading edge. It is plotted on Fig.4.2 where the distribution of the *numerical* pressure probes on the flat-plate is shown. These are numbered in a counterclockwise progression from 0, the nearest point to the trailing edge on the upper side of the plate, to 149, the nearest point to the trailing edge on the lower side of the plate. The distance between points 0 and 149 from the analytical location of the trailing edge is about 6×10^{-5} m.

The vortex distribution in the free wake at different time-steps is plotted on Fig.4.3. The first vortices shed in the field (see Fig.4.3(a)) are the trailing edge response to the impulsive introduction of the oncoming vortex when the computation is started. On the contrary, the two wake perturbations in

[1] In the case of a free convection, in fact, the velocity induced by the image vortex is opposed to the free-stream velocity
[2] A Joukowski airfoil is a Kármán-Trefftz airfoil with a vanishing trailing edge angle.

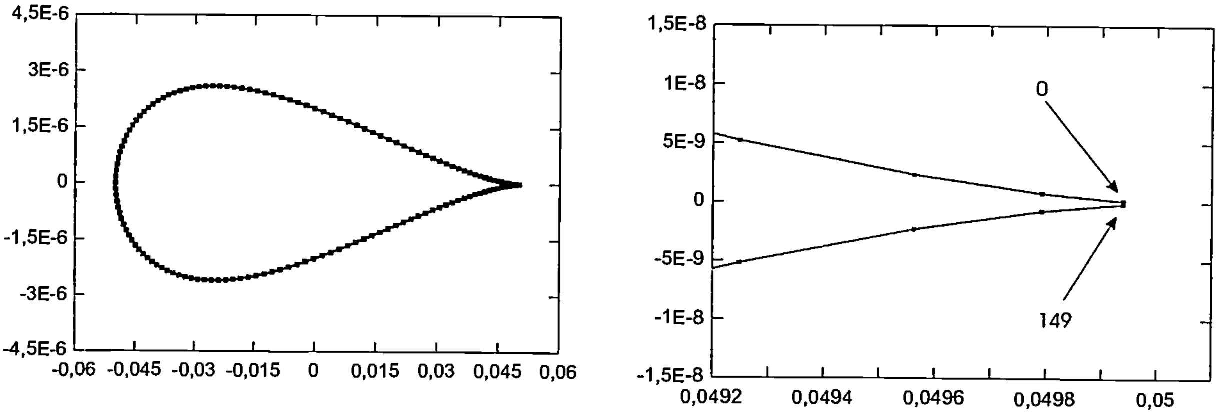

a) Numerical pressure probe distribution on the flat-plate.

b) Trailing edge region.

FIGURE 4.2: Flat-plate.

Figs.4.3(b) and 4.3(c) are the response to the vortex passage nearby the leading edge and nearby the trailing edge, respectively.

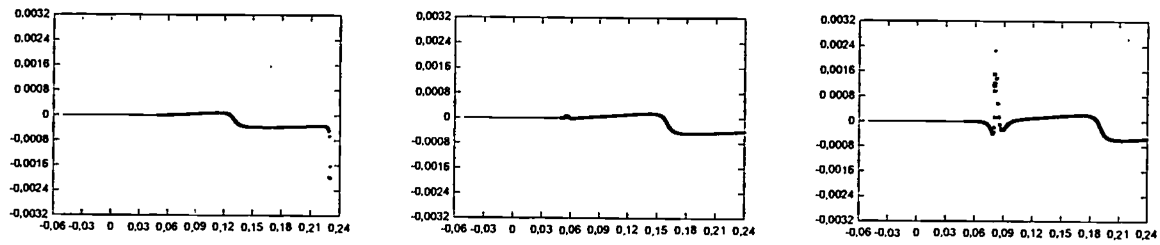

a) $t = 0.0090$ s.

b) $t = 0.0105$ s.

c) $t = 0.0120$ s.

FIGURE 4.3: Vortex distribution in the wake behind the flat-plate at different time-steps during the passage of a line-vortex. In each figure ripples from right to left are caused by: a) the impulsive introduction of the oncoming vortex when the computation is started, b) the vortex passage by the leading edge, c) the vortex passage by the trailing edge. Only ripples a) and b) can be seen in Fig.4.3(a), whereas ripples b) and c) can be seen in Figs.4.3(b) and 4.3(c).

The unsteady force on the flat-plate is plotted in Fig.4.4. A slight difference occurs in the lift component as the vortex passes by the leading edge and by the trailing edge. The quasi-singular behaviour predicted for the drag component is a consequence of the quasi-singular behaviour of the flow at the leading edge.

In Fig.4.5 the pressure coefficient in the trailing edge region is plotted. Fixed- and free-vortex path results are compared. It is interesting to notice that a reduction of the pressure jump at the trailing edge can be obtained when a free vortex convection is assumed. This is a consequence of the fact that a *vortex force*[3] is generated when a vortex is convected at a velocity different from the local flow velocity.

[3]The vortex force is proportional to $\nabla \cdot \{\omega\,(\mathrm{v}_c - \mathrm{v})\}$, where ω denotes the vorticity, v_c is the vortex convection velocity and v is the flow velocity at the vortex location (see also section 2.2.8).

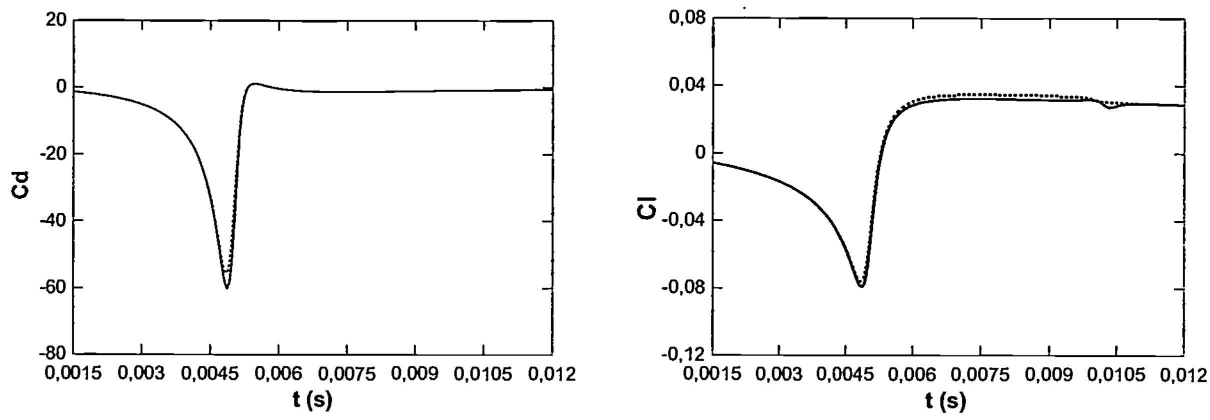

a) Drag coefficient. b) Lift coefficient.

FIGURE 4.4: Unsteady force on the flat-plate induced by a line-vortex: —— free vortex path, - - - - fixed vortex path.

4.1.2 Acoustic Results

In Fig.4.6 the acoustic pressure generated by the interaction between the vortex and the flat-plate is plotted. This has been computed by means of the acoustic analogy approach described in section 3.1. Because of the quasi-singular behaviour induced by the vortex at the airfoil leading edge, a radiation peak occurs when the oncoming vortex passes nearby the leading edge (see Fig.4.6(a)). On the contrary, when the vortex passes nearby the trailing edge, only a vanishing acoustic disturbance is generated. Furthermore, as shown in Fig.4.6(b), when both the oncoming vortex and the airfoil wake are freely convected at the local flow velocity, a slight increase of the trailing edge contribution to the noise radiation occurs. This behaviour is consistent with Howe's [13] analysis, as discussed in subsection 10.3.5 of part II.

From the results shown in the present section it follows that, in the case of a flat-plate at zero angle of attack, a fixed vortex path approximation together with a fixed wake approximation leads to consistent results. This legitimates the frozen convection assumption made by many authors, in aerodynamics as well as in aeroacoustics, when dealing with thin airfoils at small angle of attack. An idealized model based on the frozen convection hypothesis has been described in section 3.3. This model describes the noise generated when a line-vortex is convected past a flat-plate. In the following subsection, the analytical prediction based on this linear model are compared with the numerical results obtained by considering the same idealized flow configuration.

4.1.3 Comparisons with Howe's Analytical Model

In Fig.4.7 the acoustic pressure generated by the interaction between a flat-plate and a clockwise frozenly convected line-vortex is shown. The circulation of the vortex is determined by supposing a value $C_{l_{\max}} = 0.1$. The distance between the vortex trajectory and the flat-plate is $y_v = 0.001$ m. The noise prediction is made at a distance $r = 5$ m from the plate mid point. The analytical behaviour predicted by the linear model (3.16) is compared to the numerical prediction obtained by employing a fixed vortex path and a free wake formulation.

The linear model is consistent with a two-dimensional field, an aerodynamic and acoustic field indeed. In the numerical computation a flat-plate of span $l = 0.3$ m is considered to which the radiation parameter $kl \simeq 1$ corresponds. Thus, the flat-plate cannot be assumed as acoustically two-dimensional. Nevertheless, the results compare favorably, especially for the negative peak of the leading

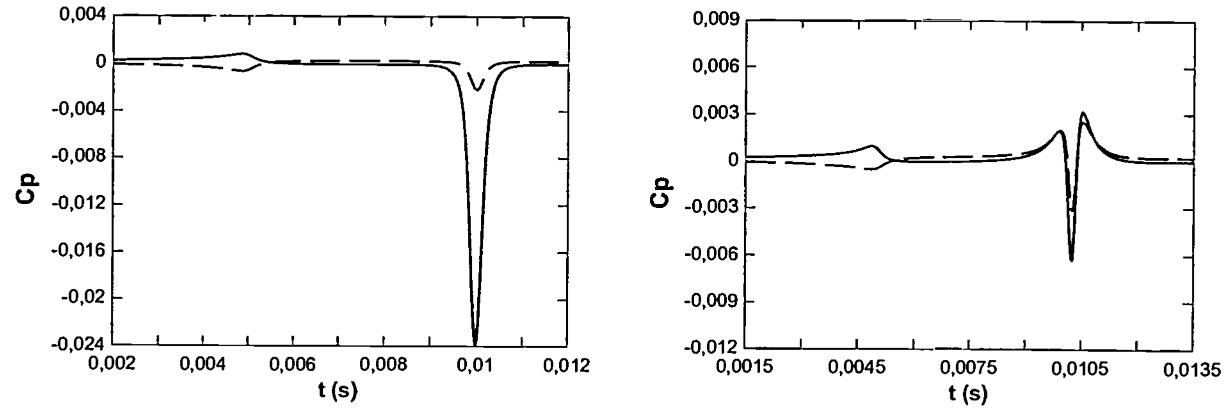

a) Fixed vortex path.

b) Free vortex path.

FIGURE 4.5: Pressure coefficient in the trailing edge region of a flat-plate induced by a line-vortex: —— point 0, - - - - point 149.

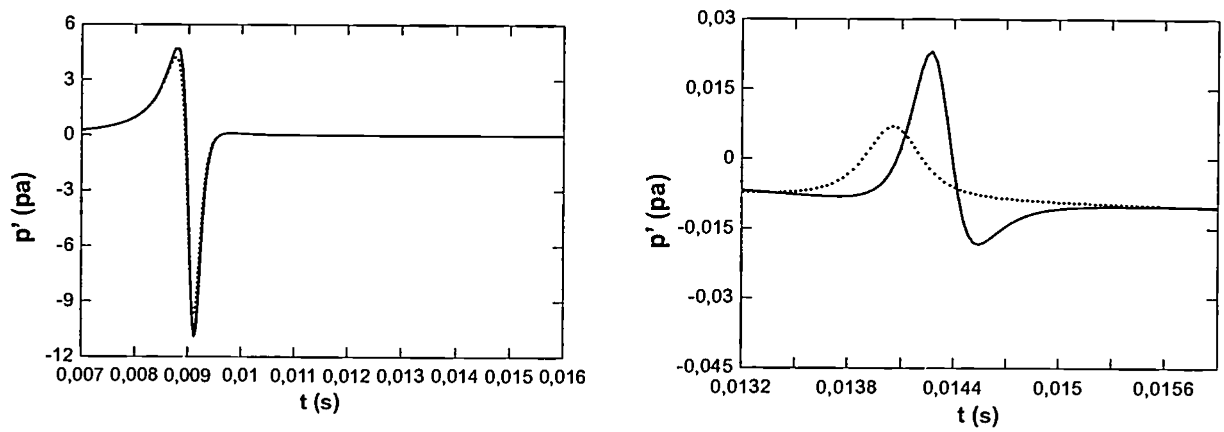

a) Leading edge contribution.

b) Trailing edge contribution.

FIGURE 4.6: Acoustic pressure at 90° to the flow. —— Free vortex path, - - - - fixed vortex path.

edge contribution. On the contrary, the numerical solution underestimates the positive peak. This is presumably due to the fact that the numerical solution is based on a thin airfoil and not on a zero-thickness plate. Thus, only a quasi-singular flow behaviour is predicted at the leading edge. On the contrary, the analytical solution is based on the Sears' response function which provides a singular behaviour at the leading edge.

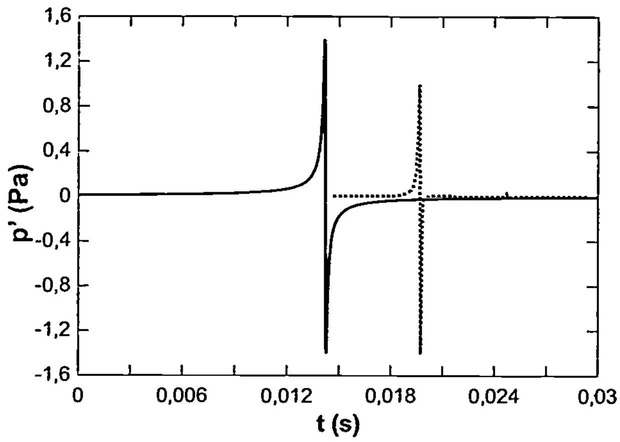

FIGURE 4.7: Comparison between the analytical solution (3.16) and a numerical prediction: —— analytical solution, - - - - numerical prediction. The time shift between the solutions is due to a different vortex initial position.

4.2 Effects of the Vortex Distortion

In this section we investigate the effects of the vortex distortion during a direct vortex-airfoil interaction. Results obtained by describing the oncoming vortex as a circular cloud of 101 vortices are compared with those obtained by concentrating the overall circulation in a line-vortex. The same comparison is made for the case of a non direct vortex-airfoil interaction by locating the vortex at a distance $y_v = 0.01\,\mathrm{m}$ above the airfoil chord line. The circulation of the impinging vortex is determined by assuming $C_{l_{max}} = 0.05$. The vortex rotates clockwise. A fixed-wake formulation is employed.

4.2.1 Aerodynamic Results

The vortex trajectory for the direct interaction case is plotted on Fig.4.8. The isolated vortex passes below the airfoil. Conversely, the cloud is split into two fragments passing above and below the airfoil.

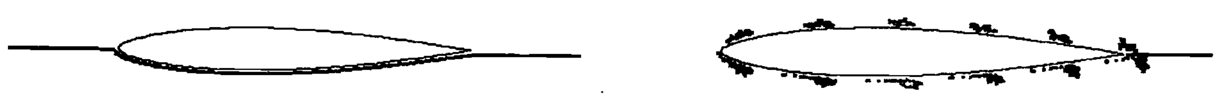

a) Isolated vortex trajectory. b) Cloud of 101 vortices at different time-steps.

FIGURE 4.8: Head-on vortex-airfoil interaction.

In the case of a non direct vortex-airfoil interaction, the oncoming cloud undergoes only a slight distortion and its trajectory is the same as if it was concentrated in a line-vortex. This is shown in Fig.4.9.

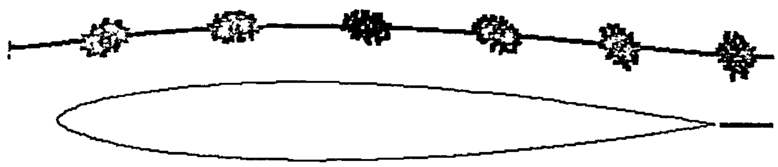

FIGURE 4.9: Non direct vortex-airfoil interaction: $y_v = 0.01\,\mathrm{m}$. Isolated vortex trajectory and a cloud of 101 vortices at different time-steps.

The circulation shed in the wake is traced in Fig.4.10. During the direct interaction of the airfoil with an isolated vortex, the flow at the trailing edge is also strongly perturbed. As a consequence, the wake circulation is three times higher than that generated by an interaction with a cloud of vortices.

During a non direct interaction, the oncoming vortex is only slightly distorted. Furthermore, as shown in Fig.4.10(b), the flow at the trailing edge remains unaffected by the spatial vorticity distribution of the incident vortex.

In Fig.4.11 the unsteady force induced by an isolated vortex is compared to the force induced by a cloud of vortices. Due to the vortex splitting, a significant difference occurs especially in the case of a

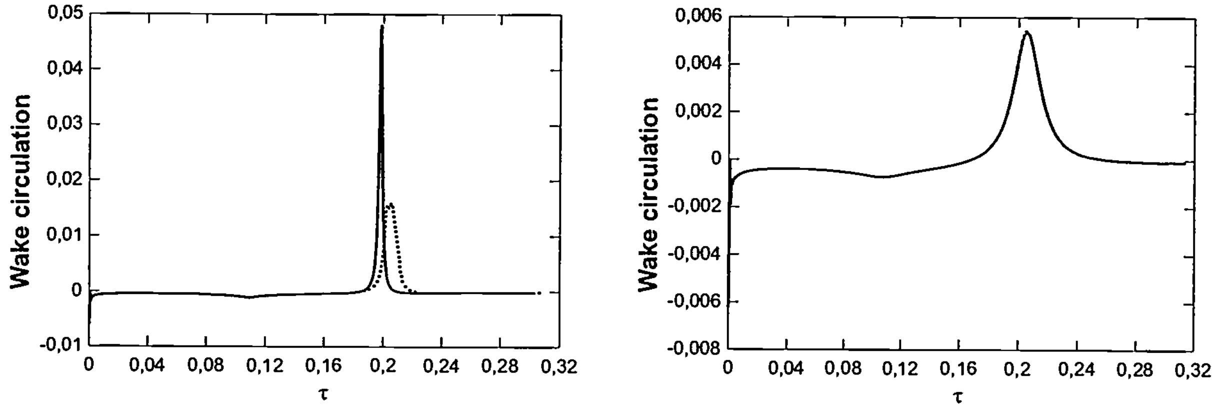

a) Direct interaction: $y_v = 0$.

b) Non direct interaction: $y_v = 0.01\,\mathrm{m}$.

FIGURE 4.10: Dimensionless circulation of the vorticity shed into the wake of the airfoil ($\gamma\Delta\tau$). —— Isolated vortex, - - - - cloud of vortices.

direct interaction. Conversely, in the case of a non direct interaction the vortex size has no significant effect on the unsteady force exerted on the airfoil.

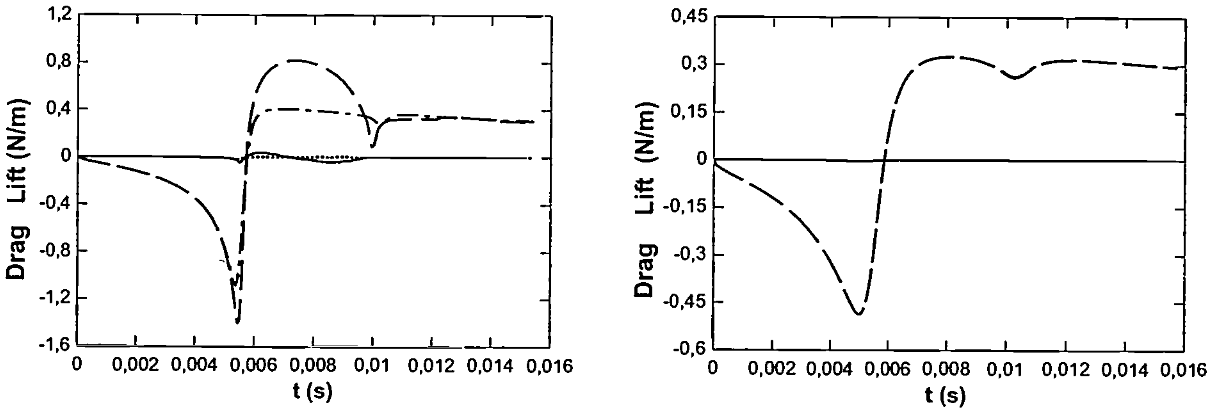

a) Direct interaction: $y_v = 0$.

b) Non direct interaction: $y_v = 0.01\,\mathrm{m}$.

FIGURE 4.11: Unsteady force on the airfoil during a vortex airfoil interaction. Isolated vortex: —— drag, — — lift; cloud of vortices: - - - - drag, - - - lift.

4.2.2 Acoustic Results

The vortex distortion and its consequent splitting are responsible for a reduction of the unsteady force exerted on the airfoil. Furthermore, as shown in Fig.4.12(a), a substantial reduction of the noise radiation occurs when the impinging vortex is described as a cloud of vortices. This reduction is particularly important in the noise contribution from the trailing edge. On the contrary, as shown in Fig.4.12(b), when a non direct interaction occurs the acoustic pressure is not affected by the size of the vortex. In this case, a line-vortex method can provide consistent results.

Finally, in Fig.4.13 the directivity of the vortex-airfoil interaction noise is plotted. It is interesting to notice that, in the case of a direct interaction, the vortex distortion and its consequent splitting yield

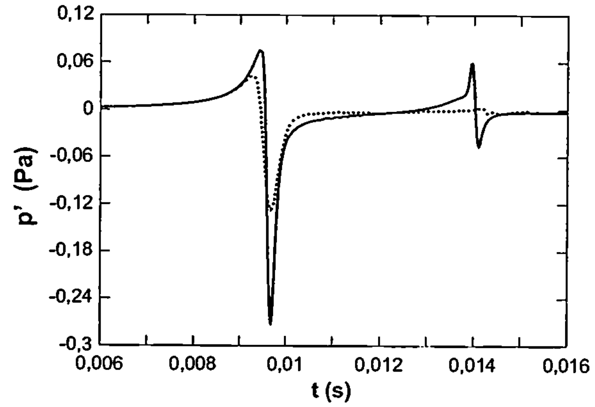

a) Direct interaction: $y_v = 0$.

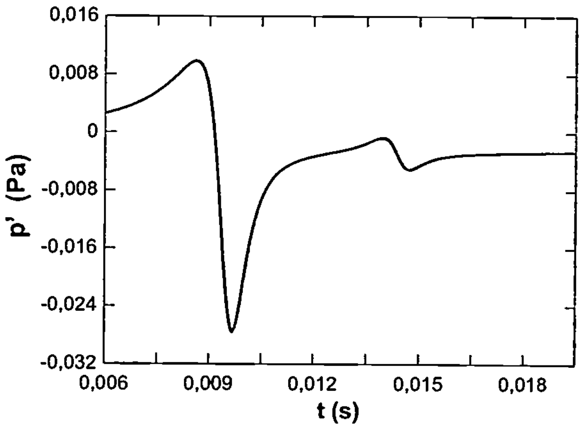

b) Non direct interaction: $y_v = 0.01$ m.

FIGURE 4.12: Acoustic pressure at 90^o to the flow generated by a vortex-airfoil interaction. —— Isolated vortex, - - - - cloud of vortices.

a substantial reduction of the noise level. Therefore, the vortex size and the vortex distance from the airfoil play a crucial role during a direct vortex-airfoil interaction.

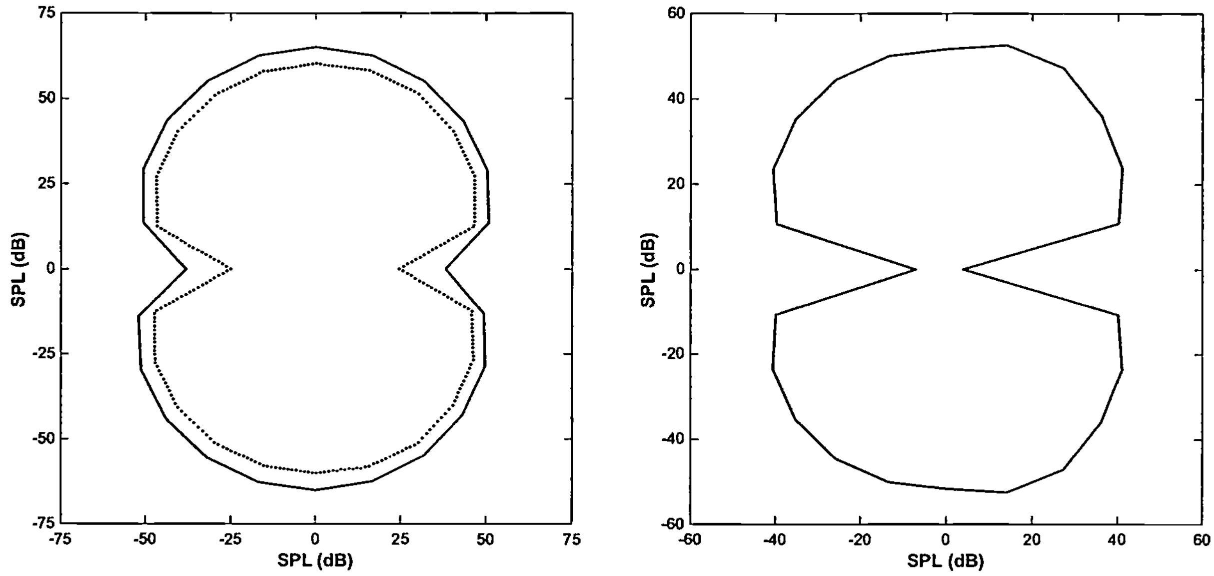

a) Direct interaction: $y_v = 0$. b) Non direct interaction: $y_v = 0.01\,\mathrm{m}$.

FIGURE 4.13: Directivity of the noise generated by a vortex-airfoil interaction. —— Isolated vortex, - - - - cloud of vortices.

4.2.3 An Example of Vortex Splitting

In order to emphasize the distortion process during a direct vortex-airfoil interaction, the circulation of an intense and large-scale vortex ($C_{l_{\max}} = 0.5$) is distributed upon a cloud of 197 vortices.

As shown in Fig.4.14, in proximity of the leading edge, the vortex is first deformed and then split into two fragments which are convected along the two sides of the airfoil. Due to the opposite induction effect of the image vortex system, the convection velocity of these two fragments is different. The upper fragment is slower and spreads across the surface. On the contrary, the lower fragment undergoes only a slight deformation after the splitting has taken place.

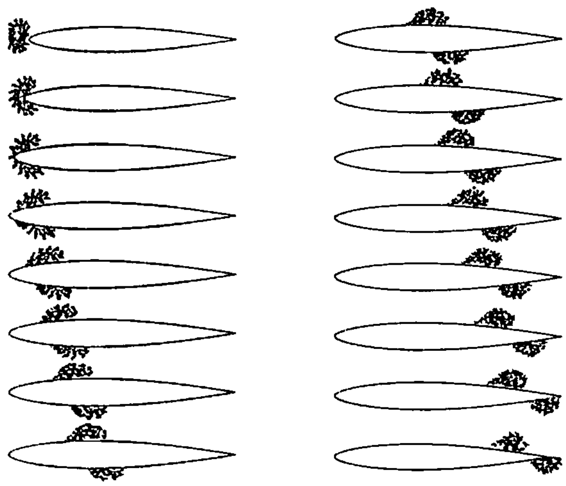

FIGURE 4.14: Direct interaction between a cloud of 197 *clockwise* vortices and an airfoil. First column: frames 1 to 8, second column: frames 9 to 16.

As these two fragments approach the trailing edge, secondary vortices are shed into the airfoil wake.

This is shown in Fig.4.15 where the wake circulation exhibits two peaks of equal sign. These correspond to the passage of the lower and upper fragments by the airfoil trailing edge.

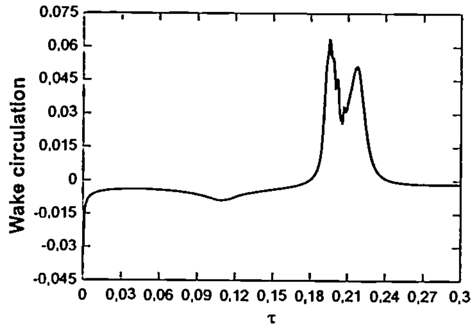

FIGURE 4.15: Airfoil wake circulation generated during a direct vortex-airfoil interaction. τ denotes the dimensionless time.

The behaviour described in this subsection is in qualitative agreement with the PIV observations made by Horner *et al.* [11] and discussed in section 2.1.

The time lag between the interaction of the two half vortices with the airfoil trailing edge generates two distinct acoustic disturbances. This effect is of fundamental importance at higher free-stream Mach numbers for two reasons:

- as discussed in chapter 9 of part II, the fluid viscosity permits the flow singularity at a trailing edge to be smoothed. However, due to a characteristic relaxation time of the fluid, the singular behaviour is smoothed only partially at high frequencies. In other words, the Kutta condition is not completely satisfied at high frequencies. As a consequence, the conversion mechanism of kinetic energy into acoustic energy at a trailing edge is enhanced at high frequencies. In gust-airfoil interaction problems, a higher free-stream Mach number corresponds to higher frequencies in the airfoil reference frame. Thus, the trailing edge contribution becomes important at high Mach numbers.

- At high free-stream Mach numbers, the airfoil is no more acoustically compact. As a consequence, the airfoil leading edge and trailing edge generate two independent acoustic contributions.

In a rod-airfoil configuration, the generation of two distinct acoustic disturbances, together with the strong nonlinear effects occuring when the vortex impinges on the airfoil leading edge, are likely to be responsible for a spectral broadening of the acoustic radiation about the main frequency.

4.3 Effects of the Airfoil Camber

In this section we investigate the effects of the airfoil camber. The following discussion aims indeed to emphasize the nonlinear character of the interaction problem. When the oncoming vortex is described as a line-vortex, that is physically consistent only at high Reynolds numbers, the flow nonlinearity is responsible for a strong, and even critical[4], dependence of both the vortex trajectory and the induced pressure field on the geometrical parameters of the problem. On the contrary, when the impinging vortex and the curvature radius of the airfoil leading-edge have a comparable scale, the flow nonlinearity acts as a rearrangement mechanism of the vorticity field during the vortex distortion. The latter aspect has been described in section 4.2. Here we demonstrate that even a slight variation of the airfoil geometry can yield remarkably different results when a line-vortex model is used.

We consider two cambered airfoils, namely $\beta = \pm 2^o$ (see Fig.2.12 for the definition of β). A clockwise line-vortex is initially located at the transverse distance $y_v = 0.005\,\mathrm{m}$ from the airfoil chord line. The vortex circulation is determined by assuming $C_{l_{\max}} = 0.1$. Both a fixed- and a free-wake formulation are used and the results are compared.

4.3.1 Aerodynamic Results

The vortex trajectory is traced in Fig.4.16. In the case of a positive camber, the fixed- and the free-wake formulations provide nearly the same vortex path. Conversely, in the case of a negative camber, the vortex trajectories differ downstream of the trailing edge. Therefore, a small variation of the airfoil camber results in a strong difference of the vortex trajectory. The divergence of the vortex trajectory shown in Fig.4.16(b) for the free-wake case is caused by an interaction with the airfoil wake. Therefore, free-wake results are more physically consistent than those obtained by means of a fixed-wake approach.

The wake circulation obtained by a free-wake formulation for two values of the airfoil camber is plotted in Fig.4.17. Consistently with the different trajectories of the oncoming vortex, a more intense generation of vorticity occurs in the case of a negative camber.

The unsteady force induced by the vortex on the airfoil at the two values of the airfoil camber is plotted in Fig.4.18. A comparison is made between fixed- and free-wake results. In the case of a positive camber, the fixed- and the free-wake formulations provide a similar behaviour. However, significant differences occur as the vortex passes by the trailing edge when the effects related to the wake become more important. In the case $\beta = -2^o$, the trailing edge contribution to the aerodynamic force depends on whether the wake is supposed to be fixed or free. An explanation of this behaviour can be found by examining the vortex trajectory near the trailing edge. As shown in Fig.4.19, when a fixed-wake formulation is employed, the vortex crosses the trailing edge steady streamline. Conversely, when a free-wake model is used, the vortex is convected above the trailing edge streamline.

The airfoil wake is plotted at different time-steps in Figs. 4.20 and 4.21 for $\beta = 2^o$ and $\beta = -2^o$, respectively. In both the positive and negative camber cases, the wake is perturbed in three points (see Figs. 4.20(c) and 4.21(c)). The first perturbation on the downstream end of the wake is the response to the impulsive introduction of the oncoming vortex when the computation is started. The second perturbation, in the center of the wake, is generated when the vortex passes nearby the airfoil leading edge. Finally, the third perturbation is caused by the vortex passage by the trailing edge. The time amplification of the leading and trailing edge wake perturbations is related to the wake strength at these points. In Figs. 4.20 and 4.21 the oncoming vortex appears as an isolated point above the airfoil.

[4]Actually, the existence of critical flow configurations, such as an airfoil angle of attack for which the vortex impinges directly on the airfoil leading edge [32], is a by-product and a drawback of an ideal flow modeling. The sensitivity of the interaction dynamics to the configuration parameters can be reduced by introducing a random perturbation of the vortex position computed at each time-step. A *random walk method*, in fact, is commonly exploited to introduce diffusive effects in an otherwise ideal flow.

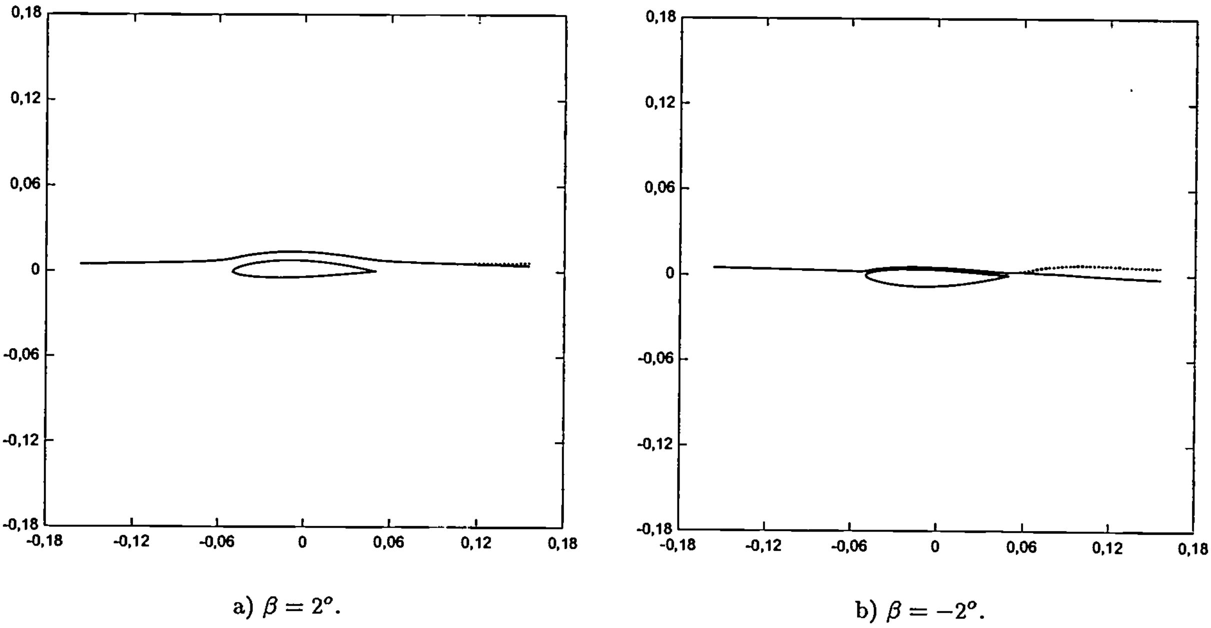

FIGURE 4.16: Vortex trajectory at different airfoil cambers. Comparison between fixed- and free-wake results: —— fixed-wake, - - - - free-wake.

4.3.2 Acoustic Results

The noise resulting from the vortex-airfoil interaction described in this section is plotted in Fig.4.22. In both the positive and negative camber cases, the trailing edge contribution to the acoustic pressure depends on the model used to describe the wake. Furthermore, concerning the main object of the present investigation, the noise level exhibits a strong dependence on the airfoil camber. Therefore, nonlinear effects may lead to erroneous results whenever a line-vortex model is used, though not adequate to describe the physics of the interaction process.

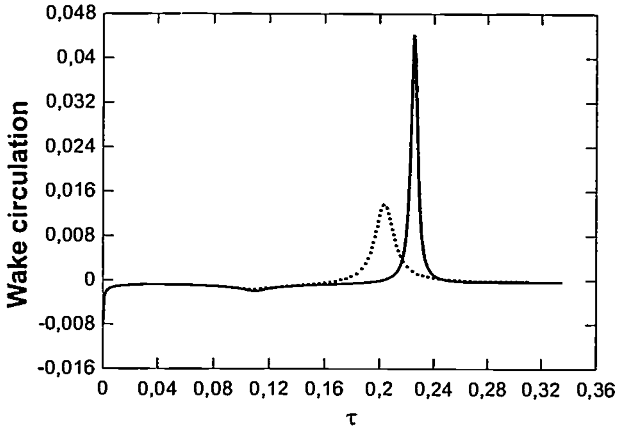

FIGURE 4.17: Dimensionless circulation of the airfoil wake ($\gamma\Delta\tau$) shed during the interaction between a vortex and a cambered airfoil. Free-wake results. —— $\beta = -2^o$, - - - - $\beta = 2^o$.

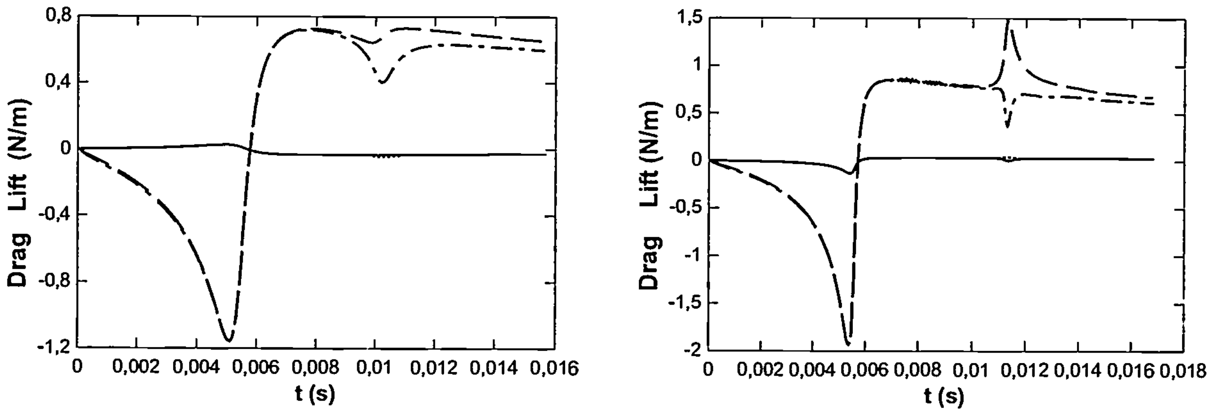

a) $\beta = 2^o$.

b) $\beta = -2^o$.

FIGURE 4.18: Unsteady force induced on a cambered airfoil by a line-vortex. Comparison between fixed- and free-wake results. Fixed-wake: —— drag, — — lift. Free-wake: - - - - drag, – - – lift.

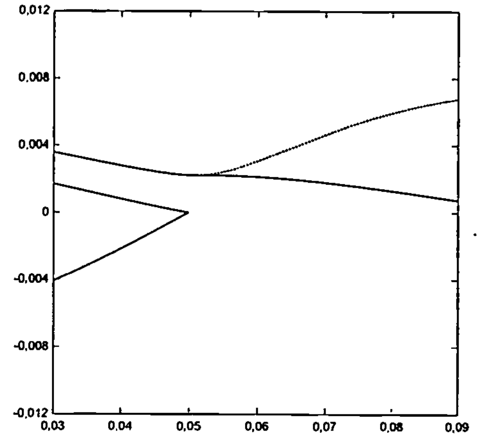

FIGURE 4.19: Vortex trajectory in proximity of the trailing edge of a cambered airfoil: $\beta = -2^o$. Comparison between fixed- and free-wake results: —— fixed-wake, - - - - free-wake.

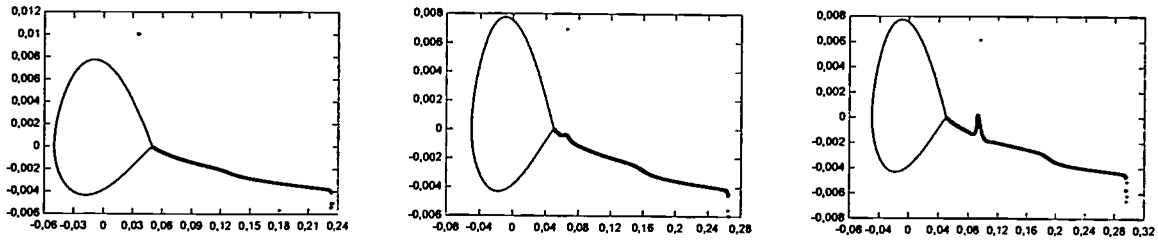

a) $t = 0.0093$s. b) $t = 0.0109$s. c) $t = 0.0124$s.

FIGURE 4.20: Vortex distribution in the airfoil Wake at different time-steps: $\beta = 2^o$. In Fig. c) three wake perturbations can be observed from right to left. These are caused by: i) the impulsive introduction of the oncoming vortex into the field when the computation is started, ii) the vortex passage nearby the leading edge, iii) the vortex passage nearby the trailing edge. The latter perturbation is more pronounced.

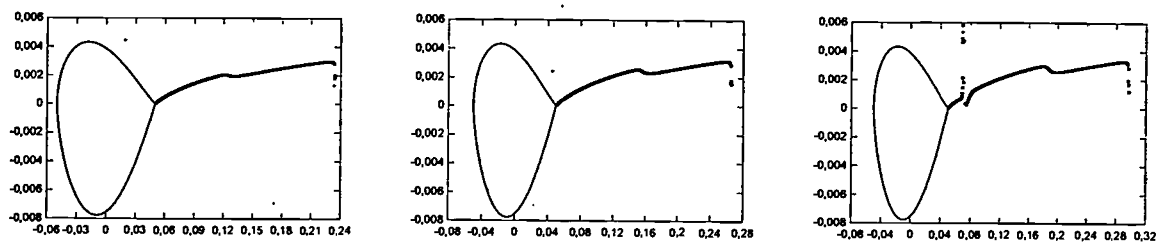

a) $t = 0.0093$s. b) $t = 0.0109$s. c) $t = 0.0124$s.

FIGURE 4.21: Vortex distribution in the airfoil wake at different time-steps: $\beta = -2^o$.

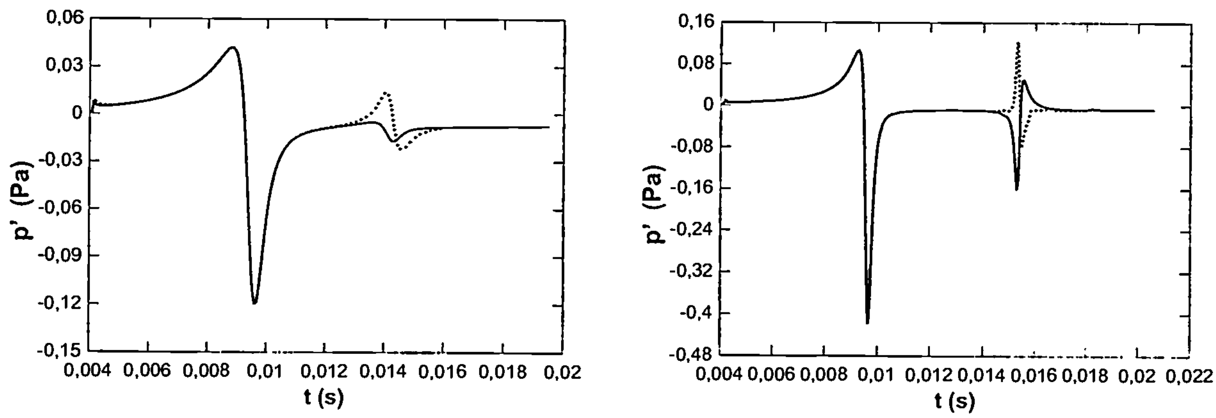

a) $\beta = 2^o$. b) $\beta = -2^o$.

FIGURE 4.22: Acoustic pressure at 90^o to the flow generated by the interaction between a line-vortex and a cambered airfoil. Comparison between fixed- and free-wake results: —— fixed-wake, - - - - free-wake.

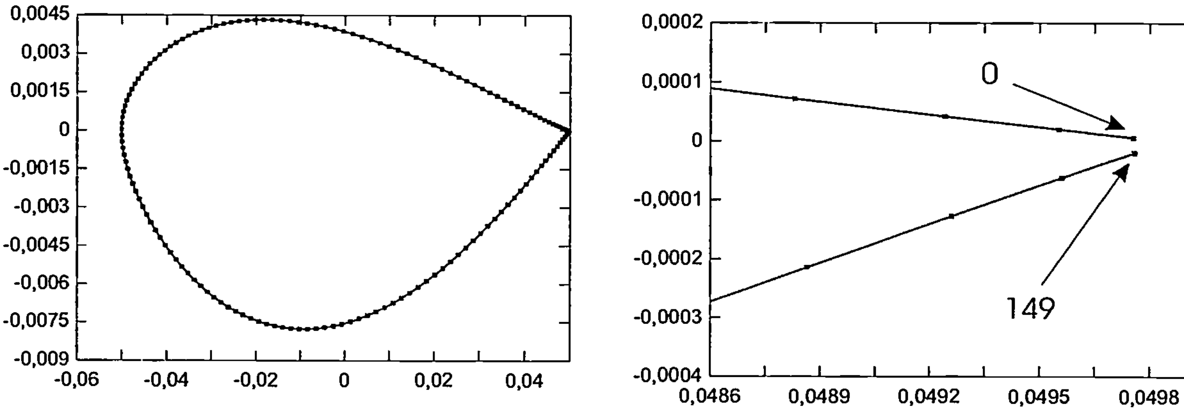

a) Numerical pressure probe distribution on the airfoil surface.

b) Trailing edge region.

FIGURE 4.23: Cambered airfoil: $\beta = -2^o$.

4.4 The Unsteady Pressure Field on the Airfoil Surface

In this section we investigate the unsteady pressure field on the airfoil surface. The case of a $\beta = -2^o$ cambered airfoil discussed in section 4.3 is subsequently considered. The analytical decomposition of $\dot{C}_p$ described in section 3.2 is used to scrutinize the reciprocal role of the various nonlinear interaction mechanisms in the generation of aerodynamic sound. Emphasis is given to the trailing edge contribution, in relation to the wake model adopted.

4.4.1 Trailing Edge Behaviour

In the example discussed in section 4.3, differences have been observed for the case $\beta = -2^o$, depending on whether a fixed- or a free-wake model are used. The origins of these differences can be found in the surface pressure field in proximity of the trailing edge

The points on the airfoil where the pressure coefficient is calculated are shown in Fig.4.23. These are numbered in a counterclockwise progression from 0, the nearest point to the trailing edge on the upper side of the airfoil (see Fig.4.23(b)), to 149, the nearest point to the trailing edge on the lower side of the airfoil. Point 74 denotes the leading edge. The distance of the points 0 and 149 from the analytical location of the trailing edge is about 2×10^{-4} m.

In Fig.4.24 a pressure jump is shown to exist between points 0 and 149 as the vortex passes by the trailing edge (see Fig.4.19). The dimensionless amplitude of this jump is 0.19 for the fixed-wake results, and 0.07 for the free-wake results. This difference is mainly due to the different trajectory of the vortex in the two cases. In fact, as already pointed out, when a fixed-wake formulation is used, the vortex crosses the steady streamline from the trailing edge. Conversely, when a free-wake formulation is used, the vortex convects above the trailing edge streamline.

Although the velocity at the trailing edge should vanish, as required by the instantaneous fulfilment of the Kutta condition, the time derivative of the pressure coefficient has a non zero value due to the second order time derivative of the complex potential (see equation (3.9)). This is plotted in Fig.4.25 where a comparison between fixed- and free-wake results shows that a free-wake model results in a reduction of the time rate of the pressure coefficient at the trailing edge.

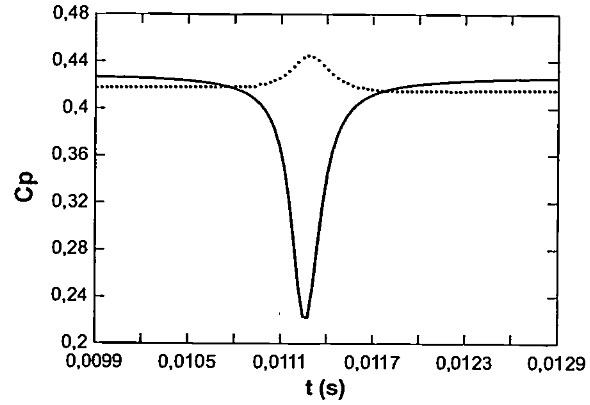

a) Fixed-wake results.

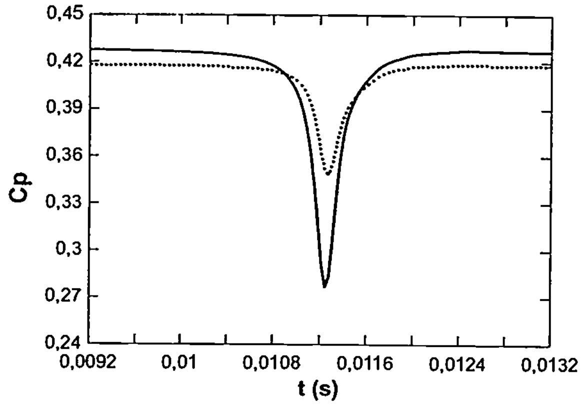

b) Free-wake results.

FIGURE 4.24: Pressure coefficient induced by a line-vortex onto the trailing edge region of a cambered airfoil: —— point 0, - - - - point 149. Comparison between fixed- and free-wake results.

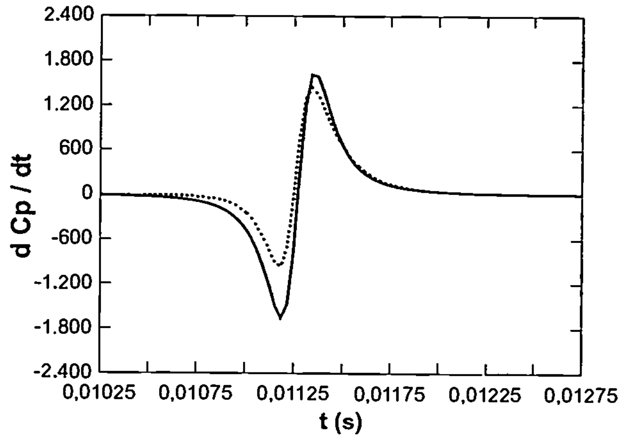

FIGURE 4.25: Time derivative of the pressure coefficient induced by a line-vortex exactly at the trailing edge of a cambered airfoil. Comparison between fixed- and free-wake results: —— fixed-wake, - - - - free-wake.

4.4.2 Aeroacoustic Sources Characterization

In this subsection we investigate the behaviour of the nonlinear interaction terms $\dot{C}_{p_v}$, $\dot{C}_{p_w}$, $\dot{C}_{p_{vw}}$ and $\dot{C}_{p_{ww}}$ on the airfoil surface. These terms have been analytically defined in section 3.2. The numerical probe distribution along the airfoil is shown in Fig.4.23. In order to compare the values that a nonlinear term takes in two different points of the airfoil, all the values have been multiplied by the local length of the discrete airfoil element $d\mathcal{L}$.

The maximum values reached by the nonlinear interaction terms are plotted in Fig.4.26(a). It can be observed that the vortex and the wake contributions tend to converge in proximity of the airfoil trailing edge (points 0 and 149). Analogously, the vortex-wake and the wake-wake interaction contributions reach nearly the same maximum values near the trailing edge. Furthermore, the nonlinear interaction contributions related to the oncoming vortex (v, vw) have a non symmetrical behaviour on the two sides of the airfoil. Conversely, the contributions related to the airfoil wake (w, ww) exhibit a quasi symmetrical pattern.

In Fig.4.26(b) the time-steps at which the four contributions reach their maximum values are plotted

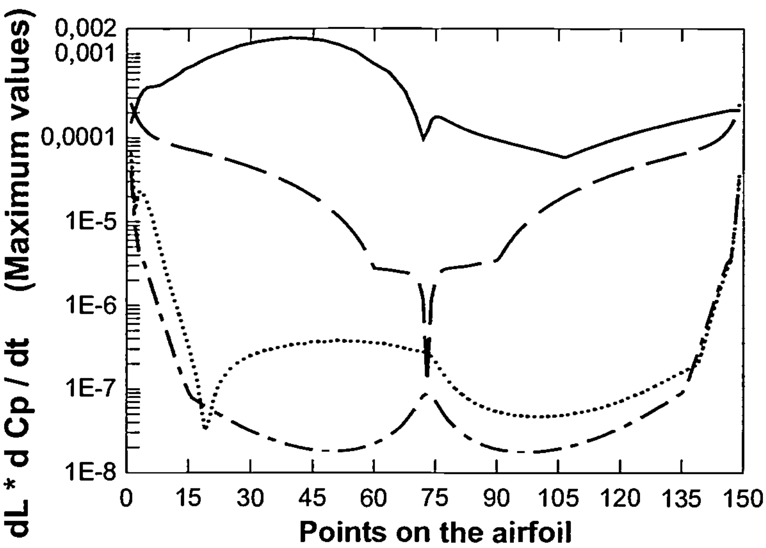

a) Maximum values of $\dot{C}_p \, d\mathcal{L}$ (dimensionless quantities). —— Vortex, — — Wake, - - - - Vortex-Wake, – – – Wake-Wake contributions.

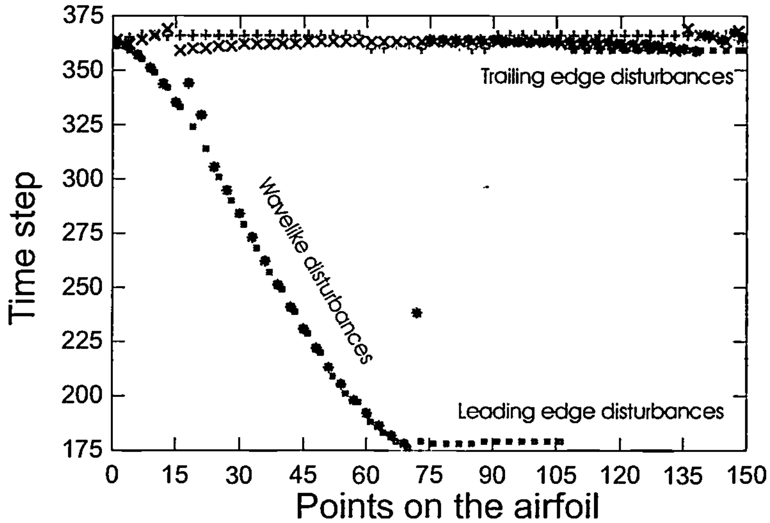

b) Time at which the maximum values of $\dot{C}_p \, d\mathcal{L}$ peaks. • Vortex, + Wake, ⋆ Vortex-Wake, × Wake-Wake contributions (values are plotted one point every three points on the airfoil).

FIGURE 4.26: Aeroacoustic sources distribution on the surface of a cambered airfoil. Free-wake formulation.

for the free-wake case. Values are gathered in three regions. The first is a line at $t \simeq$ const, related to the time at which the vortex passes by the airfoil leading edge. The second is a line with slope related to the vortex convection velocity. The third region is a line at $t \simeq$ const related to the time at which the vortex passes by the airfoil trailing edge. Thus, two types of disturbances can be distinguished. Simultaneous disturbances at the airfoil leading edge and trailing edge, and wavelike disturbances. The latter convect at the vortex velocity and represent the trace on the airfoil surface of the vortex passage. Thus, the wavelike contributions peak only on the crossed side of the airfoil. Only the vortex contribution and the vortex-wake interaction contribution can produce wavelike disturbances. On the contrary, the wake contribution and the wake-wake self interaction contribution arise only when the vortex passes by the trailing edge.

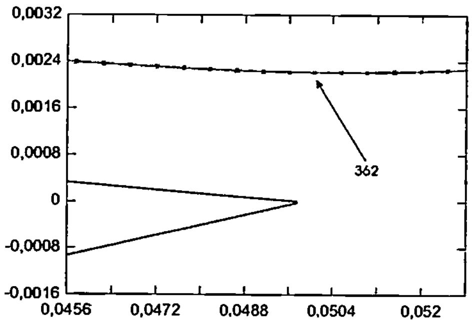

FIGURE 4.27: Vortex trajectory in proximity of the trailing edge.

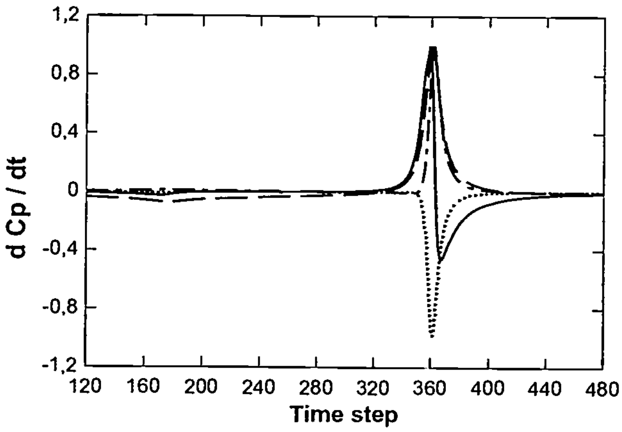

FIGURE 4.28: Normalized time derivative of the pressure coefficient. Point 0: Trailing edge region. Free-wake results. —— Vortex, — — wake, - - - - vortex-wake, – – – wake-wake contributions.

In Figs. 4.28, 4.29 and 4.30 the time trace of the nonlinear interaction terms $\dot{C}_{p_v}$, $\dot{C}_{p_w}$, $\dot{C}_{p_{vw}}$ and $\dot{C}_{p_{ww}}$ in three points of the airfoil are plotted. A free-wake model has been employed. Values have been normalized by the corresponding maximum values plotted in Fig.4.26(a).

In the trailing edge region (Fig.4.28), the vortex and the wake contributions add before the vortex has passed by the trailing edge (time-step 362 in Fig.4.27). Then they generate opposite effects. Conversely, the vortex-wake and the wake-wake interaction contributions generate opposite effects during the whole passage of the vortex by the trailing edge.

In the maximum thickness point (Fig.4.29), the vortex contribution has a peak at the time at which the vortex passes by the point itself. As previously discussed, this constitutes a wavelike disturbance and represents the trace of the vortex passage along the airfoil surface. Moreover, the vortex contribution is also characterized by leading edge and trailing edge disturbances. In the limit of an incompressible flow approximation, these disturbances reach simultaneously each point of the airfoil. The vortex-

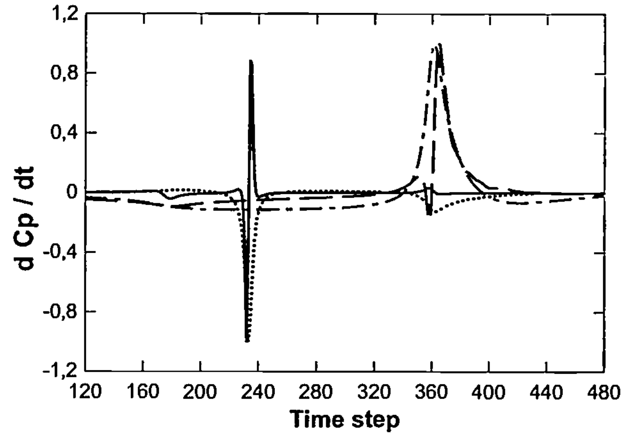

FIGURE 4.29: Normalized time derivative of the pressure coefficient. Point 44: Maximum thickness point. Free-wake results. —— Vortex, — — wake, - - - - vortex-wake, – – – wake-wake contributions.

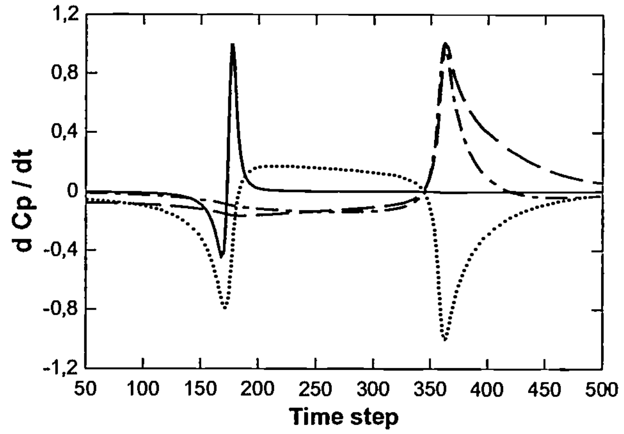

FIGURE 4.30: Normalized time derivative of the pressure coefficient. Point 74: leading edge. Free-wake results. —— vortex, — — wake, - - - - vortex-wake, – – – wake-wake contributions.

wake interaction contribution, in the maximum thickness point, exhibits a dominant wavelike nature. However, also a trailing edge disturbance can be observed. Finally, the wake contribution and the wake-wake contribution peak only when the vortex passes by the trailing edge.

At the leading edge (Fig.4.30), the vortex contribution exhibits a peak corresponding to the time at which the vortex passes by the leading edge itself. Clearly, at this location it is not possible to distinguish between a wavelike disturbance and a leading edge disturbance. The vortex-wake interaction contribution exhibits comparable peaks at times at which the vortex passes by the leading edge and by the trailing edge, respectively. Finally, the wake and the wake-wake interaction contributions arise when the vortex passes by the trailing edge.

The four contributions $\dot{C}_{p_v}$, $\dot{C}_{p_w}$, $\dot{C}_{p_{vw}}$ and $\dot{C}_{p_{ww}}$ can be integrated upon the airfoil surface in order to investigate the effect of the nonlinear interaction mechanisms on the time derivative of the aerodynamic force exerted on the airfoil. In Fig.4.31 the time derivative of the lift coefficient generated when the vortex is nearby the trailing edge is plotted. As shown in Fig.4.31(a), the vortex and the wake contributions generate opposite effects. Thus, a partial cancelation results. This happens before the vortex has passed by the trailing edge.

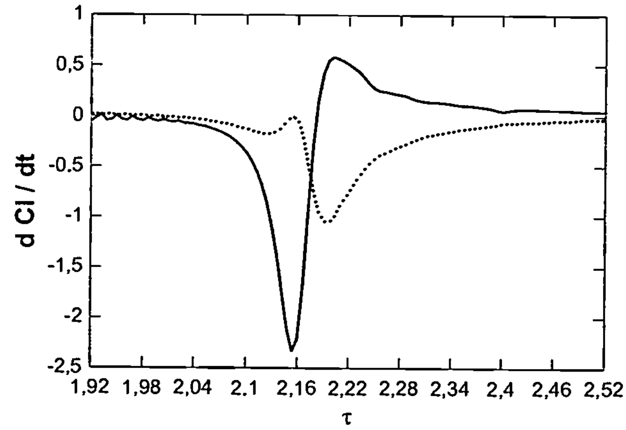

a) Vortex and wake contributions: —— $-\int_{\mathcal{L}} \dot{C}_{p_v}\, n_y \, \mathrm{d}\mathcal{L}$, - - - - $-\int_{\mathcal{L}} \dot{C}_{p_w}\, n_y \, \mathrm{d}\mathcal{L}$.

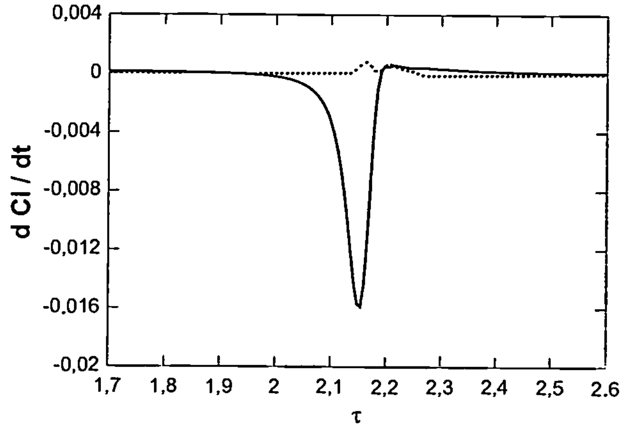

b) Vortex-wake and wake-wake interactions contributions: —— $-\int_{\mathcal{L}} \dot{C}_{p_{vw}}\, n_y \, \mathrm{d}\mathcal{L}$, - - - - $-\int_{\mathcal{L}} \dot{C}_{p_{ww}}\, n_y \, \mathrm{d}\mathcal{L}$.

FIGURE 4.31: Time derivative of the lift coefficient generated by the vortex passage by the airfoil trailing edge. Airfoil camber $\beta = -2^o$. Free-wake formulation.

4.5 Effects of the Free-Stream Velocity

In this section we consider a symmetrical airfoil embedded at a zero angle of attack in a double row of 10 counter rotating line-vortices. The circulation of each vortex is determined by assuming $C_{l_{\max}} = 0.5$. The aspect ratio of the double row is $b/a = 0.281$ (see Fig.2.11).

A fixed-wake formulation is employed, which consists in a rectilinear vortex-sheet continuously shed from the trailing edge and convected downstream of the airfoil at the free-stream velocity (see Fig.2.2). As pointed out in section 4.1, the fixed-wake formulation provides consistent results when the airfoil is at a zero angle of attack.

The oncoming vortices are initially located at a given distance upstream of the airfoil. Notwithstanding the small velocity induced at the trailing edge, vorticity is initially shed in response to the impulsive variation of the flow with respect to a steady configuration when the computation is started. Hence, the initial generation of vorticity is a consequence of the non fulfillment of the initial condition $\gamma(0) = 0$, γ denoting the wake circulation per unit length.

Due to the finite extent of the double row of vortices, only a quasi-periodic state of the flow can be achieved. As a result, the initial and final transitory phases exhibit a different behaviour.

Computations have been performed at three Mach numbers, namely $M_\infty = \{0.02, 0.06, 0.18\}$. Clearly, in terms of dimensionless variables, the aerodynamic problem is the same for the three cases.

4.5.1 Aerodynamic Results

The trajectories of the incident vortices and the wake circulation are shown in Fig.4.32. The scattering of the vortex paths is due to the finite extent of the double row. As a consequence, a quasi-periodic wake circulation is shed into the field.

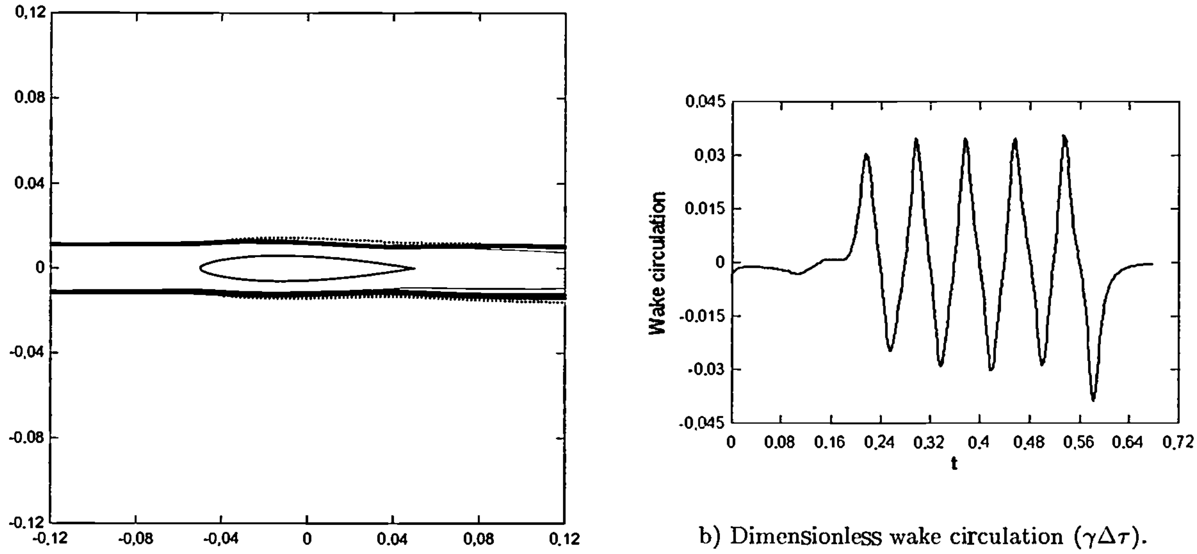

a) Trajectories of the incident vortices.

b) Dimensionless wake circulation ($\gamma\Delta\tau$).

FIGURE 4.32: Interaction between an airfoil and a Kármán vortex street made of 10 line-vortices.

In Fig.4.33 the airfoil lift and drag coefficients are plotted. It is interesting to notice that a lift cycle ends every two oncoming vortices (dominant frequency $2f_0$), whereas a drag cycle ends every time a vortex approaches the airfoil (dominant frequency f_0). This is because the drag is mainly due to the pressure suction at the leading edge which does not depend on the oncoming vortex sign. On the contrary, the lift is due to the upwash velocity whose sign depends on the oncoming vortex sign.

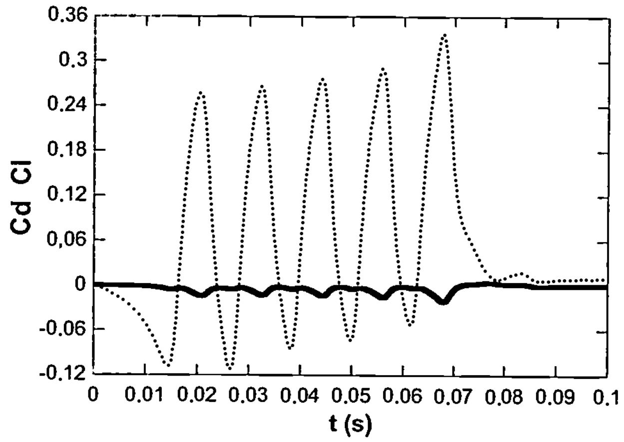

FIGURE 4.33: Unsteady force on the airfoil embedded in a double row of 10 counter rotating line-vortices. —— Cd; - - - - Cl.

4.5.2 Acoustic Results

Acoustic predictions have been performed at a distance $r = 1.4\,\mathrm{m}$. The radiation parameter kr at the three values of M_∞ has the values $kr = \{2.2, 6.6, 19.8\}$. Thus, only at the highest Mach number the observation points are in the acoustic far field.

The acoustic pressure at different Mach numbers is shown in Fig.4.34. The related spectra are traced in Fig.4.35.

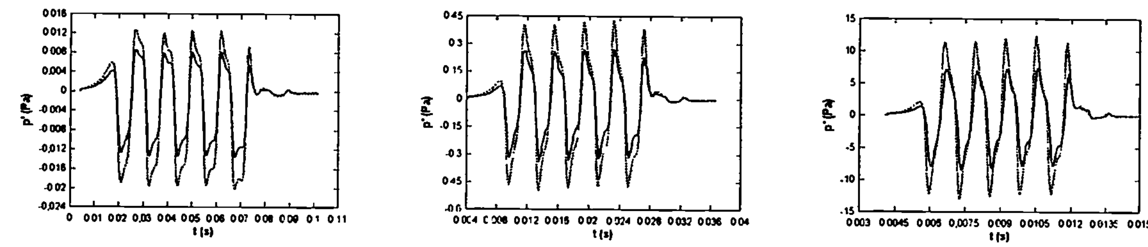

a) $M_\infty = 0.02$. b) $M_\infty = 0.06$. c) $M_\infty = 0.18$.

FIGURE 4.34: Acoustic pressure generated by an airfoil in a double row of 10 counter-rotating line-vortices. —— $\theta = 45^o$; - - - - $\theta = 90^o$.

The effect of the Mach number on the noise level is shown in Fig.4.36. The directivity pattern in Fig.4.36(a) is essentially the same at the three values of M_∞. However, as shown in Fig.4.36(b), the noise level depends on both M_∞ and the observation angle θ. At lower values of M_∞ the power law exponent is a weak function of θ and has a mean value of about 5.7. At higher values of M_∞ the power law exponent exhibits a more pronounced dependence on θ and its mean value is of about 5.9. This behaviour reflects the tendency of the acoustic directivity to exhibit lobes as the ratio between the acoustic wavelength and the airfoil chord decreases (see for example Ref. [33]).

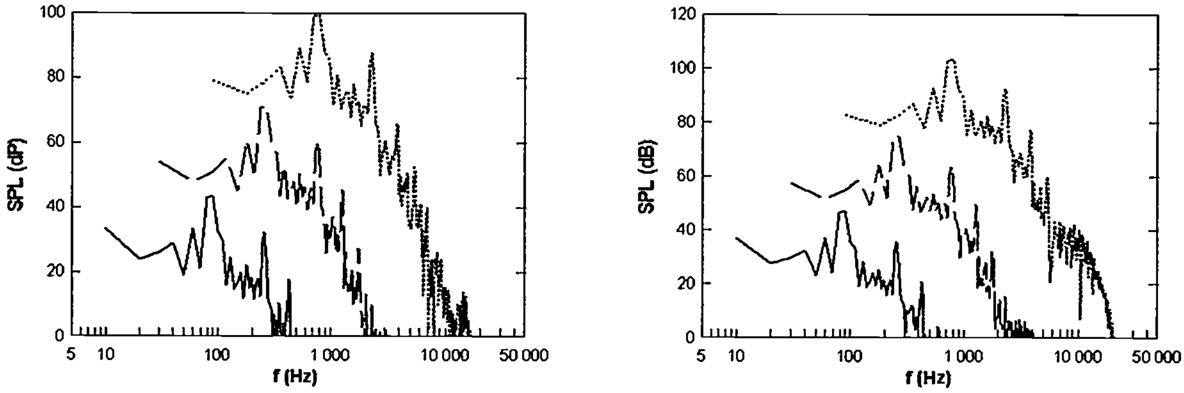

a) $\theta = 45^o$.

b) $\theta = 90^o$.

FIGURE 4.35: Spectrum of the acoustic pressure from an airfoil in a double row of 10 counter-rotating line-vortices. —— $M_\infty = 0.02$; — — $M_\infty = 0.06$; - - - - $M_\infty = 0.18$.

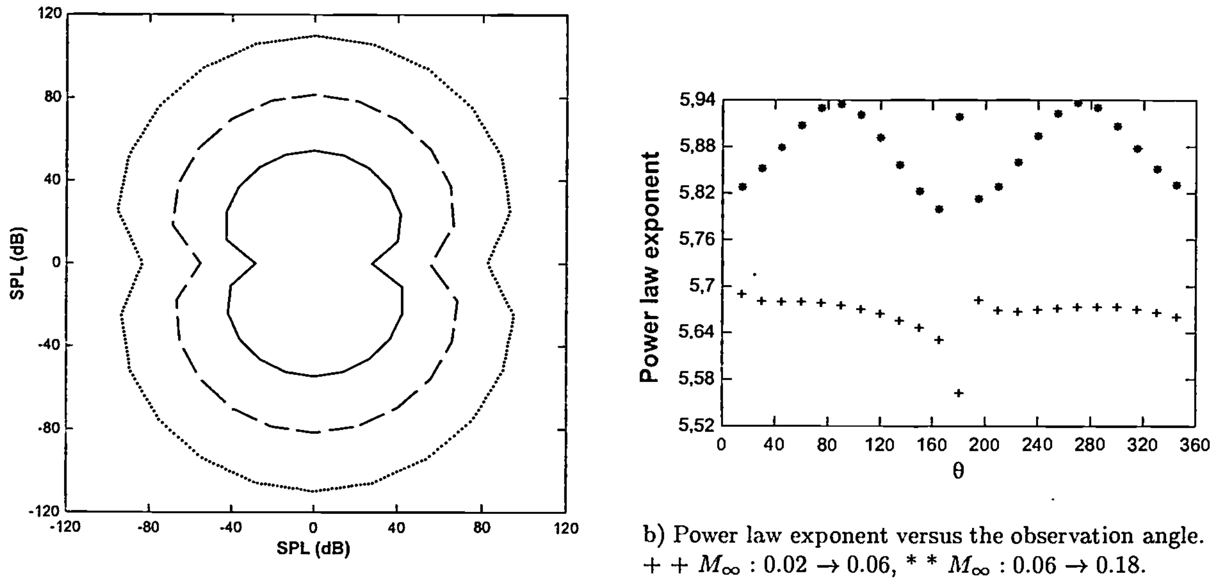

a) Directivity pattern. —— $M_\infty = 0.02$; — — $M_\infty = 0.06$; - - - - $M_\infty = 0.18$.

b) Power law exponent versus the observation angle. + + M_∞ : 0.02 → 0.06, * * M_∞ : 0.06 → 0.18.

FIGURE 4.36: Noise intensity levels at different free-stream Mach numbers generated by an airfoil in a double row of 10 counter rotating line-vortices.

4.6 Effects of the Airfoil Angle of Attack

In this section we investigate the effects of the airfoil angle of attack. A double row of 16 counter-rotating vortices is convected past an airfoil at two values of the airfoil angle of attack, namely $\alpha = \{0^o, 4^o\}$. The aspect ratio of the double row is $b/a = 0.2$. The circulation of each vortex is determined by assuming $C_{l_{\max}} = 0.6$. Previous investigations [32] showed that when a line-vortex model is used there exists a critical angle of attack at which one row impinges directly on the airfoil leading edge. This causes a dramatic increase of the noise levels. Such a behaviour is of the same nature of that investigated in section 4.3. It is related to the nonlinearity of the problem in relation to the size of the impinging vortex. Therefore, in order to reduce the sensitivity of the interaction process to the trajectories of the vortices, a cloud of vortices is herein considered. The circulation of each vortex is shared among 37 vortices of equal strength. The resulting vortex size is slightly smaller than the airfoil thickness.

The effects of the wake modeling are not investigated in the present example. Thus, a fixed-wake formulation is employed.

4.6.1 Aerodynamic Results

The arrangement of the oncoming vortices is shown in Fig.4.37.

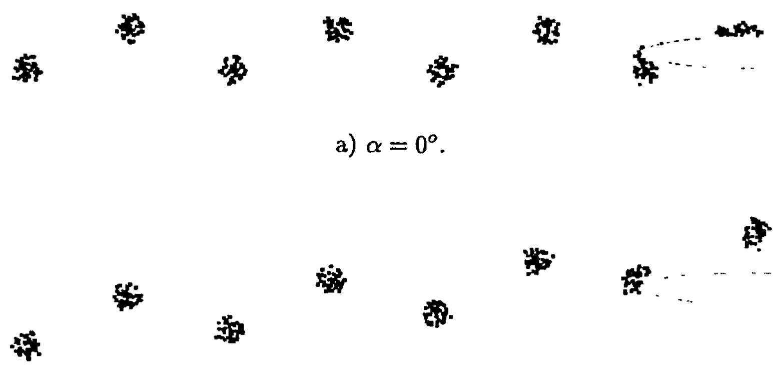

a) $\alpha = 0^o$.

b) $\alpha = 4^o$.

FIGURE 4.37: Interaction between an airfoil and a Kármán vortex street of 16 clouds of vortices at two values of the airfoil angle of attack.

In Fig.4.38 the unsteady lift and drag coefficients induced by the vortex-street are traced. Only a quasi-periodical behaviour takes place for the reasons already explained in section 4.5.

4.6.2 Acoustic Results

The spectrum of the acoustic pressure at different observation angles is shown in Fig.4.39. The main peak at the frequency of 250 Hz has nearly the same value for the two airfoil angles of attack. However, in the case of a non zero angle of attack, a peak arises at the first harmonic ($f = 500$ Hz).

The presence of a peak at the first harmonic can be physically explained in terms of deviation from a flow configuration characterized by an upwash fluctuating velocity with only odd harmonics. As shown in subsection 2.2.7, such a configuration takes place only when the airfoil is embedded symmetrically in the double row of vortices. When the airfoil has a nonzero angle of attack ($\alpha = 4^o$ in the present case), both the upper and lower rows of vortices pass above the leading edge. In addition, the lower row vortices are partially split on the airfoil leading edge (see Fig.4.37(b)). The two-dimensional linear model developed in section 3.3 can be used to validate this interpretation. Let us translate the oncoming

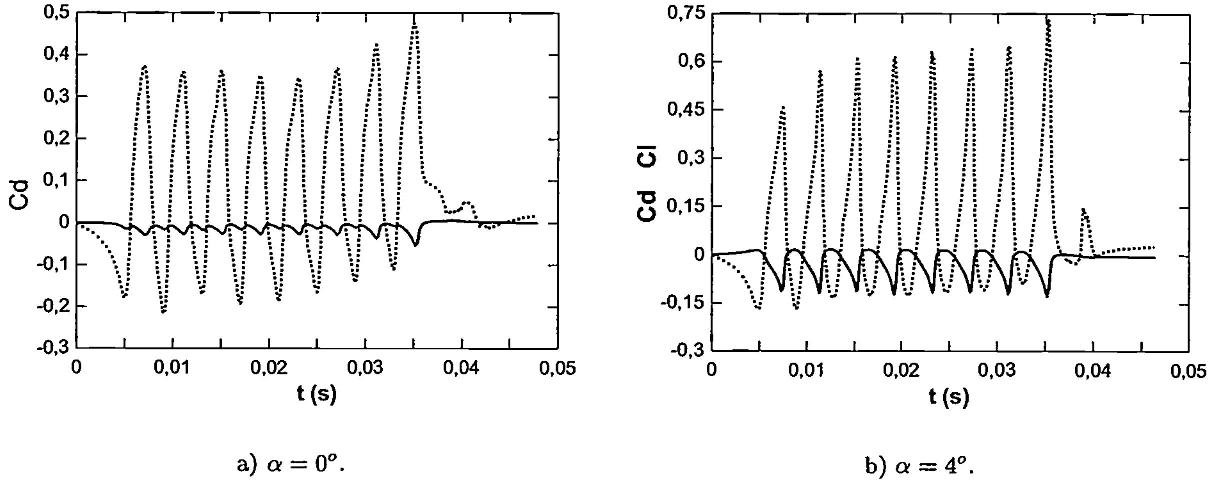

FIGURE 4.38: Unsteady force on the airfoil induced by a double row of 16 counter-rotating vortices at two values of the airfoil angle of attack: —— drag coefficient, - - - - lift coefficient.

double row of vortices of the quantity y_m in the normal direction to the flat-plate (see Fig.2.11). Then equation (4.1) takes the form

$$p(r,\theta,t) = \frac{-V_\infty^2\sqrt{M_\infty}\sin\theta}{\sqrt{r}}\frac{\rho_0\, C_{l_{\max}}\, l\, d}{\pi\sqrt{2c}} \left[\sum_{n=-\infty}^{\infty}\frac{(-1)^n\,(V_\infty t + l/2 - na/2)\, l/(b/2-(-1)^n y_m)^2}{1+(V_\infty t + l/2 - na/2)^2/(b/2-(-1)^n y_m)^2}\right]_{t-r/c_0} \tag{4.1}$$

The resulting acoustic spectrum obtained with a value $y_m = b/10$ is plotted in Fig.4.40, where it is compared to the symmetrical case $y_m = 0$. It can be observed that peaks at even harmonics arise when a non symmetrical interaction occurs.

Thus, the rise of even harmonics can be inferred to a shift between the axis of the double vortex row with respect to the leading edge, regardless of the fact that this shift is due to a nonzero angle of attack or not.

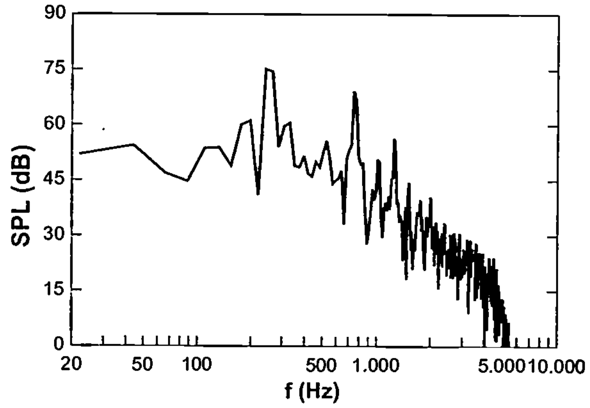

a) $\alpha = 0^o$, $\theta = 45^o$.

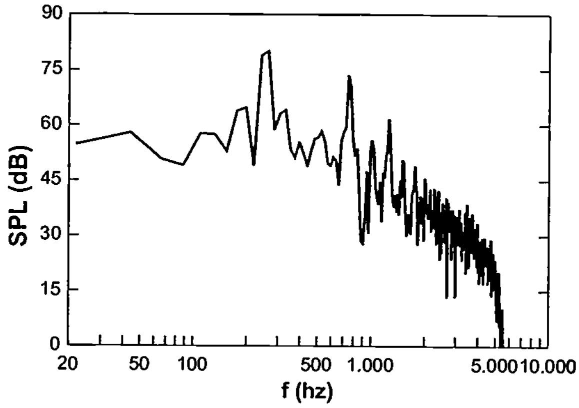

b) $\alpha = 0^o$, $\theta = 90^o$.

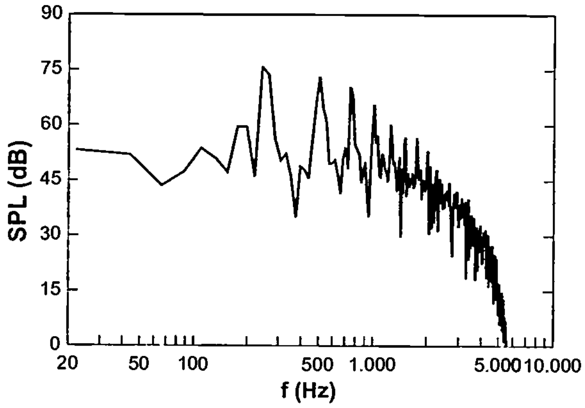

c) $\alpha = 4^o$, $\theta = 45^o$.

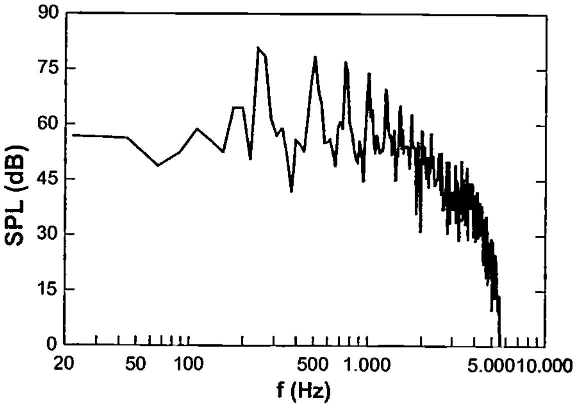

d) $\alpha = 4^o$, $\theta = 90^o$.

FIGURE 4.39: Spectrum of the acoustic pressure generated by the interaction between an airfoil and a double row of counter-rotating vortices at two values of the airfoil angle of attack.

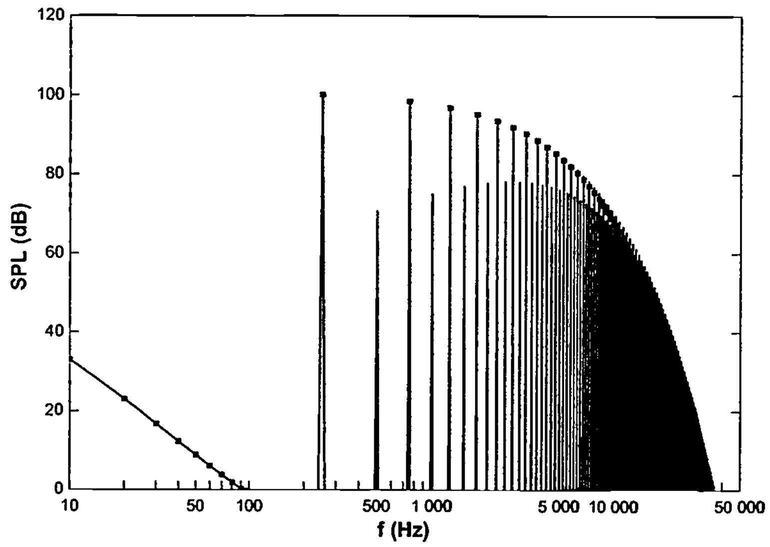

FIGURE 4.40: Spectrum of the acoustic pressure obtained by using equations (3.18) and (4.1). •• Symmetrical interaction $y_m = 0$, —— non symmetrical interaction $y_m = b/10$. The following numerical parameters have been used: 100 counter-rotating vortices, $d = 0.016\,\text{m}$, $V_\infty = 20\,\text{m/s}$, $a = 5D$, $b = 0.03a$, $C_{l_{\max}} = 0.7$, $c = 0.1\,\text{m}$, $l = 0.2\,\text{m}$, $r = 10\,\text{m}$.

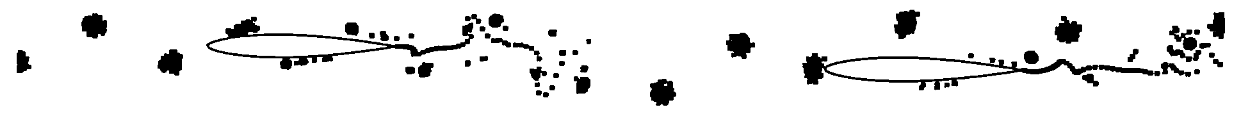

a) $\alpha = 0^o$.

b) $\alpha = 4^o$.

FIGURE 4.41: Interaction between an airfoil and a double row of 16 clouds of vortices at different angles of attack. Each cloud is constituted of 50 line-vortices.

4.7 Comparison with Experimental Results

In this section we compare experimental data of the noise radiated by an NACA-0012 airfoil in the wake of a cylinder, with a numerical prediction of the noise radiated by an airfoil in a Kármán vortex street.

A Kármán-Trefftz airfoil approximating an NACA-0012 airfoil is used in the computation, and the Kármán vortex street is described as a double row of 16 counter-rotating vortices. The aspect ratio of the double-row is $b/a = 0.25$. The oncoming vortices are described as circular clouds of 50 equal-strength vortices. The circulation of each cloud is determined by assuming a value $C_{l_{max}} = 0.65$, whereas the external size of each cloud is 5×10^{-3} m. A free-wake model is employed.

The parameter $C_{l_{max}}$ is related to circulation of the oncoming vortices by the relation

$$\Gamma = \frac{2C_{l_{max}}\, d}{c} \tag{4.2}$$

which is a dimensionless approximated form of (2.61). The vortices, in fact, are supposed to be shed from an upstream rod on which a harmonic lift coefficient $C_{l_{max}} \sin(2\pi f_0 t)$ is induced. In the present computation we adopted a value $C_{l_{max}} = 0.65$ which is in agreement with the Navier-Stokes computation described in chapter 7 (see Table 7.1).

Two interaction problems have been solved at two values of the airfoil angle of attack, namely $\alpha = \{0^o, 4^o\}$.

We present some aerodynamic results and then we compare the experimental and the predicted sound spectra. The experimental data used in this section are the same as those discussed in chapter 5.

4.7.1 Aerodynamic Results

In Fig.4.41 the distribution of the oncoming vortices and their interaction with the airfoil wake is shown. In the case $\alpha = 4^o$ the lower row vortices and the airfoil leading edge interact directly. Due to the image vortex system, the lower row vortices exhibit a stronger attitude to pass above the leading edge. As a consequence, the lower row vortices are predominantly convected along the upper side of the airfoil. This behaviour is illustrated on Fig.4.42 where snapshots of the vortex distribution past the airfoil are shown. In both cases $\alpha = 0^o$ and $\alpha = 4^o$, the oncoming vortices are partially disorganized as they pass by the airfoil leading edge.

The airfoil wake circulation is plotted in Fig.4.43. A quasi periodical behaviour can be observed for the case $\alpha = 0^o$. In the case $\alpha = 4^o$ more pronounced transient effects related to the finite extent of the vortex street can be noticed.

In Fig.4.44 the unsteady force exerted n the airfoil is plotted. A less pronounced transient behaviour can be observed.

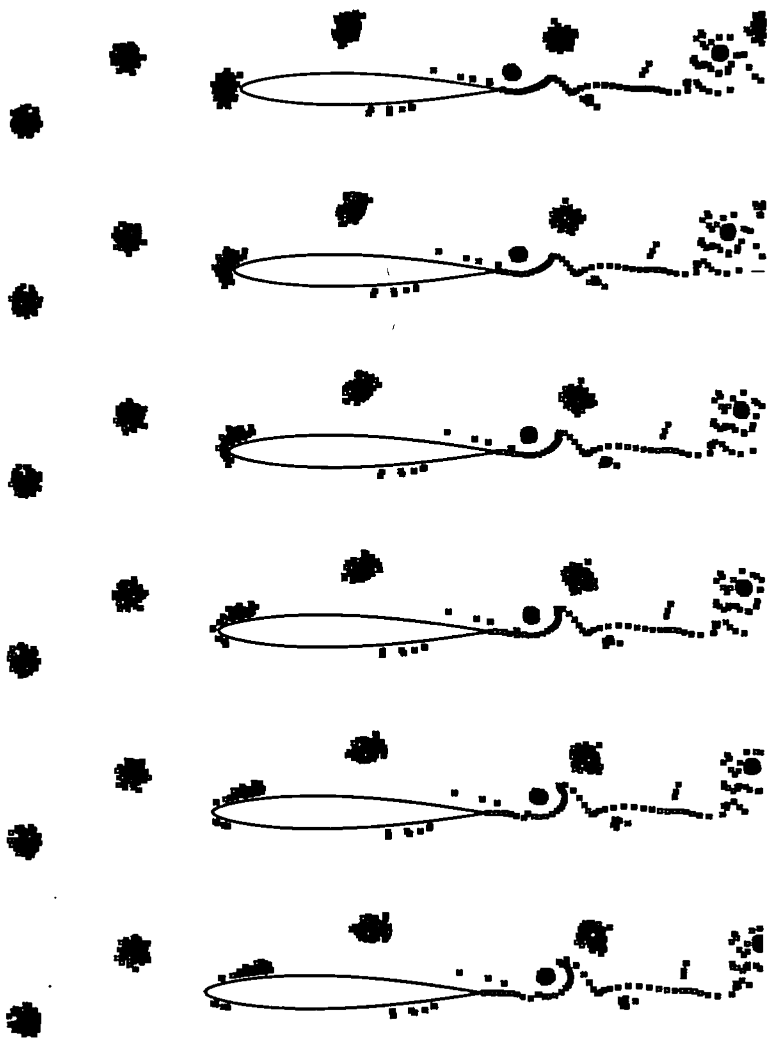

FIGURE 4.42: Snapshots of a double row of counter-rotating vortices past an airfoil at $\alpha = 4^o$. Each vortex is constituted of 50 line-vortices.

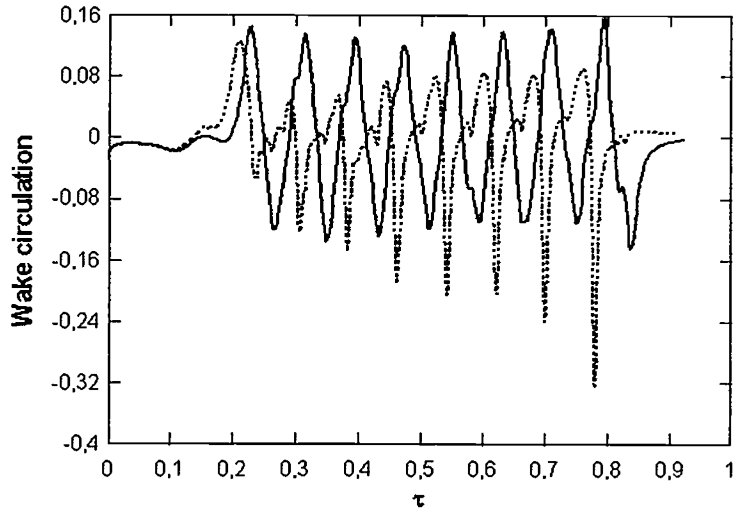

FIGURE 4.43: Airfoil wake circulation ($\gamma\Delta\tau$). —— $\alpha = 0^o$, - - - - $\alpha = 4^o$.

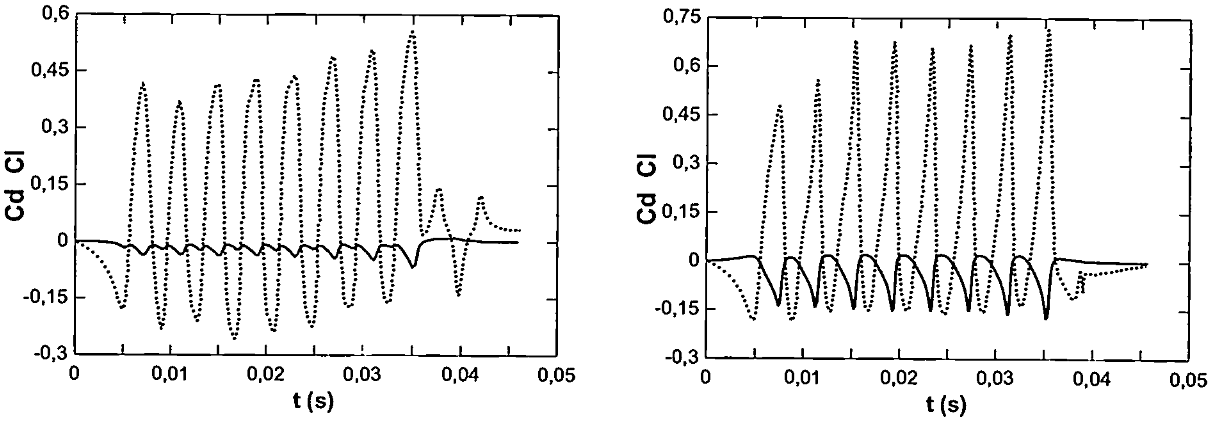

a) $\alpha = 0^o$. b) $\alpha = 4^o$.

FIGURE 4.44: Unsteady force on the airfoil induced by a double row of 16 counter rotating vortices at different angles of attack: —— drag coefficient, - - - - lift coefficient.

4.7.2 Acoustic Results

In Fig.4.45 acoustic numerical results are checked against experimental data at different observation angles. The results clearly show that the value $C_{l_{\max}} = 0.65$ used in the present computation provides a good agreement between the experimental data and the numerical prediction at the Strouhal frequency ($f_0 = 250\,\text{Hz}$). Moreover, the overall levels agree fairly well up to the third harmonic ($4f_0$). At higher frequencies the experimental levels are far below the numerical ones. This is not surprising because the aerodynamic prediction cannot feature all the aspects of the vortex dynamics. As it will be discussed in chapters 5 and 7, three-dimensional effects play an important role in the rod-airfoil configuration. These effects are not accounted for by a two-dimensional flow simulation.

Interestingly, for $\alpha = 4^o$ the numerical solutions exhibit pronounced peaks at the first harmonic ($2f_0 = 500\,\text{Hz}$). As already discussed in section 4.6, this behaviour is due to a *non symmetrical* interaction between the airfoil and the double row of vortices. More precisely, the presence of even harmonics in the acoustic spectrum at an observation angle $\theta = 90^o$ can be explained in the following way. The velocity fluctuations induced along the axis of the vortex street result from a Fourier combination of only even harmonics. This velocity has a nonzero component in the direction normal to the airfoil chord, acting as an upwash velocity. As a consequence, the spectrum of the lift induced on the airfoil exhibits even harmonics. Since, the lift fluctuations are responsible for the acoustic radiation at an observation angle $\theta = 90^o$, the presence of even harmonics in the acoustic spectrum can be consistently explained.

As an important result, first harmonic peaks appear also in the experimental data, although their amplitude remain quit smaller.

A physical explanation of the higher amplitude levels predicted at the higher harmonics ($2f_0, 3f_0, \ldots$) can be found in the following items.

- The amplitudes of the higher harmonic peaks are sensibly affected by the reciprocal positions between the vortices and the airfoil. As a consequence, any random perturbation of the vortex positions results in a reduction of the time averaged peaks of the airfoil response. In other words, the statistics smear the level of the high harmonic peaks.

- High frequency wall pressure fluctuations undergo a more important viscous dissipation.

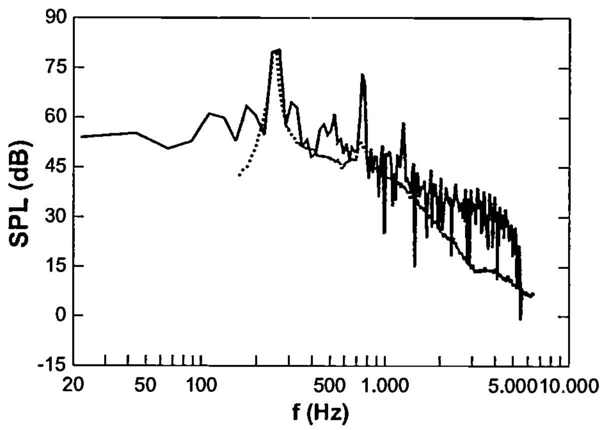

a) $\alpha = 0^o$, $\theta = 90^o$.

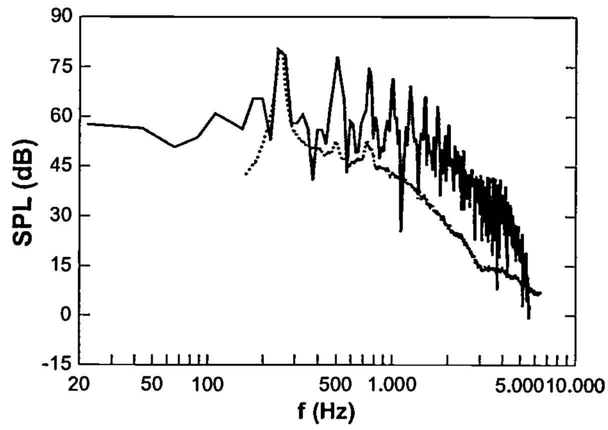

b) $\alpha = 4^o$, $\theta = 90^o$.

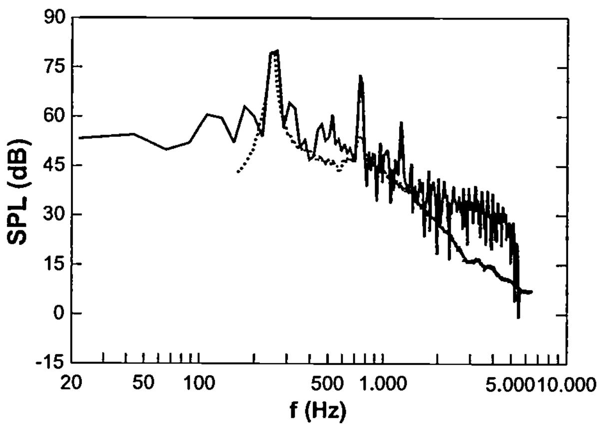

c) $\alpha = 0^o$, $\theta = 75^o$.

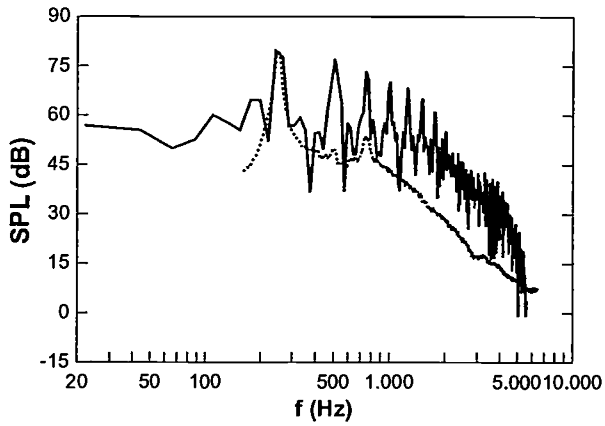

d) $\alpha = 4^o$, $\theta = 75^o$.

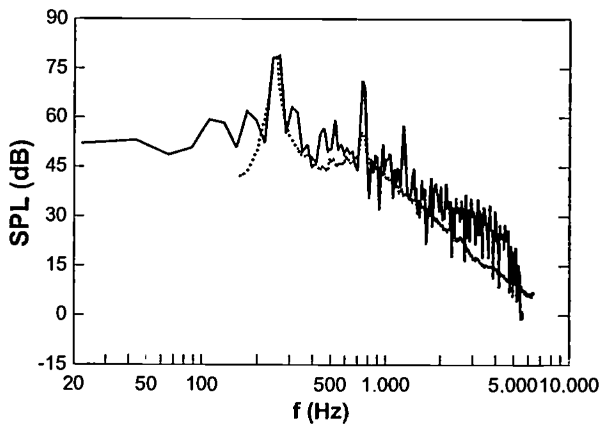

e) $\alpha = 0^o$, $\theta = 60^o$.

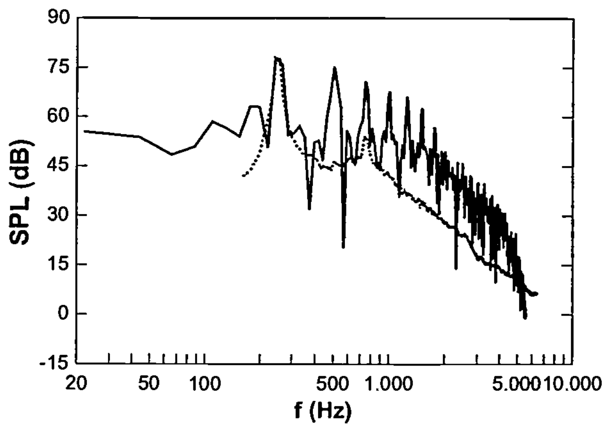

f) $\alpha = 4^o$, $\theta = 60^o$.

FIGURE 4.45: Spectrum of the acoustic pressure generated by a Kármán vortex street past an airfoil. Comparison between experimental data and numerical results: —— numerical results, - - - - experimental data.

- As it will be discussed in chapter 7, the spanwise statistical behavior of the flow in the wake of a cylinder has a dominant influence on the acoustic radiation at high harmonics.

4.8 Conclusions

In this chapter we applied the analytical formulations developed in chapters 2 and 3 in order to investigate the sound generation mechanisms in a vortex-airfoil interaction. The discrete-vortex method based on the Kármán-Trefftz conformal mapping was used to describe an incompressible, high Reynolds number vortical flow past a flat-plate and past a thick and cambered airfoil. Moreover, effects related to the finite size of the oncoming vortex were modeled by distributing the circulation of the vortex upon a cloud of line-vortices.

The analytical decomposition of the surface pressure field showed that the pressure disturbances on the airfoil surface include wavelike contributions, convected together with the vortex, and synchronized[5] contributions related to the vortex passage by the leading edge and by the trailing edge. Because of the vanishing wavelength of a line-vortex, a wavelike contribution generates only negligible effects when integrated upon the airfoil surface. On the contrary, the integrated effects are maximum when the vortex passes by the leading edge. This only acts as an effective acoustic source. Because of the vortex shedding from the trailing edge, the nonlinear interaction mechanisms cancel each other at the trailing edge. As a consequence, the airfoil trailing edge gives only a negligible contribution to the acoustic radiation.

We employed both a fixed-wake and a free-wake model in order to investigate the limits of a fixed-wake approximation. Therefore, we found that the wake model can have a strong influence on the acoustic radiation, but only through an influence on the oncoming vortex trajectory.

We showed that the role of the flow nonlinearity can be decisive when an oncoming vortex is described as a line-vortex. Even a small variation of a geometrical parameter can cause a significant variation of the oncoming vortex trajectory and the resulting interaction noise. Therefore, results must be interpreted with care when the conditions of interaction are critical.

We investigated the distortion of a vortex during a direct vortex-airfoil interaction. A reduction of the noise levels was observed when the vortex is split by the airfoil leading edge.

We found a sixth-power scaling law of the acoustic intensity from an airfoil in a Kármán vortex street ($I \propto M_\infty^6$). This confirms the compact dipolar character of the acoustic radiation from a rod-airfoil configuration at low Mach numbers.

A low Mach number linear model was used to explain the presence of a first harmonic peak in the noise radiated from an airfoil in a Kármán vortex street. It was shown that even harmonic peaks are generated by non symmetrical interactions.

We calculated the noise generated by a double row of counter-rotating vortices convected past an airfoil. The appearance of a first harmonic peak in the noise spectrum when the airfoil is at a positive angle of attack was related to the impingement of the lower row of vortices on the airfoil leading edge. Finally, comparing results with experimental data showed that the analytical approach accounts for the basic features of the interaction process, allowing an accurate prediction of the noise at the Strouhal frequency. However, significant discrepancies were found at higher harmonics. These are related to the fact that the present flow model is a crude approximation of the real flow, as it will be discussed in chapters 5, 7 and 8.

[5]The synchronized character is a by-product of an incompressible treatment.

5

Rod-Airfoil Experiment

In this chapter we present experimental results concerning the rod-airfoil configuration. The first section is devoted to the description of the experimental set-up and to the definition of the measurement protocol. The second section is concerned with the analysis and discussion of the experimental results. The third section describes a visualization experiment that was performed in a water channel by using the hydrogen bubble technique. The latter experiment was aimed to a qualitative investigation of the vortex dynamics in the rod-airfoil configuration.

5.1 Experimental Set-Up

The rod-airfoil experiment was carried out in the small anechoic room of the Ecole Centrale de Lyon (6m $\times$ 5m $\times$ 4m), where air is supplied by a low speed subsonic anechoic wind tunnel.

The reference configuration is an NACA-0012 airfoil downstream of a rod. Both the airfoil and the rod are fixed between two parallel plates and placed into the potential core of a partially flanged rectangular jet.

The airfoil has a chord $c = 0.1$ m and can rotate around its mid point, allowing non symmetrical configurations to be explored. The distance between the airfoil mid point and the center of the rod is $b = 0.162$ m. The rod diameter is $d = 0.016$ m. Both the airfoil and the rod extend by $l = 0.3$ m in the spanwise direction. The experimental set-up is sketched in Fig.5.1.

5.1.1 Acoustic Measurements

Acoustic measurements are performed at a distance $r = 1.38$ m from the airfoil mid point, at various observation angles in the airfoil mid span plane. A Brüel & Kjäer type 4191 microphone with a Brüel & Kjäer type 2669 preamplifier is used for these measurements.

The sound pressure level directivity as well as spectra are measured for various flow configurations: different free-stream velocities and different airfoil angles of attack.

The rod-alone configuration and the background noise (no airfoil, no rod) are also measured in order to check the airfoil contribution to the rod-airfoil configuration noise.

Coherence between the surface pressure field, in proximity of both the airfoil leading and trailing edge, and the acoustic pressure field at an observation angle of 90^o away from the streamwise direction is measured.

Data acquisitions are carried out with a spectral resolution of 2 Hz, from 0 to 6400 Hz, and the number of averages is 300. The Brüel & Kjäer software *Pulse* is used for the signal acquisition and analysis.

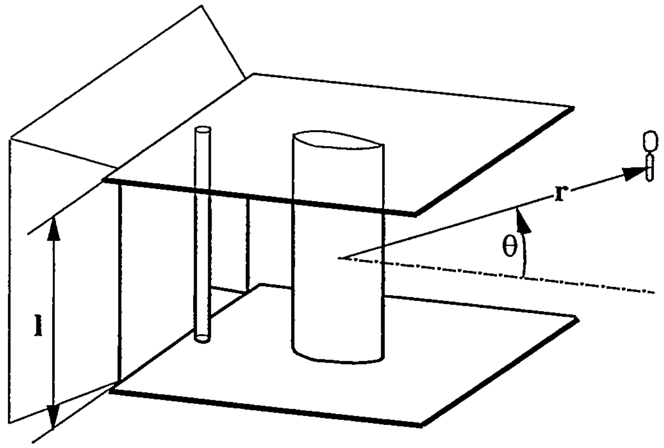

a) Overview of the rod-airfoil configuration.

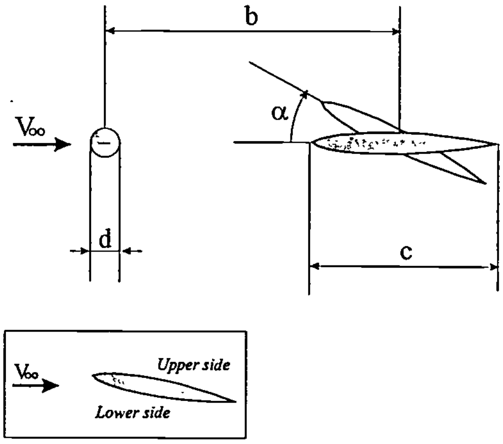

b) In-plane view of the rod-airfoil configuration.

FIGURE 5.1: Experimental set-up. The suction side for positive angle of attack is referred to as *upper* side, whereas the pressure side is referred to as *lower* side. Geometrical and flow parameters: $d = 0.016\,\mathrm{m}$, $c = 0.1\,\mathrm{m}$, $b = 0.162\,\mathrm{m}$, $l = 0.3\mathrm{m}$, $r = 1.38\mathrm{m}$, $V_\infty = 20\,\mathrm{m/s}$.

5.1.2 Surface Pressure Measurements

The turbulent flow around the airfoil is described by measuring both the correlation coefficient and the coherence function between pressure fluctuations at two separated points on the airfoil surface. The same technique is also used to investigate the statistical behaviour of the vortex shedding along the rod span. The statistical quantities used in the present work are described in appendix 5 A.

The pressure fluctuations on the surface of the airfoil are measured by means of pressure transducers. Each of them is constituted of a long metallic capillary tube which is connected to a condenser microphone through a pinhole in the wall. The capillary section is gradually increased in order to permit the insertion of the microphone. A PVC tube of 2 m length is applied at the extremity of the capillary in order to suppress the backward reflections of pressure waves at the outlet section. The PVC tube is closed on the free extremity in order to prevent a mean flow within the capillary. A sketch of the probe is shown in Fig.5.27 of appendix 5 B.

The wave propagation in the capillary tube induces a phase shift as well as an attenuation of the pressure signal transmitted to the microphone. Furthermore, the presence of discontinuities in the section of the capillary is the cause of wave reflections. This results in a modulation of the pressure amplitude measured by the microphone which depends on the frequency of the propagating disturbances. An analytical transfer function [34] is used to relate the measured pressure amplitude to the wall pressure at the inlet hole. It accounts for both the viscous amplitude attenuation and the wave reflections at the discontinuities of the capillary section. The analytical expression of the transfer function is reported in appendix 5 B.

The pressure probe distribution on the surface of the airfoil is shown on Fig.5.2. Probes are drilled only on the upper side of the airfoil, that is the suction side for a positive airfoil angle of attack.

5.2 Experimental Results

In this section we discuss the main results of the present experimental investigation.

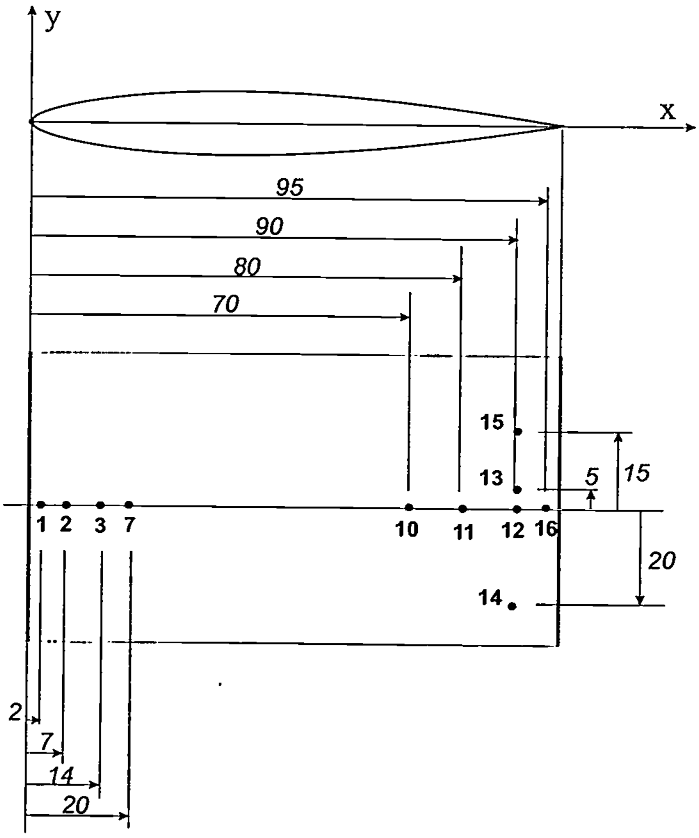

FIGURE 5.2: Distribution of the pressure transducers on the surface of the airfoil. Co-ordinates are expressed in mm.

5.2.1 Acoustic Measurements

5.2.1.1 Isolated rod noise

In order to check the airfoil contribution to the noise radiated by the rod-airfoil configuration, measurements of the noise radiated by an isolated rod are initially performed. In Fig.5.3 the spectrum of the acoustic pressure generated by the rod is compared to the spectrum of the noise radiated by the jet. The spectral contribution at frequencies less than 150 Hz is not considered because i) the far field assumption is not matched at these frequencies, ii) the jet contribution and vibrations are dominant in that range. The results clearly show that the free jet gives a negligible contribution to the noise radiated when a rod is placed into the jet. Furthermore, the noise generated by the rod exhibits a dominant peak centered at the shedding frequency $f_0 = 258\,\mathrm{Hz}$, corresponding to a Strouhal number of 0.21 ($d = 0.016\mathrm{m}$, $V_\infty = 20\,\mathrm{m/s}$). Secondary peaks also arise at the first and second harmonics ($2f_0$ and $3f_0$, respectively).

The dominant peak of the rod noise is essentially generated by the lift component of the aerodynamic force, whose frequency coincides with the vortex shedding frequency. The lift, in fact, completes a cycle every two vortices shed in the flow. Odd harmonics in the rod spectrum are also related to the lift component. Conversely, the peak at the first harmonic is generated by the drag component of the aerodynamic force whose frequency is twice the Strouhal frequency. The drag, in fact, is not affected by the sign of the vortex circulation, thus it completes a cycle every time a vortex is shed[1].

[1] Although the drag contribution should vanish at an observation angle of 90°, a normal position of the observer with respect to the airfoil chord results in the observation angle $\theta_{\mathrm{rod}} = \tan^{-1}(r/b) = 83°$ with respect to the rod. Therefore the unsteady drag contributes to the acoustic field at the first harmonic. Moreover, the rod is located slightly downstream of the bluffed extremity of the duct. Therefore, the diffraction caused by the edges is responsible for a different acoustic

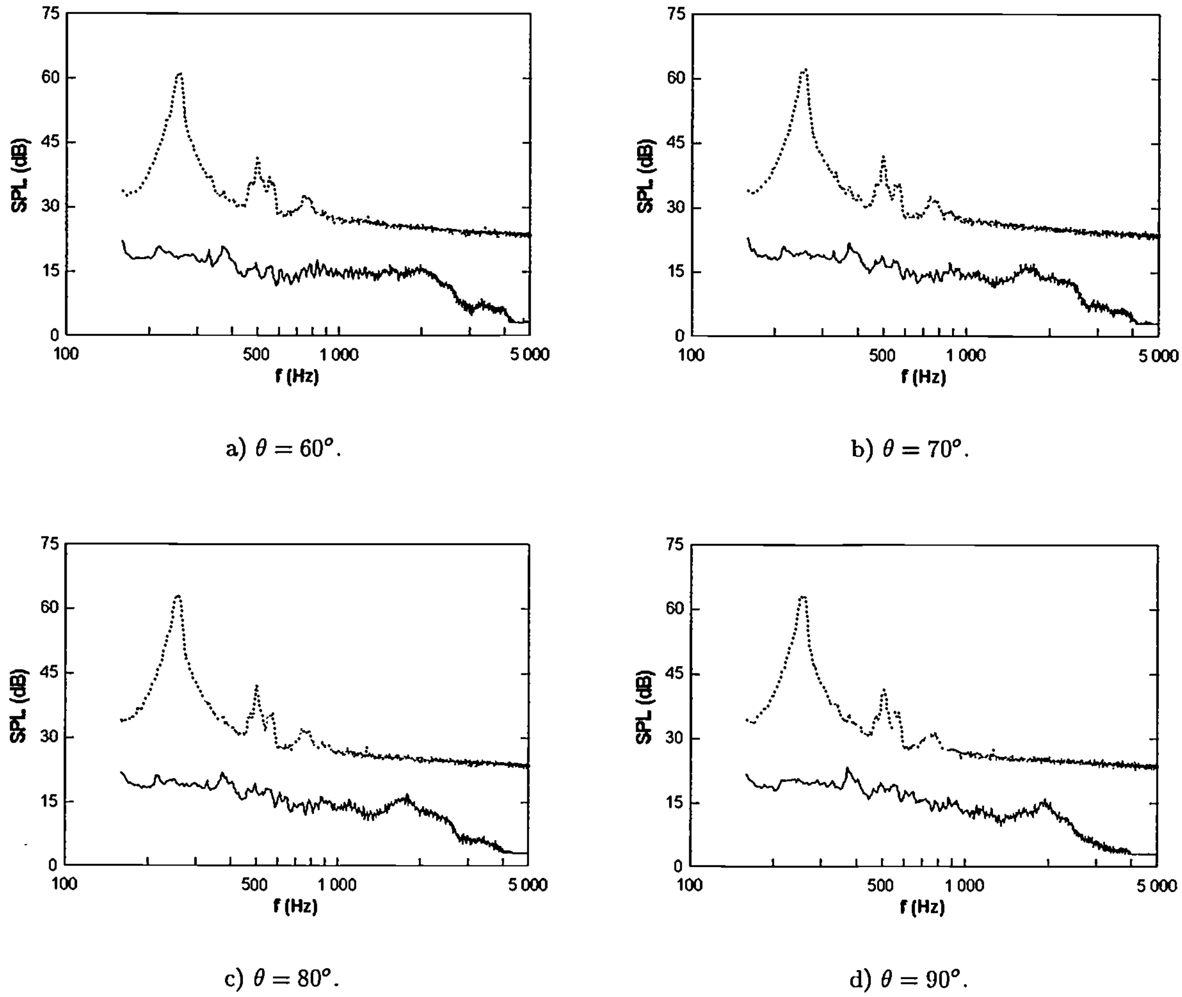

FIGURE 5.3: Spectrum of the acoustic pressure at different observation angles. —— Background noise (jet noise), - - - - rod configuration.

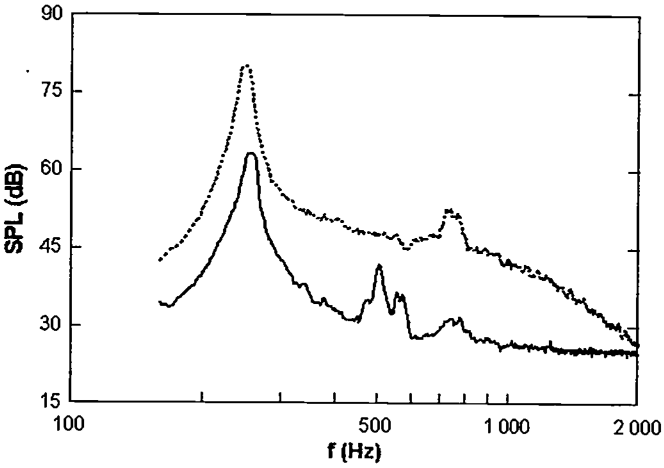

FIGURE 5.4: Spectrum of the acoustic pressure at an observation angle of 90^o away from the flow. Comparison between the noise radiated by an isolated rod and by the rod-airfoil configuration: —— rod noise, - - - - rod-airfoil noise.

5.2.1.2 Rod-airfoil configuration noise

In Fig.5.4 the noise generated by the isolated rod at the free-stream velocity of 20 m/s is compared to the noise radiated by the rod-airfoil configuration. The results show that the rod noise is far below the sound generated when an airfoil is placed into the wake of the rod. Around the main peak the rod-airfoil configuration is 17 dB louder than the rod alone configuration. Furthermore, a slight variation of the Strouhal frequency is caused by the presence of the airfoil. In the case of an isolated rod, the main peak occurs at the frequency $f_0 = 260\,\text{Hz}$, corresponding to a Strouhal number of 0.21, whereas, when the airfoil is placed into the wake of the rod, the main peak occurs at the frequency $f_0 = 246\,\text{Hz}$, corresponding to a Strouhal number of 0.2. Thus a question arises: could the airfoil have a back reaction effect onto the vortex shedding from the rod? Unfortunately, we did not performed measurements in order to give an answer to this question. However, even supposing that a weak back reaction exists, the noise amplification observed for the rod-airfoil configuration cannot be attributed to a feed-back enforcing mechanism. The distance between the rod and the airfoil, in fact, is sufficiently large to suppose as quite improbable the existence of self-sustained oscillations such those occurring in a flute or in the organ pipes. In other words, if a back reaction effect is responsible for the observed noise amplification, this effect should have a hydrodynamic character.

Another interesting aspect is the airfoil influence on the frequency distribution of the acoustic energy. The results show that the presence of the airfoil in the wake of the rod contributes to the broadening of the main peak. Moreover, a *true* broad band acoustic field is generated, which extends over a quite large frequency range. Therefore, the acoustic radiation from the rod-airfoil configuration arises at the privileged Strouhal frequency, but also exhibits a spectral broadening around the Strouhal frequency and a broad band spectral behaviour in a larger frequency range.

5.2.1.3 Airfoil noise

As shown in Fig.5.4, the noise radiated by the rod-airfoil configuration exceeds by 17 dB the noise radiated by the rod alone. Therefore, the rod-airfoil acoustic radiation is essentially generated by the airfoil interaction with rod wake, say *airfoil noise*.

In Fig.5.5 the spectrum of the airfoil noise is plotted at different observation angles and for different

behaviour with respect to that of an isolated rod.

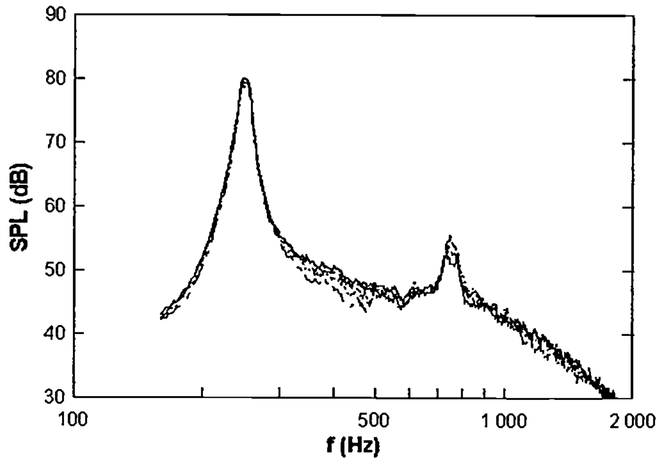

a) $\alpha = 0^o$.

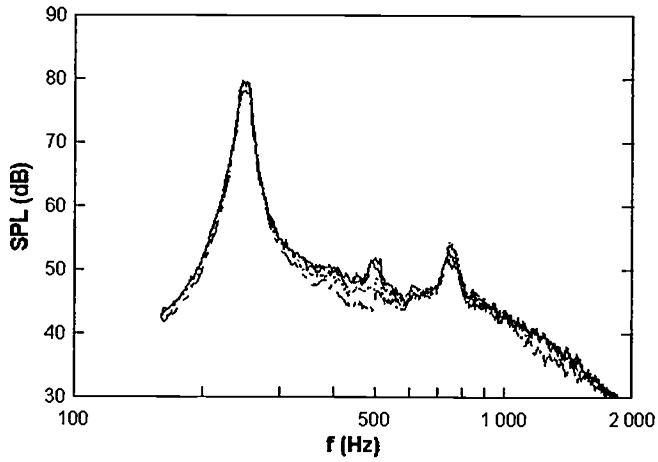

b) $\alpha = 4^o$.

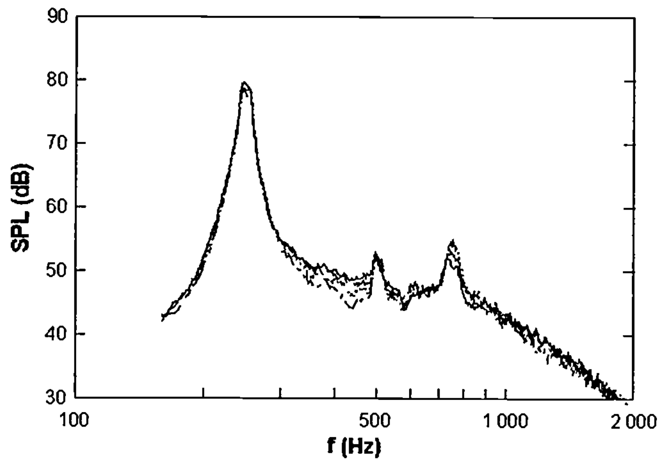

c) $\alpha = -4^o$.

FIGURE 5.5: Spectrum of the acoustic pressure radiated by the airfoil at different angle of attack. —— $\theta = 90^o$, — — $\theta = 80^o$, - - - - $\theta = 70^o$, - - - $\theta = 60^o$.

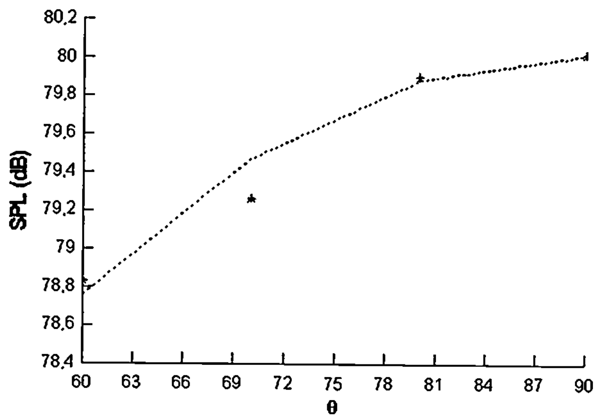

FIGURE 5.6: Directivity of the radiation peak at zero angle of attack: ⋆⋆ experimental data, - - - - $K + 20\log(\sin\theta)$.

TABLE 5.1: Airfoil noise at different observation angles: peak levels.

θ	$\alpha = 0^o$	$\alpha = 4^o$	$\alpha = -4^o$
60^o	78.8	78.1	78.6
70^o	79.2	79.0	78.7
80^o	79.9	79.2	79.6
90^o	80.0	79.5	79.7

angles of attack. It is interesting to observe that a first harmonic peak appears only when the airfoil is at nonzero angle of attack. On the contrary, a second harmonic peak is present at the three values of the airfoil angle of attack.

In Fig.5.6 the directivity of the acoustic intensity[2] radiated by the airfoil is shown for the case $\alpha = 0^o$. Unfortunately, the measurements are not in a sufficient number to detail a true sound directivity. Nevertheless, comparing with a dipolar $\sin\theta$-pattern shows that the directivity of the airfoil noise seems to fit a dipolar radiation. The values of the Strouhal peak of radiation, for different angles of attack, are reported in Table 5.1. The results show that the airfoil angle of attack has only a negligible effect on the noise levels at the Strouhal frequency. On the contrary, differences can be found in the spectral behaviour at higher frequencies. As already pointed out, the first harmonic peak appears only when the airfoil has a nonzero angle of attack. This effect is presumably due to a loss of symmetry of the interaction process. In the following of this chapter we will discuss the meaning of this assertion.

In Fig.5.7 we show the coherence function between the acoustic pressure at an observation angle of 90^o and the wall pressure at the airfoil leading edge and trailing edge. The coherence with the leading edge is maximum at the Strouhal frequency where it takes a value of about 0.9. This value is not hardly affected by the airfoil angle of attack. Nearly the same value is reached by the coherence with the trailing edge at the Strouhal frequency. Another interesting result is the broadening of the main coherence peak with the leading edge. This gives evidence of the non linear effects, such as the vortex distortion near the leading edge.

As already discussed in section (4.7), the appearance of first harmonic peaks in the acoustic spectra

[2]Integration over the main peak of radiation has been performed.

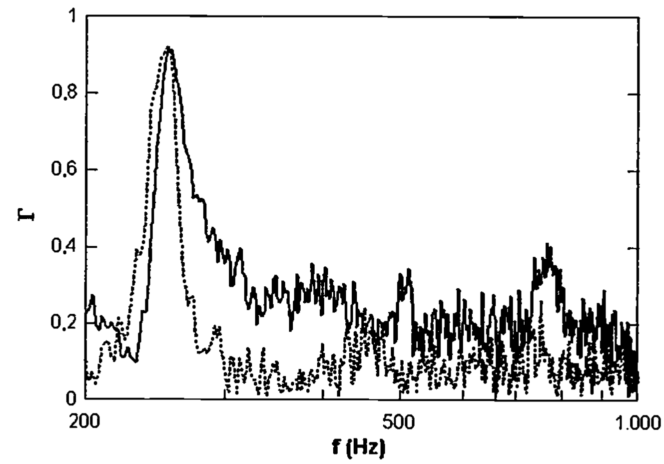

a) $\alpha = 0^o$.

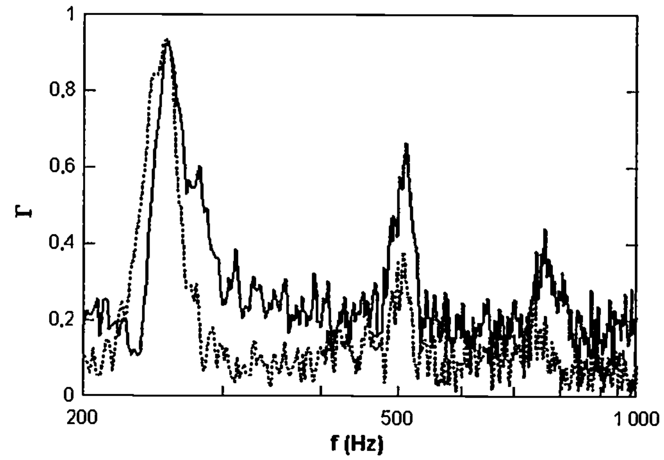

b) $\alpha = 4^o$.

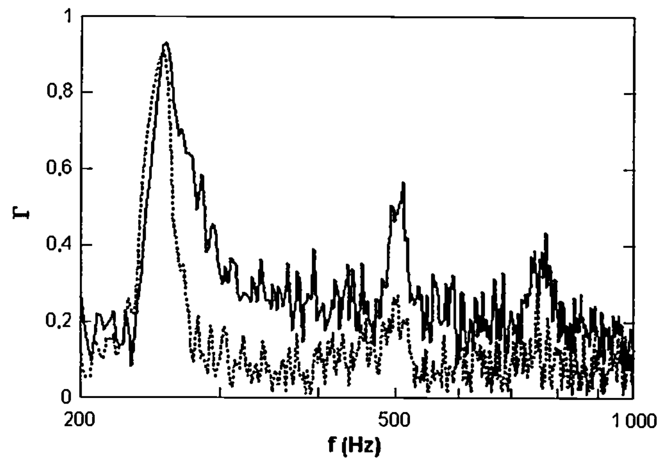

c) $\alpha = -4^o$.

FIGURE 5.7: Coherence between the radiated noise at an observation angle $\theta = 90^o$ and the wall pressure at the airfoil leading edge and trailing edge: —— probe 1 at $x/c = 0.02$, - - - - probe 16 at $x/c = 0.95$.

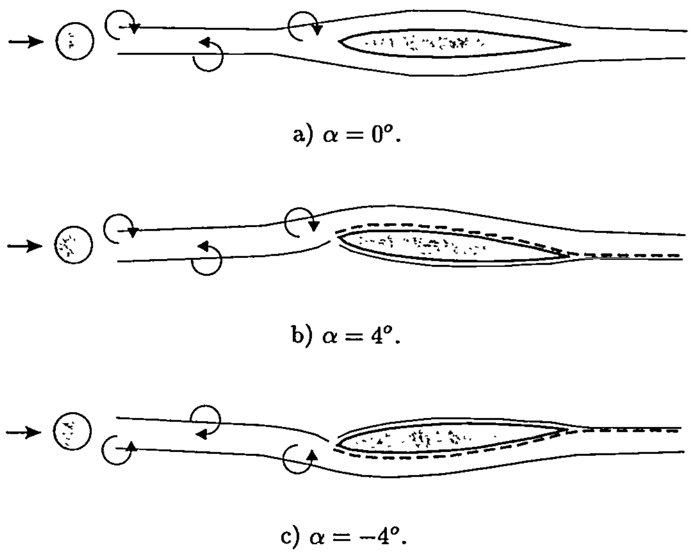

FIGURE 5.8: Qualitative picture of an interaction between a double row of counter-rotating vortices and an airfoil at different angle of attack.

of Fig.5.5 can be related to the *non symmetrical* interaction between the airfoil and the vortices shed from the rod. The velocity induced by a double row of counter-rotating vortices along the axis of the row exhibits only even harmonics. When the airfoil is at a nonzero angle of attack, such a velocity has a nonzero upwash component which is responsible for the generation of a lift with even harmonics.

A different, but not contradictory, interpretation of the phenomenon can be found by considering the coherence plotted on Figs. 5.7(b) and 5.7(c) between the acoustic field and the airfoil at $\alpha = 4^o$ and $\alpha = -4^o$, respectively. In both cases, coherence peaks arise at the first harmonic whose amplitude is smaller than that at the Strouhal frequency. These first harmonic peaks are higher for the case $\alpha = 4^o$ than for the case $\alpha = -4^o$. Hence, we can form a qualitative picture of the flow around the airfoil at different angles of attack. Fig.5.8 shows a possible scenario of the effect that changing the angle of attack has on the vortex trajectories. The lines show typical vortex trajectories past the airfoil, whereas the broken lines indicate the trajectory of a vortical fragment generated by a vortex splitting at the leading edge.

In the symmetrical case (Fig.5.8(a)), the trajectories of the vortices embrace the airfoil, generating a gust-type flow perturbation. As shown in subsection 2.2.7, the upwash velocity results from a Fourier combination of only odd harmonics $(2n-1)\, f_0$ of a main frequency $f_0 \simeq V_\infty/a$, where a is the distance between two vortices on the same row.

When the airfoil is at a nonzero angle of attack (Figs. 5.8(b) and 5.8(c)), the vortices on one of the two rows undergo a stronger interaction with the airfoil leading edge. Therefore, by supposing that the impinging vortices are split into two fragments and that the dominant one is convected along the broken lines, by considering the fact that pressure transducers are located on the upper side of the airfoil, the different behaviour observed in Figs. 5.7(b) and 5.7(c) can be consistently explained. Interestingly, the behaviour predicted in section 4.7 by means of a discrete vortex method and pictured in Fig.4.42 is in agreement with the qualitative picture on Fig.5.8.

In Fig.5.9 the effect of the free-stream velocity onto the airfoil noise is shown. The acoustic spectra obtained with four values of the free-stream velocity V_∞ are plotted in Fig.5.9(a). In Fig.5.9(b) the intensity of the main peak is plotted against the logarithm of V_∞. A linear interpolation provides a sixth-power radiation law, which is that of a compact aeroacoustic dipole.

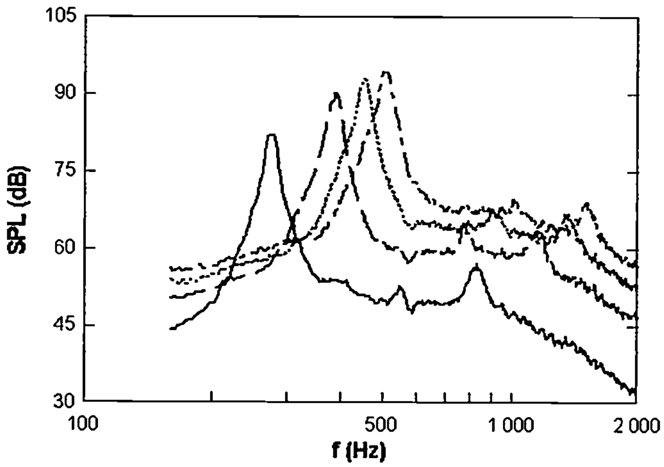

a) Spectrum of the noise radiated by the rod-airfoil configuration at different free-stream velocities ($\theta = 80°$): —— 22.5 m/s, — — 31.2 m/s, - - - - 36.3 m/s, – – – 40.8 m/s.

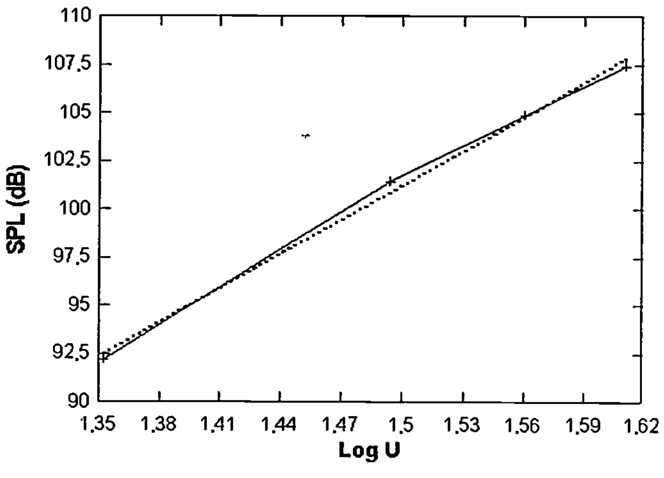

b) Noise intensity versus $\log V_\infty$ (integrated levels): —— experimental data, - - - - $12.67 + 59 \log V_\infty$.

FIGURE 5.9: Effect of the free-stream velocity on the noise radiated by the rod-airfoil system.

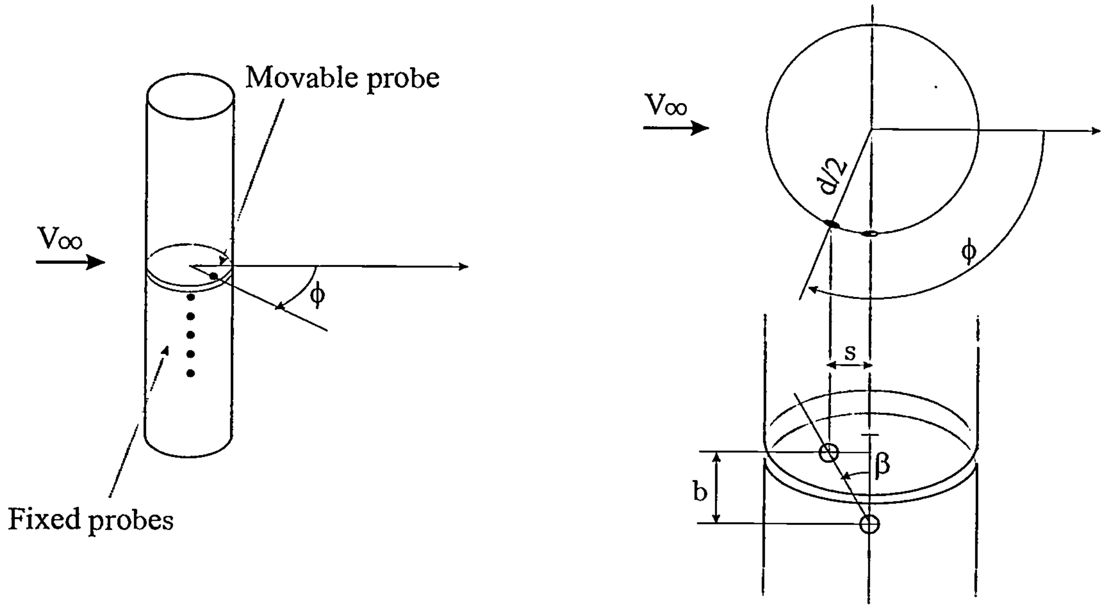

FIGURE 5.10: Rod configuration. Pressure pinholes of 0.5 mm diameter are drilled on the rod surface and communicate with external condenser microphones. 5 probes are on the fixed section, whereas only one probe is on the movable section. The distance between the movable probe and the fixed one closest to the mid span section is $b = 2\,\text{mm}$.

5.2.2 Spatial Coherence and Correlation Measurements

5.2.2.1 Rod configuration

In order to characterize the statistical behaviour of the vortical flow in the wake of the rod, preliminary measurements of wall pressure fluctuations are performed on the rod surface. The Reynolds number based on the rod diameter is 2.2×10^4 ($d = 0.016$m, $V_\infty = 20\,\text{m/s}$). The experimental arrangement is sketched in Fig.5.10. The rod is constituted of two parts. One part is fixed, the other can rotate around the rod axis with respect to the fixed part. 6 pressure pinholes are drilled on the rod: 1 on the movable section, the others on the fixed one. The fixed probes are located 90^o away from the streamwise direction. The pinholes communicate with external condenser microphones through capillary tubes. Therefore, two-point coherence and correlation measurements can be performed with both angular and spanwise spacing.

In Fig.5.11 the coherence at the Strouhal frequency and the correlation coefficient are plotted. Both these quantities are defined in appendix 5 A. The reference probe is at $\eta = 0$, η denoting the distance from the mid-span plane, made dimensionless by d. Data are fitted by a Gaussian $\exp\left(-\eta^2/2L_g^2\right)$ function, with $L_g = 4.7$ for the coherence function, and $L_g = 6.6$ for the correlation coefficient. The vortex shedding process is therefore correlated upon a distance of about 6.5 d.

In Fig.5.12 the Strouhal peaks of coherence measured at different inflow velocities V_∞ are plotted against the separation distance η. The logarithm of the coherence $\ln[\Gamma(\eta, f_0)]$ is well fitted by a quadratic polynomial. Hence the spanwise coherence, in the explored velocity range, is well fitted by a Gaussian function of the separation distance η. The correlation length L_g versus the free-stream velocity is plotted in Fig.5.13. Accordingly to literature [35], L_g decreases at increasing values of V_∞.

Cross-spectrum measurements of the fluctuating pressure are also made between a fixed reference probe at 90^o away from the streamwise direction and probes at different angular positions ϕ, with an angular step of 5^o.

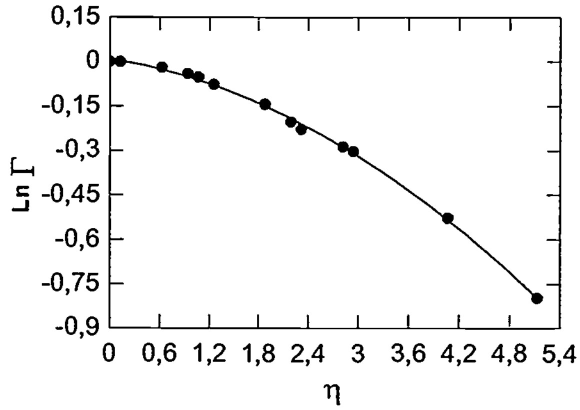

a) Coherence function $\ln(\Gamma)$.

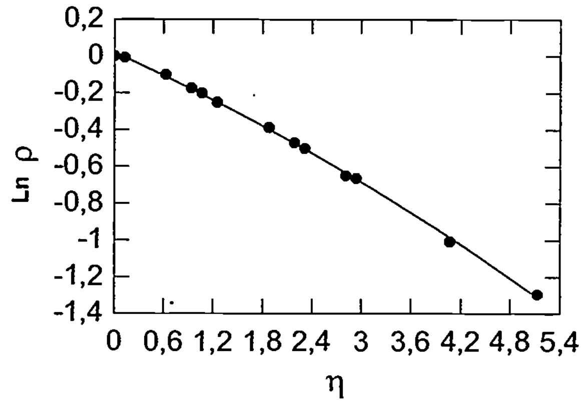

b) Correlation coefficient $\ln(\rho)$.

FIGURE 5.11: Spanwise coherence and correlation coefficient on the rod surface at $\phi = 90^o$ (logarithmic scale). ••Experimental data, —— Gaussian interpolation.

As shown in Fig.5.14(a), the cross-spectrum peaks when the movable probe is at $\phi = 100^o$. This experimental inaccuracy can be indeed justified to some extent. As sketched in Fig.5.10(b), a circumferential skew s between the fixed and the closest movable probe results in the skew angle $\beta \simeq \tan^{-1}[d\sin(\phi - \pi/2)/2b]$, where $b = 2 \times 10^{-3}\,\mathrm{m}$ is the spanwise distance between the fixed and the movable probe. In other words, the angle β measures the deviation of the movable probe from to the vertical axis cutting through the fixed probes. A skew angle $\beta = 35^o$ corresponds to $\phi = 100^o$. Fig.5.14(b) shows that also the Strouhal coherence peak is maximum when the movable probe is at $\phi = 100^o$, but it is almost maximal over a wide range of angles. Hence, $\beta \simeq 35^o$ could be interpreted as a mean vortex shedding angle. This discussion is quite far from being a quantitative analysis of the three-dimensional effects in the wake of a rod. The phenomenology, in fact, is intrinsically complex and not completely understood at present time. Nevertheless, we believe that measurements as those described in this paper can be used to investigate the three-dimensional vortex dynamics in the wake of a rod.

In Fig.5.14(b) the angular coherence at the Strouhal frequency and its peaks at the first and second harmonics are plotted against the angular position of the movable probe. At the Strouhal frequency, the coherence is almost 1 from $\phi \simeq 60^o$ to $\phi \simeq 120^o$, the maximum being reached when the movable probe is at about 100^o. Conversely, at higher harmonics, the coherence is maximum when the movable probe is 90^o away from the streamwise direction. Surprisingly, the first harmonic peak of coherence reaches a local minimum at $\phi = 100^o$, where the Strouhal peak is maximum.

The wall pressure signals corresponding to the maximum cross-spectrum amplitude are plotted in Fig.5.15. Interestingly, weak amplitude cycles reappear somewhat periodically at about 15-20 times the Strouhal period, and have a duration of about 4-5 shedding periods.

Finally, in Fig.5.16 the wall pressure signals taken at $\phi = 90^o$ along the rod span are plotted. A phase shift can be observed between signals at different spanwise positions. Furthermore, phase jumps occur sporadically. A similar behaviour was observed by Szepessy & Bearman [36] in the Reynolds number range $1 \times 10^4 - 1.3 \times 10^5$.

In this subsection we have described some effects related to the three-dimensional character of a circular cylinder flow. The spanwise loss of coherence, the wall pressure random amplitude modulation, and the phase shift between signals at different spanwise positions give evidence of the three-dimensional structure of the wake behind the rod.

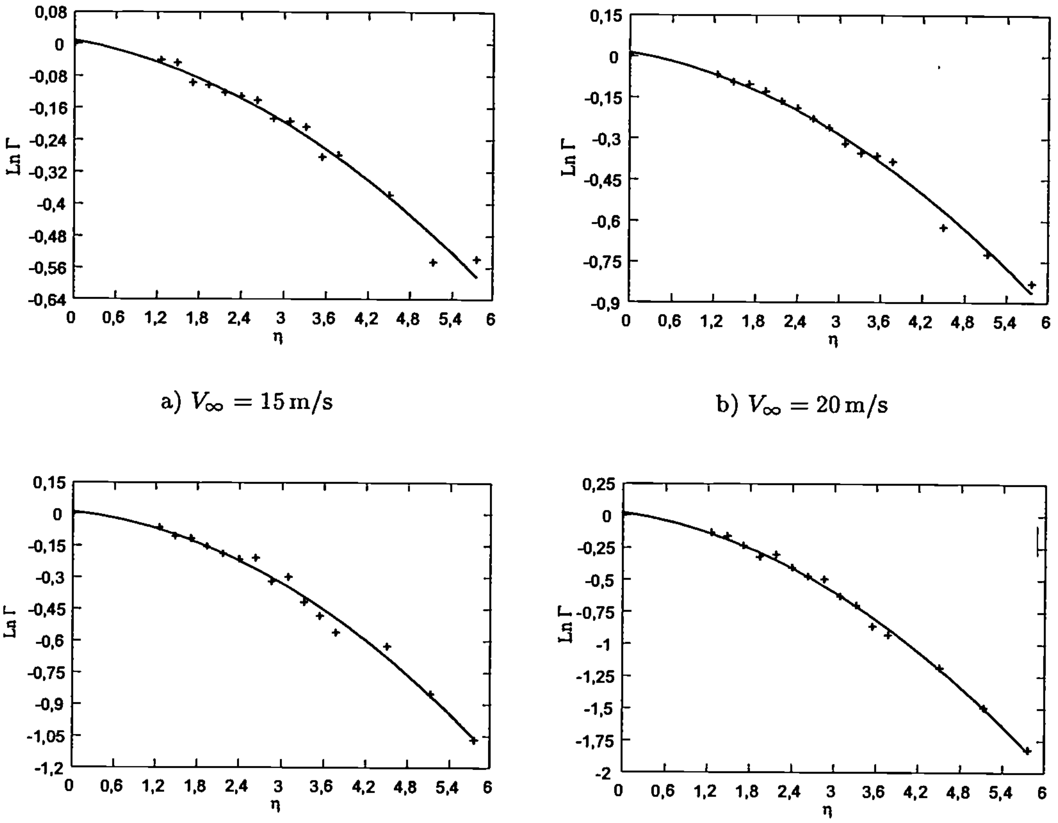

a) $V_\infty = 15\,\mathrm{m/s}$

b) $V_\infty = 20\,\mathrm{m/s}$

c) $V_\infty = 25\,\mathrm{m/s}$

d) $V_\infty = 35\,\mathrm{m/s}$

FIGURE 5.12: Experimental measurements of the spanwise coherence on the rod at different inflow velocities: ++ experimental data, —— quadratic interpolation. η denotes the spanwise separation distance, made dimensionless by the rod diameter $d = 0.016\,\mathrm{m}$.

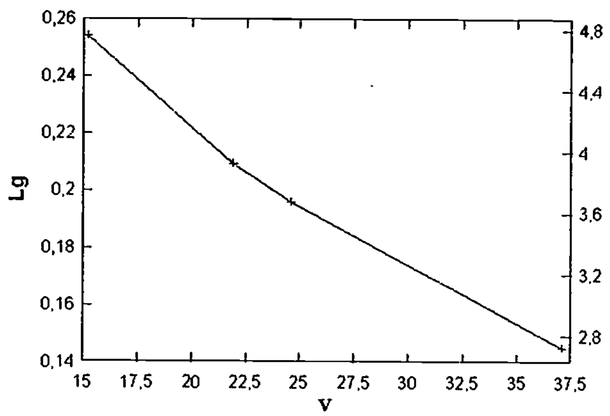

FIGURE 5.13: Measured Gaussian correlation length L_g versus the free-stream velocity V_∞. L_g made dimensionless by the rod span $l = 0.3\,\mathrm{m}$ (left axis) and by the rod diameter $d = 0.016\,\mathrm{m}$ (right axis).

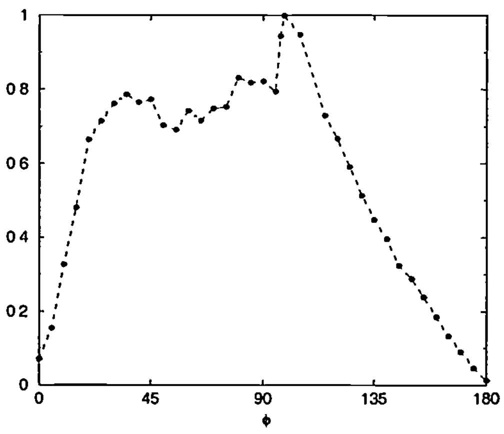

a) $|S_{12}/\max(|S_{12}|)|$ at the Strouhal frequency f_0

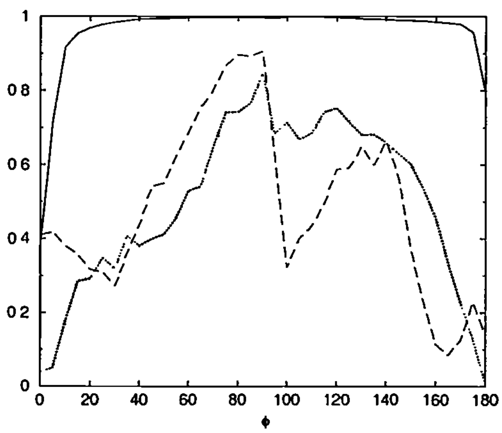

b) Maximum values of Γ at the Strouhal frequency f_0 and higher harmonics. —— f_0, — — $2f_0$, - - - - $3f_0$.

FIGURE 5.14: Cross-spectrum and coherence measurements between a reference pressure probe at $\phi = 90^o$ and probes at different ϕ.

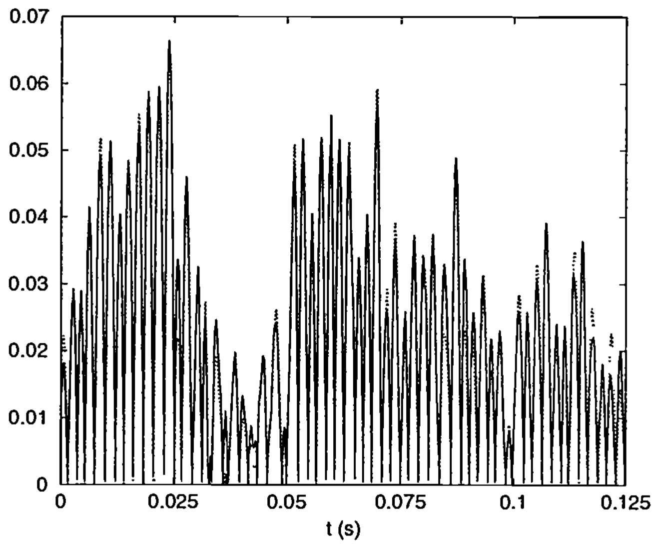

FIGURE 5.15: Wall pressure signals: —— movable probe at $\phi = 100^o$, - - - - fixed probe.

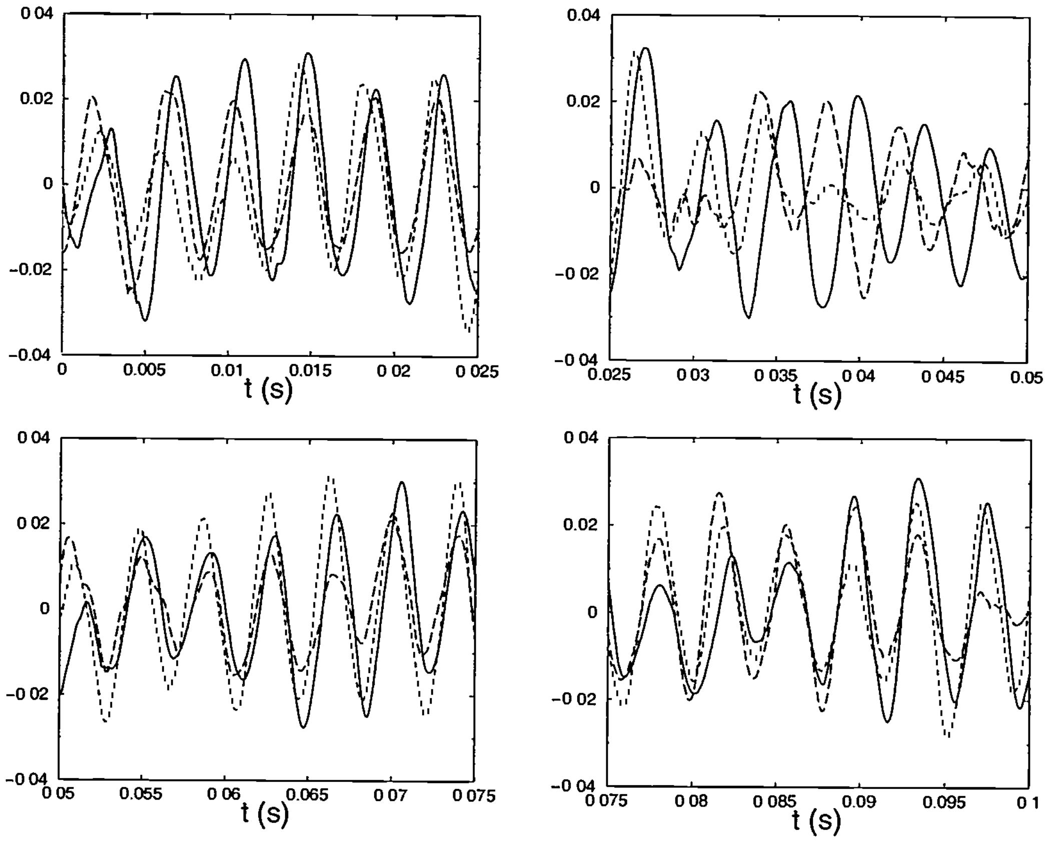

Figure 5.16: Wall pressure signals at different spanwise positions: —— $\eta = 0.125$, - - - - $\eta = 2.437$, — — $\eta = 5.250$. Pressure probes at $\phi = 90^o$.

5.2.2.2 Rod-airfoil configuration

In Fig.5.17 the power spectral density of the fluctuating pressure at the airfoil leading edge and trailing edge is plotted. The results seem to confirm the qualitative picture of the interaction dynamics described in Fig.5.8. At zero angle of attack the fluctuating upwash velocity exhibits only odd harmonics ($f_0, 3f_0, \ldots$). As a consequence, no significative peaks arise at the first harmonic. Conversely, when the airfoil is at a non zero angle of attack, a first harmonic peak appears.

Differences in the wall pressure spectra can be noticed between the cases at positive and negative angle of attack. At $\alpha = 4^o$ the main peak of the wall pressure spectrum at the leading edge is lower than that at $\alpha = -4^o$. On the contrary, the first harmonic peak is higher at $\alpha = 4^o$. The latter observation is consistent with the flow model of Fig.5.8(b): both the upper and lower row vortices pass above the instrumented side of the airfoil. In addition, the former observation could be explained by supposing that a vortex impinges on one side of the leading edge (the lower side for $\alpha = 4^o$ and the upper one for $\alpha = -4^o$), and then it is swept out the opposite side. Therefore, more intense pressure fluctuations occur on the side of the leading edge where the vortex impinges. This is true if the suction effect induced on the opposite side is less important than the *head-on* effect on the impinging side.

Another interesting aspect is that the Strouhal peak of the wall pressure at the leading edge is two orders of magnitude higher than that at the trailing edge. This can be explained by considering two factors:

- a leading edge is a discontinuity of the flow accompanied by a nearly singular behaviour. On the contrary, the behaviour of the flow at the trailing edge is smoothed by effects related to the viscosity of the fluid. Typically, unsteady vortex shedding.
- A vortex is weaker after it has passed by the airfoil leading edge. As a consequence, it induces weaker pressure fluctuations near the trailing edge.

Finally, it can be noticed that the Strouhal peak at the trailing edge is higher for $\alpha = 4^o$ than for $\alpha = -4^o$. Again, the flow picture proposed in Fig.5.8 gives a simple explanation for this different behaviour.

In Fig.5.18 the streamwise coherence of the wall pressure fluctuations near the airfoil leading edge is plotted. The coherence is maximum at the Strouhal frequency. More interestingly, the broadening of the coherence decreases as the separation distance increases. Roughly, this is a consequence of a wider variety of turbulent structures which are coherent on smaller distances. As a final remark, comparing the plots on Figs. 5.17(b) and 5.17(c) shows that the airfoil angle of attack affects only the first harmonic peak of coherence at the greatest separation distance (probes 1-7). In other words, the coherence of the flow is nearly the same on a portion of the airfoil extending about $0.15\,c$ from the leading edge. At a greater distance the coherence depends on whether the impinging vortices pass predominantly above or below the leading edge, accordingly to Fig.5.8.

The wall pressure streamwise coherence in the airfoil trailing edge region is plotted on Fig.5.19. The coherence peaks again at the Strouhal frequency. However, compared to the leading edge coherence of Fig.5.18, the separation distance seems to have a different effect on the main peaks. At small values of the separation distance the main peak of coherence emerges only slightly from a broadband behaviour. Hence, turbulent structures in a wide range of characteristic wavelengths provide nearly the same contribution to the small distance streamwise coherence. It is interesting to notice that a first harmonic peak of coherence appears only in the case $\alpha = -4^o$. This behaviour is consistent with the flow picture on Fig.5.8, according to which an impinging vortex is predominantly convected along the upper or lower side of the airfoil, depending on whether the angle of attack is negative or positive, respectively.

In Fig.5.20 the spanwise coherence in the trailing edge region is plotted. Spanwise coherence gives a good picture of the spatial coherence of turbulence, since it is not biased by the mean flow convection.

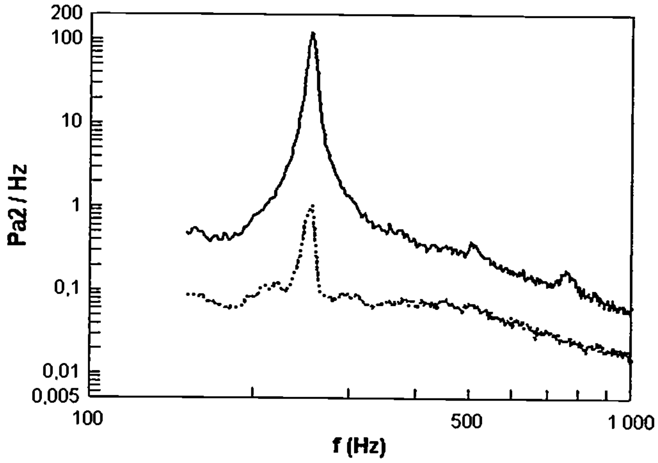

a) $\alpha = 0^o$.

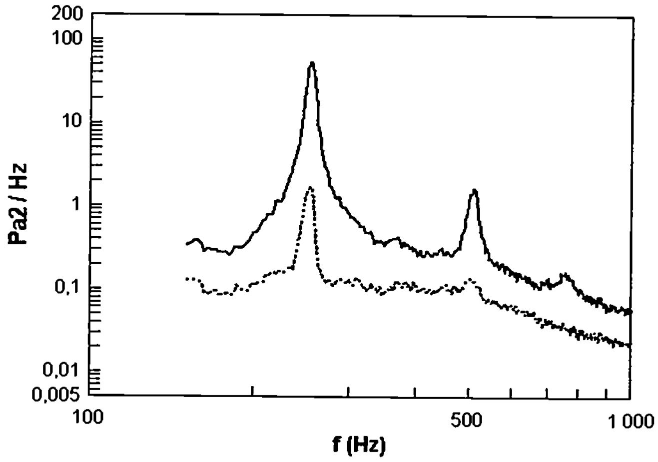

b) $\alpha = 4^o$.

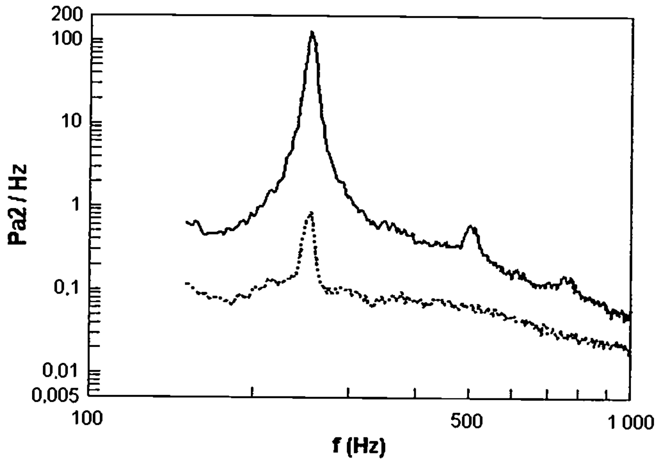

c) $\alpha = -4^o$.

FIGURE 5.17: Power spectral density of the wall pressure at the airfoil leading edge and trailing edge for different angles of attack. —— Probe 1 (leading edge), - - - - probe 16 (trailing edge).

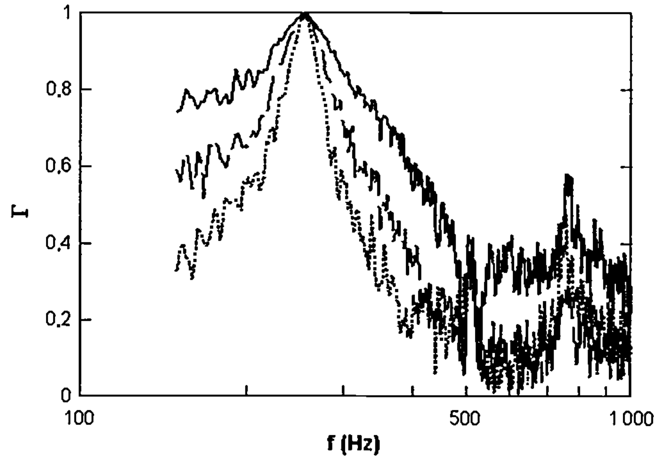

a) $\alpha = 0^o$.

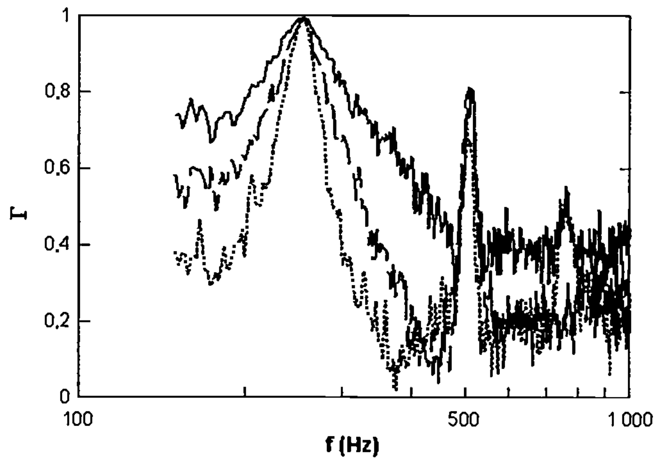

b) $\alpha = 4^o$.

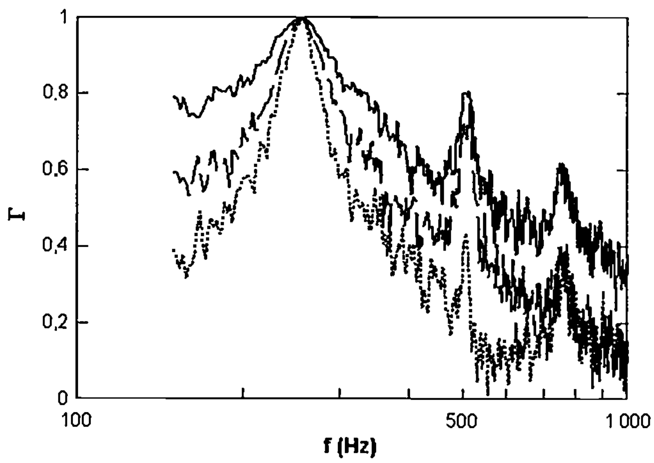

c) $\alpha = -4^o$.

FIGURE 5.18: Streamwise coherence in proximity of the airfoil leading edge for different angles of attack. Coherence between Probe 1 at $x/c = 0.02$ and: i) —— Probe 2 at $x/c = 0.07$, ii) — — Probe 3 at $x/c = 0.14$, iii) - - - - Probe 7 at $x/c = 0.20$.

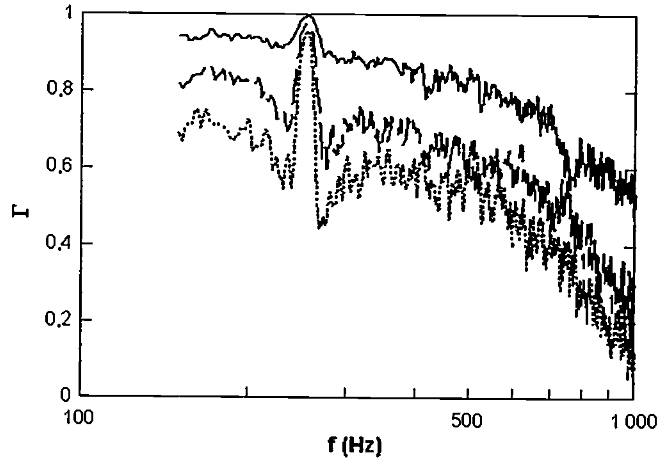

a) $\alpha = 0^o$.

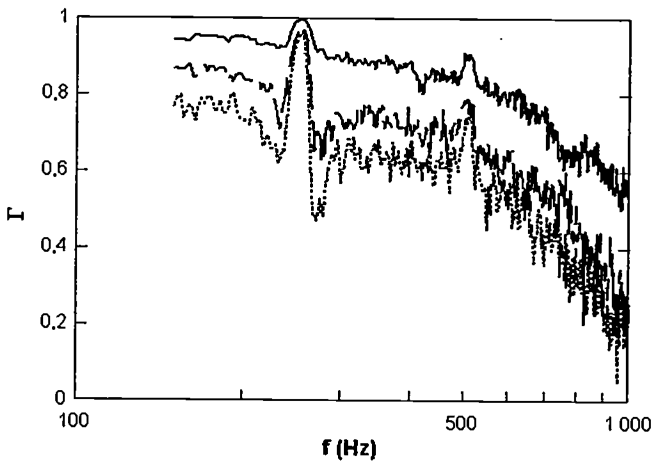

b) $\alpha = 4^o$.

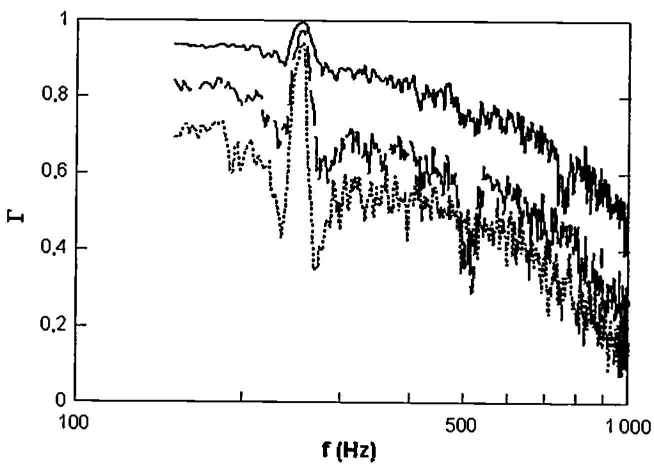

c) $\alpha = -4^o$.

FIGURE 5.19: Streamwise coherence in proximity of the airfoil trailing edge for different angles of attack. Coherence between Probe 10 at $x/c = 0.70$ and: i) —— Probe 11 at $x/c = 0.80$, ii) — — Probe 12 at $x/c = 0.90$, iii) - - - - Probe 16 at $x/c = 0.95$.

Plots on Fig.5.20 show that the overall turbulence has only a weak spatial coherence, whereas the rod vortices have large spanwise coherence. Again, the presence of lower row vortices is felt by probes in the case $\alpha = 4^o$, as revealed by the presence of the first harmonic peak.

In Figs. 5.21 and 5.22 the correlation coefficient in proximity of the airfoil leading edge and trailing edge is plotted. Unfortunately, the two-point correlation measurements are not in a sufficient number to give quantitative informations. Nevertheless, the influence of the airfoil angle of attack on the spatial correlation can be qualitatively described. Moreover, the effects related to the rod vortices are enlightened by showing the same results for an isolated airfoil (no rod) with a turbulent boundary layer[3].

In Fig.5.21 the correlation coefficient is plotted against a streamwise and spanwise separation distance, in the case of a rod-airfoil configuration. The results show that the airfoil angle of attack has only a negligible influence on the slope of the curves. On the contrary, the correlation levels are notably affected by the airfoil angle of attack. Interestingly, the effect of the angle of attack is opposite in the leading edge region (Fig.5.21(a)) and in the trailing edge region (Figs. 5.21(b) and 5.21(c)). Again, this behaviour is consistent with the flow picture of Fig 5.8, according to which at $\alpha = -4^o$ upper row vortices impinge on the upper side of the leading edge and are swept out the lower side of the airfoil.

In Fig.5.22 the correlation coefficient in the trailing edge region of an isolated airfoil (no rod) is plotted. The results show that the airfoil angle of attack has only a negligible effect on both the streamwise and spanwise correlation. Hence, the behaviour described in Fig.5.21 in the presence of a rod is likely to be caused by the presence of the incident vortices.

Finally, in Fig.5.23 the correlation coefficients measured on the isolated airfoil are compared to those measured in a rod-airfoil configuration. The results show that the large-scale vortices have an influence on both the level and the slope of the correlation curves.

[3]Transition on the isolated airfoil (no rod) was tripped by means of strip along the span of the airfoil.

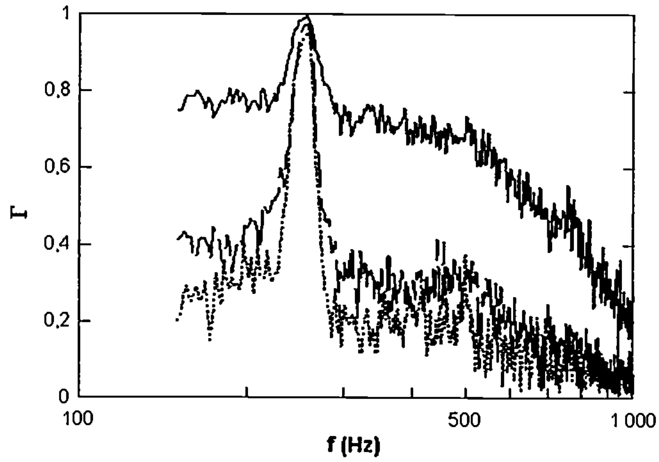

a) $\alpha = 0^o$.

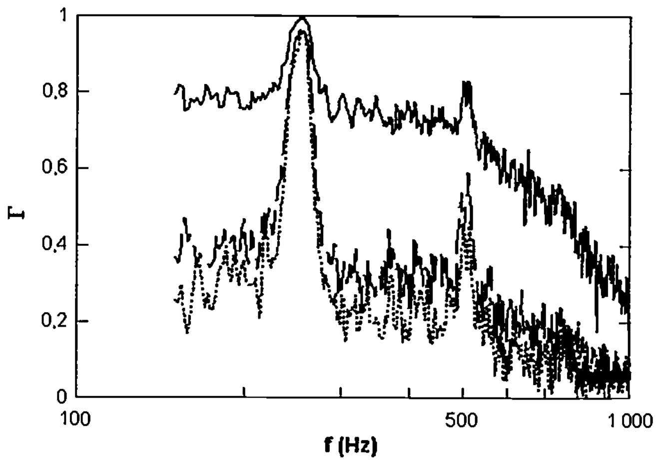

b) $\alpha = 4^o$.

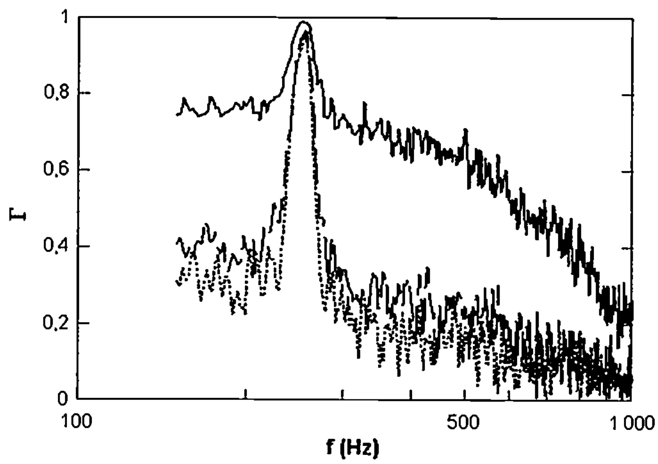

c) $\alpha = -4^o$.

FIGURE 5.20: Spanwise coherence in proximity of the airfoil trailing edge for different angles of attack. Coherence between Probe 12 at $y/c = 0$ and: i) —— probe 13 at $y/c = 0.05$, ii) — — probe 15 at $x/c = 0.15$, iii) - - - - probe 14 at $x/c = 0.20$.

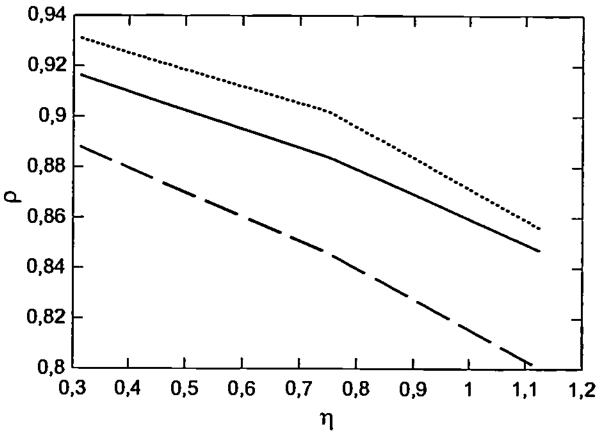

a) Streamwise correlation at the leading edge between probes 1, 2, 3 and 7.

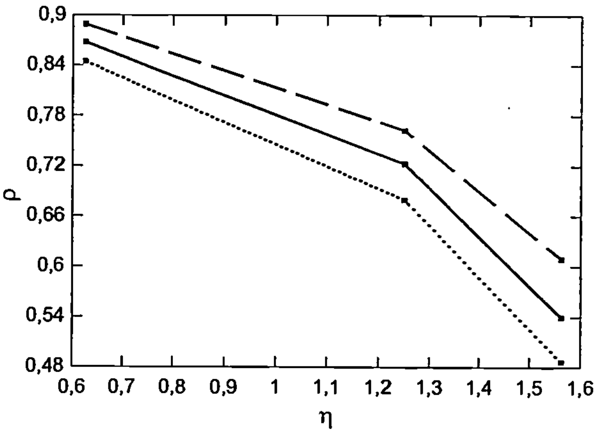

b) Streamwise correlation at the trailing edge between probes 10, 11, 12 and 16.

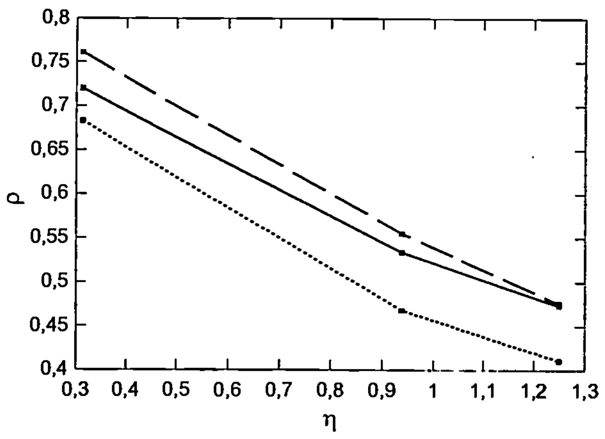

c) Spanwise correlation at the trailing edge between probes 12, 13, 15 and 14.

FIGURE 5.21: Correlation coefficient on the airfoil for different angles of attack: —— $\alpha = 0^o$, — — $\alpha = 4^o$, - - - - $\alpha = -4^o$. Rod-airfoil configuration. The separation distance η has been made dimensionless by the rod diameter d.

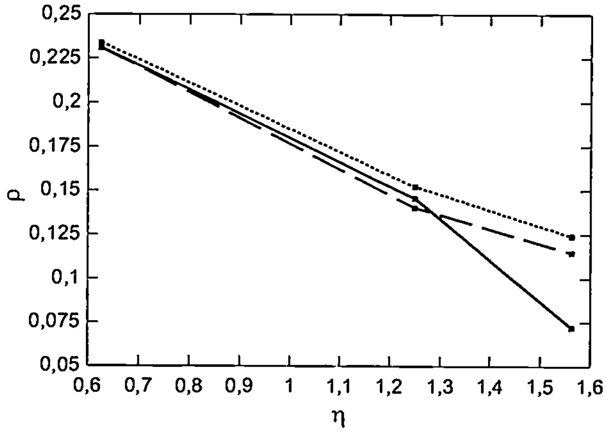

a) Streamwise correlation at the trailing edge between probes 10, 11, 12 and 16.

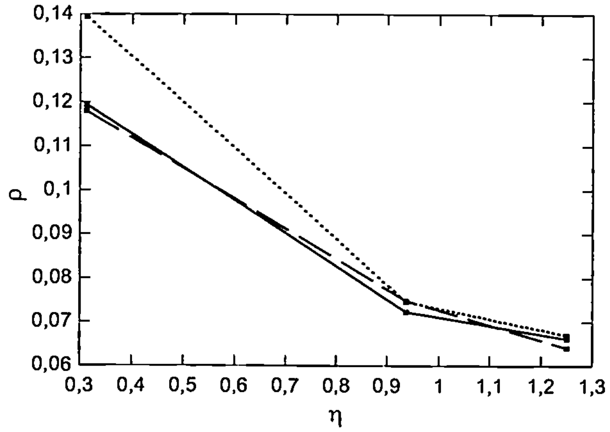

b) Spanwise correlation at the trailing edge between probes 12, 13, 15 and 14.

Figure 5.22: Correlation coefficient on the airfoil for different angles of attack: —— $\alpha = 0^o$, — — $\alpha = 4^o$, - - - - $\alpha = -4^o$. Isolated airfoil configuration. The separation distance η has been made dimensionless by the rod diameter d.

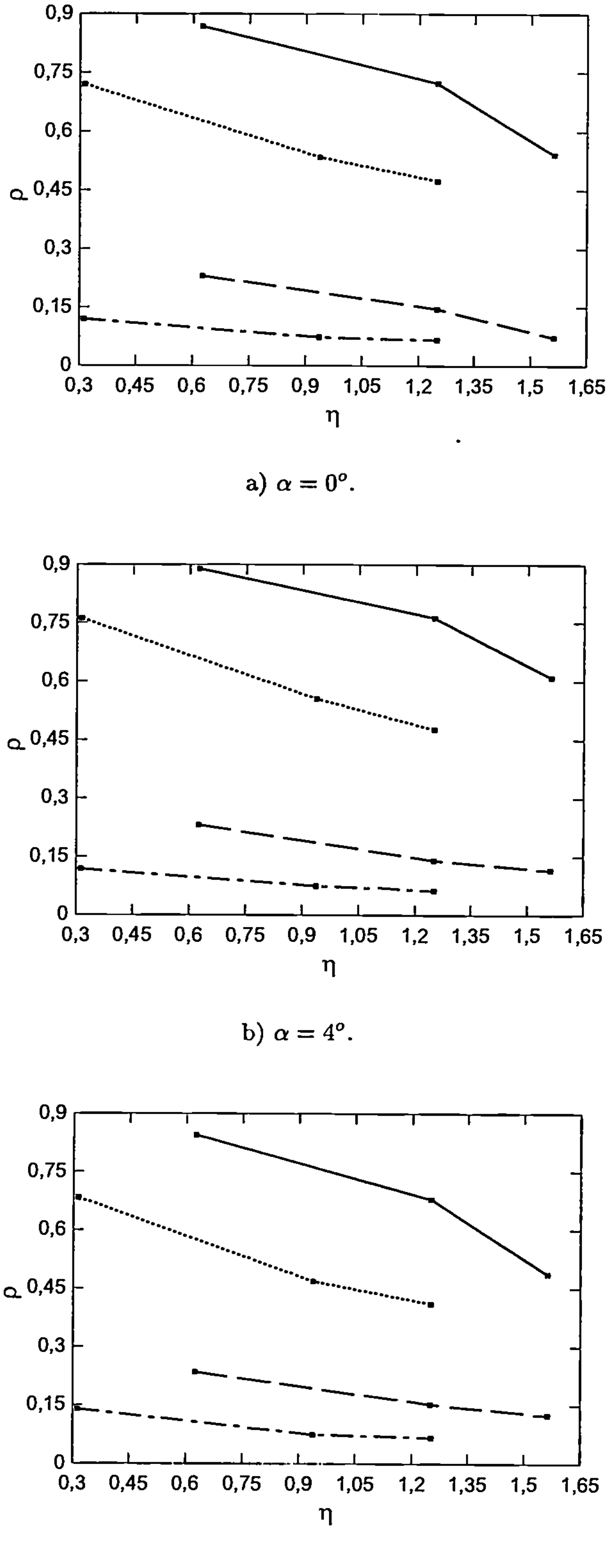

a) $\alpha = 0^o$.

b) $\alpha = 4^o$.

c) $\alpha = -4^o$.

FIGURE 5.23: Effect of the rod on the airfoil correlation coefficient for different angles of attack. Streamwise correlation (Probes 10, 11, 12 and 16): —— Rod, — — No-rod. Spanwise correlation (Probes 12, 13, 15 and 14): - - - - Rod, - - - No-rod. The separation distance η has been made dimensionless by the rod diameter d.

5.3 A Hydrogen Bubble Visualization Experiment

A visualization experiment was carried out in the *Hydra* water channel of the Politecnico di Torino.

The experimental set-up is a one-to-one reproduction of the rod-airfoil configuration used in the aeroacoustic experiments. The reference configuration is an NACA-0012 airfoil (chord: $c = 0.1\,\mathrm{m}$ thickness: $0.012\,\mathrm{m}$) located $0.112\,\mathrm{m}$ downstream of the rod, both extending by $l = 0.3\,\mathrm{m}$ in the spanwise direction. The two bodies are fixed between two plexiglass end-plates and the whole set is introduced into a rectangular water channel. Water is towed at a velocity of about $0.2\,\mathrm{m/s}$ at which the installation assures an inflow turbulence level of about 0.01. The Reynolds number is about 2500, corresponding to a shear-layer transition regime. The experimental set-up is shown in the photograph of Fig.5.24.

Electrolysis[4] is used to generate a thin layer of hydrogen bubbles from a tungsten wire of $50\,\mu\mathrm{m}$ diameter. This is stretched in the mid-span plane and located two rod diameters downstream of the rod base point. An electrical field is created between the tungsten wire and four lateral copper plates. The little hydrogen bubbles trapped by the Kármán vortex street and convected towards the airfoil are then used to visualize the vortex dynamics in the rod-airfoil configuration.

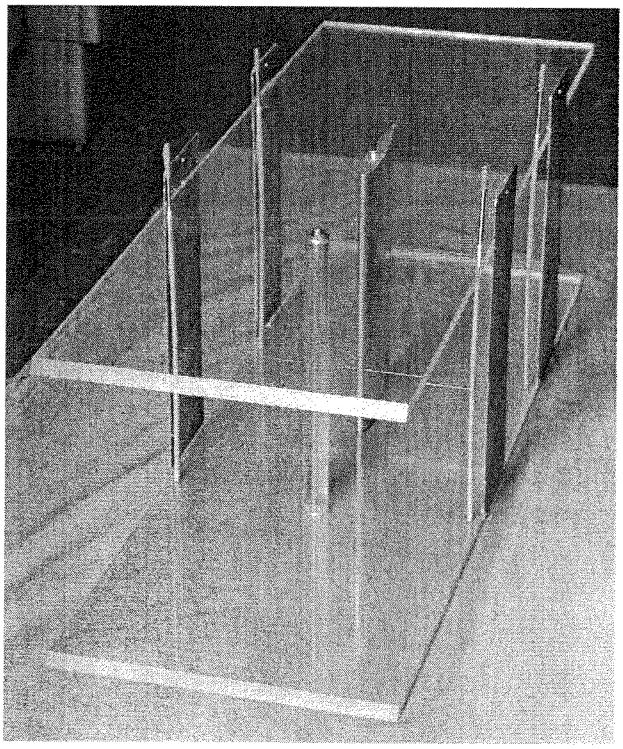

FIGURE 5.24: Set-up of the rod-airfoil hydrogen bubble visualization experiment.

Although the cylinder flow regime is the same in this experiment and in the CFD simulations performed in the present work (shear-layer transition regime), only qualitative comparisons can be made between the observed vortex dynamics and the numerical prediction discussed later on in the present work (see the RANS computations described in chapter 8).

[4]The hydrogen bubble technique was proposed by Clutter *et al.* [37]. It is based on the physical phenomenon of electrolysis and is used to visualize flow streamlines past a body immersed in a water stream. A thin wire of 10 to $50\,\mu\mathrm{m}$ diameter is stretched in the water perpendicular to the mean flow direction. This wire (tungsten or platinum, preferably) forms the negative electrode of a D.C. circuit, the surface of the body acting as the positive electrode. Hard water is sufficient, as well as a supply voltage between 10 and 250 volts. Hydrogen bubbles with a diameter between one-half and one wire diameter are produced at the negative wire electrode. After a short transient, bubbles are produced uniformly. A flat light beam parallel to the wire is then used to enlighten the bubble film.

Out of the scope of the present work, we attempt to describe a phenomenon observed during the visualization experiments.

1. The transverse distance between two successive vortices in the wake of the rod undergoes a random variation.

2. About 1-to-3 shedding cycles of Low Transverse Amplitude (LTA) occur randomly each 5-to-7 shedding cycles of High Transverse Amplitude (HTA).

3. During LTA-cycles head-on interactions between the oncoming vortices and the airfoil leading edge take place. Conversely, during HTA-cycles the Kármán vortex street tenderly embraces the airfoil.

4. A notable increasing of the shedding frequency accompanies the occurrence of LTA-cycles.

We give two explanations of such a phenomenology, the first invoking the intrinsic three-dimensional character of a circular cylinder flow, the second referring to an in-plane stability condition.

1. Suppose that the vortex shedding frequency is not constant along the span of the cylinder, which is roughly equivalent to suppose a non parallel vortex shedding. Hence, higher frequencies are associated to a streamwise compression of the Kármán vortex street, whereas lower frequencies result in a streamwise dilatation of the vortex street. By neglecting all the out-of-plane vortex induction effects, the von Kármán stability condition can be roughly applied resulting in a constant aspect ratio of the Kármán vortex street along the rod span. As a consequence, higher shedding frequencies are accompanied by a lower transverse vortex spacing. This simplified picture is in agreement with the amplitude modulation of the near-wake signals quoted in literature [36].

2. It is straightforward to demonstrate that a single infinite row of counter-rotating line-vortices realizes a condition of instable equilibrium. Consequently, its *probability* to be naturally established is essentially zero. However, if the presence of an airfoil in the wake of the rod has the effect of increasing the *domain of attraction* of the vortex aligned condition, then the random occurrence of such a limit cycle can be consistently explained.

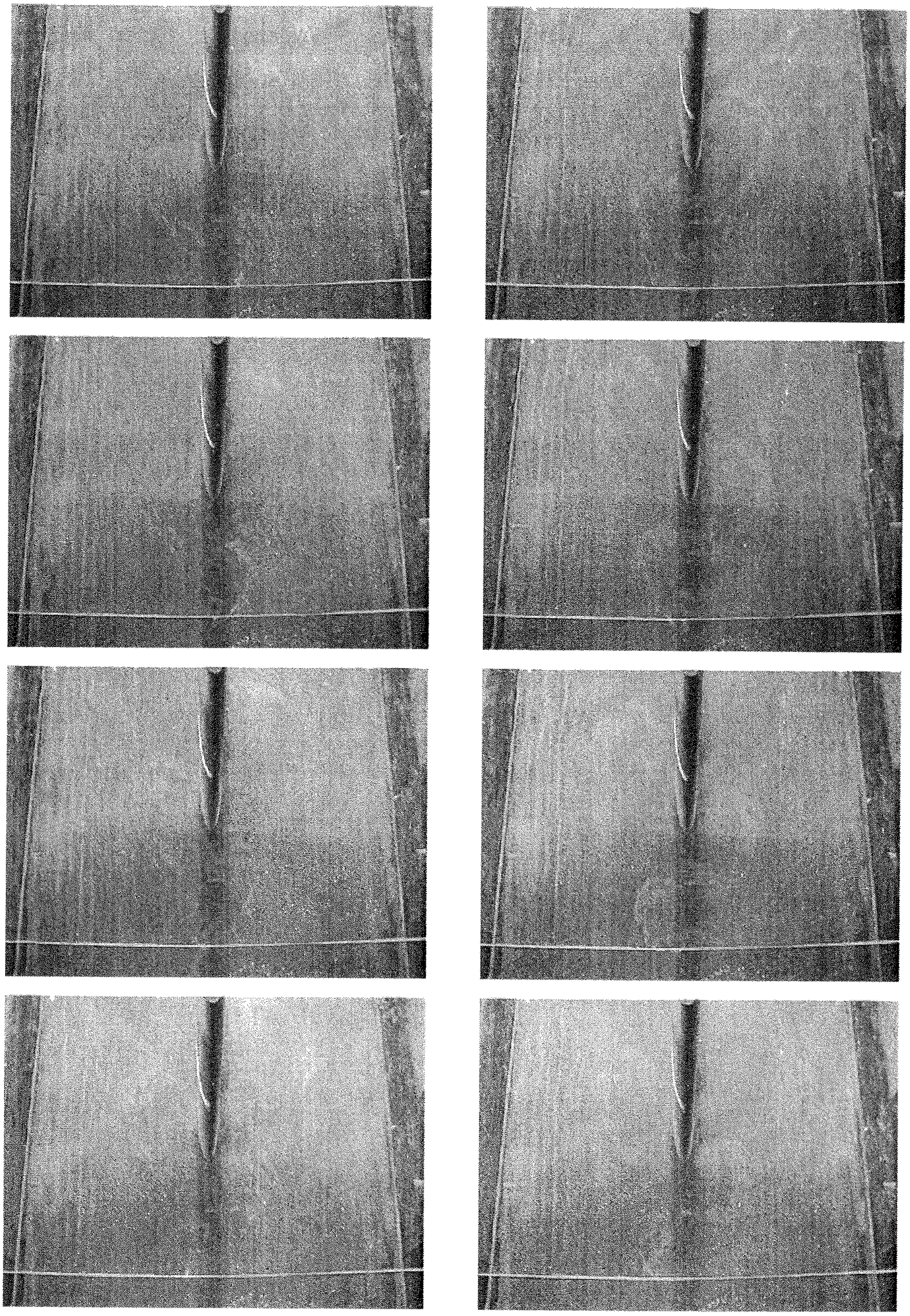

FIGURE 5.25: Snapshots of the Kármán vortex street embracing the airfoil at zero angle of attack. Figures are counterclockwisely arranged.

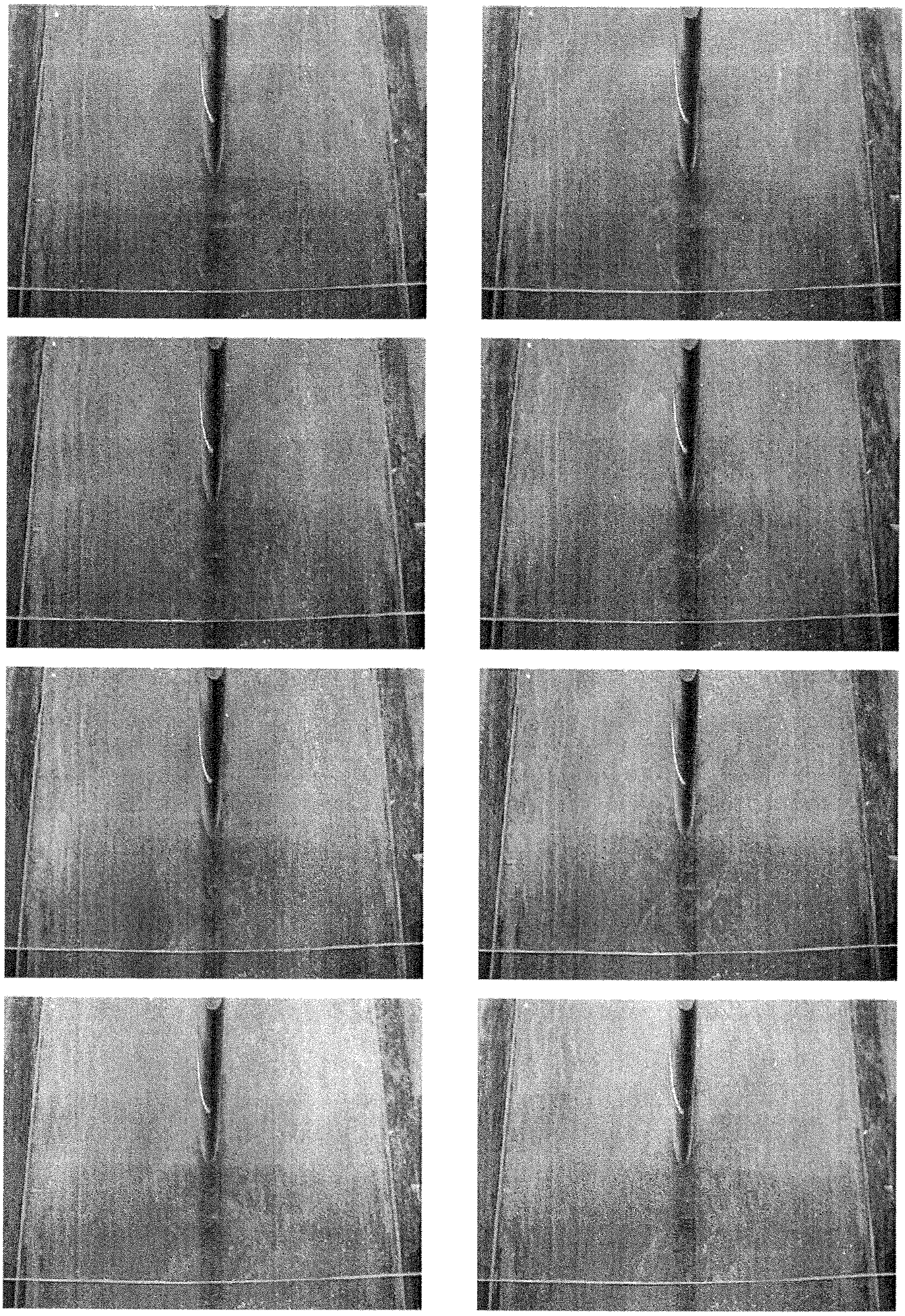

FIGURE 5.26: Snapshots of the Kármán vortex street during a LTA-cycle. Figures are counterclockwisely arranged.

5.4 Conclusions

In this chapter we experimentally investigated the acoustic field radiated by a rod-airfoil configuration, and the statistical behaviour of the fluctuating pressure field on both the rod and the airfoil surface.

Acoustic measurements showed the features listed below.

- The airfoil noise exhibits a dominant peak at the Strouhal frequency, which emerges from a broadened spectrum.

- The noise radiated by the rod-airfoil configuration is about 17 dB above the noise radiated by an isolated rod.

- Placing the airfoil into the wake of the rod also affects the frequency of the acoustic radiation peak. We did not performed measurements in order to check the existence of back reaction effects on the vortex shedding process due to the presence of the airfoil. However, even supposing that a weak back reaction exists, it is quite improbable that the observed noise amplification is due to some feed-back enforcing mechanism. Thus, the airfoil interaction with the vortices shed from the rod is the dominant cause of the noise amplification observed when the airfoil is placed downstream of the rod.

- The presence of the airfoil also contributes to the broadening of the Strouhal peak of the acoustic spectrum. Moreover, the *true* broad band spectral character of the acoustic radiation is enhanced by the presence of the airfoil.

- The airfoil angle of attack has a negligible effect on the acoustic levels at the Strouhal frequency.

- When the airfoil is at zero angle of attack, the acoustic spectrum at an observation angle of 90^o exhibits only odd harmonic peaks (f_0 and $3f_0$). On the contrary, when the airfoil is at a non zero angle of attack, a peak at the first harmonic ($2f_0$) appears. This effect was explained by considering that, when the airfoil is not symmetrically embedded in the wake of the rod, the spectrum of the upwash velocity induced by the vortex street exhibits even harmonics.

Acoustic measurements at different free-stream velocities provided a sixth-power law of the acoustic intensity. This is not surprising at a low Mach number. The main sound generation mechanism is thus of dipolar type. Furthermore, since the airfoil is acoustically compact, i.e.

$$c \ll \lambda = \frac{c_0}{f} = \frac{d}{\mathrm{St} M_\infty} \tag{5.1}$$

the directivity pattern is expected to be that of a compact dipole. This was not contradicted by the measurements.

Wall pressure measurements confirmed the aerodynamic origin of the first harmonic peak of the noise radiated when the airfoil is at a non zero angle of attack. A qualitative picture of the vortex-airfoil interaction was proposed in order to describe the influence of the angle of attack on the vortex trajectories. Such a qualitative picture was in agreement with measurements of coherence made between the acoustic and the wall pressure fluctuations. Interestingly, the behaviour predicted numerically in section 4.7 and described in Fig.4.42 agrees with the qualitative picture proposed in this chapter.

Coherence and correlation measurements of the wall pressure along the rod span provided a correlation length of the vortex shedding process of about 6.5 rod diameters. Furthermore, coherence measurements between points at different angles in the mid span plane of the rod gave evidence of a three-dimensional structure of the rod wake. These results are in agreement with the behaviour quoted in literature [36]. As an important result, three-dimensional effects are expected to be quite important in the rod-airfoil configuration.

Statistical measurements of the pressure fluctuations on the airfoil surface gave a further evidence of the existence of large, coherent vortical structures shed from the rod. These undergo a strong distortion at the airfoil leading edge, but continue to live all over the airfoil.

Finally, wall pressure measurements showed that the pressure fluctuations at the leading edge are two orders of magnitude higher than those at the trailing edge. This is not surprising because a leading edge is typically a region of quasi singular flow behaviour. On the contrary, the flow singularity at the trailing edge is smoothed by the vortex shedding process. In addition, the vortex interaction with the leading edge results in a weakening of the vortex. As a consequence, a weaker pressure field is induced by the vortex as it passes by the trailing edge.

In the final section of the present chapter we described a visualization experiment carried out in the *Hydra* water channel of the Politecnico di Torino. Hydrogen bubbles generated by electrolysis were used to visualize the large-scale vortical structures shed from the rod and convected towards the airfoil. The observations revealed the sporadic and random occurrence of vortex shedding cycles characterized by a higher Strouhal frequency and vortices nearly aligned along the wake axis. We proposed two explanations of this behaviour, the first based on the three-dimensional character of the vortex dynamics in the wake of the rod, the second based on a hypothetic effect due to the presence of the airfoil.

Appendix 5 A

Coherence Function and Correlation Coefficient

The coherence function Γ_{xy} between two signals $x(t)$ and $y(t)$ is defined as

$$\Gamma_{xy}(f) = \frac{|S_{xy}(f)|}{\sqrt{S_{xx}(f)\, S_{yy}(f)}} \tag{5.2}$$

where $S_{xy}(f)$ is the cross-power spectral density, i.e.

$$S_{xy}(f) = \mathrm{TF}\,\{C_{xy}(\tau)\} \tag{5.3}$$

with

$$C_{xy}(\tau) = \lim_{T\to\infty} \frac{1}{T} \int_0^T x(t)\, y(t-\tau)\, \mathrm{d}t \tag{5.4}$$

and TF denoting the Fourier transform.

For an ergodic process, $C_{xy}(\tau)$ can be interpreted as the correlation function between $x(t)$ and $y(t)$.

The correlation coefficient ρ is defined as

$$\rho = \frac{C_{xy}(0)}{\sqrt{C_{xx}(0)\; C_{yy}(0)}} = \frac{\int_{-\infty}^{\infty} S_{xy}(f)\; \mathrm{d}f}{\sqrt{\int_{-\infty}^{\infty} S_{xx}(f)\; \mathrm{d}f}\sqrt{\int_{-\infty}^{\infty} S_{yy}(f)\; \mathrm{d}f}} \tag{5.5}$$

Only in the case of two monochromatic signals of frequency f_0 it results that

$$\rho = \Gamma_{xy}(f_0) \tag{5.6}$$

Thus, in a rod-airfoil configuration ρ gives the correlation coefficient of the main vortices, whereas, in the case of an isolated airfoil, it gives the overall correlation (all frequencies).

Appendix 5 B

Transfer Function of the Pressure Transducer

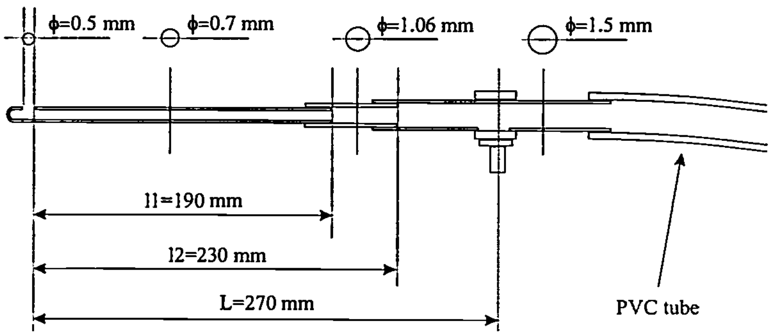

FIGURE 5.27: Pressure probe.

An analytical expression of the transfer function H for a capillary pressure probe has been proposed in [34]. It allows to correct the amplitude of the pressure fluctuation measured by the microphone P_s, in order to obtain the amplitude of the pressure P_0 at the probe inlet, namely

$$P_0 = \frac{P_s}{H} \tag{5.7}$$

In the case of a capillary tube made of three segments of different lengths, i.e. l_1, l_2 and l_3, and different sections, i.e. S_1, S_2 and S_3 (see Fig.5.27), the transfer function is given by

$$H = \frac{8}{\left|\left(\Omega + \Theta + \frac{Z_0}{\rho_0 c_0}(\Omega - \Theta)\right)\right|} \exp\left\{-\left[\alpha_1 l_1 - \alpha_2 (l_2 - l_1) + \alpha_3 (L - l_2)\right]\right\} \tag{5.8}$$

where quantities are defined as follows. The parameter α_i accounts for the viscous attenuation in the ith section. As proposed by Pierce [38] it is given by

$$\alpha = \frac{1}{\sqrt{8}}\sqrt{\frac{\omega\mu}{\rho_0 c_0^2}}\left[1 + \frac{\gamma - 1}{\sqrt{Pr}}\right]\frac{L_p}{S} \tag{5.9}$$

where ω is the frequency of the propagating disturbance, μ is the dynamic viscosity of the fluid, Pr is the Prandtl number and L_p/S denotes the ratio between the perimeter and the section of the duct. Assuming standard quantities it approximately results that

$$\alpha_i \simeq \frac{0.0102}{c_0}\sqrt{f}\frac{1}{r_i} \tag{5.10}$$

where r_i is the radius of the ith section. Ω and Θ are complex functions whose real and imaginary parts are given by

$$\begin{aligned}
\Omega_r &= I_r + \{J_r \cos[2K_2(l_2 - l_1) - J_i \sin[2K_2(l_2 - l_1)]]\} \exp\{-2\alpha_2(l_2 - l_1)\} \\
\Omega_i &= I_i + \{J_i \cos[2K_2(l_2 - l_1) + J_r \sin[2K_2(l_2 - l_1)]]\} \exp\{-2\alpha_2(l_2 - l_1)\}
\end{aligned} \tag{5.11}$$

$$\begin{aligned}
\Theta_r = {} & P_r \cos(2K_1l_1)\, e^{-2\alpha_1 l_1} - P_i \sin(2K_1l_1)\, e^{-2\alpha_1 l_1} \\
& + Q_r \cos\{2[K_2(l_2 - l_1) + K_1l_1]\}\, e^{-2[\alpha_2(l_2-l_1)+\alpha_1 l_1]} \\
& - Q_i \sin\{2[K_2(l_2 - l_1) + K_1l_1]\}\, e^{-2[\alpha_2(l_2-l_1)+\alpha_1 l_1]} \\
\Theta_i = {} & P_i \cos(2K_1l_1)\, e^{-2\alpha_1 l_1} + P_r \sin(2K_1l_1)\, e^{-2\alpha_1 l_1} \\
& + Q_i \cos\{2[K_2(l_2 - l_1) + K_1l_1]\}\, e^{-2[\alpha_2(l_2-l_1)+\alpha_1 l_1]} \\
& + Q_r \sin\{2[K_2(l_2 - l_1) + K_1l_1]\}\, e^{-2[\alpha_2(l_2-l_1)+\alpha_1 l_1]}
\end{aligned} \tag{5.12}$$

where

$$\begin{aligned}
& I_r = AC - BD, \qquad I_i = BC + AD \\
& J_r = EF - BD, \qquad J_i = -ED - BF \\
& P_r = EC + BD, \qquad P_i = ED - BC \\
& Q_r = AF + BD, \qquad Q_i = BF - AD \quad \text{with} \\
& A = 1 + a\frac{S_2}{S_1}, \qquad B = b\frac{S_2}{S_1}, \qquad C = 1 + c\frac{S_3}{S_2} \\
& D = d\frac{S_3}{S_2}, \qquad E = 1 - a\frac{S_2}{S_1}, \qquad F = 1 - c\frac{S_3}{S_2} \quad \text{and} \\
& a = \frac{K1K_2 + \alpha_2\alpha_1}{K_1^2 + \alpha_1^2}, \qquad b = \frac{K1\alpha_2 - K_2\alpha_1}{K_1^2 + \alpha_1^2} \\
& c = \frac{K3K_2 + \alpha_3\alpha_2}{K_2^2 + \alpha_2^2}, \qquad d = \frac{K2\alpha_3 - K_3\alpha_2}{K_2^2 + \alpha_2^2}
\end{aligned}$$

The complex wavenumbers k_i account for the viscous attenuation and are given by

$$\begin{aligned}
k_i &= K_i + \mathrm{i}\,\alpha_i \\
K_i &= \frac{\omega}{c_0} + \alpha_i \quad \text{with} \quad i = 1, 2, 3
\end{aligned} \tag{5.13}$$

The quantity Z_0 denotes the inlet probe impedence and is given by

$$\frac{Z_0}{\rho_0 c_0} = \frac{\omega^2 S_0}{c_0^2\, 2\pi} + \mathrm{i}\,\frac{8\omega\sqrt{S_0}}{c_0\, 3\pi^{3/2}} \tag{5.14}$$

where S_0 is the inlet section.

In Fig.5.28, the transfer function of the pressure probe sketched in Fig.5.27 is plotted. The sensibility s of the microphone has been taken into account, and the curve represents indeed the function H/s. An example of corrected wall pressure spectrum is plotted on Fig.5.29. It shows that high frequency oscillations of the measured pressure are due to a selective probe response.

The transfer function presented in this appendix was used to adjust the amplitude of the measured spectra.

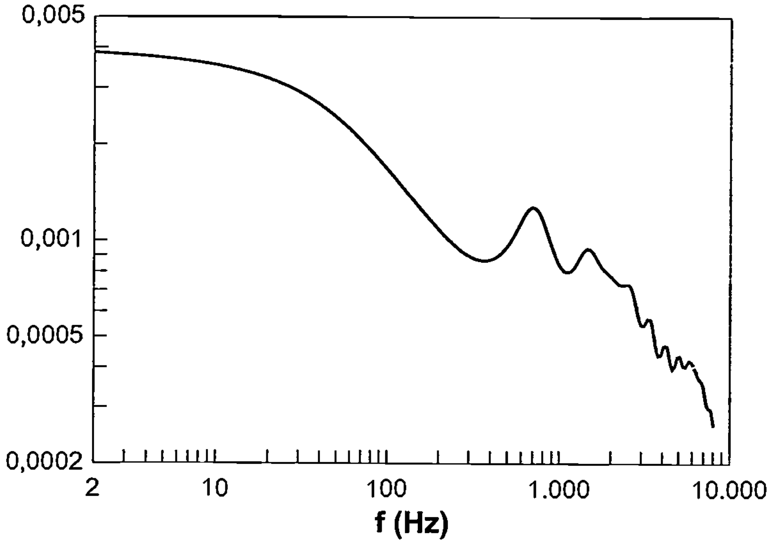

FIGURE 5.28: Transfer function of a capillary pressure probe.

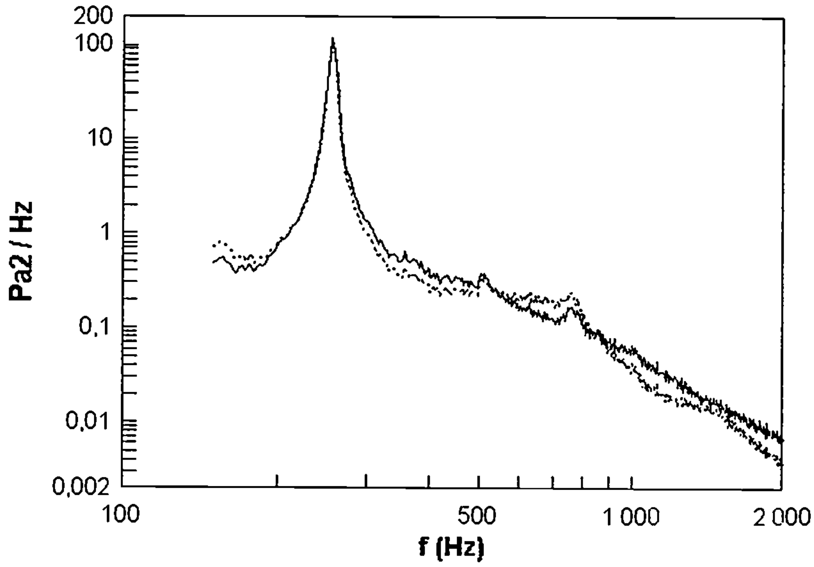

FIGURE 5.29: Comparison between a measured wall pressure spectrum and a corrected spectrum: —— corrected, - - - - measured.

6

Acoustic Analogy Formulation

In this chapter we describe the acoustic analogy formulation used throughout the present work. It is based on a retarded time solution of the Ffowcs Williams & Hawkings equation (FW-H), and allows noise predictions from aeroacoustic sources in complex motion. Farassat's thickness and loading noise formulation 1A [39] and Brentner's quadrupole noise formulation Q1A [40] are exploited and extended to a moving observer. These formulations are based upon a penetrable integration surface and upon time derivatives taken analytically inside the integrals.

The retarded time formulation is herein interpreted as an advanced time formulation, which allows a computation of the acoustic pressure field as the CFD simulation is processed. This new aeroacoustic methodology is implemented in the rotor noise prediction code *Advantia* [41], developed by the author in the present context.

In this chapter we first describe the acoustic analogy formulation. Then, results concerning the numerical assessment of the computer code *Advantia* are presented.

6.1 Introduction

Today's technological maturity of the aerospace technology concerning performances and efficiency, even more stringent certification rules and the increased sensitivity of the community result in an increasing attention to safety, emission and noise.

Low noise requirements are particularly important for aircrafts operating in and nearby populated areas. This is the case of civil helicopters and civil transport jets in landing and take-off conditions. Since a great deal of progress has been made in understanding the sound generation mechanisms, more attention is currently devoted to the development of accurate and efficient prediction methods.

Nowadays two different large groups of numerical methods are available, one based on the Computational AeroAcoustic approach (CAA), the other based on integral formulations. CAA methods consist in solving the flow governing equations including acoustic fluctuations by means of classical CFD methods (finite difference, finite volume, finite elements, etc.) with high accuracy (low-dispersion) numerical schemes. Thus, reasonable cost solutions are restricted to near field predictions. On the contrary, integral methods allow to propagate a near field *information* to the far field with a computational cost that does not depend on the observation distance. The near field information can be obtained by means of the integral method itself, as in Boundary Element Methods (BEM), or by means of a CFD/CAA method, as in a hybrid approach.

Hybrid methods are the domain of the acoustic analogy approach. This approach is based on the ideal assumption of separating the sound generation mechanism from its pure propagation. Thus, the flow governing equations are arranged in the form of a wave equation where all the terms discarded by a wave propagation pattern are gathered at the right-hand side and interpreted as source terms. Depending on both the reference wave equation and the mechanism that generates the pressure disturbances (free turbulent flows, turbulent flows bounded by solid surfaces, etc.), the acoustic analogy approach leads to different formulations. The first model was proposed by Lighthill [1] and describes the noise generated by a turbulent portion of fluid in an otherwise quiescent unbounded medium. Later on, Lighthill's model was extended by Ffowcs Williams & Hawkings [2] (FW-H) to flows confined by surfaces in arbitrary motion.

The FW-H analogy is the most appropriate theoretical support for understanding the mechanisms involved in the generation of aerodynamic sound from bodies in complex motion. This is typically the case of a helicopter rotor. The rotating wing of a helicopter generates aerodynamic noise by different mechanisms: the fluid displacement due to the blade thickness, steady and unsteady blade loadings, rotating shocks, blade-vortex interactions, blade-turbulence interactions. In the FW-H equation these mechanisms appear as source terms of an inhomogeneous wave equation.

The first solutions of the FW-H wave equation were obtained by integrating the pressure field upon the physical surface of the body. This strategy confines all the flow nonlinearities into a volume integral extended over a domain exterior to the body. Because of the computational cost required by an accurate prediction of this volume integral, for several years only the linear effects due to the body thickness and aerodynamic loading have been predicted by means of the FW-H analogy.

An important source of rotor noise is indeed related to the compressibility effects occurring in the blade tip region. At values of the advancing tip Mach number higher than ~ 0.85, shock waves appear in the flow field around the rotor, which generate an annoying impulsive noise. A prediction the so-called High-Speed Impulsive (HSI) noise requires the nonlinear effects to be taken into account in the FW-H analogy. An alternative to the computation of the volume term in the FW-H equation consists in using methods based on Kirchhoff's theorem. These methods relate the acoustic field to the pressure field upon a control surface enclosing the blade and *all* the near-blade flow nonlinearities. As in the FW-H analogy, a CFD computation provides the flow data upon the integration surface.

For several years the Kirchhoff formulations has been considered as an ineluctable alternative to the FW-H analogy for the prediction of high-speed rotor noise. Only recently, di Francescantonio [42] has shown that the FW-H analogy can be extended to a penetrable control surface and that the surface integrals account for all the nonlinear terms enclosed by the integration surface. In response to di Francescantonio [42], Brentner & Farassat [43] pointed out that, although di Francescantonio was the first to apply the FW-H analogy to a Kirchhoff-type integration surface, Ffowcs Williams had already described several implications of a penetrable surface formulation. Moreover, Brentner & Farassat discussed in great detail the conceptual difference between a Kirchhoff formulation and a FW-H penetrable formulation. Their analysis is an example of both elegance and effectiveness. It shows that, since the Kirchhoff equation follows from a linear wave equation, its application to acoustic analogy predictions requires the integration surface to be placed in the linear flow region. On the contrary, since a FW-H equation is an exact rearrangement of the flow governing equations, the placement of the integration surface is only a matter of convenience as long as the quadrupole sources are taken into account by the surface integration. Thus, the FW-H analogy allows accurate noise predictions even wnen the integration surface is not in the linear flow region.

In this chapter we are concerned with a retarded time integral solution of the FW-H equation. The mathematical formalism is that of Farassat & Succi [39] and Brentner [40], extended to a moving observer. A penetrable surface formulation is considered, as proposed by di Francescantonio [42] and Brentner & Farassat [43].

The retarded time formulation is hereafter interpreted as an advanced time formulation. This allows to compute the acoustic field as the CFD simulation is processed. The advanced time approach offers the following advantages.

1. Since the acoustic time-step is typically several orders of magnitude greater than the aerodynamic time-step, the computational time for the noise prediction at each acoustic time-step may be smaller than that required by the CFD simulation to cover an acoustic time-step. In this case,

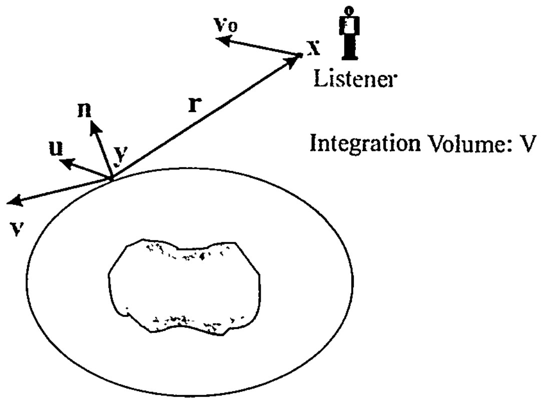

FIGURE 6.1: Scheme of the FW-H acoustic analogy. The flow field enclosed by the integration surface S is replaced by a quiescent fluid (ρ_0, p_0, $\mathbf{u} = 0$). The vectors $\mathbf{u}$ and $\mathbf{v}$ denote the velocity of the flow and the velocity of the integration surface, respectively. The listener moves at the constant velocity $\mathbf{v}_o$.

provided that a parallel architecture is used, the acoustic prediction has a negligible computational cost.

2. The advanced time is an algebraic function of the observer and point source location at the emission time. Therefore, no iterative solutions of the retarded time equation must be performed at each time-step.

3. The advanced time projection of the source status at a given time is univocal. Thus, the application of the advanced time formulation to sources in supersonic motion does not require a modification of the computational algorithms.

4. No disk-recording of the flow time history is necessary for the purpose of the acoustic computation.

This new aeroacoustic methodology is implemented in the rotor noise prediction code *Advantia* [41], developed by the author in the present context.

6.2 Aeroacoustic Formulation

Unsteady flows generate pressure fluctuations by different mechanisms. These fluctuations partially propagate as acoustic waves within the fluid medium. The acoustic analogy suggests to separate the sound generation mechanisms from its propagation. This can be made by arranging the flow governing equations in the form of a wave equation, where all the terms not accounted for by a given wave propagation pattern are moved at the right-hand side and interpreted as source terms.

The first acoustic analogy model was proposed by Lighthill [1]. It describes the sound generation from turbulent velocity fluctuations and propagating in an unbounded medium at rest. The physical adequacy of the acoustic analogy model is discussed in chapter 5 of part II. In the present chapter we focus on the extension of Lighthill's theory to account for the presence of solid surfaces in the field.

6.2.1 The FW-H Equation

The FW-H equation is the most general form of Lighthill's acoustic analogy. It can be obtained by using generalized functions in order to embed the exterior flow problem in unbounded space.

Let $f(\mathbf{x}, t) = 0$ be a control surface whose points move at the velocity $\mathbf{v}(\mathbf{x}, t)$. The surface $f = 0$ is defined such that $\nabla f = \hat{\mathbf{n}}$, where $\hat{\mathbf{n}}$ denotes the unit normal vector which points out of the surface.

Using generalized flow variables, the flow portion enclosed by the surface, i.e. $f < 0$, can be replaced by a quiescent fluid and a surface distribution of sources which restore the conservative character of the field. Therefore, the generalized continuity and the linear momentum equations can be written as

$$\begin{aligned}&\frac{\bar{\partial}}{\partial t}\left[(\rho-\rho_0)\, H(f)\right]+\frac{\bar{\partial}}{\partial x_i}\left[\rho u_i\, H(f)\right]=Q\,\delta(f) \quad \text{with}\\ &Q=\rho_0\, U_i\,\hat{n}_i \quad \text{and}\\ &U_i=\left(1-\frac{\rho}{\rho_0}\right)v_i+\frac{\rho u_i}{\rho_0}\end{aligned} \tag{6.1}$$

and

$$\begin{aligned}&\frac{\bar{\partial}}{\partial t}\left[\rho u_i\, H(f)\right]+\frac{\bar{\partial}}{\partial x_j}\left[(\rho u_i u_j+P_{ij})\, H(f)\right]=L_i\,\delta(f) \quad \text{with}\\ &L_i=P_{ij}\,\hat{n}_j+\rho u_i\,(u_n-v_n) \quad \text{and}\\ &P_{ij}=(p-p_0)\,\delta_{ij}-\tau_{ij}\end{aligned} \tag{6.2}$$

where $Q\,\delta(f)$ and $L_i\,\delta(f)$ denote surface source distributions of mass and linear momentum, respectively. The following generalized derivatives have been used in equations (7.212) and (7.213)

$$\frac{\bar{\partial}H(f)}{\partial t}=\delta(f)\,\frac{\partial f}{\partial t}=-\delta(f)\,v_n \tag{6.3}$$

$$\frac{\bar{\partial}H(f)}{\partial x_i}=\delta(f)\,\frac{\partial f}{\partial x_i}=\delta(f)\,\hat{\mathbf{n}} \tag{6.4}$$

Outside of the source region, the fluid can be considered at rest and equations (6.1) and (6.2) can be arranged in the form of a standard wave equation describing the propagation of an acoustic disturbance p' in a quiescent medium, i.e.

$$\Box^2 p' \equiv \left(\frac{1}{c^2}\frac{\partial^2}{\partial t^2}-\nabla^2\right)p'=0 \tag{6.5}$$

where c is the sound speed in the quiescent medium.

If the flow perturbations are included, equations (6.1) and (6.2) can be arranged into the FW-H equation where the flow perturbations appear as source terms of the standard wave equation. Therefore, by subtracting the divergence of equation (6.2) to the time derivative of equation (6.1), the differential form of the FW-H equation can be obtained, i.e.

$$\Box^2\left\{(\rho-\rho_0)\,c^2\,H(f)\right\}=\frac{\partial^2}{\partial x_i\partial x_j}\left\{T_{ij}\,H(f)\right\}-\frac{\partial}{\partial x_i}\left\{L_i\,\delta(f)\right\}+\frac{\partial}{\partial t}\left\{Q\,\delta(f)\right\} \tag{6.6}$$

where

$$T_{ij}=\rho\, u_i u_j+\left(p'-c^2\rho'\right)\delta_{ij}-\tau_{ij} \tag{6.7}$$

is the well-known Lighthill's stress tensor.

If the density perturbations are small, as usually happens at the observation distances, the term $(\rho-\rho_0)\,c^2$ can be replaced by p', and equation (6.6) can be interpreted as an inhomogeneous wave equation for the acoustic pressure p'.

In the aeroacoustic literature, the three source terms on the right-hand side of equation (6.6) are known as the quadrupole, loading and thickness source terms, respectively. The thickness and loading terms are surface distributions of sources, as indicated by $\delta(f)$. When the control surface encloses a physical surface, the thickness source accounts for the fluid displacement produced by the body motion, and the loading source accounts for the unsteady loading exerted by the body on the fluid. The quadrupole source is a volume distribution of sources, as indicates by $H(f)$. This accounts for all the flow nonlinearity in the domain exterior to the control surface. In the case of a body moving in an otherwise quiescent fluid, the flow nonlinearities are due to the body motion and may consist of vortical disturbances, shocks and local sound speed variations.

6.2.2 The FW-H Equation *versus* the Kirchhoff Equation

The technique of the generalized function can be also applied to the standard linear wave equation $\Box^2 p' = 0$, in order to replace the acoustic field in the region $f < 0$ by an elementary quiescent fluid $p' = 0$. A distribution of sources on the surface $f = 0$ is thus necessary to maintain the fictitious discontinuities introduced in the original field. Considering the generalized derivatives

$$\frac{1}{c}\frac{\bar{\partial}}{\partial t}\left(p' H(f)\right) = \frac{1}{c}\frac{\partial p'}{\partial t} H(f) - M_n p' \delta(f) \tag{6.8}$$

$$\frac{1}{c}\frac{\bar{\partial}}{\partial t}\left\{\frac{1}{c}\frac{\bar{\partial}}{\partial t}\left(p' H(f)\right)\right\} = \frac{1}{c^2}\frac{\partial^2 p'}{\partial t^2} H(f) - \frac{1}{c}\frac{\partial p'}{\partial t} M_n \delta(f) - \frac{1}{c}\frac{\partial}{\partial t}\left(p' M_n \delta(f)\right) \tag{6.9}$$

$$\bar{\nabla}\left(p' H(f)\right) = \nabla p' H(f) + p' \hat{\mathbf{n}}\, \delta(f) \tag{6.10}$$

$$\bar{\nabla}\cdot\bar{\nabla}\left(p' H(f)\right) = \nabla^2 p' H(f) + \nabla p' \cdot \hat{\mathbf{n}}\, \delta(f) + \nabla\cdot\left(p' \hat{\mathbf{n}}\, \delta(f)\right) \tag{6.11}$$

and subtracting equation (6.11) from equation (6.9), the generalized linear wave equation leads to the Kirchhoff (K) equation for a moving surface, i.e.

$$\bar{\Box}^2 p' H(f) = -\left(\frac{\partial p'}{\partial n} + \frac{M_n}{c}\frac{\partial p'}{\partial t}\right)\delta(f) - \frac{1}{c}\frac{\partial}{\partial t}\left\{M_n p' \delta(f)\right\} - \frac{\partial}{\partial x_i}\left\{p' \hat{n}_i \delta(f)\right\} \tag{6.12}$$

where M_n is the local normal Mach number of the surface $f = 0$.

The Kirchhoff formula for a subsonically moving surface was firstly derived by Morgans [44] in 1930. The derivation of this formula was based on classic analysis and was lengthy. The simpler procedure described above was proposed by Farassat & Myers [45] in 1988. It shows the effectiveness of the generalized function technique.

The Kirchhoff equation is valid for any physical problem governed by the standard linear wave equation. In acoustics it governs the propagation of linear flow perturbations in a medium at rest and felt by the control surface $S : f = 0$. In aeroacoustics, the linear perturbation on S are the result of all sources, regardless to their nature (linear or nonlinear, quadrupole or not, etc.), located in the interior domain $f < 0$. As a consequence, in aeroacoustics the Kirchhoff approach is only valid for S surrounding the nonlinear flow region. Moreover, the Kirchhoff equation does not account for any aerodynamic source located in the exterior domain $f > 0$, or on the surface itself. In particular, only quadrupole source terms enclosed by S are taken into account and nonlinear aerodynamic sources located on S are not handled. It follows that the use of the Kirchhoff approach in practical applications is quit limited. This is because unsteady flows extend over a large distance in the streamwise direction (e.g. jets, wakes, etc.) and would require very large integration surfaces and very large flow region accurately predicted.

This formal difficulty is removed by the FW-H equation. Being an exact rearrangement of the flow governing equations, this intrinsically accounts for the nonlinear flow perturbations on both the integration surface and the exterior domain.

The Kirchhoff formulation is attractive because no volume integration is necessary. For this reason it was used in past years for rotor noise predictions at high-speed tip Mach numbers, provided that, sufficiently far from the aerodynamic source region, the input acoustic pressure p' and its derivatives $\partial p'/\partial t$ and $\partial p'/\partial n$ are compatible with the wave equation $\Box^2 p' = 0$.

More recently [42], the FW-H formulation has been applied to rotor noise predictions by integrating the aerodynamic data upon a penetrable control surface. Since the surface source terms in equation (6.6) are compatible with the flow governing equations, the placement of the integration surface in a FW-H approach is only a matter of convenience as long as the quadrupole sources are taken into account by the surface integration. Thus, the FW-H analogy allows accurate noise predictions even when the control surface is not in the linear flow region. This is the main advantage of the FW-H aeroacoustic formulation on the Kirchhoff method.

The equivalence between the FW-H formulation and a Kirchhoff method in the linear flow region can be easily verified by introducing the linear approximations $\rho' \simeq p'/c^2$ and $u_i u_j \ll 1$ into equation (6.6). Thus, concerning the thickness noise source, it results that

$$\begin{aligned} U_i &\simeq -\frac{p'}{\rho_0 c^2} v_i + u_i \\ \rho_0 U_n \delta(f) &\simeq -p' \frac{M_n}{c} \delta(f) + \rho u_i \hat{n}_i \delta(f) \end{aligned} \tag{6.13}$$

and

$$\begin{aligned} \frac{\partial}{\partial t}\{\rho_0 U_n \delta(f)\} &\simeq -\frac{\partial}{\partial t}\left\{p' \frac{M_n}{c}\delta(f)\right\} + \hat{n}_i \delta(f) \frac{\partial}{\partial t}\{\rho u_i\} + \rho u_i \frac{\partial}{\partial t}\{\hat{n}_i \delta(f)\} \\ &= -\frac{\partial}{\partial t}\left\{p' \frac{M_n}{c}\delta(f)\right\} - \frac{\partial p'}{\partial n}\delta(f) - \rho u_i \frac{\partial}{\partial x_i}\{v_n \delta(f)\} \end{aligned} \tag{6.14}$$

where use of the relation

$$\frac{\partial}{\partial t}(\hat{n}_i \delta(f)) = -\frac{\partial}{\partial x_i}(v_n \delta(f)) \tag{6.15}$$

has been made. Analogously, the loading noise source reduces to

$$\begin{aligned} \frac{\partial}{\partial x_i}\{L_i \delta(f)\} &\simeq \frac{\partial}{\partial x_i}(p' \hat{n}_i \delta(f)) - (u_n - v_n)\frac{\delta(f)}{c^2}\frac{\partial p'}{\partial t} + \frac{u_n \delta(f)}{c^2}\frac{\partial p'}{\partial t} - \rho u_i \frac{\partial}{\partial x_i}(v_n \delta(f)) \\ &\simeq \frac{\partial}{\partial x_i}(p' \hat{n}_i \delta(f)) + \frac{v_n \delta(f)}{c^2}\frac{\partial p'}{\partial t} - \rho u_i \frac{\partial}{\partial x_i}(v_n \delta(f)) \end{aligned} \tag{6.16}$$

where use of the linearized continuity equation

$$\frac{\partial}{\partial x_i}(\rho u_i) \simeq \frac{1}{c^2}\frac{\partial p'}{\partial t} \tag{6.17}$$

has been made. Finally, substituting the linearized expressions (6.14) and (6.16) into equation (6.6), and neglecting the nonlinear quadrupole contribution, yields the Kirchhoff equation (6.12).

6.2.3 The Retarded Time Formulation of the FW-H Equation

The FW-H equation (6.6) is an exact rearrangement of the continuity and momentum equation generalized to an unbounded fluid. The flow field enclosed by a control surface is replaced by an elementary flow ($\rho = \rho_0$ and $u_i = 0$) and fulfillment of the flow governing equations is ensured by surface source distributions which ultimately act as sources of sound.

Physical surfaces possibly enclosed by the control surface have been removed and substituted by equivalent surface source distributions. Therefore, the Green's function of the unbounded three-dimensional space can be used to solve equation (6.6). The free-space Green's function is defined as $G = \delta(g)/r$, where $g = t - \tau - r/c$ and $r = |\mathbf{x} - \mathbf{y}|$. Here $\mathbf{x}$ and t are the observer position and the observer (reception) time, respectively, whereas, $\mathbf{y}$ and τ are the source position and the source (emission) time, respectively. The formal solution of equation (6.6) is thus given by

$$\begin{aligned} 4\pi p'(\mathbf{x}, t) &= \frac{\partial^2}{\partial x_i \partial x_j}\int\int_{f>0} \frac{\delta(t - \tau - r/c)}{r} T_{ij}\, dV\, d\tau \\ &- \frac{\partial}{\partial x_i}\int\int_{f=0} \frac{\delta(t - \tau - r/c)}{r} L_i\, dS\, d\tau \\ &+ \frac{\partial}{\partial t}\int\int_{f=0} \frac{\delta(t - \tau - r/c)}{r} Q\, dS\, d\tau \end{aligned} \tag{6.18}$$

where the properties of the δ–function have been exploited in order to reduce volume integrals to corresponding surface integrals. Now, a change of the integration variable can be carried out by using the well-known formula

$$\int Q(\tau)\ \delta(g(\tau)) = \sum_{n=1}^{N} \frac{Q}{|\partial g/\partial \tau|}(\tau_n^*) \qquad (6.19)$$

the sum being taken over all the zeros τ_n^* of the *retarded time equation* $g = 0$. When the source is in subsonic motion, there exists one and only one solution of the retarded time equation for any reception time. Conversely, when the source is in supersonic motion, more than one solution may exist. This physically accounts for the fact that impulses emitted at different times can be detected at the same time. The time-source derivative of g is given by

$$\frac{\partial g}{\partial \tau} = -1 + M_r \qquad (6.20)$$

where $M_r = M_i\,\hat{r}_i$ is the component of the source Mach number vector in the direction of the observer, $\hat{r}_i = (x_i - y_i)/r$ denoting the unit vector in the radiation direction. The term $|1 - M_r|$ accounts for a dilatation or contraction of the observer time scale respect to the source time scale, depending on whether the source moves far away from or towards the observer, respectively. This effect is known as *Döppler effect.*

Let us suppose that the source elements in equation (6.18) are in subsonic motion and let us denote as $[\ldots]_{\text{ret}}$ evaluation at the retarded time

$$\tau^* = t - \frac{|\mathbf{x} - \mathbf{y}(\tau^*)|}{c} \qquad (6.21)$$

Then, applying (6.19) and (6.20) to the integral expression (6.18) yields

$$\begin{aligned} 4\pi p' &= \frac{\partial^2}{\partial x_i \partial x_j} \int_{f>0} \left[\frac{T_{ij}}{r\,(1-M_r)}\right]_{\text{ret}} \mathrm{d}V \\ &- \frac{\partial}{\partial x_i} \int_{f=0} \left[\frac{L_i}{r\,(1-M_r)}\right]_{\text{ret}} \mathrm{d}S \\ &+ \frac{\partial}{\partial t} \int_{f=0} \left[\frac{Q}{r\,(1-M_r)}\right]_{\text{ret}} \mathrm{d}S \end{aligned} \qquad (6.22)$$

This is the retarded time solution of the FW-H equation (6.6). It is interesting to notice that the change of variable used to integrate the δ–function $\delta(g)$ generated a singular behaviour at the transonic condition $M_r = 1$. Fortunately, this singularity is a mathematical artefact and can be removed by applying a different change of variables. The reader should refer to chapter 7 of part II for a description of these different formulations and a discussion on the nature of the transonic singularity.

Starting from equation (6.22) different expressions of the retarded time formulation can be obtained in order to improve the practical relevance of the FW-H analogy. A first modification consists in transforming the space derivatives into time derivatives. This can be done by using the relation [46]

$$\frac{\partial}{\partial x_i} \int_{f=0} \left[\frac{L_i}{r\,(1-M_r)}\right]_{\text{ret}} \mathrm{d}S = -\frac{1}{c}\frac{\partial}{\partial t} \int_{f=0} \left[\frac{L_i\,\hat{r}_i}{r\,(1-M_r)}\right]_{\text{ret}} \mathrm{d}S - \int_{f=0} \left[\frac{L_i\,\hat{r}_i}{r^2\,(1-M_r)}\right]_{\text{ret}} \mathrm{d}S \qquad (6.23)$$

for the loading noise, and twice the same chain for the quadrupole noise. Hence, it follows that

$$\begin{aligned} 4\pi p' &= \frac{1}{c^2}\frac{\partial^2}{\partial t^2} \int_{f>0} \left[\frac{T_{rr}}{r\,(1-M_r)}\right]_{\text{ret}} \mathrm{d}V + \frac{1}{c}\frac{\partial}{\partial t} \int_{f>0} \left[\frac{3\,T_{rr} - T_{ii}}{r^2\,(1-M_r)}\right]_{\text{ret}} \mathrm{d}V + \int_{f>0} \left[\frac{3\,T_{rr} - T_{ii}}{r^3\,(1-M_r)}\right]_{\text{ret}} \mathrm{d}V \\ &+ \frac{1}{c}\frac{\partial}{\partial t} \int_{f=0} \left[\frac{L_i\,\hat{r}_i}{r\,(1-M_r)}\right]_{\text{ret}} \mathrm{d}S + \int_{f=0} \left[\frac{L_i\,\hat{r}_i}{r^2\,(1-M_r)}\right]_{\text{ret}} \mathrm{d}S \\ &+ \frac{\partial}{\partial t} \int_{f=0} \left[\frac{Q}{r\,(1-M_r)}\right]_{\text{ret}} \mathrm{d}S \end{aligned} \qquad (6.24)$$

A second modification consists in moving the time derivatives inside the integrals. This is generally convenient for numerical purposes and can be made, as shown by Farassat & Succi [39] and Brentner [40], by using the rule

$$\left.\frac{\partial}{\partial t}\right|_{\mathbf{x}} = \left[\frac{1}{1-M_r}\left.\frac{\partial}{\partial \tau}\right|_{\mathbf{x}}\right]_{\text{ret}} \tag{6.25}$$

together with the following relations

$$\frac{\partial r}{\partial \tau} = -c\,M_r \tag{6.26}$$

$$\frac{\partial \hat{r}_i}{\partial \tau} = \frac{\hat{r}_i\,c\,M_r - c\,M_i}{r} \tag{6.27}$$

$$\frac{\partial M_r}{\partial \tau} = \frac{1}{r}\left\{r\,\hat{r}_i\,\frac{\partial M_i}{\partial \tau} + c\left(M_r^2 - M^2\right)\right\} \tag{6.28}$$

In equation (6.25) the symbol $|_{\mathbf{x}}$ indicates derivatives taken at fixed observer position. It finally results that

$$p'(\mathbf{x},t) = p'_Q(\mathbf{x},t) + p'_L(\mathbf{x},t) + p'_T(\mathbf{x},t) \tag{6.29}$$

where the expressions of the thickness, loading and quadrupole noise[1] are reported below.

Thickness noise

$$\begin{aligned} 4\pi\,p'_Q(\mathbf{x},t) &= \int_{f=0}\left[\frac{\rho_0\left(\dot{U}_n + U_{\dot{n}}\right)}{r\,(1-M_r)^2}\right]_{\text{ret}} \mathrm{d}S \\ &+ \int_{f=0}\left[\frac{\rho_0\,U_n\left(r\dot{M}_r + c\left(M_r - M^2\right)\right)}{r^2\,(1-M_r)^3}\right]_{\text{ret}} \mathrm{d}S \end{aligned} \tag{6.30}$$

where $\mathbf{M}$ is the Mach number vector of a source point on the integration surface, and the remaining terms are defined as

$$\begin{aligned} &U_n = U_i\,\hat{n}_i\,, \qquad U_{\dot{n}} = U_i\,\dot{\hat{n}}_i\,, \qquad \dot{U}_n = \dot{U}_i\,\hat{n}_i \\ &M_r = M_i\,\hat{r}_i\,, \qquad \dot{M}_r = \dot{M}_i\,\hat{r}_i \end{aligned} \tag{6.31}$$

Dots on quantities denote time derivatives with respect to the source time τ. A comprehensive description of all the involved quantities is given in appendix 6 A.

Loading noise

$$\begin{aligned} 4\pi\,p'_L(\mathbf{x},t) &= \frac{1}{c}\int_{f=0}\left[\frac{\dot{L}_r}{r\,(1-M_r)^2}\right]_{\text{ret}} \mathrm{d}S \\ &+ \int_{f=0}\left[\frac{L_r - L_M}{r^2\,(1-M_r)^2}\right]_{\text{ret}} \mathrm{d}S \\ &+ \frac{1}{c}\int_{f=0}\left[\frac{L_r\left(r\dot{M}_r + c\left(M_r - M^2\right)\right)}{r^2\,(1-M_r)^3}\right]_{\text{ret}} \mathrm{d}S \end{aligned} \tag{6.32}$$

where

$$L_r = L_i\,\hat{r}_i\,, \qquad \dot{L}_r = \dot{L}_i\,\hat{r}_i\,, \qquad L_M = L_i\,M_i \tag{6.33}$$

[1]Subscripts refer to the flow quantity that generates the pressure perturbation, that is, Q, L_i and T_{ij} for the thickness, loading noise and quadrupole noise, respectively.

Quadrupole noise

$$4\pi\, p'_T(\mathbf{x},t) = \int_{f>0} \left[\frac{K_1}{c^2 r} + \frac{K_2}{c r^2} + \frac{K_3}{r^3}\right]_{\text{ret}} \mathrm{d}V \tag{6.34}$$

with

$$\begin{aligned}
K_1 &= \frac{\ddot{T}_{rr}}{(1-M_r)^3} + \frac{\ddot{M}_r T_{rr} + 3\dot{M}_r \dot{T}_{rr}}{(1-M_r)^4} + \frac{3\dot{M}_r^2 T_{rr}}{(1-M_r)^5} \\
K_2 &= \frac{-\dot{T}_{ii}}{(1-M_r)^2} - \frac{4\dot{T}_{Mr} + 2T_{\dot{M}r} + \dot{M}_r T_{ii}}{(1-M_r)^3} \\
&+ \frac{3\left\{\left(1-M^2\right)\dot{T}_{rr} - 2\dot{M}_r T_{Mr} - M_i \dot{M}_i T_{rr}\right\}}{(1-M_r)^4} + \frac{6\dot{M}_r\left(1-M^2\right)T_{rr}}{(1-M_r)^5} \\
K_3 &= \frac{2T_{MM} - \left(1-M^2\right)T_{ii}}{(1-M_r)^3} - \frac{6\left(1-M^2\right)T_{Mr}}{(1-M_r)^4} + \frac{3\left(1-M^2\right)^2 T_{rr}}{(1-M_r)^5}
\end{aligned} \tag{6.35}$$

where $T_{rr} = T_{ij}\,\hat{r}_i\,\hat{r}_j$ is the double contraction of the Lighthill's stress tensor T_{ij}, and the other terms are defined as

$$\begin{aligned}
&T_{MM} = T_{ij}\,M_i\,M_j\,, \qquad T_{Mr} = T_{ij}\,M_i\,\hat{r}_j\,, \qquad T_{\dot{M}r} = T_{ij}\,\dot{M}_i\,\hat{r}_j \\
&\dot{T}_{Mr} = \dot{T}_{ij}\,M_i\,\hat{r}_j\,, \qquad \dot{T}_{rr} = \dot{T}_{ij}\,\hat{r}_i\,\hat{r}_j\,, \qquad \ddot{T}_{rr} = \ddot{T}_{ij}\,\hat{r}_i\,\hat{r}_j
\end{aligned} \tag{6.36}$$

In the above expressions $\mathbf{M}$ is the Mach number vector of a volume source fixed in the body reference frame.

The quadrupole noise expression (6.34) is similar to that obtained by Brentner [40]. However, in Brentner's paper the volume integral in equation (6.34) is carried out in two stages. First, an integration of the aerodynamic quantity T_{ij} in the direction normal to the rotor disk is performed, providing the quantity

$$Q_{ij} = \int_{f>0} T_{ij}\,\mathrm{d}z \tag{6.37}$$

which does not depend on the observation point. Second, an integration on the rotor disk is performed by using the same expressions as in (6.35), but with Q_{ij} at the place of T_{ij}. This approximation is justified by the fact that the helicopter transonic HSI-noise is maximum in the plane of the rotor. In this case, as shown in chapter 7 of part II, Brenner's procedure is nearly exact.

A final modification consists in extending the integral formulation to an observer moving at a constant velocity $c\mathbf{M}_o$. This can be done by interpreting the time derivative of the thickness noise in equation (6.24) as a Lagrangian derivative. The other time derivatives, in fact, have been obtained by using the relation (6.25) where derivatives are taken at fixed observer position. It thus results that

$$4\pi\, p'_Q(\mathbf{x},t) \;=\; \frac{\partial}{\partial t}\int_{f=0}\left[\frac{\rho_0\,U_n}{r\,(1-M_r)}\right]_{\text{ret}} \mathrm{d}S + c\,M_{o\,i}\,\frac{\partial}{\partial x_i}\int_{f=0}\left[\frac{\rho_0\,U_n}{r\,(1-M_r)}\right]_{\text{ret}} \mathrm{d}S$$

Proceeding as in equation (6.23) to translate the space derivatives into time derivatives, yields

$$\begin{aligned}
4\pi\, p'_Q(\mathbf{x},t) \;=&\; \frac{\partial}{\partial t}\int_{f=0}\left[\frac{\rho_0\,U_n}{r\,(1-M_r)}\right]_{\text{ret}} \mathrm{d}S \\
-&\; \frac{\partial}{\partial t}\int_{f=0}\left[\frac{\rho_0\,U_n\,M_{o\,r}}{r\,(1-M_r)}\right]_{\text{ret}} \mathrm{d}S - c\int_{f=0}\left[\frac{\rho_0\,U_n\,M_{o\,r}}{r^2\,(1-M_r)}\right]_{\text{ret}} \mathrm{d}S
\end{aligned} \tag{6.38}$$

where $M_{or} = M_{oi}\,\hat{r}_i$ is the observer Mach number vector in the radiation direction. Finally, moving the time derivative inside the integral, yields

Thickness noise for a moving observer

$$
\begin{aligned}
4\pi p'_Q(\mathbf{x},t) &= \int_{f=0} \left[\frac{\rho_0\left(\dot{U}_n + U_{\dot{n}}\right)}{r\,(1-M_r)^2}\right]_{\text{ret}} \mathrm{d}S + \int_{f=0} \left[\frac{\rho_0\, U_n \left(r\dot{M}_r + c\left(M_r - M^2\right)\right)}{r^2\,(1-M_r)^3}\right]_{\text{ret}} \mathrm{d}S \\
&- \int_{f=0} \left[M_{or}\,\frac{\rho_0\left(\dot{U}_n + U_{\dot{n}}\right)}{r\,(1-M_r)^2}\right]_{\text{ret}} \mathrm{d}S - \int_{f=0} \left[M_{or}\,\frac{\rho_0\,\dot{M}_r\,U_n}{r\,(1-M_r)^3}\right]_{\text{ret}} \mathrm{d}S \\
&- \int_{f=0} \left[\frac{\rho_0\, c\, \left\{2\,M_{or}\,M_r - M_{or}\,M^2 - M_{or}\,M_r\,(1-M_r) - M_{or}\,M_r^2\right\} U_n}{r^2\,(1-M_r)^3}\right]_{\text{ret}} \mathrm{d}S \\
&- \int_{f=0} \left[\frac{M_{or}\,\rho_0\, c\, U_n}{r^2\,(1-M_r)}\right]_{\text{ret}} \mathrm{d}S
\end{aligned}
\tag{6.39}
$$

where $[\ldots]_{\text{ret}}$ denotes evaluation at the retarded time

$$
\tau^* = t - \frac{|\mathbf{x}(t) - \mathbf{y}(\tau^*)|}{c}
\tag{6.40}
$$

6.2.3.1 Non-dimensionalized FW-H Integral Equation

The formulation coded in *Advantia* is a non-dimensionalized form of equations (6.39), (6.32) and (6.34). In view of interfacing to a finite volume CFD code, the flow field is expressed in conservative variables (ρ, ρu_i, ρE,), where E is the specific total internal energy. Furthermore, since CFD solutions are commonly computed in a body reference frame, the flow velocity $\mathbf{u}$ is deprived of the velocity $\mathbf{v}$ of the control surface.

Thus, introducing a reference length l_{ref}, a reference velocity U_{ref}, a reference time $l_{\text{ref}}/U_{\text{ref}}$ and a reference dynamic pressure $p_d = \rho_0 U_{\text{ref}}^2/2$, the following non-dimensionalized expressions can be obtained (see appendix 6 B)

$$
\begin{aligned}
\frac{2\pi}{p_d} p'_Q(\mathbf{X},\theta) &= \int_{f=0} \left[\frac{\dot{V}_i\,\hat{n}_i + \dot{q}_i\,\hat{n}_i + (V_i + q_i)\,\dot{\hat{n}}_i}{R\,(1-M_r)^2} + \frac{(V_n + q_n)\left\{R\,\dot{M}_r + \frac{M_r - M^2}{M_{\text{ref}}}\right\}}{R^2\,(1-M_r)^3}\right]_{\text{ret}} \mathrm{d}S \\
&- \int_{f=0} \left[M_{or}\,\frac{\dot{V}_i\,\hat{n}_i + \dot{q}_i\,\hat{n}_i + (V_i + q_i)\,\dot{\hat{n}}_i}{R\,(1-M_r)^2}\right]_{\text{ret}} \mathrm{d}S \\
&- \int_{f=0} \left[\frac{M_{or}\,\dot{M}_r\,(V_i + q_i)\,\hat{n}_i}{R\,(1-M_r)^3}\right]_{\text{ret}} \mathrm{d}S \\
&- \int_{f=0} \left[\frac{\left\{2\,M_{or}\,M_r - M_{or}\,M^2 - M_{or}\,M_r\,(1-M_r) - M_{or}\,M_r^2\right\}(V_i + q_i)\,\hat{n}_i}{M_{\text{ref}}\,R^2\,(1-M_r)^3}\right]_{\text{ret}} \mathrm{d}S \\
&- \int_{f=0} \left[\frac{(V_i + q_i)\,\hat{n}_i\,M_{or}}{M_{\text{ref}}\,R^2\,(1-M_r)}\right]_{\text{ret}} \mathrm{d}S
\end{aligned}
\tag{6.41}
$$

$$
\begin{aligned}
\frac{2\pi}{p_d} p'_L(\mathbf{X},\theta) &= \int_{f=0} \left[\frac{M_{\text{ref}}\,\chi_r}{R\,(1-M_r)^2}\right]_{\text{ret}} \mathrm{d}S + \int_{f=0} \left[\frac{\lambda_r - \lambda_M}{R^2\,(1-M_r)^2}\right]_{\text{ret}} \mathrm{d}S \\
&+ \int_{f=0} \left[\frac{M_{\text{ref}}\,\lambda_r\left\{R\,\dot{M}_r + \frac{M_r - M^2}{M_{\text{ref}}}\right\}}{R^2\,(1-M_r)^3}\right]_{\text{ret}} \mathrm{d}S
\end{aligned}
\tag{6.42}
$$

$$\frac{2\pi}{p_d} p'_T(\mathbf{X},\theta) = \int_{f>0} \left[M_{\text{ref}}^2 \frac{K_1}{R} + M_{\text{ref}} \frac{K_2}{R^2} + \frac{K_3}{R^3} \right]_{\text{ret}} \mathrm{d}V \quad \text{with} \tag{6.43}$$

$$\begin{aligned}
K_1 &= \frac{\ddot{\Psi}_{rr}}{(1-M_r)^3} + \frac{\ddot{M}_r \Psi_{rr} + 3\dot{M}_r \dot{\Psi}_{rr}}{(1-M_r)^4} + \frac{3\dot{M}_r^2 \Psi_{rr}}{(1-M_r)^5} \\
K_2 &= \frac{-\dot{\Psi}_{ii}}{(1-M_r)^2} - \frac{4\dot{\Psi}_{Mr} + 2\Psi_{\dot{M}r} + \dot{M}_r \Psi_{ii}}{(1-M_r)^3} \\
&+ \frac{3\left\{ \left(1-M^2\right) \dot{\Psi}_{rr} - 2\dot{M}_r \Psi_{Mr} - M_i \dot{M}_i \Psi_{rr} \right\}}{(1-M_r)^4} + \frac{6\dot{M}_r \left(1-M^2\right) \Psi_{rr}}{(1-M_r)^5} \\
K_3 &= \frac{2\Psi_{MM} - \left(1-M^2\right) \Psi_{ii}}{(1-M_r)^3} - \frac{6\left(1-M^2\right) \Psi_{Mr}}{(1-M_r)^4} + \frac{3\left(1-M^2\right)^2 \Psi_{rr}}{(1-M_r)^5}
\end{aligned} \tag{6.44}$$

where square brackets enclose quantities evaluated at the retarded time θ_{ret} obtained from the dimensionless retarded time equation

$$\theta_{\text{ret}} = \theta - (\mathbf{X}(\theta) - \mathbf{Y}(\theta_{\text{ret}}))\, M_{\text{ref}} \tag{6.45}$$

In this expression the current time θ is the observer time, whereas θ_{ret} is the retarded source time.

6.2.4 The Advanced Time Formulation

The retarded time approach consists in evaluating the signal received at a given time[2] t through a summation of all the disturbances reaching the observer at the same time t. Depending on the source location in the integration domain and the kinematics of both the observer and the integration domain, these disturbances are emitted at different retarded times and cover different distances before to reach the observation point.

In this chapter we propose an advanced time approach. This merely consists in using a retarded time approach, but from the point of view of the source. Therefore, at a given time[3] the contributions from the integration domain are calculated, based on the current aerodynamic data and the current kinematics of the integration domain. At each computational time and for each source element, the time at which the corresponding disturbance will reach the observer is calculated and is referred to as *advanced time*. The observer location at the advanced time is used to calculate the relative position between the observer and a point source. The signal is finally re-composed in the observer time domain through a summation over all the computed contributions.

Let us consider the retarded time equation

$$\tau_{\text{ret}} = t - \frac{|\mathbf{x}(t) - \mathbf{y}(\tau_{\text{ret}})|}{c} \tag{6.46}$$

At an observer time $t + \mathcal{T}$ this yields

$$\tau'_{\text{ret}} = t + \mathcal{T} - \frac{|\mathbf{x}(t+\mathcal{T}) - \mathbf{y}(\tau'_{\text{ret}})|}{c} \tag{6.47}$$

Thus, setting $\tau'_{\text{ret}} \equiv t$ leads to

$$\mathcal{T} = \frac{|\mathbf{x}(t+\mathcal{T}) - \mathbf{y}(t)|}{c} \tag{6.48}$$

[2]In a retarded time approach the computational time is the reception time.

[3]In an advanced time approach the computational time is the emission time.

The quantity $t + \mathcal{T}$ is the time at which a disturbance emitted by a source element $\mathbf{y}$ at the time t will reach the observer $\mathbf{x}$. Thus, it is interpreted as the advanced time

$$t_{\text{adv}} = t + \mathcal{T} \tag{6.49}$$

Let us suppose that the observer moves at the constant velocity $c\mathbf{M}_o$. Equation (6.48) can be solved in $\mathcal{T}$, providing

$$\begin{aligned} \mathcal{T}^{\pm} &= \frac{r_i M_{oi} \pm \sqrt{(r_i M_{oi})^2 + r^2(1 - M_o^2)}}{c(1 - M_o^2)} \\ &= \frac{r}{c}\left\{\frac{M_{or} \pm \sqrt{M_{or}^2 + 1 - M_o^2}}{1 - M_o^2}\right\} \end{aligned} \tag{6.50}$$

where $r_i = x_i(t) - y_i(t)$ is the radiation vector and $M_{or} = \hat{r}_i M_{oi}$ is the observer Mach number vector in the radiation direction. Since a signal cannot be received before it is emitted, the quantity $\mathcal{T}$ must be positive. Notice that the $\mathcal{T}$ depends only on the observer velocity and not on the source velocity. The following cases can be distinguished:

a) stationary observer: $M_o = 0$. Only the solution $\mathcal{T}^+ = r/c$ is a physical solution.

b) Observer in subsonic motion: $M_o < 1$

$$M_{or} \pm \sqrt{M_{or}^2 + \alpha^2} > 0 \tag{6.51}$$

with $\alpha^2 = 1 - M_o^2$. Hence, only the solution $\mathcal{T}^+$ is a physical solution.

c) Observer in supersonic motion: $M_o > 1$

$$M_{or} \pm \sqrt{M_{or}^2 - \alpha^2} < 0 \tag{6.52}$$

with $\alpha^2 = -1 + M_o^2$. Hence,

1. observer moving far away from the source: $M_{or} > 0$. Both solutions $\mathcal{T}^{\pm}$ do not match the physical condition $\mathcal{T} > 0$.
2. observer moving towards the source: $M_{or} < 0$. Both solutions $\mathcal{T}^{\pm}$ are physical solutions, provided that $M_{or} < -\sqrt{M_o^2 - 1}$.

In the present study we assume a subsonic observer velocity. Thus, only the solution $\mathcal{T}^+$ is considered and the advanced time is given by

$$t_{\text{adv}} = t + \frac{r(t)}{c}\left\{\frac{M_{or}(t) + \sqrt{M_{or}^2(t) + 1 - M_o^2}}{1 - M_o^2}\right\} \tag{6.53}$$

It is interesting to notice that a source time t corresponds only to one value of the advanced time t_{adv}. This happens for any velocity of the source. Furthermore, the advanced time expression is given in an explicit form.

The implementation of the advanced time formulation does not require a modification of the source terms in the integrals (6.41), (6.42) and (6.43). However, difficulties may arise in the reconstruction of the signal. Due to the Döppler effect, in fact, an equally spaced discretization of the source time domain does not correspond to an equally spaced discretization of the observer time domain. This can be understood by taking the time derivative of expression (6.53), i.e.

$$\frac{\mathrm{d}t_{\text{adv}}}{\mathrm{d}t} = 1 + \frac{M_i - M_{oi}}{1 - M_o^2}\left\{M_{oi} + \frac{M_{or} M_{oi} + (1 - M_o^2)\,\hat{r}_i}{\sqrt{M_{or}^2 + 1 - M_o^2}}\right\} \tag{6.54}$$

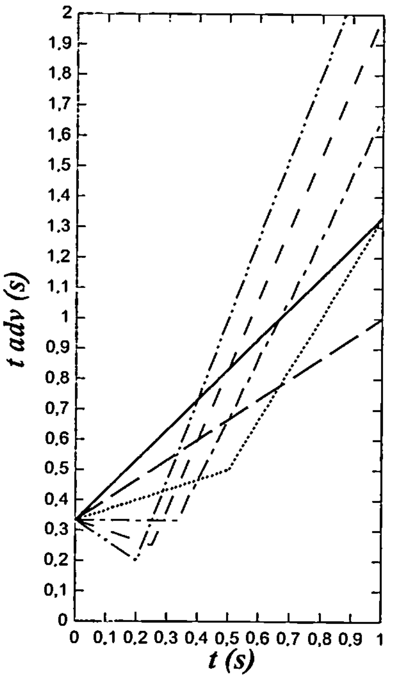

FIGURE 6.2: Advanced time *versus* current time for a source in constant motion at different Mach numbers in the direction of a fixed observer. The source initial distance from the observer is $r_o = 100\,\mathrm{m}$ and the sound speed is $c_o = 300\,\mathrm{m/s}$. Source Mach numbers: —— $M_o = 0$, — — $M_o = 0.33$, - - - - $M_o = 0.66$, - - - $M_o = 1$, - - - $M_o = 1.33$, - - - - $M_o = 1.67$.

where M_i denotes the source Mach number. Considering, for simplicity, a fixed observer position yields

$$\frac{\mathrm{d}t_{\mathrm{adv}}}{\mathrm{d}t} = 1 - M_r \tag{6.55}$$

and in discretized form

$$t^{j+1}_{\mathrm{adv}} = t^{j}_{\mathrm{adv}} + \left(1 - M^j_r\right) \Delta t \tag{6.56}$$

where Δt is the computational time-step. In Fig.6.2 the advanced time is plotted for a fixed observer and a source moving at different velocities v_o along a rectilinear trajectory. The source intercepts the observation point at $t_o = r_o/v_o$, r_o being the initial distance of the source. For $t < t_o$ and subsonic source velocities the curves have positive slopes, with values $0 < 1 - M_r \leq 1$. This situation corresponds to a contraction of the advanced time scale. For $t < t_o$ and supersonic source velocities the curves have negative slopes. Thus, signals emitted before are detected after. Finally, for $t > t_o$ the curves have positive slopes, with values $1 - M_r > 1$. This situation corresponds to a dilatation of the advanced time scale. When the computed disturbances are sampled on an equally spaced advanced time domain[4], the following situations can take place:

1. only one contribution p^j_i from the source element S_i falls in the interval $[t^j, t^{j+1}]_{\mathrm{adv}}$;
2. no contribution from the source element S_i is projected in the interval $[t^j, t^{j+1}]_{\mathrm{adv}}$;
3. more than one contribution $\left(p^j_i\right)_n$ from the source element S_i fall in the interval $[t^j, t^{j+1}]_{\mathrm{adv}}$

Since the Döppler factor is already accounted for in the source terms, contributions $\left(p^j_i\right)_n$ must not be added, but used to determine a suitable contribution p^j_i. A summation over all the source elements

[4]The same discretization used in the source computation is used in the advanced time domain.

must be made as a final step, namely $p^j = \sum_i p_i^j$, providing the pressure value at the advanced time $j\Delta t$. The procedure used in this work to build-on the pressure signal in the advanced time domain is described in appendix 6 C. It is essentially based on a linear interpolation. Although more accurate schemes can be implemented, the one herein proposed is a good compromise between accuracy and simplicity.

6.3 Numerical Assessment of *Advantia*

In this section we describe a numerical assessment of the FW-H analogy formulation implemented in the rotor noise predictor code *Advantia*.

The quadrupole contribution can be neglected at low Mach numbers. Thus, for the purposes of the present study, only the thickness and loading noise contributions, as defined in equations (6.41) and (6.42), respectively, are considered.

Advantia is a three-dimensional code in which the integral formulation is implemented by means of a first order isoparametric description of the aerodynamic data and of a Gaussian quadrature on both surface and volume elements. In the present work the FW-H acoustic analogy is applied to the circular cylinder flow in chapter 7 and to the rod-airfoil configuration in chapter 8. In both cases a two-dimensional aerodynamic field is computed and the three-dimensional aerodynamic field necessary for the acoustic prediction is recovered by a spanwise repetition of the two-dimensional solution. In order to validate this procedure, tests involving two-dimensional geometries are first discussed. Later on, a three-dimensional assessment is performed in order to validate the advanced time formulation in the case of a complex relative motion between the observer and the integration surface. The assessment strategy is the following: first, the far field radiated by a set of elementary acoustic sources is obtained directly from analytical expressions and is referred to as *analytical solution*; second, the analytical solution upon a control surface is propagated into the far field by means of the analogy formulation and is referred to as *numerical solution*; third, the numerical solution is compared to the analytical solution. Monopoles and point forces are used as elementary acoustic sources. These are kept in motion in the three-dimensional tests. A two-dimensional scattering problem is also examined, whose analytical solution is based on a series expansion.

The assessment procedure described in this chapter allows to check the linear contributions of the FW-H formulation. This is because we use analytical solutions of the standard wave equation. In chapter 7, *Advantia* will be used to predict the aerodynamic sound from an isolated rod. This configuration constitutes an aerodynamic benchmark of the FW-H formulation.

6.3.1 Two-dimensional Tests

In this section we assess a two-dimensional employment of *Advantia* by considering the following test cases:

1. the scattering of a plane wave by a rigid cylinder (see Fig.6.3(a));

2. the radiation from a pair of cylindrical monopoles (see Fig.6.3(b)).

6.3.1.1 Test 1

Consider a plane acoustic wave of wavenumber k traveling in a direction x perpendicular to the axis of a rigid cylinder of diameter D, as sketched in Fig.6.3(a). The incident pressure is given by $p_i = P \exp\{\mathrm{i}\, k\,(x - c\,t)\}$ and the pressure of the scattered wave at large distance r from the cylinder is (see

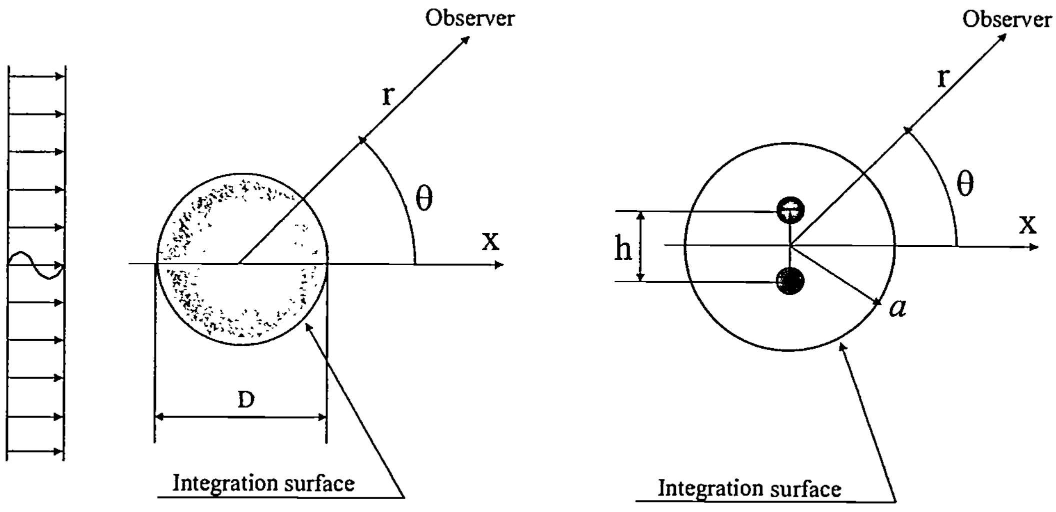

a) Test 1. b) Test 2.

FIGURE 6.3: 2D test cases scheme.

Ref.[47])

$$\begin{aligned} &p_s(r,\theta,t) \simeq -P\sqrt{\frac{D}{\pi r}}\psi_s(\theta)\exp\{\mathrm{i}\,k\,(r-c\,t)\} \quad \text{with} \\ &\psi_s(\theta) = \sqrt{\frac{2}{k\,D}}\sum_{m=0}^{\infty}\varepsilon_m \sin(\gamma_m)\exp(-\mathrm{i}\;\gamma_m)\cos(m\,\theta) \quad \text{and} \\ &\varepsilon_0 = 1, \quad \varepsilon_m = 2 \quad \text{for} \quad m > 0 \end{aligned} \tag{6.57}$$

The total pressure on the surface of the cylinder is given by

$$p_w(\theta,t) = \frac{8P}{\pi kD}\exp(-\mathrm{i}\,k\,c\,t)\sum_{m=0}^{\infty}\frac{\cos(m\theta)}{E_m}\exp\Big\{\mathrm{i}\,\Big(\frac{\pi m}{2}-\gamma_m\Big)\Big\} \tag{6.58}$$

The phase angles γ_m and the amplitudes E_m are complex combinations of Bessel functions. For $k\,D = 6$ they take the values listed in Table 6.1. Only the first nine values are considered, provided that, for $m > 9$, the phase angles γ_m and the amplitudes E_m do not give significative contributions to the summations in equations (6.57) and (6.58), respectively.

The wall pressure p_w is introduced into equation (6.42) as input data for the analogy approach. Then a numerical integration is performed upon a long cylinder of span b ($k\,b = 100$), with a spanwise discretization of about 10 segments per wavelength. The far field numerical solution ($kr = 300$) is compared to the analytical solution in equation (6.57). In Fig.6.4(a) the scattered acoustic intensity, obtained for different numbers of circumferential discretization segments, is plotted. Overlapping of the numerical solutions shows that the deviation from the analytical solution is due to the approximated form of equation (6.57). The maximum relative error of 0.057 occurs at $\theta = 0^o$. The time trace of the scattered acoustic pressure at $\theta = 0^o$ is plotted in Fig.6.4(b).

TABLE 6.1: Phase angles and amplitudes for scattering and radiation from a cylinder: $kD = 6$

m	$\gamma_m(deg)$	E_m	m	$\gamma_m(deg)$	E_m
0	133.76	0.9389	5	-1.530	2.2610
1	54.240	0.4597	6	-0.130	8.9670
2	-1.990	0.4319	7	-0.010	40.860
3	-25.09	0.4175	8	-0.000	212.60
4	-11.01	0.6965	9	-0.000	1249

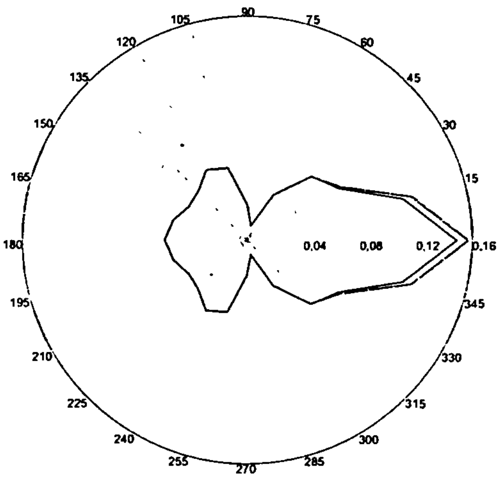

a) Directivity pattern of the scattered acoustic intensity.

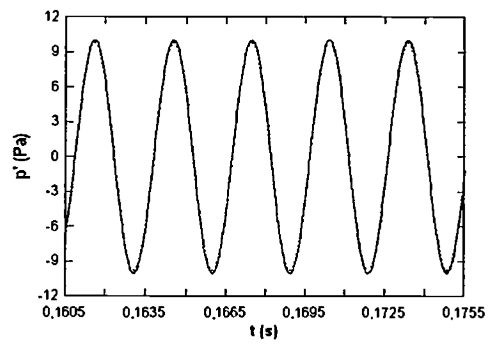

b) Time trace of the scattered acoustic pressure at an observation angle $\theta = 0°$.

FIGURE 6.4: Acoustic validation of FW-H formulation. Scattering of a plane wave by a cylinder: $kD = 6$, $kr = 300$. —— Analytical solution, — — numerical solution (5 points per wavelength), - - - - numerical solution (7 points per wavelength), – - – numerical solution (10 points per wavelength).

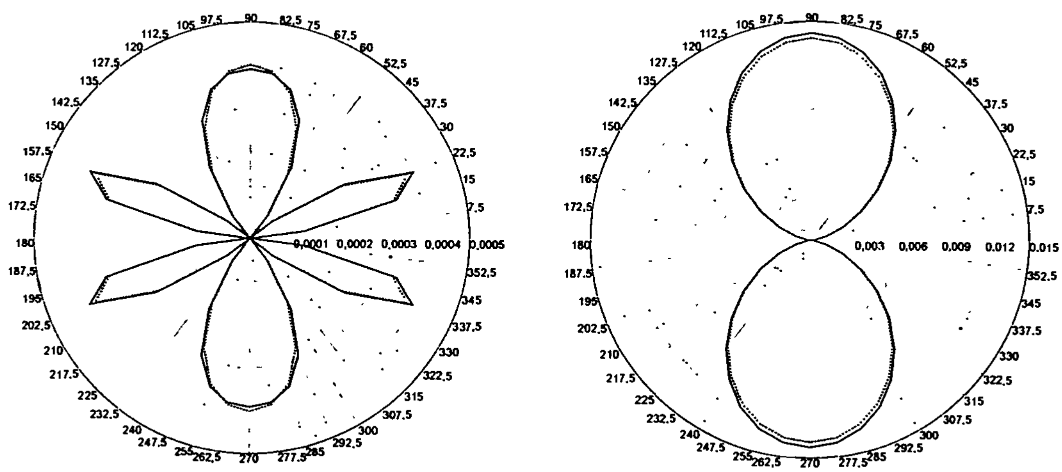

a) Directivity pattern of the radiated acoustic intensity: $kh = 8.976$, $kr = 125.6$.

b) Directivity pattern of the radiated acoustic intensity: $kh = 1.257$, $kr = 125.6$.

FIGURE 6.5: Acoustic validation of FW-H formulation. Radiation from a pair of non-compact monopoles at distance h. —— Analytical solution, - - - - numerical solution.

6.3.1.2 Test 2

The pressure and the radial velocity generated by a two-dimensional monopole source are[5] (see Ref.[47] (pp. 356-363))

$$p \simeq \rho_0 c \pi dU \sqrt{\frac{k}{8\pi r}} \exp\left\{ \mathrm{i}\left[k\left(r - ct\right)\right] - \frac{\pi}{4} \right\} \tag{6.59}$$

$$u_r \simeq \pi dU \sqrt{\frac{k}{8\pi r}} \exp\left\{ \mathrm{i}\left[k\left(r - ct\right)\right] - \frac{\pi}{4} \right\} \tag{6.60}$$

Consider two monopoles ($k = 6.28\,\mathrm{m}^{-1}$, $kd = 6.28\,10^{-3}$ and $U = 1$ m/s) placed in $(0, \pm h/2)$ and pulsating with opposite phase (see Fig.6.3(b)). The pressure and velocity field induced on a long cylindrical surface ($kb = 100$) of radius a ($ka = 12.57$) and center in the origin are introduced into equations (6.41) and (6.42). The integration surface is discretized with about 5 and 10 segments per wavelength along the circumference and the span of the cylinder, respectively. The numerical solution at a distance r ($kr = 125.6$) is then compared to the analytical solution. The radiated acoustic intensity obtained for two values of h is plotted in Figs.6.5(a) and 6.5(b). The numerical and the analytical solutions agree fairly well. The maximum relative errors is 0.025 for $kh = 8.976$ and 0.024 for $kh = 1.257$.

[5] A two-dimensional monopole source can be modeled as an infinite-span compact cylinder ($k\,d \ll 1$) with cross-section pulsating at the velocity $v_r = U \exp(-\mathrm{i}\,kct)$ (k is the acoustic wavenumber and d is the cylinder diameter.)

6.3.2 Three-dimensional Tests

In this section we investigate the capability of *Advantia* in predicting the noise radiated by acoustic sources in complex subsonic motion. The following test cases are examined:

1. acoustic monopoles translating and rotating with respect to an observer which translates at a constant velocity, as sketched in Fig.6.6;

2. radial dipoles rotating and translating with respect to a fixed observer, as sketched in Fig.6.16;

3. axial dipoles rotating and translating with respect to a fixed observer, as sketched in Fig.6.23.

The first test case is performed in order to validate the penetrable surface formulation and the thickness noise extension to a moving observer. The second and the third test cases are performed in order to show the feasibility of an advanced time prediction of the noise from a high-speed rotor.

6.3.2.1 Test 1

Harmonic monopoles of equal amplitude $q = 0.1\,\mathrm{kg/s}$, phase and frequency f are located on the vertices of a regular polygon. These monopoles rotate around the axis of the polygon at the frequency f_2, and around a vertical axis at the frequency f_1. The source distances from these normal axes are h and a, respectively. The system translates at the velocity v_y and the observer translates at the velocity v_o. The monopoles are enclosed by a control spherical surface rotating around the vertical axis at the frequency f_1.

The sound radiated by a moving harmonic monopole and received by a moving observer is used as analytical solution, namely

$$p'(\mathrm{x},t) = \rho_0 \frac{\mathrm{D}}{\mathrm{D}t}\left[\frac{Q(t)}{4\pi\, r\,(1-M_r)}\right]_{\mathrm{ret}} \tag{6.61}$$

$$u_i'(\mathrm{x},t) = \frac{\partial}{\partial x_i}\left[\frac{Q(t)}{4\pi\, r\,(1-M_r)}\right]_{\mathrm{ret}} \tag{6.62}$$

where $\mathrm{D}/\mathrm{D}t$ denotes a convective time derivative (see Ref. [48], pp. 269-275). These expressions provide both the far field acoustic solution and the *aerodynamic* field on the integration surface[6]. The latter is defined in terms of the acoustic pressure p', its time derivative $\dot{p}$, the acoustic velocity u_i' and its time derivative $\dot{u}'_i$. These quantities are evaluated numerically through a retarded time approach.

Several cases are considered in order to check the following aspects of the formulation:

a) the advanced time approach,

b) the penetrable control surface formulation,

c) the moving observer extension of the thickness noise.

In the present work, no attempt has been made to characterize the numerical accuracy of the spatial discretization. The surface integration is performed upon a sphere of radius 0.5m, with a polar discretization of 24×24 elements. A Gaussian integration is performed by using 4 points on both quadrangular and triangular elements. A linear isoparametric interpolation is used to define the aerodynamic quantities at the collocation points.

Concerning the time discretization, 200 time-steps per acoustic period are initially used for different configurations. Later on, computations are performed for one configuration down to 20 time-steps per acoustic period.

TABLE 6.2: Test 1: geometrical and kinematic parameters. N is the number of acoustic monopoles; f is the acoustic frequency; f_1 and f_2 are the rotation frequency around the vertical and the horizontal axes, respectively; $\mathbf{v}_y$ is the forward velocity of the sources; $\mathbf{v}_o$ is the observer translation velocity; M_y is the maximum Mach number of the integration surface; M_o is the observer Mach number; Err_L denotes the relative L-error; Fig. indicates the label of the corresponding figure. All the quantities are expressed in SI units. Computations are performed with a time discretization of 200 time-steps per acoustic period.

	N	f	f_1	f_2	$\mathbf{v}_y$	$\mathbf{v}_o$	M_y	M_o	Err_L	Fig.
A	1	100	0	0	$(0,0,0)$	$(0,0,0)$	0	0	1.36E-2	6.7(a)
B	4	110	0	0	$(0,0,0)$	$(0,0,0)$	0	0	1.31E-2	6.7(b)
C	1	100	20	0	$(0,0,0)$	$(0,0,0)$	0	0	1.52E-2	6.8(a)
D	4	110	20	0	$(0,0,0)$	$(0,0,0)$	0	0	8.45E-3	6.8(b)
E	1	100	20	49	$(0,0,0)$	$(0,0,0)$	0	0	1.57E-3	6.9(a)
F	4	110	20	43	$(0,0,0)$	$(0,0,0)$	0	0	8.26E-3	6.9(b)
G	1	100	20	49	$(50,40,30)$	$(0,0,0)$	0.76	0	1.88E-2	6.10(a)
H	4	110	20	43	$(50,40,30)$	$(0,0,0)$	0.76	0	6.79E-3	6.10(b)
I	1	100	20	49	$(50,40,30)$	$(-10,-30,-50)$	0.76	0.17	3.34E-5	6.11(a)
J	4	110	20	43	$(50,40,30)$	$(-10,-30,-50)$	0.76	0.17	4.19E-3	6.11(b)
K	1	100	20	49	$(50,40,30)$	$(-20,-60,-100)$	0.76	0.35	2.60E-2	6.12(a)
L	4	110	20	43	$(50,40,30)$	$(-20,-60,-100)$	0.76	0.35	5.79E-4	6.12(b)
M	1	100	20	49	$(100,80,60)$	$(-10,-30,-50)$	0.97	0.17	5.40E-2	6.13(a)
N	4	110	20	43	$(100,80,60)$	$(-10,-30,-50)$	0.97	0.17	9.45E-2	6.13(b)

The observer initial position is the same for all the presented cases, say $\mathbf{x} = (10,10,10)$ m, as well as the rotation radiuses $a = 1$ m and $h = 0.1$ m. The remaining parameters are listed in Table 6.2.

In Figs. from 6.7 to 6.13 numerical results obtained with 200 time-steps per acoustic period are checked against the analytical solutions. The plots show that the agreement between the numerical and the analytical solutions is good for all the investigated configurations. The relative L-errors, say

$$\text{Err}_L = \frac{\max_j \left| p^j_{\text{num}} - p^j_{\text{teo}} \right|}{\max_j \left| p^j_{\text{teo}} \right|} \tag{6.63}$$

for the different configurations are listed in Table 6.2.

In Fig.6.14 the relative L_2-error for Case I, say

$$\text{Err}_{L2} = \frac{\sum_j \left(p^j_{\text{num}} - p^j_{\text{teo}} \right)^2}{\sum_j \left(p^j_{\text{teo}} \right)^2} \tag{6.64}$$

is plotted against the number of samples N_s per acoustic period, from $N_s = 20$ up to $N_s = 200$. The numerical solutions corresponding to three values of N_s are plotted in Fig.6.15. The acoustic signatures exhibit a significant phase error only for $N_s = 20$.

[6]The term aerodynamic is indeed extended to denote an acoustic field.

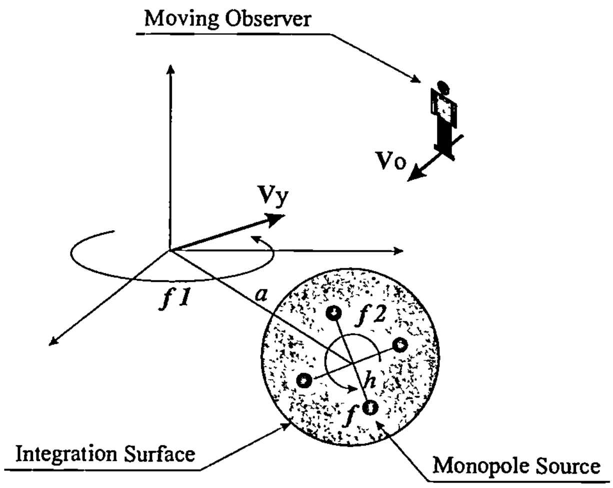

FIGURE 6.6: Scheme of Test 1. A set of equal monopoles are located on the vertices of a regular polygon. These monopoles rotate around the axis of the polygon at the frequency f_2, and around a vertical axis at the frequency f_1. These two axes of rotation are normal to each other. The system translates at the velocity $\mathbf{v}_y$ and the observer translates at the velocity $\mathbf{v}_o$. The surface integration is performed upon a sphere. It encloses the monopoles and rotates around the vertical axis at the frequency f_1.

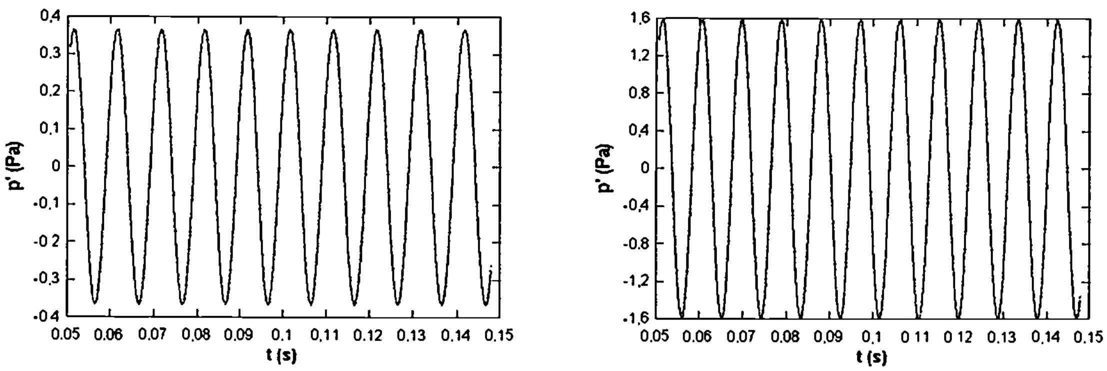

FIGURE 6.7: Test 1. Case A (left) and Case B (right). —— Analytical solution, - - - - Numerical solution.

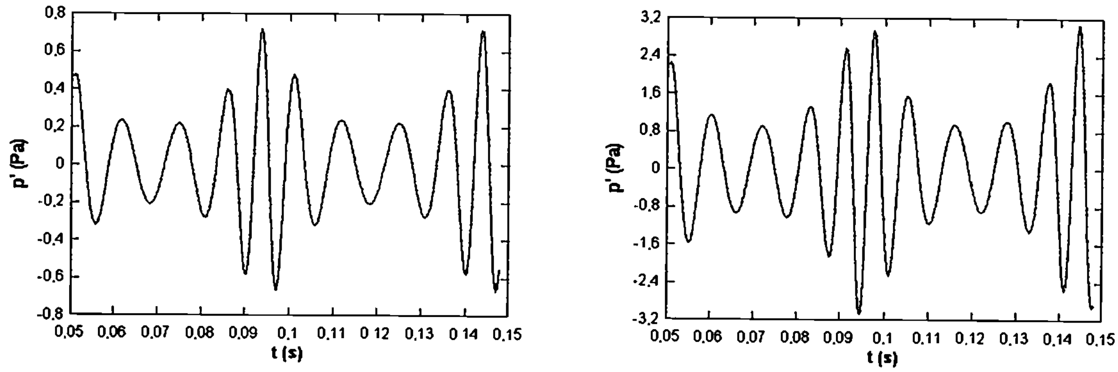

FIGURE 6.8: Test 1. Case C (left) and Case D (right). —— Analytical solution, - - - - Numerical solution.

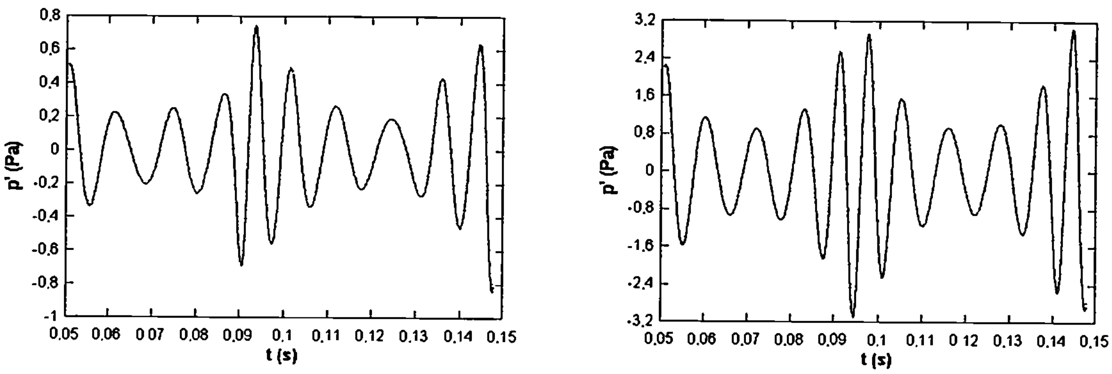

FIGURE 6.9: Test 1. Case E (left) and Case F (right). —— Analytical solution, - - - - Numerical solution.

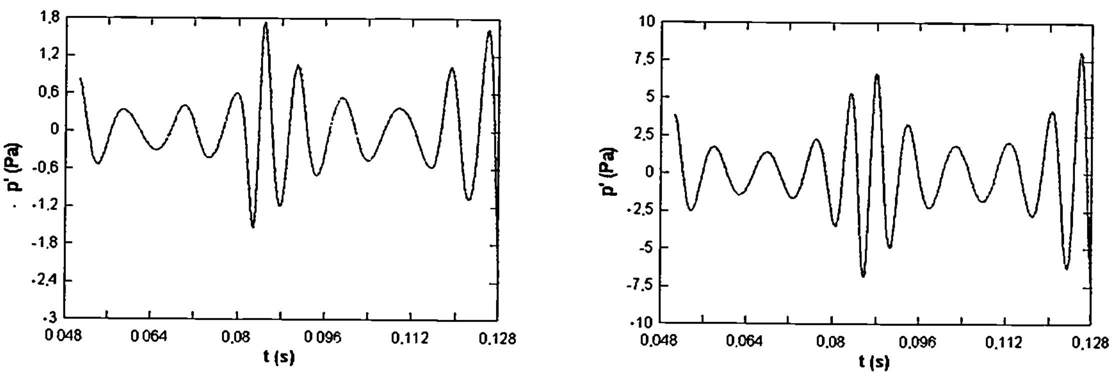

FIGURE 6.10: Test 1. Case G (left) and Case H (right). —— Analytical solution, - - - - Numerical solution.

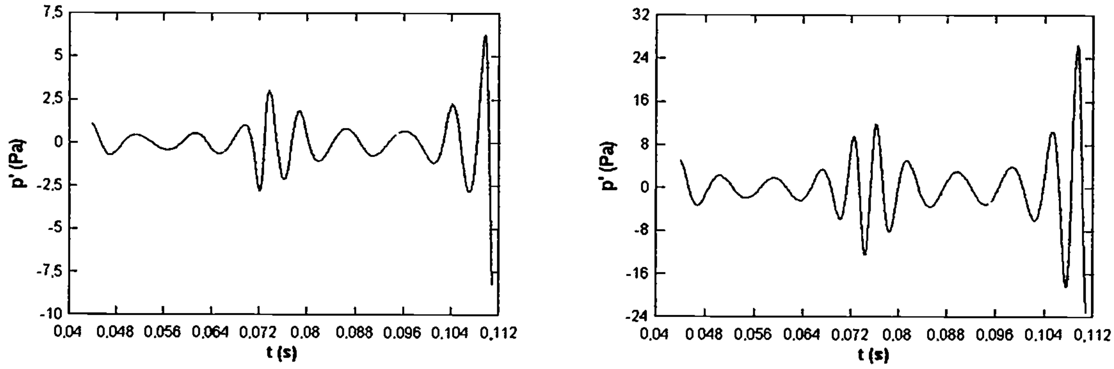

FIGURE 6.11: Test 1. Case I (left) and Case J (right). —— Analytical solution, - - - - Numerical solution.

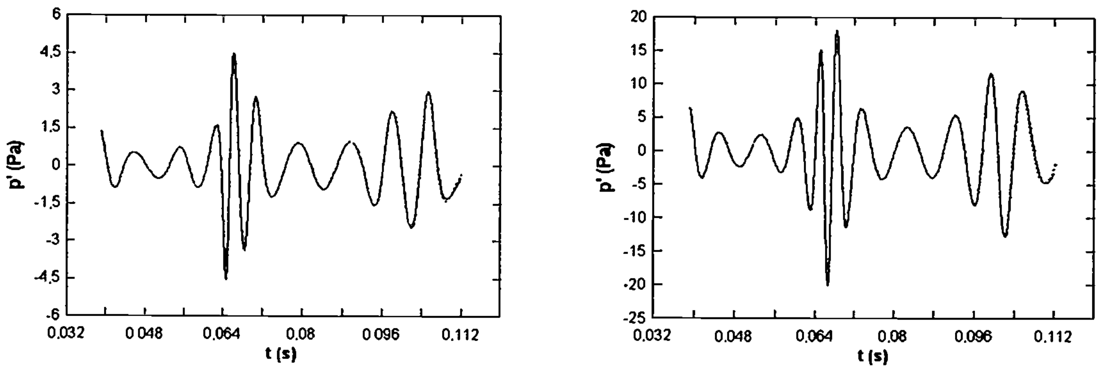

FIGURE 6.12: Test 1. Case K (left) and Case L (right). —— Analytical solution, - - - - Numerical solution.

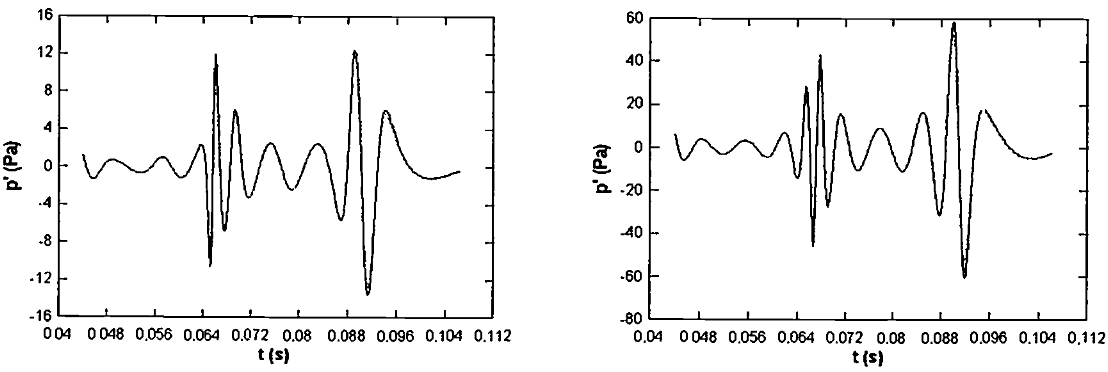

FIGURE 6.13: Test 1. Case M (left) and Case N (right).

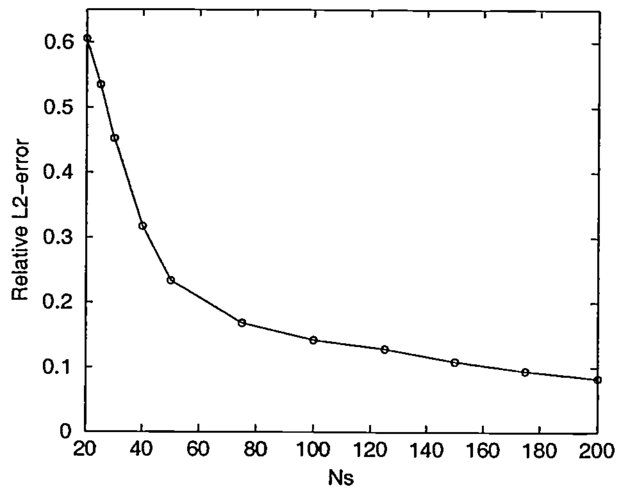

FIGURE 6.14: Test 1, Case I. Relative L_2-error *versus* the number of time-steps per acoustic period.

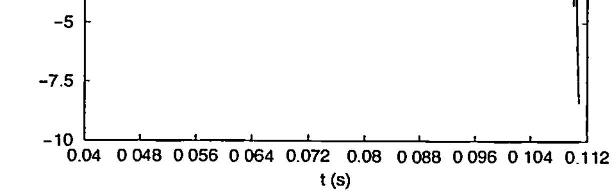

FIGURE 6.15: Test 1, Case I. Numerical solutions for three values of the number of samples N_s per acoustic period: —— $N_s = 200$, $\mathrm{Err}_{L2} = 8.24 \times 10^{-2}$; - - - - $N_s = 75$, $\mathrm{Err}_{L2} = 1.68 \times 10^{-1}$; — — $N_s = 20$, $\mathrm{Err}_{L2} = 6.05 \times 10^{-1}$.

6.3.2.2 Test 2

A radial compact dipole is described as a small disk with a pressure jump uniformly distributed upon its surface. One and three disks at a constant angle from each other are considered, rotating around a vertical axis at the frequency f_1. The system translates at the velocity $\mathbf{v}_y$, whereas the observer is fixed.

The sound radiated by a moving dipole is used as acoustic analytical solution (see Ref. [48], pp. 269-275), namely

$$p'(\mathbf{x},t) = \left[\frac{\mathbf{r}\cdot\dot{\mathbf{F}} - c\mathbf{M}\cdot\mathbf{F}}{4\pi\, c r^2\,(1-M_r)^2} + (\mathbf{r}\cdot\mathbf{F})\,\frac{\mathbf{r}\cdot\dot{\mathbf{M}} + c\left(1-M^2\right)}{4\pi\, c r^3\,(1-M_r)^3}\right]_{\text{ret}} \tag{6.65}$$

where $\mathbf{M}$ denotes the dipole Mach vector number and $\mathbf{F}$ is the unsteady force exerted on the fluid. Dots on quantities denote time derivatives.

Several cases are considered in order to check the feasibility of an advanced time prediction of the noise from a subsonic high-speed rotor. The rotation frequency is kept constant at the value $f_1 = 10$ Hz, as well as the observation point $\mathbf{x} = (5,4,3)$ m. Different Mach numbers are obtained by varying both the radius a and the forward velocity $\mathbf{v}_y$. A point force of modulus $F = 1000\,\mathrm{N}$ is introduced in the field through a pressure jump uniformly distributed on the surface of a small disk. This is obtained by flattening a sphere with a polar discretization of 5×5 elements[7]. One or three disks at a constant angle from each other are considered. The parameters for the different configurations are listed in Table 6.3.

Concerning the time discretization, 1000 time-steps per rotation period are initially used for different configurations. Later on, computations are performed for one configuration down to 100 time-steps per rotation period.

TABLE 6.3: Test 2: geometrical and kinematic parameters. N is the number of acoustic dipoles; a is the distance from the axis of rotation; $\mathbf{v}_y$ is the translation velocity of the sources; M_y is the maximum Mach number of the integration surface; Err_L denotes the relative L-error; Fig. indicates the label of the corresponding figure. All the quantities are expressed in SI units. Computations are performed with a time discretization of 1000 time-steps per rotation period.

	N	a	$\mathbf{v}_y$	M_y	Err_L	Fig.
A	1	1	$(0,0,0)$	0.18	7.10E-5	6.17(a)
B	3	1	$(0,0,0)$	0.18	1.17E-4	6.17(b)
C	1	3	$(50,50,50)$	0.81	6.49E-5	6.18(a)
D	3	3	$(50,50,50)$	0.81	2.59E-5	6.18(b)
E	1	5.4	$(0,0,0)$	0.998	1.03E-4	6.19(a)
F	3	5.4	$(0,0,0)$	0.998	1.25E-5	6.19(b)
G	1	2	$(100,100,100)$	0.88	7.35E-5	6.20(a)
H	3	2	$(100,100,100)$	0.88	1.24E-4	6.20(b)

In Figs. from 6.17 to 6.20 numerical results obtained with 1000 time-steps per rotation period are checked against analytical solutions. The plots show that, as in Test 1, the agreement between the numerical and the analytical solutions is good for all the investigated configurations. The relative L-errors, as defined in (6.63), for the different configurations are listed in Table 6.3.

[7] In this case the surface discretization has no influence on the accuracy of the solution. Simply, it provides a further check of the Gaussian integration procedure and other coded libraries.

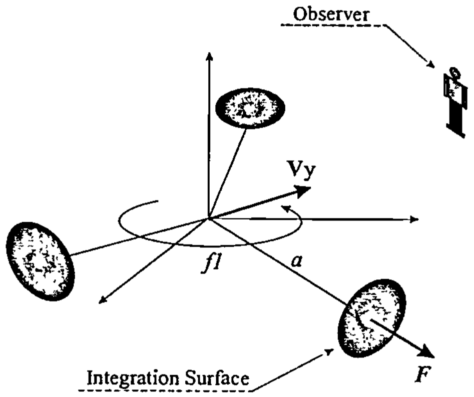

FIGURE 6.16: Scheme of Test 2. A radial compact dipole is described as a small disk with a pressure jump uniformly distributed upon its surface. One and three disks at a constant angle from each other are considered, rotating around a vertical axis at the frequency f_1. The system translates at the velocity $\mathbf{v}_y$, whereas the observer is fixed.

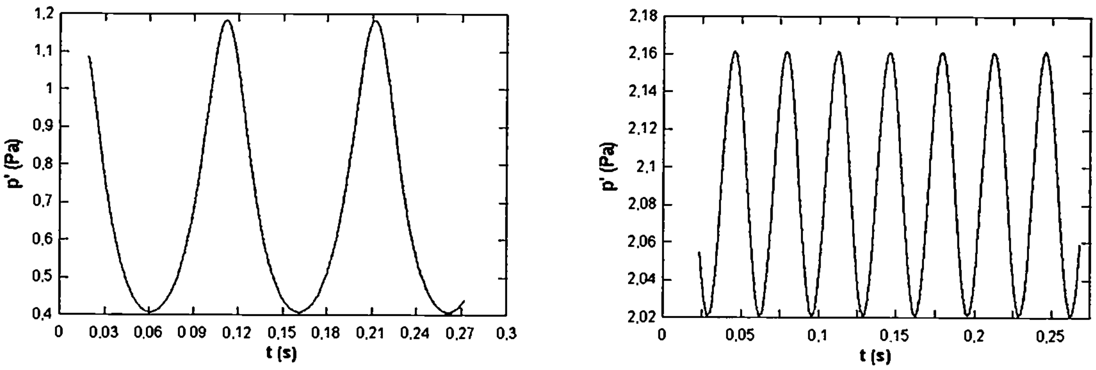

FIGURE 6.17: Test 2. Case A (left) and Case B (right). —— Analytical solution, - - - - Numerical solution.

In Fig.6.21 the relative L$_2$-error 6.64 for Case H is plotted against the number of samples N_s per rotation period, from $N_s = 100$ up to $N_s = 1000$. The numerical solutions corresponding to three values of N_s are plotted in Fig.6.22. The acoustic signatures show a significant phase error only for $N_s = 100$.

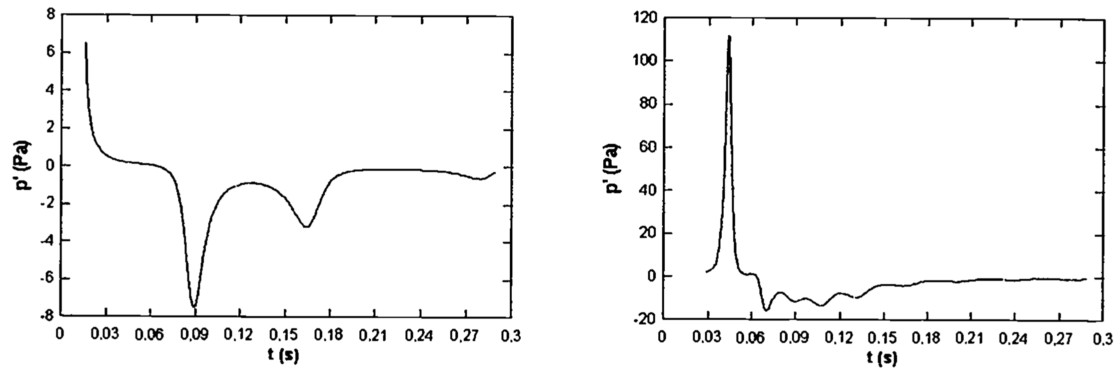

FIGURE 6.18: Test 2. Case C (left) and Case D (right). —— Analytical solution, - - - - Numerical solution.

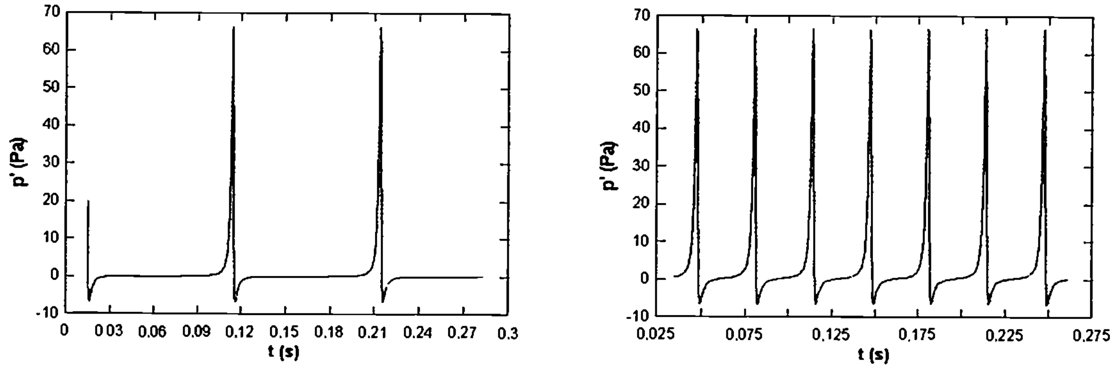

FIGURE 6.19: Test 2. Case E (left) and Case F (right). —— Analytical solution, - - - - Numerical solution.

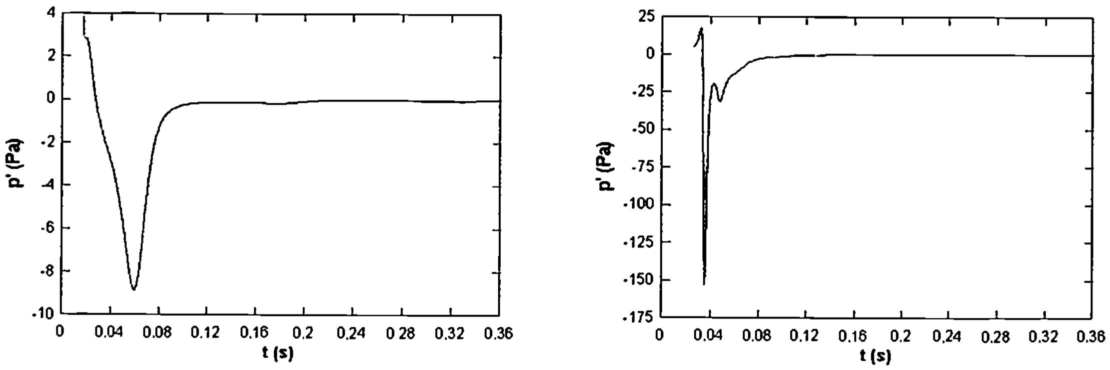

FIGURE 6.20: Test 2. Case G (left) and Case H (right). —— Analytical solution, - - - - Numerical solution.

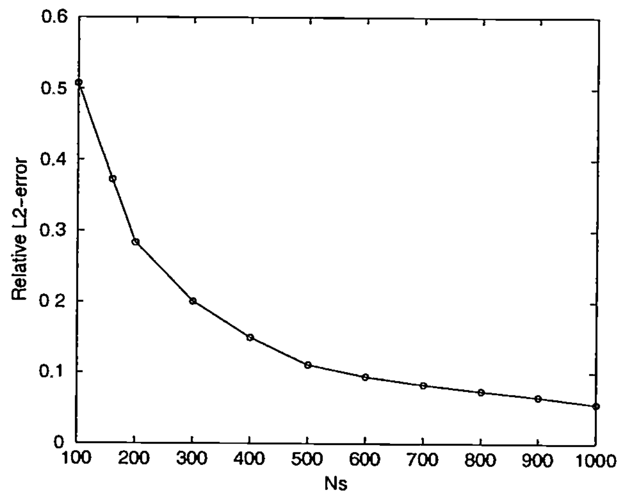

FIGURE 6.21: Test 2, Case H. Relative L2-error *versus* the number of time-steps per acoustic period.

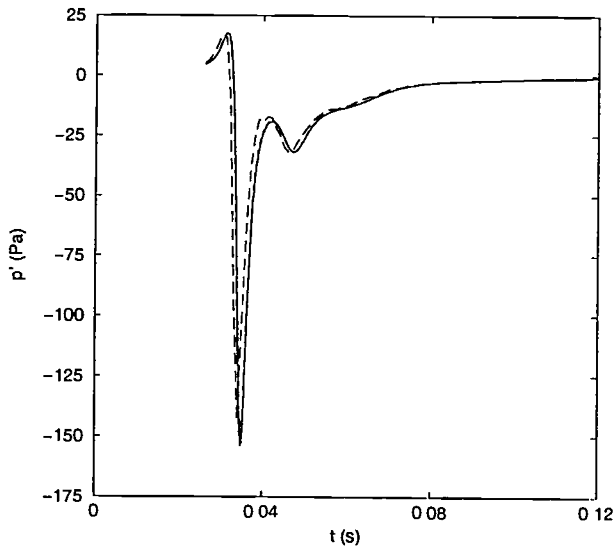

FIGURE 6.22: Test 2, Case H. Numerical solutions for three values of the number of samples N_s per rotation period: —— $N_s = 1000$, $\mathrm{Err}_{L2} = 5.56\times10^{-2}$; - - - - $N_s = 500$, $\mathrm{Err}_{L2} = 1.11\times10^{-1}$; — — $N_s = 100$, $\mathrm{Err}_{L2} = 5.07 \times 10^{-1}$.

6.3.2.3 Test 3

An axial compact dipole is described as a small disk with a pressure jump uniformly distributed upon its surface. Three and four disks at a constant angle from each other are considered, rotating around a vertical axis at the frequency f_1. The system translates at the velocity $\mathbf{v}_y$, whereas the observer is fixed. Equation (6.65) provides the acoustic analytical solution. In the present case the force has a constant direction, thus $\dot{\mathbf{F}} = 0$.

As in Test 2, several cases are considered in order to check the feasibility of an advanced time rotor-noise prediction. The rotation frequency is kept constant at the value $f_1 = 10$ Hz, as well as the observation point $\mathbf{x} = (5, 4, 3)$ m,. Different Mach numbers are obtained by varying both the radius a and the forward velocity $\mathbf{v}_y$. A point force of modulus $F = 1000\,\mathrm{N}$ is introduced in the field through a pressure jump uniformly distributed on the surface of a small disk. This is obtained by flattening a sphere composed of 5×6 elements. Three or four disks at a constant angle from each other are considered. The parameters for the different configurations are listed in Table 6.4.

Concerning the time discretization, 1600 time-steps per rotation period are initially used for different configurations. Later on, computations are performed for one configuration down to 160 time-steps per rotation period.

TABLE 6.4: Test 3: geometrical and kinematic parameters. N is the number of acoustic dipoles; a is the distance from the axis of rotation; $\mathbf{v}_y$ is the translation velocity of the sources; M_y is the maximum Mach number of the integration surface; Err_L denotes the relative L-error; Fig. indicates the label of the corresponding figure. All the quantities are expressed in SI units. Computations are performed with a time discretization of 1600 time-steps per rotation period.

	N	a	$\mathbf{v}_y$	M_y	Err_L	Fig.
A	3	1	$(0, 0, 0)$	0.18	3.00E-3	6.24(a)
B	3	3	$(0, 0, 0)$	0.55	1.89E-5	6.24(b)
C	3	3	$(100, 100, 0)$	0.97	1.03E-3	6.25(a)
D	4	3	$(100, 100, 0)$	0.97	3.53E-4	6.25(b)

In Figs. from 6.24 to 6.25 numerical results obtained with 1600 time-steps per rotation period are checked against analytical solutions. The plots show that, as in Test 1 and Test 2, the agreement between the numerical and the analytical solutions is good for all the investigated configurations. The relative L-errors, as defined in (6.63), for the different configurations are listed in Table 6.4.

In Fig.6.26 the relative L_2-error 6.64 for Case D is plotted against the number of samples N_s per rotation period, from $N_s = 160$ up to $N_s = 1600$. The numerical solutions corresponding to three values of N_s are plotted in Fig.6.27. The acoustic signatures exhibit a small phase error only for $N_s = 160$.

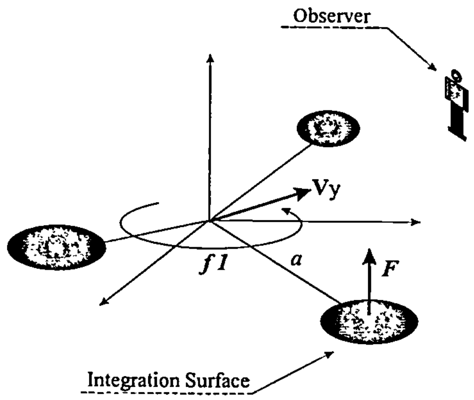

FIGURE 6.23: Scheme of Test 3. An axial compact dipole is described as a small disk with a pressure jump uniformly distributed upon its surface. Three and four disks at a constant angle from each other are considered, rotating around a vertical axis at the frequency f_1. The system translates at the velocity $\mathbf{v}_y$, whereas the observer is fixed.

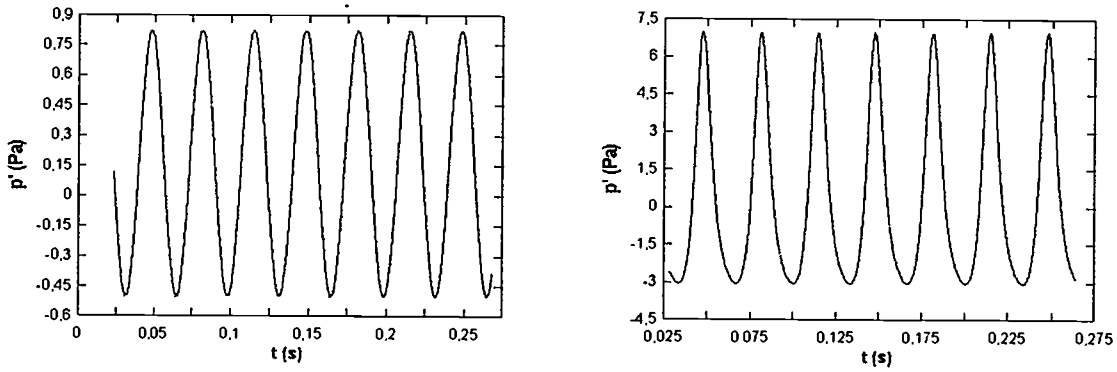

FIGURE 6.24: Test 3. Case A (left) and Case B (right). —— Analytical solution, - - - - Numerical solution.

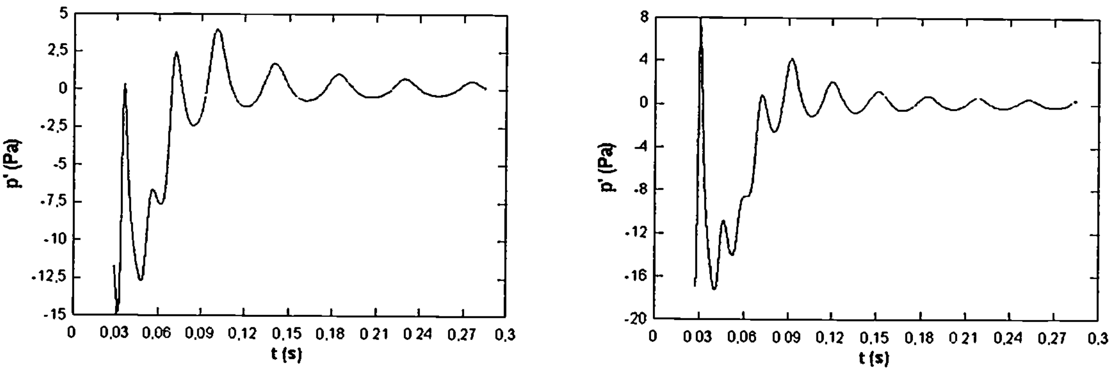

FIGURE 6.25: Test 3. Case C (left) and Case D (right). —— Analytical solution, - - - - Numerical solution.

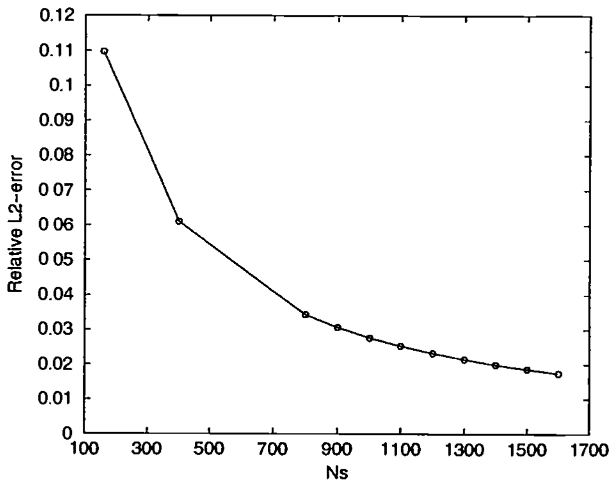

FIGURE 6.26: Test 2, Case H. Relative L_2-error *versus* the number of time-steps per acoustic period.

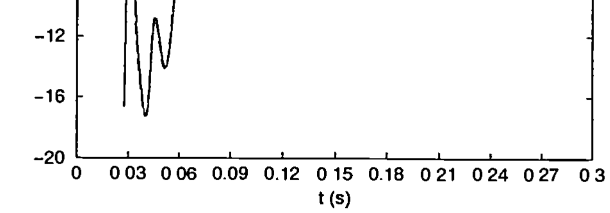

FIGURE 6.27: Test 3, Case D. Numerical solutions for three values of the number of samples N_s per rotation period: —— $N_s = 1600$, $\mathrm{Err}_{L2} = 1.74 \times 10^{-2}$; - - - - $N_s = 1100$, $\mathrm{Err}_{L2} = 2.52 \times 10^{-2}$; — — $N_s = 160$, $\mathrm{Err}_{L2} = 1.10 \times 10^{-1}$.

6.3.3 Discussion

The feasibility of an advanced time aeroacoustic prediction has been proven through several test cases. The relative L-errors in Tables 6.2, 6.3 and 6.4 show that a high level of accuracy has been obtained even in the case of surfaces moving at high Mach numbers, provided that a sufficient number of samples per period is used. Consistently, an increasing phase-error appears as the time-step is increased. This effect has been emphasized by evaluating the L_2-error. Thus, we showed that:

- the advanced time approach can be successfully applied to hybrid CFD/FW-H aeroacoustic predictions.
- The accuracy of the numerical prediction is not significantly affected by the kinematics of the problem, even at very high source Mach numbers.
- The FW-H integral formulation based on a penetrable control surface provides consistent results even when the integration surface rotates and translates at high velocities. The definition of aerodynamic quantities and their time derivatives on a rotating penetrable surface is a complicated matter. For this reason we believe that the test cases herein discussed constitute an original aspect of the present work.
- The thickness noise extension to a moving observer is consistent with an advanced time approach.

The *acoustic* assessment of *Advantia* can be successfully concluded with the awareness that: *the thickness and the loading noise contributions from a high-speed, but subsonic surface can be accurately predicted through an advanced time formulation, which is more effective and simple than a classic retarded time formulation.*

6.4 On the Feasibility of a Hybrid CFD/FW-H Aeroacoustic Prediction

In the preceeding section we showed that a FW-H formulation can be successfully applied to the prediction of complex acoustic fields, provided that a consistent acoustic field is inputed on the integration surface. In the case of a penetrable control surface, the acoustic field is expressed in terms of acoustic pressure, acoustic velocity and related time derivatives.

Throughout the present work the FW-H formulation is used to predict the aerodynamic noise from vortical flows bounded by surfaces moving at constant velocities. Since the numerical methodology implemented in *Advantia* propagates the *near* field information to the far field at a very high level of accuracy, the accuracy of the aeroacoustic prediction depends only on the accuracy of the aerodynamic solution and its time derivative on the integration surface.

6.5 Conclusions

In this chapter we showed that a retarded time solution of a generic wave equation can be computed through an advanced time approach.

When applied to the aerodynamic noise prediction, the advanced time formulation allows to progressively build the time trace of the radiated acoustic pressure by using aerodynamic data as early as these are computed by an aerodynamic solver. Hence, the traditional concept of a post-process acoustic prediction is partially surpassed. The practical advantages offered by this methodology are:

- the feasibility of an aeroacoustic prediction running parallelly to an aerodynamic prediction;
- no disk recordings of the aerodynamic data are necessary for the sake of an aeroacoustic prediction;

- the advanced time is an algebraic function of the observer and point source location at the emission time. Therefore, no iterative solutions of the retarded time equation must be performed, resulting in an increased efficiency of the numerical algorithms.

Minor results of the present study are:

- the thickness noise extension to a moving observer with time derivatives taken inside the integrals;
- a formulation of the integral FW-H equation in terms of dimensionless quantities, with velocities defined in the body reference frame.

Non trivial test cases were performed in order to assess the consistency of the advance time formulation. These were chosen in order to test all the numerical procedures involved in a rotor noise prediction.

No attempt was made in the present work to exploit the advanced time approach in the transonic regime. Nevertheless, we believe that an examination of the transonic singularity in the spirit of an advanced time prediction could suggest the way of an *ad-hoc* treatment of this regime.

As a final remark, the feasibility of an acoustic prediction running parallelly to an aerodynamic prediction could be of primary importance in the evaluation of volume contributions.

Appendix 6 A

Symbols Used in the FW-H Formulation

The aerodynamic field is introduced in equations (6.41), (6.42) and (6.43) in terms of conservative variables, namely, the flow density ρ, the linear momentum $\rho\tilde{u}_i$, $\tilde{u}_i$ being the relative velocity of the flow with respect to the integration surface $f = 0$, the specific total internal energy ρE and the specific kinetic turbulent energy ρK. A description of all the involved quantities is reported below

$$
\begin{aligned}
& p_d = \frac{1}{2}\rho_0\, U_{\mathrm{ref}}^2, \quad \theta = t\, U_{\mathrm{ref}}/l_{\mathrm{ref}}, \quad M_{\mathrm{ref}} = U_{\mathrm{ref}}/c, \quad V_i = v_i/U_{\mathrm{ref}}, \quad V_n = V_i\hat{n}_i \\
& \mathbf{X} = \mathbf{x}/l_{\mathrm{ref}}, \quad \mathbf{Y} = \mathbf{y}/l_{\mathrm{ref}}, \quad \hat{r}_i = \frac{X_i - Y_i}{|\mathbf{X}-\mathbf{Y}|}, \quad R = |\mathbf{X}-\mathbf{Y}| \\
& M_i = v_i/c, \quad M_r = M_i\,\hat{r}_i, \quad \dot{M}_r = \dot{M}_i\,\hat{r}_i, \quad \ddot{M}_r = \ddot{M}_i\,\hat{r}_i, \quad M_{or} = M_{oi}\,\hat{r}_i \\
& \tilde{u}_i = u_i - v_i, \quad \sigma = \frac{\rho}{\rho_0}, \quad q_i = \frac{(\rho\tilde{u}_i)}{(\rho_0 U_{\mathrm{ref}})}, \quad e = \frac{(\rho E)}{(\rho_0 U_{\mathrm{ref}}^2)}, \quad k = \frac{(\rho K)}{(\rho_0 U_{\mathrm{ref}}^2)} \\
& C_p = 2\left\{(\gamma-1)\left[e - \frac{q_i\,q_i}{2\,\sigma} - k\right] - \frac{p_0}{2\,p_d}\right\} \\
& \dot{C}_p = 2\,(\gamma-1)\left[\dot{e} - \frac{q_i\,\dot{q}_i}{\sigma} + \dot{\sigma}\frac{q_i\,q_i}{2\,\sigma^2} - \dot{k}\right] \\
& \lambda_i = \frac{C_p}{2}\,\hat{n}_i + V_i\,q_n + \frac{q_i\,q_n}{\sigma} \\
& \chi_i = \frac{\dot{C}_p}{2}\,\hat{n}_i + \frac{C_p}{2}\,\dot{\hat{n}}_i + \dot{V}_i q_n + V_i\,(\dot{q}_i\hat{n}_i) + V_i\left(q_i\dot{\hat{n}}_i\right) \\
& \qquad + \frac{\dot{q}_i q_n}{\sigma} + \frac{q_i\,(\dot{q}_i\hat{n}_i)}{\sigma} + \frac{q_i\left(q_i\dot{\hat{n}}_i\right)}{\sigma} - \frac{q_i q_n}{\sigma^2}\dot{\sigma} \\
& \Psi_{ij} = \frac{q_i q_j}{\sigma} + \sigma V_i V_j + q_i V_j + q_j V_i + \left(\frac{C_p}{2} - \frac{\sigma-1}{M_{\mathrm{ref}}^2}\right)\delta_{ij} \\
& q_n = q_i\hat{n}_i, \quad \lambda_M = \lambda_i\,M_i, \quad \lambda_r = \lambda_i\,\hat{r}_i, \quad \chi_r = \chi_i\,\hat{r}_i \\
& \Psi_{MM} = \Psi_{ij}\,M_i\,M_j, \quad \Psi_{Mr} = \Psi_{ij}\,M_i\,\hat{r}_j, \quad \Psi_{\dot{M}r} = \Psi_{ij}\,\dot{M}_i\,\hat{r}_j, \quad \Psi_{rr} = \Psi_{ij}\,\hat{r}_i\,\hat{r}_j \\
& \dot{\Psi}_{Mr} = \dot{\Psi}_{ij}\,M_i\,\hat{r}_j, \quad \dot{\Psi}_{rr} = \dot{\Psi}_{ij}\,\hat{r}_i\,\hat{r}_j, \quad \ddot{\Psi}_{rr} = \ddot{\Psi}_{ij}\,\hat{r}_i\,\hat{r}_j
\end{aligned}
$$

In these expressions p_0 and ρ_0 are the quiescent fluid pressure and density, respectively, M_o denotes the observer Mach number, $\hat{n}_i$ is the unit vector pointing out of the integration surface and upper dots denote derivatives with respect to the dimensionless time θ. The loading-noise term χ_i is the dimensionless time derivative of λ_i. In a similar way both $\dot{\Psi}_{ij}$ and $\ddot{\Psi}_{ij}$ can be obtained from the quadrupole noise term Ψ_{ij}.

Appendix 6 B

Nomenclature

c	Sound speed in quiescent medium
C_p	Pressure coefficient
$H()$, $\delta()$	Heaviside and Dirac delta functions
K	kinetic turbulent energy
l_{ref}	Reference length
E	Total internal energy
M_i	Mach number of the surface $f = 0$
M_{ref}, U_{ref}	Reference Mach number and reference velocity
$M_{o\,i}$	Observer Mach number vector
$M_{o\,r}$	Observer Mach number vector in the radiation direction
$\hat{n}_i$	Unit outward normal vector to the integration surface
p_0	Pressure in quiescent medium
p', ρ'	Pressure and density disturbances
p_d	Reference dynamic pressure
R	Dimensionless distance between observer and a source point
$\hat{r}_i$	Radial unit vector
t, θ	time and dimensionless time
T_{ij}	Lighthill's stress tensor
u_i	Flow velocity
$\tilde{u}_i$	Flow velocity relative to the integration surface
v_i, V_i	Velocity and dimensionless velocity of the surface $f = 0$
$\mathbf{x}$, $\mathbf{X}$	Observer position and dimensionless observer position
$\mathbf{y}$, $\mathbf{Y}$	Source position and dimensionless source position
δ_{ij}	Kronecker delta
γ	Specific heat ratio
λ_i, χ_i	Loading noise source terms
ρ, ρu_i, ρE, ρK	Aerodynamic conservative quantities
ρ_0	Flow density in quiescent medium
ρ	Flow density
σ, q_i, e, k	Dimensionless aerodynamic conservative quantities
τ_{ij}	Viscous stress tensor
Ψ_{ij}	Quadrupole noise source terms
$\Box^2$	Wave operator

Superscripts

$\dot{}$	Time derivative

Subscripts

n	Projection in the normal direction
r	Projection in the radiation direction

Abbreviations

BEM	Boundary Element Method
CAA	Computational AeroAcoustics
CFD	Computational Fluid Dynamics
FW-H	Ffowcs-Williams & Hawkings
RANS	Reynolds-Averaged Navier Stokes

Appendix 6 C

Interpolation Scheme in the Advanced Time Domain

In this appendix we describe the procedure used in the present work to build-on the acoustic signal in the advanced time domain.

At each source time-step j and for each source element i, the advanced time t^j_{adv} and the corresponding elementary sound contribution p' are computed. Then, the quantities

$$j_{\text{adv}} = \text{int}(\frac{t^j_{\text{adv}}}{\Delta t}) \tag{6.66}$$

$$w = \frac{t^j_{\text{adv}}}{\Delta t} - j_{\text{adv}} \tag{6.67}$$

are computed, j_{adv} denoting the advanced time-step and w the normalized difference between t^j_{adv} and the discrete advanced time $j_{\text{adv}}\Delta t$.

Successively, the elementary sound contribution p^j_i is computed by means of a case-procedure which depends on whether a contribution p^j_i has been already computed or not, that is

a) if $p^j_i = 0$ (not computed), then

$$p^j_i = p' \tag{6.68}$$

$$w^j_i = w \tag{6.69}$$

b) if $p^j_i \neq 0$ (already computed), then

$$p_w = \frac{p^j_i - p'}{w^j_i - w} \tag{6.70}$$

$$p^j_i = p' - p_w w \tag{6.71}$$

$$w^j_i = 0 \tag{6.72}$$

Both the values of p^j_i and w^j_i are stored. It is straightforward to verify that, once $w^j_i = 0$ has been set by a first execution of block b), successive executions do not affect the value of p^j_i.

Finally, a summation over all the source elements, say $p^j = \sum_i p^j_i$, provides the pressure value at the advanced time-step j_{adv}.

7

Spanwise Statistical Modeling of a Circular Cylinder Flow

In this chapter we propose a new method for the prediction of the aerodynamic sound generated by a *nominal two-dimensional flow* past a bluff body, which generates pulsating vortical disturbances at a privileged frequency.

The method is applied to the prediction of the noise radiated by a circular cylinder flow, with a twofold aim in mind:

1. to show how three-dimensional effects can be taken into account by an acoustic analogy prediction based on a two-dimensional flow;

2. to show the feasibility of an aerodynamic noise prediction through a hybrid RANS/FW-H formulation.

In the first part of the present chapter we describe the underlying physics of the vortex dynamics in the wake of a rod, with emphasis given to oblique vortex shedding and other three-dimensional effects.

In the second part we describe a statistical model of the flow around a rod, based on the idea of a spanwise random variation of the vortex shedding phase. An analogy in terms of spanwise correlation coefficient is also illustrated between a spanwise random phase variation and a low frequency random amplitude modulation of the pressure field on the rod surface.

In the final part of the chapter we present results concerning a RANS prediction of the flow past a circular cylinder at a Reynolds number of about $Re = 2.2 \times 10^4$, and results of a FW-H prediction of the aerodynamic noise at about one acoustic wavelength from the cylinder. Both aerodynamic and acoustic results are checked against experimental data.

7.1 Introduction

The aerodynamic sound generated by the periodic vortex shedding from a circular cylinder is a classical problem in aeroacoustics.

The *Aeolian tones* were first investigated by Strouhal [3] in 1878 by measuring the frequency of the tonal emission from a stretched wire mounted on a hand-driven rotating apparatus. Strouhal related the sound generation to the flow friction on the wire and observed that the tonal frequency is given by $f_0 = St\, U/d$, where St is a constant, U is the velocity of the cylinder and d its diameter.

This result was confirmed in 1879 by Lord Rayleigh [49] who first observed that the Strouhal number St depends on the flow Reynolds number. Moreover, Rayleigh argued that, since the wire vibrated perpendicularly to the stream, the sound could not be generated by the fluid friction. Therefore, after Bénard's 1908 observation of staggered vortices in a cylinder wake and von Kármán's 1912 stability analysis of a double row of counter-rotating vortices, Rayleigh [4] related the wire tone emission and vibration to the periodic vortex shedding from the wire.

Among the several arguments in favor of Rayleigh's fatherhood of the aerodynamic sound theory[1] that related to the Aeolian tones is well established. Indeed, as early as 1896, Rayleigh [51] observed that even motionless cylinders in a fluid stream can produce a tonal emission and that the coincidence of the vortex shedding frequency with the cylinder structural frequency only increases the sound intensity.

Once the acoustic analogy theory was established by Lighthill [1] and Curle [52], Phillips [53] succeeded in predicting the Aeolian tones on the basis of some properties of the flow, namely the vortex shedding frequency, the maximum lift coefficient induced by the counter-rotating vortices, and the spanwise correlation length.

The spanwise correlation length accounts for the three-dimensional character of the flow. A circular cylinder flow, in fact, remains two-dimensional up to Reynolds numbers of about 180. At higher values, three-dimensional fluctuations are imposed on the dominant vortex shedding. As a consequence, the wall pressure signals exhibit a random amplitude modulation. At very low Reynolds numbers this behaviour is presumably related [54] to a cellular structure of the vortex shedding, accompanied by *vortex dislocations* and oblique vortex shedding. At higher Reynolds numbers cellular shedding have never been observed, despite the randomly modulated behaviour of the wall pressure signals [36]. Therefore, vortex dislocations are likely to exist also at higher Reynolds numbers.

An oblique vortex shedding causes a spanwise variation of the vortex shedding phase. Furthermore, a statistical analogy exists between a random amplitude modulation and a random dispersion of the vortex shedding phase. Therefore, an *ad hoc* statistical model for the vortex shedding phase is described in the present chapter. The model allows to take into account, to some extent, the three-dimensional character of the flow in an acoustic analogy prediction based upon a two-dimensional flow field.

The spanwise statistical method is validated on the base of Phillips' [53] Aeolian tones model, and by comparing experimental data with an acoustic analogy prediction of the sound from a $Re = 2.2 \times 10^4$ circular cylinder flow. The acoustic field is computed by applying the Ffowcs Williams & Hawkings (FW-H) acoustic analogy to aerodynamic data computed on different surfaces around the cylinder. The aerodynamic field is obtained from a two-dimensional RANS computation. The same hybrid CFD/FW-H approach has been used by other authors [55] [56] [57] in order to validate the consistency of a FW-H formulation applied to a penetrable integration surface.

Once the acoustic analogy is tested, the present approach can be also used as a good benchmark for a CFD prediction since the accuracy of the acoustic solution hinges on the accuracy of the CFD solution.

7.2 Vortex Dynamics in the a Wake of a Circular Cylinder

In this section we describe the vortex shedding regimes in the wake of a circular cylinder. A more exhaustive discussion on the subject can be found in Ref.[58].

In Fig.7.1, experimental values of the base suction coefficient $-C_{p_B}$ are shown [2] *versus* the Reynolds number. The presence of discontinuities in the behaviour of the base suction coefficient is related to the existence of different unsteady flow regimes at different Reynolds numbers.

Re < 49: laminar steady regime (up to A). In this regime the wake of the cylinder is constituted by two symmetrical recirculating bubbles whose length grows as the Reynolds number increases.

[1]The reader should refer to Doak's review [50] for a suggestive dissertation on the Rayleigh's fatherhood of the aerodynamic sound theory.

[2]The base suction coefficient is defined as the suction coefficient $(-C_p)$ at $\phi = 0$, that is, the downstream stagnation point on the cylinder. As sketched in Fig.5.10(a), ϕ denotes the angle away from the streamwise direction.

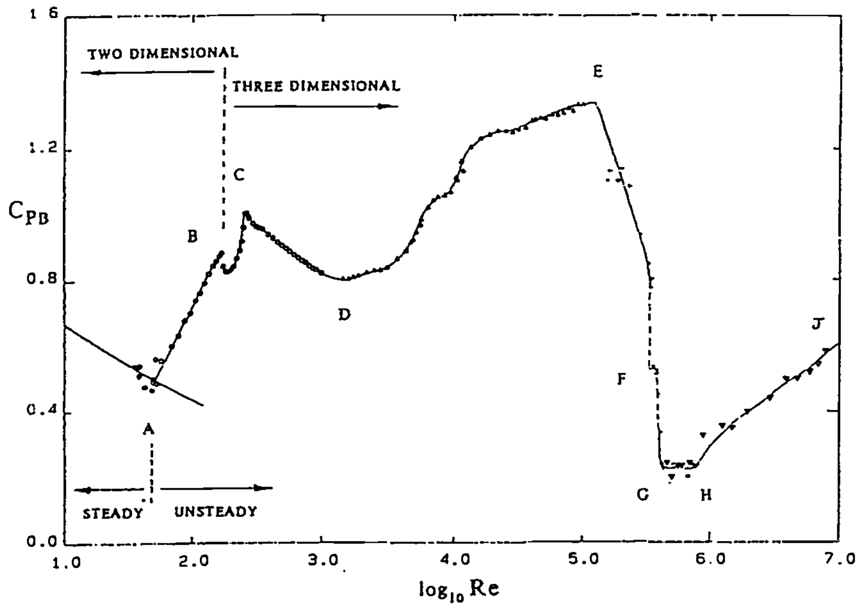

FIGURE 7.1: Base suction coefficient *versus* the Reynolds number (after [58], figure 3).

$49 < \mathbf{Re} < 140 - 194$: **laminar vortex shedding regime (A–B).** In this regime the recirculation region develops instabilities whose amplitude and amplification rate grow as the Reynolds number increases. Consequently, the Reynolds stresses in the near wake increase, the vortex formation length[3] decreases and the base suction coefficient increases. The origin of this primary instability is known to be the result of a Hopf bifurcation and scales with the cylinder diameter.

$190 \lesssim \mathbf{Re} < 260$: **wake transition regime (B–C).** This regime is characterized by a high intermittency of the flow related to the wake transition to three-dimensionality. Indeed, the transition to three-dimensionality involves two discontinuous changes of the three-dimensional instability, the former having a hysteretic nature[4]. These discontinuities mark two different mode of three-dimensional instability, which are referred to as *mode A* and *mode B* (to not be confused with the flow regimes A and B in Fig.7.1). Streamwise vortices are originated both in mode A and mode B. In mode A these vortices are due to the deformation of primary vortices, whereas in mode B these vortices are related to local shedding-phase dislocations along the span of the cylinder.

$260 < \mathbf{Re} \lesssim 1000$: **increasing disorder in the three-dimensional fine-scale (C–D).** This regime is characterized by a fine three-dimensional structure which becomes increasingly disordered as the Reynolds number increases. As a consequence, the two-dimensional Reynolds stresses decrease, the vortex formation length decreases and the base suction coefficient increases. The local maximum of the base suction in C is likely to be caused by a resonance between the frequency f_{SL} of the shear layer instability and that f_k of the primary Kármán street instability. The shear-layer instability develops by the action of a Kelvin-Helmholtz mechanism. Hence, it scales with the thickness of the separated shear layer which is a small fraction of the cylinder diameter. Consequently, the length and time scales of the shear-layer instabilities are much smaller than those related to the primary wake instability. However, a resonance between these two instability mechanisms occurs at a particular value of the Reynolds

[3]The vortex formation length is conventionally defined as the distance of a point downstream to the cylinder where the velocity fluctuation level has grown to a maximum.

[4]The Reynolds at which the discontinuity occurs depends on whether the flow speed is increased or decreased.

number. In fact, as found by Prasad & Williamson [59], the following result holds

$$\frac{f_{SL}}{f_k} = \left(\frac{\text{Re}}{262}\right)^{0.62} \tag{7.1}$$

which yields $f_{sl} = f_k$ at a Reynolds number of 262, which corresponds to the condition marked as C in Fig.7.1.

1000 < Re < 200000: shear-layer transition regime (D–E). This regime is characterized by increasing Reynolds stresses, a decreasing vortex formation length and, consistently, by an increasing base suction coefficient. This behaviour is due to the fact that the Kelvin-Helmholtz instabilities are essentially two-dimensional and contribute to the increase of the two-dimensional Reynolds stresses.

200000 < Re: critical transition (E–G). In this regime a separation-reattachment occurs upon only one side of the body. This is accompanied by a drastic reduction of the drag coefficient.

Supercritical regime (G–H). In this regime the flow is symmetric with two separation-reattachment bubbles, one on each side of the cylinder. The Strouhal number rises to a value of 0.3-0.4, which is consistent with the retarded separation and the thiner wake width.

Boundary-layer transition regime (H–J). In this regime transition to turbulent regime occurs before the separation takes place. A periodic vortex shedding is observed also in this fully turbulent regime.

7.2.1 Three-Dimensional Effects

The vortex dynamics in the wake of a bluff body is of increasing concern in many engineering areas. Effects related to the intrinsic three-dimensional character of a *nominal* two-dimensional flow must be taken into account in order to predict unsteady loading, vibrations and sound generation.

The spanwise statistical model presented in this paper is concerned with the sound from a rod. It is based on Phillips' [53] intuition of a spanwise variation of the vortex shedding phase, and is inferred by recent observations of the vortex dynamics in the wake of a rod.

Three-dimensional flow on a circular cylinder can be influenced by a number of factors which can have an *extrinsic* origin, for instance the boundary layer on the end plates, or an *intrinsic* origin, as those arising from natural instabilities. Furthermore, different three-dimensional effects have been observed at low and high Reynolds numbers.

7.2.1.1 Three-Dimensionality at Low Reynolds Numbers

Low-Reynolds-number cylinder wakes are characterized by discontinuities in the Strouhal-Reynolds number relationship, and by oblique vortex shedding. These characteristics of the wake are related to each other and are both influenced by the conditions at the ends of the cylinder, even at high aspect ratios (l/d). The Strouhal discontinuity observed by Tritton [60] near $Re = 75$ is caused by a transition from one oblique shedding mode to another one [54]. This transition can be explained by a change in the shedding pattern from one where the central flow is able to match the end conditions to one where the central flow is unable to match the end conditions and generates a cell of higher shedding frequency. Up to three coexisting frequency cells have been observed [61]. At the interface between two cells *vortex dislocations* occur during periods in which vortices move out of phase with each other. The coexistence of cells of different frequency results in a low frequency quasi-periodic amplitude modulation of the fluctuating quantities in the near wake. Furthermore, at the boundary between two cells, abrupt phase jumps can take place at the amplitude modulation frequency. In Fig.7.2 an example of velocity fluctuations at different spanwise positions across two frequency cells is shown. The near-end fluctuations have a lower frequency, say f_a. The central fluctuations have a higher frequency, say f_b.

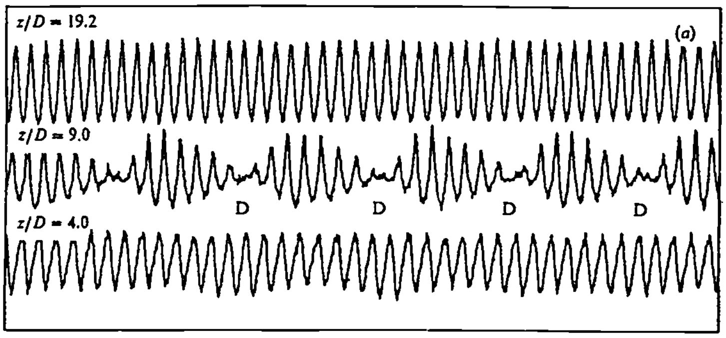

FIGURE 7.2: Time traces of velocity fluctuations along the span of a cylinder in a uniform flow at a Reynolds number Re=99.6. z/D denotes the spanwise distance from the mid-plane, made dimensionless by the cylinder diameter D. The letters D along the time axis denote *vortex dislocation* (after [54], figure 22).

The resulting amplitude modulation has a frequency $f_b - f_a$. The abrupt phase jumps at the interface between the near-end and the central frequency cell result in vortex dislocations. A sketch of a three frequency cells vortex shedding is shown in Fig.7.3.

7.2.1.2 Three-Dimensionality at High Reynolds Numbers

The main three-dimensional effect observed at higher Reynolds numbers is a spanwise variation of the vortex shedding phase, accompanied by a random amplitude modulation of the fluctuating quantities in the near wake of the rod. Since the vortex shedding is not in phase along the rod span, spanwise pressure gradients take place, which induce spanwise velocity fluctuations. Near the end plates the spanwise component of the fluctuating velocity vanishes, leading to an enhancement of the vortex shedding uniformity. Experiments conducted by Szepessy & Bearman [36] in the high-Reynolds number range $1 \times 10^4 - 1.3 \times 10^5$ show that a weak shedding mode reappears somewhat periodically at about 10-20 times the Strouhal period, and has a duration of about 3-7 shedding periods. Szepessy & Bearman also observed a phase shift between a wall pressure signal in the rod mid plane and a velocity signal near the rod, both taken 90^o away from the flow direction. The phase shift increased with the separation distances between the two transducers. Despite the observed amplitude modulation, no cellular vortex

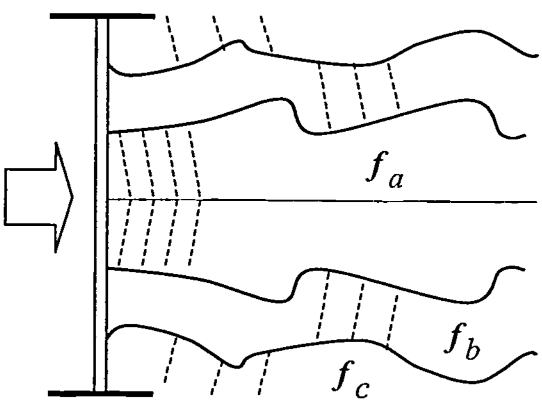

FIGURE 7.3: Three frequency cells coexisting along the span of a cylinder in a uniform flow with end plates.

shedding was observed.

7.3 A Statistical Method for Aeroacoustic Predictions

At Reynolds numbers higher than about 180 the flow past a circular cylinder is three-dimensional. This causes the wall pressure fluctuations to exhibit a modulated behaviour. The quasi-periodic amplitude modulation observed at low Reynolds numbers is related [54] to a cellular structure of the vortex shedding. Spanwise inhomogeneities such as boundary layers upon the end plates[1], nonuniform inflow conditions or a spanwise-varying diameter induce the formation of *cells*, i.e. regions of constant shedding frequency along the rod span. At the interface between two cells an abrupt frequency jump occurs. The interaction between two neighbouring cells of frequency f_a and f_b, respectively, induces a beat behaviour at the frequency $|f_a - f_b|$. When the vortices in two adjacent cells are nearly in phase, their mutual interference generates an oblique vortex shedding. Conversely, when two cells are out of phase, a contorted vortical structure, say *vortex dislocation*, is produced. Hence, oblique shedding, vortex dislocation and cellular shedding are different aspects of the same phenomenology. At higher Reynolds number random amplitude modulations have been observed [36], accompanied by spanwise phase shift and jumps along the rod span.

Both an oblique vortex shedding and a random amplitude modulation can be related to a random variation of the vortex shedding phase. Therefore, an *ad hoc* spanwise statistical model is first developed on the base of Phillips' [53] model and successively applied to the rod noise prediction.

7.3.1 Phillips' Model

Consider a motionless rod of diameter d and span l in a fluid stream with velocity V_∞. Set $l_{\text{ref}} = d$ and $U_{\text{ref}} = V_\infty$ in equations (6.41) and (6.42). Consider a fixed observation point $r_0 d(\cos\theta, \sin\theta, 0)$, r_0 being the dimensionless observation distance from the rod mid point and θ the angle away from the streamwise direction.

In the geometrical ($r_0 \gg 1$) and acoustical ($M_\infty r_0 \, 2\pi \, St \gg 1$) far field limits, provided that an integration upon the rod surface is made, equations (6.41) and (6.42) reduce to

$$p'(r_0, \theta, \tau) = \frac{p_d M_\infty r_0 \sin\theta}{4\pi} \int_{-l/2d}^{l/2d} \frac{\mathrm{d}\eta_d}{R^2 \left(1 + M_\infty r_0 \cos\theta / R\right)^2} \hat{r}_i \cdot \int_{\mathcal{L}} \left[\dot{C}_p\right] \hat{n}_i \, \mathrm{d}l \tag{7.2}$$

where $p_d = \rho_\infty V_\infty^2/2$ and $R = \sqrt{r_0^2 + \eta_d^2}$ is the dimensionless distance between the observer and a point source on the rod, with η_d denoting the dimensionless spanwise coordinate. The time derivative of the pressure coefficient is evaluated at the dimensionless retarded time

$$\tau_{\text{ret}} = \tau - R\, M_\infty \tag{7.3}$$

Supposing an observer sufficiently far from the rod, such that $r_0 \gg l/2d$, yields

$$p'(r_0, \theta, \tau) = \frac{p_d M_\infty}{4\pi\, r_0 \left(1 + M_\infty \cos\theta\right)^2} \int_{-l/2d}^{l/2d} \mathrm{d}\eta_d \quad \hat{r}_i \cdot \int_{\mathcal{L}} \left[\dot{C}_p\right] \hat{n}_i \, \mathrm{d}l \tag{7.4}$$

Finally, neglecting the unsteady drag component by substituting

$$\int_{\mathcal{L}} \left[\dot{C}_p\right] \hat{n}_i \, \mathrm{d}l \simeq - \left[\dot{C}_l\right] \hat{\jmath} \tag{7.5}$$

[1]The end conditions affect the vortex shedding over the entire rod span, even for aspect ratio of the order of 100.

into equation (7.4) leads to the *compact dipole* Aeolian tones radiation

$$p'(r_0,\theta,\tau) = \frac{-p_d\, M_\infty \sin\theta}{4\pi\, r_0\,(1+M_\infty\cos\theta)^2} \int_{-l/2d}^{l/2d} \left[\dot{C}_l\right] \mathrm{d}\eta_d \tag{7.6}$$

Although the vortex-induced fluctuating lift may be of the same amplitude along the rod span, the phase of the lift may vary stochastically as $\tilde{\varphi}(\eta_d)$. Thus, following Phillips [53], the fluctuating lift coefficient can be written as

$$C_l(\eta_d,\tau) = C_{l\,\max} \exp\left\{-\mathrm{i}\;(2\pi\, St\;\tau + \tilde{\varphi}(\eta_d))\right\} \tag{7.7}$$

Substituting equation (7.7) into equation (7.6) yields

$$p'(r_0,\theta,\tau) = \frac{\mathrm{i}\, p_d\, M_\infty\;St\;C_{l\,\max}\, l\sin\theta}{2\, r_0\, d\,(1+M_\infty\cos\theta)^2}\,\mathrm{e}^{-\mathrm{i}\,[2\pi\, St\,(\tau - M_\infty r_0)]} \int_{-\frac{1}{2}}^{+\frac{1}{2}} \mathrm{e}^{-\mathrm{i}\,\tilde{\varphi}(\eta)}\,\mathrm{d}\eta \tag{7.8}$$

where η is the spanwise coordinate made dimensionless by the rod span. Hence, the acoustic intensity is given by

$$I = I_{\det} \int_{-\frac{1}{2}}^{+\frac{1}{2}} \int_{-\frac{1}{2}}^{+\frac{1}{2}} \exp\left\{-\mathrm{i}\;(\tilde{\varphi}(\eta_1) - \tilde{\varphi}(\eta_2))\right\}\,\mathrm{d}\eta_1\,\mathrm{d}\eta_2 \tag{7.9}$$

where

$$I_{\det} = \frac{\rho_\infty\, V_\infty^6\, C_{l\max}^2\; St^2\, l^2 \sin^2\theta}{32\, c_0^3\, r_0^2\, d^2\;(1+M_\infty\cos\theta)^4} \tag{7.10}$$

denotes the far field sound intensity of a deterministic flow (fully correlated along the rod span). If the correlation length is small compared to the rod span, the double integral in equation (7.9) can be approximated as

$$\int_{-\frac{1}{2}}^{+\frac{1}{2}} \int_{-\frac{1}{2}}^{+\frac{1}{2}} \exp\left\{-\mathrm{i}\;(\tilde{\varphi}(\eta_1) - \tilde{\varphi}(\eta_2))\right\}\,\mathrm{d}\eta_1\,\mathrm{d}\eta_2 \simeq \int_{-\infty}^{+\infty} \rho(\eta)\;\mathrm{d}\eta \tag{7.11}$$

where the correlation coefficient $\rho(\eta) = \int_{-\frac{1}{2}}^{+\frac{1}{2}} \exp\left\{-\mathrm{i}\;(\tilde{\varphi}(\eta_1) - \tilde{\varphi}(\eta_1+\eta))\right\}\,\mathrm{d}\eta_1$ can be *reasonably* supposed to be Gaussian or Laplacian. In the first case it results that

$$\rho(\eta) = \exp\left(-\frac{\eta^2}{2\,L_g^2}\right) \quad \text{and} \quad I = I_{\det}\,\sqrt{2\,\pi}\,L_g \tag{7.12}$$

whereas, in the second case

$$\rho(\eta) = \exp\left(-\frac{|\eta|}{L_l}\right) \quad \text{and} \quad I = I_{\det}\,2\,L_l \tag{7.13}$$

7.3.2 The Method of the Phase Variance Distribution

The fluctuating pressure on the rod surface at 90° away from the streamwise direction is representative of the fluctuating lift. Thus, for two spanwise locations one can write $p_1(t) = P\cos(2\pi\, f_0\, t + \tilde{\varphi}_1)$ and $p_2(t) = P\cos(2\pi\, f_0\, t + \tilde{\varphi}_2)$. The related cross-correlation function is given by

$$\begin{aligned}
C_{12}(\Theta) &= \mathcal{E}\left[p_1(t)\, p_2(t+\Theta)\right] = \\
&= \frac{P^2}{2}\mathcal{E}\left[\cos\tilde{\varphi}_1\,\cos\tilde{\varphi}_2\right]\cos(2\,\pi\, f_0\,\Theta) - \frac{P^2}{2}\mathcal{E}\left[\cos\tilde{\varphi}_1\,\sin\tilde{\varphi}_2\right]\sin(2\,\pi\, f_0\,\Theta) \\
&+ \frac{P^2}{2}\mathcal{E}\left[\sin\tilde{\varphi}_1\,\cos\tilde{\varphi}_2\right]\sin(2\,\pi\, f_0\,\Theta) + \frac{P^2}{2}\mathcal{E}\left[\sin\tilde{\varphi}_1\,\sin\tilde{\varphi}_2\right]\cos(2\,\pi\, f_0\,\Theta)
\end{aligned} \tag{7.14}$$

where $\mathcal{E}\,[\,]$ denotes the expected value.

Taking the first point in $\eta = 0$ and setting $\tilde{\varphi}_2 = \tilde{\varphi}$, equation (7.14) reduces to

$$C_{1\,2}(\Theta) = \frac{P^2}{2}\mathcal{E}\,[\cos\tilde{\varphi}]\,\cos(2\,\pi\,f_0\,\Theta) - \frac{P^2}{2}\mathcal{E}\,[\sin\tilde{\varphi}]\,\sin(2\,\pi\,f_0\,\Theta) \tag{7.15}$$

This is equivalent to suppose that the flow is statistically homogenous along the rod span and that the random phase $\tilde{\varphi}$ denotes indeed a random phase shift. The corresponding spanwise correlation coefficient is given by

$$\rho(\eta) \equiv C_{1\,2}(0) = \mathcal{E}\,[\cos\tilde{\varphi}] \tag{7.16}$$

whereas, the coherence function is given by

$$\Gamma(\eta, f) = \frac{|S_{1\,2}(\eta, f)|}{\sqrt{S_{1\,1}}\sqrt{S_{2\,2}}} = \mathcal{E}\,[\cos\tilde{\varphi}]\,\delta(f - f_0) - \mathcal{E}\,[\sin\tilde{\varphi}]\,\delta(f - f_0) \tag{7.17}$$

where the cross-spectrum $S_{1\,2}$ is the Fourier transform of the cross-correlation function given in equation (7.15).

Random phase shifts may occur for different and independent causes: inflow nonuniformity, surface roughness, etc. According to the *central limit theorem*, this is sufficient to suppose that the random variable $\tilde{\varphi}$ has a Gaussian probability density. Physically this corresponds to a condition of maximum entropy, namely, the less *structured* or deterministic condition. In the present case, it is assumed that random perturbations from the incoming and surrounding turbulent flow (the rod is located in the potential core of a jet) are mainly responsible for the spanwise coherence loss of the deterministic shedding. Hence, not the shedding itself, but its deviation from periodicity is directly related to the surrounding turbulence and can thus be modeled by a Gaussian probability.

Therefore, assume a spanwise phase distribution with a Gaussian probability density $\mathcal{P}$, whose variance w is zero on the rod mid-span plane ($\eta = 0$) and increases symmetrically towards the rod extremities ($\eta = \pm 1/2$), i.e.

$$\mathcal{P}(\tilde{\varphi}, \eta) = \frac{\exp\left(-\frac{\tilde{\varphi}^2}{2\,w(\eta)}\right)}{\sqrt{2\,\pi\,w(\eta)}} \tag{7.18}$$

Clearly, a spanwisely increasing variance accounts for the intrinsic phase shift nature of $\tilde{\varphi}$. Two methods are described below to determine the value of ρ and Γ.

If $\tilde{x}$ denotes a random variable with probability density $\mathcal{P}(\tilde{x})$, the expected value of a generic function $f(\tilde{x})$ is given by $\mathcal{E}\,[f(\tilde{x})] = \int_{-\infty}^{+\infty} f(\tilde{x})\;\mathcal{P}(\tilde{x})\;\mathrm{d}\tilde{x}$. Thus, applying this fundamental property to equation (7.17) leads to

$$\mathcal{E}\,[\sin\tilde{\varphi}] = \int_{-\infty}^{+\infty} \sin\tilde{\varphi}\,\frac{\exp\left(-\frac{\tilde{\varphi}^2}{2\,w}\right)}{\sqrt{2\,\pi\,w}}\,\mathrm{d}\tilde{\varphi} = 0 \quad \text{and} \tag{7.19}$$

$$\mathcal{E}\,[\cos\tilde{\varphi}] = \int_{-\infty}^{+\infty} \cos\tilde{\varphi}\,\frac{\exp\left(-\frac{\tilde{\varphi}^2}{2\,w}\right)}{\sqrt{2\,\pi\,w}}\,\mathrm{d}\tilde{\varphi} = \exp\left(-\frac{w}{2}\right) \tag{7.20}$$

where use of the known integral $\int_{-\infty}^{+\infty}\cos(bx)\exp\left(-a\,x^2\right)\,\mathrm{d}x = \sqrt{\frac{\pi}{a}}\exp\left(-\frac{b^2}{4a}\right)$ has been made. Therefore, when $\tilde{\varphi}$ is a random variable with a symmetric probability density, the coherence function can be also interpreted as the correlation coefficient, i.e.

$$\Gamma(\eta, f) = \rho(\eta)\,\delta(f - f_0) \tag{7.21}$$

Another method for evaluating $\mathcal{E}\,[\cos\tilde{\varphi}]$ is to consider the Taylor series of $\cos\tilde{\varphi}$, writing

$$\mathcal{E}\,[\cos\tilde{\varphi}] = \mathcal{E}\left[\sum_{n=0}^{\infty}\frac{(-1)^n}{(2n)!}\tilde{\varphi}^{2n}\right] = \sum_{n=0}^{\infty}\frac{(-1)^n}{(2n)!}\mathcal{E}\,[\tilde{\varphi}^{2n}] \tag{7.22}$$

Since $\tilde{\varphi}$ has a Gaussian density probability, it results that

$$\begin{aligned}
&\mathcal{E}\left[\tilde{\varphi}^0\right] = 1 \quad \text{and, for } n \geq 1 \\
&\mathcal{E}\left[\tilde{\varphi}^{2n-1}\right] = 0 \\
&\mathcal{E}\left[\tilde{\varphi}^{2n}\right] = (2n-1)(2n-3)\cdot\ldots\cdot 3\cdot 1\cdot w^n
\end{aligned}$$

Thus, substituting into equation (7.22) and performing some algebra, i.e.

$$\begin{aligned}
\mathcal{E}\left[\cos\tilde{\varphi}\right] &= \sum_{n=0}^{\infty}\frac{(-1)^n}{(2n)!}(2n-1)(2n-3)\cdot\ldots\cdot 3\cdot 1\cdot w^n \\
&= \sum_{n=0}^{\infty}\frac{(-w)^n}{2n(2n-2)(2n-4)\cdot\ldots\cdot 4\cdot 2} \\
&= \sum_{n=0}^{\infty}\frac{\left(-\frac{w}{2}\right)^n}{n(n-1)(n-2)\cdot\ldots\cdot 3\cdot 1} \\
&= \sum_{n=0}^{\infty}\frac{1}{n!}\left(-\frac{w}{2}\right)^n = \exp\left(-\frac{w}{2}\right) \qquad (7.23)
\end{aligned}$$

the same result as in equation (7.20) is obtained.

Concluding, the spanwise correlation coefficient at $\phi = 90^o$ on the rod surface takes the form

$$\rho(\eta) = \exp\left(-\frac{w}{2}\right) \qquad (7.24)$$

Two variance distributions are considered as demonstrative examples, leading to a Gaussian and a Laplacian correlation coefficient, respectively. These are:

a) a quadratic variance distribution

$$w(\eta) = 4\,w_{\max}\eta^2 \quad \text{yielding} \qquad (7.25)$$

$$\rho(\eta) = \exp\left(-\frac{\eta^2}{2\,L_g^2}\right) \quad \text{with} \qquad (7.26)$$

$$w_{\max} = (2L_g)^{-2} \qquad (7.27)$$

b) a linear variance distribution

$$w(\eta) = 2\,w_{\max}\,|\eta| \quad \text{yielding} \qquad (7.28)$$

$$\rho(\eta) = \exp\left(-\frac{|\eta|}{L_l}\right) \quad \text{with} \qquad (7.29)$$

$$w_{\max} = L_l^{-1} \qquad (7.30)$$

where L_g and L_l denote the Gaussian and Laplacian correlation lengths, respectively, made dimensionless by the rod span.

The correlation coefficients obtained from a quadratic and a linear spanwise variance of the phase, respectively, are plotted in Fig.7.4. Numerical values, obtained from a randomly generated Gaussian distribution of $\tilde{\varphi}$, are compared with the Gaussian and Laplacian functions of the span spacing η.

By assuming a lift coefficient with the same phase distributions used to plot the correlation coefficients on Fig.7.4, equation (7.2) provides the acoustic radiation plotted on Fig.7.5. Interestingly, an amplitude modulation can be observed in the acoustic signals, resulting in a spectral broadening around the Strouhal peak.

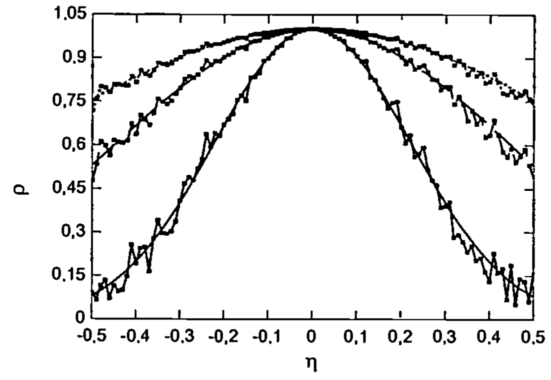

a) Gaussian correlation coefficient. Comparison between the analytical expression (7.26) and numerical values obtained by means of the quadratic variance distribution (7.27). —— $L_g = 0.222$, — — $L_g = 0.444$, - - - - $L_g = 0.666$.

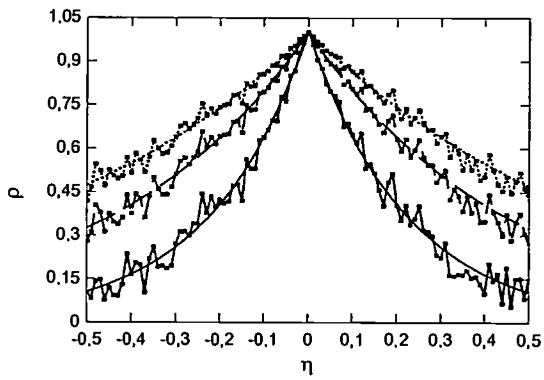

b) Laplacian correlation coefficient. Comparison between the analytical expression (7.29) and numerical values obtained by means of the linear variance distribution (7.30). —— $L_l = 0.222$, — — $L_l = 0.444$, - - - - $L_l = 0.666$.

FIGURE 7.4: Correlation coefficients resulting from random phase distributions with a quadratic (7.25) and a linear (7.28) spanwise variance of the vortex shedding phase. Lengths are made dimensionless by the rod span.

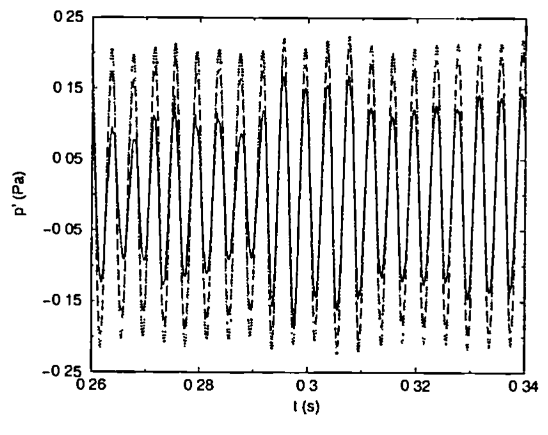

a) Time trace of the acoustic pressure.

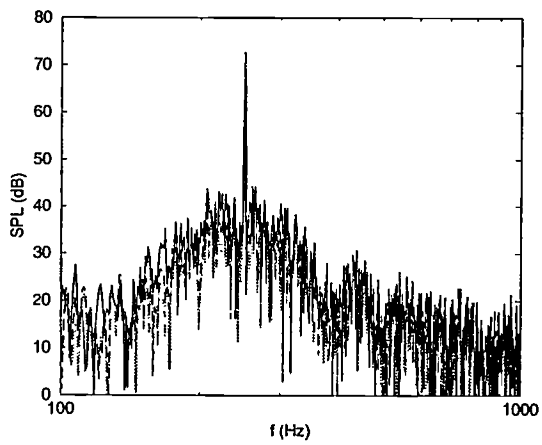

b) Spectrum of the acoustic pressure.

FIGURE 7.5: Sound from a compact rod at a distance $r_0 = 138$ and an observation angle $\theta = 90^o$, obtained by forcing a Gaussian correlation coefficient into equation (7.2): —— $L_g = 0.222$, - - - $L_g = 0.444$, - - - - $L_g = 0.666$. The values $d = 0.016\,\mathrm{m}$, $l = 0.3\,\mathrm{m}$, $V_\infty = 20\,\mathrm{m/s}$, $C_{l\max} = 0.75$, $r_0 = 138$ and $\theta = 90^o$ have been used in the computation.

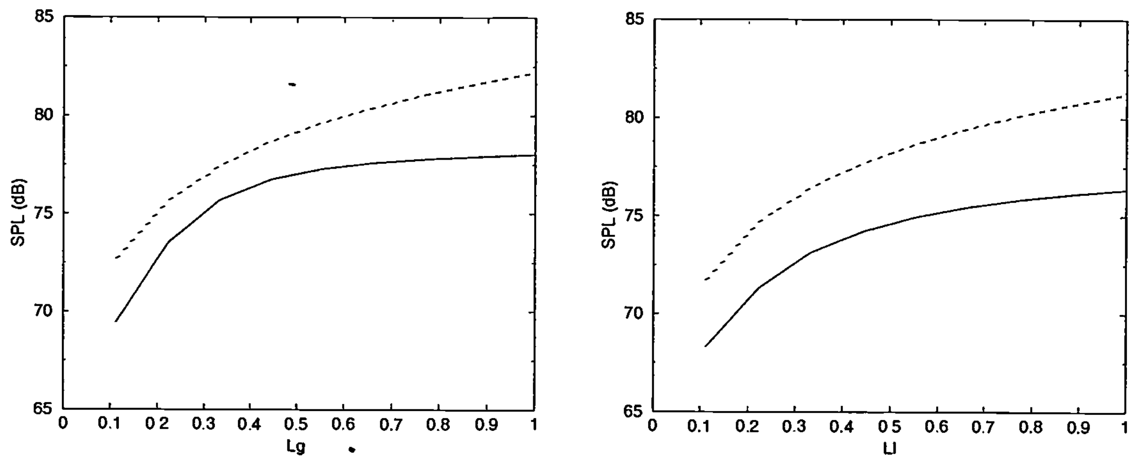

a) Gaussian spanwise correlation coefficient.
b) Laplacian spanwise correlation coefficient.

FIGURE 7.6: Sound intensity from a rod for different values of the correlation length. Comparison between Phillips' analytical results and the compact dipole formulation (7.2), with a randomly generated spanwise phase distribution of the unsteady lift coefficient. —— Compact dipole formulation, - - - - Phillips' model.

In Fig.7.6(a) the acoustic intensity obtained from equation (7.9) by assuming a Gaussian and a Laplacian correlation coefficient, as in equations (7.12) and (7.13) respectively, are compared to the acoustic intensity obtained from equation (7.2) with a Gaussian distribution of the lift phase $\tilde{\varphi}$ along the rod span. Deviations from Phillips' prediction are only due to the fact that the rod has been supposed to be finite for the numerical integration of equation (7.2). Thus, erroneous predictions can be made if the Phillips' model is applied to short rods. In this case, in fact, the approximation (7.11) is inconsistent.

7.3.3 Random Amplitude Modulation *versus* Spanwise Phase Dispersion

The random amplitude modulation observed at high Reynolds numbers can be described as

$$p(t) = \frac{P}{2}\left[\cos(2\pi\, f_0\, t) + \cos\left(2\pi\, \tilde{f}_m\, t\right)\right] \tag{7.31}$$

where $\tilde{f}_m$ denotes a random frequency which differs from f_0 only slightly. Setting $\tilde{f}_b = f_0 - \tilde{f}_m$, $\tilde{f}_b$ being the random beat frequency ($\tilde{f}_b \ll f_0$), equation (7.31) yields

$$p(t) = P\cos\left\{2\pi\left(f_0 - \frac{\tilde{f}_b}{2}\right)t\right\}\cos\left(2\pi\frac{\tilde{f}_b}{2}t\right) \simeq P\cos(2\pi f_0 t)\cos\left(\pi \tilde{f}_b t\right) \tag{7.32}$$

At two different spanwise positions the pressure signals are

$$\begin{aligned} p_1(t) &= P\cos(2\pi f_0 t)\cos\left(\pi \tilde{f}_{b1} t\right) \\ p_2(t) &= P\cos(2\pi f_0 t)\cos\left(\pi \tilde{f}_{b2} t\right) \end{aligned} \tag{7.33}$$

The resulting correlation coefficient is given by

$$\rho(\eta) = \mathcal{E}\left[\cos\left\{\pi\left(\tilde{f}_{b1} - \tilde{f}_{b2}\right)t\right\}\right] \tag{7.34}$$

This expression coincides with that given in (7.16) if the random quantity $\pi\left(\tilde{f}_{b1}-\tilde{f}_{b2}\right)t$ is interpreted as a random phase $\tilde{\varphi}$. This holds if the random process is ergodic, which is the case of the flow considered in the present study.

A major consequence of this statistical equivalence is that the spectral broadening observed in experiments around the Strouhal peak can be partially explained and modeled through a spanwise randomness of the vortex shedding phase.

7.3.4 Aeroacoustic Implementation of the Statistical Model

Statistical pressure measurements on the rod surface provide the correlation coefficient $\rho(\eta)$. This can be related to a spanwise variation of the variance $w(\eta) = -2\ \ln\{\rho(\eta)\}$. Then, $w(\eta)$ is used to generate a random phase sequence $\tilde{\varphi}(\eta_i, \tau_j)$ along the rod span.

Consistently with the observed vortex shedding behaviour, phase jumps are only permitted sporadically every two or three shedding cycles. Furthermore, jump synchronization at two different spanwise sections is avoided by slightly randomizing the time at which the phase jump occurs.

The random phase is then converted into a random perturbation of the retarded time by writing

$$\tilde{\tau}_{\mathrm{ret}}(\eta,\tau) = \tau_{\mathrm{ret}}(\eta,\tau) + \frac{\tilde{\varphi}(\eta, \tau_{\mathrm{ret}}(\eta,\tau))}{2\pi\ St} \tag{7.35}$$

where $\tau_{\mathrm{ret}}(\eta,\tau)$ denotes the deterministic retarded time obtained from the dimensionless retarded time equation (6.45).

The aeroacoustic prediction can be thus performed by forcing into equations (6.41) and (6.42) a spanwise random dispersion of the retarded time $\tilde{\tau}_{\mathrm{ret}}(\eta,\tau)$. This is equivalent to introduce a loss of coherence into the spanwise repetition of the two-dimensional aerodynamic field.

Interestingly, the same two-dimensional aerodynamic field can be used to predict the acoustic pressure by using different seeds of the random phase distribution. Then, averaged acoustic spectra can be computed in a similar way as in the experiments.

7.4 Aeroacoustic Prediction of a Circular Cylinder Flow

In this section, the sound generated by a circular cylinder flow at a Reynolds number $Re = 2.2 \times 10^4$ is the object of a numerical investigation. The acoustic field is computed in the time domain by applying the FW-H acoustic analogy to aerodynamic data calculated on different surfaces around the cylinder. The aerodynamic data are obtained from a two-dimensional RANS computation. The flow three-dimensionality is partially recovered by letting the aerodynamic field undergo a Gaussian correlation in the spanwise direction. Both aerodynamic and acoustic results are checked against experimental data.

7.4.1 Aerodynamic Computation

The compressible finite volume RANS code *Proust* [62] described in section 8.3.1 is used in the current investigation. Both the convective fluxes and the viscous terms are evaluated using a second order centered scheme. The solution is advanced in time by using an explicit second order scheme based on a five-step Runge-Kutta factorization.

Non reflecting boundary conditions and grid stretching in the outer domains are used in order to reduce spurious reflections of acoustic waves.

The turbulence model used is the two-equations Wilcox' [63] $k-\omega$ model, where k is the turbulent kinetic energy and ω is related to the turbulent dissipation. The inflow conditions and the flow parameters are $\rho_\infty = 1.225\,\mathrm{kg/m^3}$, $V_\infty = 20\,\mathrm{m/s}$, $p_\infty = 101253.6\,\mathrm{Pa}$ and $\mu_\infty = 1.78 \times 10^{-5}\,\mathrm{kg/ms}$. The turbulent kinetic energy has a uniform initial value of 0.01 as measured in experiments. The inflow boundary conditions remain the same throughout the computation.

An approximated steady potential flow is used as initial solution. Furthermore, a strong line-vortex in proximity of one separation point on the cylinder is added to the initial field in order to induce a vortex shedding as soon as the computation is started, and thus to accelerate the convergence to a periodic flow.

The computational mesh is based on 197×193 points. It is circumferentially clustered in the wake region. The minimum circumferential spacing, at the rod base point ($\phi = 0$), is $2.5 \times 10^{-3}\,d$, and the thickness of the mesh wall layer is $5 \times 10^{-4}\,d$.

The computational time-step is 6.25×10^{-8} s, corresponding to about 5×10^{5} iterations per aerodynamic cycle. 2048 aerodynamic fields are stored for the acoustic computation, covering 8.04×10^{-2} s.

7.4.2 Acoustic Computation

The rotor noise code *Advantia* described in chapter 6 is used for the acoustic prediction. For the purposes of the present investigation, only surface integrals are computed, provided that, at low Mach numbers, the volume sources give a vanishing contribution to the acoustic radiation. The consistency of this approximation is checked by comparing acoustic results obtained from different integration surfaces.

2048 aerodynamic fields are used for the acoustic computation (about 24 vortex shedding cycles, $t_{\text{fin}} = 8.04 \times 10^{-2}$ s and $\Delta f = 12.19$ Hz). The observation distance from the airfoil mid point is $r = 1.38$ m ($kr = 6.37$ for a typical Strouhal number $St = 0.2$). Integrations are performed upon the cylinder surface and upon penetrable surfaces around the cylinder. The aerodynamic field on both physical and penetrable surfaces is extracted directly from the CFD solution and a Gaussian quadrature is used to compute the surface integrals.

In order to deal with truncated time series, data are multiplied by the Tukey weighting function $w(t) = 0.815\,[1 - \cos(2\pi\, t/t_{\text{fin}})]$ before performing Fourier analyses. The energy of the original signals is preserved by scaling the windowed data.

7.4.3 Aerodynamic Results

On Fig.7.7, contours of the turbulent kinetic energy shows the vortical structures in the wake of the rod. These induce the aerodynamic force plotted in Fig.7.8. The Strouhal frequency f_0 is about 293 Hz and the corresponding Strouhal number is 0.23, which slightly differs from the experimental value of 0.2. The unsteady lift exhibits odd harmonics (f_0, $3f_0$,...), whereas the unsteady drag exhibits even harmonics ($2f_0$, $4f_0$,...). This is because the vortices shed from either sides of the cylinder give the same contribution to the drag and opposite contributions to the lift. The amplitude of the fluctuating lift is $C_{l\,\max} = 0.65$ which is greater than the experimental value of 0.5 [64] [36]. This discrepancy can be explained by considering that the experimental vortex shedding is not fully correlated along the rod span and thus results in smaller lift fluctuations. It is interesting to notice that the two-dimensional RANS prediction only features a deterministic flow unsteadiness, providing a periodic flow prediction. The spectral broadening around the Strouhal frequency in Fig.7.8(a) is indeed a by-product of the signals truncation, whose effects can be reduced by a data windowing, but not completely removed.

Fig.7.9 shows the wall pressure coefficients at $\phi = 0^o$ and $\phi = 90^o$. A comparison between Figs.7.8 and 7.9 shows that the wall pressure at the base point ($\phi = 0^o$) and the drag have similar spectral behaviours. Analogously, the wall pressure at $\phi = 90^o$ and the lift also do. This confirms Phillips' assumption of considering the wall pressure signal at $\phi = 90^o$ as representative of the fluctuating lift. The base suction coefficient is $-C_{pB} = 1.01$ which is smaller than the experimental value of about 1.2 [58].

Counter-rotating vortices are shed from the cylinder at a Strouhal number $St = 0.23$. The over-prediction of the vortex shedding frequency from a two-dimensional rod is a common CFD result [65] which can be explained to some extent. As argued by Roshko [66], the length of the mean recirculating region behind the rod results from an equilibrium between the base suction coefficient and the *in-plane*

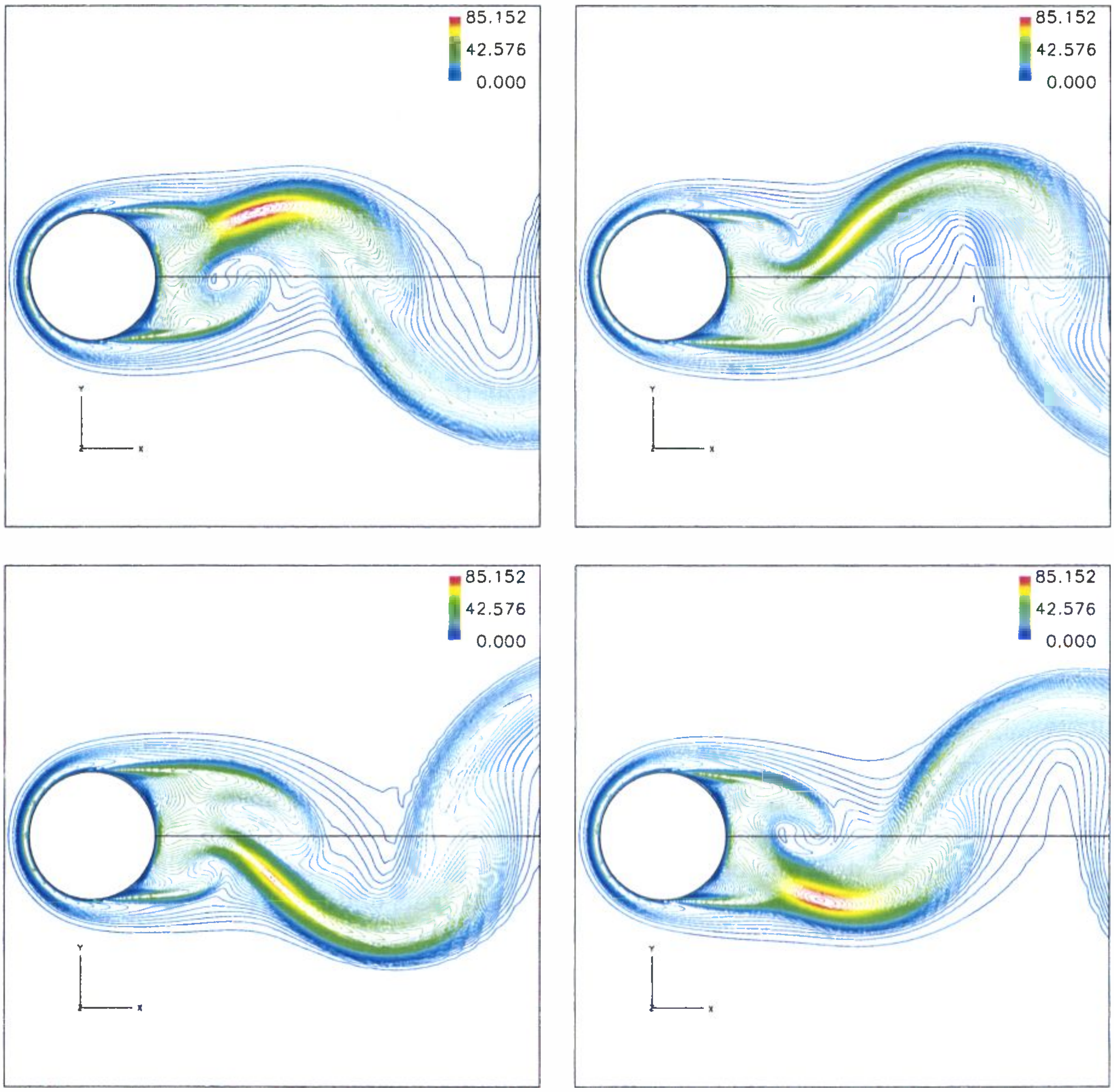

FIGURE 7.7: Kinetic turbulent energy during a vortex shedding period. Snapshots clockwisely arranged.

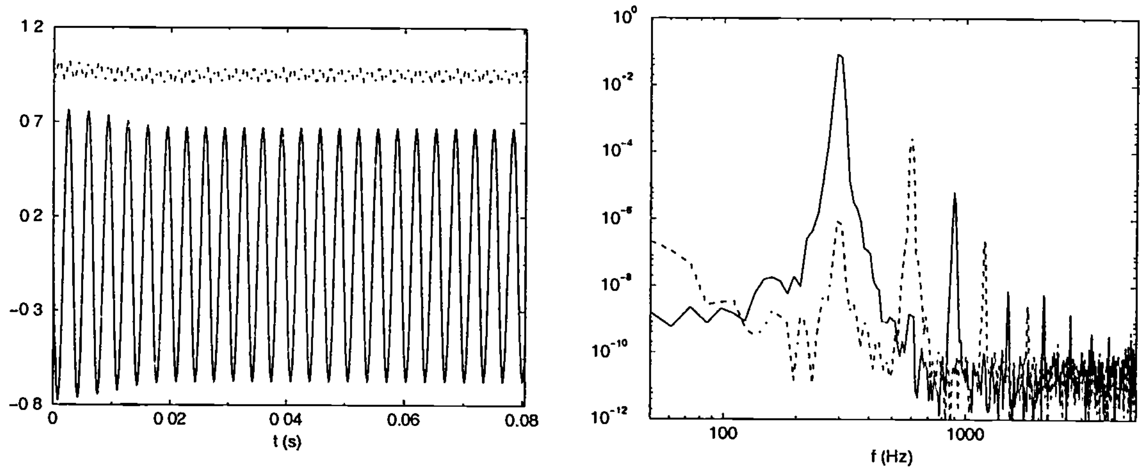

FIGURE 7.8: Aerodynamic force on the cylinder: —— C_l, - - - - C_d. Signals (left), spectra (right).

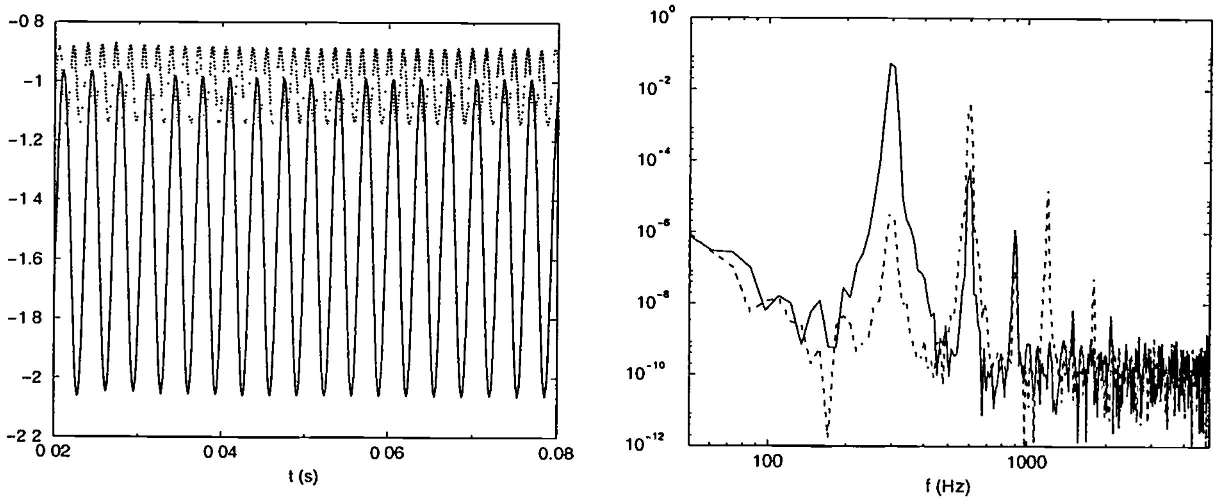

FIGURE 7.9: Pressure coefficient on the cylinder surface. —— $\phi = 90^o$, - - - - $\phi = 0^o$. Signals (left), spectra (right).

Reynolds stresses in the separated flow region. Hence, higher Reynolds stresses correspond to shorter mean recirculating regions. In a 3D flow a part of the energy extracted from the mean flow is used to maintain spanwise velocity fluctuations. As a consequence, the mean recirculating region extends farther from the cylinder and the Strouhal frequency is smaller than in a simulated 2D flow.

Letting $\langle\rangle$ denote the local average of a quantity over a vortex shedding period, the following quantities are plotted in Figs.7.10 and 7.11:
- mean pressure coefficient, i.e.

$$\langle Cp \rangle = \frac{\langle p - p_\infty \rangle}{\frac{1}{2}\rho_\infty V_\infty^2} \tag{7.36}$$

- root-mean-square pressure coefficient, i.e.

$$Cp_{\text{rms}} = \sqrt{\left\langle (Cp - \langle Cp \rangle)^2 \right\rangle} \tag{7.37}$$

- dimensionless mean velocity. i.e.

$$\langle V \rangle = \frac{\sqrt{\langle u \rangle^2 + \langle v \rangle^2}}{V_\infty} \tag{7.38}$$

- dimensionless root-mean-square velocity, i.e.

$$V_{\rm rms} = \sqrt{\left\langle (u\, n_x/V_\infty + v\, n_y/V_\infty - \langle V \rangle)^2 \right\rangle + \frac{2}{3}\langle k \rangle} \tag{7.39}$$

where $n_x = \langle u \rangle / \langle V \rangle$ and $n_y = \langle v \rangle / \langle V \rangle$ are the components of the mean flow direction and $\langle k \rangle$ denotes the mean kinetic turbulent energy[5].

The mean velocity field in Figs.7.10(a) and 7.11(c) highlights the recirculating region behind the rod. It can be observed that the downstream point of minimum $\langle V \rangle$ at $(x/d = 1.2, y = 0)$ coincides with the point of maximum $V_{\rm rms}$ (see Fig.7.11(c)). Conventionally, such a point defines the *vortex formation length* l_F. Measurements made by Szepessy & Bearman [36] over a wide range of Reynolds numbers and rod aspect ratios show a vortex formation length of about $1.5d$. Thus, consistently with Roshko's [66] model, a two-dimensional computation provides a smaller mean recirculating region behind the rod.

Fig.7.11(a) shows the pressure field on the rod surface. The $Cp_{\rm rms}$ peaks at $\phi = 91^o$, which marks the mean location of the separation point.

In Fig.7.12(a) the predicted Strouhal peak of the cross-spectrum between a wall pressure signal at $\phi = 90^o$ and that at different ϕ around the cylinder is checked against the experimental data. Discrepancies in the separated flow region can be observed up to $\phi \simeq 50^o$. Furthermore, as previously discussed, the measured cross-spectrum peaks at $\phi = 100^o$.

The cross-spectra peak values at the first and second harmonics are plotted in Fig.7.12(b) and 7.12(c), respectively. A fairly good agreement arises between experimental data and numerical predictions. Because of the major contribution given by the rod base point to the first harmonic ($2f_0$) fluctuations, the first harmonic peak of the cross-spectrum is maximum when the movable probe is at $\phi = 0^o$. In addition, a local maximum occurs at the angular position $\phi = 85^o$. At the second harmonic ($3f_0$) the computed cross-spectrum peaks when the movable probe is at $\phi = 12^o$, whereas the experimental data exhibit a maximum at about $\phi = 25^o$. Furthermore, both the numerical and the experimental cross-spectra exhibit a local maximum when the movable probe is at $\phi = 95^o$.

Comparisons between numerical and experimental values of some representative quantities are summarized in Table 7.1.

7.4.4 Acoustic Results

In this subsection acoustic results are presented and discussed. The three-dimensional flow necessary for the acoustic computation is recovered by a spanwise repetition of the computed two-dimensional flow. A deterministic repetition is referred to as 2D, whereas, a randomly perturbed repetition is referred to as 3D (spanwise statistical model). The wave propagation is of course three-dimensional, since the three-dimensional free space Green's function is used in the FW-H integral formulation.

First, the consistency of the no-quadrupole approximation is checked by comparing 2D results obtained from different integration surfaces. Second, 2D and 3D results are checked against experimental data.

[5]Equation (7.39) is based on the hypothesis of local isotropy of the turbulent velocity field, i.e. $k = \frac{3}{2}\overline{u'u'}$, where u' is the Reynolds fluctuating component of the velocity field in the $x-$direction. Clearly, in the framework of unsteady RANS modeling, a fluctuating k only reaches sense if the averaging time is longer than that associated with the slowest turbulent motions, but is much smaller than the time scale of the flow unsteadiness (the vortex shedding period in the present study).

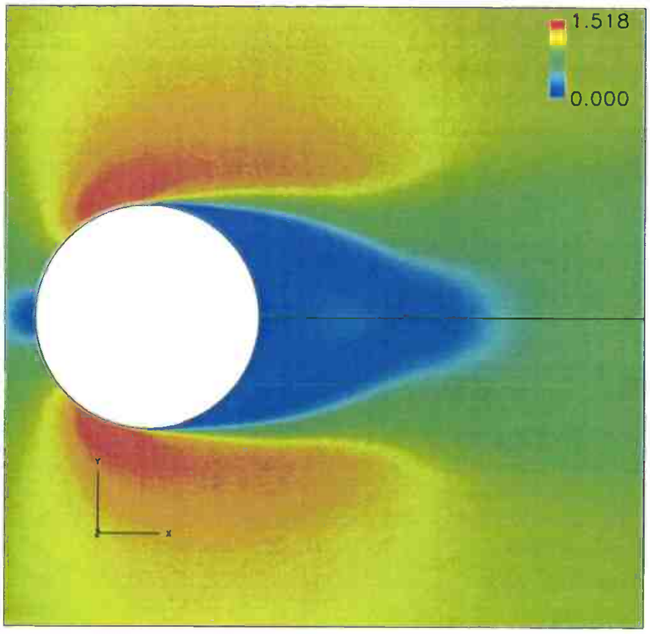

a) $\langle V \rangle$

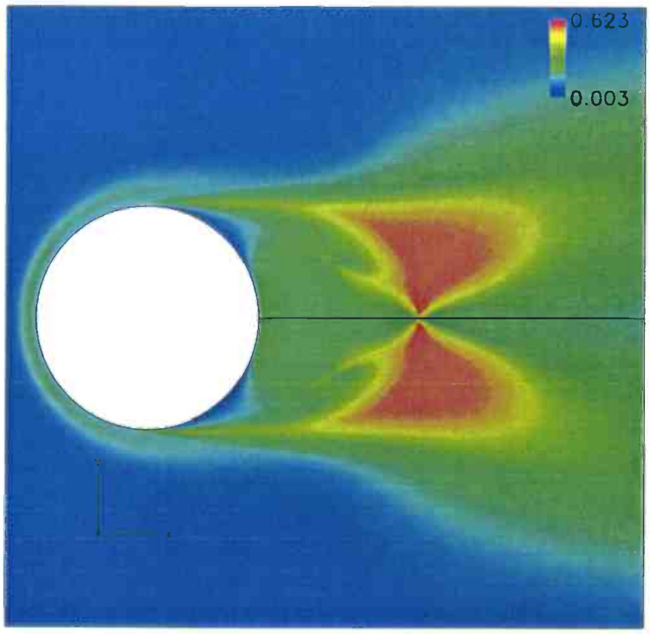

b) Vrms

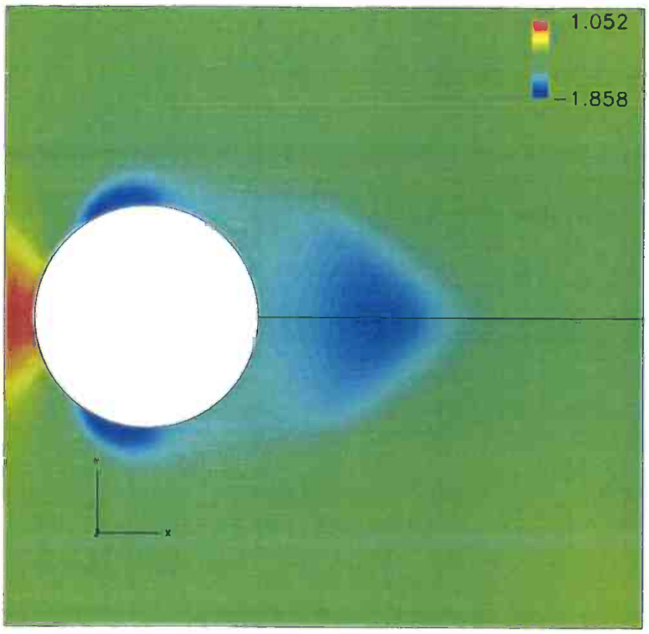

c) $\langle Cp \rangle$

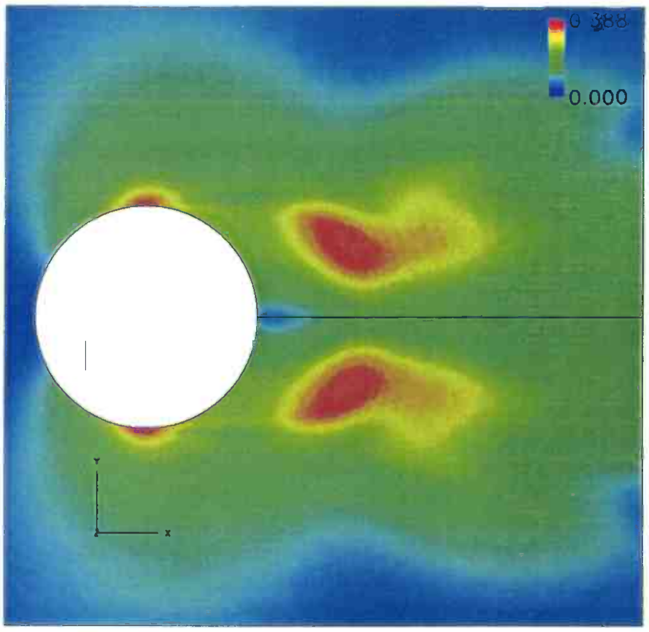

d) Cprms

FIGURE 7.10: Mean and fluctuating flow past the cylinder.

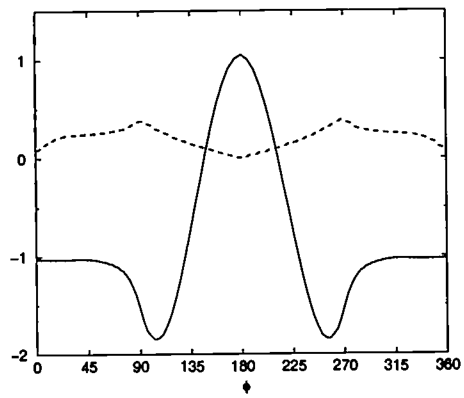

a) Wall pressure field: —— $\langle Cp \rangle$, - - - - Cprms

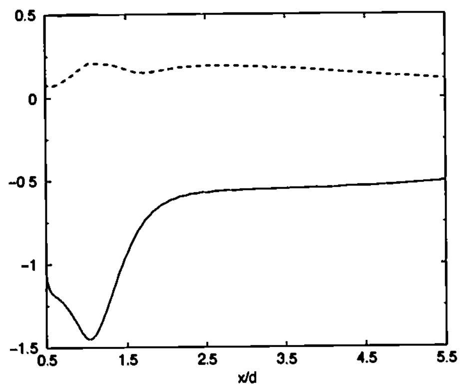

b) Pressure field in the wake of the rod ($y = 0$): —— $\langle Cp \rangle$, - - - - Cprms

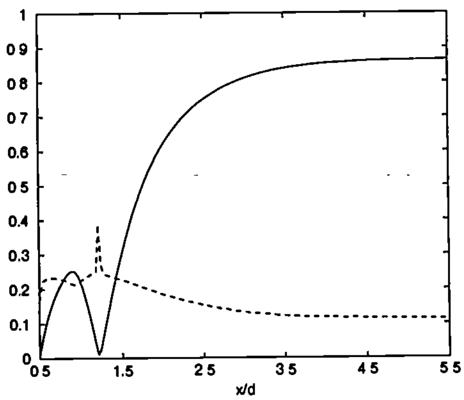

c) Velocity field in the wake of the rod ($y = 0$): —— $\langle V \rangle$, - - - - Vrms

FIGURE 7.11: Mean and fluctuating flow past the cylinder.

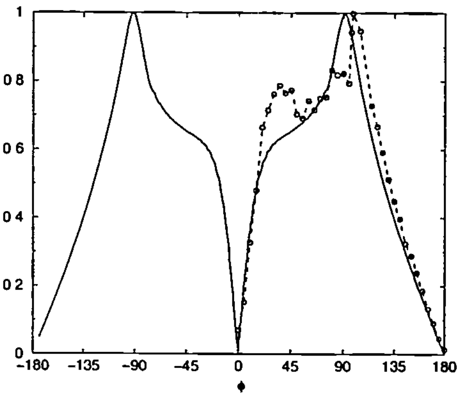

a) $f = f_0$

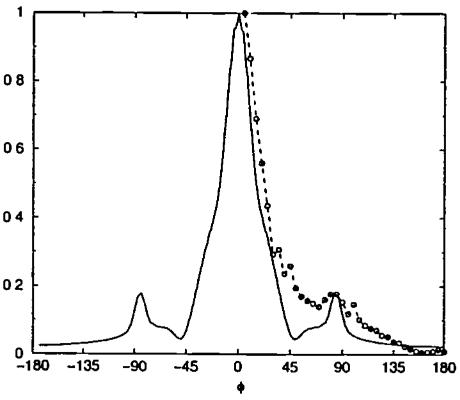

b) $f = 2f_0$

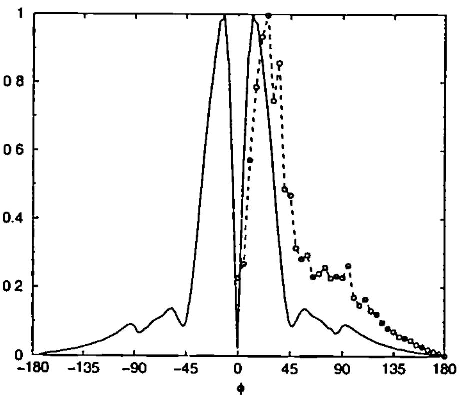

c) $f = 3f_0$

FIGURE 7.12: Peaks of the normalized cross-spectrum amplitude $|S_{12}/\max(S_{12})|$ between a reference probe at $\phi = 90^o$ and probes at different ϕ. o Experimental data, —— RANS results.

TABLE 7.1: Comparison between experimental data and RANS results. Experimental data from: a) Schewe [64], b) Williamson [58], c) Szepessy & Bearman [36]. d) The predicted drag coefficient does not account for the viscous stresses.

	Experimental	Numerical
St	0.2^a	0.234
$C_{l\,max}$	$0.5^{a,c}$	0.65
C_d	1.1^a	0.95^d
$-C_{pB}$	1.2^b	1.01
l_F	1.5^c	1.2

In Fig.7.13(b) the sound directivities computed through equations 6.41 and 6.42 applied to the surfaces on Fig.7.13(a) are plotted. The agreement within 1 dB, which is fairly good, shows both the consistency of the penetrable surface FW-H formulation and the physical adequacy of neglecting the quadrupole contribution in the acoustic prediction.

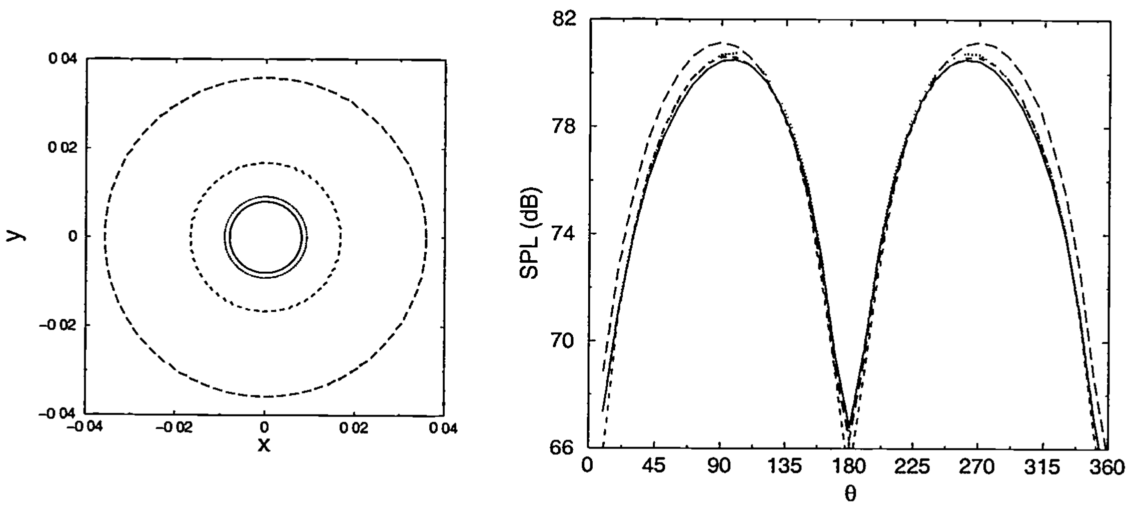

FIGURE 7.13: Directivity pattern (right) obtained by integrating upon different surfaces (left) around the cylinder: —— S1 (cylinder surface $r = 8\times10^{-3}$m), ... S2 ($r = 9.11\times10^{-3}$m), - - S3 ($r = 1.67\times10^{-2}$m), — — S4 ($r = 3.58 \times 10^{-2}$m). 2D computations.

The corresponding pressure signals computed at $\theta = 90^o$ from the 4 integration surfaces are plotted in Fig.7.14. The relative differences $\Delta p'/\max(|p'|)$ between the S1 results and those from S2 to S4 are plotted in Fig.7.15. Significant discrepancies occur only for the outer surface S4 and are likely to be due to a degraded CFD accuracy far from the cylinder. The spectra of $\Delta p'/\max(|p'|)$ in Fig.7.15(b) exhibit peaks at both even and odd harmonics. Although the reciprocal influence between physical and numerical effects on the observed discrepancies cannot be established without computing the volume contribution, these results confirm that the quadrupole contribution can be neglected in the present low Mach number aeroacoustic prediction.

In Figs.7.16 through 7.18, 3D computations are checked against 2D computations and experimental

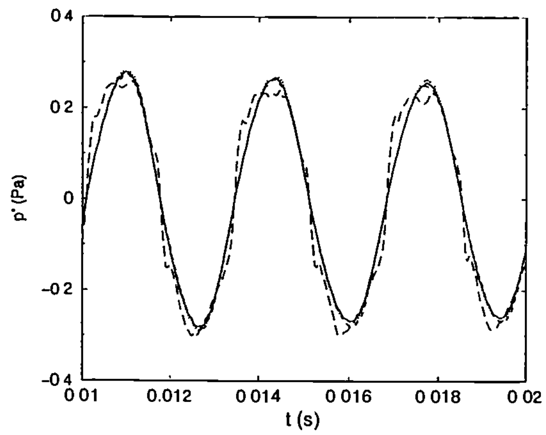

FIGURE 7.14: Acoustic pressure signals computed from: —— S1, ... S2, - - S3, — — S4. 2D computations at an observation angle $\theta = 90^o$.

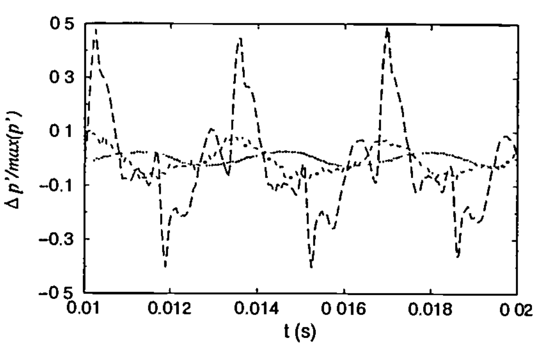

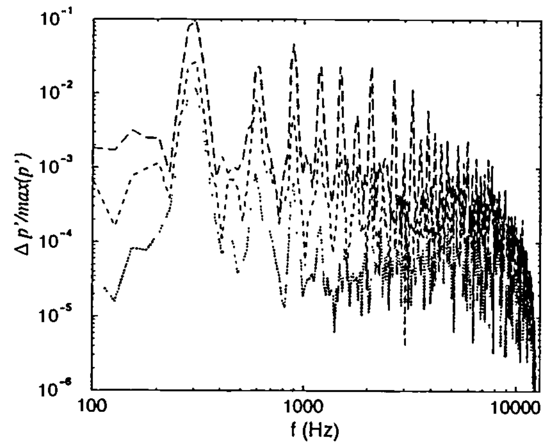

FIGURE 7.15: Relative difference between S1 results and results from: .... S2, - - S3, — — S4. 2D computations at an observation angle $\theta = 90^o$.

measurements. A Gaussian correlation length of $5\,d$ is used in the spanwise statistical model. The computed acoustic spectra at each observation point are obtained by averaging over 100 spectra, each obtained with a different value of the random generation seed.

In Fig.7.16 a comparison is shown between 2D and 3D acoustic signals. The random phase distribution along the rod span clearly results in a randomly amplitude modulation.

In Fig.7.17 2D and 3D computations are checked against experimental data. The measured power spectral density have been integrated upon frequency intervals of $\Delta f = 12\,\mathrm{Hz}$. Furthermore, in order to take into account the aerodynamic Strouhal frequency overprediction, the experimental data (f,dB) have been scaled to (f',dB'), i.e.

$$f' = \frac{\mathrm{St_{num}}}{\mathrm{St_{exp}}} f, \quad \mathrm{dB'} = \mathrm{dB} + 20 \log \left(\frac{\mathrm{St_{num}}}{\mathrm{St_{exp}}} \right) \tag{7.40}$$

where the level correction accounts for the fact that the sound level is proportional to the vortex shedding frequency, as shown in equation (7.8).

As expected from a deterministic flow prediction, 2D results only exhibit harmonic peaks without spectral broadening. On the contrary, forcing an *ad hoc* random behaviour permits to better fit the broad band noise levels. Moreover, the harmonic peaks are better predicted by 3D computations.

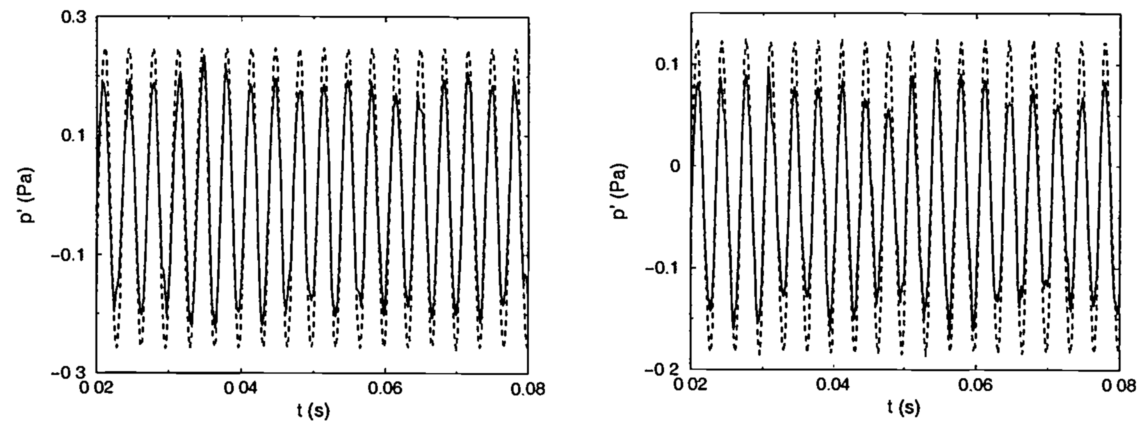

a) $\theta = 90^o$

b) $\theta = 40^o$

FIGURE 7.16: Acoustic signals: ——2D computation, - - - -3D computation.

At frequencies higher than about 3000 Hz the sound pressure level is underestimated. However, as previously pointed out, the experimental data are likely to be contaminated by the background noise (mainly, flow noise from the end plates), which persists over a wider frequency range.

In Fig.7.18 the 3D prediction of the noise directivity is compared to the measured one. Numerical results have been obtained by adding the Fourier contributions in the overall frequency range, i.e. [12 Hz, 12.4kHz], whereas the experimental values have been obtained by integrating the power spectral density upon the frequency range [100 Hz, 1000 Hz]. The agreement is good. Furthermore, a dipole-type $\sin\theta$ interpolation of the experimental data shows that the maximum radiation occurs at an observation angle slightly greater than 90^o. This is confirmed by the numerical prediction.

7.5 Conclusions

A hybrid *Aeolian tones* RANS/FW-H aeroacoustic prediction was performed at a Reynolds number of 2.2×10^4.

A deterministic periodic flow was predicted through a two-dimensional RANS approach. The Strouhal frequency was overestimated and the vortex formation length was underestimated. These results were justified by invoking the fact that, in a two-dimensional computation, all the energy extracted from the mean flow is used to maintain in-plane fluctuations.

The application of the FW-H acoustic analogy to penetrable integration surfaces around the cylinder showed that the direct contribution of the detached eddies to the overall sound remains negligible, even though the lower end of the spectrum might be affected by surrounding broad band jet noise.

Acoustic results based on the spanwise repetition of the computed two-dimensional flow only featured the spectral harmonic peaks. Therefore, in order to partially recover the three-dimensional character of the flow, a statistical behaviour of the vortex shedding phase was forced into the spanwise repetition of the aerodynamic field. Phase lags were modeled on the basis of two-point statistical measurements and allowed the acoustic signals to undergo *ad hoc* amplitude modulations. As a consequence, the spectral broadening around the shedding frequency and its harmonics was quite well featured by merely performing a two-dimensional aerodynamic computation.

This type of approach is a promising tool wherever full three-dimensional flow computations are not affordable (as in turbomachines, for instance): two-dimensional unsteady RANS provides a deterministic unsteady flow to which the statistical model may be applied.

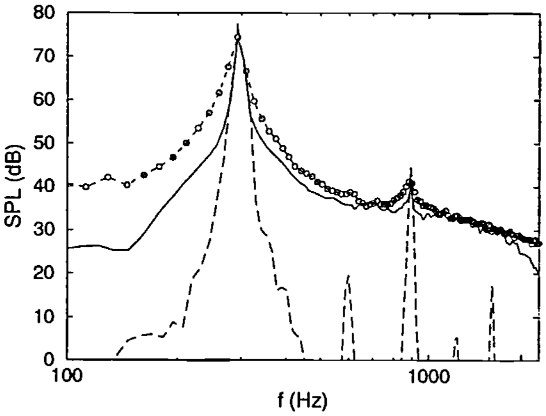

a) $\theta = 90^o$

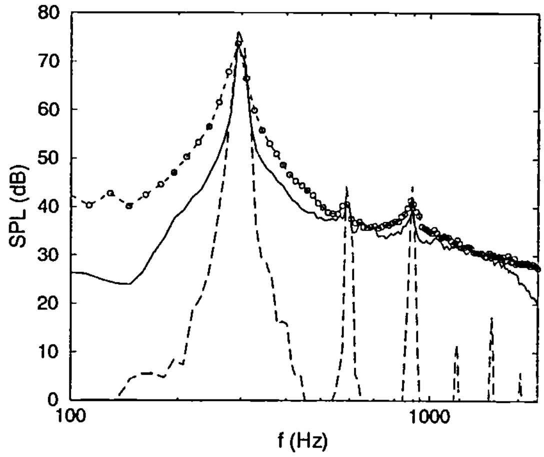

b) $\theta = 80^o$

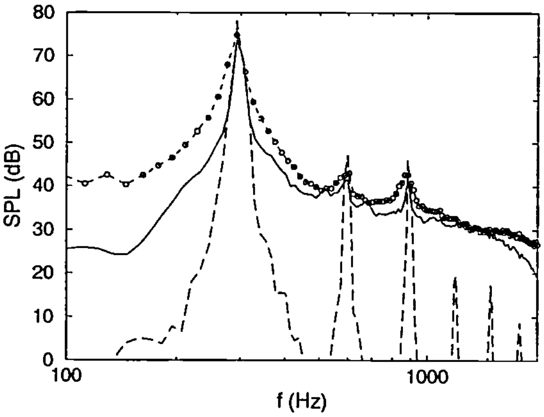

c) $\theta = 70^o$

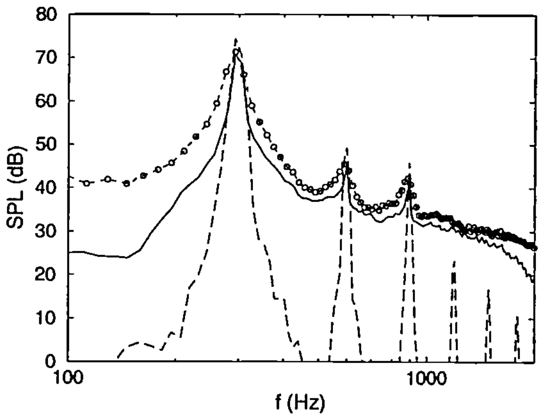

d) $\theta = 60^o$

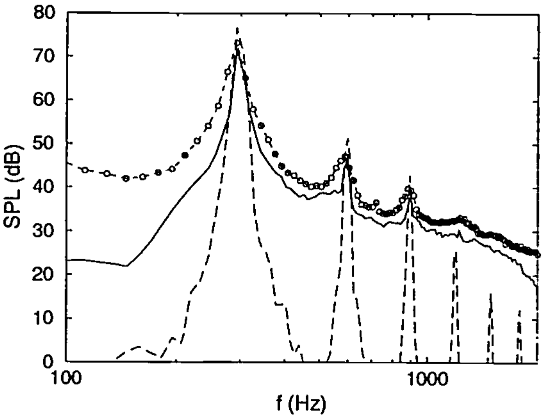

e) $\theta = 50^o$

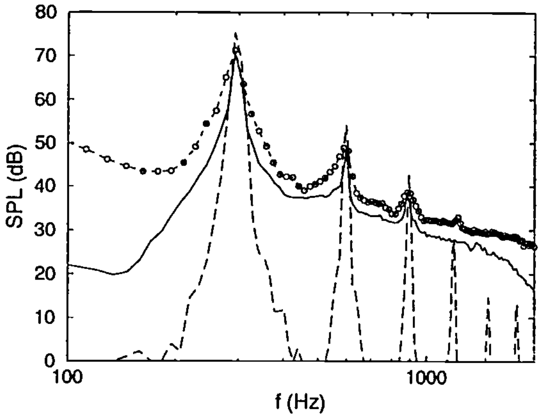

f) $\theta = 40^o$

FIGURE 7.17: Acoustic spectrum: o Experimental data, ——3D computation, — —2D computation.

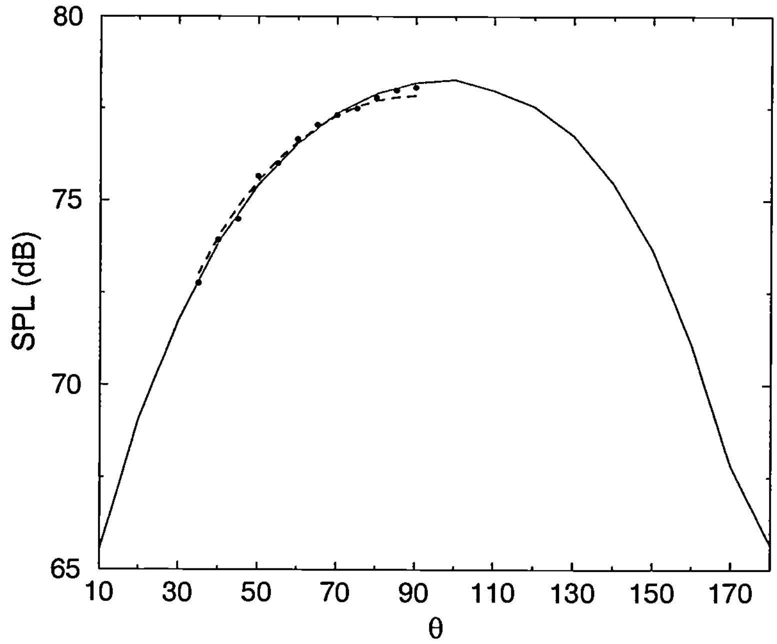

FIGURE 7.18: Directivity pattern: —— 3D computation, ••Experimental data, — — $K \sin\theta$ interpolation.

8

RANS/FW-H Rod-Airfoil Aeroacoustic Prediction

In this chapter we present results concerning a numerical aeroacoustic investigation of the rod-airfoil configuration. The capability to predict the noise generated by the unsteady flow past an obstacle hinges primarily on the accuracy of the aerodynamic simulation in modeling the physics of the flow. Therefore, more emphasis is hereafter given to the aerodynamic aspects of the rod-airfoil aeroacoustic problem.

A RANS aerodynamic computation is performed by means of the CFD solver *Proust* [62] described in section 8.3.1. The acoustic prediction is performed by means of the FW-H solver *Advantia* [41] described in section 6.2. The spanwise statistical model described in chapter 7 is exploited in order to account for the intrinsic three-dimensional character of the flow in the aeroacoustic prediction.

Two flow configurations are considered, corresponding to the values $\alpha = 0^o$ and $\alpha = -4^o$ of the airfoil angle of attack. The geometrical parameters and the free-stream velocity used in the computations are the same as those adopted in the experiments presented in chapter 5.

In the first part of the chapter we discuss the conceptual adequacy of a hybrid RANS/FW-H aeroacoustic prediction. In the second part we describe the rod-airfoil aerodynamic computation. In the third part we discuss both aerodynamic and acoustic results. These are checked against the experimental data discussed in chapter 5.

8.1 Introduction

Distortion and non-linear rearrangement of the vorticity field occur during a direct or nearly direct impingement of a vortex onto an airfoil leading edge. Furthermore, if the leading edge is sharp or the impinging vortex is intense enough, boundary-layer separation and shedding of a secondary vortex may occur.

Numerical simulations are usually performed in order to investigate vortex-body interactions in many circumstances of practical interest. Two distinct numerical approaches can be adopted to simulate a vortex-airfoil interaction. The first is the primitive (or conservative) variable approach, which consists in solving a system of governing partial differential equations, such as the Euler or the Navier-Stokes equations, with a suitable set of boundary conditions. The second is the linearized approach which is based on the following approximation: for mean potential flows with small amplitude vortical and entropic disturbances imposed upstream, the unsteady velocity field can be split into a known rotational component and an unknown potential component that satisfies a linear inhomogeneous non constant-coefficient convective wave equation.

The primitive variable approach requires long computational time and large computer memory. In addition, because of the nonlinear character of the flow, the accuracy of the unsteady solution is strongly affected by the physical consistency of the far field boundary conditions. However, classic CFD methods have proven to be quite effective in describing a vortex-body interaction problem: both distortion of the vorticity field and viscous effects can be adequately simulated. Navier-Stokes solvers require an adequate grid resolution in order to minimize the numerical dissipation of the vorticity field. Wake & Choi [67] used a $5th$ order solver to simulate the convection of a two-dimensional vortex and showed that a minimum of 14 points across the vortex was necessary in order to preserve the vortex strength.

A simplified primitive variable approach is usually performed, provided that the flow is supposed to be incompressible. It consists in describing the incident vorticity field by means of discrete vortices convected by a flow that satisfies a Laplace's equation. Boundary value methods or conformal mapping techniques are then adopted to account for the presence of a body in the flow. Discrete-vortex simulations are particularly suitable to investigate the effects of the vortex distortion in vortex-airfoil interactions. Furthermore, phenomena related to the viscosity of the fluid, such as vortex-shedding and boundary-layer separations, can be simulated by means of additional conditions. An example of a simplified primitive variable approach has been proposed in chapter 2, where a Kármán-Trefftz conformal mapping has been used to describe the unsteady vortical flow past a thick cambered airfoil.

The linearized approach is valid only for small amplitude disturbances, a requirement that is usually satisfied in many flows of practical interest. Methods based on the solution of a single linear wave equation have significant advantages over methods based on the solution of a system of nonlinear partial differential equations:

- the computational time is far shorter;
- stable and accurate differencing schemes are simpler to be derived;
- physically consistent far field boundary conditions can be imposed, which allow more accurate unsteady aerodynamic predictions.

Linearized approaches are particularly suitable for three-dimensional oblique blade-vortex interactions in highly compressible flows. Moreover, for periodic gust-airfoil interactions, the linearized approach provides an effective way to investigate the effects onto the near and far pressure field of both the wavelength of the incident vorticity field and its orientation with respect to the blade leading edge.

Numerical predictions based on potential flow modeling of isolated line-vortices convected past lifting airfoils [68] [32] show that:

- the noise level is strongly affected by the vortex trajectory;
- the vortex trajectory is a strong nonlinear function of the airfoil lift, the vortex initial position and the vortex circulation;
- the noise levels are overpredicted, especially during direct vortex-airfoil interactions. This is mainly due to the fact that a line-vortex model does not account for the vortex distortion during a close encounter.

The distortion of the vorticity field is a nonlinear rearrangement mechanism which occurs especially when the vortex and the curvature radius of the airfoil leading edge have a comparable size. Its effect onto the interaction process is twofold: on one hand, the vortex distortion smoothes the dependence of the interaction process upon some parameters of the problem. On the other hand, it reduces the loading peaks induced under critical interaction conditions (e.g. direct vortex impingement onto the leading edge). These effects have been discussed in section 4.2 where a cloud of line-vortices has been used to model a vortex of non compact size impinging onto the airfoil leading edge.

Although nonlinearity plays a dominant role in a direct vortex-airfoil interaction, it is not the only affecting factor. Vortex diffusion within the airfoil boundary-layer, vortex-shedding from the trailing edge and boundary-layer separation at the leading edge are mechanisms related to the viscosity of the fluid. These must be accounted for when a prediction is made of the vortex-airfoil interaction noise and unsteady loading.

Hardin & Lamkin [69] performed a direct numerical simulation of the unsteady aerodynamic field around a lifting Joukowski airfoil interacting with a distributed vortex. Furthermore, they exploited the theory developed by Howe [20] in order to predicted the aerodynamic sound generated by the vortex-airfoil interaction. A two-dimensional and incompressible flow was considered and the chord based Reynolds number was 200. The impinging vortex was artificially created upstream of the airfoil. Hence, Hardin & Lamkin pointed out that aerodynamic noise is generated even in the absence of the impinging vortex, as a consequence of the interaction between the boundary-layer vorticity and the airfoil trailing edge. Furthermore, they argued that the noise resulting from a direct vortex-airfoil interaction is quite less impulsive when both viscous effects and the distributed nature of the impinging vortex are taken into account. Finally, they observed that a vortex loses its organized structure and is strongly diffused after impinging onto the airfoil leading edge.

Rai [70] used a fifth-order accurate, Osher-type upwind scheme in order to solve the thin-layer, Navier-Stokes equations at each time-step in a fully implicit framework which was second-order-accurate in time. The differencing scheme was shown to preserve the vortex structure for much longer time than both central and upwind second-order accurate schemes. The vortex preserving test consisted in checking the core pressure of a Lamb-type vortex convected by a uniform flow. The fifth-order accurate method was then applied to predict the unsteady aerodynamic field generated by the interaction between a Lamb-type vortex and an NACA-0012 airfoil at a zero angle of attack. The vortex rotated clockwise, such that the image vortex convected it faster along the lower airfoil side. The Baldwin-Lomax closure model [71] was used to calculate the eddy viscosity. Three simulations were performed at different free-stream Mach numbers and different vortex parameters (circulation, initial position and core radius). The first numerical prediction was concerned with a non direct vortex-airfoil interaction at a Mach number of 0.536 and a chord based Reynolds number of 1.3×10^6. The vortex parameters were chosen in order to fit the experimental conditions of Caradonna *et al.* [72]. A good agreement was obtained between numerical and experimental results. The second numerical simulation was concerned with a direct vortex-airfoil interaction. The flow conditions were the same as in the first case, but the vortex circulation was higher. Distortion and splitting of the impinging vortex were predicted. The upper and lower vortex fragments were convected with different velocities along the respective airfoil sides, and interacted with the airfoil wake. The third computation was concerned with a non direct vortex-airfoil interaction in transonic flow conditions. The free-stream Mach number was 0.8, while all the other flow parameters were the same as in the second case. The two shocks on the upper and lower airfoil sides were perturbed from their symmetric steady positions by the presence of the vortex. Furthermore, on the lower side, the vortex-shock interaction induced a large bubble of separation from the shock foot up to the airfoil trailing edge. The structure of the lower shock was strongly affected by the vortex passage: a shock bifurcation on the wall was observed.

In the quoted investigations the impinging vortex was artificially introduced into the flow field. The same philosophy was adopted by the author in chapter 2 where vortices were located upstream of the airfoil. Contrarily, the present investigation is concerned with an unsteady RANS simulation of a rod-airfoil configuration where the impinging vortices are shed from the rod. Though more expensive, this approach reduces the arbitrariness of the vortex parameters, e.g. initial position, size and strength, and does not require a core modeling. Two flow configurations are investigated, corresponding to two values of the airfoil angle of attack.

A hybrid RANS/FW-H aeroacoustic prediction of the rod-airfoil configuration is herein performed. The same approach was exploited in chapter 7 in order to predict the noise from an isolated rod and to show the feasibility of a hybrid aeroacoustic prediction. We used unsteady RANS results regardless to their physical adequacy to represent the unsteady aerodynamic field. Contrarily, in this chapter we discuss the conceptual adequacy of an unsteady RANS computation aimed to aeroacoustic predictions.

8.2 On the Adequacy of a Hybrid RANS/FW-H Aeroacoustic Prediction

In chapter 6 we showed that the FW-H formulation can be successfully applied to noise computations by using penetrable integration surfaces which are in complex motion with respect to a moving observer. Several test cases were performed by inputing a linear field upon the integration surface.

In chapter 7 we were concerned with the feasibility of an aeroacoustic prediction through a hybrid CFD/FW-H computation. Since the FW-H equation is an exact rearrangement of the flow governing equations, an aerodynamic field was inputed on the integration surface. *Aeolian tones* were predicted and checked against experimental data showing the consistency of the hybrid approach. We assumed that unsteady RANS results are adequate to represent an unsteady flow and that they can be exploited for an aeroacoustic prediction. In this section we discuss the conceptual adequacy of a hybrid RANS/FW-H aeroacoustic prediction.

Unsteady RANS simulation consists in allowing some slow time variations of the *mean* flow field. Only some low-frequency modes (of the order of few hundred Hertz) and the mean flow are directly computed. In this approach the velocity field undergoes the following decomposition

$$\mathbf{u}(\mathbf{x},t) = \overline{\mathbf{u}}(\mathbf{x}) + \langle \mathbf{u}(\mathbf{x},t) \rangle + \mathbf{u}'(\mathbf{x},t) \tag{8.1}$$

The first term denotes the time average of the exact solution, the second term denotes a *conditioned statistical average* and the last term is a turbulent fluctuation. Thus, $\langle \mathbf{u} \rangle$ is related to the coherent modes of the unsteady flow and u' constitutes the random part of the flow. The unsteady RANS mathematical model describes the quantity $\overline{\mathbf{u}} + \langle \mathbf{u} \rangle$, whereas the random contribution u' is described by a turbulence model.

The physical adequacy of an unsteady RANS simulation can be justified to some extent: typically, if the fluctuating field is the superposition of two weakly coupled unsteady mechanisms, the first well described by a turbulent closure model, the second not accounted for by it, then the unsteady RANS strategy may be appropriate to feature the latter unsteadiness. An important question arises about a conflict between the time scales: in order to assume that the turbulence described by the model reaches a steady state during a typical cycle of the non modeled unsteadiness, the former must cover a range of frequencies which is higher than that of the latter. In other words, lower frequency components of the modeled turbulence may conflict with the non modeled unsteadiness. What happens in such a case?

1. Both low-frequency components are taken into account in some way by the non modeled unsteady description. Then they may be taken into account twice since the closure model handles the turbulent components regardless to their frequency.

2. Low-frequency components are not taken into account by the non modeled unsteady description. Then they may not be taken into account at all or in a wrong way since the RANS model considers turbulence to be statistically steady during a time which is of the same order as the typical turnover time of these largest eddies.

Another conceptual inadequacy of the unsteady RANS simulation arises from the fact that the modeled turbulent components are more likely to interact with non modeled unsteadiness in the real flow. This interaction is likely to be ill-modeled by a RANS model since two quite similar physical phenomena (both unsteady, with comparable time scales) are described in a completely different way.

In the present chapter we apply the unsteady RANS approach to describe the vortex shedding behind a cylinder at a Strouhal frequency of 250 Hz ($d = 0.016\,\mathrm{m}$, $V_\infty = 20\mathrm{m/s}$). Hence, the frequency of the coherent flow unsteadiness is sufficiently low to hope that the contamination due to a time scale conflict has a negligible effect.

Concluding, the term *Reynolds Averaged* is used throughout the present work not in its conventional definition, which implies averaging over an infinite time interval, but to denote averaging over a time which is longer than that associated with the slowest turbulent motions but is much smaller than the vortex shedding period.

8.3 The Rod-Airfoil Aerodynamic Simulation

8.3.1 The Aerodynamic Solver

The flow solver *Proust* [62] is used to compute the unsteady aerodynamic field in the rod-airfoil configuration. The main features of this CFD code are described below.

The equations solved by *Proust* are the unsteady compressible Reynolds-averaged Navier-Stokes equations. The space discretization is based on a MUSCL finite volume formulation with moving structured meshes, which uses vertex variable storage.

The convective fluxes are evaluated by using an upwind scheme. Three different schemes were implemented: Van Leer's flux vector splitting with the Hanel correction, Roe's approximate Riemann solver and Liou's advection upwind splitting method. A hybrid method combining the advantages of the central scheme in subsonic regions with the properties of the upwind scheme through discontinuities has been introduced to reduce the numerical losses in low Mach number regions. The viscous terms are computed by a second order centered scheme.

The resulting semi-discrete scheme is integrated in time using an explicit five steps Runge-Kutta time marching algorithm. Convergence toward steady states is accelerated by using local time-stepping and residual smoothing. A dual time-stepping technique is also applied for unsteady simulations.

Turbulence effects are described by two-equations models, $k - \varepsilon$ and $k - \omega$, the $k - \omega$ model being either linear or non linear.

Inlet and outlet conditions on free boundaries are imposed by retaining the outgoing characteristics, since these provide information from inside the domain. The incoming characteristics are replaced by physical boundary conditions, i.e. total pressure, total temperature and flow angles for a subsonic inlet, static pressure for a subsonic outlet. Alternatively, non reflective boundary conditions in the form proposed by Thompson are imposed on the outer boundaries. Adiabatic walls are introduced by imposing a zero-velocity condition and a zero-heat flux. Ghost cells in which the equations are not solved are built around the domain in order to impose geometrical boundary conditions, like periodicity and symmetry.

Proust code performs parallel computations in multi domains with Parallel Virtual Machines library (PVM).

8.3.2 Computational Parameters

The following code options are used in the present computation:

- two-dimensional flow;
- centered spatial scheme;
- 5 steps Runge-Kutta explicit temporal scheme without dual time-stepping technique;
- no-slip and adiabatic wall conditions on the physical surfaces;
- non-reflecting boundary conditions on the outer boundaries;

- $k - \omega$ closure model by Wilcox [63];

- molecular viscosity μ determined via the Sutherland's law.

The computational time-step is 6×10^{-8} s corresponding to about 6.5×10^4 iterations per shedding cycle.

8.3.3 Flow Parameters and Initial Conditions

Counter-rotating vortices are shed from the cylinder without artificial forcing. Nevertheless, the potential flow field of a strong line-vortex in proximity of one rod separation point is used as initial solution in order to induce a vortex shedding as soon as the computation is started. This strongly reduces the computational time required for convergence towards a permanent unsteady flow.

A uniform density field is initially set, i.e. $\rho = 1.225\,\mathrm{kg/m^3}$. The flow velocity is calculated solving analytically an approximated potential problem. $V_\infty = 20\,\mathrm{m/s}$ is the inflow velocity and $p_\infty = 101253.6\,\mathrm{Pa}$ is the free-stream pressure. Then, the pressure field is calculated via the Bernoulli equation. The reference molecular viscosity is set to $\mu_\infty = 1.78 \times 10^{-5}\,\mathrm{kg/ms}$.

The turbulent kinetic energy has a uniform initial value of 0.01 as measured in experiments, namely $\rho k = 0.5\rho\,(0.01\,V_\infty)^2$. The value of the second turbulent variable is initially set to $\omega = \rho k / A\mu_\infty$, with $A = 5$. The same value of ω is imposed on the physical surfaces.

An exponential boundary-layer is used to replace the potential solution near the physical surfaces where a no-slip initial condition is imposed. The kinetic turbulent energy is also set to zero on the walls.

The inflow boundary conditions remain the same throughout the computation.

8.3.4 Geometrical Parameters

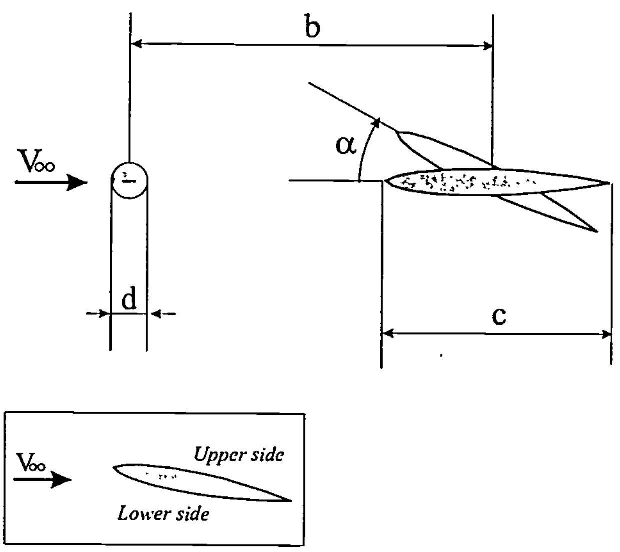

FIGURE 8.1: Geometrical parameters of the rod-airfoil configuration. $d = 0.016\,\mathrm{m}$, $c = 0.1\,\mathrm{m}$ and $b = 0.162\,\mathrm{m}$.

The geometrical parameters the rod-airfoil configuration are the same as those of the experimental configuration sketched in Fig.8.1. The Reynolds number based on the airfoil chord is about $\mathrm{Re}_c = 1.38 \times 10^5$. The Reynolds number based on the rod diameter is about $\mathrm{Re}_d = 2.2 \times 10^4$.

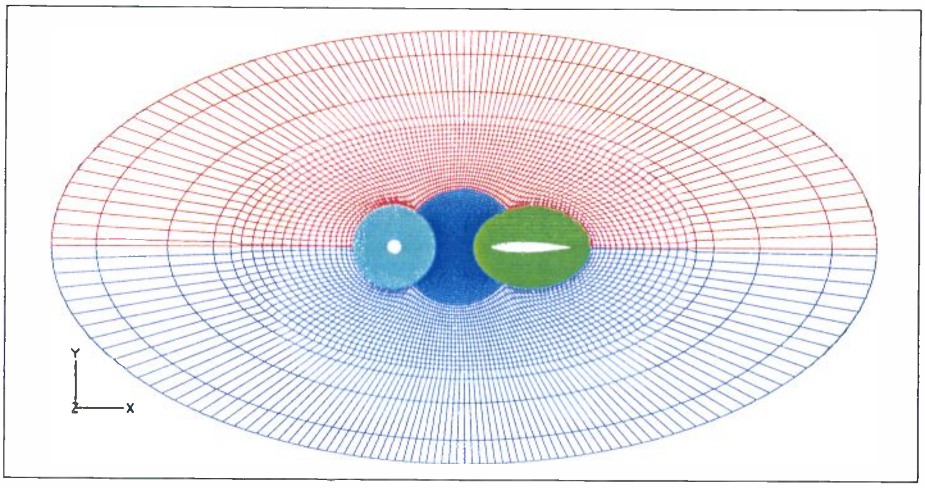

FIGURE 8.2: Overview of the computational mesh.

8.3.5 Computational Mesh

The computational mesh is based on 54640 grid points and is split into 5 structured domains. An overview of the mesh is shown in Fig.8.2. Different computational domains are plotted in different colors. These are:

1. a (201×80) O-grid around the cylinder;
2. a (201×80) O-grid around the airfoil;
3. a (101×80) rectangular grid connecting the domains 1 and 2;
4. a (180×40) rectangular grid extending the outer boundary of the computational domain;
5. a (180×40) rectangular grid extending the outer boundary of the computational domain.

The cylinder grid is circumferentially clustered in the wake region. The minimum circumferential spacing at the base point is $9.07 \times 10^{-3}\, d$, and the thickness of the mesh wall layer is $7.50 \times 10^{-4}\, d$, d denoting the rod diameter.

The airfoil grid is build around a Kármán-Trefftz airfoil fitting a NACA-0012 airfoil. The thickness of the mesh wall layer varies from $6.40 \times 10^{-5}\, c$, at the leading edge, to $1.42 \times 10^{-3}\, l$, at the airfoil thickest section, c denoting the airfoil chord. At the airfoil trailing edge the thickness of the mesh wall layer is $2.61 \times 10^{-4}\, l$.

The mesh topology is the same for the two angles of attack[1].

The parallel computation does not require averages at the block interfaces. Thus, by equal grid point distributions, the splitting of the computational domain does not affect the numerical accuracy of the solution. However, in order to reduce the numerical dissipation due to the grid stretching, the grid is smoothed at the interfaces. In Fig.8.3 the innermost region of the computational mesh is shown.

8.4 The Rod-Airfoil Acoustic Computation

The acoustic field is computed in the time domain by applying the FW-H acoustic analogy to aerodynamic data computed on various contours around the rod-airfoil equipment. The flow three-dimensionality

[1]The five block mesh used in the present computation has been obtained by using an *ad-hoc* code implemented by the author. The code allows to obtain a family of rod-airfoil meshes by simply inputing the geometrical parameters of the configuration.

is partially recovered by assuming the aerodynamic field to undergo a Gaussian correlation in the spanwise direction. Acoustic results are compared to measurements described in chapter 5.

The retarded time penetrable FW-H formulation proposed by Brentner & Farassat [43], extended to a moving observer in section 6.2 and implemented in the rotor noise code *Advantia* [41] is exploited in the present study. For the purposes of the present investigation, only surface integrals are computed, provided that, at low Mach numbers, the volume sources give a vanishing contribution to the acoustic radiation. The consistency of this approximation is checked by comparing acoustic results obtained from different integration surfaces.

The spanwise statistical model described in chapter 7 is used to force a three-dimensional random behaviour into the aeroacoustic prediction. A Gaussian correlation length of $5\,d$ is used for both the rod and the airfoil. This is roughly equivalent to suppose that the spanwise correlation length on the airfoil surface is the same as that on the rod surface. The acoustic spectra are obtained by averaging over 100 spectra.

1024 aerodynamic fields are used for the acoustic computation (about 9 vortex shedding cycles, $t_{\text{fin}} = 3.15 \times 10^{-2}$ s and $\Delta f = 32.5\,\text{Hz}$). The observation distance from the airfoil mid point is $r = 1.38\,\text{m}$ ($kr = 6.37$ for a typical Strouhal number $St = 0.2$).

Both the observer $\mathbf{X}$ and the integration surface $f = 0$ move at the constant velocity $c\mathbf{M}_o = -V_\infty \hat{\mathbf{i}}$ and the flow at infinity is at rest.

Integrations are performed upon the rod and the airfoil surface, and upon penetrable surfaces around the airfoil and the rod-airfoil system. The aerodynamic field on both physical and penetrable surfaces is extracted directly from the CFD solution. In addition, the aerodynamic data are interpolated upon penetrable surfaces which do not coincide with mesh surfaces.

In order to deal with truncated time series, data are multiplied by the Tukey weighting function $w(t) = 0.815\,[1 - \cos(2\pi\, t/t_{\text{fin}})]$ before performing Fourier analyses. The energy of the original signals is preserved by scaling the windowed data.

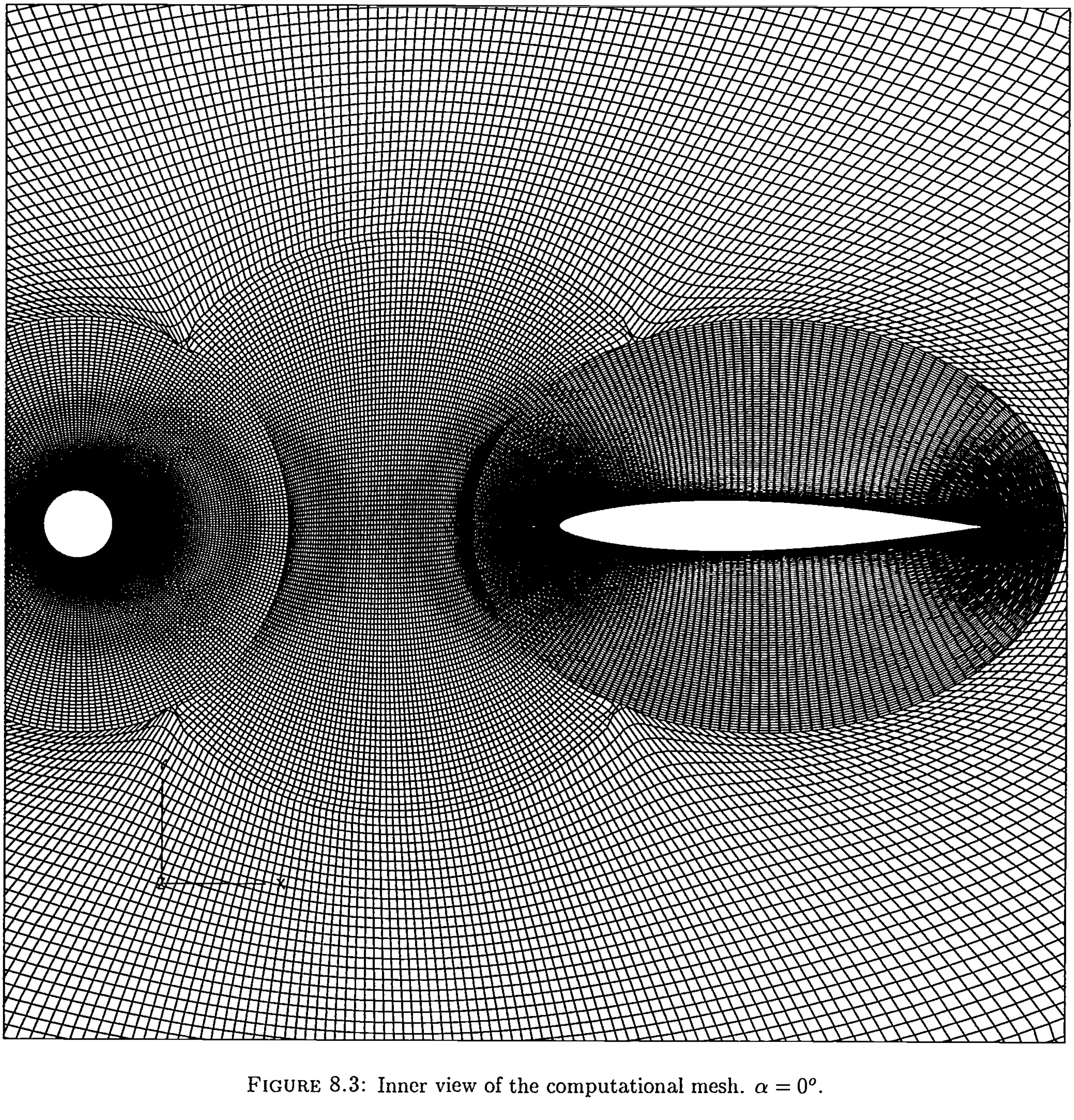

FIGURE 8.3: Inner view of the computational mesh. $\alpha = 0^o$.

8.5 Results and Discussion

In the present section, results concerning a comprehensive aeroacoustic characterization of the rod-airfoil configuration are presented and discussed. The RANS computation is performed by means of the CFD code *Proust* described in section 8.3.1 and the acoustic field is computed by means of the rotor noise code *Advantia* described in section 6.2.

8.5.1 Aerodynamic Results

A $c = 0.1\,\mathrm{m}$ airfoil is embedded in the wake of a $d = 0.016\,\mathrm{m}$ rod. The inflow velocity is 20 m/s. The unsteady RANS equations are solved on the mesh plotted in Fig.8.3. Results concerning the last 9 computed shedding cycles are discussed below.

8.5.1.1 Unsteady force on the airfoil and wall pressure field

In Fig.8.4 the computed unsteady drag and lift coefficient are plotted. The first three periods are still contaminated by transitory effects. Conversely, in the remaining part, a periodic behaviour is well established. Interestingly, at zero angle of attack the mean value of the drag is negative, resulting in a traction force exerted on the airfoil. This is due to the suction effect induced by the vortex at the leading-edge regardless to the sign of the vortex circulation. At $\alpha = -4^o$ the lift exhibits an expected negative mean value. Comparing Figs.8.4(a) and 8.4(b) shows that the unsteady drag behaviour is affected by the airfoil angle of attack.

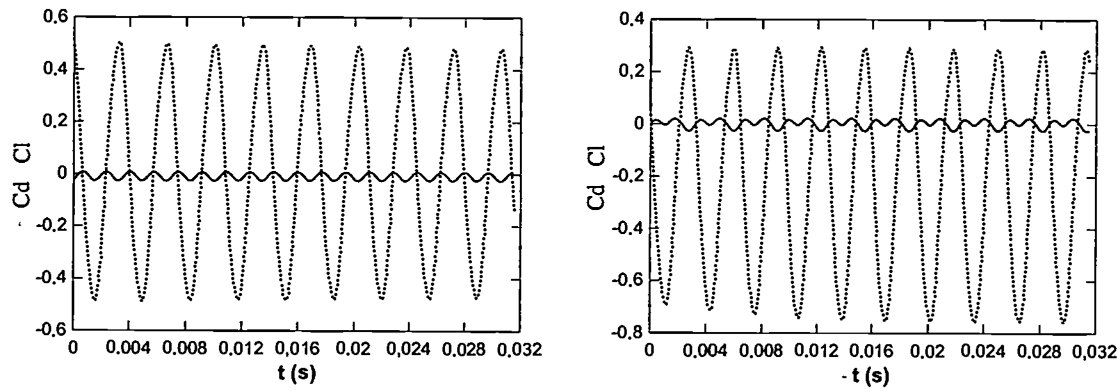

a) $\alpha = 0^o$. b) $\alpha = -4^o$.

FIGURE 8.4: Unsteady force on the airfoil: —— drag coefficient, - - - - lift coefficient.

The spectrum of the unsteady aerodynamic force exerted on the airfoil is plotted in Fig.8.5. For the case $\alpha = 0^o$ the shedding frequency f_0 has a value of 285.1 Hz, corresponding to a Strouhal number of 0.23. Conversely, for the cases $\alpha = -4^o$ the shedding frequency is $f_0 = 316.8\,\mathrm{Hz}$, corresponding to a Strouhal number of 0.25. These values differ by 14% and 26%, respectively, from the experimental value of 0.2.

Accordingly to literature, the overprediction of the vortex shedding frequency from a two-dimensional rod is a common CFD result. As mentioned in chapter 7, Kato & Ikegawa [65] investigated the flow past a rod and compared results of a two-dimensional large eddy simulation to results of a three-dimensional one. They obtained a reduction of the Strouhal number from 0.24 in the two-dimensional case to 0.2 in the three-dimensional case and a better prediction of the wall pressures in the latter case. The Strouhal frequency overprediction can be explained to some extent. As argued by Roshko [66], the length of the mean recirculating region behind the rod results from an equilibrium between the base suction coefficient and the *in-plane* Reynolds stresses in the separated flow region. Hence, higher Reynolds stresses correspond to shorter mean recirculating regions. In a three-dimensional flow a part of the energy extracted from the mean flow is used to maintain spanwise velocity fluctuations. As a consequence, the mean recirculating region extends farther from the cylinder and the Strouhal frequency is smaller than in a simulated two-dimensional flow.

Concerning the effect of the airfoil angle of attack on the Strouhal frequency, it should be argued that a possible physical mechanism responsible for such a dependence has a negligible influence on a real flow. This is because the measured Strouhal frequency is not affected by the airfoil angle of attack in the range $[-4^o, 4^o]$ (see Fig.5.5). However, experiments show that the Strouhal frequency is weakly affected by the presence of the airfoil, regardless to its angle of attack. Therefore, despite the fact that no angle of attack effects have been observed, a factor related to the presence of the airfoil is suspected to be the cause of the predicted effect of the angle of attack. Therefore, in the real flow, the effect of the airfoil angle of attack on the Strouhal frequency are likely to be smeared by the three-dimensional character of the flow.

Fig.8.5 shows that at zero angle of attack the drag spectrum exhibits predominant even harmonics peaks ($2f_0$, $4f_0$, ...), whereas the lift spectrum exhibits predominant odd harmonics peaks (f_0, $3f_0$, ...). On the contrary, at non zero angle of attack, the even and odd harmonic peaks in both the drag and the lift spectrum have comparable amplitudes.

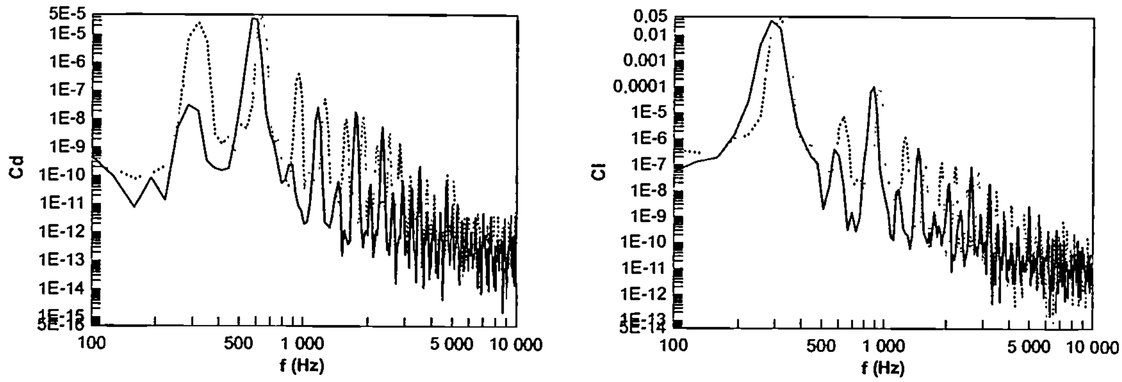

a) Unsteady drag coefficient. b) Unsteady lift coefficient.

FIGURE 8.5: Spectrum of the unsteady aerodynamic force on the airfoil: —— $\alpha = 0^o$, - - - - $\alpha = -4^o$.

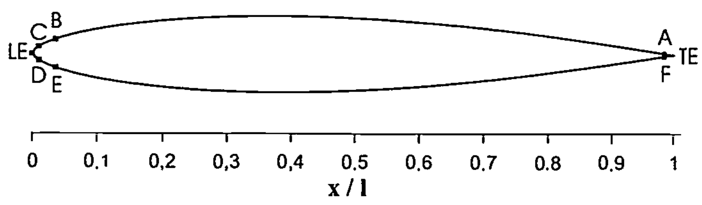

FIGURE 8.6: Numerical pressure probes (A...F) on the airfoil surface.

In Fig.8.7 the spectra of the wall pressure coefficient at two symmetrical point near the airfoil trailing edge are plotted (probes A and F in Fig.8.6). Peaks appear at both even and odd harmonics. This is a consequence of the fact that both the upper and lower vortices are split when impinging onto the airfoil leading-edge. Hence, fragments of each vortex are convected along the two airfoil sides. At zero angle of attack these peaks have the same values on the two airfoil sides. Conversely, at a non zero angle of attack the pressure fluctuations at the Strouhal frequency are nearly one order higher on the lower airfoil side. This is presumably due to the fact that at a negative angle of attack the upper row vortices undergo a stronger distortion near the airfoil leading edge. Consequently, they partially spread and their effect onto the wall pressure becomes weaker.

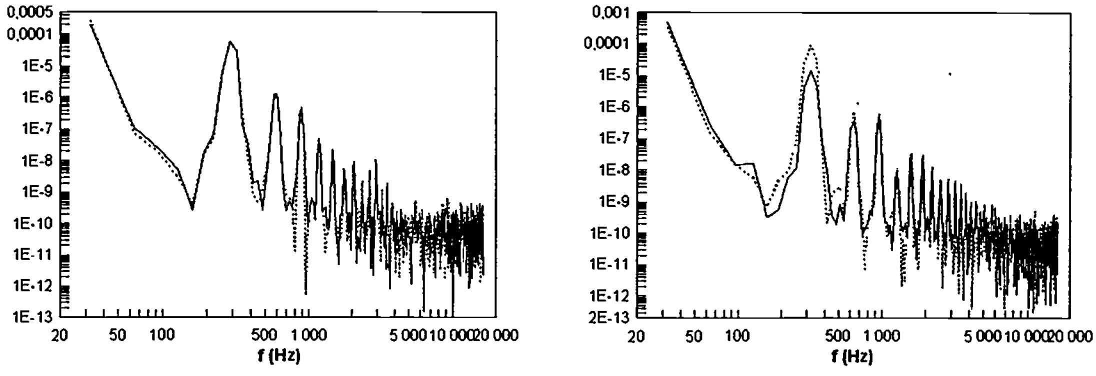

a) $\alpha = 0^o$. b) $\alpha = -4^o$.

FIGURE 8.7: Spectrum of the wall pressure coefficient. Numerical probes: —— A, - - - - F.

In Figs.8.8 and 8.9 the spectra of the wall pressure coefficient are traced for points in the neighborhood of the leading edge (probes B, C, D and E in Fig.8.6). A comparison between these results and those at the trailing edge shows that the unsteady pressure fluctuations on the airfoil surface are several orders of magnitude higher near the leading edge. The main aeroacoustic sources are therefore expected at the leading edge.

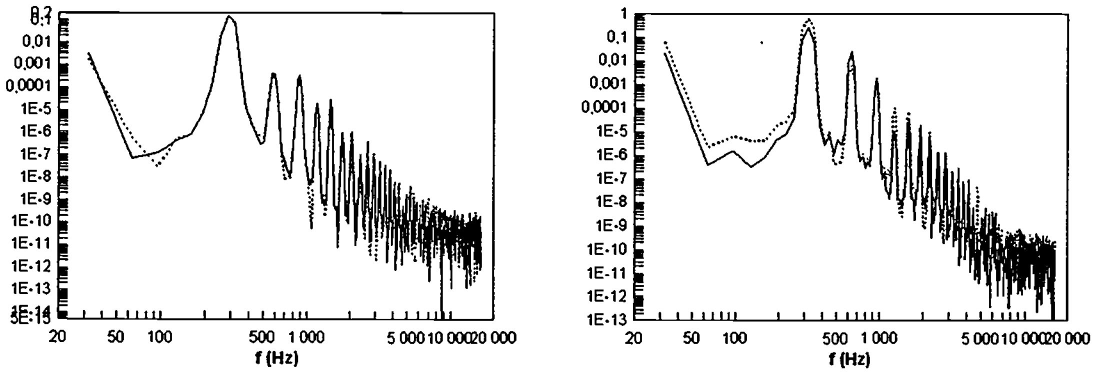

a) $\alpha = 0^o$. b) $\alpha = -4^o$.

FIGURE 8.8: Spectrum of the wall pressure coefficient. Numerical probes: —— B, - - - - E.

In Fig.8.10 the spectrum of the wall pressure exactly at the airfoil leading edge (probe LE in Fig.8.6) is compared to that at a grid point before the leading edge on the airfoil upper side (labeled LE^u). It is interesting to notice that when the airfoil is at zero angle of attack the spectral behaviour at these points is different.

Finally, in Fig.8.11 the pressure field on the airfoil surface is plotted. Non symmetrical behaviours are predicted for the case $\alpha = -4^o$, with higher fluctuating levels on the lower side of the leading edge.

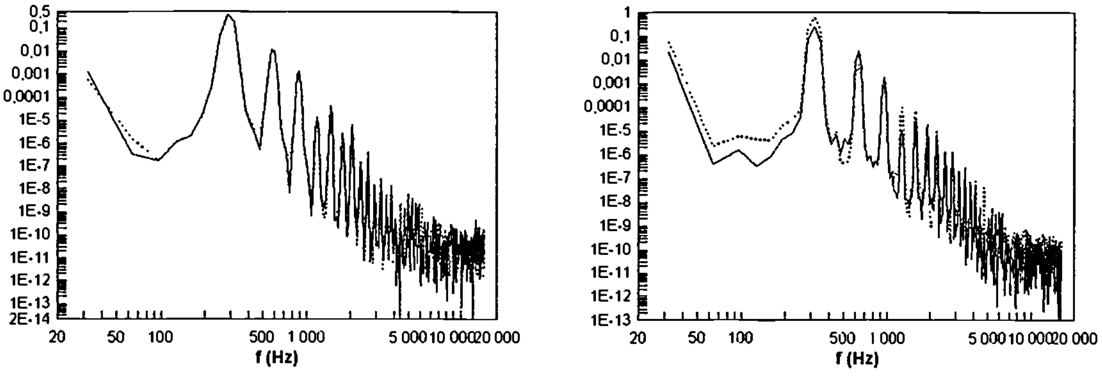

a) $\alpha = 0^o$.   b) $\alpha = -4^o$.

FIGURE 8.9: Spectrum of the wall pressure coefficient. Numerical probes: —— C, - - - - D.

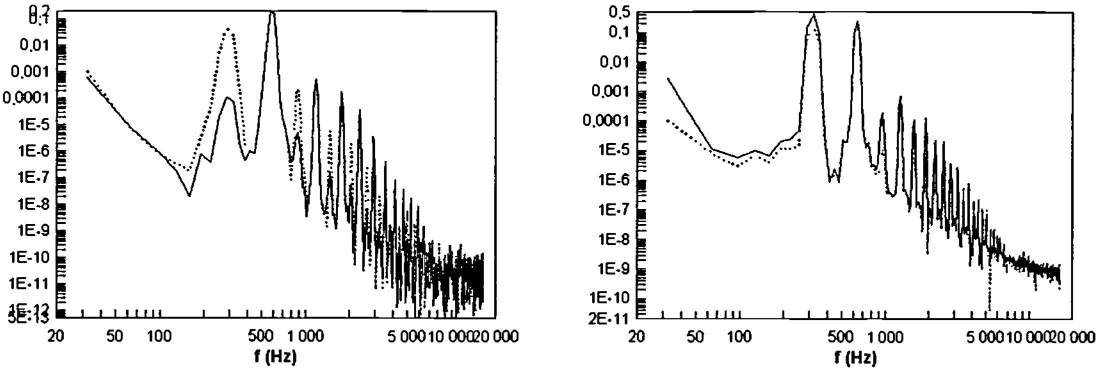

a) $\alpha = 0^o$.   b) $\alpha = -4^o$.

FIGURE 8.10: Spectrum of the wall pressure coefficient. Numerical probes: —— LE, - - - - LE^u. The separation distance between the probes is about 1×10^{-4} m.

In both cases, $Cp_{\rm rms}$ is maximum near the leading edge and decreases fast downstream, exhibiting a Sears-type behaviour.

Comparing the numerical results to the experimental ones discussed in section 5.2.2 shows that the numerical prediction overestimates the ratio between the amplitude of the pressure fluctuations at the leading edge and that at the trailing edge. Unfortunately we cannot find in the present context a reasonable explanation for this discrepancy. We can only mention that a linear $k - \omega$ model typically overestimates the turbulent kinetic energy in the neighborhood of a stagnation point when a steady RANS simulation is performed. This is due to a physical inadequacy of a turbulence model based on a local isotropy hypothesis. Accordingly, unsteady RANS predictions are expected to provide even less consistent results in a region of strong anisotropy and rapid distortion of the vorticity field.

In section 5.2.2 we showed that the amplitude of the wall pressure fluctuations increases on the upper or the lower airfoil side close to the leading edge, depending on whether the angle of attack is negative or positive, respectively. Contrarily, the numerical results herein presented exhibit an opposite trend. A stronger suction is predicted on the side of the leading edge which is opposite to that where the vortices impinge. This result is even more questionable since it strongly depends on both the vortex

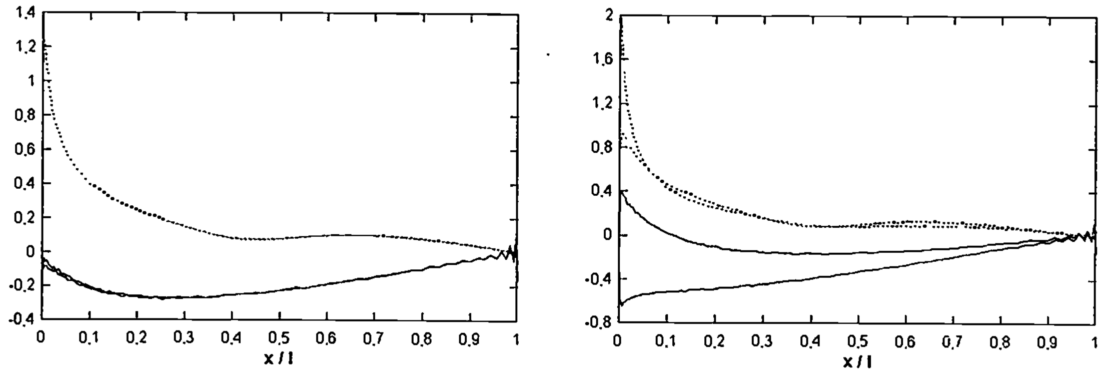

a) $\alpha = 0^o$. b) $\alpha = -4^o$.

FIGURE 8.11: Mean and fluctuating pressure coefficient on the airfoil surface: —— $\overline{Cp}$, - - - - Cp_{rms}.

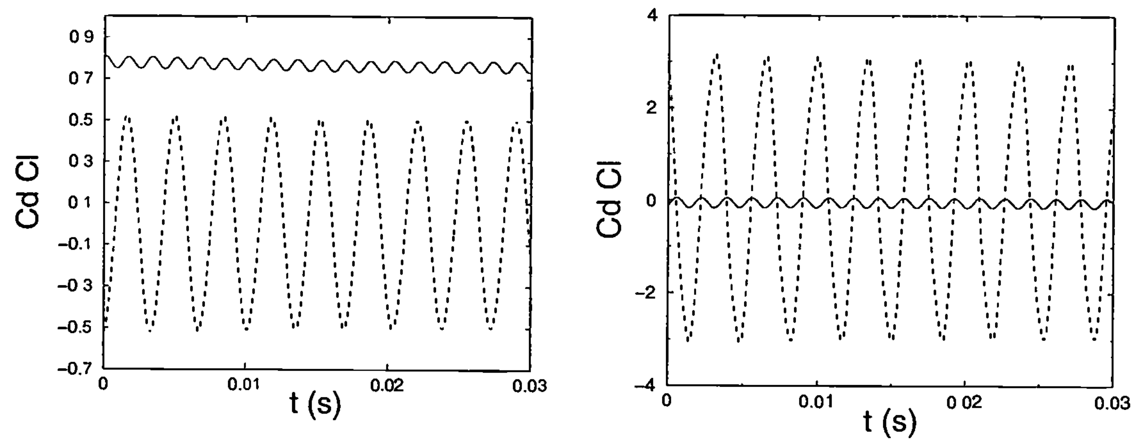

FIGURE 8.12: Force on the rod (left) and the airfoil (right): —— C_d, - - - - C_l. Reference length: d

distortion at the leading edge and the relative position between the impinging vortex and the leading edge.

From these considerations it follows that, even in a two-dimensional and apparently fairly well resolved aerodynamic computation, the problem related to the prediction of a wake, that of the rod in the present study, is the pitfall of a vortex-body numerical prediction[2].

8.5.1.2 Airfoil results *versus* rod results

In Fig.8.12 the aerodynamic force exerted on the airfoil at zero angle of attack is compared to that exerted on the rod. An interesting result is that the airfoil lift is about 6 times higher than the rod lift.

Fig.8.13(a) shows the pressure field on the rod surface. The Cp_{rms} peaks at $\phi = 95.5^o$, which marks the mean location of the separation point. The pressure field on the airfoil surface is plotted in Fig.8.13(b). As already pointed out, Cp_{rms} peaks near the leading edge, decreasing fast downstream. The fluctuating pressure level at the leading edge is about 159 times higher than that at the trailing edge. Furthermore, the maximum Cp_{rms} on the airfoil is 4.5 times higher than the maximum on the

[2]The reader should refer to chapter 10 of part II for a discussion on the *wake-prediction problem* in the context of helicopter rotor blade-vortex interaction.

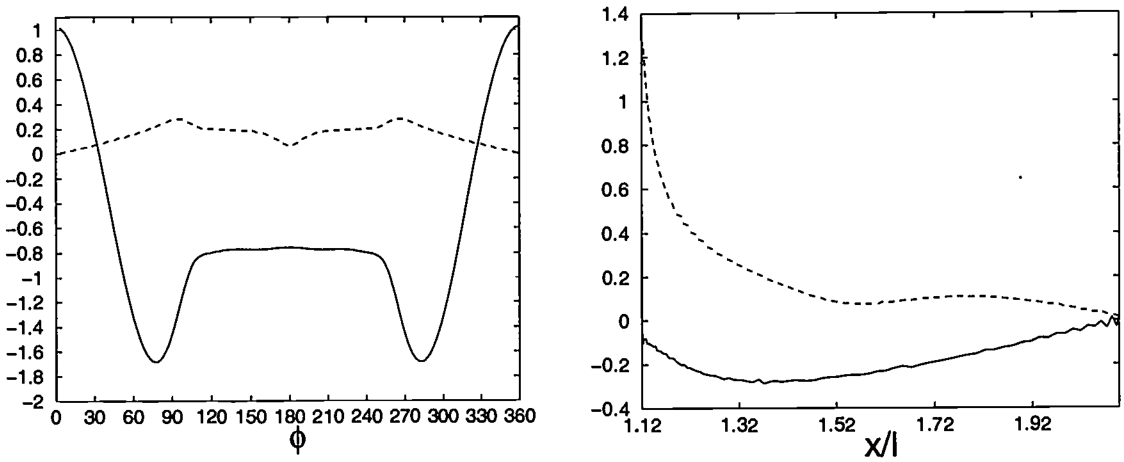

FIGURE 8.13: Pressure field on the rod (left) and the airfoil (right) surface: —— $\langle Cp \rangle$, - - - - $Cp_{\rm rms}$.

rod. This further confirms that the stronger aeroacoustic sources in the rod-airfoil configuration are expected near the airfoil leading edge.

8.5.1.3 Mean and fluctuating flow near the airfoil

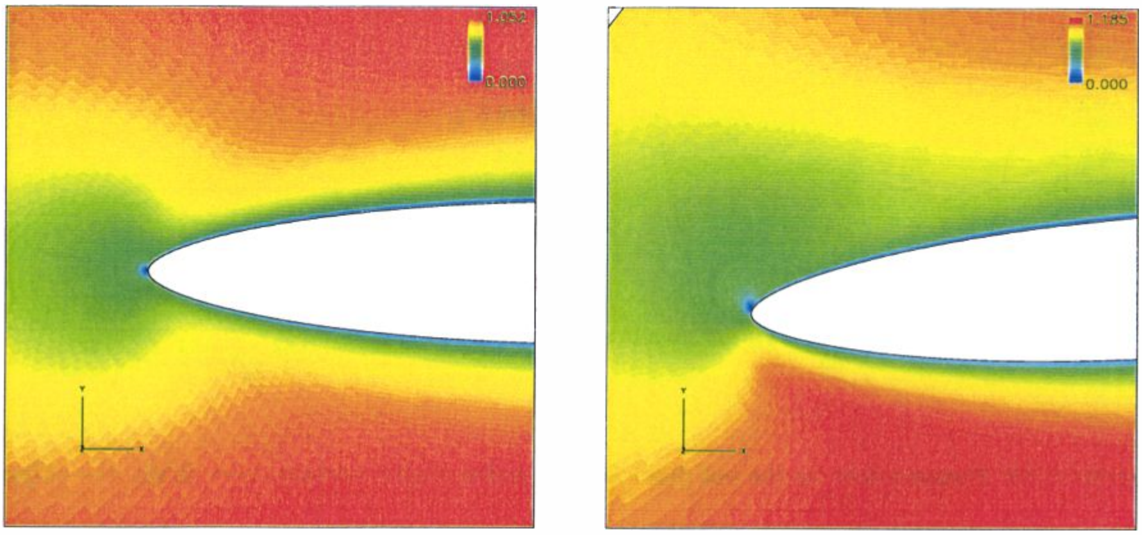

a) $\alpha = 0^o$. b) $\alpha = -4^o$.

FIGURE 8.14: Mean velocity: $\langle V \rangle$.

In this subsection, results concerning the mean and the fluctuating velocity and pressure fields near the airfoil leading edge are presented.

Letting $\langle \rangle$ denote the local average of a quantity over a vortex shedding period, the following quantities have been defined

- mean pressure coefficient

$$\langle Cp \rangle = \frac{\langle p - p_\infty \rangle}{\frac{1}{2}\rho V_\infty^2} \tag{8.2}$$

- root-mean-square pressure coefficient

$$Cp_{\text{rms}} = \sqrt{\left\langle (Cp - \langle Cp \rangle)^2 \right\rangle} \tag{8.3}$$

- dimensionless mean velocity

$$\langle V \rangle = \frac{\sqrt{\langle u \rangle^2 + \langle v \rangle^2}}{V_\infty} \tag{8.4}$$

- local dimensionless root-mean-square velocity in the local mean flow direction

$$V_{\text{rms}} = \sqrt{\left\langle (u\, n_x / V_\infty + v\, n_y / V_\infty - \langle V \rangle)^2 \right\rangle + \frac{2}{3} \langle k \rangle} \tag{8.5}$$

where $n_x = \langle u \rangle \,/\, \langle V \rangle$ and $n_y = \langle v \rangle \,/\, \langle V \rangle$ are the component of the mean flow direction and $\langle k \rangle$ denotes the mean kinetic turbulent energy[3]. Averages over the last predicted shedding period are considered in the present study.

[3]Equation (8.5) is based on the hypothesis of local isotropy of the turbulent velocity field, namely, $k = \frac{3}{2}\overline{u'u'}$, where u' is the Reynolds fluctuating component of the velocity field in the $x-$direction. Clearly, in the framework of unsteady RANS modeling, a fluctuating k only reaches sense if the averaging time is longer than that associated with the slowest turbulent motions but is much smaller than the time scale of the flow unsteadiness (the vortex shedding period in the present study).

In Fig.8.14 the mean velocity field is plotted. A symmetrical mean flow is found at zero angle of attack, with a mean location of the stagnation point exactly at the airfoil leading edge. Conversely, the mean flow is not symmetric at $\alpha = -4^o$ and exhibits a mean location of the stagnation point on the upper side of the leading edge.

In Fig.8.15 the corresponding *rms* velocity field is plotted. The strongest fluctuations are located near the leading edge. Furthermore, a slight attenuation of the fluctuating level can be observed downstream of the leading edge. Interestingly, the root-mean square velocity has higher values when the airfoil is at a non zero angle of attack. This can be partially explained by considering the fact that a stronger distortion of the vorticity field produces higher turbulent levels. However, as previously remarked, the adequacy of the adopted closure model in a region of strong anisotropy is questionable.

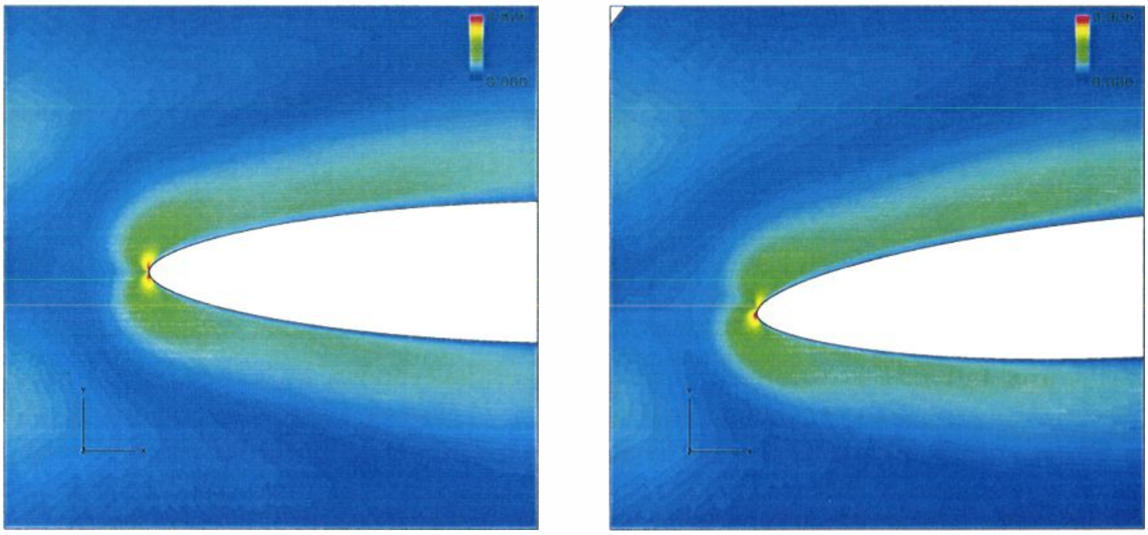

a) $\alpha = 0^o$. b) $\alpha = -4^o$.

FIGURE 8.15: Fluctuating velocity: $V_{\rm rms}$.

Finally, in Fig.8.16 the root-mean-square pressure coefficient is plotted. Strong pressure fluctuations occur in a region close to the leading edge. Therefore, the acoustic sources are expected to be concentrated in a relatively narrow region close to the leading edge. Consistently with the previous results, stronger pressure fluctuations take place when the airfoil is at non zero angle of attack.

8.5.1.4 Mean and fluctuating flow past the cylinder

Results are herein presented concerning the mean and the fluctuating flow past the cylinder. The mesh in the cylinder domain is the same for the two values of the airfoil angle of attack. Thus, possible grid effects onto the numerical solution are related to the airfoil domain and to the intermediate domain.

Previously discussed results show that the predicted Strouhal frequency is affected by the airfoil angle of attack. No reasonable explanations for this behaviour were found and we argued that, if the instability of the wake of the rod is affected by a physical mechanism related to the airfoil angle of attack, this mechanism has a negligible effect in the real flow.

In Fig.8.17 the mean pressure coefficient on the surface of the rod is plotted. Positions 0 and 200 denote the forward stagnation point of the cylinder, whereas 100 denotes the rod base point. The size of the mean separation region behind the rod is not significantly affected by the airfoil angle of attack. However, different pressure levels can be observed upstream of the separation point.

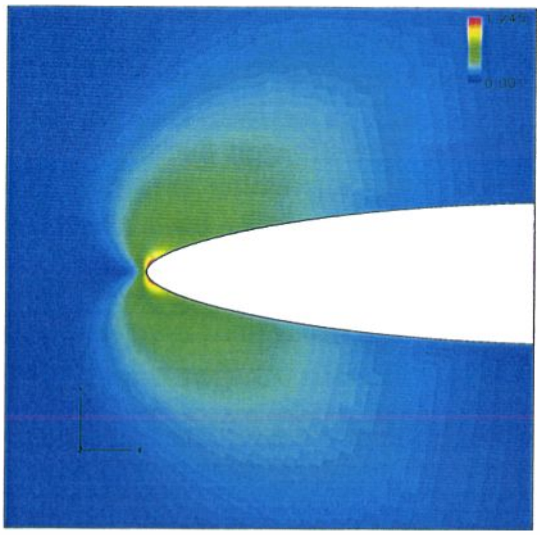

a) $\alpha = 0^o$.

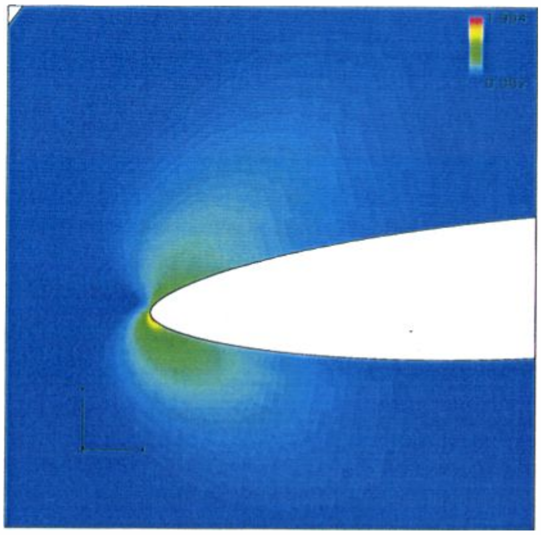

b) $\alpha = -4^o$.

FIGURE 8.16: Fluctuating pressure coefficient: $Cp_{\rm rms}$.

TABLE 8.1: Mean and fluctuating pressure in the wake of the cylinder. $-C_{pB}$ denotes the base suction coefficient; $-\langle C_p \rangle$ (MAX) is the maximum value of the mean suction coefficient occurring at $x/d = 1.05$ for $\alpha = 0^o$ and $x/d = 1.09$ for $\alpha = -4^o$; $Cp_{\rm rms}$ (BP) is the root-mean-square pressure coefficient at the base point; $Cp_{\rm rms}$ (MAX) denotes the maximum value of the root-mean-square pressure coefficient occurring at $x/d = 1.14$ for $\alpha = 0^o$ and $x/d = 1.17$ for $\alpha = -4^o$.

	$-C_{pB}$	$-\langle C_p \rangle$ (MAX)	$Cp_{\rm rms}$ (BP)	$Cp_{\rm rms}$ (MAX)
$\alpha = 0^o$	0.76	1.12	0.06	0.17
$\alpha = -4^o$	0.82	1.23	0.07	0.20

Fig.8.18 shows the root-mean-square pressure coefficient distribution on the rod surface. Higher fluctuating levels take place when the airfoil is at non zero incidence to the mean flow.

In Fig.8.19 the mean and fluctuating pressure distribution on the wake symmetry plane is plotted. It is interesting to notice that, as previously pointed out, the airfoil angle of attack has a non negligible influence on both the mean and the fluctuating part of the pressure field around the rod.

The mean and fluctuating velocity distributions downstream of the rod base point are plotted in Fig.8.20. It is interesting to observe that the location of the maximum *rms* level corresponds to that of a local minimum of the mean velocity, that is at a distance $x/d = 1.27$ from the center of the cylinder. This value is the same in the cases $\alpha = 0^o$ and $\alpha = \pm 4^o$, and provides an estimate of the vortex formation length. As argued by Roshko [66], for sufficiently high Reynolds numbers, the base suction coefficient is mainly determined by the velocity fluctuations through the action of in-plane (x, y) Reynolds stresses in the wake. From simple equilibrium considerations applied to the mean recirculating region, he obtained a relation between the base suction coefficient, the mean shear stress in the separated region and the length and width of the wake behind the rod. The length of the mean recirculating region is determined by the location of the minimum value of the mean velocity. Thus it also coincides with

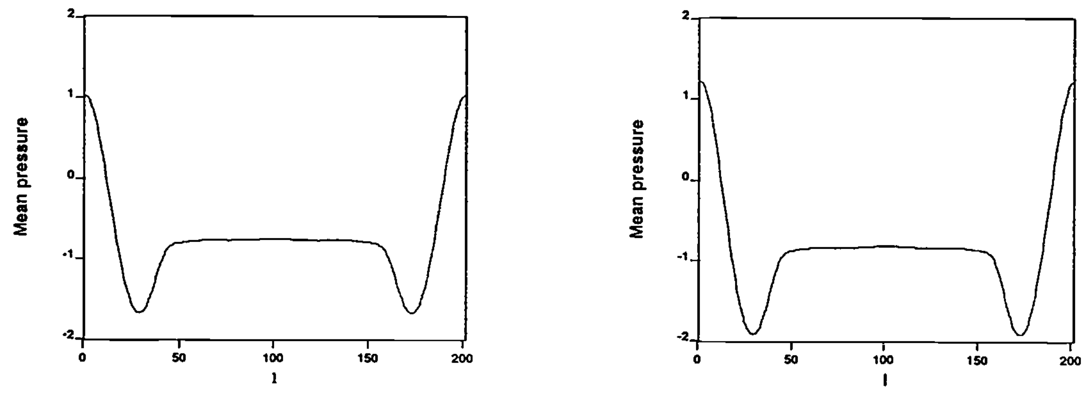

a) $\alpha = 0^o$. b) $\alpha = -4^o$.

FIGURE 8.17: Mean pressure coefficient on the cylinder surface: $\langle Cp \rangle$. Positions 0 and 200 denote the forward stagnation point of the cylinder, whereas 100 denotes the rod base point.

the vortex formation length. As discussed in section 7.4.3, the base suction coefficient $-C_{pB}$, between Re=10^3 and Re=2×10^5, is a monotonic increasing function of the Reynolds number. On the base of Roshko's model, this behaviour can be related to the increasing Reynolds stresses $\overline{\rho u'v'}$ and to the decreasing vortex formation length[4]. In the present study we investigate the effect of the airfoil angle of attack. Since the vortex formation length is the same for the two angles of attack, the Reynolds shear stresses are not implicated in the predicted effect of the airfoil angle of attack. Thus, the only reasonable explanation of the predicted behaviour is a different coupling mechanism between the vortex dynamics in the wake of the rod and the hydrodynamic field generated by the vortex-airfoil interaction.

In Tables 8.1 and 8.2 the most meaningful values of Figs.8.19 and 8.20 are summarized.

In Fig.8.21 the mean velocity field around the cylinder is plotted. A mean separation bubble can be observed behind the cylinder, having a nearly semi-elliptical shape. At about 80^o from the forward stagnation point the dimensionless mean velocity reaches the maximum value of 1.5. The only notable effect of the airfoil angle of attack is a slight extension of the upper and lower regions of higher velocity.

In Fig.8.22 the *rms* velocity field around the cylinder is plotted. A region of stronger fluctuations can be noticed in the wake of the cylinder, having the shape of a butterfly. As previously pointed out, the airfoil angle of attack affects the *rms* velocity at the formation length (see Fig.8.20). Scrutinizing Fig.8.22 shows that this difference is related to a cut of the higher fluctuation region along the wake symmetry plane. Since a significant difference occurs only at the cutting point, this behaviour can be considered as an artifact of a perfect symmetrical simulation for $\alpha = 0^o$.

The mean pressure distribution plotted in Fig.8.23 is the counterpart of the mean velocity field

[4]This also explains the discrepancies between two-dimensional and three-dimensional numerical simulations of a circular cylinder flow. The Reynolds shear stresses predicted by a two-dimensional simulation are higher than those predicted by a three-dimensional simulation at the same Reynolds number. In a two-dimensional aerodynamic field, in fact, all the energy extracted from the mean flow is expended in sustaining the in plane velocity fluctuations. Conversely, in a three-dimensional aerodynamic field, a part of the energy extracted from the mean flow is used to maintain spanwise velocity fluctuations. This results in a reduction of the in-plane Reynolds shear stresses. As an important consequence, a two-dimensional simulation underestimates the vortex formation length and overestimates both the base suction coefficient and the mean drag.

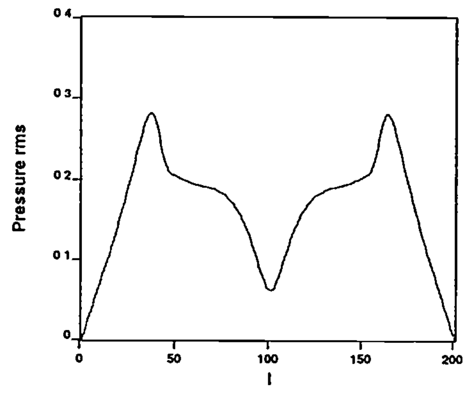

a) $\alpha = 0^o$.

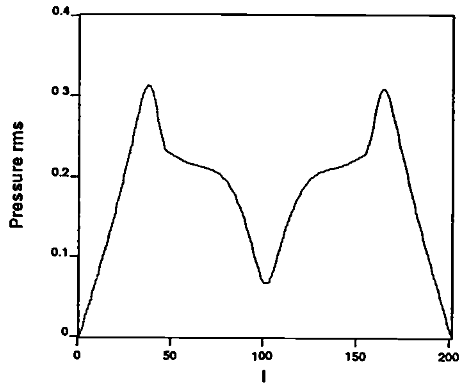

b) $\alpha = -4^o$.

FIGURE 8.18: Fluctuating pressure coefficient on the cylinder surface: Cp_{rms}. Positions 0 and 200 denote the forward stagnation point of the cylinder, whereas 100 denotes the rod base point.

TABLE 8.2: Mean and fluctuating velocity in the wake of the cylinder. $\langle V \rangle$ (MAX) denotes the maximum value of the mean dimensionless velocity occurring at $x/d = 0.94$ for both $\alpha = 0^o$ and $\alpha = -4^o$; V_{rms} (MAX) is the maximum value of the root-mean-square dimensionless velocity occurring at $x/d = 1.27$ for both $\alpha = 0^o$ and $\alpha = -4^o$.

	$\langle V \rangle$ (MAX)	V_{rms} (MAX)
$\alpha = 0^o$	0.25	0.23
$\alpha = -4^o$	0.26	0.60

plotted in Fig.8.21. A mean recirculating region can be noticed behind the cylinder. Furthermore, two symmetrical suction regions appear where the velocity is maximum.

More interestingly, the fluctuation pressure field plotted in Fig.8.24 provides an estimate of the size of the vortex core. Two symmetrical overpressure blobs, in fact, can be observed in the wake of the cylinder, having a size of about one half cylinder diameter. Furthermore, two flattened overpressure regions can be observed at about 90^o from the forward stagnation point on the rod surface, providing an estimate of the region swept by the separation point.

Finally, in Fig.8.25 the mean value of the turbulent kinetic energy is plotted.

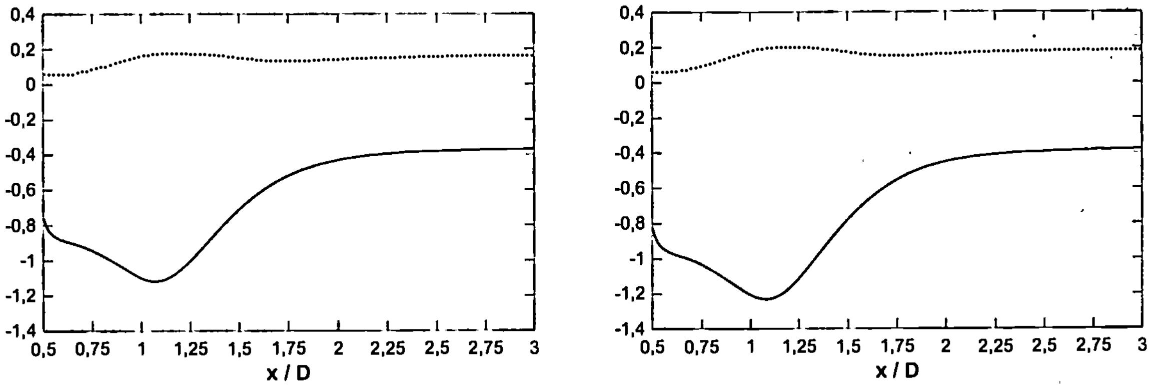

a) $\alpha = 0^o$.

b) $\alpha = -4^o$.

FIGURE 8.19: Mean and fluctuating pressure coefficient on the rod base point plane: —— $\langle Cp \rangle$, - - - - $Cp_{\rm rms}$. x/d increases from the rod towards the airfoil, $x/d = 0$ denoting the center of the rod.

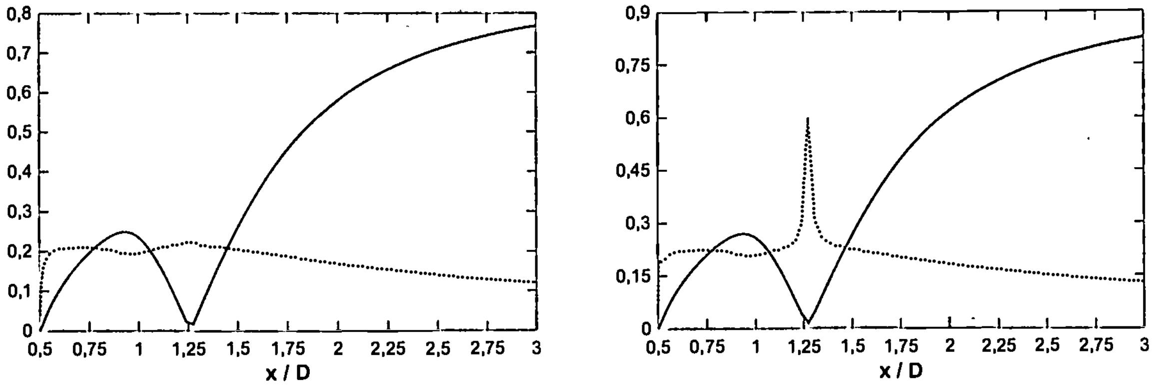

a) $\alpha = 0^o$.

b) $\alpha = -4^o$.

FIGURE 8.20: Mean and fluctuating velocity on the rod base point plane: —— $\langle V \rangle$, - - - - $V_{\rm rms}$. x/d increases from the rod towards the airfoil, $x/d = 0$ denoting the rod mid point.

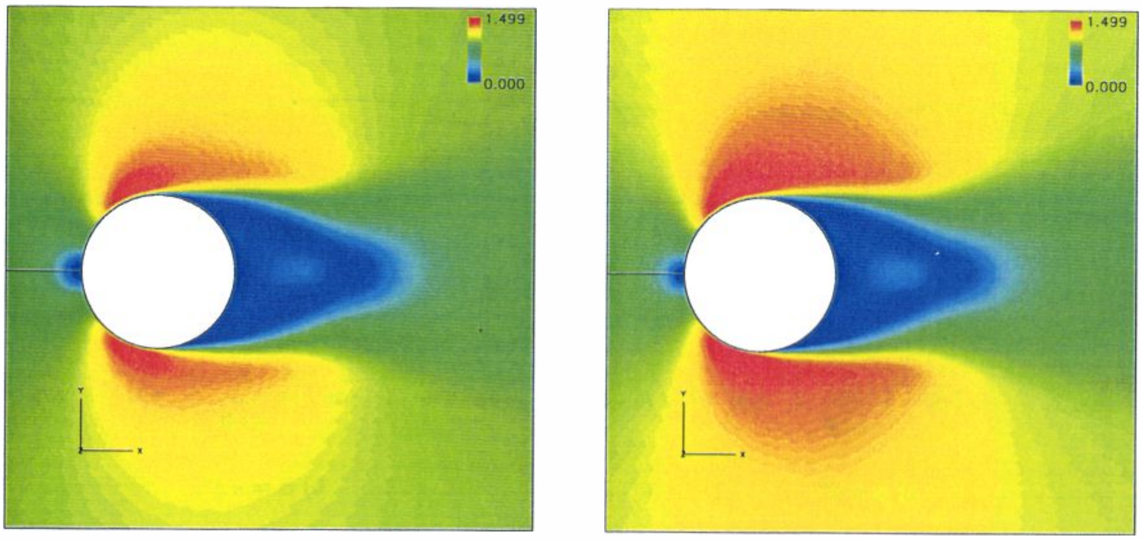

a) $\alpha = 0^o$. b) $\alpha = -4^o$.

FIGURE 8.21: Mean dimensionless velocity: $\langle V \rangle$.

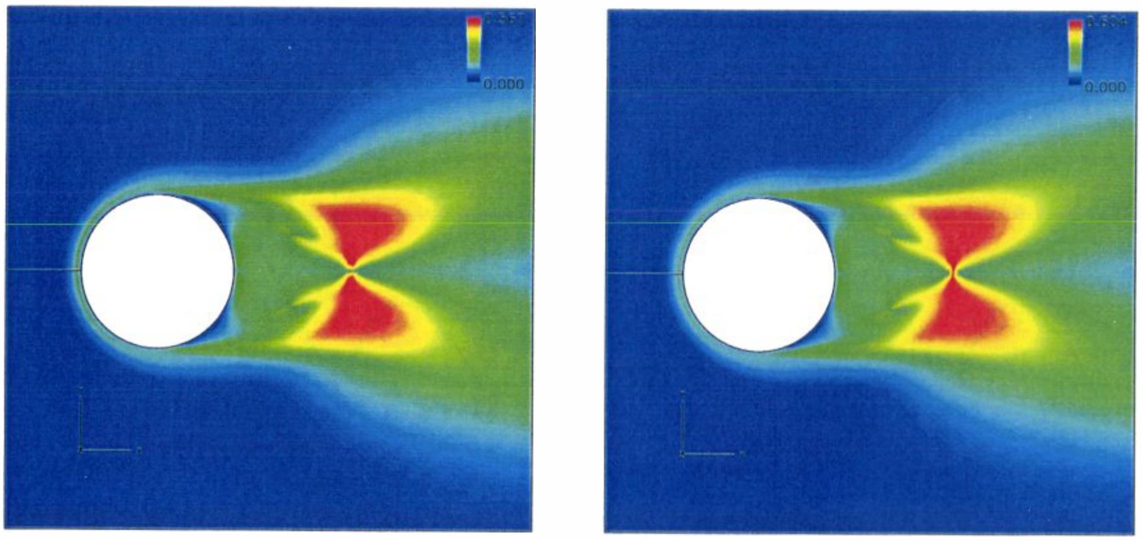

a) $\alpha = 0^o$. b) $\alpha = -4^o$.

FIGURE 8.22: Fluctuating dimensionless velocity: V_{rms}.

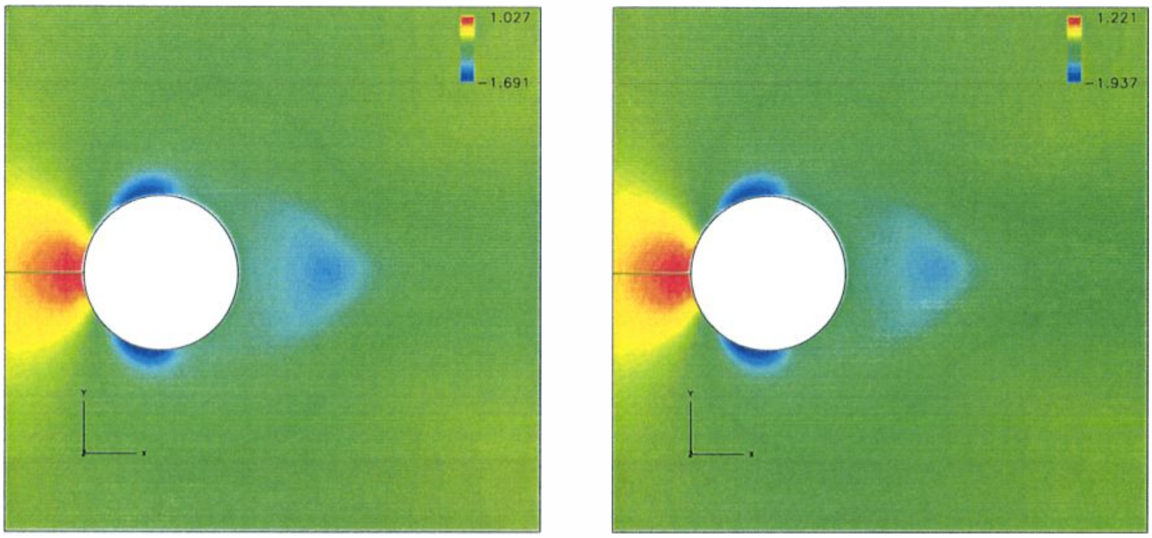

a) $\alpha = 0^o$. b) $\alpha = -4^o$.

FIGURE 8.23: Mean pressure coefficient: $\langle Cp \rangle$.

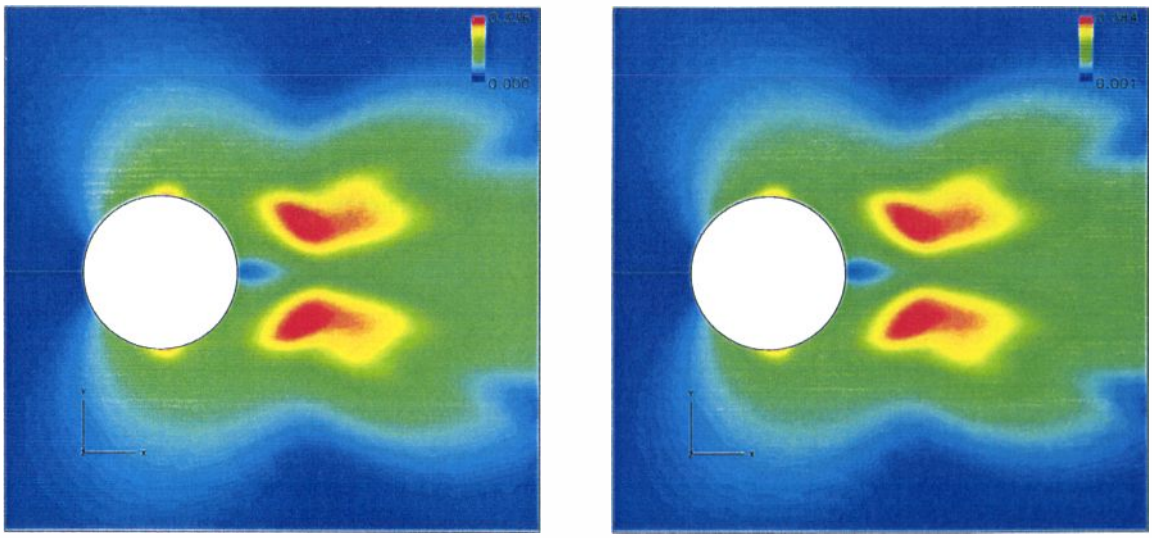

a) $\alpha = 0^o$. b) $\alpha = -4^o$.

FIGURE 8.24: Fluctuating pressure coefficient: Cp_{rms}.

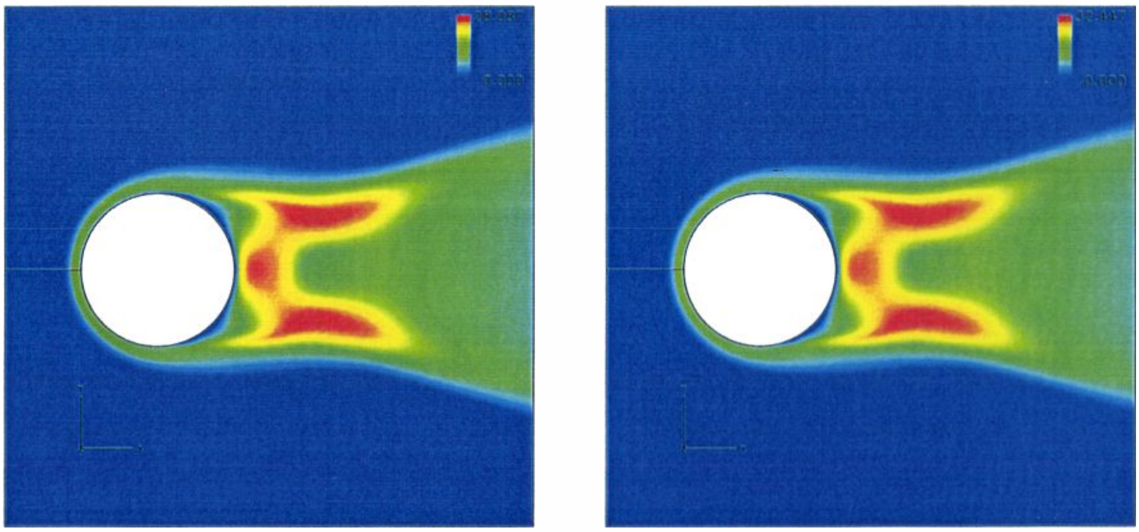

a) $\alpha = 0^o$. b) $\alpha = -4^o$.

FIGURE 8.25: Mean turbulent kinetic energy: $\overline{k}$.

8.5.1.5 Snapshots of the Rod-Airfoil Aerodynamic Field

In this subsection some snapshots are shown to illustrate the vortex dynamics in the rod-airfoil configuration. The pressure coefficient, the vorticity and the turbulent kinetic energy are plotted. Only the latter is directly computed by the CFD solver. The pressure is obtained from the total energy equation and the vorticity is computed by the post-processing visualization code. Furthermore, a visualization of the velocity field is attempted by interpolating the 5-block grid on a coarser C-grid. The relative velocity is obtained by subtracting the free-stream velocity. No attempt has been made to improve the quality of the vortex capturing[5]. Snapshots are counterclockwisely arranged in all the figures.

In Fig.8.26 snapshots of the vorticity field are plotted for the case $\alpha = 0^o$. Insight into the vortex dynamics provides the following cyclical behaviour.

1. An upper-row vortex impinges onto the airfoil leading edge, undergoing distortion and a partial splitting.

2. The greatest vortex portion is convected along the upper side of the airfoil. This fragment contains the core of the original vortex (see Fig.8.28).

3. Later on, a lower-row vortex impinges onto the airfoil leading edge. The dynamics of the vortex splitting is symmetrical to that described in items 1 and 2.

4. A constructive interaction between the upper fragment of the lower-row vortex (the faster one) and the downstream upper fragment of the upper-row vortex (the slower one) generates a sort of boundary-layer eruption on the upper side of the airfoil.

In Fig.8.27 snapshots of the turbulent kinetic energy are plotted for the case $\alpha = 0^o$. The mentioned constructive interaction between the vortex fragments leads to a progressive vortex amalgamation. It is interesting to notice that high levels of turbulent kinetic energy are generated near the airfoil leading edge. This is partially due to the inadequacy of the RANS closure model in regions of high flow anisotropy.

In Fig.8.28 snapshots of the relative velocity are plotted for the case $\alpha = 0^o$. Colors denote the instantaneous pressure coefficient. Upstream of the leading edge, the vortex cores are convected along the oncoming side of the airfoil.

Finally, in Fig.8.29 snapshots of the pressure coefficient are plotted for the case $\alpha = 0^o$. Impingement of upper-row vortices induces a pressure suction on the lower side of the airfoil leading edge. *Vice versa*, impingement of lower-row vortices induces a pressure suction on the upper side of the airfoil leading edge. As a result, the unsteady force on the airfoil is predominantly generated at the leading edge. Vortices close to the leading edge seem to be convected along the wrong side of the airfoil. Thus, the pressure field is not adequate to show the vortex trajectories near the leading edge. As a final remark, sufficiently far from the rod base point and from the airfoil leading edge, the core pressure level is nearly constant during the vortex convection. Thus, vorticity is convected across the intermediate computational domain without significant numerical dissipation. Furthermore, in the intermediate domain vortices are staggered as in a Kármán vortex street having an aspect ratio b/a of about 0.125 which differs from the theoretical value of 0.281 (see Fig.2.11). The latter value was predicted by von Kármán and is strictly valid for an infinite double row of line-vortices in an ideal fluid. This discrepancy can be partially explained by considering the opposite induction effect of the airfoil on the upper and lower row of vortices. The upper clockwise vortices tend to be towed down, *vice versa* the lower counterclockwise vortices tend to be towed up. This results in a slight reduction of the vertical spacing b of the double row.

[5]A better vortex description would be obtained by subtracting the local eddy convection velocity.

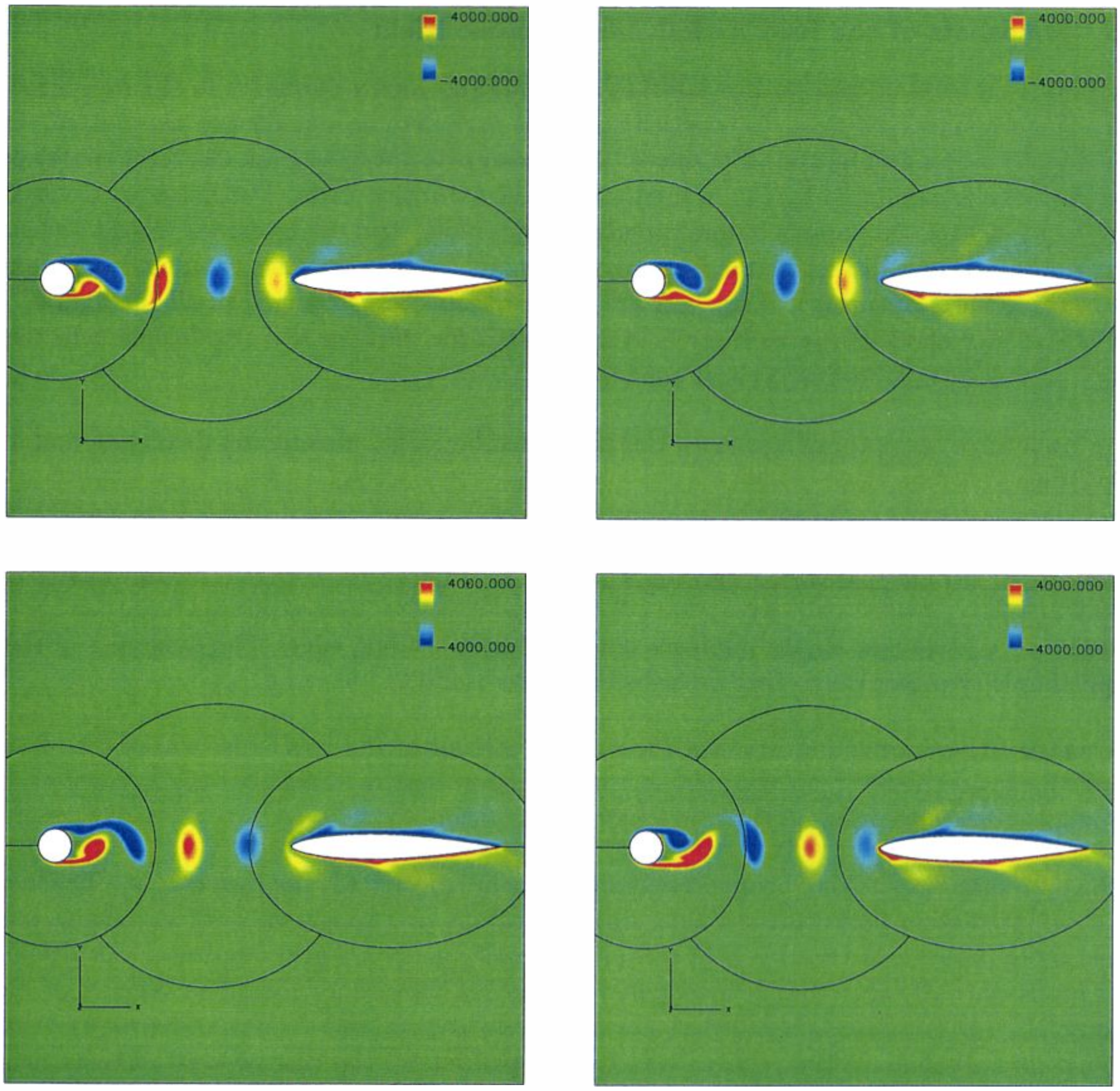

FIGURE 8.26: Instantaneous distribution of the vorticity: $\alpha = 0^o$.

In Figs.8.33 through 8.32 the same snapshots are plotted for the case $\alpha = -4^o$. Despite the non symmetrical unsteady behaviour, the vortex dynamics is nearly the same as that previously discussed for the case $\alpha = 0^o$.

As already pointed out, in all the snapshots the aspect ratio b/a of the double row of vortices is quite smaller than that predicted by von Kármán for an infinite vortex street in ideal flow, namely $b/a \simeq 0.281$.

Experimental visualizations[6] show that the value predicted by von Kármán is well fitted by the vortices in the wake of a rod. In addition, the RANS simulation of the flow around an isolated cylinder (see chapter 7) shows that the counter-rotating vortices exhibit the tendance to dispose as in a well staggered vortex street. From this considerations it follows that the presence of the airfoil is likely to be responsible for the underestimated value of b/a in the present computation.

Evaluating the relative importance between the numerical and the physical influence of the airfoil on the aspect ratio should have required different computations with different computational meshes. This was out of interest in the present work. However, some suggestions can be found in the flow behaviour described in section 5.3. The hydrogen bubble visualization experiment showed the existence of vortex

[6]See, for example, the photographs reported in Ref.[58].

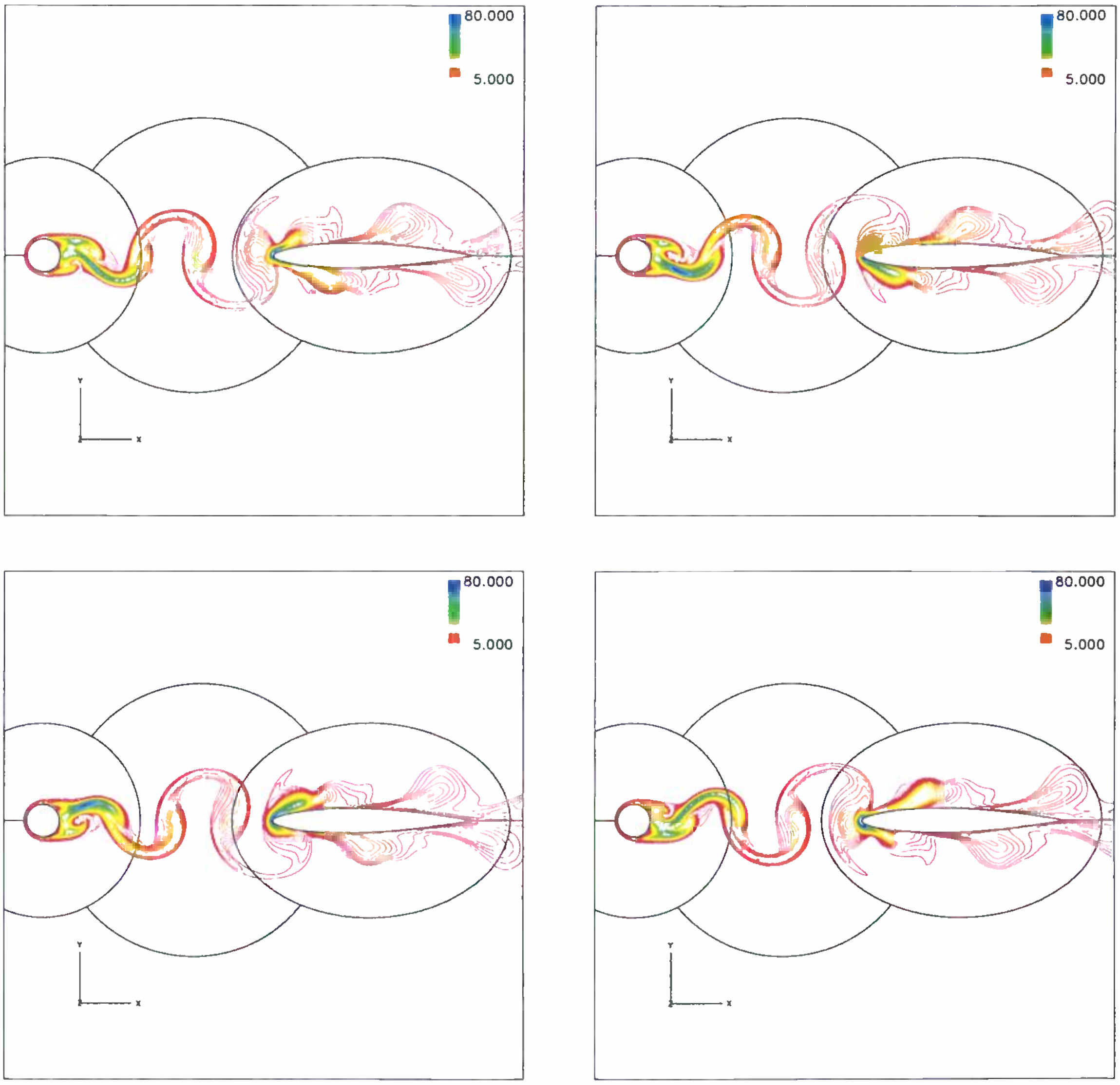

Figure 8.27: Instantaneous distribution of the turbulent kinetic energy: $\alpha = 0^o$.

shedding cycles characterized by a higher Strouhal frequency and by a smaller transverse spacing of the vortices in the wake of the rod. It was argued that this behaviour could be explained by supposing that the airfoil increases the *domain of attraction* of an otherwise improbable condition characterized by vortices aligned on the wake axis. In conclusion a question arises: could a Navier-Stokes simulation of the rod-airfoil configuration privilege this *weaker attractive* vortex aligned condition?

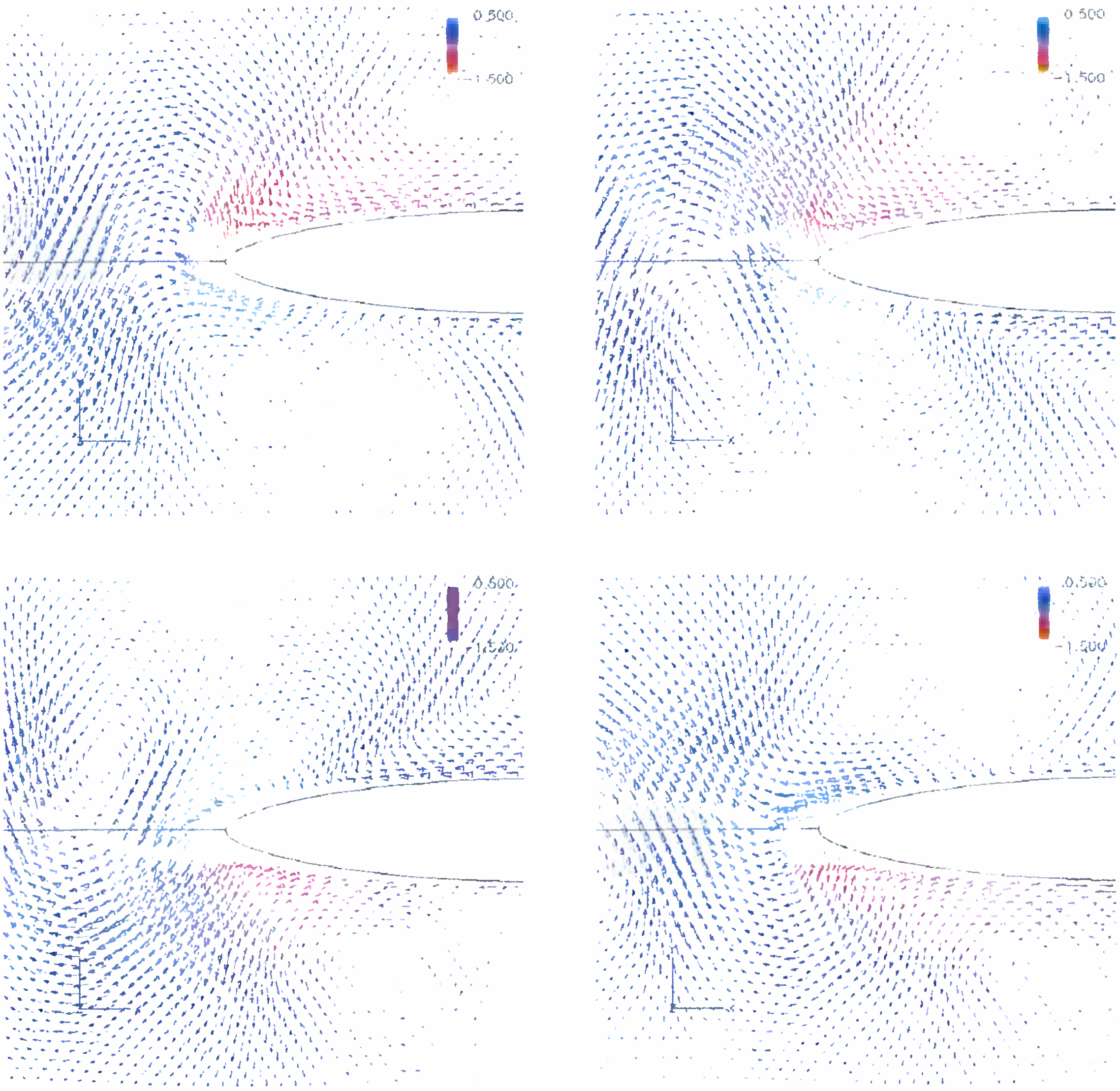

FIGURE 8.28: Instantaneous relative velocity vector field : $\alpha = 0^o$. In order to improve the quality of the visualization, the first mesh layer, that corresponding to the airfoil contour on a C-grid, has been removed.

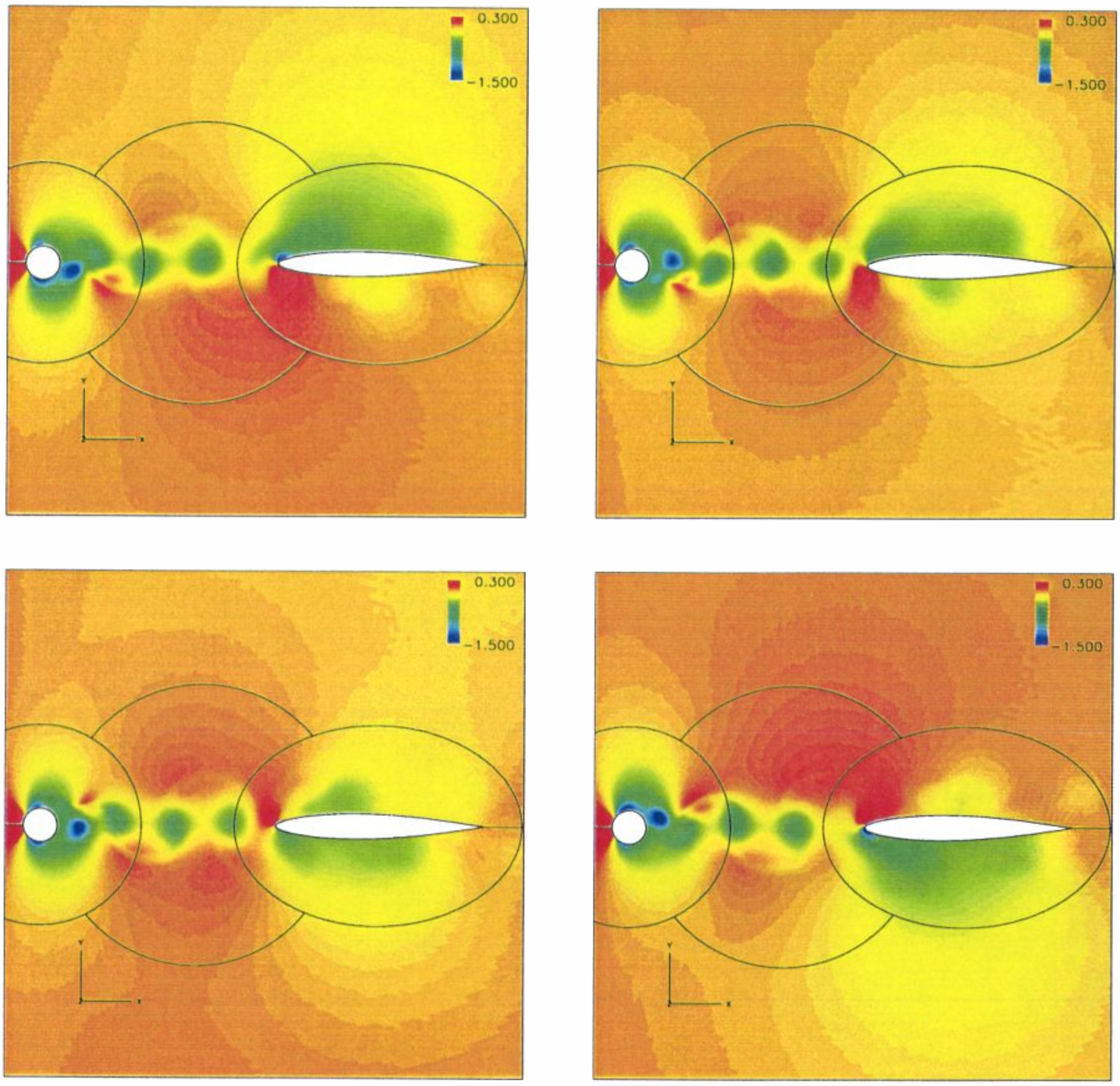

FIGURE 8.29: Instantaneous distribution of the pressure coefficient: $\alpha = 0^o$.

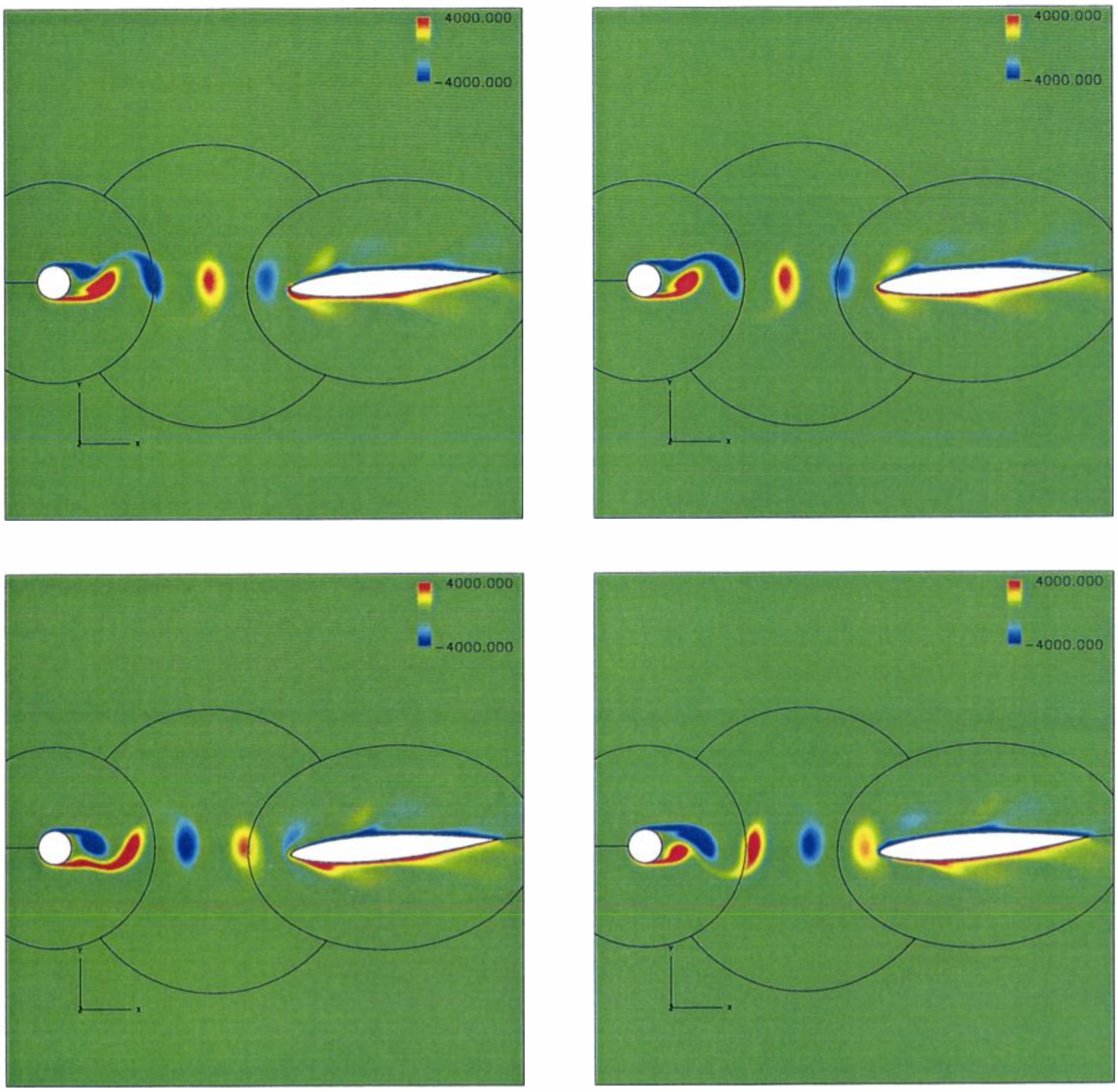

FIGURE 8.30: Instantaneous distribution of the vorticity: $\alpha = -4^o$.

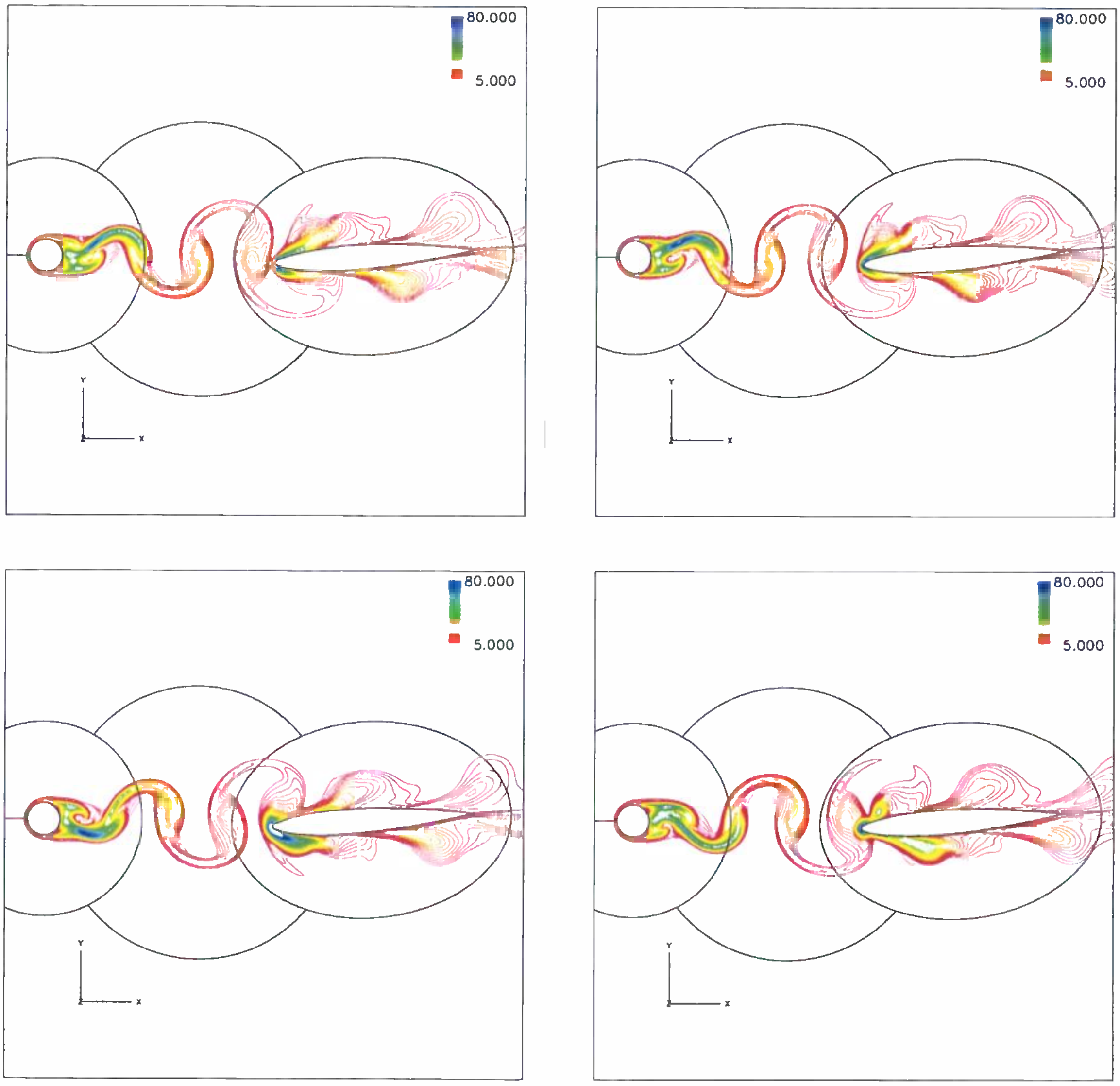

FIGURE 8.31: Instantaneous distribution of the turbulent kinetic energy: $\alpha = -4^o$.

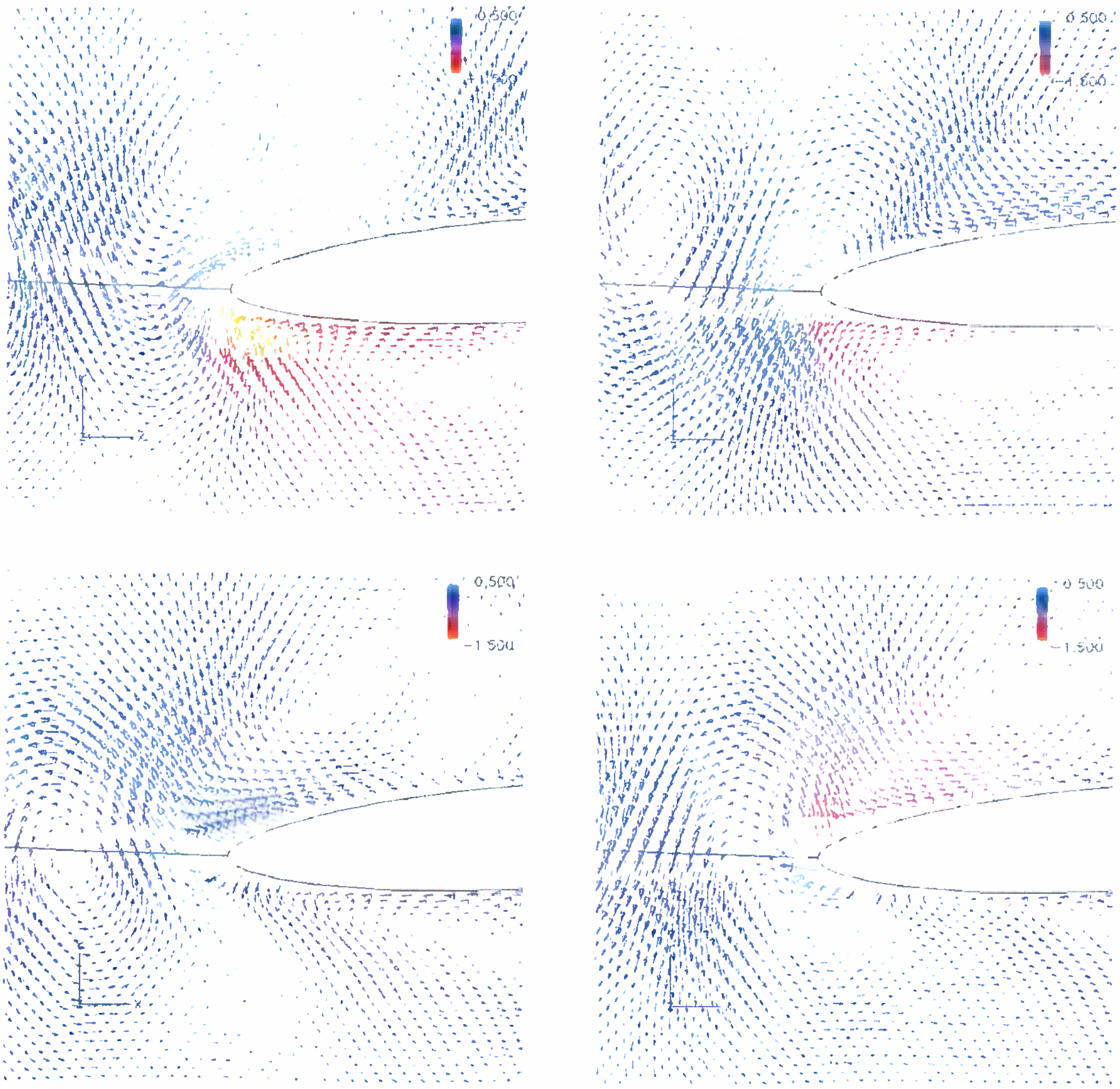

FIGURE 8.32: Instantaneous relative velocity vector field : $\alpha = -4^o$. In order to improve the quality of the visualization, the first mesh layer, that corresponding to the airfoil contour on a C-grid, has been removed.

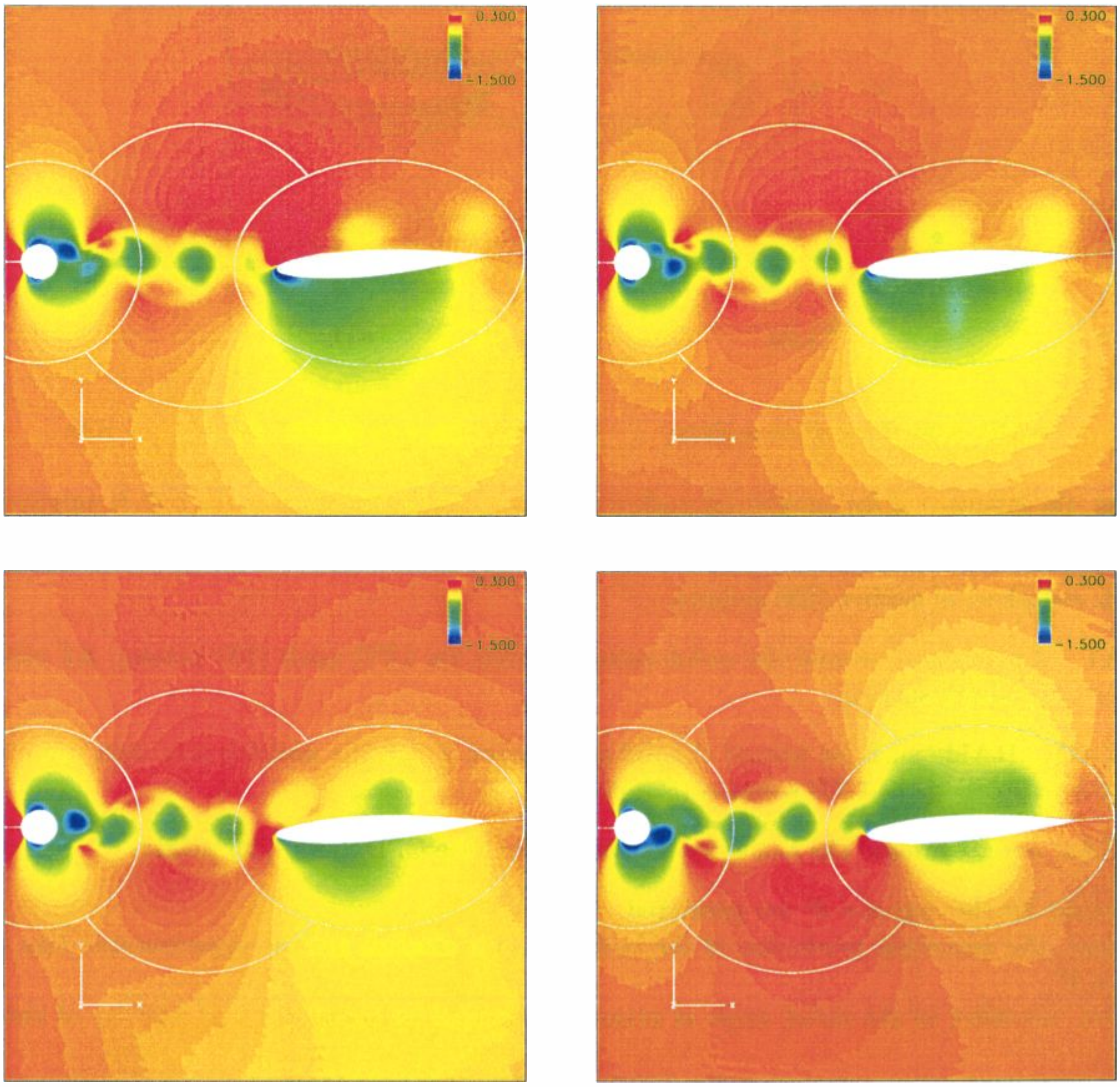

FIGURE 8.33: Instantaneous distribution of the pressure coefficient: $\alpha = -4^o$.

8.5.2 Acoustic Results

In the present section results concerning the rod-airfoil aeroacoustic prediction are presented and discussed.

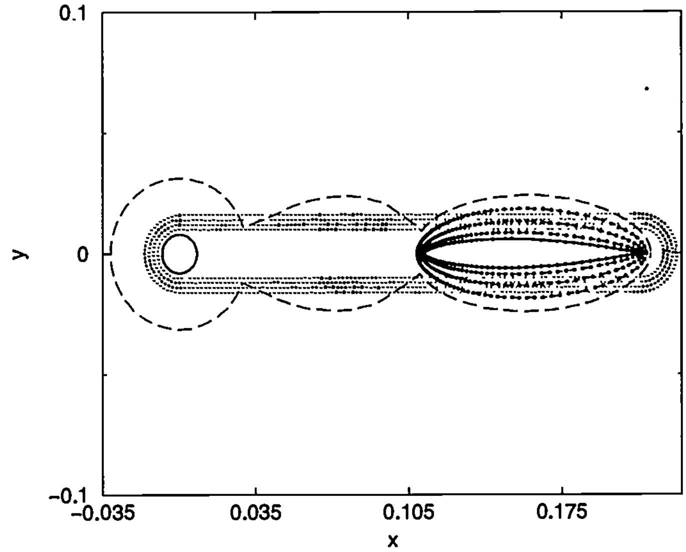

FIGURE 8.34: Integration surfaces: ——R, ••A1...A4, - - - -RAi1...RAi4, — —RAe.

First, the influence of the integration surface is investigated by integrating the FW-H equation upon the various contours plotted in Fig.8.34. These are:

- **R**: rod physical surface (200 points);
- **A1...A4**: surfaces around the airfoil extracted from the CFD mesh (200 points), **A1** coinciding with the airfoil surface;
- **RAi1...RAi4**: surfaces around the rod-airfoil upon which the aerodynamic data are obtained by interpolating the CFD solution (520 points);
- **RAe**: surface around the rod-airfoil extracted from the CFD mesh (595 points).

Only results for the case $\alpha = 0^o$ are presented.

Second, the numerical prediction of the airfoil noise is checked against experimental data for the case $\alpha = 0^o$.

Third, the effect of the airfoil angle of attack is discussed by showing the directivity of the airfoil noise.

8.5.2.1 Influence of the integration surface

In this subsection acoustic computations are performed on the base of a two-dimensional flow (no spanwise effects).

In Fig.8.35 the acoustic spectrum at $\theta = 90^o$ obtained from different integration surfaces is shown. First, the rod **R** and the airfoil **A1** contributions are compared in Fig.8.35(a) to the noise obtained by integrating upon **RAi1**, which surrounds the rod-airfoil system. The aerodynamic data on **RAi1** are obtained from a space interpolation of the CFD solution. This causes an unphysical behaviour at $1000\,\mathrm{Hz} \lesssim f$. Interestingly, as shown in Fig.8.35(b), integrations upon **RAi1...RAi4** provide unphysical but consistent results. Then, results obtained by integrating upon **A1...A4** are compared in Fig.8.35(c). Only small differences appear at even harmonics, showing again the consistency of the penetrable FW-H formulation. Finally, in Fig.8.35(d) the rod **R** and the airfoil **A1** contributions are compared to that obtained from the surface **RA**e, which is extracted from the CFD mesh and surrounds the rod-airfoil system. Now the rod-airfoil spectrum exhibits a physically reliable behaviour.

Fig.8.35(d) shows that at $\theta = 90^0$ the airfoil is $86.9 - 71.1 = 15.8$ dB louder than the rod. This corresponds to a lift amplitude ratio of 6.16, provided that at low Mach numbers the acoustic radiation is essentially dipolar. Interestingly, such a value is in good agreement with that found in Fig.8.12.

In Fig.8.36(a) the rod **R** and the airfoil **A1** acoustic signals are checked against that obtained from **RA**e. Surprisingly, the rod-airfoil system is quieter than the airfoil alone. This is because the rod and the airfoil signals are in a partial phase opposition and because the computed shedding and the rod wake are deterministic. The directivity in Fig.8.36(b) shows that, at $\theta = 90^o$, the rod-airfoil sound pressure level is about 2 dB lower than that generated by the airfoil alone.

In order to further check the consistency of the penetrable FW-H prediction, Fig.8.37 shows the relative difference between the **RA**e noise and the sum of the rod **R** and the airfoil **A1** contributions. The spectrum of $\Delta p'/\max(p')$ exhibits an enveloped broadband behaviour with harmonics peaks, the even ones being slightly higher. Such a difference may be due to numerical as well as physical effects, namely, nonlinear contributions from the flow field inside **RA**e. The even harmonics effect has been observed also in Fig.8.35(c) by integrating upon surfaces surrounding the airfoil alone. This fact plays in favor of the possible physical reliability of Fig.8.37.

8.5.2.2 Comparison with acoustic measurements

In this subsection acoustic computations are performed by forcing statistical three-dimensional effects into the aerodynamic field.

In Figs.8.38 through 8.41, acoustic results are checked against experimental data. Both the rod alone and the rod-airfoil noise are plotted. The numerical rod-airfoil noise is indeed the airfoil contribution obtained from **A1**. This is justified by the small difference previously observed between the computed airfoil noise and the rod-airfoil noise. Moreover, such a difference is even smaller if a deterministic phase opposition is smeared by some statistical effects.

The numerical prediction is performed by assuming a two-dimensional aerodynamic field (2D), and an aerodynamic field undergoing a Gaussian correlation along the rod and the airfoil spans (3D). The measured power spectral densities have been integrated upon intervals of $\Delta f = 32.5\,\text{Hz}$ in order to provide sound levels against which the numerical ones can be checked. Furthermore, the aerodynamic Strouhal frequency overprediction is taken into account by scaling the numerical results (f,dB) to (f', dB'), i.e.

$$f' = \frac{\text{St}_{\text{exp}}}{\text{St}_{\text{num}}} f, \quad \text{dB}' = \text{dB} + 20 \log \left(\frac{\text{St}_{\text{exp}}}{\text{St}_{\text{num}}} \right) \tag{8.6}$$

where the level correction accounts for the fact that the sound level is proportional to the vortex shedding frequency.

In Fig.8.38 the rod noise spectrum at $\theta = 90^o$ is plotted. The Strouhal peak is well predicted by both the 2D and 3D computations. Conversely, the second and third harmonic peaks are not well predicted. Comparing 2D and 3D results shows that the statistical model allows a quite accurate prediction of the broadband spectral behaviour. This is because the spanwise random distribution of the vortex shedding phase results in a random amplitude modulation of the acoustic signal. The second and third harmonic levels in the measurements are likely to be contaminated by installation effects. In fact, as pictured in Fig.5.1(a), the rod is located slightly downstream of the duct end. Therefore, diffraction effects may be responsible for a different acoustic behaviour with respect to that of an isolated rod.

In Fig.8.39 the rod-airfoil noise spectrum at $\theta = 90^o$ is plotted. Computations provide an overprediction of about 3 dB of the Strouhal peak. This is not surprising for the airfoil alone prediction. In

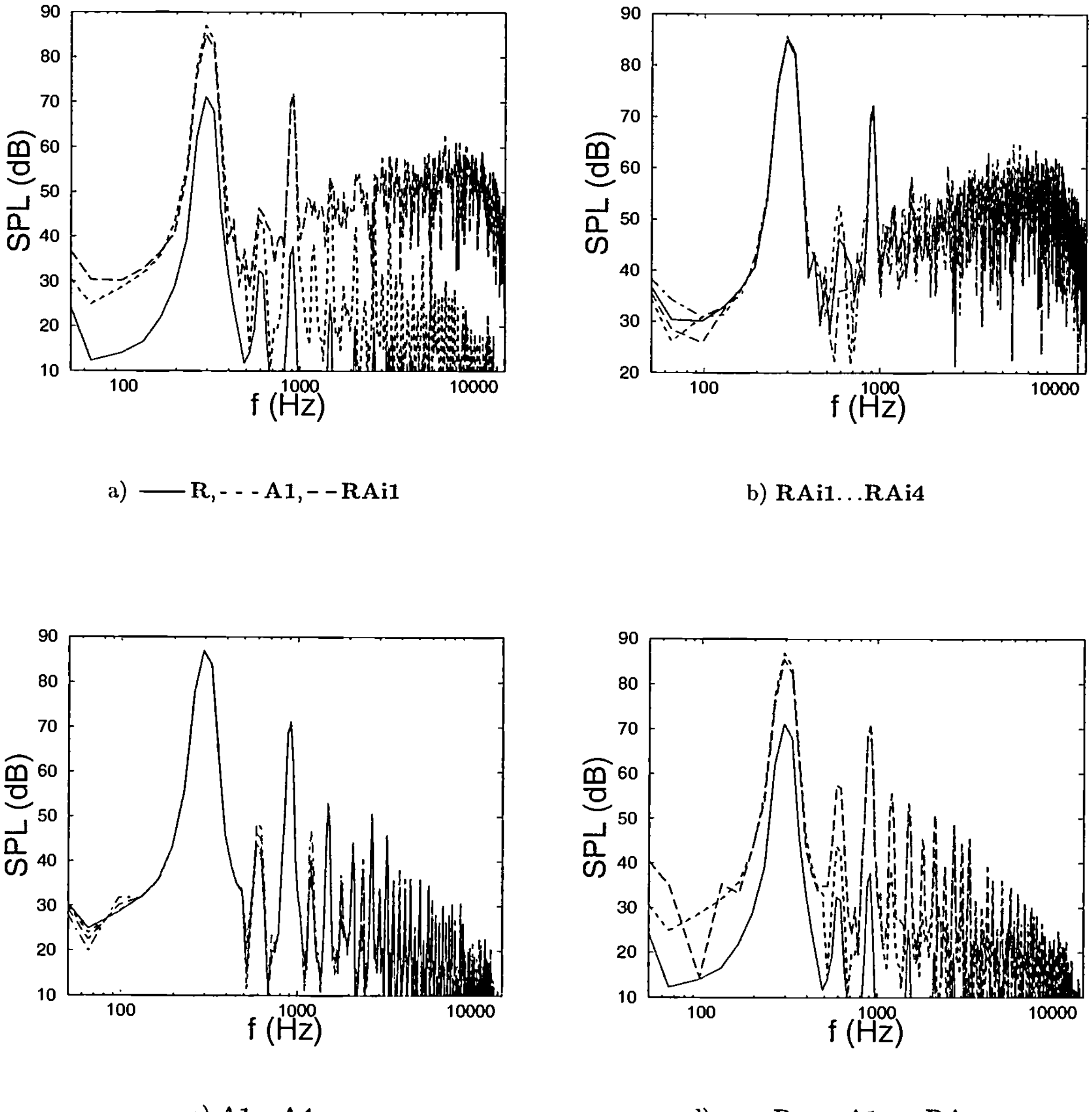

a) —— R, - - - A1, - - RAi1

b) RAi1. . .RAi4

c) A1. . .A4

d) —— R, - - - A1, - - RAe

FIGURE 8.35: Acoustic spectrum at $\theta = 90^o$ obtained from various integration surfaces. 2D aerodynamic field.

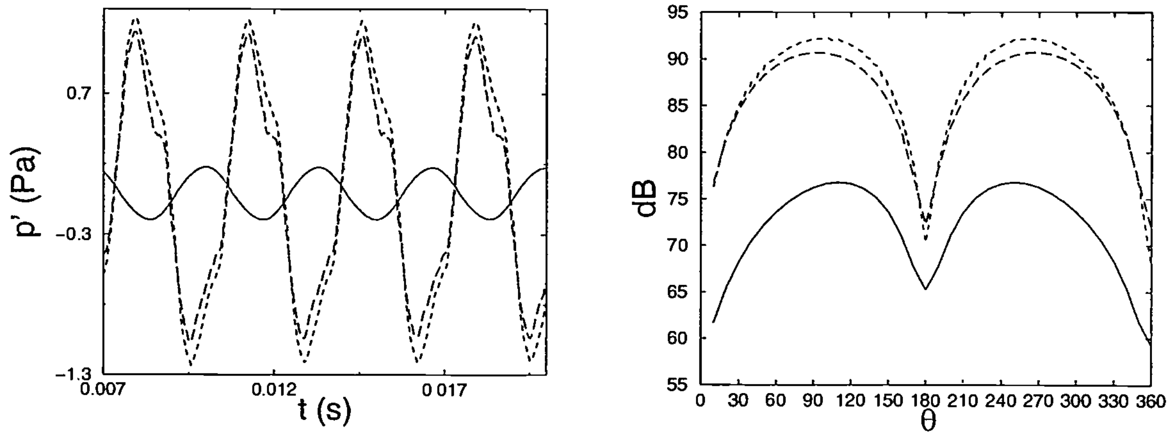

a) Time trace at $\theta = 90^o$

b) Directivity

FIGURE 8.36: Acoustic field: ——rod, - - - - airfoil, — — rod-airfoil. 2D aerodynamic field.

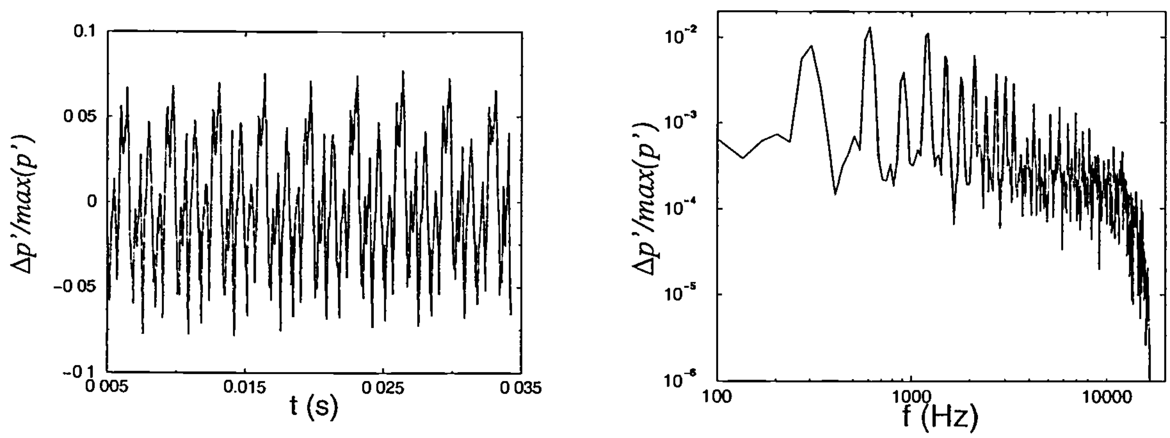

FIGURE 8.37: Relative difference between the rod-airfoil noise **RAe** and the sum of the rod **R** and the airfoil **A1** contributions at $\theta = 90^o$. Signal (left), spectrum (right). 2D aerodynamic field.

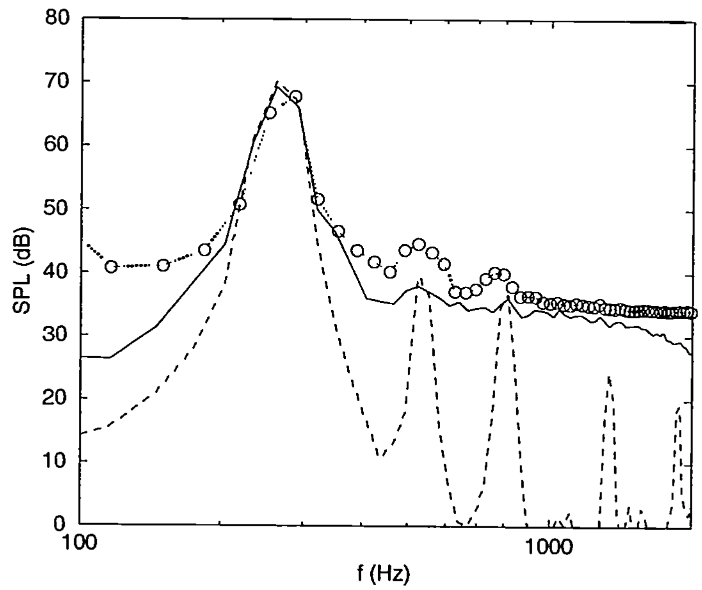

FIGURE 8.38: Rod noise spectrum at $\theta = 90^o$. Comparison between: o Experimental data, - - - - 2D prediction, —— 3D prediction.

fact, as previously discussed, the rod-airfoil system is about 2 dB quieter than the airfoil alone. The 3D results show improvements in the prediction of the third harmonic peak. Moreover, the broadband spectral behaviour is quite well featured by the 3D computation.

In Fig.8.40 the predicted rod noise spectra at different observation angles are plotted. Comparing 2D and 3D results shows that the spanwise statistical model contributes to the broadening of the main peak, reduces the higher harmonic peaks and generates a broadband spectral behaviour.

Finally, in Fig.8.41 the airfoil noise prediction is compared to rod-airfoil noise measurements at different observation angles. As for the rod noise computation, the random phase dispersion results in a better prediction of both the higher harmonic peaks and the broadband spectral behaviour.

8.5.2.3 Effects of the airfoil angle of attack

In this subsection the influence of the airfoil angle of attack onto the acoustic field is briefly discussed.

In Fig.8.42 the noise directivity obtained by applying the FW-H acoustic analogy to the pressure field upon the airfoil surface is plotted for two angles of attack, namely $\alpha = 0^o$ and $\alpha = -4^o$. Moreover, in Fig.8.43 the directivity is compared to the $\sin^2(\theta)$ dipole pattern. The results show that the airfoil angle of attack affects the noise levels only negligibly. This behaviour is confirmed by the experimental results discussed in chapter 5.

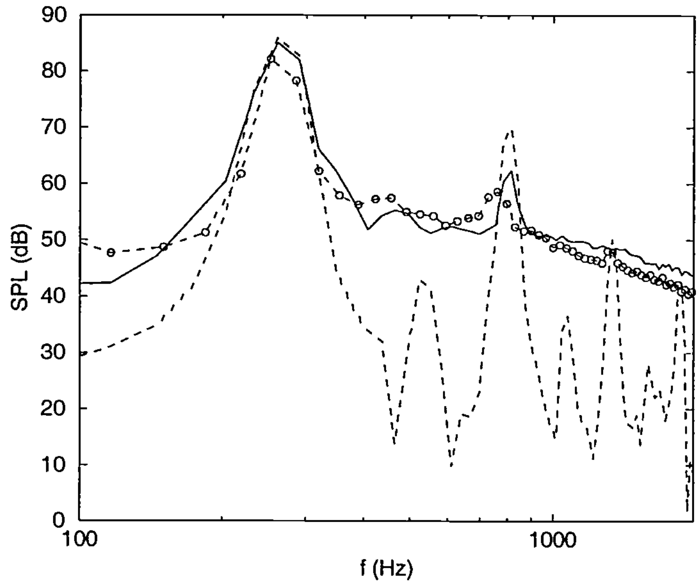

FIGURE 8.39: Rod-airfoil noise spectrum at $\theta = 90^o$. Comparison between: o Experimental data, - - - - 2D prediction, —— 3D prediction.

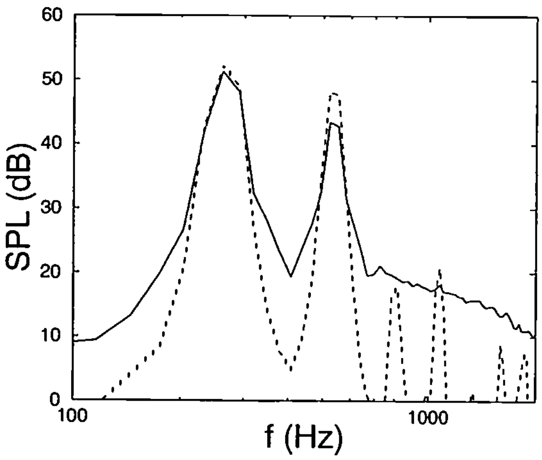

a) $\theta = 10^o$

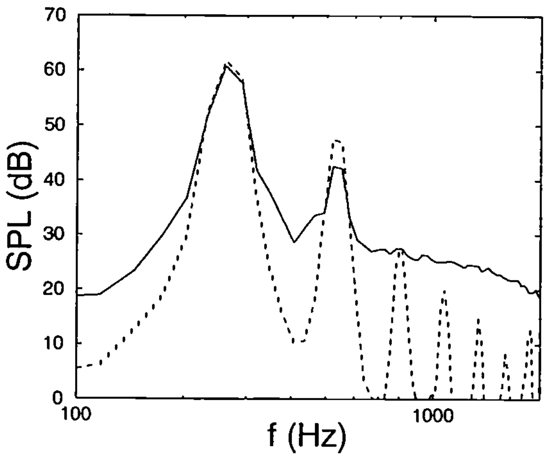

b) $\theta = 30^o$

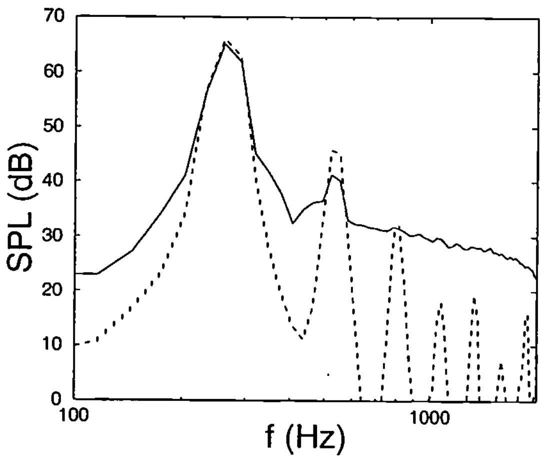

c) $\theta = 50^o$

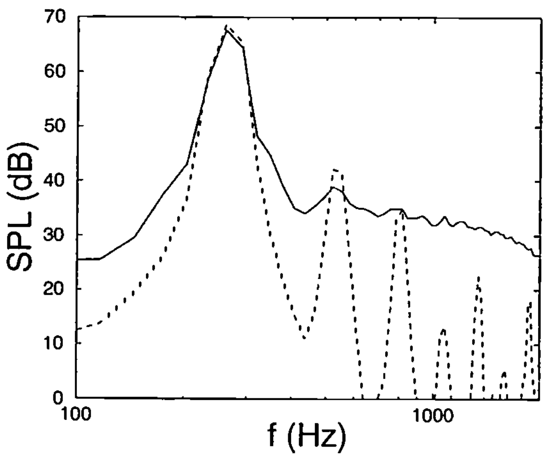

d) $\theta = 70^o$

FIGURE 8.40: Rod noise spectrum. Comparison between: - - - - 2D prediction, —— 3D prediction.

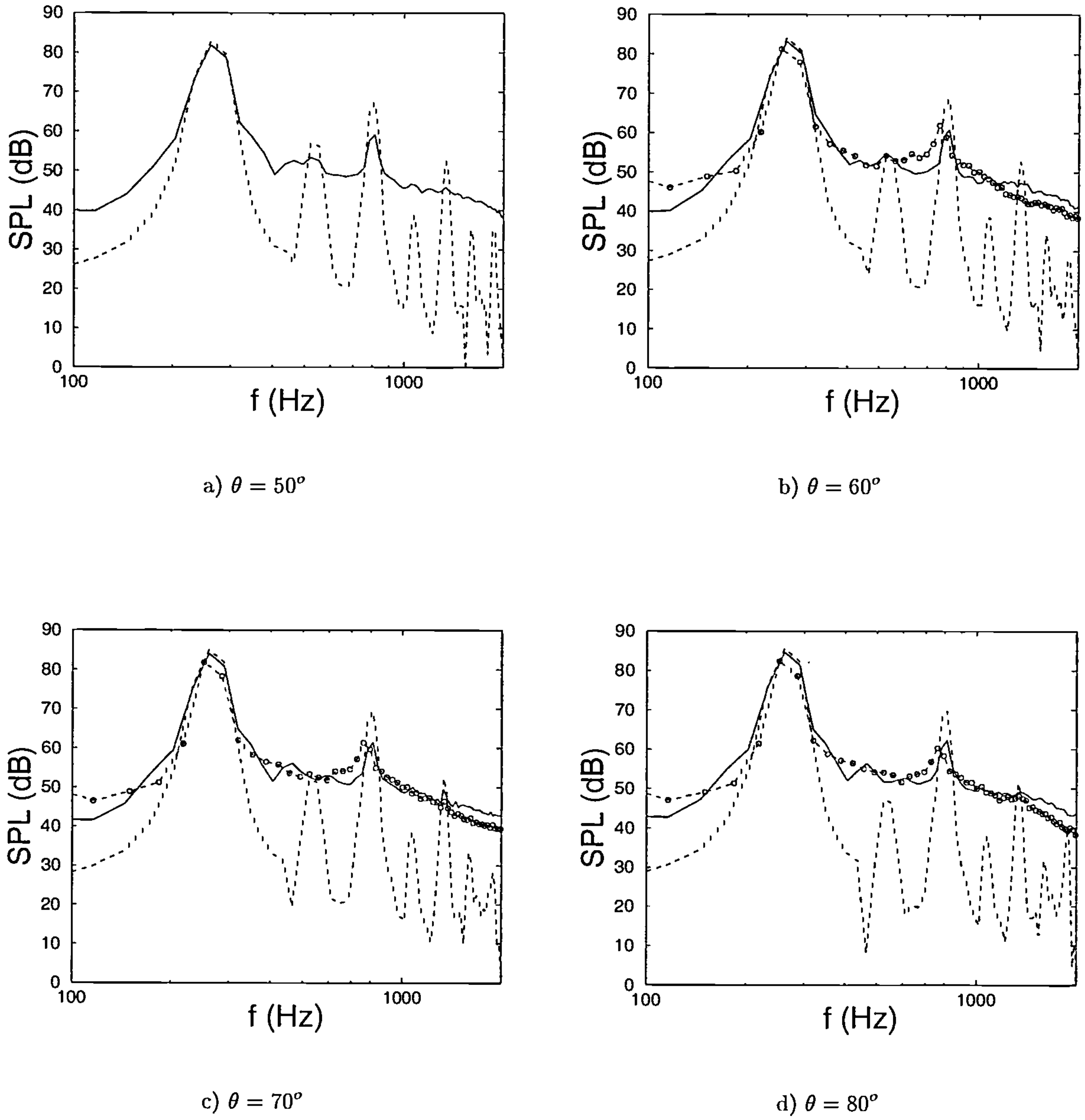

a) $\theta = 50^o$

b) $\theta = 60^o$

c) $\theta = 70^o$

d) $\theta = 80^o$

FIGURE 8.41: Rod-airfoil noise spectrum. Comparison between: o Experimental data, - - - - 2D prediction, —— 3D prediction.

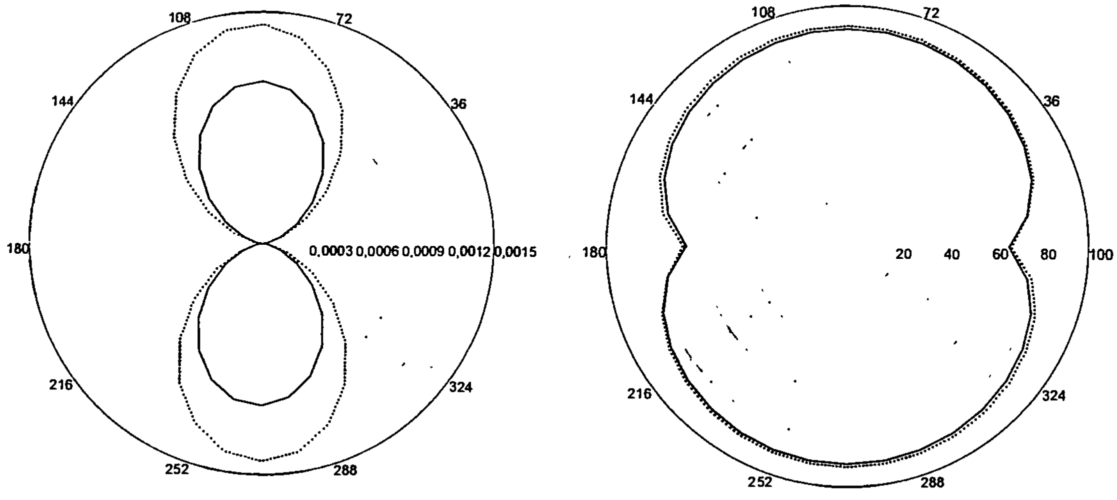

a) Acoustic intensity (W/m^2).

b) Sound pressure level (dB).

FIGURE 8.42: Airfoil noise directivity pattern: —— $\alpha = 0^o$, - - - - $\alpha = -4^o$.

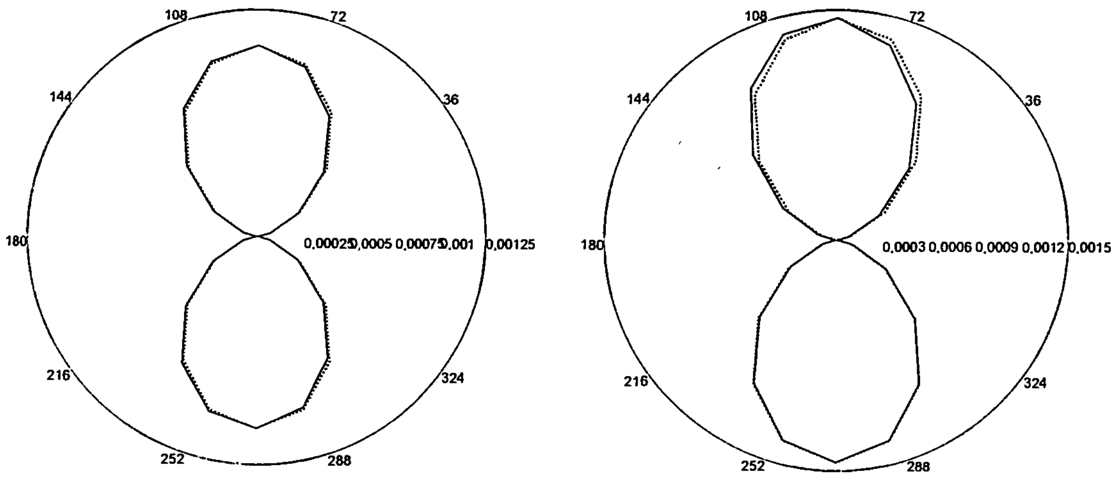

a) $\alpha = 0^o$.

b) $\alpha = -4^o$.

FIGURE 8.43: Acoustic intensity (W). —— Computed airfoil noise, - - - - dipolar radiation.

8.6 Conclusions

In this chapter we discussed results of a hybrid RANS/FW-H aeroacoustic prediction of the rod-airfoil configuration. The main features of the flow were featured by the unsteady RANS computation:

- the periodic formation of vortices in the wake of the rod was simulated without artificial forcing;
- staggered vortices were convected towards the airfoil without significative numerical dissipation;
- vortex impingements onto the airfoil leading edge were accompanied by deformation of the vorticity field and consequent vortex splitting.

However, some discrepancies with the experimental results discussed in chapter 5 were found:

- the Strouhal frequency was overpredicted;
- the computed Strouhal frequency was slightly affected by the airfoil angle of attack;
- the aspect ratio b/a of the double row of vortices shed from the rod seemed to be underestimated;
- the intensity of the pressure fluctuations near the airfoil leading edge was overestimated.

Discrepancies in items 1, 2 and 4 can be related to the unreliability of a two-dimensional computation: the rod wake is indeed characterized by a complex three-dimensional vortical flow, and a strong/rapid distortion of the vorticity field near a leading edge is an intimately three-dimensional process.

Concerning the Strouhal frequency, a two-dimensional simulation overestimates the in-plane Reynolds stresses. This results in a smaller mean recirculating region behind the rod and in a higher shedding frequency.

Concerning the dependence of the Strouhal frequency on the airfoil angle of attack, this is presumably due to a coupling mechanism between the airfoil hydrodynamic field and the flow instability generating the Kármán vortex street. The possibility of a feed-back onto the rod vortex shedding process seems to be confirmed by the experiments: introducing the airfoil in the wake of the rod affects the vortex shedding frequency. However, any coupling mechanism in experiments is likely to be smeared by the three-dimensional character of the flow.

The higher level of the pressure fluctuations predicted near the leading edge can be probably explained by considering that:

- in a three-dimensional flow, a part of the mean flow energy is used to maintain spanwise fluctuations;
- the RANS closure model used in the present investigation is inadequate for regions of high flow anisotropy.

The origin of the aspect ratio underestimation is still obscure. However, as discussed in section 5.3, an experiment performed in a water channel showed the existence of a rod shedding mode characterized by a lower transversal spacing of the vortex street and a higher shedding frequency.

Comparing the computed acoustic spectra to the experimental ones confirmed that the accuracy of the acoustic analogy prediction hinges primarily on the capability of the CFD computation in featuring the physics of the flow. An excellent agreement was obtained in terms of peak values at the Strouhal frequency and higher harmonics. On the contrary, discrepancies were found in the broadband part of the acoustic spectra. These are clearly due to the intrinsic limits of a two-dimensional RANS computation.

Hence we showed how a spanwise statistical model can be used in an acoustic analogy to account for three-dimensional effects which are not featured by a two-dimensional flow computation. Sound predictions were significantly improved and the broadband part of the sound field was quite well predicted. The model requires only an a priori knowledge of the spanwise correlation length and shape.

In the rod-airfoil configuration, the airfoil contribution was shown to be dominant. However, a fully correlated (2D) sound computation predicted partial cancelations between rod and airfoil contributions. These are not likely to be found in the non deterministic three-dimensional flow. Therefore, the airfoil contribution gives a good estimate of the overall noise.

Moreover, interesting results were found or confirmed about the choice of a suitable integration surface:

- it should coincide with grid points of the CFD domain;

- in low Mach number applications, volume sources are negligible with respect to surface sources and the physical surfaces are thus good integration surfaces.

The statistical analogy is an interesting tool for complex flow configurations where only unsteady but deterministic RANS computations can be carried out. However, our activity points towards an improvement of the rod-airfoil broadband noise prediction, without forcing any *ad hoc* flow statistical behaviour. This challenging goal requires the turbulent fluctuations to not be smeared by an average statistical treatment, as in a RANS approach. Since the Large Eddy Simulation (LES) approach is expected to provide a more realistic flow description, an LES of the rod-airfoil configuration is currently in progress.

9

Epilogue of part I

The first part of the present work was devoted to the aeroacoustic characterization of a low Mach number rod-airfoil configuration. We were concerned with:

- the vortex dynamics in the wake of the rod and the dynamics of a vortex-airfoil interaction;
- the sound generation mechanisms in a vortex-body interaction;
- the feasibility of accurate aeroacoustic predictions based on the acoustic analogy model.

The experimental activity had a supporting role in the context of our research. However, the aeroacoustic experiments described in chapter 5 and the visualization experiment described in section 5.3 shed light on many features of the rod-airfoil aeroacoustic behaviour:

- the spectral character of the acoustic far field;
- the weak dependence of the noise levels on the airfoil angle of attack;
- the influence of the airfoil angle of attack on the trajectory of the oncoming vortices;
- the influence of the vortex trajectories on the spectral behaviour of both the wall pressure field and the acoustic far field;
- the importance of three-dimensional effects in the rod wake;
- the existence of a vortex shedding mode from the rod, characterized by a higher Strouhal frequency and a smaller distance between the rows of the vortex street.

The analytical activity described in chapters 2 and 3 was the kernel of the present work. It exploited the circulation theory and a Kármán-Trefftz conformal mapping in order to describe an incompressible, high Reynolds number vortical flow past a thick and cambered airfoil. The resulting vortex method was used to investigate many aspects of a vortex-airfoil interaction problem. In addition, the limits of validity of both a line-vortex description and a fixed-wake assumption were numerically explored. An interesting aspect of the proposed methodology was the analytical decomposition of the time derivative of the wall pressure field in different contributions, each related to a nonlinear interaction mechanism. Thus, we showed the existence of wavelike contributions transported by the vortex, and contributions related to the vortex passage by the airfoil leading edge and by the trailing edge. Among these, only the contributions arising near the airfoil leading edge act as effective acoustic sources.

The analytical description of the pressure field past the airfoil was also used to find an outer expansion of the inner hydrodynamic field. Then, the inner expansion was matched to an outer acoustic solution. This MAE approach showed that the aerodynamic force and the aerodynamic moment induced by a vortex on the airfoil generate dipole and quadrupole noise, respectively.

The external aerodynamic noise can be successfully predicted through an acoustic analogy approach. We started from this assumption and moved towards an improvement of the existing methodologies. In chapter 6 we proposed a new interpretation of the retarded time approach used in the prediction of acoustic fields from moving sources. A simple hierarchical inversion between the emission time and the reception time was the fundament of an advanced time approach. This consists in projecting the current status of a source in the observer time domain where the received signal is progressively built. The practical relevance of this methodology lies on two statements:

- no retarded time equations must be solved;
- an aerodynamic noise prediction can be processed parallelly to the aerodynamic simulation.

Theoretically, the advanced time approach differs from the retarded time approach only in one aspect: a signal emitted at a given instant by a point source, moving at subsonic as well as supersonic velocity, is received only one time by an observer moving at a subsonic velocity. Consequently, only one value of the advanced time corresponds to a value of the emission time. The advanced time approach was applied to a retarded time solution of the Ffowcs Williams & Hawkings equation and was implemented in the rotor noise code *Advantia.*

A problem commonly encountered in the prediction of aerodynamic noise from bluff bodies in cross-flow is due to the intrinsic three-dimensional character of the flow. This is typically the case of a circular cylinder. In chapter 7 we proposed a spanwise statistical model for the vortex shedding phase. Then, we showed how an acoustic prediction can be performed on the base of a two-dimensional flow but accounting, to some extent, for the three-dimensional character of the real flow.

The numerical methodologies developed in chapter 6 and chapter 7 were applied in chapter 8 to the rod-airfoil aeroacoustic prediction. An unsteady RANS aerodynamic computation was performed for two airfoil angles of attack. The FW-H acoustic analogy formulation was used to compute the far pressure field. Comparing the predicted acoustic spectra with experimental results showed that the accuracy of an acoustic analogy prediction hinges primarily on the accuracy of the aerodynamic simulation in featuring the physics of the flow. Hence, an excellent agreement was found in terms of peak values, but discrepancies were found in the broad band part of the spectrum. These discrepancies were due to the limits of a two-dimensional unsteady RANS computation and were significantly reduced by forcing a spanwise random behaviour into the flow used for the acoustic analogy prediction.

A *genuine* prediction of the broadband acoustic radiation from a rod-airfoil configuration requires the random flow fluctuations to not be smeared by an average statistical treatment as in a RANS approach. Therefore a three-dimensional Large Eddy Simulation of the rod-airfoil configuration is currently in progress.

II

Aerodynamic Noise in Fluid-Body Interactions

Preface to part II

This second part deals with the aeroacoustic problem of sound generated by unsteady flows past rigid surfaces.

Aeroacoustics has a history of fifty years. In the early fifties Sir James Lighthill formulated is theory of *jet-noise*. At the end of sixties, Lighthill's formulation was extended to account for moving surfaces, as required by *rotor-noise* predictions. In the seventies the noise generated by turbulent flows past extended surfaces, say *flow-noise*, became a matter of serious military concern in the detection of ships and submarines by means of wall-mounted sonars.

Nowadays jet- rotor- and flow-noise are still fervent area of research. The high-intensity noise from the jet of a space launcher remains a subject of major importance for it causes damage on aboard satellites. The low-noise levels required to meet the international standards around airports force aircraft manufactures to produce quieter engines. The comfort requirements of commercial airplanes need the flow-noise mechanisms to be understood and controlled.

Unsteadiness in a compressible flow generates acoustic waves. When these pressure fluctuations are detected as noise by an observer in the far field, their energy is only a very small fraction of that involved in the generation process. In these terms, aerodynamic sound is a *by-product* of flow unsteadiness. Aeroacoustics, on the contrary, are not a by-product of aerodynamics. Predicting a by-product requires a deep insight into the productive process. Moreover, predicting a by-product using incomplete and inaccurate information about the productive process is a challenging goal.

As a theory of the aerodynamic by-product, aeroacoustics is intimately joined with aerodynamics. This is a necessary condition to understand the physical mechanisms by which aerodynamic sound is generated. In addition, aeroacoustics largely uses physical modeling in order to relate the behaviour of the induced wave motion to easily estimated flow quantities. Modeling is necessary, because many unsteady flow mechanisms are still unclear and unpredictable.

In developing predictive models, aeroacoustics is also concerned with the propagation of acoustic waves around diffracting obstacles. This forces aeroacoustics to leave aside aerodynamics and to become more confident with acoustics.

The dual nature of the aeroacoustic problem reflects the structure of the present work. The first four chapters are concerned with aerodynamic subjects, whereas the other six deal with aeroacoustic subjects. The aerodynamics chapters provide a *minimum* background for understanding the physics of sound generated aerodynamically. Only chapters 2 and 5 have grown-up of a relaxation of such a minimum condition. The aeroacoustic chapters are focused on some fundamental aspects concerning fluid-body interactions. A brief overview of the present part follows.

Chapter 1 introduces the reader to the physics of flow by presenting its governing equations. Different flow models are illustrated and the theory of potential flows is introduced.

Chapter 2 describes a perturbative analysis of the flow governing equations, which shows the role of nonlinearity in coupling the acoustic, vortical and entropic modes of fluctuation in a fluid. This analysis describes the physical mechanisms by which sound is generated by vortical and entropic fluctuations.

Chapter 3 is concerned with the statistical behaviour of the pressure field upon a rigid plate beneath a turbulent boundary layer. Theories and models are described, which provide the aerodynamic background for two aeroacoustic problems: flow-noise and broad-band interaction noise.

Chapter 4 illustrates the aerodynamic theories predicting the unsteady force upon an airfoil embedded in a harmonic gust. These are typically linearized theories dealing with thin airfoils at small angles of attack. Their relevance lies on the fact that the airfoil response to a generic unsteady perturbation can be determined as a superposition of elementary solutions, each related to a spectral component of the flow unsteadiness. A second order theory is also presented. This permits to relax the conditions of small airfoil thickness and small angle of attack required by a linearized theory. Both incompressible and compressible theories are discussed. These form the theoretical basis on which many aeroacoustic models of vortex-airfoil *interaction noise* are developed.

Chapter 5 is concerned with the physics of noise generated aerodynamically. In this chapter the flow governing equations are scrutinized under the light of a modal approach. Moreover, the existing jet-noise theories are reviewed and the conceptual adequacy of Lighthill's acoustic analogy is discussed.

Chapter 6 illustrates the theory of vortex sound. This represents a different interpretation of Lighthill's acoustic analogy and shows the role of vorticity in the generation of aerodynamic sound. Moreover, Howe's acoustic analogy formulation is presented. From a physical point of view, the Howe's theory provides a comprehensive and generalized approach to the aerodynamic sound problem.

Chapter 7 illustrates the Ffowcs Williams & Hawkings' acoustic analogy formulation. This extends Lighthill's theory to account for the presence of bodies moving arbitrarily into the field. Farassat' mathematical formalism is described in great detail. This allows the Ffowcs Williams & Hawkings acoustic analogy to be used for propeller- and rotor-noise predictions.

Chapter 8 is concerned with the problem of sound generation by vortical disturbances near the edge of a semi-infinite flat-plate. This flow configuration is a model problem for investigating the effects of a geometrical singularity on the acoustic radiation.

Chapter 9 deals with the problem of trailing edge noise. The flow configuration is the same as in chapter 8, but more emphasis is given to the aerodynamic mechanisms taking place near the edge of a thin airfoil in the presence of a turbulent flow.

Chapter 10 is concerned with the problem of vortex-airfoil interaction noise. Different analytical formulations are illustrated and computational methodologies are reviewed. Particular emphasis is given to the blade-vortex interaction noise which is a major source of helicopter impulsive noise.

1

Basic Equations of Fluid Mechanics

1.1 Introduction

Fluids possess the distinctive property of not having a definite shape. Under the action of a force different *elements* of a fluid portion may change their reciprocal position, but the properties of the fluid do not change.

Liquids and gases behave like fluids, whereas solids do not. This depends on both the molecular structure and the nature of the intermolecular forces. In gases under ordinary conditions, the molecules are so far from each other that they only experience a negligible attractive force which is due to their mutual electrical polarization. Conversely, in liquid and solid phases, a quite smaller intermolecular distance permits a molecular interaction of quantum nature. Therefore, the different behaviour observed in liquid and solid phases is only due to a small change of the molecular spacing.

When a fluid is observed on the molecular scale, its properties appears as strong nonuniform distributions. However, the scale adopted to observe the macroscopic behaviour of a fluid is so large compared to the typical intermolecular distance that a *continuum hypothesis* is generally supported.

The consistency of the continuum approximation depends on the value of the Knudsen number. This is defined as the ratio between the molecular mean free path l and a macroscopic reference length L. If σ, v_t and $\mathcal{N}$ denote the molecular collision section, the molecular chaotic velocity and the number of molecules per unity of volume, respectively, the mean time between two collisions is $(\mathcal{N}\,\sigma\, v_t)^{-1}$, and the mean free path is $(\mathcal{N}\,\sigma)^{-1}$. Therefore, the Knudsen number is given by

$$\mathrm{Kn} = \frac{1}{\mathcal{N}\sigma L} = \frac{m}{\sigma\, L}\,\frac{1}{\rho} \tag{1.1}$$

where m is the molecular mass and ρ is the density of the fluid. Typical values of l, in standard atmosphere, are 6.6×10^{-8} m at sea level and 1.0×10^{-2} m at an altitude of 8×10^{4} m. Thus, for standard applications, it results that $\mathrm{Kn} \ll 1$ and the continuum hypothesis is largely satisfied.

The continuum hypothesis leads to the concept of *fluid particle*, namely, a portion of fluid that is large compared to the molecular scale, but is small compared to the macroscopic scale. The fluid particle is indeed a statistical concept and its properties must be regarded as averaged quantities over a great number of molecules.

1.2 Reynolds' Transport Theorem

The behaviour of a fluid is governed by three fundamental laws: the conservation of mass, the conservation of linear momentum and the conservation of energy.

A conservation law can be expressed as an integral equation over a portion of fluid, where the rate of change of a conservative quantity $\mathcal{F}$ in a volume of the fluid is balanced by the net flux of $\mathcal{F}$

across the bounding surface and, possibly, by a production term within the considered portion of fluid. If the properties of the fluid are continuous and their derivatives exist, the integral equation may be translated into an equivalent differential form. The Reynolds' transport theorem is the kinematical tool that allows such a mathematical transformation.

Let $\mathcal{F}(\mathbf{x}, t)$ be an arbitrary continuous and single valued function denoting any property of the fluid. Let $V(t)$ be a material volume, namely, a closed volume that is always constituted by the same fluid particles and moves together with them. Thus, the evolution of the following integral quantity

$$F(t) = \iiint\limits_V \mathcal{F}(\mathbf{x}, t)\, \mathrm{d}V \tag{1.2}$$

can be related to the fluid motion. If $\boldsymbol{\xi}$ denotes the position of a fluid particle at the initial time $t = 0$, the same particle, at the generic time t, occupies the position defined by the point transformation

$$\mathbf{x} = \mathbf{x}(\boldsymbol{\xi}, t) \tag{1.3}$$

By supposing that the particle path is continuous and single valued, equation (1.3) can be inverted in order to express the particle initial position as a continuous and single valued function, i.e.

$$\boldsymbol{\xi} = \boldsymbol{\xi}(\mathbf{x}, t) \tag{1.4}$$

The continuity condition says that two close particles still remain close during their motion, whereas the single valued property is a condition on the unequivocal correspondence between a particle and its instantaneous location.

A necessary and sufficient condition for the existence of the inverse function (1.4) is that the Jacobian of the transformation

$$J = \frac{\partial(x_1, x_2, x_3)}{\partial(\xi_1, \xi_2, \xi_3)} = \frac{\mathrm{d}V}{\mathrm{d}V_0} \tag{1.5}$$

does not vanish. The quantity J represents the ratio of an elementary material volume $\mathrm{d}V$ to its initial value $\mathrm{d}V_0$. It is thus called dilatation or expansion. The evolution of J following a material volume is established by the relation

$$\frac{1}{J}\frac{\mathrm{D}J}{\mathrm{D}t} = \nabla \cdot \mathbf{v} \tag{1.6}$$

where $\mathbf{v}$ is the velocity of the fluid and $\mathrm{D}/\mathrm{D}t$ is the material (or Lagrangian) derivative, defined as

$$\frac{\mathrm{D}}{\mathrm{D}t} = \frac{\partial}{\partial t} + \mathbf{v} \cdot \nabla \tag{1.7}$$

Equation (1.6) establishes a physical relation between the divergence of the velocity field and the dilatation of a fluid particle during its motion.

The concept of material derivative together with the definition of volume dilatation can be used to describe the time evolution of the integral quantity $F(t)$ in equation (1.2). A simple variable transformation yields

$$\frac{\mathrm{d}}{\mathrm{d}t} \iiint\limits_V \mathcal{F}(\mathbf{x}, t)\, \mathrm{d}V = \frac{\mathrm{D}}{\mathrm{D}t} \iiint\limits_{V_0} \mathcal{F}\left(\mathbf{x}\left(\boldsymbol{\xi}, t\right), t\right)\, J\, \mathrm{d}V_0 \tag{1.8}$$

where the time derivative at the first member is intrinsically a material derivative. Since the volume V_0 at the second member is fixed, the derivative operator and the integral operator can be permuted yielding

$$\frac{\mathrm{d}}{\mathrm{d}t} \iiint\limits_V \mathcal{F}(\mathbf{x}, t)\, \mathrm{d}V = \iiint\limits_{V_0} J \left\{ \frac{\partial \mathcal{F}}{\partial t} + \nabla \cdot (\mathcal{F}\mathbf{v}) \right\} \mathrm{d}V_0 \tag{1.9}$$

where use of equations (1.6) and (1.7) has been made. Finally, changing back to the material volume $V(t)$ provides

$$\frac{\mathrm{d}}{\mathrm{d}t}\iiint_V \mathcal{F}(\mathbf{x},t)\,\mathrm{d}V = \iiint_V \left\{\frac{\partial\mathcal{F}}{\partial t} + \nabla\cdot(\mathcal{F}\mathbf{v})\right\}\mathrm{d}V \tag{1.10}$$

Equation (1.9) is an important kinematical result, known as *Reynolds' transport theorem*. Different form and corollaries of the theorem can be formulated. Applying Gauss' theorem to the right-hand-side of equation (1.9) yields

$$\frac{\mathrm{d}}{\mathrm{d}t}\iiint_V \mathcal{F}(\mathbf{x},t)\,\mathrm{d}V = \iiint_V \frac{\partial\mathcal{F}}{\partial t}\,\mathrm{d}V + \iint_S \mathcal{F}\,\mathbf{v}\cdot\mathbf{n}\,\mathrm{d}S \tag{1.11}$$

where $\mathbf{n}$ is the outward unit normal to the surface S. Furthermore, for a generic volume of integration $V^*(t)$, equation (1.11) becomes

$$\frac{\mathrm{d}}{\mathrm{d}t}\iiint_{V^*} \mathcal{F}(\mathbf{x},t)\,\mathrm{d}V = \iiint_{V^*} \frac{\partial\mathcal{F}}{\partial t}\,\mathrm{d}V + \iint_{S^*} \mathcal{F}\,\mathbf{b}\cdot\mathbf{n}\,\mathrm{d}S \tag{1.12}$$

where $\mathbf{b}$ is the velocity of the surface $S^*(t)$, which bounds the volume $V^*(t)$. A generalized form of the Reynolds' transport theorem for a discontinuous function $\mathcal{F}(\mathbf{x},t)$ is due to Truesdell and Toupin [73]. Let the material volume $V(t)$ be constituted by the volumes V_1 and V_2, which are separated by a surface of discontinuity $\Sigma(t)$ moving at the velocity $\mathbf{b}$. If ν is the unit normal to $\Sigma(t)$ in the direction from V_1 to V_2, the Reynolds' transport theorem can be written as

$$\frac{\mathrm{d}}{\mathrm{d}t}\iiint_V \mathcal{F}(\mathbf{x},t)\,\mathrm{d}V = \iiint_V \frac{\partial\mathcal{F}}{\partial t}\,\mathrm{d}V + \iint_S \mathcal{F}\,\mathbf{v}\cdot\mathbf{n}\,\mathrm{d}S + \iint_\Sigma (\mathcal{F}_1 - \mathcal{F}_2)\,\mathbf{b}\cdot\nu\,\mathrm{d}S \tag{1.13}$$

1.3 Governing Equations of Fluid Motion

The basic equations of fluid mechanics can be obtained by applying the conservation laws of mass, linear momentum and energy to an arbitrary volume of the fluid, and making use of the Reynolds' transport theorem.

1.3.1 The Continuity Equation

The conservation of mass leads to the continuity equation

$$\frac{\mathrm{d}}{\mathrm{d}t}\iiint_V \rho\,\mathrm{d}V = 0 \tag{1.14}$$

where the material volume $V(t)$ is supposed to enclose neither sources nor sinks. Thus, using equation (1.11) gives

$$\iiint_V \frac{\partial\rho}{\partial t}\,\mathrm{d}V + \iint_S \rho\,\mathbf{v}\cdot\mathbf{n}\,\mathrm{d}S = 0 \tag{1.15}$$

For a generic volume $V^*(t)$, equation (1.12) provides

$$\frac{\mathrm{d}}{\mathrm{d}t}\iiint_{V^*} \rho\,\mathrm{d}V = \iiint_{V^*} \frac{\partial\rho}{\partial t}\,\mathrm{d}V + \iint_{S^*} \rho\,\mathbf{b}\cdot\mathbf{n}\,\mathrm{d}S \tag{1.16}$$

At a given instant, $V^*(t)$ coincides with a given material volume. Thus, considering the continuity equation (1.15) yields

$$\iiint_{V^*} \frac{\partial \rho}{\partial t} \mathrm{d}V = -\iint_{S^*} \rho \mathbf{v} \cdot \mathbf{n} \, \mathrm{d}S \tag{1.17}$$

Then, substituting into equation (1.16) gives

$$\frac{\mathrm{d}}{\mathrm{d}t} \iiint_{V^*} \rho \mathrm{d}V = \iint_{S^*} \rho (\mathbf{b} - \mathbf{v}) \cdot \mathbf{n} \, \mathrm{d}S \tag{1.18}$$

If the volume $V^*(t)$ is supposed to be fixed, equation (1.18) becomes

$$\iiint_{V^*} \left\{ \frac{\partial \rho}{\partial t} + \nabla \cdot (\rho \mathbf{v}) \right\} \mathrm{d}V = 0 \tag{1.19}$$

The arbitrariness of the integration volume $V^*(t)$ implies that the integrand must vanish everywhere, provided that it is continuous. Therefore, the continuity equation takes the differential conservative form

$$\frac{\partial \rho}{\partial t} + \nabla \cdot (\rho \mathbf{v}) = 0 \tag{1.20}$$

It is interesting to observe that equation (1.20) is a particular case of a generic balance equation

$$\frac{\partial G}{\partial t} + \nabla \cdot \phi = \mathcal{P} \tag{1.21}$$

where G is a specific volume quantity, ϕ denotes the flux of the same quantity and $\mathcal{P}$ is a production term.

1.3.2 The Momentum Equation

The linear momentum conservation law says that the sum of the total internal force exerted on the material volume $V(t)$ through its bounding surface $S(t)$, and the total external force exerted on the mass enclosed by $S(t)$ is balanced by the rate of change of the linear momentum of the fluid in the volume $V(t)$, i.e.

$$\frac{\mathrm{d}}{\mathrm{d}t} \iiint_V \rho v_i \, \mathrm{d}V = -\iint_S P_{ij} n_j \, \mathrm{d}S + \iiint_V \rho f_i \, \mathrm{d}V \tag{1.22}$$

where P_{ij} is the internal stress tensor and f_i is an external force per unit of mass. The negative sign behind the surface integral results from having considered positive the force exerted by the exterior fluid on the surface $S(t)$. Furthermore, making use of Reynolds' transport theorem, equation (1.22) becomes

$$\iiint_V \left\{ \frac{\partial}{\partial t}(\rho v_i) + \nabla \cdot (\rho v_i \mathbf{v}) \right\} \mathrm{d}V = -\iint_S P_{ij} n_j \, \mathrm{d}S + \iiint_V \rho f_i \, \mathrm{d}V \tag{1.23}$$

and, for a generic volume of integration $V^*(t)$

$$\frac{\mathrm{d}}{\mathrm{d}t} \iiint_{V^*} \rho v_i \, \mathrm{d}V = \iiint_{V^*} \rho f_i \, \mathrm{d}V - \iint_{S^*} P_{ij} n_j \, \mathrm{d}S - \iint_{S^*} \rho v_i (\mathrm{v} - \mathbf{b}) \cdot n \, \mathrm{d}S \tag{1.24}$$

By supposing that the volume $V^*(t)$ is fixed and that the integrand functions is continuous, equation (1.24) leads to the *Cauchy equations of motion*

$$\frac{\partial}{\partial t}(\rho v_i) + \frac{\partial}{\partial x_j}(\rho v_i v_j + P_{ij}) = \rho f_i \tag{1.25}$$

The physical nature of the stress tensor P_{ij} can be enlightened by means of a statistical interpretation of the Cauchy equations. By using the method of statistical mechanics, in fact, the macroscopic properties of a system can be related to the properties of its constitutive elements.

Consider the generic balance equation (1.21). The quantity G can be regarded as a statistical average of a conservative property g, weighted by a molecular distribution function $f(\mathbf{x}, \mathbf{v}, t)$, namely

$$G(\mathbf{x}, t) = \iiint_{-\infty}^{\infty} g\, f\, \mathrm{d}u\, \mathrm{d}v\, \mathrm{d}w \tag{1.26}$$

where u, v and w are the Cartesian components of the molecular velocity.

The distribution function $f(\mathbf{x}, \mathbf{v}, t)$ is defined so that $f\,\mathrm{d}\mathbf{x}\,\mathrm{d}\mathbf{v}$ is the probable number of molecules which at the instant t have positions $\mathbf{x}$ between $\mathbf{x}$ and $\mathbf{x} + \mathrm{d}\mathbf{x}$ and velocity $\mathbf{v}$ between $\mathbf{v}$ and $\mathbf{v} + \mathrm{d}\mathbf{v}$. This distribution function is a solution of the Boltzmann equation. This an integro-differential equation which is valid at densities sufficiently low, such that the effect of collisions involving more than two molecules can be neglected.

Consistently with the conservative quantity G, a flux term can be defined as

$$\phi_i(\mathbf{x}, t) = \iiint_{-\infty}^{\infty} g\, v_i\, f\, \mathrm{d}u\, \mathrm{d}v\, \mathrm{d}w \tag{1.27}$$

If the conservative quantity coincides with the i-th component of the linear momentum, it results that

$$G = \iiint_{-\infty}^{\infty} \rho\, v_i\, f\, \mathrm{d}u\, \mathrm{d}v\, \mathrm{d}w = \rho\, \overline{v}_i \tag{1.28}$$

and

$$\phi_j = \iiint_{-\infty}^{\infty} \rho\, v_i\, v_j\, f\, \mathrm{d}u\, \mathrm{d}v\, \mathrm{d}w \equiv \rho\, \overline{v_i v_j} = \rho\, \overline{v}_i\, \overline{v}_j + \rho\, \overline{v_i' v_j'} \tag{1.29}$$

where use of the linear average properties has been made. Therefore, the balance equation (1.21) takes the form

$$\frac{\partial}{\partial t}(\rho\, \overline{v}_i) + \frac{\partial}{\partial x_j}(\rho\, \overline{v}_i\, \overline{v}_j) + \frac{\partial}{\partial x_j}(\rho\, \overline{v_i' v_j'}) = \rho\, f_i \tag{1.30}$$

By definition, the averaged velocity $\overline{v}_i$ is the velocity of the fluid particle. Thus, comparing equation (1.30) to equation (1.25) yields

$$P_{ij} = \rho\, \overline{v_i' v_j'} \tag{1.31}$$

Therefore, the force exerted internally on a fluid is a consequence of a transport phenomenon acting on the molecular scale. The stress tensor component P_{ij}, in fact, is the average flux of chaotic momentum in the i-direction, transported by the thermal molecular motion along the j-direction.

The explicit form of the internal stress tensor depends on the molecular distribution function. If a state of *absolute thermodynamic equilibrium* (mechanical, thermal and chemical equilibrium) is supposed, the distribution function has a Maxwellian form, namely

$$f(\mathbf{x}; u, v, w; t) \equiv f(u, v, w) = \mathcal{N}\, F(u')\, F(v')\, F(w') \tag{1.32}$$

with

$$F(x) = \left(\frac{m}{2\pi\, k_b\, T}\right)^{\frac{1}{2}} \exp\left(-\frac{m}{2\, k_b\, T}\, x^2\right) \tag{1.33}$$

where m is the molecular mass, k_b is the Boltzmann constant and T is the absolute temperature. The distribution function (1.32) has the important property of depending only on the fluctuating part of the molecular velocity.

The average molecular translation energy can be defined as

$$e_t = m\,\frac{\overline{v_i'v_i'}}{2} \tag{1.34}$$

Equation (1.32) provides $\overline{v_i'v_j'} = (k_b\,T/m)\,\delta_{ij}$. Therefore, in a state of absolute equilibrium, the molecular translation energy is given by

$$e_t = \frac{3}{2}\,k_b\,T \tag{1.35}$$

and for a mole of molecules

$$\mathcal{E}_t = \mathcal{N}_A\,e_t = \frac{3}{2}\,\mathcal{R}\,T \tag{1.36}$$

where $\mathcal{R} = 8.317 \times 10^3$ joule/K/Mole is the universal constant of gas and $\mathcal{N}_A = 6.023 \times 10^{26}$ is the Avogadro number.

A stress system is referred to as *hydrostatic* when all the not diagonal terms in the corresponding tensor are zero. For a fluid in a state of absolute thermodynamic equilibrium, the diagonal terms represent the thermostatic pressure p, that is, the normal stress due to the flux of chaotic momentum transported parallel to itself. It thus results that

$$P_{ij} = p\,\delta_{ij} \tag{1.37}$$

with

$$p = \rho\frac{k_b\,T}{m} = \rho\,\frac{\mathcal{R}}{\mathcal{M}}\,T = \rho\,R\,T \tag{1.38}$$

where $\mathcal{M} = m\,\mathcal{N}_A$ is the molar mass and $R = \mathcal{R}/\mathcal{M}$ is the constant of the gas.

Equation (1.38) is the *equation of state* for a *perfect gas*, namely, a fluid at rest in a state of absolute equilibrium. For a fluid in motion with vanishing gradients of the thermodynamic quantities, the hydrostatic stress system can be retained by assuming a local thermodynamic equilibrium[1]. Therefore, the normal stress can be identified with the pressure of classical thermodynamics, and the Cauchy equations (1.25) take the well-known form of the *Eulerian equations of motion*

$$\frac{\partial}{\partial t}(\rho\,v_i) + \frac{\partial}{\partial x_j}(\rho\,v_i\,v_j) = -\frac{\partial p}{\partial x_i} \tag{1.39}$$

where the external force f_i has been dropped.

In a state of non-thermodynamic equilibrium the molecular distribution function loses its universal Maxwellian form (1.32) and must be calculated solving the Boltzmann equation

$$\frac{\partial f}{\partial t} + v_i\frac{\partial f}{\partial x_i} + a_i\frac{\partial f}{\partial v_i} = \mathcal{B} \tag{1.40}$$

where v_i are the components of the molecular velocity, a_i are the components of the molecular acceleration due to an external force and $\mathcal{B}$ is an integral term describing the effect of the molecular collisions on the distribution function.

Various attempts have been made in the past in order to obtain approximate solutions of the Boltzmann equation. Enskog [74] proposed a perturbation technique based on a series expansion of

[1] A gas in any initial state which is permitted to remain undisturbed for a sufficient length of time approaches a stationary state. If the gas is isolated adiabatically and not subject to external forces, the stationary state is a uniform condition in which all of the distributions functions are Maxwellian.

the distribution function in a perturbation parameter τ, in such a way that the frequency of collisions can be varied in an arbitrary manner without affecting the relative number of collisions of a particular kind. The parameter τ measures the period of molecular collision and is thus related to the Knudsen number. If τ is small the collisions are very frequent and the gas behave like a continuum in which local equilibrium is everywhere maintained. By introducing the series expansion $f = f^{(0)}+\tau f^{(1)}+\tau^2 f^{(2)}+\ldots$ into the Boltzmann equation (1.40), and equating terms of equal power of τ, a set of equations for the functions $f^{(0)}$, $f^{(1)}$, $f^{(2)}$,... can be obtained. In principle, this method of successive approximations can be extended to systems in which the gradients of the thermodynamic quantities are quite large. In the zeroth approximation, the distribution function is locally Maxwellian and leads to the Eulerian equations of motion. Conversely, the first order perturbation leads to the *Navier-Stokes equations.* These apply to systems in which the gradients of the physical properties are small or, equivalently, in which the physical properties do not change appreciably within a distance of the order of the mean free path.

Enskog's perturbation solution of the Boltzmann equation shows that, for a fluid in motion with velocity gradients, the zeroth order term is related to the state of equilibrium, while the first order term introduces a perturbative correction that linearly relates the stress tensor to the deformation tensor, accordingly to a Newton-type constitutive relation. This result agrees with the following *Stokesian hypotheses*:

1) the stress tensor P_{ij} is a continuous function of the deformation tensor

$$e_{ij} = \frac{1}{2}\left(\frac{\partial v_i}{\partial x_j} + \frac{\partial v_j}{\partial x_i}\right) \tag{1.41}$$

and the local thermodynamic state, but it does not depend on the other kinematical quantities;

2) when no deformation occurs the stress tensor becomes hydrostatic;

3) the fluid is isotropic and the principal directions of the stress tensor coincide with those of the deformation tensor;

4) the stress tensor does not depend explicitly on the position $\mathbf{x}$.

The Newtonian constitutive relation for a stress tensor element is a particular case of a general gradient law stating that, for a sufficiently gradual variation of a scalar quantity q with respect to the position in a material, the flux vector varies linearly with its gradient ∇q. The internal friction of a fluid is generated by the molecular transport of linear momentum. As a consequence, the stress tensor elements are related to the gradient of the local velocity of the flow, that is, to the deformation tensor elements.

The stress tensor is usually written as

$$P_{ij} = p\,\delta_{ij} - \tau_{ij} \tag{1.42}$$

where δ_{ij} is the Kronecker symbol and τ_{ij} are the elements of the *viscous stress tensor*. Referring to principal axes, the viscous diagonal terms take form

$$\tau_i = a_{ij}\,d_j \tag{1.43}$$

where d_j are the principal rates of strain.

The hypothesis of fluid isotropy allows to write

$$a_{ij} = \lambda + 2\,\mu\,\delta_{ij} \tag{1.44}$$

Hence

$$\tau_i = \lambda\,\Theta + 2\,\mu\,d_i \tag{1.45}$$

where $\Theta = d_1 + d_2 + d_3$ is the divergence of the velocity field. By changing to a generic co-ordinate system, the complete internal stress tensor takes the form

$$P_{ij} = (p - \lambda\,\Theta)\,\delta_{ij} - 2\,\mu\,e_{ij} \tag{1.46}$$

where the coefficient μ is the dynamic viscosity and λ is the second coefficient of viscosity. Thus, the mean normal stress is given by

$$\overline{p} = \frac{1}{3}P_{ii} = p - \left(\lambda + \frac{2}{3}\mu\right)\Theta \tag{1.47}$$

From the continuity equation (1.20) it results that, if the fluid density ρ is constant, the velocity field is divergence free. Therefore, equation (1.47) states that, for an incompressible fluid, the thermodynamic pressure always coincides with the mean normal stress. On the contrary, for a compressible fluid, the difference between the thermodynamic pressure and the mean normal stress is proportional to the divergence of the velocity field via the bulk viscosity coefficient

$$\zeta = \lambda + \frac{2}{3}\mu \tag{1.48}$$

Stokes supposed that $\overline{p} = p$ and consequently $\lambda = -2/3\,\mu$. A monoatomic gas satisfies this *no bulk viscosity* assumption, but it is not fulfilled by polyatomic gases and liquids. However, for a nearly isochoric motion and a nearly incompressible fluid, the effect of the bulk viscosity can be generally neglected.

Concluding, for a Newtonian fluid of negligible bulk viscosity the Cauchy equations of motion (1.25) take the form of the Navier-Stokes equations

$$\frac{\partial}{\partial t}(\rho\,v_i) + \frac{\partial}{\partial x_j}(\rho\,v_i\,v_j) = -\frac{\partial p}{\partial x_i} + \frac{\partial \tau_{ij}}{\partial x_j} + \rho\,f_i \tag{1.49}$$

where the viscous terms have the constitutive form

$$\tau_{ij} = \mu\left(\frac{\partial v_i}{\partial x_j} + \frac{\partial v_j}{\partial x_i}\right) - \frac{2}{3}\,\mu\,\frac{\partial v_k}{\partial x_k}\,\delta_{ij} \tag{1.50}$$

1.3.3 The Energy Equation

The continuity equation and the Cauchy equations have been obtained from the conservation of mass and linear momentum within a fluid portion. Analogously, the conservation of energy in the balance form of the *first law of thermodynamics* applied to the material volume $V(t)$, yields

$$\frac{\mathrm{d}}{\mathrm{d}t}\iiint\limits_{V} \rho\,E\,\mathrm{d}V = \iiint\limits_{V} \rho\,\mathbf{f}\cdot\mathbf{v}\,\mathrm{d}V - \iint\limits_{S} P_{ij}v_j\cdot\mathbf{n}\,\mathrm{d}S - \iint\limits_{S} \mathbf{q}\cdot\mathbf{n}\,\mathrm{d}S \tag{1.51}$$

where $E = e + v^2/2$ is the specific total internal energy, $e = c_v T$ is the specific internal energy (c_v is the specific heat at constant volume) and $v^2/2$ is the specific kinetic energy. The first and the second integrals at the second member of equation (1.51) represent the work done by the external force and by the internal stresses, respectively, whereas the third integral accounts for the heat flux across the surface $S(t)$.

For a generic volume $V^*(t)$ the balance equation (1.51) takes the form

$$\frac{\mathrm{d}}{\mathrm{d}t}\iiint\limits_{V^*} \rho E\,\mathrm{d}V + \iint\limits_{S^*} \rho E\,(\mathbf{v}-\mathbf{b})\cdot\mathbf{n}\,\mathrm{d}S = \iiint\limits_{V^*} \rho\,\mathbf{f}\cdot\mathbf{v}\,\mathrm{d}V - \iint\limits_{S^*} P_{ij}v_j\cdot\mathbf{n}\,\mathrm{d}S - \iint\limits_{S^*} \mathbf{q}\cdot\mathbf{n}\,\mathrm{d}S \tag{1.52}$$

If the volume is fixed and the integrand functions are continuous, the *energy equation* takes the differential form

$$\frac{\partial}{\partial t}(\rho E) + \frac{\partial}{\partial x_i}(\rho v_i E) = -\frac{\partial}{\partial x_j}(P_{ij} v_j) - \frac{\partial q_i}{\partial x_i} + \rho f_i v_i \tag{1.53}$$

This equation can be simplified by subtracting the kinetic energy balance resulting from the momentum equation (1.25). Furthermore, considering a Newtonian fluid and assuming a heat conduction law of Fourier type $\mathbf{q} = -K\nabla T$, where K is the heat conductivity of the fluid, equation (1.53) becomes

$$\rho \frac{\mathrm{D}E}{\mathrm{D}t} = \nabla \cdot (K\nabla T) - p\nabla \cdot \mathbf{v} + \Gamma \tag{1.54}$$

where

$$\Gamma = (\lambda + 2\mu)\,\Theta^2 - 4\mu\,\Phi \tag{1.55}$$

The function Γ is referred to as viscous dissipation function. It depends on the deformation tensor via two of its three invariants

$$\Theta = e_{11} + e_{22} + e_{33} = \nabla \cdot \mathbf{v} \tag{1.56}$$

$$\Phi = e_{22}e_{33} - e_{23}e_{32} + e_{33}e_{11} - e_{31}e_{13} + e_{11}e_{22} - e_{12}e_{21} = -\frac{1}{2}\left(e_{ij} - \frac{1}{3}e_{kk}\delta_{ij}\right)^2 \tag{1.57}$$

$$\Psi = \det(e_{ij}) \tag{1.58}$$

which result from the characteristic equation

$$\det(e_{ij} - d\,\delta_{ij}) = \Psi - d\,\Phi + d^2\,\Theta - d^3 = 0 \tag{1.59}$$

Since it is always $\theta^2 > 2\Phi$, the function Γ is always positive.

The energy equation can be written in terms of specific entropy S, whose infinitesimal increment satisfies the thermodynamic relation

$$T\,\mathrm{d}S = \mathrm{d}E + p\,\mathrm{d}\left(\frac{1}{\rho}\right) \tag{1.60}$$

Therefore, equation (1.54) becomes

$$\rho T \frac{\mathrm{D}S}{\mathrm{D}t} = \nabla \cdot (K\nabla T) + \Gamma \tag{1.61}$$

Equations (1.54) and (1.61) show that the work done by the internal stresses has a reversible contribution due to the thermodynamic pressure, and an irreversible contribution due to the viscous terms. In fact, since the function Γ is always positive, it always causes an increment of the specific entropy of the fluid particle, acting as a dissipation function.

1.3.4 Convective Form of the Flow Governing Equations

The continuity, linear momentum and energy equations, together with the equation of state (1.38), are in sufficient number to match the number of unknown flow variables. Including a rate of mass injection for unit of volume $\dot{m}$, and a rate of heat addition for unit of volume $\dot{Q}$, the set of differential governing equations for a Stokesian fluid ($\zeta = 0$) becomes

$$\frac{\partial}{\partial t}\rho + \frac{\partial}{\partial x_i}(\rho v_i) = \dot{m} \tag{1.62}$$

$$\frac{\partial}{\partial t}(\rho v_i) + \frac{\partial}{\partial x_j}(\rho v_i v_j) = -\frac{\partial p}{\partial x_i} + \frac{\partial \tau_{ij}}{\partial x_j} + \rho f_i \tag{1.63}$$

$$\frac{\partial}{\partial t}(\rho E) + \frac{\partial}{\partial x_i}(\rho v_i E) = -\frac{\partial}{\partial x_i}(p v_i) + \frac{\partial}{\partial x_j}(\tau_{ij} v_j) - \frac{\partial q_i}{\partial x_i} + \rho f_i v_i + \dot{Q} \tag{1.64}$$

where

$$
\begin{aligned}
E &= c_v T + \frac{v^2}{2} && (1.65)\\
\tau_{ij} &= \mu\left(\frac{\partial v_i}{\partial x_j} + \frac{\partial v_j}{\partial x_i}\right) - \frac{2}{3}\mu\frac{\partial v_k}{\partial x_k}\delta_{ij} && (1.66)\\
q_i &= -K\frac{\partial T}{\partial x_i} && (1.67)\\
p &= \rho R T && (1.68)
\end{aligned}
$$

In equations (1.63) and (1.64) the injected mass has been supposed to have the local flow velocity and the local total internal energy.

Equations (1.62), (1.63) and (1.64) can be translated from their conservative form to the convective form

$$
\begin{aligned}
\frac{\mathrm{D}\rho}{\mathrm{D}t} &= -\rho\Theta + \dot{m} && (1.69)\\
\rho\frac{\mathrm{D}v_i}{\mathrm{D}t} &= -\frac{\partial p}{\partial x_i} - \frac{2}{3}\frac{\partial}{\partial x_i}(\mu\Theta) + \frac{\partial}{\partial x_j}\left\{\mu\left(\frac{\partial v_i}{\partial x_j} + \frac{\partial v_j}{\partial x_i}\right)\right\} + \rho f_i - \dot{m}\, v_i && (1.70)\\
\frac{p}{R}\frac{\mathrm{D}S}{\mathrm{D}t} &= \frac{\partial}{\partial x_i}\left(K\frac{\partial T}{\partial x_i}\right) + \frac{4}{3}\mu\Theta^2 - 4\mu\Phi + \dot{Q} - \dot{m}E && (1.71)
\end{aligned}
$$

where $\Theta = \nabla\cdot\mathbf{v}$ and

$$S = S_r + c_v \log\left(\frac{p}{p_r}\right)\left(\frac{\rho_r}{\rho}\right)^{\gamma} \tag{1.72}$$

The latter is an alternative form of the gas equation of state, with the subscript r denoting a thermodynamic reference state of the fluid and $\gamma = c_p/c_v$ being the ratio of the specific heats. Equation (1.72) has been obtained from equations (1.60), (1.61) and (1.64).

1.4 Potential Flows

As discussed in the preceeding section, the behaviour of a non-viscous and adiabatic fluid is governed by the following equations

$$\frac{\mathrm{D}\rho}{\mathrm{D}t} + \rho\nabla\cdot\mathbf{v} = 0 \tag{1.73}$$

$$\frac{\mathrm{D}\mathbf{v}}{\mathrm{D}t} + \frac{\nabla p}{\rho} = 0 \tag{1.74}$$

$$\frac{\mathrm{D}S}{\mathrm{D}t} = 0 \tag{1.75}$$

where equation (1.74) is the Eulerian equation of motion.

The equation of state relating the thermodynamic quantities (ρ, p, S) can be written as

$$\mathrm{d}\rho = \frac{1}{c^2}\,\mathrm{d}p + \left(\frac{\partial\rho}{\partial S}\right)_p \mathrm{d}S \tag{1.76}$$

where c is the local speed of sound, defined as

$$c = \sqrt{\left(\frac{\partial p}{\partial\rho}\right)_S} \tag{1.77}$$

and D /Dt denotes the material derivative, as defined in equation (1.7).

The material derivative of the velocity vector can be expressed in the useful form

$$\frac{\mathrm{D}\mathbf{v}}{\mathrm{D}t} = \frac{\partial \mathbf{v}}{\partial t} + \nabla\left(\frac{v^2}{2}\right) - \mathbf{v} \times \boldsymbol{\omega} \tag{1.78}$$

where $\boldsymbol{\omega} = \nabla \times \mathbf{v}$ is the vorticity vector.

In chapter 2 the fluid motion will be described as a combination of three modes of fluctuation: (i) the vorticity mode, governing the vorticity dynamics in a viscous incompressible fluid, (ii) the acoustic mode, governing the propagation of irrotational disturbances in a compressible fluid, (iii) the entropy mode, governing the heat transfer in a viscous fluid. When the physical mechanism of diffusion is supposed to be absent, both vorticity and entropy spots are only allowed to be convected along the fluid particle paths. Consequently, the flow is isentropic and the vorticity is entirely confined to layers of vanishing thickness. The hypothesis of irrotational flow is thus supported by the inviscid flow assumption in the Eulerian model.

The condition $\boldsymbol{\omega} = 0$ permits to express the velocity field in terms of velocity potential field ϕ by writing $\mathbf{v} = \nabla\phi$. Hence, the linear momentum equation (1.74) takes the form

$$\nabla\left(\frac{\partial \phi}{\partial t}\right) + \nabla\left(\frac{v^2}{2}\right) + \frac{\nabla p}{\rho} = 0 \tag{1.79}$$

where use of equation (1.78) has been made. This equation is satisfied everywhere in the flow field. Therefore, integrating along a particle path, from a point at infinity to the generic point $\mathbf{x}$, yields

$$\frac{\partial \phi}{\partial t} - \left(\frac{\partial \phi}{\partial t}\right)_{\infty} + \frac{v^2}{2} - \frac{v_\infty^2}{2} + \int_{p_\infty}^{p} \frac{\mathrm{d}p'}{\rho} = 0 \tag{1.80}$$

Equation (1.75) says that the entropy of a fluid particle does not change during its motion. Thus, in each point of the particle trajectory, pressure and density may vary, but following the thermodynamic isentropic transformation

$$\frac{p}{\rho^\gamma} = \frac{p_\infty}{\rho_\infty^\gamma} \tag{1.81}$$

Therefore, integrating the last term in equation (1.80) along an isentropic transformation, and assuming uniform and steady conditions at infinity, leads to

$$\frac{\partial \phi}{\partial t} + \frac{v^2 - v_\infty^2}{2} + \frac{\gamma}{\gamma - 1}\frac{p_\infty}{\rho_\infty}\left[\left(\frac{p}{p_\infty}\right)^{\frac{\gamma}{\gamma-1}} - 1\right] = 0 \tag{1.82}$$

and, equivalently

$$\frac{p}{p_\infty} = \left\{1 - \frac{\gamma - 1}{\gamma}\frac{\rho_\infty}{p_\infty}\left[\frac{\partial \phi}{\partial t} + \frac{v^2 - v_\infty^2}{2}\right]\right\}^{\frac{\gamma}{\gamma-1}} \tag{1.83}$$

Finally, by introducing the isentropic law into the sound speed definition (1.77), yields

$$c^2 = c_\infty^2\left(\frac{p}{p_\infty}\right)^{\frac{\gamma-1}{\gamma}} = c_\infty^2 - (\gamma - 1)\,\frac{v^2 - v_\infty^2}{2} - (\gamma - 1)\,\frac{\partial \phi}{\partial t} \tag{1.84}$$

where $c_\infty^2 = \gamma p_\infty / \rho_\infty$. Equations (1.83) and (1.84) relate the pressure field and the local speed of sound to the irrotational velocity field.

Consider the continuity equation (1.73) written in the quasi-linear form

$$\frac{\partial \rho}{\partial t} + \mathbf{v}\cdot\nabla\rho + \rho\nabla\cdot\mathbf{v} = 0 \tag{1.85}$$

Introducing the velocity potential field yields

$$\nabla^2\phi + \frac{1}{\rho}\frac{\partial\rho}{\partial t} + \mathbf{v}\cdot\frac{\nabla\rho}{\rho} = 0 \tag{1.86}$$

From equations (1.79) and (1.77) it follows that

$$\nabla\left(\frac{\partial\phi}{\partial t}\right) + \nabla\left(\frac{v^2}{2}\right) = -c^2\,\frac{\nabla\rho}{\rho} \tag{1.87}$$

which permits to write the last term in equation (1.86) as

$$\mathbf{v}\cdot\frac{\nabla\rho}{\rho} = -\frac{1}{c^2}\left[\frac{\partial}{\partial t}\left(\frac{v^2}{2}\right) + \nabla\phi\cdot\left(\frac{v^2}{2}\right)\right] \tag{1.88}$$

Equation (1.80) relates the generic variation of p to the generic variation of $\partial\phi/\partial t + v^2/2$ along a fluid particle path. Thus, by differentiating with respect to t and by considering the definition (1.77) of the local speed of sound, it results that

$$\frac{1}{\rho}\frac{\partial\rho}{\partial t} = -\frac{1}{c^2}\frac{\partial}{\partial t}\left(\frac{\partial\phi}{\partial t} + \frac{v^2}{2}\right) \tag{1.89}$$

Finally, substituting equations (1.88) and (1.89) into equation (1.86) provides the following scalar equation for the velocity potential

$$\nabla^2\phi - \frac{1}{c^2}\left[\frac{\partial^2\phi}{\partial t^2} + \frac{\partial}{\partial t}v^2 + \nabla\phi\cdot\nabla\left(\frac{v^2}{2}\right)\right] = 0 \tag{1.90}$$

where c^2 is a function of ϕ, as defined in equation (1.84).

With the only hypothesis of irrotational velocity field, the problem defined by the system of equations (1.73), (1.74) and (1.75) has been reduced to the solution of the single scalar equation (1.90).

When the potential field describes the propagation of small acoustic disturbances in a steady mean flow, equation (1.90) can be linearized by setting

$$\mathbf{v}(\mathbf{x},t) = \mathbf{U}(\mathbf{x}) + \mathbf{v}'(t) = \nabla\Phi + \nabla\phi' \tag{1.91}$$

with $v' \ll U$. Then, neglecting the nonlinear terms in the acoustic velocity $\mathbf{v}' = \nabla\phi'$ gives

$$c^2\,\nabla^2\phi \simeq c_0^2\,\nabla^2\Phi + c'^2\,\nabla\cdot\mathbf{U} + c_0^2\,\nabla^2\phi' \tag{1.92}$$

$$\frac{\partial^2\phi}{\partial t^2} = \frac{\partial^2\phi'}{\partial t^2} \tag{1.93}$$

$$\frac{\partial}{\partial t}v^2 \simeq 2\,\mathbf{U}\cdot\frac{\partial}{\partial t}\nabla\phi' \tag{1.94}$$

$$\nabla\phi\cdot\nabla\left(\frac{v^2}{2}\right) \simeq \mathbf{U}\cdot\nabla\left(\frac{U^2}{2}\right) + \mathbf{U}\cdot\nabla\left(\mathbf{U}\cdot\nabla\phi'\right) + \nabla\left(\frac{U^2}{2}\right)\cdot\nabla\phi' \tag{1.95}$$

where c' denotes the perturbation induced by the acoustic disturbances on the speed of sound (1.84) with respect to the local mean value c_0, namely

$$c_0^2 = c_\infty^2 + \frac{\gamma-1}{2}\left(U_\infty^2 - U^2\right) \tag{1.96}$$

$$c'^2 = -\left(\gamma-1\right)\mathbf{U}\cdot\nabla\phi' \tag{1.97}$$

Substituting equations (1.92) through (1.97) into equation (1.90) leads to the linearized potential equation

$$c_0^2\,\nabla^2\phi' - \frac{\partial^2\phi'}{\partial t^2} - 2\,\mathbf{U}\cdot\frac{\partial}{\partial t}\nabla\phi' - \mathbf{U}\cdot\nabla\left(\mathbf{U}\cdot\nabla\phi'\right) - \nabla\left(\frac{U^2}{2}\right)\cdot\nabla\phi' + c'^2\,\nabla\cdot\mathbf{U} = 0 \tag{1.98}$$

where the mean flow has been supposed to satisfy the steady potential equation

$$c_0^2\,\nabla^2\Phi - \mathbf{U}\cdot\nabla\left(\frac{U^2}{2}\right) = 0 \tag{1.99}$$

For a fluid at rest, equation (1.98) reduces to the *standard wave equation*

$$c_\infty^2\,\nabla^2\phi' - \frac{\partial^2\phi'}{\partial t^2} = 0 \tag{1.100}$$

Conversely, in the case of a uniform mean flow, equation (1.98) leads to the *convected wave equation*

$$c_\infty^2\,\nabla^2\phi' - \frac{\partial^2\phi'}{\partial t^2} - 2\,\mathbf{U}_\infty\cdot\frac{\partial}{\partial t}\nabla\phi' - U_{\infty i}U_{\infty j}\frac{\partial^2\phi'}{\partial x_i\partial x_j} = 0 \tag{1.101}$$

The pressure field can be linearized, accordingly to equation (1.91), by writing $p = P + p'$, with $p' \ll P$. Thus, equation (1.83) yields

$$p' = -\rho_\infty\left(1 - \frac{\gamma-1}{\gamma}\frac{\rho_\infty}{p_\infty}\frac{U^2 - U_\infty^2}{2}\right)^{\frac{1}{\gamma-1}}\left[\frac{\partial\phi'}{\partial t} + \mathbf{U}\cdot\nabla\phi'\right] \tag{1.102}$$

A further simplification of the aerodynamic problem consists in supposing that the acoustic disturbances have a harmonic behaviour, namely $\phi' = \hat{\phi}\,\mathrm{e}^{\mathrm{i}\omega t}$ and $p' = \hat{p}\,\mathrm{e}^{\mathrm{i}\omega t}$. Therefore, equations (1.98) and (1.102) take the form

$$(1-\mathcal{A})\frac{\partial^2\hat{\phi}}{\partial x_i^2} - M_i\,M_j\,\frac{\partial^2\hat{\phi}}{\partial x_i\partial x_j} - (\mathrm{i}\,2\,k\,M_i + \mathcal{B}_i + M_i\,\mathcal{C})\frac{\partial\hat{\phi}}{\partial x_i} + k\,(k + \mathrm{i}\,\mathcal{C})\,\hat{\phi} = 0 \tag{1.103}$$

and

$$\hat{p} = -\rho_\infty\,c_\infty\,(1-\mathcal{A})^{\frac{1}{\gamma-1}}\left[\mathrm{i}\,\hat{\phi} + M_i\,\frac{\partial\hat{\phi}}{\partial x_i}\right] \tag{1.104}$$

with

$$M_\infty = \frac{U_\infty}{c_\infty} \tag{1.105}$$

$$M_i = \frac{U_i}{c_\infty} \tag{1.106}$$

$$k = \frac{\omega}{c_\infty} \tag{1.107}$$

$$\mathcal{A} = \frac{\gamma-1}{2}\left(M^2 - M_\infty^2\right) \tag{1.108}$$

$$\mathcal{B}_i = 2\left(M_j\frac{\partial M_j}{\partial x_i}\right) \tag{1.109}$$

$$\mathcal{C} = (\gamma-1)\left(\frac{\partial M_j}{\partial x_j}\right) \tag{1.110}$$

Finally, for a uniform flow equations (1.103) and (1.104) take the form

$$\frac{\partial^2 \hat{\phi}}{\partial x_i^2} - M_i M_j \frac{\partial^2 \hat{\phi}}{\partial x_i \partial x_j} - \mathrm{i}\, 2\, k\, M_i \frac{\partial \hat{\phi}}{\partial x_i} + k^2 \hat{\phi} = 0 \tag{1.111}$$

and

$$\hat{p} = -\rho_\infty c_\infty \left[\mathrm{i}\, \hat{\phi} + M_i \frac{\partial \hat{\phi}}{\partial x_i} \right] \tag{1.112}$$

1.4.1 Green's Functions of Wave Equations

Consider the standard wave equation[2] (1.100). The Green's function $G(\mathbf{x}, t; \mathbf{y}, \tau)$ is the pulse response satisfying

$$c_\infty^2 \nabla^2 G - \frac{\partial^2 G}{\partial t^2} = \delta(\mathbf{x} - \mathbf{y})\, \delta(t - \tau) \tag{1.113}$$

With application of the Fourier transform pair

$$\begin{aligned} \mathcal{F}\{f(t)\} &= \hat{f}(\omega) = \int_{-\infty}^{\infty} f(t) \exp(-\mathrm{i}\,\omega t)\, \mathrm{d}t \\ \mathcal{F}^{-1}\left\{\hat{f}(\omega)\right\} &= f(t) = \frac{1}{2\pi} \int_{-\infty}^{\infty} \hat{f}(\omega) \exp(\mathrm{i}\,\omega t)\, \mathrm{d}\omega \end{aligned} \tag{1.114}$$

equation (1.113) becomes

$$c_\infty^2 \nabla^2 \hat{G} + k^2 \hat{G} = \delta(\mathbf{x} - \mathbf{y})\, \mathrm{e}^{\mathrm{i}\,\omega\tau}, \quad \text{with} \quad k = \frac{\omega}{c_\infty} \tag{1.115}$$

whose solution is

$$\hat{G}(\mathbf{x}, k; \mathbf{y}, \tau) = -\mathrm{e}^{\mathrm{i}\,\omega\tau} \frac{\mathrm{e}^{\mathrm{i}\,k|\mathbf{x}-\mathbf{y}|}}{4\pi\, |\mathbf{x} - \mathbf{y}|} \tag{1.116}$$

Then, transforming back to the time domain yields

$$G(\mathbf{x}, t; \mathbf{y}, \tau) = -\frac{\delta(t - \tau - |\mathbf{x} - \mathbf{y}| / c_\infty)}{4\pi\, |\mathbf{x} - \mathbf{y}|} \tag{1.117}$$

Consider now the convected wave equation (1.101). The Green's function $G_c(\mathbf{x}, t; \mathbf{y}, \tau; \mathbf{M})$ is the pulse response of the wave equation

$$c_\infty^2 \nabla^2 G_c - \frac{\partial^2 G_c}{\partial t^2} - 2\, \mathbf{U}_\infty \cdot \frac{\partial}{\partial t} \nabla G_c - U_{\infty i} U_{\infty j} \frac{\partial^2 G_c}{\partial x_i \partial x_j} = \delta(\mathbf{x} - \mathbf{y})\, \delta(t - \tau) \tag{1.118}$$

With application of the Fourier transform pair (1.114), the above equation becomes

$$\frac{\partial^2 \hat{G}_c}{\partial x_i^2} - M_i M_j \frac{\partial^2 \hat{G}_c}{\partial x_i \partial x_j} - \mathrm{i}\, 2\, k\, M_i \frac{\partial \hat{G}_c}{\partial x_i} + k^2 \hat{G}_c = \delta(\mathbf{x} - \mathbf{y})\, \mathrm{e}^{\mathrm{i}\,\omega\tau} \tag{1.119}$$

whose solution, for $M < 1$, can be obtained from a Prandtl-Glauert transformation. It thus results that

$$G_c(\mathbf{x}, k; \mathbf{y}, \tau; \mathbf{M}) = -\mathrm{e}^{\mathrm{i}\,\omega\tau} \frac{\exp\left\{ \frac{\mathrm{i}\,k r}{\beta^2} \left(M_r + \sqrt{M_r^2 + \beta^2} \right) \right\}}{r \sqrt{M_r^2 + \beta^2}} \tag{1.120}$$

[2]In acoustics, a standard waw equation describes the propagation of linear acoustic disturbances in a medium at rest.

where $r = |\mathbf{x} - \mathbf{y}|$, $M_r = M_i \hat{r}_i$, $\hat{r}_i = (x_i - y_i)/r$ and $\beta = \sqrt{1 - M^2}$ is the Prandtl-Glauert factor. Then, transforming back to the time domain provides

$$G_c(\mathbf{x}, t; \mathbf{y}, \tau; \mathbf{M}) = -\frac{\delta(g)}{4\pi r \sqrt{M_r^2 + \beta^2}} \quad \text{with}$$
$$g = t - \tau - \frac{r\left\{M_r + \sqrt{M_r^2 + \beta^2}\right\}}{c_\infty \beta^2} \tag{1.121}$$

An integral method described in chapter 7 requires the first and second spatial derivatives of the Green's function $\hat{G}_c$. These are given by [75]

$$\frac{\partial \hat{G}_c}{\partial x_i} = \left\{\frac{\mathrm{i}\,k}{\beta^2} M_i + \frac{1}{\sqrt{M_r^2 + \beta^2}} \left(\frac{\mathrm{i}\,k}{\beta^2} - \frac{1}{r\sqrt{M_r^2 + \beta^2}}\right) \left(M_r M_i + \beta^2 \hat{r}_i\right)\right\} \hat{G}_c \tag{1.122}$$

$$\begin{aligned}
\frac{\partial^2 \hat{G}_c}{\partial x_i \partial x_j} &= \frac{\left(M_r M_i + \beta^2 \hat{r}_i\right)\left(M_r M_j + \beta^2 \hat{r}_j\right)}{M_r^2 + \beta^2} \left\{-\frac{k^2}{\beta^4} - \frac{\mathrm{i}\,3k}{\beta^2 r \sqrt{M_r^2 + \beta^2}} + \frac{3}{r^2\left(M_r^2 + \beta^2\right)}\right\} \hat{G}_c \\
&- \frac{M_i\left(M_r M_j + \beta^2 \hat{r}_j\right) + M_j\left(M_r M_j + \beta^2 \hat{r}_j\right)}{\sqrt{M_r^2 + \beta^2}} \left\{\frac{k^2}{\beta^4} + \frac{\mathrm{i}\,k}{\beta^2 r \sqrt{M_r^2 + \beta^2}}\right\} \hat{G}_c \\
&+ M_i M_j \left\{-\frac{k^2}{\beta^4} + \frac{\mathrm{i}\,k}{\beta^2 r \sqrt{M_r^2 + \beta^2}} - \frac{1}{r^2\left(M_r^2 + \beta^2\right)}\right\} \hat{G}_c \\
&+ \beta^2 \left\{\frac{\mathrm{i}\,k}{\beta^2 r \sqrt{M_r^2 + \beta^2}} - \frac{1}{r^2\left(M_r^2 + \beta^2\right)}\right\} \delta_{ij} \hat{G}_c
\end{aligned} \tag{1.123}$$

where δ_{ij} is the Kronecker symbol.

1.5 The Helmholtz Decomposition

Given an arbitrary differentiable velocity field, there exists a scalar function ϕ called the scalar potential, and a vector function $\mathbf{A}$ called the vector potential, that are such that

$$\mathbf{v} = \nabla\phi + \nabla \times \mathbf{A} \tag{1.124}$$

and satisfy the relationship

$$\nabla^2 \phi = \nabla \cdot \mathbf{v} \tag{1.125}$$

and

$$\nabla^2 \mathbf{A} = -\nabla \times \mathbf{v} \equiv -\boldsymbol{\omega} \tag{1.126}$$

provided that $\mathbf{A}$ satisfies the condition

$$\nabla \cdot \mathbf{A} = 0 \tag{1.127}$$

According to Lamb [14], this result is to be attributed to Helmholtz and is usually referred to as the Helmholtz decomposition theorem. It can be noticed that equation (1.127) can always be satisfied by adding to $\mathbf{A}$ an inconsequential irrotational vector field $\nabla\eta$, namely

$$\mathbf{A}' = \mathbf{A} + \nabla\eta \tag{1.128}$$

such that $\nabla^2\eta = -\nabla \cdot \mathbf{A}$ and $\mathbf{A}'$ satisfy equation (1.127).

The Helmholtz decomposition says that a vector velocity field can be decomposed into an irrotational part $\mathbf{v}_{irr}$ and a solenoidal part $\mathbf{v}_{Sol}$, such that

$$\mathbf{v}_{Sol} = \nabla \times \mathbf{A} \quad \text{and} \tag{1.129}$$

$$\mathbf{v}_{irr} = \nabla \phi \tag{1.130}$$

From equations (1.129) and (1.126) it follows that

$$\nabla^2 \mathbf{v}_{Sol} = -\nabla \times \boldsymbol{\omega} \tag{1.131}$$

whereas, from equations (1.125) and from the continuity equation

$$\frac{\partial \rho}{\partial t} + \nabla \cdot (\rho \mathbf{v}) = 0 \tag{1.132}$$

it follows that

$$\nabla^2 \phi = -\frac{1}{\rho} \frac{\mathrm{D}\rho}{\mathrm{D}t} \tag{1.133}$$

Therefore, the dynamics of the vorticity field is described by the solenoidal part of the velocity field, as stated by equation 1.131, whereas the acoustic aspects of the flow are related to the irrotational part of the velocity field, as stated by equation 1.133.

2

Nonlinearity and Modes of Fluctuation

2.1 Introduction

The system of equations (1.69), (1.70) and (1.71) governs the behaviour of a viscous heat-conducting compressible gas.

A typical approach in fluid dynamics consists in interpreting the behaviour of a fluid as a superposition of distinct modes, whose evolution involves special quantities referred to as *invariants*. Because of the nonlinear character of the governing equations, only in a few special cases the system can be diagonalized, allowing the modes to be separated. Therefore, nonlinearity provides the interaction mechanism between the modes of fluctuation.

By expanding a disturbance field in powers of a given amplitude parameter, three modes of fluctuation can be distinguished. These are referred to as the *vorticity mode*, the *entropic mode* and the *acoustic mode*. The vorticity mode governs the behaviour of an incompressible turbulent flow, the entropic mode governs the heat transfer dynamics in a low speed flow, the acoustic mode governs the propagation of acoustic disturbances.

Chu & Kovásznay [76] proposed a perturbation method in order to reduce the system of governing equations to a set of differential equations for equal order quantities, arranged in a recursive structure where the lower order terms appear as combined source terms in the higher order equations.

2.2 A Perturbative Expansion of the Navier-Stokes Equations

The expansion of the fluctuating field in a perturbation series requires the definition of an amplitude control parameter α. This can be chosen as the maximum relative perturbation of a scalar flow variable. Thus, considering an arbitrary small space/time domain $\mathcal{D}$ and supposing that the flow properties are continuous within $\mathcal{D}$, provides the definition

$$\alpha = \frac{f - f_0}{|f_0|} \tag{2.1}$$

where f is a generic scalar variable and f_0 is its mean value within the volume $\mathcal{D}$. The value of α is controlled by the size of the domain $\mathcal{D}$, inside which f can be expanded in a power series of α. Therefore, the flow variables can be written as

$$\begin{aligned} p &= p_0 + p^{(1)} + p^{(2)} + \cdots && (2.2)\\ \rho &= \rho_0 + \rho^{(1)} + \rho^{(2)} + \cdots && (2.3)\\ v_i &= \quad v_i^{(1)} + v_i^{(2)} + \cdots && (2.4) \end{aligned}$$

where the reference system has been supposed to translate at the mean flow velocity.

Consider the continuity equation (1.62). Expanding ρ and v_i as in equations (2.3) and (2.4) yields

$$\frac{\partial \rho^{(1)}}{\partial t} + \rho_0 \frac{\partial {v_i}^{(1)}}{\partial x_i} + \frac{\partial \rho^{(2)}}{\partial t} + \rho_0 \frac{\partial {v_i}^{(2)}}{\partial x_i} + \rho^{(1)} \frac{\partial {v_i}^{(1)}}{\partial x_i} = \dot{m} + \mathrm{o}(\alpha^2) \tag{2.5}$$

This equation can be split into the following equations for equal order terms

$$\frac{\partial \rho^{(1)}}{\partial t} + \rho_0 \frac{\partial {v_i}^{(1)}}{\partial x_i} = \dot{m} \tag{2.6}$$

$$\frac{\partial \rho^{(2)}}{\partial t} + \rho_0 \frac{\partial {v_i}^{(2)}}{\partial x_i} = -\rho^{(1)} \frac{\partial {v_i}^{(1)}}{\partial x_i} + \mathrm{o}(\alpha^2) \tag{2.7}$$

It can be observed that these two equations have the same constitutive form and differ only for their source terms at the right-hand sides. Therefore, they can be written as

$$\frac{\partial \rho^{(n)}}{\partial t} + \rho_0 \frac{\partial {v_i}^{(n)}}{\partial x_i} = F^{(n)} \tag{2.8}$$

where $F^{(1)} = \dot{m}$, whereas $F^{(2)}$ accounts for the nonlinear terms of the starting equation and depends only on the flow variables at their lower order.

By supposing that the dynamic viscosity μ and the heat conductivity k are monotonic functions of the temperature, the perturbation method can be applied to the entire system of governing equations, leading to the following equations

$$\frac{\partial \rho^{(n)}}{\partial t} + \rho_0 \nabla \cdot \mathbf{v}^{(n)} = F_1^{(n)} \tag{2.9}$$

$$\rho_0 \frac{\partial \mathbf{v}^{(n)}}{\partial t} + \nabla p^{(n)} - \mu_0 \nabla^2 \mathbf{v}^{(n)} - \frac{1}{3}\mu_0 \nabla \left(\nabla \cdot \mathbf{v}^{(n)} \right) = \mathbf{F}_2^{(n)} \tag{2.10}$$

$$\frac{p_0}{R} \frac{\partial S^{(n)}}{\partial t} - k_0 \nabla^2 T^{(n)} = F_3^{(n)} \tag{2.11}$$

$$\frac{p^{(n)}}{p_0} - \frac{\rho^{(n)}}{\rho_0} - \frac{T^{(n)}}{T_0} = F_4^{(n)} \tag{2.12}$$

$$\frac{S^{(n)}}{R} - \frac{\gamma}{\gamma - 1} \frac{T^{(n)}}{T_0} + \frac{p^{(n)}}{p_0} = F_5^{(n)} \tag{2.13}$$

where $F_1^{(1)} = \dot{m}$, $\mathbf{F}_2^{(1)} = \rho_0 \, \mathbf{f}$, $F_3^{(1)} = \dot{Q}$, $F_4^{(1)} = 0$ and $F_5^{(1)} = 0$.

Equations (2.12) and (2.13) can be used to eliminate $\rho^{(n)}$ and $T^{(n)}$. Furthermore, the hypothesis of constant Prandtl number $\mathrm{Pr} = \mu \, c_p / k = 3/4$ can be invoked to eliminate one of the fluid parameters.

Introducing the dimensionless variables $\mathcal{P}^{(n)} = p^{(n)}/\gamma p_0$ and $\mathcal{S}^{(n)} = S^{(n)}/c_p$, the recursive governing equations take the form

$$\nabla \cdot \mathbf{v}^{(n)} + \frac{\partial \mathcal{P}^{(n)}}{\partial t} - \frac{\partial \mathcal{S}^{(n)}}{\partial t} = \frac{\dot{m}^{(n)}}{\rho_0} \tag{2.14}$$

$$\frac{\partial \mathbf{v}^{(n)}}{\partial t} + c_0^2 \, \nabla \mathcal{P}^{(n)} - \nu_0 \, \nabla^2 \mathbf{v}^{(n)} - \frac{1}{3}\nu_0 \, \nabla \left(\nabla \cdot \mathbf{v}^{(n)} \right) = \mathbf{f}^{(n)} \tag{2.15}$$

$$\frac{\partial \mathcal{S}^{(n)}}{\partial t} - \frac{4}{3}\nu_0 \, \nabla \mathcal{S}^{(n)} - \frac{4}{3}\nu_0 \, (\gamma - 1) \nabla^2 \mathcal{P}^{(n)} = \frac{\dot{Q}^{(n)}}{\rho_0 \, c_p \, T_0} \tag{2.16}$$

where $\mu_0 = \nu_0/\rho_0$ is the mean kinematic viscosity, c_0 is the mean speed of sound and

$$\dot{m}^{(1)} = \dot{m}, \qquad \mathbf{f}^{(1)} = \mathbf{f}, \qquad \dot{Q}^{(1)} = \dot{Q} \tag{2.17}$$

The second order source terms, as shown by Chu & Kovásznay [76], are given by

$$\begin{aligned}
\frac{\dot{m}^{(2)}}{\rho_0} &= -\nabla\cdot\left(\mathcal{P}^{(1)}\mathbf{v}^{(1)}\right)+\nabla\cdot\left(\mathcal{S}^{(1)}\mathbf{v}^{(1)}\right)\\
&\quad+\frac{\gamma-1}{2}\frac{\partial}{\partial t}\left(\mathcal{P}^{(1)}\mathcal{P}^{(1)}\right)+\frac{1}{2}\frac{\partial}{\partial t}\left(\mathcal{S}^{(1)}\mathcal{S}^{(1)}\right)\\
&\quad+\frac{1}{2}\frac{\partial}{\partial t}\left(\mathcal{S}^{(1)}\mathcal{P}^{(1)}\right)+o(\alpha^2)
\end{aligned}\tag{2.18}$$

$$\begin{aligned}
f_i^{(2)} &= -\mathcal{P}^{(1)}\frac{\partial {v_i}^{(1)}}{\partial t}+\mathcal{S}^{(1)}\frac{\partial {v_i}^{(1)}}{\partial t}\\
&\quad-\left(\mathbf{v}^{(1)}\cdot\nabla\right)v_i^{(1)}-\frac{3}{2}\frac{\partial}{\partial x_i}\left(\frac{\mu^{(1)}}{\rho_0}\nabla\cdot\mathbf{v}^{(1)}\right)\\
&\quad+\frac{\partial}{\partial x_i}\left\{\frac{\mu^{(1)}}{\rho_0}\left(\frac{\partial {v_i}^{(1)}}{\partial x_j}+\frac{\partial {v_j}^{(1)}}{\partial x_i}\right)\right\}+o(\alpha^2)
\end{aligned}\tag{2.19}$$

$$\begin{aligned}
\frac{\dot{Q}^{(2)}}{\rho_0\,c_p\,T_0} &= -\gamma\mathcal{P}^{(1)}\frac{\partial\mathcal{S}^{(1)}}{\partial t}-\left(\mathbf{v}^{(1)}\cdot\nabla\right)\mathcal{S}^{(1)}\\
&\quad+\frac{4}{3}\nabla\cdot\left\{\frac{\mu^{(1)}}{\rho_0}\nabla\left(\mathcal{S}^{(1)}+(\gamma-1)\mathcal{P}^{(1)}\right)\right\}\\
&\quad+\frac{\nu_0}{c_p\,T_0}\left(\frac{4}{3}\Theta^{(1)}\,\Theta^{(1)}-4\,\Phi^{(1)}\right)\\
&\quad-\frac{2}{3}\frac{\gamma-1}{\gamma}\nu_0\,\nabla^2\left(\gamma\mathcal{P}^{(1)}\mathcal{P}^{(1)}-2\gamma\mathcal{P}^{(1)}\mathcal{S}^{(1)}-\frac{\gamma}{\gamma-1}\mathcal{S}^{(1)}\mathcal{S}^{(1)}\right)+o(\alpha^2)
\end{aligned}\tag{2.20}$$

From equations (2.14), (2.15) and (2.16), dropping the superscript (n), the following modal evolution laws can be obtained

$$\frac{\partial\mathbf{\Omega}}{\partial t}-\nu_0\,\nabla^2\mathbf{\Omega}=\nabla\times\mathrm{f}\tag{2.21}$$

$$\frac{1}{c_0^2}\frac{\partial^2\mathcal{P}}{\partial t^2}-\nabla^2\mathcal{P}-\frac{4}{3}\frac{\gamma\nu_0}{c_0^2}\frac{\partial}{\partial t}\left(\nabla^2\mathcal{P}\right)=\frac{1}{c_0^2}\left\{\left(\frac{\partial}{\partial t}-\frac{4}{3}\nu_0\nabla^2\right)\frac{\dot{m}}{\rho_0}-\nabla\cdot\mathrm{f}+\frac{\partial}{\partial t}\left(\frac{\dot{Q}}{\rho_0 c_p T_0}\right)\right\}\tag{2.22}$$

$$\frac{\partial\mathcal{S}}{\partial t}-\frac{4}{3}\nu_0\,\nabla^2\mathcal{S}=\frac{4}{3}(\gamma-1)\,\nu_0\,\nabla^2\mathcal{P}+\frac{\dot{Q}}{\rho_0\,c_p\,T_0}\tag{2.23}$$

where

$$\mathbf{\Omega}=\nabla\times\mathbf{v}\tag{2.24}$$

is the vorticity field.

The modal-order decomposition enlightens the mechanisms according to which the generalized source terms $\dot{m}$, f and $\dot{Q}$ affect the modal dynamics. Moreover, these source terms can be interpreted as nonlinear terms generated by the interaction between the flow modes at their lower order.

Equation (2.21) shows that the vorticity mode is generated by rotational body forces. This mode has a parabolic structure and governs the behaviour of a viscous incompressible fluid. Equation (2.23) relates the entropic mode generation to heat additions. The entropic mode is of parabolic nature and affects the heat transfer dynamics in a fluid. Equation (2.22) enlightens the hyperbolic structure of the sound mode. This is generated by mass injections, non-solenoidal body forces and heat additions. The sound mode is of main concern in acoustics and in compressible fluid theories.

In equation (2.23) $\mathcal{S}$ can be split in order to further separate the entropic mode from the sound mode. Thus, setting $\mathcal{S}=\mathcal{S}_p+\mathcal{S}_s$ and $\mathcal{P}=\mathcal{P}_p$ yields

$$\frac{\partial\mathcal{S}_p}{\partial t}-\frac{4}{3}\nu_0\,\nabla^2\mathcal{S}_p=\frac{4}{3}(\gamma-1)\nu_0\nabla^2\mathcal{P}_p\quad\text{and}\tag{2.25}$$

$$\frac{\partial \mathcal{S}_s}{\partial t} - \frac{4}{3}\nu_0 \nabla^2 \mathcal{S}_s = \frac{\dot{Q}}{\rho_0 c_p T_0} \tag{2.26}$$

Equation (2.25) describes the thermal effects generated by the sound mode, and equation (2.26) describes the production, convection and diffusion of heat spots in a heat-conducting fluid, namely, the entropic mode of fluctuation.

Consider now the second order source terms (2.18), (2.19) and (2.20), and set $\mathbf{\Omega} = \mathbf{\Omega}_\Omega$ and $\mathbf{v}^{(1)} = \mathbf{v}_\Omega^{(1)} + \mathbf{v}_p^{(1)} + \mathbf{v}_s^{(1)}$. From equations (2.14) and (2.24) it follows that

$$\nabla \times \mathbf{v}_\Omega^{(1)} = \mathbf{\Omega}_\Omega^{(1)}, \qquad \nabla \cdot \mathbf{v}_\Omega^{(1)} = 0 \tag{2.27}$$

$$\nabla \times \mathbf{v}_p^{(1)} = 0, \qquad \nabla \cdot \mathbf{v}_p^{(1)} = -\frac{\partial \mathcal{P}_p{}^{(1)}}{\partial t} + \frac{\partial \mathcal{S}_p{}^{(1)}}{\partial t} + \frac{\dot{m}}{\rho_0} \tag{2.28}$$

$$\nabla \times \mathbf{v}_s^{(1)} = 0, \qquad \nabla \cdot \mathbf{v}_s^{(1)} = \frac{\partial \mathcal{S}_s{}^{(1)}}{\partial t} \tag{2.29}$$

Splitting the second order interaction terms in (2.18), (2.19) and (2.20) according to their modal nature, it formally results that

$$\dot{m}^{(2)} = \dot{m}_{pp} + \dot{m}_{p\Omega} + \dot{m}_{ps} + \dot{m}_{\Omega\Omega} + \dot{m}_{\Omega s} + \dot{m}_{ss} \tag{2.30}$$

$$f^{(2)} = f_{pp} + f_{p\Omega} + f_{ps} + f_{\Omega\Omega} + f_{\Omega s} + f_{ss} \tag{2.31}$$

$$\dot{Q}^{(2)} = \dot{Q}_{pp} + \dot{Q}_{p\Omega} + \dot{Q}_{ps} + \dot{Q}_{\Omega\Omega} + \dot{Q}_{\Omega s} + \dot{Q}_{ss} \tag{2.32}$$

where each nonlinear term can be obtained by considering the first order equations (2.21), (2.22), (2.25) and (2.26).

In free space the basic modes of fluctuation are independent from each other. Hence, analytical solutions of equations (2.21), (2.22), (2.25) and (2.26) can be obtained as superposition of Fourier components. Suppose that the space/time domain $\mathcal{D}$ does not include any solid boundary. Then set $\dot{m}$, f and $\dot{Q}$ equal to zero. The Fourier components of the vorticity, acoustic and entropic mode are respectively given by

$$\mathbf{\Omega}_\Omega^{(1)} = \mathbf{\Omega} \exp\left(\mathrm{i}\,\mathbf{k}_\Omega \cdot \mathbf{x} - \nu_0\, k_\Omega^2\, t\right) \tag{2.33}$$

$$\mathbf{v}_\Omega^{(1)} = \mathrm{i}\,\frac{\mathbf{k}_\Omega \times \mathbf{\Omega}}{k_\Omega^2} \exp\left(\mathrm{i}\,\mathbf{k}_\Omega \cdot \mathbf{x} - \nu_0\, k_\Omega^2\, t\right) \tag{2.34}$$

where $\mathbf{k}_\Omega$ is the wavenumber vector satisfying the requirement $\mathbf{k}_\Omega \cdot \mathbf{\Omega} = 0$, and Ω denotes the amplitude of the vorticity mode. For the acoustic mode

$$\mathcal{P}_p^{(1)} = \mathcal{P} \exp\left(\mathrm{i}\,\mathbf{k}_p \cdot \mathbf{x} - c\,t\right) \tag{2.35}$$

$$\mathbf{v}_p^{(1)} = \mathrm{i}\,\frac{\mathbf{k}_p\, c_0^2}{c - \frac{4}{3}\nu_0\, k_p}\mathcal{P} \exp\left(\mathrm{i}\,\mathbf{k}_p \cdot \mathbf{x} - c\,t\right) \tag{2.36}$$

$$\mathcal{S}_p^{(1)} = \frac{\frac{4}{3}\,(\gamma - 1)\,\nu_0\, k_p^2}{c - \frac{4}{3}\nu_0\, k_p}\mathcal{P} \exp\left(\mathrm{i}\,\mathbf{k}_p \cdot \mathbf{x} - c\,t\right) \tag{2.37}$$

where $\mathcal{P}$ is the complex amplitude of the pressure disturbance, $\mathbf{k}_p$ is the acoustic wavenumber vector, $\mathcal{S}_p^{(1)}$ is the entropy generated by the viscous damping of the acoustic wave, and

$$c = c_0\, k_p \left\{ \frac{2}{3}\gamma \frac{\nu_0\, k_p}{c_0} - \mathrm{i} \left[1 - \left(\frac{2}{3}\gamma \frac{\nu_0\, k_p}{c_0} \right)^2 \right] \right\} \tag{2.38}$$

is a complex number whose real part gives the rate of viscous damping of the acoustic fluctuation and the imaginary part gives the frequency of the oscillating sound mode. Finally, for the entropic mode

$$\mathcal{S}_s^{(1)} = \mathcal{S} \exp\left(\mathrm{i}\, \mathbf{k}_s \cdot \mathbf{x} - \frac{4}{3} \nu_0 \, k_s^2 \, t\right) \tag{2.39}$$

$$\mathbf{v}_s^{(1)} = \mathrm{i} \frac{4}{3} \nu_0 \, \mathbf{k}_s \mathcal{S} \exp\left(\mathrm{i}\, \mathbf{k}_s \cdot \mathbf{x} - \frac{4}{3} \nu_0 \, k_s^2 \, t\right) \tag{2.40}$$

where $\mathcal{S}$ is the complex amplitude of the entropy disturbance and $\mathbf{k}_s$ is the entropy wavenumber vector.

Suppose that the amplitude of $\mathbf{k}_\Omega$, $\mathbf{k}_p$ and $\mathbf{k}_s$ are of the same order of magnitude. Then let k indicate the largest one. The reciprocal of a wavenumber provides the length scale λ of a fluctuating field, therefore a dimensionless parameter ϵ can be defined as the ratio between λ and the medium reference length l. Letting $l \simeq \nu_0/c_0$ be the mean free molecular path, the parameter ϵ denotes the characteristic Knudsen number of the fluctuating field and is given by

$$\epsilon = \frac{\nu_0 \, k}{c_0} \tag{2.41}$$

The length parameter ϵ, together with the amplitude parameter α, can be used to estimate the relative magnitude of the various interaction terms in equations (2.18), (2.19) and (2.20). Furthermore, by applying a dimensional analysis to the first order homogeneous form of equations (2.21), (2.22), (2.25) and (2.26), it results that

$$\frac{\partial {\Omega_\Omega}^{(1)}}{\partial t} - \nu_0 \, \nabla^2 \Omega_\Omega^{(1)} = 0 \tag{2.42}$$

$$c_0^2 \, k_\Omega^2 \, \alpha \qquad \epsilon \, c_0^2 \, k_\Omega^2 \, \alpha \tag{2.43}$$

$$\frac{\partial^2 {\mathcal{P}_p}^{(1)}}{\partial t^2} - c_0^2 \, \nabla^2 \mathcal{P}_p^{(1)} - \frac{4}{3} \gamma \nu_0 \frac{\partial}{\partial t} \left(\nabla^2 \mathcal{P}_p^{(1)}\right) = 0 \tag{2.44}$$

$$c_0^2 \, k_p^2 \, \alpha \qquad c_0^2 \, k_p^2 \, \alpha \qquad \epsilon c_0^2 \, k_p^2 \, \alpha \tag{2.45}$$

$$\frac{\partial {\mathcal{S}_s}^{(1)}}{\partial t} - \frac{4}{3} \nu_0 \, \nabla^2 \mathcal{S}_s^{(1)} = 0 \tag{2.46}$$

$$c_0 \, k_s \, \alpha \qquad \epsilon c_0 \, k_s \, \alpha \tag{2.47}$$

where the following orders of magnitude have been supposed

$$\mathcal{P}_p^{(1)} = \mathcal{O}(\alpha) \tag{2.48}$$

$$\mathcal{S}_s^{(1)} = \mathcal{O}(\alpha) \tag{2.49}$$

$$\Omega_\Omega^{(1)} = \mathcal{O}(\alpha \, c_0 \, k) \tag{2.50}$$

$$\frac{\partial}{\partial x} = \mathcal{O}(k) \tag{2.51}$$

$$\frac{\partial}{\partial t}^{(\mathrm{i})} = \mathcal{O}(c_0 \, k) \qquad \text{the } \textit{inertial} \text{ time reference is } (c_0 k)^{-1} \tag{2.52}$$

$$\frac{\partial}{\partial t}^{(\mathrm{v})} = \mathcal{O}(\epsilon \, c_0 \, k) \qquad \text{the } \textit{viscous} \text{ time reference is } (\epsilon \, c_0 \, k)^{-1} \tag{2.53}$$

which further yield

$$v_p^{(1)} = \mathcal{O}(c_0 \, k) \qquad \text{from equations (2.48) and (2.36)} \tag{2.54}$$

$$\mathcal{S}_p^{(1)} = \mathcal{O}\left(\frac{k_p}{k}\,\alpha\,\epsilon\right) \qquad \text{from equations (2.48) and (2.37)} \tag{2.55}$$

$$v_s^{(1)} = \mathcal{O}\left(\frac{k_s}{k}\,c_0\,\alpha\,\epsilon\right) \qquad \text{from equations (2.49) and (2.40)} \tag{2.56}$$

$$v_\Omega^{(1)} = \mathcal{O}(c_0\,k) \qquad \text{from equations (2.50) and (2.34)} \tag{2.57}$$

For a vanishing ϵ, the above order analysis leads to the *zero order approximation*

$$\frac{\partial \Omega_\Omega{}^{(0)}}{\partial t} = 0 \tag{2.58}$$

$$\frac{\partial^2 \mathcal{P}_p{}^{(0)}}{\partial t^2} - c_0^2\,\nabla^2 \mathcal{P}_p^{(1)} = 0 \tag{2.59}$$

$$\frac{\partial \mathcal{S}_s{}^{(0)}}{\partial t} = 0 \tag{2.60}$$

where equation (2.58) states the Taylor hypothesis of vorticity frozen convection, equation (2.60) describes a similar behaviour for heat spots, and equation (2.59) is a wave equation describing the propagation of pressure disturbances in a homogeneous medium at rest.

The dimensional analysis can be applied to the second order source terms $\dot{m}^{(2)}$, $\mathrm{f}^{(2)}$ and $\dot{Q}^{(2)}$.

Consider the mass injection term, whose modal components are split into bilateral interaction terms, as in equation (2.30). From equation (2.18) it follows that

$$\begin{aligned}
\left(\frac{\dot{m}}{\rho_0}\right)_{pp} &= \underset{c_0\,k\,\alpha^2}{-\nabla\cdot\left(\mathcal{P}_p^{(1)}\,\mathrm{v}_p^{(1)}\right)} + \underset{\epsilon\,c_0\,k\,\alpha^2}{\nabla\cdot\left(\mathcal{S}_p^{(1)}\,\mathrm{v}_p^{(1)}\right)} \\
&\quad + \underset{c_0\,k\,\alpha^2}{\frac{\gamma-1}{2}\frac{\partial}{\partial t}\left(\mathcal{P}_p^{(1)}\,\mathcal{P}_p^{(1)}\right)} + \underset{\epsilon\,c_0\,k\,\alpha^2}{\frac{1}{2}\frac{\partial}{\partial t}\left(\mathcal{S}_p^{(1)}\,\mathcal{S}_p^{(1)}\right)} \\
&\quad + \underset{\epsilon\,c_0\,k\,\alpha^2}{\frac{1}{2}\frac{\partial}{\partial t}\left(\mathcal{S}_p^{(1)}\,\mathcal{P}_p^{(1)}\right)} + \mathrm{o}(\alpha^2)
\end{aligned} \tag{2.61}$$

$$\left(\frac{\dot{m}}{\rho_0}\right)_{p\Omega} = \underset{c_0\,k\,\alpha^2}{-\nabla\cdot\left(\mathcal{P}_p^{(1)}\,\mathrm{v}_\Omega^{(1)}\right)} + \underset{\epsilon\,c_0\,k\,\alpha^2}{\nabla\cdot\left(\mathcal{S}_p^{(1)}\,\mathrm{v}_\Omega^{(1)}\right)} + \mathrm{o}(\alpha^2) \tag{2.62}$$

$$\begin{aligned}
\left(\frac{\dot{m}}{\rho_0}\right)_{ps} &= \underset{\epsilon\,c_0\,\alpha^2}{-\nabla\cdot\left(\mathcal{P}_p^{(1)}\mathrm{v}_s^{(1)}\right)} + \underset{\epsilon\,c_0\,\alpha^2}{\nabla\cdot\left(\mathcal{S}_p^{(1)}\,\mathrm{v}_s^{(1)}\right)} \\
&\quad + \underset{c_0\,\alpha^2}{\nabla\cdot\left(\mathcal{S}_s^{(1)}\,\mathrm{v}_p^{(1)}\right)} + \underset{\epsilon\,c_0\,k\,\alpha^2}{\frac{\partial}{\partial t}\left(\mathcal{S}_p^{(1)}\,\mathcal{S}_s^{(1)}\right)} \\
&\quad + \frac{1}{2}\frac{\partial}{\partial t}\left(\mathcal{P}_p^{(1)}\,\mathcal{S}_s^{(1)}\right) + \mathrm{o}(\alpha^2)
\end{aligned} \tag{2.63}$$

$$c_0\, k\, \alpha^2$$

$$\left(\frac{\dot m}{\rho_0}\right)_{\Omega\Omega} = 0 \tag{2.64}$$

$$\left(\frac{\dot m}{\rho_0}\right)_{\Omega s} = \underset{c_0\, k\, \alpha^2}{\nabla \cdot \left(\mathcal{S}_s^{(1)}\, \mathbf{v}_\Omega^{(1)}\right)} + \mathrm{o}(\alpha^2) \tag{2.65}$$

$$\left(\frac{\dot m}{\rho_0}\right)_{ss} = \underset{\epsilon c_0\, k\, \alpha^2}{\nabla \cdot \left(\mathcal{S}_s^{(1)}\, \mathbf{v}_s^{(1)}\right)} + \underset{\epsilon\, c_0\, k\, \alpha^2}{\frac{1}{2}\frac{\partial}{\partial t}\left(\mathcal{S}_s^{(1)}\, \mathcal{S}_s^{(1)}\right)} + \mathrm{o}(\alpha^2) \tag{2.66}$$

where the time derivative reference scale has been supposed to depend on the corresponding flow quantity, that is

$$\frac{\partial}{\partial t}\left(\mathcal{F}_p \mathcal{G}_p\right) = \frac{\partial}{\partial t}^{(\mathrm{i})}\left(\mathcal{F}_p \mathcal{G}_p\right) \tag{2.67}$$

$$\frac{\partial}{\partial t}\left(\mathcal{F}_s \mathcal{G}_p\right) \simeq \mathcal{F}_s \frac{\partial}{\partial t}^{(\mathrm{i})}\left(\mathcal{G}_p\right) \tag{2.68}$$

$$\frac{\partial}{\partial t}\left(\mathcal{F}_s \mathcal{G}_s\right) = \frac{\partial}{\partial t}^{(\mathrm{v})}\left(\mathcal{F}_s \mathcal{G}_s\right) \tag{2.69}$$

By supposing that $\epsilon < \alpha$, terms of order $\epsilon\, \alpha^2$ can be absorbed by the truncation error and the bilateral interaction terms take the following expressions

$$\dot m_{pp} = -\rho_0 \nabla \cdot \left(\mathcal{P}_p^{(1)}\, \mathbf{v}_p^{(1)}\right) + \rho_0 \frac{\gamma - 1}{2}\frac{\partial}{\partial t}\left(\mathcal{P}_p^{(1)}\, \mathcal{P}_p^{(1)}\right) + \mathcal{O}(\epsilon\, \alpha^2) \tag{2.70}$$

$$\dot m_{p\Omega} = -\rho_0\, \nabla \cdot \left(\mathcal{P}_p^{(1)}\, \mathbf{v}_\Omega^{(1)}\right) + \mathcal{O}(\epsilon\, \alpha^2) \tag{2.71}$$

$$\dot m_{ps} = \rho_0\, \nabla \cdot \left(\mathcal{S}_s^{(1)}\, \mathbf{v}_p^{(1)}\right) + \rho_0\, \mathcal{S}_s^{(1)} \frac{\partial \mathcal{P}_p^{(1)}}{\partial t} + \mathcal{O}(\epsilon\, \alpha^2) \tag{2.72}$$

$$\dot m_{\Omega\Omega} = 0 \tag{2.73}$$

$$\dot m_{\Omega s} = \rho_0\, \nabla \cdot \left(\mathcal{S}_s^{(1)}\, \mathbf{v}_\Omega^{(1)}\right) + \mathcal{O}(\epsilon\, \alpha^2) \tag{2.74}$$

$$\dot m_{ss} = \mathcal{O}(\epsilon\, \alpha^2) \tag{2.75}$$

Analogous considerations for $\mathbf{f}^{(2)}$ and $\dot Q^{(2)}$ lead to [76]

$$\mathbf{f}_{pp} = -\mathcal{P}_p^{(1)} \frac{\partial \mathbf{v}_p{}^{(1)}}{\partial t} - \frac{1}{2}\nabla\left(\mathbf{v}_p^{(1)} \cdot \mathbf{v}_p^{(1)}\right) + \mathcal{O}(\epsilon\, \alpha^2) \tag{2.76}$$

$$\mathbf{f}_{p\Omega} = -\nabla\left(\mathbf{v}_p^{(1)} \cdot \mathbf{v}_\Omega^{(1)}\right) + \mathbf{v}_p^{(1)} \times \mathbf{\Omega}_p^{(1)} + \mathcal{O}(\epsilon\, \alpha^2) \tag{2.77}$$

$$\mathbf{f}_{ps} = \mathcal{S}_s^{(1)} \frac{\partial \mathbf{v}_p{}^{(1)}}{\partial t} + \mathcal{O}(\epsilon\, \alpha^2) \tag{2.78}$$

$$\mathbf{f}_{\Omega\Omega} = -\left(\mathbf{v}_\Omega^{(1)} \cdot \nabla\right) \mathbf{v}_\Omega^{(1)} \tag{2.79}$$

$$\mathbf{f}_{\Omega s} = \mathcal{O}(\epsilon\, \alpha^2) \tag{2.80}$$

$$\mathbf{f}_{ss} = \mathcal{O}(\epsilon\, \alpha^2) \tag{2.81}$$

and

$$\dot{Q}_{pp} = \mathcal{O}(\epsilon\,\alpha^2) \tag{2.82}$$
$$\dot{Q}_{p\Omega} = \mathcal{O}(\epsilon\,\alpha^2) \tag{2.83}$$
$$\dot{Q}_{ps} = -\left(\mathbf{v}_p^{(1)} \cdot \nabla\right) \mathcal{S}_s^{(1)} + \mathcal{O}(\epsilon\,\alpha^2) \tag{2.84}$$
$$\dot{Q}_{\Omega\Omega} = \mathcal{O}(\epsilon\,\alpha^2) \tag{2.85}$$
$$\dot{Q}_{\Omega s} = -\left(\mathbf{v}_\Omega^{(1)} \cdot \nabla\right) \mathcal{S}_s^{(1)} + \mathcal{O}(\epsilon\,\alpha^2) \tag{2.86}$$
$$\dot{Q}_{ss} = \mathcal{O}(\epsilon\,\alpha^2) \tag{2.87}$$

2.3 Physics of Modal Bilateral Interaction

The nonlinearity of fluid motion in a region sufficiently far from solid boundaries has been systematically investigated following the analysis of Chu & Kovásznay [76]. All the bilateral interaction terms have been identified and classified as generalized mass injections, body forces and heat additions. The analysis described in this chapter culminates in the physical interpretation of the bilateral interaction terms.

Consider the second order vorticity mode. It is generated by rotational body forces, as described by the parabolic equation

$$\frac{\partial \boldsymbol{\Omega}_\Omega{}^{(2)}}{\partial t} - \nu_0 \nabla^2 \boldsymbol{\Omega}_\Omega^{(2)} = \nabla \times \mathbf{f}^{(2)} =$$

$$p \Leftrightarrow p \qquad \mathcal{O}(\epsilon\,\alpha^2) \tag{2.88}$$
$$p \Leftrightarrow \Omega \qquad -v_{pj}^{(1)} \frac{\partial \Omega_i{}^{(1)}}{\partial x_j} + \Omega_j^{(1)} \frac{\partial v_{pi}{}^{(1)}}{\partial x_j} - \Omega_i^{(1)} \frac{\partial v_{pj}{}^{(1)}}{\partial x_j} \tag{2.89}$$
$$p \Leftrightarrow s \qquad \nabla \mathcal{S}_s^{(1)} \times \frac{\partial \mathbf{v}_p{}^{(1)}}{\partial t} \simeq -\nabla \mathcal{S}_s^{(1)} \times \frac{1}{c_0^2} \nabla \mathcal{P}_p^{(1)} \tag{2.90}$$
$$\Omega \Leftrightarrow \Omega \qquad -v_{\Omega j}^{(1)} \frac{\partial \Omega_{\Omega i}{}^{(1)}}{\partial x_j} + \Omega_{\Omega j}^{(1)} \frac{\partial v_{\Omega i}{}^{(1)}}{\partial x_j} + \mathcal{O}(\epsilon\,\alpha^2) \tag{2.91}$$
$$\Omega \Leftrightarrow s \qquad \mathcal{O}(\epsilon\,\alpha^2) \tag{2.92}$$
$$s \Leftrightarrow s \qquad \mathcal{O}(\epsilon\,\alpha^2) \tag{2.93}$$

The sound self-interaction, the vorticity-entropy bilateral interaction and the entropy self-interaction do not excite the vorticity mode. The sound-vorticity bilateral interaction provides the mechanisms of both the vorticity convection and the stretching of vortex tubes. The sound-entropy bilateral interaction generates vorticity when a pressure force is exerted on a fluid particle whose mass distribution is not uniform. In fact, the resulting torque induces an angular acceleration on the fluid particle. The vorticity self-interaction accounts for the vorticity self-convection. This nonlinear mechanism is of fundamental importance in the dynamics of turbulence.

Consider the second order acoustic mode. It is generated by mass injections, body forces and heat additions, as described by the hyperbolic equation

$$\frac{\partial^2 \mathcal{P}_p{}^{(2)}}{\partial t^2} - c_0^2 \nabla^2 \mathcal{P}_p^{(2)} - \frac{4}{3} \gamma \nu_0 \frac{\partial}{\partial t} \left(\nabla^2 \mathcal{P}_p^{(2)}\right) =$$
$$\left(\frac{\partial}{\partial t} - \frac{4}{3} \nu_0 \nabla^2\right) \frac{\dot{m}^{(2)}}{\rho_0} - \nabla \cdot \mathbf{f}^{(2)} + \frac{\partial}{\partial t} \left(\frac{\dot{Q}^{(2)}}{\rho_0\, c_p\, T_0}\right) =$$

$$p \Leftrightarrow p \qquad \frac{\partial^2}{\partial x_i \partial x_j}\left(v_{pi}^{(1)} v_{pj}^{(1)}\right) + c_0^2 \nabla^2 \left(\mathcal{P}_p^{(1)} \mathcal{P}_p^{(1)}\right) + \frac{\gamma - 1}{2}\frac{\partial^2}{\partial t^2}\left(\mathcal{P}_p^{(1)} \mathcal{P}_p^{(1)}\right) + \mathcal{O}(\epsilon\,\alpha^2) \tag{2.94}$$

$$p \Leftrightarrow \Omega \qquad 2\,\frac{\partial^2}{\partial x_i \partial x_j}\left(v_{\Omega i}^{(1)}\, v_{pj}^{(1)}\right) + \mathcal{O}(\epsilon\,\alpha^2) \tag{2.95}$$

$$p \Leftrightarrow s \qquad \frac{1}{\rho_0\, c_p\, T_0}\frac{\partial^2}{\partial t \partial x_i}\left(\mathcal{S}_s^{(1)}\, v_{pi}^{(1)}\right) \tag{2.96}$$

$$\Omega \Leftrightarrow \Omega \qquad \frac{\partial^2}{\partial x_i \partial x_j}\left(v_{\Omega i}^{(1)} v_{\Omega j}^{(1)}\right) \tag{2.97}$$

$$\Omega \Leftrightarrow s \qquad \mathcal{O}(\epsilon\,\alpha^2) \tag{2.98}$$

$$s \Leftrightarrow s \qquad \mathcal{O}(\epsilon\,\alpha^2) \tag{2.99}$$

The vorticity-entropy bilateral interaction and the entropy self-interaction do not excite the sound mode. The sound self-interaction accounts for the scattering of an acoustic wave by the sound field. Integration of this term over the entire flow field, with the assumption of vanishing disturbances at infinity, gives a nonzero result. As a consequence, the acoustic self interaction has a secondary source nature. The sound-vorticity bilateral interaction provides a sound scattering mechanism. The sound-entropy bilateral interaction accounts for the sound scattering by heat spots. The vorticity self-interaction is a source of acoustic disturbances. The latter result is at the basis of Lighthill's theory of aerodynamic sound.

Finally, consider the second order entropic mode. It is generated by heat additions, as described by the parabolic equation

$$\frac{\partial \mathcal{S}_s^{(2)}}{\partial t} - \frac{4}{3}\nu_0 \nabla^2 \mathcal{S}_s^{(2)} = \frac{\dot{Q}^{(2)}}{\rho_0\, c_p\, T_0} =$$

$$p \Leftrightarrow p \qquad \mathcal{O}(\epsilon\,\alpha^2) \tag{2.100}$$

$$p \Leftrightarrow \Omega \qquad \mathcal{O}(\epsilon\,\alpha^2) \tag{2.101}$$

$$p \Leftrightarrow s \qquad -\frac{1}{\rho_0\, c_p\, T_0} v_{pi}^{(1)} \frac{\partial \mathcal{S}_s^{(1)}}{\partial x_i} \tag{2.102}$$

$$\Omega \Leftrightarrow \Omega \qquad \mathcal{O}(\epsilon\,\alpha^2) \tag{2.103}$$

$$\Omega \Leftrightarrow s \qquad -\frac{1}{\rho_0\, c_p\, T_0} v_{\Omega i}^{(1)} \frac{\partial \mathcal{S}_s^{(1)}}{\partial x_i} \tag{2.104}$$

$$s \Leftrightarrow s \qquad \mathcal{O}(\epsilon\,\alpha^2) \tag{2.105}$$

The sound self-interaction, the sound-vorticity bilateral interaction, the vorticity self-interaction and the entropy self-interaction do not excite the entropic mode. The sound-entropy bilateral interaction accounts for the convection of heat spots by acoustic waves. The sound-vorticity bilateral interaction describes the convection of heat spots by vorticity fluctuations.

3

The Pressure Field at the Wall of a Turbulent Boundary-Layer

3.1 Introduction

The statistical properties of the wall-pressure fluctuations beneath a turbulent boundary-layer are of great interest in fluid mechanics. Their description has a fundamental importance in several engineering problems, such as:

1. the aerodynamic noise radiated by a turbulent boundary-layer adjacent to rigid or compliant surfaces[1].
2. The aircraft cabin noise caused by the vibrations induced by an external turbulent flow on the fuselage panels[2].
3. The conversion of a hydrodynamic pressure fluctuations into acoustic waves in the presence of geometrical singularities, e.g. edges. The model problem of a *half-plane* wetted by a turbulent flow is commonly investigated[3].
4. The trailing edge noise[4].
5. The flow noise generated on the surface of a sonar transducer mounted on submarines and ships[5].

Moreover, a great deal of interest has been devoted to a theoretical investigation of the wall-pressure statistical behaviour. This represents an effective way to explore the structure of a turbulent boundary-layer[6].

Earlier experimental measurements of wall-pressure fluctuations beneath various turbulent shear flows[7] showed that the pressure fluctuations are convected at approximately the velocity $0.81\,U_\infty$, and naturally decay after traveling a distance of few boundary-layer thicknesses.

In 1952 Lin [98] argued that, since both the mean shear gradients and the intensity of the flow fluctuations are high in a turbulent boundary-layer, there exists no a single velocity at which all the elementary pressure disturbances are convected. The *frozen convection* hypothesis introduced by Taylor

[1] Powell [77], Ffowcs Williams [78], Guo *et al.* [79]
[2] Graham [80]
[3] Chase [81], Chandiramani [82], Chase [83]
[4] Howe [84], Brooks & Hodgson [85], Howe [86]
[5] Haddle & Shudrzyk [87]
[6] Shubert & Corcos [88], Landahl [89]
[7] Laufer [90], Willmarth [91], Harrison [92], Willmarth [93], Lilley & Hodgson [94], Bull & Willis [95], Kistler & Chen [96], Corcos [97]

was thus considered too restrictive and more exhaustive models[8] were developed on the basis of two-point wall pressure statistical measurements[9].

The experimental results obtained by Willmarth & Woldridge [106] showed that the convection velocity of turbulent eddies in a boundary-layer depends on the distance between the pressure transducers. It was observed to vary between $0.56\,U_\infty$ at zero separation, and $0.83\,U_\infty$ at very large transducer separations. Such a variation was recognized to be a consequence of the fact that larger eddies are convected faster. In fact, at smaller transducer distances the correlation is dominated by small-scale-eddies which are closer to the wall and move more slowly. Conversely, since the period of decay of a convected disturbance increases with the eddy size, at larger transducer distances the correlation is dominated by large-scale eddies which are farther from the wall and move faster.

Willmarth & Woldridge attempted to relate directly the convection velocity and the eddy size by measuring the space-time wall pressure correlation into two filtered bands of low (300 Hz $< f <$ 700 Hz, $0.41 < \omega\,\delta^*/U_\infty < 0.95$) and high frequency (3000 Hz $< f <$ 5000 Hz, $4.1 < \omega\,\delta^*/U_\infty < 6.8$). Again, they observed a convection velocity increasing with the transducer separation distance and attributed this result to a not sufficiently narrow bandwidth of the frequency filtering. However, as pointed-out by Wills [107], a frequency filtering cannot distinguish between eddies of large wavelength moving faster, and eddies of smaller wavelength moving more slowly. A turbulent pressure field is indeed characterized by an energy distribution over a range of wavenumber k_x, and a phase velocity distribution $c = \omega/k_x$. Therefore, a frequency filtering isolates those fluctuations for which the product between the wavenumber and the phase-velocity is a constant.

Wills [107] measured the wall pressure wavenumber/phase-velocity spectrum for a two-dimensional turbulent boundary-layer in zero pressure gradient and defined the convection velocity as the peak-energy velocity at constant wavenumber. The convection velocity was thus observed to vary from a maximum of about $0.9\,U_\infty$ at a value of $k_x\,\delta_{995} = 1.2$, to an asymptotical value of $0.55\,U_\infty$ at higher values of $k_x\,\delta_{995}$. These results confirmed that the largest eddies extend over the whole width of the boundary-layer and are convected at the typical outer layer velocity, whereas eddies of smaller size are closer to the wall and move at lower velocities. Furthermore, Wills observed that the convection velocity decreases at very low wavenumbers and attributed this behaviour to the inaccuracy of the experimental results at frequencies less than 200 Hz.

3.2 Wall Pressure Wavenumber-Frequency Spectrum

In 1964 Corcos developed a model for the wall pressure wavenumber-frequency spectrum on the basis of the experimental results obtained by Willmarth & Woldridge's [106]. He showed that the space-time covariance of the fluctuating pressure and the corresponding spectrum at the wall of a turbulent boundary-layer can be described in terms of similarity variables. These are based on an appropriate choice of some dimensionless parameters which reduce the dispersion of the experimental data. For example, if the root-mean-square pressure at the wall of a pipe is made dimensionless by the wall mean shear stress, it exhibits a negligible dependence on the Reynolds number.

Corcos' paper is composed of two parts. The first deals with the convective properties of a turbulent boundary-layer, based on the experimental data of Willmarth & Woldridge [106]. In the second part a theoretical model of the wall-pressure field is developed. This is based on a non-homogeneous Poisson equation obtained from the continuity and linear momentum equations for an incompressible flow.

Starting from Kraichnan's [108] milestone work, most of the earlier works on the wall pressure statistical behaviour were concerned with the incompressible flow regime. A review of all these works was made by Willmarth [109]. Ffowcs Williams [78] was the first to consider the effect of fluid compressibil-

[8] Corcos [99], Bergeron [100], Chase [101], Ffowcs Williams [102], Efimtsov [103], Chase [104], Smol'Yakov & Tkachenko [105]

[9] Bull & Willis [95], Willmarth & Woldridge [106], Wills [107]

ity. He showed that the supersonic spectral elements ($\omega/k > c$, i.e. low wavenumber spectral elements) are strongly affected by the fluid compressibility and that the wall pressure wavenumber-frequency spectrum exhibits a singularity at the sonic phase speed. As demonstrated later on by Bergeron [100], such a non-integrable singularity is related to a two-dimensional form of Olbers' paradox: each element of an unbounded turbulent region generates acoustic disturbances which do not decrease rapidly enough with the distance for their integrated effect to be finite. Conversely, if the source region is supposed to have a finite extention, the singularity becomes integrable. Howe [110] interpreted the surface pressure wavenumber-frequency spectrum singularity as the response of a linear system excited at resonance: sound waves propagate parallel to the wall and are continuously enforced by turbulent elements of acoustic wavenumber. He showed that, accounting for the shear stress fluctuations, the wall pressure wavenumber-frequency spectrum does not exhibit the singular behaviour observed by Bergeron. Howe argued that the viscosity of the fluid controls the intensity of the peak at the critical wavenumber $k = |\omega|/c$. Furthermore, the shear stress fluctuations have the effect of diminishing the overall radiated acoustic intensity.

Ffowcs Williams [102] extended the Corcos similarity model in order to account for the compressibility effects at low wavenumbers. Moreover, he scrutinized the origin of the singularity at the acoustic coincidence frequency showing that, if the turbulent region is supposed to extent only over a large boundary-layer disk of radius R, the surface pressure wavenumber-frequency spectrum diverges logarithmically as the turbulent layer scale factor R/δ becomes infinitely large.

Dowling [111] applied Lighthill's acoustic analogy approach in order to determine the flow noise radiated by a turbulent boundary-layer over a planar flexible surface. He noticed an analogy between the sound generated by turbulence and equivalent sources placed between a surface with the same characteristics of the physical surface and a vortex-sheet along the outer region of the boundary-layer. The singularity at the acoustic coincidence frequency of the wall pressure wavenumber-frequency spectrum was recovered but only for rigid surface and for downstream-propagating elements. Therefore, Dowling concluded that the mean shear profile restraints the acoustic singularity for all the upstream-propagating modes.

The interest in the subconvective domain of the wall pressure wavenumber-frequency spectrum is due to the dominant contribution that low-wavenumber spectral elements give to the flow noise in both individual and array sensors for underwater acoustic applications. In fact, the higher intensity disturbances in the convective domain can be easily damped by a spatial filtering, namely, an area-averaging as suggested by Phillips' [112] theoretical results. However, a wavevector filtering generates a series of aliased lobes among which the greatest one is centered in the acoustic window $k < \omega/c$ and cannot be suppressed by adopting array sensors.

Chase & Noiseux [113] described the turbulent wall pressure wavenumber-frequency spectrum at low wavenumbers, both in planar and cylindrical flows. They expanded the nonlinear source terms in powers of the parameter $U_\infty k_x/\omega$ and M_∞. The planar case was a generalization of Bergeron's [100] result to a domain where the wavenumber does not require to be small with respect to the reciprocal of the boundary-layer thickness. The wall pressure wavenumber-frequency spectrum was shown to be singular at the acoustic wavenumber. However, if a slight compressibility is introduced in the analysis, the singularity takes a logarithmic integrable character.

In 1987 Chase [104] reexamined the structure of the wavenumber-frequency spectrum of the wall pressure fluctuations beneath a turbulent boundary-layer adjacent to a smooth rigid plane in the whole wavenumber domain. He demonstrated that the k^2 law stated by the Phillips-Kraichnan theorem ([112], [108], [114]) is well fitted only in the interval $\omega/c < k < \delta^{-1}$.

In the following sections the models proposed by Corcos, Landahl, Shubert & Corcos, Ffowcs Williams and Chase are discussed in order to provide a comprehensive description of the wavenumber-frequency spectrum of the wall pressure fluctuations beneath a turbulent boundary-layer.

3.3 Corcos' Similarity Model

Corcos' analysis is substantially based on the individuation of an appropriate set of reference quantities for a turbulent boundary-layer. The reference velocity in the outer region of the boundary-layer is the free-stream velocity U_∞, while the friction velocity $u_\tau = \sqrt{\tau_w/\rho_0}$ can be used both in the outer and the inner region. The reference lengths are the boundary-layer thickness δ in the outer region, and the displacement thickness δ^* in the inner region. The wall pressure frequency spectrum is finally made dimensionless by the quantity $q^2\delta^*/U_\infty$, where q denotes the mean flow dynamic pressure.

Let us define the wall-pressure power spectral density as the Fourier transform of the time correlation $\mathcal{R}\,(0,0,\tau)$, namely

$$\Phi\,(\omega) = \int_0^\infty \mathcal{R}\,(0,0,\tau)\cos(\omega\,\tau)\;\mathrm{d}\tau \tag{3.1}$$

The space-time correlation $\mathcal{R}$ is given by

$$\mathcal{R}\,(\xi,\eta,\tau) = \overline{p\,(x,z,t)\;p\,(x+\xi,z+\eta,t+\tau)} \tag{3.2}$$

where ξ and η denote the streamwise and the transversal transducer separation, respectively, τ is the time delay and overbar denotes ensemble average.

Willmarth & Woldridge [106] measured the fluctuating pressure upon a planar surface (x,z) beneath a boundary-layer with natural transition. They used pressure transducers with a resolution $r/\delta \simeq 0.0193$. The dimensionless spectrum $\Phi(\omega)\,U_\infty/q^2\,\delta^*$, measured at two values of the free-stream velocity, say $U_\infty = 47.6$ m/s and $U_\infty = 62.8$ m/s, were observed to be coincident at Strouhal number $\omega\,\delta^*/U_\infty$ greater than 0.14. Conversely, at lower values of the Strouhal number, the dimensionless spectra were observed to not be repeatable. This was attributed to the presence of extraneous pressure contributions, probably due to secondary flows and incoming acoustic waves.

The second step towards the Corcos' wall pressure model consists in a description of the convective properties of the pressure field.

As observed by Favre *et al.* [115], the statistical properties of a turbulent boundary-layer have a minimum of variation when measured in a reference frame moving downstream at a speed depending on the distance from the wall. Furthermore, at small values of the transversal transducer separation η, the space-time correlation function of the fluctuating streamwise velocity u peaks at values (ξ,τ) for which the quantity $\xi/\tau = U_c$ is approximately constant. Therefore, U_c can be interpreted as an eddy convection velocity.

In Fig.3.1 the longitudinal space-time correlation function $\mathcal{R}_{uu}\,(\xi,\tau)$ is plotted as a function of the dimensionless time delay $U_c\tau/\delta$ at two values of y/δ, say $y/\delta = 0.06$ and $y/\delta = 0.24$. The envelopes of the peaks of maximum velocity correlation show that, closer to the wall ($y/\delta = 0.06$), $\mathcal{R}_{uu}$ decays more rapidly than at a greater distance ($y/\delta = 0.24$). A similar qualitative behaviour was observed by Willmarth & Woldridge [106] for the pressure space-time correlation in low and high frequency bands. As shown in Fig.3.2, the correlation decays more rapidly in the higher frequency band.

Let us indicate as $\Gamma(\xi,\eta,\omega)$ the wall pressure cross-spectral density, namely, the Fourier transform of the wall pressure space-time correlation function $\mathcal{R}$, that is

$$\Gamma(\xi,\eta,\omega) = \int_{-\infty}^{+\infty} \exp(\imath\;\omega\,\tau)\,\mathcal{R}(\xi,\eta,\tau)\;\mathrm{d}\tau \tag{3.3}$$

and

$$\mathcal{R}(\xi,\eta,\tau) = \frac{1}{2\,\pi}\int_{-\infty}^{+\infty} \exp(-\imath\;\omega\,\tau)\,\Gamma(\xi,\eta,\omega)\;\mathrm{d}\omega = \frac{1}{\pi}\int_0^\infty |\Gamma|\cos(\omega\tau-\alpha)\;\mathrm{d}\omega \tag{3.4}$$

where $\Gamma = |\Gamma|\exp(\imath\;\alpha)$.

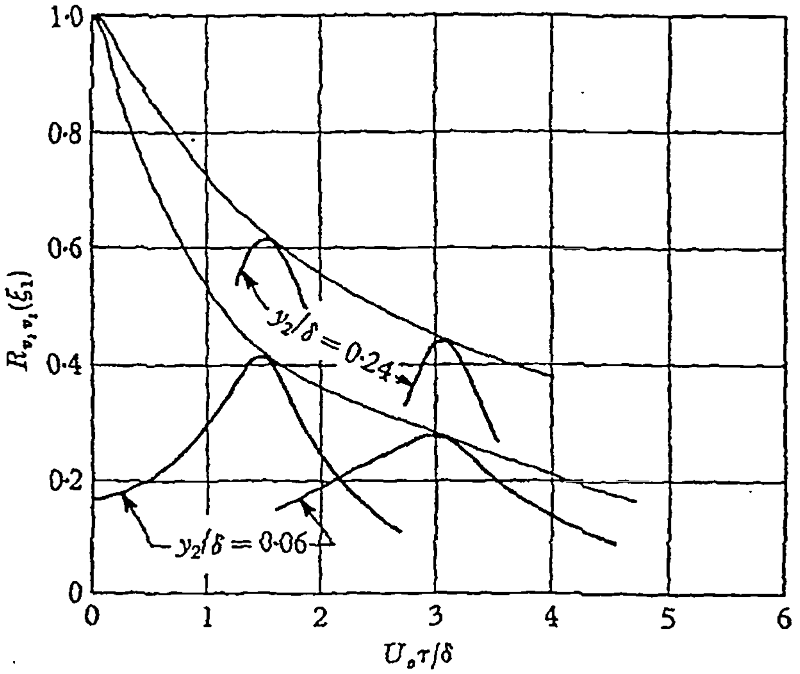

FIGURE 3.1: Space-time correlation of longitudinal velocity fluctuations v_1 at two distances y_2/δ from the wall. ξ_1 denotes the streamwise separation distance (after Corcos [99], figure 5).

The cross-spectral density at zero separation provides the power spectral density $\Phi(\omega)$ which can be used to make $|\Gamma|$ dimensionless. Thus, for the streamwise correlation, it results that

$$A = \frac{|\Gamma(\xi, 0, \omega)|}{\Phi(\omega)} \tag{3.5}$$

where the damping function A, as experimentally observed by Willmarth & Woldridge [106], Corcos [97] and Bakewell *et al.* [116], is approximately a function of the dimensionless variable $\omega\xi/U_c$ only.

Consider now two transducers separated by the streamwise distance ξ and measuring a harmonic disturbance convected at the velocity U_c, namely

$$p_1(t) = P_1 \, e^{-i\omega t}, \quad p_2(t) = P_2 \, e^{-i\omega\left(t - \frac{\xi}{U_c}\right)} \tag{3.6}$$

The correlation function between these pressure signals is

$$\mathcal{R}(\xi, \tau) = P_1 P_2 \cos\left(\omega\tau - \frac{\omega\xi}{U_c}\right) \tag{3.7}$$

By analogy with equation (3.4) the argument of the cross-spectral density is given by $\alpha = \omega\xi/U_c$. Hence, α can be used to define an average convection velocity $U_c(\omega, \xi)$.

Both the magnitude and the phase of the wall pressure cross-spectral density are function of the quantity $\omega\xi/U_c$ which can be assumed as a similarity variable. It thus follows that

$$\Gamma(\xi, 0, \omega) = \Phi(\omega) \, A\left(\frac{\omega\xi}{U_c}\right) \exp\left(i \, \frac{\omega\xi}{U_c}\right) \tag{3.8}$$

The damping function A can be interpreted as the convective memory of a vortical disturbance, whereas the similarity variable $\omega\xi/U_c$ is related to the ratio between the transducer distance ξ and the

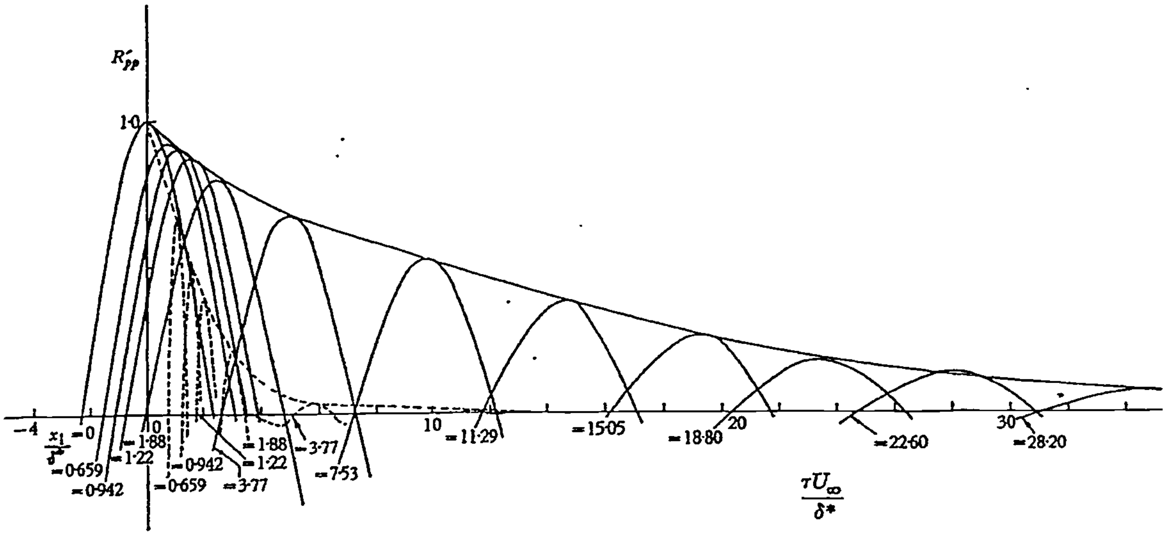

FIGURE 3.2: Peaks of the longitudinal space-time correlation of wall pressure fluctuations in a low and high frequency band. —— $300\,\mathrm{Hz} < f < 700\,\mathrm{Hz}, 0.41 < \omega\delta^*/U_\infty < 0.95$, - - - - $3000\,\mathrm{Hz} < f < 5000\,\mathrm{Hz}, 4.1 < \omega\delta^*/U_\infty < 6.8$ (after Willmarth & Woldridge [106], figure 9).

eddy size λ. In fact, letting $\lambda = U_c/f$ denote the wavelength[10] of the convected pressure disturbance yields

$$\frac{\omega\xi}{U_c} = 2\pi\frac{\xi}{\lambda} \tag{3.9}$$

Thus, the similarity rule (3.8) is physically consistent with the assumption of an eddy decay which is proportional to the eddy size, but that is not affected by the characteristic frequency of the flow U_c/δ^*. As shown in Fig.3.3, the structure of an eddy convected in a turbulent boundary-layer is corrupted after traveling a distance of approximately 6 vortical wavelengths.

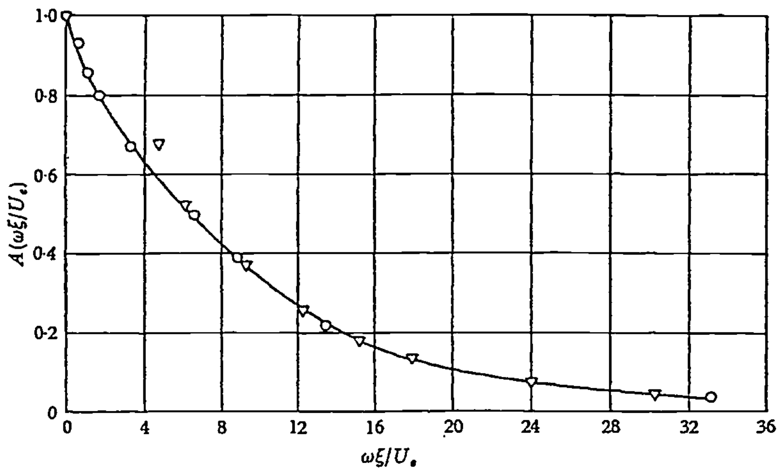

FIGURE 3.3: Amplitude of the longitudinal cross-spectral density in a boundary-layer. $\triangle$ $\omega\delta^*/U_\infty = 5.00$, o $\omega\delta^*/U_\infty = 0.68$ (after Corcos [99], figure 6).

[10]The wavelength of a vortical disturbance is a measure of the eddy size.

The same analysis for the transversal correlation yields

$$\Gamma(0,\eta,\omega) = \Phi(\omega)\, B\left(\frac{\omega\,\eta}{U_c}\right) \tag{3.10}$$

where the quantity $\omega\,\eta/U_c$ plays the role of transversal similarity variable, as shown by the measurements made by Willmarth & Woldridge [106] and Bakewell *et al.* [116]. Concluding, the wall pressure cross-spectral density takes the Corcos' similarity form

$$\Gamma(\xi,\eta,\omega) = \Phi(\omega)\, A\left(\frac{\omega\,\xi}{U_c}\right) B\left(\frac{\omega\,\eta}{U_c}\right) \exp\left(\mathrm{i}\,\frac{\omega\,\xi}{U_c}\right) \tag{3.11}$$

The convection velocity U_c, as measured by Willmarth & Woldridge [106], is a decreasing function of $\omega\,\delta^*/U_c$ and an increasing function of ξ/δ^* (see Fig.3.4). It should be defined as the velocity of the reference frame in which the rate of decay of the pressure correlation is minimum. Equivalently, its value is given by the slope, in a (ξ,τ)-plane, of the locus of points of the longitudinal correlation contours $\mathcal{R}(\xi,0,\tau)$ which have the greatest value of τ (see Fig.3.5).

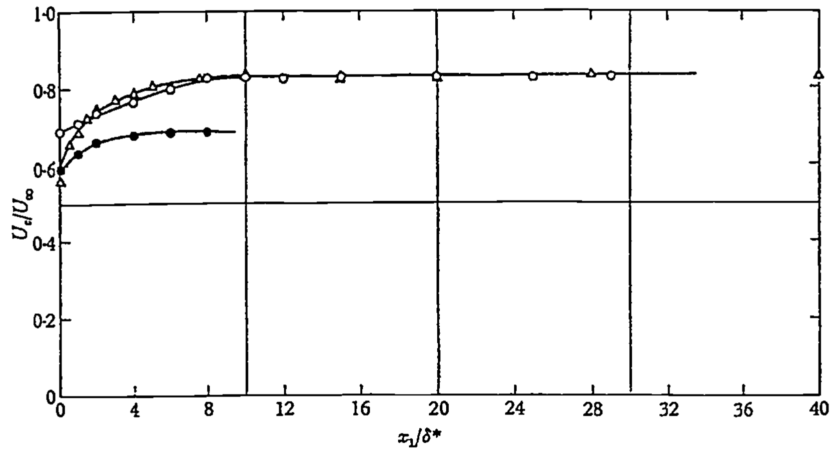

FIGURE 3.4: Local eddy convection velocity for various frequency bands. o, 300 Hz $< f <$ 700 Hz, $0.41 < \omega\delta^*/U_\infty < 0.95$; •, 3000 Hz $< f <$ 5000 Hz, $4.1 < \omega\delta^*/U_\infty < 6.8$; Δ, 105 Hz $< f <$ 10000 Hz, $0.14 < \omega\delta^*/U_\infty < 13.6$ (after Willmarth & Woldridge [106], figure 8).

The similarity hypothesis leading to the space-time correlation

$$\mathcal{R}(\xi,0,\tau) = \frac{1}{\pi}\int_0^\infty \Phi(\omega)\, A\left(\frac{\omega\,\xi}{U_c}\right) \cos\left(\omega\,\tau - \frac{\omega\,\xi}{U_c}\right)\, \mathrm{d}\omega \tag{3.12}$$

can be compared with the Taylor's frozen convection hypothesis, which says

$$p(x,z,t) = p(x - U_c\,t, z, 0) \tag{3.13}$$

and

$$\mathcal{R}_T(0,0,\tau) = \overline{p(x,z,t)\; p(x,z,t+\tau)} = \mathcal{R}_T(-U_c\tau, 0, 0) \tag{3.14}$$

From equation (3.12) it follows that

$$\mathcal{R}(0,0,\tau) = \frac{1}{\pi}\int_0^\infty \Phi(\omega)\cos(\omega\,\tau)\, \mathrm{d}\omega \tag{3.15}$$

$$\mathcal{R}(\xi,0,0) = \frac{1}{\pi}\int_0^\infty \Phi(\omega)\, A\left(\frac{\omega\,\xi}{U_c}\right) \cos\left(\frac{\omega\,\xi}{U_c}\right)\, \mathrm{d}\omega \tag{3.16}$$

and

$$\mathcal{R}\left(-U_c\tau,0,0\right)=\frac{1}{\pi}\int_0^\infty \Phi(\omega)\,A(-\omega\,\tau)\cos(\omega\,\tau)\;\mathrm{d}\omega \tag{3.17}$$

Therefore, the frozen convection hypothesis (3.14) is equivalent to suppose that no damping effect occurs, that is $A(-\omega\,\tau)=1$ in equation (3.17). Numerically, the difference between $\mathcal{R}\left(0,0,\tau\right)$ and $\mathcal{R}\left(-U_c\tau,0,0\right)$ is very small because the damping function A is close to unity at combined values of ξ and ω for which both $\mathcal{R}\left(\xi,0,0\right)$ and $\Phi\left(\omega\right)$ are not negligible.

The departure from Taylor's hypothesis was attributed by Corcos to the dispersive effect of the mean velocity gradient on the pressure disturbances convected in the boundary-layer. Such a mechanism can be described by means of a simple model based on a Poisson equation for the fluctuating pressure.

Consider an incompressible, statistically stationary turbulent flow, which satisfies the continuity equation

$$\nabla\cdot\mathbf{v}=0 \tag{3.18}$$

and the linear momentum equation

$$\frac{\partial\mathbf{v}}{\partial t}+\mathbf{v}\cdot\nabla\mathbf{v}+\frac{1}{\rho_0}\nabla p=\nu_0\nabla^2\mathbf{v} \tag{3.19}$$

Taking the divergence of equation (3.19) yields

$$\frac{\partial^2 p}{\partial x_i^2}=-\rho_0\frac{\partial^2\left(v_iv_j\right)}{\partial x_i\partial x_j} \tag{3.20}$$

Then, by subtraction of the averaged part, the following Poisson equation for the fluctuating pressure can be obtained

$$\frac{\partial^2 p'}{\partial x_i^2}=-2\rho_0\frac{\partial U_i}{\partial x_j}\frac{\partial v_j'}{\partial x_i}-\rho_0\frac{\partial^2}{\partial x_i\partial x_j}\left(v_i'v_j'-\overline{v_iv_j}\right) \tag{3.21}$$

where the averaged quantities are defined as

$$\mathbf{U}\left(\mathbf{x}\right)=\lim_{T\to\infty}\frac{1}{T}\int_{t_0}^{t_0+T}\mathbf{v}\left(\mathbf{x},t\right)\;\mathrm{d}t \tag{3.22}$$

A formal solution of equation (3.21) can be found by letting its right-hand side be a given scalar function $\mathcal{X}\left(\mathbf{x},t\right)$ and by setting the appropriate boundary conditions for p'. At the outer limit of the boundary-layer the fluctuating pressure can be assumed to vanish, whereas on the rigid planar surface the pressure can be supposed to have a zero normal derivative. The zero normal derivative condition is rigorous only for a steady boundary-layer. However, as shown by Lilley & Hodgson [94] by comparing the inertial term $\rho_0\,v_j\partial v_i/\partial x_j$ to the root-mean-square of the normal derivative of p', in the absence of a mean pressure gradient the zero normal derivative approximation affects the solution of equation (3.19) only negligibly. Hence, the formal solution of equation (3.21) with the auxiliary conditions

$$\left(p'\right)_{x_2\to\infty}=0 \tag{3.23}$$

$$\left(\partial p'/\partial x_2\right)_{x_2=0}=0 \tag{3.24}$$

is

$$p'\left(\mathbf{x},t\right)_{x_2=0}=\frac{1}{2\pi}\int_{y_2\geq 0}\frac{\mathcal{X}\left(\mathbf{y},t\right)}{\left|\mathbf{x}-\mathbf{y}\right|}\,\mathrm{d}\sigma(\mathbf{y}) \tag{3.25}$$

The two-point wall pressure correlation at a longitudinal distance ξ is

$$\mathcal{R}\left(\xi,0,\tau\right)=\frac{1}{4\pi^2}\int_{y_2\geq 0}\int_{y_2'\geq 0}\frac{\overline{\mathcal{X}(\mathbf{y},t)\,\mathcal{X}(\mathbf{y}',t+\tau)}}{\left|\mathbf{y}\right|\left|\mathbf{y}'-\hat{\mathbf{i}}\,\xi\right|}\,\mathrm{d}\sigma(\mathbf{y})\;\mathrm{d}\sigma\left(\mathbf{y}'\right) \tag{3.26}$$

where $\hat{\mathbf{i}}$ is the unit vector in the downstream direction. The time average in equation (3.26) can be written as

$$\begin{aligned}\overline{\mathcal{X}(\mathbf{y},t)\,\mathcal{X}(\mathbf{y}',t+\tau)} &= \lim_{T\to\infty}\frac{1}{T}\int_{t_0}^{t_0+T}\mathcal{X}(\mathbf{y},t)\,\mathcal{X}(\mathbf{y}',t+\tau)\;\mathrm{d}t\\ &\simeq \lim_{T\to\infty}\frac{1}{T}\int_{t_0}^{t_0+T}\mathcal{X}(\mathbf{y},t)\,\mathcal{X}\Big(\mathbf{y}+\mathbf{q}-\hat{\mathbf{i}}\,U_c(y_2)\,\tau,t\Big)\;\mathrm{d}t \qquad (3.27)\end{aligned}$$

where $\mathbf{q}=\mathbf{y}'-\mathbf{y}$ and where use of the frozen convection approximation

$$\mathcal{X}\big(\mathbf{y}',t+\tau\big)\simeq\mathcal{X}\Big(\mathbf{y}'-\hat{\mathbf{i}}\,U_c(y_2)\,\tau,t\Big) \qquad (3.28)$$

has been made.

If the source distribution $\mathcal{X}\,(\mathbf{y},t)$ is supposed to be perfectly correlated in the reference frame translating at the speed $U_c\,(y_2)$, then the averaged term (3.27) has the following form

$$\overline{\mathcal{X}\,(\mathbf{y},t)\,\mathcal{X}\,(\mathbf{y}',t+\tau)}=\rho_0^2\,\overline{\mathcal{M}'^2}\,(y_2)\,\delta(q_1-U_c\tau)\,\delta(q_2)\,\delta(q_3)\,\lambda_1\lambda_2\lambda_3 \qquad (3.29)$$

where λ_i are three length scales of the source term and $\overline{\mathcal{M}'^2}\,(y_2)$ is the source intensity. By substituting expression (3.29) into equation (3.26) and by integrating with respect to $\mathbf{q}$, the longitudinal correlation function becomes

$$\mathcal{R}\,(\xi,0,\tau)=\frac{\rho_0^2\,\lambda_1\,\lambda_3}{4\pi^2}\int_{y_2\geq 0}\frac{\overline{\mathcal{M}'^2}\,\lambda_2}{|\mathbf{y}|\,|\mathbf{y}+\hat{\mathbf{i}}\,U_c\,\tau-\hat{\mathbf{i}}\,\xi|}\,\mathrm{d}\sigma\,(\mathbf{y}) \qquad (3.30)$$

This simple model for the wall pressure correlation shows the effect of a variation of the mean flow velocity on the convective coherence loss of the wall pressure field. The effective value of $|\mathbf{y}+\hat{\mathbf{i}}\,U_c\,\tau-\hat{\mathbf{i}}\,\xi|$, with U_c being an increasing function of y_2, is always greater than the value corresponding to an average value of the convective velocity. Therefore, the correlation decreases with increasing ξ more rapidly than what it should do according to a frozen convection model.

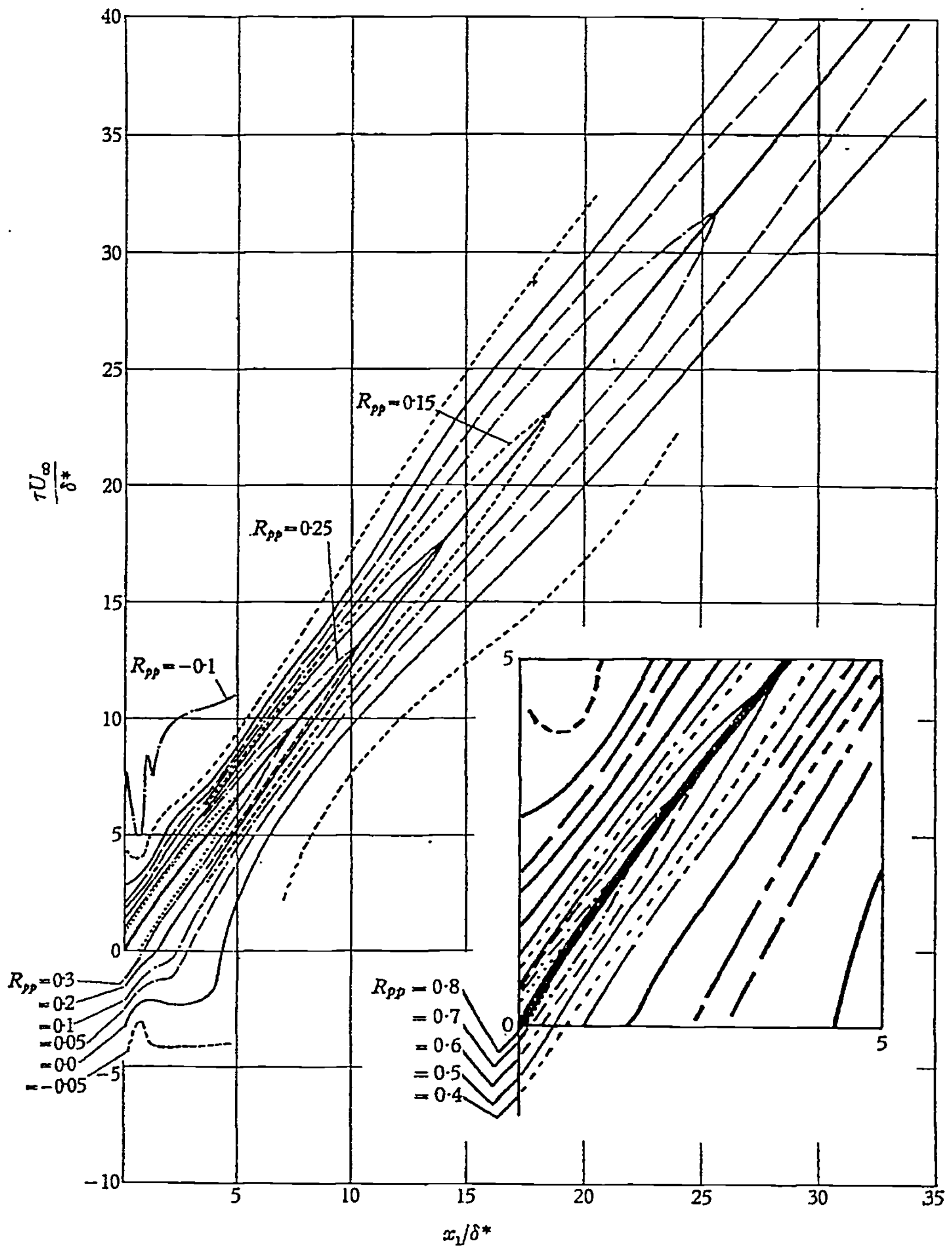

FIGURE 3.5: Contour map of the longitudinal space-time wall pressure correlation. The envelop heavy line represents the trajectory of a reference frame in which the rate of decay of the pressure correlation is minimum (after Willmarth & Woldridge [106], figure 7).

3.3.1 Wavenumber/Phase-Velocity Spectrum

The double Fourier transform of the wall pressure correlation with respect to space and time leads to the definition of the wavenumber-frequency spectrum, namely

$$E(k_1,0,\omega) = \iint_{-\infty}^{\infty} \mathcal{R}(\xi,0,\tau)\ \exp(-\mathrm{i}\ k_1\ \xi)\exp(\mathrm{i}\ \omega\,\tau)\ \mathrm{d}\xi\ \mathrm{d}\tau \tag{3.31}$$

Following Wills [107], a phase-velocity can be defined as $c = -\omega/k_1$ and a change of variable allows to translate the function $E\,(k_1,\omega)$ into the wavenumber/phase-velocity spectrum $M\,(k_1,c)$. This function is particularly appropriate for describing a convected turbulent flow, because it gives the distribution of energy over a range of phase-velocity for each wavenumber. The convection velocity $U_c(k_1)$ is thus defined as the velocity at which, for each value of k_1, the energy peaks satisfy the condition

$$\left(\frac{\partial}{\partial c}M(k_1,c)\right)_{c=U_c(k_1)} = 0 \tag{3.32}$$

Wills [107] observed that the convection velocity decreases as the wavenumber increases, varying from a maximum value of about $0.9\,U_\infty$ at $k_1\,\delta_{995} = 1.2$, to the asymptotic value of $0.55\,U_\infty$ at $k_1\,\delta_{995}$ higher than 20. This behaviour is a clear consequence of the boundary-layer mean velocity distribution. However, at values of $k_1\,\delta_{995}$ lower than 1.2, Wills observed an opposite behaviour which he attributed to a lack of the experimental accuracy at frequencies lower than 200 Hz[11].

From equation (3.31) it follows that

$$\mathcal{R}\,(\xi,\tau) = \frac{1}{4\,\pi^2}\iint_{-\infty}^{\infty} E(k_1,\omega)\ \exp(\mathrm{i}\,k_1\,\xi)\ \exp(-\mathrm{i}\,\omega\,\tau)\ \mathrm{d}k_1\,\mathrm{d}\omega \tag{3.33}$$

and by comparing to equation (3.4) the cross-spectral density takes the form

$$\Gamma(\xi,\omega) = \frac{1}{2\,\pi}\int_{-\infty}^{+\infty} E(k_1,\omega)\ \exp(\mathrm{i}\,k_1\,\xi)\ \mathrm{d}k_1 \tag{3.34}$$

Then, from equation (3.34) and from Corcos' similarity expression (3.8), the wavenumber-frequency spectrum takes the form

$$E(k_1,\omega) = 2\int_0^{\infty} \Phi\,(\omega)\,A\left(\frac{\omega\,\xi}{U_c}\right)\cos\left(\frac{\omega\,\xi}{U_c} - k_1\,\xi\right)\,\mathrm{d}\xi \tag{3.35}$$

and equivalently

$$E(k_1,\omega) = \frac{U_c\Phi\,(\omega)}{|\omega|}E_0\,(\mu+1) \tag{3.36}$$

where $\mu = k_1 U_c/\omega$, $\beta = \omega\,\xi/U_c$ and

$$E_0\,(\mu+1) = 2\int_0^{\infty} A\,(\beta)\cos\left[(\mu+1)\,\beta\right]\,\mathrm{d}\beta \tag{3.37}$$

Wills [107] proposed the following approximated form

$$E\,(k_1,\omega) = \Phi\,(\omega)\,F\left(\frac{\omega}{k_1 U_w}\right) \tag{3.38}$$

where U_w is a convection velocity depending on the frequency. Wills' experimental data showed that the function $F\,(\omega/k_1 U_w)$ fits the normal distribution

$$\exp\left\{-\left(\omega/k_1 U_w - 1\right)^2/0.04\right\} \tag{3.39}$$

with a standard deviation of $0.14\,U_\infty$.

[11]Because of the wall induction effect, the convection velocity of a very large turbulent eddy is indeed a decreasing function of the eddy size. This could be an interpretation of Wills' experimental results at low wavenumbers.

3.3.2 Discussion on the Linearizing Assumption

Kraichnan [108] was the first to investigate the nature of the source terms at the right-hand side of the Poisson equation (3.21). He separated the main contribution resulting from the interaction between the turbulent fluctuation normal to the wall and the mean shear $\partial U_1/\partial y_2$ from terms that are quadratic in the turbulent velocity fluctuation and that result from the turbulence self-interaction.

The mean velocity gradient reaches high values in the inner part of the boundary-layer. Thus the dominant term in equation (3.21) is $2\,(\partial U_1/\partial y_2)\,(\partial v_2'/\partial y_1)$. On the base of such linearizing assumption the wall pressure spatial-temporal correlation between two points $\mathbf{x}$ and $\mathbf{x}'$, with $\boldsymbol{\xi} = \mathbf{x}' - \mathbf{x}$, is given by

$$\mathcal{R}\left(\xi,\tau\right) = \frac{\rho_0^2}{\pi^2}\int_{y_2\geq 0}\int_{y_2'\geq 0} \frac{\partial U_1}{\partial y_2}\frac{\partial U_1}{\partial y_2'}\overline{\frac{\partial v_2'}{\partial y_1}\frac{\partial v_2'}{\partial y_1'}}\frac{\mathrm{d}\sigma\left(\mathbf{y}\right)\,\mathrm{d}\sigma\left(\mathbf{y}'\right)}{|\mathbf{y}-\mathbf{x}|\,|\mathbf{y}'-\mathbf{x}'|} \tag{3.40}$$

By measuring the mean velocity profile and the statistical properties of the fluctuating velocity normal to the wall, Kraichnan obtained from equation (3.40) a ratio between the wall pressure root-mean-square $\overline{(p'^2)}^{1/2}$ and the mean wall shear stress τ_w of about 6.

In a similar way Lilley & Hodgson [94] obtained a ratio of about 3, Hodgson [117] measured a ratio of 2.56 and Lilley [118] observed a variation between 1.7 and 3[12].

Starting from equation (3.21), Corcos [99] wrote the two-point wall pressure correlation in the form

$$\mathcal{R}\left(\xi,\tau\right) = \frac{\rho_0}{\pi}\int_{y_2'\geq 0}\frac{\partial U_1}{\partial y_2'}\frac{\mathcal{C}\left(\xi,\tau\right)}{|\mathbf{y}'-\mathbf{x}'|}\,\mathrm{d}\sigma\left(\mathbf{y}'\right) \tag{3.41}$$

where

$$\mathcal{C}\left(\xi,\tau\right) = \frac{\rho_0}{\pi}\int_{y_2\geq 0}\frac{\partial U_1}{\partial y_2}\overline{\frac{\partial v_2'}{\partial y_1}\frac{\partial v_2'}{\partial y_1'}}\frac{\mathrm{d}\sigma\left(\mathbf{y}\right)}{|\mathbf{y}-\mathbf{x}|} = \overline{p'\left(x,t\right)\frac{\partial v_2'}{\partial y_1'}\left(\mathbf{y}',t'\right)} \tag{3.42}$$

The correlation between the fluctuating velocity and the fluctuating wall pressure was measured by Willmarth & Woldridge [106]. By using their data, Corcos obtained a ratio $\overline{(p'^2)}^{1/2}/\tau_w \simeq 1.23$.

The discrepancy with the experimental values was related by Corcos to the fact that the linear source terms, although predominant, contributes only partially to the wall pressure fluctuations which depend on the neglected nonlinear source terms at a comparable order. Indeed, Willmarth [109] pointed out that the experimental data of pressure-velocity covariance used by Corcos did not satisfy Phillips' [53] criterion according to which, if the boundary-layer is homogeneous in planes parallel to the wall, the surface integral of the covariance over such planes must vanish.

3.4 Landahl's Wave-Guide Model

Landahl [89] investigated the possibility of relating the wall pressure statistical properties to the overall properties of a mean shear flow. His purpose was twofold:

- to individuate the conditions under which a turbulent field extracts energy from the mean flow;

- to describe the boundary-layer velocity field by means of wall pressure statistical measurements.

Landahl's wave-guide model is based on the solution of an Orr-Sommerfeld problem as a way to investigate the structure of a turbulent boundary-layer. Interestingly, the Orr-Sommerfeld equation is not applied to the solution of a stability problem for a laminar boundary-layer, but to describe the response of a boundary-layer to a turbulent excitation. Later on, the same strategy was used by Shubert & Corcos [88] who solved a boundary-layer approximation of a non-homogeneous Orr-Sommerfeld system by means of a convergent power series.

[12]These experimental values and others from several authors are collected in Tables (2) and (3) of Ref.[106].

All the theoretical works published before Landahl's analysis were based on the solution of a Poisson equation for the fluctuating pressure, with terms involving fluctuating stress and mean shear assumed as known source terms. Kraichnan [108] , Lilley & Hodgson [94] and Corcos [99] underlined the intrinsic difficulty of this approach in describing the source terms. Corcos, in particular, writing

$$\frac{\partial^2 p'}{\partial x_i^2} = -2\,\rho_0\,\frac{\partial U_1}{\partial x_2}\frac{\partial v_2'}{\partial x_1} \tag{3.43}$$

neglected all the nonlinear source terms in equation (3.21), but concluded that the mean shear interaction term, though significant, is not the primary contribution to the fluctuating pressure at low frequencies.

Landahl [89] argued that the stationary random character of a turbulent boundary-layer is a consequence of the superposition of damped waves, namely, modes of a linear eigenvalue problem where all the non-linear fluctuating terms behave like forcing terms.

In a turbulent incompressible and statistically shear flow, the fluctuating pressure satisfies the Poisson equation (3.21). In the shear layer assumption $U_1 = U\,(y)$ and $U_2 = U_3 = 0$ this takes the form

$$\nabla^2 p' = -2\rho_0 \frac{\partial U}{\partial y}\frac{\partial v'}{\partial x} + \rho_0 \nabla \cdot \mathbf{T} \tag{3.44}$$

where $\mathbf{x} = (x, y, z)$, $\mathbf{v}' = (u', v', w')$ and

$$T_i = -\frac{\partial}{\partial x_j}\left(v_j' v_i' - \overline{v_j' v_i'}\right) \tag{3.45}$$

Let us consider the momentum equation for the normal component of the fluctuating velocity

$$\frac{\partial v'}{\partial t} + U\frac{\partial v'}{\partial x} = -\frac{1}{\rho_0}\frac{\partial p'}{\partial y} + \nu \nabla^2 v' + T_y \tag{3.46}$$

From equation (3.21) and the y-derivative of equation (3.46) it follows that

$$\frac{\partial^2 p'}{\partial x^2} + \frac{\partial^2 p'}{\partial z^2} = \rho_0 \left\{ \left(\frac{\partial}{\partial t} + U\frac{\partial}{\partial x}\right)\frac{\partial v'}{\partial y} - U'\frac{\partial v'}{\partial x} - \nu\,\nabla^2\left(\frac{\partial v'}{\partial y}\right) + \frac{\partial T_x}{\partial x} + \frac{\partial T_z}{\partial z}\right\} \tag{3.47}$$

where $U' = \mathrm{d}U/\,\mathrm{d}y$. Furthermore, rearranging the Laplacian of equation (3.46) and the y-derivative of equation (3.21) yields

$$\left(\frac{\partial}{\partial t} + U\frac{\partial}{\partial x}\right)\nabla^2 v' - U''\frac{\partial v'}{\partial x} - \nu\nabla^4 v' = q \tag{3.48}$$

where $U'' = \mathrm{d}^2U/\,\mathrm{d}y^2$ and

$$q = \nabla^2 T_y - \frac{\partial}{\partial y}\left(\nabla \cdot \mathbf{T}\right) \tag{3.49}$$

If q is supposed to be known, equation (3.48) can be solved with the auxiliary conditions that v' and $\partial v'/\partial y$ vanish both on the wall and on the outer limit of the boundary-layer. Once v' has been determined, the fluctuating pressure p' can be calculated by solving equation (3.47). Finally, the remaining components u' and w' of the fluctuating velocity can be calculated by solving the momentum equation in the streamwise and spanwise direction, respectively.

The disturbance equation (3.48) is linear and its coefficients are function only of the distance y from the wall. A solution of equation (3.48) can be obtained in terms of separation of variables by using normal modes to reduce the disturbance equation to an ordinary differential equation. Thus, applying the generalized Fourier transform

$$\hat{v}\,(y, k_x, k_z, \omega) = \iiint_{-\infty}^{+\infty} \exp(-k_x\,x - k_z\,z + \omega\,t)\;v'(x, y, z, t)\;\mathrm{d}x\;\mathrm{d}z\;\mathrm{d}t \tag{3.50}$$

to equation (3.48) provides

$$
\begin{aligned}
&(U\,k_x-\omega)\,\nabla_+^2\hat{v}-U''\,k_x\,\hat{v}+\mathrm{i}\,\nu\,\nabla_+^4\hat{v}=-\mathrm{i}\,\hat{q}\\
&\hat{v}=\frac{\mathrm{d}\hat{v}}{\mathrm{d}y}=0 \qquad y=0\\
&\hat{v}=\frac{\mathrm{d}\hat{v}}{\mathrm{d}y}=0 \qquad y\to\infty
\end{aligned}
\tag{3.51}
$$

where $\nabla_+^2 = \mathrm{d}^2/\,\mathrm{d}y^2 - k^2$. Setting $\omega = k_x\,c$, $\hat{v} = -\mathrm{i}\,k\,\phi(y)$, and making lengths dimensionless by the boundary-layer thickness δ and velocities by the free-stream velocity U_∞, equation (3.51) takes the form of a non-homogeneous Orr-Sommerfeld equation, i.e.

$$
(U-c)\left(\phi''-k^2\phi\right)-U''\phi+\frac{\mathrm{i}}{k_x\,\mathrm{Re}}\left(\phi^{IV}-2\,k^2\phi''+k^4\,\phi\right)=\frac{\hat{q}}{k_x\,k}
\tag{3.52}
$$

where $k^2 = k_x^2 + k_z^2$ and Re denotes the Reynolds number based on the boundary-layer thickness and the free-stream velocity.

A formal solution of equation (3.52) can be obtained through an expansion in terms of eigenfunctions $\phi^{(n)}$ of the associated homogeneous problem. For a well-posed eigenvalue problem, there is an infinite set of discrete eigenvalues and a corresponding infinite discrete set of eigenfunctions. For boundary-layers, the eigenfunctions are called modes and form a basis for an arbitrary disturbance profile.

If $c^{(n)}$ denotes the nth eigenvalue of c for a given set of k_x, k_z and Re (real values), a generic solution of equation (3.52) is given by

$$
\begin{aligned}
&\phi=\sum_n \hat{A}^{(n)}\,\phi^{(n)} \qquad \text{with}\\
&\hat{A}^{(n)}=\frac{1}{k_x\,k\left(c-c^{(n)}\right)}\int_0^\infty \hat{q}\,\phi_+^{(n)}\,\mathrm{d}y
\end{aligned}
\tag{3.53}
$$

where $\phi_+^{(n)}$ are the corresponding eigenfunctions for the adjoint problem

$$
\begin{aligned}
&(U-c)\left(\phi_+''-k^2\phi_+\right)+2\,U'\phi_+'+\frac{\mathrm{i}}{k_x\,\mathrm{Re}}\left(\phi_+^{IV}-2\,k^2\phi_+''+k^4\,\phi_+\right)=0\\
&\phi_+=\phi_+'=0 \qquad y=0\\
&\phi_+=\phi_+'=0 \qquad y\to\infty
\end{aligned}
\tag{3.54}
$$

Disturbances can be classified with respect to their spatial amplification, temporal amplification, and both spatial and temporal amplification. Solving a spatial problem, ω is assumed to be real, while k_x and k_z are assumed to be complex. Their real parts represent the physical wavenumbers of the disturbances, while their imaginary parts represent the growth or decay rates in the streamwise and spanwise directions. Solving a temporal problem, k_x and k_z are assumed to be real, while ω is assumed to be complex. Finally, solving a both spatial and temporal problem, all the wave parameter are assumed to be complex.

Let $k_x = \alpha_R^{(n)}$ be the value of k_x for which $k_x\,c_R^{(n)} = \omega$. For a spatial stability problem, a dispersion relation $k_x = f(k_z, \omega, \mathrm{Re})$ provides the streamwise eigenvalues $\alpha^{(n)} = \alpha_R^{(n)} + \alpha_I^{(n)}$ when k_z, ω and Re are given. The denominator in equation (3.53) can be written as

$$
k_x\,k\left(c-c^{(n)}\right)=k\left\{\left(k_x-\alpha_R^{(n)}-\mathrm{i}\,\alpha_I^{(n)}\right)c_R^{(n)}+\left(\alpha_I^{(n)}-\alpha_R^{(n)}\right)c_I^{(n)}\right\}
\tag{3.55}
$$

By assuming that the variation of $c_I^{(n)}$ with k_x, for a fixed value of ω, is small, the variation of equation (3.55) is proportional to the term $k_x - \alpha_R^{(n)} - \mathrm{i}\,\alpha_I^{(n)}$. Hence, equation (3.53) has poles near the real axis of the form $(k_x - \alpha^{(n)})^{-1}$

The longitudinal cross-spectral density Γ is related to the wavenumber-frequency spectrum E by the Fourier transform

$$\Gamma(\xi,\omega) = \frac{1}{2\pi}\int_{-\infty}^{+\infty} \exp(-\mathrm{i}\, k_x\, \xi)\, E(k_x,\omega)\ \mathrm{d}k_x \tag{3.56}$$

where

$$E(k_x,\omega) = \frac{\overline{\hat{p}(k_x,\omega)\ \hat{p}(k'_x,\omega')}}{\delta(k_x - k'_x, \omega-\omega')} \tag{3.57}$$

Equation (3.47) shows a linear dependence between the fluctuating pressure and the fluctuating velocity. Thus, $\hat{p}$ has poles of the form $c^{(n)}(k_x-\alpha^{(n)})^{-1}$, and the cross-spectral density is given by

$$\Gamma(\xi,\omega) = \mathrm{i}\sum_n\sum_m \frac{\Phi^{(n,m)}(\omega)}{\alpha^{(n)}-\alpha^{*(m)}}\exp\left(\mathrm{i}\,\alpha^{(n)}\xi\right) \tag{3.58}$$

where $\Phi^{(n,m)}$ are function of both k_z and ω, which are related to the spectral functions $\hat{A}^{(n)}$ and $\hat{A}^{(m)}$ defined in (3.53). The main contribution to Γ results from the condition $m=n$, that is

$$\Gamma(\xi,\omega) = \sum_n \frac{\Phi^{(n,n)}(\omega)}{2\,\alpha_I^{(n)}}\exp\left(\mathrm{i}\,\alpha_R^{(n)}\xi - \alpha_I^{(n)}|\xi|\right) \tag{3.59}$$

Finally, accounting for the spanwise fluctuations and considering only the least attenuated mode, the cross-spectral density takes the form

$$\Gamma(\xi,\eta,\omega) = \frac{1}{2\pi}\int_{-\infty}^{+\infty}\frac{\Phi^{(0,0)}(\omega)}{2\,\alpha_I^{(0)}}\exp\left(\mathrm{i}\,\alpha_R^{(0)}\xi - \alpha_I^{(0)}|\xi| + \mathrm{i}\,k_z\eta\right)\ \mathrm{d}k_z \tag{3.60}$$

A numerical solution of the homogeneous form of equation (3.52), for given values of $\omega = k_x\, c$, k_z and Re, provides the eigenvalue $\alpha^{(0)}$. However, respect to a classic stability problem for a laminar boundary-layer, difficulties arise because of:

- the higher value of U'' near the wall of a turbulent boundary-layer;
- the larger variation range of the involved parameters. Typical values are $|k_x| = 10 \div 100$, $|k_z| = 0 \div 1000$ and $\mathrm{Re} = 5\times10^4 \div 5\times10^5$.

Landahl assumed a mean velocity profile based on Reichardt's [119] measurements in the wall region and in the logarithmic region, together with Coles' [120] universal *law of the wake*, i.e.

$$\begin{aligned}\frac{U}{u_\tau} &= k^{-1}\ln\left(1+k\,y^+\right) + \gamma\left\{1-\exp\left(-\frac{y^+}{\delta_v}\right) - \frac{y^+}{\delta_v}\exp\left(-0.33\,y^+\right)\right\}\\ &+ 1.38\left\{1+\sin\left[\left(2y^+-1\right)\frac{\pi}{2}\right]\right\}\end{aligned} \tag{3.61}$$

where u_τ is the friction velocity and $y^+ = y\,u_\tau/\nu$. Adopting the constant values $k=0.4$, $\gamma=7.4$ and $\delta_v = 11.0$, Landahl obtained the important result that the modes in a turbulent boundary-layer are always stable.

In equation (3.60) the main variation of the integrand with k_z is due to $\Phi^{(0,0)}$. Thus, the cross-spectral density can be approximated as

$$\begin{aligned}\Gamma(\xi,\eta,\omega) &\simeq \phi(\omega)\ B(\eta,\omega)\exp\left(\mathrm{i}\,\alpha_R^{(0)}\xi - \alpha_I^{(0)}|\xi|\right) \quad \text{with}\\ B(\eta,\omega) &= \frac{1}{2\pi}\int_{-\infty}^{+\infty}\hat{B}(k_z)\exp(\mathrm{i}\,k_z\eta)\ \mathrm{d}k_z \quad \text{and}\\ \hat{B}(k_z) &= \frac{\Phi^{(0,0)}}{2\,\alpha_I^{(0)}\phi(\omega)}\end{aligned} \tag{3.62}$$

If the Fourier transform $\hat{B}$ is supposed to depend only on the wave angle, namely on $k_z/\alpha_R^{(0)}$, then the spanwise decay function B is a function of $\eta\,\alpha_R^{(0)}$ and ω. Then, defining a convection velocity as $U_c = \omega/\alpha_R^{(0)}$, the cross-spectral density takes the form

$$\begin{aligned} \Gamma(\xi,\eta,\omega) &= \phi(\omega)\exp\left(\mathrm{i}\frac{\omega\,\xi}{U_c}\right) A\left(\frac{\omega\,\xi}{U_c}\right) B\left(\frac{\omega\,\eta}{U_c}\right) \quad \text{with} \\ A\left(\frac{\omega\,\xi}{U_c}\right) &= \exp\left(-\frac{\alpha_I^{(0)}}{\alpha_R^{(0)}}\frac{\omega\,|\xi|}{U_c}\right) \end{aligned} \tag{3.63}$$

This result is in agreement with Corcos' similarity hypothesis. This is therefore a consequence of the fact that the wave-propagation constants $\alpha_R^{(0)}$ and $\alpha_I^{(0)}$ are not affected by the wave orientation angle.

Landahl's [89] numerical results show that the convection velocity U_c slightly decreases when the dimensionless frequency $\omega\,\delta^*/U_\infty$ increases. The predicted values at Re= 5×10^3 are in good agreement with Willmarth & Woldridge's [106] measurements at Re$\simeq 4\times10^5$. Furthermore, the numerical prediction provides a decreasing behaviour of the convection velocity with the Reynolds number. Thus, by extrapolating the numerical results up to Re= 4×10^5, Landahl obtained a convection velocity of about $0.5\,U_\infty$, in spite of the experimental value of about $0.7\,U_\infty$.

Wills [107] measured a convection velocity that, at high wavenumbers, falls below that measured by Willmarth & Woldridge [106]. As previously discussed, this difference is a consequence of the fact that the frequency filtering used by Willmarth & Woldridge provides a convection velocity weighted towards that of the largest eddies. These structures extend over the whole width of the boundary-layer and are convected at higher velocities. Furthermore, comparing Wills' measurements to Landahl's numerical results shows a good agreement at high wavenumbers. Conversely, at low wavenumbers, the measured convection velocity is higher than the predicted one. This result is consistent with the fact that the large-scale fluctuating motion cannot be considered as a perturbation of the mean motion. Indeed, a fluctuating velocity field behaves like an eddy viscosity that reduces the effective Reynolds number. Thus, as confirmed by the comparison between Willmarth & Woldridge's measurements and Landahl's numerical results, a linear model should incorporate an additional viscosity in order to recover the experimental behaviour.

A second result of Landahl's wave guide model is about the exponential decay factor $\alpha_I^{(0)}/\alpha_R^{(0)}$ and the decay function $A(\omega\,\xi/U_c)$ in equation (3.63). The decay factor increases as the dimensionless frequency $\omega\,\delta^*/U_\infty$ increases. On the contrary, the decay factor is not hardly affected by the Reynolds number. The decay function is in excellent agreement with the experimental data. It shows that each vortical component loses its identity after traveling a distance of about 6 times its size. This result is in agreement with Millikan's [121] interpretation of the logarithmic portion of the mean velocity profile as the region of the boundary-layer where the evolution of an eddy scales only with its size.

Finally, Landahl's eigenvalue calculations show that all the waves are stable when propagating in a shear flow that is statistically homogeneous in the streamwise direction. Equivalently, the stationary random character of a turbulent boundary-layer is a consequence of the superposition of all damped waves.

3.5 Shubert & Corcos' Linear Model

The Navier-Stokes equations for an incompressible boundary-layer with separated fluctuating and mean components have the form

$$\frac{\partial v_i'}{\partial t} + U_j\frac{\partial v_i'}{\partial x_j} + v_j'\frac{\partial U_i}{\partial x_j} = -\frac{1}{\rho_0}\frac{\partial p}{\partial x_i} + \nu\frac{\partial^2 v_i'}{\partial x_j^2} + T_i \tag{3.64}$$

where

$$T_i = \frac{\partial}{\partial x_j}\left(\overline{v_i' v_j'} - v_i' v_j'\right) \tag{3.65}$$

A boundary-layer linearized form of equations (3.64) can be obtained by introducing the shear-layer assumption $\mathbf{U} = (U(y), 0, 0)$, neglecting the terms T_i, supposing the invariance of p with y and neglecting the viscous diffusion along the boundary. It thus results that

$$\frac{\partial u}{\partial t} + U\frac{\partial u}{\partial x} + v\,U' = -\frac{1}{\rho_0}\frac{\partial p}{\partial x} + \nu\frac{\partial^2 u}{\partial y^2} \tag{3.66}$$

$$\frac{\partial w}{\partial t} + U\frac{\partial w}{\partial x} = -\frac{1}{\rho_0}\frac{\partial p}{\partial z} + \nu\frac{\partial^2 w}{\partial y^2} \tag{3.67}$$

$$\frac{\partial u}{\partial x} + \frac{\partial v}{\partial y} + \frac{\partial w}{\partial z} = 0 \tag{3.68}$$

where $U' = \mathrm{d}U/\,\mathrm{d}y$ $v_i' = (u, v, w)$ and $x_i = (x, y, z)$.

If the generalized Fourier transform (3.50) is applied to equations (3.66), (3.67) and (3.68), the following system of complex ordinary partial differential equations can be obtained

$$\frac{\mathrm{d}^2\tilde{u}}{\mathrm{d}y^2} - \frac{\mathrm{i}}{\nu}(\omega - U\,k_x)\,\tilde{u} - \frac{1}{\nu}U'\,\tilde{v} = -\frac{1}{\nu}k_x\,\tilde{p} \tag{3.69}$$

$$\frac{\mathrm{d}^2\tilde{w}}{\mathrm{d}y^2} - \frac{\mathrm{i}}{\nu}(\omega - U\,k_x)\,\tilde{w} = -\frac{1}{\nu}k_z\,\tilde{p} \tag{3.70}$$

$$\mathrm{i}\,k_x\,\tilde{u} + \mathrm{i}\,k_z\,\tilde{w} - \frac{\mathrm{d}\tilde{v}}{\mathrm{d}y} = 0 \tag{3.71}$$

These equations are boundary-layer approximations of a non-homogeneous Orr-Sommerfeld equations, with pressure fluctuations acting as driving terms.

By eliminating $\tilde{p}$ and setting $U_c = \omega/k_x$, equations (3.69), (3.70) and (3.71) can be rearranged in the following homogeneous system

$$\frac{\mathrm{d}^4\tilde{v}}{\mathrm{d}y^4} + \frac{\mathrm{i}\,k_x}{\nu}(U - U_c)\frac{\mathrm{d}^2\tilde{v}}{\mathrm{d}y^2} - \frac{\mathrm{i}\,k_x}{\nu}U''\,\tilde{v} = 0 \tag{3.72}$$

$$\frac{\mathrm{d}^3\tilde{w}}{\mathrm{d}y^3} + \frac{\mathrm{i}\,k_x}{\nu}(U - U_c)\frac{\mathrm{d}\tilde{w}}{\mathrm{d}y} + \frac{\mathrm{i}\,k_x}{\nu}U'\,\tilde{w} = 0 \tag{3.73}$$

$$\mathrm{i}\,k_x\,\tilde{u} + \mathrm{i}\,k_z\,\tilde{w} - \frac{\mathrm{d}\tilde{v}}{\mathrm{d}y} = 0 \tag{3.74}$$

with the following boundary conditions on the wall ($y = 0$)

$$\tilde{v} = 0, \quad \frac{\mathrm{d}\tilde{v}}{\mathrm{d}y} = 0, \quad \frac{\mathrm{d}^3\tilde{v}}{\mathrm{d}y^3} = \frac{k^2}{\nu}\tilde{p} \tag{3.75}$$

$$\tilde{w} = 0, \quad \frac{\mathrm{d}^2\tilde{w}}{\mathrm{d}y^2} = -\mathrm{i}\frac{k_z}{\nu}\tilde{p} \tag{3.76}$$

The two remaining additional conditions for $\tilde{w}$ can be found by requiring that the effects of the fluid viscosity are negligible on the outer boundary-layer ($y \to \infty$). Thus, the viscid solution must tend to the inviscid solution as the distance from the wall increases.

Let the *critical point* denote the value y_c at which the mean velocity is equal to the convection velocity U_c. The following expression can be adopted for the mean velocity profile

$$\frac{U}{u_\tau\,\beta} = 1 - \exp\left(\frac{-y^+}{\beta}\right) \quad \text{with } \beta = 16 \tag{3.77}$$

In the inner region $y^+ \leq 50$, equation (3.77) is a good approximation of the *law of the wall* as results from Coles' [120] measurements.

The stability theory shows that viscosity plays a predominant role in the wall region as well as in the neighborhood of the critical point. On the other hand, experimental results show that a typical turbulent component of given frequency travels downstream at a convection velocity such that $y_c^+ > 100$. Thus, the outer boundary conditions would have to be imposed at distances $y^+ > y_c^+$, that is, in a region where the linear approximation should be quite inappropriate.

Setting $Y = \exp(-y/\beta)$, $\gamma = 1 - U_c/\beta U_\tau$ and $\alpha = -k_x \nu \beta^2/U_\tau$, the following solutions of equations (3.72), (3.73) and (3.74) can be obtained

- for $\tilde{v}$

$$(a) \quad \gamma\left(1 + \frac{\mathrm{i}}{\alpha\gamma}\right) - Y \tag{3.78}$$

$$(b) \quad Y \ln Y - \gamma\left(1 + \frac{\mathrm{i}}{\alpha\gamma}\right)(1 + \ln Y) + \sum_{n=1}^{\infty} a_n Y^n \tag{3.79}$$

$$(c) \quad b_n \sum_{n=0}^{\infty} Y^{(\eta+n)} \tag{3.80}$$

$$(d) \quad b_n \sum_{n=0}^{\infty} Y^{(-\eta+n)} \tag{3.81}$$

where $\eta = (\mathrm{i}\,\alpha\gamma)^{1/2}$ is chosen to have a positive real part, and

$$\begin{cases} a_1 = \frac{\alpha\gamma+3\mathrm{i}}{\alpha\gamma+\mathrm{i}} \\ a_2 = \frac{\gamma}{2\gamma(\alpha\gamma+4\mathrm{i})} \\ a_n = a_{n-1}\frac{n-2}{n}\frac{\alpha\gamma}{\gamma(\alpha\gamma+n^2\mathrm{i})} \quad \text{for} \quad n \geq 3 \end{cases} \qquad \begin{cases} b_0 = 1 \\ b_n = b_{n-1}\frac{\mathrm{i}\,\alpha[2-(\eta+n)]}{(\eta+n)[(\eta+n)^2-\mathrm{i}\,\alpha\gamma]} \end{cases} \quad \text{for} \quad n \geq 2 \tag{3.82}$$

- for $\tilde{w}$

$$(a) \quad c_n \sum_{n=0}^{\infty} Y^n \tag{3.83}$$

$$(b) \quad d_n \sum_{n=0}^{\infty} Y^{(\eta+n)} \tag{3.84}$$

$$(c) \quad d_n \sum_{n=0}^{\infty} Y^{(-\eta+n)} \tag{3.85}$$

where

$$\begin{cases} c_0 = 1 \\ c_n = c_{n-1}\frac{\gamma}{1+\mathrm{i}\,n^2/\alpha\gamma} \quad \text{for} \quad n \geq 2 \end{cases} \qquad \begin{cases} d_0 = 1 \\ d_n = d_{n-1}\frac{-\mathrm{i}\,\alpha}{(\eta+n)^2-\mathrm{i}\,\alpha\gamma} \quad \text{for} \quad n \geq 2 \end{cases} \tag{3.86}$$

All these solutions have been obtained with the condition $\gamma \neq 0$. Solutions (d) for $\tilde{v}$ and (c) for $\tilde{w}$ diverge as $y \to \infty$ and they are therefore discarded. Conversely, all the other solutions can be combined in order to satisfy the boundary condition on the wall. Solutions (c) for $\tilde{v}$ and (b) for $\tilde{w}$ decay as y increases and can be matched with the outer solutions by looking for the conditions under which the solutions (a) and (b) for $\tilde{v}$ and (a) for $\tilde{w}$ tend to their inviscid counterparts.

The inviscid forms of equations (3.69), (3.70) and (3.71) are

$$\tilde{w} = -\frac{k_z}{k_x}\frac{\tilde{p}}{\rho}\frac{1}{U - U_c} \tag{3.87}$$

$$-\mathrm{i}\, k_x \,(U - U_c)\, \tilde{u} = \frac{\mathrm{d}U}{\mathrm{d}y}\tilde{v} + \mathrm{i}\,\frac{k_x}{\rho}\tilde{p} \tag{3.88}$$

$$\mathrm{i}\, k_x \tilde{u} + \mathrm{i}\, k_x \tilde{w} + \frac{\mathrm{d}\tilde{v}}{\mathrm{d}y} = 0 \tag{3.89}$$

from which the following inviscid equation for $\tilde{v}$ can be obtained

$$(U - U_c)\,\frac{\mathrm{d}^2\tilde{v}}{\mathrm{d}y^2} - \tilde{v}\, U'' = 0 \tag{3.90}$$

with boundary conditions on the wall $\tilde{v} = \frac{\mathrm{d}\tilde{v}}{\mathrm{d}y} = 0$. Solutions of equation (3.90) have the following form

$$(a') \quad \gamma - Y \tag{3.91}$$

$$(b') \quad -\gamma + (Y - \beta)\, \ln Y - (Y - \beta)\, \log\left\{\pm\gamma\left(1 - \frac{Y}{\gamma}\right)\right\} \tag{3.92}$$

The viscous solutions (a) and (b) for $\tilde{v}$ tend to the inviscid solutions (a') and (b') if the following two conditions are satisfied

$$\begin{aligned} &\alpha\gamma \to \infty \\ &Y < |\gamma| \end{aligned} \tag{3.93}$$

For a disturbance the viscous length ν/U_τ is proportional to ν. Therefore, the former condition is consistent with the condition $\nu \to 0$. The latter condition is necessary for the expansion

$$\log\left(1 - \frac{Y}{\gamma}\right) = -\sum_{n=1}^{\infty}\frac{Y^n}{n\gamma^n} \tag{3.94}$$

and is equivalent to the conditions

$$\frac{U}{\beta\, U_\tau}\begin{cases} > \frac{U_c}{\beta U_\tau} \\ > 2 - \frac{U_c}{\beta U_\tau}\end{cases} \text{if } \frac{U_c}{\beta\, U_\tau}\begin{cases} < 1 \\ > 1\end{cases} \tag{3.95}$$

or equivalently

$$U\begin{cases} > U_c \\ < \beta\, U_\tau\end{cases} \text{if } U_c\begin{cases} < \beta\, U_\tau \\ > \beta\, U_\tau\end{cases} \tag{3.96}$$

where $\beta\, U_\tau$ is the limit value for the inner representation. Since $U_\infty/U_\tau \simeq 30$, it results that $\beta\, U_\tau \simeq 0.53\, U_\infty$.

Equations (3.72) and (3.73) do not depend on the value of k_z, which affects the solution only through the boundary conditions. As a consequence, if subscripts (1) and (2) are used to denote two solutions for two values of k_z, then equations (3.75), (3.76) and (3.74) lead respectively to

$$\frac{\tilde{v}_2}{\tilde{v}_1} = \frac{k_x^2 + k_{z\,2}^2}{k_x^2 + k_{z\,1}^2} \tag{3.97}$$

$$\frac{\tilde{w}_2}{\tilde{w}_1} = \frac{k_{z\,2}}{k_{z\,1}} \tag{3.98}$$

$$\tilde{u}_2 = \tilde{u}_1\,\frac{k_x^2 + k_{z\,2}^2}{k_x^2 + k_{z\,1}^2} + \tilde{w}_1\,\frac{k_x}{k_{z\,1}}\,\frac{k_{z\,1}^2 - k_{z\,2}^2}{k_x^2 + k_{z\,1}^2} \tag{3.99}$$

If the solution (1) is calculated with $k_{z\,1} = k_x$, then setting $k_{z\,2} = k_z$ yields

$$\frac{\tilde{v}_2}{\tilde{v}_1} = \frac{1}{2}\left[1 + \left(\frac{k_z}{k_x}\right)^2\right] \tag{3.100}$$

$$\frac{\tilde{w}_2}{\tilde{w}_1} = \frac{k_z}{k_x} \tag{3.101}$$

$$\tilde{u}_2 = \tilde{u}_1\,\frac{1}{2}\left[1 + \left(\frac{k_z}{k_x}\right)^2\right] + \tilde{w}_1\,\frac{1}{2}\left[1 - \left(\frac{k_z}{k_x}\right)^2\right] \tag{3.102}$$

The following limit cases can be distinguished

1) $k_z/k_x \ll 1$

$$\frac{\tilde{v}_2}{\tilde{v}_1} \simeq \frac{1}{2} \tag{3.103}$$

$$\frac{\tilde{w}_2}{\tilde{w}_1} \simeq 0 \tag{3.104}$$

$$\tilde{u}_2 = \frac{\tilde{u}_1 + \tilde{w}_1}{2} \tag{3.105}$$

2) $k_z/k_x \gg 1$

$$\frac{\tilde{v}_2}{\tilde{v}_1} \simeq \frac{1}{2}\left(\frac{k_z}{k_x}\right)^2 \tag{3.106}$$

$$\frac{\tilde{w}_2}{\tilde{w}_1} = \frac{k_z}{k_x} \tag{3.107}$$

$$\tilde{u}_2 = \frac{1}{2}\left(\frac{k_z}{k_x}\right)^2 (\tilde{u}_1 - \tilde{w}_1) \tag{3.108}$$

It can be observed that $\tilde{w}_2/\tilde{w}_1$ vanishes in both these limits.

Shubert & Corcos [88] obtained solutions of equations (3.72), (3.73) and (3.74) with a circular frequency ω such that $100\,\delta^\star < y_c < 1000\,\delta^\star$, and with the following values of k_x

$$k_x\,\delta^\star = k_z\,\delta^\star = 0.1;\ 1.0;\ 4.0;\ 10.0 \tag{3.109}$$

where $\delta^\star$ denotes the boundary-layer displacement thickness. The dimensionless frequency is related to the phase velocity and to the dimensionless wavenumber by the following relationship

$$\frac{\omega\,\delta^\star}{U_\infty} = \frac{U_c}{U_\tau}\,\frac{U_\tau}{U_\infty}\,k_x\,\delta^\star \tag{3.110}$$

where U_τ/U_∞ depends on the Reynolds number, $k_x\,\delta^\star$ is an arbitrary value and U_c/U_τ can be supposed to depend on the critical point $y_c^\star = y_c/\delta^\star$, as well as the mean velocity profile. In the examined range of $y_c^\star$ the mean velocity profile can be supposed to have the following logarithmic variation

$$\frac{U_c}{U_\tau} = \frac{1}{k}\ln y_c^\star + c \tag{3.111}$$

with $k \simeq 0.4$ and $c \simeq 5$. Then, for a boundary-layer with Reynolds number $R_{\delta^\star} = 50000$ ($U_\infty/U_\tau \simeq 30$), it results that $16 < U_c/U_\tau < 23$ and $0.53 < U_c/U_\infty < 0.77$ [13].

[13]It should be observed that the condition (3.96) provides $U < 0.53\,U_\infty$.

Experimental results show that the root-mean-square of the velocity fluctuations arises at some distance from the wall. According to Klebanoff's [122] measurements, u peaks at $y^\star \simeq 25$, w at $y^\star \simeq 60$ and v at $y^\star \simeq 600$.

Numerical results obtained from equations (3.72), (3.73) and (3.74) with $0.1 \leq k_x\,\delta^\star = k_z\,\delta^\star \leq 4.0$ and $y_c^\star > 50$ exhibit the following features:

1. the amplitude of the solution exhibits no tendency to peak;

2. there is no trace of a viscous sublayer;

3. the Reynolds stress coefficient

$$C_R = -\frac{<\tilde{u}\,\tilde{v}>}{|\tilde{u}|\,|\tilde{v}|} \tag{3.112}$$

is smaller than it should be required to support the assumed mean velocity profile. In fact, as it results from equation (3.88), $\tilde{u}$ and $\tilde{v}$ are about $\pi/2$ out of phase, and the fluctuating field cannot extract energy from the mean flow.

Numerical results for $k_x\,\delta^\star = k_z\,\delta^\star = 10$ and $y_c^\star = 1000$ show the existence of a viscous sublayer, but the predicted Reynolds stresses are still quite small.

As it follows from equations (3.103), (3.105) and (3.104), the behaviour predicted for the case $k_x\,\delta^\star = k_z\,\delta^\star$ is quite similar for all those turbulent structures for which $k_z/k_x \leq 1$. Thus, a linearized model cannot accurately describe the fluctuating field of a spanwise elongated turbulent structure.

Experimental results show that the spatial structure of u and v in the wall region is very elongated in the streamwise direction. According to equation (3.108), when $k_z \gg k_x$, the fluctuation $\tilde{u}$ is proportional to the difference $\tilde{u}_1 - \tilde{v}_1$, where the subscript 1 denotes the solution calculated for $k_z = k_x$. The predicted value of $\tilde{u}_1 - \tilde{v}_1$ peaks in the range $25 < y^\star < 50$, confirming the experimental behaviour of $\tilde{u}$. The peak moves towards the wall as the values of $k_x\,\delta^\star$ and $y_c^\star$ increase. The Reynolds stress coefficient C_R decreases as $k_x\,\delta^\star$ increases. Conversely, it decreases at fixed value of $k_x\,\delta^\star$ as $y_c^\star$ increases.

When $k_z \gg k_x$, equations (3.69), (3.70) and (3.71) reduce to the following equations

$$\frac{\mathrm{d}^2\tilde{u}}{\mathrm{d}y^2} - \frac{\mathrm{i}}{\nu}\,(\omega - U\,k_x)\,\tilde{u} \simeq \frac{1}{\nu}\,U'\,\tilde{v} \tag{3.113}$$

$$\frac{\mathrm{d}^2\tilde{w}}{\mathrm{d}y^2} - \frac{\mathrm{i}}{\nu}\,(\omega - U\,k_x)\,\tilde{w} = -\frac{1}{\nu}k_z\,\tilde{p} \tag{3.114}$$

$$\mathrm{i}\,k_z\,\tilde{w} - \frac{\mathrm{d}\tilde{v}}{\mathrm{d}y} = 0 \tag{3.115}$$

that govern the following boundary-layer dynamics: a pressure fluctuation induces a spanwise velocity fluctuation $\tilde{w}$ (equation (3.114)), which is compensated by a normal velocity fluctuation $\tilde{v}$ (equation (3.115)). Interaction between $\tilde{v}$ and the mean shear $\mathrm{d}U/\mathrm{d}y$ acts as a forcing term for the streamwise velocity fluctuation $\tilde{u}$ (equation (3.113)).

The mean shear $\mathrm{d}U/\mathrm{d}y$ rapidly decreases as $y^\star$ increases, while the normal velocity fluctuation $\tilde{v}$ is zero at the wall and increases at increasing $y^\star$. Thus, the source term $\tilde{v}\;\mathrm{d}U/\mathrm{d}y$ starts from zero at the wall, reaches its maximum value at some distance from the wall and then, at higher values of $y^\star$, decreases. Such a behaviour is responsible for the observed peak of the streamwise velocity fluctuation $\tilde{u}$.

3.6 Ffowcs Williams' Extension of Corcos' Model

In 1965 Ffowcs Williams [78] proposed the first model to investigate the effects of the fluid compressibility on the wall pressure wavenumber-frequency spectrum. He argued that, at low wavenumbers, i.e. at supersonic phase velocities $\omega/k \gg c$, the wall spectrum is affected by the acoustic character of the flow. In particular, at a zero wavenumber, the spectrum is entirely determined by the sound radiated by the turbulent flow in the direction normal to the wall. As a consequence, the wavenumber spectrum at $k = 0$ takes an asymptotic value estimated as $M_\infty^2\, \rho^2\, U_\infty^2\, \delta^{*2}$. Furthermore, the correlation area is proportional to the square of the mean flow Mach number M_∞. These results state that both the k^2 vanishing law of the wavenumber spectrum and the zero value of the integral scale of the surface pressure field, as predicted by Phillips [112] and Kraichnan [108], are a consequence of the flow incompressibility assumption.

The correlation area is related to the mean-square level of the force exerted by the turbulent fluctuations to the surface. Consider a two-dimensional incompressible boundary-layer which is homogeneous in planes parallel to the surface. In the absence of external pressure gradients and provided that the normal component of the velocity fluctuation vanishes both on the wall and at infinity, Phillips [112] demonstrated that

$$\int \overline{p(\mathbf{x},t)\; p(\mathbf{x}+\boldsymbol{\xi},t)}\, \mathrm{d}A(\xi) = 0 \tag{3.116}$$

Furthermore, Kraichnan [108] showed that equation (3.116) is equivalent to the condition

$$\lim_{k_1,k_3\to 0} E(0,k_1,k_3) = 0 \tag{3.117}$$

where $E(0,k_1,k_3)$ is the wavenumber spectrum ($\omega = 0$) given by

$$E(0,k_1,k_3) = \frac{1}{(2\pi)^2} \int_{-\infty}^{\infty} \int_{-\infty}^{\infty} \mathcal{R}(\xi,\eta,0)\, \exp\left[-\mathrm{i}\,(k_1\xi_1 + k_3\xi_3)\right]\, \mathrm{d}\xi\, \mathrm{d}\eta \tag{3.118}$$

and $\mathcal{R}$ is the space-time correlation function defined in (3.2).

Ffowcs Williams' [78] model is based on the idea that the wall pressure beneath a turbulent boundary-layer can be described accordingly to an acoustic analogy model. The fluctuating flow field behaves like an acoustic source whereas the surface acts as a diffracting entity. This is the approach that Curle [52] adopted in order to extend Lighthill's acoustic analogy model to account for the presence of a solid surface in the flow field. Curle's equation for the fluctuating pressure induced by the adjacent turbulent field on a rigid planar surface is

$$p(\mathbf{y},t) = \frac{1}{2\pi} \iiint_V \frac{\partial^2}{\partial z_i \partial z_j} T_{ij}\Big(\mathbf{z}, t - \frac{r}{c}\Big)\, \frac{\mathrm{d}z}{r} \tag{3.119}$$

Denote as $P(\mathbf{k},\omega)$ the generalized space-time Fourier transform of the wall pressure, i.e.

$$p(\mathbf{y},t) = \frac{1}{(2\pi)^3} \iint P(\mathbf{k},\omega)\, \mathrm{e}^{\mathrm{i}\,\mathbf{k}\cdot\mathbf{y}}\, \mathrm{e}^{\mathrm{i}\,\omega\, t}\, \mathrm{d}\mathbf{k}\, \mathrm{d}\omega \tag{3.120}$$

and $W_{ij}(\mathbf{z},\omega)$ the Fourier transform of the turbulence stress tensor, namely

$$T_{ij}\Big(\mathbf{z}, t - \frac{r}{c}\Big) = \frac{1}{2\pi} \int W_{ij}(\mathbf{z},\omega)\, \mathrm{e}^{\mathrm{i}\omega\left(t - \frac{r}{c}\right)}\, \mathrm{d}\omega \tag{3.121}$$

Substituting equations (3.120) and (3.121) into equation (3.119) yields the following expression of the space-time Fourier transform of the wall pressure

$$P(\mathbf{k},\omega) = \int_0^\infty \theta_{ij}(z_2,\mathbf{k},\omega) \left\{ \delta_{i2} \sqrt{\left(\frac{\omega}{c}\right)^2 - k^2} + k_i \right\} \left\{ \delta_{j2} \sqrt{\left(\frac{\omega}{c}\right)^2 - k^2} + k_j \right\} \frac{\mathrm{i}\, \exp\left\{ -\mathrm{i}\, z_2 \left[\left(\frac{\omega}{c}\right)^2 - k^2 \right]^{\frac{1}{2}} \right\}}{\left[\left(\frac{\omega}{c}\right)^2 - k^2 \right]^{\frac{1}{2}}}\, \mathrm{d}z_2 \tag{3.122}$$

where

$$\theta_{ij}(z_2,\mathbf{k},\omega) = \int_{S(z_2=\text{const})} W_{ij}(\mathbf{z},\omega)\, \mathrm{e}^{-\mathrm{i}\,\mathbf{k}\cdot\mathbf{z}}\, \mathrm{d}S \tag{3.123}$$

Equation (3.122) shows the existence of a critical frequency ω for any wavenumber k, above which the wall pressure results from the superposition of sound waves, and below which the pressure decays exponentially. These two cases can be expressed in their limit form as

- $|\omega/k| \gg c$

$$P(\mathbf{k},\omega) = \int_0^\infty \theta_{ij}(z_2,\mathbf{k},\omega) \left\{\left(\frac{\omega}{c}\right)\delta_{i2} + k_i\right\} \left\{\left(\frac{\omega}{c}\right)\delta_{j2} + k_j\right\} \frac{\mathrm{i}\exp\left\{-\mathrm{i}\, z_2\left(\frac{\omega}{c}\right)\right\}}{\left(\frac{\omega}{c}\right)}\, \mathrm{d}z_2 \tag{3.124}$$

- $|\omega/k| \ll c$

$$P(\mathbf{k},\omega) = \int_0^\infty \theta_{ij}(z_2,\mathbf{k},\omega) \left\{k\delta_{i2} + k_i\right\} \left\{k\delta_{j2} + k_j\right\} \frac{\exp\left\{-\mathrm{i}\, k\, z_2\right\}}{k}\, \mathrm{d}z_2 \tag{3.125}$$

from which it follows that

$$P(0,\omega) = \int_0^\infty \theta_{22}(z_2,0,\omega)\, \mathrm{i}\frac{\omega}{c} \exp\left\{-\mathrm{i}\, z_2\frac{\omega}{c}\right\} \mathrm{d}z_2 \tag{3.126}$$

$$P(\mathbf{k},0) = \int_0^\infty \theta_{ij}(z_2,\mathbf{k},0) \left\{k\,\delta_{i2} + k_i\right\} \frac{\exp\left\{-\mathrm{i}\, k\, z_2\right\}}{k}\, \mathrm{d}z_2 \tag{3.127}$$

Equation (3.126) shows that the effect of compressibility is to ensure a finite value of the wavenumber spectral density[14] as k tends to zero. This result disagrees with Phillips' result according to which the instantaneous surface force should vanish.

At first order the time variation of the wall pressure at a given point can be interpreted, consistently with Taylor frozen convection hypothesis, as simply related to the spatial streamwise variation within the size of the moving eddy. On this assumption, Lilley and Hodgson [94] and Hodgson [117] translated the low wavenumber k^2 prediction of Kraichnan's theory into an equivalent ω^2 vanishing law for the frequency spectrum. However, equation (3.127) shows the physical inconsistency of the k^2-ω^2 equivalence assumption.

Finally, a dimensional analysis applied to the wall pressure spectrum in the form of equations (3.126) and (3.127), shows that the k^2- and the ω^2-vanishing laws are well approximated for $k \gtrsim M_\infty/\delta^*$ and $\omega \gtrsim c M_\infty/\delta^*$, respectively (see Fig.3.6).

The approach based on the acoustic analogy model was later on improved by Ffowcs Williams [102] in order to extend the applicability of Corcos' model to the spectral region dominated by the compressible character of the flow.

Ffowcs Williams' model is build on the idea that, if the acoustic analogy is well posed, the acoustic character of all those low wavenumber spectral elements with supersonic phase velocity is intrinsically accounted for. Furthermore, if the acoustic source is described in terms of Corcos' similarity hydrodynamic law, the wall pressure must be consistent with the similarity scheme.

Let us consider the approximated form of Lighthill's equation

$$\frac{1}{c^2}\frac{\partial^2 p}{\partial t^2} - \nabla^2 p = \rho_0 \frac{\partial^2 (u_i u_j)}{\partial x_i \partial x_j} \equiv Q \tag{3.128}$$

[14]The wavenumber spectral density can be obtained by multiplying equation (3.126) by its complex conjugate.

$$\theta_{ij} \sim \bar{\rho} U \delta^{*3}.$$

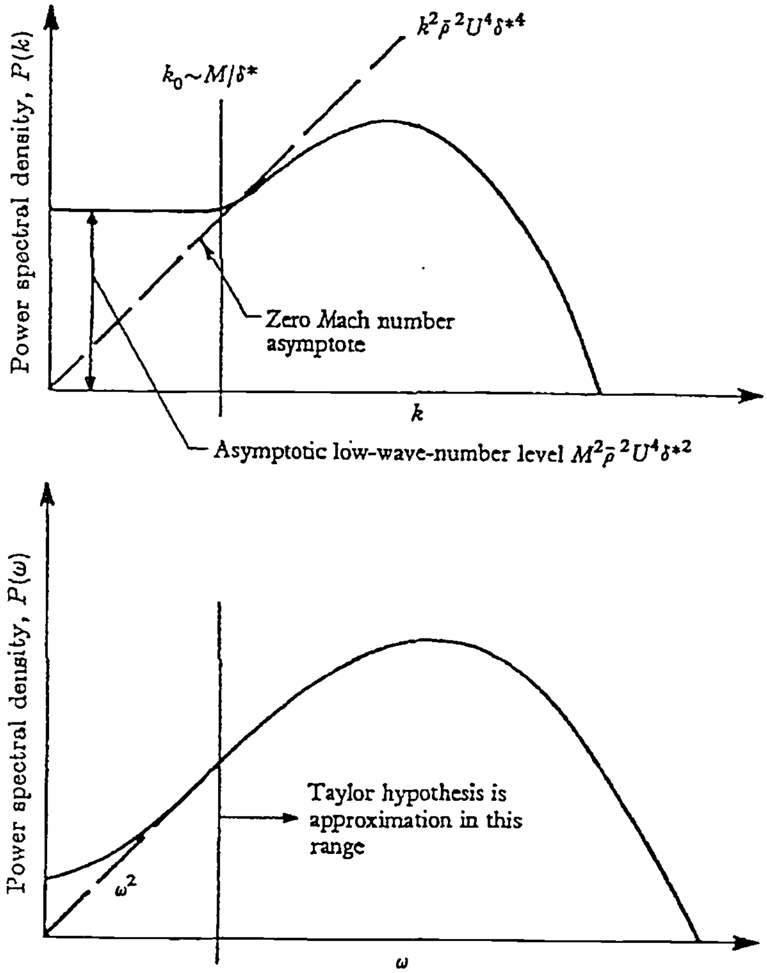

FIGURE 3.6: Qualitative behaviour of the wall pressure wavenumber-frequency spectrum induced by a turbulent boundary-layer (after Ffowcs Williams [78], figure 4).

where the flow in the source region has been approximately supposed to be incompressible. Equation (3.128) can be applied to describe the pressure field in proximity of a planar physical surface on which the auxiliary condition $\partial p/\partial y = 0$ is satisfied. Clearly, the acoustic pressure field satisfies a radiation condition on the outer boundary $y \to \infty$.

If $P(y, k_\alpha, \omega)$ denotes the spatial/time Fourier transform of $p(y, x_\alpha, t)$[15] in planes parallel to the boundary $y = 0$, i.e.

$$p(y, x_\alpha, t) = \int_0^\infty P(y, k_\alpha, \omega)\, \mathrm{e}^{\mathrm{i}\, k_\alpha x_\alpha} \mathrm{e}^{\mathrm{i}\omega t}\, \mathrm{d}^2 k_\alpha\, \mathrm{d}\omega \tag{3.129}$$

then equation (3.128) becomes

$$\left\{\frac{\partial^2}{\partial y^2} + \Psi_1^2\right\} P = -Q \quad \text{with}$$
$$\Psi_1^2 = \frac{\omega^2}{c^2} - k_\alpha^2 \quad \text{and} \quad \frac{\omega^2}{c^2} > k_\alpha^2 \tag{3.130}$$

and

$$\left\{\frac{\partial^2}{\partial y^2} - \Psi_2^2\right\} P = -Q \quad \text{with}$$
$$\Psi_2^2 = k_\alpha^2 - \frac{\omega^2}{c^2} \quad \text{and} \quad \frac{\omega^2}{c^2} < k_\alpha^2 \tag{3.131}$$

where Q is the spatial/time Fourier transform of $\mathcal{Q}$. The Green's function of equation (3.130) is

$$G(y, z) = A\, \mathrm{e}^{\mathrm{i}\, \Psi_1 \eta} + B\, \mathrm{e}^{-\mathrm{i}\, \Psi_1 \eta} + \frac{\mathrm{sgn}(z-y)}{2\, \Psi_1} \sin\left[\Psi_1(z-y)\right] \tag{3.132}$$

The radiation condition requires

$$\left\{\frac{\partial G}{\partial y} + \mathrm{i}\, \Psi_1\, G\right\}_{y\to\infty} = 2\,\mathrm{i}\ \Psi_1\, A\, \mathrm{e}^{\mathrm{i}\, \Psi_1 \eta} + \frac{1}{2}\, \mathrm{e}^{-\mathrm{i}\, \Psi_1(z-y)} = 0 \tag{3.133}$$

which gives

$$A = \frac{\mathrm{i}}{4\Psi_1}\, \mathrm{e}^{-\mathrm{i}\, \Psi_1 z} \tag{3.134}$$

Furthermore, the condition of vanishing normal derivative at $y = 0$ yields

$$B = \frac{\mathrm{i}}{4\Psi_1}\, \mathrm{e}^{\mathrm{i}\, \Psi_1 z} + \frac{\mathrm{i}}{2\Psi_1}\, \mathrm{e}^{-\mathrm{i}\, \Psi_1 z} \tag{3.135}$$

Thus, substituting into equation (3.132) provides the following expression for the supersonic phase velocity spectral elements of G

$$G(y, z) = \frac{\mathrm{i}}{2\Psi_1} \cos\left[\Psi_1(z-y)\right] + \frac{\mathrm{i}}{2\Psi_1}\, \mathrm{e}^{-\mathrm{i}\, \Psi_1(z+y)} + \frac{\mathrm{sgn}(z-y) \sin\left[\Psi_1(z-y)\right]}{2\Psi_1} \tag{3.136}$$

A similar procedure applied to equation (3.131) yields the following expression for the subsonic phase velocity spectral elements of G

$$G(y, z) = -\frac{\mathrm{i}}{2\Psi_2} \cosh\left[\Psi_2(z-y)\right] - \frac{\mathrm{i}}{2\Psi_2}\, \mathrm{e}^{-\Psi_2(z+y)} + \frac{\mathrm{sgn}(z-y) \sinh\left[\Psi_2(z-y)\right]}{2\Psi_2} \tag{3.137}$$

[15] $k_\alpha = (k_1, k_2) = (k_x, k_z)$; $x_\alpha = (x_1, x_2) = (x, z)$.

The wall pressure can be obtained by convoluting equations (3.130) and (3.131) with their respective Green's functions. It thus results that

$$P(0,k_\alpha,\omega) = -\int_0^\infty G(0,z)\,Q^*(z,k_\alpha,\omega)\;\mathrm{d}z \tag{3.138}$$

Then, substituting the Green's functions (3.136) and (3.137) into equation (3.138) yields the following asymptotic expressions

- $\omega^2/k_\alpha^2 > c^2$, i.e. supersonic phase velocity,

$$P(0,k_\alpha,\omega) = \frac{-\mathrm{i}}{\Psi_1}\int_0^\infty \mathrm{e}^{-\mathrm{i}\,\Psi_1 z} Q^*(z,k_\alpha,\omega)\;\mathrm{d}z \tag{3.139}$$

- $\omega^2/k_\alpha^2 < c^2$, i.e. subsonic phase velocity,

$$P(0,k_\alpha,\omega) = \frac{1}{\Psi_2}\int_0^\infty \mathrm{e}^{-\Psi_2 z} Q^*(z,k_\alpha,\omega)\;\mathrm{d}z \tag{3.140}$$

The wavenumber-frequency spectrum $E(k_\alpha,\omega)$ can be obtained by Fourier transforming the correlation function $R(\xi_\alpha,\tau)$, i.e.

$$E(k_\alpha,\omega) = \frac{1}{(2\,\pi)^3}\int_0^\infty R(\xi_\alpha,\tau)\,\mathrm{e}^{-\mathrm{i}\,(k_\alpha\xi_\alpha+\omega\,\tau)}\;\mathrm{d}^2\xi_\alpha\,\mathrm{d}\tau \tag{3.141}$$

where

$$R(\xi_\alpha,\tau) = \overline{p(x_\alpha,t)\;p(x_\alpha+\xi_\alpha,t+\tau)} \tag{3.142}$$

Thus, substituting equations (3.139) and (3.140) into equation (3.141) provides

- $\omega^2/k_\alpha^2 > c^2$

$$R(\xi_\alpha,\tau) = \int_0^\infty\!\!\int_0^\infty \frac{\mathrm{e}^{-\mathrm{i}\,\Psi_1(z-z')}}{\Psi_1^2}\overline{Q(z,x_\alpha,t)\,Q(z',x_\alpha+\xi_\alpha,t+\tau)}\,\mathrm{d}z\,\mathrm{d}z' \tag{3.143}$$

- $\omega^2/k_\alpha^2 < c^2$

$$R(\xi_\alpha,\tau) = \int_0^\infty\!\!\int_0^\infty \frac{\mathrm{e}^{-\Psi_2(z+z')}}{\Psi_2^2}\overline{Q(z,x_\alpha,t)\,Q(z',x_\alpha+\xi_\alpha,t+\tau)}\,\mathrm{d}z\,\mathrm{d}z' \tag{3.144}$$

Finally, setting

$$S(z,z',k_\alpha,\omega) = \frac{1}{(2\,\pi)^3}\int_0^\infty \overline{Q(z,x_\alpha,t)\,Q(z',x_\alpha+\xi_\alpha,t+\tau)}\,\mathrm{e}^{-\mathrm{i}\,(k_\alpha\xi_\alpha+\omega\,\tau)}\,\mathrm{d}^2\xi_\alpha\,\mathrm{d}\tau \tag{3.145}$$

the wavenumber frequency spectrum (3.141) takes the form

- $\omega^2/k_\alpha^2 > c^2$

$$E(k_\alpha,\omega) = \int_0^\infty\!\!\int_0^\infty \frac{\mathrm{e}^{-\mathrm{i}\,\Psi_1(z-z')}}{\Psi_1^2}S(z,z',k_\alpha,\omega)\;\mathrm{d}z\,\mathrm{d}z' \tag{3.146}$$

- $\omega^2/k_\alpha^2 < c^2$

$$E(k_\alpha,\omega) = \int_0^\infty\int_0^\infty \frac{e^{-\Psi_2(z+z')}}{\Psi_2^2} S(z,z',k_\alpha,\omega)\,dz\,dz' \tag{3.147}$$

Since the term S denotes a turbulent source, it can be described in terms of Corcos' similarity hypothesis. Thus, let us consider the Fourier transform of Lighthill's stress tensor

$$Q(z,k_\alpha,\omega) = \frac{1}{(2\pi)^3}\int_{-\infty}^{\infty}\left\{\frac{\partial^2 T_{zz}}{\partial z^2} + \frac{\partial^2 T_{z\alpha}}{\partial z\partial x_\alpha} + \frac{\partial^2 T_{\alpha\beta}}{\partial x_\alpha \partial x_\beta}\right\} e^{-i(k_\alpha x_\alpha+\omega\tau)}\,d^2x_\alpha\,dt \tag{3.148}$$

which can be integrated by parts taking the form

$$Q(z,k_\alpha,\omega) = Q_1(z,k_\alpha,\omega) + Q_2(z,k_\alpha,\omega) + Q_3(z,k_\alpha,\omega) \tag{3.149}$$

with

$$Q_1(z,k_\alpha,\omega) = \frac{1}{(2\pi)^3}\int_{-\infty}^{\infty}\frac{\partial^2 T_{zz}}{\partial z^2} e^{-i(k_\alpha x_\alpha+\omega\tau)}\,d^2x_\alpha\,dt \tag{3.150}$$

$$Q_2(z,k_\alpha,\omega) = \frac{i\,2\,k_\alpha}{(2\pi)^3}\int_{-\infty}^{\infty}\frac{\partial T_{z\alpha}}{\partial z}\, e^{-i(k_\alpha x_\alpha+\omega\tau)}\,d^2x_\alpha\,dt \tag{3.151}$$

$$Q_3(z,k_\alpha,\omega) = -\frac{k_\alpha^2}{(2\pi)^3}\int_{-\infty}^{\infty} T_{\alpha\alpha}\, e^{-i(k_\alpha x_\alpha+\omega\tau)}\,d^2x_\alpha\,dt \tag{3.152}$$

These three integrals have characteristic magnitudes in the ratios

$$|Q_1| : |Q_2| : |Q_3| = 1 : k\Delta : (k\Delta)^2. \tag{3.153}$$

where Δ is a reference boundary-layer scale. A similar decomposition of $S(z,z',k_\alpha,\omega)$ yields

$$S_1(z,z',k_\alpha,\omega) = \frac{\partial^2}{\partial z^2}\frac{\partial^2}{\partial z'^2} T_1(z,z',k_\alpha,\omega) \quad \text{with} \tag{3.154}$$

$$T_1(z,z',k_\alpha,\omega) = \frac{1}{(2\pi)^3}\int_{-\infty}^{-\infty} \overline{T_{zz}(z,x_\alpha,t)\,T_{zz}(z',x_\alpha+\xi_\alpha,t+\tau)}\, e^{-i(k_\alpha\xi_\alpha+\omega\tau)}\,d^2\xi_\alpha\,d\tau$$

$$S_2(z,z',k_\alpha,\omega) = 4\,k_\alpha^2\frac{\partial^2}{\partial z\partial z'} T_2(z,z',k_\alpha,\omega) \quad \text{with} \tag{3.155}$$

$$T_2(z,z',k_\alpha,\omega) = \frac{1}{(2\pi)^3}\int_{-\infty}^{-\infty} \overline{T_{z\alpha}(z,x_\alpha,t)\,T_{z\alpha}(z',x_\alpha+\xi_\alpha,t+\tau)}\, e^{-i(k_\alpha\xi_\alpha+\omega\tau)}\,d^2\xi_\alpha\,d\tau$$

$$S_3(z,z',k_\alpha,\omega) = k_\alpha^4 T_3(z,z',k_\alpha,\omega) \quad \text{with} \tag{3.156}$$

$$T_3(z,z',k_\alpha,\omega) = \frac{1}{(2\pi)^3}\int_{-\infty}^{-\infty} \overline{T_{\alpha\alpha}(z,x_\alpha,t)\,T_{\alpha\alpha}(z',x_\alpha+\xi_\alpha,t+\tau)}\, e^{-i(k_\alpha\xi_\alpha+\omega\tau)}\,d^2\xi_\alpha\,d\tau$$

The wall pressure wavenumber-frequency contributions corresponding to these three contributions of S are

$$E_1(k_\alpha,\omega) = \begin{cases} \left(\frac{\omega^2}{c^2} - k_\alpha^2\right) F_1(k_\alpha,\omega) & \text{for } \frac{\omega^2}{c^2} > k_\alpha^2 \\ \left(k_\alpha^2 - \frac{\omega^2}{c^2}\right) F_1(k_\alpha,\omega) & \text{for } \frac{\omega^2}{c^2} < k_\alpha^2 \end{cases} \tag{3.157}$$

$$E_2(k_\alpha,\omega) = k_\alpha^2\, F_2(k_\alpha,\omega) \tag{3.158}$$

$$E_3(k_\alpha,\omega) = \frac{k_\alpha^4}{\left|\frac{\omega^2}{c^2} - k_\alpha^2\right|}\, F_3(k_\alpha,\omega) \tag{3.159}$$

where F_1, F_2 and F_3 are characteristic spectral functions representing the integrated influence of the boundary-layer turbulence. These terms are not influenced by the fluid compressibility if the acoustic analogy is well posed.

According to the relation (3.153), at wavenumbers much less than Δ^{-1}, the main contribution to the spectrum is given by equation (3.157). Thus, separating the two limit cases, yields

- supersonic wave speed: $\Delta^{-2} \gg \omega^2/c^2 \gg k_\alpha^2$

$$E(k_\alpha,\omega) \simeq \frac{\omega^2}{c^2} F_{1\mathrm{a}}^*(k_\alpha,\omega) \tag{3.160}$$

- subsonic wave speed: $\Delta^{-2} \gg k_\alpha^2 \gg \omega^2/c^2$

$$E(k_\alpha,\omega) \simeq k_\alpha^2 F_{1\mathrm{b}}^*(k_\alpha,\omega) \tag{3.161}$$

Since the source elements are quadratic in the turbulence fluctuating quantities, the function $F_1^*(k_\alpha,\omega)$ tends asymptotically to a finite value as both k_α and ω tend to zero. Therefore, both equations (3.160) and (3.161) agree with Ffowcs Williams' 1965 result [78], as plotted in Fig.3.6.

If the condition $\Delta^{-2} \gg k_\alpha^2$ is not verified, all the three contributions of Q must be considered. Nevertheless, if $k_\alpha^2 \gg \omega^2/c^2$, then E_{1b}, E_2 and E_3 have all the same limit form

$$E(k_\alpha,\omega) \simeq k_\alpha^2 F(k_\alpha,\omega) \tag{3.162}$$

Both equations (3.160) and (3.161) can be rewritten in terms of dimensionless quantities, i.e.

- supersonic wave speed: $(\Delta k_\alpha)^2 \ll (\omega\Delta/c)^2 \ll 1$

$$E(k_\alpha,\omega) = \rho_0^2\, U_\infty^3\, \Delta^3 \left(\frac{U_\infty}{c}\right)^2 \left(\frac{\omega\,\Delta}{U_\infty}\right)^2 F\left(\Delta k_\alpha, \frac{\omega\,\Delta}{U_\infty}\right) \tag{3.163}$$

- subsonic wave speed: $(\omega\Delta/c)^2 \ll (\Delta k_\alpha)^2 \ll 1$

$$E(k_\alpha,\omega) = \rho_0^2\, U_\infty^3\, \Delta^3\, (\Delta k_\alpha)^2\, F\left(\Delta k_\alpha, \frac{\omega\,\Delta}{U_\infty}\right) \tag{3.164}$$

The singularity at the acoustically coincident wavenumber in the spectral contribution (3.159) is a consequence of the fact that the wave field radiated by an unbounded distribution of surface sources is singular. Therefore, it is a consequence of the so-called *scale effect.* In order to describe this singular behaviour, the boundary-layer turbulence can be supposed to be bounded at a large radius R. Solving directly equation (3.128) the wavenumber-frequency spectrum, at the acoustic coincident frequency, takes the form

$$E(k_\alpha,\omega) = \pi \int_0^\infty S(z,z',k_\alpha,\omega)\, \delta(k_\alpha^2 - \omega^2/c^2)\, \ln\left(\frac{R}{\Delta}\right)\, \mathrm{d}z\, \mathrm{d}z' \tag{3.165}$$

which shows that the field diverges logarithmically as the scale of the turbulence, say R/Δ, tends to infinity.

The stress tensor elements which contribute to S in equation (3.165) are those whose axes lie in the boundary-layer plane. In fact, elements involving surface normal components integrate to zero. The source term S is thus proportional to k^4 (ω^4/c^4 at the acoustically coincident wavenumber) and equation (3.165) can be expressed as

$$E(k_\alpha,\omega) = \ln\left(\frac{R}{\Delta}\right) \left(\frac{\omega}{c}\right)^4 \delta\left(k^2 - \left(\frac{\omega}{c}\right)^2\right) F(k_\alpha,\omega) \tag{3.166}$$

and, in the non-dimensional form

$$E(k_\alpha,\omega) = \rho_0^2 U_\infty^3 \Delta^3 \ln\left(\frac{R}{\Delta}\right) \left(\frac{\omega\,\Delta}{c}\right)^4 \delta\left((\Delta k_\alpha)^2 - \left(\frac{\omega\,\Delta}{c}\right)^2\right) F\left(\Delta k_\alpha, \frac{\omega\,\Delta}{U_\infty}\right) \tag{3.167}$$

This expression shows explicitly the singular behaviour of the acoustically coincident spectral elements. Together with equations (3.163) and (3.164), it describes the structure of the wall pressure field for all the wavenumber-frequency elements.

The function $F\left(\Delta k_\alpha, \frac{\omega\Delta}{U_\infty}\right)$ is the characteristic spectrum of the integrated boundary-layer turbulence. It has a purely hydrodynamic nature and can be expressed in a similarity form. According to Corcos [99], the cross-spectral density $\Gamma(\xi_\alpha,\omega)$ has the following similarity structure

$$\Gamma(\xi_\alpha,\omega) = \phi(\omega)\, A\left(\frac{\omega\,\xi_1}{U_c}\right) B\left(\frac{\omega\,\xi_2}{U_c}\right) \mathrm{e}^{\mathrm{i}\,\frac{\omega\,\xi_1}{U_c}} \tag{3.168}$$

The cross-spectral density is related to the wavenumber-frequency spectrum by the double Fourier transform

$$E(k_\alpha,\omega) = \frac{1}{(2\,\pi)^2} \int_{-\infty}^{\infty}\int_{-\infty}^{\infty} \Gamma(\xi_\alpha,\omega)\, \mathrm{e}^{-\mathrm{i}\,k_\alpha \xi_\alpha}\, \mathrm{d}^2\xi_\alpha \tag{3.169}$$

Thus, substituting equation (3.168) into equation (3.169) yields

$$\begin{aligned} E(k_\alpha,\omega) = \frac{1}{(2\,\pi)^2}\,\phi(\omega)\,\frac{U_c^2}{\omega^2} &\int_{-\infty}^{\infty} A\left(\frac{\omega\,\xi_1}{U_c}\right) \exp\left[-\mathrm{i}\,\frac{\omega\,\xi_1}{U_c}\left(1+\frac{k_1 U_c}{\omega}\right)\right] \mathrm{d}\left(\frac{\omega\,\xi_1}{U_c}\right) \\ &\int_{-\infty}^{\infty} B\left(\frac{\omega\,\xi_2}{U_c}\right) \exp\left[-\mathrm{i}\,\frac{\omega\,\xi_2}{U_c}\frac{k_2 U_c}{\omega}\right] \mathrm{d}\left(\frac{\omega\,\xi_2}{U_c}\right) = \\ &= \phi(\omega)\,\frac{U_c^2}{\omega^2}\mathcal{A}\left(1+\frac{k_1 U_c}{\omega}\right) \mathcal{B}\left(\frac{k_2 U_c}{\omega}\right) \end{aligned} \tag{3.170}$$

where

$$\mathcal{A}(\alpha) = \frac{1}{2\pi}\int_{-\infty}^{\infty} A(\beta)\, e^{-\mathrm{i}\,\alpha\beta}\, \mathrm{d}\beta \tag{3.171}$$

$$\mathcal{B}(\alpha) = \frac{1}{2\pi}\int_{-\infty}^{\infty} B(\beta)\, e^{-\mathrm{i}\,\alpha\beta}\, \mathrm{d}\beta \tag{3.172}$$

(3.173)

Finally, in agreement with equation (3.170), the function F in equation (3.167) can be written as

$$F\left(\Delta k_\alpha, \frac{\omega\,\Delta}{U_\infty}\right) = \left(\frac{U}{\omega\,\Delta}\right)^2 \phi_0\!\left(\frac{\omega\,\Delta}{U_\infty}\right) \mathcal{A}_0\!\left(1 + \frac{k_1 U_c}{\omega}\right) \mathcal{B}_0\!\left(\frac{k_2 U_c}{\omega}\right) \tag{3.174}$$

where

$$\phi_0\!\left(\frac{\omega\,\Delta}{U_\infty}\right) = \int_{-\infty}^{\infty} F\left(\Delta k_\alpha, \frac{\omega\,\Delta}{U_\infty}\right) \mathrm{d}^2\left(\Delta k_\alpha\right) \quad \text{and} \tag{3.175}$$

$$\int_{-\infty}^{\infty} \mathcal{A}_0^*\left(x\right) \mathrm{d}x = \int_{-\infty}^{\infty} \mathcal{B}_0^*\left(x\right) \mathrm{d}x = 1 \tag{3.176}$$

Equations (3.163), (3.164) and (3.167) can be linearly combined into a single equation where $F\left(\Delta k_\alpha, \frac{\omega\Delta}{U_\infty}\right)$ is given by equation (3.174). Setting $M_\infty = U_\infty/c$ and calling a_0, a_1 and a_2 the coefficients of the combination, it follows that

$$\begin{aligned} E(k_\alpha, \omega) = \rho_0^2\, U_\infty^3\, \Delta^3\, \phi_0\!\left(\frac{\omega\,\Delta}{U_\infty}\right) \mathcal{A}_0\!\left(1 + \frac{k_1 U_\infty}{\omega}\right) \mathcal{B}_0\!\left(\frac{k_2 U_\infty}{\omega}\right) \\ \left\{a_0 \left(\frac{U_\infty k}{\omega}\right)^2 + a_1\, M_\infty^2 + a_2\, M_\infty^4 \ln\!\left(\frac{R}{\Delta}\right) \delta\left[\left(\frac{U_\infty\, k}{\omega}\right)^2 - M_\infty^2\right]\right\} \end{aligned} \tag{3.177}$$

This is the form proposed by Ffowcs Williams [102] for the wavenumber-frequency spectrum.

The function which is commonly measured is the frequency spectrum of the pressure field $\phi(\omega) = \int_\infty E(k_\alpha, \omega)\ \mathrm{d}^2 k_\alpha$. According to equation (3.177), it is given by

$$\phi(\omega) = \rho_0^2\, U_\infty^3\, \Delta \left(\frac{\omega\Delta}{U}\right)^2 \phi_0\!\left(\frac{\omega\Delta}{U}\right)^2 \left\{\alpha + \beta\, M_\infty^2 + \gamma\, M_\infty^4 \ln\!\left(\frac{R}{\Delta}\right)\right\} \tag{3.178}$$

where

$$\alpha = a_0 \int_{-\infty}^{\infty} \mathcal{A}_0\!\left(1 + \frac{k_1 U_\infty}{\omega}\right) \mathcal{B}_0\!\left(\frac{k_2 U_\infty}{\omega}\right) \left(\frac{k U_\infty}{\omega}\right)^2 \mathrm{d}^2\left(\frac{k_\alpha U_\infty}{\omega}\right) \tag{3.179}$$

$$\beta = a_1 \int_{-\infty}^{\infty} \mathcal{A}_0\!\left(1 + \frac{k_1 U_\infty}{\omega}\right) \mathcal{B}_0\!\left(\frac{k_2 U_\infty}{\omega}\right) \mathrm{d}^2\left(\frac{k_\alpha U_\infty}{\omega}\right) \tag{3.180}$$

$$\begin{aligned} \gamma = a_2 \int_{-\infty}^{\infty} \mathcal{A}_0\!\left(1 + \frac{k_1 U_\infty}{\omega}\right) \mathcal{B}_0\!\left(\frac{k_2 U_\infty}{\omega}\right) \\ \delta\!\left(\left(\frac{k_1 U_\infty}{\omega}\right)^2 + \left(\frac{k_2 U_\infty}{\omega}\right)^2 - M_\infty^2\right) \mathrm{d}^2\left(\frac{k_\alpha U_\infty}{\omega}\right) \end{aligned} \tag{3.181}$$

$$\simeq a_2\, \pi\, \mathcal{A}_0(1)\ \mathcal{B}_0(0) \quad \text{when } M_\infty \text{ is sufficiently small} \tag{3.182}$$

According to this model the frequency spectrum vanishes as ω^2 when the frequency tends to zero. Such a result is commonly accepted but experimental validations are difficult because of the background noise at very low frequencies.

3.7 Chase's Wall Pressure Spectrum Model

By means of matched asymptotic expansions, Bergeron [100] obtained a low wavenumber solution for a nearly incompressible turbulent boundary-layer. The same equation was solved by Chase & Noiseux [113] by adopting a perturbation procedure. Their results constitute the starting point of Chase's [104] successive investigation where the author re-examined all the aspects of the problem and suggested a comprehensive model for the wall pressure wavenumber-frequency spectrum. In the present section the model proposed by Chase is briefly presented.

Adopting dimensionless quantities $x = x'/\delta$, $t = t' U_\infty/\delta$, $u_i = u_i'/U_\infty$ and $p = (p' - p_0)/\rho_0 U_\infty^2$, δ denoting the boundary-layer thickness, the linear momentum and the continuity equation for an inviscid fluid take the form

$$\left[\frac{\partial \mathbf{u}}{\partial t} + (\mathbf{u}\cdot\nabla)\,\mathbf{u}\right](1 + M_\infty^2\, p) = -\nabla p \tag{3.183}$$

$$\nabla\cdot\mathbf{u} = -M_\infty^2\left[\frac{\partial p}{\partial t} + (\mathbf{u}\cdot\nabla)\,p + p\nabla\cdot\mathbf{u}\right] \tag{3.184}$$

The mean flow can be separated from the fluctuating part by substituting $\mathbf{u} = \mathbf{U}(y) + \mathbf{u}'$ into equations (3.183) and (3.184). Then, rearranging and neglecting terms of order higher than M_∞^2, Bergeron [100] obtained the following equation

$$\begin{aligned} L(\nabla^2 p) - 2\frac{\mathrm{d}U}{\mathrm{d}y}\frac{\partial^2 p}{\partial x \partial y} - M_\infty^2\, L^3(p) = \\ 2\frac{\mathrm{d}U}{\mathrm{d}y}\frac{\partial T_2}{\partial x} - L(\nabla\cdot\mathbf{T}) + M_\infty^2\left\{2\frac{\mathrm{d}U}{\mathrm{d}y}\frac{\partial S_2}{\partial x} - L\left(\nabla\cdot\mathbf{S} - L(\nabla\cdot[p\,\mathbf{u}'])\right)\right\} \end{aligned} \tag{3.185}$$

where

$$L = \frac{\partial}{\partial t} + U(y)\,\frac{\partial}{\partial x} \tag{3.186}$$

$$T_i = \frac{\partial\left(u_i' u_j'\right)}{\partial x_j} = \frac{\partial T_{ij}}{\partial x_j} \tag{3.187}$$

$$\mathbf{S} = \mathbf{u}'\left[L(p) + (\mathbf{u}'\cdot\nabla)\,p\right] - \frac{1}{2}\nabla\left(p^2\right) \tag{3.188}$$

Introducing the Fourier representation

$$\theta(x,y,z,t) = \int_{-\infty}^{\infty} \mathrm{d}\omega \int_{-\infty}^{\infty}\int_{-\infty}^{\infty} \exp\left[\mathrm{i}\,(k_x\, x + k_z\, z - \omega t)\right]\hat{\theta}(y,k_x,k_z,\omega)\; \mathrm{d}k_x\, \mathrm{d}k_z \tag{3.189}$$

into equation (3.185) yields

$$\begin{aligned} &(\omega - k_x U)\left[\frac{\mathrm{d}^2}{\mathrm{d}y^2} - K^2\right]\hat{p} + 2\,k_x\frac{\mathrm{d}U}{\mathrm{d}y}\frac{\mathrm{d}\hat{p}}{\mathrm{d}y} + M_\infty^2\,(\omega - k_x U)^3\,\hat{p} = \\ &-2\,k_x\frac{\mathrm{d}U}{\mathrm{d}y}\hat{T}_2 - (\omega - k_x U)\left[\frac{\mathrm{d}\hat{T}_2}{\mathrm{d}y} + \mathrm{i}\,\left(k_x \hat{T}_1 + k_z \hat{T}_3\right)\right] \\ &-M_\infty^2\left\{2\,k_x\frac{\mathrm{d}U}{\mathrm{d}y}\,\hat{S}_2 + (\omega - k_x U)\left[\frac{\mathrm{d}\hat{S}_2}{\mathrm{d}y} + \mathrm{i}\,\left(k_x \hat{S}_1 + k_z\,\hat{S}_3\right)\right]\right\} \\ &+\mathrm{i}\,(\omega - k_x U)^2\left[\frac{\mathrm{d}}{\mathrm{d}y}(p\,\hat{u}_2) + \mathrm{i}\,\left[k_x\,(p\,\hat{u}_1) + k_z\,(p\,\hat{u}_3)\right]\right] \end{aligned}$$

where $K^2 = k_x^2 + k_z^2$. Finally, changing to physical variables and operating a co-ordinate rotation such that x_3 lies along the wavevector argument $\mathbf{K}$, namely

$$K^2\,\hat{T}_{33} = k_x^2\,\hat{T}_{xx} + 2\,k_x\,k_z\,\hat{T}_{xz} + k_z^2\,\hat{T}_{zz} \tag{3.190}$$

$$K\,\hat{T}_{32} = k_x\,\hat{T}_{xy} + k_z\,\hat{T}_{zy} \tag{3.191}$$

equation (3.190) takes the form obtained by Chase & Noiseux [113], i.e.

$$\left\{(\omega - k_x\,U)\left[\frac{\mathrm{d}^2}{\mathrm{d}y^2} - K^2 + \frac{1}{c^2}\,(\omega - k_x\,U)^2\right] + 2\,k_x\frac{\mathrm{d}U}{\mathrm{d}y}\frac{\mathrm{d}}{\mathrm{d}y}\right\}\hat{p} = \rho\,\hat{S} + \rho\,\hat{S}_M \tag{3.192}$$

where

$$\rho\,\hat{S} = -2\,\rho\,k_x\,\frac{\mathrm{d}U}{\mathrm{d}y}\left(\frac{\mathrm{d}\hat{T}_{22}}{\mathrm{d}y} + \mathrm{i}\,K\,\hat{T}_{32}\right) - \rho\,(\omega - k_x\,U)\left(\frac{\mathrm{d}^2\hat{T}_{22}}{\mathrm{d}y^2} + \mathrm{i}\,2\,K\,\frac{\mathrm{d}\hat{T}_{32}}{\mathrm{d}y} - K^2\,\hat{T}_{33}\right) \tag{3.193}$$

and

$$\begin{aligned}\rho\,\hat{S}_M = &-\left(\rho\,c^2\right)^{-1}\left[2\,k_x\,\frac{\mathrm{d}U}{\mathrm{d}y}\hat{S}_2 + (\omega - k_x\,U)\left(\frac{\mathrm{d}\hat{S}_2}{\mathrm{d}y} + \mathrm{i}\;K\hat{S}_3\right)\right] \\ &+\mathrm{i}\;(\omega - k_x\,U)^2\left[\frac{\mathrm{d}\,(p\,\hat{u}_2)}{\mathrm{d}y} + \mathrm{i}\;\,(p\,\hat{u}_3)\right]\end{aligned} \tag{3.194}$$

Consider first the incompressible case ($c \to \infty$) and eliminate $\hat{p}$ from equation (3.192) in favor of the more convenient variable

$$f = \left(\hat{p} + \rho\,\hat{T}_{22}\right)\frac{\phi}{\omega} \tag{3.195}$$

where

$$\phi = \left(1 - k_x\frac{U(y)}{\omega}\right)^{-1} \tag{3.196}$$

Equation (3.192) becomes

$$f'' - \left(K^2 + \frac{\phi''}{\phi}\right)f = \rho K\left[K\frac{\hat{T}_{33} - \hat{T}_{22}}{\omega - k_x\,U} - \frac{\mathrm{i}\;2\,\hat{T}_{32}}{\omega - k_x\,U}\right] \tag{3.197}$$

where primes denote derivation with respect to y. The boundary conditions $|\hat{p}(\infty)| < \infty$ and $\hat{p}'(0) = 0$ lead respectively to

$$|f(\infty)| < \infty \tag{3.198}$$

$$\frac{f'(0)}{f(0)} = k_x\frac{U'(0)}{\omega} \tag{3.199}$$

If $G_1(y)$ and $G_2(y)$ denote two Green's functions of the homogeneous form of equation (3.197) with boundary conditions

$$|G_1(\infty)| < \infty \tag{3.200}$$

$$\frac{G_2'(0)}{G_2(0)} = k_x\frac{U'(0)}{\omega} \tag{3.201}$$

the solution of equation (3.197), evaluated at $y = 0$, is

$$\hat{p}(0,\mathbf{K},\omega) = -\rho\,K\,\omega\,\mathcal{W}^{-1}\,G_2(0)\int_0^\infty G_1(1)\left[K\frac{\hat{T}_{33} - \hat{T}_{22}}{\omega - k_x\,U} - \mathrm{i}\,2\left(\frac{\hat{T}_{32}}{\omega - k_x\,U}\right)'\right]\mathrm{d}y \tag{3.202}$$

where $\mathcal{W}$ denotes the Wronskian of G_1 and G_2. Thus, integrating by parts yields

$$\hat{p}(0,\mathbf{K},\omega) = -\rho\mathcal{W}^{-1}G_2(0)\int_0^\infty \phi\left[K^2\left(\hat{T}_{33}-\hat{T}_{22}\right)G_1(y) + \mathrm{i}\,2K\hat{T}_{32}G_1'(y)\right]\mathrm{d}y \tag{3.203}$$

The Green's functions G_1 and G_2 can be calculated by a perturbation technique applied to the equation

$$f'' - \left[s^2 + \epsilon V'' + \epsilon^2\left(VV'' + 2V'^2\right) + \mathcal{O}(\epsilon^2)\right]f = 0 \tag{3.204}$$

obtained by substituting $\zeta = y/\delta$, $s = K\delta$ and $V(\zeta) = U(y)/U_\infty$ into the homogeneous form of equation (3.197) and by dropping terms of order higher than ϵ^2, where

$$\epsilon = \frac{k_x U_\infty}{\omega} \ll 1 \tag{3.205}$$

Expanding f in a power series of ϵ, namely

$$f = f_0 + \epsilon f_1 + \epsilon^2 f_2 + \ldots \tag{3.206}$$

and solving equation (3.204) for successive orders of f yields

$$G_1(\zeta) = \mathrm{e}^{-s\zeta} + \epsilon\left[\mathrm{e}^{s\zeta}\,S_+(\zeta) - 2\,S_1\sinh(s\,\zeta)\right] + \mathcal{O}(\epsilon^2) \tag{3.207}$$

$$G_2(\zeta) = \cosh(s\,\zeta) + \frac{\epsilon}{2}\left[\mathrm{e}^{s\zeta}\,S_+(\zeta) + \mathrm{e}^{-s\zeta}\,S_-(\zeta)\right] + \mathcal{O}(\epsilon^2) \tag{3.208}$$

where

$$S_\pm(\zeta) = \int_0^\zeta \mathrm{e}^{\mp 2sz}V'(z)\,\mathrm{d}z \tag{3.209}$$

and $S_1 = S_+(1)$. The Wronskian takes the form

$$\mathcal{W} = K\left[1 + 2\epsilon S_1 + \mathcal{O}(\epsilon^2)\right] \tag{3.210}$$

The nonlinear source terms in equation (3.197) vanishes at some distance δ_1 from the wall. Thus, supposing that $K\delta_1 \ll 1$, expanding the term $\hat{T}_{ij}$ to the first order in ϵ and $K\delta_1$, and introducing equations (3.207), (3.208) and (3.210) into equation (3.203) provides the following integral form of the wall pressure spectrum at low wavenumbers and in the incompressible case

$$\hat{p}(0,\mathbf{K},\omega) = -\rho\int_0^\infty \mathrm{d}y\left[K\left(\hat{T}_{33}-\hat{T}_{22}\right) - \mathrm{i}\,2\hat{T}_{32}\left(K - \frac{k_x U'(y)}{\omega}\right)\right] \tag{3.211}$$

This result agrees with Kraichnan-Phillips' theorem according to which

$$\lim_{K\to 0}\hat{p}(0,\mathbf{K},\omega) \to 0 \tag{3.212}$$

Consider now the compressible case. The contribution of $\hat{S}_M$ in equation (3.192) is of higher order in ϵ and can be neglected. Hence, equation (3.192) has the following solution

$$\hat{p}(0,\mathbf{K},\omega) = -\rho\mathcal{W}^{-1}G_2(0)$$
$$\int_0^\infty \mathrm{d}y\left[\left(\hat{T}_{33}-\hat{T}_{22}\right)K^2\phi\,G_1(y) + \hat{T}_{22}\left(\frac{\omega^2}{c^2}\right)\phi^{-1}G_1 + \mathrm{i}\,2\hat{T}_{32}\,K\,\phi\,G_1'\right] \tag{3.213}$$

where G_1 and G_2 are Green's functions of the homogeneous equation

$$f'' - \left(K^2 - \frac{\omega^2}{c^2}\phi^2 + \frac{\phi''}{\phi}\right)f = 0 \tag{3.214}$$

At first order in ϵ, equation (3.214) has the same solution of the homogeneous form of equation (3.197), with arguments K^2 replaced by $K^2 - \omega^2/c^2$. Thus, introducing the condition $K\delta \ll 1$ yields

$$\phi \to 1 \tag{3.215}$$

$$G_1 \to 1 \tag{3.216}$$

$$\mathcal{W} \to \left(K^2 - \frac{\omega^2}{c^2}\right)^{1/2} \tag{3.217}$$

$$\frac{\mathrm{d}G_1}{\mathrm{d}y} \to -\left(K^2 - \frac{\omega^2}{c^2}\right)^{1/2} + k_x \frac{U'}{\omega} \tag{3.218}$$

which leads to

$$\hat{p}(0, \mathbf{K}, \omega) \to -\rho \int_0^\infty \left\{ \frac{K^2 \hat{T}_{33}}{\sqrt{K^2 - \frac{\omega^2}{c^2}}} - \hat{T}_{22}\sqrt{K^2 - \frac{\omega^2}{c^2}} - \mathrm{i}\, 2K \left[1 - \frac{k_x U'(y)}{\omega\sqrt{K^2 - \frac{\omega^2}{c^2}}}\right] \hat{T}_{32} \right\} \mathrm{d}y \tag{3.219}$$

where, for $K < \omega/c$, the argument $\left(K^2 - \omega^2/c^2\right)^{1/2}$ must be replaced by $\mathrm{i}\,\left(\omega^2/c^2 - K^2\right)^{1/2}$.

Equation (3.219) describes the wall pressure beneath a slightly compressible ($U_\infty/c \ll 1$) turbulent boundary-layer in the low wavenumber limit ($k_x U_\infty/\omega \ll 1$).

At the same low order in $k_x U_\infty/\omega$, but with no upper limit for $K\delta$, the wall pressure is given by equation (3.219) with a factor $\exp\left[-\left(K^2 - \omega^2/c^2\right)^{1/2} y\right]$ added to the integrand. It thus results that

$$\hat{p}(\mathbf{K}, \omega) = -\rho K \int_0^\infty \mathrm{e}^{-K_c y} \left[\frac{K}{K_c}\hat{T}_{33} - \mathrm{i}\, 2\hat{T}_{32} - \frac{K_c}{K}\hat{T}_{22} + \mathrm{i}\, 2\frac{k_x}{K_c}\frac{U'}{\omega}\hat{T}_{32}\right] \mathrm{d}y \tag{3.220}$$

where

$$K_c = \begin{cases} \left(K^2 - \frac{\omega^2}{c^2}\right)^{1/2} & \text{for} \quad k > \frac{\omega}{c} \\ \mathrm{i}\left(\frac{\omega^2}{c^2} - K^2\right)^{1/2} & \text{for} \quad k < \frac{\omega}{c} \end{cases} \tag{3.221}$$

In the incompressible limit ($K_c \to K$), equation (3.220) reduces to

$$\hat{p}(\mathbf{K}, \omega) = -\rho \int_0^\infty \mathrm{e}^{-K y} \left[\left(\hat{T}_{33} - \mathrm{i}\, 2\hat{T}_{32} - \hat{T}_{22}\right) K + \mathrm{i}\, 2k_x \frac{U'}{\omega}\hat{T}_{32}\right] \mathrm{d}y \tag{3.222}$$

Equation (3.219) leads to an approximated form of the wall pressure wavenumber-frequency spectral density where the various cross-terms are neglected. It results that

$$P(\mathbf{K}, \omega) \simeq P_T + P_U \tag{3.223}$$

where the pure turbulence contribution P_T and the mean shear contribution P_U are respectively given by

$$P_T(\mathbf{K}, \omega) = \left(\frac{K}{|K_c|}\right)^2 P_{33} + 4P_{32} + \left(\frac{|K_c|}{K^2}\right)^2 P_{22} \tag{3.224}$$

with

$$P_{ij}(\mathbf{K}, \omega) = \rho^2 K^2 \int_0^\omega \mathrm{d}y \int_0^\omega \mathrm{d}y' \exp(-K_c^* y - K_c y')\, E_{ijij}(y, y', \mathbf{K}, \omega) \tag{3.225}$$

and

$$P_U(\mathbf{K}, \omega) = 4\rho^2 k_x^2 \left(\frac{K}{|K_c|}\right)^2 \omega^{-2}$$
$$\int_0^\infty \mathrm{d}y \int_0^\infty \mathrm{d}y' \exp\left(-k_x y - K_c y'\right) U'(y)\, U'(y')\, E_{3232}(y, y', \mathbf{K}, \omega) \tag{3.226}$$

The cross-spectral densities of the fluctuating velocity products are given by

$$E_{ijkl}(y, y', \mathbf{K}, \omega) = \frac{\overline{T^*_{ij}(y, \mathbf{K}, \omega)\, T_{kl}(y', \mathbf{K}', \omega')}}{\delta(K' - K)\, \delta(\omega - \omega')} \tag{3.227}$$

For the incompressible case, equation (3.222) yields

$$P_T(\mathbf{K}, \omega) = \rho^2 K^2 \int_0^\infty \mathrm{d}y \int_0^\infty \mathrm{d}y' \exp\left[-K\,(y' + y)\right] S(y, y', K, \omega) \tag{3.228}$$

$$P_U(\mathbf{K}, \omega) = 4\,\rho^2\, k_x^2\, \omega^{-2} \int_0^\infty \mathrm{d}y \int_0^\infty \mathrm{d}y' \exp\left[-K\,(y' + y)\right] U'(y)\, U'(y')\, E_{3232}(y, y', K, \omega) \tag{3.229}$$

where

$$S(y, y', K, \omega) = \frac{\overline{\hat{T}^*_s(y, \mathbf{K}, \omega)\, \hat{T}_s(y', \mathbf{K}', \omega')}}{\delta(K' - K)\, \delta(\omega - \omega')} \tag{3.230}$$

and

$$\hat{T}_s = \hat{T}_{33} - \hat{T}_{22} - \mathrm{i}\, 2\hat{T}_{32} \tag{3.231}$$

In 1980 Chase [101] proposed a four-dimensional orthotropic similarity model for the nonlinear source terms $S(y, y', \mathbf{K}, \omega)$ and $E_{3232}(y, y', \mathbf{K}, \omega)$. Furthermore, in a successive work, Chase [104] revisited such an earlier model and extended the analysis to the compressible case.

Suppose that the source layer is bounded in thickness with a scale $b\,\delta$, b being a constant that does not depend on the quantities $\mathbf{K}$ and ω. Then, let us assume an exponential profile for the source spectrum $S(y, y', \mathbf{K}, \omega)$ and let us write

$$S(y, y', \mathbf{K}, \omega) = \exp\left[-\frac{y + y'}{b\,\delta}\right] S^0(y, y', \mathbf{K}, \omega) \tag{3.232}$$

If the wave pattern is convected at a velocity u, which does not depend on y and y', both the velocity and the pressure spectra have a sharp convective ridge $\delta(\omega - u\,k_1)$, where $\omega' = \omega - u\,k_1$ denotes the frequency measured in the convected frame of reference. In a boundary-layer the wave interaction associated with the nonlinear terms in the Navier-Stokes equations induces a loss of time correlation in the convected frame. Let $h\,v^*$ denote a characteristic turbulence velocity, where h is a scale factor of unit order. It can be supposed that the correlation loss due to a time delay τ is comparable to the correlation loss due to a spatial separation $h\,v^*\tau$ in a plane parallel to the wall. Furthermore, in terms of statistical average, the correlation contributions due to space and time add quadratically. Hence, a space-time separation (ζ, τ) is equivalent to $\left(\sqrt{\zeta^2 + h^2 v^{*2} \tau^2}, 0\right)$. As a consequence, $S^0(y, y', \mathbf{K}, \omega)$ depends on $\mathbf{K}$ and ω only via the argument

$$K_+^2 = \frac{(\omega - u\,k_x)^2}{(h\,v^*)^2} + K^2 \tag{3.233}$$

A further restriction on the form of S^0 is given by the following transformation

$$S^0(y, y', \mathbf{K}, \omega) = \int_{-\infty}^{\infty} \mathrm{d}k_2 \exp\left[\mathrm{i}\,k_2\,(y' - y)\right] \sigma^0(\xi, \mathbf{k}, \omega) \tag{3.234}$$

where $\mathbf{k} = (k_1, k_2, k_3)$ and $\xi = (y\,y')^{1/2}$ is the geometric mean distance from the wall.

As done for the planar source spectrum S^0, the term $\sigma^0(\xi, \mathbf{k}, \omega)$ can be supposed to depend on $\mathbf{k}$ and ω via the argument $k_+^2 = k_2^2 + \gamma^2 K_+^2$, where γ is a constant.

The terms $\hat{T}_{ij}$ can be obtained by convolution of the Fourier transform of v_i and v_j, namely .

$$\hat{T}_{ij}(y, y', \mathbf{K}, \omega) = \int_{-\infty}^{\infty} \mathrm{d}^2\mathbf{K}' \int_{-\infty}^{\infty} \mathrm{d}\omega' \, \hat{v}_i(y, \mathbf{K}', \omega') \, \hat{v}_j(y, \mathbf{K} - \mathbf{K}', \omega - \omega') \tag{3.235}$$

In the subconvective domain ($k_1 \lesssim \omega/U$) the second integral in equation (3.235) can include a region where both $\hat{v}_i$ and $\hat{v}_j$ have a convective structure and the resulting spectral density of $\hat{T}_{ij}$ is relatively large. The necessary condition for the existence of such a region is

$$\left|\frac{\omega'}{k_1'}\right| \simeq u(y, \mathbf{k}') \quad \text{and} \tag{3.236}$$

$$\left|\frac{\omega' - \omega}{k_1'} - k_1\right| \simeq u(y, \mathbf{k}' - \mathbf{k}) \tag{3.237}$$

where u is a convection speed associated with the boundary-layer waves. Thus, supposing a domain where the spectra of the velocity products scale with the distance from the wall, and considering the frequency dependence in a mean convected frame yields

$$S^0(y, y', \mathbf{K}, \omega) = v^{*3} \, \xi^3 \, F_s\left(k_+ \, \xi, \frac{y'}{y}, \frac{\mathbf{K}}{k_+}\right) \tag{3.238}$$

and

$$\sigma^0(\xi, \mathbf{K}, \omega) = v^{*3} \, \xi^4 \, \phi_\sigma\left(k_+ \, \xi, \frac{k_2}{k_+}, \frac{\mathbf{K}}{k_+}\right) \tag{3.239}$$

The dependence of σ^0 on k_2/k_+ and $\mathbf{K}/k_+$ has not a significant effect on the integral expression (3.234). Hence, it can be written

$$\sigma^0(\xi, \mathbf{K}, \omega) = v^{*3} \, \xi^4 \, \phi(k_+ \, \xi) \tag{3.240}$$

From equations (3.228), (3.230), (3.238) and (3.240), the following expression for the pure turbulence contribution of the wall pressure spectral density can be obtained

$$P_T(\mathbf{K}, \omega) = \rho^2 \, K^2 \, v^{*3} \int_0^{\infty} \mathrm{d}y \int_0^{\infty} \mathrm{d}y' \mathrm{e}^{-K(y+y')} \mathrm{e}^{-\frac{y+y'}{b\delta}} \int_{-\infty}^{\infty} \mathrm{d}k_2 \, \mathrm{e}^{\mathrm{i}\, k_2(y'-y)} \, \xi^4 \, \phi(k_+ \xi) \tag{3.241}$$

Changing to variables $\zeta_2 = y' - y$ and $\xi = \sqrt{y\, y'}$, provided that

$$\int_0^{\infty} \mathrm{d}y \int_0^{\infty} \mathrm{d}y' = 2 \int_0^{\infty} \xi \, \mathrm{d}\xi \int_{-\infty}^{\infty} \left(\zeta_2^2 + 4\xi^2\right)^{-1/2} \mathrm{d}\zeta_2 \quad \text{and} \tag{3.242}$$

$$y + y' = \left(\zeta_2^2 + 4\xi^2\right)^{1/2} \tag{3.243}$$

the pure turbulence contribution of the wall pressure spectral density takes the form

$$\begin{aligned} P_T(\mathbf{K}, \omega) &= 2\rho^2 K^2 v^{*3} \int_0^{\infty} \mathrm{d}\xi \, \xi \\ &\int_{-\infty}^{\infty} \mathrm{d}\zeta_2 \left(\zeta_2^2 + 4\,\xi^2\right)^{-1/2} \exp\left[-\left(K + \frac{1}{b\,\delta}\right) \left(\zeta_2^2 + 4\,\xi^2\right)^{1/2}\right] \\ &\int_{-\infty}^{\infty} \mathrm{d}k_2 \, \mathrm{e}^{\mathrm{i}\, k_2 \zeta_2} \, \xi^4 \, \phi(k_+ \, \xi) = \\ &= 2\,\rho^2 \, K^2 \, v^{*3} \int_{-\infty}^{\infty} \mathrm{d}k_2 \int_0^{\infty} \mathrm{d}\xi \, \xi^5 \, \phi(k_+ \, \xi) \\ &\int_{-\infty}^{\infty} \mathrm{d}\zeta_2 \left(\zeta_2^2 + 4\,\xi^2\right)^{-1/2} \exp\left[-\left(K + \frac{1}{b\,\delta}\right) \left(\zeta_2^2 + 4\,\xi^2\right)^{1/2}\right] \mathrm{e}^{\mathrm{i}\, k_2 \zeta_2} \end{aligned} \tag{3.244}$$

The following identity is verified

$$\int_{-\infty}^{\infty} \mathrm{d}\zeta_2 \left(\zeta_2^2 + 4\xi^2\right)^{-1/2} \exp\left[-\beta \left(\zeta_2^2 + 4\xi^2\right)^{1/2}\right] \exp\left[\mathrm{i}\,(k_2 + \alpha)\,\zeta_2\right] =$$
$$= 2K_0\left(2\xi \left[(k_2 + \alpha)^2 + \beta^2\right]^{1/2}\right) \tag{3.245}$$

where K_0 denotes the modified Bessel function. Thus, since $\alpha = 0$ and $\beta = K + 1/b\delta$ in equation (3.244), it results that

$$P_T(\mathbf{K}, \omega) = 4\,\rho^2\, K^2\, v^{*3} \int_{-\infty}^{\infty} \mathrm{d}k_2 \int_0^{\infty} \mathrm{d}\xi\, \xi^5\, \phi(k_+\xi)\; K_0\left(2\,\xi \left[\left(k_2^2 + \left(k + \frac{1}{b\,\delta}\right)^2\right)^{1/2}\right]\right) \tag{3.246}$$

By assuming a decreasing behaviour of the function $\phi(k_+\xi)$ at large values of its argument, that is $\phi(z) \simeq (1+z)^{-\lambda}$ ($\phi(z) \simeq 1$ for $z \lesssim 1$, $\phi(z) \simeq z^{-\lambda}$ for $z \gtrsim 1$), the pure turbulence contribution to the wall pressure spectrum in the incompressible limit takes the form

$$P_T(\mathbf{K}, \omega) = C_T\, \rho^2\, v^{*3}\, K^2 \left[K_+^2\; + (b\,\delta)^{-2}\right]^{-5/2} \quad \text{if} \quad \lambda > 5 \tag{3.247}$$

$$P_T(\mathbf{K}, \omega) = C_T\, \rho^2\, v^{*3}\, K^2 \left[K^2\; + (b\,\delta)^{-2}\right]^{-(5-\lambda)/2}$$
$$\left[K_+^2\; + (b_0\,\delta)^{-2}\right]^{-\lambda/2} \quad \text{if} \quad \lambda < 5 \tag{3.248}$$

where C_T is a constant factor and b_0 is a scale coefficient of the same order of b. If $\lambda = 3$ it results that

$$P_T(\mathbf{K}, \omega) = C_T\, \rho^2\, v^{*3}\, \frac{K^2}{K^2 + (b\,\delta)^{-2}}\, \frac{1}{\left[K^2 + \left(\frac{\omega - u\,k_x}{h\,v^*}\right)^2 + (b_0\,\delta)^{-2}\right]^{3/2}} \tag{3.249}$$

In the range $(b\,\delta)^{-1} \lesssim K \lesssim \omega/U_\infty + (b_0\,\delta)^{-1}$ the wall pressure spectrum takes the *white wavevector* form

$$P_T(\mathbf{K}, \omega) = \frac{C_T\, \rho^2\, v^{*3}}{\left[(\omega/h\,v^*)^2 + (b_0\,\delta)^{-2}\right]^{3/2}} \tag{3.250}$$

In the same range of K and for $\lambda < 5$ it results that

$$P_T(\mathbf{K}, \omega) = C_T\, \rho^2\, v^{*3}\, K^{\lambda-3} \left[(\omega/h\,v^*)^2 + (b_0\,\delta)^{-2}\right]^{-\lambda/2} \tag{3.251}$$

which shows that P_T varies as $K^{\lambda-3}$.

Equation (3.240) shows that, if $K_+\,\xi \gtrsim 1$, then

$$\sigma^0(\xi, \mathbf{K}, \omega) \simeq v^{*3}\, \xi^{(4-\lambda)}\, K_+^{-\lambda} \tag{3.252}$$

If $\lambda \lesssim 4$, then the integral of $\sigma^0(\xi, \mathbf{K}, \omega)$ over the three-dimensional wavevector and the frequency domains diverges. Furthermore, if $\lambda = 4$ then the divergence is logarithmic.

Consider now the mean shear contribution P_U in equation (3.229). Assuming a logarithmic wall layer profile yields

$$U'(y)\, U'(y') = \left(\frac{Av^*}{y}\right) \left(\frac{Av^*}{y'}\right) = A^2 v^{*2} \xi^{-2} \tag{3.253}$$

where $A \simeq 2.5$. Thus, substituting into equation (3.229) provides

$$P_U(\mathbf{K},\omega) = 4\,\rho^2\,k_x^2\,\omega^{-2}\,A^2\,v^{*2}\int_0^\infty \mathrm{d}y \int_0^\infty \mathrm{d}y'\,\mathrm{e}^{-K(y+y')}\,\xi^{-2}\,E_{3232}(y,y',\mathbf{K},\omega) \tag{3.254}$$

Then, using for $E_{3232}(y,y',\mathbf{K},\omega)$ the same modeling procedure used to describe the function $S(y,y',\mathbf{K},\omega)$ provides

$$P_U(\mathbf{K},\omega) = 16\,A^2\,\rho^2\,v^{*3}\left(\frac{v^*\,k_x}{\omega}\right)^2\int_0^\infty \mathrm{d}k_2\int_0^\infty \mathrm{d}\xi\,\xi^3\,\phi_{32}(k_+\,\xi)\,K_0\left(2\,\xi\sqrt{k_2^2+\left(k+\frac{1}{b\,\delta}\right)^2}\right) \tag{3.255}$$

Supposing that the term $\phi_{32}(k_+\,\xi)$ have the same decreasing behaviour of $\phi(k_+\,\xi)$ for $\lambda \geq 3$ and integrating equation (3.255) yields

$$P_U(\mathbf{K},\omega) = C_U\,\rho^2\,v^{*3}\,k_x^2\,K^2\left(\frac{v^*}{\omega}\right)^2\left[K_+^2\,+(b_0\,\delta)^{-2}\right]^{-3/2} \tag{3.256}$$

where b_0 is a scale parameter which may differ only slightly from the equivalent parameter b_0 in the pure turbulence contribution P_T.

The slightly compressibility condition requires that $|k_x|\,U_\infty/\omega \ll 1$ then, equation (3.233) yields $K_+ \simeq \omega/h\,v^*$. Equivalently, if $K_+\,b_0\,\delta \gtrsim 1$, then $(v^*\,\omega)^2 \simeq \left[K_+\,+(b_0\,\delta)^{-2}\right]^{-1}$. Hence, for $\lambda \geq 3$, the mean shear contribution to the wall pressure spectrum takes the form

$$P_U(\mathbf{K},\omega) = C_U\,\rho^2\,v^{*3}\,k_x^2\,K^2\left[K_+^2\,+(b_0\,\delta)^{-2}\right]^{-5/2} \tag{3.257}$$

Finally, by adding the pure turbulence and the mean shear contributions, the wall pressure spectrum takes the form

$$P(\mathbf{K},\omega) = \frac{\rho^2\,v^{*3}}{\left[K_+^2\,+(b_0\,\delta)^{-2}\right]^{5/2}}\left\{C_T\,K^2\left[\frac{K_+^2\,+(b_0\,\delta)^{-2}}{K^2+(b\,\delta)^{-2}}\right]^{\frac{5-\lambda}{2}}+C_U\,k_x^2\right\}\quad \text{for}\quad 3\leq\lambda<5 \tag{3.258}$$

$$P(\mathbf{K},\omega) = \frac{\rho^2\,v^{*3}}{\left[K_+^2\,+(b_0\,\delta)^{-2}\right]^{5/2}}\left\{C_T\,K^2+C_U\,k_x^2\right\}\quad \text{for}\quad \lambda>5 \tag{3.259}$$

Consider now the slightly compressible case. The four-dimensional orthotropic similarity model applied to describe the source spectra $S(y,y',\mathbf{K},\omega)$ and $E_{3232}(y,y',\mathbf{K},\omega)$ (see equation (3.232) for S), can be adopted for each source component E_{ijij} in equation (3.225). By supposing that the source spectra E_{2222}, E_{3333} and E_{3232} are in the ratio of the constants C_2, C_3 and $(1-C_2-C_3)/4$, with $0 \leq C_i \leq 1$, and by supposing that the flow compressibility affects the pressure spectral density only via the term $K/|K_c|$ in equation (3.224), the slightly compressible extension of equations (3.258) and (3.259) is

$$P(\mathbf{K},\omega) = \frac{\rho^2\,v^{*3}}{\left[K_+^2\,+(b_0\,\delta)^{-2}\right]^{5/2}}$$
$$\left[C_2\left(\frac{|K_c|}{K}\right)^2+C_3\left(\frac{|K_c|}{K}\right)^{-2}+1-C_2-C_3\right]C_T\,K^2\left[\frac{K_+^2\,+(b_0\,\delta)^{-2}}{K^2+(b\,\delta)^{-2}}\right]^{\frac{5-\lambda}{2}}$$

$$+\frac{\rho^2\, v^{*3}}{\left[K_+^2\, + (b_0\, \delta)^{-2}\right]^{5/2}}\, C_U \left(\frac{|K_c|}{K}\right)^{-2} k_x^2 \qquad \text{for} \quad 3 \leq \lambda < 5 \tag{3.260}$$

$$P(\mathbf{K},\omega) = \frac{\rho^2\, v^{*3}}{\left[K_+^2\, + (b_0\, \delta)^{-2}\right]^{5/2}} \left[C_2 \left(\frac{|K_c|}{K}\right)^{2} + C_3 \left(\frac{|K_c|}{K}\right)^{-2} + 1 - C_2 - C_3\right] C_T\, K^2$$

$$+\frac{\rho^2\, v^{*3}}{\left[K_+^2\, + (b_0\, \delta)^{-2}\right]^{5/2}}\, C_U \left(\frac{|K_c|}{K}\right)^{-2} k_x^2 \qquad \text{for} \quad \lambda > 5 \tag{3.261}$$

It can be noticed that, if $C_2 \neq 0$, the wall pressure spectrum does not vanish at a zero wavenumber. Furthermore, if the spectra E_{ijij} are supposed to be equal ($C_2 = C_3 = 1/6$) then for $K = 0$ the term $C_2\, |K_c|^2$ in equation (3.261) is equal to $C_2\, \omega^2/c^2$. In this case the wall pressure spectrum takes the same structural limit form given by the term proportional to a_1 in equation (3.177) obtained by Ffowcs Williams [102].

The wall pressure wavenumber-frequency spectrum can be used to define some statistical functions. Then, comparing these functions with experimental data allows the constant quantities in equations (3.259) and (3.261) to be determined.

From the simplified form of equation (3.259) ($\lambda = 3$, $b_0 = b$)

$$P(\mathbf{K},\omega) = \frac{\rho^2 v^{*3}}{\left[K_+^2 + (b\delta)^{-2}\right]^{5/2}} \left\{ C_T K^2 \left[\frac{K_+^2 + (b\delta)^{-2}}{K^2 + (b\delta)^{-2}}\right] + C_U k_x^2 \right\} \tag{3.262}$$

Chase [104] obtained the space/frequency cross-spectrum, the wall pressure spectrum and the space-time pressure correlation at zero time delay. Then, comparing these statistical quantities with experimental data, Chase obtained the following values of the constant quantities

$$h = 3 \qquad C_T h = 0.014 \qquad C_U h = 0.466 \qquad b = 0.75 \tag{3.263}$$

where the constant h enters the definition (3.233).

4

Gust-Response Aerodynamic Theories

4.1 Introduction

The interest in the aerodynamic response of an airfoil embedded in a vortical flow arose in the 1920s when higher flight speeds required the aerodynamic unsteady loadings to be predicted and the aeroelasticity problems to be accurately solved. The earlier models dealt with thin airfoils of infinite span, embedded at zero angle of attack in a uniform parallel incompressible flow, with harmonic velocity disturbances imposed upstream and convected without distortion.

By considering only small amplitude disturbances, it is possible to linearize the unsteady aerodynamic problem with respect to the steady mean flow. This permits to uncouple the time-dependent component of the flow from the steady component. The problem becomes that of finding an irrotational and solenoidal flow satisfying some boundary conditions on the airfoil surface, the Kelvin's conservation theorem of the total flow circulation, and the Kutta condition at the airfoil trailing edge. The circulation around the airfoil changes in response to any flow unsteadiness, as required by the Kutta condition to be instantaneously fulfilled. Consequently, vortices are shed from the trailing edge in order to ensure the conservation of the total flow circulation. Thus, the airfoil wake represents a recorded history of the unsteady flow around the airfoil and the velocity field depends on the entire history of such flow.

An unsteady airfoil theory for incompressible flows based on the concepts of circulation theory [5] was proposed by von Kármán & Sears [123]. This theory recovers the results predicted by Theodorsen [124] for a linearized sinusoidally oscillatory motion of a flat-plate, and some primary results obtained by Küssner [125].

On the base of von Kármán & Sears' [123] unsteady airfoil theory, Sears [126] derived an analytical expression for the unsteady lift induced by a vortical sinusoidal gust convected past a thin airfoil. Later on, Filotas [127] extended Sears' analysis to an oblique sinusoidal gust.

The mathematical treatment of a linearized gust-airfoil interaction problem consists in splitting the velocity field into the sum of a solenoidal (rotational) part and a potential (irrotational) part, as described in section 1.5. The solenoidal part is a known function of the imposed upstream disturbances and represents a vortical wave decoupled by the steady-state aerodynamic field. The potential part is an unknown function of both the mean flow and the vortical disturbances. The solenoidal and the potential parts are coupled by the boundary conditions on the airfoil surface. For a compressible flow the potential part of the unsteady velocity field is governed by a constant coefficient, homogeneous, convective wave equation that reduces to a Laplace's equation if the flow is supposed to be incompressible.

Theoretical analyses of the unsteady aerodynamic field past an airfoil in a compressible flow were performed by Possio [128] and by Amiet [129, 130]. The former obtained an integral equation relating the pressure field on the surface of a thin airfoil to a sinusoidally fluctuating velocity field around the airfoil. The latter proposed analytical procedures for the gust-airfoil interaction problem in the high-and low-frequency limit.

The mean steady flow about a real airfoil with nonzero thickness, camber and angle of attack is no longer a parallel uniform flow. Goldstein & Atassi [131] developed a second order theory for the gust-airfoil interaction problem that accounts for the dependence of the unsteady velocity field on the mean potential flow around the airfoil. They showed that the vortical waves are distorted by the mean flow around the airfoil and that the distortion affects significantly both the amplitude and the phase of the unsteady velocity field. In the case of a thin airfoil with small angle of attack and camber, Goldstein & Atassi's second order theory provides explicit analytical formulae for the unsteady lift induced by longitudinal and transverse gusts.

4.2 Possio's Integral Equation

In 1938 Possio [128], making use of the acceleration potential, obtained an integral equation for the pressure jump across a flat-plate oscillating in a compressible stream. In this subsection the same equation will be obtained by means of the velocity potential.

A flat-plate of chord l and equation $z = z_s(x)\exp(-\mathrm{i}\,\omega t)$, oscillating at the frequency ω, can be described by a distribution of two-dimensional acoustic dipoles whose potential field has the form

$$\phi(x,z) = \frac{\mathrm{i}\, z\beta_\infty}{4}\int_0^l a(\xi)\,\frac{\lambda H_1^{(2)}(\lambda)\,\mathrm{e}^{\mathrm{i}\,\mu(x-\xi)}}{(x-\xi)^2+\beta_\infty^2 z^2}\,\mathrm{d}\xi \tag{4.1}$$

where $a(\xi)$ is the complex amplitude of the dipole distribution and where

$$\lambda = \frac{\omega\sqrt{(x-\xi)^2+\beta_\infty^2 z^2}}{\beta_\infty^2 c_\infty} \tag{4.2}$$

$$\mu = \frac{\omega M_\infty}{\beta_\infty^2 c_\infty} \tag{4.3}$$

with $\beta_\infty^2 = 1 - M_\infty^2$. The amplitude a of the dipole distribution can be related to the pressure jump across the airfoil surface by applying the linearized pressure equation to the dipole distribution (4.1), and by subtracting the limit as $z \to 0^+$ to the limit as $z \to 0^-$. It thus results that

$$\Delta p(x) = -\rho_\infty a(\xi) \tag{4.4}$$

The next step is to impose the linearized slip condition

$$w(x) = \mathrm{i}\,\omega z_s(x) + V_\infty \frac{\mathrm{d}z_s}{\mathrm{d}x} \tag{4.5}$$

on the flat-plate, $w(x)$ denoting the complex amplitude of the surface velocity in the z-direction. Therefore, considering that

$$w(x) = \frac{\partial\phi}{\partial z} \tag{4.6}$$

yields Possio's equation

$$w(\overline{x}) = -\frac{1}{\rho V_\infty}\int_0^1 \Delta p(\overline{\xi})\, K(\overline{x}-\overline{\xi}, M_\infty, \overline{\omega})\,\mathrm{d}\overline{\xi} \quad \text{with} \tag{4.7}$$

$$\begin{aligned} K(\overline{\xi}', M_\infty, \overline{\omega}) &= \frac{\overline{\omega}}{4\beta_\infty}\mathrm{e}^{\mathrm{i}\overline{\omega} M_\infty^2 \overline{\xi}'/\beta_\infty^2}\left[\frac{\mathrm{i}\, M_\infty \overline{\xi}'}{|\overline{\xi}'|} H_1^{(2)}\left(\frac{\overline{\omega} M_\infty |\overline{\xi}'|}{\beta_\infty^2}\right) - H_0^{(2)}\left(\frac{\overline{\omega} M_\infty |\overline{\xi}'|}{\beta_infty^2}\right)\right] \\ &+ \frac{\mathrm{i}\,\overline{\omega}\beta_\infty}{4}\mathrm{e}^{-\mathrm{i}\overline{\omega}\overline{\xi}'}\left[\frac{2}{\pi\beta_\infty}\ln\left(\frac{1+\beta_\infty}{M_\infty}\right) + \int_0^{\overline{\omega}\overline{\xi}'/\beta_\infty} \mathrm{e}^{\mathrm{i}\,\nu} H_0^{(2)}(M_\infty |\nu|)\,\mathrm{d}\nu\right] \end{aligned} \tag{4.8}$$

where $\overline{x} = x/l$, $\overline{\xi} = \xi/l$, $\overline{\xi}' = \overline{x} - \overline{\xi}$ and $\overline{\omega} = \omega l/V_\infty$.

4.3 Sears' Gust-Response Solution

In 1938 von Kármán & Sears [123] obtained formulae for the lift and the moment of a two-dimensional flat-plate in an arbitrary unsteady flow. Later on the analysis was applied by Sears [126] to determine the unsteady lift and the moment exerted on a thin airfoil passing through a sinusoidal upwash gust.

Von Kármán & Sears' theory exploits the basic concepts of the circulation theory [5], according to which the total circulation around an airfoil in nonuniform motion vary, and vorticity is shed from the trailing edge into the field. The analysis is based on a flat-wake hypothesis which is satisfied by a small amplitude oscillating airfoil. A conformal mapping technique is used to describe the unsteady aerodynamic field around a rigid two-dimensional flat-plate. The flow is supposed to be incompressible and inviscid.

Consider an infinite-span flat-plate extending from -1 to 1 in the streamwise direction. The airfoil wake extends from 1 to ∞ on the plane of the plate. The vorticity distribution over the plate is composed by a *quasi-steady* contribution $\gamma_0(x)$, which would be produced by the plate motion if the wake had no effect, and by a vorticity distribution $\gamma_1(x)$ induced by the wake. Equivalently, the circulation Γ around the flat-plate has a quasi-steady contribution Γ_0 and a wake contribution Γ_1.

The vorticity distribution $\mathrm{d}\gamma_1(x)$ induced by a wake segment of intensity $\gamma(\xi)\,\mathrm{d}\xi$ and satisfying the zero velocity Kutta condition is given by

$$\mathrm{d}\gamma_1(x) = \frac{1}{\pi}\frac{\gamma(\xi)\,\mathrm{d}\xi}{\xi - x}\sqrt{\frac{1-x}{1+x}}\sqrt{\frac{\xi+1}{\xi-1}} \tag{4.9}$$

Integrating over the length of the wake yields the wake contribution to the vorticity distribution

$$\gamma_1(x) = \frac{1}{\pi}\sqrt{\frac{1-x}{1+x}}\int_1^\infty \frac{\gamma(\xi)}{\xi - x}\sqrt{\frac{\xi+1}{\xi-1}}\,\mathrm{d}\xi \tag{4.10}$$

Furthermore, the wake contribution to the airfoil circulation can be obtained by integrating the vorticity distribution (4.10) over the flat-plate. It thus results that

$$\Gamma_1 = \int_1^\infty \left(\sqrt{\frac{\xi+1}{\xi-1}} - 1\right)\gamma(\xi)\;\mathrm{d}\xi \tag{4.11}$$

The total circulation of the airfoil-wake system must vanish. Thus

$$\Gamma_0 + \Gamma_1 + \int_1^\infty \gamma(\xi)\;\mathrm{d}\xi = 0 \tag{4.12}$$

and, by using equation (4.11),

$$\Gamma_0 + \int_1^\infty \sqrt{\frac{\xi+1}{\xi-1}}\gamma(\xi)\;\mathrm{d}\xi = 0 \tag{4.13}$$

The total momentum[1] of a vortex distribution on both the flat-plate and its wake is given by

$$\begin{aligned} I &= \rho\int_{-1}^1 (\gamma_0(x) + \gamma_1(x))\,x\,\mathrm{d}x + \rho\int_1^\infty \gamma(\xi)\,\xi\,\mathrm{d}\xi \\ &= \rho\int_{-1}^1 \gamma_0(x)\,x\,\mathrm{d}x + \frac{\rho}{\pi}\int_{-1}^1 \sqrt{\frac{1-x}{1+x}}x\,\mathrm{d}x\int_1^\infty \frac{\gamma(\xi)}{\xi - x}\sqrt{\frac{\xi+1}{\xi-1}}\,\mathrm{d}\xi + \rho\int_1^\infty \gamma(\xi)\,\xi\,\mathrm{d}\xi \\ &= \rho\int_{-1}^1 \gamma_0(x)\,x\,\mathrm{d}x + \rho\int_1^\infty \gamma(\xi)\,\sqrt{\xi^2-1}\,\mathrm{d}\xi \end{aligned} \tag{4.14}$$

[1] In literature the same quantity is usually referred to as *hydrodynamic impulse*.

where use of (4.10) has been made.

The lift exerted on the flat-plate is the time derivative of the total momentum, namely

$$L = -\frac{\mathrm{d}I}{\mathrm{d}t} \tag{4.15}$$

In order to carry out the time derivative of the wake contribution to the total momentum (4.14), consider the generic integral of form

$$A = \int_1^{1+V_\infty t} \gamma(\xi)\, f(\xi)\, \mathrm{d}\xi \tag{4.16}$$

which represents a generic contribution at the instant t generated by a wake convected at the velocity V_∞. The wake can be supposed to be stationary relative to the fluid, whereas the airfoil translates at the velocity V_∞. Therefore, space and time can be considered as two explicit forms of the same convective variable $(x - V_\infty t)$. It is convenient to express γ in a body frame of reference by means of the Galilean transformation $\sigma = -\xi + 1 + V_\infty t$. Hence, the generic integral (4.16) takes the form

$$A = \int_0^{V_\infty t} \gamma(\sigma)\, f(\sigma, t)\, \mathrm{d}\sigma \tag{4.17}$$

Now, if $f(\sigma = V_\infty t, t) = 0$ then the time derivative of (4.17) takes the form

$$\frac{\mathrm{d}A}{\mathrm{d}t} = \int_0^{V_\infty t} \gamma(\sigma) \left(\frac{\partial f}{\partial t}\right)_\sigma \mathrm{d}\sigma \tag{4.18}$$

and changing back to the variable ξ yields

$$\frac{\mathrm{d}A}{\mathrm{d}t} = V_\infty \int_1^{1+V_\infty t} \gamma(\xi)\, \frac{\partial f}{\partial \xi}\, \mathrm{d}\xi \tag{4.19}$$

This result can be used to differentiate the total momentum (4.14) and to obtain the lift expression

$$L = -\rho\frac{\mathrm{d}}{\mathrm{d}t}\int_{-1}^{1} \gamma_0(x)\, x\, \mathrm{d}x - \rho V_\infty \int_1^\infty \frac{\gamma(\xi)\,\xi}{\sqrt{\xi^2 - 1}}\, \mathrm{d}\xi \tag{4.20}$$

Finally, using the condition (4.13) that the total circulation must vanish, the lift can be also written in the form

$$L = -\rho\frac{\mathrm{d}}{\mathrm{d}t}\int_{-1}^{1} \gamma_0(x)\, x\, \mathrm{d}x + \rho V_\infty \Gamma_0 + \rho V_\infty \int_1^\infty \frac{\gamma(\xi)}{\sqrt{\xi^2 - 1}}\, \mathrm{d}\xi \tag{4.21}$$

This shows that the lift is composed by three contributions:

1. the quasi-steady contribution, i.e.

$$L_0 = \rho V_\infty \Gamma_0 \tag{4.22}$$

2. the apparent mass contribution, i.e.

$$L_1 = -\rho\frac{\mathrm{d}}{\mathrm{d}t}\int_{-1}^{1} \gamma_0(x)\, x\, \mathrm{d}x \tag{4.23}$$

3. the wake contribution, i.e.

$$L_2 = \rho V_\infty \int_1^\infty \frac{\gamma(\xi)}{\sqrt{\xi^2 - 1}}\, \mathrm{d}\xi \tag{4.24}$$

If the motion of the flat-plate is periodic, both the quasi-steady circulation Γ_0 and the wake vorticity distribution are periodic, the latter being convected at the free-stream velocity V_∞. Thus, let us write

$$\Gamma_0 = G_0\, \mathrm{e}^{\mathrm{i}\,\omega t} \tag{4.25}$$

$$\gamma(\xi) = g\, \mathrm{e}^{\mathrm{i}\,\omega t}\, \mathrm{e}^{-\mathrm{i}\,\omega\xi/V_\infty} \tag{4.26}$$

where G_0 and g are constant. Hence, the quasi-steady and apparent-mass lift contributions are given by

$$L_0 = \rho V_\infty\, G_0\, \mathrm{e}^{\mathrm{i}\,\omega t} \tag{4.27}$$

$$L_1 = -\mathrm{i}\,\omega\rho\, \mathrm{e}^{\mathrm{i}\,\omega t} \int_{-1}^{1} g(x)\, x\, \mathrm{d}x \tag{4.28}$$

with

$$G_0 = \int_{-1}^{1} g_0(x)\ \mathrm{d}x \tag{4.29}$$

From equation (4.11) it follows that the total circulation around the airfoil is given by

$$\Gamma_a = \Gamma_0 + \Gamma_1 = \mathrm{e}^{\mathrm{i}\,\omega t} \left\{ G_0 + g \int_1^\infty \left(\sqrt{\frac{\xi+1}{\xi-1}} - 1 \right) e^{-\mathrm{i}\,\omega\xi/V_\infty}\, \mathrm{d}\xi \right\} \tag{4.30}$$

Since the total circulation of the system must be constant, an increment of circulation $\mathrm{d}\Gamma_a$ must be canceled by a wake vortical element shed from the trailing edge in the time interval $\mathrm{d}t$, namely

$$\mathrm{d}\Gamma_a = -\gamma(1)\, V_\infty\, dt \tag{4.31}$$

Thus, from equation (4.30) and the edge condition (4.31) the following relation between G_0 and g can be obtained

$$-\frac{G_0}{g} = \int_1^\infty \left(\frac{1+\xi}{\sqrt{\xi^2-1}} - 1 \right) e^{-\mathrm{i}\,\omega\xi/V_\infty}\, \mathrm{d}\xi + \frac{V_\infty}{\mathrm{i}\,\omega} \mathrm{e}^{-\mathrm{i}\,\omega/V_\infty} \tag{4.32}$$

$$= K_0(\mathrm{i}\,\omega/V_\infty) + K_1(\mathrm{i}\,\omega/V_\infty) \tag{4.33}$$

where K_0 and K_1 denote the modified Bessel functions of second kind.

Finally, substituting γ from (4.26), with g obtained from (4.33), into the wake contribution (4.24), yields

$$L_2 = -\rho V_\infty G_0 \mathrm{e}^{\mathrm{i}\,\omega t} \frac{K_0(\mathrm{i}\,\omega/V_\infty)}{K_0(\mathrm{i}\,\omega/V_\infty) + K_1(\mathrm{i}\,\omega/V_\infty)} \tag{4.34}$$

The three lift contributions (4.27), (4.28) and (4.34) provide the airfoil response to a generic periodic motion.

Consider a thin airfoil of chord l with upwash velocity w measured positive downward, namely

$$w = V_\infty \mathrm{e}^{\mathrm{i}\,\omega t} \left\{ A_0 + 2 \sum_{n=1}^{\infty} A_n \cos(n\theta) \right\} \tag{4.35}$$

where θ is related to x through the following expression

$$x = \frac{l}{2} \cos\theta \tag{4.36}$$

The resulting total lift acting on the airfoil is given by

$$L = \pi\rho l V_\infty^2 \mathrm{e}^{\mathrm{i}\,\omega t} \left\{ (A_0 + A_1)\, C(\omega^*/2) + (A_0 - A_2)\, \mathrm{i}\,\omega^*/4 \right\} \tag{4.37}$$

where $\omega^* = \omega l/V_\infty$ denotes the reduced frequency and

$$C(\omega^*/2) = \frac{K_1(\mathrm{i}\,\omega^*/2)}{K_0(\mathrm{i}\,\omega^*/2) + K_1(\mathrm{i}\,\omega^*/2)} \tag{4.38}$$

is the complex Theodorsen's function.

The total lift expression (4.37) can be also used to determine the response of an airfoil at rest to a convected sinusoidal gust of form

$$v(x,t) = W \mathrm{e}^{\mathrm{i}\,\omega(t - x/V_\infty)} = W \mathrm{e}^{\mathrm{i}\,\omega t} \mathrm{e}^{-\mathrm{i}\,\frac{\omega^*}{2}\cos\theta} \tag{4.39}$$

where the upwash velocity v is measured positive upward. By exploiting the identity

$$\mathrm{e}^{\mathrm{i}\,z\cos\theta} = J_0(z) + 2\sum_{n=1}^{\infty} \mathrm{i}^{\,n}\, J_n(z)\cos(n\theta) \tag{4.40}$$

where $J_n(z)$ denotes the Bessel function of first kind and order n, the sinusoidal gust (4.39) takes the form

$$v(x,t) = W \mathrm{e}^{\mathrm{i}\,\omega t} \left\{ J_0(\omega^*/2) + 2\sum_{n=1}^{\infty} (-\mathrm{i})^n\, J_n(z)\cos(n\theta) \right\} \tag{4.41}$$

where use of the property $J_n(-z) = (-1)^n J_n(z)$ has been made. Comparing the velocity expressions (4.35) and (4.39) yields

$$A_0 = \frac{W}{U_\infty} J_0(\omega^*/2) \tag{4.42}$$

$$A_n = (-\mathrm{i})^n \frac{W}{U_\infty} J_n(\omega^*/2) \quad \text{for} \quad n \geq 1 \tag{4.43}$$

Therefore, the lift expression (4.37) takes the form of an airfoil lift response to a vertical sinusoidal gust, namely

$$L = \pi\rho l V_\infty W \mathrm{e}^{\mathrm{i}\,\omega t} \{ [J_0(\omega^*/2) - \mathrm{i}\, J_1(\omega^*/2)]\, C(\omega^*/2) + [J_0(\omega^*/2) + J_2(\omega^*/2)]\, \mathrm{i}\,\omega^*/4 \} \tag{4.44}$$

Finally, using the recurrence formula

$$2n\, J_n(z) = J_{n-1}(z) + J_{n+1}(z) \tag{4.45}$$

the airfoil response (4.44) can be written as

$$L = \pi\rho l V_\infty W e^{\mathrm{i}\,\omega t} S(\omega^*/2) \tag{4.46}$$

where

$$S(\omega^*/2) = [J_0(\omega^*/2) - \mathrm{i}\, J_1(\omega^*/2)]\, C(\omega^*/2) + \mathrm{i}\, J_1(\omega^*/2) \tag{4.47}$$

is the well-known Sears' function.

In 1936 Küssner [125] in Germany and contemporarily Cicala [132] in Italy calculated the lift acting on a vertically oscillating airfoil by applying a thin airfoil theory. Their analysis can be now applied in order to determine the local pressure jump induced on the airfoil surface by a convected harmonic gust.

The vorticity distribution along a thin airfoil is the solution of an integral equation resulting from the imposition of the slip condition on the airfoil surface and satisfying the Kutta condition at the trailing edge. By assuming a small amplitude periodic motion, the integral equation takes the form

$$w(x) = \frac{1}{2\pi} \int_{-l/2}^{l/2} \left[\frac{1}{x - \xi} - \frac{\mathrm{i}\,\omega}{V_\infty} \int_{\xi}^{\infty} \frac{e^{-\mathrm{i}\,\omega(\xi' - \xi)/V_\infty}}{x - \xi'}\, \mathrm{d}\xi \right] \gamma(\xi)\, \mathrm{d}\xi \tag{4.48}$$

where w is measured positive downward and is given by (4.35). Following Glauert [133], the vorticity distribution can be expanded in the series

$$\gamma(\theta) = -V_\infty \left\{ 2B_0 \tan(\theta/2) + 4 \sum_{n=1}^{\infty} B_n \frac{\sin(n\theta)}{n} \right\} \tag{4.49}$$

which intrinsically satisfies the Kutta condition at the trailing edge. Thus, by introducing the expansion (4.49) into the integral equation (4.48), the expansion coefficients take the form

$$B_0 = -C(\omega^*/2)\,(A_0 + A_1) + A_1 \tag{4.50}$$

$$B_n = -\frac{\mathrm{i}\,\omega^*}{4} A_{n-1} - nA_n + \frac{\mathrm{i}\,\omega^*}{4} A_{n+1} \quad \text{for} \quad n \geq 1 \tag{4.51}$$

Then, substituting (4.42) and (4.43) into (4.50) and (4.51), and applying the recurrence rule (4.45) give

$$B_0 = -C(\omega^*/2)\,\frac{W}{U_\infty}\,(J_0(\omega^*/2) - \mathrm{i}\,J_1(\omega^*/2)) - \mathrm{i}\,\frac{W}{U_\infty} J_1(\omega^*/2) \tag{4.52}$$

$$B_n = 0 \tag{4.53}$$

As a result, the vorticity distribution takes the form

$$\gamma(\theta) = 2W \tan(\theta/2)\, S(\omega^*/2) \tag{4.54}$$

and the pressure jump across the airfoil surface is given by

$$\Delta p(x,t) = \rho V_\infty \gamma(\theta)\, \mathrm{e}^{\mathrm{i}\,\omega t} = 2\rho V_\infty W \sqrt{\frac{1 - 2x/l}{1 + 2x/l}}\, S(\omega^*/2)\, \mathrm{e}^{\mathrm{i}\,\omega t} \tag{4.55}$$

4.4 Filotas' Model of Oblique Gust-Airfoil Interaction

Filotas [134], following the analysis of Chu & Widnall [135], generalized the Sears' gust response solution to an infinite-span wing flying subsonically through a sinusoidal gust at an arbitrary skew angle.

Consider an oblique Sears-type gust of reduced frequency $\omega^* = \omega l / V_\infty$, that is

$$w(x,y,t) = w_0 \exp\left\{-\mathrm{i}\,\left[k_1 2\,(x - V_\infty t)\,/l + k_2 2y/l\right]\right\} \tag{4.56}$$

with $k_1 = \omega^*/2$. The gust is convected past a thin wing of section chord l. The instantaneous lift coefficient at the spanwise position y induced by the gust can be written as

$$C_l(y,t) = T(k_1, k_2, M_\infty)\, \alpha(y,t) \tag{4.57}$$

where T is the aerodynamic transfer function and $\alpha(y,t) = w(0,y,t)\,/V_\infty$ is the instantaneous angle of attack at midchord.

As shown by Graham [6], in the subcritical case ($\mathcal{M} < 1$) the loading coefficient per unit upwash induced by an oblique gust is related to that induced by an incompressible parallel gust through the relationship (10.50). Thus, by applying the similarity rules of Graham for the case $\mathcal{M} \ll 1$, the aerodynamic transfer function takes the form

$$T_A(k_1, k_2, M_\infty) = a_0 \beta^{-1} S(k_1/\beta^2)\, F(k_1/\beta^2, k_2/\beta, M_\infty) \tag{4.58}$$

where

$$a_0 = T_A(0,0,0) = 2\pi \tag{4.59}$$

is the two-dimensional steady lift curve slope, $S(k_1) = T(k_1, 0, 0)/a_0$ is the Sears' function (4.47), and the function F accounts for unsteady compressible effects and the obliqueness of the gust. The function F has the form

$$F(K_1, K_2, M_\infty) = F_1\left(\sqrt{M_\infty^4 K_1^2 + K_2^2}, \tan^{-1}\left(\frac{K_2}{M_\infty^2 K_1}\right)\right) F_2\left(\sqrt{K_1^2 + K_2^2}, \tan^{-1}\left(\frac{K_2}{K_1}\right)\right) \tag{4.60}$$

with

$$F_1(r, \theta) = \frac{J_0(r e^{i\theta}) - i J_1(r e^{i\theta})}{I_0(r \sin\theta) + I_1(r \sin\theta)} \tag{4.61}$$

$$F_2(k, \lambda) = \frac{T(k, \lambda)}{T(k, \pi/2)} \equiv \frac{T(k, lambda)}{S(k)} \tag{4.62}$$

where J_n and I_n are Bessel functions and T denotes the normalized incompressible Filotas' gust transfer function [127].

By considering the Sears' function approximated expression

$$S(k) \simeq \sqrt{\frac{k + 0.1811}{0.1811 + 1.569k + 2\pi k^2}} \exp\left\{i k \left[1 - \frac{\pi^2/2}{1 + 2\pi k}\right]\right\} \tag{4.63}$$

Filotas [127] obtained the following approximated functions

$$\begin{aligned} F_1(r, \theta) \quad &\simeq \quad \sqrt{\frac{4\pi + 2\cos^2\theta\, r^3 + \pi \sin\theta\, r^4}{4\pi + \pi \cos^2\theta\, r^2 + \pi r^4}} \\ &\quad \exp\left\{-i r \cos\theta \left[\frac{\frac{1}{2}(\pi/2 - \theta) + r\cos\theta}{(\pi/2 - \theta) + r\cos\theta}\right]\right\} \end{aligned} \tag{4.64}$$

$$\begin{aligned} F_2(r, \theta) \quad &\simeq \quad \sqrt{\frac{2\pi + r^3}{1 + \pi r^2 + \pi r^4/2} \frac{2\pi + \pi \sin^2\lambda\, r^2 + \pi r^4/2}{2\pi + \sin^2\lambda\, r^3 + \pi \cos\lambda\, r^4/2}} \\ &\quad \exp\left\{i k \left[1 - \sin\lambda - \pi^2/(2 + 4\pi k) + \frac{\pi\lambda(2 + \cos\lambda)/2}{1 + \pi k(2 + \cos\lambda)}\right]\right\} \end{aligned} \tag{4.65}$$

4.5 Amiet's Theory of Low- and High-Frequency Unsteady Flow Past a Thin Airfoil

Amiet investigated the aerodynamic problem of a thin airfoil in a compressible stream and proposed analytical procedures for both low- and high-frequency unsteady flows.

4.5.1 Low-Frequency Case

As shown by Küssner [136] and by Amiet & Sears [137], the convected wave equation (10.29) for the perturbation velocity potential ϕ, with time-dependent boundary conditions, can be reduced to a standard wave equation for zero mean flow by applying a Galilean and a Lorentz combined transformation. The Galilean transformation

$$x' = x - M_\infty c_0 t, \quad y' = y, \quad z' = z, \quad t' = t \tag{4.66}$$

changes equation (10.29) into a standard wave equation. In addition, the Lorentz transformation

$$X = \frac{x' + M_\infty c_0 t}{\beta}, \quad Y = y', \quad Z = z', \quad T = \frac{t' + M_\infty x'/c_0}{\beta} \tag{4.67}$$

reestablishes the relative motion between the stream and the surface of the body. Thus, the combined transformation

$$x = \beta X, \quad y = Y, \quad z = Z, \quad t = \frac{T - M_\infty X/c_0}{\beta} \tag{4.68}$$

reduces the linearized potential equation (10.29) to the following standard wave equation

$$\phi_{XX} + \phi_{YY} + \phi_{ZZ} - \frac{1}{c_0^2}\phi_{TT} = 0 \tag{4.69}$$

but leaves the body at rest.

Let ϵ be a parameter related to the ratio between the characteristic dimension of the body b and the acoustic wavelength λ, namely

$$\epsilon = \frac{2\pi}{\beta^2}\frac{b}{\lambda} = \frac{M_\infty}{1 - M_\infty^2}\frac{\omega b}{U_\infty} = \frac{M_\infty}{1 - M_\infty^2}k \tag{4.70}$$

where $k = \omega b/U_\infty$ is the reduced frequency.

In the low-frequency limit $\epsilon \ll 1$, neglecting terms of order $\mathcal{O}(\epsilon^2)$ and of higher order, the second-order time derivative in equation (4.69) can be neglected and the problem reduces to that of solving the Laplace's equation

$$\phi_{XX} + \phi_{YY} + \phi_{ZZ} = 0 \tag{4.71}$$

In 1976, Amiet [130] discussed the consistency of such low-frequency approximation when the problem is solved in terms of small perturbation pressure instead of perturbation velocity potential, and a boundary condition on the velocity is imposed on the body. This is the case of lifting bodies with shed vorticity. Consider a point force acting as a harmonic dipole with axis in the y-direction, namely

$$\mathbf{F} = \hat{\jmath}\, F\, \delta(x)\,\delta(y)\,\delta(z)\, e^{i\,\omega\,t} \tag{4.72}$$

The acoustic field is the solution of the following convected wave equation

$$\left(1 - M_\infty^2\right) p_{xx} + p_{yy} + p_{zz} - \frac{2\,M_\infty}{c_0} p_{xt} - \frac{1}{c_0^2} p_{tt} = \nabla \cdot \mathbf{F} \tag{4.73}$$

that is

$$p(x,y,z,t) = \frac{F}{4\pi}\exp\left\{i\left(\omega\,t + \epsilon\,M_\infty\frac{x}{b}\right)\right\}\frac{\partial}{\partial y}\left[\frac{1}{\sigma}\exp\left(-i\,\epsilon\frac{\sigma}{b}\right)\right] \tag{4.74}$$

where $\sigma = \sqrt{x^2 + \beta^2\left(y^2 + z^2\right)}$.

The pressure perturbation is related to the perturbation velocity potential by the following linear expression

$$p = -\rho_0\left(\phi_t + M_\infty\, c_0\, \phi_x\right) \tag{4.75}$$

which can be solved in the variable ϕ leading to

$$\phi(x,y,z,t) = -\frac{1}{\rho_0\, M_\infty\, c_0}\int_{-\infty}^{x} p\left(\xi, y, z, t - \frac{x - \xi}{M_\infty\, c_0}\right)\, d\xi \tag{4.76}$$

The perturbation velocity normal to the mean flow can be calculated by using equation (4.74) into equation (4.76) and differentiating with respect to y. Thus, on the axis ahead of the dipole, it results that

$$v(x < 0,0,0,t) = -\frac{\beta^2\, F\, \mathcal{I}}{8\,\pi\,\rho_0\, M_\infty\, c_0\, b^2}\exp\left\{i\left(\omega\,t - k\frac{x}{b}\right)\right\} \tag{4.77}$$

where

$$\mathcal{I} = \frac{b^2}{x^2}\left[1 + i\frac{x}{b}\left(k^* - \epsilon\right)\right]\exp\left[i\frac{x}{b}\left(k^* + \epsilon\right)\right] - k^{*2}\beta^2\int_1^\infty \exp\left[i\frac{x}{b}\left(k^* + \epsilon\right)\xi\right]\frac{d\xi}{\xi} \tag{4.78}$$

and $k^* = \epsilon/M_\infty$ is the reduced frequency k divided by β^2.

In order to investigate the consistency of the low-frequency approximation, the solution $\tilde{p}$ of the transformed equation

$$p_{XX} + p_{YY} + p_{ZZ} = \nabla \cdot \mathbf{F} \tag{4.79}$$

can be compared with the exact solution (4.74). It thus results that

$$\tilde{p}(x, y, z, t) = \frac{F}{4\pi} \exp\left\{\mathrm{i}\left(\omega t + \epsilon M_\infty \frac{x}{b}\right)\right\} \frac{\partial}{\partial y}\left(\frac{1}{\sigma}\right) \tag{4.80}$$

while the perturbation velocity is given by equation (4.77) with $\mathcal{I}$ having the following approximated expression

$$\tilde{\mathcal{I}} = \frac{b^2}{x^2}\left(1 + \mathrm{i}\frac{x}{b}k^*\right)\exp\left(\mathrm{i}\frac{x}{b}k^*\right) - k^{*2}\int_1^\infty \exp\left(\mathrm{i}\frac{x}{b}k^*\xi\right)\frac{\mathrm{d}\xi}{\xi} \tag{4.81}$$

Thus, comparing equation (4.74) to equation (4.80) and equation (4.78) to equation (4.81) yield

$$\tilde{p} = p + \mathcal{O}(\epsilon^2) \tag{4.82}$$

$$\tilde{v} = v + \mathcal{O}(\epsilon^2) \tag{4.83}$$

As a result, in the low-frequency limit $\epsilon \ll 1$, the exact and the approximated solutions for both the pressure and the velocity differ by terms of order $\mathcal{O}(\epsilon^2)$.

The same analysis for a line force yields different results. In fact, in a two-dimensional case, even though the $\mathcal{O}(\epsilon)$ terms in the pressure expressions p and $\tilde{p}$ are identical, the $\mathcal{O}(\epsilon)$ terms in the velocities v and $\tilde{v}$ differ. Following Amiet [130], it can be written

$$p(x, y, t) = -\frac{\mathrm{i}\,\omega\, y\, F}{4\beta c_0 \sigma}\exp\left\{\mathrm{i}\left(\omega t + \epsilon M_\infty \frac{x}{b}\right)\right\} H_1^{(2)}\left(\epsilon\frac{\sigma}{b}\right) \tag{4.84}$$

and

$$v(x, 0, t) = -\frac{\beta F \mathcal{I}}{b \rho_0 M_\infty c_0}\exp\left\{\mathrm{i}\left(\omega t - k\frac{x}{b}\right)\right\} \tag{4.85}$$

where

$$\begin{aligned}\mathcal{I} = {} & \frac{\mathrm{i}\beta}{2\pi}k^* \ln\left(\frac{1+\beta}{M_\infty}\right) \\ & + \frac{k^*}{4}\left[\mathrm{i}\, M_\infty \frac{x}{|x|} H_1^{(2)}(\epsilon\ frac|x|b) - H_0^{(2)}\left(\epsilon\frac{|x|}{b}\right)\right]\exp\left(\mathrm{i}\, k^*\frac{x}{b}\right) \\ & + \frac{\mathrm{i}}{4}\frac{x}{b}\left(k^{*2} - \epsilon^2\right)\int_0^1 \exp\left(\mathrm{i}\, k^*\frac{x}{b}\xi\right) H_0^{(2)}\left(\epsilon\frac{|x|}{b}\xi\right)\,\mathrm{d}\xi\end{aligned} \tag{4.86}$$

Interestingly, equation (4.86) is the kernel of Possio's [128] integral equation. The approximated solution is

$$\tilde{p}(x, y, t) = \frac{\beta y F}{2\pi\sigma^2}\exp\left\{\mathrm{i}\left(\omega t + \epsilon M_\infty \frac{x}{b}\right)\right\} \tag{4.87}$$

and

$$\begin{aligned}\tilde{\mathcal{I}} = {} & -\frac{b}{2\pi x}\exp\left(\mathrm{i}\, k^*\frac{x}{b}\right) \\ & + \mathrm{i}\frac{k^*}{2\pi}\left[\gamma + \ln\left(k^*\frac{x}{b}\right) + \frac{\mathrm{i}\pi}{2} - \mathrm{i}\, k^*\frac{x}{b}\int_0^1 \ln(\xi)\exp\left(\mathrm{i}\, k^*\frac{x}{b}\xi\right)\mathrm{d}\xi\right]\end{aligned} \tag{4.88}$$

Then, expanding the Hankel functions for small values of the parameter ϵ yields

$$\tilde{p} = p + \mathcal{O}(\epsilon^2) \tag{4.89}$$

$$\tilde{\mathcal{I}} = \mathcal{I} - \mathrm{i}\frac{k^*}{2\pi} f(M_\infty) + \mathcal{O}(\epsilon^2) \tag{4.90}$$

where

$$f(M_\infty) = (1-\beta)\ln M_\infty + \beta\ln(1+\beta) - \ln 2 \tag{4.91}$$

Concluding, when no condition must be imposed on the velocity, the generalized Prandtl- Glauert transformation, together with the low-frequency assumption of neglecting the second- order time derivative in the transformed wave equation, yields consistent solutions both in two- and three-dimensional cases. On the contrary, when a wake of shed vorticity is present, provided that a condition on the velocity has been imposed, the low-frequency approximation leads to consistent results only in three-dimensional problems.

4.5.2 High-Frequency Case

In 1976 Amiet [129] proposed an analytical procedure for a gust-airfoil interaction problem. It is based on the separation of the leading edge and the trailing edge effects on the unsteady pressure distribution upon a thin rectangular wing embedded in a high-frequency, oblique gust.

Because of the short-wavelength character of the gust, a twofold simplification of the interaction problem is possible. First, as observed by Amiet in writing equation (10.68), at high frequencies the unsteady pressure on a rectangular airfoil differs from that induced on a similar infinite-span wing only in a small tip-region. Therefore, the three-dimensional pressure field can be approximated by a spanwise Fourier superposition of two-dimensional solutions of the interaction problem between an infinite-span wing and an oblique gust. The second simplification consists in the fact that, at high frequencies, the leading edge and the trailing edge contributions to the airfoil response are essentially independent. Therefore, these can be separately determined and matched in an iterative scheme.

Landahl [138] showed that the pressure distribution on the surface of an infinite-span airfoil embedded in a parallel gust of arbitrary wavelength can be determined by alternatively solving a leading edge problem, where the airfoil chord is supposed to extend infinitely in the downstream direction, and a trailing edge problem, where the chord is permitted to extend infinitely in the upstream direction. The leading edge solution satisfies both the upstream boundary condition and the slip velocity condition on the airfoil, but does not satisfy the condition of pressure continuity at the trailing edge and across the wake. On the contrary, the trailing edge solution satisfies both the downstream wake boundary condition and the slip velocity condition, but does not satisfy the upstream boundary condition. These two solutions can be matched in an iterative scheme which converges as faster as smaller is the wavelength of the gust.

Adamczyk [139] determined the response of an infinite-span swept wing to an oblique gust, by considering the first two terms of the series resulting from the iteration scheme. The leading edge and the trailing edge problems were solved by means of the Wiener-Hopf technique.

Amiet [129] extended Adamczyk's analysis in order to account for a difference between the free-stream velocity and the convection velocity of the gust. The leading edge and the trailing edge problems were solved in terms of Schwartzchild solution for a semi- infinite boundary-value problem.

The linearized equation for the perturbation velocity potential ϕ is

$$\frac{\partial^2\phi}{\partial x^2} + \frac{\partial^2\phi}{\partial y^2} + \frac{\partial^2\phi}{\partial z^2} - M_\infty^2\frac{\mathrm{D}^2\phi}{\mathrm{D}t^2} = 0 \tag{4.92}$$

where quantities have been made dimensionless by the semichord b and the mean flow velocity U_∞. Furthermore, $\mathrm{D}/\mathrm{D}t = (b/U_\infty)\partial/\partial t + \partial/\partial x$ is the linearized form of the dimensionless Lagrangian derivative.

Let us consider a sinusoidal Sears-type gust

$$w(x,y,t) = w_0 \exp\left\{ \mathrm{i} \left[-k_x \left(x - \frac{U_\infty}{b} t \right) - k_y\, y \right] \right\} = w(x,y)\, \mathrm{e}^{\mathrm{i}\,\omega\, t} \tag{4.93}$$

with $w(x,y) = w_0 \exp(-\mathrm{i}\, k_x\, x - \mathrm{i}\, k_y\, y)$, $k_x = \omega b/U_\infty$ and $k_y = k_x \tan\Lambda$. The boundary conditions for an airfoil in the plane $z = 0$ embedded in the gust are

$$\phi(x,y,0,t) = 0 \qquad \text{for} \quad x \le 0 \tag{4.94}$$

$$\frac{\partial\phi}{\partial z}(x,y,0,t) = -b\, w(x,y)\, \mathrm{e}^{\mathrm{i}\,\omega\, t} \qquad \text{for} \quad 0 < x \le 2 \tag{4.95}$$

$$\frac{\partial\phi}{\partial z}(x,y,0,t) \qquad \text{continuous for all } x \tag{4.96}$$

$$\frac{\mathrm{D}\phi}{\mathrm{D}t}(x,y,0,t) = 0 \qquad \text{for} \quad x \ge 2 \tag{4.97}$$

The boundary condition (4.95) states that the flow velocity has a normal vanishing component on the airfoil, whereas, the boundary condition (4.97) requires that the fluctuating pressure $p = -\rho_0\, \mathrm{D}\phi/\mathrm{D}t$ has no discontinuities at the trailing edge and across the wake.

Since the airfoil has an infinite span, the potential ϕ has the same y-dependence of the incident gust. Thus, the following variables separation can be performed

$$\phi(x,y,z,t) = \Phi(x,z)\, \mathrm{e}^{\mathrm{i}\,(\omega t - k_y\, y)} \tag{4.98}$$

Moreover, making the following change of variables

$$\Phi(x,z) = \hat{\Phi}(x,z) \exp\left(\mathrm{i}\, \frac{k_x\, x\, M_\infty^2}{\beta^2} \right) \tag{4.99}$$

$$X = x \qquad Z = \beta\, z \tag{4.100}$$

$$\tag{4.101}$$

equation (4.92) takes the form

$$\frac{\partial^2 \hat{\Phi}}{\partial X^2} + \frac{\partial^2 \hat{\Phi}}{\partial Z^2} + \mu^2\, \hat{\Phi} = 0 \tag{4.102}$$

with boundary conditions

$$\hat{\Phi}(X,0) = 0 \qquad \text{for} \quad X \le 0 \tag{4.103}$$

$$\frac{\partial\hat{\Phi}}{\partial Z}(X,0) = -\frac{b\, w_0}{\beta} \exp\left(-\mathrm{i}\, \frac{k_x\, X}{\beta^2} \right) \qquad \text{for} \quad 0 < X \le 2 \tag{4.104}$$

$$\frac{\partial\hat{\Phi}}{\partial Z}(X,0) \qquad \text{continuous for all } X \tag{4.105}$$

$$\left(\mathrm{i}\, \frac{k_x}{\beta^2} + \frac{\partial}{\partial X} \right) \hat{\Phi}(X,0) = 0 \qquad \text{for} \quad X \ge 2 \tag{4.106}$$

where

$$\mu^2 = \frac{k_x^2\, M_\infty^2 - k_y^2\, \beta^2}{\beta^4} = \frac{k_x^2 + k_y^2}{\beta^2} \sin^2\Lambda \left(\frac{M_\infty^2}{\sin^2\Lambda} - 1 \right) \tag{4.107}$$

and

$$\hat{\Phi}(X,Z) = \phi(x,z) \tag{4.108}$$

It can be noticed that μ^2 is negative for $M_\infty/\sin\Lambda < 1$. In this case no sound is radiated from the airfoil.

Consider first a generic Sears-type parallel gust, namely

$$w(x) = w_0 \exp(-\mathrm{i}\, k_x\, x) \tag{4.109}$$

The boundary-value problem takes the form

$$\hat{\Phi}_{XX} + \hat{\Phi}_{ZZ} + \mu^2 \hat{\Phi} = 0 \tag{4.110}$$

$$\hat{\Phi}(X,0) = 0 \qquad \text{for} \quad X \leq 0 \tag{4.111}$$

$$\frac{\partial \hat{\Phi}}{\partial Z}(X,0) = -\frac{b}{\beta}\, w(X)\, \exp(-\mathrm{i}\, \mu M_\infty X) \qquad \text{for} \quad 0 < X \leq 2 \tag{4.112}$$

$$\frac{\partial \hat{\Phi}}{\partial Z}(X,0) \qquad \text{continuous for all } X \tag{4.113}$$

$$\left(\mathrm{i}\, k^* + \frac{\partial}{\partial X}\right) \hat{\Phi}(X,0) = 0 \qquad \text{for} \quad X \geq 2 \tag{4.114}$$

where $k^* = k_x/\beta^2$, $k_y = 0$ and $\mu = M_\infty\, k^*$.

The boundary-value problem posed by equations (4.110) through (4.114) can be solved in terms of iteratively matched Schwartzchild solutions. The first is the solution of the semi-infinite leading edge problem (equation (4.110) with boundary conditions (4.111), (4.112) and (4.113)). The second solution is that of a semi-infinite trailing edge problem (equation (4.110) with boundary conditions (4.112), (4.113) and (4.114)).

The generic solution of equation (4.110) with boundary conditions

$$\hat{\Phi}(X,0) = F(X) \qquad \text{for} \quad X > 0 \tag{4.115}$$

$$\frac{\partial \hat{\Phi}}{\partial Z}(X,0) = 0 \qquad \text{for} \quad X < 0 \tag{4.116}$$

is referred to as Schwartzchild solution. It is given by

$$\hat{\Phi}(X,Z) = \frac{1}{\pi} \int_0^\infty G(X,\xi,Z)\, F(\xi)\, \mathrm{d}\xi \quad \text{with}$$

$$G(X,\xi,0) = (-X/\xi)^{1/2}\, [1/(\xi - X)]\, \exp\{-\mathrm{i}\, \mu\, (\xi - X)\} \quad \text{for} \quad X < 0 \tag{4.117}$$

The first term in the iterative scheme is the solution of equation (4.110), satisfying the no flow condition (4.112) through the airfoil surface. It is thus given by a distribution of elementary sources whose intensity is related to the gust upwash velocity $w(x)$, namely

$$\phi^{(0)}(x,z) = -\frac{\mathrm{i}\, b}{2\beta} \int_{-\infty}^{\infty} \exp\{\mathrm{i}\, \mu\, M_\infty\, (x-\xi)\}\, H_0^{(2)} \left\{\mu \left[(x-\xi)^2 + \beta^2 z^2\right]^{1/2}\right\} w(\xi)\, \mathrm{d}\xi \tag{4.118}$$

where use of the physical co-ordinates (x,z,t) has been made.

The zeroth-order solution $\phi^{(0)}$ can be corrected in order to satisfy the boundary condition (4.111). Thus, let us write

$$\phi^{(1)} = \phi^{(0)} + \psi^{(1)} \tag{4.119}$$

where $\psi^{(1)}$ denotes the leading edge correction. The first-order correction $\psi^{(1)}$ can be found in the form of Schwartzchild solution applied to the boundary- value problem

$$\frac{\partial^2 \psi^{(1)}}{\partial x^2} + \frac{\partial^2 \psi^{(1)}}{\partial z^2} + \mu^2\, \psi^{(1)} = 0 \tag{4.120}$$

$$\psi^{(1)}(x,0) = -\phi^{(0)}(x) \qquad \text{for} \quad x < 0 \tag{4.121}$$

$$\frac{\partial \psi^{(1)}}{\partial z}(x,0) = 0 \qquad \text{for} \quad x > 0 \tag{4.122}$$

Hence, considering equation (4.117) yields[2]

$$\psi^{(1)}(x,0) = -\frac{1}{\pi}\int_0^\infty (x/\xi)^{1/2} \exp\{-\mathrm{i}\,(1-M_\infty)\,\mu\,(\xi+x)\}\,\phi^{(0)}(-\xi,0)\,\frac{\mathrm{d}\xi}{\xi+x} \tag{4.123}$$

The first-order solution $\phi^{(1)}$ can be further corrected in order to satisfy the boundary condition (4.114). Thus, let us write

$$\phi^{(2)} = \phi^{(1)} + \psi^{(2)} \tag{4.124}$$

where $\psi^{(2)}$ denotes the trailing edge correction.

The pressure and the velocity potential are related by the relationships

$$P\,\mathrm{e}^{\mathrm{i}\omega t} = -\rho_0\,\frac{\mathrm{D}\phi}{\mathrm{D}t} \tag{4.125}$$

$$\phi(x,t) = -\frac{b}{\rho_0\,U_\infty}\int_{-\infty}^{x} P(\xi,z)\exp\{-\mathrm{i}\,k\,(x-\xi)\}\,\mathrm{d}\xi \tag{4.126}$$

Thus, the boundary condition (4.114) is equivalent to the condition $P = 0$. Furthermore, because the pressure and the potential are linearly related, P satisfies the Helmholtz equation (4.110), the vanishing normal derivative boundary condition (4.112) and the wake condition $P = 0$. Thus, it is more convenient to find the trailing edge correction in terms of pressure, that is $P^{(2)} = P^{(1)} + \chi^{(2)}$, with $\chi^{(2)}$ satisfying the boundary-value problem

$$\frac{\partial^2\chi^{(2)}}{\partial x^2} + \frac{\partial^2\chi^{(2)}}{\partial z^2} + \mu^2\,\chi^{(1)} = 0 \tag{4.127}$$

$$\chi^{(2)}(x,0) = -P^{(1)}(x) \qquad \text{for} \quad x > 2 \tag{4.128}$$

$$\frac{\partial\chi^{(2)}}{\partial z}(x,0) = 0 \qquad \text{for} \quad x < 2 \tag{4.129}$$

which can be solved in terms of Schwartzchild solution. From equation (4.117) it follows that

$$\begin{aligned}\psi^{(2)}(x,0) = -\frac{1}{\pi}\int_0^\infty \left(\frac{2-x}{\xi}\right)^{1/2} &\exp\{-\mathrm{i}\,(1+M_\infty)\,\mu\,(\xi+2-x)\}\\ P^{(1)}(2+\xi,0)\,&\frac{\mathrm{d}\xi}{\xi+2-x}\end{aligned} \tag{4.130}$$

where $P^{(1)}$ is related to $\phi^{(1)}$ by equation (4.125).

The iterative scheme[3] could be continued finding higher-order corrections $\psi^{(n)}$ and $\chi^{(n)}$ up to the required order of accuracy.

Substituting the parallel gust upwash (4.109) into equation (4.118) and integrating, the zeroth-order solution takes the form

$$\phi_s^{(0)}(x,0) = -\frac{b\,w_0}{k}\,\mathrm{e}^{-\mathrm{i}\,k\,x} \tag{4.131}$$

Then, introducing $\phi_s^{(0)}$ into equation (4.123) provides the leading edge correction

$$\phi_s^{(1)}(x,0) = (1-\mathrm{i})\;E\,[k^*\,(1-M_\infty)\,x]\,\phi^{(0)}(x,0) \tag{4.132}$$

where

$$E(x) = \int_0^x (2\,\pi\,t)^{-1/2}\,\mathrm{e}^{\mathrm{i}\,t}\,\mathrm{d}t \tag{4.133}$$

[2]The sign of x must be changed in equation (4.117) because $\psi^{(1)}$ is specified for $x<0$ and $\psi_z^{(1)}$ for $x>0$ rather than the contrary as in equations (4.115) and (4.116).

[3]The convergence of the iteration scheme is as faster as smaller is the gust wavelength.

is a combination of Fresnel integrals. The first-order pressure, obtained from equations (4.125) and (4.132), is given by

$$P_s^{(1)}(x,0) = -\rho_0\, U_\infty\, w_0\, [\pi\, k\, x\, (1 + M_\infty)]^{-1/2}\ \mathrm{e}^{-\mathrm{i}\,\mu(1-M)x - \mathrm{i}\,\pi/4} \tag{4.134}$$

Finally, the trailing edge correction can be found by introducing $P^{(1)}$ into equation (4.130) and integrating. An approximated result for the second-order solution is given by Amiet [129] in the form

$$\begin{aligned} P_s^{(2)}(x,0) \;&\simeq\; P_s^{(1)}(x,0) - \rho_0\, U_\infty\, w_0\, [2\,\pi\, k\, (1 + M_\infty)]^{-1/2} \\ &\quad \{1 - (1+\mathrm{i})\, E^*(2\mu\,(2-x))\}\ \mathrm{e}^{-\mathrm{i}\,\mu(1-M_\infty)x - \mathrm{i}\,\pi/4} \end{aligned} \tag{4.135}$$

where E^* denotes the complex conjugate of E.

The first and the second order pressure distributions (4.134) and (4.135) on the airfoil can be integrated in order to obtain the lift induced by a parallel Sears-type gust. It thus results that

$$L_s^{(1)} = (1-\mathrm{i})\, M^{1/2}\, (\pi\,\mu\,\beta)^{-1}\, E^*\, [2\mu\, (1 - M_\infty)] \tag{4.136}$$

$$\begin{aligned} L_s^{(2)} \;&\simeq\; L_s^{(1)} + \frac{\mathrm{i}}{\beta\, (\pi\mu)^{3/2}} \sqrt{\frac{M_\infty}{1 - M_\infty}} \\ &\left\{ \left[\sqrt{\frac{2}{1+M_\infty}} E^*\, [2\mu\, (1 + M_\infty)] - \frac{1-\mathrm{i}}{2} \right] \mathrm{e}^{-\mathrm{i}\, 2\mu(1-M_\infty)} + \frac{1+\mathrm{i}}{2} - E^*(4\mu) \right\} \end{aligned} \tag{4.137}$$

where both $L_s^{(1)}$ and $L_s^{(2)}$ are normalized by the factor $-2\pi\, \rho_0\, b\, U_\infty\, w_0/\beta$. Adamczyk [139] had obtained equations (4.134) to (4.137) before Amiet [129] by means of the Wiener-Hopf technique. Interestingly, the high-frequency limit of equation (4.136) is

$$\lim_{\mu\to\infty} L_s^{(1)} = -\frac{\mathrm{i}\,\beta}{\pi\, k\, \sqrt{M_\infty}} \propto k^{-1} \tag{4.138}$$

The Sears function for an incompressible flow behaves as $k^{-1/2}$ for small values of the gust wavelength. Therefore, it should be concluded that the flow compressibility has a predominant effect at high frequencies.

If a Sears-type skewed gust is considered ($k_y \neq 0$) the iterative scheme applies in the same way as for a parallel gust, but the exponential factor in equations (4.123) and (4.130) must be replaced by

$$-\mathrm{i}\,\mu\,(1 - M_\infty) \to -\left(\frac{k_y^2}{\beta^2} - \mu^2\right)^{1/2} + \mathrm{i}\,\mu\, M_\infty \tag{4.139}$$

$$-\mathrm{i}\,\mu\,(1 + M_\infty) \to -\left(\frac{k_y^2}{\beta^2} - \mu^2\right)^{1/2} - \mathrm{i}\,\mu\, M_\infty \tag{4.140}$$

respectively. Consider now a parallel gust convected at other than the free-stream velocity U_∞, namely a Kemp-type gust given by

$$w(x) = w_0\, \exp(-\mathrm{i}\ \lambda_x\, x) \tag{4.141}$$

where $\lambda_x \neq k_x$.

By making use of equation (4.141) into equation (4.118) and integrating, the zeroth-order solution takes the form

$$\phi_k^{(0)}(x,0) = -\mathrm{i}\ \frac{b\, w_0}{\beta} \left[\mu^2 - (\lambda_x + M_\infty\, \mu)^2\right]^{-1/2} \mathrm{e}^{-\mathrm{i}\ \lambda_x\, x} \tag{4.142}$$

It can be observed that, for $\lambda_x = k_x$ it results that

$$\left[\mu^2 - (\lambda_x + M_\infty \mu)^2\right]^{-1/2} = -\mathrm{i}\,\frac{\beta}{k_x} \tag{4.143}$$

and equation (4.142) reduces to equation (4.131).

From equations (4.125) and (4.142) it follows that

$$P_k^{(0)}(x,0) = -\mathrm{i}\,\frac{\rho_0\,U_\infty}{b}\,(k_x - \lambda_x)\,\phi_k^{(0)}(x,0) \tag{4.144}$$

Thus, inserting equation (4.142) into equation (4.123) and integrating leads to the leading edge correction $\psi^{(1)}$. As a result

$$\phi_k^{(0)}(x,0) + \psi^{(1)}(x,0) = (1+\mathrm{i})\,E^*\left[x\,(\mu\,(1-M_\infty) - \lambda_x)\right]\phi_k^{(0)}(x,0) \tag{4.145}$$

This is not the first-order solution $\phi_k^{(1)}$ because the zeroth order solution $\phi_k^{(0)}$ does not satisfy the wake condition (4.114). Thus a first-order trailing edge correction must be found by considering equation (4.130) and integrating. It thus results that

$$\chi^{(1)}(x,0) = \{(1+\mathrm{i})\,E^*\{(2-x)\,[\mu\,(1+M_\infty) + \lambda_x]\} - 1\}\,P_k^{(0)}(x,0) \tag{4.146}$$

Finally, adding $\chi^{(1)}$ to the pressure corresponding to equation (4.145), the first-order solution can be obtained. Its integrated value provides the following expression for the first-order normalized lift

$$\begin{aligned}
L_k^{(1)} = {} & \frac{i-\mathrm{i}}{\pi\lambda_x}\left[\mu^2 - (\lambda_x + M_\infty\,\mu)^2\right]^{-1/2} \\
& \left\{k_x\left(1 - \frac{\lambda_x/\mu}{1-M_\infty}\right)^{1/2} E^*\left[2\mu\,(1-M_\infty)\right] - (k_x - \lambda_x)\,\mathrm{e}^{-\mathrm{i}2\lambda_x} E^*\left\{2\left[\mu\,(1-M_\infty) - \lambda_x\right]\right\}\right\} \\
& + \frac{\mathrm{i}}{\pi}k_x\,(\lambda_x - 1)\left[\mu^2 - (\lambda_x + M_\infty\,\mu)^2\right]^{-1/2} \\
& \{(1+\mathrm{i})\left(1 + \frac{\lambda_x/\mu}{1+M_\infty}\right)^{1/2} \mathrm{e}^{-\mathrm{i}2\lambda_x} E^*\left[2\mu\,(1+M_\infty)\right] \\
& - (1+\mathrm{i})\,E^*\left\{2\left[\mu\,(1+M_\infty) + \lambda_x\right]\right\} + 1 - \mathrm{e}^{-\mathrm{i}2\lambda_x}\}
\end{aligned} \tag{4.147}$$

By comparing the analytical approximated results with Graham [6] numerical solution of the exact problem, Amiet [129] estimated that the cut-off limit for real ν is about $\pi/4$. Above this value the Landahl's separation technique gives accurate aerodynamic results.

4.6 Goldstein & Atassi's Gust-Airfoil Second Order Theory

Chu & Kovásznay [76] demonstrated that three modes of fluctuation can exist independently from each other in a disturbance flow field, namely, the *vorticity mode*, the *entropy mode* and the *acoustic mode*. The vorticity mode has a divergence-free velocity field. It governs the behaviour of an incompressible turbulent flow. The entropy mode governs the heat transfer dynamics in a low speed flow. The acoustic mode governs the propagation of acoustic disturbances within a flow field.

Based on a modal decomposition, the perturbation velocity $\mathbf{u}$ at any point $\mathbf{x}$ of an unsteady compressible and vortical flow around a three-dimensional obstacle can be split into the sum of a solenoidal, rotational part $\mathbf{u}_R$ and an irrotational part $\nabla\phi$. The solenoidal part $\mathbf{u}_R$ is a known function of the imposed upstream distortion field and the mean flow variables. The irrotational part $\nabla\phi$ is related to the acoustic pressure disturbance p' by the linear relationship

$$p' = -\rho_0 \frac{\mathrm{D}_0\phi}{\mathrm{D}t} \tag{4.148}$$

where $\mathrm{D}_0/\mathrm{D}t$ denotes the convective derivative based on the mean flow velocity, and $\rho_0 = \rho_0(\mathbf{x})$ is the local density of the mean flow.

By assuming a steady mean potential flow, the perturbation potential ϕ can be described by the linear, inhomogeneous convected wave equation

$$\frac{\mathrm{D}_0}{\mathrm{D}t}\left(\frac{1}{c_0^2}\frac{\mathrm{D}_0\phi}{\mathrm{D}t}\right) - \frac{1}{\rho_0}\nabla\cdot(\rho_0\nabla\phi) = \frac{1}{\rho_0}\nabla\cdot(\rho_0\,\underline{\mathrm{f}}u_R) \tag{4.149}$$

where $c_0 = c_0(\mathbf{x})$ denotes the local mean sound speed. In equation (4.149) the vortical disturbance acts as a dipole-type source term whose strength $\rho_0\,\mathbf{u}_R$ is a known function of the imposed upstream distortion field.

Far upstream from the obstacle the fluid density ρ_0 is constant and $\mathbf{u}_R$ approaches the imposed solenoidal vortical disturbance. Thus, the source term vanishes and the outgoing wave solution ϕ approaches zero as $x \to -\infty$. Conversely, near the obstacle the mean flow induces a distortion on the vortical disturbance and destroys its solenoidal character. Therefore, the distortion effect of the obstacle is to generate an acoustic mode of fluctuation. Moreover, a solid surface in a fluctuating velocity field has the effect of coupling the vortical and the acoustic modes. The vanishing normal velocity boundary condition yields

$$\frac{\partial\phi}{\partial n} = -\mathbf{u}_R\cdot\mathbf{n} \tag{4.150}$$

where $\mathbf{n}$ denotes the unit vector normal to the surface of the obstacle.

For a uniform parallel flow, no distortion of the vortical disturbance occurs and the divergence-free character of the convected vortical disturbance is retained even in proximity of the body. Therefore, for a flat-plate at zero angle of attack, the surface modal coupling effect is the only sound generation mechanism.

Equation (4.149) was used by Goldstein [140] in order to extend the *rapid-distortion theory* of turbulence[4]. The rapid-distortion theory describes the effects induced by mean flow gradients on a turbulent flow which is distorted in a time which is short relative to the Lagrangian integral scale. Thus, viscous effects are neglected by this theory.

Goldstein [140] applied the rapid-distortion theory to describe the interaction between vortical and entropic disturbances and a generic obstacle immersed in a mean compressible flow. The obstacle is neither required to have a small transverse dimension, as in a Sears-type [126] aerodynamic problem, nor to be a Lighthill- type [144] blunt body.

Goldstein & Atassi [131] used the same rapid-distortion approximation in order to investigate the interaction between generic airfoils and convected sinusoidal gusts in incompressible flows. Their second-order analyses provide useful formulae for the airfoil unsteady loading at low frequencies (the gust wavelength is large compared to the airfoil chord).

Myers & Kerschen [145] applied Goldstein's [140] formulation in order to develop a complete first order high-frequency subsonic model for the gust-airfoil interaction problem. They investigated the noise generated when short-wavelength vortical disturbances are convected past an airfoil at non zero angle of attack in a compressible flow. Myers & Kerschen concluded that the influence of the airfoil mean loading on the acoustic far field is significant even for small incidence angles. Furthermore, they

[4]The *rapid-distortion* theory was developed by Hunt [141] on the base of the preliminary works by Prandtl [142] and Batchelor & Proudman [143]

showed that, at high frequencies, all the important source terms are located in a region around the airfoil leading edge.

The influence of the mean loading on the aerodynamic noise from a blade in a vortical flow was firstly investigated by Goldstein *et al.* [9]. They showed that the quadrupole noise contribution from a loaded airfoil is proportional to the mean flow circulation and tends to become important and comparable to the dipole noise contribution at higher airfoil loadings. This is a consequence of the distortion induced by the mean flow gradients in proximity of the airfoil onto the impinging vortical disturbances.

In the present section the second-order gust-airfoil interaction theory of Goldstein & Atassi [131] is described. It will be shown how the mean steady potential flow around an arbitrary airfoil affects the aerodynamic response function of the airfoil when it is embedded in a small-amplitude periodic gust.

Consider a two-dimensional incompressible and inviscid flow. The Euler's governing equations become

$$\nabla \cdot \mathbf{V} = 0 \tag{4.151}$$

$$\left(\frac{\partial}{\partial t} + \mathbf{V} \cdot \nabla\right) \mathbf{V} = -\nabla P \tag{4.152}$$

where quantities have been made dimensionless by the airfoil semi-chord $c/2$, the reference velocity U_∞, the reference time $c/2U_\infty$ and the reference pressure $\rho_0 U_\infty^2$.

The velocity and pressure fields can be split into the sum of a steady contribution and a fluctuating perturbation contribution by writing

$$\mathbf{V} = \mathbf{v}(\mathbf{x}) + \epsilon\, \mathbf{u}(\mathbf{x}, t) + \ldots \tag{4.153}$$

$$P = p(\mathbf{x}) + \epsilon\, p'(\mathbf{x}, t) + \ldots \tag{4.154}$$

where ϵ is a small amplitude parameter and $\mathbf{u}$ and p' are of order unity.

By assuming an irrotational steady flow, the steady velocity satisfies the conditions

$$\nabla \cdot \mathbf{v} = \nabla \times \mathbf{v} = 0 \tag{4.155}$$

Since the unsteady velocity field is divergence-free, a stream function ψ can be introduced, such that

$$u_1 = \frac{\partial \psi}{\partial x_2}, \qquad u_2 = -\frac{\partial \psi}{\partial x_1} \tag{4.156}$$

Taking the curl of equation (4.152) and neglecting terms of order ϵ^2 gives

$$\left(\frac{\partial}{\partial t} + \mathbf{v} \cdot \nabla\right) \Omega = 0 \tag{4.157}$$

where Ω is the negative of the vorticity and is related to the stream function by the Poisson equation

$$\Omega \equiv \frac{\partial u_1}{\partial x_2} - \frac{\partial u_2}{\partial x_1} = \nabla^2 \psi \tag{4.158}$$

By introducing the steady potential Φ and the stream function Ψ, provided that

$$\mathbf{v} \cdot \nabla = |\mathbf{u}|^2 \frac{\partial}{\partial \Phi} \tag{4.159}$$

equation (4.157) can be written as

$$\left(\frac{\partial}{\partial t} + |\mathbf{v}|^2 \frac{\partial}{\partial \Phi}\right) \Omega = 0 \tag{4.160}$$

which has the formal solution

$$\Omega = f\left(\int_{-\infty}^{\Phi}\left(|\mathrm{v}|^{-2}-1\right)\,\mathrm{d}\Phi + \Phi - t, \Psi\right) \tag{4.161}$$

where f is an arbitrary function of its arguments.

Far upstream from a lifting airfoil the steady potential and the stream function behave like

$$\Phi \simeq \Phi_0 + x_1 \tag{4.162}$$

$$\Psi \simeq E_0 + x_2 + \beta \ln|\mathrm{x}| \tag{4.163}$$

where Φ_0, β and E_0 are constants, β being a parameter related to the airfoil lift. Thus, in order to approach the vorticity of a longitudinal and transverse periodic gust imposed upstream, equation (4.161) must have the form

$$\Omega = -\mathrm{i}\,|k|\exp\left\{\mathrm{i}\,k_1\left[\int_{-\infty}^{\Phi}\left(|\mathrm{v}|^{-2}-1\right)\,\mathrm{d}\Phi + \Phi - \Phi_0 - t\right] + \mathrm{i}\,k_2\left(\Psi - E_0\right)\right\} \tag{4.164}$$

where $k = k_1 + \mathrm{i}\,k_2$ and the normalization factor $-\mathrm{i}\,|k|$ is chosen as a matter of convenience. However, it should be observed that, far upstream from the airfoil, say $x_1 \to -\infty$, the vortical wave (4.164) takes the limit form

$$\Omega = -\mathrm{i}\,|k|\exp\left\{\mathrm{i}\,\left[k_1\left(x_1 - t\right) + k_2\left(\beta\ln|\mathrm{x}| + x_2\right)\right]\right\} \tag{4.165}$$

which differs from a Sears-type vortical wave $\Omega = -\mathrm{i}\,|k|\exp\{\mathrm{i}\,[k_1(x_1-t)+k_2x_2]\}$ if the perturbation parameter β differs from zero.

Without loss of generality it can be supposed through out the present analysis that both the streamwise and transverse wavenumbers k_1 and k_2 are positive.

The aerodynamic interaction problem has been reduced to the solution of the Poisson equation (4.158) for the unsteady stream function ψ, with the source term given by (4.164). The boundary conditions are the slip condition $\mathbf{u}\cdot\mathbf{n} = 0$ on the airfoil surface, the Kutta condition at the trailing edge and the continuity of both the pressure and the normal velocity across the vortex-sheet downstream of the airfoil. In order to simplify the analysis, suppose that the mean steady flow is slightly perturbed from a uniform parallel flow by a thin airfoil with a small angle of attack and small camber. Thus, denoting as α an airfoil perturbation parameter, the mean velocity field has the form

$$\mathrm{v}(\mathrm{x}) = \hat{i}_1 + \alpha\mathrm{v}^{(1)}(\mathrm{x}) \tag{4.166}$$

where $\mathrm{v}^{(1)}$ is of order unity.

The unsteady perturbation flow quantities can be supposed to have the form

$$\mathbf{u}(\mathbf{x},t) = \exp(-\mathrm{i}\,k_1\,t)\left[\mathbf{u}^{(0)}(\mathrm{x}) + \alpha\mathbf{u}^{(1)}(\mathrm{x}) + \ldots\right] \tag{4.167}$$

$$p'(\mathrm{x},t) = \exp(-\mathrm{i}\,k_1\,t)\left[p^{(0)}(\mathrm{x}) + \alpha p^{(1)}(\mathrm{x}) + \ldots\right] \tag{4.168}$$

$$\psi(\mathrm{x},t) = \exp(-\mathrm{i}\,k_1\,t)\left[\psi^{(0)}(\mathrm{x}) + \alpha\psi^{(1)}(\mathrm{x}) + \ldots\right] \tag{4.169}$$

Thus, by substituting equation (4.169) into equations (4.157) and (4.158), and by equating terms of equal power of α, the following perturbation problem can be obtained

$$\left(-\mathrm{i}\,k_1 + \frac{\partial}{\partial x_1}\right)\nabla^2\psi^{(0)} = 0 \tag{4.170}$$

$$\left(-\mathrm{i}\,k_1 + \frac{\partial}{\partial x_1}\right)\nabla^2\psi^{(1)} = -\mathrm{v}^{(1)}\cdot\nabla\left(\nabla^2\psi^{(0)}\right) \tag{4.171}$$

where

$$u_1^{(0)} = \frac{\partial \psi^{(0)}}{\partial x_2}, \qquad u_2^{(0)} = -\frac{\partial \psi^{(0)}}{\partial x_1} \tag{4.172}$$

$$u_1^{(1)} = \frac{\partial \psi^{(1)}}{\partial x_2}, \qquad u_2^{(1)} = -\frac{\partial \psi^{(1)}}{\partial x_1} \tag{4.173}$$

Equation (4.170) is related to the first-order theory of Sears. It can be integrated giving

$$\nabla^2 \psi^{(0)} = -\mathrm{i}\, |k|\, \mathrm{e}^{\mathrm{i}\,\mathbf{k}\cdot\mathbf{x}} \tag{4.174}$$

which can be substituted into equation (4.171) yielding

$$\left(-\mathrm{i}\, k_1 + \frac{\partial}{\partial x_1}\right) \nabla^2 \psi^{(1)} = -\,|k|\, \mathbf{k}\cdot\mathbf{v}^{(1)} \mathrm{e}^{\mathrm{i}\,\mathbf{k}\cdot\mathbf{x}} \tag{4.175}$$

In equation (4.174) the normalization factor $-\mathrm{i}\,|k|$ has been chosen to be compatible with equation (4.164). Setting $z = x_1 + \mathrm{i}\,x_2$, $W^{(1)} = \Phi^{(1)} + \Psi^{(1)}$ and $\zeta^{(1)} = v_1^{(1)} - \mathrm{i}\,v_2^{(1)}$, with $\mathrm{d}W^{(1)}/\mathrm{d}z = \zeta^{(1)}$, Goldstein & Atassi [131] obtained the following formal solution of equation (4.175)

$$\psi^{(1)} = -\frac{1}{|k|}\left[\frac{k}{2}\mathcal{F}_+ - \overline{\frac{k}{2}\mathcal{F}_-} - \mathrm{e}^{\mathrm{i}\,\mathbf{k}\cdot\mathbf{x}}\, \Re\Big(kW^{(1)}(z)\Big)\right] + f(x_2)\, \mathrm{e}^{\mathrm{i}\,k_1 x_1} + \tilde{F}(z) + \tilde{G}(\overline{z}) \tag{4.176}$$

where f is an arbitrary function of x_2, where $\tilde{F}$ and $\tilde{G}$ are analytic function of z and $\overline{z}$, respectively, and where

$$\mathcal{F}_\pm(\mathbf{k},\mathbf{x}) = \pm \exp\left(\pm\frac{1}{2}\mathrm{i}\, k\overline{z}\right) \mathcal{H}_\pm(z) \tag{4.177}$$

with

$$\mathcal{H}_\pm(z) = \int_{\mp\infty}^{z} \zeta^{(1)}(z) \exp\left(\pm\frac{1}{2}\mathrm{i}\, k\overline{z}\right) \mathrm{d}z \tag{4.178}$$

The functions $\mathcal{H}_\pm$ are analytic multivalued functions of z. In fact, $\zeta^{(1)}(z)$ behaves like $\mathrm{i}\,\Gamma/z$ for large z, $\alpha\Gamma$ being the steady circulation around the airfoil. Thus, it should be supposed that the branch cut of $\mathcal{H}_+$ lies along the positive real axis and that the branch cut of $\mathcal{H}_-$ lies along the negative real axis.

The velocity $\mathbf{u}^{(1)}$ can be obtained by differentiating the stream function (4.176). It can be split into the sum of a homogeneous solution, namely

$$\begin{aligned} u_1^h(x_1,x_2) &= f'(x_2)\, \mathrm{e}^{\mathrm{i}\,k_1 x_1} + F(z) + G(\overline{z}) \\ u_2^h(x_1,x_2) &= -\mathrm{i}\, k_1 f(x_2)\, \mathrm{e}^{\mathrm{i}\,k_1 x_1} + \mathrm{i}\, \{F(z) - G(\overline{z})\} \end{aligned} \tag{4.179}$$

and a particular solution

$$\begin{aligned} u_1^p(x_1,x_2) &= -\frac{1}{|k|}\left\{J_+ - \overline{J_-} - \mathrm{i}\, k_2\, \mathrm{e}^{\mathrm{i}\,\mathbf{k}\cdot\mathbf{x}}\, \Re\Big(k\left[W^{(1)}(z) - W_0\right]\Big)\right\} \\ u_2^p(x_1,x_2) &= \frac{1}{|k|}\left\{J_+ + \overline{J_-} - k_1\, \mathrm{e}^{\mathrm{i}\,\mathbf{k}\cdot\mathbf{x}}\, \Re\Big(k\left[W^{(1)}(z) - W_0\right]\Big)\right\} \end{aligned} \tag{4.180}$$

where

$$J_\pm(\mathbf{k},\mathbf{x}) = \frac{k^2}{4} \exp\left(\pm\frac{1}{2}\mathrm{i}\, k\overline{z}\right) \left[\mathcal{H}_\pm(z) - D_\pm \overline{\mathcal{H}_\pm(z)}\right] \tag{4.181}$$

with

$$D_\pm = \frac{\int_{-1}^{1} \Delta\zeta^{(1)}(x_1) \exp\left(\pm\frac{1}{2}\mathrm{i}\, \overline{k} x_1\right)\, \mathrm{d}x_1}{\int_{-1}^{1} \overline{\Delta\zeta^{(1)}(x_1)} \exp\left(\mp\frac{1}{2}\mathrm{i}\, k x_1\right)\, \mathrm{d}x_1} \tag{4.182}$$

The arbitrary functions f, F and G and the complex constant W_0 can be determined by requiring the boundary conditions to be satisfied, whereas, the constants $D_\pm$ are such that

$$\Delta u_1^p(x_1) = 0, \qquad \Delta u_2^p(x_1) = 0 \quad \text{for} \quad x_1 < -1 \tag{4.183}$$

and that

$$\begin{aligned} \Delta u_1^p(x_1) &= \frac{\mathrm{i}\,k_2}{|k|}\,\mathrm{e}^{\mathrm{i}\,k_1 x_1}\,\Re\Big(kW^{(1)}(z)\Big) \\ \Delta u_2^p(x_1) &= -\frac{\mathrm{i}\,k_1}{|k|}\,\mathrm{e}^{\mathrm{i}\,k_1 x_1}\,\Re\Big(kW^{(1)}(z)\Big) \quad \text{for} \quad x_1 \geq -1 \end{aligned} \tag{4.184}$$

where $\Delta f(x_1)$ denotes the jump in the function $f(x_1, x_2)$ across the real axis at the point x_1. The conditions (4.183) derive from the fact that $\Delta\zeta^{(1)}(x_1) = \Delta W^{(1)}(x_1) = 0$ for $x_1 < -1$ and lead to

$$\Delta u_1^{(1)}(x_1) = \Delta u_1^h(x_1)\,, \qquad \Delta u_2^{(1)}(x_1) = \Delta u_2^h(x_1) \quad \text{for} \quad x_1 < -1 \tag{4.185}$$

The conditions (4.184) derive from the fact that $\Delta\zeta^{(1)}(x_1) = 0$ and that $\Delta W^{(1)}(x_1)$ is constant for $x_1 \geq -1$ and yield

$$\begin{aligned} \Delta u_1^{(1)}(x_1) &= \frac{\mathrm{i}\,k_2}{|k|}\mathrm{e}^{\mathrm{i}\,k_1 x_1}\Re\Big(kW^{(1)}(z)\Big) + \Delta u_1^h(x_1) \\ \Delta u_2^{(1)}(x_1) &= -\frac{\mathrm{i}\,k_1}{|k|}\mathrm{e}^{\mathrm{i}\,k_1 x_1}\Re\Big(kW^{(1)}(z)\Big) + \Delta u_2^h(x_1) \quad \text{for} \quad x_1 \geq -1 \end{aligned} \tag{4.186}$$

For a lifting airfoil the complex potential $W^{(1)}(z)$ behaves like $\mathrm{i}\,\Gamma \ln z$ as $z \to \infty$. As a result

$$\mathcal{H}_+(z) \simeq \frac{2\Gamma}{\bar{k}z}\exp\left(\frac{1}{2}\mathrm{i}\,\bar{k}z\right) \quad \text{for} \quad 0 \leq \arg(z) \leq 2\pi, \quad z \to \infty \tag{4.187}$$

$$\mathcal{H}_-(z) \simeq -\frac{2\Gamma}{\bar{k}z}\exp\left(-\frac{1}{2}\mathrm{i}\,\bar{k}z\right) \quad \text{for} \quad |\arg(z)| \leq \pi, \quad z \to \infty \tag{4.188}$$

and, from the definition (4.181)

$$J_\pm = \mathcal{O}\Big(\frac{1}{z}\Big) \quad \text{as} \quad z \to \infty \tag{4.189}$$

Thus, it can be concluded that $\mathbf{u}^p$ diverges as $|k|^{-1}\exp(\mathrm{i}\,\mathbf{k}\cdot\mathbf{x})\,\Re(\mathrm{i}\,k\Gamma\ln z)$ as $z \to \infty$. On the other hand, since it is impossible to choose the functions f, F and G in equation (4.179) in order to cancel the diverging terms of $\mathbf{u}^p$, the solution $\mathbf{u}^h + \mathbf{u}^p$ describes indeed the behaviour of the velocity field only in the airfoil inner region.

In order to determine the outer expansion of $\mathbf{u}$, let us consider the following result which is valid for a generic steady, two-dimensional, potential flow

$$\Phi - \Phi_0 + \mathrm{i}\,(\Psi - E_0) = z + \alpha\left\{\mathrm{i}\,\Gamma\ln z + (a + \mathrm{i}\,b)\,z^{-1} + \mathrm{i}\,(e - e_0) + \mathcal{O}\big(z^{-2}\big)\right\} \quad \text{as} \quad z \to \infty \tag{4.190}$$

where a, b and e are real constant and $e_0 = E_0/\alpha$. The term z denotes the potential of a uniform stream, whereas terms within the brackets denote the steady perturbation induced by the airfoil angle of attack, thickness and camber. The expression (4.190) can be written as

$$\Phi - \Phi_0 + \mathrm{i}\,(\Psi - E_0) = z + \alpha\Big(W^{(1)}(z) - W_0\Big) + \mathcal{O}\big(\alpha\, z^{-2}\big) \tag{4.191}$$

where

$$W^{(1)}(z) - W_0 = \mathrm{i}\,\left(\Gamma\ln z + \frac{b - \mathrm{i}\,a}{z} + e - e_0\right) \tag{4.192}$$

and

$$W_0 = \lim \Phi^{(1)}(x_1, x_2) + \mathrm{i}\, e_0 \quad \text{as} \quad x_1 \to -\infty \quad \text{with} \quad x_2 \text{ finite} \tag{4.193}$$

Then, since $|\mathrm{d}(\Phi + \mathrm{i}\,\Psi)/\mathrm{d}z|^2 = |\mathbf{v}|^2 \to 1$ as $z \to \infty$, equation (4.165) has the following limit form

$$\begin{aligned}\Omega &= -\mathrm{i}\,|k| \exp\left\{\mathrm{i}\left[\Re\left(k\,\overline{(\Phi - \Phi_0 + \mathrm{i}\,\Psi - \mathrm{i}\,E_0)}\right) - k_1 t\right]\right\} \\ &= -\mathrm{i}\,|k| \exp\left\{\mathrm{i}\left[\mathbf{k}\cdot\mathbf{x} - \alpha\,\Re\left(k\,\left(W^{(1)}(z) - W_0\right)\right) - k_1 t\right]\right\} + \mathcal{O}(\alpha^2, \alpha\, z^{-2}) \\ &\quad \text{as} \quad z \to \infty, \quad \alpha \to 0, \quad 0 < \arg(z) < 2\pi\end{aligned} \tag{4.194}$$

Equations (4.158) and (4.194) can be used to determine the velocity field at large distance from the airfoil. It results that, within an error $\mathcal{O}(\alpha^2, \alpha\, z^{-2})$

$$\begin{aligned}u_1^{\text{out}} &= -\frac{1}{|k|}\exp\left\{\mathrm{i}\left[\mathbf{k}\cdot\mathbf{x} - \alpha\,\Re\left(k\,\left(W^{(1)}(z) - W_0\right)\right) - k_1 t\right]\right\}\left[k_2 + \alpha\,\Gamma\,\Re\left(\frac{k^2}{\overline{k}z}\right)\right] \\ &\quad + [\mathcal{F}(z) + \mathcal{G}(\overline{z})]\exp(-\mathrm{i}\,k_1 t) \\ u_2^{\text{out}} &= \frac{1}{|k|}\exp\left\{\mathrm{i}\left[\mathbf{k}\cdot\mathbf{x} - \alpha\,\Re\left(k\,\left(W^{(1)}(z) - W_0\right)\right) - k_1 t\right]\right\}\left[k_1 - \alpha\,\Gamma\,\Im\left(\frac{k^2}{\overline{k}z}\right)\right] \\ &\quad + \mathrm{i}\,[\mathcal{F}(z) - \mathcal{G}(\overline{z})]\exp(-\mathrm{i}\,k_1 t)\end{aligned} \tag{4.195}$$

where $\mathcal{F}$ and $\mathcal{G}$ are arbitrary analytic functions of their arguments. It should be demonstrated that the pressure field obtained by inserting the far field velocity in the momentum equation (4.152) is uniformly bounded at infinity only if there is a constant M such that

$$\mathcal{F}(z) = \frac{M}{z} + o(z^{-1}) \quad \text{and} \quad \mathcal{G}(z) = -\frac{M}{\overline{z}} + o(\overline{z}^{-1}) \tag{4.196}$$

Furthermore, the pressure field can be continuous only if $M = 0$. It thus follows that $\mathcal{F}(z) = o(z^{-1})$ and $\mathcal{G}(z) = o(\overline{z}^{-1})$.

From equations (4.172) and (4.174) the following far field expression for the zeroth order velocity can be obtained

$$\begin{aligned}u_1^{(0)} &= -\frac{k_2}{|k|}\mathrm{e}^{\mathrm{i}\,\mathbf{k}\cdot\mathbf{x}} + \mathcal{O}(z^{-2}) \\ u_2^{(0)} &= \frac{k_1}{|k|}\mathrm{e}^{\mathrm{i}\,\mathbf{k}\cdot\mathbf{x}} + \mathcal{O}(z^{-2})\end{aligned} \tag{4.197}$$

Therefore, by matching the outer expansion (4.195) of the velocity field with the inner expansion

$$\mathbf{u}(\mathbf{x}, t) = \exp(-\mathrm{i}\,k_1\,t)\left[\mathbf{u}^{(0)}(\mathbf{x}) + \alpha\left(\mathbf{u}^h(\mathbf{x}) + \mathbf{u}^p(\mathbf{x})\right)\right] \tag{4.198}$$

where $\mathbf{u}^{(0)}$, $\mathbf{u}^h$ and $\mathbf{u}^p$ are given by equations (4.197), (4.179) and (4.180), respectively, the matching conditions $u_i^h, u_2^h \to 0$ as $z \to \infty$ can be found. Furthermore, the inner and outer expansions of the pressure field can be matched in some intermediate domain only if a more severe requirement is satisfied, that is

$$\begin{aligned}u_1^h &= -\frac{\Gamma}{2\,|k|}\left[\frac{kD_+}{\overline{z}} + \overline{\left(\frac{kD_-}{\overline{z}}\right)}\right] + o(z^{-1}) \\ u_2^h &= \frac{\mathrm{i}\,\Gamma}{2\,|k|}\left[\frac{kD_+}{z} - \overline{\left(\frac{kD_-}{\overline{z}}\right)}\right] + o(z^{-1}) \quad \text{as} \quad z \to \infty\end{aligned} \tag{4.199}$$

On the other hand, since the inner particular solution $\mathbf{u}^{(p)}$ diverges as $z \to \infty$, this expression provides the outer behaviour of the velocity field.

A homogeneous solution must be found that satisfies the boundary condition (4.199) at infinity and permits the velocity field to satisfy the boundary condition on the wake and the airfoil surface. In addition, singularities at the airfoil leading edge and trailing edge must be removed from the solution.

The zeroth order velocity $\mathbf{u}^{(0)}$ is the solution of a Sears-type problem and is given by

$$\mathbf{u}^{(0)} = -\left(\hat{\imath}_1 k_2 - \hat{\imath}_2 k_1\right) |k|^{-1} \mathrm{e}^{\mathrm{i}\,\mathbf{k}\cdot\mathbf{x}} + {}^{H}\mathbf{u}^{(0)} \tag{4.200}$$

where ${}^{H}\mathbf{u}^{(0)}$ is a homogeneous solution that decays like z^{-2} as $z \to \infty$. Both ${}^{H}\mathbf{u}^{(0)}$ and $\mathbf{u}^{(0)}$ exhibit jumps across the airfoil and the wake surface, namely

- on the airfoil surface, i.e. $-1 < x_1 < 1$

$$\Delta u_1^{(0)} = \Delta {}^{H}u_1^{(0)} = h_s(x_1) + h_b(x_1) \tag{4.201}$$
$$\Delta u_2^{(0)} = \Delta {}^{H}u_2^{(0)} = 0 \tag{4.202}$$

where

$$h_s(x_1) = \frac{2k_1}{|k|} S(x_1) \sqrt{\frac{1-x_1}{1+x_1}} = -\Delta p^{(0)} \tag{4.203}$$

and

$$h_b(x_1) = \frac{2k_1}{|k|} \Omega_0 \exp\{\mathrm{i}\,k_1 (x_1 - 1)\} \tag{4.204}$$
$$+ \frac{2\mathrm{i}\,k_1^2}{|k|} S(k_1) \exp(\mathrm{i}\,k_1 x_1) \int_1^{x_1} \exp(-\mathrm{i}\,k_1 x_1) \sqrt{\frac{1-x_1}{1+x_1}}\, \mathrm{d}x_1 \tag{4.205}$$

with

$$S(k_1) = \left\{\frac{1}{2} \mathrm{i}\,\pi k_1 \left[H_1^{(1)}(k_1) - \mathrm{i}\,H_0^{(1)}(k_1)\right]\right\}^{-1} \tag{4.206}$$

denoting the complex conjugate Sears function. It can be noticed that $h_s(x_1)$ has a square-root singularity at the airfoil leading edge, and that $h_b(x_1)$ is bounded at the airfoil edges ($h_b(-1) = 0$ and $h_b(1) = 2k_1\,|k|^{-1}\,\Omega_0$).

- In the wake region, i.e. $x_1 > 1$

$$\Delta u_1^{(0)} = \Delta {}^{H}u_1^{(0)} = \frac{2k_1}{|k|} \Omega_0 \exp\{\mathrm{i}\,k_1 (x_1 - 1)\} \tag{4.207}$$
$$\Delta u_2^{(0)} = \Delta {}^{H}u_2^{(0)} = 0 \tag{4.208}$$

where

$$\Delta {}^{H}u_1^{(0)}(1) = \frac{2k_1}{|k|} \Omega_0 = \frac{4k_1}{|k|} \exp(\mathrm{i}\,k_1) \left[\frac{J_0(k_1) + \mathrm{i}\,J_1(k_1)}{H_1^{(1)}(k_1) - \mathrm{i}\,H_0^{(1)}(k_1)}\right] \tag{4.209}$$

Then, the zeroth order velocity can be written as

$$u_1^{(0)} = {}^{b}u_1^{(0)} + \frac{k_1}{|k|} S(k_1)\, \Re\left\{-\mathrm{i}\sqrt{\frac{z-1}{z+1}}\right\}$$
$$u_2^{(0)} = {}^{b}u_2^{(0)} - \frac{k_1}{|k|} S(k_1)\, \Im\left\{-\mathrm{i}\sqrt{\frac{z-1}{z+1}}\right\} \tag{4.210}$$

where ${}^h\mathbf{u}$ is bounded and satisfies the Cauchy-Riemann conditions

$$\frac{\partial {}^h u_1}{\partial x_1} + \frac{\partial {}^h u_2}{\partial x_2} = 0 \qquad \frac{\partial {}^h u_2}{\partial x_1} - \frac{\partial {}^h u_1}{\partial x_2} = 0 \tag{4.211}$$

In order to determine the boundary conditions on the airfoil and the wake surface, let us suppose that the airfoil shape is defined by:

- angle of attack: $\alpha\beta$;
- mean camber line: $x_2 = \alpha y_c(x_1)$;
- thickness distribution: $\alpha b(x_1)$;
- upper and lower surfaces: $x_2 = \alpha f_\pm(x_1)$;

and that the wake is defined by the function

$$x_2 = \alpha g(x_1) + \epsilon \tilde{g}(x_1, t) + \alpha\epsilon\tilde{\tilde{g}}(x_1, t) \tag{4.212}$$

From the theory of unsteady inviscid flow, the following linearized boundary conditions can be obtained for the first order velocity field

- on the airfoil surface, i.e. $-1 < x_1 < 1$

$$\Delta u_2^{(1)} = \frac{\mathrm{d}}{\mathrm{d}x_1}\left\{[y_c(x_1) - \beta x_1]\,\Delta^H u_1^{(0)}(x_1) - \frac{k_2}{|k|}b(x_1)\exp(\mathrm{i}\,k_1 x_1)\right\} \tag{4.213}$$

- In the wake region, i.e. $x_1 > 1$

$$\Delta u_2^{(1)} = -\frac{2k_1}{|k|}\Omega_0\frac{\mathrm{d}}{\mathrm{d}x_1}\left\{\Psi^{(1)}(x_1, 0)\exp\left[\mathrm{i}\,k_1\,(x_1 - 1)\right]\right\} \tag{4.214}$$

where it has been supposed that $g(x_1) = -\Psi^{(1)}(x_1, 0)$.

By requiring that the pressure is continuous across the wake, it can be obtained

$$\Delta u_1^{(1)} = -\frac{2k_1}{|k|}\Omega_0\frac{\mathrm{d}}{\mathrm{d}x_1}\left\{\left[\Phi^{(1)}(x_1, 0) + K_0\right]\exp\left[\mathrm{i}\,k_1\,(x_1 - 1)\right]\right\} \quad \text{for} \quad x_1 > 1 \tag{4.215}$$

where K_0 is an arbitrary constant of integration.

By supposing that $y_c(x_1)$ and $b(x_1)$ go to zero fast enough at the airfoil edges, the only singularities in the boundary condition (4.213) are due to the term

$$\beta\frac{\mathrm{d}}{\mathrm{d}x_1}\left\{x_1\Delta^H u_1^{(0)}(x_1)\right\} \tag{4.216}$$

with $\Delta^H u_1^{(0)}(x_1)$ given by (4.201). These singularities can be removed by introducing a new homogeneous velocity

$$\begin{aligned} u_1^H &= u_1^h + \beta\frac{k_1}{|k|}S(k_1)\,\Re\left(\frac{\mathrm{d}}{\mathrm{d}z}\left[z - z\sqrt{\frac{z-1}{z+1}}\right]\right) \\ u_2^H &= u_2^h - \beta\frac{k_1}{|k|}S(k_1)\,\Im\left(\frac{\mathrm{d}}{\mathrm{d}z}\left[z - z\sqrt{\frac{z-1}{z+1}}\right]\right) \end{aligned} \tag{4.217}$$

whose jump across the airfoil surface and the wake satisfy the conditions

$$\Delta u_1^H(x_1) = \Delta u_1^h(x_1)\,, \qquad \Delta u_2^H(x_1) = \Delta u_2^h(x_1) \quad \text{for} \quad |x_1| > 1 \tag{4.218}$$

and

$$\Delta u_2^H(x_1) = \Delta u_2^h(x_1) + 2\beta \frac{k_1}{|k|} S(k_1) \frac{\mathrm{d}}{\mathrm{d}x_1}\left(x_1\sqrt{\frac{1-x_1}{1+x_1}}\right) \quad \text{for} \quad |x_1| < 1 \tag{4.219}$$

Since $\mathbf{u}^H = \mathbf{u}^h + \mathcal{O}\left(|z|^{-2}\right)$ as $z \to \infty$, $\mathbf{u}^H$ satisfies the same boundary conditions as $\mathbf{u}^h$, also the condition at infinity (4.199). In addition, u_1^H and u_2^H have the form (4.179) where $f(x_2)$ must be put equal to zero in order to satisfy the condition (4.199). Thus, since $\Delta u_1^{(1)} = \Delta u_1^h = 0$ and $\Delta u_2^{(1)} = \Delta u_2^h = 0$ for $x < -1$, from the theory of piecewise analytic functions it follows that

$$\begin{aligned} u_1^H - \mathrm{i}\, u_2^H &= \frac{1}{2\pi\mathrm{i}} \int_{-1}^{\infty} \frac{\Delta u_1^H(x_1) - \mathrm{i}\,\Delta u_2^H(x_1)}{x_1 - z}\, \mathrm{d}x_1 \\ \overline{u_1^H} - \mathrm{i}\, \overline{u_2^H} &= \frac{1}{2\pi\mathrm{i}} \int_{-1}^{\infty} \frac{\Delta \overline{u_1^H}(x_1) - \mathrm{i}\,\Delta \overline{u_2^H}(x_1)}{x_1 - z}\, \mathrm{d}x_1 \end{aligned} \tag{4.220}$$

for all z outside the cut $-1 < x < \infty$.

The velocity jumps Δu_1^H and Δu_2^H can be obtained by inserting (4.180), (4.186), (4.217), (4.218) and (4.219) into the boundary conditions (4.213), (4.214) and (4.215), and by using (4.200) and (4.201). It thus results

$$\Delta u_1^H(x_1) = -\frac{2k_1}{|k|}\Omega_0 \frac{\mathrm{d}}{\mathrm{d}x_1}\left\{\left[\Phi^{(1)}(x_1,0) + K_1\right] \exp\left[\mathrm{i}\, k_1\,(x_1-1)\right]\right\} \quad \text{for} \quad x_1 \geq 1 \tag{4.221}$$

$$\begin{aligned} \Delta u_2^H(x_1) = &-\frac{2k_1}{|k|}\Omega_0 \frac{\mathrm{d}}{\mathrm{d}x_1}\left\{\Psi^{(1)}(x_1,0) \exp\left[\mathrm{i}\, k_1\,(x_1-1)\right]\right\} \\ &+\frac{\mathrm{i}\, k_1}{|k|} \exp(\mathrm{i}\, k_1 x_1)\, \Re\left(k\Delta W^{(1)}(1)\right) \quad \text{for} \quad x_1 > 1 \end{aligned} \tag{4.222}$$

and

$$\begin{aligned} \Delta u_2^H(x_1) = &-\frac{\mathrm{i}}{|k|}\left[r_+(x_1) - r_-(x_1)\right] + \frac{\mathrm{i}\, k_1}{|k|} \exp(\mathrm{i}\, k_1 x_1)\, \Re\left(k\Delta W^{(1)}(x_1)\right) \\ &-\frac{k_2}{|k|}\frac{\mathrm{d}}{\mathrm{d}x_1}\left\{b(x_1)\exp(\mathrm{i}\, k_1 x_1)\right\} + \frac{\mathrm{d}}{\mathrm{d}x_1}\left\{y_c(x_1)\, \Delta^H u_1^{(0)}(x_1)\right\} \\ &-\beta\frac{\mathrm{d}}{\mathrm{d}x_1}\left\{x_1 h_b(x_1)\right\} \quad \text{for} \quad -1 < x_1 < 1 \end{aligned} \tag{4.223}$$

where

$$\begin{aligned} r_\pm(x_1) = &\frac{k^2}{4}\exp\left(\pm\frac{1}{2}\mathrm{i}\, k x_1\right) \int_{-1}^{x_1} \Delta\zeta^{(1)}(x_1) \exp\left(\pm\frac{1}{2}\mathrm{i}\,\overline{k} x_1\right)\, \mathrm{d}x_1 \\ &-\frac{k^2}{4}\exp\left(\pm\frac{1}{2}\mathrm{i}\, k x_1\right) D_\pm \int_{-1}^{x_1} \overline{\Delta\zeta^{(1)}(x_1)} \exp\left(\mp\frac{1}{2}\mathrm{i}\, k x_1\right)\, \mathrm{d}x_1 \end{aligned} \tag{4.224}$$

Furthermore, by requiring that the velocity jump Δu_1^H is finite at the trailing edge, the limit of (4.220) as z approaches the real axis is

$$\begin{aligned} \Delta u_1^H(x_1) = &-\frac{2}{\pi}\sqrt{\frac{1-x_1}{1+x_1}}\left\{P\int_{-1}^{1}\sqrt{\frac{1+\tilde{x}_1}{1-\tilde{x}_1}}\frac{R(\tilde{x}_1)}{\tilde{x}_1 - x_1}\,\mathrm{d}\tilde{x}_1\right\} \\ &+\frac{k_1\Omega_0}{|k|}\int_1^{\infty}\sqrt{\frac{\tilde{x}_1+1}{\tilde{x}_1-1}}\frac{\frac{\mathrm{d}}{\mathrm{d}\tilde{x}_1}\left\{\left[\Phi^{(1)}(\tilde{x}_1,0)+K_1\right]\exp\left[\mathrm{i}\, k_1\,(\tilde{x}_1-1)\right]\right\}}{\tilde{x}_1 - x_1}\,\mathrm{d}\tilde{x}_1 \end{aligned} \tag{4.225}$$

where

$$R(x_1) = -\frac{k_2}{|k|}\frac{\mathrm{d}}{\mathrm{d}x_1}\{[y_c(x_1) - \beta x_1]\exp(\mathrm{i}\,k_1x_1)\} + \frac{1}{4}\frac{\mathrm{d}}{\mathrm{d}x_1}\left\{b(x_1)\,\Delta^H u_1^{(0)}(x_1)\right\}$$
$$-\frac{\mathrm{i}}{|k|}\left\{q^+(x_1) + \overline{q^-(x_1)}\right\} + \frac{\mathrm{i}\,k_1}{|k|}\exp(\mathrm{i}\,k_1x_1)\,\Re\left\{k\left[\left\langle W^{(1)}(x_1)\right\rangle - W_0\right]\right\} \tag{4.226}$$

with

$$q^{\pm}(x_1) = \frac{k^2}{4}\exp\left(\pm\frac{1}{2}\mathrm{i}\,kx_1\right)\int_{\mp\infty}^{x_1}\left\langle\zeta^{(1)}(x_1)\right\rangle\exp\left(\pm\frac{1}{2}\mathrm{i}\,\overline{k}x_1\right)\,\mathrm{d}x_1$$
$$-\frac{k^2}{4}\exp\left(\pm\frac{1}{2}\mathrm{i}\,kx_1\right)D_{\pm}\int_{\mp\infty}^{x_1}\left\langle\zeta^{(1)}(x_1)\right\rangle\exp\left(\mp\frac{1}{2}\mathrm{i}\,kx_1\right)\,\mathrm{d}x_1 \tag{4.227}$$

In the above expressions, for any function $f(x_1, x_2)$ it results that

$$\langle f(x_1)\rangle = \frac{f(x_1, 0^+) + f(x_1, 0^-)}{2} \tag{4.228}$$

The constant K_1 can be determined by requiring that $\mathbf{u}^H$ satisfies the condition (4.199) at infinity. Therefore, by inserting equations (4.221) and (4.222) into equations (4.220) and integrating by parts, it can be shown that, for any $\delta > 0$, there exist two constants $\tilde{a}$ and $\tilde{b}$, such that

$$u_1^H - \mathrm{i}\,u_2^H \sim \tilde{a}/z \quad \text{and} \quad \overline{u_1}^H - \mathrm{i}\,\overline{u_2}^H \sim \tilde{b}/z \quad \text{as} \quad z \to \infty \quad \text{for} \quad \delta < \arg z < 2\pi - \delta \tag{4.229}$$

As a consequence, the solution $\mathbf{u}^H$ obtained by integration of equations (4.220) can match the condition at infinity (4.199). However, this is possible only if the following condition is satisfied

$$\int_{C_0}\mathbf{u}^H\cdot\mathrm{d}\mathbf{S} = -\int_{-1}^{\infty}\Delta u_1^H(x_1)\,\mathrm{d}x_1 = \frac{-\mathrm{i}\,\pi\Gamma}{|k|}\left(\overline{kD_-} - kD_+\right) \tag{4.230}$$

C_0 being a large circle enclosing the airfoil, with a perforation corresponding to the airfoil wake. Therefore, by substituting equations (4.221) and (4.225) into the condition (4.230) and integrating, an equation for the constant K_1 can be obtained.

An inner solution $\mathbf{u}^H$ has been determined that satisfies all the equations and boundary conditions governing the problem. However, this solution is nonuniformly valid at the airfoil edges. The second term on the right-hand side of (4.217), in fact, causes the $\mathcal{O}(\alpha\epsilon)$ term to be more singular at the airfoil edges than the $\mathcal{O}(\epsilon)$ Sears solution. This singular behaviour can be removed by introducing the slightly strained co-ordinate $\eta = \xi_1 + \mathrm{i}\,\xi_2 = z/(1 - \mathrm{i}\,\alpha\beta)$ into the solution (4.167) and expanding for small values of $\alpha\beta\eta$. It thus results that

$$\begin{aligned}
u_1\exp(\mathrm{i}\,k_1t) &= u_1^{(0)}(\xi_1,\xi_2) + \alpha u_1^p(\xi_1,\xi_2) + u_1^H(\xi_1,\xi_2) + \alpha\beta D_\xi\,{}^b u_1^{(0)}(\xi_1,\xi_2)\\
&- \alpha\beta\frac{k_1}{|k|}S(k_1)\,\Re\left\{1 - \sqrt{\frac{\eta-1}{\eta+1}}\right\} + \mathcal{O}(\alpha^2)
\end{aligned} \tag{4.231}$$

$$\begin{aligned}
u_2\exp(\mathrm{i}\,k_1t) &= u_2^{(0)}(\xi_1,\xi_2) + \alpha u_2^p(\xi_1,\xi_2) + u_2^H(\xi_1,\xi_2) + \alpha\beta D_\xi\,{}^b u_2^{(0)}(\xi_1,\xi_2)\\
&- \alpha\beta\frac{k_1}{|k|}S(k_1)\,\Re\left\{\mathrm{i}\left[1 - \sqrt{\frac{\eta-1}{\eta+1}}\right]\right\} + \mathcal{O}(\alpha^2)
\end{aligned} \tag{4.232}$$

where

$$D_\xi = \xi_2\frac{\partial}{\partial\xi_1} - \xi_2\frac{\partial}{\partial\xi_2} \tag{4.233}$$

with $\mathbf{u}^{(0)}$, ${}^b\mathbf{u}^{(0)}$, $\mathbf{u}^p$ and $\mathbf{u}^H$ given by (4.200), (4.210), (4.180) and (4.220), respectively.

The solution for the gust-airfoil interaction problem is now complete. A uniformly valid inner velocity field has been determined. This solution matches the outer expansion (4.199). The next step consists in using the velocity field to determine the pressure field and the airfoil unsteady lift.

Consistently with the expansions (4.154) and (4.168), the unsteady pressure on the airfoil surface can be written as

$$p_s^{\pm} = \epsilon\, e^{-i k_1 t} \left\{ p^{(0)}(\xi_1, \pm 0) + \alpha \left[p^{(1)}(\xi_1, \pm 0) + \left(y_c \pm \frac{b}{2} \right) \left(\frac{\partial p^{(0)}}{\partial \xi_2} \right)_{\xi_2 = \pm 0} \right] + \mathcal{O}\left(\alpha^2\right) \right\} \tag{4.234}$$

Inserting equations (4.153), (4.154), (4.166), (4.231), (4.232) and (4.168) into the momentum equation (4.152), using (4.200), (4.211) and (4.210) and equating the ξ_2 component of the $\mathcal{O}(\epsilon)$ yields

$$\left(\frac{\partial p^{(0)}}{\partial \xi_2} \right)_{\xi_2 = \pm 0} = 0 \quad \text{for} \quad |\xi_1| < 1 \tag{4.235}$$

whereas equating the ξ_1 component of $\mathcal{O}(\alpha\epsilon)$ yields

$$\begin{aligned} &\frac{\mathrm{d}}{\mathrm{d}\xi_1} \left[\Delta p^{(1)}(\xi_1) - \frac{k_2}{|k|} \exp(i k_1 \xi_1)\, \Delta v_1^{(1)}(\xi_1) + \left\langle v_1^{(1)}(\xi_1) \right\rangle \Delta^H u_1(0)(\xi_1) \right] - \frac{k_2^2}{|k|} \exp(i k_1 \xi_1)\, \Delta v_2^{(1)}(\xi_1) \\ &= \left(i k_1 - \frac{\partial}{\partial \xi_1} \right) \left[\Delta u_1^p(\xi_1) + \Delta u_1^H(\xi_1) \right] \\ &\quad \text{for} \quad |\xi_1| < 1 \end{aligned} \tag{4.236}$$

The airfoil fluctuating lift per unit span can be written as

$$L' = L_0' + \alpha L_1' \tag{4.237}$$

where L_0' is the fluctuating lift obtained by Sears for a flat-plate at zero-incidence, namely

$$\frac{L_0'}{\rho c U^2 \epsilon / 2} \exp(i k_1 t) = \int_{-1}^{1} \Delta p^{(0)}(\xi_1)\, \mathrm{d}\xi_1 = 2\pi \frac{k_1}{|k|} \exp(-i k_1 t)\, S(k_1) \tag{4.238}$$

with S denoting the complex conjugate Sears function (4.206), and L_1' denoting the $\mathcal{O}(\alpha\epsilon)$ contribution to the lift given by

$$\frac{L_1'}{\rho c U^2 \alpha \epsilon / 2} \exp(i k_1 t) = \int_{-1}^{1} \Delta p^{(1)}(\xi_1)\, \mathrm{d}\xi_1 \tag{4.239}$$

By evaluating the integral in (4.239), an expression for L_1' can be obtained which depends on the velocities $\mathbf{v}$ and $\mathbf{u}$. However, for a zero-thickness airfoil a significant simplification is possible and a specific formula for L_1' can be obtained which depends only on the steady velocity $\mathbf{v}$. It results that

$$\begin{aligned} L_1' &= \rho c \epsilon U^2 \exp(-i k_1 t) \\ &\left[-\frac{i \Gamma k_1}{2|k|} \left(D_+ - \overline{D_-} \right) + i k_1 \int_{-1}^{1} (1 - x_1)\, R_0(x_1)\, \mathrm{d}x_1 - C(k_1) \int_{-1}^{1} R_0(x_1)\, \mathrm{d}x_1 \right] \end{aligned} \tag{4.240}$$

where $D_\pm$ is given by (4.182),

$$C(k_1) = \frac{H_1^{(1)}(k_1)}{H_1^{(1)}(k_1) - i H_0^{(1)}(k_1)} \tag{4.241}$$

is the complex conjugate of the Theodorsen function [124],

$$R_0 = \frac{\mathrm{i}}{|k|}\sqrt{\frac{1+x_1}{1-x_1}}\left\{k_1 \exp\left(\mathrm{i}\, k_1 x_1\right) \Re(k a_0) + \frac{\mathrm{d}}{\mathrm{d}x_1}\left[q_0^+(x_1) - \overline{q_0^-(x_1)}\right]\right\} \tag{4.242}$$

with

$$q_0^{\pm}(x_1) = \frac{k}{2}\exp\left(\frac{\pm\mathrm{i}\, k x_1}{2}\right)$$
$$\left[\int_{\mp\infty}^{x_1}\left\langle v_2^{(1)}(\xi_1)\right\rangle \exp\left(\pm\frac{1}{2}\imath m\bar{k}x_1\right)\,\mathrm{d}x_1 + D_{\pm}\int_{\mp\infty}^{x_1}\left\langle v_2^{(1)}(\xi_1)\right\rangle \exp\left(\mp\frac{1}{2}\mathrm{i}\, k x_1\right)\,\mathrm{d}x_1\right] \tag{4.243}$$

and

$$a_0 = \left\langle W^{(1)}(x_0)\right\rangle - W_0 \tag{4.244}$$

x_0 being the point where the surface of the airfoil crosses the x_1 axis, and W_0 being defined in (4.193).

Atassi [146] demonstrated that, for a thin airfoil with a small camber and a small angle of attack, moving in a periodic gust, the unsteady lift L_1' can be constructed through a linear superposition of three independent components accounting for the effects produced by the thickness, the camber and the angle of attack. Thus, by denoting as $\alpha\theta$, $\alpha\beta$ and αm the airfoil thickness, angle of attack and camber, respectively, the unsteady lift L_1' can be written as

$$L_1'(k_1, k_2, \beta, m, \theta) = \theta L_\theta'(k_1, k_2) + \beta L_\beta'(k_1, k_2) + m L_m'(k_1, k_2) \tag{4.245}$$

For a zero-thickness airfoil, Atassi [146] obtained specific formulae for the angle of attack and camber contributions:

- *angle of attack contribution*, i.e.

$$\frac{L_\beta'}{\pi\rho c U^2 \epsilon \exp(-\mathrm{i}\, k_1 t)} = \frac{k_1}{|k|}\left[-\left(\mathrm{i}\,\Re(k a_{0\beta}) + \frac{4k_1k_2}{|k|^2}\right)S(k_1) + \Theta_+\left(\frac{k}{2}\right) - \overline{\Theta_-\left(\frac{k}{2}\right)}\right]$$
$$+\ \mathrm{i}\frac{C(k_1)}{|k|}\left[\Lambda_+\left(\frac{k}{2}\right) - \overline{\Lambda_-\left(\frac{k}{2}\right)}\right] \tag{4.246}$$

where

$$\Theta_{\pm}(z) = \pm\mathrm{i}\frac{\pi z J_1(z)\,\Im\left(H_{\pm}(z)\,\overline{J_{\pm}(z)}\right) - \overline{J_{\pm}(z)}}{J_{\pm}(z)} \tag{4.247}$$

$$\Lambda_{\pm}(z) = \pm\mathrm{i}\,\pi z^2\Im\left(H_{\pm}(z)\,\overline{J_{\pm}(z)}\right) \tag{4.248}$$

$$J_{\pm}(z) = J_0(z) \pm J_1(z) \tag{4.249}$$

$$H_{\pm}(z) = H_0^{(1)}(z) \pm H_1^{(1)}(z) \tag{4.250}$$

J_0, J_1, $H_0^{(1)}$ and $H_1^{(1)}$ denoting the Bessel and Hankel functions of the complex variable x, and $a_{0\beta} = \mathrm{i}\,(x_0 - e_{0\beta})$.

- *camber contribution*, i.e.

$$\frac{L_m'}{\pi\rho c U^2 \epsilon \exp(-\mathrm{i}\, k_1 t)} = \frac{-\mathrm{i}\,4k_1}{|k|}\left[\Re\left(\frac{k a_{0m}}{4}\right) + \frac{8k_2\left(k_1^2 - k_2^2\right)}{|k|^4}\right]S(k_1)$$
$$+\frac{16k_1k_2}{|k|^3}\left[\pi k_1 G\left(\frac{k_1}{2}\right) - E\left(\frac{k_1}{2}\right)\right] + \frac{4C(k_1)}{|k_1|}\left[F_+\left(\frac{k}{2}\right) - \overline{F_-\left(\frac{k}{2}\right)}\right] \tag{4.251}$$

where

$$E(k_1) = k_1 J_2(k_1) + C(k_1)\left[k_1 J_+(k_1) - J_1(k_1)\right] \tag{4.252}$$

$$G(z) = \Im\left(\overline{H_1^{(1)}(z)} J_1(z)\right) \tag{4.253}$$

$$F_\pm(z) = \frac{z}{\overline{z}} \frac{\pi z J_\pm(z)\, G(z) - \overline{J_1(z)}}{J_1(z)} \tag{4.254}$$

The lift function $L'_1 = L'_0 + \alpha\left(\beta L'_\beta + m L'_m\right)$ accounts for the effects of the gust distortion due to the steady aerodynamic field. Nevertheless, as in a steady thin airfoil theory, it linearly depends on the airfoil angle of attack and camber.

5

Theories of Aerodynamically Generated Noise

5.1 Introduction

Lighthill's 1952 primary work is usually referred to as the starting point of aeroacoustics. However, as pointed out by Doak [50], Lighthill's theory of sound generated aerodynamically can be inserted in a larger context permeated by the *classical* theories developed by Stokes, Kirchhoff and Rayleigh to describe the fluctuating *types of motion*, say modes, in a fluid medium. From Rayleigh's 1877 book [147] a fundamental concept emerges: the coexistence in a generic small-amplitude fluctuating motion of three distinct modes describing the propagation of acoustic waves, the vortex dynamics and the behaviour of entropy spots. Although Rayleigh did not detail the modal coupling mechanisms, his studies showed two ways for more exhaustive investigations. The first led to a modal approach describing the generation of second order fluctuating motions by interaction of first order flow perturbations. The second was concerned with the role of physical boundaries in coupling different modes of fluctuation. Thus, both *jet-noise* and *interaction noise*, the main topics of modern aeroacoustics, can be founded on Rayleigh's primary intuitions.

In 1958 Chu & Kovásznay [76] shed light on the role of nonlinearity in the generation of modes of fluctuation. They classified the second order bilateral interaction terms according to their source-like behaviour. They showed that Lighthill's stress tensor is a source for the acoustic mode, generated by the self-interaction of the vortical mode. In these terms, the generation of noise by turbulence is only a particular aspect of a more general modal coupling dynamics in a fluid.

A classical approach in the aerodynamics of wings consists in defining surface distributions of singularities whose strength permits to satisfy both boundary conditions and compatibility conditions. In 1936 Gutin [148] developed a theory to predict the noise generated by a rotating propeller. The propeller surface was described as a moving distribution of mass, density and linear momentum density sources generating acoustic waves in a medium at rest. Therefore, Gutin was the first to relate the acoustic mode of fluctuation in a fluid to generalized sources of aerodynamic noise and to physical boundaries. In these terms Lighthill's acoustic analogy could be considered as an extension of Gutin's model and the fluctuating Reynolds' stresses can be interpreted as moving source distributions of linear momentum density flux.

In 1972 Doak [50] reviewed the existing theories of noise generated aerodynamically, giving emphasis to Lilley's [149] theory of mixing noise for a unidirectional, transversely shared turbulent mixing layer. A generalized Rayleigh's approach was used in order to show the similarities between the existing theories and to develop an unified jet aeroacoustic theory. Contrarily to previous models, Doak's theory is explicitly formulated for a generic nonlinear fluctuating motion and no restrictions are made on the mean velocity and the temperature gradients.

5.2 Rayleigh's Approach and Phillips' Theory

Starting from the linearized equations of mass, linear momentum and energy, Rayleigh obtained three sets of equations, which are uncoupled in a portion of fluid in which the linearization is supported and where no physical boundaries are present.

In a similar way, Doak [50] considered the exact transport equations and obtained three sets of coupled equations that exhibit common aspects with Chu & Kovásznay's [76] perturbative recursive equations described in chapter 2, and include, as a special case, a wave equation previously obtained by Phillips [150].

Consider a Newtonian fluid of nonzero bulk viscosity ζ (see (1.48)) and define the following set of variables[1]

$$r = \ln p \quad \sigma = \ln \frac{p}{\rho^{\gamma}} \quad c^2 = \gamma \frac{p}{\rho} \quad k = \frac{K}{\rho\, c_p}$$
$$\nu = \frac{\mu}{\rho} \quad \eta = \frac{4}{3}\nu + \frac{\chi}{\rho} \quad \mathrm{Pr} = \frac{\nu}{k} \quad \dot{q}_{\mathrm{e}} = \frac{\dot{Q}}{\rho\, c_v} \tag{5.1}$$

where $\eta = 2\zeta/\rho$ and $\chi = 2\lambda$. By rearranging the flow governing equations presented in chapter 1, the following equations can be obtained

$$\frac{\mathrm{D}r}{\mathrm{D}t} - \frac{\mathrm{D}\sigma}{\mathrm{D}t} = -\gamma \frac{\partial v_i}{\partial x_i} \tag{5.2}$$

$$\begin{aligned}
&\left\{c^2 \frac{\partial}{\partial x_i} + \eta \left[\frac{\partial}{\partial x_i} + \frac{\partial [\ln(\rho\eta)]}{\partial x_i}\right] \left[\frac{\mathrm{D}}{\mathrm{D}t} - (\gamma-1)\, k \frac{\partial^2}{\partial x_j^2}\right]\right\} r = \\
&\quad \gamma f_i - \gamma \frac{\mathrm{D}v_i}{\mathrm{D}t} + \gamma \nu \left[\frac{\partial}{\partial x_j} + \frac{\partial [\ln(\rho\nu)]}{\partial x_j}\right] \left[\frac{\partial v_i}{\partial x_j} + \frac{\partial v_j}{\partial x_i} - 2\frac{\partial v_k}{\partial x_k}\delta_{ij}\right] + \\
&\quad \eta \left[\frac{\partial}{\partial x_i} + \frac{\partial [\ln(\rho\eta)]}{\partial x_i}\right] \left[k \frac{\partial^2 \sigma}{\partial x_j^2} + \frac{\dot{q}_{\mathrm{i}} + \dot{q}_{\mathrm{e}}}{T}\right]
\end{aligned} \tag{5.3}$$

and

$$k \frac{\partial^2 \sigma}{\partial x_j^2} - \frac{\mathrm{D}\sigma}{\mathrm{D}t} = -(\gamma-1)\, k \frac{\partial^2 r}{\partial x_j^2} - \frac{\dot{q}_{\mathrm{i}} + \dot{q}_{\mathrm{e}}}{T} \tag{5.4}$$

where $\dot{q}_{\mathrm{i}}$ is the following positive definite *internal dissipation function*

$$\begin{aligned}
\dot{q}_{\mathrm{i}} = &\frac{\gamma k \mathrm{Pr}}{c_p} \left\{\frac{c_p}{\mathrm{Pr}} \frac{\partial [\ln(KT)]}{\partial x_j} \frac{\partial T}{\partial x_j} + \left(\frac{4}{3} + \frac{\chi}{\mu}\right) \left(\frac{\partial v_k}{\partial x_k}\right)^2\right\} + \\
&\frac{\gamma k \mathrm{Pr}}{c_p} \left(\frac{\partial v_i}{\partial x_j} + \frac{\partial v_j}{\partial x_i} - 2\frac{\partial v_k}{\partial x_k}\delta_{ij}\right) \frac{\partial v_i}{\partial x_j}
\end{aligned} \tag{5.5}$$

Equation (5.4) is a generalized inhomogeneous scalar diffusion equation for the entropy mode of fluctuation.

Taking the curl of equation (5.3), a generalized vector equation for the convection and diffusion of the vorticity mode can be obtained. Conversely, rearranging equations (5.2) and (5.4) leads to

$$\frac{\mathrm{D}r}{\mathrm{D}t} - (\gamma-1)\, k \frac{\partial^2 r}{\partial x_j^2} = -\gamma \frac{\partial v_i}{\partial x_i} + k \frac{\partial^2 \sigma}{\partial x_j^2} + \frac{\dot{q}_{\mathrm{i}} + \dot{q}_{\mathrm{e}}}{T} \tag{5.6}$$

[1] As far as possible, the nomenclature used in this chapter is the same used in chapter 1.

By taking the divergence of equation (5.3) and subtracting from it the material derivative of equation (5.6), the following generalized equation for the sound mode of fluctuation can be obtained

$$\begin{aligned}&\frac{\partial}{\partial x_i}\left[\eta\left(\frac{\partial}{\partial x_i}+\frac{\partial\left[\ln\left(\rho\eta\right)\right]}{\partial x_i}\right)\left(\frac{\mathrm{D}}{\mathrm{D}t}-(\gamma-1)\,k\frac{\partial^2}{\partial x_j^2}\right)\right]r+\\&\left\{\frac{\mathrm{D}}{\mathrm{D}t}\left((\gamma-1)\,k\frac{\partial^2}{\partial x_j^2}\right)+\frac{\partial}{\partial x_i}\left(c^2\frac{\partial}{\partial x_i}\right)-\frac{\mathrm{D}^2}{\mathrm{D}t^2}\right\}r=\\&\gamma\frac{\partial f_i}{\partial x_i}-\gamma\frac{\partial v_i}{\partial x_j}\frac{\partial v_j}{\partial x_i}+\frac{\partial}{\partial x_i}\left\{\gamma\nu\left[\frac{\partial}{\partial x_j}+\frac{\partial\left[\ln\left(\rho\nu\right)\right]}{\partial x_j}\right]\left[\frac{\partial v_i}{\partial x_j}+\frac{\partial v_j}{\partial x_i}-2\frac{\partial v_k}{\partial x_k}\delta_{ij}\right]\right\}+\\&\left\{\frac{\partial}{\partial x_i}\left[\eta\left(\frac{\partial}{\partial x_i}+\frac{\partial\left[\ln\left(\rho\eta\right)\right]}{\partial x_i}\right)\right]-\frac{\mathrm{D}}{\mathrm{D}t}\right\}\left\{k\frac{\partial^2\sigma}{\partial x_j^2}+\frac{\dot{q}_\mathrm{i}+\dot{q}_\mathrm{e}}{T}\right\}\end{aligned}\tag{5.7}$$

Equation (5.7) has the form of a convected inhomogeneous scalar wave equation for a viscous heat-conducting nonuniform acoustic medium.

Equations (5.3), (5.4) and (5.7) can be linearized with respect to a uniform flow with constant mean velocity $\overline{v}_i$, constant thermodynamic variables $\overline{c}$, $\overline{p}$, $\overline{T}$ and $\overline{\rho}$, constant viscous and thermal properties $\overline{\mu}$, $\overline{\eta}$ and $\overline{k}$. Thus, denoting by primes the fluctuating components and neglecting second order terms, the following set of linearized equations can be obtained

$$\left\{\left[\overline{\eta}+(\gamma-1)\,\overline{k}\right]\frac{\overline{\mathrm{D}}}{\mathrm{D}t}+\overline{c}^2\right\}\frac{\partial^2 r'}{\partial x_i^2}-\frac{\overline{\mathrm{D}}^2 r'}{\mathrm{D}t^2}=\gamma\frac{\partial f_i'}{\partial x_i}+\overline{\eta}\left\{\frac{\partial^2}{\partial x_i^2}-\frac{\overline{\mathrm{D}}}{\mathrm{D}t}\right\}\left(\overline{k}\frac{\partial^2\sigma'}{\partial x_j^2}+\frac{\dot{q}_\mathrm{e}'}{\overline{T}}\right)\tag{5.8}$$

$$\left\{\overline{\nu}\,\nabla\times\nabla\times+\frac{\overline{\mathrm{D}}}{\mathrm{D}t}\right\}\left(\nabla\times\mathbf{v}_\mathrm{s}'\right)_i=\left(\nabla\times\mathbf{f}'\right)_i\tag{5.9}$$

$$\left\{\overline{k}\frac{\partial^2}{\partial x_i^2}-\frac{\overline{\mathrm{D}}}{\mathrm{D}t}\right\}\sigma'=-(\gamma-1)\,\overline{k}\,\frac{\partial^2 r'}{\partial x_i^2}-\frac{\dot{q}_\mathrm{e}'}{\overline{T}}\tag{5.10}$$

where

$$\frac{\overline{\mathrm{D}}}{\mathrm{D}t}=\frac{\partial}{\partial t}+\overline{v}_j\frac{\partial}{\partial x_j}\tag{5.11}$$

and $\mathbf{v}_\mathrm{s}'$ is the solenoidal component of the fluctuating velocity.

Equation (5.9) describes the convection and diffusion of the vorticity mode. In the small perturbation limit, the vorticity mode is uncoupled from both the acoustic and the entropic modes. These latter two modes, on the contrary, are coupled to each other.

The second term on the right-hand side of equation (5.8) can be written as

$$-(\gamma-1)\,\overline{k}^2\frac{\partial^4 r'}{\partial x_i^2\partial x_j^2}+\overline{k}\left(\overline{\eta}-\overline{k}\right)\frac{\partial^4\sigma'}{\partial x_i^2\partial x_j^2}+\left[\left(\overline{\eta}-\overline{k}\right)\frac{\partial^2}{\partial x_i^2}-\frac{\overline{\mathrm{D}}}{\mathrm{D}t}\right]\left(\frac{\dot{q}_\mathrm{e}'}{\overline{T}}\right)\tag{5.12}$$

Consider the Stokes number[2] $\epsilon=f\,\overline{\nu}/\overline{c}^2$. It results that $\epsilon\ll 1$ for a large range of frequency f. Hence, the first term on the right-hand side of equation (5.10) and the first two terms in equation (5.12), being of higher order in ϵ, can be neglected and equations (5.8), (5.9) and (5.10) take the form

$$\left\{\left[\overline{\eta}+(\gamma-1)\,\overline{k}\right]\frac{\overline{\mathrm{D}}}{\mathrm{D}t}+\overline{c}^2\right\}\frac{\partial^2 r'}{\partial x_i^2}-\frac{\overline{\mathrm{D}}^2 r'}{\mathrm{D}t^2}=\gamma\frac{\partial f_i'}{\partial x_i}+\left\{\left(\overline{\eta}-\overline{k}\right)\frac{\partial^2}{\partial x_i^2}-\frac{\overline{\mathrm{D}}}{\mathrm{D}t}\right\}\left(\frac{\dot{q}_\mathrm{e}'}{\overline{T}}\right)\tag{5.13}$$

$$\left\{\overline{\nu}\,\nabla\times\nabla\times+\frac{\overline{\mathrm{D}}}{\mathrm{D}t}\right\}\left(\nabla\times\mathbf{v}_\mathrm{s}'\right)_i=\left(\nabla\times\mathbf{f}'\right)_i\tag{5.14}$$

$$\left\{\overline{k}\frac{\partial^2}{\partial x_i^2}-\frac{\overline{\mathrm{D}}}{\mathrm{D}t}\right\}\sigma'=-\frac{\dot{q}_\mathrm{e}'}{\overline{T}}\tag{5.15}$$

[2]This is the same parameter utilized by Chu & Kovásznay and defined in equation (2.41).

In the small Stokes number limit the coupling between small amplitude modes of fluctuation is only due to the boundary conditions: the velocity continuity condition couples all the three types of motion, the temperature continuity condition couples the acoustic and the entropic modes.

In 1960 Phillips [150] obtained an exact convected wave equation for the logarithmic pressure. This is a special case of equation (5.7) for the particular conditions $f_i = \dot{q}'_e = \chi = 0$. However, Phillips did not notice the generalized Rayleigh form of his equation. This was merely interpreted as a wave equation in a moving non-homogeneous medium, with a right-hand side accounting for the fluid viscosity effects, and describing the production of acoustic waves by velocity and entropy fluctuations. This physical interpretation is imprecise in two points:

- Phillips did not extract from the viscous terms the part responsible for the damping of the wave propagation, which should be written on the left-hand side, as done by Doak in equation (5.7) and by Chu & Kovásznay in their iterative set of equations (2.21), (2.22) and (2.23).
- The term $-\gamma(\partial v_i/\partial x_j)(\partial v_j/\partial x_i)$ is not a pure source term, but it also accounts for a shear refraction contribution that should be moved to the left-hand side.

In order to shed light on the latter point, let us consider the following simplified inviscid form of the Phillips' equation

$$\frac{\partial}{\partial x_i}\left(c^2\frac{\partial r}{\partial x_i}\right) - \frac{\mathrm{D}^2 r}{\mathrm{D}t^2} = -\gamma\frac{\partial v_i}{\partial x_j}\frac{\partial v_j}{\partial x_i} \tag{5.16}$$

and apply to it the material derivative operator. For an inviscid fluid, the following exact relation is satisfied

$$-\gamma\frac{\mathrm{D}}{\mathrm{D}t}\left(\frac{\partial v_i}{\partial x_j}\frac{\partial v_j}{\partial x_i}\right) = 2\frac{\partial v_j}{\partial x_i}\frac{\partial}{\partial x_j}\left(c^2\frac{\partial r}{\partial x_i}\right) + 2\gamma\frac{\partial v_i}{\partial x_j}\frac{\partial v_j}{\partial x_k}\frac{\partial v_k}{\partial x_i} \tag{5.17}$$

Thus, the material derivative of equation (5.16) takes the form

$$\frac{\mathrm{D}}{\mathrm{D}t}\left\{\frac{\partial}{\partial x_i}\left(c^2\frac{\partial r}{\partial x_i}\right) - \frac{\mathrm{D}^2 r}{\mathrm{D}t^2}\right\} - 2\frac{\partial v_j}{\partial x_i}\frac{\partial}{\partial x_j}\left(c^2\frac{\partial r}{\partial x_i}\right) = 2\gamma\frac{\partial v_i}{\partial x_j}\frac{\partial v_j}{\partial x_k}\frac{\partial v_k}{\partial x_i} \tag{5.18}$$

where the shear layer refraction contribution has been isolated and moved to the left-hand side.

The following linearized form of equation (5.18), for a model shear layer $v_i = \overline{v}_1(x_2) + u_i$, was obtained by Lilley [149]

$$\begin{aligned}\frac{\overline{\mathrm{D}}_1}{\mathrm{D}t}\left\{\frac{\partial}{\partial x_i}\left(\overline{c}^2\frac{\partial r'}{\partial x_i}\right) - \frac{\overline{\mathrm{D}}_1^2 r'}{\mathrm{D}t^2}\right\} - 2\frac{\partial \overline{v}_1}{\partial x_2}\frac{\partial}{\partial x_1}\left(\overline{c}^2\frac{\partial r'}{\partial x_2}\right) = \\ 6\gamma\frac{\partial \overline{v}_1}{\partial x_2}\frac{\partial u_2}{\partial x_k}\frac{\partial u_k}{\partial x_1} + 2\gamma\frac{\partial u_i}{\partial x_j}\frac{\partial u_j}{\partial x_k}\frac{\partial u_k}{\partial x_i}\end{aligned} \tag{5.19}$$

where

$$\frac{\overline{\mathrm{D}}_1}{\mathrm{D}t} = \frac{\partial}{\partial t} + \overline{v}_1(x_2)\frac{\partial}{\partial x_1} \tag{5.20}$$

An analysis of the order of magnitude of equation (5.19) is useful to enlighten some mechanisms involved in the internal generation and propagation of acoustic waves in a shear layer configuration. The relative magnitude of the refraction term is given by

$$2\frac{\partial \overline{v}_1}{\partial x_2}\frac{\partial}{\partial x_1}\left(\overline{c}^2\frac{\partial r'}{\partial x_2}\right) / \frac{\mathrm{D}}{\mathrm{D}t}\left\{\frac{\partial}{\partial x_i}\left(c^2\frac{\partial r}{\partial x_i}\right)\right\} = \mathcal{O}\left(\frac{V_s}{L_s f}\right) \tag{5.21}$$

where V_s is a shear layer reference velocity, L_s is the shear layer thickness and f is a characteristic frequency in the convected frame of reference. Considering that

$$\frac{V_s}{L_s f} = M_s\frac{\lambda}{L_s} \tag{5.22}$$

at a given Mach number M_s, the refraction term becomes significant for an acoustic wavelength λ greater than, or comparable to, the shear layer thickness. Furthermore, a comparison between the refraction term and the source term provides the following result

$$\frac{\partial \overline{v}_1}{\partial x_2}\frac{\partial}{\partial x_1}\left(\overline{c}^2\frac{\partial r'}{\partial x_2}\right)/\gamma\frac{\partial \overline{v}_1}{\partial x_2}\frac{\partial u_2}{\partial x_k}\frac{\partial u_k}{\partial x_1} = \mathcal{O}\left(\frac{L_t^2}{\lambda^2}\right) \tag{5.23}$$

where L_t is the length scale of the turbulent eddies, which is comparable to the shear layer thickness.

Concluding, the greater is the difficulty in distinguishing the refraction term from the source term ($L_t/\lambda \ll 1$ in equation (5.23)), the greater is their influence on the propagative behaviour ($\lambda/L_s \gg 1$ in equation (5.21)). Therefore, an adequate use of a jet-noise aeroacoustic model requires the refraction contribution to be separated *a priori* from the source term and to be moved to the left-hand side of the wave equation.

5.3 Lighthill's Acoustic Analogy

Pressure fluctuations generated somewhere in a fluid may propagate as acoustic disturbances within the fluid medium. On the ideal assumption of separating the sound generation mechanisms from its pure propagation, the flow governing equations can be arranged in the form of an inhomogeneous wave equation where all those terms discarded by the propagation pattern are gathered at right-hand side and interpreted as source terms. Such a model is referred to as *acoustic analogy model.*

Depending on both the reference wave equation and the mechanism that generates the pressure disturbances (free turbulent flows, turbulent flows confined by solid surfaces, etc.), the acoustic analogy approach leads to different formulations. The first model was proposed by Lighthill [1] and describes the noise generated by a turbulent portion of fluid and propagating in a quiescent unbounded medium. Despite its concise formulation, Lighthill's theory succeeded in predicting the so-called *eighth-power law*, describing the dependence of the jet-noise intensity on the mean jet velocity.

More detailed measurements showed that Lighthill's acoustic analogy is too concise to provide a clear identification of all the cause-effect mechanisms in the noise generation from turbulent mixing regions. Indeed, Lighthill [1] first discussed the physical consistency of the acoustic analogy model. He argued that the sound back reaction onto the aerodynamic source of noise restraints the validity of the acoustic analogy approach. A brief discussion about Lighthill's model is reported below.

The Navier-Stokes equations (1.62) and (1.63), in the absence of both mass injections and external forces, take the form

$$\frac{\partial \rho}{\partial t} + \frac{\partial (\rho v_i)}{\partial x_i} = 0 \tag{5.24}$$

$$\frac{\partial (\rho v_i)}{\partial t} + \frac{\partial (\rho v_i v_j)}{\partial x_j} = -\frac{\partial p}{\partial x_i} + \frac{\partial \tau_{ij}}{\partial x_j} \tag{5.25}$$

with

$$\tau_{ij} = \mu\left(\frac{\partial v_i}{\partial x_j} + \frac{\partial v_j}{\partial x_i}\right) - \left(\frac{2}{3}\mu - \chi\right)\frac{\partial v_k}{\partial x_k}\delta_{ij} \tag{5.26}$$

Expanding the expression

$$-\frac{\partial}{\partial t}\left[\mathrm{E}q.(5.24)\right] + \frac{\partial}{\partial x_i}\left[\mathrm{E}q.(5.25)\right] + c_0^2\frac{\partial^2 \rho}{\partial x_i^2} - c_0^2\frac{\partial^2 \rho}{\partial x_i^2} = 0 \tag{5.27}$$

leads to the Lighthill's equation

$$c_0^2\frac{\partial^2 \rho}{\partial x_i^2} - \frac{\partial^2 \rho}{\partial t^2} = -\frac{\partial^2 T_{ij}}{\partial x_i \partial x_j} \tag{5.28}$$

where

$$T_{ij} = \rho v_i v_j + \left(p - c_0^2 \rho\right) \delta_{ij} - \tau_{ij} \tag{5.29}$$

is the Lighthill's stress tensor.

The constant c_0 is mathematically arbitrary. However, it can be identified with the sound speed by supposing the existence of a region of fluid surrounding the aeroacoustic source region with a uniform mean temperature $T_0 = c_0^2/\gamma R$. Therefore, the acoustic analogy can be established by supposing that the terms $\partial^2 T_{ij}/\partial x_i \partial x_j$ are of second order in the exterior region where they can be neglected. This is equivalent to suppose a quiescent fluid exterior to the source region.

Equation (5.28) can be interpreted as a standard wave equation for the acoustic pressure, provided that the acoustic approximation

$$p - p_0 = c_0^2 \left(\rho - \rho_0\right) \tag{5.30}$$

is used. The consistency of this approximation can be investigated beneath the light of Stokes-Kirchhoff-Rayleigh's theories.

Consider the linearized Rayleigh equation (5.13) for the acoustic mode of fluctuation ($r' \simeq p'/p_0$) in a quiescent fluid in the absence of body forces and heat additions, namely

$$c_0^2 \left[\frac{\eta_0 + (\gamma - 1)\, k_0}{c_0^2} \frac{\partial}{\partial t} + 1\right] \frac{\partial^2 p'}{\partial x_i^2} - \frac{\partial^2 p'}{\partial t^2} = 0 \tag{5.31}$$

This equation has been obtained in the limit of both small amplitude fluctuations

$$\frac{p - p_0}{p_0} \ll 1 \qquad \frac{\rho - \rho_0}{\rho_0} \ll 1 \qquad \frac{v_i}{c_0} \ll 1 \tag{5.32}$$

and small but non vanishing Stokes number $\omega \left[\eta_0 + (\gamma - 1)\, k_0\right] / c_0^2$. Under the same hypothesis equation (5.28) can be linearized yielding

$$\begin{aligned} c_0^2 \frac{\partial^2}{\partial x_i^2} \left(\rho - \rho_0\right) - \frac{\partial^2}{\partial t^2} \left(\rho - \rho_0\right) = \\ -\rho_0 \frac{\partial^2 \left(v_i v_j\right)}{\partial x_i \partial x_j} - \frac{\partial^2}{\partial x_i^2} \left\{p - p_0 - c_0^2 \left(\rho - \rho_0\right) + \eta_0 \frac{\partial}{\partial t} \left(\rho - \rho_0\right)\right\} \end{aligned} \tag{5.33}$$

Consider now the linearized Rayleigh equation (5.10) for the thermal type of motion in a quiescent fluid and in the absence of heat additions, namely

$$\left\{k_0 \frac{\partial^2}{\partial x_i^2} - \frac{\partial}{\partial t}\right\} \sigma' = -\,(\gamma - 1)\, k_0 \frac{\partial^2 r'}{\partial x_i^2} \tag{5.34}$$

In the small amplitude approximation ($r' \simeq p'/p_0$ and $\sigma' \simeq p'/p_0 - \gamma \rho'/\rho_0$) equation (5.34) takes the form

$$\frac{\partial}{\partial t}\left(\frac{p - p_0}{p_0}\right) - \gamma \frac{\partial}{\partial t}\left(\frac{\rho - \rho_0}{\rho_0}\right) - (\gamma - 1)\, k_0 \frac{\partial^2}{\partial x_i^2}\left(\frac{p - p_0}{p_0}\right) - k_0 \frac{\partial^2 \sigma'}{\partial x_i^2} = 0 \tag{5.35}$$

The second time-derivative of $(p - p_0)/p_0$ obtained from equation (5.35) can be substituted into equation (5.33), providing

$$\begin{aligned} -\frac{1}{c_0^2} \frac{\partial^2}{\partial t^2} \left(p - p_0\right) + \frac{\gamma - 1}{c_0^2} k_0 \frac{\partial^2}{\partial x_i^2} \frac{\partial}{\partial t} \left(p - p_0\right) + \frac{k_0 p_0}{\gamma} \frac{\partial^2}{\partial x_i^2} \frac{\partial \sigma'}{\partial t} = \\ -\rho_0 \frac{\partial^2 \left(v_i v_j\right)}{\partial x_i \partial x_j} - \frac{\partial^2}{\partial x_i^2} \left(p - p_0\right) - \eta_0 \frac{\partial^2}{\partial x_i^2} \frac{\partial}{\partial t} \left(\rho - \rho_0\right) \end{aligned} \tag{5.36}$$

Then, substituting $\rho - \rho_0 = (p - p_0)/c_0^2 - (\rho_0/\gamma)\,\sigma'$ yields

$$c_0^2\left[\frac{\eta_0 + (\gamma-1)\,k_0}{c_0^2}\frac{\partial}{\partial t} + 1\right]\frac{\partial^2 p'}{\partial x_i^2} - \frac{\partial^2 p'}{\partial t^2} = -\rho_0 c_0^2\frac{\partial^2 (v_i v_j)}{\partial x_i \partial x_j} + \frac{\rho_0 c_0^2}{\gamma}(\eta_0 - k_0)\frac{\partial^2}{\partial x_i^2}\frac{\partial \sigma'}{\partial t} \tag{5.37}$$

Finally, by neglecting terms of higher order in the Stokes number, equation (5.37) takes the form

$$c_0^2\left[\frac{\eta_0 + (\gamma-1)\,k_0}{c_0^2}\frac{\partial}{\partial t} + 1\right]\frac{\partial^2 p'}{\partial x_i^2} - \frac{\partial^2 p'}{\partial t^2} = -\rho_0 c_0^2\frac{\partial^2 (v_i v_j)}{\partial x_i \partial x_j} \tag{5.38}$$

Comparing the homogeneous linearized Rayleigh equation (5.31) to the linearized form of the Lighthill equation (5.38) shows that Lighthill's acoustic analogy is rigorous only in the vanishing Stokes number limit.

A more suitable version of Lighthill's acoustic analogy theory can be obtained by rearranging equation (5.28) in the following form

$$\frac{\partial^2 p}{\partial x_i^2} - \frac{1}{c_0^2}\frac{\partial^2 p}{\partial t^2} = -\frac{\partial^2 (\rho v_i v_j) - \tau_{ij}}{\partial x_i \partial x_j} - \frac{1}{c_0^2}\frac{\partial^2}{\partial t^2}\left(p - c_0^2 \rho\right) \tag{5.39}$$

In the acoustic field of a nearly quiescent Stokesian fluid, even at first order in the Stokes number, Stokes-Kirchhoff-Rayleigh's theories states that $(\rho - \rho_0) = (p - p_0)/c_0^2$. Indeed, because of the parabolic nature of the entropic mode of fluctuation, the thermal effects on the mass density fluctuations are typically confined to a region closer to the source, and do not propagate farther away from it. Thus, by comparing equation (5.28) to equation (5.39) and by applying the uniqueness theorem of a wave equation solution, it follows that the difference between the source distributions

$$\frac{\partial^2}{\partial x_i^2}\left(p - c_0^2\rho\right) \quad \text{and} \quad \frac{1}{c_0^2}\frac{\partial^2}{\partial t^2}\left(p - c_0^2\rho\right) \tag{5.40}$$

is of higher order in the Stokes number, even in the source region.

Concluding, the Lighthill equation (5.28) and equation (5.39) are perfectly equivalent in a practical use, but the second is conceptually more rigorous since it can be directly reduced to a correct Rayleigh equation for the acoustic mode of fluctuation.

5.4 Doak's Momentum Potential Theory

Between 1970 and 1973 Doak ([151], [50] and [152]) developed a unified theory of noise generated aerodynamically. This is based on the identification of acoustic, thermal and turbulent motions in a small amplitude fluctuating field, and on the extension of the modal approach to nonlinear fluctuating motions.

In the present section only the main guidelines of Doak's theory are described. The reader should refer to the original works for an exhaustive treatment.

The starting point of Doak's theory is the linear momentum density decomposition in its solenoidal and irrotational parts, i.e.

$$\rho \mathbf{v} = \mathbf{B} - \nabla\psi \tag{5.41}$$

with $\mathbf{B} = \nabla \times \mathbf{A}$. The vector $\mathbf{B}$ is purely solenoidal ($\nabla \cdot \mathbf{B} = 0$) and the vector $\nabla\psi$ is purely irrotational ($\nabla \times \nabla\psi = 0$). It thus results that

$$\nabla \cdot (\rho \mathbf{v}) = -\nabla^2 \psi \tag{5.42}$$

$$\nabla \times (\rho \mathbf{v}) = \nabla \times (\nabla \times \mathbf{A}) \tag{5.43}$$

where $\mathbf{A}$ and ψ are the vector and scalar linear momentum density potential, respectively. Therefore, the continuity equation (5.24) takes the form

$$\frac{\partial \rho}{\partial t} = \nabla^2 \psi \tag{5.44}$$

which involves only the solenoidal part of the linear momentum density.

In the case of a time-stationary process, the generic flow quantity g can be decomposed into its mean stationary part and its fluctuating part by writing

$$g(x,t) = \overline{g}(x) + g'(x,t) \tag{5.45}$$

with

$$\overline{g}(x) = \frac{1}{T}\int_{-T/2}^{+T/2} g(x,t)\,\mathrm{d}t \tag{5.46}$$

$$\overline{g'}(x,t) = \frac{1}{T}\int_{-T/2}^{+T/2} g'(x,t)\,\mathrm{d}t = 0 \tag{5.47}$$

T is one period if g is a periodic function, and the limit $T \to \infty$ if g is a random quantity.

As shown by Doak [151], for a time-stationary process in the linear momentum density and in the mass density, the time averaged part of the scalar potential ψ can be supposed to be identically zero without loss of generality. Therefore, the linear momentum density can be written as

$$\rho\mathbf{v} = \overline{\mathbf{B}} + \mathbf{B}' - \nabla\psi' \tag{5.48}$$

with $\overline{\rho\mathbf{v}} = \overline{\mathbf{B}}$. Therefore, the fluctuating counterpart of equation (5.44) is

$$\frac{\partial \rho'}{\partial t} = \nabla^2 \psi' \tag{5.49}$$

In analogy with electromagnetisms, ψ' and $\mathbf{B}$ can be defined as the pykodynamic and the pykostatic part of the linear momentum density, respectively. In these terms, the acoustic problem is reduced to the determination of the pykodynamic and the pykostatic contributions of the fluctuating pressure.

In a earlier work Doak [151] considered an inviscid, non-heat-conducting fluid with negligible external forcing and heating. Thus, he showed that when the linear momentum and the energy transport equations are linearized in all their fluctuating quantities, except the solenoidal linear momentum fluctuations[3], the acoustic and the thermal parts of the fluctuating mass density, the scalar potential and the pykodynamic part of the fluctuating pressure have a physically meaningful nature.

In a successive work Doak [152] showed that the existing theories of aerodynamically generated noise can be interpreted as special cases of a generalized theory, whose applicability is ensured by the fact that second-order terms in the solenoidal part of the fluctuating linear momentum density have been retained in the formulation.

In spite of Doak's complete formulation, only a simplified equation is reported below which is valid in regions where neither mean velocity gradients, nor mean temperature and/or pressure gradients are significantly large[4]. Therefore, the simplified form of Doak's equation is an inhomogeneous convected wave equation for the acoustic fluctuating pressure p', i.e.

$$\left(\overline{c}^2\delta_{ij} - \frac{\overline{B_i}\,\overline{B_j}}{\overline{\rho}^2}\right)\frac{\partial^2 p'}{\partial x_i \partial x_j} - \frac{\partial^2 p'}{\partial t^2} - 2\frac{\overline{B_j}}{\overline{\rho}}\frac{\partial^2 p'}{\partial x_j \partial t} \simeq \frac{\partial^2 Q'_{ij}}{\partial x_i \partial x_j} \tag{5.50}$$

[3] Second-order solenoidal linear momentum fluctuation were retained as possible sources.

[4] In the flow portion where the flow quantities change appreciably over distances of the same order of the acoustic wavelength, as in high shear regions or at the boundaries of shock cells in over-expanded jets, suitable boundary conditions must be used in order to describe such regions as localized discontinuities.

where the equivalent quadrupole source is given by

$$Q'_{ij} \simeq \frac{\overline{B_i}B'_j + \overline{B_j}B'_i + B'_iB'_j}{\overline{\rho}} \tag{5.51}$$

6

Theory of Vortex Sound

6.1 Introduction

The theory of *vortex sound* is due to Powell [153] [154]. It is based on the concept that the vorticity within a compact eddy in a weakly compressible isentropic medium drives a near hydrodynamic field and feeds an acoustic far field. Therefore, sources of aerodynamic noise are associated with regions of the flow field with non-vanishing vorticity.

The theory of vortex sound did not receive a great attention until Howe [20] showed the consistency of Powell's formulation with Lighthill's acoustic analogy. Howe demonstrated that it is possible to manipulate the Lighthill's stress tensor in such a manner that Powell's source term would be seen to be dominant at low turbulence Mach numbers. Howe's discussion on the consistency of Powell's theory is illustrated in section 6.2. Less rigorously, we will show hereafter how the concept of *vortex force* due to Prandtl [155] can be used to justify the theory of vortex sound.

The equation of motion for an ideal and incompressible fluid can be written as

$$\frac{\partial \mathbf{v}}{\partial t} = -\nabla\left(p + \frac{v^2}{2}\right) + \mathbf{v} \times \boldsymbol{\omega} + \mathbf{f} \tag{6.1}$$

where $\mathbf{f}$ denotes an external force per unit mass. Equation (6.1) shows that the term $\mathbf{v} \times \boldsymbol{\omega}$ acts as an equivalent body force called the *vortex force*. The concept of vortex force is the fundament of the *circulation theory* developed by Kármán & Burgers' [5], that describes the response of a wing to unsteady flow conditions. A body force $\mathbf{f}$ exerted on a compressible fluid provides a dipole acoustic source which is proportional to $\nabla \cdot \mathbf{f}$. Thus, in acoustic analogy, the term $\nabla \cdot (\mathbf{v} \times \boldsymbol{\omega})$ acts as a dipole source of aerodynamic noise.

6.2 Sound Radiation by a Compact Turbulent Eddy

As primarily shown by Lighthill [1], rearranging the momentum and the continuity equations yields

$$\Box^2 \rho \equiv \frac{\partial^2 \rho}{\partial t^2} - c_0^2 \nabla^2 \rho = \frac{\partial^2 T_{ij}}{\partial x_i \partial x_j} \tag{6.2}$$

where ρ is the fluid density, c_0 is the speed of sound in free space and $T_{ij} = \rho u_i u_j + p_{ij} - c_0^2 \rho \delta_{ij}$ is Lighthill's stress tensor. Since the propagation of acoustic perturbations in free space is governed by $\Box^2 \rho = 0$, the right-hand side of equation (6.2) can be formally regarded as a quadrupole source distribution which generates acoustic waves in an ideal fluid at rest.

A turbulent eddy of size l and characteristic velocity U generates sound with frequency of the order U/l. If the acoustic wavelength $\lambda = \mathcal{O}(l/M)$, with $M = U/c$, greatly exceeds the eddy size (low turbulent Mach number) then, as shown by Crow [156], the sound generation problem can be formulated as a singular perturbation problem and solved by means of matched asymptotic expansions. Therefore, Crow showed that the acoustic source is

$$\rho_0 \frac{\partial^2 (v_i v_j)}{\partial x_i \partial x_j} \tag{6.3}$$

where $\mathbf{v}$ is the divergence-free vortically induced velocity field. It is given by

$$\mathbf{v} = \nabla \times \mathbf{A} \quad \text{with} \\ \mathbf{A} = \frac{1}{4\pi} \int \frac{\boldsymbol{\omega}(\mathbf{y})}{|\mathbf{x}-\mathbf{y}|} \, \mathrm{d}^3\mathbf{y} \tag{6.4}$$

As a result,

$$\mathbf{v} = \mathcal{O}\left(m/|\mathbf{v}|^3\right) \quad \text{as} \quad |\mathbf{v}| \to \infty \tag{6.5}$$

provided that the total hydrodynamic impulse

$$\mathbf{m} = \int \mathbf{y} \times \boldsymbol{\omega} \, \mathrm{d}^3\mathbf{y} \tag{6.6}$$

converges.

Employing the Helmholtz decomposition described in section 1.5, the velocity field can be written as

$$\mathbf{u} = \mathbf{v} + \nabla\phi \tag{6.7}$$

where the velocity potential ϕ is such that

$$\nabla^2\phi = \nabla \cdot \mathbf{u} = -\frac{1}{\rho}\frac{\mathrm{D}\rho}{\mathrm{D}t} \tag{6.8}$$

Equation (6.8) implies that

$$\phi = \mathcal{O}(lUM^2) \tag{6.9}$$

in the eddy region.

The result (6.3) obtained by Crow [156] can be used to find a formal solution of equation (6.2). Thus, a convolution with the free space Green's function yields

$$\frac{\rho}{\rho_0} = \frac{1}{4\pi c_0^2} \int \frac{\partial^2 (v_i v_j)}{\partial y_i \partial y_j} \frac{\delta(t - \tau - |\mathbf{x}-\mathbf{y}|/c_0)}{|\mathbf{x}-\mathbf{y}|} \, \mathrm{d}^3\mathbf{y} \, \mathrm{d}\tau \tag{6.10}$$

Since $\nabla \cdot \mathbf{v} = 0$, the following vector identity is verified

$$\frac{\partial^2 (v_i v_j)}{\partial y_i \partial y_j} = \nabla \cdot (\boldsymbol{\omega} \times \mathbf{v}) + \nabla^2 \left(\frac{v^2}{2}\right) \tag{6.11}$$

As a result, at a low turbulent Mach number, a turbulent eddy is acoustically equivalent to a dipole of strength $\rho_0 \nabla \cdot (\boldsymbol{\omega} \times \mathbf{v})$ and an isotropic quadrupole of strength $\rho_0 v^2/2$.

The Green's function depends on $\mathbf{x}$ and $\mathbf{y}$ only in the combination $\mathbf{x}-\mathbf{y}$. Hence

$$\frac{\partial}{\partial y_i}\left(\frac{\delta(t - \tau - |\mathbf{x}-\mathbf{y}|/c_0)}{|\mathbf{x}-\mathbf{y}|}\right) = -\frac{\partial}{\partial x_i}\left(\frac{\delta(t - \tau - |\mathbf{x}-\mathbf{y}|/c_0)}{|\mathbf{x}-\mathbf{y}|}\right) \tag{6.12}$$

and equation (6.10) can be written as

$$\begin{aligned} \frac{\rho}{\rho_0} &= -\frac{1}{4\pi c_0^2}\frac{\partial}{\partial x_i} \int (\boldsymbol{\omega} \times \mathbf{v}) \frac{\delta(t - \tau - |\mathbf{x}-\mathbf{y}|/c_0)}{|\mathbf{x}-\mathbf{y}|} \, \mathrm{d}^3\mathbf{y} \, \mathrm{d}\tau \\ &+ \frac{1}{4\pi c_0^2}\frac{\partial^2}{\partial x_i \partial x_j} \int \left(\frac{v^2}{2}\right) \frac{\delta(t - \tau - |\mathbf{x}-\mathbf{y}|/c_0)}{|\mathbf{x}-\mathbf{y}|} \, \mathrm{d}^3\mathbf{y} \, \mathrm{d}\tau \end{aligned} \tag{6.13}$$

If $|\mathbf{x}| \gg |\mathbf{y}|$ then

$$\frac{\partial}{\partial x_i} \simeq -\frac{x_i}{|\mathbf{x}|\, c_0} \frac{\partial}{\partial t} \tag{6.14}$$

and equation (6.13) becomes

$$\frac{\rho}{\rho_0} = \frac{\mathbf{x}}{4\pi c_0^3 |\mathbf{x}|^2} \cdot \frac{\partial}{\partial t} \int (\boldsymbol{\omega} \times \mathbf{v})(t - |\mathbf{x} - \mathbf{y}|/c_0, \mathbf{y})\, \mathrm{d}^3\mathbf{y} \tag{6.15}$$

$$+ \frac{1}{8\pi c_0^4 |\mathbf{x}|} \frac{\partial^2}{\partial t^2} \int v^2(t - |\mathbf{x} - \mathbf{y}|/c_0, \mathbf{y})\, \mathrm{d}^3\mathbf{y} \tag{6.16}$$

where integration over τ has been performed by exploiting the properties of the Dirac δ-function. The order of magnitude of the two integrals in equation (6.16) can be estimates as follows.

Consider the momentum equation[1] (1.63) ($\dot{m} = 0$, $f_i = 0$). Changing from the conservative to the convective form yields

$$\frac{\partial u_i}{\partial t} + u_j \frac{\partial u_i}{\partial x_j} = -\frac{1}{\rho} \frac{\partial p}{\partial x_i} + \frac{1}{\rho} \frac{\partial \tau_{ij}}{\partial x_j} \tag{6.17}$$

Then, using the vector identity

$$(\mathbf{u} \cdot \nabla)\, \mathbf{u} = \nabla \left(\frac{u^2}{2} \right) + \boldsymbol{\omega} \times \mathbf{u} \tag{6.18}$$

introducing the stagnation enthalpy

$$B = h + \frac{u^2}{2} \tag{6.19}$$

with h denoting the specific enthalpy, and recalling the thermodynamic relation

$$\mathrm{d}h = T\, \mathrm{d}S + \mathrm{d}p/\rho \tag{6.20}$$

with S denoting the specific entropy, equation (6.17) can be written in Crocco's form

$$\frac{\partial u_i}{\partial t} + \frac{\partial B}{\partial x_i} = -(\boldsymbol{\omega} \times \mathbf{u})_i + T \frac{\partial S}{\partial x_i} + \frac{1}{\rho} \frac{\partial \tau_{ij}}{\partial x_j} \tag{6.21}$$

Hence, the inviscid isentropic momentum equation can be written as

$$\frac{\partial \mathbf{v}}{\partial t} + \nabla \left\{ \int \frac{\mathrm{d}p}{\rho} + \frac{u^2}{2} + \frac{\partial \phi}{\partial t} \right\} = -\boldsymbol{\omega} \times \mathbf{v} - \boldsymbol{\omega} \times \nabla \phi \tag{6.22}$$

where use of the Helmholtz decomposition (6.7) has been made. Taking the scalar product of this equation with $\mathbf{v}$, and recalling that $\nabla \cdot \mathbf{v} = 0$ yields

$$\frac{1}{2} \frac{\partial v^2}{\partial t} + \nabla \cdot \left\{ \mathbf{v} \left[\int \frac{\mathrm{d}p}{\rho} + \frac{u^2}{2} + \frac{\partial \phi}{\partial t} \right] \right\} = -\mathbf{v} \cdot \boldsymbol{\omega} \times \nabla \phi \tag{6.23}$$

This equation can be used to estimate the order of magnitude of the second integral in equation (6.16), namely

$$I_2 = \frac{1}{8\pi c_0^4 |\mathbf{x}|} \frac{\partial^2}{\partial t^2} \int v^2(t - |\mathbf{x} - \mathbf{y}|/c_0, \mathbf{y})\, \mathrm{d}^3\mathbf{y} \tag{6.24}$$

Integrating equation (6.23) over all space and applying the divergence theorem, the second term on the left-hand side gives a vanishing contribution because, as it results from (6.5), the term

$$\mathbf{v} \left[\int \frac{\mathrm{d}p}{\rho} + \frac{u^2}{2} + \frac{\partial \phi}{\partial t} \right] \tag{6.25}$$

[1] In this section the flow velocity is denoted as u_i.

tends to zero at least as fast as $|\mathbf{y}|^{-3}$ as $|\mathbf{y}| \to \infty$. Therefore,

$$\frac{1}{2}\frac{\partial^2}{\partial t^2}\int v^2\,\mathrm{d}^3\mathbf{y} \simeq -\frac{\partial}{\partial t}\int \mathbf{v}\cdot(\boldsymbol{\omega}\times\nabla\phi)\,\mathrm{d}^3\mathbf{y} \tag{6.26}$$

The integration on the right-hand side is confined to the flow region of non-vanishing vorticity. Thus, making use of (6.9) yields

$$I_2 = \mathcal{O}\left(\frac{lM^6}{|\mathbf{x}|}\right) \tag{6.27}$$

In order to estimate the order of magnitude of the first integral in equation (6.16), namely

$$I_1 = \frac{\mathbf{x}}{4\pi c_0^3\,|\mathbf{x}|^2}\cdot\frac{\partial}{\partial t}\int(\boldsymbol{\omega}\times\mathbf{v})(t-|\mathbf{x}-\mathbf{y}|/c_0,\mathbf{y})\,\mathrm{d}^3\mathbf{y} \tag{6.28}$$

consider that, for $|\mathbf{x}| \gg |\mathbf{y}|$, the retarded time can be approximated as $t - |\mathbf{x}|/c_0 + \mathbf{x}\cdot\mathbf{y}/c_0\,|\mathbf{x}|$. Furthermore, the variation in retarded time can be expanded as a Taylor series

$$(\boldsymbol{\omega}\times\mathbf{v})\left(\mathbf{y},t-\frac{|\mathbf{x}|}{c_0}+\frac{\mathbf{x}\cdot\mathbf{y}}{c_0\,|\mathbf{x}|}\right) \simeq (\boldsymbol{\omega}\times\mathbf{v})\left(\mathbf{y},t-\frac{|\mathbf{x}|}{c_0}\right)+\frac{\mathbf{x}\cdot\mathbf{y}}{c_0\,|\mathbf{x}|}\frac{\partial}{\partial t}(\boldsymbol{\omega}\times\mathbf{v})\left(\mathbf{y},t-\frac{|\mathbf{x}|}{c_0}\right)+\dots \tag{6.29}$$

The first term on the right-hand side of (6.29) yields a vanishing contribution to the integral of equation (6.28) because the integrand $\boldsymbol{\omega}\times\mathbf{v}$ can be expressed through (6.18) as a divergence. Therefore, the leading term in the far field density perturbation is

$$I_1 \simeq \frac{\mathbf{x}}{4\pi c_0^4\,|\mathbf{x}|^3}\cdot\frac{\partial^2}{\partial t^2}\int(\mathbf{x}\cdot\mathbf{y})\,(\mathbf{x}\cdot\boldsymbol{\omega}\times\mathbf{v})\,\mathrm{d}^3\mathbf{y} \tag{6.30}$$

which is of order

$$I_1 = \mathcal{O}\left(\frac{lM^4}{|\mathbf{x}|}\right) \tag{6.31}$$

As a result, for small turbulence Mach numbers M, $I_1 \gg I_2$. Moreover, the estimate (6.31) leads to Lighthill's [1] U^8 law.

From the above analysis it follows that, as firstly proposed by Powell [153], the source of aerodynamic sound in low Mach number turbulence can be identified with those flow regions of non-vanishing vorticity. More precisely, the Lighthill's equation (6.2) is equivalent to Powell's equation

$$\Box^2\rho = \rho_0\nabla\cdot(\boldsymbol{\omega}\times\mathbf{v}) \tag{6.32}$$

where the term on the right-hand side can be calculated by assuming that the flow is incompressible.

6.3 Howe's acoustic Analogy

In 1975 Howe [20] reformulated the Lighthill's acoustic analogy in terms of a convected wave equation for the stagnation enthalpy, with source terms incorporating the concept of vortex sound and the effects due to entropy inhomogeneities.

The thermodynamic relation (6.20) yields

$$\frac{1}{T}\frac{\mathrm{D}T}{\mathrm{D}t} = \frac{1}{c_p}\frac{\mathrm{D}S}{\mathrm{D}t}+\frac{1}{\rho c_p T}\frac{\mathrm{D}p}{\mathrm{D}t} \tag{6.33}$$

where c_p is the specific heat at constant pressure. The differential form of the equation of state of an ideal gas $p = \rho RT$, that is

$$\frac{\mathrm{d}p}{p} = \frac{\mathrm{d}\rho}{\rho}+\frac{\mathrm{d}T}{T} \tag{6.34}$$

and the continuity equation

$$\frac{\mathrm{D}\rho}{\mathrm{D}t} = -\rho\nabla \cdot \mathbf{u} \tag{6.35}$$

lead to

$$\frac{1}{p}\frac{\mathrm{D}p}{\mathrm{D}t} = -\nabla \cdot \mathbf{u} + \frac{1}{T}\frac{\mathrm{D}T}{\mathrm{D}t} \tag{6.36}$$

Hence, arranging equations (6.33) and (6.36) gives

$$\frac{1}{\rho c^2}\frac{\mathrm{D}p}{\mathrm{D}t} + \nabla \cdot \mathbf{u} = \frac{1}{c_p}\frac{\mathrm{D}S}{\mathrm{D}t} \tag{6.37}$$

The Crocco's equation (6.21) for an inviscid flow takes the form

$$\frac{\partial \mathbf{u}}{\partial t} + \nabla B = -\omega \times \mathbf{u} + T\nabla S \tag{6.38}$$

Then, taking the divergence of equation (6.38) and subtracting the partial time derivative of equation (6.37) yields

$$\frac{\partial}{\partial t}\left(\frac{1}{\rho c^2}\frac{\mathrm{D}p}{\mathrm{D}t}\right) - \nabla^2 B = \nabla \cdot \{\omega \times \mathbf{u} - \mathbf{T}\nabla\mathbf{S}\} + \frac{\partial}{\partial t}\left(\frac{1}{c_p}\frac{\mathrm{D}S}{\mathrm{D}t}\right) \tag{6.39}$$

The first term on the left-hand side of equation (6.39) can be expanded as follows

$$\frac{\partial}{\partial t}\left(\frac{1}{\rho c^2}\frac{\mathrm{D}p}{\mathrm{D}t}\right) = \frac{\mathrm{D}}{\mathrm{D}t}\left(\frac{1}{\rho c^2}\frac{\partial p}{\partial t}\right) + \frac{1}{\rho c^2}\frac{\partial u_j}{\partial t}\frac{\partial p}{\partial x_j} + u_j\left\{\frac{\partial}{\partial t}\left(\frac{1}{\rho c^2}\right)\frac{\partial p}{\partial x_j} - \frac{\partial}{\partial x_j}\left(\frac{1}{\rho c^2}\right)\frac{\partial p}{\partial t}\right\} \tag{6.40}$$

The last term on the right-hand side vanishes because the term $\rho c^2 = \gamma p$ is a function of the pressure alone (γ = const.). The other terms on the right-hand side of equation (6.40) are transformed as follows. Concerning the first term,

$$\frac{1}{\rho}\frac{\partial p}{\partial t} = \frac{1}{\rho}\frac{\mathrm{D}p}{\mathrm{D}t} - \frac{1}{\rho}\mathbf{u} \cdot \nabla p = \frac{\mathrm{D}B}{\mathrm{D}t} - T\frac{\mathrm{D}S}{\mathrm{D}t} \tag{6.41}$$

where use of the thermodynamic relation (6.20) and the momentum equation

$$\frac{\mathrm{D}\mathbf{u}}{\mathrm{D}t} = \frac{\nabla p}{\rho} \tag{6.42}$$

has been made. Concerning the second term,

$$\frac{\partial u_j}{\partial t}\frac{\partial p}{\partial x_j} = -\nabla p \cdot (\nabla B + \omega \times \mathbf{u} - T\nabla S) \tag{6.43}$$

where use of Crocco's equation (6.38) has been made. Thus, substituting (6.41) and (6.43) into equation (6.40) and considering equation (6.39) leads to the Howe's [20] acoustic analogy equation for the stagnation enthalpy, i.e.

$$\left\{\frac{\mathrm{D}}{\mathrm{D}t}\left(\frac{1}{c^2}\frac{\mathrm{D}}{\mathrm{D}t}\right) - \frac{\nabla \cdot p}{\rho c^2} - \nabla^2\right\} B =$$
$$\left(\nabla + \frac{\nabla p}{\rho c^2}\right) \cdot (\omega \times \mathbf{u} - T\nabla S) + \frac{\partial}{\partial t}\left(\frac{1}{c_p}\frac{\mathrm{D}S}{\mathrm{D}t}\right) + \frac{\mathrm{D}}{\mathrm{D}t}\left(\frac{T}{c^2}\frac{\mathrm{D}S}{\mathrm{D}t}\right) \tag{6.44}$$

In an ideal, homentropic and irrotational flow, the Crocco's equation (6.21) becomes

$$\frac{\partial}{\partial t}(\nabla\phi) + \nabla B = 0 \tag{6.45}$$

where ϕ is the velocity potential. Thus, a first integral of the momentum equation is

$$\dot{\phi} + B = f(t) \tag{6.46}$$

The velocity potential ϕ is undefined to within an arbitrary function of time. Thus, the function $f(t)$ can be set equal to a constant or zero. Equation (6.41) for a homentropic flow yields

$$\frac{1}{\rho}\frac{\partial p}{\partial t} = \frac{\mathrm{D}B}{\mathrm{D}t} \tag{6.47}$$

Hence, applying the Lagrangian derivative to equation (6.46) and substituting equation (6.47) leads to the pressure equation

$$\frac{1}{\rho}\frac{\partial p}{\partial t} = -\frac{\mathrm{D}\dot{\phi}}{\mathrm{D}t} \tag{6.48}$$

The continuity equation for a homentropic and irrotational flow has the form

$$\frac{1}{\rho c^2}\frac{\mathrm{D}p}{\mathrm{D}t} + \nabla^2\phi = 0 \tag{6.49}$$

Then, applying the time derivative

$$\frac{\partial}{\partial t}\left(\frac{1}{\rho c^2}\frac{\mathrm{D}p}{\mathrm{D}t}\right) + \nabla^2\dot{\phi} = 0 \tag{6.50}$$

and considering equation (6.40) yields

$$\frac{\mathrm{D}}{\mathrm{D}t}\left(\frac{1}{\rho c^2}\frac{\mathrm{D}p}{\mathrm{D}t}\right) + \frac{1}{\rho c^2}\nabla\dot{\phi}\cdot\nabla p + \nabla^2\dot{\phi} = 0 \tag{6.51}$$

Finally, substituting equation (6.48) gives

$$\left\{\frac{\mathrm{D}}{\mathrm{D}t}\left(\frac{1}{c^2}\frac{\mathrm{D}}{\mathrm{D}t}\right) - \frac{1}{\rho c^2}\nabla p\cdot\nabla - \nabla^2\right\}\dot{\phi} = 0 \tag{6.52}$$

This convective wave equation governs the propagation of sound in irrotational homentropic flows. It contains the nonlinear propagation operator of equation (6.44).

All terms on the right-hand side of equation (6.44) vanish in irrotational and homentropic regions of the flow. Thus, the sources of aerodynamic sound are indeed confined in regions in which $\boldsymbol{\omega} \neq 0$ and $\nabla S \neq 0$.

When $S = \text{const}$, equation (6.44) becomes

$$\left\{\frac{\mathrm{D}}{\mathrm{D}t}\left(\frac{1}{c^2}\frac{\mathrm{D}}{\mathrm{D}t}\right) - \frac{\nabla\cdot(\rho\nabla)}{\rho}\right\}B = \frac{1}{\rho}\nabla\cdot(\rho\,\boldsymbol{\omega}\times\mathbf{u}) \tag{6.53}$$

At low Mach numbers, when the flow is at rest at infinity where $\rho = \rho_0$ and $c = c_0$, neglecting nonlinear effects of propagation and the scattering of sound by vorticity and taking $\rho = \rho_0$ and $c = c_0$ equation (6.53) takes the form

$$\left(\frac{1}{c_0^2}\frac{\partial^2}{\partial t^2} - \nabla^2\right)B = \nabla\cdot(\boldsymbol{\omega}\times\mathbf{u}) \tag{6.54}$$

In the far field the acoustic pressure is given by

$$p \simeq \rho_0 B \tag{6.55}$$

which is the linearized form of equation (6.47). Therefore, equation (6.54) reduces to Powell's equation (6.32).

If equation (6.44) describes the interaction between a flow field and a rigid surface, a boundary condition for B is required. In the immediate vicinity of the surface Crocco's equation (6.21) becomes

$$\frac{\partial \mathbf{u}}{\partial t} + \nabla B = 0 \tag{6.56}$$

Hence, on a rigid surface the normal derivative of the stagnation enthalpy vanishes, that is

$$\frac{\partial B}{\partial n} = 0 \tag{6.57}$$

6.4 Vortex Sound and Rigid Surfaces

The analysis of section 6.2 shows that the dipole source $\nabla \cdot (\omega \times \mathbf{v})$ in free space is acoustically equivalent to a quadrupole distribution, provided that the vorticity is concentrated within an acoustically compact region. Clearly, the situation is different if the vortical region is located near a rigid surface. In this case the wall pressure fluctuations act as dipole-type aeroacoustic sources, which are more effective.

In this section two methods will be described which allow to solve equation (6.32) in the presence of a rigid body. The first was proposed by Howe [157], the second is due to Möring [158].

6.4.1 Howe's Compact Green's Function

Howe [157] proposed a formal procedure for calculating the leading order monopole and dipole terms in the multipole expansion of the acoustic field generated by a source in proximity of a solid surface.

Consider first a harmonic source ($k_0 = \omega/c_0$) near a body of characteristic size l. Suppose that the body is acoustically compact, that is $k_0 l \ll 1$. The Green's function $G(\mathbf{x}, \mathbf{y}; \omega)$ of the Helmholtz equation

$$\left(\nabla^2 + k_0^2\right) G(\mathbf{x}, \mathbf{y}; \omega) = \delta(\mathbf{x} - \mathbf{y}) \tag{6.58}$$

in the presence of a body can be determined by solving a scattering problem in which the spherical wave

$$G(\mathbf{x}, \mathbf{y}; \omega) = \frac{-\mathrm{e}^{\mathrm{i}\, k_0 |\mathbf{x}-\mathbf{y}|}}{4\pi\, |\mathbf{x} - \mathbf{y}|} \tag{6.59}$$

generated by a point source in $\mathbf{x}$, say the free-space Green's function, is scattered by the body surface S. If $\mathbf{y}$ is close to S, the compactness condition $k_0 l \ll 1$ permits $G(\mathbf{x}, \mathbf{y}; \omega)$ to be expanded in the form

$$G(\mathbf{x}, \mathbf{y}; \omega) = \frac{-\mathrm{e}^{\mathrm{i}\, k_0 |\mathbf{x}|}}{4\pi\, |\mathbf{x}|} \left\{ 1 - \frac{\mathrm{i}\, k_0 x_i}{|\mathbf{x}|} \left(y_i - \phi_i^*(\mathbf{y})\right) + \sum_{n \geq 2} (k_0 l)^n\, \Phi_n\left(\frac{\mathbf{x}}{|\mathbf{x}|}, \mathbf{y}\right) \right\} \quad \text{for}$$
$$\mathbf{y} \sim \mathcal{O}(l)\,,\, |\mathbf{x}| \to \infty \tag{6.60}$$

The first term represents the incident wave (6.59) evaluated at $\mathbf{y} = 0$. The second term is $\mathcal{O}(k_0 l)$ and represents the leading order effect due to the surface S. The other terms are of order $(k_0 l)^2$ or smaller and can be neglected. The function $\phi_i^*(\mathbf{y})$ is the velocity potential of the incompressible fluid motion generated by a translational rigid motion of S in the i-direction at unit speed. Therefore, $\phi_i^*(\mathbf{y})$ is defined by the shape of the body and satisfies

$$\frac{\partial \phi_i^*(\mathbf{y})}{\partial y_n} = n_i \quad \text{on} \quad S \tag{6.61}$$

Furthermore, the function $Y_i(\mathbf{y}) \equiv y_i - \phi_i^*(\mathbf{y})$ is a solution of Laplace's equation satisfying $\partial Y_i/\partial n = 0$ on S.

The time-domain low frequency Green's function can be obtained by transforming the first two terms of the Green's function (6.60), that is

$$G(\mathbf{x},\mathbf{y};t,\tau) = \int G(\mathbf{x},\mathbf{y};\omega)\exp\{-\mathrm{i}\,\omega\,(t-\tau)\}\,\mathrm{d}\omega \tag{6.62}$$

It thus follows that

$$\begin{aligned} G(\mathbf{x},\mathbf{y};t,\tau) &\simeq \frac{1}{4\pi\,|\mathbf{x}|}\left(\delta(t-\tau-|\mathbf{x}|/c_0)+\frac{\mathbf{x}\cdot\mathbf{Y}}{c_0\,|\mathbf{x}|}\delta'(t-\tau-|\mathbf{x}|/c_0)\right) \\ &\simeq \frac{1}{4\pi\,|\mathbf{x}|}\delta\left(t-\tau-|\mathbf{x}|/c_0+\frac{\mathbf{x}\cdot\mathbf{Y}}{c_0\,|\mathbf{x}|}\right) \\ &\simeq \frac{1}{4\pi\,|\mathbf{x}-\mathbf{Y}|}\delta(t-\tau-|\mathbf{x}-\mathbf{Y}|/c_0) \quad \text{as} \quad |\mathbf{x}|\to\infty \end{aligned} \tag{6.63}$$

Finally, replacing $\mathbf{x}$ by $\mathbf{X}=\mathbf{x}-\phi_i^*(\mathbf{x})$, the Green's function (6.63) can be made symmetric, in accordance with reciprocity. Therefore

$$G(\mathbf{x},\mathbf{y};t,\tau) = \frac{1}{4\pi\,|\mathbf{X}-\mathbf{Y}|}\delta(t-\tau-|\mathbf{X}-\mathbf{Y}|/c_0) \tag{6.64}$$

is the compact Green's function satisfying $\partial G/\partial x_n = \partial G/\partial y_n = 0$ on the body surface S and the reciprocal requirement according to which the noise in $\mathbf{y}$ generated by a point source in $\mathbf{x}$ is equal to the noise in $\mathbf{x}$ generated by a point source in $\mathbf{y}$. In the frequency domain the corresponding compact Green's function is

$$G(\mathbf{x},\mathbf{y};\omega) = \frac{-\mathrm{e}^{\mathrm{i}\,k_0|\mathbf{X}-\mathbf{Y}|}}{4\pi\,|\mathbf{X}-\mathbf{Y}|} \tag{6.65}$$

The above analysis can be extended to account for the presence of a low Mach number mean flow. The coefficients in the convected wave equation (6.52) are function of both mean (steady) and perturbation (unsteady) quantities. Small-amplitude acoustic disturbances satisfy a linearized version of this equation. Thus, the convective derivative can be approximated as

$$\frac{\mathrm{D}}{\mathrm{D}t} \simeq \frac{\partial}{\partial t}+\mathbf{U}\cdot\nabla \tag{6.66}$$

where $\mathbf{U}(\mathbf{x})$ is the mean flow velocity. Furthermore, since the mean flow is time independent, the time derivative $\dot{\phi}$ can be replaced by the perturbation potential ϕ'.

At low Mach numbers ($M^2 \ll 1$, $\mathbf{M}=\mathbf{U}(\mathbf{x})/c$) variations in the mean density and sound speed can be neglected in the linearized version of equation (6.52) which reduces to

$$\left\{\frac{1}{c_0^2}\left(\frac{\partial}{\partial t}+\mathbf{U}\cdot\nabla\right)^2-\nabla^2\right\}\phi' = 0 \tag{6.67}$$

Setting $\phi'(\mathbf{x},t)=\hat{\phi}'(\mathbf{x})\,\mathrm{e}^{-\mathrm{i}\,\omega t}$, equation (6.67) becomes

$$(k_0^2+\nabla^2+2\mathrm{i}\,k_0\mathbf{M}\cdot\nabla)\,\hat{\phi}' = 0 \tag{6.68}$$

where terms of order M^2 have been neglected.

The reciprocal theorem in the presence of a mean flow applies as follows. Let $\phi'_A(\mathbf{x},t)$ be the solution of the convected wave equation

$$\left\{\frac{1}{c_0^2}\left(\frac{\partial}{\partial t}+\mathbf{U}\cdot\nabla\right)^2-\nabla^2\right\}\phi'_A(\mathbf{x},t) = \delta(\mathbf{x}-\mathbf{x}_A)\,\mathrm{e}^{-\mathrm{i}\,\omega t} \tag{6.69}$$

and let $\phi'_B(\mathbf{x},t)$ be the solution of the reverse convected wave equation

$$\left\{\frac{1}{c_0^2}\left(\frac{\partial}{\partial t} - \mathbf{U}\cdot\nabla\right)^2 - \nabla^2\right\}\phi'_B(\mathbf{x},t) = \delta(\mathbf{x}-\mathbf{x}_B)\,\mathrm{e}^{-\mathrm{i}\,\omega t} \tag{6.70}$$

Then the reciprocal theorem states that $\phi'_A(\mathbf{x}_B,t) = \phi'_B(\mathbf{x}_A,t)$.

Accordingly to the reciprocal theorem in the presence of a mean flow, the compact Green's function of equation (6.68) must be defined by considering the reverse flow problem

$$\left(k_0^2 + \nabla^2 - 2\mathrm{i}\,k_0\mathbf{M}\cdot\nabla\right)G(\mathbf{x},\mathbf{y};\omega) = \delta(\mathbf{x}-\mathbf{y}) \tag{6.71}$$

Consider a flow past a stationary acoustically compact rigid surface S. The mean flow can be expressed as

$$U_i(\mathbf{y}) = \mathbf{U}_0\cdot\nabla Y_i(\mathbf{y}) \tag{6.72}$$

where $\mathbf{U}_0$ is the uniform mean velocity at large distance from S and $Y_i = y_i - \phi_i^*(\mathbf{y})$ is a solution of Laplace's equation satisfying $\partial Y_i/\partial n = 0$ on S, with $\phi_i^*(\mathbf{y})$ denoting the velocity potential of the incompressible fluid motion generated by a translational rigid motion of S in the i-direction at unit speed. Thus, applying the Taylor's [159] transformation

$$G(\mathbf{x},\mathbf{y};\omega) = \tilde{G}(\mathbf{x},\mathbf{y};\omega)\,\mathrm{e}^{\mathrm{i}\,k_0\mathbf{M}_0\cdot\mathbf{Y}} \tag{6.73}$$

where $\mathbf{M}_0 = \mathbf{U}_0/c_0$, equation (6.71) takes the Helmholtz form

$$\left(\nabla^2 + k_0^2\right)\tilde{G} = \delta(\mathbf{x}-\mathbf{y})\,\mathrm{e}^{-\mathrm{i}\,k_0\mathbf{M}_0\cdot\mathbf{X}} \tag{6.74}$$

Thus, the no-flow compact Green's functions (6.64) and (6.65) lead respectively to

$$G(\mathbf{x},\mathbf{y};t,\tau) = \frac{1}{4\pi\,|\mathbf{X}-\mathbf{Y}|}\delta\left(t-\tau-|\mathbf{X}-\mathbf{Y}|/c_0 + \mathbf{M}_0\cdot(\mathbf{X}-\mathbf{Y})/c_0\right) \tag{6.75}$$

and

$$G(\mathbf{x},\mathbf{y};\omega) = \frac{-\mathrm{e}^{\mathrm{i}\,k_0\{|\mathbf{X}-\mathbf{Y}|-\mathbf{M}_0\cdot(\mathbf{X}-\mathbf{Y})\}}}{4\pi\,|\mathbf{X}-\mathbf{Y}|} \tag{6.76}$$

6.4.2 Möring's Vector Green's Function

A formal solution of Powell-Howe's vortex-sound equation

$$\left(\frac{1}{c_0^2}\frac{\partial^2}{\partial t^2} - \nabla^2\right)B = \nabla\cdot(\omega\times\mathbf{u}) \tag{6.77}$$

with boundary condition $\mathbf{n}\cdot\nabla B = 0$ on the body surface S is

$$B(\mathbf{x},t) = \int_V \nabla\cdot(\omega\times\mathbf{u})\,G\,\mathrm{d}^3\mathbf{y}\,\mathrm{d}\tau \tag{6.78}$$

where V is the region outside the body with non-vanishing vorticity and G is the solution of

$$\left(\frac{1}{c_0^2}\frac{\partial^2}{\partial t^2} - \nabla^2\right)G = \delta(\mathbf{x}-\mathbf{y},t-\tau) \quad \text{with} \quad \mathbf{n}\cdot\nabla G = 0 \quad \text{on} \quad S \tag{6.79}$$

In the far field B reduces to p'/ρ_0. Thus, integrating equation (6.78) by parts yields

$$p'(\mathbf{x},t) = -\rho_0\int_V (\omega\times\mathbf{u})_i\,\frac{\partial G}{\partial y_i}\,\mathrm{d}^3\mathbf{y}\,\mathrm{d}\tau \tag{6.80}$$

Möring [158] argued that the formal solution (6.80) can be expressed as a function of the vorticity ω only. He defined a *vector Green's function* $\mathbf{G}$ as

$$\nabla \times \mathbf{G} = \nabla G \tag{6.81}$$

If $\mathbf{G}$ exists, equation (6.80) can be written as

$$p'(\mathbf{x}, t) = -\rho_0 \int_V (\omega \times \mathbf{u}) \cdot (\nabla \times \mathbf{G}) \, \mathrm{d}^3\mathbf{y} \, \mathrm{d}\tau \tag{6.82}$$

and integrating by parts

$$p'(\mathbf{x}, t) = -\rho_0 \int_V \nabla \times (\omega \times \mathbf{u}) \cdot \mathbf{G} \, \mathrm{d}^3\mathbf{y} \, \mathrm{d}\tau \tag{6.83}$$

Then, considering the vorticity equation

$$\frac{\partial \omega}{\partial t} + \nabla \times (\omega \times \mathbf{u}) = 0 \tag{6.84}$$

yields

$$p'(\mathbf{x}, t) = \rho_0 \int_V \frac{\partial \omega}{\partial \tau} \cdot \mathbf{G} \, \mathrm{d}^3\mathbf{y} \, \mathrm{d}\tau \tag{6.85}$$

Finally, integrating by parts, i.e.

$$p'(\mathbf{x}, t) = -\rho_0 \int_V \omega \cdot \frac{\partial \mathbf{G}}{\partial \tau} \, \mathrm{d}^3\mathbf{y} \, \mathrm{d}\tau \tag{6.86}$$

and considering that $\mathbf{G}$ depends on t and τ only via $t - \tau$, yields

$$p'(\mathbf{x}, t) = \rho_0 \frac{\partial}{\partial t} \int_V \omega \cdot \mathbf{G} \, \mathrm{d}^3\mathbf{y} \, \mathrm{d}\tau \tag{6.87}$$

The formal solution (6.87) proposed by Möring [158] depends linearly on the vorticity field. Therefore, the contributions from several vortices add linearly.

The existence condition (6.81) of the vector Green's function $\mathbf{G}$ is equivalent to $\nabla^2 G = 0$. However, the Green's function G is the solution of

$$\nabla^2 G = \frac{1}{c_0^2} \frac{\partial^2 G}{\partial t^2} - \delta(\mathbf{x} - \mathbf{y}, t - \tau) \tag{6.88}$$

The δ-function vanishes if $\mathbf{y} \neq \mathbf{x}$. Thus, provided that $\mathbf{y}$ is in the vortical flow and $\mathbf{x}$ is in the far field, and provided that the term

$$\frac{1}{c_0^2} \frac{\partial^2 G}{\partial t^2} \tag{6.89}$$

vanishes to lowest order in the Mach number, $\nabla^2 G$ vanishes and the vector Green's function $\mathbf{G}$ exists.

6.5 Sound Radiation from a Line-Vortex Near a Rigid Half-Plane

In this section the theory of vortex sound is employed to determine the noise radiated by a line-vortex convected past the edge of a semi-infinite rigid plate under the action of only the image vortex system. This model problem was first studied by Crighton [160] by means of matched asymptotic expansions. Later on, the same problem posed in terms of vortex sound, was solved by Howe [20] by means of the compact Green's function technique, and by Möring [158] by means of the vector Green's function technique. Howe's and Möring's analyses are described below.

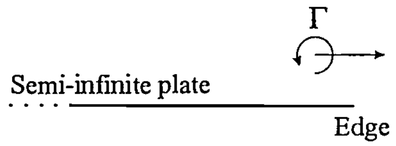

FIGURE 6.1: Line-vortex near the edge of a semi-infinite rigid plate.

Consider a line-vortex with circulation Γ near the edge of a rigid half-plane $x_1 < 0$, $x_2 = 0$, as sketched on Fig.6.1. The vortex moves under the induction of the image vortex and generates a vorticity field

$$\boldsymbol{\omega} = \Gamma\delta(\mathbf{y} - \mathbf{y}_{\mathrm{w}}(t))\,\hat{e}_3 \tag{6.90}$$

where $\mathbf{y}_{\mathrm{w}}(t)$ denotes the vortex path and $\hat{e}_3$ is the unit vector taken out of the paper.

Let us consider the Powell-Howe's equation

$$\left\{\frac{1}{c_0^2}\frac{\partial^2}{\partial t^2} - \nabla^2\right\} B = \nabla\cdot(\boldsymbol{\omega}\times\mathbf{u}) \tag{6.91}$$

with

$$\boldsymbol{\omega}\times\mathbf{u} = \Gamma\,\hat{e}_3\times\dot{\mathbf{y}}_{\mathrm{w}}(t)\,\delta(\mathbf{y} - \mathbf{y}_{\mathrm{w}}(t)) \tag{6.92}$$

Following Howe [20], equation (6.91) can be solved by means of a convolution with the compact Green's function G, which is the solution of

$$\begin{aligned}&\left\{\frac{1}{c_0^2}\frac{\partial^2}{\partial \tau^2} - \frac{\partial^2}{\partial y_i^2}\right\} G = \delta(\mathbf{x} - \mathbf{y}, t - \tau) \quad \text{with}\\ &\frac{\partial G}{\partial y_2} = 0 \quad \text{on} \quad y_1 < 0, \quad y_2 = 0\end{aligned} \tag{6.93}$$

The Green's function G can be determined by using the reciprocal theorem: the acoustic far field in $\mathbf{x}$ generated by a point source in $\mathbf{y}$ close to the edge of a semi-infinite plate is equal to the noise in $\mathbf{y}$ generated by a source point in $\mathbf{x}$. Clearly, as $|\mathbf{x}| \to \infty$, the problem becomes that of determining the scattering of a plane acoustic wave by a semi-infinite plate. As quoted in chapter 8, this scattering problem was solved by Crighton & Leppington [161] by means of the Weiner-Hopf technique. In the frequency domain, the Green's function is

$$\tilde{G} = \tilde{G}_i + \tilde{G}_s \tag{6.94}$$

where

$$\tilde{G}_i = \frac{1}{4\pi\,|\mathbf{x} - y_3\hat{e}_3|}\exp\left\{-\mathrm{i}\,\omega\left(t - \frac{|\mathbf{x} - y_3\hat{e}_3|}{c_0}\right)\right\} \tag{6.95}$$

$$\tilde{G}_s = \frac{-\mathrm{i}}{\pi\sqrt{2\pi}}\frac{\phi^*(\mathbf{x})\,\phi^*(\mathbf{y})}{|\mathbf{x} - y_3\hat{e}_3|^{3/2}}\left(\frac{\omega}{c_0}\right)^{\frac{1}{2}}\exp\left\{\mathrm{i}\left[\frac{\pi}{4} - \omega\left(t - \frac{|\mathbf{x} - y_3\hat{e}_3|}{c_0}\right)\right]\right\} \tag{6.96}$$

The contribution $\tilde{G}_i$ represents the incident field without scattering, whereas the contribution $\tilde{G}_s$ represents the leading approximation to the field scattered by the semi-infinite rigid plate. The function $\phi^*(\mathbf{x})$ is the velocity potential field for incompressible irrotational flow around a half-plane, that is

$$\phi^*(\mathbf{x}) = \sqrt{R}\sin\left(\frac{\theta}{2}\right) \tag{6.97}$$

where $R = \sqrt{x_1^2 + x_2^2}$ and $\tan\theta = x_2/x_1$.

The Green's function for a two-dimensional application can be obtained by integrating (6.95) and (6.96) over all values of y_3. As obtained by Howe [20] by using the method of stationary phase, the two-dimensional contribution G_i is independent of $\mathbf{y}$ and is therefore significant only in problems involving monopole sources. The two-dimensional scattered contribution is given by

$$\tilde{G}_s(\mathbf{x},\mathbf{y},\omega) \simeq \frac{\phi^*(\mathbf{x})\,\phi^*(\mathbf{y})}{\pi\,|\mathbf{x}|}\exp\left\{-i\omega\left(t-\frac{|\mathbf{x}|}{c_0}\right)\right\} \tag{6.98}$$

Therefore, multiplying by $(2\pi)^{-1}\exp(i\omega\tau)$ and integrating provide the time-domain compact Green's function

$$G_s(\mathbf{x},\mathbf{y},t,\tau) \simeq \frac{\phi^*(\mathbf{x})\,\phi^*(\mathbf{y})}{\pi\,|\mathbf{x}|}\delta\left(t-\tau-\frac{|\mathbf{x}|}{c_0}\right) \tag{6.99}$$

Using the Green's function (6.99) to convolute equation (6.91) yields

$$\begin{aligned} p' &\simeq \rho_0\frac{\phi^*(\mathbf{x})}{\pi R}\int \nabla\cdot(\Gamma\,\hat{e}_3\times\dot{\mathbf{y}}_{\mathrm{w}}(\tau)\,\delta(\mathbf{y}-\mathbf{y}_{\mathrm{w}}(\tau)))\,\phi^*(\mathbf{y})\,\delta\left(t-\tau-\frac{R}{c_0}\right)\,\mathrm{d}^3\mathbf{y}\,\mathrm{d}\tau \\ &= -\frac{\rho_0\,\Gamma\phi^*(\mathbf{x})}{\pi R}\left[\hat{e}_3\cdot\dot{\mathbf{y}}_{\mathrm{w}}(\tau)\times\nabla\phi^*\right]_{\mathrm{ret}} \end{aligned} \tag{6.100}$$

where square brackets enclose quantities evaluated at the retarded vortex position $\mathbf{y}_{\mathrm{w}}(t-R/c_0)$. Since

$$\dot{\mathbf{y}}_{\mathrm{w}}(\tau)\times\nabla\phi^* = -\left(\dot{\mathbf{y}}_{\mathrm{w}}(\tau)\cdot\nabla\Psi\right)\hat{e}_3 \tag{6.101}$$

where Ψ is the stream function conjugate to ϕ^*, the solution (6.100) can be written as

$$p' \simeq \frac{\rho_0\,\Gamma\sin(\theta/2)}{\pi\sqrt{R}}\left[\frac{\mathrm{D}\Psi}{\mathrm{D}t}\right]_{\mathrm{ret}} \tag{6.102}$$

where $\mathrm{D}/\mathrm{D}t$ denotes the rate at which the vortex crosses the streamlines Ψ =const of a hypothetical potential flow with velocity potential $\phi^*(\mathbf{y})$, that is

$$\Psi(\mathbf{y}) = -\sqrt{\sigma}\cos\left(\frac{\psi}{2}\right) \tag{6.103}$$

where $\sigma = \sqrt{y_{w1}^2+y_{w2}^2}$ and $\psi = \tan(y_{w2}/y_{w1})$ are the vortex polar co-ordinates.

The result (6.102) agrees with the prediction made by Crighton [160] by means of matched asymptotic expansions. It states that the noise is generated only when the vortex is near the edge. Far from the edge, in fact, the vortex moves along a streamline. Thus, the term $\mathrm{D}\Psi/\mathrm{D}t$ vanishes and the vortex is silent.

Interestingly, the acoustic field (6.102) exhibits a $\sin^2(\theta/2)$ directivity pattern which is typical for semi-infinite rigid plates.

The vector Green's function procedure of Möring [158] can be used to solve the same model problem. Thus, considering the formal solution (6.86) and substituting the vorticity field induced by a line-vortex provide

$$p' = \rho_0\Gamma\frac{\partial}{\partial t}\int \delta(\mathbf{y}-\mathbf{y}_{\mathrm{w}}(\tau))\,\hat{e}_3\cdot\mathbf{G}\,\mathrm{d}^3\mathbf{y}\,\mathrm{d}\tau \tag{6.104}$$

The vector Green's function $\mathbf{G}$ exists since

$$\frac{\partial^2 G}{\partial y_i^2} = \frac{\phi^*(\mathbf{x})}{\pi R}\left(\frac{\partial^2\phi^*(\mathbf{y})}{\partial y_i^2}\right)\delta\left(t-\tau-\frac{R}{c_0}\right) = 0 \tag{6.105}$$

Thus, applying the definition (6.81) yields

$$\mathbf{G}(\mathbf{x},\mathbf{y},t,\tau) = \frac{\phi^*(\mathbf{x})\,\Psi(\mathbf{y})}{\pi R}\delta\left(t-\tau-\frac{R}{c_0}\right)\hat{e}_3 \tag{6.106}$$

Finally, substituting the vector Green's function (6.106) into (6.104) yields

$$p' = \frac{\rho_0 \Gamma \sin(\theta/2)}{\pi\sqrt{R}} \left[\frac{\mathrm{D}\Psi}{\mathrm{D}t}\right]_{\mathrm{ret}} \tag{6.107}$$

which coincides with the solution (6.102) obtained by both Crighton [160] and Howe [20].

7

Aeroacoustics of Solid Boundaries in Arbitrary Motion

7.1 Introduction

Today's technological maturity of the aerospace technology concerning performances and efficiency, even more stringent certification rules and the increased sensitivity of the community result in an increasing attention to safety, emission and noise.

Low noise requirements are particularly important for aircrafts operating in and nearby populated areas. This is the case of civil helicopters and civil transport jets in landing and take-off conditions. Since a great deal of progress has been made in understanding the sound generation mechanisms, more attention is currently devoted to the development of accurate and efficient prediction methods.

Nowadays two different large groups of numerical methods are available, one based on the Computational AeroAcoustic approach (CAA), the other based on integral formulations. CAA methods consist in solving the flow governing equations including acoustic fluctuations by means of classical CFD methods (finite difference, finite volume, finite elements, etc.) with high accuracy (low-dispersion) numerical schemes. Thus, reasonable cost solutions are restricted to near field predictions. On the contrary, integral methods allow to propagate a near field *information* to the far field with a computational cost that does not depend on the observation distance. The near field information can be obtained by means of the integral method itself, as in Boundary Element Methods (BEM), or by means of a CFD/CAA method, as in a hybrid approach.

Hybrid methods are the domain of the acoustic analogy approach. This approach is based on the ideal assumption of separating the sound generation mechanism from its pure propagation. Thus, the flow governing equations are arranged in the form of a wave equation where all the terms discarded by a wave propagation pattern are gathered at the right-hand side and interpreted as source terms. Depending on both the reference wave equation and the mechanism that generates the pressure disturbances (free turbulent flows, turbulent flows bounded by solid surfaces, etc.), the acoustic analogy approach leads to different formulations. The first model was proposed by Lighthill [1] and describes the noise generated by a turbulent portion of fluid in an otherwise quiescent unbounded medium. Later on, Lighthill's model was extended by Ffowcs Williams & Hawkings [2] (FW-H) to flows confined by surfaces in arbitrary motion.

The FW-H analogy is the most appropriate theoretical support for understanding the mechanisms involved in the generation of aerodynamic sound from bodies in complex motion. This is typically the case of a helicopter rotor. The rotating wing of a helicopter generates aerodynamic noise by different mechanisms: the fluid displacement due to the blade thickness, steady and unsteady blade loadings, rotating shocks, blade-vortex interactions, blade-turbulence interactions. In the FW-H equation these mechanisms appear as source terms of an inhomogeneous wave equation.

The first solutions of the FW-H wave equation were obtained by integrating the pressure field upon the physical surface of the body. This strategy confines all the flow nonlinearities into a volume integral extended over a domain exterior to the body. Because of the computational cost required by an accurate prediction of this volume integral, for several years only the linear effects due to the body thickness and aerodynamic loading have been predicted by means of the FW-H analogy.

An important source of rotor noise is indeed related to the compressibility effects occurring in the blade tip region. At values of the advancing tip Mach number higher than ~ 0.85, shock waves appear in the flow field around the rotor, which generate an annoying impulsive noise. A prediction the so-called High-Speed Impulsive (HSI) noise requires the nonlinear effects to be taken into account in the FW-H analogy. An alternative to the computation of the volume term in the FW-H equation consists in using methods based on Kirchhoff's theorem. These methods relate the acoustic field to the pressure field upon a control surface enclosing the blade and *all* the near-blade flow nonlinearities. As in the FW-H analogy, a CFD computation provides the flow data upon the integration surface.

For several years the Kirchhoff (K) formulations has been considered as an ineluctable alternative to the FW-H analogy for the prediction of high-speed rotor noise. Only recently, di Francescantonio [42] has shown that the FW-H analogy can be extended to a penetrable control surface and that the surface integrals account for all the nonlinear terms enclosed by the integration surface. In response to di Francescantonio [42], Brentner & Farassat [43] pointed out that, although di Francescantonio was the first to apply the FW-H analogy to a Kirchhoff-type integration surface, Ffowcs Williams had already described several implications of a penetrable surface formulation. Moreover, Brentner & Farassat discussed in great detail the conceptual difference between a K formulation and a FW-H penetrable formulation. Their analysis is an example of both elegance and effectiveness. It shows that, since the K equation follows from a linear wave equation, its application to acoustic analogy predictions requires the integration surface to be placed in the linear flow region. On the contrary, since a FW-H equation is an exact rearrangement of the flow governing equations, the placement of the integration surface is only a matter of convenience as long as the quadrupole sources are taken into account by the surface integration. Thus, the FW-H analogy allows accurate noise predictions even when the integration surface is not in the linear flow region.

Depending on the mathematical formalism used to obtain integral solutions of both the K equation and the FW-H equation, singularities may appear in the final expressions of the noise radiated by a moving surface. Diverging behaviours typically occur in transonic kinematic conditions (for example, when the velocity component of a surface rotor element in the observation direction is sonic). Fortunately, these singularities do not have a physical origin and can be removed by using different mathematical manipulations. The greatest contributions to the development of suitable analytical formulations for rotor noise predictions have been done by Farassat and coworkers at NASA Langley Research Center (LRC in the last quarter 20^{th} century. The strategy developed at LRC consists in using the most suitable formulation for each blade element, depending on whether it moves subsonically or supersonically.

In the present chapter a first section is devoted to the description of some physical effects related to the movement of an acoustic source. Later on, some elements of generalized functions theory and differential geometry are introduced. These provide the mathematical formalism by which the aeroacoustic theory of solid boundaries in arbitrary motion can be developed. Then the K approach and the FW-H acoustic analogy methods are described and discussed in great detail. Formal solutions are derived for both the K and the FW-H equation and for both the subsonic and the supersonic regime. In section 7.10 an advanced time approach is presented, which allows to perform acoustic analogy predictions by using aerodynamic data as soon as they are computed by a CFD solver. Finally, in section 7.11, a convective form of the FW-H equation is used to describe the aerodynamic sound generation by unsteady flows past stationary surfaces.

7.2 Acoustic Fields of Moving Elementary Sources

In this section the effects related to the motion of an acoustic source are illustrated with reference to the model problem of an elementary acoustic source in arbitrary motion.

The sound radiated from a moving source differs from that radiated when the same source is stationary. The well-known Döppler effect is one of the two effects related to the source motion. It consists in a frequency shift of the detected acoustic signal and is easily experienced by a listener approached by a whistling train. As the train passes by the listener and recede from him, the detected whistle undergoes a frequency fall. The second effect due to the source motion is an amplitude variation of the detected signal and is usually referred to as Döppler amplification.

7.2.1 Noise from a Moving Monopole

The Döppler frequency shift and amplification can be illustrated by considering the acoustic field generated by a monopole of strength $Q(t)$ moving along the path $\mathbf{x} = \mathbf{x}_s(t)$ in a quiescent medium. The radiated acoustic pressure is described by the wave equation

$$\frac{1}{c^2}\frac{\partial^2 p}{\partial t^2} - \nabla^2 p = \rho_0 \frac{\partial}{\partial t}\left\{Q(t)\,\delta(\mathbf{x} - \mathbf{x}_s(t))\right\} \tag{7.1}$$

where ρ_0 is the medium density and c is the sound speed. Making use of the free space Green's function

$$G(\mathbf{x}, t; \mathbf{y}, \tau) = \frac{\delta(t - \tau - |\mathbf{x} - \mathbf{y}|/c)}{4\pi\,|\mathbf{x} - \mathbf{y}|} \tag{7.2}$$

the solution of equation (7.1) can be easily obtained. This takes the form

$$p(\mathbf{x}, t) = \rho_0 \frac{\partial}{\partial t}\int \frac{Q(\tau)\,\delta(\mathbf{y} - \mathbf{x}_s(\tau))\,\delta(t - \tau - |\mathbf{x} - \mathbf{y}|/c)}{4\pi\,|\mathbf{x} - \mathbf{y}|}\,\mathrm{d}^3\mathbf{y}\,\mathrm{d}\tau \tag{7.3}$$

Exploiting the properties of the δ-function to evaluate the $\mathbf{y}$-integral yields

$$p(\mathbf{x}, t) = \rho_0 \frac{\partial}{\partial t}\int \frac{Q(\tau)\,\delta(t - \tau - |\mathbf{x} - \mathbf{x}_s(\tau)|/c)}{4\pi\,|\mathbf{x} - \mathbf{x}_s(\tau)|}\,\mathrm{d}\tau \tag{7.4}$$

The integral in the above equation has the form $\int Q(\tau)\,\delta(g(\tau))\,\mathrm{d}\tau$. It can be further simplified by performing a change of variable and exploiting the properties of the δ-function. Thus, let us consider the general result

$$\int Q(\tau)\,\delta(g(\tau))\,\mathrm{d}\tau = \sum_{n=1}^{N} \frac{Q(\tau_n^*)}{\left|\frac{\partial g}{\partial \tau}(\tau_n^*)\right|} \tag{7.5}$$

where the sum is taken over all the zeros τ_n^* of the equation $g(\tau) = 0$. In the present case the function $g(\tau)$ is given by

$$g(\tau) = t - \tau - |\mathbf{x} - \mathbf{x}_s(\tau)|/c \tag{7.6}$$

and its derivative is

$$\frac{\mathrm{d}g}{\mathrm{d}\tau} = -1 + \frac{1}{c}\frac{x_i - x_{si}}{|\mathbf{x} - \mathbf{x}_s(\tau)|}\frac{\mathrm{d}x_{si}}{\mathrm{d}\tau} = -1 + M_r \tag{7.7}$$

where $c\,M_r$ is the projection of the source velocity on the radiation direction, i.e.

$$c\,M_r = \mathbf{v}_s \cdot \hat{\mathbf{r}} \tag{7.8}$$

with

$$v_{si} = \frac{\mathrm{d}x_{si}}{\mathrm{d}\tau} \tag{7.9}$$

and

$$\hat{r}_i = \frac{x_i - x_{si}}{|\mathbf{x} - \mathbf{x}_s(\tau)|} \tag{7.10}$$

Hence, substituting equations (7.6) and (7.7) into equation (7.5) and considering that

$$\mathcal{Q}(\tau) = \frac{Q(\tau)}{4\pi\,|\mathbf{x} - \mathbf{x}_s(\tau)|} \tag{7.11}$$

the expression (7.4) takes the form

$$p(\mathbf{x}, t) = \rho_0 \sum_{n=1}^{N} \frac{\partial}{\partial t} \left\{ \frac{Q(\tau_n^*)}{4\pi\,|\mathbf{x} - \mathbf{x}_s(\tau_n^*)|\,|1 - M_r(\tau_n^*)|} \right\} \tag{7.12}$$

where τ_n^* are solutions of the *retarded time equation*

$$\tau_n^* = t - |\mathbf{x} - \mathbf{x}_s(\tau_n^*)|\,/c \tag{7.13}$$

and represent the times at which signals detected at the same time t are emitted by the source. If the source moves subsonically, only one emission time τ^* corresponds to a given reception time t. Conversely, if the source moves supersonically, more than one solutions of the retarded time equation (7.13) may exist. This physically accounts for the fact that impulses emitted at different times can be detected at the same time.

The relationship between the emission and the reception time can be enlightened by evaluating the time derivative of the retarded time τ_n^*. From equation (7.13) it follows that

$$\frac{\partial \tau_n^*}{\partial t} = 1 - \frac{1}{c} \frac{x_i - x_{si}(\tau_n^*)}{|\mathbf{x} - \mathbf{x}_s(\tau_n^*)|} \frac{\mathrm{d}x_{si}}{\mathrm{d}\tau_n^*} \frac{\partial \tau_n^*}{\partial t} \tag{7.14}$$

leading to

$$\frac{\partial \tau_n^*}{\partial t} = \frac{1}{1 - M_r(\tau_n^*)} \tag{7.15}$$

The factor $1 - M_r(\tau_n^*)$ accounts for the Döppler frequency shift. For an approaching subsonic source it results that $0 \leq M_r \leq 1$ and $(1 - M_r)^{-1} \geq 1$. This corresponds to a *contraction* of the reception time scale, resulting in higher detected frequencies. Conversely, for a receding subsonic source it results that $-1 \leq M_r \leq 0$ and $0.5 \leq (1 - M_r)^{-1} \leq 1$. This corresponds to a *dilatation* of the reception time scale, resulting in lower detected frequencies. Moreover, for the case of an approaching supersonic source it may be $M_r > 1$ and $(1 - M_r)^{-1} < 0$. This physically accounts for the fact that signals emitted later are detected earlier.

Consider a monopole moving subsonically and let $[\ldots]_{\text{ret}}$ denote evaluation at the retarded time τ^*. The relationship (7.15) can be used to translate the reception time derivative into an emission time derivative by writing

$$\frac{\partial}{\partial t}[\ ]_{\text{ret}} = \left[\frac{1}{1 - M_r} \frac{\partial}{\partial \tau}\right]_{\text{ret}} \tag{7.16}$$

Hence equation (7.12) takes the form

$$p(\mathbf{x}, t) = \rho_0 \left[\frac{1}{1 - M_r} \frac{\partial}{\partial \tau} \left\{ \frac{Q}{4\pi r\,(1 - M_r)} \right\}\right]_{\text{ret}} \tag{7.17}$$

where $r = |\mathbf{x} - \mathbf{x}_s(\tau^*)|$ is the observer distance from the source at its retarded time location. Taking explicitely the retarded time derivatives yields

$$p(\mathbf{x}, t) = \rho_0 \left[\frac{1}{1 - M_r} \left\{ \frac{1}{4\pi r\,(1 - M_r)} \frac{\partial Q}{\partial \tau} - \frac{Q}{4\pi r^2\,(1 - M_r)} \frac{\partial r}{\partial \tau} + \frac{Q}{4\pi r\,(1 - M_r)^2} \frac{\partial M_r}{\partial \tau} \right\}\right]_{\text{ret}} \tag{7.18}$$

Then, making use of the following relations

$$\frac{\partial r}{\partial \tau} = -c\, M_r \tag{7.19}$$
$$\frac{\partial \hat{r}_i}{\partial \tau} = \frac{\hat{r}_i\, c\, M_r - c\, M_i}{r} \tag{7.20}$$
$$\frac{\partial M_r}{\partial \tau} = \frac{1}{r}\left\{ r\,\hat{r}_i\,\frac{\partial M_i}{\partial \tau} + c\left(M_r^2 - M^2\right)\right\} \tag{7.21}$$

the acoustic pressure from a subsonically moving monopole takes the form

$$\begin{aligned} p(\mathbf{x},t) &= \frac{\rho_0}{4\pi}\left[\frac{\dot{Q}}{r\,(1-M_r)^2} + \frac{Q\,cM_r}{r^2\,(1-M_r)^2} + \frac{Q}{r^2\,(1-M_r)^3}\left\{r\,\dot{M}_r + c\left(M_r^2 - M^2\right)\right\}\right]_{\text{ret}} \\ &= \frac{\rho_0}{4\pi}\left[\frac{\dot{Q}}{r\,(1-M_r)^2} + \frac{Q}{r^2\,(1-M_r)^3}\left\{r\,\dot{M}_r + c\left(M_r - M^2\right)\right\}\right]_{\text{ret}} \end{aligned} \tag{7.22}$$

where

$$\dot{M}_r = \hat{r}_i\,\frac{\partial M_i}{\partial \tau} \tag{7.23}$$

In equation (7.22), the $\mathcal{O}\left(r^{-1}\right)$-term dominates the far field, whereas the $\mathcal{O}\left(r^{-2}\right)$-term dominates the near field. The factors $(1-M_r)^2$ and $(1-M_r)^3$ are responsible for the Döppler amplification in the far and near field, respectively.

7.2.2 Noise from a Moving Dipole

Consider a point force $\mathbf{F}(t)$ moving along the path $\mathbf{x}_s(t)$ in a quiescent medium. The radiated acoustic pressure is described by the wave equation

$$\frac{1}{c^2}\frac{\partial^2 p}{\partial t^2} - \nabla^2 p = \frac{\partial}{\partial x_i}\left\{F_i(t)\,\delta(\mathbf{x}-\mathbf{x}_s(t))\right\} \tag{7.24}$$

The solution is

$$p(\mathbf{x},t) = \sum_{n=1}^{N}\frac{\partial}{\partial x_i}\left[\frac{F_i}{4\pi r\,|1-M_r|}\right]_{\text{ret}} \tag{7.25}$$

The observer space derivative can be translated into an observer time derivative by using the relationship

$$\frac{\partial}{\partial x_i}\left[\frac{F_i}{r\,|1-M_r|}\right]_{\text{ret}} = -\frac{1}{c}\frac{\partial}{\partial t}\left[\frac{F_i\hat{r}_i}{r\,|1-M_r|}\right]_{\text{ret}} - \left[\frac{F_i\hat{r}_i}{r^2\,|1-M_r|}\right]_{\text{ret}} \tag{7.26}$$

By considering a subsonic dipole and using the relation (7.16), the acoustic field (7.25) takes the form

$$4\pi\, p(\mathbf{x},t) = -\frac{1}{c}\left[\frac{\dot{F}_r}{r\,(1-M_r)^2}\right]_{\text{ret}} - \frac{1}{c}\left[\frac{F_r\left\{r\dot{M}_r + c\left(M_r - M^2\right)\right\}}{r^2\,(1-M_r)^3}\right]_{\text{ret}} - \left[\frac{F_r - F_M}{r^2\,(1-M_r)^2}\right]_{\text{ret}} \tag{7.27}$$

where $\dot{F}_r = \dot{F}_i\hat{r}_i$ and $F_M = F_iM_i$.

Comparing the monopole and the dipole noise expressions in (7.22) and (7.27), respectively, shows that higher order Döppler factors appear for higher order multipole sources.

7.3 Generalized Functions

Discontinuous functions encountered in various physical problems can be easily handled by using some results of the generalized functions theory. The functional approach introduced by Schwartz in 1950 to formulate his theory of distributions [162] is the first tentative to define generalized functions as mathematical objects. The functional approach is indeed the most popular approach to generalized functions, since it extends, with a minimum of abstraction, the concepts of ordinary differentiation and integration to discontinuous functions.

In this section some rudiments of Schwartz functional approach are illustrated with emphasis given to some aerodynamic and aeroacoustic applications.

7.3.1 Definition

The delta function $\delta(x)$ introduced by Dirac in the form

$$\int_{-\infty}^{\infty} \phi(x)\, \delta(x)\; \mathrm{d}x = \phi(0) \tag{7.28}$$

is a generalized function in Schwartz theory of distributions. No ordinary function, in fact, could satisfy the sifting property, an ordinary function being a locally Lebesgue integrable function with a finite integral over any bounded region. The Dirac delta function can be introduced in mathematics by changing the way to think of an ordinary function. This can be done by introducing the functional

$$F\,[f] = \int_{-\infty}^{\infty} f(x)\, \phi(x)\; \mathrm{d}x \tag{7.29}$$

where the function $\phi(x)$ comes from a given space of functions which is referred to as the *test function space*. The relationship (7.29) maps the test function space into real or complex numbers. According to an ordinary definition, a function $f(x)$ is represented by a table of ordered pairs $(x, f(x))$ where, for each x, $f(x)$ is unique. Now, according to the definition (7.29), a function $f(x)$ is represented by a table of its functional values over a given test function space.

A familiar example of this new way of thinking about functions is the Fourier transform of a function f periodic with period 2π, i.e.

$$F\,[\phi_n] = \frac{1}{2\pi} \int_0^{2\pi} f(x) \exp(\mathrm{i}\, nx)\; \mathrm{d}x \tag{7.30}$$

where $\phi_n = \exp(\mathrm{i}\, nx)$ $(n = 0, \pm 1, \pm 2, \ldots)$ constitute the test function space. The table $F\,[\phi_n]$ contains the same information as $f(x)$. Hence, the Fourier coefficients $F\,[\phi_n]$ can be interpreted as functional values of $f(x)$ on the test function space ϕ_n.

A special test function space is one constituted by all infinitely differentiable functions with bounded support, hereafter referred to as D. The support Supp_ϕ of a function $\phi(x)$ is the closure of the set on which $\phi(x) \neq 0$. The functional $F[\phi]$ of an ordinary function $f(x)$ over the test function space D has the following two properties:

1. *linearity*. Considered two test functions ϕ_1 and ϕ_2, then

$$F\,[\alpha\phi_1 + \beta\phi_2] = \alpha F\,[\phi_1] + \beta F\,[\phi_2] \tag{7.31}$$

   where α and β are two arbitrary constants.

2. *Continuity*. Consider a sequence ϕ_n of test functions satisfying the following two properties:

   (a) there exists a bounded interval I such that for all n, $\mathrm{Supp}_{\phi_n} \subset I$;

(b) $\lim_{n\to\infty} \phi_n^{(k)} = 0$ uniformly for all k.

Hence, the functional $F[\phi]$ is continuous in the sense that $\lim_{n\to\infty} F[\phi_n] = 0$.

The continuous linear functionals on space D are now defined as generalized functions on D. Moreover, the space of generalized functions on D is hereafter referred to as D'.

A typical example of space D mapping into generalized functions is that constituted by the test functions

$$\phi(x;a) = \begin{cases} \exp\left(-\frac{a^2}{a^2-x^2}\right) & \text{for} \quad |x| < a \\ 0 & \text{for} \quad |x| \geq a \end{cases} \tag{7.32}$$

for a given $a > 0$. A sequence satisfying the property b) coming from D is, for example,

$$\phi_n(x) = \frac{1}{n}\phi(x;a) \tag{7.33}$$

A key point of the generalized function theory is that even non ordinary functions can generate some continuous linear functionals on D. This is typically the case of the Dirac delta functional defined as

$$\delta[\phi] = \phi(0) \tag{7.34}$$

Since $\delta[\phi]$ satisfies both linearity and continuity it can be regarded as a generalized function.

7.3.2 Generalized Differentiation

The derivative of a generalized function is a concept which allows to handle partial differential equations in the presence of discontinuous fields.

Let $f(x)$ be an ordinary function with a continuous first derivative, and let $F'[\phi]$ denote the functional of its derivative, that is

$$F'[\phi] = \int f'\phi \, \mathrm{d}x \tag{7.35}$$

Integrating by parts and using the fact that the test function ϕ has a compact support yield

$$F'[\phi] = -\int f\phi' \, \mathrm{d}x \equiv -F[\phi'] \tag{7.36}$$

Since $\phi' \in D$, $F[\phi']$ is a functional on D. Hence, equation (7.36) can be used to define the derivative of all generalized functions in D'. For higher order derivatives we can write

$$F^{(n)}[\phi] = (-1)^n F[\phi(n)] \qquad (n = 1, 2, \ldots) \tag{7.37}$$

which illustrates the fundamental theorem that *generalized functions have derivatives of all orders.* As a consequence, even locally Lebesgue integrable functions that are discontinuous are infinitely differentiable when regarded as generalized functions.

A first result concerns the derivative of the Dirac delta function. Using the definition (7.34) into the formula (7.37) provides

$$\begin{aligned} \delta'[\phi] &= -\delta[\phi'] \\ &\equiv -\phi'(0) \end{aligned} \tag{7.38}$$

A second result concerns the derivative of the Heaviside function

$$h(x) = \begin{cases} 1 & (x > 0) \\ 0 & (x < 0) \end{cases} \tag{7.39}$$

In functional notation $h(x)$ can be written as

$$H[\phi] = \int_0^\infty \phi(x)\ \mathrm{d}x \tag{7.40}$$

The Heaviside function is discontinuous at $x = 0$. However, its generalized derivative can be obtained by using the formula (7.37) to write

$$\begin{aligned} H'[\phi] &= -H\left[\phi'\right] \\ &= -\int_0^\infty \phi'(x)\ \mathrm{d}x \\ &= \phi(0) \\ &\equiv \delta[\phi] \end{aligned} \tag{7.41}$$

Hence, we can symbolically write

$$h'(x) = \delta(x) \tag{7.42}$$

where h' signifies generalized differentiation of h.

A general result concerns the derivative of discontinuous functions. Let $f(x)$ be a piecewise smooth function with one discontinuity at x_0 represented by the jump

$$\Delta f = f\left(x_0^+\right) - f\left(x_0^-\right) \tag{7.43}$$

Let ϕ be in D with support $\mathrm{Supp}_\phi = [a, b]$, and let $x_0 \in \mathrm{Supp}_\phi$. Then, the generalized derivative of $f(x)$ can be obtained by writing

$$\begin{aligned} F'[\phi] &= -F\left[\phi'\right] \\ &= -\int_a^b f(x)\,\phi'(x)\ \mathrm{d}x \\ &= -\int_0^{x_0^-} f(x)\,\phi'(x)\ \mathrm{d}x - \int_{x_0^+}^b f(x)\,\phi'(x)\ \mathrm{d}x \end{aligned} \tag{7.44}$$

Integrating by parts yields

$$\begin{aligned} F'[\phi] &= \int_a^b f'(x)\,\phi(x)\ \mathrm{d}x + \left[f\left(x_0^+\right) - f\left(x_0^-\right)\right]\phi(x_0) \\ &= \int_a^b f'(x)\,\phi(x)\ \mathrm{d}x + \Delta f\,\phi(x_0) \end{aligned} \tag{7.45}$$

that can be symbolically written as

$$\overline{f'}(x) = f'(x) + \Delta f\,\delta(x - x_0) \tag{7.46}$$

where overbar denotes generalized derivative.

In the more general case in which the function $f(x)$ has n discontinuities at x_i with jumps $\Delta f_i = f\left(x_i^+\right) - f\left(x_i^-\right)$, then

$$\overline{f'}(x) = f'(x) + \sum_{i=1}^n \Delta f_i \delta(x - x_i) \tag{7.47}$$

The generalized derivative concept can be extended to accounts for multidimensional discontinuities. Let $f(\mathrm{x})$ have a jump Δf across the surface $g(\mathrm{x}) = 0$, i.e.

$$\Delta f = f\left(g = 0^+\right) - f\left(g = 0^-\right) \tag{7.48}$$

Then, as shown for example in Ref. [163], the differentiation operations can be generalized as

$$\overline{\nabla} f = \nabla f + \Delta f \nabla g \, \delta(g) \tag{7.49}$$
$$\overline{\nabla} \cdot \mathbf{f} = \nabla \cdot \mathbf{f} + \nabla g \cdot \Delta \mathbf{f} \, \delta(g) \tag{7.50}$$
$$\overline{\nabla} \times \mathbf{f} = \nabla \times \mathbf{f} + \nabla g \times \Delta \mathbf{f} \, \delta(g) \tag{7.51}$$

7.3.3 Generalized Integration

By definition, the integral functional $G[\phi]$ of the functional $F[\phi]$ is such that

$$G'[\phi] = F[\phi] \tag{7.52}$$

For example, the Heaviside function is a generalized integral of the Dirac delta function.

Let $C[\phi]$ be a generalized function such that

$$C'[\phi] = 0 \tag{7.53}$$

As shown in Ref. [164], the only solution of equation (7.53) in D' is

$$C[\phi] = \int c \, \phi(x) \, \mathrm{d}x \tag{7.54}$$

where c is an arbitrary function. Now, if $G[\phi]$ is the generalized integral of $F[\phi]$, then $(G + C)[\phi] = G[\phi] + C[\phi]$ is also an integral of $F[\phi]$. This result corresponds to the indefinite integration of an ordinary function, i.e.

$$\int f(x) \, \mathrm{d}x = g(x) + c \tag{7.55}$$

where the indefinite constant c is interpreted as a constant distribution $C[\phi]$.

7.3.4 Some Useful Elements and Results of Differential Geometry

In this subsection we illustrate some results which will be used to describe some aerodynamic and aeroacoustic applications of the generalized function theory.

7.3.4.1 Multiplication of a generalized function with a C^∞ function

Consider the generalized function $F[\phi]$ and the C^∞ function $a(x)$. It results that

$$a \, F[\phi] = F[a\phi] \tag{7.56}$$

where the left-hand side is defined by the right-hand side. A typical example is

$$a\delta(\phi) = \delta(a\phi) = a(0) \, \delta(0) \tag{7.57}$$

that can be symbolically written as

$$a(x) \, \delta(x) = a(0) \, \delta(x) \tag{7.58}$$

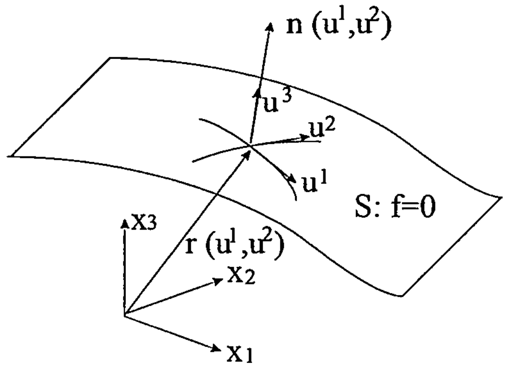

FIGURE 7.1: Gaussian co-ordinates on the surface $f(\mathbf{x}) = 0$ and normal extension.

7.3.4.2 Multidimensional delta functions

The multidimensional interpretation of $\delta(\mathbf{x})$ is

$$\int \phi(\mathbf{x})\,\delta(\mathbf{x})\,\mathrm{d}\mathbf{x} = \phi(0) \tag{7.59}$$

where

$$\delta(\mathbf{x}) = \delta(x_1)\,\delta(x_1)\ldots\delta(x_n) \tag{7.60}$$

is defined in a n-dimensional space.

The sifting properties (7.34) and (7.38) can be extended to a multidimensional δ–function by writing

$$\int \delta(\mathbf{x})\,\phi(\mathbf{x})\,\mathrm{d}\mathbf{x} = \phi(0) \tag{7.61}$$

$$\int \left(\frac{\partial}{\partial x_j}\delta(\mathbf{x})\right)\phi(\mathbf{x})\,\mathrm{d}\mathbf{x} = -\frac{\partial \phi}{\partial x_j}(0) \tag{7.62}$$

7.3.4.3 Some important results from differential geometry

Consider the local Gaussian co-ordinates (u_1, u_2) on the surface $f(\mathbf{x}) = 0$ and extend these co-ordinates along normals to the surface, as sketched in Fig.7.1. Define the local tangent vectors on the surface by

$$\mathbf{r}_1 = \frac{\partial \mathbf{r}}{\partial u_1}$$
$$\mathbf{r}_2 = \frac{\partial \mathbf{r}}{\partial u_2} \tag{7.63}$$

and set

$$g_{ij} = \mathbf{r}_i \cdot \mathbf{r}_j \tag{7.64}$$

$$g_{(2)} = det(g_{ij}) = g_{11}\,g_{22} - g_{12}^2 \equiv |\mathbf{r}_1 \times \mathbf{r}_2|^2 \tag{7.65}$$

$$g^{ii} = \frac{g_{ii}}{g_{(2)}},\; g^{ij} = \frac{-g_{ij}}{g_{(2)}} \quad \text{i.e.} \quad g^{ij}\,g_{jk} = \delta_{ki}, \quad \delta_{ki} \text{ denoting the Kronecker delta} \tag{7.66}$$

$$\mathbf{n}_i = \frac{\partial \mathbf{n}}{\partial u_i} \tag{7.67}$$

$$\mathbf{r}_{ij} = \frac{\partial^2 \mathbf{r}}{\partial u^i \partial u^j} \tag{7.68}$$

$$b_{ij} = \mathbf{r}_{ij} \cdot \mathbf{n} = -\mathbf{r}_i \cdot \mathbf{n}_j \tag{7.69}$$

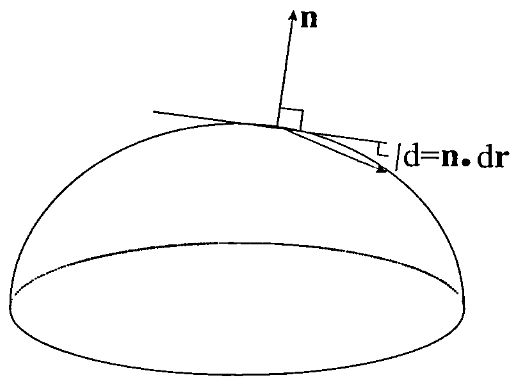

FIGURE 7.2: Geometrical meaning of Π.

$$b_i^j = g^{jk} b_{ki} \tag{7.70}$$

$$\Gamma_{ijk} = \frac{1}{2}\left[\frac{\partial g_{jk}}{\partial u^i} + \frac{\partial g_{ki}}{\partial u^j} - \frac{\partial g_{ij}}{\partial u^k}\right] \tag{7.71}$$

$$\Gamma_{ij}^k = g^{kl}\Gamma_{ijl} \tag{7.72}$$

where g^{ij} are elements of the inverse of the matrix $\{g_{ij}\}$, $\mathbf{n}$ is the unit normal to $f = 0$ pointing in the region $f > 0$, Γ_{ijk} is the Christoffel symbol of first kind and Γ_{ij}^k is the Christoffel symbol of second kind. The above symbols are now used to illustrate some differential geometry results.

- Denoting as $\mathrm{d}l$ an element of length of a curve on the surface $f = 0$, *the first fundamental form* says
$$\mathrm{d}l^2 = g_{ij}\, \mathrm{d}u^i\, \mathrm{d}u^j \tag{7.73}$$
where the summation convention on repeated index is used.

- The element of surface area $\mathrm{d}S$ is given by
$$\mathrm{d}S = \sqrt{g_{(2)}}\, \mathrm{d}u^1\, \mathrm{d}u^2 \tag{7.74}$$

- *The second fundamental form* says
$$\Pi = b_{ij}\, \mathrm{d}u^i\, \mathrm{d}u^j \tag{7.75}$$
where $\Pi \simeq 2\mathbf{n} \cdot \mathrm{d}\mathbf{r}$ (see Fig.7.2).

- The Weingarten formula says
$$\mathbf{n}_i = -b_i^j \cdot \mathbf{r}_j \tag{7.76}$$

- The Gauss formula says
$$\mathbf{r}_{ij} = \Gamma_{ij}^k\, \mathbf{r}_k + b_{ij}\, \mathbf{n} \tag{7.77}$$

- A useful results is
$$\frac{\partial\sqrt{g_{(2)}}}{\partial u^i} = \Gamma_{ik}^k \sqrt{g_{(2)}} \tag{7.78}$$

- Let us parameterize a curve in space by the length parameter s, such that the unit tangent $\mathbf{t}$ to the curve is
$$\mathbf{t} = \frac{\mathrm{d}\mathbf{r}}{\mathrm{d}s} \tag{7.79}$$

and the local curvature k is given by

$$k\,\mathbf{N} = \frac{\mathrm{d}\mathbf{t}}{\mathrm{d}s} = \mathbf{k} \tag{7.80}$$

where

$$k = \left|\frac{\mathrm{d}^2\mathbf{r}}{\mathrm{d}s^2}\right| \tag{7.81}$$

and $\mathbf{N}$ is an unit vector pointing to the center of curvature. For a curve on a surface, the local curvature vector $\mathbf{k}$ has components along the tangent and normal directions to the surface, i.e.

$$\begin{aligned} \mathbf{k} &= \mathbf{r}_{ij}\frac{\mathrm{d}u^i}{\mathrm{d}s}\frac{\mathrm{d}u^j}{\mathrm{d}s} + \mathbf{r}_i\frac{\mathrm{d}^2u^i}{\mathrm{d}s^2} \\ &= \left(\frac{\mathrm{d}^2u^k}{\mathrm{d}s^2} + \Gamma^k_{ij}\frac{\mathrm{d}u^i}{\mathrm{d}s}\frac{\mathrm{d}u^j}{\mathrm{d}s}\right)\mathbf{r}_k + \left(b_{ij}\frac{\mathrm{d}u^i}{\mathrm{d}s}\frac{\mathrm{d}u^j}{\mathrm{d}s}\right)\mathbf{n} \\ &= \mathbf{k}_g + \mathbf{k}_n \end{aligned} \tag{7.82}$$

where $\mathbf{k}_g$ is the *geodesic* curvature vector and $\mathbf{k}_n$ is the *normal* curvature vector.

- There are two orthogonal directions on a surface along which the normal curvature is maximum (k_1) and minimum (k_2). Hence, the Euler's formula says

$$k_n(\alpha) = k_1\cos^2\alpha + k_2\sin^2\alpha \tag{7.83}$$

- The following curvatures can be also defined
  - Mean curvature

$$\begin{aligned} H &= \frac{1}{2}(k_1 + k_2) \\ &= \frac{1}{2}\left(k_n(\alpha) + k_n\left(\alpha + \frac{\pi}{2}\right)\right) \end{aligned} \tag{7.84}$$

  - Gaussian curvature

$$\begin{aligned} K &= k_1 k_2 \\ &= b^1_1 b^2_2 - b^1_2 b^2_1 \end{aligned} \tag{7.85}$$

- Let us displace the surface $S : f = 0$ defined as $\mathbf{r}(u^1, u^2)$ by the constant distance a along the local normal to S. The resulting surface S' is defined as $\mathbf{r}'(u^1, u^2, a) = \mathbf{r}(u^1, u^2) + a\mathbf{n}(u^1, u^2)$. Hence, an important result is

$$\sqrt{g'_{(2)}} = \left(1 - 2Ha + K\,a^2\right)\sqrt{g_{(2)}} \tag{7.86}$$

- By setting $u^3 = a$, the three-dimensional space near the surface S can be parameterized by (u^1, u^2, u^3) and $g_{(3)}$, the determinant of the coefficients of the three-dimensional first fundamental form, is given by

$$g_{(3)} = g'_{(2)}(u^1, u^2, u^3) = \left(1 - 2Hu^3 + K\,u^3u^3\right)^2 g_{(2)}(u^1, u^2) \tag{7.87}$$

from which an important result can be obtained by differentiation, i.e.

$$\left(\frac{\partial\sqrt{g'_{(2)}}}{\partial u^3}\right)_{u^3=0} = \left(\frac{\partial\sqrt{g'_{(2)}}}{\partial n}\right)_S = -2\,H\sqrt{g_{(2)}} \tag{7.88}$$

- An important result concerns the divergence of a vector field $\mathbf{Q}$ in the vicinity of the surface S. Let parameterize the space in the vicinity of S by introducing the Gaussian co-ordinates $\left(u^1, u^2, u^3\right)$. Denoting as Q^i the contravariant components of $\mathbf{Q}$ we can write

$$\nabla \cdot \mathbf{Q} = \frac{1}{\sqrt{g_{(3)}}} \frac{\partial}{\partial u^i} \left\{ \sqrt{g_{(3)}} Q^i \right\} \tag{7.89}$$

Making use of the relation $g_{(3)} = g'_{(2)}\left(u^1, u^2, u^3\right)$ yields

$$(\nabla \cdot \mathbf{Q})_S = \left\{ \frac{\partial}{\partial u^1} \left\{ \sqrt{g'_{(2)}} Q^1 \right\} + \frac{\partial}{\partial u^2} \left\{ \sqrt{g'_{(2)}} Q^2 \right\} + \frac{\partial Q^3}{\partial u^3} + \frac{Q^3}{\sqrt{g'_{(2)}}} \frac{\partial \sqrt{g'_{(2)}}}{\partial u^3} \right\} \tag{7.90}$$

Now, using the result (7.88) allows to write

$$(\nabla \cdot \mathbf{Q})_S = \nabla_2 \cdot \mathbf{Q}_t + \frac{\partial Q_n}{\partial n} - 2 H Q_n \tag{7.91}$$

where $\mathbf{Q}_t$ is the surface component of $\mathbf{Q}$, $\mathbf{Q}_n$ is the normal component of $\mathbf{Q}$, $\nabla_2 \cdot \mathbf{Q}_t$ is the surface divergence of $\mathbf{Q}_t$, and H is the local mean curvature of S. The above relation can be used to obtain the following useful result

$$\begin{aligned} \nabla \cdot \{ p \hat{\mathbf{n}}\, \delta(f) \} &\equiv \nabla \cdot \{ \tilde{p} \hat{\mathbf{n}}\, \delta(f) \} \\ &= \nabla \cdot (\tilde{p} \hat{\mathbf{n}})\, \delta(f) + \tilde{p}\, \delta'(f) \\ &= \left\{ \nabla_2 \cdot (\tilde{p} \hat{\mathbf{n}})_t + \frac{\partial \tilde{p}}{\partial n} - 2 H_f \tilde{p} \right\} \delta(f) + \tilde{p}\, \delta'(f) \\ &= -2 H_f \tilde{p}\, \delta(f) + \tilde{p}\, \delta'(f) \end{aligned} \tag{7.92}$$

where use of the restriction property $\partial \tilde{p} / \partial n = 0$ has been made (see subsection 7.3.4.7).

Further details about the differential geometry theory can be found in the book of Kreyszig [165].

7.3.4.4 Integration of $\phi(\mathrm{x})\, \delta(f)$

Consider the surface $f = 0$ and suppose that $|\nabla f| = 1$ [1]. An equivalent form of the integral

$$I = \int \phi(\mathrm{x})\, \delta(f)\, \mathrm{dx} \tag{7.93}$$

is herein derived.

Let us parameterize the three-dimensional space in the vicinity of the surface $f = 0$ by the Gaussian variables $\left(u^1, u^2, u^3\right)$, as shown in Fig.7.1. Denoting as $g_{(3)}$ the determinant of the coefficients of the three-dimensional first fundamental form, it results that

$$\begin{aligned} \mathrm{dx} &= \sqrt{g_{(3)}}\, \mathrm{d}u^1\, \mathrm{d}u^2\, \mathrm{d}u^3 \\ &= \sqrt{g'_{(2)}\left(u^1, u^2, u^3\right)}\, \mathrm{d}u^1\, \mathrm{d}u^2\, \mathrm{d}u^3 \end{aligned} \tag{7.94}$$

Now, substituting into equation (7.93) and making use of the relation (7.74) give

$$\begin{aligned} I &= \int \phi(\mathrm{x})\, \delta\left(u^3\right) \sqrt{g'_{(2)}}\, \mathrm{d}u^1\, \mathrm{d}u^2\, \mathrm{d}u^3 \\ &= \int \{\phi(\mathrm{x})\}_{u^3=0} \sqrt{g_{(2)}}\, \mathrm{d}u^1\, \mathrm{d}u^2 \\ &= \int_{f=0} \phi(\mathrm{x})\, \mathrm{d}S \end{aligned} \tag{7.95}$$

which shows that I provides the surface integral of ϕ over the surface $f = 0$.

[1] If $|\nabla f| \neq 1$, then we can always redefine the surface as $f_1 = f / |\nabla f|$.

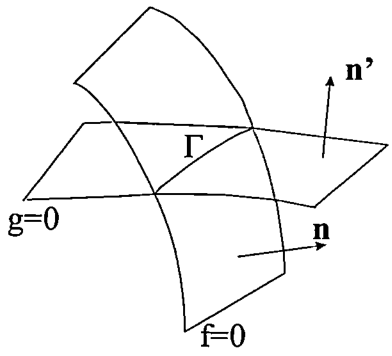

FIGURE 7.3: Integration of $\phi(\mathrm{x})\,\delta(f)\,\delta(g)$ upon two intersecting surfaces $f=0$ and $g=0$.

7.3.4.5 Integration of $\phi(\mathrm{x})\,\delta'(f)$

Again, consider the surface $f=0$ and suppose that $|\nabla f|=1$. An equivalent form of the integral

$$I' = \int \phi(\mathrm{x})\,\delta'(f)\;\mathrm{dx} \tag{7.96}$$

is herein derived.

Introducing the local Gaussian co-ordinates (u^1,u^2,u^3) upon and near the surface $f=0$ allows to write

$$I' = \int \phi(\mathrm{x})\,\delta'(u_3)\,\sqrt{g'_{(2)}}\,\mathrm{d}u^1\,\mathrm{d}u^2\,\mathrm{d}u^3 \tag{7.97}$$

Making use of the sifting property (7.62) yields

$$I' = -\int \frac{\partial}{\partial u_3}\left\{\phi(\mathrm{x})\,\sqrt{g'_{(2)}}\right\}_{u^3=0}\mathrm{d}u^1\,\mathrm{d}u^2 \tag{7.98}$$

Equations (7.88) and (7.74) can be now used to write

$$\begin{aligned} I' &= \int\left\{-\frac{\partial\phi}{\partial u_3}+2\,H_f\phi\right\}\sqrt{g_{(2)}}\,\mathrm{d}u^1\,\mathrm{d}u^2 \\ &= \int_{f=0}\left\{-\frac{\partial\phi}{\partial n}+2H_f(\mathrm{x})\,\phi(\mathrm{x})\right\}\mathrm{d}S \end{aligned} \tag{7.99}$$

where $\partial\phi/\partial n$ stands for the normal derivative of ϕ, and $H_f(\mathrm{x})$ denotes the local mean curvature of the surface $f=0$. The normal unit vector to the surface $f=0$ points in the direction of $f>0$.

7.3.4.6 Integration of $\phi(\mathrm{x})\,\delta(f)\,\delta(g)$

Singular generalized functions are not, in general, defined pointwise. They define a functional when are multiplied by a test function and appear under an integral sign. This means that when a singular generalized function appears in the solution of a real physical problem, it is always in an intermediate stage of the analysis. For the same reason, multiplications of two arbitrary generalized functions generally may be not defined.

The product of two generalized functions reaches a physical sense in one special case. Consider the surfaces $f=0$ and $g=0$ intersecting along the curve Γ, as sketched in Fig.7.3. Let $\hat{\mathbf{n}}=\nabla f$ and $\hat{\mathbf{n}}'=\nabla g$ denote the unit normal vector to the surfaces $f=0$ and $g=0$, respectively. On the local plane normal to the Γ-curve take the vectors $u_1=f$ and $u_2=g$. Then define $u_3=\Gamma$ as the distance along the Γ-curve. Extending u_1 and u_2 in the space near the plane, along the local normal direction to the plane, we have

$$\mathrm{dx} = \frac{du_1\, du_2\, du_3}{\sin\theta} \tag{7.100}$$

where $\sin\theta = \left|\hat{\mathbf{n}} \times \hat{\mathbf{n}}'\right|$. This result can be used to interprete the integral

$$I = \int \phi(\mathbf{x})\, \delta(f)\, \delta(g)\; \mathrm{dx} \tag{7.101}$$

In fact, using equation (7.100) into equation (7.101) gives

$$\int \phi(\mathbf{x})\, \delta(f)\, \delta(g)\; \mathrm{dx} = \int_{\substack{f=0\\ g=0}} \frac{\phi(\mathbf{x})}{\sin\theta}\, \mathrm{d}\Gamma \tag{7.102}$$

7.3.4.7 Restriction to the support of a delta function

Consider the expression

$$E = \phi(\mathbf{x})\, \delta(f) \tag{7.103}$$

Denoting as $\tilde{\phi}(\mathbf{x})$ the restriction of $\phi(\mathbf{x})$ to the support of the delta function, that is the surface $f = 0$, then E can be also written as

$$E = \tilde{\phi}(\mathbf{x})\, \delta(f) \tag{7.104}$$

This second form is advantageous since it allows to exploit two important properties

$$\frac{\partial\tilde{\phi}}{\partial n} = 0 \tag{7.105}$$

and

$$\nabla\tilde{\phi} = \nabla_2\tilde{\phi} \tag{7.106}$$

where $\nabla_2\tilde{\phi}$ is the surface gradient of $\tilde{\phi}(\mathbf{x})$ on $f = 0$. Therefore, using the restriction of $\phi(\mathbf{x})$ to the support of the delta function in expressions involving $\phi(\mathbf{x})\, \delta(f)$ allows to reduce the algebraic manipulations. This can be illustrated by considering the following one-dimensional example. Taking the derivatives with respect to x of both sides of the equation

$$\phi(x)\, \delta(x) = \phi(0)\, \delta(x) \tag{7.107}$$

yields

$$\phi'(x)\, \delta(x) + \phi(x)\, \delta'(x) = \phi(0)\, \delta'(x) \tag{7.108}$$

which shows that the generalized function on the right-hand side is simpler than that on the left-hand side.

7.3.5 The Divergence Theorem

The divergence theorem can be easily demonstrated by using generalized functions. Moreover, an extension of the theorem to discontinuous fields can be easily obtained by interpreting derivatives as generalized derivatives.

Let Ω be a finite volume and $\phi(\mathbf{x})$ a C^1 vector field. Consider the discontinuous vector field

$$\phi_1(\mathbf{x}) = \begin{cases} \phi(\mathbf{x}) & \text{for} \quad \mathbf{x} \in \Omega \\ 0 & \text{for} \quad \mathbf{x} \notin \Omega \end{cases} \tag{7.109}$$

Thus, the vector field $\phi_1(\mathbf{x})$ is discontinuous across the boundary $f \equiv \partial\Omega$ of the control volume Ω. Using the relationship (7.50) yields

$$\overline{\nabla} \cdot \phi_1 = \nabla \cdot \phi_1 + \Delta\phi_1 \cdot \hat{\mathbf{n}}\, \delta(f) \tag{7.110}$$

where $\Delta\phi_1 = -\phi(f=0)$ and $\hat{\mathbf{n}} = \nabla f$, provided that $|\nabla f| = 1$.

Integrating $\overline{\nabla} \cdot \phi_1$ over the unbounded three-dimensional space yields

$$\int \overline{\nabla} \cdot \phi_1 = 0 \tag{7.111}$$

Then, using the property (7.95) and considering that

$$\nabla \cdot \phi_1 = \begin{cases} \nabla \cdot \phi & \text{for} \quad \mathbf{x} \in \Omega \\ 0 & \text{for} \quad \mathbf{x} \notin \Omega \end{cases} \tag{7.112}$$

lead to

$$\int_{\Omega} \nabla \cdot \phi \,\mathrm{d}\mathbf{x} - \int_{\partial\Omega} \phi_n \,\mathrm{d}S = 0 \tag{7.113}$$

where $\phi_n = \phi \cdot \hat{\mathbf{n}}$. Equation (7.113) is the divergence theorem.

Suppose now that the vector field is discontinuous across the surface $g = 0$. Equation (7.111) is still valid, but the divergence in equation (7.113) must be regarded as a generalized operator. Therefore, the divergence theorem takes the general form

$$\int_{\Omega} \nabla \cdot \phi \,\mathrm{d}\mathbf{x} - \int_{\partial\Omega} \phi_n \,\mathrm{d}S + \int_{S_g} \Delta\phi_{n'} \,\mathrm{d}S = 0 \tag{7.114}$$

where $\hat{\mathbf{n}'} = \nabla g$ denotes the unit vector normal to the surface $g = 0$, $\Delta\phi_{n'} = \Delta\phi \cdot \hat{\mathbf{n}'}$ and S_g is the portion of the surface $g = 0$ enclosed in the region Ω.

The divergence theorem is used in physics to derive conservation laws in differential form. Therefore, the generalization (7.114) implies that the conservation laws are still valid for discontinuous vector fields, provided that the derivatives are interpreted as generalized derivatives.

7.3.6 The Transport Theorem

As shown in chapter 1, the transport theorem is used in the derivation of conservation laws. Here we show how generalized functions can be used to obtain two forms of the theorem.

Consider first the expression

$$\dot{I} = \frac{\mathrm{d}}{\mathrm{d}t} \int_{\Omega(t)} Q(\mathbf{x}, t)\, \mathrm{d}\mathbf{x} \tag{7.115}$$

where $\Omega(t)$ is a time-dependent region of space and $Q(\mathbf{x}, t)$ is a C^1 function. We are interested in taking the derivative inside the integral. If we suppose that the integral in equation (7.115) is continuous in time, then we can replace $\mathrm{d}/\mathrm{d}t$ with $\overline{\mathrm{d}}/\mathrm{d}t$ and bring the derivative inside the integral. Hence, we can write

$$\begin{aligned} \dot{I} &= \frac{\overline{\mathrm{d}}}{\mathrm{d}t} \int h(f)\, Q(\mathbf{x}, t)\, \mathrm{d}\mathbf{x} \\ &= \int \left\{ \frac{\partial f}{\partial t} \delta(f)\, Q(\mathbf{x}, t) + h(f)\, \frac{\partial Q}{\partial t} \right\} \mathrm{d}\mathbf{x} \\ &= \int_{\partial\Omega(t)} \frac{\partial f}{\partial t} Q(\mathbf{x}, t)\, \mathrm{d}S + \int_{\Omega(t)} \frac{\partial}{\partial t} Q(\mathbf{x}, t)\, \mathrm{d}\mathbf{x} \end{aligned} \tag{7.116}$$

where the surface $f = 0$ denotes the boundary $\partial\Omega(t)$, such that $f > 0$ in Ω and $\hat{\mathbf{n}}' = \nabla f = -\hat{\mathbf{n}}$ is the unit inward vector normal to the surface. In equation (7.116) use of equation (7.95) has been made. Let $v_{n'}$ and v_n denote the local normal velocities in the direction of inward and outward normals, respectively. Thus, substituting $\partial f/\partial t = v_n$ into equation (7.116), the well-known form of the transport theorem follows, i.e.

$$\dot{I} = \int_{\partial\Omega(t)} v_n Q(\mathbf{x},t)\ \mathrm{d}S + \int_{\Omega(t)} \frac{\partial}{\partial t} Q(\mathbf{x},t)\ \mathrm{d}\mathbf{x} \tag{7.117}$$

Consider now a *restriction* of the transport theorem to the boundary $\partial\Omega(t)$ and write

$$\dot{I} = \frac{\mathrm{d}}{\mathrm{d}t} \int_{\partial\Omega(t)} Q(\mathbf{x},t)\ \mathrm{d}S \tag{7.118}$$

Again, we are interested in taking the time derivative inside the integral. First, convert the surface integral into a volume integral by introducing the delta function $\delta(f)$, i.e.

$$\dot{I} = \frac{\mathrm{d}}{\mathrm{d}t} \int Q(\mathbf{x},t)\, \delta(f)\ \mathrm{d}\mathbf{x} \tag{7.119}$$

where $f = 0$ describes the boundary $\partial\Omega(t)$. Now, consider the restriction of $Q(\mathbf{x},t)$ to the support $f = 0$ of the delta function, i.e.

$$\dot{I} = \frac{\mathrm{d}}{\mathrm{d}t} \int \tilde{Q}(\mathbf{x},t)\, \delta(f)\ \mathrm{d}\mathbf{x} \tag{7.120}$$

Supposing that the integral in equation (7.118) is continuous in time, the time derivative $\mathrm{d}/\mathrm{d}t$ can be replaced by the generalized $\bar{\mathrm{d}}/\mathrm{d}t$ that can be bring inside the integral. Hence, we can write

$$\begin{aligned} \dot{I} &= \int \left\{ \frac{\partial f}{\partial t} \delta'(f)\, \tilde{Q}(\mathbf{x},t) + \delta(f)\, \frac{\partial \tilde{Q}}{\partial t} \right\} \mathrm{d}\mathbf{x} \\ &= \int \left\{ -\tilde{v}_n \delta'(f)\, \tilde{Q}(\mathbf{x},t) + \delta(f)\, \frac{\partial \tilde{Q}}{\partial t} \right\} \mathrm{d}\mathbf{x} \end{aligned} \tag{7.121}$$

where $\tilde{v}_n$ denotes the velocity normal to the surface $f = 0$, restricted to the surface. Then, using equations (7.95) and (7.99) into equation (7.121) gives

$$\begin{aligned} \dot{I} &= \int_{\partial\Omega(t)} \frac{\partial}{\partial n} \left\{ \tilde{Q}(\mathbf{x},t)\, \tilde{v}_n \right\} \mathrm{d}S - \int_{\partial\Omega(t)} 2 v_n H_f Q(\mathbf{x},t)\ \mathrm{d}S + \int_{\partial\Omega(t)} \frac{\partial \tilde{Q}}{\partial t}\, \mathrm{d}S \\ &= \int_{\partial\Omega(t)} \left\{ \frac{\partial \tilde{Q}}{\partial t} - 2 v_n H_f Q(\mathbf{x},t) \right\} \mathrm{d}S \end{aligned} \tag{7.122}$$

where use of the property (7.105) has been made. In equation (7.122) $\partial\tilde{Q}/\partial t$ stands for

$$\frac{\partial \tilde{Q}}{\partial t} = \frac{\partial Q}{\partial t} + v_n \frac{\partial Q}{\partial n} \tag{7.123}$$

Therefore equation (7.118) takes the final form

$$\dot{I} = \int_{\partial\Omega(t)} \left\{ \frac{\partial Q}{\partial t} + v_n \frac{\partial Q}{\partial n} - 2 v_n H_f Q(\mathbf{x},t) \right\} \mathrm{d}S \tag{7.124}$$

Concluding, we have demonstrated that

$$\frac{\mathrm{d}}{\mathrm{d}t} \int_{\Omega(t)} Q(\mathbf{x},t)\ \mathrm{d}\mathbf{x} = \int_{\partial\Omega(t)} v_n Q(\mathbf{x},t)\ \mathrm{d}S + \int_{\Omega(t)} Q(\mathbf{x},t)\ \mathrm{d}\mathbf{x} \tag{7.125}$$

$$\frac{\mathrm{d}}{\mathrm{d}t} \int_{\partial\Omega(t)} Q(\mathbf{x},t)\ \mathrm{d}S = \int_{\partial\Omega(t)} \left\{ \frac{\partial Q}{\partial t} + v_n \frac{\partial Q}{\partial n} - 2 v_n H_f Q(\mathbf{x},t) \right\} \mathrm{d}S \tag{7.126}$$

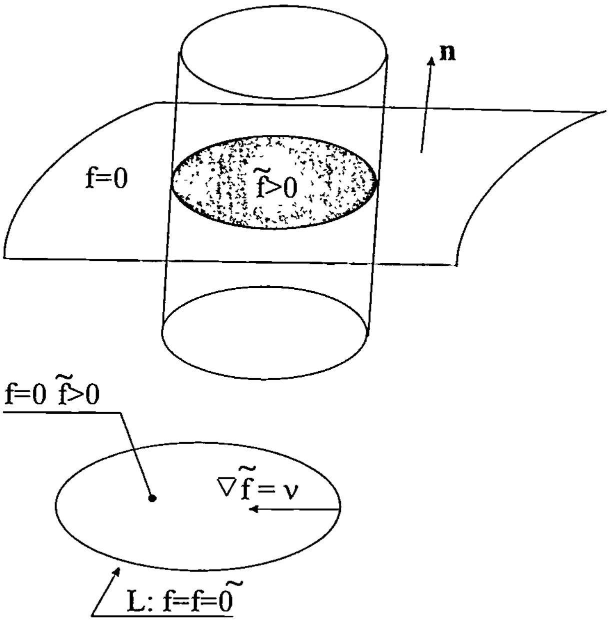

FIGURE 7.4: Definition of an open surface as $f(\mathbf{x},t)=0$ and $\tilde{f}(\mathbf{x},t)>0$. The edge is defines by $f=\tilde{f}=0$ and ν denotes the unit inward geodesic normal.

7.3.7 Solutions of Standard Inhomogeneous Wave Equations

In this subsection we illustrate some aeroacoustic applications of the generalized function theory.

As will be shown later on in this chapter, the wave equations describing the various mechanisms of aerodynamic sound generation in the presence of moving surfaces may have the following inhomogeneous forms

$$\begin{aligned}
\overline{\Box^2}\left(p' H(f)\right) &= Q(\mathbf{x},t)\,\delta(f) && (7.127)\\
\overline{\Box^2}\left(p' H(f)\right) &= \frac{\partial}{\partial t}\left\{Q(\mathbf{x},t)\,\delta(f)\right\} && (7.128)\\
\overline{\Box^2}\left(p' H(f)\right) &= \nabla\cdot\left\{\mathbf{Q}(\mathbf{x},t)\,\delta(f)\right\} && (7.129)\\
\overline{\Box^2}\left(p' H(f)\right) &= Q(\mathbf{x},t)\,H\left(\tilde{f}\right)\delta(f) && (7.130)\\
\overline{\Box^2}\left(p' H(f)\right) &= Q(\mathbf{x},t)\,\delta\left(\tilde{f}\right)\delta(f) && (7.131)\\
\overline{\Box^2}\left(p' H(f)\right) &= \tilde{Q}(\mathbf{x},t)\,H\left(\tilde{f}\right)\delta'(f) && (7.132)\\
\overline{\Box^2}\left(p' H(f)\right) &= Q(\mathbf{x},t)\,H(f) && (7.133)\\
\overline{\Box^2}\left(p' H(f)\right) &= \frac{\partial^2}{\partial x_i \partial x_j}\left\{Q(\mathbf{x},t)\,H(f)\right\} && (7.134)
\end{aligned}$$

where

$$\overline{\Box^2}=\frac{1}{c^2}\frac{\overline{\partial}^2}{\partial t^2}-\overline{\nabla^2} \qquad (7.135)$$

is the generalized D'Alambertian wave operator. In the above equations, $f(\mathbf{x},t)$ denotes a moving surface, usually assumed to be closed. Conversely, an open surface, such as a blade surface element, is described by $f(\mathbf{x},t)=0$ and $\tilde{f}(\mathbf{x},t)>0$, where $f(\mathbf{x},t)=0$ and $\tilde{f}(\mathbf{x},t)=0$ denote the edge of the open surface, as sketched in Fig.7.4. In equation (7.132), $\tilde{Q}(\mathbf{x},t)$ denotes the restriction of $Q(\mathbf{x},t)$ to the support of $\delta(f)$.

As already discussed in section 7.2, the Green's function of the wave equation $\overline{\Box}^2 = 0$ in unbounded space is

$$G(\mathbf{y},\tau;\mathbf{x},t) = \begin{cases} \frac{\delta(g)}{4\pi r} & \tau \leq t \\ 0 & \tau > t \end{cases} \tag{7.136}$$

where

$$g = t - \tau - \frac{r}{c} \tag{7.137}$$

and

$$r = |\mathbf{x} - \mathbf{y}| \tag{7.138}$$

In the above expressions, $(\mathbf{x}, t)$ and $(\mathbf{y}, \tau)$ are the observer and source space-time variables, respectively.

7.3.7.1 Solutions of $\overline{\Box}^2\,(p'\,H(f)) = Q(\mathbf{x},t)\,\delta(f)$

Three formal solutions of equation (7.127) are given here. Using the Green's function (7.137), the formal solution of equation (7.127) is

$$4\pi p'(\mathbf{x},t) = \int \frac{1}{r} Q(\mathbf{y},\tau)\,\delta(f)\,\delta(g)\;\mathrm{d}\mathbf{y}\,\mathrm{d}\tau \tag{7.139}$$

where the time integration is over $(-\infty, t)$ and the space integration is over the entire unbounded space. In the above equation we have used the hypothesis that $|\nabla f| = 1$.

A change of variable $\tau \rightarrow g$ can be performed in equation (7.139) in order to exploit the properties of the δ–function. Since the Jacobian of the transformation is unity, an integration over g gives

$$4\pi p'(\mathbf{x},t) = \int \frac{1}{r}\,[Q(\mathbf{y},\tau)\,\delta(f)]_{\mathrm{ret}}\;\mathrm{d}\mathbf{y} \tag{7.140}$$

where $[\;]_{\mathrm{ret}}$ stands for evaluation at the retarded time.

Consider now the surface Σ given by

$$F(\mathbf{y};\mathbf{x},t) = [f(\mathbf{y},\tau)]_{\mathrm{ret}} = f\left(\mathbf{y}, t - \frac{r}{c}\right) = 0 \tag{7.141}$$

This is referred to as *influence surface* and represents the locus of points on $f = 0$ whose emitted signals are detected simultaneously at the time t by an observer in $\mathbf{x}$. The Σ–surface is generated by the curves of the intersection of $f = 0$ and the *collapsing sphere* $g = 0$ for $-\infty < \tau \leq t$. These curves of intersection are called the Γ–curves. Using the influence surface $F = 0$ in equation (7.140) yields

$$4\pi p'(\mathbf{x},t) = \int \frac{1}{r}\,[Q(\mathbf{y},\tau)]_{\mathrm{ret}}\,\delta(F)\;\mathrm{d}\mathbf{y} \tag{7.142}$$

Equation (7.95) can be now used to reduce the volume integral in the above equation to a surface integral. However, since $|\nabla F| \neq 1$, a modification of equation (7.95) is first necessary, i.e.

$$\int \phi(\mathbf{x})\,\delta(f)\;\mathrm{d}\mathbf{x} = \int_{f=0} \frac{\phi(\mathbf{x})}{|\nabla f|}\,\mathrm{d}S \tag{7.143}$$

This can be used in equation (7.142) to obtain

$$4\pi p'(\mathbf{x},t) = \int_{F=0} \frac{1}{r}\,[Q(\mathbf{y},\tau)]_{\mathrm{ret}}\,\frac{\mathrm{d}\Sigma}{|\nabla F|} \tag{7.144}$$

By differentiation of $F = 0$ with respect to $\mathbf{y}$ we obtain

$$\nabla F = \left[\nabla f + \frac{\partial f}{\partial \tau}\frac{\partial \tau}{\partial r}\nabla r\right]_{\mathrm{ret}} \tag{7.145}$$

with

$$\nabla f = \hat{\mathbf{n}} \tag{7.146}$$
$$\frac{\partial f}{\partial \tau} = -v_n \tag{7.147}$$
$$\frac{\partial \tau}{\partial r} = -\frac{1}{c} \tag{7.148}$$
$$\nabla_y r = -\hat{\mathbf{r}} \tag{7.149}$$

where v_n is the local normal velocity on $f = 0$. It thus results that

$$\nabla F = [\hat{\mathbf{n}} - M_n \hat{\mathbf{r}}]_{\text{ret}} \tag{7.150}$$

and

$$|\nabla F| = \left[\left(1 + M_n^2 - 2M_n \cos\theta\right)^{\frac{1}{2}}\right]_{\text{ret}} \equiv \Lambda_{\text{ret}} \tag{7.151}$$

where $M_n = v_n/c$ and $\cos\theta = \hat{\mathbf{n}} \cdot \hat{\mathbf{r}}$ is the cosine of the angle between the local normal to $f = 0$ and the radiation direction $\hat{\mathbf{r}} = (\mathbf{x} - \mathbf{y})/r$. Hence, we can write the first formal solution of equation (7.127) as

$$4\pi p'(\mathbf{x}, t) = \int_{F=0} \frac{1}{r} \left[\frac{Q(\mathbf{y}, \tau)}{\Lambda}\right]_{\text{ret}} \mathrm{d}\Sigma \tag{7.152}$$

The retarded time formulation described in section 7.2 for elementary point sources can be generalized to the case of a surface source distribution. Therefore, let us introduce the Lagrangian variable η on the surface $f = 0$ in equation (7.139), such that the Jacobian of the transformation is unity. Since $\mathbf{y} = \mathbf{y}(\eta, \tau)$, a change of variable $\tau \to g$ generates the Döppler factor $\partial g/\partial \tau = 1 - M_r$. Now, integrating equation (7.139) with respect to g and then using the result (7.95) to integrate $\delta(f)$, the second formal solution of equation (7.127) results, which can be written as

$$4\pi p'(\mathbf{x}, t) = \int_{f=0} \left[\frac{Q(\mathbf{y}, \tau)}{r\,|1 - M_r|}\right]_{\text{ret}} \mathrm{d}S \tag{7.153}$$

where $M_r = M_i \hat{r}_i$ denotes the projection of the surface local Mach number in the radiation direction.

The third formal solution of equation (7.127) can be obtained by using equation (7.102) to integrate $\delta(f)\,\delta(g)$ in equation (7.139). Since $|\nabla g| = c^{-1} \neq 1$, a modification of equation (7.102) is first necessary, which yields

$$4\pi p'(\mathbf{x}, t) = \int\int_{\substack{f=0\\g=0}} \frac{c\,Q(\mathbf{y}, \tau)}{r \sin\theta}\,\mathrm{d}\Gamma\,\mathrm{d}\tau \tag{7.154}$$

where θ is again the angle between the local normal to $f = 0$ and the radiation direction $\hat{\mathbf{r}} = (\mathbf{x} - \mathbf{y})/r$. In the above expression, the time integral extends between the times when the collapsing sphere $g = 0$ enters and leaves the surface $f = 0$.

It is interesting to observe that the three formal solutions (7.152), (7.153) and (7.154) of equation (7.127), can be obtained directly from equation (7.139) by applying the variable transformation

$$\mathrm{d}\mathbf{y}\ \mathrm{d}\tau = \frac{c\,\mathrm{d}\Gamma\,\mathrm{d}\tau\,\mathrm{d}f\,\mathrm{d}g}{\sin\theta} = \frac{\mathrm{d}\Sigma\,\mathrm{d}F\,\mathrm{d}g}{\Lambda} = \frac{\mathrm{d}S\,\mathrm{d}f\,\mathrm{d}g}{|1 - M_r|} \tag{7.155}$$

7.3.7.2 Solutions of $\overline{\square^2}\,(p'\,H(f)) = \frac{\partial}{\partial t}\,\{Q(\mathbf{x}, t)\,\delta(f)\}$

Three formal solutions of equation (7.128) can be obtained by applying the procedures used for equation (7.127). Since the operator $\square^2$ commutates with the operator $\partial/\partial t$, the formal solutions are

$$4\pi p'(\mathbf{x}, t) = \frac{\partial}{\partial t} \int_{F=0} \frac{1}{r} \left[\frac{Q(\mathbf{y}, \tau)}{\Lambda}\right]_{\text{ret}} \mathrm{d}\Sigma \tag{7.156}$$

$$= \frac{\partial}{\partial t}\int_{f=0}\left[\frac{Q(\mathbf{y},\tau)}{r\,|1-M_r|}\right]_{\mathrm{ret}}\mathrm{d}S \tag{7.157}$$

$$= \frac{\partial}{\partial t}\int\int_{\substack{f=0\\g=0}}\frac{c\,Q(\mathbf{y},\tau)}{r\sin\theta}\,\mathrm{d}\Gamma\,\mathrm{d}\tau \tag{7.158}$$

where θ is again the angle between the local normal to $f=0$ and the radiation direction $\hat{\mathbf{r}} = (\mathbf{x}-\mathbf{y})/r$. In equation (7.158), the time integral extends between the times when the collapsing sphere $g=0$ enters and leaves the surface $f=0$.

7.3.7.3 Solutions of $\overline{\Box}^2\,(p'\,H(f)) = \nabla\cdot\{\mathbf{Q}(\mathbf{x},t)\,\delta(f)\}$

Again, three formal solutions of equation (7.129) are given here. These can be obtained by considering that the operator $\Box^2$ commutates with the operator $\partial/\partial x_i$, and by using the relation

$$\frac{\partial}{\partial x_i}\left[\frac{\delta(g)}{r}\right]_{\mathrm{ret}} = -\frac{1}{c}\frac{\partial}{\partial t}\left[\frac{\hat{r}_i\delta(g)}{r}\right]_{\mathrm{ret}} - \left[\frac{\hat{r}_i\delta(g)}{r^2}\right]_{\mathrm{ret}} \tag{7.159}$$

in the final step of the procedure used to solve equations (7.127) and (7.128). Therefore, the three formal solutions are

$$4\pi p'(\mathbf{x},t) = -\frac{1}{c}\frac{\partial}{\partial t}\int_{F=0}\frac{1}{r}\left[\frac{Q_r(\mathbf{y},\tau)}{\Lambda}\right]_{\mathrm{ret}}\mathrm{d}\Sigma - \int_{F=0}\frac{1}{r^2}\left[\frac{Q_r(\mathbf{y},\tau)}{\Lambda}\right]_{\mathrm{ret}}\mathrm{d}\Sigma \tag{7.160}$$

$$= -\frac{1}{c}\frac{\partial}{\partial t}\int_{f=0}\left[\frac{Q_r(\mathbf{y},\tau)}{r\,|1-M_r|}\right]_{\mathrm{ret}}\mathrm{d}S - \int_{f=0}\left[\frac{Q_r(\mathbf{y},\tau)}{r^2\,|1-M_r|}\right]_{\mathrm{ret}}\mathrm{d}S \tag{7.161}$$

$$= -\frac{1}{c}\frac{\partial}{\partial t}\int\int_{\substack{f=0\\g=0}}\frac{c\,Q_r(\mathbf{y},\tau)}{r\sin\theta}\,\mathrm{d}\Gamma\,\mathrm{d}\tau - \int\int_{\substack{f=0\\g=0}}\frac{c\,Q_r(\mathbf{y},\tau)}{r^2\sin\theta}\,\mathrm{d}\Gamma\,\mathrm{d}\tau \tag{7.162}$$

where $Q_r = Q_i\hat{r}_i$.

7.3.7.4 Solutions of $\overline{\Box}^2\,(p'\,H(f)) = Q(\mathbf{x},t)\,H\big(\tilde{f}\big)\,\delta(f)$

Equation (7.130) can be solved by applying the procedure used to obtain the solution (7.152) of equation (7.127). By letting $\tilde{F}(\mathbf{y};\mathbf{x},t) = \tilde{f}(\mathbf{y},t-r/c) = \left[\tilde{f}(\mathbf{y},\tau)\right]_{\mathrm{ret}}$, the formal solution of equation (7.130) is

$$4\pi p'(\mathbf{x},t) = \int_{\substack{F=0\\ \tilde{F}>0}}\frac{1}{r}\left[\frac{Q(\mathbf{y},\tau)}{\Lambda}\right]_{\mathrm{ret}}\mathrm{d}\Sigma \tag{7.163}$$

7.3.7.5 Solutions of $\overline{\Box}^2\,(p'\,H(f)) = Q(\mathbf{x},t)\,\delta\big(\tilde{f}\big)\,\delta(f)$

The formal solution of equation (7.127) is

$$4\pi p'(\mathbf{x},t) = \int\frac{1}{r}Q(\mathbf{y},\tau)\,\delta(f)\,\delta\big(\tilde{f}\big)\,\delta(g)\;\mathrm{d}\mathbf{y}\,\mathrm{d}\tau \tag{7.164}$$

This equation is similar to equation (7.102) with $\sin\theta$ replaced by $\left|\nabla F\times\nabla\tilde{F}\right|$, here denoted as Λ_0. Hence, it results that

$$4\pi p'(\mathbf{x},t) = \int_{\substack{F=0\\ \tilde{F}=0}}\frac{Q}{r\Lambda_0}\,\mathrm{d}L \tag{7.165}$$

where L is the edge of the Σ–surface described by $F=\tilde{F}=0$. We can also write

$$\Lambda_0 = \Lambda\tilde{\Lambda}\sin\theta' \tag{7.166}$$

where

$$\Lambda^2 = 1 + M_n^2 - 2M_n \cos\theta \tag{7.167}$$

$$\tilde{\Lambda}^2 = 1 + M_\nu^2 - 2M_\nu \cos\tilde{\theta} \tag{7.168}$$

$$\mathbf{N} = \frac{\nabla F}{|\nabla F|} = \frac{\mathbf{n} - M_n \hat{\mathbf{r}}}{\Lambda} = \frac{1 - M_n \cos\theta}{\Lambda} \hat{\mathbf{n}} + \frac{M_n \sin\theta}{\Lambda} \hat{\mathbf{t}}_1 \tag{7.169}$$

$$\tilde{\mathbf{N}} = \frac{\nabla \tilde{F}}{\left|\nabla \tilde{F}\right|} = \frac{\boldsymbol{\nu} - M_\nu \hat{\mathbf{r}}}{\tilde{\Lambda}} \tag{7.170}$$

$$\cos\theta' = \mathbf{N} \cdot \tilde{\mathbf{N}} \tag{7.171}$$

with $\boldsymbol{\nu}$ denoting the unit inward geodesic normal to the L−edge, as sketched in Fig.7.4, and $\hat{\mathbf{t}}_1$ is the unit vector along the projection of $\hat{\mathbf{r}}$ on the local tangent plane of $f = 0$.

7.3.7.6 Solutions of $\overline{\Box^2}\,(p' H(f)) = \tilde{Q}(\mathbf{x}, t)\, H\left(\tilde{f}\right) \delta'(f)$

The formal solution of equation (7.132) is

$$\begin{aligned} 4\pi p'(\mathbf{x}, t) &= \int \frac{1}{r} \tilde{Q}(\mathbf{y}, \tau)\, h\left(\tilde{f}\right) \delta'(f)\, \delta(g)\, \mathrm{d}\mathbf{y}\, \mathrm{d}\tau \\ &= \int \frac{1}{r} \left[\tilde{Q}(\mathbf{y}, \tau)\right]_{\text{ret}} h\left(\tilde{F}\right) \delta'(F)\, \mathrm{d}\mathbf{y} \end{aligned} \tag{7.172}$$

This equation is in the form of equation (7.96), with a minor modification due to the fact that $|\nabla F| = \Lambda \neq 1$, namely

$$\int \phi(\mathbf{x})\, \delta'(F)\, \mathrm{d}\mathbf{y} = \int_{F=0} \left\{ -\frac{1}{|\nabla F|} \frac{\partial}{\partial n} \left(\frac{\phi}{|\nabla F|} \right) + \frac{2H_F \phi}{|\nabla F|^2} \right\} \mathrm{d}\Sigma \tag{7.173}$$

where H_F is the local mean curvature of the Σ−surface $F = 0$. Hence, equation (7.172) can be written as

$$4\pi p'(\mathbf{x}, t) = \int_{F=0} \left\{ -\frac{1}{\Lambda} \frac{\partial}{\partial N} \left(\frac{\left[\tilde{Q}\right]_{\text{ret}} h\left(\tilde{F}\right)}{r\Lambda} \right) + \frac{2H_F \left[\tilde{Q}\right]_{\text{ret}} h\left(\tilde{F}\right)}{r\Lambda^2} \right\} \mathrm{d}\Sigma \tag{7.174}$$

Using

$$\frac{\partial}{\partial N} h\left(\tilde{F}\right) = \mathbf{N} \cdot \nabla \tilde{F}\, \delta\left(\tilde{F}\right) \tag{7.175}$$

in equation (7.174) yields

$$4\pi p'(\mathbf{x}, t) = \int_{F=0} \left\{ -\frac{1}{\Lambda} \frac{\partial}{\partial N} \left(\frac{\left[\tilde{Q}\right]_{\text{ret}}}{r\Lambda} \right) h\left(\tilde{F}\right) - \frac{\left[\tilde{Q}\right]_{\text{ret}} \mathbf{N} \cdot \nabla \tilde{F}\, \delta\left(\tilde{F}\right)}{r\Lambda^2} + \frac{2H_F \left[\tilde{Q}\right]_{\text{ret}} h\left(\tilde{F}\right)}{r\Lambda^2} \right\} \mathrm{d}\Sigma \tag{7.176}$$

From equation (7.171) it follows that $\mathbf{N} \cdot \nabla \tilde{F} = \left|\nabla \tilde{F}\right| \cos\theta'$ which can be used in the above expression to write

$$4\pi p'(\mathbf{x}, t) = \int_{F=0} \left\{ -\frac{1}{\Lambda} \frac{\partial}{\partial N} \left(\frac{\left[\tilde{Q}\right]_{\text{ret}}}{r\Lambda} \right) h\left(\tilde{F}\right) - \frac{\left[\tilde{Q}\right]_{\text{ret}} \left|\nabla \tilde{F}\right| \cos\theta'\, \delta\left(\tilde{F}\right)}{r\Lambda^2} + \frac{2H_F \left[\tilde{Q}\right]_{\text{ret}} h\left(\tilde{F}\right)}{r\Lambda^2} \right\} \mathrm{d}\Sigma \tag{7.177}$$

Then, using the relation

$$\int_{F=0} \phi(\mathbf{x}) \left|\nabla \tilde{F}\right| \delta\left(\tilde{F}\right) \mathrm{d}\Sigma = \int_{\substack{F=0 \\ \tilde{F}=0}} \frac{\phi}{\sin\theta'}\, \mathrm{d}L \tag{7.178}$$

gives

$$4\pi p'(\mathbf{x},t) = \int_{\substack{F=0\\ \tilde{F}>0}} \left\{ -\frac{1}{\Lambda}\frac{\partial}{\partial N}\left(\frac{\left[\tilde{Q}\right]_{\text{ret}}}{r\Lambda}\right) + \frac{2H_F\left[\tilde{Q}\right]_{\text{ret}}}{r\Lambda^2} \right\} \mathrm{d}\Sigma - \int_{\substack{F=0\\ \tilde{F}=0}} \frac{\left[\tilde{Q}\right]_{\text{ret}} \cot\theta'}{r\Lambda^2}\,\mathrm{d}L \tag{7.179}$$

where θ' is the angle between $\mathbf{N} = \nabla F / |\nabla F|$ and $\tilde{\mathbf{N}} = \nabla\tilde{F} / \left|\nabla\tilde{F}\right|$, and $\mathrm{d}L$ is the element of the edge $F = \tilde{F} = 0$.

The first term on the right-hand side of equation (7.179) can be simplified by writing

$$\frac{\partial}{\partial N}\left(\frac{\left[\tilde{Q}\right]_{\text{ret}}}{r\Lambda}\right) = \frac{1}{r\Lambda}\frac{\partial\tilde{Q}_{\text{ret}}}{\partial N} + \tilde{Q}_{\text{ret}}\frac{\partial}{\partial N}\left(\frac{1}{r\Lambda}\right) \tag{7.180}$$

and observing that

$$\frac{\partial\tilde{Q}_{\text{ret}}}{\partial N} = \left[\frac{\partial\tilde{Q}}{\partial N}\right]_{\text{ret}} + \left[\frac{\partial\tilde{Q}}{\partial\tau}\frac{\partial\tau}{\partial N}\right]_{\text{ret}} \tag{7.181}$$

where

$$\begin{aligned}
\left[\frac{\partial\tau}{\partial N}\right]_{\text{ret}} &= [\nabla\tau\cdot\mathbf{N}]_{\text{ret}} \\
&= \left[-\frac{\nabla r}{c}\cdot\mathbf{N}\right]_{\text{ret}} \\
&= \left[\frac{\hat{\mathbf{r}}}{c}\cdot\mathbf{N}\right]_{\text{ret}}
\end{aligned} \tag{7.182}$$

and

$$\begin{aligned}
\left[\frac{\partial\tilde{Q}}{\partial N}\right]_{\text{ret}} &= \left[\nabla\tilde{Q}\cdot\mathbf{N}\right]_{\text{ret}} \\
&= \left[\nabla\tilde{Q}\cdot\hat{\mathbf{n}}\,\frac{1-M_n\cos\theta}{\Lambda} + \nabla\tilde{Q}\cdot\hat{\mathbf{t}}_1\,\frac{M_n\sin\theta}{\Lambda}\right]_{\text{ret}} \\
&= \left[\frac{\partial\tilde{Q}}{\partial t_1}\frac{M_n\sin\theta}{\Lambda}\right]_{\text{ret}}
\end{aligned} \tag{7.183}$$

where use of equation (7.169) has been made, together with the restriction property (7.105) yielding to $\nabla\tilde{Q}\cdot\hat{\mathbf{n}} = \partial\tilde{Q}/\partial n = 0$. Hence, using equations (7.182) and (7.183) in equation (7.181), the formal solution (7.179) takes the form

$$\begin{aligned}
4\pi p'(\mathbf{x},t) &= \int_{\substack{F=0\\ \tilde{F}>0}} \left\{ -\frac{1}{r\Lambda^2}\left[\frac{\partial\tilde{Q}}{\partial t_1}\frac{M_n\sin\theta}{\Lambda} + \frac{1}{c}\hat{\mathbf{r}}\cdot\mathbf{N}\frac{\partial\tilde{Q}}{\partial\tau}\right]_{\text{ret}} - \frac{\tilde{Q}_{\text{ret}}}{\Lambda}\frac{\partial}{\partial N}\left(\frac{1}{r\Lambda}\right) + \frac{2H_F\left[\tilde{Q}\right]_{\text{ret}}}{r\Lambda^2} \right\} \mathrm{d}\Sigma \\
&- \int_{\substack{F=0\\ \tilde{F}=0}} \frac{\left[\tilde{Q}\right]_{\text{ret}}\cot\theta'}{r\Lambda^2}\,\mathrm{d}L
\end{aligned} \tag{7.184}$$

Farassat & Farris [166] derived the following expression for the local mean curvature H_F of the $\Sigma-$surface

$$\begin{aligned}
H_F = &- \frac{M_n}{r\Lambda}\left(1 - \frac{\sin^2\theta}{2\Lambda^2}\right) + \frac{(1-M_r)^2}{\Lambda^3}H_f + \frac{1-M_r}{\Lambda^3}\left(\hat{\mathbf{r}}_t\cdot\mathbf{q} + k_1\tilde{\lambda^1}\tilde{\gamma^1} + k_2\tilde{\lambda^2}\tilde{\gamma^2}\right) \\
&+ \frac{\sin^2\theta}{2\Lambda^3}\left(\frac{\dot{M}_n}{c} + M^2 k_\gamma\right) + \frac{1}{\Lambda^3}(\boldsymbol{\gamma}\cdot\mathbf{q})(\boldsymbol{\lambda}\cdot\hat{\mathbf{r}}_t)
\end{aligned} \tag{7.185}$$

where

$$\cos\theta = \hat{r}_n = \hat{\mathbf{r}} \cdot \hat{\mathbf{n}} \tag{7.186}$$
$$\hat{\mathbf{r}}_t = \hat{\mathbf{r}} - \hat{\mathbf{n}}\cos\theta \tag{7.187}$$
$$\mathbf{M}_t = \mathbf{M} - M_n\hat{\mathbf{n}} \tag{7.188}$$
$$\mathbf{q} = \frac{1}{c}\hat{\mathbf{n}} \times \boldsymbol{\omega} \tag{7.189}$$
$$\boldsymbol{\lambda} = \hat{\mathbf{n}} \times \hat{\mathbf{r}}_t \tag{7.190}$$
$$\boldsymbol{\gamma} = \hat{\mathbf{n}} \times \mathbf{M}_t \tag{7.191}$$
$$\dot{M}_n = \hat{\mathbf{n}} \cdot \dot{\mathbf{M}} \tag{7.192}$$

In the above expressions, k_1 and k_2 are the local principal curvatures of the surface $f = 0$, k_γ is the local normal curvature of $f = 0$ along γ, $\left(\tilde{\lambda^1}, \tilde{\lambda^2}\right)$ and $\left(\tilde{\gamma^1}, \tilde{\gamma^2}\right)$ are the components of $\boldsymbol{\lambda}$ and $\boldsymbol{\gamma}$ in principal directions with respect to unit basis vectors, respectively, and $\boldsymbol{\omega}$ is the angular velocity of the surface $f = 0$.

7.3.7.7 Solutions of $\overline{\square}^2\,(p'\,H(f)) = Q(\mathbf{x}, t)\,H(f)$

Three formal solutions of equation (7.133) are given here. Using the Green's function (7.137), the formal solution of equation (7.133) is

$$4\pi p'(\mathbf{x}, t) = \int \frac{1}{r} Q(\mathbf{y}, \tau)\,H(f)\,\delta(g)\;\mathrm{d}\mathbf{y}\,\mathrm{d}\tau \tag{7.193}$$

where the time integration is over $(-\infty, t)$ and the space integration is over the entire unbounded space.

A change of variable $\tau \to g$ can be performed in equation (7.193) in order to exploit the properties of the $H-$function. Since the Jacobian of the transformation is unity, an integration over g provides

$$4\pi p'(\mathbf{x}, t) = \int \frac{1}{r}\left[Q(\mathbf{y}, \tau)\,H(f)\right]_{\mathrm{ret}}\,\mathrm{d}\mathbf{y} \tag{7.194}$$

Introducing the influence surface Σ given by

$$F(\mathbf{y}; \mathbf{x}, t) = \left[f(\mathbf{y}, \tau)\right]_{\mathrm{ret}} = 0 \tag{7.195}$$

into equation (7.194) yields

$$\begin{aligned} 4\pi p'(\mathbf{x}, t) &= \int \frac{1}{r}\left[Q(\mathbf{y}, \tau)\right]_{\mathrm{ret}} H(F)\;\mathrm{d}\mathbf{y} \\ &= \int_{F>0} \frac{1}{r}\left[Q(\mathbf{y}, \tau)\right]_{\mathrm{ret}}\,\mathrm{d}V_\Sigma \end{aligned} \tag{7.196}$$

which is the first formal solution of equation (7.133).

By denoting as Ω the collapsing sphere $r - c\,(t - \tau) = 0$, the second formal solution of equation (7.133) can be written as

$$\begin{aligned} 4\pi p'(\mathbf{x}, t) &= \int_{-\infty}^{t} \frac{\mathrm{d}\tau}{t - \tau} \int_\Omega \left[Q(\mathbf{y}, \tau)\right]_{\mathrm{ret}} H(F)\;\mathrm{d}\Omega(\mathbf{y}) \\ &= \int_{-\infty}^{t} \int_\Omega \left[\frac{c\,Q(\mathbf{y}, \tau)}{r}\right]_{\mathrm{ret}} H(F)\;\mathrm{d}\Omega(\mathbf{y})\;\mathrm{d}\tau \end{aligned} \tag{7.197}$$

The third formal solution of equation (7.133) can be obtained by introducing the Lagrangian variable η on and near the surface $f = 0$ in equation (7.193), such that the Jacobian of the transformation is unity. Since $\mathbf{y} = \mathbf{y}(\eta, \tau)$, a change of variable $\tau \to g$ generates the Döppler factor $\partial g/\partial \tau = 1 - M_r$. Then, integrating equation (7.193) with respect to g provides the retarded time solution of equation (7.133), i.e.

$$4\pi p'(\mathbf{x}, t) = \int_{f>0} \left[\frac{Q(\mathbf{y}, \tau)}{r\,|1 - M_r|} \right]_{\text{ret}} \mathrm{d}V_S \tag{7.198}$$

where $M_r = M_i \hat{r}_i$ denotes the projection of the volume local Mach number in the radiation direction.

7.3.7.8 Solutions of $\overline{\Box}^2 (p' H(f)) = \partial^2 \{Q_{ij}(\mathbf{x}, t)\, H(f)\} / \partial x_i \partial x_j$

Three formal solutions of equation (7.134) are given here. These can be obtained by applying the procedures used to solve equation (7.133), and by exploiting the fact that the operator $\Box^2$ commutates with the operator $\partial^2/\partial x_i \partial x_j$. Hence, the three formal solutions are

$$\begin{aligned}
4\pi p'(\mathbf{x}, t) &= \frac{\partial^2}{\partial x_i \partial x_j} \int_{F>0} \frac{1}{r} \left[Q_{ij}(\mathbf{y}, \tau)\right]_{\text{ret}} \mathrm{d}V_\Sigma && (7.199)\\
&= \frac{\partial^2}{\partial x_i \partial x_j} \int_{-\infty}^{t} \int_{\Omega} \left[\frac{c\, Q_{ij}(\mathbf{y}, \tau)}{r} \right]_{\text{ret}} H(F)\; \mathrm{d}\Omega(\mathbf{y})\; \mathrm{d}\tau && (7.200)\\
&= \frac{\partial^2}{\partial x_i \partial x_j} \int_{f>0} \left[\frac{Q_{ij}(\mathbf{y}, \tau)}{r\,|1 - M_r|} \right]_{\text{ret}} \mathrm{d}V_S && (7.201)
\end{aligned}$$

The observer space-derivatives can be translated into observer time-derivatives by applying twice the rule (7.159), namely

$$\frac{\partial^2}{\partial x_i \partial x_j} \left[\frac{\delta(g)}{r} \right]_{\text{ret}} = \frac{1}{c^2} \frac{\partial^2}{\partial t^2} \left[\frac{\hat{r}_i \hat{r}_j}{r} \delta(g) \right]_{\text{ret}} + \frac{1}{c} \frac{\partial}{\partial t} \left[\frac{3\hat{r}_i \hat{r}_j - \delta_{ij}}{r^2} \delta(g) \right]_{\text{ret}} + \left[\frac{3\hat{r}_i \hat{r}_j - \delta_{ij}}{r^3} \delta(g) \right]_{\text{ret}} \tag{7.202}$$

where δ_{ij} denotes the Kronecker symbol. Hence, the formal solutions (7.200) and (7.201) take the form

$$\begin{aligned}
4\pi p'(\mathbf{x}, t) &= \frac{1}{c} \frac{\partial^2}{\partial t^2} \int_{-\infty}^{t} \int_{\Omega} \frac{Q_{rr}}{r} H(F)\; \mathrm{d}\Omega(\mathbf{y})\; \mathrm{d}\tau \\
&+ \frac{\partial}{\partial t} \int_{-\infty}^{t} \int_{\Omega} \frac{3\,Q_{rr} - Q_{ii}}{r^2} H(F)\; \mathrm{d}\Omega(\mathbf{y})\; \mathrm{d}\tau \\
&+ c \int_{-\infty}^{t} \int_{\Omega} \frac{3\,Q_{rr} - Q_{ii}}{r^3} H(F)\; \mathrm{d}\Omega(\mathbf{y})\; \mathrm{d}\tau && (7.203)
\end{aligned}$$

and

$$\begin{aligned}
4\pi p'(\mathbf{x}, t) &= \frac{1}{c^2} \frac{\partial^2}{\partial t^2} \int_{f>0} \left[\frac{Q_{rr}}{r\,|1 - M_r|} \right]_{\text{ret}} \mathrm{d}V_S \\
&+ \frac{1}{c} \frac{\partial}{\partial t} \int_{f>0} \left[\frac{3\,Q_{rr} - Q_{ii}}{r^2\,|1 - M_r|} \right]_{\text{ret}} \mathrm{d}V_S \\
&+ \int_{f>0} \left[\frac{3\,Q_{rr} - Q_{ii}}{r^3\,|1 - M_r|} \right]_{\text{ret}} \mathrm{d}V_S && (7.204)
\end{aligned}$$

where the quantity Q_{rr} is the double contraction $Q_{ij} \hat{r}_i \hat{r}_j$.

7.4 The Kirchhoff Formula and the Curle equation

In 1955 Curle [52] extended Lighthill's acoustic analogy in order to describe the aerodynamic noise from turbulent flows past stationary surfaces. The Curle's method is based on the Kirchhoff formula

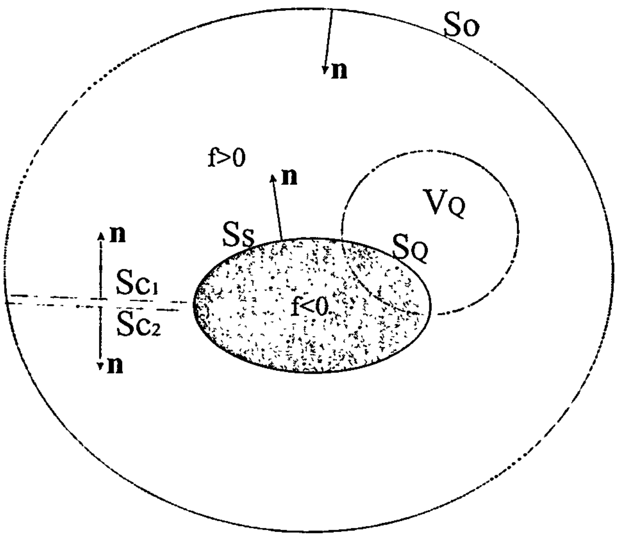

FIGURE 7.5: Configuration used to illustrate the Kirchhoff formula for a stationary surface. The volume V is delimited by an inner stationary surface S and an outer stationary surface S_o, connected by the coincident oriented surfaces S_{c1} and S_{c2}. V_Q denotes a source region adjacent to the portion S_Q of the inner surface.

for linear wave fields in domains bounded by stationary surfaces. Therefore, let us first derive the Kirchhoff formula for a stationary surface.

Consider the volume V delimited by an inner stationary surface S and an outer stationary surface S_o, as shown in Fig.7.5. Suppose that the volume V includes a source region V_Q. The volume portion V_Q is adjacent to a portion of S, denoted as S_Q. The remaining portion of S is denoted as S_s. The outer and the inner surfaces are connected by the coincident oriented surfaces S_{c1} and S_{c2}, which make the volume V simply connected. The unit normal $\hat{\mathbf{n}}$ to S, S_o, S_{c1} and S_{c2} points into the volume V. The inner surface $S_Q \cup S_s$ may be a physical surface or a control surface, say *Kirchhoff surface.* In the latter case, the actual sources can be partially or completely contained by $S_Q \cup S_s$. Because of its generality, this configuration is useful to illustrate the classic Kirchhoff formula for a stationary surface.

Suppose that the scalar quantity $\phi(\mathbf{x}, t)$ satisfies the linear wave equation $\Box^2\phi = Q(\mathbf{x}, t)$ in the volume V $(f > 0)$, and that the source distribution $Q(\mathbf{x}, t)$ vanishes exterior to the source region V_Q. Thus, a formal solution of the wave equation $\Box^2\phi = Q(\mathbf{x}, t)$ can be found by using the Green's formula, i.e.

$$\begin{aligned} \phi(\mathbf{x}, t)\; H(f) &= \int_{-\infty}^{t} \int_{V_Q} Q(\mathbf{y}, \tau)\, G(\mathbf{x}, t; \mathbf{y}, \tau)\; \mathrm{d}\mathbf{y}\, \mathrm{d}\tau \\ &+ \int_{-\infty}^{t} \int_{S \cup S_o} \left\{ \phi \frac{\partial G}{\partial y_i} - G \frac{\partial \phi}{\partial y_i} \right\} \hat{n}_i\, \mathrm{d}S_y\, \mathrm{d}\tau \end{aligned} \tag{7.205}$$

where $G(\mathbf{x}, t; \mathbf{y}, \tau) = \delta(g)\,/4\pi r$ is the free-space Green's function, with $r = |\mathbf{x} - \mathbf{y}|$ and $g = t - \tau - r/c$. Suppose now that the outer surface S_o is sufficiently far from the source region, such that no waves can reach it in the time interval of interest $(r_{S_o} > ct)$. Moreover, the integrals upon the surfaces S_{c1} and S_{c2} cancel each other. Hence, the surface integral at the right-hand side of equation (7.205) reduces to the surface $S_Q \cup S_s$, that is

$$\phi(\mathbf{x}, t)\; H(f) = \int_{-\infty}^{t} \int_{V_Q} Q(\mathbf{y}, \tau)\, G(\mathbf{x}, t; \mathbf{y}, \tau)\; \mathrm{d}\mathbf{y}\, \mathrm{d}\tau$$

$$+ \int_{-\infty}^{t} \int_{S_Q \cup S_s} \left\{ \phi \frac{\partial G}{\partial y_i} - G \frac{\partial \phi}{\partial y_i} \right\} \hat{n}_i \, \mathrm{d}S_y \, \mathrm{d}\tau \tag{7.206}$$

The gradient of the Green's function in the above equation can be evaluated as follows

$$\begin{aligned} \frac{\partial G}{\partial y_i} &= \frac{\delta(g)}{4\pi} \frac{\partial (r^{-1})}{\partial y_i} + \frac{1}{4\pi r} \frac{\partial g}{\partial y_i} \\ &= -\frac{\delta(g)}{4\pi r^2} \frac{\partial r}{\partial y_i} + \frac{\delta'(g)}{4\pi r} \frac{\partial g}{\partial y_i} \\ &= \frac{\delta(g)\, \hat{r}_i}{4\pi r^2} - \frac{\delta'(g)\, \hat{r}_i}{4\pi r c} \end{aligned} \tag{7.207}$$

where use of $\nabla_y r = -\hat{\mathbf{r}}$ has been made. Then, substituting into equation (7.206) yields

$$\begin{aligned} 4\pi\, \phi(\mathbf{x}, t)\, H(f) &= \int_{-\infty}^{t} \int_{V_Q} \frac{Q(\mathbf{y}, \tau)}{r}\, \delta(g)\, \mathrm{d}\mathbf{y}\, \mathrm{d}\tau \\ &+ \int_{-\infty}^{t} \int_{S_Q \cup S_s} \left\{ \frac{\phi\, \hat{r}_n}{r^2}\, \delta(g) - \frac{\phi\, \hat{r}_n}{rc}\, \delta'(g) - \frac{\phi_n}{r}\, \delta(g) \right\} \mathrm{d}S_y\, \mathrm{d}\tau \end{aligned} \tag{7.208}$$

where $\phi_n = \nabla\phi \cdot \hat{\mathbf{n}}$ and $\hat{r}_n = \hat{\mathbf{r}} \cdot \hat{\mathbf{n}}$. Finally, integrating with respect to τ leads to the classic Kirchhoff formula for a stationary surface

$$\begin{aligned} 4\pi\, \phi(\mathbf{x}, t)\, H(f) &= \int_{V_Q} \frac{[Q]_{\mathrm{ret}}}{r}\, \mathrm{d}\mathbf{y} \\ &+ \int_{S_Q \cup S_s} \frac{[\phi]_{\mathrm{ret}}\, \hat{r}_n}{r^2}\, \mathrm{d}S_y + \int_{S_Q \cup S_s} \frac{\left[c^{-1}\dot{\phi}\, \hat{r}_n - \phi_n\right]_{\mathrm{ret}}}{r}\, \mathrm{d}S_y \end{aligned} \tag{7.209}$$

where $\dot{\phi} = \partial\phi / \partial\tau$.

The Curle equation can be now derived by substituting $\phi = p'$ and $Q(\mathbf{y}, \tau) = \partial^2 T_{ij} / \partial y_i \partial y_j$ into equation (7.209), T_{ij} being the Lighthill's stress tensor. Moreover, since the Kirchhoff formula is valid for a linear wave field, the linearized momentum equation in the normal direction can be used to write $p'_n = -\rho_0 \dot{u}_n$, where u_n is the normal component of the flow velocity. Hence, equation (7.209) takes the form of the Curle equation

$$\begin{aligned} 4\pi\, p'(\mathbf{x}, t)\, H(f) &= \frac{\partial^2}{\partial x_i \partial x_j} \int_{V_Q} \frac{[T_{ij}]_{\mathrm{ret}}}{r}\, \mathrm{d}\mathbf{y} \\ &+ \int_{S_Q \cup S_s} \frac{[p']_{\mathrm{ret}}\, \hat{r}_n}{r^2}\, \mathrm{d}S_y + \int_{S_Q \cup S_s} \frac{\left[c^{-1}\dot{p}'\, \hat{r}_n + \rho_0 \dot{u}_n\right]_{\mathrm{ret}}}{r}\, \mathrm{d}S_y \end{aligned} \tag{7.210}$$

If the integration surface is a physical rigid surface, then $p'_n = -\rho_0 \dot{u}_n = 0$ on $S_Q \cup S_s$ and the Curle equation takes the form

$$\begin{aligned} 4\pi\, p'(\mathbf{x}, t)\, H(f) &= \frac{\partial^2}{\partial x_i \partial x_j} \int_{V_Q} \frac{[T_{ij}]_{\mathrm{ret}}}{r}\, \mathrm{d}\mathbf{y} \\ &+ \int_{S_Q \cup S_s} \frac{[p']_{\mathrm{ret}}\, \hat{r}_n}{r^2}\, \mathrm{d}S_y + \int_{S_Q \cup S_s} \frac{\left[c^{-1}\dot{p}'\, \hat{r}_n\right]_{\mathrm{ret}}}{r}\, \mathrm{d}S_y \end{aligned} \tag{7.211}$$

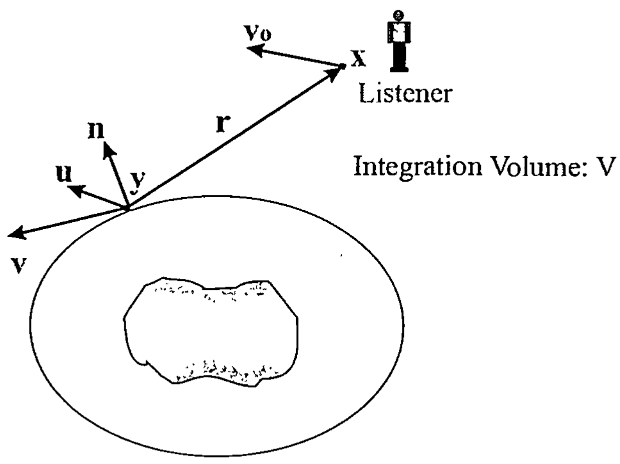

FIGURE 7.6: Scheme of the FW-H acoustic analogy. The flow field enclosed by the integration surface S is replaced by a quiescent fluid (ρ_0, p_0, $\mathbf{u} = 0$). The vectors $\mathbf{u}$ and $\mathbf{v}$ denote the velocity of the flow and the velocity of the integration surface, respectively. The listener moves at the constant velocity $\mathbf{v}_o$.

7.5 The Ffowcs Williams and Hawkings Equation

The FW-H equation is the most general form of Lighthill's acoustic analogy. It can be obtained by using generalized functions in order to embed the exterior flow problem in unbounded space.

Let $f(\mathbf{x}, t) = 0$ be a control surface whose points move at the velocity $\mathbf{v}(\mathbf{x}, t)$. The surface $f = 0$ is defined such that $\nabla f = \hat{\mathbf{n}}$, where $\hat{\mathbf{n}}$ denotes the unit normal vector pointing out of the surface. Using generalized flow variables, the flow portion enclosed by the surface, i.e. $f < 0$, can be replaced by a quiescent fluid and a surface distribution of sources which restore the conservative character of the field. Therefore, the generalized continuity and the linear momentum equations can be written as

$$\begin{aligned}
&\frac{\bar{\partial}}{\partial t}\left[(\rho - \rho_0)\, H(f)\right] + \frac{\bar{\partial}}{\partial x_i}\left[\rho\, u_i\, H(f)\right] = Q\,\delta(f) \quad \text{with} \\
&Q = \rho_0\, U_i\, \hat{n}_i \quad \text{and} \\
&U_i = \left(1 - \frac{\rho}{\rho_0}\right) v_i + \frac{\rho\, u_i}{\rho_0}
\end{aligned} \tag{7.212}$$

and

$$\begin{aligned}
&\frac{\bar{\partial}}{\partial t}\left[\rho\, u_i\, H(f)\right] + \frac{\bar{\partial}}{\partial x_j}\left[(\rho\, u_i\, u_j + P_{ij})\, H(f)\right] = L_i\,\delta(f) \quad \text{with} \\
&L_i = P_{ij}\,\hat{n}_j + \rho\, u_i\,(u_n - v_n) \quad \text{and} \\
&P_{ij} = (p - p_0)\,\delta_{ij} - \tau_{ij}
\end{aligned} \tag{7.213}$$

where $Q\,\delta(f)$ and $L_i\,\delta(f)$ denote surface source distributions of mass and linear momentum, respectively. The following generalized derivatives have been used in equations (7.212) and (7.213)

$$\frac{\bar{\partial} H(f)}{\partial t} = \delta(f)\,\frac{\partial f}{\partial t} = -\delta(f)\, v_n \tag{7.214}$$

$$\frac{\bar{\partial} H(f)}{\partial x_i} = \delta(f)\,\frac{\partial f}{\partial x_i} = \delta(f)\,\hat{\mathbf{n}} \tag{7.215}$$

Outside of the source region, the fluid can be considered at rest and the previous equations (7.212) and (7.213) can be reduced to the standard wave equation describing the propagation of an acoustic disturbance p' in a quiescent medium, i.e.

$$\Box^2 p' \equiv \left(\frac{1}{c^2} \frac{\partial^2}{\partial t^2} - \nabla^2 \right) p' = 0 \tag{7.216}$$

where c is the sound speed in the quiescent medium.

If the flow perturbations are included, equations (7.212) and (7.213) can be arranged into the FW-H equation where the flow perturbations appear as source terms of the standard wave equation. Therefore, by subtracting the divergence of equation (7.213) to the time derivative of equation (7.212), the differential form of the FW-H equation can be obtained, i.e.

$$\Box^2 \left\{ (\rho - \rho_0)\, c^2\, H(f) \right\} = \frac{\partial^2}{\partial x_i \partial x_j} \left\{ T_{ij}\, H(f) \right\} - \frac{\partial}{\partial x_i} \left\{ L_i\, \delta(f) \right\} + \frac{\partial}{\partial t} \left\{ Q\, \delta(f) \right\} \tag{7.217}$$

where

$$T_{ij} = \rho\, u_i u_j + \left(p' - c^2 \rho' \right) \delta_{ij} - \tau_{ij} \tag{7.218}$$

is the well-known Lighthill's stress tensor.

If the density perturbations are small, as usually happens at the observation distances, the term $(\rho - \rho_0)\, c^2$ can be replaced by p' and equation (7.217) can be interpreted as an inhomogeneous wave equation for the acoustic pressure.

In the aeroacoustic literature, the three source terms on the right-hand side of equation (7.217) are known as the quadrupole, loading and thickness source terms, respectively.

The thickness and loading terms are surface distributions of sources, as indicated by $\delta(f)$. When the control surface encloses a physical surface, the thickness source accounts for the fluid displacement produced by the body motion, and the loading source accounts for the unsteady loading exerted by the body on the fluid. The quadrupole source is a volume distribution of sources, as indicates by $H(f)$. This accounts for all the flow nonlinearity in the domain exterior to the control surface.

In the case of a body moving in an otherwise quiescent fluid, the flow nonlinearities are due to the body motion and may consist of vortical disturbances, shocks and local sound speed variations.

7.6 The Kirchhoff Equation

The technique of the generalized function can be also applied to the standard linear wave equation $\Box^2 p' = 0$, in order to replace the acoustic field in the region $f < 0$ by an elementary quiescent fluid $p' = 0$. A distribution of sources on the surface $f = 0$ is thus necessary to maintain the fictitious discontinuities introduced in the original field. Considering the generalized derivatives

$$\frac{1}{c} \frac{\bar{\partial}}{\partial t} \left(p'\, H(f) \right) = \frac{1}{c} \frac{\partial p'}{\partial t} H(f) - M_n\, p'\, \delta(f) \tag{7.219}$$

$$\frac{1}{c} \frac{\bar{\partial}}{\partial t} \left\{ \frac{1}{c} \frac{\bar{\partial}}{\partial t} \left(p'\, H(f) \right) \right\} = \frac{1}{c^2} \frac{\partial^2 p'}{\partial t^2} H(f) - \frac{1}{c} \frac{\partial p'}{\partial t} M_n\, \delta(f) - \frac{1}{c} \frac{\partial}{\partial t} \left(p'\, M_n\, \delta(f) \right) \tag{7.220}$$

$$\overline{\nabla} \left(p'\, H(f) \right) = \nabla p'\, H(f) + p'\, \hat{\mathbf{n}}\, \delta(f) \tag{7.221}$$

$$\overline{\nabla} \cdot \overline{\nabla} \left(p'\, H(f) \right) = \nabla^2 p'\, H(f) + \nabla p' \cdot \hat{\mathbf{n}}\, \delta(f) + \nabla \cdot \left(p'\, \hat{\mathbf{n}}\, \delta(f) \right) \tag{7.222}$$

and subtracting equation (7.222) from equation (7.220), the generalized linear wave equation leads to the Kirchhoff (K) equation for a moving surface, i.e.

$$\overline{\Box^2} \left(p' H(f) \right) = - \left(\frac{\partial p'}{\partial n} + \frac{M_n}{c} \frac{\partial p'}{\partial t} \right) \delta(f) - \frac{1}{c} \frac{\partial}{\partial t} \left\{ M_n\, p'\, \delta(f) \right\} - \frac{\partial}{\partial x_i} \left\{ p'\, \hat{n}_i\, \delta(f) \right\} \tag{7.223}$$

where M_n is the local normal Mach number of the surface $f = 0$.

The Kirchhoff formula for a subsonically moving surface was firstly derived by Morgans [44] in 1930. The derivation of this formula was based on classic analysis and was lengthy. The simpler procedure described above was proposed by Farassat & Myers [45] in 1988. It shows the effectiveness of the generalized function technique.

7.7 The FW-H Equation *versus* the K Equation

The Kirchhoff equation is valid for any physical problem governed by the standard linear wave equation. In acoustics it governs the propagation of linear flow perturbations in a medium at rest and felt by the control surface $S : f = 0$. In aeroacoustics, the linear perturbation on S are the result of all sources, regardless to their nature (linear or nonlinear, quadrupole or not, etc.), located in the interior domain $f < 0$. As a consequence, in aeroacoustics the Kirchhoff approach is only valid for S surrounding the nonlinear flow region. Moreover, the Kirchhoff equation does not account for any aerodynamic source located in the exterior domain $f > 0$, or on the surface itself. In particular, only quadrupole source terms enclosed by S are taken into account and nonlinear aerodynamic sources located on S are not handled. It follows that the use of the Kirchhoff approach in practical application is quit limited. This is because unsteady flows extend over a large distance in the streamwise direction (e.g. jets, wakes, etc.) and would require very large integration surfaces and very large flow region accurately predicted.

This formal difficulty is removed by the FW-H equation. Being an exact rearrangement of the flow governing equations, this intrinsically accounts for the nonlinear flow perturbations on both the integration surface and the exterior domain.

The Kirchhoff formulation is attractive because no volume integration is necessary. For this reason it was used in past years for rotor noise predictions at high-speed tip Mach numbers, provided that, sufficiently far from the aerodynamic source region, the input acoustic pressure p' and its derivatives $\partial p'/\partial t$ and $\partial p'/\partial n$ are compatible with the wave equation $\Box^2 p' = 0$.

More recently [42], the FW-H formulation has been applied to rotor noise predictions by integrating the aerodynamic data upon a penetrable control surface. Since the surface source terms in equation (7.217) are compatible with the flow governing equations, the placement of the integration surface in a FW-H approach is only a matter of convenience as long as the quadrupole sources are taken into account by the surface integration.

Thus, the FW-H analogy allows accurate noise predictions even when the control surface is not in the linear flow region. This is the main advantage of the FW-H aeroacoustic formulation on the Kirchhoff method.

The equivalence between the FW-H formulation and a Kirchhoff method in the linear flow region can be easily verified by introducing the linear approximations $\rho' \simeq p'/c^2$ and $u_i u_j \ll 1$ into equation (7.217). Thus, concerning the thickness noise source, it results that

$$U_i \simeq -\frac{p'}{\rho_0 c^2} v_i + u_i$$

$$\rho_0 U_n \delta(f) \simeq -p' \frac{M_n}{c} \delta(f) + \rho u_i \hat{n}_i \delta(f) \tag{7.224}$$

and

$$\begin{aligned}
\frac{\partial}{\partial t}\{\rho_0 U_n \delta(f)\} &\simeq -\frac{\partial}{\partial t}\left\{p' \frac{M_n}{c}\delta(f)\right\} + \hat{n}_i \delta(f) \frac{\partial}{\partial t}\{\rho u_i\} + \rho u_i \frac{\partial}{\partial t}\{\hat{n}_i \delta(f)\} \\
&= -\frac{\partial}{\partial t}\left\{p' \frac{M_n}{c}\delta(f)\right\} - \frac{\partial p'}{\partial n}\delta(f) - \rho u_i \frac{\partial}{\partial x_i}\{v_n \delta(f)\}
\end{aligned} \tag{7.225}$$

where use of the relation

$$\frac{\partial}{\partial t}(\hat{n}_i \delta(f)) = -\frac{\partial}{\partial x_i}(v_n \delta(f)) \tag{7.226}$$

has been made. Analogously, the loading noise source reduces to

$$\begin{aligned}\frac{\partial}{\partial x_i}\{L_i\,\delta(f)\} &\simeq \frac{\partial}{\partial x_i}\left(p'\,\hat{n}_i\,\delta(f)\right) - (u_n - v_n)\frac{\delta(f)}{c^2}\frac{\partial p'}{\partial t} + \frac{u_n\,\delta(f)}{c^2}\frac{\partial p'}{\partial t} - \rho\,u_i\frac{\partial}{\partial x_i}\left(v_n\,\delta(f)\right)\\ &\simeq \frac{\partial}{\partial x_i}\left(p'\,\hat{n}_i\,\delta(f)\right) + \frac{v_n\,\delta(f)}{c^2}\frac{\partial p'}{\partial t} - \rho\,u_i\frac{\partial}{\partial x_i}\left(v_n\,\delta(f)\right)\end{aligned} \tag{7.227}$$

where use of the linearized continuity equation

$$\frac{\partial}{\partial x_i}(\rho\,u_i) \simeq \frac{1}{c^2}\frac{\partial p'}{\partial t} \tag{7.228}$$

has been made. Finally, substituting the linearized expressions (7.225) and (7.227) into equation (7.217), and neglecting the nonlinear quadrupole contribution, yields the Kirchhoff equation (7.223).

7.8 Solutions of the FW-H Equation

In this section the most popular formal solutions of the FW-H equation (7.217) are obtained on the base of the model solutions described in subsection 7.3.7. The notoriety of these formulations lies on their numerical relevance and convenience.

Different formulae are proposed for subsonic and supersonic applications. In the subsonic case, the most suitable formulation is based on a Lagrangian change of variable, which generates the transonic Döppler factor $1-M_r$ in the dominator of the integrands. For supersonic surfaces, there exist directions in which $M_r = 1$ and thus mathematical singularities appear in the subsonic formulation. This forces to use, in the supersonic regime, different formulations which do not contain the Döppler singularity.

Aerodynamic noise predictions based on the integral approach are performed by dividing the integration surface into panels, and the contribution of each panel is evaluated separately and summed. In rotor-noise applications, the tip-region of the advancing blade is frequently in supersonic motion. Although a supersonic formula can be used to compute the noise from a subsonic surface, it is expedient to use the most suitable formulation for each panel. Therefore, formulations containing the Döppler factor $1 - M_r$ are used for subsonic panels, and *ad hoc* formulations deprived of the transonic singularity are used for supersonic panels. Such a hybrid subsonic/supersonic formulation requires the integral solutions to be extended to an open surface (e.g. a panel). It can be shown that no additional terms appear in the subsonic formulation when applied to an open surface. On the contrary, one edge line integral generally appears when the supersonic formulation is extended to an open surface.

The aeroacoustic sources in the FW-H equation can be divided into surface and volume sources. The surface sources, denoted by $\delta(f)$, accounts for the thickness and loading noise contributions. The volume source, denoted by $H(f)$, accounts for the quadrupole contribution. When the integration surface $f = 0$ coincide with the body surface, the surface sources account for the displacement effect induced by the body motion on the surrounding fluid (thickness noise), and for the aerodynamic force exerted by the body on the surrounding fluid (loading noise). The volume contribution accounts for all the flow nonlinearities in the vicinity of the rotor blade. In helicopter rotors in high-speed forward flight, the quadrupole source gives a significant contribution to the High-Speed Impulsive (HSI) noise. HSI noise is associated with the presence of shocks and a transonic flow around the advancing rotor blades. When the supersonic flow region extends off the blade into the field, a phenomenon referred to as delocalization [2], HSI noise becomes dominant over all the other rotor noise sources.

In the following subsections, the surface and volume contributions are treated separately. Suitable formulations for both subsonic and supersonic sources are illustrated. Moreover, two approximated procedures for the volume noise evaluation are described. The first consists in integrating the

[2] When delocalization occurs, shocks on the blades can extend far beyond the blade tips.

quadrupole sources along lines normal to the rotor disc, and then treating the integrated sources as surface sources distributed upon the rotor disc. The second approximated procedure consists in interpreting the quadrupole sources in the presence of shocks as surface sources distributed upon the flow discontinuity surfaces.

7.8.1 Surface Noise

The surface noise in the FW-H equation is described by

$$\overline{\Box}^2 \{p' H(f)\} = \frac{\partial}{\partial t}\{Q\,\delta(f)\} - \frac{\partial}{\partial x_i}\{L_i\,\delta(f)\} \tag{7.229}$$

where

$$Q = \rho_0\,U_i\,\hat{n}_i, \qquad U_i = \left(1 - \frac{\rho}{\rho_0}\right) v_i + \frac{\rho\,u_i}{\rho_0} \tag{7.230}$$

and

$$L_i = P_{ij}\,\hat{n}_j + \rho\,u_i\,(u_n - v_n)\,, \qquad P_{ij} = (p - p_0)\,\delta_{ij} - \tau_{ij} \tag{7.231}$$

7.8.1.1 Subsonic surface

In the subsonic regime ($M_r < 1$), a suitable formal solution of equation (7.229) is the well-known Formulation 1 of Farassat [39]. This can be obtained by using the retarded time formulae (7.157) and (7.161) for the thickness (Q) and loading noise (L), respectively, that is

$$4\pi p'_Q(\mathbf{x},t) = \frac{\partial}{\partial t}\int_{f=0}\left[\frac{Q(\mathbf{y},\tau)}{r\,(1-M_r)}\right]_{\text{ret}} \mathrm{d}S \tag{7.232}$$

$$4\pi p'_L(\mathbf{x},t) = \frac{1}{c}\frac{\partial}{\partial t}\int_{f=0}\left[\frac{L_r(\mathbf{y},\tau)}{r\,(1-M_r)}\right]_{\text{ret}} \mathrm{d}S + \int_{f=0}\left[\frac{L_r(\mathbf{y},\tau)}{r^2\,(1-M_r)}\right]_{\text{ret}} \mathrm{d}S \tag{7.233}$$

where $L_r = L_i \hat{r}_i$.

A more effective formal solution of equation (7.229) can be obtained by taking, in equations (7.232) and (7.233), the time derivatives inside the integrals. As shown in section 7.2, this can be made by using the rule

$$\left.\frac{\partial}{\partial t}\right|_{\mathbf{x}} = \left[\frac{1}{1-M_r}\left.\frac{\partial}{\partial \tau}\right|_{\mathbf{x}}\right]_{\text{ret}} \tag{7.234}$$

together with the following relations

$$\frac{\partial r}{\partial \tau} = -c\,M_r \tag{7.235}$$

$$\frac{\partial \hat{r}_i}{\partial \tau} = \frac{\hat{r}_i\,c\,M_r - c\,M_i}{r} \tag{7.236}$$

$$\frac{\partial M_r}{\partial \tau} = \frac{1}{r}\left\{r\,\hat{r}_i\,\frac{\partial M_i}{\partial \tau} + c\,\left(M_r^2 - M^2\right)\right\} \tag{7.237}$$

In equation (7.234) the symbol $|_{\mathbf{x}}$ indicates derivatives taken at fixed observer position. Hence, the well-known Formulation 1A of Farassat [39] can be obtained, i.e.

$$4\pi\,p'_Q(\mathbf{x},t) = \int_{f=0}\left[\frac{\rho_0\left(\dot{U}_n + U_{\dot{n}}\right)}{r\,(1-M_r)^2}\right]_{\text{ret}} \mathrm{d}S$$

$$+ \int_{f=0} \left[\frac{\rho_0 U_n \left(r\dot{M}_r + c\left(M_r - M^2\right)\right)}{r^2 (1 - M_r)^3} \right]_{\text{ret}} \mathrm{d}S \tag{7.238}$$

$$\begin{aligned} 4\pi p'_L(\mathbf{x},t) &= \frac{1}{c}\int_{f=0} \left[\frac{\dot{L}_r}{r(1-M_r)^2} \right]_{\text{ret}} \mathrm{d}S \\ &+ \int_{f=0} \left[\frac{L_r - L_M}{r^2(1-M_r)^2} \right]_{\text{ret}} \mathrm{d}S \\ &+ \frac{1}{c}\int_{f=0} \left[\frac{L_r\left(r\dot{M}_r + c\left(M_r - M^2\right)\right)}{r^2(1-M_r)^3} \right]_{\text{ret}} \mathrm{d}S \end{aligned} \tag{7.239}$$

where $\mathbf{M}$ is the Mach number vector of a source point on the integration surface, and the remaining terms are defined as

$$\begin{array}{lll} U_n = U_i \hat{n}_i\,, & U_{\dot{n}} = U_i \dot{\hat{n}}_i\,, & \dot{U}_n = \dot{U}_i \hat{n}_i \\ M_r = M_i \hat{r}_i\,, & \dot{M}_r = \dot{M}_i \hat{r}_i & \\ L_r = L_i \hat{r}_i\,, & \dot{L}_r = \dot{L}_i \hat{r}_i\,, & L_M = L_i M_i \end{array} \tag{7.240}$$

In the above equations dots on quantities denote time derivatives with respect to the source time τ.

7.8.1.2 Supersonic surface

The surface contribution of the FW-H equation is herein derived for a supersonic open surface $\tilde{f}(\mathbf{x},t) > 0$, e.g. a panel, $f = \tilde{f} = 0$ describing the edge of the panel. The extension of the open surface formulation to a closed surface is trivial.

Let $\nabla\tilde{f} = \boldsymbol{\nu}$ denote the unit inward geodesic normal at the edge. The surface noise for a single panel is described by

$$\overline{\Box}^2\left\{p' H(f)\right\} = \frac{\partial}{\partial t}\left\{Q\,H\!\left(\tilde{f}\right)\,\delta(f)\right\} - \frac{\partial}{\partial x_i}\left\{L_i\,H\!\left(\tilde{f}\right)\,\delta(f)\right\} \tag{7.241}$$

The monopole source term can be written as

$$\begin{aligned} \frac{\partial}{\partial t}\left\{Q\,H\!\left(\tilde{f}\right)\,\delta(f)\right\} &\equiv \frac{\partial}{\partial t}\left\{\tilde{Q}\,H\!\left(\tilde{f}\right)\,\delta(f)\right\} \\ &= \frac{\partial\tilde{Q}}{\partial t}\,H\!\left(\tilde{f}\right)\,\delta(f) - cM_\nu\,\tilde{Q}\,\delta\!\left(\tilde{f}\right)\,\delta(f) \\ &- cM_n\tilde{Q}\,H\!\left(\tilde{f}\right)|\nabla f|\,\delta'(f) \end{aligned} \tag{7.242}$$

where $\tilde{Q}$ denotes the restriction to $f = 0$ of the monopole source (7.230), and $M_\nu = \mathbf{M}\cdot\boldsymbol{\nu}$ is the local Mach number in the direction of the geodesic normal. Let notice that $|\nabla f|$ multiplying $\delta'(f)$ is not restricted to the surface of the panel. Therefore, it cannot be set $|\nabla f| = 1$. The dipole source can be written as

$$\begin{aligned} -\frac{\partial}{\partial x_i}\left\{L_i\,H\!\left(\tilde{f}\right)\,\delta(f)\right\} &\equiv -\frac{\partial}{\partial x_i}\left\{\tilde{L}_i\,H\!\left(\tilde{f}\right)\,\delta(f)\right\} \\ &= -\left(\nabla_2\cdot\tilde{\mathbf{L}}_t - 2H_f\tilde{L}_n\right)H\!\left(\tilde{f}\right)\,\delta(f) \\ &- \tilde{L}_\nu\,\delta\!\left(\tilde{f}\right)\,\delta(f) - \tilde{L}_n\,H\!\left(\tilde{f}\right)|\nabla f|\,\delta'(f) \end{aligned} \tag{7.243}$$

where $\tilde{L}_i$ denotes the restriction to $f=0$ of the dipole source (7.231), $\nabla_2 \cdot \tilde{\mathbf{L}}_t$ is the surface divergence of $\tilde{\mathbf{L}}$, $\tilde{L}_n$ is the component of $\tilde{\mathbf{L}}$ normal to the panel, $\tilde{L}_\nu = \tilde{\mathbf{L}} \cdot \boldsymbol{\nu}$ is the component of $\tilde{\mathbf{L}}$ in the direction of the geodesic normal, and H_f is the local mean curvature of the panel. Again, it cannot be set $|\nabla f| = 1$. Hence, the surface noise expression (7.241) becomes

$$\overline{\Box}^2 \left\{p' H(f)\right\} = q_1 H\left(\tilde{f}\right)\, \delta(f) + \tilde{q}_2 H\left(\tilde{f}\right)\, \delta'(f) + q_3\, \delta\left(\tilde{f}\right)\, \delta(f) \tag{7.244}$$

where

$$\begin{aligned} q_1 &= \frac{\partial \tilde{Q}}{\partial t} - \left(\nabla_2 \cdot \tilde{\mathbf{L}}_t - 2H_f \tilde{L}_n\right) && (7.245)\\ q_2 &= -|\nabla f| \left(cM_n \tilde{Q} + \tilde{L}_n\right) && (7.246)\\ q_3 &= -cM_\nu \tilde{Q} - \tilde{L}_\nu && (7.247)\end{aligned}$$

The solution of equation (7.244) can be found by using the results of subsections 7.3.7.4, 7.3.7.6 and 7.3.7.5 in order to determine the contributions related to the source terms q_1, $\tilde{q}_2$ and q_3. Setting $p' = p_1' + p_2' + p_3'$, from equation (7.163) it follows that

$$4\pi p_1'(\mathbf{x}, t) = \int_{\substack{F=0\\ \tilde{F}>0}} \frac{[q_1]_{\text{ret}}}{r\Lambda}\, \mathrm{d}\Sigma \tag{7.248}$$

From equation (7.184) it follows that

$$\begin{aligned} 4\pi p_2'(\mathbf{x}, t) &= \int_{\substack{F=0\\ \tilde{F}>0}} \left\{ -\frac{1}{r\Lambda^2} \left[\frac{\partial q_2}{\partial t_1} \frac{M_n \sin\theta}{\Lambda} + \frac{1}{c} \hat{\mathbf{r}} \cdot \mathbf{N} \frac{\partial q_2}{\partial \tau}\right]_{\text{ret}} - \frac{[q_2]_{\text{ret}}}{\Lambda} \frac{\partial}{\partial N} \left(\frac{1}{r\Lambda}\right) + \frac{2H_F [q_2]_{\text{ret}}}{r\Lambda^2} \right\} \mathrm{d}\Sigma \\ &- \int_{\substack{F=0\\ \tilde{F}=0}} \frac{[q_2]_{\text{ret}} \cot\theta'}{r\Lambda^2}\, \mathrm{d}L && (7.249)\end{aligned}$$

Finally, from equation (7.165) it follows that

$$4\pi p_3'(\mathbf{x}, t) = \int_{\substack{F=0\\ \tilde{F}=0}} \frac{q_3}{\Lambda_0 r}\, \mathrm{d}L \tag{7.250}$$

Now, adding the above contributions p_1', p_2' and p_3', and making use of the following relations (see subsection 7.3.7.6)

$$\begin{aligned} \hat{\mathbf{r}} \cdot \mathbf{N} &= -\frac{M_n - \cos\theta}{\Lambda} && (7.251)\\ \frac{\partial}{\partial N}\left(\frac{1}{r\Lambda}\right) &= -\frac{\nabla\Lambda \cdot \mathbf{N}}{r\Lambda^2} - \frac{M_n - \cos\theta}{r^2\Lambda^2} && (7.252)\\ \frac{\cot\theta'}{\Lambda^2} &= \frac{\tilde{\Lambda}\, \cos\theta'}{\Lambda\Lambda_0} && (7.253)\end{aligned}$$

the formal solution of equation (7.241) takes the form

$$\begin{aligned} 4\pi p'(\mathbf{x}, t) &= \int_{\substack{F=0\\ \tilde{F}>0}} \frac{1}{r\Lambda} \left[q_1 - \frac{\partial \tilde{q}_2}{\partial t_1} \frac{M_n \sin\theta}{\Lambda^2} + \frac{\partial q_2}{\partial \tau} \frac{M_n - \cos\theta}{c\Lambda^2}\right]_{\text{ret}} \mathrm{d}\Sigma \\ &+ \int_{\substack{F=0\\ \tilde{F}>0}} \frac{1}{r\Lambda^2} \left[\left(2H_f + \frac{\nabla\Lambda \cdot \mathbf{N}}{\Lambda} + \frac{M_n - \cos\theta}{r\Lambda}\right) \tilde{q}_2\right]_{\text{ret}} \mathrm{d}\Sigma \\ &+ \int_{\substack{F=0\\ \tilde{F}=0}} \frac{1}{r\Lambda_0} \left[q_3 - \frac{\tilde{\Lambda} \cos\theta'}{\Lambda} \tilde{q}_2\right]_{\text{ret}} \mathrm{d}L && (7.254)\end{aligned}$$

7.8.2 Volume Noise

The quadrupole noise (T) in the FW-H equation is described by

$$\overline{\Box}^2 \{p' H(f)\} = \frac{\partial^2}{\partial x_i \partial x_j} \{T_{ij} H(f)\} \tag{7.255}$$

where

$$T_{ij} = \rho\, u_i u_j + (p' - c^2 \rho')\, \delta_{ij} - \tau_{ij} \tag{7.256}$$

is Lighthill's stress tensor.

7.8.2.1 Subsonic volume

In the subsonic regime ($M_r < 1$), a suitable formal solution of equation (7.255) is given by the retarded time solution (7.204), i.e.

$$\begin{aligned} 4\pi p'_T(\mathbf{x}, t) &= \frac{1}{c^2} \frac{\partial^2}{\partial t^2} \int_{f>0} \left[\frac{T_{rr}}{r\,(1 - M_r)} \right]_{\text{ret}} \mathrm{d}V_S \\ &+ \frac{1}{c} \frac{\partial}{\partial t} \int_{f>0} \left[\frac{3\,T_{rr} - T_{ii}}{r^2\,(1 - M_r)} \right]_{\text{ret}} \mathrm{d}V_S \\ &+ \int_{f>0} \left[\frac{3\,T_{rr} - T_{ii}}{r^3\,(1 - M_r)} \right]_{\text{ret}} \mathrm{d}V_S \end{aligned} \tag{7.257}$$

where the quantity T_{rr} is the double contraction $T_{ij}\hat{r}_i\hat{r}_j$ of Lighthill's stress tensor. In the above expression $\mathbf{M}$ is the Mach number vector of a volume source fixed in the body reference frame.

A more effective formal solution of equation (7.255) can be obtained by taking the time derivatives inside the integrals. This can be made by applying the rule (7.234) and by using the relations (7.235), (7.236) and (7.237) together with

$$\frac{\partial^2 M_r}{\partial \tau^2} = \ddot{M}_r + \frac{3c}{r} \left(\dot{M}_r - M_i \dot{M}_i \right) + \frac{3c^2 M_r}{r^2} \left(M_r^2 - M^2 \right)^2 \tag{7.258}$$

Hence, the quadrupole noise in the subsonic regime is given by

$$4\pi\, p'_T(\mathbf{x}, t) = \int_{f>0} \left[\frac{K_1}{c^2\, r} + \frac{K_2}{c\, r^2} + \frac{K_3}{r^3} \right]_{\text{ret}} \mathrm{d}V_S \tag{7.259}$$

with

$$\begin{aligned} K_1 &= \frac{\ddot{T}_{rr}}{(1 - M_r)^3} + \frac{\ddot{M}_r\, T_{rr} + 3\, \dot{M}_r\, \dot{T}_{rr}}{(1 - M_r)^4} + \frac{3\, \dot{M}_r^2\, T_{rr}}{(1 - M_r)^5} \\ K_2 &= \frac{-\dot{T}_{ii}}{(1 - M_r)^2} - \frac{4\, \dot{T}_{Mr} + 2\, T_{\dot{M}r} + \dot{M}_r\, T_{ii}}{(1 - M_r)^3} \\ &\quad + \frac{3\left\{ \left(1 - M^2\right)\, \dot{T}_{rr} - 2\, \dot{M}_r\, T_{Mr} - M_i\, \dot{M}_i\, T_{rr} \right\}}{(1 - M_r)^4} + \frac{6\, \dot{M}_r\, \left(1 - M^2\right)\, T_{rr}}{(1 - M_r)^5} \\ K_3 &= \frac{2\, T_{MM} - \left(1 - M^2\right)\, T_{ii}}{(1 - M_r)^3} - \frac{6\, \left(1 - M^2\right)\, T_{Mr}}{(1 - M_r)^4} + \frac{3\, \left(1 - M^2\right)^2\, T_{rr}}{(1 - M_r)^5} \end{aligned} \tag{7.260}$$

where

$$\begin{aligned} &T_{MM} = T_{ij}\, M_i\, M_j\,, \qquad T_{Mr} = T_{ij}\, M_i\, \hat{r}_j\,, \qquad T_{\dot{M}r} = T_{ij}\, \dot{M}_i\, \hat{r}_j \\ &\dot{T}_{Mr} = \dot{T}_{ij}\, M_i\, \hat{r}_j\,, \qquad \dot{T}_{rr} = \dot{T}_{ij}\, \hat{r}_i\, \hat{r}_j\,, \qquad \ddot{T}_{rr} = \dot{T}_{ij}\, \hat{r}_i\, \hat{r}_j \end{aligned} \tag{7.261}$$

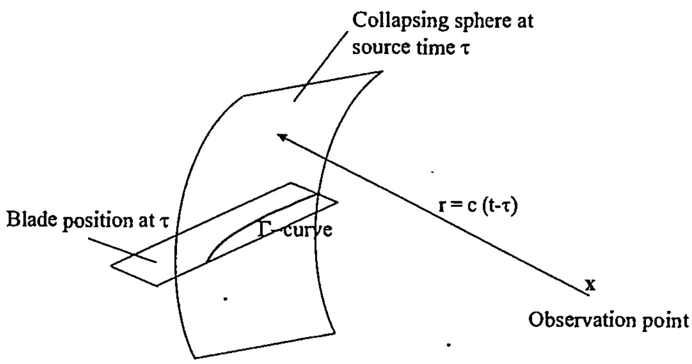

FIGURE 7.7: Intersection between the collapsing sphere and a rotor blade.

7.8.2.2 Supersonic volume

In the supersonic regime ($M_r \geq 1$), a suitable formal solution of equation (7.255) is Farassat & Brentner's [167] collapsing-sphere formula (7.203), that is

$$\begin{aligned} 4\pi p'_T(\mathbf{x},t) &= \frac{1}{c}\frac{\partial^2}{\partial t^2}\int_{-\infty}^{t}\int_{\Omega}\frac{T_{rr}}{r}\,H(F)\ \mathrm{d}\Omega(\mathbf{y})\ \mathrm{d}\tau \\ &+ \frac{\partial}{\partial t}\int_{-\infty}^{t}\int_{\Omega}\frac{3\,T_{rr}-Tii}{r^2}\,H(F)\ \mathrm{d}\Omega(\mathbf{y})\ \mathrm{d}\tau \\ &+ c\int_{-\infty}^{t}\int_{\Omega}\frac{3\,T_{rr}-T_{ii}}{r^3}\,H(F)\ \mathrm{d}\Omega(\mathbf{y})\ \mathrm{d}\tau \end{aligned} \tag{7.262}$$

7.8.2.3 Approximate collapsing-sphere formulations

In this subsection we describe a first approximated procedure to evaluate the quadrupole contribution in rotor-noise predictions.

Let us consider the collapsing-sphere formulation (7.262). The collapsing sphere is defined by the equation $g = \tau - t + r/c = 0$, where τ and t the source and observer time, respectively, and r is the distance between the observer position $\mathbf{x}$ and the point source $\mathbf{y}$. The observer co-ordinates $(\mathbf{x}, t)$ are held fixed during the integration. Hence, the solution to $g = 0$ can be interpreted as a sphere centered on the observer $\mathbf{x}$ and radius r, which collapses as τ approaches t (see Fig.7.7).

In equation (7.262) the quadrupole sources are integrated over the entire collapsing sphere. However, since the Lighthill stress tensor T_{ij} vanishes away from the nonlinear flow region, only the collapsing sphere portion near the blade contributes to the integrals in equation (7.262).

As first shown by Yu *et al.* [168], for an observer in the far field, the collapsing sphere can be locally approximated by a cylinder with axis passing through the observer and perpendicular to the rotor plane (see Fig.7.8). Moreover, if the observer is supposed to be in the rotor plane, an integration of the quadrupole sources in equation (7.262) can be performed in the direction normal to the rotor disc independently of the observer position. Hence, the integration over the approximate collapsing sphere can be carried out in two stages. The Lighthill stress tensor is first integrated along the direction normal to the rotor plane. Thus, denoting as z the co-ordinate normal to the rotor disc, a new source tensor can be defined as

$$Q_{ij} = \int_{f>0} T_{ij}\,\mathrm{d}z \tag{7.263}$$

The surface source Q_{ij} is then integrated upon the Γ−curves which are the intersection of the collapsing sphere and the rotor blade (see Fig.7.7). Thus, the approximate collapsing-sphere formulation takes the form

$$\begin{aligned} 4\pi p'_T(\mathbf{x},t) &= \frac{1}{c}\frac{\partial^2}{\partial t^2}\int_{-\infty}^{t}\int_{\substack{f^+=0\\ g=0}} \frac{Q_{rr}}{r}\,\mathrm{d}\Gamma\,\mathrm{d}\tau \\ &+ \frac{\partial}{\partial t}\int_{-\infty}^{t}\int_{\substack{f^+=0\\ g=0}} \frac{3\,Q_{rr}-Q_{ii}}{r^2}\,\mathrm{d}\Gamma\,\mathrm{d}\tau \\ &+ c\int_{-\infty}^{t}\int_{\substack{f^+=0\\ g=0}} \frac{3\,Q_{rr}-Q_{ii}}{r^3}\,\mathrm{d}\Gamma\,\mathrm{d}\tau \end{aligned} \tag{7.264}$$

where f^+ denotes the rotor disk plane, including the blade surface.

Starting from the solution (7.264), a subsonic and a supersonic quadrupole noise formula can be obtained.

For subsonic moving sources, a retarded time formulation with time derivatives taken inside the integrals is the most suitable formulation. This can be derived by first considering the variable transformation (7.155), i.e.

$$\frac{c\,\mathrm{d}\Gamma\,\mathrm{d}\tau}{\sin\theta} = \frac{\mathrm{d}S}{|1-M_r|} \tag{7.265}$$

When the observer is in the rotor plane, $\sin\theta = 1$ and equation (7.264) can be written as

$$\begin{aligned} 4\pi p'_T(\mathbf{x},t) &= \frac{1}{c^2}\frac{\partial^2}{\partial t^2}\int_{f^+=0}\left[\frac{Q_{rr}}{r\,|1-M_r|}\right]_{\mathrm{ret}}\mathrm{d}S \\ &+ \frac{1}{c}\frac{\partial}{\partial t}\int_{f^+=0}\left[\frac{3\,Q_{rr}-Q_{ii}}{r^2\,|1-M_r|}\right]_{\mathrm{ret}}\mathrm{d}S \\ &+ \int_{f^+=0}\left[\frac{3\,Q_{rr}-Q_{ii}}{r^3\,|1-M_r|}\right]_{\mathrm{ret}}\mathrm{d}S \end{aligned} \tag{7.266}$$

Then, taking the time derivatives inside the integrals by using the rule (7.234) together with the relations (7.235), (7.236), (7.237) and (7.258), yields the well-known Formulation Q1A of Brentner [40], i.e.

$$4\pi\,p'_T(\mathbf{x},t) = \int_{f^+=0}\left[\frac{K'_1}{c^2\,r} + \frac{K'_2}{c\,r^2} + \frac{K'_3}{r^3}\right]_{\mathrm{ret}}\mathrm{d}S \tag{7.267}$$

with

$$K'_1 = \frac{\ddot{Q}_{rr}}{(1-M_r)^3} + \frac{\ddot{M}_r\,Q_{rr} + 3\,\dot{M}_r\,\dot{Q}_{rr}}{(1-M_r)^4} + \frac{3\,\dot{M}_r^2\,Q_{rr}}{(1-M_r)^5}$$

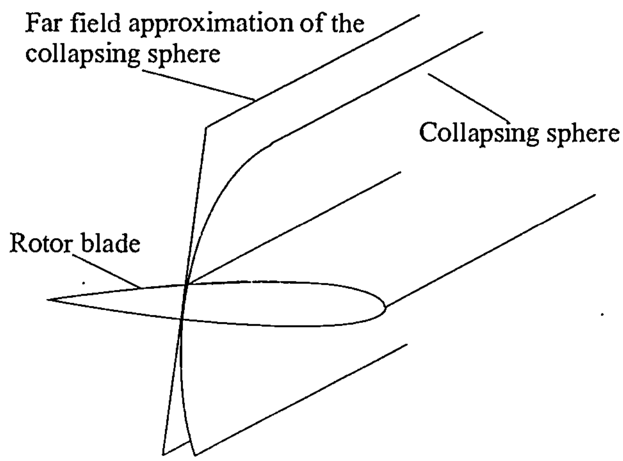

FIGURE 7.8: Collapsing sphere approximated by a cylinder in the source region.

$$K_2' = \frac{-\dot{Q}_{ii}}{(1-M_r)^2} - \frac{4\,\dot{Q}_{Mr} + 2\,Q_{\dot{M}r} + \dot{M}_r\,Q_{ii}}{(1-M_r)^3}$$
$$+\frac{3\left\{\left(1-M^2\right)\dot{Q}_{rr} - 2\,\dot{M}_r\,Q_{Mr} - M_i\,\dot{M}_i\,Q_{rr}\right\}}{(1-M_r)^4} + \frac{6\,\dot{M}_r\,\left(1-M^2\right)Q_{rr}}{(1-M_r)^5}$$
$$K_3' = \frac{2\,Q_{MM} - \left(1-M^2\right)Q_{ii}}{(1-M_r)^3} - \frac{6\,\left(1-M^2\right)Q_{Mr}}{(1-M_r)^4} + \frac{3\,\left(1-M^2\right)^2 Q_{rr}}{(1-M_r)^5} \tag{7.268}$$

where

$$Q_{MM} = Q_{ij}\,M_i\,M_j\,, \qquad Q_{Mr} = Q_{ij}\,M_i\,\hat{r}_j\,, \qquad Q_{\dot{M}r} = Q_{ij}\,\dot{M}_i\,\hat{r}_j$$
$$\dot{Q}_{Mr} = \dot{Q}_{ij}\,M_i\,\hat{r}_j\,, \qquad \dot{Q}_{rr} = \dot{Q}_{ij}\,\hat{r}_i\,\hat{r}_j\,, \qquad \ddot{Q}_{rr} = \dot{Q}_{ij}\,\hat{r}_i\,\hat{r}_j \tag{7.269}$$

In the above expression $\mathbf{M}$ is the Mach number vector of a surface source fixed in the body reference frame.

For supersonic moving sources, a singularity free solution can be obtained by first considering the variable transformation (7.155), i.e.

$$\frac{c\,\mathrm{d}\Gamma\,\mathrm{d}\tau}{\sin\theta} = \frac{\mathrm{d}\Sigma}{\Lambda} \tag{7.270}$$

When the observer is in the rotor plane, $\sin\theta = 1$. Furthermore, assuming that the rotor is nominally in the rotor tip-path plane y_1, y_2, and that the blade is sufficiently thin with not significantly blunted edges, allows to write $\Gamma \simeq 1$ and

$$c\,\mathrm{d}\Gamma\,\mathrm{d}\tau \simeq \mathrm{d}\Sigma \tag{7.271}$$

Using the above change of variable in equation (7.264) yields

$$\begin{aligned} 4\pi p_T'(\mathbf{x},t) &= \frac{1}{c^2}\frac{\partial^2}{\partial t^2}\int_{f^+=0}\frac{[Q_{rr}]_{\mathrm{ret}}}{r}\,\mathrm{d}\Sigma \\ &+ \frac{1}{c}\frac{\partial}{\partial t}\int_{f^+=0}\frac{[3\,Q_{rr} - Q_{ii}]_{\mathrm{ret}}}{r^2}\,\mathrm{d}\Sigma \\ &+ \int_{f^+=0}\frac{[3\,Q_{rr} - Q_{ii}]_{\mathrm{ret}}}{r^3}\,\mathrm{d}\Sigma \end{aligned} \tag{7.272}$$

where f^+ denotes the entire $y_1\,y_2$–plane. Since the integration domain is fixed in time, the observer-time derivatives can be bring inside the integrals without worrying about the limits of integration. Furthermore, since the tensor Q_{ij} is defined in the $\mathbf{x}$–frame of reference, which is fixed to the undisturbed medium, it results that

$$\left.\frac{\partial\,[Q_{ij}]_{\mathrm{ret}}}{\partial t}\right|_{\mathbf{x}} = \left[\left.\frac{\partial}{\partial\tau}\right|_{\mathbf{x}} Q_{ij}\right]_{\mathrm{ret}} \tag{7.273}$$

Now, introducing the reference frame η fixed with the rotor blade gives

$$\left.\frac{\partial Q_{ij}}{\partial\tau}\right|_{\eta} = \left.\frac{\partial}{\partial\tau}\right|_{\mathbf{x}} Q_{ij} + \mathbf{V}\cdot\nabla_\eta Q_{ij} \tag{7.274}$$

where $\mathbf{V} = \partial\eta/\partial\tau$ is the velocity of the point η specified in the frame fixed to the undisturbed medium. Then, using equation (7.274) into equation (7.273) yields

$$\begin{aligned} \left.\frac{\partial\,[Q_{ij}]_{\mathrm{ret}}}{\partial t}\right|_{\mathbf{x}} &= \left[\left.\frac{\partial Q_{ij}}{\partial\tau}\right|_{\eta} - \mathbf{V}\cdot\nabla_\eta Q_{ij}\right]_{\mathrm{ret}} \\ &\equiv [L_\tau\,Q_{ij}]_{\mathrm{ret}} \end{aligned} \tag{7.275}$$

where $Q_{ij}|_\eta$ denote the components of the tensor Q_{ij} represented in co-ordinates that are instantaneously aligned with the moving frame. Since $\hat{\mathbf{r}}$ does not depend upon t or τ, the operator L_τ operates on Q_{ij} only. Hence, equation (7.272) takes the form

$$\begin{aligned} 4\pi p'_T(\mathbf{x},t) &= \frac{1}{c^2}\int_{f^+=0} \frac{\hat{r}_i\hat{r}_j\left[L_\tau^2 Q_{ij}\right]_{\text{ret}}}{r}\,\mathrm{d}\Sigma \\ &+ \frac{1}{c}\frac{\partial}{\partial t}\int_{f^+=0} \frac{\left[3\hat{r}_i\hat{r}_j\,L_\tau Q_{ij} - L_\tau Q_{ii}\right]_{\text{ret}}}{r^2}\,\mathrm{d}\Sigma \\ &+ \int_{f^+=0} \frac{\left[3\,Q_{rr} - Q_{ii}\right]_{\text{ret}}}{r^3}\,\mathrm{d}\Sigma \end{aligned} \tag{7.276}$$

The above singularity free solution can be used for both subsonic and supersonic quadrupole noise predictions. It was obtained by Farassat & Brentner [169] and is referred to as Formulation Q2.

Equation (7.276) can be algebraically simplified by setting

$$\mathbf{V} = \mathbf{V}_F + \boldsymbol{\omega}\times\boldsymbol{\eta} \tag{7.277}$$

where $\mathbf{V}_F$ is the forward velocity of the rotor, and $\boldsymbol{\omega}$ is the angular velocity of the rotor. Hence, as shown in Ref.[169], the operator L_τ^2 takes the form

$$L_\tau^2 = \left.\frac{\partial^2}{\partial\tau^2}\right|_\eta - 2\mathbf{V}\cdot\nabla\left.\frac{\partial}{\partial\tau}\right|_\eta + \left(\mathbf{V}\cdot\nabla'\right)^2 + \left(\boldsymbol{\omega}\times\mathbf{V}_F\right)\cdot\nabla \tag{7.278}$$

where ∇' does not operate on $\mathbf{V}$.

The approximate collapsing-sphere procedure is rigorous for an observer in the far field and in the rotor plane. Since the HSI noise is maximum in the rotor plane, the approximate formulae (7.267) and (7.276), referred to as Formulation Q1A and Formulation Q2, respectively, allow a quite accurate prediction of the quadrupole noise in helicopter applications.

Formulation Q1A can be only applied to subsonic sources because of the presence of the Döppler factor $1 - M_r$ in the denominator of the integrands. Formulation Q2 is valid for both subsonic and supersonic sources and is quite simple.

Because of high flow gradients at the leading edge of a blade and across a shock trace, the accuracy of Formulation Q2 is remarkably affected by the accuracy of the numerical evaluation of the source spatial derivatives.

When delocalization occurs, Formulation Q1A can be only used to integrate the quadrupole sources up to the sonic circle (see Fig.7.9). On the contrary, Formulation Q2 can be used to account for all the significative quadrupole sources beyond the blade tip.

Farassat & Brentner [169] used Formulation Q2 to perform volume noise predictions in the presence of delocalization. They showed that the sources over the blades and beyond the tips have a different effect on the shape of the acoustic signature. The sources around and in the vicinity of the blades account for the peak level, whereas, the sources beyond the tip determine the steepening and the broadening of the waveform.

7.8.2.4 On the surface nature of the quadrupole sources in the presence of shocks

In this subsection we describe a second approximated procedure to evaluate the quadrupole contribution in rotor-noise predictions.

The FW-H equation has been obtained by handling the flow discontinuity across the surface $f = 0$ through generalized functions. Since there may be other discontinuities in the flow across shocks or thin vortical wakes, the quadrupole contribution in equation (7.217) is intrinsically represented by

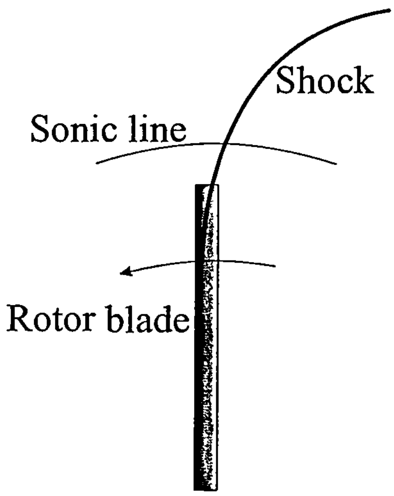

FIGURE 7.9: Transonic flow past a rotating blade: the phenomenon of delocalization.

generalized derivatives. In the presence of a flow discontinuity across the moving surface $k(\mathbf{x},t)=0$, the volume sources include a surface source distribution whose strength depends on the flow jump across the surface $k=0$. This can be shown by taking into account extrinsically the generalized nature of the quadrupole source in equation (7.217). Thus, let us write

$$\frac{\overline{\partial}\{T_{ij}H(f)\}}{\partial x_i} = \frac{\partial\{T_{ij}H(f)\}}{\partial x_i} + \Delta\{T_{ij}H(f)\}\,\hat{m}_i\,\delta(k) \tag{7.279}$$

$$\begin{aligned}\frac{\overline{\partial}^2\{T_{ij}H(f)\}}{\partial x_i\partial x_j} &= \frac{\partial\{T_{ij}H(f)\}}{\partial x_i\partial x_j} + \Delta\left\{\frac{\partial\{T_{ij}H(f)\}}{\partial x_i}\right\} m_j\,\delta(k)\\ &+\frac{\partial}{\partial x_j}\{\Delta\{T_{ij}H(f)\}\,\hat{m}_i\,\delta(k)\}\end{aligned} \tag{7.280}$$

where $\Delta=(\cdot)_2-(\cdot)_1$ denotes the jump of a flow quantity across the discontinuity surface, and $\hat{\mathbf{m}}=\nabla k$ is the unit normal to the discontinuity surface $k=0$, pointing into region 2. Equation (7.280) shows that, in the presence of a flow discontinuity surface, the quadrupole source can be decomposed into a volume term which is familiar in the jet-noise theory, and two surface terms of monopole and dipole types, respectively.

Farassat *et al.* [170] argued that the surface contribution to the quadrupole noise is dominant in the presence of rotating shocks on rotor blades. Therefore, they performed HSI noise predictions by taking into account only monopole and dipole source distributions upon the shock surface.

7.8.3 Solution of the FW-H Equation for a Stationary Surface

For a stationary surface, the monopole and dipole source terms (7.230) and (7.231) become $U_i=u_i$ and $L_i=(p-p_0)\,\hat{n}_i=p'\hat{n}_i$, respectively (the viscous stresses τ_{ij} having been neglected). Using the subsonic results derived in subsections 7.8.1.1 and 7.8.2.1 allows to write the formal solution of the FW-H equation for a stationary surface as

$$\begin{aligned}4\pi\,p'(\mathrm{x},t)\,H(f) &= \frac{\partial^2}{\partial x_i\partial x_j}\int_{f>0}\frac{[T_{ij}]_{\mathrm{ret}}}{r}\,\mathrm{dy}\\ &+\int_{S_Q\cup S_s}\frac{[p']_{\mathrm{ret}}\,\hat{r}_n}{r^2}\,\mathrm{d}S_y+\int_{S_Q\cup S_s}\frac{\left[c^{-1}\dot{p}'\,\hat{r}_n+\rho_0\dot{u}_n\right]_{\mathrm{ret}}}{r}\,\mathrm{d}S_y\end{aligned} \tag{7.281}$$

which coincides with the Curle equation (7.281).

7.8.4 Solution of the FW-H Equation for a Moving Observer

The integral formulation of the FW-H equation can be extended to an observer moving at the constant velocity $c\mathbf{M}_o$. This is done by interpreting the time derivative of the thickness noise in equation (6.24) as a Lagrangian derivative. The other time derivatives, in fact, have been obtained by using the rule (7.234) where derivatives are taken at fixed observer position. Thus, let us write the thickness noise expression for a subsonic surface as

$$4\pi p'_Q(\mathbf{x},t) = \frac{\partial}{\partial t}\int_{f=0}\left[\frac{\rho_0 U_n}{r(1-M_r)}\right]_{\text{ret}} \mathrm{d}S + cM_{oi}\frac{\partial}{\partial x_i}\int_{f=0}\left[\frac{\rho_0 U_n}{r(1-M_r)}\right]_{\text{ret}} \mathrm{d}S \quad .$$

Then, using the relation (7.159) in order to translates space derivatives into time derivatives, yields

$$\begin{aligned} 4\pi p'_Q(\mathbf{x},t) &= \frac{\partial}{\partial t}\int_{f=0}\left[\frac{\rho_0 U_n}{r(1-M_r)}\right]_{\text{ret}} \mathrm{d}S \\ &- \frac{\partial}{\partial t}\int_{f=0}\left[\frac{\rho_0 U_n M_{or}}{r(1-M_r)}\right]_{\text{ret}} \mathrm{d}S - c\int_{f=0}\left[\frac{\rho_0 U_n M_{or}}{r^2(1-M_r)}\right]_{\text{ret}} \mathrm{d}S \end{aligned} \tag{7.282}$$

where $M_{or} = M_{oi}\hat{r}_i$ is the observer Mach number vector in the radiation direction. Finally, moving the time derivative inside the integral, yields

$$\begin{aligned} 4\pi p'_Q(\mathbf{x},t) &= \int_{f=0}\left[\frac{\rho_0\left(\dot{U}_n + U_{\dot{n}}\right)}{r(1-M_r)^2}\right]_{\text{ret}} \mathrm{d}S + \int_{f=0}\left[\frac{\rho_0 U_n\left(r\dot{M}_r + c\left(M_r - M^2\right)\right)}{r^2(1-M_r)^3}\right]_{\text{ret}} \mathrm{d}S \\ &- \int_{f=0}\left[M_{or}\frac{\rho_0\left(\dot{U}_n + U_{\dot{n}}\right)}{r(1-M_r)^2}\right]_{\text{ret}} \mathrm{d}S - \int_{f=0}\left[M_{or}\frac{\rho_0 \dot{M}_r U_n}{r(1-M_r)^3}\right]_{\text{ret}} \mathrm{d}S \\ &- \int_{f=0}\left[\frac{\rho_0 c\left\{2M_{or}M_r - M_{or}M^2 - M_{or}M_r(1-M_r) - M_{or}M_r^2\right\}U_n}{r^2(1-M_r)^3}\right]_{\text{ret}} \mathrm{d}S \\ &- \int_{f=0}\left[\frac{M_{or}\rho_0 c U_n}{r^2(1-M_r)}\right]_{\text{ret}} \mathrm{d}S \end{aligned} \tag{7.283}$$

where $[\ldots]_{\text{ret}}$ denotes evaluation at the retarded time

$$\tau^* = t - \frac{|\mathbf{x}(t) - \mathbf{y}(\tau^*)|}{c} \tag{7.284}$$

7.9 Solutions of the K Equation

As discussed for the FW-H equation, the more effective numerical approach for rotor-noise computations based on the K equation consists in using a hybrid subsonic/supersonic formulation in which the supersonic formulae are extended to an open surface, namely, a supersonic panel.

7.9.1 Stationary Surface

In this subsection a formal solution of the K equation for the special case of a stationary surface is derived. Setting $M_n = 0$ into equation (7.223) gives

$$\overline{\Box}^2\left(p'H(f)\right) = -\frac{\partial p'}{\partial n}\delta(f) - \frac{\partial}{\partial x_i}\left\{p'\hat{n}_i\delta(f)\right\} \tag{7.285}$$

whose formal solution can be written as

$$4\pi\, p'(\mathbf{x},t) = -\int_{f=0} \frac{[p'_n]_{\text{ret}}}{r}\, \mathrm{d}S - \frac{\partial}{\partial x_i}\int_{f=0} \frac{[p']_{\text{ret}}\,\hat{n}_i}{r}\, \mathrm{d}S \tag{7.286}$$

where $p'_n = \partial p'/\partial n$. The following algebra can be now performed

$$\begin{aligned}
\frac{\partial}{\partial x_i}\left\{\frac{[p']_{\text{ret}}\,\hat{n}_i}{r}\right\} &= \frac{\hat{n}_i}{r}\frac{\partial}{\partial x_i}\left[p'\right]_{\text{ret}} + \left[p'\right]_{\text{ret}}\hat{n}_i\frac{\partial\left(r^{-1}\right)}{\partial x_i} \\
&= \frac{\hat{n}_i}{r}\left[\frac{\partial p'}{\partial \tau}\frac{\partial \tau}{\partial x_i}\right]_{\text{ret}} - \left[p'\right]_{\text{ret}}\frac{\hat{n}_i}{r^2}\frac{\partial r}{\partial x_i} \\
&= -\frac{\hat{n}_i}{r}\left[\frac{\partial p'}{\partial \tau}\frac{\hat{r}_i}{c}\right]_{\text{ret}} - \left[p'\right]_{\text{ret}}\frac{\hat{n}_i\hat{r}_i}{r^2} \\
&= -\frac{c^{-1}\hat{r}_n}{r}\left[\frac{\partial p'}{\partial \tau}\right]_{\text{ret}} - \left[p'\right]_{\text{ret}}\frac{\hat{r}_n}{r^2}
\end{aligned} \tag{7.287}$$

where $\hat{r}_n = \hat{\mathbf{r}}\cdot\hat{\mathbf{n}}$ and $\nabla_x r = \hat{\mathbf{r}}$. Then, substituting into equation (7.285) gives

$$4\pi\, p'(\mathbf{x},t) = -\int_{f=0} \frac{[p'_n]_{\text{ret}}}{r}\, \mathrm{d}S + \int_{f=0} \frac{c^{-1}\hat{r}_n}{r}\left[\frac{\partial p'}{\partial \tau}\right]_{\text{ret}} \mathrm{d}S + \int_{f=0} \left[p'\right]_{\text{ret}}\frac{\hat{r}_n}{r^2}\,\mathrm{d}S \tag{7.288}$$

which coincides with the classic Kirchhoff formula (7.209), provided that $V_Q \to 0$ and that $\phi \equiv p'$. The condition $V_Q \to 0$ means that the acoustic sources are enclosed by the surface $f = 0$.

7.9.2 Subsonic Surface

In this subsection a formal solution of the K equation (7.223) for a deformable surface moving subsonically is derived.

Convoluting the wave equation (7.223) with the free-space Green's function gives

$$\begin{aligned}
4\pi\phi(\mathbf{x},t)\; H(f) = &- \int_{-\infty}^{t}\iiint \frac{1}{r}\left(\frac{\partial p'}{\partial n} + c^{-1}M_n\frac{\partial p'}{\partial \tau}\right)\delta(f)\,\delta(g)\;\mathrm{d}\mathbf{y}\,\mathrm{d}\tau \\
&- \frac{1}{c}\frac{\partial}{\partial t}\int_{-\infty}^{t}\iiint \frac{M_n\, p'}{r}\delta(f)\,\delta(g)\;\mathrm{d}\mathbf{y}\,\mathrm{d}\tau \\
&- \frac{\partial}{\partial x_i}\int_{-\infty}^{t}\iiint \frac{p'\,\hat{n}_i}{r}\delta(f)\,\delta(g)\;\mathrm{d}\mathbf{y}\,\mathrm{d}\tau
\end{aligned} \tag{7.289}$$

The divergence operator in the last term can be taken in the integral, where it operates only on $\delta(g)/r$ that depends on the observer co-ordinates $\mathbf{x}$. Then, the spatial derivative can be translated into a time derivative by using the rule

$$\frac{\partial}{\partial x_i}\left(\frac{\delta(g)}{r}\right) = -\frac{1}{c}\frac{\partial}{\partial t}\left(\frac{\hat{r}_i\,\delta(g)}{r}\right) - \frac{\hat{r}_i\,\delta(g)}{r^2} \tag{7.290}$$

Hence, equation (7.289) takes the form

$$\begin{aligned}
4\pi\phi(\mathbf{x},t)\; H(f) = &- \int_{-\infty}^{t}\iiint \frac{1}{r}\left(\frac{\partial p'}{\partial n} + c^{-1}M_n\frac{\partial p'}{\partial \tau}\right)\delta(f)\,\delta(g)\;\mathrm{d}\mathbf{y}\,\mathrm{d}\tau \\
&- \frac{1}{c}\frac{\partial}{\partial t}\int_{-\infty}^{t}\iiint \frac{M_n\, p'}{r}\delta(f)\,\delta(g)\;\mathrm{d}\mathbf{y}\,\mathrm{d}\tau
\end{aligned}$$

$$+ \quad \frac{1}{c}\frac{\partial}{\partial t}\int_{-\infty}^{t}\iiint \frac{p'\hat{r}_n}{r}\delta(f)\,\delta(g)\;\mathrm{d}\mathbf{y}\,\mathrm{d}\tau$$

$$+ \quad \int_{-\infty}^{t}\iiint \frac{p'\hat{r}_n}{r^2}\delta(f)\,\delta(g)\;\mathrm{d}\mathbf{y}\,\mathrm{d}\tau \tag{7.291}$$

where $\hat{r}_n = \hat{r}_i\hat{n}_i$. Setting

$$Q_1(\mathbf{y},\tau) = -\frac{1}{r}\left(\frac{\partial p'}{\partial n} + c^{-1}M_n\frac{\partial p'}{\partial \tau}\right) + \frac{p'\hat{r}_n}{r^2} \tag{7.292}$$

$$Q_2(\mathbf{y},\tau) = \frac{\hat{r}_n - M_n}{r}p' \tag{7.293}$$

equation (7.291) can be written in the compact form

$$\begin{aligned} 4\pi\phi(\mathbf{x},t)\;H(f) \quad &= \quad \int_{-\infty}^{t}\iiint Q_1(\mathbf{y},\tau)\,\delta(f)\,\delta(g)\;\mathrm{d}\mathbf{y}\,\mathrm{d}\tau \\ &+ \quad \frac{1}{c}\frac{\partial}{\partial t}\int_{-\infty}^{t}\iiint Q_2(\mathbf{y},\tau)\,\delta(f)\,\delta(g)\;\mathrm{d}\mathbf{y}\,\mathrm{d}\tau \end{aligned} \tag{7.294}$$

Let us now parameterize the surface $f = 0$ by introducing the Gaussian co-ordinates (u^1, u^2) with domain $\mathcal{D}_S$. Then, let us parameterize the space near the surface $f = 0$ by extending (u_1, u_2) along the normal to $f = 0$ and by taking $u_3 = f$. It thus results that

$$\mathrm{d}\mathbf{y} = \sqrt{g'_{(2)}}\,\mathrm{d}u^1\,\mathrm{d}u^2\,\mathrm{d}u^3 \tag{7.295}$$

where $g'_{(2)}(u^1,u^2,u^3) = \left(1 - 2Hu^3 + K\,u^3\,u^3\right)^2\,g_{(2)}(u^1,u^2)$, $g_{(2)}$ being the determinant of the coefficients of the first fundamental form (see subsection 7.3.4.3). We assume that the domain $\mathcal{D}_S$ is time independent, whereas, for a deformable surface, the determinant $g_{(2)}$ is a function of time τ. Hence, equation (7.294) takes the form

$$\begin{aligned} 4\pi\phi(\mathbf{x},t)\;H(f) \quad &= \quad \int_{-\infty}^{t}\iiint Q_1(u^1,u^2,u^3,\tau)\,\delta(u^3)\,\delta(g)\,\sqrt{g'_{(2)}}\,\mathrm{d}u^1\,\mathrm{d}u^2\,\mathrm{d}u^3\,\mathrm{d}\tau \\ &+ \quad \frac{1}{c}\frac{\partial}{\partial t}\int_{-\infty}^{t}\iiint Q_2(u^1,u^2,u^3,\tau)\,\delta(u^3)\,\delta(g)\,\sqrt{g'_{(2)}}\,\mathrm{d}u^1\,\mathrm{d}u^2\,\mathrm{d}u^3\,\mathrm{d}\tau \\ &= \quad \int_{-\infty}^{t}\iint_{\mathcal{D}_S} Q_1(u^1,u^2,0,\tau)\,\delta(g)\,\sqrt{g_{(2)}}\,\mathrm{d}u^1\,\mathrm{d}u^2\,\mathrm{d}\tau \\ &+ \quad \frac{1}{c}\frac{\partial}{\partial t}\int_{-\infty}^{t}\iint_{\mathcal{D}_S} Q_2(u^1,u^2,0,\tau)\,\delta(g)\,\sqrt{g_{(2)}}\,\mathrm{d}u^1\,\mathrm{d}u^2\,\mathrm{d}\tau \end{aligned} \tag{7.296}$$

Now, integrating with respect to τ, provided that $\partial g/\partial\tau = 1 - M_r$, gives

$$\begin{aligned} 4\pi\phi(\mathbf{x},t)\;H(f) \quad &= \quad \iint_{\mathcal{D}_S}\left[\frac{Q_1(u^1,u^2,0,\tau)\,\sqrt{g_{(2)}}}{1-M_r}\right]_{\mathrm{ret}}\mathrm{d}u^1\,\mathrm{d}u^2 \\ &+ \quad \frac{1}{c}\frac{\partial}{\partial t}\iint_{\mathcal{D}_S}\left[\frac{Q_2(u^1,u^2,0,\tau)\,\sqrt{g_{(2)}}}{1-M_r}\right]_{\mathrm{ret}}\mathrm{d}u^1\,\mathrm{d}u^2 \end{aligned}$$

Using the rule (7.16) to translate the observer time derivative into a source time derivative gives

$$\begin{aligned}
4\pi\phi(\mathbf{x},t)\; H(f) &= \iint\limits_{\mathcal{D}_S} \left[\frac{Q_1\sqrt{g_{(2)}}}{1-M_r}\right]_{\text{ret}} \mathrm{d}u^1\,\mathrm{d}u^2 \\
&+ \frac{1}{c}\iint\limits_{\mathcal{D}_S} \left[\frac{1}{1-M_r}\frac{\partial}{\partial\tau}\left\{\frac{Q_2\sqrt{g_{(2)}}}{1-M_r}\right\}\right]_{\text{ret}} \mathrm{d}u^1\,\mathrm{d}u^2
\end{aligned}$$

This is the formal solution of the K equation (7.223) for a deformable subsonic surface [3]. It was originally obtained by Morgans [44] by using the Green's formula, and later on by Farassat & Myers [45] by using the above method. Moreover, the latter authors wrote equation (7.297) in the following useful form

$$4\pi\phi(\mathbf{x},t)\; H(f) = \int_{\mathcal{D}_S}\left[\frac{E_1}{r\,(1-M_r)}\right]_{\text{ret}} \mathrm{d}\Sigma + \int_{\mathcal{D}_S}\left[\frac{p'\,E_2}{r^2\,(1-M_r)}\right]_{\text{ret}} \mathrm{d}\Sigma \tag{7.297}$$

where

$$\begin{aligned}
E_1 &= \left(M_n^2-1\right)\frac{\partial p'}{\partial n} + M_n\,\mathbf{M}_t\cdot\nabla_2 p' - c^{-1}M_n\dot{p}' + \frac{\dot{M}_r\,(\hat{r}_n - M_n)\,p'}{c\,(1-M_r)^2} \\
&+ \frac{1}{c\,(1-M_r)}\left\{\left(\dot{\hat{n}}_r - \dot{M}_n - \dot{\hat{n}}_M\right)p' + (\hat{r}_n - M_n)\,\dot{p}' + (\hat{r}_n - M_n)\,p'\,\dot{\sigma}\right\} &(7.298)\\
E_2 &= \frac{-\hat{r}_n\left(M_r^2+M^2\right) + M_n\left(M_r+M^2\right)}{(1-M_r)^2} &(7.299)\\
\Sigma &= \left[\sqrt{g_{(2)}}\right]_{\text{ret}} \mathrm{d}u^1\,\mathrm{d}u^2 &(7.300)\\
\dot{p}' &= \frac{\partial p'}{\partial\tau} + c\,M_n\frac{\partial p'}{\partial n} + c\mathbf{M}_t\cdot\nabla_2 p' \quad \text{(Lagrangian derivative)} &(7.301)\\
\mathbf{M}_t\cdot\nabla_2 p' &= M_1\frac{\partial p'}{\partial u_1} + M_2\frac{\partial p'}{\partial u_2} &(7.302)\\
\dot{\sigma} &= \frac{1}{\sqrt{g_{(2)}}}\frac{\partial}{\partial\tau}\sqrt{g_{(2)}} &(7.303)
\end{aligned}$$

and

$$\begin{aligned}
\dot{M}_r &= \dot{M}_i\,\hat{r}_i \qquad & \dot{M}_n &= \dot{M}_i\,\hat{n}_i \\
\dot{\hat{n}}_r &= \dot{\hat{n}}_i\,\hat{r}_i \qquad & \dot{\hat{n}}_M &= \dot{\hat{n}}_i\,M_i
\end{aligned} \qquad (7.304)\ (7.305)$$

7.9.3 Supersonic Surface

In this section we derive the supersonic Kirchhoff formula for an open surface. The extension to a closed surface is trivial.

Let us define the panel $\hat{f} > 0$ on the surface $f(\mathbf{x}, \mathbf{t})$, with edge $\hat{f} = 0$ and local unit geodesic normal to the edge $\nabla\hat{f} = \boldsymbol{\nu}$ (see Fig.7.4). The K equation (7.223) for the panel becomes

$$\begin{aligned}
\overline{\Box}^2\left(p'H(f)\right) = &- \left(\frac{\partial p'}{\partial n} + \frac{M_n}{c}\frac{\partial p'}{\partial t}\right) H\left(\tilde{f}\right)\,\delta(f) - \frac{1}{c}\frac{\partial}{\partial t}\left\{M_n p'\,H\left(\tilde{f}\right)\,\delta(f)\right\} \\
&- \frac{\partial}{\partial x_i}\left\{p'\,\hat{n}_i\,H\left(\tilde{f}\right)\,\delta(f)\right\}
\end{aligned} \tag{7.306}$$

[3]Because of the transonic Döppler singularity, equation (7.297) is unsuitable for supersonically moving surfaces.

The second term at the right-hand side of the above equation can be written as

$$\begin{aligned}
\frac{1}{c}\frac{\partial}{\partial t}\left\{M_n p' H\left(\tilde{f}\right)\,\delta(f)\right\} &\equiv \frac{1}{c}\frac{\partial}{\partial t}\left\{\tilde{M}_n \tilde{p}' H\left(\tilde{f}\right)\,\delta(f)\right\} \\
&= \frac{1}{c}\frac{\partial}{\partial t}\left\{\tilde{M}_n \tilde{p}'\right\} H\left(\tilde{f}\right)\,\delta(f) \\
&- M_n M_\nu p'\delta(f)\,\delta\left(\tilde{f}\right) - \tilde{M}_n^2 \tilde{p}' H\left(\tilde{f}\right)|\nabla f|\,\delta'(f) \qquad (7.307)
\end{aligned}$$

where a tilde over a function stands for the restriction of the function to the surface $f = 0$. The symbol $M_\nu = \mathbf{M}\cdot\boldsymbol{\nu}$ is the local Mach number of the edge in the direction of the geodesic normal. We have removed the restriction sign where it is not necessary. Let notice that $|\nabla f|$ multiplying $\delta'(f)$ is not restricted to the surface of the panel. Therefore, it cannot be set $|\nabla f| = 1$. The third term at the right-hand side of the above equation can be written as

$$\begin{aligned}
\frac{\partial}{\partial x_i}\left\{p'\hat{n}_i H\left(\tilde{f}\right)\,\delta(f)\right\} &\equiv \frac{\partial}{\partial x_i}\left\{\tilde{p}'\hat{n}_i H\left(\tilde{f}\right)\,\delta(f)\right\} \\
&= -2H_f p' H\left(\tilde{f}\right)\,\delta(f) + \tilde{p}' H\left(\tilde{f}\right)|\nabla f|\,\delta'(f) \qquad (7.308)
\end{aligned}$$

where use of the divergence result (7.92) has been made. Hence, the governing equation (7.306) becomes

$$\overline{\Box}^2\left(p'H(f)\right) = q_1 H\left(\tilde{f}\right)\,\delta(f) + \tilde{q}_2 H\left(\tilde{f}\right)\,\delta'(f) + q_3\,\delta\left(\tilde{f}\right)\,\delta(f) \qquad (7.309)$$

where

$$\begin{aligned}
q_1 &= -\left\{\frac{\partial p'}{\partial n} + c^{-1}M_n\frac{\partial p'}{\partial t} + c^{-1}\frac{\partial}{\partial t}\left(\tilde{M}_n\tilde{p}'\right) - 2H_f p'\right\} \qquad (7.310) \\
\tilde{q}_2 &= -\left(1 - \tilde{M}_n^2\right)\tilde{p}' \qquad (7.311) \\
q_3 &= M_n M_\nu p' \qquad (7.312)
\end{aligned}$$

The solution of equation (7.309) can be obtained by using the results of subsections 7.3.7.4, 7.3.7.6 and 7.3.7.5 in order to determine the contributions related to the source terms q_1, $\tilde{q}_2$ and q_3. Setting $p' = p_1' + p_2' + p_3'$, from equation (7.163) it follows that

$$4\pi p_1'(\mathbf{x}, t) = \int_{\substack{F=0\\ \tilde{F}>0}} \frac{[q_1]_{\text{ret}}}{r\Lambda}\,\mathrm{d}\Sigma \qquad (7.313)$$

From equation (7.184) it follows that

$$\begin{aligned}
4\pi p_2'(\mathbf{x}, t) &= \int_{\substack{F=0\\ \tilde{F}>0}} \left\{-\frac{1}{r\Lambda^2}\left[\frac{\partial\tilde{q}_2}{\partial t_1}\frac{M_n\sin\theta}{\Lambda} + \frac{1}{c}\hat{\mathbf{r}}\cdot\mathbf{N}\frac{\partial\tilde{q}_2}{\partial\tau}\right]_{\text{ret}} - \frac{[\tilde{q}_2]_{\text{ret}}}{\Lambda}\frac{\partial}{\partial N}\left(\frac{1}{r\Lambda}\right) + \frac{2H_F\,[\tilde{q}_2]_{\text{ret}}}{r\Lambda^2}\right\}\mathrm{d}\Sigma \\
&- \int_{\substack{F=0\\ \tilde{F}=0}} \frac{[\tilde{q}_2]_{\text{ret}}\cot\theta'}{r\Lambda^2}\,\mathrm{d}L \qquad (7.314)
\end{aligned}$$

Finally, from equation (7.165) it follows that

$$4\pi p_3'(\mathbf{x}, t) = \int_{\substack{F=0\\ \tilde{F}=0}} \frac{q_3}{\Lambda_0 r}\,\mathrm{d}L \qquad (7.315)$$

Now, adding the above contributions p_1', p_2' and p_3', and making use of the following relations (see subsection 7.3.7.6)

$$\hat{\mathbf{r}}\cdot\mathbf{N} = -\frac{M_n - \cos\theta}{\Lambda} \qquad (7.316)$$

$$\frac{\partial}{\partial N}\left(\frac{1}{r\Lambda}\right) = -\frac{\nabla\Lambda\cdot\mathbf{N}}{r\Lambda^2} - \frac{M_n - \cos\theta}{r^2\Lambda^2} \tag{7.317}$$

$$\frac{\cot\theta'}{\Lambda^2} = \frac{\tilde{\Lambda}\,\cos\theta'}{\Lambda\Lambda_0} \tag{7.318}$$

the formal solution of the K equation (7.223) for a supersonic panel takes the form obtained by Farassat & Myers [171], i.e.

$$\begin{aligned} 4\pi p'(\mathbf{x},t) &= \int_{\substack{F=0\\ \tilde{F}>0}} \frac{1}{r\Lambda}\left[q_1 - \frac{\partial\tilde{q}_2}{\partial t_1}\frac{M_n\sin\theta}{\Lambda^2} + \frac{\partial\tilde{q}_2}{\partial\tau}\frac{M_n-\cos\theta}{c\Lambda^2}\right]_{\mathrm{ret}} \mathrm{d}\Sigma \\ &+ \int_{\substack{F=0\\ \tilde{F}>0}} \frac{1}{r\Lambda^2}\left[\left(2H_f + \frac{\nabla\Lambda\cdot\mathbf{N}}{\Lambda} + \frac{M_n-\cos\theta}{r\Lambda}\right)\tilde{q}_2\right]_{\mathrm{ret}} \mathrm{d}\Sigma \\ &+ \int_{\substack{F=0\\ \tilde{F}=0}} \frac{1}{r\Lambda_0}\left[q_3 - \frac{\tilde{\Lambda}\cos\theta'}{\Lambda}\tilde{q}_2\right]_{\mathrm{ret}} \mathrm{d}L \end{aligned} \tag{7.319}$$

After taking all the derivatives explicitly, the above result leads to the well-known Formulation 3 of Farassat [172] [173].

7.10 The Advanced Time Approach

As shown by Casalino [41], a hierarchical inversion between the emission time and the reception time changes a retarded time formulation into an advanced time formulation. This approach allows to compute the acoustic field as the CFD simulation is processed. The advanced time approach offers the following advantages.

- Since the acoustic time-step is typically several orders of magnitude greater than the aerodynamic time-step, the computational time for the noise prediction at each acoustic time-step may be smaller than that required by the CFD simulation to cover an acoustic time-step. In this case, provided that a parallel architecture is used, the acoustic prediction has a negligible computational cost.

- The advanced time is an algebraic function of the observer and point source location at the emission time. Hence, no iterative solutions of the retarded time equation must be performed at each time-step.

- The advanced time projection of the current source status at a given time is univocal. Thus, the application of the advanced time formulation to sources in supersonic motion does not require a modification of the computational algorithms.

- No disk-recording of the flow time history is necessary for the purpose of the acoustic computation.

In this section we describe the fundamental aspects of the advanced time approach. The retarded time approach consists in evaluating the signal received at a given time[4] t through a summation of all the disturbances reaching the observer at the same time t. Depending on the source location in the integration domain and the kinematics of both the observer and the integration domain, these disturbances are emitted at different retarded times and cover different distances before to reach the observation point.

The advanced time approach merely consists in using a retarded time approach, but from the point of view of the source. Therefore, at a given time[5] the contributions from the integration domain

[4] In a retarded time approach the computational time is the reception time.
[5] In an advanced time approach the computational time is the emission time.

are calculated, based on the current aerodynamic data and the current kinematics of the integration domain. At each computational time and for each source element, the time at which the corresponding disturbance will reach the observer is calculated and is referred to as *advanced time*. The observer location at the advanced time is used to calculate the relative position between the observer and a point source. The signal is finally re-composed in the observer time domain through a summation over all the computed contributions.

Let us consider the retarded time equation

$$\tau_{\text{ret}} = t - \frac{|\mathbf{x}(t) - \mathbf{y}(\tau_{\text{ret}})|}{c} \tag{7.320}$$

At an observer time $t + \mathcal{T}$ this yields

$$\tau'_{\text{ret}} = t + \mathcal{T} - \frac{|\mathbf{x}(t+\mathcal{T}) - \mathbf{y}(\tau'_{\text{ret}})|}{c} \tag{7.321}$$

Thus, setting $\tau'_{\text{ret}} \equiv t$ leads to

$$\mathcal{T} = \frac{|\mathbf{x}(t+\mathcal{T}) - \mathbf{y}(t)|}{c} \tag{7.322}$$

The quantity $t + \mathcal{T}$ is the time at which a disturbance emitted by a source element $\mathbf{y}$ at the time t will reach the observer $\mathbf{x}$. Thus, it is interpreted as the advanced time

$$t_{\text{adv}} = t + \mathcal{T} \tag{7.323}$$

Let us suppose that the observer moves at the constant velocity $c\mathbf{M}_o$. Equation (7.322) can be solved in $\mathcal{T}$, providing

$$\begin{aligned} \mathcal{T}^{\pm} &= \frac{r_i M_{oi} \pm \sqrt{(r_i M_{oi})^2 + r^2(1 - M_o^2)}}{c(1 - M_o^2)} \\ &= \frac{r}{c}\left\{\frac{M_{or} \pm \sqrt{M_{or}^2 + 1 - M_o^2}}{1 - M_o^2}\right\} \end{aligned} \tag{7.324}$$

where $r_i = x_i(t) - y_i(t)$ is the radiation vector and $M_{or} = \hat{r}_i M_{oi}$ is the observer Mach number vector in the radiation direction. Since a signal cannot be received before it is emitted, the quantity $\mathcal{T}$ must be positive. Notice that the $\mathcal{T}$ depends only on the observer velocity and not on the source velocity. The following cases can be distinguished:

a) observer at rest: $M_o = 0$. Only the solution $\mathcal{T}^+ = r/c$ is a physical solution.

b) Observer in subsonic motion: $M_o < 1$

$$M_{or} \pm \sqrt{M_{or}^2 + \alpha^2} > 0 \tag{7.325}$$

with $\alpha^2 = 1 - M_o^2$. Hence, only the solution $\mathcal{T}^+$ is a physical solution.

c) Observer in supersonic motion: $M_o > 1$

$$M_{or} \pm \sqrt{M_{or}^2 - \alpha^2} < 0 \tag{7.326}$$

with $\alpha^2 = -1 + M_o^2$. Hence,

1. observer moving far away from the source: $M_{or} > 0$. Both solutions $\mathcal{T}^{\pm}$ do not match the physical condition $\mathcal{T} > 0$.

2. observer moving towards the source: $M_{or} < 0$. Both solutions $\mathcal{T}^{\pm}$ are physical solutions, provided that $M_{or} < -\sqrt{M_o^2 - 1}$.

By assuming a subsonic observer velocity, only the solution $\mathcal{T}^{+}$ must be considered and the advanced time is given by

$$t_{\text{adv}} = t + \frac{r(t)}{c} \left\{ \frac{M_{or}(t) + \sqrt{M_{or}^2(t) + 1 - M_o^2}}{1 - M_o^2} \right\} \tag{7.327}$$

It is interesting to notice that a source time t corresponds only to one value of the advanced time t_{adv}. This happens for any velocity of the source. Furthermore, the advanced time expression is given by an explicit form.

The implementation of the advanced time formulation does not require a modification of the source terms in the integrals (6.41), (6.42) and (6.43). However, difficulties may arise in the reconstruction of the signal. Due to the Döppler effect, in fact, an equally spaced discretization of the source time domain does not correspond to an equally spaced discretization of the observer time domain. This can be understood by taking the time derivative of expression (7.327), i.e.

$$\frac{\mathrm{d}t_{\text{adv}}}{\mathrm{d}t} = 1 + \frac{M_i - M_{oi}}{1 - M_o^2} \left\{ M_{oi} + \frac{M_{or} M_{oi} + (1 - M_o^2)\, \hat{r}_i}{\sqrt{M_{or}^2 + 1 - M_o^2}} \right\} \tag{7.328}$$

where M_i denotes the source Mach number. Considering, for simplicity, a fixed observer position yields

$$\frac{\mathrm{d}t_{\text{adv}}}{\mathrm{d}t} = 1 - M_r \tag{7.329}$$

and in discretized form

$$t_{\text{adv}}^{j+1} = t_{\text{adv}}^{j} + \left(1 - M_r^j\right) \Delta t \tag{7.330}$$

where Δt is the computational time-step. In Fig.7.10 the advanced time is plotted for a fixed observer and a source moving at different velocities v_o along a rectilinear trajectory. The source intercepts the observation point at $t_o = r_o/v_o$, r_o being the initial distance of the source. For $t < t_o$ and subsonic source velocities the curves have positive slopes, with values $0 < 1 - M_r \leq 1$. This situation corresponds to a contraction of the advanced time scale. For $t < t_o$ and supersonic source velocities the curves have negative slopes. Thus, signals emitted before are detected after. Finally, for $t > t_o$ the curves have positive slopes, with values $1 - M_r > 1$. This situation corresponds to a dilatation of the advanced time scale. When the computed disturbances are sampled on an equally spaced advanced time domain[6], the following situations can take place:

1. only one contribution p_i^j from the source element S_i falls in the interval $[t^j, t^{j+1}]_{\text{adv}}$;
2. no contribution from the source element S_i is projected in the interval $[t^j, t^{j+1}]_{\text{adv}}$;
3. more than one contribution $\left(p_i^j\right)_n$ from the source element S_i falls in the interval $[t^j, t^{j+1}]_{\text{adv}}$

Since the Döppler factor is already accounted for in the source terms, contributions $\left(p_i^j\right)_n$ must not be added, but used to determine a suitable contribution p_i^j. A summation over all the source elements must be made as a final step, namely $p^j = \sum_i p_i^j$, providing the pressure value at the advanced time $j\Delta t$. The procedure used by Casalino [41] to build-on the pressure signal in the advanced time domain is essentially based on a linear interpolation and is described in subsection 7.10.1.

[6] The same discretization used in the source computation is used in the advanced time domain.

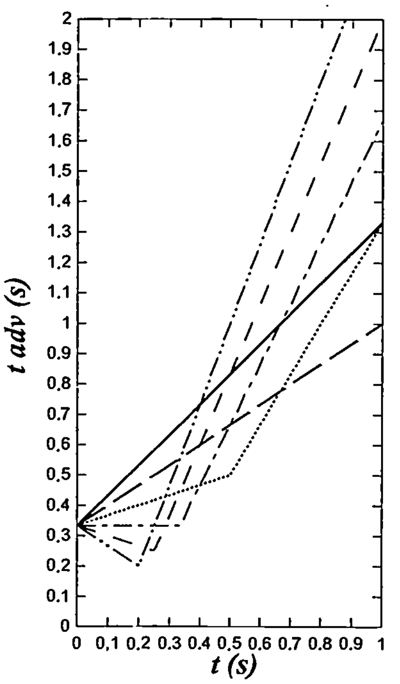

FIGURE 7.10: Advanced time versus current time for a source in constant motion at different Mach numbers in the direction of a fixed observer. The source initial distance from the observer is $r_o =$ 100 m and the sound speed is $c_o = 300$ m/s. Source Mach numbers: —— $M_o = 0$, — — $M_o = 0.33$, - - - - $M_o = 0.66$, - - - $M_o = 1$, - - - $M_o = 1.33$, - - - - $M_o = 1.67$.

7.10.1 Interpolation Scheme in the Advanced Time Domain

In this subsection we describe the method used by Casalino [41] to build-on the acoustic signal in the advanced time domain. Although more accurate schemes can be implemented, the one herein presented is a good compromise between accuracy and simplicity.

At each source time-step j and for each source element i, the advanced time t^j_{adv} and the corresponding elementary sound contribution p' are computed. Then, the quantities

$$j_{\text{adv}} = \text{int}(\frac{t^j_{\text{adv}}}{\Delta t}) \tag{7.331}$$

$$w = \frac{t^j_{\text{adv}}}{\Delta t} - j_{\text{adv}} \tag{7.332}$$

are computed, j_{adv} denoting the advanced time-step and w the normalized difference between t^j_{adv} and the discrete advanced time $j_{\text{adv}}\Delta t$.

Later on, the elementary sound contribution p^j_i is computed by means of a case-procedure which depends on whether a contribution p^j_i has been already computed or not, that is

a) if $p^j_i = 0$ (not computed), then

$$p^j_i = p' \tag{7.333}$$

$$w^j_i = w \tag{7.334}$$

b) if $p^j_i \neq 0$ (already computed), then

$$p_w = \frac{p^j_i - p'}{w^j_i - w} \tag{7.335}$$

$$p_i^j = p' - p_w w \tag{7.336}$$
$$w_i^j = 0 \tag{7.337}$$

Both the values of p_i^j and w_i^j are stored. It is straightforward to verify that, once $w_i^j = 0$ has been set by a first execution of block b), successive executions do not affect the value of p_i^j.

Finally, a summation over all the source elements, say $p^j = \sum_i p_i^j$, provides the pressure value at the advanced time-step j_{adv}.

7.11 Noise from a Steady Surface in a Moving Fluid Medium

In this section we address the problem of the noise generated by a turbulent flow past a steady surface. This is a typical problem in aeroacoustics and is usually referred to as *flow noise*.

7.11.1 Convected FW-H Equation

The acoustic analogy formulation discussed in section 7.8 can be used to describe the noise generated by un unsteady flow past a stationary surface and detected by a stationary observer immersed in the stream. The effects of the mean flow convection on the acoustic propagation can be taken into account by supposing that both the surface and the observer translate at the mean flow velocity, but in the direction opposite to the stream. Thus, the velocity fluctuations used in the acoustic analogy are perturbations with respect to the mean flow velocity, such that the fluid is at rest far from the surface. An alternative approach is herein described. It consists in rearranging the continuity and linear momentum equations in the form of a convected wave equation.

Let us write the continuity equation in the form

$$\frac{\mathrm{D}_\infty \rho}{\mathrm{D}t} \equiv \frac{\partial \rho}{\partial t} + U_{\infty i}\frac{\partial \rho}{\partial x_i} = -\frac{\partial (\rho u_i)}{\partial x_i} + U_{\infty i}\frac{\partial \rho}{\partial x_i} = -\frac{\partial (\rho \tilde{u}_i)}{\partial x_i} \tag{7.338}$$

where $\tilde{u}_i = u_i - U_{\infty i}$ is the flow velocity in a reference frame convected by the mean flow velocity $\mathbf{U}_\infty$. Taking into account the presence of a surface $S = f(\mathbf{x})$ by means of generalized derivatives gives

$$\frac{\mathrm{D}_\infty}{\mathrm{D}t}\left\{(\rho - \rho_\infty) H(f)\right\} + \frac{\partial}{\partial x_i}\left\{\rho \tilde{u}_i H(f)\right\} = (\rho - \rho_\infty)\frac{\mathrm{D}_\infty}{\mathrm{D}t} H(f) + \rho \tilde{u}_i \frac{\partial}{\partial x_i} H(f) \tag{7.339}$$

For a stationary surface it results that

$$\frac{\mathrm{D}_\infty}{\mathrm{D}t} H(f) = \frac{\partial}{\partial t} H(f) + U_{\infty i}\frac{\partial}{\partial x_i} H(f) = U_{\infty i}\frac{\partial}{\partial x_i} H(f) \tag{7.340}$$

Hence, the generalized continuity equation takes the form

$$\frac{\mathrm{D}_\infty}{\mathrm{D}t}\left\{(\rho - \rho_\infty) H(f)\right\} + \frac{\partial}{\partial x_i}\left\{\rho \tilde{u}_i H(f)\right\} = (\rho - \rho_\infty) U_{\infty j}\frac{\partial}{\partial x_j} H(f) + \rho \tilde{u}_j \frac{\partial}{\partial x_j} H(f) \tag{7.341}$$

Let us now write the linear momentum equation in the form

$$\frac{\mathrm{D}_\infty}{\mathrm{D}t}(\rho \tilde{u}_i) = -\frac{\partial p}{\partial x_i} + \frac{\partial \tau_{ij}}{\partial x_j} - \frac{\partial (\rho \tilde{u}_i \tilde{u}_j)}{\partial x_j} \tag{7.342}$$

Then, defining the relative Lighthill's stress tensor as

$$\tilde{T}_{ij} = \rho \tilde{u}_i \tilde{u}_j + \left\{p - c_\infty^2 (\rho - \rho_\infty)\right\}\delta_{ij} - \tau_{ij} \tag{7.343}$$

equation (7.342) takes the form

$$\frac{\mathrm{D}_\infty}{\mathrm{D}t}\left(\rho\tilde{u}_i\right) + c_\infty^2 \frac{\partial\left(\rho - \rho_\infty\right)}{\partial x_i} = -\frac{\partial \tilde{T}_{ij}}{\partial x_j} \tag{7.344}$$

Again, taking into account the presence of a stationary surface by means of generalized derivatives gives

$$\begin{aligned}\frac{\mathrm{D}_\infty}{\mathrm{D}t}\left\{\rho\tilde{u}_i H(f)\right\} + c_\infty^2 \frac{\partial}{\partial x_i}\left\{\left(\rho - \rho_\infty\right) H(f)\right\} &= \\ -\frac{\partial}{\partial x_j}\left\{\tilde{T}_{ij} H(f)\right\} + \left\{\rho\tilde{u}_i\tilde{u}_j + p\delta_{ij} - \tau_{ij}\right\}\frac{\partial}{\partial x_j} H(f) &+ \rho\tilde{u}_i U_{\infty j}\frac{\partial}{\partial x_j} H(f)\end{aligned} \tag{7.345}$$

Now, arranging the generalized continuity and linear momentum equations in the form

$$\frac{\mathrm{D}_\infty}{\mathrm{D}t}\left\{\mathrm{Eq.}\,(7.341)\right\} - \frac{\partial}{\partial x_i}\left\{\mathrm{Eq.}\,(7.345)\right\} \tag{7.346}$$

leads to the convected FW-H equation

$$\begin{aligned}\Box_c^2\left\{\left(\rho - \rho_\infty\right) H(f)\right\} \equiv & \left\{\frac{1}{c_\infty^2}\frac{\mathrm{D}_\infty^2}{\mathrm{D}t^2} - \nabla^2\right\}\left\{\left(\rho - \rho_\infty\right) c_\infty^2 H(f)\right\} = \\ & \frac{\partial^2}{\partial x_i \partial x_j}\left\{\tilde{T}_{ij} H(f)\right\} - \frac{\partial}{\partial x_i}\left\{\tilde{L}_i \delta(f)\right\} + \frac{\partial}{\partial t}\left\{\tilde{Q}\delta(f)\right\}\end{aligned} \tag{7.347}$$

where, provided that $|\nabla f| = 1$, the quadrupole, loading and thickness noise sources are given by

$$\tilde{T}_{ij} = \rho\tilde{u}_i\tilde{u}_j + \left\{p - c_\infty^2\left(\rho - \rho_\infty\right)\right\}\delta_{ij} - \tau_{ij} \tag{7.348}$$

$$\tilde{L}_i = \rho\left(\tilde{u}_i - U_{\infty i}\right)\left(\tilde{u}_j + U_{\infty j}\right) + \rho_\infty U_{\infty i} U_{\infty j} + p\delta_{ij} - \tau_{ij} \tag{7.349}$$

$$\tilde{Q} = \left(\rho - \rho_\infty\right) U_{\infty i} + \rho\tilde{u}_i \tag{7.350}$$

Formal solutions of equation (7.347) can be obtained in the time domain by using the convected Green's function (1.121). An alternative approach consists in Fourier transforming equation (7.347) and using the Green's function (1.120) in the frequency domain. This approach has been used by Lockard [174] among others, and is described in the following subsection.

7.11.2 The Frequency Approach

Applying the Fourier transform pair (1.114) to equation (7.347) gives

$$\begin{aligned}\left\{\frac{\partial^2}{\partial x_i^2} - M_i M_j \frac{\partial^2}{\partial x_i \partial x_j} - \mathrm{i}\, 2\, k\, M_i \frac{\partial}{\partial x_i} + k^2\right\}\left\{H(f)\, c_\infty^2 \hat{\rho}'(\mathbf{x}, k)\right\} = \\ -\frac{\partial^2}{\partial x_i \partial x_j}\left\{\hat{\tilde{T}}_{ij}(\mathbf{x}, k)\; H(f)\right\} + \frac{\partial}{\partial x_i}\left\{\hat{\tilde{L}}_i(\mathbf{x}, k)\; \delta(f)\right\} - \mathrm{i}\; k\, c_\infty \hat{\tilde{Q}}(\mathbf{x}, k)\; \delta(f)\end{aligned} \tag{7.351}$$

where $k = \omega/c_\infty$ is the acoustic wavenumber and $\mathbf{M} = \mathbf{U}_\infty/c_\infty$ is the mean flow Mach vector number.

The Green's function for the above wave equation has been derived in section 1.4.1 and is given by

$$G_c(\mathbf{x}, k; \mathbf{y}) = -\frac{\exp\left\{\frac{\mathrm{i}\,kr}{\beta^2}\left(M_r + \sqrt{M_r^2 + \beta^2}\right)\right\}}{r\sqrt{M_r^2 + \beta^2}} \tag{7.352}$$

where $r = |\mathbf{x} - \mathbf{y}|$, $M_r = M_i \hat{r}_i$, $\hat{r}_i = (x_i - y_i)/r$, and $\beta = \sqrt{1 - M^2}$ is the Prandtl-Glauert factor. The formal solution of equation (7.351) for $M < 1$ can be now written as

$$\begin{aligned} 4\pi H(f)\, c_\infty^2 \hat{\rho}'(\mathbf{x}, k) = & - \int G_c(\mathbf{x}, k; \mathbf{y}) \frac{\partial^2}{\partial y_i \partial y_j} \left\{ \hat{\hat{T}}_{ij}(\mathbf{y}, k)\; H(f) \right\} \,\mathrm{d}\mathbf{y} \\ & + \int G_c(\mathbf{x}, k; \mathbf{y}) \frac{\partial}{\partial y_i} \left\{ \hat{\hat{L}}_i(\mathbf{y}, k)\; \delta(f) \right\} \,\mathrm{d}\mathbf{y} \\ & - \mathrm{i}\, k\, c_\infty \int G_c(\mathbf{x}, k; \mathbf{y})\, \hat{\hat{Q}}(\mathbf{y}, k) \,\mathrm{d}\mathbf{y} \end{aligned} \tag{7.353}$$

The volume integrals are extended to the entire three-dimensional space. The dipole and the quadrupole terms can be simplified by moving the Green's function inside the derivative operators and applying the Green's theorem to show that the integral of the divergence is zero. This permits to transfer the spatial derivatives on the Green's function. Furthermore, the properties of the δ–function can be exploited in order to write equation (7.353) in the form

$$\begin{aligned} 4\pi H(f)\, c_\infty^2 \hat{\rho}'(\mathbf{x}, k) = & - \int \hat{\hat{T}}_{ij}(\mathbf{y}, k)\; H(f) \frac{\partial^2}{\partial y_i \partial y_j} G_c(\mathbf{x}, k; \mathbf{y}) \,\mathrm{d}\mathbf{y} \\ & - \int \hat{\hat{L}}_i(\mathbf{y}, k)\; \delta(f) \frac{\partial}{\partial y_i} G_c(\mathbf{x}, k; \mathbf{y}) \,\mathrm{d}\mathbf{y} \\ & - \mathrm{i}\, k\, c_\infty \int G_c(\mathbf{x}, k; \mathbf{y})\, \hat{\hat{Q}}(\mathbf{y}, k) \,\mathrm{d}\mathbf{y} \end{aligned} \tag{7.354}$$

The spatial derivatives of the Green's function can be evaluated by considering the analytical expressions (1.122) and (1.123), together with the property

$$\frac{\partial}{\partial y_i} G_c(\mathbf{x}, k; \mathbf{y}) = -\frac{\partial}{\partial x_i} G_c(\mathbf{x}, k; \mathbf{y}) \tag{7.355}$$

8

Sound Radiated by Turbulence Near a Scattering Half-Plane

8.1 Introduction

The problem of turbulence near a trailing edge generating aerodynamic sound has been treated by many authors as an acoustic diffraction problem involving a half-plane and turbulent pressure fluctuations.

A scattering body in proximity of an acoustic source converts part of the near field kinetic energy into far field noise. The intensity of the acoustic field usually exceeds that radiated by the same source into an unbounded medium. The efficiency of this conversion mechanism depends on the shape of the body, the reciprocal position between the source and the body, and the boundary conditions associated with the body surface.

According to Lighthill's [1] acoustic analogy, a turbulent portion of fluid in a quiescent medium is acoustically equivalent to a distribution of quadrupole sources. Curle [52] showed that the presence of a *hard* body (zero normal derivative of the wall pressure fluctuations) in a fluctuating aerodynamic field is equivalent to a distribution of surface dipoles. If the body is acoustically compact the surface dipoles are in phase and act as a single dipole. The strength of this acoustic dipole is proportional to the total force exerted on the fluid. The acoustic intensity from quadrupole and dipole source distributions are proportional to the eighth and sixth power of a characteristic flow velocity, respectively. As a consequence, at low Mach numbers the pressure fluctuations induced on the surface of a rigid body provide a more effective sound generation mechanism. A *soft* body (zero wall pressure fluctuation) is acoustically equivalent to a surface distribution of monopole sources. In this case a fourth power scaling law can be obtained, provided that the body is acoustically compact.

Starting from Lighthill's and Curle's theories of aerodynamic sound, Powell [77] showed that an infinite plane bounding a turbulent field does not produce an enhancement of the power law of the acoustic intensity. A planar surface is indeed equivalent to an image distribution of quadrupoles with phase depending on the boundary condition imposed on the surface. When a *pressure-release* condition is imposed, the plane acts as an image distribution of source with opposite phase and its local motion does not increase the radiation efficiency of the incident field.

Following Powell's analysis, Ffowcs Williams [175] investigated the effects of the surface motion on the sound radiated by a turbulent boundary-layer supported by an infinite homogeneous compliant plate. The compliant attribute allows to neglect the structural elastic forces with respect to the inertial terms. Thus, the surface motion can be described by means of a linear differential equation $p = f(v_n)$ which relates the wall pressure distribution P to the surface normal velocity v_n. Consistently with the acoustic analogy approach, Ffowcs Williams neglected the effects of the surface response on the structure of the turbulent field. Therefore, he showed that the effect of the surface is simply to reflect the quadrupole sound generated by turbulence. In terms of reflection coefficient, the influence of the infinite plane on the spectrum of the radiated pressure field can be written as $P = T_+ + RT_-$ where the terms T_+ and T_- account for the incident turbulent field and the image source distribution, respectively. The reflection coefficient R is real for propagating waves and does not exceed the unit value in absolute magnitude. Thus, the far field intensity does not exceed that due to the sum of the real and the image quadrupole source distributions. The sign of R depends on the surface response and determines the phase between the incident and the reflected acoustic field. For non-propagating components the reflexion coefficient can be complex and the surface motion can produce an increase of the near field pressure fluctuations.

Ffowcs Williams & Hall [176] discussed the problem of the sound generated by turbulence near the edge of a semi-infinite flat-plate. The presence of a scattering sharp edge implies that the reference length and velocity are not imposed by the turbulent field. As a consequence, Curle's dimensional analysis does not apply and the sixth power law of a compact surface distribution of dipoles is replaced by a fifth power law. The turbulent eddies which are responsible for this radiation enhancement are those characterized by a quadrupole structure with axes normal to the edge. These sources generate an acoustic far field whose intensity is increased by the factor $(k\,r_0)^{-3}$ both for rigid and soft surfaces, provided that the acoustic wavenumber k and the eddy distance from the edge r_0 satisfy the condition $2\,k\,r_0 \ll 1$. Finally, the noise directivity predicted by Ffowcs Williams & Hall has a $\sin^2(\theta/2)$ pattern when the plate is rigid, and a $\cos^2(\theta/2)$ pattern when a pressure release boundary condition is imposed on the plate surface, θ being the observation angle away from the streamwise direction.

Crighton & Leppington [161] solved the scattering problem of a distribution of quadrupoles near the edge of a semi-infinite compliant surface. They made use of the reciprocal theorem according to which the acoustic field at the listener location $\mathbf{x}_0$ generated by a monopole source in $\mathbf{x}$ is equal to the acoustic field at $\mathbf{x}$ generated by a monopole source in $\mathbf{x}_0$. Thus, if the observation point $\mathbf{x}_0$ is in the acoustic far field the problem is equivalent to that of determining the field in $\mathbf{x}$ generated by an incident plane wave. Furthermore, by differentiating with respect to $\mathbf{x}$, the acoustic field at the location $\mathbf{x}_0$ due to a multipole source of arbitrary order can be determined.

The problem of an incident plane wave scattered by the edge of a semi-infinite plate was solved by Crighton & Leppington by using the Wiener-Hopf technique applied to the system of equations

$$\phi_0(x,y) = \exp\{\mathrm{i}\; k_0\,(x\cos\theta_0 + y\sin\theta_0)\} \tag{8.1}$$

$$\left(\nabla^2 + k_0^2\right)\phi(x,y) = 0 \tag{8.2}$$

$$\phi(x,0^+) - \phi(x,0^-) = \frac{m}{\rho}\left\{\phi'(x,0) + \mathrm{i}\; k_0\cos\theta_0\exp(\mathrm{i}\; k_0\,x\,\cos\theta_0)\right\} \quad \text{for} \quad x<0 \tag{8.3}$$

Equation (8.1) represents an incident pressure field of wavenumber $k = \omega/c_0$ and reduced wavenumber $k_0 = k\,\sin\alpha_0$. The angles θ_0 and α_0 are related to the polar representation of the listener location $\mathbf{x}_0 = (r_0\sin\alpha_0\cos\theta_0, r_0\sin\alpha_0\cos\theta_0, r_0\cos\alpha_0)$, as sketched in Fig.8.1. Equation (8.2) represents the wave equation for the scattered potential field written in the Helmholtz form, and equation (8.3) follows from the boundary condition on the plate ($x<0$, $y=0$)

$$\Delta\left[p(x,0)\,\mathrm{e}^{-\mathrm{i}\omega t}\right] = m\frac{\mathrm{d}}{\mathrm{d}t}\left(v(x)\,\mathrm{e}^{-\mathrm{i}\omega t}\right) \tag{8.4}$$

which yields

$$p(x,0^-) - p(x,0^+) \equiv \mathrm{i}\;\rho_0\,\omega\,\left\{\phi(x,0^-) - \phi(x,0^+)\right\} = -\mathrm{i}\;m\,\omega\,v(x) \tag{8.5}$$

where m is the specific mass of the plate and $v(x)$ is the plate velocity in the positive y-direction. The no slip condition on the surface of the plate leads to

$$v(x) = \frac{\partial}{\partial y}\left(\phi + \phi_0\right)_{y=0} = \phi'(x,0) + \mathrm{i}\; k_0\,\sin\theta_0\exp\left(\mathrm{i}\; k_0\,x\cos\theta_0\right) \tag{8.6}$$

Thus, the boundary condition (8.3) can be obtained from equations (8.5) and (8.6).

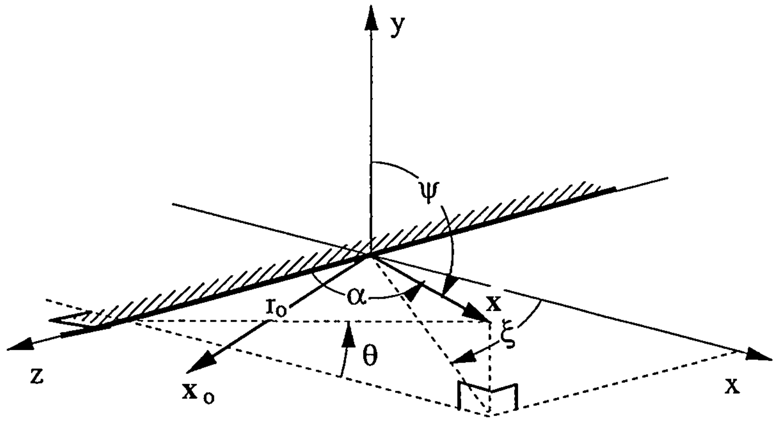

FIGURE 8.1: Scheme of the half-plane co-ordinate system. $\mathbf{x}_0$ denotes the observer location, whereas $\mathbf{x}$ denotes the source location.

The quadrupole sources near the edge can be related to the properties of the turbulent flow, namely, the *rms* velocity U and the integral correlation length l. Combining U and l, the following reference quantities can be defined: a characteristic frequency $\omega = U/l$, a reference Mach number $M = U/c_0$, and a characteristic wavenumber $k = M\,l^{-1}$.

Calling η the ratio of the scattered pressure amplitude to the direct pressure amplitude, $\epsilon = 2\,\rho\,l/m$ the fluid loading parameter and $\mu = 2\,\rho/m$, Crighton & Leppington [161] estimated the magnitude of η in two limit cases under the condition $k\,r \ll 1$, namely

- relatively rigid surface: $\frac{\mu}{k} = \frac{\epsilon}{M} \ll 0$

$$\eta \propto (kr)^{-3/2} = (l/r)^{3/2}\; M^{-3/2} \tag{8.7}$$

- relatively limp surface: $\frac{\mu}{k} = \frac{\epsilon}{M} \gg 0$

$$\eta \propto k^{-1}\, r^{-3/2} \mu^{-1/2} = (l/r)^{3/2}\, \epsilon^{-1/2}\, M^{-1} \tag{8.8}$$

The amplification ratio for a rigid plate, as expressed by equation (8.7), recovers that obtained by Ffowcs Williams & Hall [176] according to which the effect of an edge in proximity of a turbulent flow is that of increasing the radiated noise intensity by a factor $(k\,r)^{-3}$. This enhancement is related to the fifth power intensity law through the chain

$$I \simeq \eta^2 I_{\text{quadrupole}} \propto \eta^2 M^8 \propto U^5 \tag{8.9}$$

Conversely, for a limp surface, equation (8.8) shows two important results:

- the scattered pressure field vanishes as the surface mass m tends to zero ($\epsilon \to \infty$);
- the scattered intensity varies as U^6/ϵ in place of U^5, as obtained by Ffowcs Williams & Hall [176].

In a successive work Crighton & Leppington [177] extended their analysis to the scattering by both rigid and soft wedgelike bodies, with characteristic dimensions larger than the acoustic wavelength. They showed that the scattered intensity of the near pressure field generated by a quadrupole source with axes perpendicular to the edge depends on the typical fluctuation velocity in the form predicted by the expression

$$I \propto U^{4+\frac{2}{p/q}} = U^{4+\frac{1}{1-e/2\pi}} \tag{8.10}$$

where $(p/q)\pi$ and e are the exterior and the interior wedge angle, respectively. If the interior angle e tends to zero, a fifth power law predicted for a thin plate is recovered. Conversely, for $e \to \pi$ (infinite plane), a sixth power law results. These results agree with those obtained by Ffowcs Williams & Hall [176] and Crighton & Leppington [161], but disagree with Ffowcs Williams's [175] results according to which the effect of an infinite plane supporting a distribution of quadrupole sources is simply to reflect the incident field without modifying the quadrupole radiation character of the turbulent boundary-layer.

The models developed by Ffowcs Williams & Hall [176] and Crighton & Leppington [161] [177], are based on the extension of Lighthill acoustic analogy theory to an edge diffraction problem involving a semi-infinite plate or a wedge-like body. These models relate the radiated noise intensity to an assumed turbulent velocity, that is, to a measurable property of the quadrupole source distribution. Chase [81] [83] and Chandiramani [82] proposed a different treatment of the edge diffraction problem. Their approaches consist in relating the far field acoustic spectrum to the wavevector-frequency spectral density of the hydrodynamic pressure field near the edge. Therefore, in a first step the acoustic problem is solved by looking for a relation between the spectrum of the scattered acoustic field and the spectrum of the incident pressure field. In a second step the driving hydrodynamic spectrum is described by means of a hydrodynamic semi-empirical model.

Both Chase [81] and Chandiramani [82] considered only the case of a turbulent one-side wall jet crossing obliquely the edge of a rigid semi-infinite plate without wetting its surface.

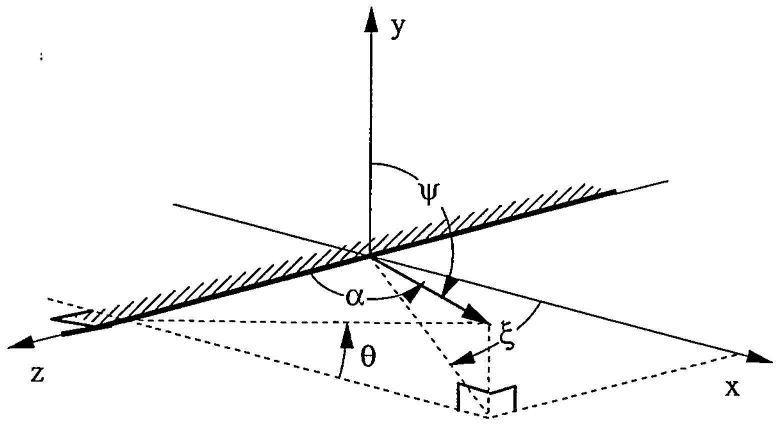

FIGURE 8.2: Scheme of the half-plane co-ordinate system.

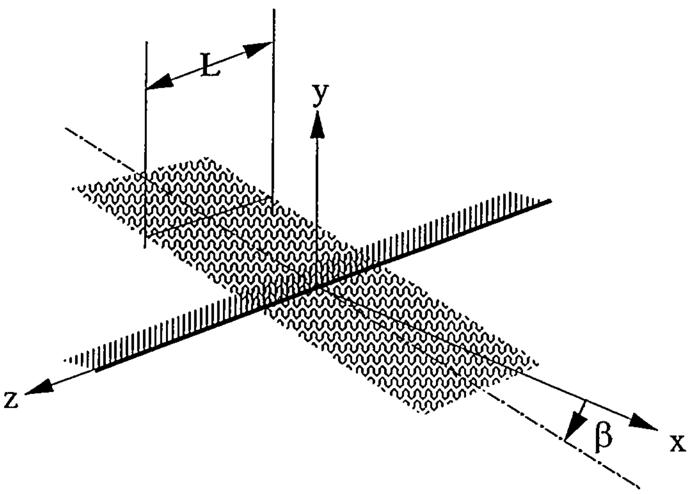

FIGURE 8.3: Turbulent ribbon wetting one side of a half-plane. β denotes the angle between the axis of the ribbon and the normal to the edge on the plane of the plate. L denotes the width of the ribbon.

Chase [81] used the modified isotropic convective similarity model [178] in order to describe the wall pressure field induced by a turbulent boundary-layer. By defining the radiated sound power per unit frequency and per unit solid angle as

$$\Pi(\omega, \phi, \theta) = (\rho\, c)^{-1}\, r^2\, P(\omega, r) \tag{8.11}$$

where $P(\omega, r)$ denotes the frequency spectral density of the radiated pressure (see Figs.8.2 and 8.3), Chase obtained the following results:

- for $\omega\delta/U_c \gtrsim 5\cos\beta$, $\Pi(\omega, \alpha, \theta)$ varies as ω^{-2} and nearly as U_∞^6;
- for $0.5 \lesssim \omega\delta/U_c \lesssim 5\cos\beta$, $\Pi(\omega, \alpha, \theta)$ does not depend on ω and varies as U_∞^4

where β is the angle between the ribbon direction and the normal to the edge, and where δ and U_c are the eddy size and convection velocity, respectively. Furthermore, the total acoustic power per unit solid angle varies as U_∞^5, in agreement with Ffowcs Williams & Hall's [176] result.

Chandiramani [82] proposed a slight modification of Chase's approach. He described the diffraction of evanescent incident waves with harmonic components[1]

$$P^i(x, y, z) = \frac{P_b}{2} \exp\left\{\mathrm{i}\,\left(k_{1_0} x + k_{2_0} y - k_{3_0} z\right)\right\} \tag{8.12}$$

The wavenumbers k_{1_0} and k_{2_0} are real, whereas k_{3_0} is imaginary positive and determines an exponential decay of the incident waves as y tends to zero[2]. The hydrodynamic near field driving pressure is described accordingly a Corcos' similarity model [99] and the frequency spectral density of the scattered acoustic pressure takes the form

$$P^s(r, \theta, \omega) \propto \frac{\rho^2\, U_c^2\, U_\infty^4}{r\, \omega^2}\, \sin^2(\theta/2) \tag{8.13}$$

where θ denotes the observation angle away from the streamwise direction.

Later on, Chase [83] refined his previous model by describing the pseudo-sound near field as a distribution of harmonic evanescent waves generated by the turbulent ribbon on one side of the semi-infinite plate. A different expression for the wavevector-frequency spectral density of the hydrodynamic pressure was used. The resulting model fits the spectrum of both the near and the far pressure field of a jet-flow. For a particular choice of a dimensionless parameter ($\nu = 2$), the spectrum does not depend on the large-eddy scale δ at frequency well above the convective large-eddy frequency U_c/δ. The resulting spectrum has a similarity character and yields a radiate far field spectrum ($\nu = 0$, $\beta = 0$ and $\alpha = \pi/2$) of the form

$$P(r, \theta, \omega) \propto \rho^2\, v^4\, \omega^{-2}\, (U_c/r)\, (U_c/c)\, (L/r)\, \sin^2(\theta/2) \tag{8.14}$$

where v is a dispersion velocity that characterizes the coherence of the hydrodynamic pressure in the convected frame of reference, and L is the width of the turbulent ribbon crossing the edge.

Equation (8.14) can be compared to the analogous form (8.13) obtained by Chandiramani. It is interesting to notice that, if v is supposed to be proportional to U_∞, these two expressions have nearly the same structural form.

When fluctuations occur in the flow past a trailing edge, vorticity is shed into the field. Despite its viscous origin, this process is commonly described by means of an inviscid model and an appropriate condition at the trailing edge. Briefly, a fluctuations in an inviscid flow induce a singular behaviour at the trailing edge. This singular behaviour can be smoothed by shedding a vortical wake which satisfies a Kutta condition at the trailing edge.

As discussed in chapter 9, the effect of the vortex shedding onto the trailing edge noise is a disputed argument in theoretical aeroacoustics. The present chapter is concerned with the scattering of an

[1] The term $\exp(-\mathrm{i}\omega t)$ has been dropped.

[2] This exponential decay has been introduced by Chandiramani in order to control the behaviour of the hydrodynamic forcing term.

acoustic field by the edge of a half-plane as a model of the aerodynamic noise from an edge in a turbulent flow. The procedure commonly adopted to solve this scattering problem consists in two steps:

- the solution of an acoustic diffraction problem,

- the description of the acoustic sources in terms of hydrodynamic elements associated with the turbulent flow in proximity of the edge.

All the analyses quoted above are based on this procedure and do not account for the vortex shedding process. Nevertheless, the theoretical works of Jones [179], Candel [180] and Rienstra [181], and the experimental work of Heavens [182] showed that the acoustic scattering approach can be extended in order to account for the presence of a vortical wake. In this way, the effects of the vortex shedding onto the trailing edge noise can be taken into account. Rienstra, in particular, showed that the vortex shedding induced by an incident acoustic wave at the edge of a semi-infinite flat-plate in a uniform flow can couple the acoustic field and the hydrodynamic field. As a result, acoustic power can be absorbed or released by the vortical wake depending on both the Mach number and the orientation angle of the incident acoustic waves.

In the following sections the half-plane scattering models developed by Ffowcs Williams & Hall [176], Chase [83] and Rienstra [181] are described in greater detail.

8.2 Ffowcs Williams & Hall's Model

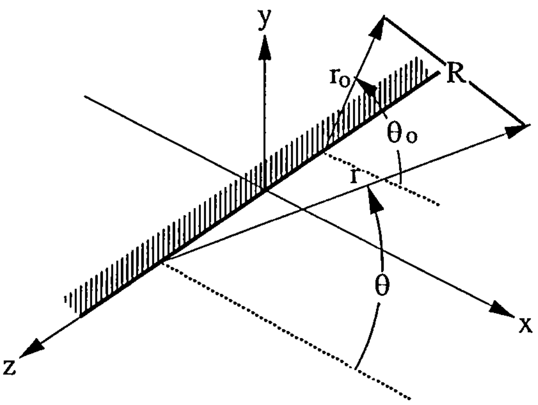

FIGURE 8.4: Scheme of the half-plane co-ordinate system used by Ffowcs Williams & Hall's [176].

By assuming that changes in p are exactly balanced by changes in $c^2\,\rho$ and by neglecting the viscous effects, Lighthill's equation (5.28) takes the form

$$\nabla^2 p - \frac{1}{c^2}\frac{\partial^2 p}{\partial t^2} = -\frac{\partial^2\left(\rho\, v_i\, v_j\right)}{\partial y_i \partial y_j} \tag{8.15}$$

whose frequency counterpart is

$$\nabla^2 p^* + k^2\, p^* = -\left\{\frac{\partial^2\left(\rho\, v_i\, v_j\right)}{\partial y_i \partial y_j}\right\}^* \tag{8.16}$$

where stars denote Fourier transform and $k = \omega/c$ is the acoustic wavenumber. A formal solution of the inhomogeneous Helmholtz equation (8.16) for a half-plane geometry can be obtained by convoluting with a tailored Green's function G which satisfies

$$\left(\nabla^2 + k^2\right) G = -4\pi\, \delta(\mathbf{x} - \mathbf{y}) \tag{8.17}$$

$$\frac{\partial G}{\partial n} = 0 \quad \text{on the half-plane} \tag{8.18}$$

It thus results that

$$4\pi\, p^*(\mathbf{x}, \omega) = \int_{V_0(\mathbf{y})} (\rho\, v_i\, v_j)^* \, \frac{\partial^2 G}{\partial y_i \partial y_j}\, \mathrm{d}V \tag{8.19}$$

where $V_0\,(\mathbf{y})$ denotes the portion of fluid containing the quadrupole sources of noise.

As shown by Macdonald [183], the Green's function for the half-plane has the following far field ($kr \gg 1$) expression

$$G(r, \theta, z | r_0, \theta_0, z_0) = \frac{\mathrm{e}^{\mathrm{i}\,\pi/4}}{\sqrt{\pi}} \left\{ \frac{\mathrm{e}^{-\mathrm{i}\,k\,R}}{R} \int_{-\infty}^{U_R} \mathrm{e}^{-\mathrm{i}\,U^2}\, \mathrm{d}U + \frac{\mathrm{e}^{-\mathrm{i}\,k\,R'}}{R'} \int_{-\infty}^{U_{R'}} \mathrm{e}^{-\mathrm{i}\,U^2}\, \mathrm{d}U \right\} \tag{8.20}$$

where use of the cylindrical co-ordinates has been made by setting

$$\begin{aligned}
R &= \sqrt{r^2 + r_0^2 - 2r\, r_0 \cos(\theta - \theta_0) + (z - z_0)^2} \\
R' &= \sqrt{r^2 + r_0^2 - 2r\, r_0 \cos(\theta + \theta_0) + (z - z_0)^2} \\
D &= \sqrt{(r + r_0)^2 + (z - z_0)^2}
\end{aligned} \tag{8.21}$$

and where the terms U_R and $U_{R'}$ are defined as

$$\begin{aligned}
U_R &= 2\left(\frac{k\, r\, r_0}{D + R}\right) \cos\!\left(\frac{\theta - \theta_0}{2}\right) \\
U_{R'} &= 2\left(\frac{k\, r\, r_0}{D + R'}\right) \cos\!\left(\frac{\theta + \theta_0}{2}\right)
\end{aligned} \tag{8.22}$$

In the geometric far field ($r \gg r_0$) it results that

$$\begin{aligned}
D + R &\simeq D + R' \simeq 2\sqrt{r^2 + (z - z_0)^2} \\
U_R &\simeq \sqrt{2\, k\, r_0 \sin\phi}\, \cos\!\left(\frac{\theta - \theta_0}{2}\right) \\
U_{R'} &\simeq \sqrt{2\, k\, r_0 \sin\phi}\, \cos\!\left(\frac{\theta + \theta_0}{2}\right)
\end{aligned} \tag{8.23}$$

where

$$\sin\phi = \frac{r}{\sqrt{r^2 + (z - z_0)^2}} \tag{8.24}$$

Hence, the formal solution of equation (8.19) is given by

$$4\pi\, p^*(r, \theta, z, \omega) = \iiint \mathcal{T}^*\, r_0\, \mathrm{d}r_0\, \mathrm{d}\theta_0\, \mathrm{d}z_0 \tag{8.25}$$

where

$$\mathcal{T} \;=\; \rho v_r^2 \frac{\partial^2 G}{\partial r_0^2} + \rho v_z^2 \frac{\partial^2 G}{\partial z_0^2}$$

$$
\begin{aligned}
&+ \quad \rho v_\theta^2 \left(\frac{1}{r_0^2}\frac{\partial^2 G}{\partial \theta_0^2} + \frac{1}{r_0}\frac{\partial G}{\partial r_0}\right) + \rho v_r v_z \left[\frac{\partial}{\partial r_0}\left(\frac{\partial G}{\partial z_0}\right) + \frac{\partial}{\partial z_0}\left(\frac{\partial G}{\partial r_0}\right)\right] \\
&+ \quad \rho v_r v_\theta \left[\frac{\partial}{\partial r_0}\left(\frac{1}{r_0}\frac{\partial G}{\partial \theta_0}\right) + \frac{1}{r_0}\frac{\partial}{\partial \theta_0}\left(\frac{\partial G}{\partial r_0}\right) - \frac{1}{r_0^2}\frac{\partial G}{\partial \theta_0}\right] \\
&+ \quad \rho v_\theta v_z \left[\frac{1}{r_0}\frac{\partial}{\partial \theta_0}\left(\frac{\partial G}{\partial z_0}\right) + \frac{\partial}{\partial z_0}\left(\frac{1}{r_0}\frac{\partial G}{\partial \theta_0}\right)\right]
\end{aligned}
\tag{8.26}
$$

Consider the case of an eddy close to the edge and satisfying the condition $2\,k\,r_0 \ll 1$ ($U_R \ll 1$, $U_{R'} \ll 1$). The Fresnel integral in equation (8.20) has the following series expansion

$$
\frac{\mathrm{e}^{\mathrm{i}\,\pi/4}}{\sqrt{\pi}} \int_{-\infty}^{x} \mathrm{e}^{-\mathrm{i}\,u^2}\, du \simeq \frac{1}{2} + \frac{\mathrm{e}^{\mathrm{i}\,\pi/4}}{x}\,(1 + \mathcal{O}(x)) \tag{8.27}
$$

Since $R'^2 = R^2 + 4r\,r_0 \sin\theta \sin\theta_0$, in the geometric far field $R' \simeq R + 2r\,r_0 \sin\theta \sin\theta_0$, which yields $kR \simeq kR'$. Thus, the Green's function (8.20) takes the simplified form

$$
G(r,\theta,z|r_0,\theta_0,z_0) = \frac{\mathrm{e}^{-\mathrm{i}\,k\,R}}{R}\left\{1 + \frac{2\mathrm{e}^{\mathrm{i}\,\pi/4}}{\sqrt{\pi}}\sqrt{2\,k\,r_0 \sin\phi}\cos(\theta_0/2)\cos(\theta/2) + \mathcal{O}(k\,r_0)\right\} \tag{8.28}
$$

where $R \simeq \sqrt{r^2 + (z - z_0)^2}$ and $\sin\phi = r/\sqrt{r^2 + (z-z_0)^2}$

Differentiating the half-plane Green's function (8.28) as in equation (8.26) shows some fundamental properties of the half-plane diffraction problem:

- the acoustic radiation from quadrupoles with both axes normal to the edge is amplified by a factor $(2\,k\,r_0)^{-3/2}$ with respect to a free-turbulence radiation;
- the contribution from quadrupoles with only one axis normal to the edge is only enhanced by a factor $(2\,k\,r_0)^{-1/2}$;
- the contribution from quadrupoles with both axes parallel to the edge is not affected by the presence of the edge.

Therefore, only terms of greater order $(2\,k\,r_0)^{-3/2}$ in equation (8.26) can be retained, i.e.

$$
\begin{aligned}
\frac{\partial^2 G}{\partial r_0^2} &\simeq -k^2\,\frac{\mathrm{e}^{-\mathrm{i}\,k\,R}}{R}\,\frac{2\mathrm{e}^{\mathrm{i}\,\pi/4}}{\sqrt{\pi}}\,\sqrt{\sin\phi}\,\cos(\theta_0/2)\,\cos(\theta/2)\,(2\,k\,r_0)^{-3/2} \\
\frac{1}{r_0}\frac{\partial G}{\partial r_0} &\simeq 2\,k^2\,\frac{\mathrm{e}^{-\mathrm{i}\,k\,R}}{R}\,\frac{2\mathrm{e}^{\mathrm{i}\,\pi/4}}{\sqrt{\pi}}\,\sqrt{\sin\phi}\,\cos(\theta_0/2)\,\cos(\theta/2)\,(2\,k\,r_0)^{-3/2} \\
\frac{1}{r_0^2}\frac{\partial^2 G}{\partial \theta_0^2} &\simeq -k^2\,\frac{\mathrm{e}^{-\mathrm{i}\,k\,R}}{R}\,\frac{2\mathrm{e}^{\mathrm{i}\,\pi/4}}{\sqrt{\pi}}\,\sqrt{\sin\phi}\,\cos(\theta_0/2)\,\cos(\theta/2)\,(2\,k\,r_0)^{-3/2} \\
\frac{1}{r_0^2}\frac{\partial G}{\partial \theta_0} &\simeq -2\,k^2\,\frac{\mathrm{e}^{-\mathrm{i}\,k\,R}}{R}\,\frac{2\mathrm{e}^{\mathrm{i}\,\pi/4}}{\sqrt{\pi}}\,\sqrt{\sin\phi}\,\sin(\theta_0/2)\,\cos(\theta/2)\,(2\,k\,r_0)^{-3/2} \\
\frac{\partial}{\partial r_0}\left(\frac{1}{r_0}\frac{\partial G}{\partial \theta_0}\right) &\simeq k^2\,\frac{\mathrm{e}^{-\mathrm{i}\,k\,R}}{R}\,\frac{2\mathrm{e}^{\mathrm{i}\,\pi/4}}{\sqrt{\pi}}\,\sqrt{\sin\phi}\,\sin(\theta_0/2)\,\cos(\theta/2)\,(2\,k\,r_0)^{-3/2} \\
\frac{1}{r_0}\frac{\partial}{\partial \theta_0}\left(\frac{\partial G}{\partial r_0}\right) &\simeq -k^2\,\frac{\mathrm{e}^{-\mathrm{i}\,k\,R}}{R}\,\frac{2\mathrm{e}^{\mathrm{i}\,\pi/4}}{\sqrt{\pi}}\,\sqrt{\sin\phi}\,\sin(\theta_0/2)\,\cos(\theta/2)\,(2\,k\,r_0)^{-3/2}
\end{aligned}
\tag{8.29}
$$

Substituting into equation (8.25) and neglecting all those terms of order smaller than $(2\,k\,r_0)^{-3/2}$ provides the final form of the far pressure field, i.e.

$$
p^*(r,\theta,z,\omega) \;=\; k^2\,\frac{\mathrm{e}^{\mathrm{i}\,\pi/4}}{2\pi^{3/2}}\,\cos(\theta/2)\iiint\left\{-\rho v_r^2\cos(\theta_0/2) + \rho v_\theta^2\cos(\theta_0/2) + 2\rho v_r v_\theta \sin(\theta_0/2)\right\}^*
$$

$$(2\,k\,r_0)^{-3/2}\sqrt{\sin\phi}\,\frac{\mathrm{e}^{-\mathrm{i}\,k\,R}}{R}\,r_0\,\mathrm{d}r_0\,\mathrm{d}\theta_0\,\mathrm{d}z_0 \tag{8.30}$$

Consider a turbulent element whose size is much smaller than an acoustic wavelength and for which $(\rho v_r^2)^*$, $(\rho v_\theta^2)^*$ and $(\rho v_r v_\theta)^*$ are perfectly correlated. The acoustic field from this element is

$$p^*(r,\theta,z,\omega) = k^2\,\frac{\mathrm{e}^{\mathrm{i}\,\pi/4}}{2\pi^{3/2}}\cos(\theta/2)\,\sqrt{\sin\phi}\frac{\mathrm{e}^{-\mathrm{i}\,k\,R}}{R}\left\{\left(\rho v_r^2-\rho v_\theta^2\right)^* I_1 + 2\,(\rho v_r v_\theta)^*\,I_2\right\} \tag{8.31}$$

where

$$I_1 = \iiint \cos(\theta_0/2)\,(2\,k\,r_0)^{-3/2}\,r_0\,\mathrm{d}r_0\,\mathrm{d}\theta_0\,\mathrm{d}z_0$$

$$I_2 = \iiint \sin(\theta_0/2)\,(2\,k\,r_0)^{-3/2}\,r_0\,\mathrm{d}r_0\,\mathrm{d}\theta_0\,\mathrm{d}z_0 \tag{8.32}$$

If this elementary source region occupies the field portion $r_1 < r_0 < r_2$, $\theta_1 < \theta_0 < \theta_2$, $z_1 < z_0 < z_2$, as

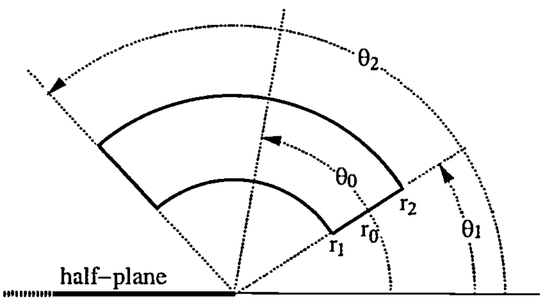

FIGURE 8.5: Idealized model of a turbulent eddy near the edge of a half-plane.

sketched in Fig.8.5, the volume integrals in equation (8.31) become

$$\begin{aligned} I_{\substack{1\\2}} &= (2k)^{-3/2}\,(z_2-z_1)\int_{\theta_1}^{\theta_2}\begin{matrix}\cos\\ \sin\end{matrix}(\theta_0/2)\,\mathrm{d}\theta_0\int_{r_1}^{r_2} r_0^{-3/2} = \\ &= (2k)^{-3/2}\,\Delta z\,4\,\begin{matrix}[+\sin(\theta_2/2)-\sin(\theta_1/2)]\\ [-\cos(\theta_2/2)+\cos(\theta_1/2)]\end{matrix}\left(r_2^{1/2}-r_1^{1/2}\right) \end{aligned} \tag{8.33}$$

Conversely, if the turbulent element is a cylinder of diameter 2δ with center in the edge of the half-plane, it results that

$$\begin{aligned} I_1 &= 0 \\ I_2 &= \frac{\sqrt{2}}{\pi}\,V\,(k\delta)^{-3/2} \end{aligned} \tag{8.34}$$

where $V = \pi\delta^2\Delta z$ is the eddy volume. Finally, if the eddy occupies a small region for which

$$\begin{aligned} \theta_{\substack{1\\2}} &= \overline{\theta_0} \mp \Delta\theta/2 \\ r_{\substack{1\\2}} &= \overline{r_0} \mp \Delta r/2 \end{aligned} \tag{8.35}$$

with $\Delta\theta \ll 1$ and $\Delta r \ll 1$, then it results that

$$I_{\substack{1\\2}} = (2k\overline{r_0})^{-3/2}\,V\,\begin{matrix}\cos(\overline{\theta_0}/2)\\ \sin(\overline{\theta_0}/2)\end{matrix} \tag{8.36}$$

where $V = \overline{r_0}\,\Delta r\,\Delta\theta\,\Delta z$ is the eddy volume.

The velocity field can be decomposed into a stationary part (U_r, U_θ, U_z) and a fluctuating part (u'_r, u'_θ, u'_z). If the fluctuating velocity is supposed to be of small amplitude, the following linearizing relationships can be introduced into equation (8.31)

$$\begin{aligned} \left(\rho v_r^2\right)^* &\simeq 2\rho_0 U_r\, u_r'^* \\ \left(\rho v_\theta^2\right)^* &\simeq 2\rho_0 U_\theta\, u_\theta'^* \\ \left(\rho v_r v_\theta\right)^* &\simeq \rho_0 U_r\, u_\theta'^* + \rho_0 U_\theta\, u_r'^* \end{aligned} \tag{8.37}$$

yielding

$$\begin{aligned} p^*(r,\theta,z,\omega) = k^2\,\frac{\mathrm{e}^{\mathrm{i}\,\pi/4}}{\pi^{3/2}}\,\cos(\theta/2)\,\sqrt{\sin\phi}\frac{\mathrm{e}^{-\mathrm{i}\,k\,R}}{R}\,\rho_0\,\left(2k\overline{r_0}\right)^{-3/2}\,V \\ \left\{\left(U_\theta\, u_\theta'^* - U_r\, u_r'^*\right)\cos\left(\overline{\theta_0}/2\right) + \left(U_r\, u_\theta'^* + U_\theta\, u_r'^*\right)\sin\left(\overline{\theta_0}/2\right)\right\} \end{aligned} \tag{8.38}$$

where use of the integral volume expressions (8.36) has been made.

An approximated formula for the radiated acoustic intensity can be obtained by neglecting any effect of cross-correlation in equation (8.38). Thus, calling α the normalized turbulent intensity, it results that

$$I(r,\theta,z,\omega) = \frac{p^*\overline{p^*}}{\rho_0 c} \simeq \frac{k^4\sin\phi\cos^2(\theta/2)\,\rho_0 U_\infty^4\alpha^2\,V^2\cos^2\beta}{\pi^3 cR^2\,\left(2k\overline{r_0}\right)^3}\left\{\cos^2\left(\overline{\theta_0}/2\right) + \sin^2\left(\overline{\theta_0}/2\right)\right\} \tag{8.39}$$

where β is the angle between the mean flow and the normal to the edge in the plane of the plate. Setting $\overline{r_0}$ equal to the eddy correlation length δ, the maximum value of the radiated intensity is given by

$$I_{\max} \simeq \frac{\rho_0\,k\,U_\infty^4\,\alpha^2\,V^2}{\pi^3\,c\,R^2\,\delta^3} \tag{8.40}$$

The characteristic frequency of an eddy of size δ, convected at the velocity U is of order $U/(2\delta)$, thus setting $k \simeq \pi U/c\delta$ into equation (8.40) yields

$$I_{\max} \simeq \frac{\rho_0\,U_\infty^5\,\alpha^2\,V^2}{\pi^2\,c^2\,R^2\,\delta^4} \tag{8.41}$$

where we have also supposed that the convection velocity is of the same order of the free-stream velocity U_∞.

The expression 8.41 is the main result of Ffowcs Williams & Hall's [176] analysis. It shows that the far field acoustic intensity scattered by a half-plane is proportional to the fifth power of the flow velocity when the turbulent quadrupole source is close to the edge ($2\,k\overline{r_0} \ll 1$). Furthermore, equation (8.39) shows that the noise level can be reduced by sweeping the half-plane edge with respect to the flow direction ($\beta \neq 0$).

Consider now the case of an eddy far from the edge at a distance such that $(k\,r_0)^{1/2} \gg 1$. Let us substitute the Green's function (8.20) into equation (8.19) and then let us differentiate. Terms containing the Fresnel integrals I_R and $I_{R'}$, and others containing the factors $(k\,r_0)^{-1/2}$ and $(k\,r_0)^{-3/2}$ have a dominant effect.

An analysis of the order of magnitude of the various terms at fixed observer position θ and at variable eddy location $\overline{\theta_0}$ shows the existence of three fundamental regions (see Fig.8.6), namely:

A) $0 \le \overline{\theta_0} < \pi - \theta$

the half-plane behaves like an infinite rigid flat-plate and the edge have a negligible effect of order $(k\,r_0)^{-1/2}$. The radiated pressure is given by

$$4\pi\,p^*(r,\theta,z,\omega) = -k^2\iiint\left(\rho v_i v_j\right)^*\left\{\mathcal{R}_i\mathcal{R}_j\frac{\mathrm{e}^{-\mathrm{i}\,k\,R}}{R} + \mathcal{R}'_i\mathcal{R}'_j\frac{\mathrm{e}^{-\mathrm{i}\,k\,R'}}{R'}\right\}\,r_0\,\mathrm{d}r_0\,\mathrm{d}\theta_0\,\mathrm{d}z_0 \tag{8.42}$$

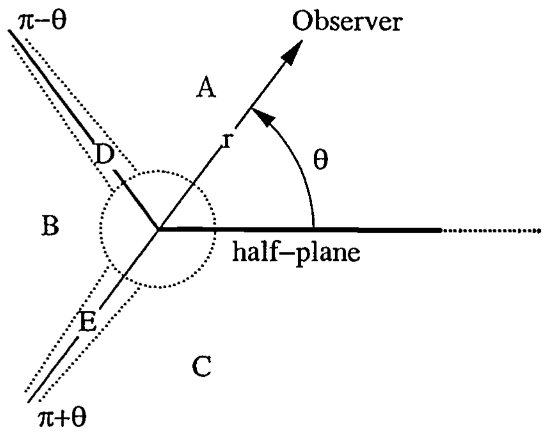

FIGURE 8.6: Noise generated by a compact turbulent eddy sufficiently far from the edge of a half-plane $(k\,r_0)^{1/2} \gg 1$.Intensity regions.

where

$$
\begin{aligned}
v_i &= (v_r, v_\theta, v_z) \\
\mathcal{R}_i &= \left(\frac{\partial R}{\partial r_0}, \frac{1}{r_0}\frac{\partial R}{\partial \theta_0}, \frac{\partial R}{\partial z_0}\right) \\
\mathcal{R}'_i &= \left(\frac{\partial R'}{\partial r_0}, \frac{1}{r_0}\frac{\partial R'}{\partial \theta_0}, \frac{\partial R'}{\partial z_0}\right)
\end{aligned}
\tag{8.43}
$$

B) $\pi - \theta < \overline{\theta_0} < \pi + \theta$

the radiated noise is nearly that of an eddy in free-turbulence, having the edge a negligible effect of order $(k\,r_0)^{-1/2}$. The acoustic pressure is given by

$$4\pi\, p^*(r,\theta,z,\omega) = -k^2 \iiint (\rho v_i v_j)^* \, \mathcal{R}_i \mathcal{R}_j \frac{\mathrm{e}^{-\mathrm{i}\,k\,R}}{R}\, r_0\, \mathrm{d}r_0\, \mathrm{d}\theta_0\, \mathrm{d}z_0 \tag{8.44}$$

C) $\pi + \theta < \overline{\theta_0} \leq 2\pi$

in the geometrical shadow of the observer location the radiated pressure is a factor $(k\,r_0)^{1/2}$ lower than that from the other regions.

Between the regions A and B there is a buffer region D where I_R and $I_{R'}$ are of greater order than $(k\,r_0)^{-1/2}$ and the radiated pressure has the form

$$4\pi\, p^*(r,\theta,z,\omega) = -k^2 \iiint (\rho v_i v_j)^* \left\{ \mathcal{R}_i \mathcal{R}_j \frac{\mathrm{e}^{-\mathrm{i}\,k\,R}}{R}\, I_R + \mathcal{R}'_i \mathcal{R}'_j \frac{\mathrm{e}^{-\mathrm{i}\,k\,R'}}{R'}\, I_{R'} \right\} r_0\, \mathrm{d}r_0\, \mathrm{d}\theta_0\, \mathrm{d}z_0 \tag{8.45}$$

Likewise, between the regions B and C there is a region E where $I_{R'}$ is of order $(k\,r_0)^{-1/2}$ and can be neglected compared to I_R. The radiated pressure is thus given by

$$4\pi\, p^*(r,\theta,z,\omega) = -k^2 \iiint (\rho v_i v_j)^* \, \mathcal{R}_i \mathcal{R}_j \frac{\mathrm{e}^{-\mathrm{i}\,k\,R}}{R}\, I_R\, r_0\, \mathrm{d}r_0\, \mathrm{d}\theta_0\, \mathrm{d}z_0 \tag{8.46}$$

In a final step, Ffowcs Williams & Hall [176] discussed the effects of a pressure release boundary condition ($p^* = 0$) on the surface of the half-plane. The problem is solved by introducing the appropriate

Green's function $\tilde{G}$ into the formal solution

$$4\pi\, p^*(\mathbf{x},\omega) = \int_{V_0(\mathbf{y})} (\rho\, v_i\, v_j)^* \, \frac{\partial^2 \tilde{G}}{\partial y_i \partial y_j}\, \mathrm{d}V - \int_S \rho\, v_n^2 \frac{\partial \tilde{G}}{\partial n}\, \mathrm{d}S \tag{8.47}$$

with $\tilde{G} = 0$ on the half-plane.

The far field ($kr \gg 1$) expression of $\tilde{G}$ was obtained by Macdonald [183] in the form

$$\tilde{G}(r,\theta,z|r_0,\theta_0,z_0) = \frac{\mathrm{e}^{\mathrm{i}\,\pi/4}}{\sqrt{\pi}} \left\{ \frac{\mathrm{e}^{-\mathrm{i}\,k\,R}}{R} \int_{-\infty}^{U_R} \mathrm{e}^{-\mathrm{i}\,U^2}\, \mathrm{d}U - \frac{\mathrm{e}^{-\mathrm{i}\,k\,R'}}{R'} \int_{-\infty}^{U_{R'}} \mathrm{e}^{-\mathrm{i}\,U^2}\, \mathrm{d}U \right\} \tag{8.48}$$

whose only difference with respect to its rigid-surface counterpart (8.20) is the sign of the image term.

For turbulence close to the edge ($2\,k\,r_0 \ll 1$), $\tilde{G}$ reduces to

$$\tilde{G}(r,\theta,z|r_0,\theta_0,z_0) = \frac{\mathrm{e}^{-\mathrm{i}\,k\,R}}{R} \left\{ 1 + \frac{2\mathrm{e}^{\mathrm{i}\,\pi/4}}{\sqrt{\pi}} \sqrt{2\,k\,r_0 \sin\phi}\, \sin(\theta_0/2)\sin(\theta/2) + \mathcal{O}(k\,r_0) \right\} \tag{8.49}$$

where the term $\cos(\theta_0/2)\cos(\theta/2)$ in G is replaced by $\sin(\theta_0/2)\sin(\theta/2)$. As a consequence, the surface boundary condition in Ffowcs Williams & Hall's analysis affects only the directivity of the acoustic field.

8.3 Chase's Model

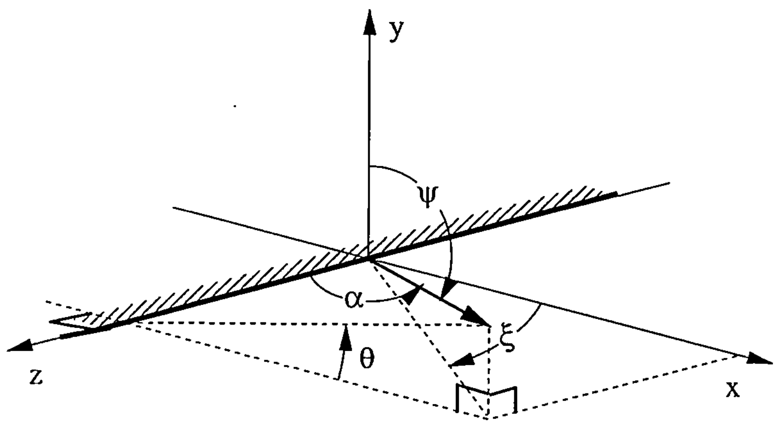

FIGURE 8.7: Scheme of the half-plane co-ordinate system.

Consider a rigid half-plane ($y_1 < 0, y_3$), whose upper side is crossed by a turbulent flow along a ribbon of width L, as sketched in Figs.8.8 and 8.7. The acoustic analogy approach applied to a generic volume $V\,(\mathbf{y})$ enclosed by the surface $S\,(\mathbf{y})$ and containing an aeroacoustic source region $V_0\,(\mathbf{y})$ yields

$$\begin{aligned} 4\pi\, p^*(\mathbf{x},\omega) &= \int_{V_0(\mathbf{y})} T_{ij}^* \frac{\partial^2 G}{\partial y_i \partial y_j}\, \mathrm{d}V \\ &- \int_{S(\mathbf{y})} (\rho v_n v_i + p_i)^* \, \frac{\partial G}{\partial y_i}\, \mathrm{d}S + \mathrm{i}\,\omega \int_{S(\mathbf{y})} (\rho v_n)^*\, G\, \mathrm{d}S \end{aligned} \tag{8.50}$$

where G is a generic Green's function of the Helmholtz equation

$$\left(\nabla^2 + k^2\right) G = -4\,\pi\, \delta(\mathbf{x} - \mathbf{y}) \tag{8.51}$$

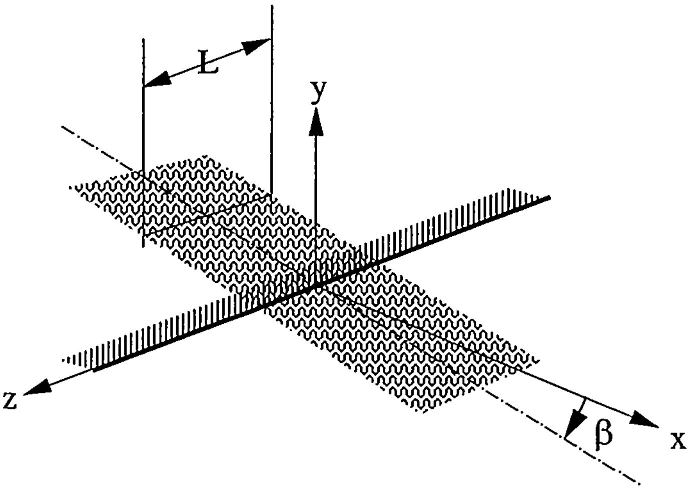

FIGURE 8.8: Turbulent ribbon wetting one side of a half-plane. β denotes the angle between the axis of the ribbon and the normal to the edge on the plane of the plate. L denotes the width of the ribbon.

T_{ij} is Lighthill's stress tensor, v_n is the normal component of the fluid velocity outward from the volume V and p_i is the vector stress exerted by the fluid on the surface S.

Equation (8.50) is verified for a field point $\mathbf{x}$ outside the source volume $V_0\,(\mathbf{y})$. If the analysis is restricted to the lower half-space and the spillover of Lighthill's sources is neglected, equation (8.50) becomes

$$4\pi p^*(\mathbf{x},\omega) = -\int_{\substack{y_2=0\\-\infty<y_1<\infty}} \left(\rho v_2^2 + p\right)^* \frac{\partial G}{\partial y}\,\mathrm{d}S + \mathrm{i}\,\omega \int_{\substack{y_2=0\\-\infty<y_1<\infty}} (\rho v_2)^*\, G\,\mathrm{d}S \tag{8.52}$$

Equation (8.52) can be simplified if G is obtained by imaging, with opposite sign, the half-plane Green's function G_{HP}, that is, $G(\mathbf{x},\mathbf{y}) = G_{\mathrm{HP}}(\mathbf{x},\mathbf{y}) - G_{\mathrm{HP}}(\mathbf{x},\mathbf{y}')$. The normal derivative of G_{HP} vanishes on the half-plane, and the Green's function G satisfies the following conditions on the plane $y_2 = 0$:

- for $y_1 < 0$, $\frac{\partial G}{\partial y_2} = 0$
- for $y_1 > 0$, $\frac{\partial G}{\partial y_2} = 2\frac{\partial}{\partial y_2}G_{\mathrm{HP}}$ and $G = 0$

Thus, substituting into equation (8.52) yields

$$2\pi p^*(\mathbf{x},\omega) = -\int_{S_+} \mathrm{d}S\,\left(p + \rho v_2^2\right) \frac{\partial G_{\mathrm{HP}}}{\partial y_2} \tag{8.53}$$

where S_+ denotes the half-plane downstream extension.

The diffracted wave vanishes on S_+. This can be easily demonstrated by considering an integration volume $V\,(\mathbf{y})$ bounded by the upper (S_U) and lower (S_L) half-plane surfaces, and by using the free-space Green's function G_0 in equation (8.50). It thus results that

$$4\pi p^*(\mathbf{x},\omega) = \int_{V_0(\mathbf{y})} T_{ij}^* \frac{\partial^2 G_0}{\partial y_i \partial y_j}\,\mathrm{d}V + \int_{S_L} (p_U - p_L)^* \frac{\partial G_0}{\partial y_2}\,\mathrm{d}S \tag{8.54}$$

Since $\partial G_0 / y_2 = 0$ when the observer is on the half-plane extension S_+, the fluctuating pressure on S_+ has a pure hydrodynamic nature and can be described without considering the diffraction by the rigid plate (the second integral in equation 8.54).

The aeroacoustic problem (8.53) was solved by Chase [81] by assuming the wavevector component $p_0 \exp\{\mathrm{i}\,(k_{1_0}\,x_1 + k_{3_0}\,x_3)\}$ as driving pressure on S_+. Thus, the radiated pressure is given by

$$\frac{p^*(\mathbf{x},\omega)}{p_0} = (4\pi)^{-1}\,r^{-1}\mathrm{e}^{\mathrm{i}\,k_\alpha r}\,L\,\sin(\theta/2)\,\frac{(2\,k_\alpha \sin\alpha \sec\beta)^{1/2}}{\left|\tilde{k}_{1_0} - k_\alpha\,\sin\Psi\,\cos(\xi+\beta)\right|^{1/2}}\,\frac{\sin(m\,L/2)}{m\,L/2} \tag{8.55}$$

where $k_\alpha = \omega/c$ is the acoustic wavenumber, $\tilde{k}_{1_0}$ and $\tilde{k}_{3_0}$ are the streamwise and transverse components of the flow-related wavevector, respectively, and

$$m = \tilde{k}_{3_0} - \tilde{k}_{1_0}\tan\beta - k_\alpha\,\sec\beta\,\cos\alpha \tag{8.56}$$

The frequency spectral density of the radiated pressure at the observer location $\mathbf{x}$ can be related to the driving pressure wavevector-frequency spectral density $P(\mathbf{k},\omega)$ by convoluting the solution (8.55), that is

$$P(\omega,\mathbf{x}) = \int T(\mathbf{k},\omega,\mathbf{r})\;P(\mathbf{k},\omega)\;\mathrm{d}^2\mathbf{k} \tag{8.57}$$

where $T(\mathbf{k},\omega,\mathbf{r}) = |p^*(\mathbf{x},\omega)/p_0|^2$ is the absolute square of the radiated pressure per unit driving pressure, as defined in equation (8.55).

The transfer function $T(\mathbf{k},\omega,\mathbf{r})$ peaks for excitation wavenumbers in the acoustic range, as results from the denominator $\left|\tilde{k}_{1_0} - k_\alpha\,\sin\Psi\,\cos(\xi+\beta)\right|^{1/2}$. However, $P(\mathbf{k},\omega)$ is small in that range. On the other hand, $P(\mathbf{k},\omega)$ peaks for a streamwise convection velocity U_c, that is, at the wavenumber $\tilde{k}_{1_0} = \omega/U_c$. Hence, by supposing $U_c \ll c$, the denominator of $T(\mathbf{k},\omega,\mathbf{r})$ can be approximated by $\tilde{k}_{1_0}$ and equation (8.57) takes the form

$$P(\omega,\mathbf{x}) = 2\,(4\pi)^{-2}\,k_\alpha\left(\frac{L}{r}\right)^2\sec\beta\,\sin\alpha\,\sin^2(\theta/2)\int_{-\infty}^{\infty}\mathrm{d}\tilde{k}_{3_0}$$
$$\int\frac{\mathrm{d}\tilde{k}_{1_0}}{\tilde{k}_{1_0}}\,\frac{\sin^2\left[\left(\tilde{k}_{3_0} - \tilde{k}_{1_0}\tan\beta - k_\alpha\,\sec\beta\,\cos\alpha\right)L/2\right]}{\left[\left(\tilde{k}_{3_0} - \tilde{k}_{1_0}\tan\beta - k_\alpha\,\sec\beta\,\cos\alpha\right)L/2\right]^2}\,P\left(\tilde{k}_{1_0},\tilde{k}_{3_0},\omega\right) \tag{8.58}$$

where the integral over the streamwise component $\tilde{k}_{1_0}$ covers the convective peak region ω/U_c.

By neglecting the transverse inhomogeneity of the ribbon caused by the lateral flow boundaries, and by supposing that $L \gg \left(\Delta\tilde{k}_{3_0}\right)^{-1}$, $\Delta\tilde{k}_{3_0}$ being the transverse half-width of the wavenumber/frequency spectrum $P\left(\tilde{k}_{1_0},\tilde{k}_{3_0},\omega\right)$, the double integral in equation (8.58) can be approximated as

$$S(\omega) = \frac{2\pi}{L}\int\frac{\mathrm{d}\tilde{k}_{1_0}}{\tilde{k}_{1_0}}\,P\left(\tilde{k}_{1_0},\tilde{k}_{1_0}\tan\beta + k_\alpha\,\sec\beta\,\cos\alpha,\omega\right) \tag{8.59}$$

Furthermore, since $\tilde{k}_{1_0} \simeq \omega/U_c \gg k_\alpha$, for a large range of β, the $\tilde{k}_{3_0}$ argument of $P\left(\tilde{k}_{1_0},\tilde{k}_{3_0},\omega\right)$ can be replaced by the term $\tilde{k}_{1_0}\tan\beta$. Thus, it follows that

$$S(\omega) = 2\pi\left(\frac{U_c}{\omega L}\right)\int\mathrm{d}\tilde{k}_{1_0}\,P\left(\tilde{k}_{1_0},\omega\tan\beta/U_c,\omega\right) \tag{8.60}$$

which can be substituted into equation (8.58) yielding

$$P(\omega,\mathbf{x}) = \frac{1}{4\pi}\left(\frac{U_c}{\omega L}\right)\,k_\alpha\left(\frac{L}{r}\right)^2\sec\beta\,\sin\alpha\,\sin^2(\theta/2)\int\mathrm{d}\tilde{k}_{1_0}\,P\left(\tilde{k}_{1_0},\omega\tan\beta/U_c,\omega\right) \tag{8.61}$$

A similar result can be obtained by following the evanescent wave approach of Chandiramani [82]. Consider an incident elementary wave

$$p^i(\mathbf{x}) = p_0 \exp\{\mathrm{i}\ (k_{1_0}\, x_1 + k_{3_0}\, x_3 - k_{2_0}\, x_2)\} \tag{8.62}$$

where k_{1_0} and k_{3_0} are real and satisfy the conditions $|k_{1_0}| > k_\alpha$ and $|k_{3_0}| \leq k_\alpha$, while k_{2_0} is positive imaginary and is given by

$$k_{2_0} = \mathrm{i}\ \left(k_0^2 - k_\alpha^2\right)^{1/2} = \mathrm{i}\ \left(k_{1_0}^2 - k_d^2\right)^{1/2} \tag{8.63}$$

with $k_0 = \left(k_{1_0}^2 + k_{3_0}^2\right)^{1/2}$ and $k_d = \left(k_\alpha^2 - k_{3_0}^2\right)^{1/2}$.

By applying the Weiner-Hopf technique to the half-plane diffraction problem, Chandiramani obtained the following expression for the scattered far pressure field

$$p^s(\mathbf{x}) = C(k_{1_0}, k_{3_0}, x_3)\ I(k_{1_0}, k_{3_0}, x_1, x_2) \tag{8.64}$$

with

$$C(k_{1_0}, k_{3_0}, x_3) = \mathrm{i}\ (2\pi)^{-1}\ (k_d - k_{1_0})^{-1/2}\ p_0\, k_{2_0}\, \mathrm{e}^{\mathrm{i}\, k_{3_0}\, x_3} \quad \text{and} \tag{8.65}$$

$$I(k_{1_0}, k_{3_0}, x_1, x_2) = \int_{-k_d}^{k_d} (k_d - k_1)^{1/2}\, (k_1 - k_{1_0})^{-1}\, \left(k_d^2 - k_1^2\right)^{-1/2} \exp\left\{\mathrm{i}\ \left[k_1 x_1 + \left(k_d^2 - k_1^2\right)^{1/2} x_2\right]\right\}\, \mathrm{d}k_1 \tag{8.66}$$

Chase [83] generalized these results to a flow of finite lateral extent by introducing an appropriate function $g(2\tilde{x}_3/L)$ which: (i) modulates the incident field along the transverse co-ordinate $\tilde{x}_3 = x_3 \cos\beta + x_1 \sin\beta$, (ii) has unitary value at $\tilde{x}_3 = 0$, (iii) vanishes for values of its argument $2\tilde{x}_3/L \gg 1$. Thus, defining the incident field as

$$p^i(\mathbf{x}, \omega) = g(2\tilde{x}_3/L) \int \exp\{\mathrm{i}\ (k_{1_0}\, x_1 + k_{3_0}\, x_3 - k_{2_0}\, x_2)\}\ \hat{p}(\mathbf{k}, \omega)\ \mathrm{d}^2\mathbf{k} \tag{8.67}$$

where $\hat{p}(\mathbf{k}, \omega)$ is the amplitude of the wavenumber/frequency Fourier component of the hydrodynamic pressure in the plane $y = 0$, the scattered pressure takes the form

$$p^s(\mathbf{x}\,\omega) = \int \mathrm{d}^2\mathbf{k}\, \hat{p}(\mathbf{k}, \omega)\ H^s(\mathbf{k}, \mathbf{x}) \tag{8.68}$$

where

$$H^s(\mathbf{k}, \mathbf{x}) = \int_{-\infty}^{\infty} \mathrm{d}k'_{3_0}\, h\, \hat{g}\, \left[(k'_{3_0} - k_{3_0})\, h\right]\ C(k'_{1_0}, k'_{3_0}, x_3)\ I(k'_{1_0}, k'_{3_0}, x_1, x_2) \tag{8.69}$$

$$h = \frac{L}{2} \sec\beta \tag{8.70}$$

$$k'_{1_0} = k_{1_0} + \left(k'_{3_0} - k_{3_0}\right)\ \tan\beta \tag{8.71}$$

In the far field limit $k_d r \gg 1$ and $r \gg h$, the method of stationary phase provides

$$H^s(\mathbf{k}, \mathbf{x}) \simeq -\sqrt{2}\left(\frac{h}{r}\right) \mathrm{e}^{\mathrm{i}\, k_\alpha r} \sqrt{\sin\alpha}\ \sin(\theta/2)\ k_\alpha^{1/2}\, \left(k'_{1_0} + k_\alpha \sin\alpha\right)^{1/2} \left[k'_{1_0} - k_\alpha\ \sin\alpha\ \cos\theta\right]^{-1} \hat{g}\left[(k_\alpha \cos\alpha - k_{3_0})\, h\right] \tag{8.72}$$

Thus, the frequency spectral density of the scattered pressure takes the form

$$P^s(\mathbf{x}, \omega) = \int P(\mathbf{k}, \omega)\, |H^s(\mathbf{k}, \mathbf{x})|^2\ \mathrm{d}^2\mathbf{k} \tag{8.73}$$

If the transverse extension of the turbulent ribbon is supposed to largely exceed the large eddy scale δ, and if the wavenumber/frequency hydrodynamic pressure spectrum is supposed to have a sharp convective peak at $k_{1_0} = \omega/U_c$, with $U_c \ll c$, then a good approximation of $P^s(\mathbf{x},\omega)$ is

$$P^s(\mathbf{x},\omega) \simeq \frac{1}{\pi}\left(\frac{U_c}{\omega L}\right) k_\alpha \left(\frac{L}{r}\right)^2 \sec\beta \, \sin\alpha \, \sin^2(\theta/2) \int \mathrm{d}\tilde{k}_{1_0} \, P\Big(\tilde{k}_{1_0}, \omega \tan\beta/U_c, \omega\Big) \tag{8.74}$$

where use of the relation

$$\int_{-\infty}^{\infty} \mathrm{d}k_{3_0} \, |\hat{g}(k_{3_0} h)|^2 \simeq (\pi\, h)^{-1} \tag{8.75}$$

has been made. It should be observed that equation (8.74), apart from the constant factor of 4^{-1}, coincides with equation (8.61) obtained by Chase [81].

Chase [83] proposed the following expression for the hydrodynamic pressure wavenumber/frequency spectrum

$$P(\mathbf{k},\omega) \doteq c_v \, \rho^2 \, v^3 \, \delta^{-2(\nu-2)} \, \tilde{k}_{1_0}^2 \, k_*^{-2\nu-1} \tag{8.76}$$

where

$$k_*^2 = \frac{\left(\omega - U_c \tilde{k}_{1_0}\right)^2}{v^2} + \tilde{k}_{1_0}^2 + \tilde{k}_{3_0}^2 + \delta^{-2} \tag{8.77}$$

This model describes the main features of a turbulent shear layer: the convective peaking at $\tilde{k}_{1_0} = \omega/U_c$, the peak depth dependence on the dispersion velocity v (a measure of the turbulence level), and the ω^2 frequency dependence imposed by the term $\tilde{k}_{1_0}^2$. Furthermore, the dimensionless parameters ν and c_v can be adjusted in order to fit a given experimental behaviour. In fact, the value $\nu = 2$ provides an expression for $P(\mathbf{k},\omega)$ that features quite well the similarity character[3] of a turbulent boundary-layer. Conversely, the value $\nu = 7/3$ better features a jet-flow behaviour.

Thus, making use of equation (8.76) into equation (8.74) and integrating, the frequency spectrum of the far pressure field scattered by a rigid half-plane in the opposite side of an impinging turbulent ribbon, takes the final form

$$\begin{aligned} P^s(\mathbf{x},\omega) \quad &= \left[\frac{\Gamma(\nu)}{\sqrt{\pi}\Gamma(\nu+1/2)}\right] c_v \, \rho^2 \, v^4 \, \omega^{-1} \, (\omega\, r/U_c)^{-1} \, (L/r) \, (U_c/c) \, (\omega\delta/U_c)^{-2(\nu-2)} \\ &\sec\beta \, \sin\alpha \, \sin^2(\theta/2) \, \left[\sec^2\beta + (\omega\delta/U_c)^{-2}\right]^{-\nu} \end{aligned} \tag{8.78}$$

where Γ denotes the gamma function.

8.4 Rienstra's Model

Vortex shedding plays a complex role in the physics of trailing edge noise. Howe [13] investigated the effect of vortex shedding induced by a fluctuating hydrodynamic field, such as an impinging gust or a turbulent boundary-layer. He concluded that the shed vorticity has a silencer effect because it induces a pressure field which is in opposite phase with respect to the impinging vortical disturbance.

Vortex shedding is also produced when acoustic disturbances interact with a trailing edge. Jones [179] considered the harmonic field of a line source parallel to the trailing edge of a semi-infinite plate in a subsonic flow. He concluded that the imposition of the Kutta condition has a notable effect only in the neighborhood of the wake.

Heavens [182] investigated experimentally the diffraction of a sound pulse from an airfoil trailing edge in a subsonic flow. He observed that the intensity of the diffracted wave greatly increases when unsteady perturbative phenomena, such as a boundary-layer separation, take place in the flow.

[3]The spectrum of the wall pressure beneath a turbulent boundary-layer does not depend on the scale δ at frequencies well above the convective large-eddy frequency U_c/δ.

Rienstra [181] examined the effect of the Kutta condition on the diffraction of cylindrical sound pulse, plane sound pulse and harmonic waves by the edge of a semi-infinite plate. He demonstrated that the vortex shedding process can absorb or release acoustic energy, depending on both the value of the flow Mach number and the source location. Some details of Rienstra's analysis are hereafter discussed.

Consider a rigid semi-infinite plate ($x \leq 0, y = 0$) in a uniform subsonic flow with velocity U_0. The fluid is supposed to be inviscid. Pressure and density of the fluid at infinity are p_0 and ρ_0, respectively.

A flow field perturbed by an acoustic field can be described by a convective wave equation for the potential ϕ of the acoustic velocity. If the acoustic field is generated by an impulsive source, the wave equation has the form

$$\phi_{xx} + \phi_{yy} - M_0^2\,(\phi_{tt} + 2\,\phi_{xt} + \phi_{xx}) = 4\pi\,a\,\delta(x - x_0)\;\delta(y - y_0)\;\delta(t) \tag{8.79}$$

where $M_0 = U_0/c_0$ is the flow Mach number. The acoustic pressure is related to the velocity potential through the linear expression

$$p = -\phi_t - \phi_x \tag{8.80}$$

Equations (8.79) and (8.80) have been made dimensionless by means of a reference length L, a reference time L/U_0, a reference potential $U_0\,L$ and a reference pressure $\rho_0 U_0^2$.

The boundary conditions to be applied on the plane $y = 0$ are

$\phi_y(x < 0, 0) = 0$	slip condition on the plate	(8.81)
$\phi_y\big(x > 0, 0^+\big) = \phi_y\big(x > 0, 0^-\big)$	continuity of $v\,(= \phi_y)$ across the wake	(8.82)
$p\big(x > 0, 0^+\big) = p\big(x > 0, 0^-\big)$	continuity of p across the wake	(8.83)

If a vortex-sheet lies in the half-plane ($x > 0, y = 0$), both ϕ and $u\,(= \phi_x)$ may have there a bounded discontinuity.

The physical condition to be applied at the trailing edge is that of finite net force or, equivalently, a condition of integrable pressure. When a vortex shedding occurs this generic edge condition is replaced by an explicit Kutta condition which requires a finite pressure or, equivalently, a finite velocity at the trailing edge.

Finally, a radiation condition must be satisfied by the diffracted acoustic field. For the pulse problem this condition is imposed by supposing the existence, at any time t, of a circle outside which the acoustic field is identically zero. Conversely, for the harmonic problem, a convective form of Sommerfeld's radiation condition must be imposed.

The diffraction harmonic problem with vortex shedding was solved by Jones [179] whose results are reported below.

Consider the Prandtl-Glauert type transformations

$$\begin{aligned}
&\beta = \sqrt{1 - M_0^2} \\
&x = \beta\,X = \beta\,R\,\cos\Theta \\
&y = Y = R\,\sin\Theta \\
&k = \omega\,M_0 = \beta\,K \\
&\Theta_1 = \mathrm{i}\,\cosh^{-1}(1/M_0)
\end{aligned} \tag{8.84}$$

Fourier transforming equation (8.79) yields

$$\hat{\phi}_{XX} + \hat{\phi}_{YY} + K^2\,\hat{\phi} + \mathrm{i}\,2\,K\,M_0\,\hat{\phi}_X = 4\pi\,a\,\delta(X - X_0)\;\delta(Y - Y_0) \tag{8.85}$$

where use of the mapping rules (8.84) has been made. The continuous solution of equation (8.85)[4] is

$$\hat{\phi}_c(x,y,\omega) = -\frac{a}{\beta}\, G\Big(X, Y, \frac{\omega}{\beta}\Big)\ \exp\{\mathrm{i}\ K M_0\,(X - X_0)\} \tag{8.86}$$

where $G(x,y,\omega)$ is the half-plane Green's function. It is given by

$$G(x,y,\omega) = G_1(x,y,\omega) + G_2(x,y,\omega) \tag{8.87}$$

with

$$\begin{aligned} G_{1,2}(x,y,\omega) &= \int_{-\infty}^{Ur_{1,2}} \exp\left(-\mathrm{i}\ k\, r_{1,2}\cosh u\right)\,\mathrm{d}u \\ Ur_{1,2} &= \pm\mathrm{asinh}\left\{2\frac{\sqrt{r\,r_0}}{r_{1,2}}\cos\left(\frac{\theta \mp \theta_0}{2}\right)\right\} \quad \text{and} \end{aligned} \tag{8.88}$$

$$r_{1,2} = \left\{r^2 + r_0^2 - 2\,r\,r_0\,\cos(\Theta - \Theta_0)\right\}^{1/2} \tag{8.89}$$

The potential field of a vortex-sheet on the half-plane $x > 0$, $y = 0$ was determined by Jones in terms of eigensolutions of equation (8.85). It is given by

$$\begin{aligned} \hat{\phi}_e(x,y,\omega) &= \frac{\mathrm{e}^{\mathrm{i}\,\pi/4}}{\sqrt{\pi}}\left[F(\Gamma_1) + F(\overline{\Gamma}_1)\right]\,\exp(-\mathrm{i}\ K\,R + \mathrm{i}\ K\,M_0\,X) \\ &- \ 2\,H(-y)\cosh(\omega\,y)\,\exp(-\mathrm{i}\,\omega\,x) \end{aligned} \tag{8.90}$$

with

$$\begin{aligned} \Gamma_1 &= (2\,K\,R)^{1/2}\,\sin\left(\frac{\Theta - \Theta_1}{2}\right) \\ \overline{\Gamma}_1 &= (2\,K\,R)^{1/2}\,\sin\left(\frac{\Theta + \Theta_1}{2}\right) \end{aligned} \tag{8.91}$$

and

$$F(z) = \exp\left(\mathrm{i}\ z^2\right)\int_z^{\infty}\exp\left(-\mathrm{i}\ z'^2\right)\,\mathrm{d}z' \tag{8.92}$$

The function $F(z)$ denotes the Fresnel's integral and H denotes the Heaviside function which marks a discontinuity across the vortex-sheet on the half-plane $x > 0$, $y = 0$.

The general solution of the harmonic diffraction problem with vortex shedding from the trailing edge can be written as

$$\hat{\phi}_k(x,y,\omega) = \hat{\phi}_c(x,y,\omega) + A(\omega)\,\hat{\phi}_e(x,y,\omega) \tag{8.93}$$

where $A(\omega)$ denotes the intensity of the wake and depends on the incident acoustic field via the Kutta condition. It results that

$$A(\omega) = -2\frac{\alpha}{\beta}\left(\frac{1 - M_0}{1 + M_0}\right)^{1/4}\left(\frac{\pi}{\omega\,R_0}\right)^{1/2}\sin(\Theta_0/2)\exp\left\{-\mathrm{i}\ \left(\frac{\pi}{4} + k\,R_0 + K\,M_0\,X_0\right)\right\} \tag{8.94}$$

Transforming back into the time domain and applying equation (8.80) to obtain the diffracted pressure yields

$$p_c(x,y,t) = 2\,a\frac{\delta(T)}{\beta^2\,M_0}\,\frac{1 - M_0\,\cos\Theta_0}{\cos\Theta + \cos\Theta_0}\,\frac{\sin(\Theta/2)\sin(\Theta_0/2)}{(R\,R_0)^{1/2}} + \ldots \tag{8.95}$$

[4]The continuous solution of equation (8.85) results from a classical diffraction problem with flow and no vortex shedding.

and

$$p_e(x,y,t)) = 2\,a\frac{\delta(T)}{\beta^2}\,\frac{\sin(\Theta/2)\sin(\Theta_0/2)}{(R\,R_0)^{1/2}} \tag{8.96}$$

where

$$T = t - \frac{M_0}{\beta}\,(R + R_0) + \frac{M_0^2}{\beta}\,(X - X_0) \tag{8.97}$$

The continuous solution $p_c(x,y,t)$ has been expressed with the only front term retained. This term, in fact, is the only affected by the Kutta condition. The eigensolution $p_e(x,y,t)$ has been obtained by transforming the term $A(\omega)\,p_e(x,y,t)$. The total diffracted pressure is thus given by

$$p_k(x,y,t) \equiv (1+r)\,p_c = 2\,a\frac{\delta(T)}{\beta^2\,M_0}\,\frac{1 + M_0\,\cos\Theta_0}{\cos\Theta + \cos\Theta_0}\,\frac{\sin(\Theta/2)\sin(\Theta_0/2)}{(R\,R_0)^{1/2}} \tag{8.98}$$

with

$$r = \frac{p_e}{p_c} = M_0\,\frac{\cos\Theta + \cos\Theta_0}{1 - M_0\,\cos\Theta_0} + \ldots \tag{8.99}$$

At fixed Θ_0, the maximum and the minimum values of r are

$$\begin{aligned} r_{\max}(\Theta = 0) &= M_0\,\tfrac{1+\cos\Theta_0}{1-M_0} & \left(0 \le r_{\max} \le \frac{2\,M_0}{1 - M_0}\right) \\ r_{\min}(\Theta = \pm\pi) &= M_0\,\tfrac{-1+\cos\Theta_0}{1+M_0} & \left(\frac{-2\,M_0}{1 + M_0} \le r_{\min} \le 0\right) \end{aligned} \tag{8.100}$$

The vortex-sheet causes an increase of the diffracted pressure in the circular sector seen by the source and its image, that is, for $|\Theta| < \pi - \Theta_0$. The amplification r factor achieves its maximum $r_{\max}$ when the field point is close to the wake ($\theta \simeq 0$).

Consider now a harmonic plane wave. The normal to the wave fronts makes the angle θ_i with the plate. The propagation direction θ_s of the acoustic waves is thus given by

$$\begin{aligned} \sin\theta_s &= \frac{\sin\theta_i}{\left(1 + 2\,M_0\,\cos\theta_i + M_0^2\right)^{1/2}} \\ \cos\theta_s &= \frac{\cos\theta_i + M_0}{\left(1 + 2\,M_0\,\cos\theta_i + M_0^2\right)^{1/2}} \end{aligned} \tag{8.101}$$

By setting

$$\begin{aligned} \sin\Theta_s &= \frac{\beta\sin\theta_s}{\left(1 - M_0^2\sin^2\theta_s\right)^{1/2}} \\ \cos\Theta_s &= \frac{\cos\theta_s}{\left(1 - M_0^2\sin^2\theta_s\right)^{1/2}} \end{aligned} \tag{8.102}$$

and

$$\begin{aligned} \Gamma_s &= (2\,K\,R)^{1/2}\,\sin\!\left(\frac{\Theta - \Theta_s}{2}\right) \\ \overline{\Gamma}_s &= (2\,K\,R)^{1/2}\,\sin\!\left(\frac{\Theta + \Theta_s}{2}\right) \quad \text{and} \end{aligned} \tag{8.103}$$

the incident field is given by

$$p_i(x,y,t) = a\exp(\mathrm{i}\,\omega\,T_i) \tag{8.104}$$

$$\phi_i(x,y,t) = \frac{\mathrm{i}\;a\beta^2}{\omega\,(1 - M_0\cos\Theta_s)}\exp(\mathrm{i}\,\omega\,T_i) \tag{8.105}$$

where

$$T_i = t - (M_0/\beta)\ R\cos(\Theta - \Theta_s) + \left(M_0^2/\beta\right)\ X \tag{8.106}$$

The continuous solution of the acoustic diffraction problem has been determined by Jones [184]. It is given by

$$\phi_c(x,y,t) = \frac{\mathrm{i}\ a\beta^2}{\omega\left(1 - M_0\cos\Theta_s\right)} \frac{1}{\sqrt{\pi}} \exp(\mathrm{i}\,\pi/4 + \mathrm{i}\,\omega\,T_d)\left[F(\Gamma_s) + F(\overline{\Gamma}_s)\right] \tag{8.107}$$

$$p_c(x,y,t) = \frac{a}{\sqrt{\pi}} \exp(\mathrm{i}\,\pi/4 + \mathrm{i}\,\omega\,T_d)\left[F(\Gamma_s) + F(\overline{\Gamma}_s) - \frac{\mathrm{i}\ M_0\sin(\Theta/2)\cos(\Theta_s/2)}{1 - M_0\cos\Theta_s}\left(\frac{2}{K\,R}\right)^{1/2}\right] \tag{8.108}$$

where

$$T_d = t - \frac{M_0}{\beta}R + \frac{M_0^2}{\beta}X \tag{8.109}$$

The first term in equation (8.108) is proportional to $\phi_c(x,y,t)$. Therefore, the two contributions of the diffracted pressure separately satisfy the wave equation and the half-plane boundary conditions in the absence of a vortex-sheet. However, the second term introduces a non integrable singularity at the trailing edge that must be removed by imposing a Kutta condition. The discontinuous solution is thus given by

$$p(x,y,t) = p_c + p_e = \frac{a}{\sqrt{\pi}} \exp\left(\mathrm{i}\,\pi/4 + \mathrm{i}\,\omega\,T_d\right)\left[F(\Gamma_s) + F(\overline{\Gamma}_s)\right] \tag{8.110}$$

where

$$p_e(x,y,t) = \mathrm{i}\ \frac{a}{\sqrt{\pi}} \exp\left(\mathrm{i}\,\pi/4 + \mathrm{i}\,\omega\,T_d\right) \frac{M_0\sin(\Theta/2)\cos(\Theta_s/2)}{1 - M_0\cos\Theta_s}\left(\frac{2}{K\,R}\right)^{1/2} \tag{8.111}$$

Hence, the amplification factor is

$$r = \frac{\mathrm{i}\ M_0\sin(\Theta/2)\cos(\Theta_s/2)}{1 - M_0\cos\Theta_s}\left(\frac{2}{K\,R}\right)^{1/2}\left[F(\Gamma_s) + F(\overline{\Gamma}_s)\right]^{-1} \tag{8.112}$$

In the far field limit ($k\,R \to \infty$) r reduces to

$$r \simeq M_0\frac{\cos\Theta - \cos\Theta_s}{1 - M_0\cos\Theta_s} \tag{8.113}$$

and its maximum and minimum values are

$$\begin{aligned} r_{\max}(\Theta = 0) &= M_0\ \tfrac{1-\cos\Theta_s}{1-M_0} & \left(0 \le r_{\max} \le \frac{2\,M_0}{1 - M_0}\right) \\ r_{\min}(\Theta = \pm\pi) &= M_0\ \tfrac{-1-\cos\Theta_s}{1+M_0} & \left(\frac{-2\,M_0}{1 + M_0} \le r_{\min} \le 0\right) \end{aligned} \tag{8.114}$$

The amplification factor is positive in the angular sector $|\Theta| < \Theta_s$, where the Kutta condition has an enhancement effect of the diffracted acoustic field.

The harmonic solutions (8.108) and (8.110) can be used to determine the diffracted field of a plane pulse $p_i(x,y,t) = a\,\delta(T_i)$. Rienstra [181] obtained the following solution

$$\begin{aligned} p_c(x,y,t) &= a\,H(\Theta_s - \Theta)\ \delta(T_i) + a\,H(-\Theta_s - \Theta)\ \delta(\overline{T}_i) + \frac{a}{2\pi}\frac{H(T_d)}{\sqrt{T_d}}\left(\frac{2\,M_0\,R}{\beta}\right)^{1/2} \\ &\left[T_i^{-1}\sin\left(\frac{\Theta - \Theta_s}{2}\right) + \overline{T}_i^{-1}\sin\left(\frac{\Theta + \Theta_s}{2}\right) + \frac{2\beta}{R}\frac{\sin(\Theta/2)\cos(\Theta_s/2)}{1 - M_0\cos\Theta_s}\right] \end{aligned} \tag{8.115}$$

$$\begin{aligned} p(x,y,t) &= p_c + p_e = a\,H(\Theta_s - \Theta)\ \delta(T_i) + a\,H(-\Theta_s - \Theta)\ \delta(\overline{T}_i) \\ &+ \frac{a}{2\pi}\frac{H(T_d)}{\sqrt{T_d}}\left(\frac{2\,M_0\,R}{\beta}\right)^{1/2}\left[T_i^{-1}\sin\left(\frac{\Theta - \Theta_s}{2}\right) + \overline{T}_i^{-1}\sin\left(\frac{\Theta + \Theta_s}{2}\right)\right] \end{aligned} \tag{8.116}$$

where

$$\overline{T}_i = t - \frac{M_0}{\beta} R \cos(\Theta + \Theta_s) + \frac{M_0^2}{\beta} X \tag{8.117}$$

and

$$p_e(x, y, t) = -\frac{a}{2\pi} \frac{H(T_d)}{\sqrt{T_d}} \left(\frac{2 M_0 R}{\beta} \right)^{1/2} \frac{2\beta}{R} \frac{\sin(\Theta/2) \cos(\Theta_s/2)}{1 - M_0 \cos \Theta_s} \tag{8.118}$$

Therefore, as in the case of a harmonic plane wave, a vortex-sheet causes an increase of the diffracted pressure in the angular sector $|\Theta| < \Theta_s$.

The influence of the Kutta condition on the diffracted acoustic field can be investigated by calculating the amplification factor of the far pressure field caused by a vortex-sheet downstream of the trailing edge. The net effect can be obtained from a balance between the energy absorbed by the vortex shedding to the incident acoustic field and to the mean flow, and the acoustic energy generated by the interaction of the shed vorticity with the trailing edge. The net acoustic power can be calculated by integrating the acoustic energy flux upon two half-planes, one just above the vortex-sheet, the other just below the vortex-sheet. These two half-planes are connected at the trailing edge. The acoustic energy flux can be calculated by using the definition of Morfey [185]

$$\mathbf{I} = -\rho_0 U_0^3 \phi_t \left\{ \left(\phi_x + M_0^2 p \right) \hat{\imath} + \phi_y \hat{\jmath} \right\} \tag{8.119}$$

Thus, for the harmonic plane wave, the acoustic power P is given by

$$P(\theta_i, f) = \frac{\rho_0 U_\infty^4 a^2}{2\pi f} M_0 \cos^2(\theta_i/2) \, (1 + M_0 \cos \theta_i) \, (1 - M_0 + 2 M_0 \cos \theta_i) \tag{8.120}$$

f being the frequency of the wave. The last factor in equation (8.120) is responsible for the change of sign of the acoustic power P. It results that $P > 0$ for

$$M_0 < \frac{1}{1 - 2 \cos \theta_i} < 1/3 \tag{8.121}$$

As a result, if the mean flow Mach number is less then 1/3, the diffracted acoustic power is always reduced by the vortex shedding.

9

Trailing Edge Noise

9.1 Introduction

A solid surface immersed in a turbulent flow has a dual influence on the far pressure field. On one hand, it affects the structure of the flow field and, consequently, of the aerodynamic source of sound. On the other hand, a solid surface constitutes an acoustic impedence discontinuity which affects the pattern of the scattered acoustic field. The noise from a trailing edge is a *singular* problem for which the separation of these two effects can lead to physically inconsistent theoretical models.

A trailing edge in a fluctuating flow field generates an unsteady vortical wake. This phenomenon can be regarded as an unsteady boundary-layer separation due to the viscosity of the fluid. An inviscid model of the vortex shedding process consists in imposing an edge condition onto the aerodynamic field. Since the vortex shedding smoothes the singular behaviour of the flow at the trailing edge, a Kutta-Joukowski condition[1] is commonly imposed at the trailing edge. This requires that the flow velocity is finite at the trailing edge.

The physical connection between the smoothing effect of the vortical wake and the Kutta condition is not completely clear. The experimental works of Archibald [186] and Satyanarayana & Davis [187], for example, show that the Kutta condition is only partially fulfilled at the trailing edge of an airfoil in a high frequency fluctuating field. A viscous flow, in fact, has a characteristic relaxation time over which the flow reacts to an imposed disturbance. If this relaxation time is greater than the characteristic period of the perturbation field, the flow would not have enough time to fully satisfy the Kutta condition.

From these preliminary considerations it follows that the aeroacoustic sources are significantly affected by the hypothesis made on the behaviour of the flow at a trailing edge. This is a first difficulty in modeling the trailing edge noise. Another difficulty lies on the fact that an edge does not distinguish between an acoustic and a vortical disturbance. As a result, the unsteady pressure field induced by the wake itself can couple with the vortex shedding process causing an increase of the noise levels. A further difficulty is related to the diffraction effect of a boundary shear flow. This imposes some restrictions on the applicability of an acoustic analogy approach which is based on a rough separation between the description of the turbulent field, the aeroacoustic sources and the diffracting properties of the edge. Depending on the strategy used to face these difficulties, different theoretical results can be obtained concerning the role of the Kutta condition on the noise levels, as well as other underlying aspects of the problem.

Crighton [188], following the work of Orszag & Crow [189], investigated the interaction between an acoustic incident field, an unstable shear layer and the trailing edge of a flat-plate. He showed that, at low Mach numbers, a Kutta condition induces a change in the flow velocity dependence of the acoustic intensity from U_∞^4 to U_∞^2, provided that the vortex-sheet is unstable.

Jones [179] investigated the diffraction of the acoustic field generated by a source near the edge of a

[1]The Kutta-Joukowski condition is usually referred to as Kutta-condition.

semi-infinite flat-plate. He concluded that the Kutta condition causes an intense beaming effect along the plane of the plate.

Crighton & Leppington [190] found no significant effects of the Kutta condition on the acoustic radiation.

Davis [191] determined the noise generated by the vortex shedding from the trailing edge of a semi-infinite flat-plate, with and without the imposition of a Kutta condition. He found that, without a Kutta condition, the far field noise has a $\sin^2(\theta/2)$ directivity pattern and an intensity level increasing as U_∞^3. Conversely, with a Kutta condition, a beaming effect along the wake takes place and the noise intensity level increases as U_∞. Howe [84] pointed out that both Crighton's [188] and Davis' [191] analysis are erroneous since the radiation condition of outgoing waves at infinity is not satisfied.

Howe [13] demonstrated that the imposition of the Kutta condition removes the flow singularity at a sharp edge. As a consequence, it always leads to a reduction of the noise levels (see subsection 10.3.5). The wake intensity, in fact, is related in both amplitude and phase to the incident vortical disturbances and generates a sound field which cancels that generated by the incident turbulent field.

Rienstra [181] showed that the vortex shedding process extracts energy from both the incident acoustic field and the mean flow reducing the far field noise intensity (see section 8.4). However, the interaction between the trailing edge and the unsteady pressure field induced by the wake generates a noise radiation whose energy may exceed that absorbed by the wake.

In chapter 8, some models have been discussed which describe the problem of the trailing edge noise as an acoustic scattering problem involving a fluctuating pressure field near the edge and a semi-infinite plate. Ffowcs Williams & Hall [176] and Crighton & Leppington [161] [177] examined the scattering problem in the context of Lighthill's acoustic analogy theory. They related the acoustic far field to the turbulent quadrupole sources. Chase [81], [83] and Chandiramani [82] proposed a procedure to relate the far field acoustic spectrum to measurable statistical properties of the hydrodynamic pressure field in proximity of the edge. These properties are formally synthesized by the wavenumber/frequency spectrum of the driving pressure field. Rienstra [181] discussed the half-plane scattering problem of an acoustic incident field in the presence of a vortex-sheet shed from the trailing edge.

In the present chapter the problem of the trailing edge noise is discussed by giving more emphasis to the noise generation mechanisms occurring when vortical disturbances are convected past a trailing edge.

Crighton [160], using the method of matched asymptotic expansions, determined the noise radiated by a line-vortex convected past the edge of a semi-infinite flat-plate. The vortex moves under the influence of the image vortex and generates an unsteady near field driving an acoustic far field (see section 6.5). The radiated noise intensity was shown to have a $\sin^2(\theta/2)$ directivity pattern and a third power dependence on the flow velocity. The latter result was in agreement with the general result obtained by Ffowcs Williams & Hall [176] and Crighton & Leppington [161] according to which the effect of the interaction between a fluctuating turbulent flow and the edge of a semi-infinite plate is to increase the far field acoustic intensity by a factor of M_∞^{-3}. In fact, the acoustic energy radiated by a vortex filament in free space or in the presence of an infinite rigid plate follows a sixth power law [192].

Amiet [193] related the acoustic spectrum to the wall pressure spectrum by means of an airfoil response function. In order to adopt a wall pressure distribution with the same characteristics it would have in the absence of the trailing edge, Amiet assumed that the turbulence was statistically stationary when convected past the trailing edge. Thus, he showed that the noise radiated from the edge of a semi-infinite flat-plate is generated by dipole sources induced by the turbulent flow near the trailing edge.

Howe [13] discussed the general problem of the noise from an airfoil interacting with a frozenly convected turbulent eddy. By supposing a small flow Mach number such that $M_\infty^2 \ll 1$, the aerodynamic problem was posed in terms of an incompressible potential flow problem. In addition, the acoustic problem was formulated in terms of Howe's [20] acoustic analogy theory, which describes the aerodynamic noise generated by vorticity and by entropy gradients (see chapter 6). In the limit of a frozen convection hypothesis Howe showed that, when a line-vortex is convected past the edge of a semi-infinite flat-plate, a Kutta condition results in a vortex shedding that exactly cancel the sound generated by the vortex-edge interaction. Furthermore, in the case of an acoustically compact airfoil, the effect of the vortex shedding is to annhilate the field diffracted by the trailing edge. Thus, at low Mach numbers, the effect of a Kutta condition is always to reduce the far field noise. Since the fulfillment level of the Kutta condition decreases as the frequency of the fluctuating flow increases, the effectiveness of the vortical wake in reducing the radiated noise decreases at higher frequency. As a consequence, a trailing edge in a turbulent flow acts as a source of high frequency noise.

Howe [84] revisited the problem of the trailing edge noise and proposed a comprehensive theory. This includes, as special cases, the models developed by Ffowcs Williams & Hall [176], Crighton [160], Chase [81] [83] and Chandiramani [82]. All these models were shown to give essentially the same results when properly interpreted. Extending his previous formulation [13], Howe examined the influence of the Kutta condition on the noise levels by assuming a wake convection velocity w which differs from the convection velocity v of the vortical disturbances within the boundary-layer. Hence, he found that the sound pressure level with no Kutta condition imposed exceeds by a factor $(1-w/v)^{-2}$ the level predicted by imposing a Kutta condition. This factor diverges when the Kutta condition is absolutely satisfied, i.e. when $w = v$.

Howe's analysis revealed that the edge condition can have a critical influence on the radiation from a trailing edge and showed the importance of an experimental investigation of the flow behaviour near a trailing edge. Brooks & Hodgson [85] performed an experimental investigation of the low Mach number trailing edge noise generated by an NACA-0012 airfoil at several angles of attack and with different degrees of edge bluntness. The airfoil was provided of roughness trips on both its sides in order to ensure a well developed turbulent boundary-layer. Brooks & Hodgson discussed the theories developed by Chandiramani [82], Chase [83] and Howe [84] by relating the statistical behaviour of the far pressure field to the wall pressure statistical behaviour. This was described by means of two-points correlation measurements between pressure transducers mounted on the airfoil surface.

In order to investigate the vortex shedding process in terms of a wake convection velocity w, as proposed by Howe [84], Brooks & Hodgson [85] performed coherence measurements between a cross hot wire just downstream of the edge and a pressure transducer near the edge. No vortex shedding was detected. From this result and the verified consistency of the evanescent wave model of Chase [83] in the edge region without the modification proposed by Howe, Brooks & Hodgson concluded that the prediction of trailing edge noise requires the wake convection velocity to be vanishing small compared to the eddy convection velocity within a turbulent boundary-layer. On the other hand, the condition $w \to 0$ in Howe's formulation reduces the difference between the acoustic far field predicted by imposing or not a Kutta condition. Finally, for an airfoil with a sharp trailing edge, Brooks & Hodgson observed a good agreement with the theoretical U_∞^5 power law and the $\sin^2(\theta/2)$ directivity pattern.

The continuous improvements in both the computational fluid dynamics techniques and the computer performances allow numerical investigations of the physical mechanisms involved in the generation of aerodynamic sound. Some numerical studies have been devoted in the last years to the trailing edge noise. Singer *et al.* [194] used a RANS/FW-H[2] hybrid approach to predict the noise radiated by a two-dimensional trailing edge in a turbulent flow. Manoha *et al.* [195] performed a LES/FW-H[3] hybrid simulation in order to calculate the noise generated by a blunt trailing edge of a three-dimensional plate. Unfortunately, both these analyses did not attempt to relate the flow behaviour in proximity of a trailing edge to the sound generation mechanisms.

In the following of the present chapter Amiet's [193] trailing edge dipole model and Howe's [84] trailing edge noise theory are presented.

[2]Reynolds-averaged Navier Stokes flow simulation and Ffowcs Williams & Hawkings acoustic analogy formulation.

[3]Large-eddy filtered Navier Stokes flow simulation and Ffowcs Williams & Hawkings acoustic analogy formulation.

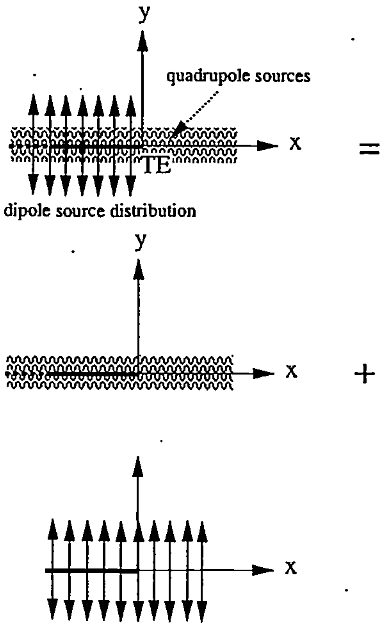

FIGURE 9.1: Amiet's solution scheme of the trailing edge noise problem.

9.2 Amiet's Trailing Edge Noise Model

Consider a semi-infinite flat-plate ($-2b \leq x \leq 0$, $z = 0$) embedded in a statistically stationary turbulent field which is unaffected by the presence of the trailing edge. The spectral components of the surface pressure field are convected at the velocity U_c along the streamwise direction x and take the form

$$P = P_0 \exp\{\mathrm{i}\,\omega\,(t - x/U_c) - \mathrm{i}\,k_y\,y\} = P_0 \exp\{-\mathrm{i}\,(k_x\,x - k_y\,y) + \mathrm{i}\,\omega\,t\} \tag{9.1}$$

where $k_x = \omega/U_c$ and k_y are the streamwise and the spanwise wall pressure wavenumbers, respectively. As sketched in Fig.9.1, the flow field results from a combination of an unbounded distribution of quadrupole sources in the x-direction and an induced dipole distribution on the plate. Having supposed a statistical stationary turbulent field, this flow configuration can be interpreted as the superposition of two configurations: the first consists of the same quadrupole distribution, together with an infinite dipole distribution in both the upstream and the downstream extensions; the second configuration is constituted by an infinite dipole distribution. As argued by Schwartzchild [196], the second dipole distribution is such that the first dipole distribution on the downstream plate extension is canceled by applying a Kutta condition at the trailing edge and by imposing a no-flow condition on the plate surface.

In a previous work Amiet [129] obtained from the general Schwartzchild's solution the high frequency response function of an airfoil in a turbulent flow (see section 4.5). Amiet's analysis was based on the assumption that the vorticity shed from the trailing edge is convected at the free stream velocity[4] U_∞. In terms of surface pressure jump induced by the pressure disturbances (9.1), Amiet's high frequency airfoil response for $k_y = 0$ (parallel gust-airfoil interaction) has the form

$$g(x,\omega,U_c) = \left\{(1+\mathrm{i})\,E^*\left[-\frac{x}{b}\,(1+M_\infty)\,\mu + k_x\right] - 1\right\}\exp(-\mathrm{i}\,k_x\,x) \quad \text{for} \quad -2b \leq x \leq 0 \tag{9.2}$$

where b denotes the airfoil semi-chord,

$$\mu = \frac{M_\infty\,\omega\,b}{U_c\,(1 - M_\infty^2)} \tag{9.3}$$

[4]This assumption conflicts with the turbulent statistical stationary hypothesis. In the trailing edge noise analysis, in fact, a convection velocity U_c has been supposed, which is smaller than U_∞.

and

$$E^*(x) = \int_0^x (2\,\pi\,\xi)^{-1/2}\, e^{-i\,\xi}\, d\xi \tag{9.4}$$

is a combination of Fresnel's integrals.

The pressure measured at a given point and at a given frequency results from a superposition of spectral components (9.1), for which the product $k_x\,U_c$ is a constant. As a consequence, the sound field at a given frequency results from a superposition of the sound generated by all these spectral components. Experimental data show that the convection velocity is a weak function of the frequency. However, by assuming a constant average value $U_c = 0.8\,U_\infty$, a given value of ω is associated to a single value of the wavenumber k_x. With this assumption a standard integral technique can be applied to relate the radiated sound spectral components to the spectral components of the surface pressure jump defined in equation (9.2).

By supposing that $M_\infty\,k_x\,d \gg 1$, with d denoting the airfoil span, and by assuming a one-side turbulent boundary-layer, Amiet [193] obtained the following expression for the far field acoustic spectrum in the mid-span plane $y = 0$

$$S_{pp}(x, z, \omega) = d\left(\frac{\omega\,b\,z}{2\,\pi\,c_0\,\sigma^2}\right)^2 \int_0^\infty S_{qq}(\omega, y)\; dy\,|\mathcal{L}|^2 \tag{9.5}$$

where $\sigma^2 = x^2 + \beta^2\,z^2$, $\beta^2 = 1 - M_\infty^2$, $S_{qq}(\omega, y)$ is the spanwise cross-spectrum of the wall pressure fluctuations, and

$$\mathcal{L} = \frac{1}{b}\int_{-2b}^{0} g(\xi, \omega, U_c)\; e^{-i\,\mu\,\xi(M_\infty - x/\sigma)}\, d\xi \tag{9.6}$$

Substituting the response function (9.2) into equation (9.6) and integrating yields

$$\begin{aligned}\mathcal{L} = {} & 1 - e^{-i\,2\Theta} + \frac{1}{\Theta}(1+i) \\ & \left\{\sqrt{\frac{1 + M_\infty + k_x/\mu}{1 + k_x/\sigma}}\; E^*\left[2\,\mu\,(1 + x/\sigma)\right] e^{-i\,2\Theta} - E^*\left[2\,(1 + M_\infty)\,\mu + 2\,k_x\right]\right\}\end{aligned} \tag{9.7}$$

where $\Theta = k_x + \mu\,(M_\infty - x/\sigma)$.

On the base of Corcos' [99] similarity model, it can be written

$$S_{qq}(\omega, y) = S_{qq}(\omega, 0)\; B(\omega\,y/U_c) \tag{9.8}$$

As a result

$$\int_0^\infty S_{qq}(\omega, y)\; dy = \frac{U_c\,S_{qq}(\omega, 0)}{\omega}\int_0^\infty B(\eta)\, d\eta \tag{9.9}$$

where $B\,(\omega\,y/U_c)$ is an exponentially decaying function of its argument. Its integrated value, based on Corcos' measurements, is approximately 2.1.

Finally, by changing to polar observer co-ordinates and by supposing a turbulent boundary-layer on both the plate sides, the far field acoustic spectrum takes the form

$$S_{pp}(r, \theta, \omega) = 2\,d\left\{\frac{\omega\,b\,\sin\theta}{2\,\pi\,c_0\,r\,(1 - M_\infty^2\sin^2\theta)}\right\}^2\; 2.1\,\frac{U_c}{\omega}\;|\mathcal{L}|^2\; S_{qq}(\omega, 0) \tag{9.10}$$

where r is the observer distance from the trailing edge and $\theta = \tan^{-1}(z/x)$ is the observation angle with respect to the streamwise direction.

Equation (9.10) relates the far field acoustic spectrum S_{pp} to the wall pressure spectrum S_{qq} near the trailing edge.

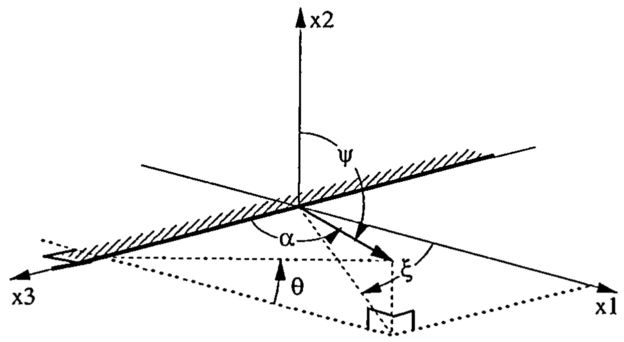

FIGURE 9.2: Scheme of the half-plane co-ordinate system.

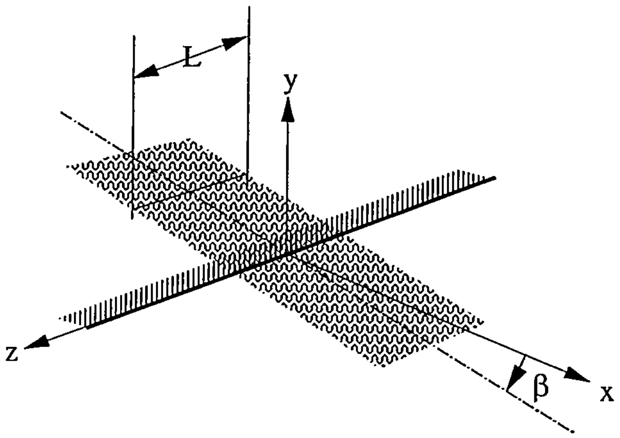

FIGURE 9.3: Turbulent ribbon wetting one side of a half-plane. β denotes the angle between the axis of the ribbon and the normal to the edge on the plane of the plate. L denotes the width of the ribbon.

9.3 Howe's Theory of Trailing Edge Noise

Consider an ideal fluid and neglect the dissipation due to the viscosity and the heat transfer. From equation (1.61) it follows that $\mathrm{D}S/\mathrm{D}t$. Thus, for inlet uniform conditions, a boundary-layer wall jet flow is also isentropic. As shown by Howe [20], when the acoustic medium is in motion it is convenient to express the Lighthill's acoustic analogy in terms of total enthalpy B which satisfies the following wave equation

$$\left\{\frac{\mathrm{D}}{\mathrm{D}t}\left(\frac{1}{c^2}\frac{\mathrm{D}}{\mathrm{D}t}\right)+\frac{1}{c^2}\frac{\mathrm{D}\mathbf{v}}{\mathrm{D}t}\cdot\nabla-\nabla^2\right\}B=\nabla\cdot(\boldsymbol{\omega}\times\mathbf{v})-\frac{1}{c^2}\frac{\mathrm{D}\mathbf{v}}{\mathrm{D}t}\cdot(\boldsymbol{\omega}\times\mathbf{v}) \tag{9.11}$$

where c is the local speed of sound and $\boldsymbol{\omega}=\nabla\times\mathbf{v}$ is the vorticity vector. The total enthalpy B is defined as

$$B=h+\frac{v^2}{2} \tag{9.12}$$

where $h=\int \mathrm{d}p/\rho$ is the specific enthalpy.

For a homentropic flow the momentum equation written in Crocco's form

$$\frac{\partial\mathbf{v}}{\partial t}+\nabla B=-\boldsymbol{\omega}\times\mathbf{v}+T\nabla S \tag{9.13}$$

yields

$$\frac{1}{c^2}\frac{\mathrm{D}\mathbf{v}}{\mathrm{D}t}\cdot(\nabla B+\boldsymbol{\omega}\times\mathbf{v})=-\frac{1}{c^2}\frac{\mathrm{D}\mathbf{v}}{\mathrm{D}t}\cdot\frac{\partial\mathbf{v}}{\partial t}=\frac{1}{\rho c^2}\nabla p\cdot\frac{\partial\mathbf{v}}{\partial t} \tag{9.14}$$

which can be introduced into equation (9.11) providing the convected wave equation

$$\left\{\frac{\mathrm{D}}{\mathrm{D}t}\left(\frac{1}{c^2}\frac{\mathrm{D}}{\mathrm{D}t}\right)-\nabla^2\right\}B=\nabla\cdot(\boldsymbol{\omega}\times\mathbf{v})-\frac{1}{\rho c^2}\nabla p\cdot\frac{\partial\mathbf{v}}{\partial t} \tag{9.15}$$

In order to simplify equation (9.15), the following approximations can be introduced.

- The boundary-layer/wall jet turbulent eddies are frozenly convected past the trailing edge.
- The eddy convection velocity is approximated by the mean shear velocity $\mathbf{V}=\mathbf{V}(x_2)=(V_1,0,V_3)$. Consequently, the dipole source term in equation (9.15) can be approximated as $\nabla\cdot(\boldsymbol{\omega}\times\mathbf{V})$.
- A vortical wake $\overline{\omega}$ is shed from the trailing edge where a Kutta condition is imposed. The vorticity shed is supposed to be convected at the velocity $\mathbf{W}=(W_1,0,W_3)$ along the plane of the plate downstream of the trailing edge.
- The mean shear velocity $\mathbf{V}$ and the wake convection velocity $\mathbf{W}$ satisfy the condition M_v^2, $M_w^2 \ll 1$. Thus, the effect of fluid compressibility are not significant near the trailing edge, and the speed of sound in the wave operator can be assumed to be constant.
- Second order terms in the material derivative of B are neglected, it thus results that

$$\left(\frac{\mathrm{D}}{\mathrm{D}t}\right)^2B=\left(\frac{\partial}{\partial t}+U_0\frac{\partial}{\partial x_1}\right)^2B \tag{9.16}$$

  where U_0 is the mean flow velocity

Therefore, equation (9.15) takes the simplified form

$$\left\{\frac{1}{c^2}\left(\frac{\partial}{\partial t}+U_0\frac{\partial}{\partial x_1}\right)^2-\nabla^2\right\}B=\nabla\cdot(\boldsymbol{\omega}\times\mathbf{V})+\nabla\cdot(\overline{\boldsymbol{\omega}}\times\mathbf{W}) \tag{9.17}$$

The flow in the vicinity of the plate is irrotational and can be described in terms of velocity potential ϕ by means of Bernoulli's equation

$$\frac{\partial\phi}{\partial t}=-B \tag{9.18}$$

which yields the zero normal velocity boundary condition

$$\frac{\partial B}{\partial n}=0 \tag{9.19}$$

provided that the plate is rigid.

By supposing that turbulent eddies convected at different velocity $\mathbf{V}$ are not correlated, the problem described by equations (9.17) and (9.19) can be simplified by describing B as a combination of solutions related to independent incident turbulent layer. Thus, setting

$$\boldsymbol{\omega}(x_1-V_1\,t,x_2,x_3-V_3\,t)\times\mathbf{V}(x_2)=\int_0^\infty \mathrm{Q}(x_1-V_1\,t,y,x_3-V_3\,t)\;\delta(x_2-y)\;\mathrm{d}y \tag{9.20}$$

$$\overline{\boldsymbol{\omega}}(x_1-W_1\,t,x_3-W_3\,t)\times\mathbf{W}=\delta(x_2)\int_0^\infty \mathrm{q}(x_1-W_1\,t,y,x_3-W_3\,t)\;\mathrm{d}y \tag{9.21}$$

$$B=\int_0^\infty \mathcal{B}\,\mathrm{d}y \tag{9.22}$$

$$\mathcal{B}=\mathcal{B}_Q+\mathcal{B}_q \tag{9.23}$$

and substituting into equations (9.17) and (9.19) yields

$$\left\{\frac{1}{c^2}\left(\frac{\partial}{\partial t}+U_0\frac{\partial}{\partial x_1}\right)^2-\nabla^2\right\}\mathcal{B}_Q=\nabla\cdot\{\mathbf{Q}\,\delta(x_2-y)\} \tag{9.24}$$

$$\left\{\frac{1}{c^2}\left(\frac{\partial}{\partial t}+U_0\frac{\partial}{\partial x_1}\right)^2-\nabla^2\right\}\mathcal{B}_q=\nabla\cdot\{\mathbf{q}\,\delta(x_2)\} \tag{9.25}$$

$$\frac{\partial}{\partial x_2}\left(\mathcal{B}_Q+\mathcal{B}_q\right)=0 \quad \text{for} \quad x_1<0, \quad x_2=0 \tag{9.26}$$

Let us consider the Fourier transform

$$\begin{aligned}
&\mathbf{Q}(x_1-V_1\,t,y,x_3-V_3\,t)=\\
&=\iint_{-\infty}^{\infty}\mathrm{d}\mu_1\,\mathrm{d}\mu_3\,\hat{\mathbf{Q}}(\mu_1,y,\mu_3)\exp\{\mathrm{i}\,(\mu_1\,x_1+\mu_3\,x_3)-\mathrm{i}\,(\mu_1\,V_1\,t+\mu_3\,V_3\,t)\}=\\
&=\iint_{-\infty}^{\infty}\mathrm{d}\mu_1\,\mathrm{d}\mu_3\,\hat{\mathbf{Q}}(\mu_1,y,\mu_3)\exp\{\mathrm{i}\,(\mu_1\,x_1+\mu_3\,x_3)\}\exp(-\mathrm{i}\,\omega_y\,t)
\end{aligned} \tag{9.27}$$

where $\omega_y(y)=\mu_1V_1+\mu_3V_3$ denotes the convective frequency. The solution of the diffraction problem (9.24) in the small mean flow Mach number limit is

$$\begin{aligned}
\mathcal{B}_Q=&-\frac{1}{2}\iint_{-\infty}^{\infty}\mathrm{d}\mu_1\,\mathrm{d}\mu_3\frac{\boldsymbol{\mu}\cdot\hat{\mathbf{Q}}}{\gamma(\mu_1)}\exp\{\mathrm{i}\,[\mu_1\,x_1+\gamma(\mu_1)\,(y-x_2)+\mu_3\,x_3]\}\exp(-\mathrm{i}\,\omega_y\,t)\\
&-\mathrm{i}\,\frac{\operatorname{sign}(x_2)}{4\,\pi}\int_{-\infty+\mathrm{i}\,\epsilon}^{+\infty+\mathrm{i}\,\epsilon}\mathrm{d}k\iint_{-\infty}^{\infty}\mathrm{d}\mu_1\,\mathrm{d}\mu_3\\
&\frac{\boldsymbol{\mu}\cdot\hat{\mathbf{Q}}\exp\{\mathrm{i}\,[(k-M_0\,\omega_y/c)\,x_1+\Gamma(k)\,|x_2|+\gamma(\mu_1)\,y+\mu_3\,x_3]\}}{\sqrt{\lambda+k}\sqrt{\lambda-(\mu_1+M_0\,\omega_y/c)}\,[k-(\mu_1+M_0\,\omega_y/c)]}\exp(-\mathrm{i}\,\omega_y\,t)
\end{aligned} \tag{9.28}$$

where $\epsilon\to 0^+$, $\boldsymbol{\mu}=(\mu_1,-\gamma(\mu_1)\,,\mu_3)$,

$$\lambda=\begin{cases}\operatorname{sign}(\omega_y)\sqrt{\left(\frac{\omega_y}{c}\right)^2-\mu_3^2} & \text{for} \quad \left(\frac{\omega_y}{c}\right)^2>\mu_3^2\\ \mathrm{i}\sqrt{\mu_3^2-\left(\frac{\omega_y}{c}\right)^2} & \text{for} \quad \left(\frac{\omega_y}{c}\right)^2<\mu_3^2\end{cases} \tag{9.29}$$

$$\gamma(\mu_1)=\begin{cases}\operatorname{sign}(\omega_y)\sqrt{\lambda^2-\left(\mu_1+\frac{M_0\,\omega_y}{c}\right)^2} & \text{for} \quad \lambda^2>\left(\mu_1+\frac{M_0\,\omega_y}{c}\right)^2\\ \mathrm{i}\sqrt{\left(\mu_1+\frac{M_0\,\omega_y}{c}\right)^2-\lambda^2} & \text{for} \quad \lambda^2<\left(\mu_1+\frac{M_0\,\omega_y}{c}\right)^2\end{cases} \tag{9.30}$$

$$\Gamma(k)=\begin{cases}\operatorname{sign}(\omega_y)\sqrt{\lambda^2-k^2} & \text{for} \quad \lambda^2>k^2\\ \mathrm{i}\sqrt{k^2-\lambda^2} & \text{for} \quad \lambda^2<k^2\end{cases} \tag{9.31}$$

The branches of $\sqrt{\lambda+k}$ and $\sqrt{\lambda-(\mu_1+M_0\,\omega_y/c)}$ are chosen to be positive or to have positive imaginary parts on the real k_1 and μ_1 axes, respectively.

The solution (9.28) includes two contributions, the first constitutes the evanescent wave field generates by the dipole source $\mathbf{Q}$ in the absence of the plate, the second accounts for the presence of the diffracting plate. Setting

$$\begin{aligned}
\nu_1&=\frac{\mu_1V_1+\mu_3\,(V_3-W_3)}{W_1}\\
\nu_3&=\mu_3
\end{aligned} \tag{9.32}$$

that is $\nu_1 W_1 + \nu_3 W_3 = \omega_y$ and

$$\mathbf{q}(x_1 - W_1\,t, y, x_3 - W_3\,t) = \\ = \iint_{-\infty}^{\infty} \mathrm{d}\nu_1\,\mathrm{d}\nu_3\,\hat{\mathbf{q}}(\nu_1, y, \nu_3) \exp\{\mathrm{i}\,(\nu_1\,x_1 + \nu_3\,x_3) - \mathrm{i}\,(\nu_1 W_1 t + \nu_3 W_3 t)\} \tag{9.33}$$

yields

$$\mathcal{B}_q = -\frac{1}{2} \iint_{-\infty}^{\infty} \mathrm{d}\nu_1\,\mathrm{d}\nu_3 \frac{\boldsymbol{\nu}\cdot\hat{\mathbf{q}}}{\gamma(\nu_1)} \exp\{\mathrm{i}\,[\nu_1\,x_1 - \gamma(\nu_1)\,x_2 + \mu_3\,x_3]\} \exp(-\mathrm{i}\,\omega_y\,t)$$
$$-\mathrm{i}\,\frac{\mathrm{sign}(x_2)}{4\,\pi} \int_{-\infty+\mathrm{i}\,\epsilon}^{+\infty+\mathrm{i}\,\epsilon} \mathrm{d}k \iint_{-\infty}^{\infty} \mathrm{d}\nu_1\,\mathrm{d}\nu_3$$
$$\frac{\boldsymbol{\nu}\cdot\hat{\mathbf{q}} \exp\{\mathrm{i}\,[(k - M_0\,\omega_y/c)\,x_1 + \Gamma(k)\,|x_2| + \gamma\,(\nu_1)\;z + \mu_3\,x_3]\}}{\sqrt{\lambda + k}\sqrt{\lambda - (\nu_1 + M_0\,\omega_y/c)}\,[k - (\nu_1 + M_0\,\omega_y/c)]} \exp(-\mathrm{i}\,\omega_y\,t) \tag{9.34}$$

where $\boldsymbol{\nu} = (\nu_1, -\gamma(\nu_1), \nu_3)$. The branch of $\sqrt{\lambda - (\nu_1 + M_0\,\omega_y/c)}$ is chosen to be positive or to have a positive imaginary part on the real axis ν_1.

The strength of the wake dipole $\mathbf{q}$ can be related to the incident dipole strength $\mathbf{Q}$ by applying a Kutta condition onto the trailing edge. Hence, requiring the flow to leave the plate tangentially provides

$$\frac{\partial}{\partial x_2}(\mathcal{B}_Q + \mathcal{B}_q) \to 0 \quad \text{as} \quad x_1 \to 0^+ \quad \text{and} \quad x_2 = 0 \tag{9.35}$$

that is

$$\frac{\partial}{\partial x_2}\mathcal{B}_Q + \frac{\partial}{\partial x_2}\mathcal{B}_q =$$
$$\frac{\mathrm{i}}{2} \iint_{-\infty}^{\infty} \mathrm{d}\mu_1\,\mathrm{d}\mu_3 \left(\boldsymbol{\mu}\cdot\hat{\mathbf{Q}}\,\mathrm{e}^{\mathrm{i}\,\gamma(\mu_1)\,z}\,\gamma\,(\mu_1) + \boldsymbol{\nu}\cdot\hat{\mathbf{q}}\,\gamma\,(\nu_1)\right) \exp\{\mathrm{i}\,[(k - M_0\,\omega_y/c)\,x_1 + \mu_3\,x_3 - \omega_y t]\}$$
$$-\frac{\mathrm{i}}{4\,\pi} \int_{-\infty+\mathrm{i}\,\epsilon}^{+\infty+\mathrm{i}\,\epsilon} \mathrm{d}k \iint_{-\infty}^{\infty} \mathrm{d}\mu_1\,\mathrm{d}\mu_3\,\sqrt{\lambda - k}\,\exp\{\mathrm{i}\,[(k - M_0\,\omega_y/c)\,x_1 + \mu_3\,x_3 - \omega_y t]\}\,\mathcal{K} \tag{9.36}$$

with

$$\mathcal{K} = \frac{\boldsymbol{\mu}\cdot\hat{\mathbf{Q}}\,\mathrm{e}^{\mathrm{i}\,\gamma(\mu_1)\,z}}{\sqrt{\lambda - (\mu_1 + M_0\,\omega_y/c)}\,[k - (\mu_1 + M_0\,\omega_y/c)]} + \frac{\boldsymbol{\nu}\cdot\hat{\mathbf{q}}}{\sqrt{\lambda - (\nu_1 + M_0\,\omega_y/c)}\,[k - (\nu_1 + M_0\,\omega_y/c)]} \tag{9.37}$$

Only the diffraction contribution (second integral) in equation (9.36) is singular. Thus, as shown by Howe [84], the condition

$$\frac{\boldsymbol{\mu}\cdot\hat{\mathbf{Q}}\mathrm{e}^{\mathrm{i}\,\gamma(\mu_1)\,z}}{\sqrt{\lambda - (\mu_1 + M_0\,\omega_y/c)}} = -\frac{\boldsymbol{\nu}\cdot\hat{\mathbf{q}}}{\sqrt{\lambda - (\nu_1 + M_0\,\omega_y/c)}} \tag{9.38}$$

is sufficient to ensure that $\partial\mathcal{B}/\partial x_2 \to 0$ at the trailing edge.

It can be observed that if $\mathbf{W} = \mathbf{V}$ then $\mu = \nu$, and the edge condition (9.38) leads to a vanishing sum of $\mathcal{B}_Q$ and $\mathcal{B}_q$. Therefore, no edge noise is radiated when the incident and the shed vorticity are convected at the same velocity.

Let us introduce the polar co-ordinates (R, θ, α) (see Fig.9.2) by setting

$$\begin{aligned} x_1 &= R \sin\alpha \cos\theta \\ x_2 &= R \sin\alpha \sin\theta \\ x_3 &= R \cos\alpha \end{aligned} \tag{9.39}$$

The far field limit of $\mathcal{B}_Q$ has the form

$$\begin{aligned} \mathcal{B}_Q = & \frac{-\mathrm{i}\sqrt{M_{v_1}}\sin(\theta/2)\sqrt{\sin\alpha}}{R\sqrt{2}\,(1 - M_{v_R})\,(1 - M_{v_1}\sin\alpha - M_{v_3}\cos\alpha)^{1/2}} \\ & \int_{-\infty}^{\infty} \frac{\mathrm{d}\omega}{\omega} \tilde{\boldsymbol{\mu}} \cdot \hat{\mathbf{Q}} \exp\left\{ -\frac{|\omega|\, z}{V_1}\,(1 - M_{v_3}\cos\alpha) + \frac{\mathrm{i}\,\omega}{c}\,(R - M_0\, x_1 - ct) \right\} \end{aligned} \tag{9.40}$$

where $M_{v_i} = V_i/C$ and $M_{v_R} \simeq M_v \sin\alpha\cos\theta$ are the eddy convection Mach number and its projection in the observer direction, respectively, and

$$\begin{aligned} \tilde{\mu}_1 &= \frac{\omega}{V_1}\,(1 - M_{v_3}\cos\alpha) \\ \tilde{\mu}_2 &= -\mathrm{i}\,\frac{|\omega|}{V_1}\,(1 - M_{v_3}\cos\alpha) \\ \tilde{\mu}_3 &= \frac{\omega}{c}\cos\alpha \end{aligned} \tag{9.41}$$

At low mean flow Mach number, the radial velocity in the far field is given by

$$v = c\, M_{0_R} + \frac{p}{\rho_0\, c} \tag{9.42}$$

which yields

$$\frac{v^2}{2} \simeq \frac{M_{0_R}\, p}{\rho_0} \tag{9.43}$$

p being the acoustic pressure. It thus results that

$$\mathcal{B}_Q \simeq \frac{p_Q}{\rho_0} + \frac{M_{0_R}\, p_Q}{\rho_0} \tag{9.44}$$

and

$$p_Q = \frac{\rho_0}{1 + M_{0_R}}\, \mathcal{B}_Q \tag{9.45}$$

A similar procedure provides the far field expression of the wake contribution p_q. This, can be added to p_Q in order to obtain the far field acoustic radiation generated by a turbulent boundary-layer convected past a trailing edge and by a vortical wake shed from the trailing edge. Finally, by integrating with respect to y, the far field acoustic pressure takes the form

$$\begin{aligned} p(R, \theta, \alpha, t) = & \frac{-\mathrm{i}\,\rho_0 \sin(\theta/2)\sqrt{\sin\alpha}}{R\sqrt{2}\,(1 + M_{0_R})\,(1 - M_{W_R})} \int_{-\infty}^{\infty} \frac{\mathrm{d}\omega}{\omega} \int_0^{\infty} \mathrm{d}y \\ & \frac{\sqrt{M_{v_1}}\,(1 - \sigma(y))\, \tilde{\boldsymbol{\mu}} \cdot \hat{\mathbf{Q}} \exp\left\{ -\frac{|\omega| y}{V_1}\,(1 - M_{v_3}\cos\alpha) + \frac{\mathrm{i}\omega}{c}\,(R - M_0\, x_1 - ct) \right\}}{(1 - M_{v_R})\,(1 - M_{v_1}\sin\alpha - M_{v_3}\cos\alpha)^{1/2}} \end{aligned} \tag{9.46}$$

where the function $\sigma(y) = W/V(y)$ results from having applied the Kutta condition (9.38) with $\tilde{\nu}_1 = (\omega/W_1)(1 - M_{w_3}\cos\alpha)$ and $\lambda = (\omega/c)\sin\alpha$. Interestingly, if $\sigma = 1$ the acoustic pressure p vanishes because the incident and the shed vorticity generate equal and opposite far field perturbations.

Consider a boundary-layer/wall jet flow (see Fig.9.3) for which

$$\tan\beta = \frac{V_3}{V_1} = \frac{W_3}{W_1} \ll 1 \tag{9.47}$$

From the definitions (9.41) it follows that

$$\begin{aligned} \tilde{\mu}_1 &\simeq \frac{\omega}{V_1} \\ \tilde{\mu}_2 &\simeq -\mathrm{i}\frac{|\omega|}{V_1} \\ \tilde{\mu}_3 &= \frac{\omega}{c}\cos\alpha \end{aligned} \tag{9.48}$$

The dipole source is thus approximated by

$$\tilde{\boldsymbol{\mu}} \cdot \hat{\mathbf{Q}} \equiv \tilde{\boldsymbol{\mu}} \cdot \hat{\boldsymbol{\omega}} \times \mathbf{V}(y) \simeq -\tilde{\mu}_2 \hat{\omega}_3 V_1 = -\mathrm{i}\ |\omega|\ \hat{\omega}_3 \tag{9.49}$$

where $\hat{\boldsymbol{\omega}} = (\omega_1, \hat{\omega_2}, \omega_3)$ is the Fourier transform of the incident vorticity $\boldsymbol{\omega}$, defined in equation (9.27). Equation (9.49) shows that the most important contribution to the trailing edge noise is generated by the component of the vorticity parallel to the edge.

By supposing that the eddy convection velocity V does not depend on the distance y from the plate, and by introducing the Strouhal number $\omega\, l_1/V_1 \simeq \mu_1\, l_1$ based on the vorticity correlation scale l_1 in the x_1-direction, the acoustic pressure (9.46) takes the form

$$\begin{aligned} p(R,\theta,\alpha,t) \simeq{}& \frac{-\rho_0\ \sin(\theta/2)\sqrt{\sin\alpha\, M_v\ \cos\beta}\,(1-\sigma(y))}{R\sqrt{2}\,(1+M_{0_R})\,(1-M_{W_R})\,(1-M_{V_R})\sqrt{1-M_{v_1}\sin\alpha}} \\ & \frac{2\,V_1}{l_1}\int_0^\infty \mathrm{d}\left(\frac{\omega\, l_1}{V_1}\right)\int_0^\infty \mathrm{d}y\, \mathrm{e}^{-\mu_1 y}\, \mathrm{e}^{\mathrm{i}\frac{\omega}{c}(R - M_0 x_1 - ct)}\,\hat{\omega}_3(\mu_1, y, \mu_3) \end{aligned} \tag{9.50}$$

As a result, the mean square pressure is given by

$$\begin{aligned} \langle p^2 \rangle ={}& \frac{\rho_0^2\, 2\, M_v\, V_1^2\ \cos^3\beta\ \sin^2(\theta/2)\ \sin\alpha\,(1-\sigma)^2}{R^2\, l_1^2\ (1+M_{0_R})^2\,(1-M_{W_R})^2\,(1-M_{V_R})^2\,(1-M_{v_1}\sin\alpha)} \\ & \iint_0^\infty \mathrm{d}\,(\mu_1\, l_1)\ \mathrm{d}\,(\overline{\mu}_1\, l_1) \iint_0^\infty \mathrm{d}y\, \mathrm{d}\overline{y}\, \mathrm{e}^{-(\mu_1 y + \overline{\mu}_1 \overline{y})}\ \langle \hat{\omega}_3(\mu_1, y, \mu_3)\ \hat{\omega}_3(\overline{\mu}_1, \overline{y}, \mu_3)\rangle \end{aligned} \tag{9.51}$$

The correlation of $\hat{\omega}_3$ can be written in terms of a dimensionless vorticity spectral density ϕ_{33}, the vorticity correlation scales l_1, l_2 and l_3 in the $(1,2,3)$-directions, the length scale of the boundary-layer/wall jet mean velocity profile l_0, and the wetted span segment L. It thus results that

$$\begin{aligned} &\langle \hat{\omega}_3(\mu_1, y, \mu_3)\ \hat{\omega}_3(\overline{\mu}_1, \overline{y}, \overline{\mu}_3)\rangle = \\ &\quad l_1\, v^2\left(\frac{l_1\, l_3}{l_0\, l_2}\right)\phi_{33}\left(l_1\mu_1, l_3\mu_3, \frac{\overline{y}-y}{l_2}, \frac{y}{l_0}\right)\delta(l_1\mu_1 + l_1\overline{\mu}_1)\,\frac{\sin\left[L\,(\mu_3+\overline{\mu}_3)/2\right]}{2\pi\left[L\,(\mu_3+\overline{\mu}_3)/2\right]}\, L \end{aligned} \tag{9.52}$$

which can be substituted into equation (9.51) in order to obtain

$$\begin{aligned} \langle p^2 \rangle \simeq{}& \frac{\rho_0^2\, M_v\, V^2\, v^2\ \cos^3\beta}{\pi\, R^2}\left(\frac{l_3\, L}{l_0\, l_2}\right)\frac{\sin^2(\theta/2)\ \sin\alpha\,(1-\sigma)^2}{(1+M_{0_R})^2\,(1-M_{W_R})^2\,(1-M_{V_R})^2\,(1-M_{v_1}\sin\alpha)} \\ & \int_0^\infty \mathrm{d}\,(\mu_1\, l_1)\iint_0^\infty \mathrm{d}y\, \mathrm{d}\overline{y}\, \mathrm{e}^{-\mu_1(y+\overline{y})}\,\phi_{33}\left(l_1\mu_1, l_3\mu_3, \frac{\overline{y}-y}{l_2}, \frac{y}{l_0}\right) \end{aligned} \tag{9.53}$$

Finally, setting

$$C_X = \frac{2}{l_0 l_2} \int_0^\infty \mathrm{d}(\mu_1 l_1) \iint\limits_0^\infty \mathrm{d}y\, \mathrm{d}\overline{y}\, \mathrm{e}^{-\mu_1 (y+\overline{y})}\, \phi_{33}\left(l_1\mu_1, l_3\mu_3, \frac{\overline{y}-y}{l_2}, \frac{y}{l_0}\right) \tag{9.54}$$

equation (9.53) becomes

$$\langle p^2 \rangle = \frac{\rho_0^2 V^2 v^2 \cos^3\beta\, M_v\, C_X}{2\,\pi} \left(\frac{l_3\, L}{R^2}\right) \sin^2(\theta/2)\, \sin\alpha \\ \frac{(1-\sigma)^2}{(1+M_{0_R})^2\,(1-M_{W_R})^2\,(1-M_{V_R})^2\,(1-M_{v_1}\sin\alpha)} \tag{9.55}$$

This is a generalized form of Ffowcs Williams & Hall's [176] result (see section 8.2)

$$\langle p^2 \rangle = \frac{1}{\pi^2} \rho_0^2 v^2 V^2 M_v \left(\frac{\delta}{R}\right)^2 \left(\frac{\Delta}{\delta^3}\right)^2 \sin\alpha\, \sin^2(\theta/2)\, \cos^2\beta \tag{9.56}$$

which describes the acoustic radiation generated by a compact eddy of volume Δ, characteristic turbulent correlation scale δ and mean square turbulent velocity v^2, convected at the velocity V past the edge of a semi-infinite plate. In fact, by dropping the Döppler factors related to the mean flow and to the vorticity convection, and by neglecting the effect of the wake, equation (9.55) becomes

$$\langle p^2 \rangle = \frac{C_X \rho_0^2 V^2 v^2 M_v}{2\,\pi} \left(\frac{l_3\, L}{R^2}\right) \sin^2(\theta/2)\, \sin\alpha\, \cos^3\beta \tag{9.57}$$

Considering a distribution of $\mathcal{N}$ uncorrelated eddies with total spanwise extention L and effective mean square volume

$$\Delta_E^2 = \mathcal{N}\,\langle \Delta^2 \rangle \simeq \frac{L}{\delta/\cos\beta}\,\delta^6 \tag{9.58}$$

equation (9.56) becomes

$$\langle p^2 \rangle \simeq \frac{1}{\pi^2} \rho_0^2 v^2 V^2 M_v \left(\frac{L\,\delta}{R^2}\right) \sin\alpha\, \sin^2(\theta/2)\, \cos^3\beta \tag{9.59}$$

which has the same form of Howe's equation (9.57).

In order to describe the effect of forward flight it is convenient to assume an observer fixed position relatively to the mean flow, and a flat-plate moving at the velocity U_0. The observer location at the emission time is defined by the polar co-ordinates (R, Θ, ϕ) which are related to the Cartesian co-ordinates through the relations

$$\begin{aligned} x_1 &= r\,(M_0 + \cos\Theta) \\ x_2 &= r\cos\phi \sin\Theta \\ x_3 &= r\sin\phi \sin\Theta \end{aligned} \tag{9.60}$$

Thus, by substituting into equation (9.55), the mean square pressure in the flyover plane ($\phi = 0$) takes the form

$$\langle p^2 \rangle = \frac{\rho_0\, V^2 v^2 \cos^3\beta\, M_v\, C_X}{2\,\pi} \left(\frac{l_3\, L}{R^2}\right) \sin\alpha \\ \frac{(1-\sigma)^2\,(1-M_0+M_{v_1})\sin^2(\Theta/2)}{(1+M_0\,\cos\Theta)\,[1+(M_0-M_{w_1})\cos\Theta]^2\,\,[1+(M_0-M_{v_1})\cos\Theta]^2} \tag{9.61}$$

The formal solutions (9.28) and (9.34), together with the condition (9.38), can be used to express the fluctuating pressure on the flat-plate. Howe [84] demonstrated that, by neglecting the diffraction contribution of the plate, the correlation of the wall pressure is given by

$$\langle p(x_1, x_3, t)\, p(x_1 + X_1, x_3 + X_3, t + \tau)\rangle = \frac{\rho_0^2}{4} \iint\limits_{-\infty}^{+\infty} \mathrm{d}\mu_1\, \mathrm{d}\mu_3 \iint\limits_{0}^{\infty} \mathrm{d}y\, \mathrm{d}\overline{y} \frac{(1-\sigma(y))^2}{|\gamma(\mu_1)|^2}$$
$$\Phi_i\left(l_1\,\mu_1, l_3\,\mu_3, \frac{\overline{y}-y}{l_2}, \frac{y}{l_0}\right) \exp\left\{-2\,y\,|\gamma(\mu_1)| + \mathrm{i}\,[\mu_1 X_1 + \mu_3 X_3 - \omega_y\,\tau]\right\} \tag{9.62}$$

where the incident vorticity spectrum Φ_i has been introduced in analogy with equation (9.52) by setting

$$\left\langle \left\{\boldsymbol{\mu}\cdot\hat{\mathbf{Q}}(\mu_1, y, \mu_3)\right\} \left\{\overline{\boldsymbol{\mu}}\cdot\hat{\mathbf{Q}}(\overline{\mu}_1, \overline{y}, \overline{\mu}_3)\right\}\right\rangle =$$
$$-\Phi_i\left(l_1\mu_1, l_3\mu_3, \frac{\overline{y}-y}{l_2}, \frac{y}{l_0}\right) \delta(l_1\mu_1 + l_1\overline{\mu}_1)\, \frac{\sin\left[L\left(\mu_3+\overline{\mu}_3\right)/2\right]}{2\pi\left[L\left(\mu_3+\overline{\mu}_3\right)/2\right]}\, L \tag{9.63}$$

In equation (9.62) the assumption has been made that a significant correlation exists only between turbulent eddies convected at the same velocity, namely, $\omega_y = \overline{\omega}_y$.

Having neglected the diffraction contribution of the plate, the wall pressure fluctuations are indeed pseudo-sound fluctuations induced by incident harmonic vortical disturbances. An evanescent wavenumber/frequency spectrum $\Pi(\mu_1, \mu_3, \omega)$ can be thus defined in analogy with Chandiramani [82] and Chase [83]. Thus, let us write

$$\langle p(x_1, x_3, t)\, p(x_1 + X_1, x_3 + X_3, t + \tau)\rangle =$$
$$\iiint\limits_{-\infty}^{+\infty} \Pi(\mu_1, \mu_3, \omega) \exp\left\{\mathrm{i}\;(\mu_1\, x_1 + \mu_3\, x_3 - \omega\tau)\right\}\, \mathrm{d}\mu_1\, \mathrm{d}\mu_3\, \mathrm{d}\omega \tag{9.64}$$

Comparing equation (9.64) to equation (9.62) yields the following form of the wavenumber/frequency spectrum

$$\Pi(\mu_1, \mu_3, \omega) = \int_0^\infty f(\mu_1, y, \mu_3)\; \delta(\omega - \omega_y)\; \mathrm{d}y \tag{9.65}$$

where

$$f(\mu_1, y, \mu_3) = \frac{\rho_0^2\,(1-\sigma(y))^2}{4\,|\gamma(\mu_1)|^2} \exp\left\{-2\,y\,|\gamma\,(\mu_1)|\right\} \int_0^\infty \Phi_i\left(l_1\mu_1, l_3\mu_3, \frac{\overline{y}-y}{l_2}, \frac{y}{l_0}\right) \mathrm{d}\overline{y} \tag{9.66}$$

The far field solution (9.46) can be used to express the spectral density $S(\omega)$, defined by $\langle p^2\rangle = \int_0^\infty S(\omega)\, \mathrm{d}\omega$, in terms of the function $f(\mu_1, \mu_3, z)$. It results that

$$S(\omega) = \frac{2\,L}{\pi\, c\, R^2} \frac{\sin\alpha\, \sin^2(\theta/2)}{(1+M_{0_R})^2\,(1-M_{w_R})^2} \int_0^\infty \frac{f(\tilde{\mu}_1, \tilde{\mu}_3, y)}{(1-M_{v_R})^2\,(1-M_{v_1}\,\sin\alpha)}\, \mathrm{d}y \tag{9.67}$$

and, equivalently

$$S(\omega) = \frac{2\,L}{\pi\, R^2} \frac{\sin\alpha\, \sin^2(\theta/2)\, \cos\beta}{(1+M_{0_R})^2\,(1-M_{w_R})^2} \int_{-\infty}^\infty \frac{M_v\, \Pi(\mu_1, \tilde{\mu}_3, \omega)}{(1-M_{v_R})^2\,(1-M_{v_1}\,\sin\alpha)}\, \mathrm{d}\mu_1 \tag{9.68}$$

Finally, by supposing that the eddy convection velocity is constant and by neglecting the Döppler factors related to the mean flow and to the vorticity convection, equation (9.68) becomes

$$S(\omega) = \frac{2\,L}{\pi\, R^2}\, \sin\alpha\, \sin^2(\theta/2)\; M_v\, \cos\beta \int_{-\infty}^\infty \Pi\left(\mu_1, \frac{\omega}{c}\cos\alpha, \omega\right)\, \mathrm{d}\mu_1 \tag{9.69}$$

which has the same structural form of Chase's result (8.74).

10

Interaction Noise

10.1 Introduction

A vortical flow on the surface of a body is a common source of unsteady loading, aerodynamic sound and structural vibrations.

In several engineering configurations devices are arranged so that downstream bodies are embedded in wakes from upstream bodies. Typical examples are those of a bank of heat exchanger tubes in which vortices from upstream cylinders impinge on downstream cylinders, a turbomachinery stage where the wake from inlet vanes is chopped by the rotor blades, and a helicopter rotor whose blades may interact with the tip-vortices shed from the preceeding blades.

In a cavity, a vortex-sheet is shed from the upstream corner and impinges onto the downstream corner. In this case difficulties arise because of the existence of a nonlinear coupling mechanism between low-frequency modes of the separated shear-layer, the low-frequency unsteadiness of the recirculating flow within the cavity, and the acoustic disturbances propagating upstream from the downstream corner.

An unsteady shear-layer impinging on a sharp edge can generate self-sustained oscillations if a phase compatibility occurs between the upstream propagating acoustic waves and a shear-layer vorticity mode. As a consequence, self-excitement of the selected vorticity mode enforces a tonal emission. The discrete tones radiation from an isolated airfoil in a laminar regime and the sound emitted by an organ pipe are typical examples of self-sustained oscillations[1].

Under some conditions of powered descent, the tip-vortices shed from the main rotor blades of a helicopter can impinge on the following blades. This periodic interaction can be described by means of theories based on the airfoil response to a gust. These theories relate the unsteady pressure field on the airfoil surface to the wavenumber of the impinging gust and other interaction parameters.

The first section of the present chapter describes the underlying physics of a vortex-body interaction. In the second section, some analytical models for the vortex-airfoil interaction problem are presented. The third section is concerned with the numerical prediction of the blade-vortex interactions.

10.2 Physics of Vortex-Body Interaction

A vortex-body interaction problem is predominantly affected by three factors:

- the distance of the oncoming vortex,

- the orientation of the oncoming vortex with respect to the body surface,

- the characteristic wavelength of the vorticity field.

[1]The reader should refer to the works of Tam [197], Goldstein [198] and Rockwell [199] for an exhaustive treatment of the subject.

The orientation of the impinging vorticity vector has a fundamental role in blade-vortex interaction. For example, depending on the flight conditions of a helicopter, blade-vortex interactions may occur with different angles, varying between three extreme cases: parallel, streamwise and normal interaction. In terms of unsteady loading and sound generation, the most severe conditions occur when the blade leading edge is parallel to the vorticity vector. Based on this assumption, two-dimensional analyses are commonly performed, despite the fact that a strong vortex-body interaction is an intimately three-dimensional phenomenon[2].

A streamwise blade-vortex interaction, as shown by Bodstein [200], exhibits elements of great complexity. For example, the existence of a local separation zone induced by a spanwise pressure gradient, a vortex breakdown near the maximum thickness location or upstream of the leading edge in the case of a direct blade-vortex interaction, and strong vortex-wake interactions.

A normal vortex-body interaction involves both a vortex bending and a vortex chopping. When the airfoil is sufficiently thin, the vortex is chopped but not significantly bended. The vortex chopping is accompanied by a *compression* of the vortex core on one blade side and an *expansion* on the opposite side. Both the compressed and the expanded portions of the vortex propagates away from the surface as the vortex moves along the blade. The terms compression and expansion do not refer to phenomena related to the compressibility of the fluid, but to the strength of the vorticity field. A review of this interaction mechanism is given by Marshall & Grant [7].

A parallel vortex-airfoil interaction is accompanied by a deformation of the vorticity field in the plane normal to the airfoil. The vortex distortion is as stronger as smaller is the distance between the oncoming vortex and the airfoil. Therefore, a *direct interaction* usually indicates a parallel interaction with the vortex impinging directly onto the airfoil leading edge[3]. Accordingly, a *nearly direct interaction* is defined as that occurring when the deviation of the vortex trajectory from the airfoil plane is a fraction of the airfoil thickness.

The vorticity field is strongly distorted during a direct or nearly direct vortex-airfoil interaction. Furthermore, the pressure field induced on the airfoil surface depends on the vorticity distribution especially when the vortex is at a small distance from the airfoil. As a result, the distortion of the vortex must be taken into account when a prediction is made of the unsteady loading and noise generation during a vortex-leading edge interaction. On the contrary, when the oncoming vortex is sufficiently far from the airfoil, the unsteady pressure field induced on the airfoil surface depends only on the overall vortex circulation. In this case the distortion of the vorticity field can be neglected in favor of a line-vortex description.

The characteristic wavelength of the vorticity field is the *size* of an isolated vortex, as well as the wavelength of a gust. In the case of a Kármán vortex street from an upstream rod, for example, the wavelength of the vorticity field is the distance between two vortices on the same row. The influence of the gust wavelength on the unsteady flow past an airfoil is combined with the influence of the skew angle. In fact, as shown by Graham [6], the gust parameter affecting the interaction dynamics depends on both the skew angle and the gust wavelength. The influence of the size of an isolated vortex can be related to the distortion of the vorticity field. The vortex distortion, in fact, is a nonlinear rearrangement mechanism occurring when the curvature radius of the leading edge and the impinging vortex have a comparable scale. On the contrary, when the vortex is of small size compared to the curvature radius of the leading edge, say *compact*, the flow nonlinearity is responsible for a strong dependence of both the vortex trajectory and the induced pressure field on the upstream position of the vortex. In these terms the size of an oncoming vortex affects the dynamics of a vortex-airfoil interaction. Moreover, as observed by Kaykayoglu & Rockwell [8], when a compact vortex moves along the airfoil surface, it induces a wavelike pressure disturbance. The amplitude and the wavelength of

[2]The *rapid-distortion* theory of turbulence developed by Prandtl [142], Batchelor & Proudman [143] and Hunt [141] shows that a strong blocking of a nearly two-dimensional vorticity field originates transversal velocity fluctuations.

[3]A direct interaction is commonly referred to in literature as a head-on interaction.

this convected disturbance affect both the resulting unsteady loading and interaction noise.

In three cases the fluid viscosity has an important role on the interaction dynamics:

- the vortex impingement on a sharp edge;
- the convection of an intense vortex along a planar surface;
- the convection of vortical disturbances past a trailing edge;

In the first case, as described in section 10.2.2, a strong opposite secondary vortex is shed from the leading edge. In the second case, as shown by Doligalski & Valker [201], a local boundary-layer separation may occur. This is accompanied by an eruption of the boundary-layer which transfers a portion of the wall-layer vorticity into the outer flow. In the third case, a vortical wake is shed from the trailing edge.

Some experimental results are described in the following subsections, concerning with parallel vortex-body interactions. Three configurations are considered: vortices impinging onto rounded leading edges, vortices impinging onto sharp leading edges, vortex-corner interactions in the presence of recirculating flows.

10.2.1 Vortex-Airfoil Interaction

Gursul & Rockwell [10] investigated the interaction between a vortex street and an elliptical airfoil. Experiments were carried out in a water channel. The vortex streets impinging onto the elliptical airfoil were generated by using upstream plates of different thickness. The Reynolds number based on the plate thickness was in the range 309 − 619. The free-stream velocity was $U_\infty = 9.65 \times 10^{-2}$ s and kept constant in the experiments. Gursul & Rockwell showed that the interaction process is strongly affected by two factors:

- the wavelength of the oncoming vorticity field, namely the distance between two next vortices on the same row;
- the offset distance between the axis of the vortex street and the streamwise axis of the elliptical airfoil.

Two vortex streets of different wavelength were considered: a large scale vortex street, and a small scale vortex street. Three flow configurations were observed:

a) both the small scale and the large scale vortex streets, at small values of the offset distance, are split into two separate rows which embrace the airfoil.

b) Both the small scale and large scale vortex streets, at large values of the offset distance, are convected along one side of the airfoil and preserve their structure.

c) When one row impinges directly on the airfoil leading edge, only the large scale vortices are split into less coherent structures. Moreover, these vortices are stretched in the cross-stream direction, but no boundary-layer separation occurs. The small scale vortex street, on the contrary, behave as described in a) or in b).

Horner *et al.* [11] investigated the interaction between a vortex and a rotating blade. The blade had an NACA-0015 symmetric section of chord 0.149 m. The wind tunnel speed was 47 m/s, whereas the rotor tip velocity was 59.25 m/s. Different blade-vortex intersection configurations were investigated by means of Particle Image Velocimetry (PIV). During a direct blade-vortex interaction, the PIV data showed some basic mechanisms. In proximity of the leading edge the vortex is first deformed and then split into two fragments which are convected along the two airfoil sides. Because of the opposite induction effect of the image vortex system, the convection velocity is different along the two airfoil sides. The slower fragment spreads across the surface, whereas the faster one undergoes a slight distortion. As the vortex fragments approach the trailing edge, secondary vortices are shed into the airfoil wake. Finally, a further interaction occurs in the airfoil wake between the main vortex fragments and the secondary vortices.

Lee & Bershader [12] investigated a direct blade-vortex interaction by means of holographic interferograms. The blade section was an NACA-0012 of 0.05 m chord and the span extended by 0.05 m. The chord based free-stream Reynolds number was in the range $0.9 \times 10^6 - 1.3 \times 10^6$. The free-stream Mach number was in the range $0.5 - 0.7$. Lee & Bershader observed that the impinging vortex induces two opposite pressure peaks near the leading edge. These peaks collapse as the vortex passes above the leading edge. As a consequence, a pressure wave is radiated from the airfoil into the field. Moreover, a boundary-layer separation on the lower side of the leading edge was observed. This implies that the effects related to the viscosity of the fluid play an important role in a strong blade-vortex interaction.

10.2.2 Vortex-Wedge Interaction

Rogler [202] investigated the impingement of distributed vorticity upon the leading edge of a flat-plate. Nonlinearity and viscosity were shown to have a predominant effect near the leading edge where vortex shedding occurs at a rate that depends on the incident vorticity field. Such a mechanism was thus related to the existence of a pressure singularity at the leading edge that Rogler determined in the form of a $r^{-1/2}$ law for the fluctuating pressure amplitude, with r denoting the distance from the leading edge. Ziada & Rockwell [203] observed the impingement of a row of vortices on the sharp leading edge of a wedge. They investigated the strong dependence of the interaction dynamics upon the transverse distance between the incident vortex and the edge and observed the following flow features.

- Because of the induction effect of the image vortex system, the impinging vortex exhibits the tendency to pass above the leading edge. As a consequence, the vorticity field undergoes a different distortion at positive and negative values of the offset distance (see Fig.10.1).

- A vortex of opposite circulation is shed from the leading edge towards the underside of the wedge. Such a secondary vortex is stronger at negative values of offset.

- The aerodynamic force induced on the wedge has its maximum value at zero offset and drops at slight leading edge displacement. Moreover, in agreement with Rogler's [202] analysis and observations, Ziada & Rockwell observed a strong induced effect only in the vicinity of the edge.

Kaykayoglu & Rockwell [8] investigated the interaction between a periodic row of vortices with the sharp leading edge of a wedge. They interpreted the instantaneous pressure field on the wedge surface as downstream propagating waves on the basis of the following expressions

$$\begin{aligned}
&\frac{\mathrm{D}p}{\mathrm{D}t} = 0 \quad \text{with} \quad \frac{\mathrm{D}}{\mathrm{D}t} = \frac{\partial}{\partial t} + U_c \frac{\partial}{\partial x} \\
&p \simeq \hat{\mathrm{p}} e^{-\mathrm{i}\{2\pi f t - \phi(x)\}} \\
&U_c = \frac{2\pi f}{\mathrm{d}\phi / \mathrm{d}x} = f\lambda
\end{aligned} \tag{10.1}$$

In these expressions f and ϕ denote the frequency and the streamwise phase of the induced disturbance, respectively, whereas U_c and λ are the phase velocity and the wavelength of the convected vorticity disturbances, respectively. According to (10.1) a higher phase velocity is related to a larger vorticity wavelength and to a smaller phase variation. As a consequence, the force induced by an elongated vorticity structure has a higher amplitude. Kaykayoglu & Rockwell argued that, because of the rapid distortion of the vorticity field, a wavelike description of the unsteady pressure field is not consistent in proximity of the edge. The phase variation, in fact, while negligible along the lower side of the wedge, showed an abrupt jump on the upper side. This jump was associated with the flow *sweeping* about the edge. On the contrary, downstream of the edge region, the long wavelength measured on the upper side of the wedge was related to the elongation of the incident vortex, whereas the shorter wavelength on the lower side was related to the secondary vortex shedding. Kaykayoglu & Rockwell supported the existence of a singularity at the leading edge and suggested that an inviscid model of the vortex-wedge interaction should not incorporate a leading edge Kutta condition.

10.2.3 Vortex-Corner Interaction in a Cavity

The vortex-corner interaction in a cavity coexists with a zone of recirculating flow. A large-scale vortex impinging on the downstream corner is constituted by a number of small-scale vortices originated by a hydrodynamic instability of the separated shear-layer along the aperture of the cavity. Such instability exhibits a convective character. As a consequence, a nonlinear coupling between the low-frequency modes of the recirculating flow and the vortex shedding process can generate a low-frequency modulation of the flow within the cavity.

Numerical simulations [204] [205] show that the existence of a modulated flow behaviour is related to the length of the cavity. For large values of the cavity length the recirculating zone takes the form of a large eddy that is convected downstream by the mean stream and that overshadows the role of the smaller vortices. On the contrary, for small and moderate values of the cavity length the low-frequency unsteadiness of the recirculating flow can enforce a low-frequency flapping of the shear-layer.

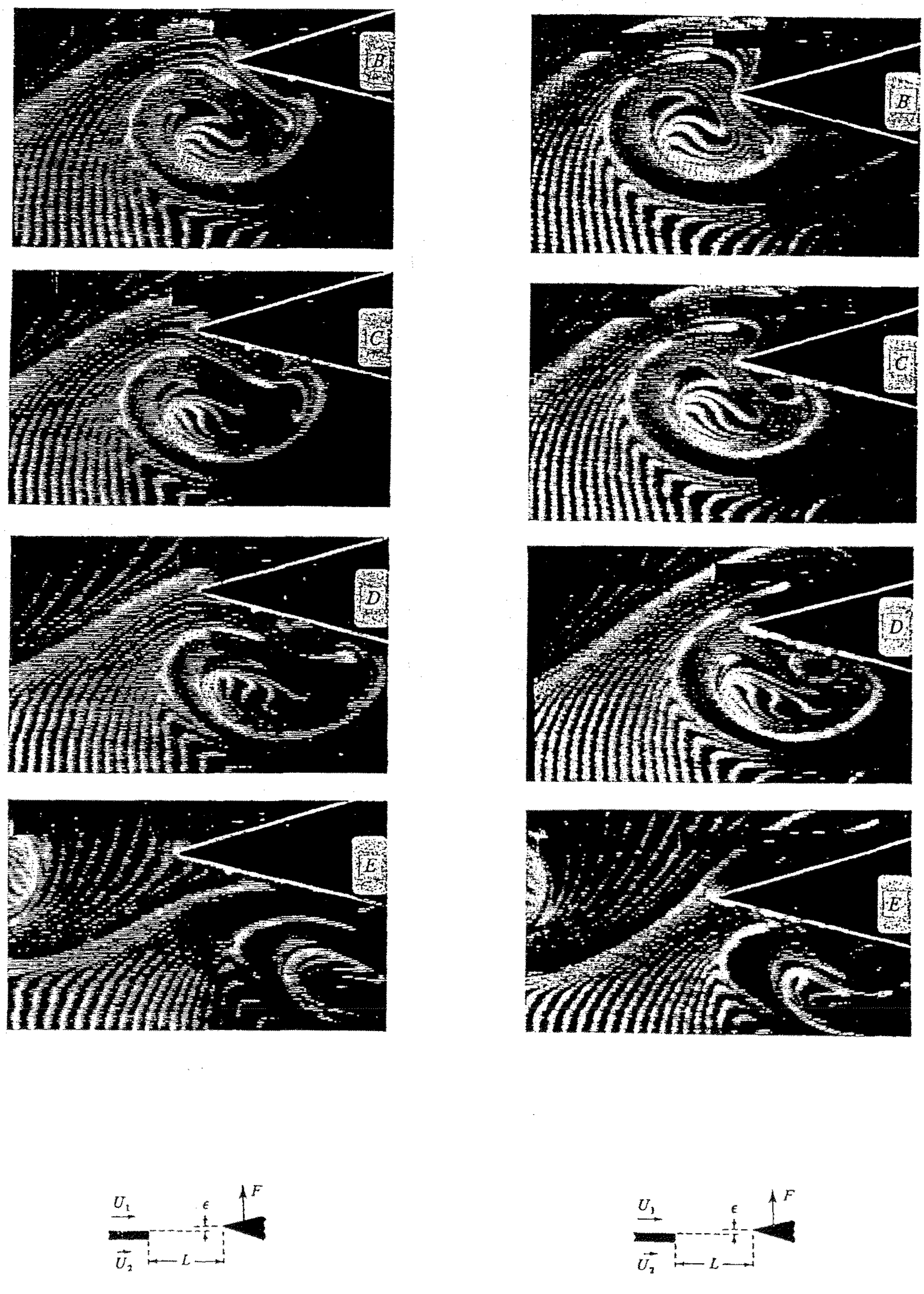

FIGURE 10.1: Impingement of a row of vortices onto the sharp leading edge of a wedge for two values of the vertical offset ϵ. Hydrogen bubble snapshots: first column $\epsilon/\theta_R = 0.2$, second column $\epsilon/\theta_R = 1.2$, θ_R denoting the thickness of the upstream plate (after Ziada & Rockwell [203], figures 4 and 5).

10.3 Blade-Vortex Interaction Noise

As discussed in chapter 7, sound is generated when an unsteady force is exerted on a fluid portion. The force acts as an acoustic dipole with axis parallel to the line of action of the force.

A steady aerodynamic force exerted on the surface of an airfoil in accelerated motion is unsteady in the fluid reference frame. Therefore, a lift distribution on the rotating blades of a propeller is equivalent to a distribution of dipoles on the rotor plane which radiate noise predominantly in the direction normal to the rotor plane [4]. When an airfoil is embedded in an unsteady flow, the resulting unsteady force provides the same noise generation mechanism.

Flow unsteadiness is usually associated with vortical flows. When the vorticity field exhibits a spatially organized structure it is better referred to as a *gust*. For example, the tip-vortices shed from the blades of a helicopter in steady flight conditions can impinge with regularity on the following blades. As a consequence, the tip-vortices act as an oblique harmonic gust convected towards a steady airfoil. Even when an airfoil is embedded in a turbulent flow, a Fourier decomposition of the impinging vorticity field, supported by a linear flow assumption, permits a description of the interaction problem in terms of a gust-airfoil interaction. In section 10.3.1 an equivalence is shown to exist between a gust and a pair of vorticity waves.

Sears [126] obtained an analytical expression of the unsteady lift induced by a space-harmonic gust on a thin airfoil. The gust was supposed to be frozenly convected past the airfoil by an incompressible flow. Different gust-response theories were developed successively in order to extend Sears' model to compressible, oblique, high- and low- frequency gusts.

As discussed in chapter 7, a classic aeroacoustic approach takes advantage of the acoustic analogy theory in order to relate the acoustic far field to the pressure distribution on the airfoil surface. Indeed, the wall pressure field depends on the gust-airfoil interaction dynamics, as predicted by a wing-gust aerodynamic theories. Thus, the radiated acoustic field can be ultimately related to the properties of the incident gust.

Widnall [206] investigated the sound generated by the interaction between a two-dimensional airfoil and an obliquely incident vortex. The airfoil was assumed to be chordwise compact, but not necessarily spanwise compact. The vortex was supposed to remain stationary as it was convected past the airfoil. The velocity field induced by the vortex was decomposed into Fourier components. These components were introduced into Filotas' [127] airfoil response function in order to determine the fluctuating pressure field on the airfoil surface. Finally, the sound generated by the blade-vortex interaction was determined by using the pressure field induced on the airfoil surface.

Amiet [207] described the acoustic field generated by an airfoil immersed in a turbulent flow. He related the spectral behaviour of the far pressure field to the spectral properties of the incident turbulent flow. For the case of an airfoil in a low Mach number stream, the Sears' function was used as airfoil response function.

Amiet [130] demonstrated that a generalized Prandtl-Glauert transformation can be used to reduce a small perturbation problem in a compressible stream to a standard wave equation in a medium at rest. Furthermore, in the low-frequency limit, the second-order time derivative in the transformed wave equation can be neglected leading to a Laplace's equation. The solution of this Laplace's equation can be matched to an outer compressible solution, allowing a prediction of the acoustic far field.

Amiet [129] proposed an analytical procedure to calculate the unsteady lift induced by a compressible high-frequency gust on a thin airfoil. The method was based on the assumption that, as shown by Landahl [138], the leading edge and the trailing edge aerodynamic problems, at high frequencies, can be separately solved and matched in a converging iterative scheme. Amiet solved the leading edge and the trailing edge problem in terms of Schwartzchild solution up to a second-order matched solution.

Martinez & Widnall [208] used the first two terms in the series of Adamczyk's [139] iteration

[4]As discussed in chapter 7, a transonic rotor generates a high impulsive noise mainly in the rotor plane.

scheme in order to predict the pressure field induced by an oblique high-frequency compressible gust on a rectangular thin blade. A three-dimensional surface pressure distribution was recovered by means of a spanwise Fourier superposition of two-dimensional solutions.

Martinez & Widnall [209] extended their previous formulation to the case of a rotating blade encountering an oblique high-frequency gust. The pressure field on the blade surface was build via a spanwise Fourier superposition of two-dimensional solutions, but having linearly increasing magnitudes along the blade span.

Models based on airfoil gust-response theories are particularly suitable in relating the spectral properties of the acoustic far field to those of the incident turbulent flow. However, in order to understand the aerodynamic mechanisms involved in a vortex-airfoil interaction, different analysis must be developed.

Howe [13] exploited the vortex-sound acoustic analogy [20] in order to describe the interaction noise generated by a turbulent eddy frozenly convected past an acoustically compact airfoil in a low subsonic stream. He showed that imposing a Kutta condition at the airfoil trailing edge always leads to a reduction of the interaction noise.

Howe [24] showed that fictitious acoustic sources can be introduced when the vorticity shed from the airfoil trailing edge is not properly convected. As a consequence, inaccurate noise predictions can be performed if these spurious sources are not removed.

As remarked in section 10.2, distortion and nonlinear rearrangement of the vorticity field occur during a direct or nearly direct vortex-airfoil interaction. Furthermore, if the leading edge is sharp or the impinging vortex is intense enough, boundary-layer separation and shedding of a secondary vortex can take place. No one of the aforementioned analyses accounts for the distortion of the incident vorticity field. Even Goldstein & Atassi' s [131] second order gust-response theory accounts only for a steady deflection of the convected sinusoidal gust. In this scenario numerical prediction are usually performed in order to investigate vortex-body interactions in circumstances of practical interest, such as the helicopter Blade-Vortex Interaction (BVI).

BVI predictions involve two different scales of simulation: the local scale, where the physics of the vortex interaction is investigated from a basic point of view, and the global scale of the rotor, where the wake convection problem is predominant. Classic CFD methods have proven to be quite effective in describing the local interaction problem: both distortion of the vorticity field and viscous effects can be adequately simulated. However, Navier-Stokes solvers require an adequate grid resolution in order to minimize the numerical dissipation of the vortical disturbances. Wake & Choi [67] used a 5th order solver to simulate the convection of a two-dimensional vortex and showed that a minimum of 14 points across the vortex core was required by their high-accuracy discretization scheme in order to preserve the vortex strength. Therefore, the central problem in the numerical prediction of helicopter BVI is the prediction of the wake on its global scale. In subsection 10.4 some numerical methods for the BVI problem are described.

10.3.1 Equivalence between a Vorticity Wave and a Harmonic Gust

As discussed in chapter 6, the generation of aerodynamic sound is always related to the presence of vorticity or entropy gradients in the flow. Neglecting both viscous dissipation and heat conduction, Howe [20] obtained the following convected wave equation

$$\left\{\frac{\mathrm{D}}{\mathrm{D}t}\left(\frac{1}{c^2}\frac{\mathrm{D}}{\mathrm{D}t}\right)+\frac{1}{c^2}\frac{\mathrm{D}\mathbf{v}}{\mathrm{D}t}\cdot\nabla-\nabla^2\right\}B=\nabla\cdot(\omega\times\mathbf{v}-T\nabla S)-\frac{1}{c^2}\frac{\mathrm{D}\mathbf{v}}{\mathrm{D}t}\cdot(\omega\times\mathbf{v}-T\nabla S) \tag{10.2}$$

which shows that, in the presence of a mean flow, the specific stagnation enthalpy B plays the role of an acoustic variable.

Equation (10.2) can be linearized by splitting the velocity field into a steady, irrotational and isentropic base flow $\mathbf{U}$ and a fluctuating part $\mathbf{v}'$ induced by the vorticity ω. In the remaining part of the present subsection the specific stagnation enthalpy B, the pressure p and the vorticity $\boldsymbol{\omega}$ will denote perturbation quantities. By neglecting second order terms, equation (10.2) takes the form

$$\left\{\frac{1}{c_0^2}\left(\frac{\partial}{\partial t}+\mathbf{U}\cdot\nabla\right)^2-\nabla^2\right\}B=\nabla\cdot(\boldsymbol{\omega}\times\mathbf{U})\equiv\gamma(\mathbf{x},t) \tag{10.3}$$

Setting $\mathbf{U}=U_0\nabla\Phi$ and Fourier transforming equation (10.3), the following convected wave equation in the frequency domain can be obtained

$$\{\nabla^2+2\,\mathrm{i}\,k_0\,M_0\,\nabla\Phi\cdot\nabla-M_0^2\,\nabla\Phi\cdot\nabla\,(\nabla\Phi\cdot\nabla)+k_0^2\}\,\hat{B}=\hat{\gamma}(\mathbf{x},\omega) \tag{10.4}$$

where

$$\hat{B}(\omega)=\frac{1}{2\pi}\int_{-\infty}^{\infty}B(t)\,\mathrm{e}^{\mathrm{i}\,\omega t}\,\mathrm{d}t \tag{10.5}$$

and

$$\hat{\gamma}(\mathbf{x},\omega)=\nabla\cdot(\hat{\boldsymbol{\omega}}\times\mathbf{U}) \tag{10.6}$$

By linearizing the momentum equation (6.38) written in Crocco's form for a inviscid homentropic irrotational flow, the following expressions for the fluctuating velocity in a vorticity-free field can be obtained

$$\hat{\mathbf{v}'}=-\frac{\mathrm{i}}{\omega}\nabla\hat{B} \tag{10.7}$$

As proposed by Taylor [159], at a sufficiently low Mach number, such that terms involving M_0^2 can be neglected, equation (10.4) can be transformed into a Helmholtz equation by setting

$$\hat{\mathcal{B}}=\hat{B}\,\mathrm{e}^{\mathrm{i}\,M_0\,k_0\,\Phi} \tag{10.8}$$

It thus results that

$$\nabla^2\hat{\mathcal{B}}+k_0^2\,\hat{\mathcal{B}}=\hat{\gamma}(\mathbf{x},\omega)\,\mathrm{e}^{\mathrm{i}\,M_0\,k_0\,\Phi} \tag{10.9}$$

Consider the vorticity field of a line-vortex of circulation Γ convected along the path $\mathbf{y}(t)$, i.e.

$$\begin{aligned}\omega_1&=\omega_2=0\\ \omega_3&=\Gamma\,\delta\,(\mathbf{x}-\mathbf{y}(t))\end{aligned} \tag{10.10}$$

The source term in equation (10.3) takes the form

$$\gamma(\mathbf{x},t)=U\,\mathbf{n}\cdot\nabla\omega_3 \tag{10.11}$$

where $\mathbf{n}$ is the unit normal to the path of the vortex and U denotes the modulus of the local mean velocity. A formal solution of equation (10.9) is

$$\hat{\mathcal{B}}(\mathbf{x},\omega)=\int_V G(\mathbf{x},\mathbf{z},\omega)\,\hat{\gamma}(\mathbf{z},\omega)\,\mathrm{e}^{\mathrm{i}\,M_0\,k_0\,\Phi(\mathbf{z})}\,\mathrm{d}\mathbf{z} \tag{10.12}$$

where V is a region of non-vanishing $\hat{\gamma}$, $G(\mathbf{x},\mathbf{z},\omega)$ is the Green's function of the Helmholtz equation[5] and

$$\hat{\gamma}(\mathbf{x},\omega)=\frac{1}{2\pi}\int_{-\infty}^{\infty}\gamma(\mathbf{x},t)\,\mathrm{e}^{\mathrm{i}\,\omega t}\,\mathrm{d}t \tag{10.13}$$

From equations (10.10), (10.11) and (10.12) it follows that

$$\hat{\mathcal{B}}(\mathbf{x},\omega)=\frac{\Gamma}{2\pi}\int_{-\infty}^{+\infty}U\mathrm{e}^{\mathrm{i}\,M_0\,k_0\,\Phi(\mathbf{z})}\mathrm{e}^{\mathrm{i}\,\omega t}G(\mathbf{x},\mathbf{z},\omega)\,\mathbf{n}\cdot\nabla\delta\,(\mathbf{x}-\mathbf{z}(t))\,\mathrm{d}z_1\,\mathrm{d}z_2\,\mathrm{d}t \tag{10.14}$$

[5] A Green's function tailored to the particular problem have been assumed.

Then, exploiting the properties of the delta-function yields

$$\hat{\mathcal{B}}(\mathbf{x},\omega) = \frac{\Gamma}{2\pi}\int_{-\infty}^{+\infty} U\, \mathrm{e}^{\mathrm{i}\, M_0\, k_0\, \Phi(\mathbf{y})}\, \mathrm{e}^{\mathrm{i}\,\omega t}\, \nabla G\cdot \mathbf{n}\; \mathrm{d}t \tag{10.15}$$

Equation (10.15) describes the acoustic field generated by a distribution of dipoles along the vortex trajectory, with axis normal to the trajectory. Therefore, a convected line-vortex is spectrally equivalent to an infinite sum of *vorticity waves* with frequency ω and wave speed U.

Consider now a line-vortex convected by a uniform incompressible flow $\mathbf{U} = (U, 0)$. Equations (10.8) and (10.15) lead to

$$\hat{\mathcal{B}}(\mathbf{x},\omega) = \frac{\Gamma}{2\pi}\int_{-\infty}^{+\infty} \mathrm{e}^{\mathrm{i}\,\omega \frac{y_1}{U}}\, \frac{\partial}{\partial y_2} G_i(\mathbf{x},\mathbf{y})\; \mathrm{d}y_1 \tag{10.16}$$

where

$$G_i(\mathbf{x},\mathbf{y}) = \frac{1}{2\pi}\ln\left(|\mathbf{x}-\mathbf{y}|\right) \tag{10.17}$$

is the Green's function for the incompressible problem ($k_0 \to 0$). From equation (10.7) the following expression for the fluctuating velocity induced by the vortex can be obtained

$$\hat{v}_1'(\mathbf{x},\omega) = -\mathrm{sign}\,(x_2)\,\frac{\Gamma}{4\pi^2\,U}\mathrm{e}^{\mathrm{i}\,k_1 x_1}\,\mathrm{e}^{-|k_1 x_2|} \tag{10.18}$$

$$\hat{v}_2'(\mathbf{x},\omega) = -\mathrm{i}\,\frac{\Gamma}{4\pi^2\,U}\mathrm{e}^{\mathrm{i}\,k_1 x_1}\,\mathrm{e}^{-|k_1 x_2|} \tag{10.19}$$

where $k_1 = \omega/U$. Then, changing to the time domain yields

$$v_1'(\mathbf{x},t) = -\mathrm{sign}\,(x_2)\,\frac{\Gamma}{4\pi^2\,U}\mathrm{e}^{\mathrm{i}\,(k_1 x_1-\omega t)}\,\mathrm{e}^{-|k_1 x_2|} \tag{10.20}$$

$$v_2'(\mathbf{x},t) = -\mathrm{i}\,\frac{\Gamma}{4\pi^2\,U}\mathrm{e}^{\mathrm{i}\,(k_1 x_1-\omega t)}\,\mathrm{e}^{-|k_1 x_2|} \tag{10.21}$$

If two parallel vorticity waves of equal strength are placed at a distance $2\,\epsilon$ from each other, the induced velocity on the centerline vanishes in the x_1-direction, whereas the normal component is given by

$$v_2'(\mathbf{x},t) = -\mathrm{i}\,\frac{\Gamma}{2\pi^2\,U}\mathrm{e}^{\mathrm{i}\,(k_1 x_1-\omega t)}\,\mathrm{e}^{-|k_1 \epsilon|} \tag{10.22}$$

A sinusoidal gust frozenly convected at velocity U in the x_1-direction has the form

$$v_2'(\mathbf{x},t) = \mathcal{A}\,\mathrm{e}^{\mathrm{i}\;k_1(x_1-Ut)} = \mathcal{A}\,\mathrm{e}^{\mathrm{i}\,(k_1 x_1-\omega t)} \tag{10.23}$$

Therefore, provided that

$$\mathcal{A} = -\mathrm{i}\,\frac{\Gamma}{2\pi^2\,U}\,\mathrm{e}^{-|k_1\epsilon|} \tag{10.24}$$

a gust is equivalent to a pair of vorticity wakes.

10.3.2 General Features of Helicopter Blade-Vortex Interaction

Two important aerodynamic phenomena occur when a helicopter rotor operates in high-speed flight conditions: (i) the presence of a transonic flow on the advancing side of the rotor, (ii) the presence of an extended vortex system around the rotor. Unsteady transonic conditions on the rotor blades are responsible for high vibration levels, power divergence, component fatigue and aerodynamic noise. The helical tip-vortex system interacts with the rotating blades and generates aerodynamic noise and vibrations. Furthermore, blade-vortex interaction can also occur in transonic flow conditions. Both these

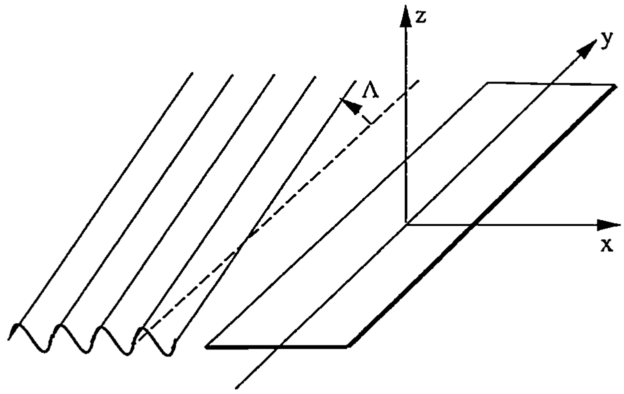

FIGURE 10.2: Modeling scheme of a gust-airfoil interaction.

two aerodynamic phenomena generate a high impulsive aerodynamic noise which is usually referred to as *blade slap noise.*

A rotor interacts with a tip-vortex under a wide range of relative orientation angles. However, the underlying physics of a blade-vortex interaction can be described by considering a rectangular blade of infinite aspect ratio and an infinite line-vortex at a skew angle Λ. In Fig.10.2 a blade-gust interaction is sketched. In this case Λ denotes the angle between the blade axis and the gust wavefronts.

By supposing that the oncoming gust is frozenly convected past the airfoil,the interaction is steady in a co-ordinate system (x', y') that translates along the blade at the velocity of the intersection point between the blade centerline and the vortex projection onto the plane of blade, that is

$$\begin{aligned} x' &= x \\ y' &= y - U_\infty \cot \Lambda \end{aligned} \tag{10.25}$$

When $\Lambda = \pi/2$ the vortex is perpendicular to the blade and the speed of the intersection point is zero. Conversely, when $\Lambda = 0$ the vortex is parallel to the blade and the speed of the intersection point is infinite. As a result, a two-dimensional problem is intrinsically unsteady.

The condition $\Lambda = \pi/2$, usually referred to as low-speed interaction, occurs principally during a hovering flight. On the contrary, the condition $\Lambda = 0$, usually referred to as high-speed interaction, occurs during a high-speed flight and a descent flight.

Finally, it can be noticed that when $\Lambda < \tan^{-1}(M_\infty)$ the intersection point translates at a supersonic speed.

Consider an oblique gust of wavenumber k. The streamwise and spanwise wavenumbers are given by

$$\begin{aligned} k_x &= k \cos \Lambda \\ k_y &= k \sin \Lambda \\ \Lambda &= \tan^{-1}\left(\frac{k_y}{k_x}\right) \end{aligned} \tag{10.26}$$

The trace velocity U_t of the moving co-ordinate system and the free-stream velocity U_r relative to this system are given by

$$U_t = U_\infty \frac{k_x}{k_y} \tag{10.27}$$

$$U_r = U_\infty \sqrt{1 + \frac{k_x^2}{k_y^2}} \tag{10.28}$$

Graham [6] showed that, depending on the value of a gust parameter which is related to the free-stream Mach number and to the intersection angle Λ, the space of solutions of a gust-airfoil interaction problem can be divided into two subspaces. Each subspace is represented by a model problem whose solution is known. Therefore, by means of appropriate similarity rules, any solution of a blade-vortex interaction problem can be related to the model solution of the related subspace. The two model solutions are that of an incompressible oblique blade-vortex interaction, and that of a two-dimensional compressible problem.

Suppose that the aerodynamic field of a small-amplitude gust frozenly convected past a thin airfoil can be described by a linearized form of the velocity potential equation (1.90). Setting $\mathbf{v}' = \nabla\phi$, where ϕ is a perturbation velocity potential, the linearized potential equation takes the form

$$\left(1 - M_\infty^2\right)\phi_{xx} + \phi_{yy} + \phi_{zz} - \frac{2\,M_\infty}{c_0}\phi_{xt} - \frac{1}{c_0^2}\phi_{tt} = 0 \tag{10.29}$$

where the x-axis is parallel to the mean flow.

Consider a thin blade lying on the plane $z = 0$, with section chord l parallel to the x-axis. Then suppose that the blade is embedded in the upwash gust

$$w = w_0\,\mathrm{e}^{\mathrm{i}\,\{k_x(x - U_\infty t) + k_y\,y\}} = w_0\,\mathrm{e}^{\mathrm{i}\,(\omega\,t - k_x x - k_y\,y)} \tag{10.30}$$

where $\omega = k_x\,U_\infty$. The boundary condition on the blade surface can be imposed in the form of a vanishing normal velocity, i.e.

$$\phi_z = w_0\,\mathrm{e}^{\mathrm{i}\,(\omega\,t - k_x x - k_y\,y)} \quad \text{for} \;\; z = 0, \quad -\frac{l}{2} \le x \le \frac{l}{2} \tag{10.31}$$

By using the transformation

$$\phi'(x,z) = \phi(x,y,z,t)\exp\left[-\mathrm{i}\,(\omega\,t - k_y\,y)\right] \tag{10.32}$$

into equation (10.29), the aerodynamic interaction problem is described by the equation

$$\left(1 - M_\infty^2\right)\phi'_{xx} + \phi'_{zz} - \frac{2\,\mathrm{i}\,\omega\,M_\infty}{c_0}\phi'_x + \left(\frac{\omega^2}{c_0^2} - k_y^2\right)\phi' = 0 \tag{10.33}$$

Finally, introducing the Prandtl-Glauert transformation

$$X = \frac{2\,x}{l}, \quad Y = \frac{2\,y}{l}, \quad Z = \beta\,\frac{2\,z}{l} \quad \text{with} \qquad \beta^2 = 1 - M_\infty^2 \tag{10.34}$$

and the Reissner [210] transformation

$$\Phi(X,Z) = \phi'(x,z)\,\exp\left(-\mathrm{i}\,\frac{k_x\,x\,M_\infty^2}{\beta^2}\right) \tag{10.35}$$

equation (10.33) takes the form

$$\Phi_{XX} + \Phi_{ZZ} + K^2\left(1 - \frac{1}{\mathcal{M}^2}\right)\Phi = 0 \tag{10.36}$$

where

$$\mathcal{M} = \frac{k_x}{k_y}\frac{M_\infty}{\beta} = \frac{M_\infty}{\beta}\cot\Lambda \tag{10.37}$$

is Graham's gust parameter and

$$K = K_x \frac{M_\infty}{\beta^2} \quad \text{with} \quad K_x = \frac{k_x\, l}{2} \tag{10.38}$$

is the reduced transformed streamwise wavenumber.

In the same transformed plane the boundary condition (10.31) takes the form

$$\Phi_Z = -\frac{w_0\, l}{2\,\beta} \exp\left(-\mathrm{i}\, K_x \frac{X}{\beta^2}\right) \quad \text{for } Z = 0, \quad -1 \le X \le 1 \tag{10.39}$$

whereas the linearized pressure equation

$$p = -\rho_\infty \left(\frac{\partial}{\partial t} + U_\infty \frac{\partial}{\partial x}\right) \phi \tag{10.40}$$

yields

$$C_p = -\frac{4}{U_\infty\, l} \exp\left(\mathrm{i}\, \frac{K_x}{\beta^2}\, X\, M_\infty^2\right) \left(\mathrm{i}\, \frac{K_x}{\beta^2}\, \Phi + \Phi_X\right) \tag{10.41}$$

where C_p denotes the pressure coefficient.

The Kutta condition at the trailing edge and the continuity of the pressure across the wake must be imposed as additional conditions. Thus, it results that

$$\Delta \left(\mathrm{i}\, \frac{K_x}{\beta^2}\, \Phi + \Phi_X\right) = 0 \quad \text{for } Z = 0, \quad X \ge 1 \tag{10.42}$$

The boundary condition at infinity depends on whether equation (10.36) is elliptic or hyperbolic. If $\mathcal{M} < 1$ the problem is elliptic and a vanishing disturbance condition must be imposed at infinity, namely

$$\Phi \to 0 \quad \text{as } R \to \infty \tag{10.43}$$

Conversely, if $\mathcal{M} > 1$ the problem is hyperbolic and a Sommerfeld radiation condition must be imposed at infinity, namely

$$\exp\left\{\mathrm{i}\, K \left(1 - \frac{1}{\mathcal{M}^2}\right) R\right\} \Phi \to 0 \quad \text{as } Z \to \pm\infty \tag{10.44}$$

with $R = \sqrt{X^2 + Z^2}$.

Consider the *subcritical* case $\mathcal{M} \le 1$. Setting $\mathcal{X}^2 = -K^2\left(1 - 1/\mathcal{M}^2\right)$, equation (10.36) can be written as

$$\Phi_{XX} + \Phi_{ZZ} - \mathcal{X}^2 \Phi = 0 \tag{10.45}$$

In the subspace of solutions $\Phi = \Phi\left(M_\infty, K_x, K_y\right)$ of equation (10.45)[6] with boundary condition (10.39), a line at fixed values of $\mathcal{X}$ and K_x/β^2 defines a set of similar solutions. Intersections between two distinct lines are not possible. Furthermore, each line intersects the surface $\mathcal{M} = 0$ ($M_\infty = 0$) only in one point. This surface consists of all the incompressible oblique solutions. Therefore, each solution can be related to its incompressible counterpart $\Phi(M_\infty^-, K_x^-, K_y^-)$ via the following similarity rules

$$\begin{aligned} M_\infty^- &= 0 \\ K_x^- &= \frac{K_x}{\beta^2} \\ K_y^- &= \frac{K_y}{\beta}\sqrt{1 - \mathcal{M}^2} \end{aligned} \tag{10.46}$$

[6] It should be reminded that $K_x = k_x\, l/2$ and $K_y = k_y\, l/2$.

No similarity rules are required in order to satisfy the boundary condition (10.43) at infinity.

Consider the *supercritical* case $\mathcal{M} \geq 1$. Setting $\mathcal{X}^2 = K^2\left(1 - 1/\mathcal{M}^2\right)$, equation (10.36) can be written as

$$\Phi_{XX} + \Phi_{ZZ} + \mathcal{X}^2\Phi = 0 \tag{10.47}$$

Again, in the subspace of solutions $\Phi = \Phi\left(M_\infty, K_x, K_y\right)$ of equation (10.47) with boundary condition (10.39), a line at fixed values of $\mathcal{X}$ and K_x/β^2 defines a set of similar solutions. Intersections between two distinct lines are not possible. Furthermore, each line intersects the surface $\mathcal{M} = \infty$ ($K_y = 0$) only in one point. This surface consists of all the compressible parallel ($\Lambda = 0$) solutions. Thus, each solution can be related to its compressible parallel counterpart $\Phi(M_\infty^+, K_x^+, K_y^+)$ via the following similarity rules

$$\begin{aligned} M_\infty^+ &= M_\infty\sqrt{1 - \frac{1}{\mathcal{M}^2}} \\ K_x^+ &= K_x\left(1 + \frac{K_y^2}{K_x^2}\right) \\ K_y^+ &= 0 \end{aligned} \tag{10.48}$$

The boundary condition (10.44) at infinity is automatically satisfied by all the similar solution at constant value of $\mathcal{X}$.

It is interesting to notice that, if $\mathcal{M} = 1$ then $K_y = M_\infty K_x/\beta$ and the two sets of similarity rules (10.46) and (10.48) overlap.

Equations (10.28) and (10.37) provide the free-stream Mach number relative to the moving axis system

$$M_r = \sqrt{M_\infty^2 + \beta^2\mathcal{M}^2} \tag{10.49}$$

At low subsonic free-stream it results that $M_r \simeq \mathcal{M}$. Therefore, the subcritical and supercritical flows correspond to subsonic and supersonic velocities, respectively, of the free-stream relatively to the moving co-ordinate system (10.25).

From equation (10.41) and the similarity rules (10.46) and (10.48), Graham [6] obtained the following expressions for the loading coefficient per unit upwash

- subcritical flow: $\mathcal{M} < 1$

$$\begin{aligned} C_{\Delta p}\left(M_\infty, K_x, K_y\right) = {} & C_{\Delta p^-}\left(0, \frac{K_x}{\beta^2}, \frac{K_y}{\beta}\sqrt{1-\mathcal{M}^2}\right) \\ & \frac{1}{\beta}\exp\left(\mathrm{i}\,\frac{K_x}{\beta^2}\,X\,M_\infty^2\right)\exp\left\{\mathrm{i}\,K_y Y\left[\frac{1}{\beta}\sqrt{1-\mathcal{M}^2} - 1\right]\right\} \end{aligned} \tag{10.50}$$

- supercritical flow: $\mathcal{M} > 1$

$$\begin{aligned} C_{\Delta p}\left(M_\infty, K_x, K_y\right) = {} & C_{\Delta p^+}\left(M_\infty\sqrt{1 - \frac{1}{\mathcal{M}^2}}, K_x\left[1 + \frac{K_y^2}{K_x^2}\right], 0\right) \\ & \sqrt{1 + \frac{K_y^2}{K_x^2}}\exp\left\{\mathrm{i}\,K_y\left(\frac{K_y}{K_x}X - Y\right)\right\} \end{aligned} \tag{10.51}$$

- critical flow: $\mathcal{M} = 1$

$$C_{\Delta p}\left(M_\infty, K_x, K_y\right) = C_{\Delta p^\pm}\left(0, \frac{K_x}{\beta^2}, 0\right)\frac{1}{\beta}\exp\left\{\mathrm{i}\left(\frac{K_x}{\beta^2}\,X\,M_\infty^2 - K_y Y\right)\right\} \tag{10.52}$$

where $C_{\Delta p^-}$, $C_{\Delta p^+}$ and $C_{\Delta p^\pm}$ are the loading coefficients induced by a unitary oblique gust in an incompressible flow, by a parallel gust in a compressible flow and by a parallel gust in an incompressible flow, respectively. The former solution can be expressed in terms of Filotas' [127] gust-response function, the second can be obtained by means of Possio's [128] integral equation for a two-dimensional unsteady compressible flow, whereas the third is the solution obtained by Sears [126] for a two-dimensional incompressible gust.

10.3.3 Amiet's Analysis

Amiet investigated the aeroacoustic problem of a thin airfoil embedded in a turbulent stream. The unsteady pressure field on a flat-plate was modeled as a distribution of acoustic dipoles whose strength is related to the incident turbulent field by means of an aerodynamic gust-response function.

Consider a harmonic dipole in the point $(x_1, y_1, z_1 = 0)$, with axis normal to the plane $z = 0$ and strength $F(x_1, y_1, \omega)$. The acoustic far field radiated in a uniformly moving medium has the following expression

$$p\,(x,y,z,\omega;x_1,y_1) = \frac{\mathrm{i}\,\omega\, z}{4\,\pi\, c_0\,\sigma^2}\,F(x_1,y_1,\omega)\exp\left\{\mathrm{i}\,\omega\left[t+\frac{M\,(x-x_1)-\sigma}{c_0\beta^2}+\frac{x x_1+y y_1\beta^2}{c_0\beta^2\sigma}\right]\right\} \tag{10.53}$$

where the x–axis is parallel to the flow, $\sigma = \sqrt{x^2+\beta^2(y^2+z^2)}$ and $\beta = \sqrt{1-M^2}$. As a consequence, the power spectral density of the sound radiated by a distribution of dipoles is

$$\begin{aligned} S_{pp}\,(x,y,z,\omega) &= \iiiint p\,(x,y,z,\omega;x_1,y_1)\;p^\star\,(x,y,z,\omega;x_2,y_2)\;\mathrm{d}x_1\,\mathrm{d}x_2\,\mathrm{d}y_1\,\mathrm{d}y_2 \\ &= \left(\frac{\omega z}{4\,\pi\,c_0\,\sigma^2}\right)^2 \iiiint S_{ww}(x_1,x_2,\eta,\omega)\,\mathrm{e}^{\,\mathrm{i}\,\frac{\omega}{c_0\beta^2}\left[\left(M-\frac{x}{\sigma}\right)(x_1-x_2)+\frac{\eta\beta^2 y}{\sigma}\right]}\,\mathrm{d}x_1\,\mathrm{d}x_2\,\mathrm{d}y_1\,\mathrm{d}y_2 \end{aligned} \tag{10.54}$$

where $\eta = y_2 - y_1$ and $S_{ww}(x_1, x_2, \eta, \omega)$ is the cross power spectral density of the dipole strength distribution.

As shown in chapter 7, a solid boundary in a turbulent field is equivalent to a distribution of acoustic dipoles whose strength is related to the pressure induced on the body surface. Thus, a flat-plate can be modeled as a distribution of dipoles whose strength is given by the pressure jump between its upper and lower sides.

Consider a rectangular airfoil of chord $2b$ and span $2d$ and let the airfoil spanwise direction y be normal to the free-stream velocity U. Then, suppose that a frozen vertical gust convected in the x-direction, has the generic form

$$w(x,y,t) = \iint_{-\infty}^{+\infty} \hat{w}(k_x,k_y)\;\mathrm{e}^{\mathrm{i}\,[k_x(x-U\,t)+k_y y]}\,\mathrm{d}k_x\,\mathrm{d}k_y \tag{10.55}$$

where $\hat{w}$ is a gust spectral component of wavenumbers k_x and k_y.

In a linear approximation, the pressure jump induced on the airfoil surface can be related to the gust spectral components by means of an aerodynamic transfer function $g(x, k_x, k_y)$. Thus, it results that

$$\Delta p(x,y,t) = 2\,\pi\,\rho_0\,U\,b \iint_{-\infty}^{+\infty} \hat{w}(k_x,k_y)\;g(x,k_x,k_y)\;\mathrm{e}^{\mathrm{i}\,(-k_x\,U\,t+k_y y)}\,\mathrm{d}k_x\,\mathrm{d}k_y \tag{10.56}$$

or, equivalently

$$\Delta p(x,y,t) = 2\,\pi\,\rho_0\,b \iint_{-\infty}^{+\infty} \hat{w}(k_x,k_y)\;g(x,k_x,k_y)\;\mathrm{e}^{\mathrm{i}\,k_y y}\,\mathrm{d}k_y\;\mathrm{e}^{\mathrm{i}\,\omega t}\,\mathrm{d}\omega \tag{10.57}$$

where the change of variable $\omega = -k_x U$ has been performed in order to isolate the following time-spectral component

$$\Delta\hat{p}(x,y,\omega) = 2\,\pi\,\rho_0\,b\int_{-\infty}^{+\infty} \hat{w}(K_x,k_y)\;g(x,K_x,k_y)\;\mathrm{e}^{\mathrm{i}\,k_y y}\,\mathrm{d}k_y \tag{10.58}$$

with $K_x = -\omega/U$.

The cross power spectral density of the pressure jump between two points on the airfoil surface is given by

$$S_{ww}(x_1,x_2,y_1,y_2,\omega) = \lim_{T\to\infty}\left\{\frac{\pi}{T}\,E\left[\Delta\hat{p}^\star(x_1,y_1,\omega)\;\Delta\hat{p}(x_2,y_2,\omega)\right]\right\} \tag{10.59}$$

where $E[\ldots]$ denotes the expected value of a random quantity. The only non-deterministic quantity in $\Delta\hat{p}(x,y,\omega)$ is $\hat{w}(K_x,k_y)$. Thus, substituting equation (10.58) into equation (10.59) yields

$$\begin{aligned} S_{ww}(x_1,x_2,y_1,y_2,\omega) &= (2\,\pi\,\rho_0\,b)^2\iint_{-\infty}^{+\infty} g^\star(x_1,K_x,k_{y_1})\;g(x_2,K_x,k_{y_2}) \\ &\mathrm{e}^{\mathrm{i}\,(-k_{y_1}y_1+k_{y_2}y_2)}\lim_{T\to\infty}\left\{\frac{\pi}{T}\,E\left[\hat{w}^\star(K_x,k_{y_1})\;\hat{w}(K_x,k_{y_2})\right]\right\}\,\mathrm{d}k_{y_1}\,\mathrm{d}k_{y_2} \end{aligned} \tag{10.60}$$

Because of the statistical orthogonality of the wavevectors, the ensemble average of the gust velocity can be written in the form

$$E\left[\hat{w}^\star(K_x,k_{y_1})\;\hat{w}(K_x,k_{y_2})\right] = \frac{U\,T}{\pi}\,\delta(k_{y_1}-k_{y_2})\,\Phi(K_x,k_{y_1}) \tag{10.61}$$

with

$$\Phi(K_x,k_{y_1}) = \int_{-\infty}^{+\infty}\phi(K_x,k_{y_1},k_z)\;\mathrm{d}k_z \tag{10.62}$$

and $\phi(k_x,k_y,k_z)$ denoting the energy spectrum of the turbulent velocity field. Thus, making use of equation (10.61) in equation (10.60), the cross power spectral density of the pressure jump takes the form

$$S_{ww}(x_1,x_2,\eta,\omega) = (2\pi\rho_0\,b)^2\,U\int_{-\infty}^{+\infty} g^\star(x_1,K_x,k_y)\,g(x_2,K_x,k_y)\,\mathrm{e}^{\mathrm{i}\,k_y\eta}\Phi(K_x,k_y)\;\mathrm{d}k_y \tag{10.63}$$

The cross-spectral density S_{ww} of the airfoil loading can be now substituted into equation (10.54) in order to obtain an expression for the power spectral density of the acoustic far field radiated by the airfoil. This is given by

$$\begin{aligned} S_{pp}\,(x,y,z,\omega) &= \left(\frac{\omega z\rho_0\,b}{2\,c_0\,\sigma^2}\right)^2 U\iiiint\!\!\int_{-\infty}^{+\infty} g^\star(x_1,K_x,k_y)\,g(x_2,K_x,k_y) \\ &\mathrm{e}^{\mathrm{i}\,k_y\eta}\Phi(K_x,k_y)\;\mathrm{d}k_y\mathrm{e}^{\mathrm{i}\,\frac{\omega}{c_0\beta^2}\left[\left(M-\frac{x}{\sigma}\right)(x_1-x_2)+\frac{\eta\beta^2 y}{\sigma}\right]}\,\mathrm{d}x_1\,\mathrm{d}x_2\,\mathrm{d}y_1\,\mathrm{d}y_2 \end{aligned} \tag{10.64}$$

or equivalently

$$S_{pp}\,(x,y,z,\omega) = \left(\frac{\omega z\rho_0\,b}{2\,c_0\,\sigma^2}\right)^2 U\int_{-\infty}^{+\infty}|\mathcal{P}(x,K_x,k_y)|^2\;\Phi(K_x,k_y)\;\mathrm{d}k_y\iint_{-d}^{+d}\mathrm{e}^{\mathrm{i}\,\eta\left(\frac{\omega}{c_0\,\sigma}\,y+k_y\right)}\,\mathrm{d}y_1\,\mathrm{d}y_2 \tag{10.65}$$

where

$$\mathcal{P}(x,K_x,k_y) = \int_{-b}^{+b} g(x_0,K_x,k_y)\, \mathrm{e}^{-\mathrm{i}\frac{\omega}{c_0\beta^2}\left(M-\frac{x}{\sigma}\right)x_0}\, \mathrm{d}x_0 \tag{10.66}$$

is an airfoil loading function that, in the small frequency limit, reduces to the airfoil sectional lift induced by a unitary gust.

Finally, if the latter double integral in equation (10.65) is evaluated analytically, the acoustic power spectral density takes the form

$$\begin{aligned} S_{pp}(x,y,z,\omega) &= \left(\frac{\omega z \rho_0 b}{c_0\,\sigma^2}\right)^2 U d\pi \\ & \int_{-\infty}^{+\infty} \left\{ \frac{\sin^2\left[d\left(\frac{\omega}{c_0\,\sigma}\,y + k_y\right)\right]}{\pi d\left(\frac{\omega}{c_0\,\sigma}\,y + k_y\right)^2} \right\} |\mathcal{P}(x,K_x,k_y)|^2\;\Phi(K_x,k_y)\;\mathrm{d}k_y \end{aligned} \tag{10.67}$$

An important property of the acoustic far field can be derived from equation (10.67) by letting the airfoil span tend to infinity. Because of the mathematical property

$$\lim_{d\to\infty} \left\{ \frac{\sin^2\left[d\left(\frac{\omega}{c_0\,\sigma}\,y + k_y\right)\right]}{\pi d\left(\frac{\omega}{c_0\,\sigma}\,y + k_y\right)^2} \right\} = \delta\left(\frac{\omega}{c_0\,\sigma}\,y + k_y\right) \tag{10.68}$$

equation (10.67) has the following limit expression

$$S_{pp}(x,y,z,\omega) = \left(\frac{\omega z \rho_0 b}{c_0\,\sigma^2}\right)^2 U d\pi \left|\mathcal{P}\left(x,K_x,\frac{\omega}{c_0\,\sigma}\,y\right)\right|^2\;\Phi\left(K_x,\frac{\omega}{c_0\,\sigma}\,y\right) \tag{10.69}$$

which shows that an observer at a distance y from the airfoil mid-span plane can listen only the gust component with spanwise wavenumber $k_y = -\omega/c_0\,\sigma$. At low Mach number it results that

$$k_y \simeq -k\,\sin\theta \tag{10.70}$$

where θ is the angle between the line joining the airfoil mid-point to the observer and its projection onto the mid-span plane $y = 0$. Since, $k_y = k\,\sin\Lambda$, then $\theta = -\Lambda$. In particular, on the plane $y = 0$ the skewed spectral components give opposite effects, whereas the only contribution to the acoustic far field is given by the parallel spectral components.

Equation (10.67) relates the acoustic far field to the incident turbulent field via the airfoil response function $g(x,k_x,k_y)$. As shown by Graham, depending on both the flow conditions and the characteristic parameters of the incident gust, the airfoil response function can be expressed in terms of Filotas' or Sears' gust-response functions, or determined by solving Possio's integral equation. Furthermore, Amiet proposed a low-frequency and a high-frequency solution procedure for a small perturbation flow, with time-dependent boundary conditions. The low-frequency approximation was based on a generalization of the Prandtl-Glauert technique to a time dependent compressible problem, whereas the high-frequency problem was solved in terms of Schwartzchild solution applied to a skewed gust. Both the low- and the high-frequency approximation are discussed in section 4.5.

10.3.4 Martinez & Widnall's Analysis

Martinez & Widnall [208] developed an aeroacoustic model for the wing-gust interaction problem. Both the aerodynamic and the acoustic problem were solved in terms of separated leading edge and trailing edge boundary-value problems, matched in an iterative converging scheme, as first proposed by Landahl [138].

Adamczyk [139] and Amiet [129] applied the same iterative scheme to obtain analytical expressions for the wing response to a high-frequency gust. Adamczyk used the Wiener-Hopf technique to solve the leading edge and the trailing edge boundary-value problems, whereas Amiet solved the same problems in terms of Schwartzchild solution of a semi-infinite boundary-value problem.

Martinez & Widnall [208] extended Adamczyk's analysis in order to describe the noise generated by the interaction between a skewed Sears-type gust and a wing of both finite and infinite span. The main results of Martinez & Widnall's analysis are reported below.

By applying the Wiener-Hopf technique both to the leading and the trailing edge problem in which the boundary-value problem (4.102) with boundary conditions from (4.103) to (4.106) can be separated, the following expression for the far pressure field can be obtained

$$
\begin{aligned}
P(x,y,z,t) \simeq\; & \sqrt{\frac{2}{\pi}} \frac{\rho_0 w_0 U_\infty \exp(\mathrm{i}\,\omega\, t - \mathrm{i}\; k_y\, y)}{\beta\sqrt{\frac{k_x}{\beta^2}+\mu}} \frac{1}{(x^2+z^2)^{1/4}} \\
& \exp\left\{\mathrm{i}\left[\frac{k_x M_\infty^2 \cos\theta}{\beta^2} - \mu\sqrt{1-M_\infty^2\sin^2\theta}\right]\sqrt{x^2+z^2}\right\} \\
& \left\{\frac{(1-\cos\theta^*/2)\,\mathrm{e}^{-\mathrm{i}\pi/4}/\sqrt{2} - E^*\left[2\mu\,(1-\cos\theta^*)\right]}{\left(1-M_\infty^2\sin^2\theta\right)^{1/4}}\right\}
\end{aligned}
\qquad (10.71)
$$

where the same notation as in section 4.5.2 has been used, and where

$$
\theta = \tan^{-1}\left(\frac{z}{x}\right) \qquad (10.72)
$$

$$
\theta^* = \tan^{-1}\left(\beta\,\tan\theta\right) \qquad (10.73)
$$

Equation (10.71) describes the far pressure field generated by the interaction of an oblique gust with an infinite-span wing. It can be used to obtain the acoustic far field of a rectangular wing of span $2\,l$. Consider the function

$$
\mathcal{S} = \sqrt{\frac{2}{\pi}} \frac{\sin\left(k_y - k_y^*\right)\, l/b}{k_y - k_y^*} \qquad (10.74)
$$

The k_y-Fourier transform of $\mathcal{S}$ is $\exp\left(-\mathrm{i}\; k_y^*\, y\right)$ for $|y| < l/b$ and zero elsewhere. Therefore, by adding a factor $\mathcal{S}$ to the right-hand side of equation (10.71) and integrating over k_y from $-\infty$ to ∞ leads to an approximated form of the rectangular wing response to a vertical gust $w_0 \exp\left(\omega t - k_x x - k_y^* y\right)$, i.e.

$$
P_{2l}(x,y,z,t) \simeq \frac{1}{\sqrt{2\pi}} \int_{-\infty}^{\infty} \mathrm{d}k_y\, \mathcal{S}\, \mathrm{e}^{-\mathrm{i}\; k_y\, y}\, \tilde{P}(x,y,z,t) \qquad (10.75)
$$

where $\tilde{P}(x,y,z,t)$ is the function $P(x,y,z,t)$ defined in equation (10.71), deprived of the factor $\mathrm{e}^{-\mathrm{i}\; k_y\, y}$.

By substituting equation (10.71) into equation (10.75) and using the method of stationary phase to evaluate the asymptotic behaviour of $P_{2l}(x,y,z,t)$, Martinez & Widnall [208] obtained the acoustic far field generated by the interaction between a finite-span wing and a skewed gust. In spherical co-ordinates (r_a, θ_a, ψ) it takes the form

$$
\begin{aligned}
P_{2l}(x_a,y,z,t) \simeq\; & \frac{-\mathrm{i}\,\rho_0 w_0 U_\infty \sqrt{2\,M_\infty}}{\pi\, r_a} \frac{D(\theta_a,\psi)}{(1+M_\infty\,\cos\theta_a \sin\psi)^2} \\
& \exp\left\{\frac{\mathrm{i}\,\omega}{1+M_\infty\,\cos\theta_a\sin\psi}\left[t - \frac{b\, r_a}{c_0}\right]\right\}
\end{aligned}
\qquad (10.76)
$$

where $x_a = x - (U/b)\,t$, $\theta_a = \tan^{-1}(z/x_a)$, $r_a = \sqrt{x_a^2 + y^2 + z^2}$, $(1 + M_\infty \cos\theta_a \sin\psi)^2$ denotes the amplitude Doppler factor and $D(\theta_a, \psi)$ is the directivity factor which is given by

$$D(\theta_a,\psi) \;=\; \frac{\sin\left\{\frac{\omega b}{U_\infty}\frac{l}{b}\left(\frac{M_\infty \cos\psi}{1+M_\infty\cos\theta_a\sin\psi} - \tan\Lambda^*\right)\right\}}{\frac{\omega b}{U_\infty}\left(\frac{M_\infty\cos\psi}{1+M_\infty\cos\theta_a\sin\psi} - \tan\Lambda^*\right)} \frac{1}{\sqrt{1+M_\infty\left\{1-\frac{\beta^2\cos^2\psi}{(1+M_\infty\cos\theta_a\sin\psi)^2}\right\}^{1/2}}}\,(F_1+F_2+F_3) \tag{10.77}$$

with

$$\begin{aligned}
F_1 &= \frac{-\mathrm{i}\,\sin\theta_a\sin\psi/\sqrt{2}}{\sqrt{\frac{1}{\beta^2}\left\{1-\frac{\beta^2\cos^2\psi}{(1+M_\infty\cos\theta_a\sin\psi)^2}\right\}^{1/2} - \frac{M_\infty}{\beta^2} - \frac{\cos\theta_a\sin\psi}{1+M_\infty\cos\theta_a\sin\psi}}}\\
F_2 &= \mathrm{i}\,(1+M_\infty\cos\theta_a\sin\psi)\left\{1-\frac{\beta^2\cos^2\psi}{(1+M_\infty\cos\theta_a\sin\psi)^2}\right\}^{1/4}\\
F_3 &= 1+\sqrt{2}\,\mathrm{e}^{-\mathrm{i}\,3\pi/4}E^*\left(\frac{2\omega\, bM_\infty}{U_\infty}F_4\right)\\
F_4 &= \frac{1}{\beta^2}\left\{1-\frac{\beta^2\cos^2\psi}{(1+M_\infty\cos\theta_a\sin\psi)^2}\right\}^{1/2} - \frac{M_\infty^2}{\beta^2}\frac{\cos\theta_a\sin\psi}{1+M_\infty\cos\theta_a\sin\psi}
\end{aligned} \tag{10.78}$$

where the identities $k_x = (\omega\, b/U_\infty)\tan\Lambda$ and $k_y^* = (\omega\, b/U_\infty)\tan\Lambda^*$ have been used (see 10.26).

Martinez & Widnall [208] showed that for $\mu(\Lambda^*) > \pi/4$ (a real value of μ corresponds to a supersonic spanwise propagation speed of the gust in the wing reference frame), the sound at a generic far field location results from the combination of disturbances from every point on the wing, except the trailing edge. Conversely, for $\mu^2(\Lambda^*) < -(\pi/4)^2$ (subsonic gust spanwise propagation speed), the far field noise mainly results from the wing tip sections.

10.3.5 Howe's Analysis

In this subsection the model problem of a line-vortex convected past a thin airfoil by a low Mach number flow is illustrated. The analysis is that proposed by Howe [13] to describe the influence of vortex shedding on the interaction noise generated by an acoustically compact airfoil.

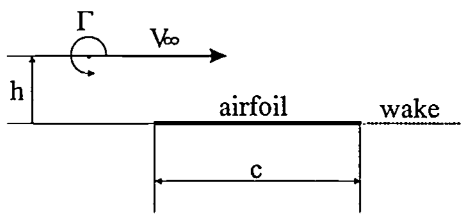

FIGURE 10.3: Interaction between a thin airfoil of chord $c = 2a$ and a line-vortex of circulation Γ.

Consider a flat-plate of chord $c = 2a$ $(-a \le x_1 \le a,\ x_2 = 0)$ in a uniform parallel stream of velocity V_∞. Suppose that the mean flow Mach number $M_\infty = V_\infty/c_0$ is sufficiently small that $M_\infty^2 \ll 1$. This allows to suppose that the flow is incompressible, but does not eliminate the convective effects on the acoustic radiation, which are of order $\mathcal{O}(M_\infty)$.

Suppose that a line-vortex of circulation Γ is frozenly convected by the mean flow along the path $x_2 = h$ parallel to the airfoil chord (see Fig.10.3). Since the image vortex system disturbs the vortex path as the vortex passage by the airfoil edges, the vortex circulation is sufficiently small to suppose that the vortex path is not significantly perturbed from the constant value $x_2 = h$. The incident line-vortex induces the singular vorticity field

$$\omega = \Gamma\, \delta(x_1 - V_\infty t)\; \delta(x_2 - h)\; \hat{e}_3 \tag{10.79}$$

where $\hat{e}_3$ is the unit vector taken out of the paper (parallel to the airfoil edges).

Assuming an ideal and homentropic fluid, Howe's [20] inhomogeneous wave equation for the stagnation enthalpy takes the form of equation (6.53). At low mean flow Mach numbers, the speed of sound can be regarded as constant and equal to c_0. Furthermore, by linearizing the wave operator, equation (6.53) becomes

$$\left(\frac{1}{c_0^2}\frac{\mathrm{D}^2}{\mathrm{D}t^2} - \nabla^2\right) B = \nabla \cdot (\omega \times \mathbf{u}) \tag{10.80}$$

As the vortex is convected past the airfoil, vorticity is shed from the airfoil trailing edge into the field. In a linear approach the airfoil wake can be described as a vortex-sheet convected along the plane $x_1 > 0, x_2 = 0$ at the free-stream velocity V_∞. The strength of the vortex-sheet can be determined by requiring that a Kutta condition is satisfied at the airfoil trailing edge.

The vortex dipole associated with the incident vortex is

$$\nabla \cdot (\omega \times \mathbf{u}) = \Gamma\, V_\infty \frac{\partial}{\partial x_2}\{\delta(x_1 - V_\infty t)\; \delta(x_2 - h)\} \tag{10.81}$$

The vortex force distribution associated with the vortex-sheet is

$$\omega \times \mathbf{u} = Z(\mathbf{x}, t)\; \delta(x_2)\; \hat{e}_2 \tag{10.82}$$

where the wake strength Z can be obtained from the Crocco's equation

$$\frac{\partial \mathbf{u}}{\partial t} + \nabla B = -\omega \times \mathbf{u} \tag{10.83}$$

Since the normal velocity is continuous across the vortex-sheet, integrating across a small interval normal to the vortex-sheet yields

$$Z = -\,[B]_2^1 \tag{10.84}$$

where $[\ldots]_2^1$ denotes the jump in crossing the wake in the $+x_2$ direction. For an irrotational flow equation (10.83) is equivalent to Bernoulli's equation

$$B + \frac{\partial \phi}{\partial t} = 0 \tag{10.85}$$

where the function ϕ is the velocity potential. Hence, the wake strength in (10.84) can be written as

$$Z = \left[\frac{\partial \phi}{\partial t}\right]_2^1 \tag{10.86}$$

The wake is convected at the free-stream velocity V_∞, thus

$$\frac{\mathrm{D}\phi}{\mathrm{D}t} \equiv \frac{\partial \phi}{\partial t} + V_\infty \frac{\partial \phi}{\partial x_1} = 0 \tag{10.87}$$

Furthermore, the pressure is continuous across the vortex-sheet, thus

$$\left[\frac{\mathrm{D}\phi}{\mathrm{D}t}\right]_2^1 = 0 \tag{10.88}$$

Hence, arranging (10.86), (10.87) and (10.88) gives

$$Z = V_\infty (u_2 - u_1) = V_\infty \gamma(x_1, t) \tag{10.89}$$

where $\gamma(x_1, t)$ is the wake circulation density. The vortex dipole corresponding to the vortex-sheet is

$$\nabla \cdot (\omega \times \mathbf{u}) = V_\infty \frac{\partial}{\partial x_2} \{\gamma(x_1, t)\ \delta(x_2)\} \tag{10.90}$$

Substituting (10.81) and (10.90) into equation (10.80) yields

$$\left(\frac{1}{c_0^2}\frac{\mathrm{D}^2}{\mathrm{D}t^2} - \nabla^2\right) B = \Gamma\, V_\infty \frac{\partial}{\partial x_2} \{\delta(x_1 - V_\infty t)\ \delta(x_2 - h)\} + V_\infty \frac{\partial}{\partial x_2} \{\gamma(x_1, t)\ \delta(x_2)\} \tag{10.91}$$

Equation (10.91) can be solved by making use of the Green's function technique. The wavelength of the acoustic disturbances generated by the vortex-airfoil interaction is of order

$$\lambda \sim \frac{2a}{M_\infty} \tag{10.92}$$

Therefore, if M_∞ is sufficiently small, the airfoil is acoustically compact and a low frequency Green's function can be used to solve equation (10.91). As discussed in subsection 6.4.1, the compact Green's function tailored to the airfoil in the presence of a mean flow is

$$G(\mathbf{x}, \mathbf{y}, t, \tau) = \frac{1}{4\pi\, |\mathbf{X} - \mathbf{Y}|} \delta \left\{ t - \tau - \frac{|\mathbf{X} - \mathbf{Y}|}{c_0} + \mathbf{M} \cdot \frac{(\mathbf{X} - \mathbf{Y})}{c_0} \right\} \tag{10.93}$$

where $\mathbf{M}$ is the mean flow Mach number, $X_i = x_i - \phi_i^*(\mathbf{x})$ and $Y_i = y_i - \phi_i^*(\mathbf{y})$, with ϕ_i^* denoting the velocity potential of the incompressible fluid motion generated by a translational rigid motion of the airfoil in the i-direction at unit speed. Equivalently, X_i represents the potential of incompressible flow about the airfoil which at large distances is of unit velocity in the i-direction. Clearly, in a two-dimensional field $X_3 = x_3$.

The potential X_i can be determined by using the conformal transformation

$$z \equiv x_1 + \mathrm{i}\, x_2 = \frac{1}{2}\left(\zeta + \frac{a^2}{\zeta}\right) \tag{10.94}$$

which maps a circle of radius a into a flat-plate of chord $2a$. The complex potential past the circle, which is of unit velocity in the i-direction at a large distance from the airfoil, is

$$W(\zeta) = \frac{1}{2}\left(\zeta \mathrm{e}^{-\mathrm{i}\,\theta_i} + \frac{a^2}{\zeta}\mathrm{e}^{\mathrm{i}\,\theta_i}\right) \tag{10.95}$$

Thus, substituting the inverse conformal mapping $\zeta = z + \sqrt{z^2 - a^2}$ yields

$$X_i = \Re\left\{z \cos\theta_i - \mathrm{i}\sqrt{z^2 - a^2} \sin\theta_i\right\} \tag{10.96}$$

It should be observed that, as $|z|/a \to \infty$, $X_i \to \Re\left\{z\mathrm{e}^{-\mathrm{i}\,\theta_i}\right\} = x_i$.o

The conformal mapping technique can be also employed to determine the wake circulation density γ. Imposing the zero-velocity Kutta condition in the ζ-plane leads to

$$\Gamma\left\{\frac{1}{\zeta_v - a} + \frac{1}{\zeta_v^* - a}\right\} + \int_a^\infty \frac{\gamma(\xi)}{a}\left(\frac{\xi + a}{\xi - a}\right)^{\frac{1}{2}} \mathrm{d}\xi = 0 \tag{10.97}$$

where ζ_v is the location of the incident vortex[7].

Using the Fourier transform result

$$\delta(x_1 - V_\infty t) = \frac{1}{2\pi V_\infty} \iint_{-\infty}^{\infty} \delta(x_1 - y_1) \exp\left\{ \mathrm{i}\,\omega \left(\frac{y_1}{V_\infty} - t \right) \right\} \mathrm{d}y_1\, \mathrm{d}\omega \tag{10.98}$$

the singular vorticity field (10.79) induced by the incident vortex can be written as

$$\omega = \frac{\Gamma}{2\pi V_\infty} \hat{e}_3 \iint_{-\infty}^{\infty} \delta(x_1 - y_1)\, \delta(x_2 - h) \exp\left\{ \mathrm{i}\,\omega \left(\frac{y_1}{V_\infty} - t \right) \right\} \mathrm{d}y_1\, \mathrm{d}\omega \tag{10.99}$$

The Fourier transform of the wake circulation should have the same form of the incident vorticity wave (10.99). Therefore, $\gamma_0(\omega) \exp\{\mathrm{i}\,\omega\xi/V_\infty\} \exp(-\mathrm{i}\,\omega t)$ is the wake spectral component of frequency ω. The Kutta condition (10.97) yields

$$\frac{\Gamma}{2\pi V_\infty} \int_{-\infty}^{\infty} \left\{ \frac{1}{\zeta_v - a} + \frac{1}{\zeta_v^* - a} \right\} \exp\left(\mathrm{i} \frac{\omega y_1}{V_\infty} \right) \mathrm{d}y_1 + \gamma_0(\omega) \int_a^{\infty} \frac{\exp\{\mathrm{i}\,\omega\xi/V_\infty\}}{a} \left(\frac{\xi + a}{\xi - a} \right)^{\frac{1}{2}} \mathrm{d}\xi = 0 \tag{10.100}$$

where $\zeta_v = y_1 + \mathrm{i}\,h + \sqrt{(y_1 + \mathrm{i}\,h)^2 - a^2}$ is the vortex position in the ζ-plane. From equation (10.100) it follows that

$$\gamma_0(\omega) = \frac{-\Gamma\,\mathrm{sgn}(\omega)}{\pi V_\infty} \exp\left\{ -\frac{|\omega|\,h}{V_\infty} \right\} \left\{ \frac{J_0(\omega a/V_\infty) + \mathrm{i}\, J_1(\omega a/V_\infty)}{H_0^{(1)}(\omega a/V_\infty) + \mathrm{i}\, H_1^{(1)}(\omega a/V_\infty)} \right\} \tag{10.101}$$

Let us now determine the wake and the incident vortex contributions to the acoustic far field.

The noise generated by the wake vorticity $\gamma_0(\omega) \exp\{\mathrm{i}\,\omega\xi/V_\infty\} \exp(-\mathrm{i}\,\omega t)$ can be determined by integrating the noise generated by harmonic wake component

$$\gamma_0 \exp\{\mathrm{i}\,\omega\xi/V_\infty\} \exp(-\mathrm{i}\,\omega t) = \gamma_0 \exp\{-\mathrm{i}\,k_1 V_\infty (t - \xi/V_\infty)\} \tag{10.102}$$

over all frequencies $\omega \equiv k_1 V_\infty$.

Using the low frequency Green's function (10.93) to solve equation (10.91) provides the wake contribution

$$B_w = \frac{V_\infty \gamma_0}{4\pi} \iiiint_{-\infty}^{\infty} \mathrm{d}y_1\, \mathrm{d}y_2\, \mathrm{d}y_3\, \mathrm{d}\tau \frac{\partial}{\partial y_2} \left(\exp\{-\mathrm{i}\,k_1 V_\infty (t - \xi/V_\infty)\} \right)$$
$$\frac{1}{|\mathbf{X} - \mathbf{Y}|} \delta\left\{ t - \tau - \frac{|\mathbf{X} - \mathbf{Y}|}{c_0} + \mathbf{M} \cdot \frac{(\mathbf{X} - \mathbf{Y})}{c_0} \right\} \tag{10.103}$$

In order to relate the stagnation enthalpy to the acoustic pressure, consider the Bernoulli's equation (6.46). It can be written as

$$B = -\left(\frac{\mathrm{D}\phi}{\mathrm{D}t} - \mathbf{u} \cdot \nabla\phi \right) \tag{10.104}$$

whose linearized form is

$$\begin{aligned} B &= \frac{p}{\rho_0} + \mathbf{U} \cdot \nabla\phi \\ &= \frac{p}{\rho_0} \left(1 + \frac{\rho_0 c_0 \nabla\phi}{p} \cdot \mathbf{M} \right) \end{aligned} \tag{10.105}$$

where p, ϕ and B denote disturbance quantities and $\mathbf{U}$ is the mean flow. In the far field the acoustic pressure and velocity are related by

$$\frac{\partial\phi}{\partial r} \simeq \frac{p}{\rho_0 c_0} \tag{10.106}$$

[7]The same approach has been used by von Kármán & Sears' [123] and by Chiocchia & Casalino [32].

which can be written as

$$\frac{\rho_0 c_0 \nabla\phi}{p} \simeq \frac{\mathbf{x}}{|\mathbf{x}|} \tag{10.107}$$

Thus, substituting (10.107) into (10.105) yields

$$B = \frac{p}{\rho_0}\left(1 + \mathbf{M}\cdot\frac{\mathbf{x}}{|\mathbf{x}|}\right) \tag{10.108}$$

As shown by Howe [13], integrating equation (10.103), taking the observer in the far field and using (10.108) lead to

$$\frac{p}{\rho_0} \simeq \frac{-\mathrm{i}\, V_\infty \gamma_0\, a\, \sin\theta}{4\,(1 + M_\infty\cos\theta)}\left(\frac{\pi k_1 M_\infty}{2R}\right)^{\frac{1}{2}} H_1^{(1)}(k_1 a)\exp\left\{-\mathrm{i}\left[k_1 V_\infty t_{\mathrm{ret}} - \frac{\pi}{4}\right]\right\} \tag{10.109}$$

where

$$t_{\mathrm{ret}} = t - \frac{R}{a\,(1 + M\cos\theta)} \tag{10.110}$$

is the retarded time, R is the distance of the observer from the airfoil and θ is the angle between the observation direction and the $+x_1$ axis.

Finally, the noise generated by the airfoil wake of circulation density $\gamma_0(\omega)\exp\{\mathrm{i}\,\omega\xi/V_\infty\}$ can be calculated by substituting (10.101) into equation (10.109), and integrating over all frequencies. It thus results that

$$\frac{p}{\rho_0} \simeq \frac{\mathrm{i}\,\Gamma V_\infty a \sin\theta\; \mathrm{e}^{\mathrm{i}\frac{\pi}{4}}}{4\pi h\,(1 + M_\infty\cos\theta)}\left(\frac{M_\infty \pi}{2Rh}\right)^{\frac{1}{2}}$$
$$\int_{-\infty}^{\infty}\sqrt{\nu}\ \mathrm{sgn}(\nu)\ \exp\left(-|\nu| - \mathrm{i}\frac{\nu}{h}V_\infty t_{\mathrm{ret}}\right) H_1^{(1)}\left(\frac{\nu a}{h}\right)\left\{\frac{J_0\left(\frac{\nu a}{h}\right) + \mathrm{i}\,J_1\left(\frac{\nu a}{h}\right)}{H_0^{(1)}\left(\frac{\nu a}{h}\right) + \mathrm{i}\,H_1^{(1)}\left(\frac{\nu a}{h}\right)}\right\}\mathrm{d}\nu \tag{10.111}$$

where the variable transformation $\nu = \omega h/V_\infty$ has been performed. This integral can be evaluated explicitly in two extreme cases:

- $a/h \ll 1$, vortex passing at large distance from the airfoil, i.e.

$$\frac{p}{\rho_0} \simeq \frac{\Gamma V_\infty \sin\theta}{4\,(1 + M_\infty\cos\theta)}\left(\frac{M_\infty}{2Ra}\right)^{\frac{1}{2}}\left[\left(\frac{a}{R_v}\right)^{\frac{3}{2}}\sin\left(\frac{3\theta_v}{2}\right)\right]_{\mathrm{ret}} \tag{10.112}$$

  where (R_v, θ_v) are the polar co-ordinate of the incident vortex.

- $a/h \gg 1$, vortex passing at small distance from the airfoil, i.e.

$$\frac{p}{\rho_0} \simeq \frac{\Gamma V_\infty \sin\theta}{4\pi\,(1 + M_\infty\cos\theta)}\left(\frac{M_\infty}{Ra}\right)^{\frac{1}{2}}\left[\frac{a/h}{1 + (V_\infty t - a)^2/h^2}\right]_{\mathrm{ret}} \tag{10.113}$$

The noise generated by the incident vorticity wave (10.99) can be determined by integrating the noise generated by a harmonic incident gust over all frequencies.

Consider the Sears-type gust

$$\mathbf{u} = \mathbf{A}\exp\{\mathrm{i}\,[k_1\,(x_1 - V_\infty t) + k_2 x_2]\} \tag{10.114}$$

and the associated vorticity field

$$\omega = \mathrm{i}\,\mathbf{k}\times\mathbf{A}\exp\{\mathrm{i}\,[k_1\,(x_1 - V_\infty t) + k_2 x_2]\} \tag{10.115}$$

Since the gust is incompressible, $\mathbf{k} \cdot \mathbf{A} \equiv k_1 A_1 + k_2 A_2 = 0$. Therefore, equation (10.115) can be written as

$$\omega = \mathrm{i}\, A_2 \frac{k_1^2 + k_2^2}{k_1} \exp\left\{\mathrm{i}\left[k_1 \left(x_1 - V_\infty t\right) + k_2 x_2\right]\right\} \tag{10.116}$$

Following Howe [13], the acoustic pressure generated by the incident vortical gust (10.116) can be determined by convoluting equation (10.91) with the low frequency Green's function (10.93). Then, taking the observer in the far field and using equation (10.108) provide

$$\frac{p}{\rho_0} \simeq \frac{A_2 V_\infty\, a \sin\theta}{\left(1 + M_\infty \cos\theta\right)} \left(\frac{\pi k_1 M_\infty}{2R}\right)^{\frac{1}{2}} J_1(k_1 a) \exp\left\{-\mathrm{i}\left[k_1 V_\infty t_{\mathrm{ret}} - \frac{\pi}{4}\right]\right\} \tag{10.117}$$

This solution can be used to determine the far pressure field generated by the vortex passage past the airfoil. Thus, convoluting the vorticity wave (10.99), leads to

$$\frac{p}{\rho_0} \simeq \frac{-\mathrm{i}\,\Gamma V_\infty a \sin\theta\, \mathrm{e}^{\mathrm{i}\frac{\pi}{4}}}{4\pi h \left(1 + M_\infty \cos\theta\right)} \left(\frac{M_\infty \pi}{2Rh}\right)^{\frac{1}{2}}$$
$$\int_{-\infty}^{\infty} \sqrt{\nu}\ \mathrm{sgn}(\nu)\ \exp\Big(-|\nu| - \mathrm{i}\frac{\nu}{h} V_\infty t_{\mathrm{ret}}\Big)\, J_1\Big(\frac{\nu a}{h}\Big)\ \mathrm{d}\nu \tag{10.118}$$

Again, this integral can be evaluated explicitly in two extreme cases:

- $a/h \ll 1$, vortex passing at large distance from the airfoil, i.e.

$$\frac{p}{\rho_0} \simeq \frac{-3\,\Gamma V_\infty \sin\theta}{16\left(1 + M_\infty \cos\theta\right)} \left(\frac{M_\infty}{2Ra}\right)^{\frac{1}{2}} \left[\left(\frac{a}{R_v}\right)^{\frac{5}{2}} \sin\Big(\frac{5\theta_v}{2}\Big)\right]_{\mathrm{ret}} \tag{10.119}$$

- $a/h \gg 1$, vortex passing at small distance from the airfoil, i.e.

$$\frac{p}{\rho_0} \simeq \frac{\Gamma V_\infty \sin\theta}{4\pi\left(1 + M_\infty \cos\theta\right)} \left(\frac{M_\infty}{Ra}\right)^{\frac{1}{2}} \left[\frac{\left(V_\infty t + a\right) a/h^2}{1 + \left(V_\infty t + a\right)^2/h^2} - \frac{a/h}{1 + \left(V_\infty t - a\right)^2/h^2}\right]_{\mathrm{ret}} \tag{10.120}$$

The two terms in the retarded-time brackets of equation (10.120) account for the scattering effects of the airfoil leading and trailing edges, respectively. An important result is that the diffraction of the trailing edge is exactly canceled by the wake contribution (10.113). Howe [13] argued that such an exact cancelation is a consequence of the linear assumptions made by supposing that both the incident vortex and the wake are convected at constant velocity along rectilinear paths. Furthermore, Howe showed that the exact cancelation of the trailing edge diffraction contribution is related to the fact that, when the vortex is convected at the free-stream velocity V_∞, the normal velocity vanishes at all points of the wake. In this case the flow conditions are steady in a convected frame of reference and no sound is radiated.

In conclusion, the vortex shedding smoothes the large pressure gradients near the trailing edge, reducing the diffraction contribution of the trailing edge. However, nonlinear effects related to the image vortex system are responsible for the generation of a trailing edge noise contribution.

10.4 BVI Numerical Predictions

Blade-vortex interaction occurs in the flow field about the main rotor of a helicopter, especially when it operates in steady, descending flight conditions, when the rotor wake is forced to remain in the rotor disk. The resulting interaction between tip-vortices and advancing blades is a complex three-dimensional, unsteady, viscous and compressible phenomenon that induces unsteady loadings and high impulsive noise levels.

Three mechanisms are involved in BVI:

- the vortex shedding from the blade-tips;
- the vortex convection in the rotor wake;
- the vortex interaction with one or more oncoming blades.

Because of the different order of magnitude between the local scale of the blade and the global scale of the rotor, a comprehensive numerical simulation of a blade-vortex interaction is still prohibitive. Therefore, simplified numerical predictions must be performed by separately investigating the local and the global scale of the phenomenon.

10.4.1 Local Simulations

The unsteady aerodynamic field about a lifting airfoil in a vortical flow can be described only numerically. Two distinct numerical approaches can be adopted to simulate vortex-airfoil interactions. The first is the primitive (or conservative) variable approach, which consists in solving a system of governing partial differential equations, such as the Euler or the Navier-Stokes equations, with a suitable set of boundary conditions. The second is the linearized approach which is based on the following approximation: for mean potential flows with small amplitude vortical and entropic disturbances imposed upstream, the unsteady velocity field can be split into a known rotational component and an unknown potential component that satisfies a linear inhomogeneous nonconstant-coefficient convective wave equation.

The primitive variable approach requires a long computational time and large computer memory. In addition, because of the nonlinear character of the flow, the accuracy of the unsteady solution may be strongly affected by the physical consistency of the far field boundary conditions.

A simplified primitive variable approach is usually performed, provided that the flow is assumed to be incompressible. It consists in describing the incident vorticity field by means of discrete-vortices convected by a flow which is a solution of a Laplace's equation. Boundary value methods or conformal mapping techniques are then adopted in order to account for the presence of a body in the field. Discrete-vortex simulations are particularly suitable to investigate the effects of the vortex distortion during a direct blade-vortex interaction. Furthermore, phenomena related to the viscosity of the fluid, such as vortex-shedding and boundary-layer separations, can be simulated but these require additional conditions.

The linearized approach is valid only for small amplitude disturbances, a requirement that is usually satisfied in many flows of practical interest. Methods based on the solution of a single linear wave equation have significant advantages over methods based on the solution of a system of nonlinear partial differential equations:

- the computational time is far shorter;
- stable and accurate differencing schemes are simpler to be derived;
- physically consistent far field boundary conditions can be determined, which permit more accurate unsteady aerodynamic predictions.

Linearized approaches are particularly suitable for three-dimensional oblique blade-vortex interactions in highly compressible flows. Moreover, for periodic gust-airfoil interactions, the linearized approach provides an effective way to investigate the effects onto the near and far pressure field of both the wavelength of the incident vorticity field and its orientation with respect to the blade leading edge.

Numerical predictions based on potential flow modeling of isolated line-vortices convected past lifting airfoils [68, 32, 211] show that:

- the noise level is strongly affected by the vortex trajectory;

- the vortex trajectory is a strong nonlinear function of the airfoil lift, the vortex initial position and the vortex circulation;

- the line-vortex models overpredict the noise levels, especially during a direct vortex-airfoil interaction. This is mainly due to the fact that a line-vortex model does not account for the vortex distortion during a closer encounter.

The distortion of the vorticity field is a nonlinear rearrangement mechanism which occurs especially when the vortex and the curvature radius of the airfoil leading edge have a comparable scale. The effect of the vortex distortion on the interaction dynamics is twofold: on one hand it smoothes the dependence of the interaction process upon some parameters of the problem, on the other hand it reduces the loading peaks induced under critical interaction conditions [211].

Although nonlinearity plays a dominant role in the direct interaction between a vortex and an airfoil, it is not the only affecting factor. Vortex diffusion within the airfoil boundary-layer, vortex-shedding from the trailing edge and boundary-layer separation at the leading edge are viscosity related mechanisms that must be accounted for when a prediction is attempted of the BVI noise and unsteady loading. Moreover, when an oblique blade-vortex interaction occurs in high Mach number flows, both compressible and three-dimensional effects have an important influence on the acoustic power and directivity.

In the following subsections some analyses and numerical simulations of blade-vortex and gust-airfoil interactions are reviewed. Three different approaches are presented, based on the discrete-vortex model, the Navier-Stokes equations and the linearized convected wave equation.

10.4.1.1 Discrete-Vortex Simulations

Lee & Smith [212] investigated the effect of the vortex distortion by describing the impinging vorticity field by multiple vortex elements convected in a two-dimensional flow. The airfoil surface was described by means of an integral boundary-element method. An adaptative panel distribution on the airfoil surface as the vortices move along the airfoil was used in order to accurately predict the effects induced by the vorticity field.

Consider an unsteady, incompressible, inviscid, and rotational flow. In terms of vorticity $\omega\,\hat{k} = \nabla\times\mathbf{u}$, the linear momentum equation can be written as

$$\frac{\partial\omega}{\partial t} + \mathbf{u}\cdot\nabla\omega = 0 \tag{10.121}$$

As shown in section 1.5, the velocity field can be decomposed into a solenoidal field $\mathbf{u}_\omega$ and an incompressible, irrotational, potential field $\mathbf{u}_\phi$. Therefore,

$$\mathbf{u} = \mathbf{u}_\omega + \mathbf{u}_\phi \tag{10.122}$$

where

$$\nabla\cdot\mathbf{u}_\omega = 0 \tag{10.123}$$
$$\nabla\times\mathbf{u}_\phi = 0 \tag{10.124}$$

A vector potential $\mathbf{A}$ and a scalar potential ϕ can be defined such that

$$\nabla^2\mathbf{A} = -\omega \quad \text{with} \quad \mathbf{u}_\omega = \nabla\times\mathbf{A} \tag{10.125}$$

and

$$\nabla^2\phi = 0 \quad \text{with} \quad \mathbf{u}_\phi = \nabla\phi \tag{10.126}$$

These two fields are coupled by the boundary condition of zero normal velocity

$$\frac{\partial \phi}{\partial n} + \mathbf{u}_\omega \cdot \mathbf{n} = 0 \tag{10.127}$$

on the airfoil surface.

By integrating the linear momentum equation (1.74) along a streamline, provided that $\mathbf{u} = \nabla\phi + \mathbf{u}_\omega$, the following form of the unsteady Bernoulli equation can be obtained

$$C_p = 1 - u^2 - 2\frac{\partial \phi}{\partial t} - 2\int_l \frac{\partial \mathbf{u}_\omega}{\partial t} \cdot \mathrm{d}\mathbf{l} \tag{10.128}$$

where C_p is the pressure coefficient.

The total circulation in the flow is conserved, hence

$$\begin{aligned} &\frac{\mathrm{d}\Gamma(t)}{\mathrm{d}t} = 0 \quad \text{with} \\ &\Gamma(t) = \Gamma_a + \Gamma_v + \Gamma_w \end{aligned} \tag{10.129}$$

where Γ_a denotes the circulation around the airfoil, Γ_v is the circulation of the interacting vortices and Γ_w is the circulation of the vorticity shed from the trailing edge. The instantaneous value of Γ_w can be determined by requiring that the pressure jump between the upper and lower airfoil sides vanishes at the trailing edge. Thus, from equations (10.128) and (10.129) it follows that

$$\frac{\mathrm{d}\Gamma_a}{\mathrm{d}t} = -\frac{\mathrm{d}\Gamma_w}{\mathrm{d}t} = \frac{1}{2}\left(u_{-TE}^2 - u_{+TE}^2\right) \tag{10.130}$$

where u_{-TE} and u_{+TE} respectively denote the velocity immediately below and above the trailing edge on the airfoil surface.

The airfoil surface can be described as a surface distribution of sources with strength taken constant in each boundary panel. The scalar potential field is thus given by

$$\phi(\mathbf{x}_i, t) = \mathbf{U}_\infty \cdot \mathbf{x}_i + \sum_j \frac{q_j(t)}{2\pi}\int_j \ln|\mathbf{x}_i - \mathbf{x}_j|\,\mathrm{d}s_j + \frac{\gamma_a(t)}{2\pi}\int_j \tan^{-1}\left(\frac{y_i - y_j}{x_i - x_j}\right)\mathrm{d}s_j \tag{10.131}$$

where $q_j(t)$ denotes the source strength of the panel j and $\gamma_a(t)$ is the airfoil circulation per unit length.

By applying the boundary condition (10.127) at each surface panel, with ϕ given by equation (10.131), a set of linear equations for q_j and γ_a can be obtained and solved at each time-step.

A vortex is shed from the trailing edge at each time-step and its intensity is given by a discretized form of equation (10.130). These vortices are moved to their new positions at the local velocity $\mathbf{u} = \mathbf{u}_{\omega V} + \mathbf{u}_{\omega W} + \nabla\phi$, where $\mathbf{u}_{\omega V}$ is the velocity induced by the impinging vortices and $\mathbf{u}_{\omega W}$ is the velocity induced by the shed vortices. Both $\mathbf{u}_{\omega V}$ and $\mathbf{u}_{\omega W}$ can be determined through the Biot-Savart law.

In order to investigate the effects of the vortex distortion, the initial vorticity field is modeled as multiple, discrete-vortex elements clustered in a circular cloud. The vortex core is that of a Rankine vortex, having a uniform vorticity distribution. A second order Runge-Kutta time integration algorithm is adopted in order to reduce the numerical diffusion of the incident vorticity field. Furthermore, the numerical instability is minimized by:

- assuming vortex elements of equal area, that is, of equal circulation;
- locating each vortex in the centroid of a cloud surface element;
- assuming an aspect ratio of each cloud element close to 1.

Lee & Smith [212] investigated the interaction between an isolated vortex and an NACA-0012 airfoil and observed that:

1. the amount of vortex distortion, the airfoil lift and the mixing of the impinging vortex with the airfoil wake are affected by the size and the strength of the impinging vortex;

2. the main effect of the vortex distortion is to reduce the unsteady loading peaks;

3. when the vortex passes by the airfoil trailing edge an appreciable lift variation occurs;

4. the unsteady pressure terms have an important effect on the airfoil lift.

Park & Lee [213] used an Euler-Lagrangian method in order to calculate the unsteady, viscous, incompressible flow field of a Rankine vortex impinging on the sharp leading edge of a wedge. The vorticity field was described by means of a random vortex method, the convection velocity of each vortical element was calculated by means of a fast vortex method, and the physical domain was mapped into a numerical domain by means of a Schwartz-Christoffel transformation.

In terms of vorticity ω, the incompressible, unsteady Navier-Stokes equation has the form

$$\frac{\partial \omega}{\partial t} + (\mathbf{u} \cdot \nabla)\,\omega = \frac{1}{\mathrm{Re}}\nabla^2\omega \quad \text{with} \tag{10.132}$$

$$\nabla \cdot \mathbf{u} = 0 \tag{10.133}$$

where Re is a reference Reynolds number.

Consider the Schwartz-Christoffel transformation which maps the numerical domain ζ into the physical domain z, i.e.

$$z = a\int \left\{(\zeta - s_j)^{\alpha/\pi - 1} + (\zeta + s_j)^{\alpha/\pi - 1}\right\} \mathrm{d}\zeta + b \tag{10.134}$$

where a and b are the parameters of the transformation, α is the wedge interior angle and s_j is a constant associated with the edge rounding off, which avoids the leading edge singularity. The complex velocity in the physical domain is given by

$$V(z) = V(\zeta)\,\frac{\mathrm{d}\zeta}{\mathrm{d}z} \tag{10.135}$$

where $V(\zeta)$ is the complex velocity in the numerical domain. The vorticity field consists of:

- incident vortical elements, which are blob-vortices arranged in a Rankine vortex;

- vortex-sheets which are shed from some generation points within a numerical boundary-layer along the wedge surface;

- blob-vortices originated when a vortex-sheet crosses the numerical boundary-layer.

Impinging vortex elements are convected by means of a two-step Runge-Kutta time integration scheme, i.e.

$$\begin{aligned} \mathbf{x}^{n+1/2} &= \mathbf{x}^n + \frac{\Delta t}{2}\,\mathbf{u}(\mathbf{x}^n) \\ \mathbf{x}^{n+1} &= \mathbf{x}^n + \Delta t\,\mathbf{u}\left(\mathbf{x}^{n+1/2}\right) \end{aligned} \tag{10.136}$$

whereas vortex-sheets and surface vortices are convected by means of a first-order Euler method, i.e.

$$\mathbf{x}^{n+1} = \mathbf{x}^n + \Delta t\,\mathbf{u}(\mathbf{x}^n) \tag{10.137}$$

In equations (10.136) and (10.137) both blob-vortices and vortex-sheets, are convected at the local flow velocity $\mathbf{u}$.

By separating the advection part of equation (10.132) from its diffusion part, the local velocity of a blob-vortex can be rigorously calculated by means of the Biot-Savart law, provided that the vorticity field ω is known. Then, a random walk method can be employed in order to simulate the viscous diffusion mechanism. It thus results that

$$\mathbf{x}^{n+1} = \mathbf{x}^{n+1}_{\text{convection}} + \eta \tag{10.138}$$

where η is a random Gaussian distribution with mean value 0 and a variance proportional to Δt and the kinematic viscosity ν.

The convection velocity of a vortex-sheet can be calculated from Prandtl's boundary-layer equation

$$\frac{\partial \omega}{\partial t} + (\mathbf{u} \cdot \nabla)\,\omega = \frac{1}{\mathrm{Re}} \frac{\partial^2 \omega}{\partial y^2} \quad \text{with} \tag{10.139}$$

$$\omega = -\frac{\partial u}{\partial y} \quad \text{and} \tag{10.140}$$

$$\nabla \cdot \mathbf{u} = 0 \tag{10.141}$$

By defining the vortex-sheet strength as the circulation per unit length, i.e.

$$\gamma = \lim_{\Delta y \to 0} \int_{y}^{y-\Delta y} \omega \, dy \tag{10.142}$$

the vorticity field is given by

$$\omega(\mathbf{x}, t) = \sum_j \gamma_j \, b(x_j(t) - x) \; \delta(y_j(t) - y) \tag{10.143}$$

where x and y are the local body-fitted co-ordinates and b is a linear smoothing function given by

$$b(x) = \begin{cases} 1 - 2\,|x|\,/h, & |x| < h/2 \\ 0, & \text{otherwise} \end{cases} \tag{10.144}$$

h being the length of the vortex-sheet. Therefore, the tangential and normal velocity of the ith vortex-sheet at the time-step n can be obtained from equations (10.140), (10.141) and (10.143). It follows that

$$u_i^n \equiv u(x_i(n\Delta t)\,, y_i(n\Delta t)) = U_\delta^n(x_i) + \sum_j \gamma_j \, b(x_j(t) - x_i) \; H\big(y_j^n - y_i\big) \tag{10.145}$$

$$\begin{aligned} v_i^n \equiv v(x_i(n\Delta t)\,, y_i(n\Delta t)) &= -\frac{\partial U_\delta^n(x_i)}{\partial x}\, y_i \\ &-\frac{1}{h} \sum_j \gamma_j \left[b\Big(x_i + \frac{h}{2} - x_j^n\Big) - b\Big(x_i - \frac{h}{2} - x_j^n\Big) \right] \min\big(y_i, y_j^n\big) \end{aligned} \tag{10.146}$$

Equation (10.137) is used to convect a vortex-sheet to the next time-step location, whereas a random walk method is performed to simulate the boundary-layer viscous diffusion. Consistently with equation (10.139), a random perturbation is imposed only in the y-direction.

The local convection velocity of a blob-vortex can be calculated by means of the Biot-Savart law. However, in order to reduce the computational time, a fast vortex method can be performed. It consists in solving the following Poisson equation

$$\nabla^2 \mathbf{u} \simeq \sum_j g(\mathbf{x} - \mathbf{x}_j) \tag{10.147}$$

where g denotes the discretized Laplacian of the velocity induced by a blob-vortex. A Sculley [28] blob-vortex model

$$u_\theta = \frac{\Gamma}{2\pi r}\frac{1}{1+a^2/r^2} \tag{10.148}$$

is assumed, and equation (10.147) is solved on a discretized numerical domain with the normal boundary condition on the body surface satisfied via the image method. The velocity at each vortex location is finally calculated by means of a cubic spline interpolation of the values computed at the grid points.

The numerical simulation is performed by calculating, at each time-step, the velocity convection of each vortical element in the flow field, moving them to the next time-step locations, and by using equation (10.145) to calculate the tangential velocity at some generation points on the wedge surface. Whenever the surface velocity is greater than a control value, a vortex-sheet is generated and its strength is such that the no-slip boundary condition is satisfied at the generation point. Furthermore, when a vortex-sheet crosses the numerical boundary-layer it is converted into a blob-vortex which is added to the field.

Park & Lee [213] showed that, when a Rankine vortex is initially located above the centerline of the wedge, a secondary vortex is shed toward the underside of the wedge as the oncoming vortex approaches the leading edge. The secondary vortex is of opposite circulation and less intense than the incident one. Furthermore, distortion and splitting of the incident vortex occur, but do not depend upon the viscosity of the fluid. Conversely, the vortex shedding from the leading edge is due to a viscous interaction process.

Chiocchia & Casalino [32] used a conformal mapping technique in order to describe the unsteady aerodynamic field of a double row of counter-rotating vortices convected past a Kármán-Trefftz airfoil. A vortex-sheet was shed from the airfoil trailing edge in order to satisfy a zero-velocity unsteady Kutta condition. The model accounted for all the induction effects between the oncoming vortices, the airfoil and the airfoil wake, but the latter was convected at a constant velocity. The interaction noise was successively predicted by using an acoustic analogy approach and the unsteady pressure field on the airfoil surface.

Consider a Kármán-Trefftz conformal transformation, which maps the outer region of a circle in the complex ζ-plane into the outer region of an airfoil in the complex z-plane, namely

$$z = (\theta/4)\,\frac{(\zeta+1/4)^\theta + (\zeta-1/4)^\theta}{(\zeta+1/4)^\theta - (\zeta-1/4)^\theta} \tag{10.149}$$

where $\theta = 2-\epsilon/\pi$ and ϵ is the value of the trailing edge angle. The circle is centered in $\zeta_c = -a + \mathrm{i}b$, intersects the real axis at $\xi_{TE} = 1/4$ and has radius $R_c = \sqrt{(\xi_{TE}+a)^2+b^2}$. The point ξ_{TE} maps into the airfoil trailing edge $x_{TE} = \theta/4$.

Making the change of variable $\zeta' = \zeta - \zeta_c$ and letting a line-vortex of circulation Γ ($k = \Gamma/2\pi$) occupy the position ζ_v, the complex potential field can be written as

$$W(\zeta') = W_s + W_v + W_w \tag{10.150}$$

where W_s denotes the steady potential of a Kármán-Trefftz airfoil, W_v is the contribution of the incident vortex, and W_w is the potential of a wake shed from the airfoil trailing edge, as required by an unsteady Kutta condition. Quantities in the following expressions are made dimensionless by the free-stream velocity V_∞ and by the airfoil chord.

The steady potential contribution is given by

$$W_s(\zeta') = \mathrm{e}^{-\mathrm{i}\alpha}\zeta' + \frac{R_c^2}{\zeta'}\mathrm{e}^{\mathrm{i}\alpha} + \mathrm{i}\frac{\Gamma_s}{2\pi}\ln\zeta' \tag{10.151}$$

where α is the airfoil angle of attack and $\Gamma_s = 4\pi R_c \sin(\alpha + \beta)$ is the airfoil steady circulation, which depends on the airfoil camber $\beta = \tan^{-1}[b/(\xi_{TE} + a)]$.

The vortex potential contribution is given by

$$W_v(\zeta') = -\mathrm{i}\,k \left\{ \ln\left(\zeta' - \zeta_v'\right) - \ln\left(\zeta' - \frac{R_c^2}{\zeta_v'^*}\right) + \ln\zeta' \right\} \tag{10.152}$$

where the first and the second term describe the potential field of a vortex at ζ_v' and its image within the circle, whereas the third term accounts for a vortex added to the circle center in order to cancel the image vortex when the incident one is infinitely far.

Finally, supposing that the wake is a continuous distribution of vorticity along the real axis ξ, its potential contribution is given by

$$W_w(\zeta') = -\frac{\mathrm{i}}{2\pi} \int_{\xi_{TE}}^{\xi_F} \ln\left(\frac{\zeta' - \zeta_w'}{\zeta' - R_c^2/\zeta_w'^*}\right) \gamma(\xi)\,\mathrm{d}\xi \tag{10.153}$$

where $\gamma(\xi)$ is the specific circulation of the vortex-sheet shed from the airfoil trailing edge.

In order to account for the flow unsteadiness, the motion of the oncoming vortex must be taken into account in the complex formulation. Therefore, the following history is assumed to describe the vortex-airfoil interaction process.

a) A vortex of given intensity is located at an arbitrary upstream position, sufficiently far from the airfoil. As a result, a vanishing velocity is induced at the trailing edge and the vortex-sheet has a vanishing circulation γ. The circulation around the airfoil is thus initially due to the only steady-state contribution Γ_s.

b) As the vortex moves towards the airfoil, a wake is progressively shed from the trailing edge, allowing the Kutta condition to be instantaneously fulfilled. The instantaneous reaction of the flow around the airfoil is a consequence of both the incompressible and inviscid character of the flow: the flow perturbations induced by the oncoming vortex propagate at an infinite velocity, no relaxation effects occur at the trailing edge.

c) The trajectory of the oncoming vortex is instantaneously perturbed from the steady-state streamlines by the induction of the whole vorticity field, namely, the image vortex, the wake already shed into the field and the image system of the wake.

The circulation of the wake progressively shed from the trailing edge depends on the instantaneous perturbation induced by all the preexisting vortical disturbances (the oncoming vortex, the wake already shed and the respective images) at the trailing edge. A physically consistent condition requires that the velocity induced at the trailing edge is finite. This condition is equivalent to a zero velocity condition applied onto ξ_{TE} in the circle plane. Hence, the circulation of the vortex-sheet can be determined by requiring that it induces a velocity at ξ_{TE} which exactly cancels the velocity induced by the preexisting vortical disturbances. This is the form of the unsteady Kutta condition adopted in the present fixed-wake approach.

Since the steady potential satisfies the Kutta condition at the trailing edge by definition, the zero velocity Kutta condition in the circle-plane takes the form

$$(V^*)_{\xi_{TE}} = \left(\frac{\mathrm{d}W_v}{\mathrm{d}\zeta}\right)_{\xi_{TE}} + \left(\frac{\mathrm{d}W_w}{\mathrm{d}\zeta}\right)_{\xi_{TE}} = 0 \tag{10.154}$$

Introducing equations (10.152) and (10.153) into equation (10.154), setting $\zeta'_{TE} = R_c \,\mathrm{e}^{-\mathrm{i}\beta}$ and rearranging yields

$$\int_{\xi_{TE}}^{\xi_F} \frac{2R_c \cos\beta + \xi - \xi_{TE}}{R_c \,\mathrm{e}^{-\mathrm{i}\beta} (\xi - \xi_{TE})} \gamma(\xi)\,\mathrm{d}\xi = \Gamma\,\phi(\zeta_v) \tag{10.155}$$

where

$$\phi(\zeta_v) = \frac{1}{R_c \,\mathrm{e}^{-\mathrm{i}\beta} - \zeta'_v} + \frac{1}{R_c \,\mathrm{e}^{-\mathrm{i}\beta}} - \frac{\zeta'^{*}_v}{\zeta'^{*}_v R_c \,\mathrm{e}^{-\mathrm{i}\beta} - R_c^2} \tag{10.156}$$

Then, changing back to the airfoil-plane and using the identity $\gamma(x)\,\mathrm{d}x = \gamma(\xi)\,\mathrm{d}\xi$ leads to the integral equation

$$\int_{x_{TE}}^{x_{TE}+V_\infty t} \left\{ 1 - 4\,R_c \cos\beta \left[1 - \left(\frac{x+\theta/4}{x-\theta/4} \right)^{\frac{1}{\theta}} \right] \right\} \gamma(x)\,\mathrm{d}x = \Gamma\,\phi(\zeta_v) \tag{10.157}$$

where the upper limit of integration results from having supposed that the wake is convected at the free-stream velocity V_∞ along the real axis.

It is expedient to express the wake in a body frame of reference by means of the Galilean transformation $\sigma = -x + x_{TE} + \tau$, with $\tau = V_\infty t$. Thus, equation (10.157) takes the form

$$\int_0^\tau \left\{ 1 - 4R_c \cos\beta \left[1 - \left(\frac{\tau - \sigma + \theta/2}{\tau - \sigma} \right)^{\frac{1}{\theta}} \right] \right\} \gamma(\sigma)\,\mathrm{d}\sigma = \Gamma\phi(\zeta_v) \tag{10.158}$$

with the initial condition $\gamma(0) = 0$ which is consistent with the condition of zero initial velocity at the trailing edge.

Interestingly, for $\zeta_c = 0$ and $\theta = 2$, which correspond to a flat-plate, the kernel in equation (2.38) reduces to $\sqrt{(\tau + 1 - \sigma)/(\tau - \sigma)}$, which is the same of the integral equation obtained by Wagner [21] for an impulsive start of a flat-plate at a small incidence.

The known term ϕ in (10.156) is a function of the instantaneous vortex position ζ_v. The corresponding position in the z-plane is given by $z_v(\tau) = z_v^o + \int_0^\tau V_c(z_v)\,\mathrm{d}\tau'$, where z_v^o is the initial position of the vortex. The convection velocity V_c is given by the following expression in which use of Routh's theorem has been made

$$V_c^\star(z_v) = \left(\frac{\mathrm{d}\tilde{W}}{\mathrm{d}\zeta} \right)_{\zeta_v} \left(\frac{\mathrm{d}\zeta}{\mathrm{d}z} \right)_{\zeta_v} - \mathrm{i}\frac{\Gamma}{4\pi} \left(\frac{\mathrm{d}^2\zeta/\mathrm{d}z^2}{\mathrm{d}\zeta/\mathrm{d}z} \right)_{\zeta_v} \tag{10.159}$$

where $\tilde{W}$ is the overall complex potential deprived of the self-vortex contribution.

Since the vortex velocity V_c is an implicit function of time, equation (10.158) must be solved by successive updates of the vortex position. Moreover, in order to account for the wake contribution, an integral extending from 0 to τ requires to be calculated at each time-step.

An acoustic analogy prediction requires the unsteady pressure field on the airfoil surface. This is given by the Bernoulli's equation

$$C_p(z,\tau) = 1 - V(z,\tau)\,V^*(z,\tau) - 2\,\Re\left(\frac{\partial}{\partial\tau} W(\zeta,\tau) \right)_{\zeta(z)} \tag{10.160}$$

where C_p is the pressure coefficient and V is complex the velocity in the airfoil-plane.

10.4.1.2 Navier-Stokes Simulations

Hardin & Lamkin [69] computed the unsteady aerodynamic field around a lifting Joukowski airfoil interacting with a distributed vortex.

By supposing a two-dimensional incompressible flow, the Navier-Stokes equations can be written as

$$\nabla^2 \psi = -\omega \tag{10.161}$$

$$\frac{\partial \omega}{\partial t} + \frac{\partial \Psi}{\partial y}\frac{\partial \omega}{\partial x} - \frac{\partial \Psi}{\partial x}\frac{\partial \omega}{\partial y} = \nu\, \nabla^2 \omega \tag{10.162}$$

where Ψ denotes the stream function, such that $u = \Psi_y$ and $v = -\Psi_x$, ω is the vorticity of the flow and ν is the kinematic viscosity of the fluid. Hardin & Lamkin solved sequentially in time the coupled equations (10.161) and (10.162) at a chord based Reynolds number of 200 with a no-slip boundary condition imposed on the airfoil surface.

The oncoming vortex is given by

$$\omega = \omega_0\, \mathrm{e}^{-\gamma r^2} \quad \text{for} \quad r \le r_c \tag{10.163}$$

and it is introduced into the field upstream of the airfoil. The cut-off radius r_c is an input parameter which determines the size of the vorticity field, whereas the parameter γ is such that the vorticity strength at r_c is reduced of one percent of the maximum value ω_0 in the vortex center. Therefore, it results that

$$\gamma = \frac{-\ln(0.01)}{r_c^2} \tag{10.164}$$

The input parameter ω_0 is related to the vortex circulation Γ_0 by the relationship

$$\Gamma_0 = \int_0^{2\pi}\int_0^{r_c} \omega\, r\, \mathrm{d}r\, \mathrm{d}\theta = \frac{0.99\,\pi\,\omega_0}{\gamma} \tag{10.165}$$

In order to predict the radiated acoustic field from the vorticity field around the airfoil, Hardin & Lamkin [69] exploited the theory developed by Howe [20]. For an isentropic and low Mach number flow, provided that the characteristic wavelength of the acoustic field is much larger than the airfoil chord, the far pressure field is given by

$$p(\mathrm{x}, t) = \frac{-\rho_0}{4\pi c_0\, x\left(1 + \mathbf{M}_0 \cdot \frac{\mathrm{x}}{x}\right)} \frac{\partial}{\partial t} \iiint\limits_V \left[(\omega \times \mathrm{v}) \cdot \nabla \left\{ \left(\frac{\mathrm{x}}{x} - \mathbf{M}_0 \right) \cdot \mathrm{y} \right\} \right]_{\mathrm{ret}} \mathrm{dy} \tag{10.166}$$

where ρ_0 and c_0 are the ambient density and speed of sound, respectively, and $\mathbf{M}_0$ is the mean flow Mach number. The integration extends over the total volume of the flow and the integrand is evaluated at the retarded time $t - (x - \mathbf{M}_0 \cdot \mathrm{x})/c_0$.

Hardin & Lamkin observed that aerodynamic noise is generated even in the absence of the impinging vortex, as a consequence of the interaction between the boundary-layer fluctuations and the trailing edge. Furthermore, they argued that the noise resulting from a direct vortex-airfoil interaction is quite less impulsive when both viscous effects and the distributed nature of the impinging vortex are taken into account. Finally, they observed that a vortex loses its organized structure and is strongly diffused after it have impinged onto the airfoil leading edge. Therefore Hardin & Lamkin argued that helicopter BVI noise is mainly generated by the first encounter between a tip-vortex and an oncoming blade.

Rai [70] used a fifth-order accurate, Osher-type upwind scheme in order to solve the thin-layer Navier-Stokes equations with an implicit scheme which was second-order-accurate in time.

The differencing scheme was demonstrated to preserve the vortex structure for much longer time than both central and upwind second-order accurate schemes. The vortex preserving test consisted in checking the core pressure of a lamb-type vortex, namely

$$u_\theta = \frac{\Gamma}{2\pi r}\frac{1}{1 + a^2/r^2} \tag{10.167}$$

convected by a uniform flow. The increasing rate of the core pressure was assumed as representative of the numerical vortex decay induced by the numerical scheme.

The first numerical prediction was concerned with a non direct vortex-airfoil interaction at a Mach number of 0.536 and a chord based Reynolds number of 1.3×10^6. The vortex parameters were chosen in order to fit the experimental conditions of Caradonna *et al.* [72]. A good agreement was obtained between numerical and experimental results.

The second numerical simulation was concerned with a direct vortex-airfoil interaction. The flow conditions were the same as in the first case, but the vortex circulation was higher. Distortion and splitting of the impinging vortex were predicted. The upper and lower vortex fragments were convected with different velocities along the respective airfoil sides, and interacted with the airfoil wake.

The third computation was concerned with a non direct vortex-airfoil interaction in transonic flow conditions. The free-stream Mach number was 0.8, while all the other flow parameters were the same as in the second case. The two shocks on the upper and lower airfoil sides were perturbed from their symmetric steady positions by the presence of the vortex. Furthermore, on the lower side, the vortex-shock interaction induced a large bubble of separation from the shock foot, up to the airfoil trailing edge. Furthermore, the structure of the lower shock was strongly affected by the vortex passage and a shock bifurcation near the wall was observed.

10.4.1.3 Linearized Models

Atassi *et al.* [33] used an integral Kirchhoff method in order to relate the far pressure field to the aerodynamic field past a flat-plate interacting with a three-dimensional gust. The aerodynamic solution scheme was developed by Scott & Atassi [214] and was shown to provide accurate numerical results only in the airfoil near field. In fact, as discussed by Atassi & Scott [215], the far field direct solution largely differed from the solution obtained by propagating the near pressure field into the far field through an integral approach.

Consider a two-dimensional airfoil of chord c, placed at nonzero angle of attack into a uniform stream of velocity U_∞ parallel to the x_1 axis. Let

$$\mathbf{u}_\infty = \mathbf{a}\, e^{\mathrm{i}\,\mathbf{k}\cdot(\mathbf{x}-\hat{\imath}\,U_\infty t)} \tag{10.168}$$

be a solenoidal ($\mathbf{a}\cdot\mathbf{k} = 0$), small amplitude ($a \ll U_\infty$) gust, imposed upstream onto the flow. Let the velocity field be decomposed into the sum of a steady mean potential flow and an unsteady fluctuating field, namely

$$\mathbf{u}(\mathbf{x}, t) = \mathbf{U}(\mathbf{x}) + \mathbf{u}'(\mathbf{x}, t) \tag{10.169}$$

Then, let us decompose the unsteady velocity $\mathbf{u}'$ into the sum of a known vortical (solenoidal and rotational) component $\mathbf{u}_R$ and a potential (irrotational) component $\nabla\phi$, that is

$$\mathbf{u}'(\mathbf{x}, t) = \mathbf{u}_R + \nabla\phi \tag{10.170}$$

For a flat-plate at zero angle of attack the unsteady velocity can be decoupled from the mean flow and $\mathbf{u}_R$ reduces to the upstream gust $\mathbf{u}_\infty$.

Let us consider the motion of an ideal fluid (inviscid and not-heat conducting) governed by the Euler equations. These can be linearized with respect to the steady mean flow and arranged as a convective wave equation for the potential ϕ, i.e.

$$\frac{\mathrm{D}_0}{\mathrm{D}t}\left(\frac{1}{c_0^2}\frac{\mathrm{D}_0\phi}{\mathrm{D}t}\right) - \frac{1}{\rho_0}\nabla\cdot(\rho_0\nabla\phi) = \frac{1}{\rho_0}\nabla\cdot(\rho_0\,\mathbf{u}_R) \tag{10.171}$$

where ρ_0 and c_0 are the local mean flow density and speed of sound, respectively, and $\mathrm{D}_0/\mathrm{D}t$ is the convective derivative associated to the mean velocity. The fluctuating pressure is given by

$$p = -\rho_0(\mathbf{x})\,\frac{\mathrm{D}_0\phi}{\mathrm{D}t} \tag{10.172}$$

For a uniform and parallel mean flow, because of the solenoidal character of the vortical disturbance, equation (10.171) reduces to

$$\frac{1}{c_0^2}\frac{\mathrm{D}_0^2\phi}{\mathrm{D}t^2} - \nabla^2\phi = 0 \tag{10.173}$$

which describes the aerodynamic field around a flat-plate, embedded in a small amplitude solenoidal gust.

For a flat-plate, the boundary conditions of (i) vanishing normal velocity on the airfoil surface and (ii) pressure continuity across the wake take the form

$$\frac{\partial\phi}{\partial x_2} = -a_2\,\mathrm{e}^{\mathrm{i}\,;k_1(x_1-U_\infty t)+\mathrm{i}\,k_3x_3} \quad \text{for} \quad -\frac{c}{2}\le x_1\le\frac{c}{2}, \qquad x_2=0 \tag{10.174}$$

$$\frac{\mathrm{D}_0}{\mathrm{D}t}(\Delta\phi) = 0 \quad \text{for} \quad x_1 > \frac{c}{2}, \qquad x_2 = 0 \tag{10.175}$$

Furthermore, the unsteady potential ϕ satisfies the far field condition

$$\nabla\phi \to 0 \quad \text{as} \quad x_1 \to -\infty \tag{10.176}$$

Equation (10.173) and the boundary conditions (10.174), (10.175) and (10.176) can be made dimensionless by the reference length $c/2$, the reference velocity U_∞, the reference time $c/2U_\infty$, the reference gust amplitude a and the reference potential $c\,a/2$. It thus results that

$$M_\infty^2\frac{\mathrm{D}^2\phi}{\mathrm{D}t^2} - \nabla^2\phi = 0 \tag{10.177}$$

$$\frac{\partial\phi}{\partial x_2} = -a_2\,\mathrm{e}^{\mathrm{i}\,k_1(x_1-t)+\mathrm{i}\,k_2x_2} \quad \text{for} \quad -1\le x_1\le 1, \qquad x_2 = 0 \tag{10.178}$$

$$\frac{\mathrm{D}}{\mathrm{D}t}(\Delta\phi) = 0 \quad \text{for} \quad x_1 > 1, \qquad x_2 = 0 \tag{10.179}$$

$$\nabla\phi \to 0 \quad \text{as} \quad x_1 \to -\infty \tag{10.180}$$

where

$$\frac{\mathrm{D}}{\mathrm{D}t} = \frac{\partial}{\partial t} + \frac{\partial}{\partial x_1} \tag{10.181}$$

and

$$k_1 = \frac{\omega\,c}{2U_\infty} \tag{10.182}$$

is the streamwise wavenumber, with ω denoting the angular frequency of the upstream disturbance.

Equation (10.177) can be reduced to a Helmholtz equation by introducing the Prandtl-Glauert transformation

$$x = x_1 \tag{10.183}$$

$$y = \beta x_2 \tag{10.184}$$

$$z = x_3 \tag{10.185}$$

with $\beta^2 = 1 - M_\infty^2$, and by setting

$$\varphi = \phi\,\mathrm{e}^{\mathrm{i}\,\frac{k_1M_\infty^2}{\beta^2}x}\,\mathrm{e}^{\mathrm{i}\,k_1t-\mathrm{i}\,k_3x} \tag{10.186}$$

Therefore, the wave equation takes the form

$$\frac{\partial^2\varphi}{\partial x^2} + \frac{\partial^2\varphi}{\partial y^2} + \left\{\left(\frac{k_1M_\infty}{\beta^2}\right)^2 - \left(\frac{k_3}{\beta}\right)^2\right\}\varphi = 0 \tag{10.187}$$

and the boundary conditions (10.178), (10.179) and (10.180) take the form

$$\frac{\partial \varphi}{\partial y} = -\frac{a_2}{\beta}\, \mathrm{e}^{\mathrm{i}\, k_1 x} \qquad \text{for} \quad -1 \le x \le 1, \qquad y = 0 \tag{10.188}$$

$$\left(-\frac{\mathrm{i}\, k_1}{\beta^2} + \frac{\partial}{\partial x}\right)(\Delta\varphi) = 0 \qquad \text{for} \quad x > 1, \qquad y = 0 \tag{10.189}$$

$$\nabla\varphi \to 0 \qquad \text{as} \quad x \to -\infty \tag{10.190}$$

Finally, the wake boundary condition (10.189) can be integrated leading to

$$\Delta\varphi = \Delta\varphi_{\mathrm{TE}}\, \mathrm{e}^{\frac{\mathrm{i}\, k_1}{\beta^2}(x-1)} \quad \text{for} \quad x > 1, \qquad y = 0 \tag{10.191}$$

where $\Delta\varphi_{\mathrm{TE}}$ is the potential jump at the airfoil trailing edge.

The boundary-value problem defined by the Helmholtz equation (10.187) and the boundary conditions (10.188), (10.190) and (10.191) can be solved numerically. Then, the pressure field can be obtained from the potential field by means of equation (10.172).

The pressure distribution on the flat-plate can be calculated by means of a Possio [128] solver. This strategy was adopted by Atassi *et al.* [215] in order to test the numerical solution of the boundary-value problem.

As shown by Atassi *et al.* [33], the pressure field satisfies a Helmholtz equation in the transformed Prandtl-Glauert plane (x, y, z), that is

$$\left(\nabla^2 + K^2\right) P = 0 \tag{10.192}$$

where

$$K = \sqrt{\left(\frac{k_1 M_\infty}{\beta^2}\right)^2 - \left(\frac{k_3}{\beta}\right)^2} \tag{10.193}$$

and

$$P = \frac{p}{\rho_0\, a_2\, U_\infty}\, \mathrm{e}^{-\mathrm{i}\,(\omega t - k_3 x_3)}\, \mathrm{e}^{-\mathrm{i}\, M_\infty\, K_1\, x} \tag{10.194}$$

with

$$K_1 = \frac{k_1\, M_\infty}{\beta^2} = \frac{\pi}{\beta^2}\frac{c}{\lambda} \tag{10.195}$$

By using the Green's theorem, the transformed pressure P in a field point can be related to the values taken upon the airfoil surface. It thus results that

$$P(\mathrm{x}) = \frac{1}{2\pi}\int_{-1}^{1}\left(\Delta P \frac{\partial G}{\partial y_2} - G \frac{\partial\, (\Delta P)}{\partial y_2}\right) \mathrm{d}y_1 \tag{10.196}$$

where $\mathrm{x} = (x, y, z)$ denotes the observer location in the transformed Prandtl-Glauert plane, $\mathrm{y} = (y_1, y_2, y_3)$ is a source point in the transformed Prandtl-Glauert plane and G is the free-space Green's function of the Helmholtz equation (10.192), say

$$G(|\mathrm{x}-\mathrm{y}|) = -\mathrm{i}\ (\pi/2)\ H_0^{(2)}(K\,|\mathrm{x}-\mathrm{y}|) \tag{10.197}$$

For a flat-plate, the condition of vanishing normal velocity is equivalent to the condition $\partial P/\partial y_2 = 0$. Thus, substituting equation (10.197) into equation (10.196) yields

$$P(\mathrm{x}) = \frac{-\mathrm{i}\ K y}{4}\int_{-1}^{1} \Delta P(y_1)\, \frac{H_1^{(2)}(K\,|\mathrm{x}-\mathrm{y}|)}{|\mathrm{x}-\mathrm{y}|}\, \mathrm{d}y_1 \tag{10.198}$$

In the far field, say $|\mathbf{x}| \gg |\mathbf{y}|$, the formal solution (10.198) provides the following acoustic pressure

$$\begin{aligned} p(r,\theta) &= \frac{\beta\sqrt{K}}{\sqrt{8\pi}} \frac{\mathrm{e}^{\mathrm{i}\,\pi/4}}{\sqrt{r}} \frac{\sin\theta}{\left(1 - M_\infty^2 \sin^2\theta\right)^{3/4}} F(\alpha) \\ & \exp\left\{-\mathrm{i}\,r\left[K\left(1 - M_\infty^2\sin^2\theta\right)^{1/2} - M_\infty K_1 \cos\theta\right]\right\} + \mathcal{O}\left(r^{-3/2}\right) \end{aligned} \tag{10.199}$$

where both the observer and the source point are located in the physical plane (r and θ denote the observer polar co-ordinates). The function F is the Fourier transform of the pressure jump along the x_1 axis, namely

$$F(\alpha) = \int_{-1}^{1} \Delta p(y_1)\ \mathrm{e}^{\mathrm{i}\,\alpha\, y_1}\, \mathrm{d}y_1 \tag{10.200}$$

where $\Delta p(y_1) = p(y_1, 0^+) - p(y_1, 0^-)$ and

$$\alpha = \frac{K\cos\theta}{\sqrt{1 - M_\infty^2 \sin^2\theta}} - M_\infty K_1 \tag{10.201}$$

In order to compute the acoustic intensity, the far field acoustic velocity must be determined. This can be obtained by integrating the linearized Euler equation

$$\rho_0 \frac{\mathrm{D}_0 \mathbf{u}_a}{\mathrm{D}t} = -\nabla p \tag{10.202}$$

with p given by equation (10.199). Hence,

$$u_{a\,1} = M_\infty \frac{K\cos\theta - M_\infty K_1 \left(1 - M_\infty^2\sin^2\theta\right)^{1/2}}{K_1\left(1 - M_\infty^2\sin^2\theta\right)^{1/2} - M_\infty K\cos\theta}\, p \tag{10.203}$$

$$u_{a\,2} = \frac{\beta^2 M_\infty K \sin\theta}{K_1\left(1 - M_\infty^2\sin^2\theta\right)^{1/2} - M_\infty K\cos\theta}\, p \tag{10.204}$$

$$u_{a\,1} = \frac{M_\infty k_3 \left(1 - M_\infty^2\sin^2\theta\right)^{1/2}}{K_1\left(1 - M_\infty^2\sin^2\theta\right)^{1/2} - M_\infty K\cos\theta}\, p \tag{10.205}$$

For an isentropic irrotational flow Goldstein [216] proposed the following expression for the acoustic intensity vector

$$\mathbf{I} = (p + \rho_0 U_\infty u_{a\,1}) \left[\left(u_{a\,1} + \frac{\rho'}{\rho_0} U_\infty\right) \hat{\imath}_1 + u_{a\,2}\,\hat{\imath}_2 + u_{a\,3}\,\hat{\imath}_3\right] \tag{10.206}$$

Thus, substituting equations (10.199), (10.203), (10.204) and (10.205) into equation (10.206), and averaging over a period, yields the mean acoustic intensity vector

$$\begin{aligned} \tilde{\mathbf{I}} = \frac{1}{16\pi} \frac{\beta^4 M_\infty K}{K_1\, r} & \frac{\sin^2\theta}{\left[\left(1 - M_\infty^2\sin^2\theta\right)^{1/2} - K M_\infty \cos\theta / K_1\right]^2} |F(\alpha)|^2 \\ & \left[\frac{\beta^2 K \hat{r}}{1 - M_\infty^2\sin^2\theta} + \frac{k_3\,\hat{\imath}_3}{\left(1 - M_\infty^2\sin^2\theta\right)^{1/2}}\right] + \mathcal{O}(r^{-2}) \end{aligned} \tag{10.207}$$

where $\hat{r}$ is the unit vector in the observation direction. Finally, from the flux of the averaged intensity vector across a cylindrical surface around the airfoil, the following expression for the acoustic power can be obtained

$$\mathcal{P} = \frac{\beta^6 M_\infty K^2}{K_1 8\pi} \int_0^\pi \frac{\sin^2\theta}{\left[\left(1 - M_\infty^2\sin^2\theta\right)^{1/2} - K M_\infty\cos\theta/K_1\right]^2} \frac{|F(\alpha)|^2}{\left(1 - M_\infty^2\sin^2\theta\right)}\, \mathrm{d}\theta \tag{10.208}$$

Atassi *et al.* [33] concluded that both the acoustic power and the directivity strongly depend on the gust parameter K_1. For $K_1 \lesssim \pi/2$ ($c < \lambda/2$), the pressure directivity is a smooth function of the observation angle with a typical dipole pattern. Conversely, for $K_1 \gtrsim \pi/2$ ($c > \lambda/2$), the directivity pattern exhibits several lobes.

The acoustic intensity radiated when the airfoil interacts with an oblique gust is generally lower than that generated by a parallel interaction. The difference is significant when $K \ll K_1$ and vanishes when $K \simeq K_1$. Indeed, if $K \leq 0$ no sound is radiated.

Finally, at moderate and high values of the mean flow Mach number, the acoustic power reaches a maximum as the reduced frequency k_1 increases. As a result, a significant noise reduction can be obtained by avoiding frequencies around the peak value of $\mathcal{P}$.

Patrick *et al.* [217] investigated the feasibility of an inverse acoustic prediction. This consists in determining the spectral behaviour of a vortical flow on the base of the sound generated by its interaction with a streamlined body.

The inverse aeroacoustic problem includes a gust inverse problem, which consists in determining the unsteady velocity field from the unsteady pressure distribution on the body surface, and an acoustic inverse problem, which consists in determining the surface pressure field from the acoustic field. Some requirements guarantee the uniqueness of the solution for both the gust and the acoustic inverse problems.

Consider first the gust inverse problem for a flat-plate in incompressible flow with an imposed transverse gust. The pressure jump on the plate was expressed by Sears [126] in the form

$$\Delta p(x_1, k_1) = 2\pi\,\rho_0\,U_\infty \sqrt{\frac{1-x_1}{1+x_1}}\,a_2(k_1)\;S(k_1)\;\mathrm{e}^{\mathrm{i}\,k_1 t} \tag{10.209}$$

where

$$S(k_1) = \frac{1}{\frac{\pi}{2}k_1\left(H_0^{(2)}(k_1) - \mathrm{i}\,H_1^{(2)}(k_1)\right)} \tag{10.210}$$

is the Sears' function. In this case the transverse gust amplitude a_2 can be uniquely determined from the pressure jump on the flat-plate. If a longitudinal disturbance is imposed on the upstream flow and its wavenumber k_2 is known, then the longitudinal gust amplitude a_1 can be determined from the continuity condition $\mathbf{a}\cdot\mathbf{k} = 0$. Finally, if the gust is three-dimensional, the inverse solution is not unique since the third component a_3 cannot be determined.

Consider now the inverse acoustic problem for a flat-plate in incompressible flow with an imposed three-dimensional gust. In the small mean flow Mach number limit, equation (10.199) reduces to

$$p(r,\theta) = \sqrt{\frac{K}{8\pi}}\,\frac{\sin\theta}{\sqrt{r}}\,\exp\left\{-\mathrm{i}\,r\,K + \pi/4\right\}\int_{-1}^{1}\Delta p(y_1)\;\mathrm{e}^{\mathrm{i}\,K\,\cos\theta\,y_1}\,\mathrm{d}y_1 \tag{10.211}$$

Setting

$$f(r,\theta) = p(r,\theta)\sqrt{\frac{8\pi}{K}}\,\frac{\sqrt{r}}{\sin\theta}\,\exp\left\{\mathrm{i}\,r\,K - \pi/4\right\} \tag{10.212}$$

equation (10.211) can be written as

$$\int_{-1}^{1}\Delta p(y_1)\;\mathrm{e}^{\mathrm{i}\,K\,\cos\theta\,y_1}\,\mathrm{d}y_1 = f(r,\theta) \tag{10.213}$$

A collocation technique can be exploited in order to discretize equation (10.213). Setting $y_1 = -\cos\alpha$, the pressure jump can be assumed as given by the series expansion

$$\Delta p(\alpha) = A_0\,\cot\left(\frac{\alpha}{2}\right) + \sum_{n=1}^{\infty} A_n\,\sin(n\alpha) \tag{10.214}$$

which is physically consistent with both the square root singular behaviour at the leading edge of the flat-plate and the Kutta condition at the trailing edge. Thus, substituting into equation (10.213) and integrating yields

$$f(r,\theta) = A_0\,\pi\,[J_0(K\cos\theta) - \mathrm{i}\,J_1(K\cos\theta)] + \sum_{n=1}^{\infty} A_n\,\pi\,(-\mathrm{i})^{n-1}\,n\frac{J_n(K\cos\theta)}{K\cos\theta} \tag{10.215}$$

where J_n is the nth Bessel function of first kind. Equation (10.215) is the discretized form of the Fredholm integral equation of first kind (10.213). It can be written as

$$M\,A = f \tag{10.216}$$

where M is a $m \times n$ matrix, with $m \geq n$, whose elements are combinations of Bessel functions, A is a $n \times 1$ matrix containing the discretized pressure jump and f is a $m \times 1$ matrix containing the known far field data.

Rayleigh [51] demonstrated that a source of sound could not be determined uniquely from its far field radiation, provided that the acoustic field is governed by a standard wave equation. However, for a harmonic disturbance governed by the Helmholtz equation, the inverse solution can be unique. Theorems on the uniqueness of an inverse acoustic problem governed by the Helmholtz equation have been formulated by Colton & Kress [218]. However, even though the uniqueness requirements are satisfied, the inverse problem can be ill-posed and its solution can be quite difficult. The ill-posedness of the inverse problem is a consequence of the discrete dependence of the solution on the far field data. As a consequence, the linear system can be ill-conditioned and extremely sensitive to the far field input data.

The matrix M has been obtained by projecting the unknown pressure jump on a solution which is physically consistent with the flow behaviour at the leading edge and the trailing edge of the flat-plate. Nevertheless, since the elements in the columns of M decrease as the column number increases, the linear system is ill-conditioned. This follows from the property of the Bessel functions

$$J_n(n) \simeq \frac{1}{\sqrt{2\pi\,z}}\left(\frac{\mathrm{e}z}{2n}\right)^n \quad \text{as} \quad n \to \infty \tag{10.217}$$

Patrick *et al.* [217] used two methods to solve the linear problem (10.216). The first method is based on the singular value decomposition of M. It consists in finding the matrices U, Σ and V such that

$$M = U\,\Sigma\,\overline{V}^t \tag{10.218}$$

where Σ is $m \times n$ diagonal matrix whose first n terms are the singular values σ_i and the remaining $m-n$ terms are zero, U is a $m \times m$ matrix containing the left singular vectors in its columns, and V is a $n \times n$ matrix containing the left singular vectors in its columns. Overbars denote complex conjugates. The solution of the linear system (10.216) is thus given by

$$A = \sum_{\sigma_i \neq 0} \frac{(f \cdot u_i)}{\sigma_i} v_i \tag{10.219}$$

Divisions by very small singular values is responsible for large errors in the solution. Therefore, a regularization method must be incorporated into the solution (10.219) in order to reduce the sensitivity of the pressure jump on the far field data. Patrick *et al.* adopted the spectral cut-off method, which consists in avoiding summation over singular values smaller than a cut-off value, and the Tikhonov [219] method, which makes use of the parameter β to write the solution as

$$A = \sum_{\sigma_i \neq 0} \frac{\sigma_i\,(f \cdot u_i)}{\beta + \sigma_i^2} v_i \tag{10.220}$$

The second method is a simple regularization technique which consists in multiplying both the sides of equation (10.216) by the adjoint matrix of M, namely

$$\overline{M}^t M\, A = \overline{M}^t f \tag{10.221}$$

The solution is thus given by

$$A = \left(\overline{M}^t M\right)^{-1} \overline{M}^t f \tag{10.222}$$

Patrick *et al.* showed that, although the simple regularization technique provides accurate results, the method based on the singular value decomposition is more general.

10.4.2 Global Rotor-Wake Simulations and the Wake-Preserving Problem

Three-dimensional rotor/wake CFD computations have been performed for many years, but these were mainly concerned with the prediction of rotor performances [220, 221]. These do not require a high accuracy in the prediction of the wake convection. On the contrary, aeroacoustic BVI predictions require that the rotor/vortex passage distance is predicted within a small fraction of the blade chord and that the vortex core is preserved during its motion. Simple estimates show that the grid required to preserve and accurately predict the wake is enormous. Therefore full CFD predictions of helicopter BVI will remain un practical for many years.

An alternative to using large computational resources is to introduce some modeling in the vortex treatment in order to reduce the numerical vortex diffusion. A typical approach consists in modifying the flow equations by adding some artificial terms which reduce a vortex dissipation and preserve its strength. The *Vorticity confinement* method [222], for example, consists in adding the acceleration term

$$\epsilon\,\mathbf{P} = -\epsilon\,\mathbf{n} \times \omega \tag{10.223}$$

with

$$\mathbf{n} = \frac{\nabla\omega}{|\nabla\omega|} \tag{10.224}$$

to the right-hand side of the linear momentum equation. This acceleration is in the direction of the tangential flow induced by the vortex and is proportional to the vorticity ω. Since a non vortical flow portion is not affected by this term, the circulation of the vortex is unaffected by the artificial source term. The effect of this term is to drive vorticity inward the center of the vortex. Therefore, the size of the vortex results from an equilibrium between the confinement acceleration and the numerical dissipation. It can be varied by changing the value of the parameter ϵ.

Bibliography

[1] Lighthill, M. J., "On Sound Generated Aerodynamically: 1. General Theory," *Proceeding of The Royal Society*, Vol. A211, 1952, pp. 564–578.

[2] Ffowcs Williams, J. E. and Hawkings, D. L., "Sound Generated by Turbulence and Surfaces in Arbitrary Motion," *Philosophical Transactions of the Royal Society*, Vol. A264, No. 1151, 1969, pp. 321–342.

[3] Strouhal, V., "Ueber eine Besondere Art der Tonerregung," *Annalen der Physik und Chemie (Leipzig)*, Vol. 3, No. 5, 1878, pp. 216–251.

[4] Rayleigh, J. W. S., "Aeolian Tones," *Philosophical Magazine*, Vol. 29, 1915, pp. 434–444.

[5] von Kármán, T. and Burgers, J. M., *General Aerodynamic Theory, Perfect Fluids. Aerodynamic Theory.*, Vol. II, Durand, Stanford, 1934.

[6] Graham, J. M. R., "Similarity Rules for Thin Airfoils in non-Stationary Subsonic Flows," *Journal of Fluid Mechanics*, Vol. 43, No. 4, 1970, pp. 753–766.

[7] Marshall, J. S. and Grant, J. R., "Penetration of a Blade into a Vortex Core: Vorticity Response and Unsteady Blade Forces," *Journal of Fluid Mechanics*, Vol. 306, 1996, pp. 83–109.

[8] Kaykayoglu, R. and Rockwell, D., "Vortices Incident upon a Leading Edge: Instantaneous Pressure Fields," *Journal of Fluid Mechanics*, Vol. 156, 1985, pp. 439–461.

[9] Goldstein, M. E., Dittmar, J. H., and Gelder, T. F., "Combined Quadrupole-Dipole Model for Inlet Flow Distortion Noise," *NASA TN D-7676*, May 1974.

[10] Gursul, I. and Rockwell, D., "Vortex Street Impinging upon an Elliptical Leading Edge," *Journal of Fluid Mechanics*, Vol. 211, 1990, pp. 211–242.

[11] Horner, M. B., McD. Galbraith, R. A., and Coton, F. N., "Examination of a Vortex Deformation During Blade-Vortex Interaction," *American Institute of Aeronautics and Astronautics Journal*, Vol. 34, No. 6, June 1996, pp. 1188–1194.

[12] Lee, S. and Bershader, D., "Head-On Parallel Blade-Vortex Interaction," *American Institute of Aeronautics and Astronautics Journal*, Vol. 32, No. 1, 1994, pp. 16–22.

[13] Howe, M. S., "The Influence of Vortex Shedding on The Generation of Sound by Convected Turbulence," *Journal of Fluid Mechanics*, Vol. 76, No. 4, 1976, pp. 711–740.

[14] Lamb, H., *Hydrodynamics*, Dover Publishers 6th Ed., 1932.

[15] Clements, R. R. and Maull, D. J., "The Representation of Sheets of Vorticity by Discrete Vortices," *Prog. Aeron. Sci*, Vol. 16, 1975, pp. 129–146.

[16] Saffman, P. G. and Baker, G. R., "Vortex Interactions," *Annual Review of Fluid Mechanics*, Vol. 11, 1979, pp. 95–122.

[17] Leonard, A., "Vortex Methods for Flow Simulation," *Journal of Computational Physics*, Vol. 37, 1980, pp. 289–335.

[18] Aref, H., "Integrable, Chaotic, and Turbulent Vortex Motion in Two-dimensional Flows," *Annual Review of Fluid Mechanics*, Vol. 15, 1983, pp. 345–389.

[19] Sarpkaya, T., "Computational Methods with Vortices - The 1988 Freeman scholar lecture," *Journal of Fluids Engineering*, Vol. 111, 1989, pp. 5–52.

[20] Howe, M. S., "Contributions to the Theory of Aerodynamic Sound, with Application to Excess Jet Noise and the Theory of the Flute," *Journal of Fluid Mechanics*, Vol. 71, 1975, pp. 625–673.

[21] Wagner, H., "Über die Entstchung des Dynamischen Auftriebes von Tragflügeln," *ZAMM*, Vol. 5, No. 1, 1925, pp. 17–35.

[22] Brown, C. E. and Michael, W. H., "Effect of Leading Edge Separation on the Lift of a Delta Wing," *Journal of the Aeronautica Sciences*, Vol. 21, 1954, pp. 690–695.

[23] Peters, M. C. A. M. and Hirschberg, A., "Acoustically Induced Periodic Vortex Shedding at Sharp Edged Open Channel Ends: Simple Vortex Model," *Journal of Sound and Vibration*, Vol. 161, No. 2, 1993, pp. 281–299.

[24] Howe, M. S., "Emendation of the Brown & Michael Equation, with Application to Sound Generation by Vortex Motion Near a Half-Plane," *Journal of Fluid Mechanics*, Vol. 329, 1996, pp. 89–101.

[25] Milne-Thompson, L. M., *Theoretical Hydrodynamics*, Macmillian, London, 1968.

[26] Sallet, D. W., "The Lift Force Due to von Karman's vortex wake," *J. Hydronaut.*, Vol. 7, 1973, pp. 161–165.

[27] Roger, M., *Aeroacoustics*, Lecture note of Ecole Centrale de Lyon, Lyon, 2000.

[28] Sculley, M. P., "Computation of Helicopter Rotor Wake Geometry and Its Influence on Rotor Harmonic Loads," *Massachusetts Inst. of Technology, ASRL TR-178-1, Boston, MA*, 1975.

[29] Beale, J. T. and Majda, A., "High Order Accuracy Vortex Methods with Explicit Velocity Kernels," *Journal of Computational Physics*, Vol. 58, 1985, pp. 188–208.

[30] Howe, M. S., *Acoustic of Fluid-Structure Interactions*, Cambridge Monographs on Mechanics, 1998.

[31] Abromowitz, M. and Stegun, I. A., *Handbook of Mathematical Functions With Formulas, Graphs, and Mathematical Tables*, Dover Publications, New York, 1965.

[32] Chiocchia, G. and Casalino, D., "An Analytical Model of the Interaction Noise between Vortices and a Wing Profile," *Atti del XV Congresso Nazionale AIDAA, Torino, Italy*, 1999.

[33] Atassi, H. M., Dusey, M., and Davis, C. M., "Acoustic Radiation from a Thin Airfoil in Nonuniform Subsonic Flows," *American Institute of Aeronautics and Astronautics Journal*, Vol. 31, No. 1, 1993, pp. 12–19.

[34] Pérennès, S., *Caractérisation des sources de bruit aérodinamique à basses fréquences de dispositifs hypersustentateurs*, Ph.D Thesis, Ecole Centrale de Lyon, 1999.

[35] Iida, A., Otaguro, T., Kato, C., and Fujita, H., "Prediction of Aerodynamic Sound Spectra from a Circular Cylinder," *Proceedings of the 5th Triennial International Symposium on Fluid Control, Measurements and Visualization, Hayama, Japan*, Vol. 1, 1999, pp. 121–126.

[36] Szepessy, S. and Bearman, P. W., "Aspect Ratio and End Plate Effects on Vortex Shedding from a Circular Cylinder," *Journal of Fluid Mechanics*, Vol. 234, 1992, pp. 191–217.

[37] Clutter, D. W., Smith, O. M. O., and Brazier, J. G., *Aerosp. Engrg.*, Vol. 20, 1961.

[38] Pierce, A. D., *Acoustics. An Introduction to its Physical Principles and Applications*, McGraw-Hill, 1981.

[39] Farassat, F. and Succi, G. P., "The Prediction of Helicopter Discrete Frequency Noise," *Vertica*, Vol. 7, No. 4, 1983, pp. 309–320.

[40] Brentner, K. S., "An Efficient and Robust Method for Predicting Helicopter High-Speed Impulsive Noise," *Journal of Sound and Vibration*, Vol. 203, No. 1, 1997, pp. 87–100.

[41] Casalino, D., "An Advanced Time Approach for Acoustic Analogy Predictions," *Accepted for publication by the Journal of Sound and Vibration*, 2002.

[42] di Francescantonio, P., "A New Boundary Integral Formulation for the Prediction of Sound Radiation," *Journal of Sound and Vibration*, Vol. 202, No. 4, 1997, pp. 491–509.

[43] Brentner, K. S. and Farassat, F., "Analytical Comparison of the Acoustic Analogy and Kirchhoff Formulation for Moving Surfaces," *American Institute of Aeronautics and Astronautics Journal*, Vol. 36, No. 8, 1998, pp. 1379–1386.

[44] Morgans, W. R., "The Kirchhoff Formula Extended to a Moving Surface," *Philisophical Magazine*, Vol. 9, 1930, pp. 141–161.

[45] Farassat, F. and Myers, M. K., "Extension of Kirchhoff's Formula to Radiation from Moving Surfaces," *Journal of Sound and Vibration*, Vol. 123, No. 3, 1988, pp. 451–461.

[46] Farassat, F., "Discontinuities in Aerodynamics and Aeroacoustics: the Concept and Applications of Generalized Derivatives," *Journal of Sound and Vibration*, Vol. 55, No. 2, 1977, pp. 156–193.

[47] Morse, P. M. and Ingard, K. U., *Theoretical Acoustics*, McGraw-Hill, 1968.

[48] Rienstra, S. W. and Hirschberg, A., *An Introduction to Acoustics*, Extended and revised edition of IWDE92-06, 2001.

[49] Rayleigh, J. W. S., "Acoustical Observations II," *Philosophical Magazine*, Vol. 7, 1879, pp. 149–162.

[50] Doak, P. E., "Analysis of Internally Generated Sound in Continuous Materials: 2. A Critical Review of the Conceptual Adequacy and Physical Scope of Existing Theories of Aerodynamic Noise, with Special Reference to Supersonic Jet Noise," *Journal of Sound and Vibrations*, Vol. 25, No. 2, 1972, pp. 263–335.

[51] Rayleigh, J. W. S., *The Theory of Sound*, Vol. I,II, London: Macmillan, 1896.

[52] Curle, N., "The Influence of Solid Boundaries upon Aerodynamic Sound," *Proceeding of The Royal Society*, Vol. A231, 1955, pp. 505–514.

[53] Phillips, O. M., "The intensity of Aeolian tones," *Journal of Fluid Mechanics*, Vol. 1, 1956, pp. 607–624.

[54] Williamson, C. H. K., "Oblique and Parallel Modes of Vortex Shedding in the Wake of a Circular Cylinder at Low Reynolds Numbers," *Journal of Fluid Mechanics*, Vol. 206, 1989, pp. 579–627.

[55] Brentner, K. S., "A Superior Kirchhoff Method for Aeroacoustic Noise Prediction: The Ffowcs Williams-Hawkings Equation," *134th Meeting of the Acoustical Society of America*, 1997.

[56] Cox, J. S., Rumsey, C. L., and Brentner, K. S., "Computation of Sound Generated by Viscous Flow Over a Circular Cylinder," *NASA Technical Memorandum 110339*, 1997.

[57] Brentner, K. S. and Farassat, F., "An Analytical Comparison of the Acoustic Analogy and Kirchhoff Formulation for Moving Surfaces," *American Helicopter Society 53rd Annual Forum*, 1997.

[58] Williamson, C. H. K., "Vortex Dynamics in the Cylinder Wake," *Annual Review of Fluid Mechanics*, Vol. 28, 1996, pp. 477–539.

[59] Prasad, A. and Williamson, C. H. K., "The Instability of the Shear Layer Separating from a Bluff Body," *Journal of Fluid Mechanics*, Vol. 333, 1997, pp. 375–402.

[60] Tritton, D. J., "Experiments on the Flow Past a Circular Cylinder at Low Reynolds Numbers," *Journal of Fluid Mechanics*, Vol. 45, 1959, pp. 203.

[61] König, M., Heisenlohr, H., and Eckelmann, H., "Visualisation of the Spanwise Cellular Structure of the Laminar Wake of Wall-Bounded Circular Cylinders," *Phys. Fluids A*, Vol. 4, 1992, pp. 869.

[62] Ferrand, P., Aubert, S., Smati, L., Bron, O., and Atassi, H. M., "Nonlinear Interaction of Upstream Propagating Sound with Unsteady Transonic Flow in a Nozzle," *American Institute of Aeronautics and Astronautics Paper 98-2213*, 1998.

[63] Wilcox, D. C., "Comparison of Two Equations Turbulence Models for Boundary Layers with Pressure Gradient," *American Institute of Aeronautics and Astronautics Journal*, Vol. 31, No. 8, 1993, pp. 1414–1421.

[64] Schewe, G., "On the Force Fluctuations Acting on a Cylinder in Crossflow from Subcritical up to Transcritical Reynolds Numbers," *Journal of Fluid Mechanics*, Vol. 133, 1983, pp. 265–285.

[65] Kato, C. and Ikegawa, M., "Large Eddy Simulation of Unsteady Turbulent Wake of a Circular Cylinder Using the Finite Element Method," *Advances in Numerical Simulation of Turbulent Flows, ASME, FED*, Vol. 117, 1991, pp. 49–56.

[66] Roshko, A., "Perspectives on Bluff Body Aerodynamics," *J. Wind Ind. Aerodyn.*, 1993, pp. 49–79.

[67] Wake, B. E. and Choi, D., "Vortex Prediction and Convection Using Upwinded Navier-Stokes Solver," *American Helicopter Society Specialists' Meeting for Aeromechanics Technology and Product Design for 21st Century, Bridgeport, CT,*, Oct. 1995.

[68] Hardin, J. C. and Mason, J. P., "A New Look at Sound Generation by Blade/Vortex Interaction," *ASME Winter Annual Meeting, New Orleans, LA*, 1984.

[69] Hardin, J. C. and Lamkin, S. L., "Aeroacoustic Interaction of a Distributed Vortex with a Lifting Joukowski Airfoil," *American Institute of Aeronautics and Astronautics Paper 84-2287*, 1984.

[70] Rai, M. M., "Navier-Stokes Simulations of Blade-Vortex Interaction using High-Order Accurate Upwind Schemes," *American Institute of Aeronautics and Astronautics Paper 87-0543*, 1987.

[71] Baldwin, B. S. and Lomax, H., "Thin Layer Approximation and Algebraic Model for Separated Turbulent Flow," *American Institute of Aeronautics and Astronautics Paper 78-257*, 1978.

[72] Caradonna, F. X., Laub, G. H., and Tung, C., "An Experimental Investigation of the Parallel Blade-Vortex Interaction," *10th European Rotorcraft Forum, The Hague, Netherlands*, Aug. 1984.

[73] Truesdell, C. A. and Toupin, R., *Handbuch der Physik III/1*, S. Flugge, 1960.

[74] Enskog, D., "Kinetische Theorie der Vorgänge in mässig verdünnten Gasen," *Arkiv. Mat., Astron. Fysik Stockholm*, Vol. 16, 1922.

[75] Di Francescantonio, P. and Casalino, D., "Green's Function Discretization Scheme for Sound Propagation in Nonuniform Flows," *American Institute of Aeronautics and Astronautics Journal*, Vol. 37, No. 10, 1999, pp. 1161–1172.

[76] Chu, B. T. and Kovásznay, L. S. B., "Nonlinear Interactions in a Viscous Heat-Conducting Compressible Gas," *Journal of Fluid Mechanics*, Vol. 3, 1958, pp. 494–514.

[77] Powell, A., "Aerodynamic Noise and the Plane Boundary," *Journal of the Acoustical Society of America*, Vol. 32, No. 8, 1960, pp. 982–990.

[78] Ffowcs Williams, J. E., "Surface-Pressure Fluctuations Induced by Boundary-Layer Flow at Finite Mach Number," *Journal of Fluid Mechanics*, Vol. 22, No. 3, 1965, pp. 507–519.

[79] Guo, Y. P., Joshi, M. C., Bent, P. H., and Yamamoto, K. J., "Surface Pressure Fluctuations on Aircraft Flaps and their Correlation with Far-Field Noise," *Journal of Fluid Mechanics*, Vol. 415, 2000, pp. 175–202.

[80] Graham, W. R., "A Comparison of Models for the Wavenumber-Frequency Spectrum of Turbulent Boundary Layer Pressures," *Journal of Sound and Vibration*, Vol. 206, No. 4, 1997, pp. 541–565.

[81] Chase, D. M., "Sound Radiated by Turbulent Flow off a Rigid Half-Plane as Obtained from a Wavevector Spectrum of Hydrodynamic Pressure," *Journal of the Acoustical Society of America*, Vol. 52, No. 3, 1972, pp. 1011–1023.

[82] Chandiramani, K. L., "Diffraction of Evanescent Waves, with Applications to Aerodynamically Scattered Sound and Radiation from Unblaffed Plates," *Journal of the Acoustical Society of America*, Vol. 55, No. 1, 1974, pp. 19–29.

[83] Chase, D. M., "Noise Radiated from an Edge in Turbulent Flow," *American Institute of Aeronautics and Astronautics Journal*, Vol. 13, No. 8, 1975, pp. 1041–1047.

[84] Howe, M. S., "A Review of the Theory of Trailing-Edge Noise," *Journal of Sound and Vibration*, Vol. 61, No. 3, 1978, pp. 437–465.

[85] Brooks, T. F. and Hodgson, T. H., "Trailing Edge Noise Prediction from Measured Surface Pressures," *Journal of Sound and Vibration*, Vol. 78, No. 1, 1981, pp. 69–117.

[86] Howe, M. S., "Trailing Edge Noise at Low Mach-Numbers," *Journal of Sound and Vibration*, Vol. 225, No. 2, 1999, pp. 211–238.

[87] Haddle, G. P. and Shudrzyk, E. J., "The Physics of Flow Noise," *Journal of the Acoustical Society of America*, Vol. 46, No. 1, 1969, pp. 130–157.

[88] Shubert, G. and Corcos, G. M., "The Dynamics of Turbulence near a Wall According to a Linear Model," *Journal of Fluid Mechanics*, Vol. 29, No. 1, 1967, pp. 113–135.

[89] Landahl, M. T., "A Wave-Guide Model for Turbulent Shear Flow," *Journal of Fluid Mechanics*, Vol. 29, No. 3, 1967, pp. 441–459.

[90] Laufer, J., "Investigation of Turbulent Flow in a Two-Dimensional Channel," *NACA Rep. 1053*, 1951.

[91] Willmarth, W. W., "Wall Pressure Fluctuations in a Turbulent Boundary Layer," *Journal of the Acoustical Society of America*, Vol. 28, 1956.

[92] Harrison, M., "Pressure Fluctuations on the Wall adjacent to a Turbulent Boundary Layer," *US Navy David Taylor Model Basin Rep. 1260*, 1958.

[93] Willmarth, W. W., "Space-time Correlations of the Fluctuating Wall Pressure in a Turbulent Boundary Layer," *Journal of Aerospace Sciences*, Vol. 25, 1958.

[94] Lilley, G. M. and Hodgson, T. H., "On Surface Pressure Fluctuations in Turbulent Boundary Layers," *AGARD Rep. No. 276*, 1960.

[95] Bull, M. K. and Willis, J. L., "Some Results of Experimental Investigations of the Surface Pressure Field due to a Turbulent Boundary Layer," *Dept. Astroeng., Univ. Southampton Rep. No. 99*, 1961.

[96] Kistler, A. L. and Chen, W. S., "A Fluctuating Pressure Field in a Supersonic Turbulent Boundary Layer," *Journal of Fluid Mechanics*, Vol. 16, 1963, pp. 41–64.

[97] Corcos, G. M., "Pressure Fluctuations in Shear Flows," *University of California Inst. of Eng. Res. Report*, Vol. 183, No. 2, 1962.

[98] Lin, C. C., "On Taylor's Hypothesis and the Acceleration Terms in the Navier-Stokes equations," *Quarterly Applied Mathematics*, Vol. 10, No. 4, 1953, pp. 295–306.

[99] Corcos, G. M., "The Structure of a Turbulent Pressure Field in Boundary-Layer Flows," *Journal of Fluid Mechanics*, Vol. 18, 1964, pp. 353–378.

[100] Bergeron, R. F., "Aerodynamic Sound and the Low-Wavenumber Wall-Pressure Spectrum of Nearly Incompressible Boundary-Layer Turbulence," *Journal of the Acoustical Society of America*, Vol. 54, No. 1, 1973, pp. 123–133.

[101] Chase, D. M., "Modeling the Wavevector-Frequency Spectrum of Turbulent Boundary Layer Wall Pressure," *Journal of Sound and Vibration*, Vol. 70, No. 1, 1980, pp. 29–67.

[102] Ffowcs Williams, J. E., "Boundary-Layer Pressures and the Corcos Model: a Development to Incorporate Low-Wavenumber Constraints," *Journal of Fluid Mechanics*, Vol. 125, 1982, pp. 9–25.

[103] Efimtsov, B. M., "Characteristics of the Field of Turbulent Wall Pressure Fluctuations at Large Reynolds Numbers," *Soviet Physics - Acoustics*, Vol. 28, No. 4, 1982, pp. 289–292.

[104] Chase, D. M., "The Character of the Turbulent Wall Pressure Spectrum at Subconvective Wavenumbers and a Suggested Comprehensive Model," *Journal of Sound and Vibration*, Vol. 112, No. 1, 1987, pp. 125–147.

[105] Smol'Yakov, A. V. and Tkachenko, V. M., "Model of a Field of Pseudosonic Turbulent Wall Pressures and Experimental Data," *Soviet Physics - Acoustics*, Vol. 37, No. 6, 1991, pp. 627–631.

[106] Willmarth, W. W. and Woldridge, C. E., "Measurements of the Fluctuating Pressure at the Wall beneath a Thick Turbulent Boundary Layer," *Journal of Fluid Mechanics*, Vol. 14, 1962, pp. 187–210.

[107] Wills, J. A. B., "Measurements of the Wave-Number/Phase Velocity Spectrum of Wall Pressure beneath a Turbulent Boundary Layer," *Journal of Fluid Mechanics*, Vol. 45, No. 1, 1970, pp. 65–90.

[108] Kraichnan, R. H., "Pressure Field within Homogeneous Anisotropic Turbulence," *Journal of the Acoustical Society of America*, Vol. 28, 1956, pp. 1–64.

[109] Willmarth, W. W., "Pressure Fluctuations beneath Turbulent Boundary Layers," *Annual Review of Fluid Mechanics*, 1975, pp. 13–38.

[110] Howe, M. S., "The Rôle of Surface Shear Stress Fluctuations in the Generation of Boundary Layer Noise," *Journal of Sound and Vibration*, Vol. 65, No. 2, 1979, pp. 159–164.

[111] Dowling, A. P., "Flow-Acoustic Interaction Near a Flexible Wall," *Journal of Fluid Mechanics*, Vol. 128, 1983, pp. 181–198.

[112] Phillips, O. M., "Surface Noise from a Plane Turbulent Boundary Layer," *ARC Rep. 16*, 1954.

[113] Chase, D. M. and Noiseux, C. F., "Turbulent Wall Pressure at Low Wavenumbers: Relation to Nonlinear Sources in Planar and Cylindrical Flow," *Journal of the Acoustical Society of America*, Vol. 72, No. 3, 1982, pp. 975–982.

[114] Kraichnan, R. H., "Pressure Fluctuations in Turbulent Flow over a Flat Plate," *Journal of the Acoustical Society of America*, Vol. 28, No. 3, 1956, pp. 378–390.

[115] Favre, A. J., Gaviglio, J. J., and Dumas, R., "Space-Time Double Correlations and Spectra in Turbulent Boundary Layer," *Journal of Fluid Mechanics*, Vol. 2, 1957, pp. 313–342.

[116] Bakewell, H. P., Carey, G. F., Libuka, J. J., Schloemer, H. H., and von Winkle, W. A., "Wall Pressure Correlations in Turbulent Pipe Flow," *U.S. Navy Under-water Sound Laboratory Report*, Vol. 559, 1962.

[117] Hodgson, T. H., "Pressure Fluctuations in Shear Flow Turbulence," *College of Aeronautics, Cranfield, Note No. 129*, 1960.

[118] Lilley, G. M., "Wall Pressure Fluctuations under Turbulent Boundary Layers at Subsonic and Supersonic Speeds," *College of Aeronautics, Cranfield, COA Note 140*, 1963.

[119] Reichardt, H., "Vollständige Darstellung der turbulenten Geschwindigkeitsverteilung in glatten Leitungen," *Z. Angev. Math. Mech.*, Vol. 31, 1951.

[120] Coles, D., "The Law of the Wake in the Turbulent Boundary Layer," *Journal of Fluid Mechanics*, Vol. 1, 1956, pp. 191–226.

[121] Millikan, C., "A Critical Discussion of Turbulent Flows in Channels and Circulars Tubes," *Proc. 5th Int. Cong. Appl. Mech., Cambridge*, 1938.

[122] Klebanoff, P. S., "Characteristics in a Boundary Layer With Zero Pressure Gradient," *NACA Technical Note No. 3178*, 1954.

[123] von Kármán, T. and Sears, W. R., "Airfoil Theory for Non-Uniform Motion," *Journal of the Aeronautical Sciences*, Vol. 5, No. 10, 1938, pp. 379–390.

[124] Theodorsen, T., "General Theory of Aerodynamic Instability and the Mechanism of Flutter," *NACA Advance Restricted Report (also NACA Tech. Rep. No. 496, 1949)*, 1935.

[125] Küssner, H. G., "Zusammenfassender Bericht über den instationärem Auftrieb von Flügeln," *Luftfahrtforsch*, Vol. 13, 1936, pp. 410–424.

[126] Sears, W. R., "Some Aspects of Non-Stationary Airfoil Theory and its Practical Application," *Journal of the Aeronautical Sciences*, Vol. 8, No. 3, 1941, pp. 104–108.

[127] Filotas, L. T., "Theory of Airfoil Response in a Gusty Atmosphere - Part I Aerodynamic Transfer Function," *Inst. for Aerospace Studies, Univ. of Toronto, UTIAS Rep. No. 139, ASFOR 69-2150TR*, 1969.

[128] Possio, C., "L'azione aerodinamica sul profilo oscillante in un fluido compressibile a velocitá iposonora," *L'Aerotecnica*, Vol. 18, No. 4, 1938, pp. 441–458.

[129] Amiet, R. K., "High Frequency Thin-Airfoil Theory for Subsonic Flow," *American Institute of Aeronautics and Astronautics Journal*, Vol. 14, No. 8, 1976, pp. 1076–1082.

[130] Amiet, R. K., "Low-Frequency Approximations in Unsteady Small Perturbation Subsonic Flows," *Journal of Fluid Mechanics*, Vol. 75, No. 3, 1976, pp. 545–552.

[131] Goldstein, M. E. and Atassi, H. M., "A Complete Second-Order Theory for the Unsteady Flow about an Airfoil Due to periodic Gust," *Journal of Fluid Mechanics*, Vol. 74, No. 4, 1976, pp. 741–765.

[132] Cicala, P., "Le azioni aerodinamiche sul profilo oscillante," *L'Aerotecnica*, Vol. 16, 1936, pp. 652–665.

[133] Glauert, H., "The Force and Moment on an Oscillating Airfoil," *British A.R.C., R. & M., No. 1242*, 1929.

[134] Filotas, L. T., "Oblique Compressible Sears Function," *American Institute of Aeronautics and Astronautics Journal*, Vol. 12, No. 11, 1974, pp. 1601–1603.

[135] Chu, S. and Widnall, S. E., "Prediction of Unsteady Airloads for Oblique Blade-Gust Interaction in Compressible Flow," *American Institute of Aeronautics and Astronautics Journal*, Vol. 12, No. 9, 1974, pp. 1228–1235.

[136] Küssner, H. G., "Allgemeine Tragflächen Theorie," *NACA Tech. Memo. no. 979*, 1940.

[137] Amiet, R. and Sears, W. R., "The Aerodynamic Noise of Small-Perturbation Subsonic Flows," *Journal of Fluid Mechanics*, Vol. 44, 1970, pp. 227–235.

[138] Landahl, M., *Unsteady Transonic Flow*, Pergamon Press, New York, 1961.

[139] Adamczyk, J. J., "The Passage of an Infinite Swept Airfoil Through an Oblique Gust," *Journal of Aircraft*, Vol. 11, No. 5, 1974, pp. 281–287.

[140] Goldstein, M. E., "Unsteady Vortical and Entropic Distortions of Potential Flows Round Arbitrary Obstacles," *Journal of Fluid Mechanics*, Vol. 89, No. 3, 1978, pp. 433–468.

[141] Hunt, J. C. R., "A Theory of Turbulent Flow round Two-Dimensional Bluff Bodies," *Journal of Fluid Mechanics*, Vol. 61, No. 4, 1973, pp. 625–706.

[142] Prandtl, L., "Attaining a Steady Air Stream in Wind Tunnels," *NACA Tech. Memo. no. 726*, 1933.

[143] Batchelor, G. K. and Proudman, I., "The effects of Rapid Distortion of a Fluid in Turbulent Motion," *Q. J. Mech. Appl. Maths.*, Vol. 7, 1954, pp. 83–103.

[144] Lighthill, M. J., "Drift," *Journal of Fluid Mechanics*, Vol. 1, 1956, pp. 31–53.

[145] Myers, M. R. and Kerschen, E. J., "Effect of Airfoil Mean Loading on Convected Gust Interaction Noise," *Proceeding of the AIAA/NASA 9th Aeroacoustics Conference, Williamsburg, Virginia*, 1984.

[146] Atassi, H. M., "The Sears Problem for a Lifting Airfoil Revisited - New Results," *Journal of Fluid Mechanics*, Vol. 141, 1984, pp. 109–122.

[147] Rayleigh, J. W. S., *The Theory of Sound*, Vol. I,II, New York: Dover Publications, 1877.

[148] Gutin, L., "On the Sound Field of a Rotating Propeller," *NACA TM 1195 (from Physik. Zeitschr. der Sowjetunion, Bd. 9, Heft 1, 1936, pp. 57-71)*, 1948.

[149] Lilley, G. M., "Appendix: Generation of sound in mixing region," *Lockheed-Georgia Company Fourth Monthly Progress Report, Contract F-33615-71-C-1663*, 1971.

[150] Phillips, O. M., "On the Generation of Sound by Supersonic Turbulent Shear Layers," *Journal of Fluid Mechanics*, Vol. 9, 1960, pp. 1–28.

[151] Doak, P. E., "On the Interdependence between Acoustic and Turbulent Fluctuating Motions in a Moving Fluid," *Journal of Sound and Vibration*, Vol. 19, 1971, pp. 211–225.

[152] Doak, P. E., "Analysis of Internally Generated Sound in Continuous Materials: 3. The momentum potential field description of fluctuating fluid motion as a basis for a unified theory of internally generated sound," *Journal of Sound and Vibrations*, Vol. 26, No. 1, 1973, pp. 91–120.

[153] Powell, A., "Vortex Sound," *Rept No 61-70, Department of Engineering University of California, Los Angeles*, 1961.

[154] Powell, A., "Theory of Vortex Sound," *Journal of the Acoustical Society of America*, Vol. 36, 1964, pp. 177–195.

[155] Prandtl, L., "Tragflügeltheorie I. Mitteilungen, Nachrichten," *Ges. Wiss. Göttingen, Math-Phys. Kl. 107-137 (also 1920 N.A.C.A. T.N. 10: Calculation of Core of Rolled Up Vortices By Energy)*, 1918.

[156] Crow, S. C., "Aerodynamic Sound Emission as a Singular Perturbation Problem," *Studies in Applied Mathematics*, Vol. 49, 1970, pp. 21–44.

[157] Howe, M. S., "Multiple Scattering of Sound by Turbulence and Other Inhomogeneities," *Journal of Sound and Vibration*, Vol. 27(4), 1973, pp. 455–476.

[158] Möring, W., "On vortex Sound at Low Mach Number," *Journal of Fluid Mechanics*, Vol. 85, 1978, pp. 685–691.

[159] Taylor, K., "A Transformation of the Acoustic Equation with Implications for Wind-Tunnel and Low-Speed Flight Tests," *Proceedings of the Royal Society of London*, Vol. A363, 1978, pp. 271–281.

[160] Crighton, D. G., "Radiation from Vortex Filament Motion Near a Half-Plane," *Journal of Fluid Mechanics*, Vol. 51, 1972, pp. 357–362.

[161] Crighton, D. G. and Leppington, F. G., "Scattering of Aerodynamic Noise by a Semi-Infinite Compliant Plate," *Journal of Fluid Mechanics*, Vol. 43, 1970, pp. 721–736.

[162] Schwartz, L., *Theories des Distributions*, Vol. I and II, Actualities Scientifiques et Industrielles, Hermann and Cie, Paris, 1957.

[163] Farassat, F., "Introduction to Generalized Functions With Applications in Aerodynamics and Aeroacoustics," *NASA Technical Paper 3428*, 1994.

[164] Richards, I. and Heekyung, Y., *Theory of Distributions: A New-Technical Introduction*, Cambridge University Press, 1990.

[165] Kreyszig, E., *Differential Geometry*, Dover Books, 1991.

[166] Farassat, F. and Farris, M., "The Mean Curvature of the Influence Surface of Wave Equation with Sources on a Moving Surface," *Math. Meth. Appl. Sci.*, Vol. 22, 1999, pp. 1485–1503.

[167] Brentner, K. S. and Farassat, F., "The Uses and Abuses of the Acoustic Analogy in Helicopter Rotor Noise Prediction," *Journal of the American Helicopter Society*, Vol. 33, 1988, pp. 29–36.

[168] Yu, Y. H., Caradonna, F. X., and Schmitz, F. H., "The Influence of the Transonic Flow Field on High-Speed Helicopter Impulsive Noise," *Proceedings of the Fourth European Rotorcraft and Powered Lift Aircraft Forum*, Vol. 58, 1978.

[169] Brentner, K. S. and Farassat, F., "Supersonic Quadrupole Noise Theory for High-Speed Helicopter Rotors," *Journal of Sound and Vibration*, Vol. 218(3), 1998, pp. 481–500.

[170] Farassat, F., Lee, Y. J., Tadghighi, H., and Holtz, R., "High-Speed Helicopter Rotor Noise-Shock Waves as a Potent Source of Sound," *AHS/RAS International Technical Specialists' Meeting on Rotorcraft Acoustic and Rotor Fluid Dynamics*, 1991.

[171] Farassat, F. and Myers, M. K., "The Kirchhoff Formula for a Supersonically Moving Surface," *American Institute of Aeronautics and Astronautics Paper 95-062*, 1995.

[172] Farassat, F., "Theoretical Analysis of Linearized Acoustics and Aerodynamics of Advanced Supersonic Propellers," *AGARD-CP-366*, 1985.

[173] Farassat, F., Padula, S. L., and Dunn, M. H., "Advanced Turboprop Noise Prediction Based on Recent Theoretical Results," *Journal of Sound and Vibration*, Vol. 119(1), 1987, pp. 53–79.

[174] Lockard, D., "Advanced Turboprop Noise Prediction Based on Recent Theoretical Results," *Journal of Sound and Vibration*, Vol. 229(4), 2000, pp. 897–911.

[175] Ffowcs Williams, J. E., "Sound Radiated from Turbulent Boundary Layers Formed on Compliant Surfaces," *Journal of Fluid Mechanics*, Vol. 22, No. 2, 1965, pp. 347–358.

[176] Ffowcs Williams, J. E. and Hall, L. H., "Aerodynamic Sound Generation by Turbulent Flow in the Vicinity of a Scattering Half-Plane," *Journal of Fluid Mechanics*, Vol. 40, 1970, pp. 657–670.

[177] Crighton, D. G. and Leppington, F. G., "On the Scattering of Aerodynamic Noise," *Journal of Fluid Mechanics*, Vol. 46, 1971, pp. 577–597.

[178] Chase, D. M., "Turbulent-Boundary-Layer Pressure Fluctuations and Wavenumber Filtering by Non-Uniform Spatial Averaging," *Journal of the Acoustical Society of America*, Vol. 46, 1969, pp. 1350–1365.

[179] Jones, D. S., "Aerodynamic Sound Due to a Source Near a Half-Plane," *Journal of the Institute of Mathematics and its Applications*, Vol. 9, 1972, pp. 114–122.

[180] Candel, S. M., "Diffraction of a Plane Wave by a Half Plane in a Subsonic and Supersonic Medium," *Journal of the Acoustical Society of America*, Vol. 54, 1973, pp. 1008–1016.

[181] Rienstra, S. W., "Sound Diffraction at a Trailing Edge," *Journal of Fluid Mechanics*, Vol. 108, 1981, pp. 443–460.

[182] Heavens, S. N., "An Experimental Study of Sound Diffraction at an Airfoil Trailing Edge," *Journal of Fluid Mechanics*, Vol. 84, 1978, pp. 331–335.

[183] Macdonald, H. M., "A class of Diffraction Problem," *Proc. Lon. Math. Soc*, Vol. 14, 1915, pp. 410–427.

[184] Jones, D. S., *The Theory of Electromagnetism*, Pergamon, 1964.

[185] Morfey, C. L., "Sound Transmission and Generation in Ducts with Flow," *Journal of Sound and Vibration*, Vol. 14, 1971, pp. 37–55.

[186] Archibald, F. S., "Unsteady Kutta Condition at High Values of the Reduced Frequency Parameter," *Journal of Aircraft*, Vol. 12, 1975, pp. 545–550.

[187] Satyanarayana, B. and Davis, S., "Experimental Studies of Unsteady Trailing-Edge Condition," *American Institute of Aeronautics and Astronautics Journal*, Vol. 16, 1978, pp. 125–129.

[188] Crighton, D. G., "Radiation Properties of a Semi-Infinite Vortex Sheet," *Proceedings of the Royal Society of London*, Vol. A330, 1972, pp. 185–193.

[189] Orszag, S. A. and Crow, S. C., "Instability of a Vortex Sheet leaving a Semi-Infinite Plate," *Studies in Applied Mathematics*, Vol. 49, 1970, pp. 167–181.

[190] Crighton, D. G. and Leppington, F. G., "Radiation Properties of the Semi-Infinite Vortex Sheet: the Initial Value Problem," *Journal of Fluid Mechanics*, Vol. 64, 1974, pp. 393–414.

[191] Davis, S. S., "Theory of Discrete Vortex Noise," *American Institute of Aeronautics and Astronautics Journal*, Vol. 13, 1975, pp. 375–380.

[192] Obermeier, F., "Berechnung aerodynamisch erzeugter shallfelder mittels der Methode der "Matched Asymptotic Expansion"," *Acustica*, Vol. 18, 1967, pp. 238–240.

[193] Amiet, R. K., "Noise Due to Turbulent Flow past a Trailing Edge," *Journal of Sound and Vibration*, Vol. 47, 1976, pp. 387-393.

[194] Singer, B. A., Brentner, K. S., and Lockard, D. P., "Simulation of Acoustic Scattering from a Trailing Edge," *37th Aerospace Sciences Meeting & Exhibit, January 11-14, 199, Reno, NV*, 1999.

[195] Manoha, E., Troff, B., and Sagaut, P., "Trailing-Edge Noise Prediction Using Large-Eddy Simulation," *American Institute of Aeronautics and Astronautics Journal*, Vol. 38, No. 4, 2000, pp. 575–583.

[196] Schwartzchild, K., "Die Beugung und Polarisation des Lichts durch einen Spalt-I," *Mathematische Annalen*, Vol. 55, 1902, pp. 177–247.

[197] Tam, C. K. W., "Discrete Tones of Isolated Airfoils," *Journal of the Acoustical Society of America*, Vol. 55, No. 6, 1974, pp. 1173–1177.

[198] Goldstein, M. E., "The Coupling between Flow Instabilities and Incident Disturbances at a Leading-Edge," *Journal of Fluid Mechanics*, Vol. 104, 1981, pp. 217–246.

[199] Rockwell, D., "Oscillations of Impinging Shear-Layers," *American Institute of Aeronautics and Astronautics Journal*, Vol. 21, No. 5, 1983, pp. 645–664.

[200] R.Bodstein, G. C., George, A. R., and Hui, C. Y., "The Three-Dimensional Interaction of a Streamwise Vortex with a Large-Chord Lifting Surface: Theory and Experiment," *Journal of Fluid Mechanics*, Vol. 322, 1996, pp. 51–79.

[201] Doligalski, T. L. and Valker, J. D. A., "The boundary Layer Induced by a Convected Rectilinear Vortex," *Journal of Fluid Mechanics*, Vol. 139, 1984, pp. 1–30.

[202] Rogler, H., "The Interaction Between Vortex-Array Representations of Free-Stream Turbulence and Semi-Infinite Flat Plates," *Journal of Fluid Mechanics*, Vol. 87, No. 3, 1978, pp. 583–606.

[203] Ziada, S. and Rockwell, D., "Vortex-Leading-Edge Interaction," *Journal of Fluid Mechanics*, Vol. 118, 1982, pp. 79–107.

[204] Najm, H. N. and Ghoniem, A. F., "Numerical Simulation of the Convective Instability in a Dump Combustor," *American Institute of Aeronautics and Astronautics Journal*, Vol. 29, No. 6, 1991, pp. 911–919.

[205] Pereira, J. C. F. and Sousa, J. M. M., "Experimental and Numerical Investigation of Flow Oscillations in a Rectangular Cavity," *ASME Journal of Fluids Engineering*, Vol. 117, 1995, pp. 68–74.

[206] Widnall, S., "Helicopter Noise do to Blade-Vortex Interaction," *Journal of Acoustic Society of America*, Vol. 51, No. 1, 1971, pp. 354–365.

[207] Amiet, R. K., "Acoustic Radiation from an Airfoil in a Turbulent Stream," *Journal of Sound and Vibration*, Vol. 41, No. 4, 1975, pp. 407–420.

[208] Martinez, R. and Widnall, S., "Unified Aerodynamic-Acoustic Theory for a Thin Rectangular Wing Encountering a Gust," *American Institute of Aeronautics and Astronautics Journal*, Vol. 18, No. 6, 1980, pp. 636–645.

[209] Martinez, R. and Widnall, S., "An Aeroacoustic Model for High-Speed, Unsteady Blade-Vortex Interaction," *American Institute of Aeronautics and Astronautics Journal*, Vol. 21, No. 9, 1983, pp. 1225–1231.

[210] Reissner, E., "On the Application of Mathieu Functions in the Theory of Subsonic Compressible Flow past Oscillating Airfoils," *NACA Tech. Note 2363*, 1951.

[211] Casalino, D., Chiocchia, G., and Roger, M., "Interaction Noise from an Airfoil in a Kármán Vortex Street," *American Institute of Aeronautics and Astronautics Paper 2001-2213*, 2001.

[212] Lee, D. J. and Smith, C. A., "Effect of Vortex Core Distortion on Blade-Vortex Interaction," *American Institute of Aeronautics and Astronautics Journal*, Vol. 29, No. 9, 1991, pp. 375–380.

[213] Park, J. H. and Lee, D. J., "Numerical Simulation of Vortex-Wedge Interaction," *American Institute of Aeronautics and Astronautics Journal*, Vol. 32, No. 6, 1994, pp. 1126–1134.

[214] Scott, J. R. and Atassi, H. M., "Numerical Solution of Periodic Vortical Flows About a Thin Airfoil," *American Institute of Aeronautics and Astronautics Paper 89-1691*, 1989.

[215] Atassi, H. M. and Scott, J. R., "Acoustic Radiation from Lifting Airfoils in Compressible Subsonic Flow," *American Institute of Aeronautics and Astronautics Paper 90-3911*, 1990.

[216] Goldstein, M. E., *Aeroacoustics*, McGraw-Hill, New York, 1976.

[217] Patrick, S. M., Atassi, H. M., and Blake, W. K., "Inverse Problems in Aerodynamics and Aeroacoustics," *Active Control of Vibration and Noise, ASME DE*, Vol. 75, 1994, pp. 309–319.

[218] Colton, D. and Kress, R., *Inverse Acoustic and Electromagnetic Scattering Theory*, Springer - Verlag, 1992.

[219] Tikhonov, A. N., "Solutions of Incorrectly Formulated Problems and the Regularization Method," *Soviet Mathematics*, Vol. 4, 1963, pp. 1035–1038.

[220] Wake, B. and Baeder, J., "Evaluation of a Navier-Stokes Analysis Method for Hover Performance Prediction," *Journal of the American Helicopter Society*, Vol. 41, No. 1, 1996, pp. 1–17.

[221] Ahamad, J. and Strawn, R., "Hovering Rotor and Wake Calculations with an Overset-Grid Navier-Stokes Solver," *55th Annual Forum of the American Helicopter Society, Montreal, Canada*, May 1999.

[222] Wang, C., Bridgeman, J., Steinhoff, J., and Wenren, Y., "The Application of Computational Vorticity Confinement to Helicopter Rotor and Body Flows," *49th Annual Forum of the American Helicopter Society*, 1993.

Abstract

This work deals with the aeroacoustic problem of sound generated by unsteady flows past rigid surfaces. It is the outcome of a PhD research shared among the *Dipartimento di Ingegneria Aeronautica e Spaziale* at *Politecnico di Torino*, and the *Laboratoire de Mécanique des Fluides et d'Acoustique* at *Ecole Centrale de Lyon*.

The model problem of an airfoil embedded in the fluctuating wake of a rod is investigated in the first part. Such a flow configuration is an effective benchmark for developing and validating numerical methodologies of aeroacoustic prediction. Furthermore, the rod-airfoil configuration is of great academic concern, for it allows to investigate some underlying mechanisms involved in the generation of vortex-airfoil interaction noise. The numerical and theoretical relevance of the rod-airfoil configuration reflects the structure of the first part.

An analytical model based on the circulation theory is initially developed. This is used to investigate the influence of the airfoil geometry and the vortex size on the far pressure field, for a given distribution of vortices convected past an airfoil. Particular emphasis is given to the nonlinear effects related to the airfoil thickness and camber, the interaction of the airfoil wake with the incident vortices, and the vortex distortion near the airfoil leading edge. The limits of applicability of the frozen convection hypothesis and other linear approximations are discussed in great detail.

Wall pressure and acoustic measurements are carried out with a twofold aim in mind: (i) to obtain data for comparisons with numerical results, (ii) to investigate the three-dimensional character of a *nominal* two-dimensional flow.

Numerical results are obtained by means of a hybrid RANS/Ffowcs-Williams & Hawkings approach. The RANS solver is a finite volume code developed at LMFA, and the FW-H solver is the rotor-noise code *Advantia*. The latter has been developed in the context of the present study and is based on the so-called *advanced time approach*, firstly proposed by the author.

The intrinsic three-dimensional behaviour of the flow past a bluff body is described for the first time by means of a *spanwise statistical model*. This allows to perform acoustic analogy predictions by using a two-dimensional aerodynamic field, but accounting, to some extent, for the three-dimensional character of the flow.

The hybrid RANS/FW-H approach and the spanwise statistical model are applied to the rod-airfoil system. It is shown that, despite the tonal character of the RANS solution, the spectral broadening around the tonal frequency, as observed in the experiments, is partially recovered.

The second part of the work illustrates theories and models in fluid-body aeroacoustics. It is only concerned with sound generation in the absence of acoustic feed-back. Therefore, only external flows are considered, the propagation problem in complex geometries is not addressed, and the aeroacoustic feed-back in resonant configurations is not examined. Three unsteady flow configurations are considered:

- vortical flows past motionless surfaces,
- surfaces moving in a fluid at rest,
- vortical flows interacting with moving surfaces.

The first case is of main concern in the flow noise theory. A turbulent boundary layer upon a fuselage panel induces noise and vibrations. Small-wavenumber turbulent fluctuations past an airfoil trailing edge are a source of high-frequency broad band noise. This kind of problems dealing with acoustically non-compact surfaces are investigated by means of infinite or semi-infinite plates.

The second case is of main concern in the rotor noise theory. Helicopter rotors operating in quite uniform flows generate noise because of the unsteady loading exerted on the surrounding fluid. Furthermore, the blade motion may induce the formation of vortical flows (wakes and turbulent boundary layers), and shocks in transonic conditions. Both turbulence and shocks are important sources of aerodynamic noise.

The third case is of main concern in the rotor-stator noise theory. Rotor blades in turbomachines interact with incoming flow disturbances. This happens when atmospheric turbulence is ingested by a fan, or when a stator wake is chopped by a downstream rotor.

Unsteady aerodynamic theories are presented in the second part as an [illegible]ctable theoretical basis for developing aeroacoustic models. Nevertheless, the author's feeling in writing this part [illegible] *sound is an aerodynamic by-product, but aeroacoustics are not a by-product of aerodynamics.*